Geophysical Monograph Series

Including
IUGG Volumes
Maurice Ewing Volumes
Mineral Physics Volumes

Geophysical Monograph Series

135 **Prediction in Geomorphology** *Peter R. Wilcock and Richard M. Iverson (Eds.)*

136 **The Central Atlantic Magmatic Province: Insights from Fragments of Pangea** *W. Hames, J. G. McHone, P. Renne, and C. Ruppel (Eds.)*

137 **Earth's Climate and Orbital Eccentricity: The Marine Isotope Stage 11 Question** *André W. Droxler, Richard Z. Poore, and Lloyd H. Burckle (Eds.)*

138 **Inside the Subduction Factory** *John Eiler (Ed.)*

139 **Volcanism and the Earth's Atmosphere** *Alan Robock and Clive Oppenheimer (Eds.)*

140 **Explosive Subaqueous Volcanism** *James D. L. White, John L. Smellie, and David A. Clague (Eds.)*

141 **Solar Variability and Its Effects on Climate** *Judit M. Pap and Peter Fox (Eds.)*

142 **Disturbances in Geospace: The Storm-Substorm Relationship** *A. Surjalal Sharma, Yohsuke Kamide, and Gurbax S. Lakhima (Eds.)*

143 **Mt. Etna: Volcano Laboratory** *Alessandro Bonaccorso, Sonia Calvari, Mauro Coltelli, Ciro Del Negro, and Susanna Falsaperla (Eds.)*

144 **The Subseafloor Biosphere at Mid-Ocean Ridges** *William S. D. Wilcock, Edward F. DeLong, Deborah S. Kelley, John A. Baross, and S. Craig Cary (Eds.)*

145 **Timescales of the Paleomagnetic Field** *James E. T. Channell, Dennis V. Kent, William Lowrie, and Joseph G. Meert (Eds.)*

146 **The Extreme Proterozoic: Geology, Geochemistry, and Climate** *Gregory S. Jenkins, Mark A. S. McMenamin, Christopher P. McKay, and Linda Sohl (Eds.)*

147 **Earth's Climate: The Ocean–Atmosphere Interaction** *Chunzai Wang, Shang-Ping Xie, and James A. Carton (Eds.)*

148 **Mid-Ocean Ridges: Hydrothermal Interactions Between the Lithosphere and Oceans** *Christopher R. German, Jian Lin, and Lindsay M. Parson (Eds.)*

149 **Continent-Ocean Interactions Within East Asian Marginal Seas** *Peter Clift, Wolfgang Kuhnt, Pinxian Wang, and Dennis Hayes (Eds.)*

150 **The State of the Planet: Frontiers and Challenges in Geophysics** *Robert Stephen John Sparks and Christopher John Hawkesworth (Eds.)*

151 **The Cenozoic Southern Ocean: Tectonics, Sedimentation, and Climate Change Between Australia and Antarctica** *Neville Exon, James P. Kennett, and Mitchell Malone (Eds.)*

152 **Sea Salt Aerosol Production: Mechanisms, Methods, Measurements, and Models** *Ernie R. Lewis and Stephen E. Schwartz*

153 **Ecosystems and Land Use Change** *Ruth S. DeFries, Gregory P. Anser, and Richard A. Houghton (Eds.)*

154 **The Rocky Mountain Region—An Evolving Lithosphere: Tectonics, Geochemistry, and Geophysics** *Karl E. Karlstrom and G. Randy Keller (Eds.)*

155 **The Inner Magnetosphere: Physics and Modeling** *Tuija I. Pulkkinen, Nikolai A. Tsyganenko, and Reiner H. W. Friedel (Eds.)*

156 **Particle Acceleration in Astrophysical Plasmas: Geospace and Beyond** *Dennis Gallagher, James Horwitz, Joseph Perez, Robert Preece, and John Quenby (Eds.)*

157 **Seismic Earth: Array Analysis of Broadband Seismograms** *Alan Levander and Guust Nolet (Eds.)*

158 **The Nordic Seas: An Integrated Perspective** *Helge Drange, Trond Dokken, Tore Furevik, Rüdiger Gerdes, and Wolfgang Berger (Eds.)*

159 **Inner Magnetosphere Interactions: New Perspectives From Imaging** *James Burch, Michael Schulz, and Harlan Spence (Eds.)*

160 **Earth's Deep Mantle: Structure, Composition, and Evolution** *Robert D. van der Hilst, Jay D. Bass, Jan Matas, and Jeannot Trampert (Eds.)*

161 **Circulation in the Gulf of Mexico: Observations and Models** *Wilton Sturges and Alexis Lugo-Fernandez (Eds.)*

162 **Dynamics of Fluids and Transport Through Fractured Rock** *Boris Faybishenko, Paul A. Witherspoon, and John Gale (Eds.)*

163 **Remote Sensing of Northern Hydrology: Measuring Environmental Change** *Claude R. Duguay and Alain Pietroniro (Eds.)*

164 **Archean Geodynamics and Environments** *Keith Benn, Jean-Claude Mareschal, and Kent C. Condie (Eds.)*

165 **Solar Eruptions and Energetic Particles** *Natchimuthukonar Gopalswamy, Richard Mewaldt, and Jarmo Torsti (Eds.)*

166 **Back-Arc Spreading Systems: Geological, Biological, Chemical, and Physical Interactions** *David M. Christie, Charles Fisher, Sang-Mook Lee, and Sharon Givens (Eds.)*

167 **Recurrent Magnetic Storms: Corotating Solar Wind Streams** *Bruce Tsurutani, Robert McPherron, Walter Gonzalez, Gang Lu, José H. A. Sobral, and Natchimuthukonar Gopalswamy (Eds.)*

168 **Earth's Deep Water Cycle** *Steven D. Jacobsen and Suzan van der Lee (Eds.)*

169 **Magnetic ULF Waves: Synthesis and New Directions** *Kazue Takahashi, Peter J. Chi, Richard E. Denton, and Robert L. Lysak (Eds.)*

170 **Earthquakes: Radiated Energy and the Physics of Faulting** *Rachel Abercrombie, Art McGarr, Hiroo Kanamori, and Giulio Di Toro (Eds.)*

171 **Subsurface Hydrology: Data Integration for Properties and Processes** *David W. Hyndman, Frederick D. Day-Lewis, and Kamini Singha (Eds.)*

Geophysical Monograph 172

Volcanism and Subduction: The Kamchatka Region

John Eichelberger
Evgenii Gordeev
Pavel Izbekov
Minoru Kasahara
Jonathan Lees
Editors

American Geophysical Union
Washington, DC

Published under the aegis of the AGU Books Board

Library of Congress Cataloging-in-Publication Data

Volcanism and subduction : the Kamchatka region / John Eichelberger ... [et al.], editors.
p. cm. -- (Geophysical monograph ; 172)
ISBN 978-0-87590-436-8
1. Volcanism--Russia (Federation)--Kamchatskaia oblast'. 2. Subduction zones--Russia (Federation)--Kamchatskaia oblast'. I. Eichelberger, J. C. (John Charles)

QE527.2.R8V65 2007
551.210957'7--dc22

2007041340

ISBN 978-0-87590-436-8
ISSN 0065-8448

Printed in the United States of America.

CONTENTS

B. Topical Studies

Section III: Volcanism

A. Overview

B. Topical Studies

PREFACE

Long before introduction of the subduction paradigm, it was recognized that there was a “Pacific Ring of Fire” characterized by explosive eruptions, devastating earthquakes, and far-reaching tsunamis. This belt of closely coupled tectonism and volcanism girdles a hemispheric ocean. We chose a segment of this ring as the subject of this volume, a choice that deserves some explanation. An astronaut arriving here, had Earth’s oceans gone the way of Mars’ oceans, would certainly be drawn to this deep kinked furrow in the planet’s skin, but there are more reasons than topography.

One reason is the high level of activity. Five of Earth’s ten largest earthquakes of the 20th century occurred in this segment, and over a span of only 12 years. Volcanism is likewise robust. Exceptional volcanic events include the great Katmai/Novarupta eruption of 1912, by far the largest on Earth in the last hundred years; the Bezymianny and Shiveluch collapse/Plinian events of 1956 and 1964, respectively; and the Great Tolbachik Fissure Eruption of 1975 with a vent span of 30 km. At this writing, 5 volcanoes of the Kurile-Kamchatka system and 3 of Aleutian-Alaska are in continuous to frequent intermittent low-level eruption. Tsunamis of the past century have obliterated whole villages, Severo-Kurilsk in 1952 and Valdez, Alaska in 1964. Here is a place where Earth’s interior dynamics are illuminated dramatically and sometimes tragically by earthquakes, deformation, and melting.

Obviously the activity does not end at the geographic limits of this volume. Vigorous subduction continues uninterrupted south of the Kuriles into Japan. At the other end, volcanism but not seismicity diminishes in southeastern Alaska where the plate boundary becomes the Queen Charlotte transform fault of western Canada. The chosen segment does, however, coincide with relative lack of visibility within the global geoscience community. This is somewhat ironic, because the Aleutian arc is a place where important aspects of the subduction paradigm were first introduced.

One impediment to science in this region is the harsh environment. The weather is often cold and stormy, and supply points are few and far. In most cases, a helicopter or ship or both are required. The high cost of transportation and support are exacerbated by the need for budgeting weather days. Scientists stuck in bad weather and unaccustomed to this fact of northern life have been known to contact their embassies for help in improving flying conditions. Field seasons are generally limited to mid June to mid September, and maintaining operation of geophysical instruments through the long winter is difficult. A team or expedition approach to field work is often needed, though happily this has benefits in encouraging cross-discipline collaboration and cross-culture understanding.

The new driving force toward scientific understanding of this part of the world is the concern shared by all governments about natural hazards. Significant local populations are at risk to earthquakes and eruptions, and the entire northern Pacific basin is at risk to tsunamis generated here. For volcanology, the risk for jet aircraft encountering ash clouds from explosive eruptions has motivated rapid growth of volcano observatories in Alaska, Kamchatka, and in Sakhalin for the Kuriles. Some 25,000 passengers and equally impressive amounts of cargo are carried by roughly 200 large aircraft per day along the Kurile-Kamchatka-Aleutian volcanic line en route between eastern Asia and North America. Approximately one hundred volcanoes in this subduction segment are capable of erupting ash clouds to flight levels.

Before the growth in volcano monitoring, for which a triggering event was the near-disastrous encounter of a wide-body passenger jet with an ash cloud from Redoubt volcano over southcentral Alaska in 1989, only the Soviet Union maintained volcano observatories in the region. Alaska Volcano Observatory (AVO) now employs dense seismic networks on 30 volcanoes, as well as continuously recording, telemetered GPS networks on four of them. The Kamchatka Volcanic Eruption Response Team (KVERT) monitors 10 Kamchatka and northern Kurile volcanoes seismically in real time. Both in Kamchatka and Alaska, a great deal of work has gone into developing stand-alone telemetered geophysical stations that can withstand the rigors of the environment for long periods without expensive helicopter visits.

An important parallel development was the use of satellite-based remote sensing observations to detect and warn of volcano unrest and eruption. Nowhere in the world is satellite data used so intensively for volcano hazard mitigation as at the observatories of Alaska, Kamchatka, and Sakhalin. Rapidly advancing technology has changed not just the resolution of satellite systems but also the kinds of data that can be acquired, including volcano deformation, eruption cloud composition, and estimation of effusion rate. Although seismic data from dense proximal networks remains the preferred means of detecting activity precursory to eruptions, satellite remote sensing makes possible monitoring of volcanoes for which ground installations are prohibitively expensive and provides essential confirmation of explosive ash production where ground stations are present.

Another societal imperative motivating geoscience investigations of active processes is the need for economical, clean,

Volcanism and Subduction: The Kamchatka Region
Geophysical Monograph Series 172

10.1029/172GM01

reliable energy for isolated communities. Important use of geothermal energy has been a reality in Kamchatka and the Kurile Islands for some time, and is under serious consideration in Alaska. With concern about oil spills in rich fisheries and rising oil prices, geothermal will likely grow so that northern coastal communities can remain viable.

In order to view the geophysics of this region as a whole and to encourage development of international and interdisciplinary investigations, workers from Hokkaido, Kamchatka and Alaska formed the Japan-Kamchatka-Alaska Subduction Processes Consortium (JKASP). Five biennial meetings, each attracting 100 to 200 scientists and students, have taken place to date: 1998 in Petropavlovsk-Kamchatsky, 2000 in Sapporo, 2002 in Fairbanks, 2004 in Petropavlovsk-Kamchatsky, and 2006 in Sapporo. The present volume is an outgrowth of the birth of this geoscience community.

The contents of the volume span a broad range of disciplines within the general theme of subduction processes. Students will rapidly appreciate that this classic subduction zone lacks the classic simplicity of textbook cartoons, wonder at the relationship of present-day topography to tectonic history, and find that the crowning volcano at Earth's sharpest subduction corner is not andesite but basalt. For scientists of more southern experience, we hope that the book will serve as a stimulating and useful introduction to the research and the researchers of the far north Pacific. For those who have worked here, we hope that the papers herein will point the way to new connections, collaborations, and directions. Most of all, we hope that through these and other efforts the window of opportunity for collaboration that has opened among Japan, Russia, and the US will remain open; that the Kurile-Kamchatka-Aleutian-Alaska subduction system will be a shared natural geodynamic laboratory of our countries, and indeed of the world.

The editors thank the US National Science Foundation, the Russian Academy of Sciences, and the US Geological Survey for support that has made this volume possible.

John Eichelberger
Evgenii Gordeev
Pavel Izbekov
Minoru Kasahara
Jonathan Lees

Introduction: Subduction's Sharpest Arrow

John C. Eichelberger[1]

Alaska Volcano Observatory, Geophysical Institute, University of Alaska Fairbanks, Fairbanks, Alaska, USA

In the center of the 6000-km reach of Kurile-Kamchatka-Aleutian-Alaska subduction is arguably Earth's most remarkable subduction cusp. The Kamchatka-Aleutian junction is a sharp arrowhead mounted on the shaft of the Emperor Seamount Chain. This collection of papers provides context, definition, and suggestions for the origin of the junction, but a comprehensive understanding remains elusive, in part because of the newness of international collaborations. Necessary cross-border syntheses have been impeded by the adversarial international relations that characterized the 20th century. For much of this period, Kamchatka and the Kurile Islands were part of the Soviet Union, a mostly closed country. The entire region was swept by World War II, abundant remnants of which are wrecked ships and planes, unexploded ordnance, and Rommel stakes.

Of the three countries with a direct interest in this region, Russia has the longest presence. Russia established settlements in Kamchatka beginning in the early 18th century, then colonized the Aleutians, Kodiak, and southeast Alaska following A. Chirikov's and V. Bering's discovery voyage from Petropavlovsk-Kamchatsky in 1741. Hokkaido was the last territory area added permanently to Japan, during the latter half of the 19th century. Similarly, the United States purchased the Aleutians and Alaska from Russia in 1867 in the interest of territorial expansion, whaling, and harvesting of fur.

The strategic importance of the region to the US and Russia increased dramatically with World War II, when Japan began launching military operations from the northern Kuriles and occupied the American Near Islands (so named because they are close to Kamchatka) of the Aleutians. At the same time, Alaska and Kamchatka airfields were needed to ferry materiel in support of the Soviet Union's war effort against Nazi Germany. An immediate American response to these events was to build a road through Canada to Fairbanks, providing what is still Alaska's only land link to the rest of the United States. In contrast to Alaska, Kamchatka is geographically continuous with Russia but still lacks a land transportation connection. During the war, American soldiers wrote of the Aleutian Islands as a sort of cold, damp hell, while American school teachers more often described them as a flower garden with an advanced native culture. In any case, they were a remote and exotic place to those Americans who even knew they existed. This is still the largely true, and few Americans are aware of the hardships the Aleuts endured during the war, nor of the rich legacy of Russian culture that persists in Alaska among Native people.

Hardly better for science than World War II was the Cold War. The situation changed from the US and Soviet Union allied against Japan to the US and Japan allied against the Soviet Union. Kamchatka and Alaska became armed camps, with the US testing its largest nuclear weapons on Kamchatka's doorstep in the western Aleutians and with Kamchatka off-limits even to most Russians. The Soviet Union did, however, maintain a robust geoscience effort in Kamchatka. Likewise, the United States, in part in support of defense activities, conducted extensive geological and geophysical work in the Aleutians.

The end of the Cold War brought an end to most travel prohibitions. A lingering border dispute over the southern Kuriles is now being addressed in a positive way by Russia and Japan in terms of access for hazard monitoring and science. But easing of tensions did not make travel easy, only possible. Issues of expense, language, culture, and cumbersome visa procedures remain. Air routes are inconvenient and expensive.

For Russians, the Kurile-Kamchatka-Aleutian-Alaska region is a fabled part of their history, and Kamchatka is the one place in their vast country where spectacular volcanism and the greatest earthquakes can be studied firsthand. It is perhaps not surprising, then, that only recently did the state of knowledge of Aleutian/Alaska volcanoes reach the level of knowledge about Kamchatka volcanoes. The record of eruption from historical

[1]Currently at Volcano Hazards Program, USGS, Reston, VA.

Volcanism and Subduction: The Kamchatka Region
Geophysical Monograph Series 172

10.1029/172GM02

documents and careful tephrochronology in Kamchatka, some of which is presented here in the overview paper on volcanism by V. Ponomereva and coauthors, still surpasses that of Aleutia/Alaska. The Kurile Islands, posing transportation and telemetry difficulties in their central portion and lingering international tension in the south, remain the least known.

The positioning of the Emperor seamount chain as the shaft at the Kamchatka-Aleutian arrowhead may or may not be a coincidence, but what seems not a coincidence is the prodigious rate of magma production inboard of this junction, represented by the largely mafic Kliuchevskaya group and its more silicic northern neighbor, Shiveluch. In this volume, M. Portyangin and coauthors suggest an answer in large-scale slab melting, as the Pacific slab, torn open under the western Aleutians, dives into hot mantle under Kamchatka. In tectonic overview papers, G. Avdieko and coauthors and D. Scholl wrestle with the meaning of the cusp from vantage points from the west and east of it, respectively. A. Lander and M. Shapiro focus on constraining the onset of the modern volcanic and subduction regime of Kamchatka with seismic data. Intriguing related problems are the welding of arc fragments to Kamchatka as the eastern capes, the origin and behavior of neighboring microplates, and the apparent double arcs of Kamchatka, one young and robust and the other old and dying.

On either side of the arrow's point are two almost matching arc pairs: continental Kamchatka Peninsula with oceanic Kurile Islands, and continental Alaska Peninsula with oceanic Aleutian Islands. We use the term "arc" for the volcanic expression of subduction in deference to history and to economy of letters, but the volcanoes more properly comprise "supra-subduction zone volcanism". Much of the segment of interest is not an island arc because, except for the Aleutians, the arrangement is not arcuate and, except for the Aleutians and Kuriles, the volcanoes are not islands. The arcuate shape seems irrelevant and to call continent-sited volcanoes "islands" is even worse. Continental margin subduction faithfully follows the shape of the unsubductable continental margin, as is clear along Kamchatka and Alaska. Kurile subduction is a straight line pinned to continental margins at both ends, Hokkaido and Kamchatka. D. Scholl suggests that the Aleutians, a true arc and perhaps an inspiration for the term, "budded" off continental margin subduction of the Alaska Peninsula and progressed westward, turning to the right as it went until it was parallel to Pacific Plate motion and became a transform fault. We should perhaps view the western end as "free", unconstrained by a continental margin because it is perpendicular to it, and hence able to migrate in either direction. Confusingly, arguments can be made for migration in either direction: southward because older "supra-subduction zone volcanism" extends north of the current junction and northward if the east coast capes of the Kamchatka Peninsula represent prior positions of the junction. Indeed, the current plate boundary, the "corner" representing the northern limit of the subducting Pacific plate, is not where the Aleutian arc/trench pair meets Kamchatka but north of this at a back-arc shear zone. Bering Island seems destined to become another cape on the east coast of Kamchatka.

Scholl argues that the Aleutians, and Avdeiko and coauthors and Lander and Shapiro argue that the eastern volcanic front of Kamchatka, record a large forward jump in volcanism due to jamming of subduction by arc fragments. For the Aleutians, this resulted in capture by North America of the Bering microplate. But now the western Aleutians are being fritted and torn from the North American/Bering plate. For Kamchatka, the postulated jump caused the death of Sredinny Range volcanoes and rise of the prolific and caldera-rich volcanism of the eastern Kamchatka Peninsula. It would seem then that the only steady state subduction regimes are the Kuriles and the Alaska Peninsula, though the latter has a relative dearth of older volcanic rocks on its Mesozoic basement, giving the impression of a very recent start to volcanic growth. These interpretations remain speculative. For example, Scholl observes that the age of Bering microplate crust is poorly known and Ponomareva and coauthors show that the Sredinny Range can be viewed as back-arc volcanism arising from the modern subduction configuration.

The volume is divided into three themes: tectonics, earthquakes, and volcanism. Each section begins with one or more overview papers that not only provide background and context, but also new ideas. They are followed by topical studies focusing on specific features or processes. Of course, the ultimate goal should be a holistic view that encompasses all these manifestations of subduction. It is clear that we are far from that. But although the discussions of tectonics are highly speculative, they pose hypotheses that are clearly testable with more data on age and origin of terranes and on current rates of deformation. Perhaps the greatest progress is evident in seismology, with an understanding of earthquake distribution in time and space based on slab age, convergence rate, stress distribution, and formation of asperities. The diversity of volcanic expression of subduction, in contrast to all other tectonic domains, seems most resistive to solution, though increasingly under attack by new sophisticated geochemical techniques and synthesis with geophysical results. An accompanying DVD provides a view of eruptions in Kamchatka and of the style of field work conducted there not previously available outside Russia.

If there is one place where tectonic, seismic, and volcanic interpretations seem to be converging, it is the arrow itself. The subduction of the torn Pacific plate corner, the seismically inferred rounding of its leading edge, and geochemical inference of a large slab component in resultant eruption products are internally consistent. It is towards such a synthesis of geological, geophysical, and geochemical techniques at the micro and macro scales that this volume strives.

Viewing the Tectonic Evolution of The Kamchatka-Aleutian (KAT) Connection With an Alaska Crustal Extrusion Perspective

David W. Scholl

Department of Geophysics, Standford University, Standford, California, USA, and College of Natural Science and Mathematics, University of Alaska, Fairbanks, Alaska, USA

The Kamchatka and Aleutian (KAT) arc-trench systems meet orthogonally at Cape Kamchatka Peninsula. The KAT connection is the intersection of the NE-striking Kamchatka subduction zone and the NW-striking, transform setting of the western, Komandorsky sector of the Aleutian Ridge. Deciphering the origin and evolution of the KAT connection is challenging because of the paucity of constraining information about the age and latitude of formation of major crustal blocks of the deep water Bering Sea Basin.

It is proposed that in the late early Eocene (~50 Ma) the combined tectonic machinery of subduction zone obstruction and continental margin extrusion created the tectonic and rock architecture of the Aleutian-Bering Sea region. Accretion of the Olyutorsky arc to the north Kamchatka-Koryak subduction zone forced the offshore formation of the Aleutian subduction zone (SZ), added a sector of Pacific crust—Aleutia—to the North America plate, and established the KAT connection. Subsequently, but also in the middle Eocene, extrusion of Alaska crust southwestward across the Beringian margin connecting Alaska and NE Russia buckled Aleutia and forced the offshore formation of the Shirshov and Bowers SZs. Extrusion was driven by northward oblique underthrusting beneath British Columbia and SE Alaska.

In the early Tertiary the Aleutian and Kamchatka SZs, linked at the KAT connection, thus consumed northwest moving crust of the Pacific Basin and within the Bering Sea the Beringian, Shirshov, and Bowers SZs accommodated SW extruding Alaska and captured Aleutia crust. Since the early Miocene extrusion space has been provided by the Aleutian SZ. Arc-arc collisions at the KAT connection have been guided by the right-lateral Bering-Kresta shear zone, which lies at the Bering Sea base of the Komandorsky section and terminates at Cape Kamchatka Peninsula. In the past the tectonic connection with Kamchatka may have been farther to the north.

1. INTRODUCTION

The northwestern corner of the Pacific basin, as widely recognized, is an unusual right-angle confluence of two lengthy arc-trench systems, those of the Kamchatka and

Volcanism and Subduction: The Kamchatka Region
Geophysical Monograph Series 172

10.1029/172GM03

Aleutian subduction zones. Their tectonic contact is, for the convenience of this paper, dubbed the KAT connection (Fig. 1A). The KAT connection is widely believed to be an intermittent collision zone between the arc massifs of the two subduction zones. Collision began in the late Neogene or earlier in the Tertiary as terranes or blocks of arc crust of the far western or Komandorsky sector of the Aleutian Ridge entered the Kamchatka subduction zone (SZ) from the east. The eastward projecting promontory of the Cape Kamchatka Peninsula physiographically marks the collision zone (Fig. 1B; Watson and Fujita, 1985; Zinkevich et al., 1985; Zoneshain et al., 1990; Baranov et al., 1991; Geist and Scholl, 1994; Seliverstov, 1998; Gaedicke et al., 2000; Freitag et al., 2001; McLeish et al. 2002). In the past, the collision zone may have been farther to the north.

Collision at the KAT connection is the kinematic consequence of the circumstance that the Cape Kamchatka Peninsula is the intersection of the NE-striking Kamchatka SZ and the right-lateral transform plate boundary striking NW along the Komandorsky sector of the Aleutian Ridge (Fig 1B). The transform boundary along the far western Aleutian Ridge is a complex, distributed shear zone that embraces the width of the arc massif from trench floor to the backarc (Cormier, 1975; Geist and Scholl, 1994; Gaedicke et al., 2000, Freitag, 2001; Kozhurin, this volume).

So how did the KAT connection come to be? This paper explores an hypothesis that Pacific rim tectonism created, in the Aleutian-Bering Sea region, the geometry of the offshore subduction zones of the Aleutian-Shirshov-Bowers system that led to arc-arc collision at the KAT connection (Fig. 1A). The scenario outlined in this paper is based on the published ideas and data of many colleagues as cited. The tectonic sketch advance is speculative because constraining information is lacking to test assumptions that must be made about the ages and origins of key crustal blocks and terranes that construct the Aleutian-Bering Sea region. Compounding matters, the paucity of regional paleomagnetic data east of Kamchatka means that assumptions have also to be made about the paleogeographic origins of the crustal blocks of the Bering Sea Basin and the Cenozoic style(s) of north Pacific rim tectonism that brought the key pieces of the KAT junction together. A spotty but improving GPS data set for the Aleutian Ridge, however, apparently reveals the fundamental nature of westward block transport toward collision with Kamchatka (Oldow et al. 1999; Avé' Lallemant and Oldow, 2000); Gordeev et al., 2001; Steblov et al., 2003, Cross and Freymueller, 2007). Nonetheless, the troubling circumstances of insufficient regional information to constrain models apply equally to all evolutionary schemes that have been suggested for the origin of the Aleutian-Bering Sea region and thus the KAT connection.

Three tectonic models for the early Tertiary genesis of the Aleutian SZ have been posited. The most accepted of these is the clogging or occlusion model describing the tectonic jamming of the north Kamchatka-Koryak SZ then occupying the northwestern-most or Cape Navarin corner of the Pacific Basin (Fig 1A). Southwest of the corner, subduction was obstructed by docking or accretion of the northward migrating Olyutorsky arc complex (Fig. 2A; Zonenshain et al., 1990, Garver et al., 2000). Suturing of the exotic arc complex to the north Kamchatka-Koryak margin forced formation of a new offshore subduction zone—the Aleutian SZ. The driving force was continuing slab pulls beneath Alaska and Kamchatka, west and east, respectively, of the obstructed north Kamchatka-Koryak SZ.

The colliding arc complex is also referred to as the Achaivayam-Valagin or Olyutor-Valaginskii arc complex (see discussion in Park et al., 2002; Sukhov et al., 2004; Chekhovich et al., 2006, Chekhovich and Sukhov, 2006). This Late Cretaceous–early Tertiary arc complex is commonly viewed as having formed well south of it present location either proximal to the NW margin of the Pacific Basin or far offshore. The arc complex would thus be exotic to the Aleutian-Bering Sea Region. This arc complex is usually shown as including the Shirshov and Bowers Ridges of the Bering Sea Basin (Fig. 1A).

In various forms, models for the formation of the Aleutian-Bering Sea region as a consequence of terrane(s) accretion and subduction zone occlusion have been explored and thought through by many authors, for example Ben- Avraham and Cooper (1981), Cooper et al. (1987), Zonenshain et al. (1990), Stavsky et al. (1988; 1990), Seliverstov (1998), Worrall (1991), Scholl et al., (1992), Zinkevich and Tsukanov, (1992), Baranov et al. (1991), Park et al. (2002), Sukhov et al. (2004) and Garver et al. (2000, 2004).

A contrasting model ascribes the origin of the Aleutian-Bering Sea region to the plate-boundary-driven deformation of the north Pacific margin (Scholl et al., 1989). Formation in place of the offshore Aleutian-Shirshov-Bowers subduction zone systems is linked to the SW extrusion of the Beringian margin that trends southeastward from the Koryak margin at Cape Navarin, NE Russia, to the western tip of the Alaska Peninsula (Fig. 1A). Before the formation of the offshore subduction zone system, probably in the late early Eocene about 50 Ma (Jicha et al., 2006), the Beringian margin is inferred to have been the northernmost sector of the dominantly transform boundary separating the North America plate and that of either the Kula or Pacific plate (Moore, 1972; Scholl et al., 1975, 1986; Cooper et al., 1987a; Haeussler et al., 2003; Nokelberg et al., 2005). Figure 2 suggests that the Beringian margin was highly obliquely underthrust by Pacific Basin crust.

Figure 1A. Physiographic and bathymetric index maps of northeastern Russia, Alaska, and the north Pacific-Aleutian-Bering Sea region. Mercator-projection map derived from This Dynamic Planet (http://www.minerals.si.edu/tdpmap/index.htm). Major tectonic elements are identified on companion Figure 1B.

Seaward displacement and deformation of the Beringian margin is conjectured to have been effected by the extrusion of western Alaska toward the Bering Sea region. Tectonic push-out or extrusion of Beringian crust toward and along the Beringian margin is hypothesized to have buckled the oceanic crust then residing in the area of the modern Bering Sea Basin leading to establishment of the Shirshov, Bowers, and Aleutian SZs (Fig. 2B). The extrusion or escape model for the genesis of the Aleutian-Bering Sea region has been outlined by Scholl and Stevenson (1989,1991), Scholl et al. (1992, 1994), Scholl, (1999), and Lizarralde et al. (2002) and most completely by Redfield et al. (in press). Southwestward extrusion of western Alaska and Bering Sea crust is on-going today as the Bering block identified with regional seismic and geologic data assembled and interpreted by Mackey et al. (1997) and Fujita et al. (2002). Enhanced movement of the Bering block southward toward the Aleutian SZ and westward toward the Kamchatka-Koryak margin is presently driven by the late Neogene collision of the Yakutat block with the eastern end of the Alaska SZ (Fig. 1B; see also Mazzotti and Hyndman, 2002; Eberhart-Phillips et al. 2006).

A third model merges or couples the tectonic machinery of the first two scenarios as forcing the formation of the Aleutian-Bering Sea region and its three offshore SZs (see Fig. 10; Scholl et al., 1992; Cooper et al., 1992; Scholl 1994). The occlusion-extrusion or coupled model is explored in this paper as the working hypothesis principally because it is evident that the Late Cretaceous-early Tertiary Olyutorsky

Figure 1B. Major tectonic elements of the north Pacific rim and offshore Aleutian-Bering Sea region and north Pacific Basin. Active and inactive strike-slip faults (F) and shear zones (SZ), and major Beringian shelf basins (B).

arc complex was accreted to the Kamchatka margin of the western Bering Sea at the same time as, or just before, the arc volcanic construction of the Aleutian Ridge began to form in the middle Eocene (Levoshova et al., 1997, 2000; Zonenshain et al., 1990; Seliverstov, 1998; Garver et al., 2000; Garver et al., 2004, Jicha et al., 2006, Chekhovich and Sukhov, 2006). Paleomagnetic data also document that the Aleutian Ridge, which is not known to include pre-Tertiary rock, is not an exotic terrane but formed effectively in place (Harbert, 1987) as a western addition to the much older continental crust of the Alaska Peninsula (Burk, 1965). Similarly, the Aleutian SZ is viewed as a westward continuation of the Alaska SZ (Scholl et al., 1975; 1986; 1987). Farther west, the newly formed Aleutian SZ was presumably connected by a NW-trending, right-lateral shear zone or transform system to the older Kamchatka SZ (Lonsdale, 1988). In this way the KAT connection was first established that ultimately led to the collisions of blocks of the far western sectors of the Aleutian arc massif with the landward slope of the Kamchatka Trench (Fig. 2).

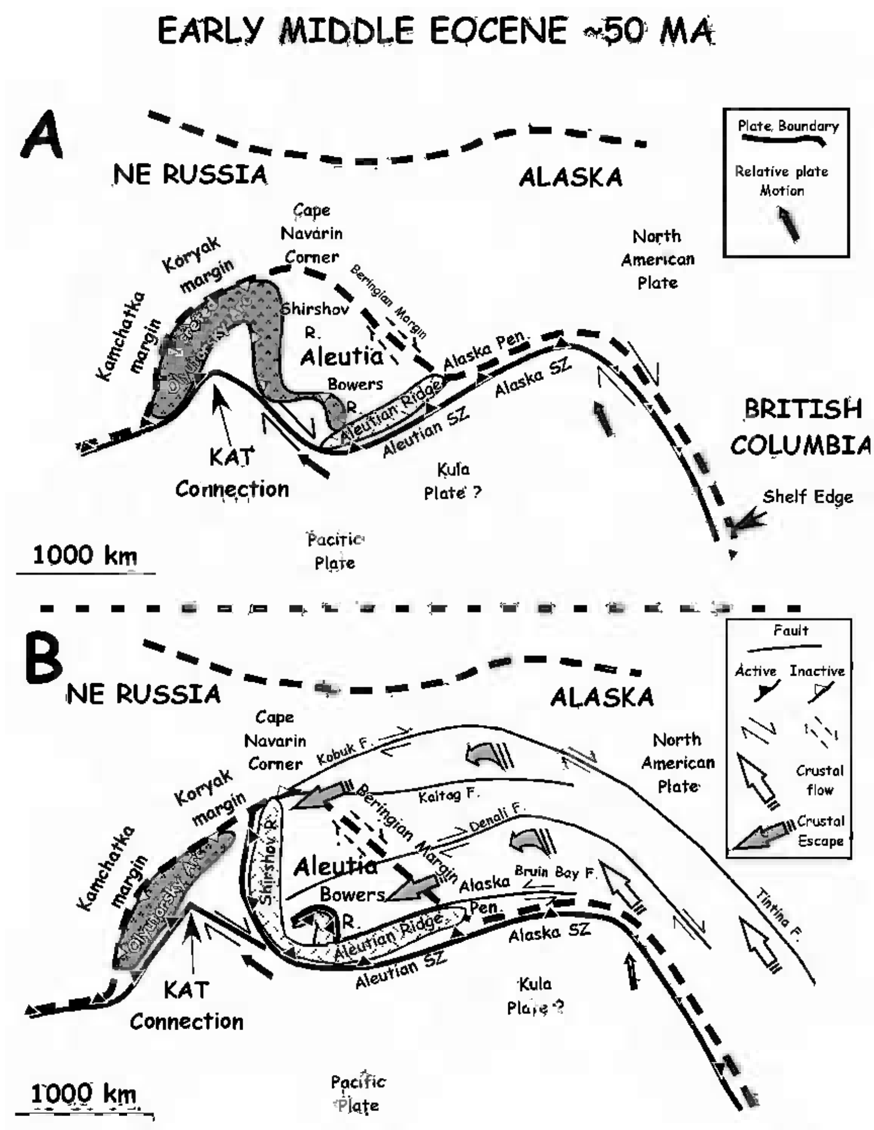

Figure 2. Two general models, (A) subduction zone (SZ) occlusion of the Kamchatka-Koryak margin, and (B) plate boundary extrusion of the Beringian margin, have been proposed for the origin of the offshore Aleutian SZ, accretion of a sector of Pacific lithosphere (Aleutia) to the North America plate, and consequent formation of the Aleutian-Bering Sea region. (A) Accretion of a Pacific-basin born, and thus exotic to the Bering Sea, Olyutorsky-Shirshov-Bowers arc complex to the Kamchatka-Koryak margin occludes (jams) the SZs of the Pacific's northwestern rim and forces offshore formation of the Aleutian SZ. (B) Plate-boundary driven lateral crustal streaming and extrusion of the Pacific's northeastern rim forces the in-place formation of the offshore Aleutian-Shirshov-Bowers SZ system.

This paper presents a model that merges both plate-boundary modifying forces to create the Aleutian Bering Sea region and the Kamchatka-Aleutian or KAT tectonic connection.

In the coupled model, the Bowers and Shirshov Ridges would have formed in-situ as a consequence of extrusion of western Alaska and Bering shelf crust toward the Beringian plate margin. Woven into the working hypothesis are the recent findings in the north Pacific concerning the age, origin, and tectonic implications of the prominent change in trend or bend in the Hawaiian-Emperor seamount chain (Figs. 1A and B; Tarduno et al., 2003, Pare´s and Moore, 2005; Sharp and Clague, 2006; Steinberger and Gaina, 2007). The beginning age of the sweeping bend, which required about 8 Myr to complete, is ~50 Ma (Sharp and Clague, 2006). This age matches the final docking time of the Late Cretaceous-early Tertiary massif of the Olyutorsky arc complex (Garver et al., 2000; Garver et al., 2004; Chekhovich and Sukhov, 2006) and the best estimate of the origin of the Aleutian SZ (Jicha et al., 2006).

The coupled model considers that the Bering block of Mackey et al. (1997) and Fujita et al., 2002) is the westernmost part of a laterally moving crustal track that extends northwestward from NW British Columbia in a broad counterclockwise curving arc through central Alaska to the KAT connection (Fig. 2). The northward and westward moving track of British Columbia, Alaska, and Bering crust is collectively referred to (see discussion below) as the North Pacific Rim orogenic stream or NPRS (Redfield et al. in press). The plate boundary forces and suprasubduction zone setting described by Mazzotti et al (in press) that have long mobilized a Pacific rim orogenic float (Oldow et al., 1990) are those involved in laterally moving the NPRS. The expanse of Bird's (1996) computer simulations of north Pacific rim tectonism is effectively that of the NPRS.

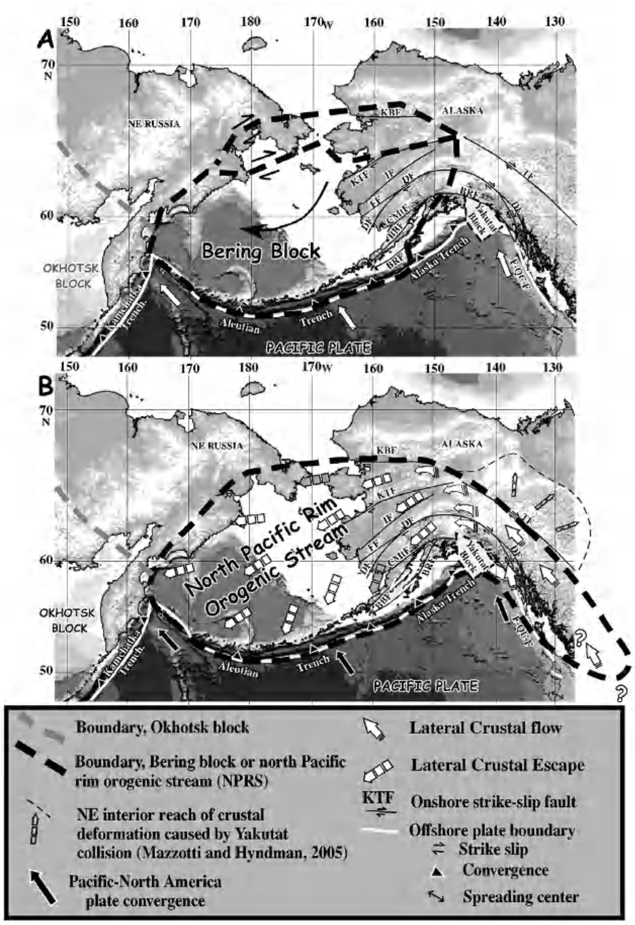

Figure 3. Upper diagram (A) sketches outline of the Bering Block of Mackey et al. (1997) and Fujita et al. (2002). Lower diagram (B) sketches outline of the CCW flowing north Pacific orogenic stream the leading front of which is the Bering Block (Redfield et al., in press). Abbreviations of strike-slip faults match full names shown on Figure 1B.

2. MAJOR CRUSTAL BLOCK

2.1 The Bering Block

2.1.1 Observations. Seismic and geological observations of Mackey et al. (1997) and Fujita et al. (2002) define the Bering block as the largest tectonostratigraphic element of the KAT connection. The Bering block includes much of western Alaska and the whole of the Aleutian Ridge including the KAT connection (Fig. 3). The Bering block rotates clockwise and deforms the Koryak and northern Kamchatka margins of the Bering Sea.

The Okhotsk microplate exists west of the Bering block and, as documented by Bourgeois et al. (2006) and Pedoja et al. (2006), the westward extrusion of the Okhotsk lithospheric slab (Riegel et al., 1993) toward the Kuril-Kamchatka SZ is importantly involved in the KAT collisional processes. Extrusion of the Okhotsk microplate forces Kamchatka to overrun the Komandorsky Basin that forms the western side of the deep water Bering Sea Basin (Figs. 1A and 3).

2.1.2 Interpretations. Kinematically, the Bering block can be viewed as the westward or leading edge of the NPRS as described by Redfield et al. (in press) and that embraces the regional tectonic concepts of the orogenic float of Oldow et al. (1990), Mazzotti and Hyndman (2002), and Mazzotti et al. (in press) (Fig. 3). The Bering block can be tectonically added, as the leading edge, to the laterally moving crust included within the great family of strike-slip faults that strike northwestward along the British Columbia margin and coastal region (e.g., Tintina, Denali, Fairweather, Queen Charlotte, etc fault systems) and curve through the so-called Alaska oroclinal bend to fan out southwestward toward the Bering Sea (e.g., the Kobuk, Kaltag, Iditarod-Nixon Fork, Denali, Farwell, Castle Mountain, Bruin Bay and Border Ranges, etc fault systems; Fig. 3B; Redfield et al., in press). This view is based on the observation that the major shear systems of the NPRS are or have been active in the late Cenozoic (Mackey et al. 1977; Page et al., 1991; Fujita et al., 2002); Haeussler et al., 2004). In western Alaska the southwestward expanding pattern of strike-slip faults implies the faults are slip lines bordering differentially extruding gores of Alaskan and Bering shelf crust. The pattern is similar to that of the differentially extruding and rotating crustal slices of SE Asia (Tapponnier et al., 1982, 1986) and Anatolia (Nyst and Thatcher, 2004).

2.1.3 Issues. The notion that the northward and westward moving North Pacific Rim orogenic stream existed in the early Tertiary is based on the absence of significant interior Alaska mountain building yet the recording of hundreds of kilometers of offsets across, and localized deformation along, the curving pattern of regional strike-slip faults that tectonically connect western Alaska and British Columbia (Redfield et al., in press). The concept of a currently extruding western crustal track is based on the seismically defined Bering block, deformation along its western or NE Russian edge, and a limited but growing inventory of epicentral and fault mechanism data stretching eastward back into central Alaska (Page et al., 1991, 1995; Eberhart-Phillipps, 2006). To test this idea an extensive network of GPS stations is needed in western Alaska and on the Bering shelf. Extrusion or tectonic escape can be identified if crustal blocks are detected moving westward and southwestward toward the Aleutian SZ at a rate exceeding a component of motion in these directions generated by convergence between the North America and Pacific plates. The complex movement of blocks of crust documented by Nyst and Thatcher (2004) for the extruding Anatolian microplate implies that similar patterns of crustal shearing, extension, and both large and small scale rotations will be true for the hypothesized NPRS (Mackey et al. 1997; Fujita et al. (2002).

2.2 Komandorsky Basin

2.2.1 Observations. The broad expanse of the Komandorsky Basin, the far western part of deep water Bering Sea Basin, lies north of the KAT connection (Fig. 1B). The Bering-Kresta shear zone trending along the southern edge of the basin most likely separates its oceanic crustal framework from that of the arc massif of the Komandorsky sector of the Aleutian Ridge (Seliverstov, 1984; Baranov et al, 1991; Geist and Scholl, 1994). To the east, the arc crustal mass of Shirshov Ridge separates the oceanic basement of the Komandorsky Basin from that of the Aleutian and Bowers Basins (Figs. 1A and 1B).

Muzurov et al. (1989), Baranov et al. (1991) and Valyasho et al. (1993), established that the Komandorsky basin was formed by a style of rear or backarc spreading in a direction parallel to the axis of the arc. Baranov et al. (1991) note that opening of the Komandorsky Basin in a NW-SE direction took place parallel to the active Pacific-North America (PAC/NAM) transform boundary of the Bering-Kresta shear zone. Opening was thus parallel to relative plate motion (Plate 1 and Fig. 4). The opening of the Miocene Komandorsky Basin is similar to the opening of the backarc Andaman Sea subparallel to the relative motion between the India-Australia plate and that of the Sumatra sector of the Eurasian plate (Subarya et al., 2006). Although concentrated at the Bering-Kresta shear zone, transform shearing is distributed southward across the width of the Komandorsky sector of the Aleutian Ridge to the Stellar shear zone in the Aleutian Trench (Fig. 1B and Plate 1, see also Fig. 7; Cormier, 1975; Seliverstov, 1984; Baranov, 1991; Geist and Scholl, 1994; Gaedicke et al., 2000; Freitag et al., 2001; Kozhurin, this volume**)**.

Magnetic anomalies constrain the emplacement of rear-arc crust between about 20 and 10 Ma and document that the speed of opening increased southward toward the Bering-Kresta shear zone (Fig. 4; Valyasho et al., 1993). The young age is consistent with the relatively thin sedimentary sequence (1–2 km) filling the basin, the late Cenozoic age of its basal sediment at DSDP Site 191, and ~9 Ma age (K-Ar) of the underlying basement (Creager, Scholl, et al., 1973; Baranov et al., 1991; Cooper 1987a, b). The thickest (3+ km) sedimentary sequences occur in trench-shaped depressions at the base of the basin's northern Kamchatka margin (Baranov et al., 1991). The basin's high heat flow (typically > 100 mW/m^2 and as high as 230 mW/m^2) is also consistent with its young crust (Fig. 1B, Plate 1, and Fig. 7); Cormier, 1975; Cooper et al., 1987b, Baranov et al., 1991). In the northwestern Pacific, emplacement of crust in the Komandorsky basin took place after the earlier Tertiary opening of the Kuril Basin of the Sea of Okhotsk and, farther south, the Sea of Japan (Baranov, et al., 2002).

2.2.2 Interpretations. The Aleutian SZ is at least older than the oldest known arc igneous rock at ~46 Ma (Jicha et al., 2006), and the crust of the Komandorsky Basin was emplaced 25–35 Myr later (between ~20–10 Ma; Valyasho et al., 1993). The direction of spreading was parallel to the Bering-Kresta shear zone (Figs. 1A and Plate 1). So it seems evident that the direction of spreading was controlled by the pre-existing strike of the Aleutian Ridge's transform or Komandorsky sector and that its NW trend may not have significantly changed since at least the early Miocene.

Yogodzinski et al. (1993) recognized that the Komandorsky Basin resides in a transform-boundary setting similar to that

Plate 1. Index map of gravity (lows are in blue tones and highs in orange and red) and magnetic anomalies (white lines) adapted from Norton (in press) for the northwestern most or Meiji corner of the Pacific Basin. Mid Cretaceous oceanic crust, which lacks a pattern of magnetic anomalies, underlies the Meiji corner. Older early Mesozoic or M-series anomalies are recorded to the south on the western side of the ridge of the Emperor Seamounts. East of the ridge are Late Cretaceous and early Tertiary magnetic anomalies (Chrons 33 to 20 in black numbers). Fracture zones are traced with thin red lines. See also Miller et al. (2006).

Pink line with 0, 5, 10, and 20 Myr ticks (white numbers) tracks the WNW movement of the Pacific plate toward the Kamchatka subduction zone during the past 20 Myr. The high bathymetric relief lying east of the Emperor Seamounts and including Stalemate Fracture Zone, Emperor Trough, and an unnamed cluster of seamounts between them, began to obliquely enter the western sectors of the Aleutian subduction zone ~20 Myr ago. Tectonism of the Aleutian Ridge was a likely consequence (Vallier et al., 1992, 1996), causing or contributing importantly to the fragmentation of the arc massif and rapid transport of block toward the Kamchatka Trench and the tear in the Pacific plate underlying the Near and Komandorsky Islands sector of the ridge (Yogodzinski et al., 2001). Potentially, entrance of high relief into the western sector of the subduction zone also stimulated rear-arc spreading in the Komandorsky Basin from ~20 to ~10 Ma (Baranov et al., 1991; Valyashko et al., 1993).

of the Andaman Sea. They also conjecture that Miocene spreading involved the westward transport of blocks of arc crust along the Bering-Kresta shear zone. Their collision with Kamchatka significantly changed arc-volcanic processes operating along the far western Aleutian Ridge.

Formation of the mostly early Miocene crust in the Komandorsky basin requires that either room was tectonically opened for its emplacement or that older, pre-existing crust was assimilated or buried in place, an hypothesis considered by Scholl and Creager (1973) and Cormier (1975). But the mapping of fossil spreading centers and companion magnetic anomalies and fractures zones document that crustal replacement was by backarc spreading (Baranov et al. 1991). Evidence is unknown to the author that Komandorsky spreading was accompanied by displacement of Kamchatka to the NW (by a minimum of several hundred kilometers), or Shirshov Ridge to the east over the older crust of the Aleutian Basin, or the subduction of this crust beneath the basin's Beringian margin (Scholl et al., 1986; Cooper et al., 1987a, b; 1992). Hence older crust existing in the area of the Komandorsky Basin—a part of the Aleutia terrane of Marlow and Cooper (1983)—was evidently removed to the west in the early and middle Miocene by basin-edge subduction below northern Kamchatka (see Fig. 10).

Hochstaedter et al., 1991 cites the eruption and geochemical characteristics of the Vyvenka igneous bodies (15–6 Ma.) in northern Kamchatka as recording the westward subduction of Komandorsky crust beneath Kamchatka. The existence of a sediment-filled trench at the base of the eastern Kamchatka margin is arguable evidence for west-directed subduction of the pre-existing crust occupying the basin prior to the early Miocene (Baranov et al., 1991; Avdeiko et al., this volume).

Tectonic circumstances that reinitiated subduction beneath the northern margin of Kamchatka and the emplacement of early Neogene crust in the Komandorsky Basin are unknown. But the southern crust of the Komandorsky Basin resides above a probable regional tear in the subducting Pacific plate that passes deeply beneath the basin (Creager and Boyd, 1991). The tear, the southern edge of which lies parallel to and below the Bering-Kresta shear zone (Fig. 1B), begins near Buldir Island (176 deg E; Fig. 1A and Plate 1), the westernmost subaerial volcanic edifice of the Aleutian Ridge, and extends northwestward ~1000 km to dive westward below Kamchatka (Yogodzinski et al., 1994, 1995, 2001; Peyton et al., 2001; Levin et al., 2002; Park et al., 2002, Kelemen et al., 2003; Levin et al., 2005).

It is tempting to link crustal emplacement in the Komandorsky Basin to early Miocene tearing of the Pacific slab highly obliquely underthrusting the western and far western sectors of the Aleutian Ridge. Tearing may have initiated asthenospheric upwelling in the Komandorsky Basin, a general concept explored by Cormier (1975). Although backarc basins are characterized by high heat flow (Hyndman et al. 2005), ascent of the asthenosphere is consistent with the basin's exceptionally high heat flow that increases toward the southern end of the basin where the massive and submerged Piip volcano erupts in a graben just north of the Bering-Kresta shear zone (Fig. 1B and Plate 1; Cormier, 1975; Cooper et al. 1987b; Baranov et al., 1991). As noticed by Yogodzinski et al. (1993, 2001), the slab tear posit is supported by the Neogene and younger eruption of calc-alkaline magma and high magnesium andesite ("adakite") along the western sectors of the Aleutian Ridge and including at Piip volcano.

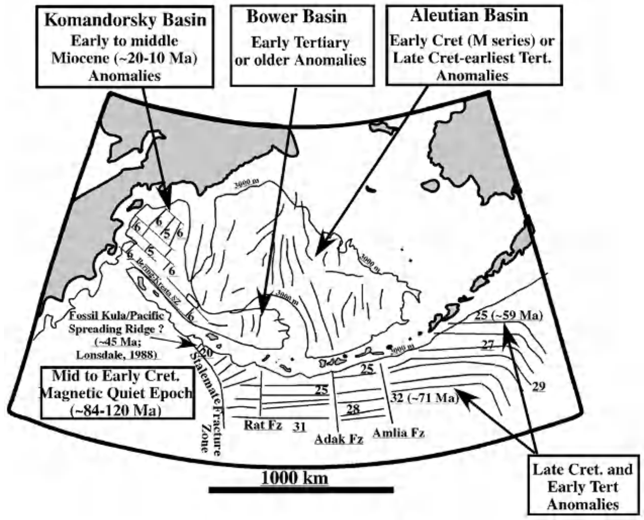

Figure 4. Drawing of magnetic anomaly patterns, showing Chron numbers, for north Pacific and Bering Sea Basin region. Aleutian Basin pattern from Cooper et al. (1992); Komandorsky Basin pattern and age estimates from Valyasho et al. (1993)—see also Baranov et al., (1991); north Pacific pattern from various sources (see Figure 4 and Atwater, 1989; Atwater and Severinghaus, 1989; and Norton, in press).

An alternative model is to recognize that slab tearing may have been a consequence of the re-initiation of subduction westward beneath northern Kamchatka. Subduction start-up would have led to rifting of the Shirshov forearc, the end of subduction beneath it, and the beginning of asthenospheric ascent or upwelling to nourish within-basin spreading behind the east or trailing edge of the westward subducting sector of Aleutia (Yogodzinski et al., 1993). Upwelling beneath the basin could have promoted the tearing away of the Pacific slab then residing deep beneath it, but connected across the Komandorsky sector's transform fault system to the Pacific Basin south of the Aleutian Ridge. Tearing and falling away of the Pacific lithosphere north of the ridge was evidently focused below the Being-Kresta shear zone. Melting of the heated edge of the Pacific plate would have favored the ascent of adakitic magma along the western sectors of the Aleutian Ridge and including at Piip volcano (Fig. 1B and Plate 1; Yogodzinski et al., 1994, 1995).

2.2.3 Issues. Capture of the basement of the Aleutian Basin on the east side of Shirshov Ridge—Aleutia—was apparently in the late early Eocene (~50 Ma) and thus most likely involved accretion of a sector of Pacific or Kula plate because the only other candidate plate, the Resurrection plate (Haeussler et al., 2003; Farris et al., 2006), had by 50 Ma disappeared beneath Alaska and the Pacific margin of British Columbia (Fig; 2, also see Fig. 10A). Prior to its replacement between ~20 and ~10 Ma, the westward expanse of Aleutia would have included the existing area of the Komandorsky Basin (See Figs. 10A and B).

Allowing that in some form the Aleutia replacement scenario and accompanying slab tearing is correct, it is not obvious why westward subduction beneath northern Kamchatka to accommodate basinal crust generated by spreading did not happen until at least 25 Myr after the formation of the Aleutian-Bering Sea region. Possibly, the removal mechanism was driven by the heating and eclogite densification of the fossil slab of Aleutia dipping westward beneath northern Kamchatka. Vallier et al. (1987, 1994, 1996) also speculate that early Miocene entrance of high bathymetric relief into the western sectors of the early Miocene Aleutian SZ may have led to significant tectonism of the Aleutian Ridge west of about Amchitka Island (Plate 1) and the consequent rapid movement of crustal blocks toward the Kamchatka subduction zone. These concepts are explored further below.

2.3 Far Northwest Pacific and Coastal Kamchatka.

2.3.1 Observations. Oceanic crust of the Pacific plate forms the south side of the KAT connection. The age of this crust is not accurately known because it was created at a north Pacific spreading center during the Cretaceous Long Normal Polarity Chron (~83–119 Ma) and thus lacks a reversal fabric of magnetic anomalies, (Plate 1 and Fig. 4; Mammerickx and Sharman, 1988, Lonsdale, 1988; Sukhov et al., 2004; Sager, 2005; Norton, in press; Miller and Kennett, 2006). However, paleomagnetic and age dating studies establish that the oceanic crust south of the Aleutian Trench and flanking the northern base of Detroit Seamount formed at ~81 Ma at a paleolatitude of ~36 degs N (Fig. 1A; Tarduno and Cottrell, 1997; Cottrell and Tarduno, 2003; Tarduno et al., 2005). The volcanic edifice of Detroit Seamount rises above the northern end of the NNW-trending ridge of the Emperor Seamounts. Detroit was eruptively emplaced at about 76 Ma, at a paleolatitude near 34 deg N (Duncan and Keller, 2004, Tarduno et al., 2005), and proximal to a spreading center most like trending NW-SE parallel to Obruchev Rise (Keller et al., 2004; Norton, in press). The rise is the deeply sediment-buried ridge that connects Detroit and Meiji Seamounts (Fig. 1A; Scholl et al., 1977; Scholl et al., 2003; Kerr et al., 2005). Meiji, bathymetrically and by continuity, is presumably the northernmost of the Emperor Seamounts, was probably emplaced toward 80 Ma, a paleontologically based age assessment because rock alteration of recovered basalt core has significantly reset the K-Ar clock (Creager, Scholl, et al., 1973; Duncan and Keller, 2004). The Meiji edifice is poised to orthogonally enter the Kamchatka SZ at the Kronotsky Peninsula (~55 deg N; Figs. 1A, 1B and Plate 1).

A significant tectonic and physiographic companion to the KAT connection is Obruchev Rise, which is carried on the Pacific plate and trends parallel to the Komandorsky transform sector and enters the Kamchatka Trench at Cape Kronotsky (Plate 1). Both the Komandorsky sector of the Aleutian Ridge and the Obruchev sector of the Emperor Seamounts thus terminate at paired, effectively non-migrating collision zones. Orthogonal collisions at these capes have probably been ongoing since at least the mid Tertiary. Based on GPS data, the Komandorsky sector of the Aleutian Ridge enters the Kamchatka SZ at close to the speed of the rise (~80 km/Myr; Avé Lallemant and Oldow, 2000; Gordeev et al., 2001; Steblov, et al., 2003). Effectively, the Komandorsky sector is, like the Obruchev Rise, part of the Pacific plate.

2.3.2 Interpretations. When the formation of the Aleutian SZ created the KAT connection (Fig. 2), the Late Cretaceous ocean crust and cresting Obruchev Rise and Emperor Seamounts resided at least 2500 km to the SE. Detroit Seamount, for example, was positioned in the general vicinity of 35 deg N and perhaps as far east as 150 deg W (Engebretson et al., 1984; Tarduno et al., 2003; Norton, 1995; in press). Thus much of the length of the Pacific plate along which the original transform connection between the Aleutian and Kamchatka SZs was established has been subducted (Plate 1).

Most authors agree that the Cape Kamchatka Peninsula records late Cenozoic collision of the Aleutian Ridge's Komandorsky sector with eastern Kamchatka (Watson and Fujita, 1985; Zinkevich et al., 1985; Zoneshain et al., 1990; Baranov et al., 1991; Geist and Scholl, 1994; Seliverstov, 1998; Gaedicke et al., 2000; Freitag et al., 2001; McElflesh et al., 2002). Views differ about what tectonic and structural processes formed the other two eastern peninsulas, Kronotsky and Shipunsky, south of the Cape Kamchatka Peninsula (Fig. 1A and Plate 1). The accretion of sectors of

Pacific-basin born arc massifs is commonly suggested (see for example Seliverstov, 1998; Alexeiev et al., 2006, Avdeiko et al., this volume). Alternatively, from Shipunsky to at least the Cape Kamchatka Peninsula, Park et al. (2002) envision a northward migrating collisional scheme sequentially adding sectors of the Aleutian Ridge to eastern Kamchatka.

However, as noted by Park et al. (2002), the existing base of data does not clearly define when the eastern capes formed, how they were created, or if their formations are tectonically kindred. It is equally plausible to suppose that the prominent capes of eastern Kamchatka record the orthogonal subduction of bathymetric relief, Kruzenstern Fracture Zone at Shipunsky (Plate 1; Bürgmann et. al, 2005), Obruchev Rise at Kronotsky, and the Komandorsky sector of the Aleutian Ridge at Cape Kamchatka Peninsula (Fig. 1A and Plate 1). Crustal elevation to form the capes could be effected by collisional underthrusting and consequent upper plate shortening or underplating. The underthrusting oceanic or arc relief need not be coastally exposed.

It is not known how much of the length of the Obruchev Rise has entered the Kamchatka SZ to potentially build the elevated structure of the Kronotsky Peninsula, but the deformed slab dipping beneath it suggest a period of at least several million years (Gorbatov et al., 1997). The rise's thick sediment cover provided by the deposition of the Meiji drift body implies a subducted length of at least 1000 km (Scholl and Rea, 2002; Scholl et al., 2003). At the present convergent speed of ~80 km/Myr, the Pacific crust immediately south of the KAT connection approached the Aleutian Trench in the vicinity of Near Pass approximately 10 Myr ago (Fig. 1B and Plate 1; Norton, in press; Miller et al., 2006), or about the time when spreading ceased in the Komandorsky Basin (Baranov et al., 1991; Valyasho et al., 1993). The Obruchev Rise has thus probably been underthrusting and building the Kronotsky Peninsula since the middle Miocene if not before.

2.3.3 Issues. That collisional processes are the cause for the seaward-projecting peninsulas of eastern Kamchatka might be tested with submarine sampling. Where bathymetric ridges underun a convergent margin sedimentary and igneous material from the summit area of the ridge can be detached and accreted to the landward trench slope. Accretion of ridge material has been described from the collision zone of the Nazca Ridge and the Peru Trench (Kulm et al., 1974) and where the Louisville Ridge—the south Pacific's tectonic "twin" of the Hawaiian-Emperor seamount chain—collides with the Tonga Ridge (Ballance et al., 1989). Potentially, oceanic material accreted from the underthrusting Obruchev Rise can be recovered from the landward trench slope east of Kronotsky Peninsula (Plate 1; Gorbatov et al., 1997; Bürgmann et al., 2005). If oceanic debris exists on Kamchatka's landward trench slope, then invaluable information about the history of underthrusting, much as described by Ballance et al., (1989) for the Tonga Ridge, can be obtained.

2.4 Aleutian and Bowers Basins

2.4.1 Observations. The Aleutian and Bowers Basins occupy the eastern side of the deep water Bering Sea Basin (Fig. 1A). The larger Aleutian Basin is flanked to the northwest and northeast, respectively, by the NE-striking Koryak and the NW-striking Beringian continental margins. Arc massifs border the other sides of the basin: Shirshov Ridge to the west and Bowers and Aleutian Ridges to the south. Prominent N-S striking magnetic anomalies are recorded in both the Aleutian and Bowers Basins, and the velocity structure of their basement rock is typical of oceanic crust (Fig. 4; Shor, 1964, Cooper et al., 1987a, b, 1992; Stone, 1988). The age of the magnetic anomalies that stripe the Aleutian Basin has been tentatively identified as Chrons M1 through M 13, younging to the east, of early Cretaceous age (Cooper et al., 1976a, b, 1977). The age of the magnetic pattern in Bowers Basin is poorly constrained. Both basins are characterized by heat flow averaging near 60 mW/m2, which is higher than that expected of Cretaceous crust but not atypical of suprasubduction zone or backarc settings (Hyndman et al., 2005).

The sedimentary sequence underlying the abyssal floor of the Aleutian Basin is typically 2–3 km thick, but the section is as thick as 10–12 km in fossil trenches at the base of the Beringian margin, along the length of the Koryak margin, and below the outward curving, northern side of Bowers Ridge (Fig. 5; Cooper et al., 1987b, 1992). Shirshov Ridge is not flanked by a sediment-filled trench along either its Kamchatka or Alaska-facing sides (Figs. 4 and 5: Rabinowitz and Cooper, 1977; Baranov et al., 1991).

The Beringian continental margin bordering the Aleutian Basin along its Alaska side is underlain by a subsided and erosionally decapitated fold belt—the Beringian fold belt (Fig. 6)—of broadly deformed shallow marine and nonmarine beds of late Jurassic, Late Cretaceous, and early Tertiary age. These units are collectively referred to by Worrall (1991) as the Carapace Sequence. Units of the Beringian fold belt accumulated in a forearc setting. No deep water or accretionary complex facies have been recovered along the Beringian margin by dredging or drilling (see summarizing map and descriptions of Grantz et al., 2002). The Mesozoic rocks are unconformably overlain by little-deformed Eocene and younger generally marine shelf facies beds that accumulated to thicknesses as much as 10–12 km

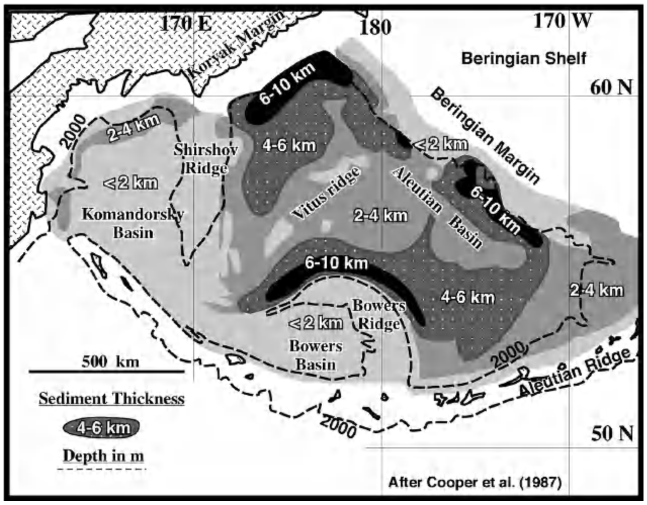

Figure 5. Isopach map of sediment thickness in Bering Sea Basin. Thick (6–10 km) trench-filling sequences, presumably identifying abandoned subduction zones of early Tertiary age, rest at the base of sectors of the Beringian margin, the Koryak margin, and north of Bowers Ridge.

in margin-paralleling basins (e.g., Navarin and St. George; Fig. 6) (Marlow et al. 1987; Worrall, 1991; Grantz et al., 2002). The prominent unconformity is referred to as the "top of Cretaceous" unconformity by Marlow et al. (1987) and the "Red Event" surface by Worrall (1991) (Fig. 6).

The NW margin of the Aleutian Basin, the southern Koryak margin of NE Russia, exposes at and southwest of Cape Navarin shallow marine and non-marine units of middle and late Cenozoic age unconformably overlying deformed early Tertiary and older Cretaceous and Jurassic sequences (Marlow et al. 1987; Worrall, 1991; Grantz et al., 2002). The Mesozoic sequences are recognized as accretionary complexes generally similar to those exposed along the northern margin of the Gulf of Alaska (Plafker et al., 1994). Southwest along the Koryak margin, the Late Cretaceous Olyutosky arc massif that many authors project offshore to include Shirshov Ridge is thrust over the early and middle Eocene margin and basinal flysch sequences (Garver et al., 2004, Chekhovich et al, 2006; Chekhovich and Sukhov, 2006).

The Alaska border of the Aleutian Basin is thus constructed of a framework of broadly deformed miogeoclinal rocks of a Jurassic, Cretaceous, and early Tertiary forearc setting topped unconformably by little deformed basinal sequences of submerged Eocene and younger shelf and upper slope beds (Fig. 6). In contrast, the complementary Koryak margin of NE Russia is an assembly of deformed accretionary eugeosynclinal sequences of Jurassic, Cretaceous, and earliest Tertiary age and accreted arc complexes unconformably overlain by younger, less deformed and subaerially exposed miogeosynclinal deposits (Stavsky et al., 1988, 1990; Zonenshain et al., 1990; see regional maps of Worrall, 1981 and Grantz et al., 2002).

A sediment-filled trench section overlying the oceanic crust of the Aleutian Basin is conspicuous beneath the base

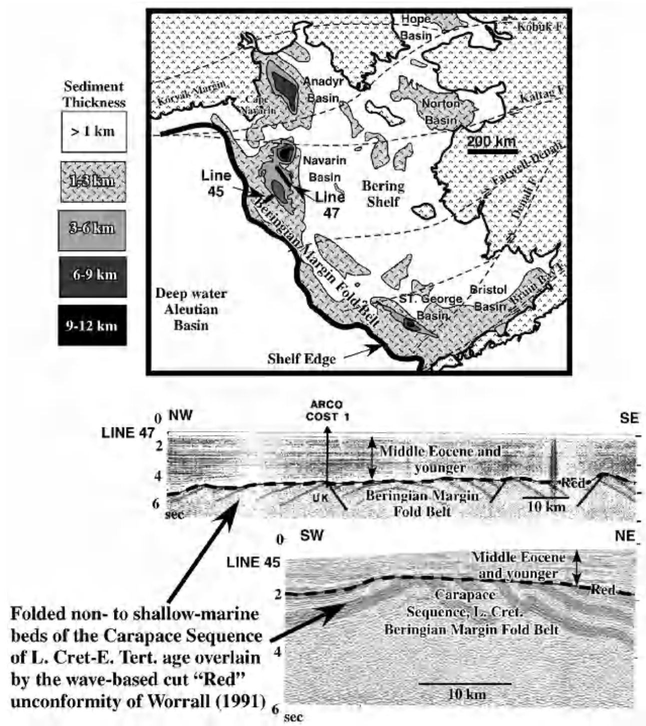

Figure 6. Seismic sections imaging the wave-eroded and depositionally buried antiformal and fault structures of the Beringian margin fold belt of Late Cretaceous and early Tertiary beds. The "Red" unconformity of Worrall (1991) formed until the late middle Eocene (~45-42 Ma). The Beringian margin fold belt is the basement for large, margin paralleling shelf basins largely filled with shelfal deposits of late Eocene and younger age. The history of these basins (e.g., Anadyr, Navarin, St. George) extends back into the Cretaceous when the Beringian margin was largely a transform plate boundary between the North America and Kula or Izanagi plates of the north Pacific Basin (see Norton, in press). Index map and seismic sections are adapted from Worrall (1991). Offshore continuations of onshore, western Alaska strike-slip faults are hypothetical and guided seaward by major shelf structures, volcanic centers, and offsets in the NW-SE trend of the Beringian margin. It is posited that Anadyr and Navarin basins were originally aligned but relative Cenozoic motion across the right-lateral Kobuk and Kaltag fault systems and extrusion of the north Pacific rim orogenic stream (NPRS) offset the basins by more than 200 km (see Figures 1B and 3). Extrusion also juxtaposed the Mesozoic accretionary complexes of the Koryak margin and the similar age but shallow marine and continental deposits of the Beringian Carapace sequence.

of the Koryak margin and also along sectors of the modern Beringian margin (Fig 5; Cooper et al. 1987a, b; Marlow et al., 1987; Worrall, 1981; Klemperer et al., 2002; Grantz et al., 2002). The oldest sampled sedimentary sequence that drapes the margins of the Aleutian and Bowers Basin and extends over the basin floor is Oligocene. Over the basin the oldest sediment recovered by DSDP drilling (at Site 190, Fig. 1A) is middle Miocene (Creager, Scholl et al., 1973; Scholl et al., 1987; Marlow et al., 1987). Drilling at Site 190 was targeted to reach basement but failed to do so. Thus no direct information exists about the age of the oceanic crust of the Aleutian Basin or the much smaller Bowers Basin inside the arc of Bowers Ridge (Fig. 1A). In contrast, the largely early Miocene age of the igneous crust flooring the Komandorsky Basin is known (Muzurov et al., 1989, Baranov et al., 1991).

2.4.2 Interpretations. It has long been supposed that the basement of the Aleutian Basin is a sector of Pacific oceanic crust (Shor, 1964; Ewing et al.1965) generated at a north Pacific spreading center but captured by the North America plate with the formation of the Aleutian-Bering Sea region. (Scholl et al., 1975; Cooper et al., 1976a, b; 1977). This exotic terrane was given the name "Aleutia" by Marlow and Cooper (1983). The principal reason for the capture concept is the prominent basement magnetic anomalies and their N-S, arc-normal trend (Figs. 2 and 4), characteristics not typical of a basin formed by backarc spreading (Stone, 1988).

The time of entrapment of the oceanic crust of Aleutian is constrained by the middle Eocene age (~46 Ma) of the Aleutian Ridge (Jicha et al., 2006). If the trapped crust is indeed early Cretaceous in age, it could be a sector of the Izanagi plate that was incorporated into the Kula plate at its apparent formation at ~83 Ma (Engebretson et al., 1984, 1985; Cooper et al., 1976a, b; Scholl et al., 1986; Norton, in press). If the anomaly pattern is younger than about 83 Ma and older than early to middle Eocene, then the captured sector is not of the Izanagi plate. In the Late Cretaceous and early Tertiary an eastward-migrating spreading ridge separated the Kula plate to the west from the Resurrection plate subducting eastward beneath British Columbia (Fig. 2; Haeussler et al., 2003). Potentially, the N-S pattern of Aleutia's magnetic fabric may be a sector of Kula plate generated west of the eastward migrating Kula-Resurrection spreading ridge (Haeussler et al., 2003; also see Fig. 10A).

Probably during or soon after crustal capture, rifting in the backarc east of Shirshov Ridge formed the now sediment-buried and seamount-populated NE-trending Vitus ridge, a short-lived spreading ridge trending roughly parallel to those that in the early Miocene opened the adjacent Komandorsky Basin (Cooper et al., 1992; Fig. 1B, also see Figs. 10A and B). A phase of post-capture backarc spreading may also have formed Bowers Basin behind a northeastward migrating Bowers Ridge. Three views have been stated about this possibility, (1) basin formation as part of the early Miocene opening of the Komandorsky Basin (Yogodzinski et al., 1993), (2) basin formation tied to regional scale deformation of western Alaska and the Aleutian Bering Sea region (Cooper et al. 1992), and (3) basin formation linked to extrusion-driven formation of the Bowers and Shirshov SZs (Scholl and Stevenson, 1989; Scholl et al., 1992).

2.4.3 Issues. Knowing the age and latitude of formation of the crust of the Aleutian Basin—Aleutia—is central to reconstructing the configuration of plates and the pattern of crustal ages occupying the high north Pacific when the Aleutian-Bering Sea region formed in the middle Eocene. Although it seems likely the Aleutian Basin is floored by lower Cretaceous crust, this inference has not been confirmed by drilling nor has a wealth of newly collected magnetic data been integrated into the age analysis (Bering Sea EEZ-SCAN Staff, 1991). The age of the probably younger Vitus ridge is also not directly known, nor is that of Bowers Basin (Fig. 1. The age of oceanic crust underlying the Aleutian and the Bowers Basins remains equally uncertain.

Placing N-S magnetically patterned crust of early Cretaceous age in the Bering Sea region at the time of the middle Eocene entrapment of Aleutia, remains problematic for several reasons: (1) confirmation is lacking of their M13–M1 age assignment, (2) the discovery of the Resurrection plate implies that the N-S pattern could have been generated in the Late Cretaceous and early Tertiary west of the eastward migrating Kula/Resurrection spreading center (Haeussler et al. 2003), and (3) the unresolved problem of whether a significant change in motion of the Pacific plate is signaled by the prominent, middle Eocene bend in the Hawaiian-Emperor Seamount chain (Tarduno et al., 2003; Steinberger et al., 2004; Koppers and Staudigel, 2005; Andrews et al. 2006; Sharp and Claque, 2006; Stock, 2006; Steinberger and Gaina, 2007).

Until age and formative latitude data are in hand, for example as are now available for the Detroit sector of the NW Pacific Basin (Tarduno and Cottrell, 1997; Tarduno et al., 2003), the reasons for, and setting of, the Eocene formation of the Aleutian-Bering Sea region and its KAT connection will remain unresolved.

2.5 Shirshov and Bowers Ridges

2.5.1 Observations. Based on geophysical data and dredge sampling, Shirshov and Bowers Ridges, which, respectively, flank the western edge and part of the southern edge of the Aleutian Basin (Fig. 1A), are recognized as the massifs of volcanic arcs. The northern end of Shirshov Ridge is connected to NE Russia at Cape Olyutorsky (Fig. 1A). Rock assemblages of the accreted Late Cretaceous-early Tertiary Olyutorsky arc are exposed at the cape and also extend farther to the north along the Koryak margin (Levoshova et al., 1997, 2000, Seliverstov, 1998; Garver et al., 2000); Garver et al., 2004; Chekhovich et al., 2006; Chekhovich and Sukhov, 2006). Shortening structures suggestive of a collisional contact between the cape and the ridge are not mapped at Cape Olyutorsky, for example as they are farther to the south at the KAT connection ((Shapiro et al., 1984; Tsukanov and Zinkevich, 1987; Geist and Scholl, 1994).

Basement rock of Shirshov Ridge is extensionally faulted normal to its longitudinal, N-S length, as documented by prominent ridge-paralleling half-grabens (Baranov et al. 1991) mapped prominently by gravity anomalies (Plate 1). Basement highs at depths of 1000–2000 m cresting the northern and central sectors of the ridge are truncated by wave-based erosional platforms (Scholl et al., 1975; Baranov et al., 1991). Neither side of the N-S-trending ridge is flanked by sediment-filled trench structures revealed by satellite gravity (Plate 1) and seismic-reflection-based sediment thickness maps (Fig. 5; Scholl et al., 1975; Rabinowitz and Cooper, 1977; Cooper et al., 1987b; Baranov et al., 1991).

Mafic ocean crust and chert deposits of Late Cretaceous and Triassic age have been reported from dredge samples recovered from the ridge (Bogdanov et al., 1983; Savotsin et al., 1996; Gladenkov, 1990). Dating of Cretaceous beds is based on the radiolaria taxa included within the chert, an assemblage that is also found in similar chert deposits exposed in the nearby Koryak mountains, which are fjord-scarred (Fig. 1A). Hence, ice-rafting of Koryak-derived Mesozoic material to the surface of the offshore Shirshov Ridge is a troubling concern.

Arc volcanic material collected from the southern end of Shirshov Ridge includes feldspar of late Oligocene age (K-Ar date of 27.8 Ma +/- 1.1) that has to be view as minimal (Scholl et al., 1975; Cooper, 1987a, b). The sampled sector of the ridge trends NW-SE, thus striking parallel to the major fracture zones of the Komandorsky Basin and the Aleutian Ridge (Figs. 1B and 4) and very different from the ridge's prominent N-S alignment and strike of it graben system (Plate 1: Baranov et al., 1991). As a consequence it possible that the dated late Oligocene arc material from the southern extremity of Shirshov Ridge is actually a fragment of the Aleutian Ridge rifted away during the Miocene formation of the Komandorsky Basin or, earlier, the Bowers Basins (Scholl et al., 1989; Cooper et al., 1992 and Yogodzinski et al., 1993). Arc material dredged farther to the north by Russian colleagues has not been radiometrically dated (Baranov, written communication, 2006) but N-MORB amphibolite recovered from the ridge is reported at ~47 Ma (Sukhov et al., 1987). Well preserved diatom and silicoflagellates assemblages have been recovered from overlying stratified deposits of Miocene and Oligocene age (Gladenkov, 1990).

Bowers Ridge appears to be structurally connected to the southern end of Shirshov Ridge (Rabinowitz, 1974). Late Cenozoic deposits of the Aleutian Basin that bury the connection are deformed above it. Submerged sectors of the summit of Bowers Ridge as deep as 1000 m are, similar to Shirshov Ridge, wave-truncated platforms of former islands. The summit platform of the eastern end of Bowers Ridge abuts and merges with the wave-flattened summit platform of the Aleutian Ridge (Fig. 1A).

The northern side of Bowers Ridge is flanked by a prominent trench structure filled with a sequence of Aleutian Basin sediment as thick as 10 km (Fig. 5). The infilling Bowers Ridge trench sequence exhibits only slight post-depositional deformation, suggestive of minor late Cenozoic shortening between Alaska and the ridge (Marlow et al., 1990). Older, underlying sedimentary material at the base of the ridge's northern slope are more deformed, but not greatly so, and a frontal accretionary prism wider than 10–15 km is not evident (Cooper et al., 1987a, b).

Basement of calk-alkaline arc breccia was recovered in 1970 by the Scripps Institution of Oceanography from the north side of Bowers Ridge (http://walrus.wr.usgs.gov/infobank/m/m170bs/html/m-1-70-bs.meta.html; Creager, Scholl et al., 1973). The breccia was too altered to date by K-Ar methodology (Scholl et al., 1975). Drilling on the southern slope of Bowers Ridge (DSDP Leg 19) did not reach basement or sediment older than late Miocene (Creager, Scholl et al., 1973). Decades earlier, G. Dallas Hanna (1929) described diatom-bearing sediment of late Miocene age recovered by dredging the submerged flank of Bowers Ridge. This study was probably the first attempt to decipher the geologic history of the Bering Sea Basin.

2.5.2 Interpretations. Geophysical and sample data document that the Shirshov and Bowers Ridges were, like the Aleutian Ridge, largely constructed by arc volcanism. It is also evident that both Shirshov and Bowers Ridges were formerly emergent arc massifs that sometime in the mid Cenozoic subsided below wave-base erosion to depths of >1500 m. On Shirshov Ridge, Oligocene sediment recovered at depths of 1400–1500 m contain neritic and sublittoral diatoms, documenting subsidence, and possibly recording that arc-extinction occurred after the late Oligocene (Gladenkov, 1990). The present Aleutian Ridge, although still volcanically active, exhibits a similar history of wave-base truncation and subsidence of its crestal summit platform to depth of several hundred meters and as deep as ~1500 m along the flanks of the ridge (Scholl et al., 1987).

Deformation studies by Marlow et al. (1990) of the sedimentary sequence filling the Bowers Ridge trench and seismicity and GPS data from the Aleutian Ridge (Oldow et al., 1999; Avé' Lallemant and Oldow, 2000: Cross and Freymueller, 2007) imply that Bowers Ridge is tectonically disconnected from the clockwise rotation and westward transport of blocks of Aleutian arc crust moving along the Pacific-North America plate boundary toward the Kamchatka subduction zone (Geist et al., 1988: Geist and Scholl, 1992). Evidently, an active right-lateral shear zone separates the Aleutian and Bowers Ridges (Ryan and Scholl, 1989, 1993). Also, only modest late Cenozoic basement deformation or possibly magmatism has occurred in the subsurface structural septum connecting the western end of Bowers Ridge and the southern end of the physiographic relief of Shirshov Ridge (Rabinowitz, 1974). Apparent vertical deformation in late Cenozoic sediment overlying the septum is not understood.

Evidence of collisional impact between the Aleutian and Bowers Ridges has not been recognized, and both appear to be arc massifs of similar age, possibly built upon thrust-thickened oceanic crust (Savotsin et al., 1986). Thus Bowers is viewed as having formed effectively in place as a northward projecting, westward curving growth added constructionally to the larger Aleutian Ridge.

Shirshov Ridge is physiographically the submarine extension of the promontory of the Olyutosky Peninsula (Fig. 1A), which is underlain by a framework of Late Cretaceous arc rocks accreted to the margin most likely in early and middle Eocene time (Stavsky et. al, 1988; 1990; Levashova et al., 2000, Garver et al. 2000; Garver et al., 2004; Chekhovich and Sukhov, 2006; Chekhovich et al., 2006). The submerged extension is in itself not confirming evidence that the ridge is the seaward continuation of the Late Cretaceous arc massif that forms the peninsula. For example, the Cenozoic Aleutian Ridge is not the seaward extension of the continental framework of the Permo-Triassic, Jurassic, and Cretaceous rocks that underlie the Alaska Peninsula (Burk, 1965, Nokleberg et al., 1994). So it can be entertained that Shirshov Ridge was similarly constructed in the Tertiary seaward of an existing framework of Cretaceous and older rocks of the Koryak-Kamchatka margin.

Unlike Bowers Ridge, Shirshov Ridge is not flanked by a preserved structural trough of a sediment-filled trench (Fig. 5). Most likely, as surmised by Baranov et al., (1991), a trench and eastward-dipping subduction zone formerly lay at the base of the ridge's western or Kamchatka-facing side. Destruction of the structural trench was likely a consequence of ridge extension and fracturing during the creation of the early and middle Miocene crust of the Komandorsky Basin. Older, probably Cretaceous, Pacific oceanic crust of Aleutia and western fragments of the Shirshov Ridge were presumably swept into a north Kamchatka-south Koryak SZ bordering the western side of the Basin (Baranov et al., 1991; Hochstaedter et al., 1994; Park et al., 2002)

The relations noted above are drawn upon to conjecture that Bowers and Shirshov arc systems are not exotic to the Bering Sea Basin region but rather formed there in the early Tertiary in response to plate-boundary-driven tectonism of the far north Pacific rim and offshore areas. Although subduction continues beneath much of the length of the Aleutian Ridge, subduction beneath Bowers and Shirshov ridges waned and ended in the Oligocene or early Neogene. This inference is based on the 1000–2000 m depth of ridge crest subsidence (Dietrick et al., 1977), the Oligocene age of recovered shallow water taxa from the crest of Shirshov Ridge (Gladenkov, 1990), the radiometric age (minimum) of late Oligocene of arc fragmental material recovered from the southern end of Shirshov Ridge (Cooper et al. 1987a), and the early Miocene inception of spreading in Komandorsky Basin (Muzurov et al., 1989; Baranov et al., 1991).

2.5.3 Issues. As discussed earlier, lacking definitive age and paleolatitude controls, the formative place and age of initial arc activity for Shirshov and Bowers Ridges cannot be established. If the ridges are mostly Mesozoic igneous accumulations overlain by Cenozoic deposits, then these arc massifs could have formed in the north Pacific Basin well south of the Bering Sea Basin and thus would be exotic to it. If the igneous basement of these ridges is Cretaceous in age and exhibit OIB geochemical characteristics, then their formation as part of the NW extension of the north Pacific's Hawaii-Emperor seamount chain can also be hypothesized (Steinberger and Gaina, 2007).

If they formed in the Eocene, then they did so within the setting of the Bering Sea Basin because outboard of them construction of Aleutian Ridge appears to have gotten underway in the middle Eocene or a little earlier (Jicha et al., 2006). Reconstructing the tectonic setting and deciphering the cause for the formation of the Aleutian Bering Sea region and its subsequent evolution thus requires at the least accurate information about when Bowers and Shirshov began to formed and when arc volcanism ceased along them.

2.6 The Aleutian Ridge and the KAT Connection

2.6.1 Observations. The critical tectonic element of the KAT connection is the westward extension of the Aleutian sector of the PAC/NAM boundary to the Kamchatka SZ, which is either the eastern edge of the Okhotsk microplate (block) or a tectonically simpler southward striking continuation of the PAC/NAM plate boundary (Fig. 3; Riegel et al., 1993; Bourgeois et al., 2006; Pedoja et al., 2006). In its curving path across the north rim of the Pacific Basin, the ~2200-km-long Aleutian Ridge extends to within ~100 km of Kamchatka (Figs. 7 and 8). The width of the ridge ranges from ~250 to 75 km, narrowing west of about 180 deg. longitude and markedly so west of Near Pass (172 E) across the Komandorsky sector of the Aleutian Ridge (Fig. 8).

In relief, the ridge rises ~7 km above the generally smooth, flat, and thickly (1–2 km) sedimented floor of the Aleutian Trench to the south and 3–4 km above the abyssal plain of the Bering Sea Basin to the north. The lateral continuity of the ridge's arc massif is disrupted in the forearc by large NNE-SSW-trending submarine canyons, and along the crest of the ridge by tectonically controlled between-island passes and ridge-axis elongated summit basins (Figs. 7 and 8).

The Aleutian Ridge is an arc construct of Cenozoic age flanked to the south, and presumably to the north, by older oceanic crust. Although not known to include pre-Eocene crust, the ridge buds westward from the tip of the Alaska Peninsula underlain by continental basement of late Paleozoic and Mesozoic age (Fig. 1A: Burk, 1965; Nokleberg et al., 1994; Vallier et al., 1994). Beneath its structural summit the arc massif is 30–35 km thick, an

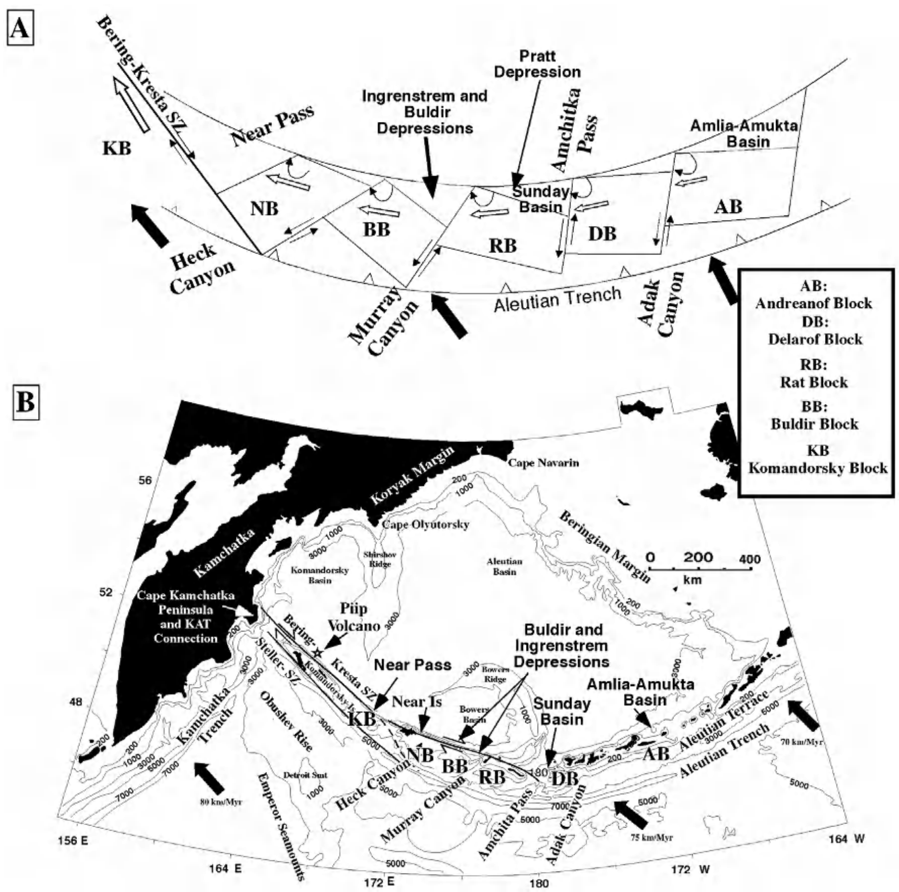

Figure 7. Geographic and tectonic setting maps for Aleutian Ridge. Top panel (A) is diagrammatic model of clockwise rotation and westward translation of blocks of the arc massif moving toward the Kamchatka subduction zone. Rotating blocks leave trail-edge basins along their northern sides (e. g. Amlia-Amukta Basin, Sunday Basin, Buldir Depression) and large, left-lateral tear canyons along their eastern flanks (e. g., Adak, Murray, and Heck Canyons). The far western or Komandorsky block is effectively moving to the NW with the Pacific plate. Bottom panel (B) shows that via the right-lateral Bering-Kresta shear zone, which runs along the base of the Bering Sea side of the Komandorsky block, westward moving blocks of the Aleutian massif are guided toward collision with Kamchatka at the Kamchatka-Aleutian or KAT tectonic connection, which is presently located at the Cape Kamchatka Peninsula.

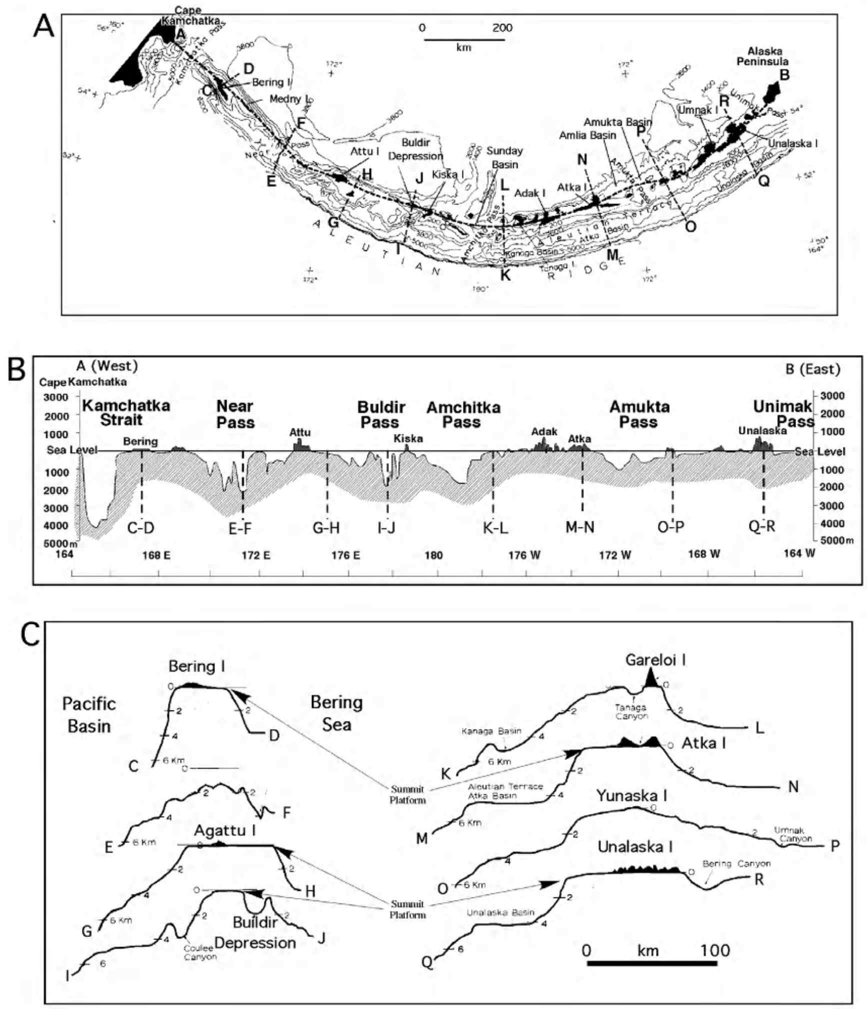

Figure 8. (A) Index map showing locations of longitudinal (W-E along-ridge) and transverse (S-N across ridge) bathymetric profiles of the Aleutian Ridge. Longitudinal profile (B) shows, in the westward direction of increasing obliquity of convergence, increasing deepening of between-island passes separating the major CW and westward translating blocks of the arc massif (see Figure 7). Transverse profiles (C) display the westward narrowing of the width of the arc massif, in particular west of Amchitka Pass (profile I-J). Both physiographic measurements are consistent with the GPS-documented determination that westward blocks of the arc massif move with increasing speed toward the Kamchatka subduction zone.

unusual thickness for an intra-oceanic arc (Fig. 9; Shor, 1964; Grow, 1973; Fliedner and Klemperer, 1999; Holbrook et al., 1999, Lizarralde, et al., 2002; Shillington, et al., 2004; Takahashi et al., 2007; Calvert et al., in press). Arc crust thins seaward beneath the submerged forearc and landward below the backarc slope descending toward the Bering Sea Basin (Fig. 9).

The oldest radiometrically-documented age for arc volcanic material is middle and late Eocene (Vallier et al., 1994; Jicha et al., 2006). Late to middle Eocene fossiliferous sequences are widely exposed in the Aleutian and Komandorsky Islands (Scholl et al., 1987; Vallier et al., 1994). The report of early Eocene or late Paleocene beds from the Komandorsky Islands (Shmidt, 1978; Rostovtseva and Shapiro, 1998) is based on a poorly identified planktonic foraminifera fauna (K. McDougall, written communication, 2006). The linked paleomagnetic stratigraphy is permissive of the older Tertiary ages (Minyuk and Gladenkov, 2007). However, the basalt and andesite flows underlying the basal sedimentary units have middle and late Eocene K-Ar ages (45–37 Ma; Tsvetkov, 1991). If these dates are correct, and the "flows" are not sills or lie beneath a thrust, basement cannot be overlain by the fossiliferous beds of older early Eocene or late Paleocene age.

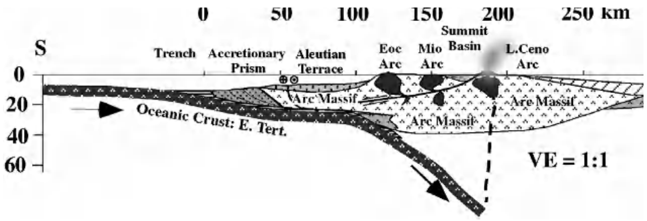

Figure 9. Idealized cross-section through the Aleutian Ridge showing major structural and tectonic units. Frontal accretionary prism is late Cenozoic in age and consists principally of turbiditic sediment transported westward along the trench axis from Alaskan drainages. The basins of the deep-water Aleutian Terrace and the ridge's summit area are late Cenozoic in age. Since at least the late Eocene the axis of arc volcanism has shifted progressively northward toward the Bering Sea Basin or backarc. Information is from various source but in particular from Shor (1964), Grow, 1973, Scholl et al. (1987), Ryan and Scholl, (1989, 1993), Vallier et al. (1994), Fliedner and Klemperer (1999), Holbrook at al. (1999), and Lizarralde et al., 2002.

The ^{39}Ar-^{40}Ar determination of Jicha et al (2006) dates the Aleutian Ridge's oldest securely known volcanogenic material at ~46 Ma, or middle Eocene. The sample was dredged immediately west of Kiska Island from the submerged eastern wall of Murray Canyon (Fig. 7). This age closely matches the oldest K-Ar dated lava reported by Tsvetkov (1991) from the Komandorsky Islands farther to the west. Initiation of the Aleutian SZ that produced these middle Eocene magmatic rocks must necessarily have been earlier. Because the start-out phase of arc growth is a voluminous outpouring across a broad front (see discussion in Jicha et al., 2006), it can be surmised that middle Eocene basement rock recovered from the crestal region of the Aleutian Ridge is not going to be significantly younger than the massif deeply buried beneath the ridge's forearc and backarc slopes, or the missing seaward sector, probably on the order of 60 km, of the arc massif removed by subduction erosion (von Huene and Scholl, 1991; Jicha et al., 2006; Scholl and von Huene, 2007). Thus the initiation of the new offshore Aleutian SZ is earlier than 46 Ma but most likely, unless the paleontologically-based Komandorsky early Eocene or late Paleocene ages are confirmed, not before ~50 Ma, in the late early Eocene.

Structurally, except for its far western or Komandorsky sector, from south to north the ridge in cross section is constructed of a frontal prism of accreted trench material of late Miocene and younger age bordering a submerged forearc of arc crust of Eocene age. The submerged forearc basement is overlain by dredge-recovered samples of Oligocene and younger slope-conforming sediment and, beneath the deep water (3500–4500 m) Aleutian Terrace, basin-filling sequences of late Miocene and younger beds (Figs. 8 and 9; Scholl et al., 1987). At the summit of the ridge, island exposures of the middle Eocene igneous massif are intruded by late Eocene, Neogene, and younger bodies and unconformably overlain by lava and sediment. The greater width of the summit of the ridge is truncated by a wave-beveled surface, the summit platform, cut across Miocene and older rocks (Fig. 8). During the past ~5 Myr, the arcuate alignment of dormant and active centers of the Aleutian volcanic arc has been constructed generally along the northern edge of summit platform. North of the ridge crest the sediment-covered surface of the Eocene basement descends toward the abyssal floor of the Bering Sea (Fig. 9; Scholl et al., 1987).

The Komandorsky section, above which Bering and Medny Islands rise, is narrower (~75 km), presumably lacks a frontal prism of accreted debris, and lacks active or dormant summit volcanoes (Fig. 7). However, just beyond the northern or Bering Sea base of the sector, Piip Volcano has built nearly to sea level from a graben-like depression. The depression borders to the north the principal trace of the Bering-Kresta shear zone that separates crust of the Komandorsky Basin from that of the Aleutian Ridge (Fig. 1B, Plate 1, and Fig. 7; Baranov et., 1991; Yogodzinski et al., 1993, 1994, 1995, 2001; Geist and Scholl, 1994). Piip appears to be a "bleeding" transform construct.

Tectonically, the Aleutian arc massif is arranged along the far northern sector of the PAC/NAM boundary (Fig. 1B). With respect to the trend or strike of the ridge, from east to west plate convergence is NW and orthogonal near the Alaska Peninsula and increasingly oblique westward (to the left or west of NW). West of the Near Islands, relative motion is highly oblique to virtually strike slip along the Komandorsky sector (Vallier et al., 1994; Fig. 7). Based on regional studies of bathymetric, seismic, paleomagnetic, and geologic data, the width of the ridge involved in ridge-parallel or longitudinal shearing broadens to the west, in particular west of Amchitka Pass and then more so west of Near Pass where the right-lateral Bering-Kresta shear zone passes along the northern base of the Komandorsky sector (Figs. 1B and 7; Cormier, 1975; Geist et al., 1988; Ryan and Scholl, 1989; Geist and Scholl, 1994).

GPS and seismic motion studies appear to document that the major plate boundary is now the Bering-Kresta shear zone (Avé' Lallemant and Oldow, 2000; Gordeev et al., 2001; Steblov, et al., 2003). However, differential right-lateral shearing occurs across the width of the Komandorsky sector defining the Komandorsky shear zone of Freitag et al. (2001). The impact of the collisional process at the KAT connection is exhibited by a horizontal gradient of vertical tectonism at Cape Kamchatka Peninsula that increases southward away from the Bering Kresta shear zone and toward that of the western most reach of the Aleutian Trench and the Steller SZ

(Fig. 1B, Plate 1 and Fig. 7; Gaedicke et al., 2000; Freitag et al., 2000). Gaedicke et al. (2000), McElflesh et al. (2002), and Kozhurin (this volume) document that the kinematics of arc-arc collision across the north-south width of the KAT connection is as expected, complicated.

2.6.2 Interpretations. Abandonment of the Beringian-Koryak margin plate boundary circuit required that a new one be established between the Alaska Peninsula and northern end of the Kamchatka Trench—i.e. the KAT connection. It has also been hypothesized that the Eocene Aleutian Ridge and underlying subduction zone only extended westward to roughly the position of Shirshov Ridge, which, it is exploratively argued below, evolved coevally with or soon after arc magmatism began to construct the new Aleutian Ridge (Scholl et al., 1989, 1992; Yogodzinski et al., 1995; Lizarralde et al., 2000; Fig. 10). Tectonic connectivity to the Kamchatka SZ was evidently establish by a long, NW-striking transform boundary (Lonsdale, 1988), probably one slightly underthrust orthogonally similar to the modern Queen Charlotte transform shear system of British Columbia (Yorath, 1987; Gabrieles et al., 2006) and the Andaman sector of the northern Sumatra transform system (Subarya et al., 2006).

Oblique convergence has fragmented the arc massif into clockwise rotating blocks and narrower, arc-subparallel crustal slivers (Geist et al., 1988; Geist and Scholl, 1992). Oblique convergence has also acted to progressively transport the blocks northwestward toward the Kamchatka SZ. The Komandorsky Islands of Bering and Medny, for example, have on geologic grounds (Rostovtseva and Shapiro, 1998), the narrow width of the Komandorsky arc massif, and the Bering Sea location of the Bering-Kresta shear zone, been identified as the former Pacific forearc of the Near Islands sector displaced ~500 km westward (Plate 1, Figs. 7 and 9). Allowing that westward transport of Aleutian terranes has been underway since the Eocene, then arc-arc collision at the KAT connection was inevitable (e.g., Watson and Fujita, 1985; Zinkevich et al., 1985; Geist and Scholl, 1994; Seliverstov, 1998; Gaedicke et al., 2000; Freitag et al., 2001).

Expanding on the speculative lead of Vallier et al. (1987, 1992, 1994, 1996), it is tempting to suppose that a rapid phase of breakup and fragmentation of the western sector of the Aleutian arc massif and movement of blocks toward the Kamchatka SZ was initiated by the early Miocene oblique entrance of high bathymetric relief into the western sectors of the Aleutian Trench (Fig. 1A, Plate 1, and Fig. 10B). Some of the tectonizing relief remains in the northwestern corner of the Pacific basin, for example, the unsubducted section of Stalemate Ridge, the long-deceased Kula/Pacific spreading center north of the ridge, groups of adjacent seamounts between them (Plate 1), and possibly a more northerly trending line of older and either subducted edifices of the Emperor Seamounts or at the formation of the Aleutian subduction zone trapped and abandoned in the Bering Sea Basin (Steinberger and Gaina, 2007).

Other tectonic consequences of obliquely underthrusting relief would have been shearing and faulting of the oceanic crust seaward of the trench and rapid tectonic erosion of the submerged forearc (Vallier et al., 1996; Mortera-Gutiérrez et al., 2003). Crustal fracturing of the underthrusting plate and strong coupling with the base of the arc massif may have contributed importantly to moving the principal transform boundary from the Aleutian Trench and forearc to the backarc setting of the Bering-Kresta shear zone (Vallier et al., 1994). Such a circumstance could also have led to tearing away the Pacific plate of the north Pacific Basin from it's subducted extension residing beneath the Komandorsky Basin. Tearing would have promoted asthenospheric upwelling and spreading in the basin that got underway in the early Miocene (Baranov et al., 1991).

Because the relative plate motion between the Pacific and North America plates appears to have changed little since the late Eocene (Engebretson et al., 1984, 1985; Lonsdale, 1988; Cande et al., 1995; Norton, 1995), it is presumed that the strike of the connecting Komandorsky transform has remained much the same during the past ~45 Myr. Modern GPS and teleseismic data document that transport of Aleutian terranes toward the KAT connection is presently underway (Avé' Lallemant and Oldow, 2000; Gordeev et al. 2001; Steblov, et al., 2003; Cross and Freymueller, 2007).

As shown on Figure 10B, the southward extrusion of Alaska and Bering shelf crust as the tectonic forward sector the NPRS may have, with respect to Kamchatka, moved the KAT connection progressively southward with time, possibly from Karaginsky Island via Ozernoy Peninsula to reach Cape Kamchatka Peninsula (Fig. 1A and Plate 1).

2.6.3 Issues. A geologic connection between the present trench-separated onshore Cape Kamchatka Peninsula and the offshore Komandorsky Islands has long been postulated (Markov et al., 1969; Zinkevich et al., 1985; 1987; Watson and Fujita, 1985, Scholl et al., 1989; Zonenshain et al., 1990; Baranov et al., 1991; Alexeiev et al., 2006). Although Eocene and younger Tertiary sedimentary units are comparable, igneous basement of Late Cretaceous age is widely exposed on the Kamchatka Peninsula (Zinkovich et., 1985; Fedorchuk et al. 1991; Zinkovich and Tuskanov, 1992; Chekhovich et al, 2006, Chekhovich and Sukhov, 2006) but unreported from the Komandorsky Islands. The oldest reported igneous basement rock on Bering and Medny Islands (Plate 1 and Fig. 8) is middle Eocene or perhaps somewhat older (Shmidt, 1978; Tsvetkov,1991; Rostovtseva and Shapiro, 1998; Minyuk and Gladenkov, 2007). If the similarity of stratigraphic sections is to be interpreted as documenting arc-arc collision at the KAT connection, then either the existence of Cretaceous basement must be demonstrated for the Komandorsky sector of the Aleutian Ridge or the thrust offloading of its stratigraphic sequence onto older Kamchatka basement.

Although no igneous rocks older than middle Eocene have been identified anywhere along the Aleutian Ridge (Tsvetkov, 1991; Vallier et al., 1994; Jicha et al., 2006), perhaps the most profitable exposure to search for Cretaceous basement is the exceptionally precipitous trench slope south of Bering Island (Plate 1 and Fig. 8). Finding rocks of Cretaceous age here would falsify most perceptions of the evolution of the Aleutian Ridge and the KAT connection (in particular the author's), but not the Kronotsky arc collision concept of Alexeiev et al. (2006) that generically links the Komandorsky sector of the Aleutian Ridge with the crust exposed at Cape Kamchatka Peninsula.

Alternatively, the seaward projection of the Cape Kamchatka Peninsula can be viewed as physiographically recording past collisional events that involved the subduction of incoming Komandorsky basement crust and much of its sedimentary carapace. Subduction of arc crust beneath Kamchatka could have formed the cape via crustal thrusting or underplating of the Cretaceous Olyutorsky arc massif by younger Aleutian crust (Zonenshain et al., 1990; Seliverstov 1998; Stavsky et al. 1990, Worrall, 1991; Zinkevich and Tsukanov, 1992; Baranov et al., 1991; Sukhov et al., 2004, and Garver et al., 2000; Garver et al. 2004; Chekhovitch and Sukhov, 2006). Arc subduction, however, also caused crustal shortening inboard of the peninsula demonstrated by the Kumroch thrust belt (Shapiro et al., 1984; Tsukanov and Zinkevich, 1987; Geist and Scholl, 1994). An example of the collisional style of tectonism exhibited at the KAT connection is expressed where the Cocos Ridge orthogonally enters the Middle America SZ at Costa Rica. Underthrusting is manifested by the coastal uplift of Late Cretaceous igneous basement and farther inboard the Fila Costeña, a growing fold belt of Eocene and younger marine and non-marine continental margin deposits (Fisher et al., 2004).

3. ESTABLISHING THE KAT CONNECTION

3.1. Review of Basic Concepts

The most commonly described plate-tectonic scenarios for the origin of the Aleutian SZ and thus the KAT connection are:

(1) Terrane accretion along the northwestern most or north Kamchatka-Koryak margin of the Pacific Basin tectonically occluded this subduction zone and forced the offshore formation of the Aleutian SZ and the captured of the Pacific-born Shirshov and Bowers Ridges in the newly formed Bering Sea Basin
(2) Plate-boundary coupling and drive in the northeastern or British Columbia and Alaska sector of the north Pacific margin caused extrusion of Alaska and Bering shelf continental crust westward toward the plate boundary of the Beringian margin and forced the in-place formation of the offshore Aleutian-Bowers-Shirshov subduction zone system, and
(3) A combination or coupling of the plate-boundary forces arising from occlusion and extrusion buckling of the sector of Pacific plate then occupying the northwestern Pacific to form the Aleutian SZ directly seaward and on strike with the Alaska SZ. The Shirshov and Bowers SZs formed at the same time or shortly after within the setting of the newly created Bering Sea Basin.

Primarily because verifying age and formative paleolatitude information is lacking for the arc massifs of Shirshov and Bowers Ridges and the igneous oceanic crust of the Aleutian Basin, is it not possible to select the model that best explains what is unavailable as critically constraining observations. Nonetheless, known and emerging information identifies the early and middle Eocene as a time of enhanced tectonism in the north Pacific Basin and along the periphery of its rim.

For onshore and subshelf areas, the older and emerging evidence record:

1) the early to middle Eocene age of accretion or suturing of the Late Cretaceous-early Tertiary Olyutorsky arc to the northern Kamchatka-southern Koryak margin of NE Russia (Zonenshain et al., 1990; Garver et al., 2000; Garver et al., 2004; Chekhovich and Sukhov, 2006),
2) the early to middle Eocene wave-beveling and subsidence along the length of the Beringian margin of a former coastal mountain system, the Beringian margin fold belt, constructed of shallow marine and nonmarine Jurassic, Cretaceous, and earliest Tertiary sequences (Fig. 6; Marlow et al., 1987, Worrall, 1991).
3) the middle Eocene recording of significant counterclockwise rotation of crustal blocks in western Alaska (Hillhouse and Coe, 1994), and
4) early to late Eocene prominent movement along the family of major, right-lateral strike-slip faults of western Alaska and their curving connections to those of SE Alaska and northern British Columbia (Figs. 1B, 2, 3, 10A and 10B); Hickman et al., 1990; Plafker et al., 1994; Ridgway et al., 1997; Cole et al., 1999; Miller et al., 2002; Gabrieles et al., 2006).

For the offshore north Pacific, emerging and older observations record:

1) the early middle Eocene age of the birthing of the Aleutian SZ (Jicha et al. 2006),
2) in the northeastern Pacific, the early to middle Eocene subduction of the Resurrection plate beneath the rim of the Gulf of Alaska and associated continental magmatism and structuring (Haeussler et al., 2003; Farris et al., 2006),
3) the early to middle Eocene record of a prominent reorientation of north Pacific spreading centers (Chrons 24–23; Engebretson et al. 1984, 1985; Lonsdale, 1988; Atwater 1989; Atwater and Severinghaus, 1989), and
4) the early to middle Eocene age of the bend in the Hawaiian-Emperor Seamount chain that presumably records mantle dynamics and/or possibly a change in motion of the Pacific plate with respect to North America (Tarduno et al., 2003; Steinberger et al., 2004; Andrews et al. 2006; Koppers and Staudigel, 2005; Sharp and Claque, 2006; Stock, 2006; Steinberger and Gaina, 2007).

The thematic spectrum and geographic sweep of onshore and offshore observations draw attention to the likelihood that the Aleutian SZ, and also those of the Bowers and Shirshov Ridges, came into existence as a consequence of the offshore focusing of convergent stresses directed extrusively seaward from the circum-north Pacific rim rather than landward by a prominent change in the northward motion of the Pacific plate. This inference prompts consideration of the possibility that the Aleutian SZ was forced into being as the collective consequence of middle Eocene subduction zone blockage along the northern Kamchatka-southern Koryak margin and coeval extrusion of Bering shelf crust outward and across the Beringian margin.

3.2. Exploring the Coupled Scenario

3.2.1 Phase 1, Subduction Zone Occlusion and Capture of Aleutia. The author favors the high-latitude origin and near-continent migration of the Olyutorsky arc complex described by Sukhov et al. (2004), and Chekhovich and Sukhov (2006). But with respect to the coupled model explored here, the distance and azimuth of arc migration are, in fact, not significant issues unless an early or middle Eocene accretion time is made impossible (Fig. 10A). Garver et al. (2000, 2004) established that suturing along Kamchatka began in the early Eocene and was completed by about ~52 Ma. Further to the north within the domain of the Bering Sea Basin, collisional occlusion occurred between ~45 and 50 Ma (Chekhovich and Sukhov, 2006). The jammed NE-SW-striking north Kamchatka-Koryak margin lies in proximity to the right-angle change in the strike of the Pacific margin at the Cape Navarin corner of the Pacific basin (Fig. 1A and 2). The structural buttress of this corner may have limited the northward travel of the Olyutorsky arc complex.

As envisioned by many authors, clogging of this sector of subduction zone forced the northwest moving Pacific plate to establish a replacement subduction zone —the Aleutian SZ—seaward of the blocked one and to also establish a new plate boundary connecting the Alaska and Kamchatka SZs (Fig. 2; see overviewing discussions of Scholl et al., 1992 and Garver et al., 2000). The driving force creating the Aleutian SZ at ~50 Ma and its connection to Kamchatka arose from continuing slab pull beneath the Alaska and the Kuril-Kamchatka margins. These forces applied a horizontal, NW-SE oriented most-compressive axis (S_1) to the sector of oceanic crust lying offshore (SE) of the tectonically encumbered north Kamchatka-Koryak SZ. Seaward step-out of the plate boundary to the Aleutian SZ relaxed the stress field and captured the oceanic crustal area of Aleutia, probably a sector of the Kula plate, and attached it to the North America plate (Marlow and Cooper, 1983; Scholl et al., 1986). It is presumed that trench occlusion and subduction stoppage was not geologic "instantaneous" but occurred over a period of several million years. Capture was likely attended by slab detachment and crustal heating inboard of the stopped north Kamchatka-Koryak SZ and possibly also along the Beringia margin. The Beringian margin was effectively abandoned as the principal trace of the PAC/NAM boundary but continue to accommodate continued outflow of the NPRS.

It is significant that the Aleutian SZ formed off the Alaska Peninsula on-strike with the SW-trending Alaska SZ (Figs. 2 and 10A). Formation of the new subduction zone just here may have been conditioned by a focusing of buckling forces at the prominent change in trend of the margin from the SW strike of the Alaska Peninsula to the NW strike of the Beringian margin. Focusing would have been augmented by extrusion (see below) of Alaskan and Beringian crust toward this margin. Possibly crucial to the seaward positioning of the Aleutian SZ was the existence off the Alaska Peninsula of a west-trending fracture zone offsetting the N-S magnetic fabric of the oceanic crust of Aleutia then occupying the northwestern most corner of the Pacific Basin (see discussions in Scholl et al., 1992, 1994).

An equally important matter concerns identifying the north Pacific spreading system that generated the N-S magnetic fabric of the captured Aleutia. If the anomaly pattern is early Cretaceous in age it was likely created along a sector of the Izanagi-Farallon spreading center later captured by the Kula plate at the time of its formation in the Late Cretaceous at ~83 Ma (Cooper et al., 1976a, b; Engebretson et al, 1984; Scholl et al., 1986) If the crustal fabric of Aleutia is latest Cretaceous

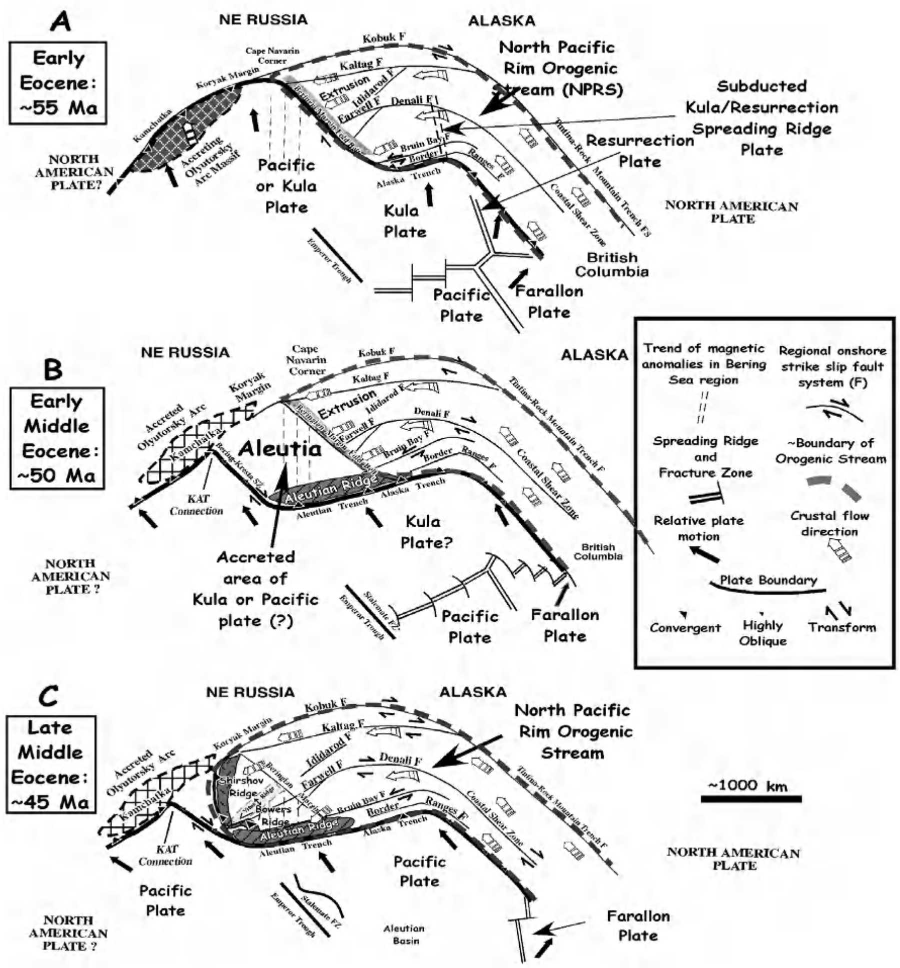

Figure 10A. Diagrammatic drawings of the coupled or merged scenario for the origin of the Aleutian-Bering Sea region and the establishment of the KAT tectonic connection between the Kamchatka and Aleutian subduction zones. Top cartoon (A) sketches the early Eocene setting of the high north Pacific mapping in the northeastern Pacific the CCW flow of the north Pacific rim orogenic stream (NPRS) that extrudes across the Beringian plate margin, the eastward and northward subduction of the Resurrection plate and its trailing Kula/Resurrection spreading ridge, and in the northwestern Pacific the accretion of the Olyutorsky arc complex to Kamchatka-Koryak margin. A pattern of N-S magnetic anomalies, possibly generated at the Kula/Resurrection ridge in the Late Cretaceous/Early Tertiary, lies in the northwestern most region—the Cape Navarin Corner—of the Pacific Basin. (B) Accretion of the Olyutorsky arc jams the Koryak subduction zone and forces the offshore formation of the Aleutian subduction zone as a seaward continuation of the older Alaska subduction zone. (C) Continued extrusion of the NPRS toward the Beringian margin forces the in-place formation of the offshore subduction zones of Shirshov and Bower Ridges. Formation of the Aleutian-Bering Sea region is thus exploratively linked to the consequence of the accretion of an exotic arc terrane, the Olyutorsky arc, to the NW corner of the Pacific Basin and, from its NE corner, the virtually simultaneous plate boundary driven, SW push out of the NPRS toward the Bering Sea region.

and earliest Tertiary in age, then it may have been generated in the wake of the eastward migrating Kula-Resurrection spreading system (Fig. 10A; Haeussler et al., 2003).

3.2.2 Phase 2, Extrusion of the North Pacific Rim Orogenic Stream (NPRS). The coupled model posits that in the middle Eocene somewhat after ~50 Ma an episode of forceful expulsion of the leading Alaska and Beringian crust of the NPRS occurred toward the Beringian margin (Redfield et al., in press). The Tectonic outflow forced the offshore creation of the west-facing Shirshov and northeast-facing Bowers SZs within the Aleutia terrane captured in the Bering

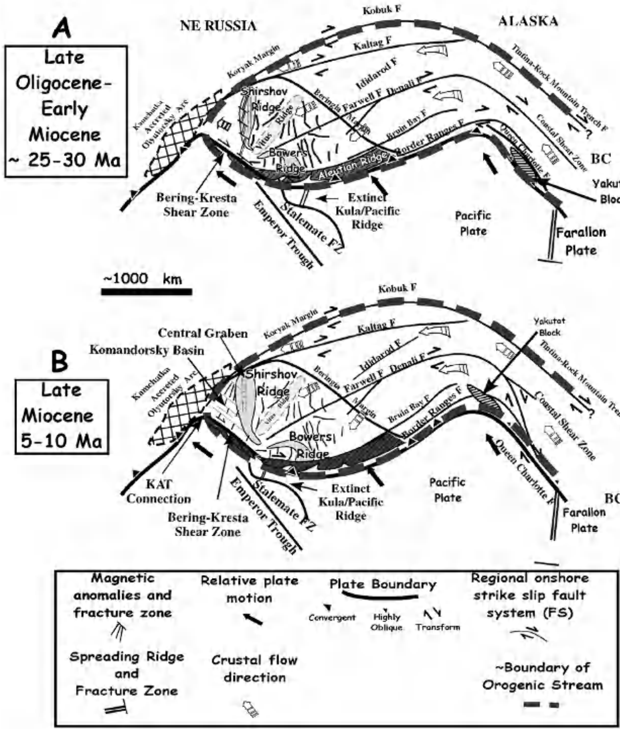

Figure 10B. For unknown reasons, probably in the late Oligocene or early Miocene arc volcanism ended at the Shirshov and Bowers subduction zones and the arc massifs of both ridges subsided below wave-base erosion to depths of 1500-2000 m. Cessation of subduction at these ridges transferred the SW boundary of the north Pacific rim orogenic stream to the Aleutian subduction zone and thus to include the whole of the Bering Block of Mackey et al. (1997) and Fujita et al. (2002) (Fig. 3). This transfer would have allowed collisional tectonism at the KAT connection to move southward with respect to eastern Kamchatka, perhaps from Karaginsky Island to Ozernoy Peninsula to reach Cape Kamchatka Peninsula.
The top diagrammatic drawing (A) shows that beginning ~20 Ma backarc spreading in a direction parallel to the Bering-Kresta shear zone commenced in the Komandorsky Basin and presumably replaced older crust of Aleutia, which was subducted westward beneath northern Kamchatka (Baranov et al., 1991; Hochstaedter et al., 1994). Spreading is shown initiating along the Shirshov forearc and linked to the ridge's longitudinal extension and fracturing (Baranov et al., 1991). Spreading may have been initiated by the sinking of warmed and eclogized Pacific crust hanging below the occluded and Eocene abandoned SZ of the Kamchatka-Koryak margin (Fig 10A). Adopting the views of Vallier et al. (1992, 1996), diagrams (A) and (B) conjecture that the oblique entrance of high bathymetric relief (Plate 1) into the western sector of the Aleutian subduction zone disrupted the arc massif and began the westward transport of CW rotating blocks toward the Kamchatka subduction zone, a process that may have contributed to the opening of the slab window beneath the Bering-Kresta shear zone that remains a residual manifestation of Miocene spreading and crustal replacement in Komandorsky Basin (Yogodzinski et al. 1995). Along the opposite or NE margin of the Pacific Basin the Yakutat block moving northward with the orogenic stream enters the eastern end of the Alaska subduction zone and contributes significantly to tightening the bend of the so-called Alaska "orocline" and enhance extrusion of western Alaska and Bering crust toward the Aleutian subduction zone (Eberhart-Phillips, 2006; Redfield et al., in press).

Sea. This conjecture means that the two ridges are neither exotic terranes nor part of the Olyutorsky arc complex that jammed the north Kamchatka-Koryak SZ hypothesized to have nucleated the Aleutian SZ.

The principal, most compressive, NW-SE oriented stress direction (S_1) that forged the Aleutian subduction was coupled to a SW-NE oriented intermediate axis (S_2) of horizontal stress generated by extrusive crustal push-out along the Beringian margin. Establishment of the Aleutian SZ rotated the principal horizontal stress axis to face the Beringian margin, thus favoring the formation of the Shirshov and Bowers SZs. Although critical age information is lacking to confirm the initial Eocene creation of their arc massifs, it is assumed they formed tectonically immediately after that of the Aleutian SZ if not virtually co-tectonically.

The N-S strike of Shirshov Ridge sub-parallels the magnetic fabric of Aleutia, a circumstance that may have conditioned the trend of the ridge's subduction zone. Alternatively, the subduction zone may have nucleated along the northern section of Stalemate Ridge (fracture zone) or the older Pacific-Kula plate boundary of the Emperor Trough (Fig. 1A and Plate 1; Grow and Atwater, 1970; Mammerickx and Sharman, 1988; Lonsdale, 1988; Norton, 1995, in press) or possibly the NW extension of the ridge of the Emperor Seamounts (Steinberger and Gaina, 2007). In the middle Eocene one or more of these north-trending crustal fault zones likely projected into the area of the present Aleutian Basin (Scholl et al., 1986, 1992). No remnant remains of the Shirshov Trench, which was presumably subducted westward beneath the northern Kamchatka margin when in the early Miocene rifting of Shirshov Ridge accompanied spreading and the opening of Komandorsky Basin (Baranov et al., 1991).

Thus, in the middle Eocene, the role of the Aleutian SZ is envisioned as mostly absorbing the northwestward moving oceanic plate (Kula or Pacific) whereas the tectonically kindred Shirshov and Bowers SZs provided, within the tectonic framework of the North America plate, most of the crustal take up for its southwestwardly extruding at the leading edge of the laterally moving NPRS (Figs. 2, 3, and 10A). Also consumed at these subduction zones were areas of the accreted Aleutia terrane equivalent spatially to the SW advance of the orogenic stream.

3.2.2.1 Mechanics and Kinematics of Extrusion. A kinematic requirement for the outflow of crust toward the Shirshov and Bowers SZs is that the regional strike-slip faults of western Alaska extended seaward and to the southwest to the edges of the Beringian shelf and across it and the oceanic crust of Aleutia to reach the northern and eastern ends of Shirshov and Bowers SZs, respectively (Fig. 10A). Trench rollback along the Aleutian and Shirshov SZs would have assisted, perhaps significantly so, crustal expulsion toward them. Presumably, rollback of the Bowers SZ opened Bowers Basin (Cooper et al., 1992).

The extrusion model also requires that any track or triangular-shaped gore of extruding crust radiating outward from central Alaska toward the Bering Sea is bordered by strike slip faults exhibiting conjugate or opposed directions of relative offset (i.e., right vs. left lateral). The sense of displacement across the conjugates can reverse if the expulsion rate of a crustal gore is retarded or increased over a neighboring one (Tapponnier et al., 1982; 1986).

The newly formed Shirshov Ridge, as diagrammatically shown on Figures 2 and 10A, probably connected to the south with the western end of the northwestward curving Aleutian SZ (Scholl et al., 1989; 1992; Cooper et al., 1992). During the past 45 Myr the western or Komandorsky terminus of the arc massif has been transported westward at least 1000–1500 km from its Eocene position (Scholl et al., 2003). Restoring the transport blocks to the east roughly relocates the ridge's western end and connection to Shirshov Ridge between longitude 175 deg E and 180 deg, i.e., near present Kiska Island (Plate 1, Figs. 7, and 8). As diagrammed by Cooper et al. (1992), the conjectured confluence of the Aleutian and Shirshov SZs would have been tectonically unstable. So it is supposed the northeast or Alaska-facing Bowers SZ in part formed to resolve instabilities. Once initiated, the offshore Aleutian-Bowers-Shirshov system of subduction zones was completed.

The opposite facing Shirshov and Bowers SZs presumably also evolved to handle differentially outflowing tracks of Alaska and Beringian crust. The track of extruding crust accommodated by the Shirshov SZ evidently extended southward from the right-lateral Kobuk fault at the southern base of the Brooks Range southward to included the Kaltag, Iditarod, and Denali-Farwell fault systems of central Alaska (Figs. 1B, 2, 10A and 10B). Bowers SZ perhaps served mainly to accommodate seaward crustal push-out south of the Denali-Farwell system to at least the Bruin Bay fault of the Alaska Peninsula. In the early Tertiary this fault was an active left-lateral shear that offset older material at least 65 km prior to the early Miocene (Fig. 10A; Dettermen and Reed, 1980). The Bruin Bay fault remains closely linked to an active, full-crustal left-lateral shear zone striking northeast along the axis of southern Cook Inlet (Fig. 1A; Fisher et al., 2006).

As diagrammed on Figs. 10A and 10B, a southern, NE-SW striking transform fault connected Shirshov and Bower SZs. The separation between them would have increased as extrusion continued and also as backarc spreading formed Bowers Basin to the south and the subsurface Vitus ridge to the north (Cooper et al., 1992). Alternatively, or in combination with backarc spreading, separation could have been aided by differential outflow of Alaska crust, much like that envisioned and modeled by Tapponnier et al. (1982, 1986) for southeast Asia. For example, if the Iditarod and Denali-Farwell fault systems extended seaward to the posited Shirshov-Bowers transform, a faster relative rate of extruding crust north of them would have then favored a growing left-lateral offset (Figs. 2 and 10A; Scholl et al., 1992; Redfield et al., in press). The mechanics of this notion requires that after its capture, the crust of Aleutia was sheared in place by differentially extruding gores of Alaskan crust bordered by crust penetrating, regional-scale strike-slip faults.

3.2.2.2 Tectonic Significance of the Beringian Fold Belt. The deeply eroded and subsided Beringian margin fold belt running the length of the seaward edge of the Beringian shelf apparently documents that in the Late Cretaceous and early Tertiary the Beringian margin was the Pacific Basin-North America plate boundary linking the subduction zones of southern Alaska and the Koryak-Kamchatka margin (Figs. 6 and 10A). Before its demise, the Beringian margin fold belt records that the margin was shortened across its width. A coastal mountain system was likely created (Worrell, 1991). The orientation of the Beringian margin, if not greatly different from now, was subparallel to the azimuth of transform motion between the Pacific or Kula and the North America plates. As a consequence the margin was longitudinally sheared along its length by a wide zone of right-lateral wrench faults (Worrell, 1991; Figs. 1B and 6). Building of the Beringian fold belt may in part reflect the consequences of margin-parallel shearing (Worrell, 1991), but it is thought to principally record the impact of SW-directed crustal extrusion against the dominantly transform, probably highly obliquely underthrust margin (Scholl et al. 1992).

Onshore, seaward extrusion of the NPRS was attended by rapid motion along the family of strike slip faults tracking through western Alaska, in particular the Kobuk, Kaltag, Iditarod, Denali, Farwell, Castle Mountain and Bruin Bay fault systems (Patton and Hoare, 1968; Tolson, 1987; Worrell 1991; Parry et al., 2001; Miller et al., 2002; Plafker et al., 1994). Eastward this ensemble of faults curve south to tectonically connect with the margin-parallel Tintina-Rocky Mountain Trench, Coastal shear zone, and Queen Charlotte shear systems of the Canadian Pacific margin. In the early and middle Eocene, the most inboard of these shear zones, the Tintina-Rock Mountain Trench fault system, was in rapid motion (Figs. 1B, 10A; Gabrieles et al., 2006). In effect, during the formation of the Beringian margin fold belt the lateral motion of the NPRS was accommodated by crustal extrusion across the dominantly transform Beringian margin, some of the motion of which was stored as shortening strain in the fold belt (Figs. 6 and 10A).

A modern-day example of an extrusion-forged Beringian-style fold belt is that of the Alaska Peninsula, which is the present thrust-elevated southeastern edge of the Beringian shelf (Fig. 1A; Burke, 1965; Nokleberg et al., 1994; Gladenkov, 2006). Late Cenozoic thrusting and mountain building that constructed the peninsula may reflect a pulse of extruding Alaska-Beringian crust of the NPRS arising from the late Miocene movement of the Yakutat block through the eastern end of the Alaska SZ (Mackey et al., 1997).

A prominent example of a PAC-NAM transform boundary where the principal shortening stress is oriented normal to it is the San Andreas margin of northern and central California. Folding normal to the San Andreas fault zone built the California Coast Ranges during the past 5–6 Myr. Shortening is linked to the seaward push-out of the elevated crust of the Basin and Range of Nevada against a small component of convergence of the Pacific plate (Page et al., 1998; Thompson, 1999). The deformational workings of the California setting is similar to that proposed for the early Tertiary Beringian margin where extrusional outflow of the NPRS is envisioned as creating the Beringian margin fold belt even as the margin was the PAC-NAM boundary. The Queen Charlotte sector of the British Columbia is an additional example of a modern PAC-NAM transform margin exhibiting evidence that the principal horizontal stress is oriented normal to its trend, evidently caused here by a small measure of orthogonal convergence and underthrusting (Yorath, 1987; Gabrieles et al., 2006).

The demise and subsidence of the Beringian margin fold belt is viewed as signaling the shift of the leading edge of the NPRS from the Beringian margin to the offshore Aleutian-Bowers-Shirshov system. The middle Eocene shift times the transformation of Beringian margin to effectively a passive one characterized by many kilometers of subsidence. Trench rollback at Shirshov and the Aleutian Ridge probably significantly contributed to the rapid late Eocene and sustained formation of the large outer shelf basins of Anadyr, Navarin, and St George (Fig. 6).

3.2.2.3 Cause of Rapid Extrusion. An important question concerns what tectonic circumstance in the middle Eocene drove the Beringian margin seaward with sufficient force to buckle the offshore oceanic crust and create the subduction zones of Shirshov and Bowers Ridges? Rapid lateral mobilization of the NPRS westward around the Pacific's northern periphery may have been in response to subduction of the Kula-Resurrection spreading ridge eastward below the British Columbia margin (Figs. 2 and 10A; Haeussler et al., 2003). Ridge subduction opened a latitudinally wide slab window beneath this margin that swept inland and exerted an extra-regional heating, magmatic, and deformation impact over the western Canadian and U. S. Cordillera (Bradley et al., 1993, 2000; Haeussler et al., 2003; Farris et al., 2006; Gabrieles, et. al., 2006). In the early Tertiary, the northern reach of the Kula-Resurrection spreading ridge had earlier passed eastward beneath the width of southern Alaska (Fig. 10A). The consequent slab-window heated the Alaska interior across which the family of strike-slip faults radiates outward toward the Beringian margin (Figs. 1B and 2; Cole et al., 2006). Still earlier, in the earliest Tertiary, the eastward migrating ridge may have swept obliquely beneath this margin, possibly explaining the eruption there of early Eocene basaltic centers (54–49 Ma) (Davis et al., 1989).

Subduction of the Resurrection plate and its trailing Kula/Resurrection spreading center heated and magmatically intruded the crust across much of the width and length of the NPRS. Drawing on the suprasubduction zone deformational processes and mechanisms described for the north Pacific rim by Hyndman et al. (2005), Mazzotti and Hyndman (2005), and Mazzotti et al. (in press), a thermally weakened lower crust fostered a pulse of early and middle Eocene extrusion of coastal and interior crust toward the Beringian margin. The driving force was supplied by the NNE oblique underthrusting motion of the Resurrection plate beneath the British Columbia margin and, after its subduction at ~50 Ma, the NNW convergence of the Kula plate or its Pacific plate capturer beneath southern Alaska (Haeussler et al., 2003).

4. CONCLUDING STATEMENT

As lamented, the absence of constraining age and paleolatitude information for the major crustal bodies of the Aleutian Basin (i.e., Shirshov and Bowers Ridges and Aleutia), reigning uncertainties that a significant Eocene change in motion of the Pacific plate is signaled by the Hawaiian-Emperor bend, and the paucity of Beringian and western Alaska GPS data, combine to vex assessing the soundness of the Pacific rim, extrusion part of the coupled model. The extrusion component of the coupled model was nonetheless adopted to explore its ramifications for the evolution of the Aleutian-Bering Sea region and also to draw attention to investigations needed to both challenge and confirm leading but contrasting ideas about the origin and evolution of the KAT connection. Testing is in particular needed to evaluate the reality of the hypothesized NPRS (Redfield et al., in press), which is linked to the guiding concept of the orogenic crustal float (Oldow et al., 1990; Mazzotti and Hyndman, 2002; Mazzotti et al., in press), to effect lateral mobilization and extrusion of Pacific-rim crust at the extra-regional scale required.

Acknowledgments. Many colleagues, but in particular John Eichelberger, encouraged me to write this paper exploring the notion that crustal extrusion participated in forging the origin of the Aleutian-Bering Sea region and establishing at Cape Kamchatka Peninsula the tectonic connection of the Aleutian and Kamchatka subduction zones. Andy Stevenson, Roland von Huene, Tracy Vallier, and Tim Redfield were especially helpful in thinking through the role that extrusion tectonism played and also did not play. Idea formulation and testing benefited importantly from conversations with John Garver. Improvements in the presentation of information and ideas were importantly guided by the reviewing comments of John Eichelberger and an anonymous referee.

REFERENCES

Alexeiev, D. V., C. Gaedicke, N. V. Tsukanov, and R. Freitag, 2006, Collision of the Kronotskiy arc at the NE Eurasia margin and structural evolution of the Kamchatka-Aleutian junction: International Journal of Earth Science (Geologische Rundschau), v. 95, No. 6, p. 977–993. DOI 10.1007/s00531-006-0080-z.

Andrews, D. L., R. G. Gordon and B. C. Horner-Johnson, 2006, Uncertainties in plate reconstructions relative to the hotspots; Pacific-hotspot rotations and uncertainties for the past 68 million years: Geophysical Journal International v. 166, p. 939–951; doi: 10.1111/j.1365-246X.2006.03029-x.

Atwater, T, 1989, Plate tectonic history of the northeast Pacific and western North America, *in,* E. L. Winterer, D. M. Hussong, and R. W. Decker, (editors), The geology of North America (DENAG), v. N, The eastern Pacific crust and Hawaii: Geological Society of America, p. 21–72.

Atwater, T, and J. Severinghaus, 1989, Tectonic maps of the northeastern Pacific, *in,* E. L. Winterer, D. M. Hussong, and R. W. Decker (editors), The geology of north America (DENAG), v. N, The eastern Pacific crust and Hawaii: Geological Society of America, p. 15–20.

Avé Lallemant, H. G., and J. S Oldow, 2000, Active displacement partitioning and arc-parallel extension of the Aleutian volcanic arc based on Global Positioning System geodesy and kinematic analysis: Geology, v. 28, No. 8, p. 739–742.

Avdeiko, G. P., D. P. Savelyev, A. A. Palueva, and S. V., Popruzhenko, this volume, Evolution of the Kurile-Kamchatkan volcanic arcs and geodynamics of the Kamchatka-Aleutian junction, *in* Volcanism and subduction at the Kamchatka Peninsula and Adjacent Arcs, J. C. Eichelberger and E. Gordeev (editors): American Geophysical Union, Monograph.

Ballance, P. F., D. W. Scholl, T. L. Vallier, A. J. Stevenson, F. Ryan, and R. H. Herzer, 1989, Subduction of a Late Cretaceous seamount of the Louisville Ridge at the Tonga Trench—a model of normal and accelerated tectonic erosion: Tectonics, v. 8, p. 953–962.

Baranov, B. V., N. I. Seliverstov, A. V., Murav'ev, and E. L. Muzurov, 1991, The Komandorsky Basin as a product of spreading behind a transform plate boundary: Tectonophysics, v. 199, p. 237–269.

Baranov, B. H., K. Wong, K. Dozorova, B. Karp, T. Ludmann and V. Karnaukh, 2002, Opening geometry of the Kurile Basin (Okhotsk Sea) as inferred from structural data: Island Arc, v. 11, p. 206–219.

Bazhenov, M. L., V. S. Burtman, O. A. Krezhovskikh, and M. N. Shapiro, 1992, Paleomagnetism of Paleogene rocks of the central-east Kamchatka and Komandorsky Islands: tectonic implications: Tectonophysics, v. 201, p. 157–173.

Bering Sea EEZ-SCAN Scientific Staff, 1991, Atlas of the U.S. Exclusive Economic Zone, Bering Sea: United States Geological Survey Miscellaneous Investigations Series 1-2053, 145 pp

Bird, P., 1996, Computer simulations of Alaskan neotectonic: Tectonics, v. 15, p. 225–236.

Ben-Avraham, B. Z., and A. K. Cooper, 1981, Early evolution of the Bering Sea by collision of oceanic rises and north Pacific subduction zones: Geological Society of America Bulletin, v. 93, p. 485–495.

Bradley, D. C., P. Haeussler and T. M. Kusky, T. M., 1993, Timing of early Tertiary ridge subduction in southern Alaska: U.S. Geological Survey Bulletin 2068, p. 163–177.

Bradley, D. C., R. Parrish, W. Clendenen, D. Lux, P. Layer, M. Heizler, and D. T. Donley, 2000, New geochronological evidence for the timing of early Tertiary ridge subduction in southern Alaska: U.S. Geological Survey Professional Paper 1615, p. 5–21.

Bogdanov, N. A., V. S., Vishnevskaya and A. N. Sukhov, 1983, Upper Cretaceous deposits from the Shirshov Ridge (Bering Sea): Doklady Akademii Nauk, USSR, v. 273, p, 1183–1187 (in Russian).

Bourgeois, J., T. Pinegina, V. Ponomareva, and N. Zaretskaia, 2006, Holocene tsunamis in the southwestern Bering Sea, Russian Far East, and their tectonic implications: Geological Society of America Bulletin, v. 118, No. 3, p. 449–463, DOI: 10.1130/B25726.1.

Burk, C. A., 1965, Geology of the Alaska Peninsula—island arc and continental margin (Part 1): Geological Society of America Memoir 99, 250 p.

Bürgmann, R., M. G. Kogan, G. M. Steblov, G. Hilley, V. E. Levin and E. Apel, 2005, Interseismic coupling and asperity distribution along the Kamchatka subduction zone: Journal of Geophysical Research, v. 110, B07405, doi:10.1029/2005JB003648.

Calvert, A. J., S. L. Klemperer, N. Takahashi, and B. Kerr, in press, 3-D Crustal Structure of the Mariana Island Arc from Seismic Tomography: Journal of Geophysical Research.

Cande, S. C, C. A. Raymond, J. Stock and W. Haxby, 1995, Geophysics of the Pitman Fracture Zone and Pacific-Antarctic plate motions during the Cenozoic: Science, v. 270, p. 947–953.

Chekhovich, V. D. and A. N. Sukhov, 2006, Breakup of the Late Cretaceous Achaivayam-Valagin volcanic arc in the Paleocene (terranes of southern Koryakia and eastern Kamchatka): Doklady Earth Sciences, v. 497A, No. 6, pp. 893–896.

Chekhovich, V. D., A. N. Sukhov, N. I. Filatova, V. S. Vishnevskaya and I. A. Basov, 2006, New data on Cretaceous volcanic arcs of the northeastern Asian margin: Doklady Earth Sciences, v. 407A, No. 3, p. 381–384.

Cole, R. B., K. D. Ridgway, P. W. Layer and J. Drake, 1999, Kinematics of basin development during the transition from terrane accretion to strike-slip tectonics, Late Cretaceous-early Tertiary Cantwell Formation, south Central Alaska: Tectonics, v. 18, p. 1224–1244.

Cole, R. B., S. W. Nelson. P. W. Layer and P. J. Oswald, 2006, Eocene volcanism above a depleted mantle slab window in southern Alaska: Geological Society of America Bulletin, v. 118; No. 1/2; p. 140–158; doi: 10.1130/B25658.1.

Cooper, A. K., M. S., Marlow, and D. W., Scholl, 1976a, Mesozoic magnetic lineations in the Bering Sea marginal basin: Journal of Geophysical Research, v. 81, p. 1916–1934.

Cooper, A. K., D. W., Scholl M. S. and Marlow, 1976b, A plate tectonic model for the evolution of the eastern Bering Sea basin: Geological Society of America Bulletin, v. 87, p. 1119–1126.

Cooper, A. K., M. S. Marlow and D. W. Scholl, 1977, The Bering Sea—A multifarious marginal basin: *in* Island Arcs Deep Sea Trenches and Back-Arc basins, M. Talwani and W. C. Pitman III (editors): Maurice Ewing Series, v. 1, American Geophysical Union, p. 437–450.

Cooper, A. K., M. S. Marlow, and D. W. Scholl, 1987a, Geologic framework of the Bering Sea crust: *in* D. W. Scholl, A. Grantz, and J. G. Vedder (editors), Geology and Resource Potential of the Continental Margin of Western North America and Adjacent Ocean Basins—Beaufort Sea to Baja California: Circum-Pacific Council for Energy and Mineral Resources, Earth Science Series, v. 6, p. 73–102, Houston, Texas.

Cooper, A. K., D. W. Scholl, and M. S. Marlow, 1987b, Structural framework, sedimentary sequences, and hydrocarbon potential of the Aleutian and Bowers Basins, Bering Sea: *in* D. W. Scholl, A. Grantz, and J. G. Vedder, (editors), Geology and Resource Potential of the Continental Margin of Western North America and Adjacent Ocean Basins—Beaufort Sea to Baja California: Circum-Pacific Council for Energy and Mineral Resources, Earth Science Series, v. 6, p. 476–502, Houston, Texas.

Cooper, A. K., M. S. Marlow, D. W. Scholl, and A. J. Stevenson, 1992, Evidence for Cenozoic crustal extension in the Bering Sea: Tectonics, v. 11, p. 719–731.

Cormier, V. F., 1975, Tectonics near the junction of the Aleutian and Kuril-Kamchatka arcs and a mechanism for the middle Tertiary magmatism in the Kamchatka Basin: Geological Society of America Bulletin, v. 86, p. 443–453.

Cottrell, R. D. and J. A. Tarduno, 2003, A Late Cretaceous pole for the Pacific plate: implications for apparent and true polar wander and the drift of hotspots: Tectonophysics v. 362, p. 321– 333.

Creager, J. S., D. W. Scholl and others, 1973, Initial Report of the Deep Sea Drilling Project, v. 19: U.S. Government Print. Office, Wash., D. C., 913 pp.

Creager, K. C. and T. M. Boyd, 1991, The geometry of Aleutian subduction: three dimensional kinematic flow model: Journal of Geophysical Research, v. 96, p. 2293–2307.

Cross, R. S and J. T. Freymueller, 2007, Plate coupling variation and block translation in the Andreanof segment of the Aleutian arc determined by subduction zone modeling using GPS data: Geophysical Research Letters, v. 34, L06304, doi:10.1029/2006GL028970.

Davis, A. S., L-B G. Pickthorn, T. L Vallier, and M. S. Marlow, 1989, Petrology and age of volcanic-arc rocks from the continental margin of the Bering Sea: implications for early Eocene relocation of plate boundaries: Canadian Journal of Earth Sciences, v. 26, p. 1474–1490.

Detrick, R. S., J. G. Sclater, and J. Thiede (1977), The subsidence of aseismic ridges: Earth Planetary Science Letters, v. 34, p. 185–196.

Detterman, R. L., and B. L. Reed, 1980, Stratigraphy, structure, and economic geology of the Iliamna Quadrangle, Alaska: U. S. Geological Survey Bulletin 1368-B, p. B1-B86, 1 sheet, scale 1:250,000.

Doubrovine, P. V. and J. A. Tarduno, 2005, Late Cretaceous paleolatitude of the Hawaiian Hot Spot: New paleomagnetic data from Detroit Seamount (ODP Site 883): Geochemistry Geophysics Geosystems, v.5, No. 11, Q11L04 DOI 10.1029/2004GC000745.

Duncan R. A. and R. A. Keller, 2004, Radiometric ages for basement rocks from the Emperor Seamounts, ODP Leg 197: Geochemistry Geophysics Geosystems,v. 5, No. 8, Q08L03 DOI 10.1029/2004GC000704.

Eberhart-Phillips, D., D. H. Christensen, T. M Brocher, R. Hansen, N. A. Ruppert, P. J. Haeussler and G. A. Abers, 2006, Imaging the Transition from Aleutian subduction to Yakutat collision in central Alaska with local earthquakes and active source data,: Journal of Geophysical Research, v. 111, B11303, doi:10.1029/2005JB004240.

Engebretson, D. C., A. Cox and R. G. Gordon, 1984, Relative motions between oceanic plates of the Pacific Basin; Basin: Journal of Geophysical Research, v. 89, p. 10,291–10,310.

Engebretson, D. C., A. Cox, and R. G. Gordon, 1985, Relative motions between oceanic and continental plates in the Pacific Basin: Geological Society of America Special Paper 206, 59 p.

Ewing, M., W. J. Ludwig, and J. Ewing, 1965, Oceanic structural history of the Bering Sea: Journal of Geophysical Research, v. 70, No. 18, p. 4593–4600.

Farris, D. W., P. Haeussler, R. Friedman, S. R. Paterson, R. W. Saltus and R. Ayuso, 2006, Emplacement of the Kodiak batholith and slab-window migration: Geological Society of America Bulletin, v. 118, No. 11/12, p. 1360–1367; doi:1130/B25718.1.

Fedorchuk, A. V., M. I. Karpenko and A. Z. Zhuravlev, 1991, Age of ophiolites of the Cape Kamchatskiy Peninsula: Doklady Akademii Nauk, v. 316, No. 6, p. 1457–1460.

Fisher, D. M., T. W. Gardner, P. S. Sak, J. Sanchez, K. Murphy and P. Vannucchi, 2004, Active thrusting in the inner fore arc of an erosive convergent margin, Pacific Coast, Costa Rica: Tectonics, v. 23, TC 2007, doi:10.1029/2002TC001464.

Fisher, M. A., N. A., Ruppert, F. H. Wilson, D. Comer, R. Sliter, and F. Wong, 2006, Geologic setting and regional seismicity of the erupting Augustine volcano, lower Cook Inlet, Alaska: the influence of bedrock geology on volcanic processes: Geological

Society of America, Abstracts with Programs, Philadelphia, PA, Oct., 22–25. v. 38, No. 7, p. 350, Paper No. 142.

Fliedner, M. and Klemperer, S. L., 1999, Structure of an island-arc: Wide-angle seismic studies in the eastern Aleutians, Alaska: Journal of Geophysical Research, v. 104, p. 10,667–10,694.

Freitag, R. C., Gaedicke, B. Baranov and N. Tsukanov, 2001, Collisional processes at the junction of the Aleutian-Kamchatka arcs: new evidence from fission track analysis: Terra Nova, v. 13, p. 433–442.

Fujita. K., K. G. Mackey, R. C. McCaleb, L. V. Gunbina, V. N. Kovalev, V. S. Imaev, V. N. Smirnov, 2002, Seismicity of Chukotka, northeastern Russia, *in* Tectonic Evolution of the Bering Shelf–Chukchi Sea–Arctic Margin and Adjacent Landmasses, E. L. Miller, A. Grantz, and S. L. Klemperer, (editors): Geological Society of America Special Paper 360, p. 259–272.

Gabrieles, H., D. C. Murphy, and J. K. Mortensen, 2006, Cretaceous and Cenozoic dextral orogen-parallel displacements, magmatism, and paleogeography, northcentral Canadian Cordillera, *in* J. W. Haggart, H. Monger and R. J. Enkin, (Editors), Evidence for Major Lateral Displacements in the North American Cordillera: Geological Association of Canada, Special Paper 46. p, 255–276.

Gaedicke, C., B. Baranov, N. Seliverstov, D. Alexeiev, N. Tsukanov, and R. Freitag, 2000, Structure of an active arc-continental collision area: the Aleutia-Kamchatka junction: Tectonophysics, v. 325, p. 64–85.

Garver, J. I., A. V. Soloviev, M. E. Bullen and M. T. Brandon, 2000, Towards a more complete record of magmatism and exhumation in continental arcs, using detrital fission-track thermochrometry, Physics and Chemistry of the Earth (A), v. 25, No. 6-7, p. 565–570.

Garver, J. I., J. Hourigan, A. Soloviev, and M. T. Brandon, 2004, Collision of the Olyutorsky terrane, Kamchatka: Geological Society of America Abstracts with Program, v. 36, No. 5, p 121.

Geist, E. L., J. R. Childs, and D. W. Scholl, 1988, The origin of summit basins of the Aleutian Ridge: implications for block rotation of an arc massif: Tectonics, v. 7, p. 327–341.

Geist, E. L., and Scholl, D. W., 1992, Application of continuum models to deformation of the Aleutian Island Arc: Journal of Geophysical Research, v. 97, p. 4953–4967.

Geist, E. L. and D. W. Scholl, 1994, Large-scale deformation related to the collision of the Aleutian Arc with Kamchatka: Tectonics, v. 13, No. 2, p. 538–560.

Geist, E. L., T. L. Vallier and D. W. Scholl, 1994, Origin, transport, and emplacement of exotic island-arc terranes exposed in eastern Kamchatka, Russia: Geological Society of America Bulletin, v. 106, p. 1182–1194.

Gladenkov, A. Yu., 1990, Geology of the western Bering Sea region: International Geology v. 32, No. 12, p. 1171–1184.

Gladenkov, A. Yu., 2006, Neogene Diatoms from the Sandy Ridge section, Alaska Peninsula: significance for stratigraphic and paleogeographic reconstructions: Stratigraphy and Geological Correlation, v. 14, No. 1, p. 73–90.

Gorbatov, A., V. Kostoglodov and G. Suarez, 1997, Seismicity and structure of the Kamchatka subduction zone: Journal of Geophysical Research, v. 102, No. B8, p. 17,883–17,898.

Gordeev, E. I., Gusev, A. A., Levin, V. E., Bakhtiarov, V. F., Pavlov, V. M., Chebrov, V. N., and Kasahara, M., 2001. Preliminary analysis of deformation at the Eurasia-Pacific-North America plate junction from GPS data: Geophysical Journal International, v. 147, p. 189–198.

Grow, J. A., 1973, Crustal and upper mantle structure of the central Aleutian arc: Geological Society of America Bulletin, v. 84, p. 2169–2192.

Grow, J. A., and T. Atwater, 1970, Mid-Tertiary tectonic transition in the Aleutian arc: Geological Society of America Bulletin, v. 81, p. 3715–3722.

Grantz, A., D. W. Scholl, J. Toro and S. L. Klemperer, 2002, Geologic structure of Bering and Chukchi shelves adjacent to Bering-Chukchi deep seismic transect and tectonostratigraphic terranes of adjacent landmasses, *in* Tectonic Evolution of the Bering Shelf–Chukchi Sea–Arctic Margin and Adjacent Landmasses, E. L. Miller, A. Grantz, and S. L. Klemperer, (editors): Geological Society of America Special Paper 360, plate 1.

Haeussler, P. J., D. C. Bradley, R. E. Wells and M. L. Miller, 2003, Life and death of the Resurrection plate: Evidence for its existence and subduction in the northeastern Pacific in Paleocene–Eocene time: Geological Society of America Bulletin, v. 115, No. 7, p 867–880.

Haeussler, P. J., D. P. Schwartz, T. E. Dawson, H. D. Stenner, J. J. Lienkaemper, B. Sherrod, F. R. Cinti, P. Montone, P. Craw, A. J. Crone, and S. F. Personius, 2004, Surface rupture and slip distribution of the Denali and Totschunda Faults in the 3 November 2002 M 7.9 earthquake, Alaska: Bulletin of the Seismological Society of America, v. 94, No. 6B, p. S23–S52.

Harbert. W., 1987, New paleomagnetic data from the Aleutian Islands; implications for terrane migration and deposition of the Zodiac Fan: Tectonics, v. 6, No. 5 p. 585–602.

Hanna, G. D., 1929, Fossil diatoms dredge from Bering Sea: Transaction of San Diego Museum of Natural History, v. 5, p. 287–296.

Hillhouse. J. W., and R. S. Coe, 1994, Paleomagnetic data from Alaska, *in* G. Plafker and H. C Berg, H. C. (editors), The Geology of Alaska: The geology of north America (DENAG), v. G-1: The Geological Society of America, Boulder, CO, p. 797–812.

Hochstaedter A. G., P. K. Kepezhinskas, M. J. Defant, M. S. Drummond, and H. Bellon, 1994, On the tectonic significance of arc volcanism in northern Kamchatka: Journal of Geology, v. 102, p. 639–654.

Hickman. R. G., K. W. Sherwood, C. Craddock, 1990, Structural evolution of the early Tertiary Cantwell basin, south central Alaska: Tectonics, v. 9, No. 6, p. 1433–1449.

Holbrook, W. S., D. Lizarralde, S. McGeary, N. Bangs and J. Diebold, 1999, Structure and composition of the Aleutian Island arc and implications for continental crustal growth: Geology, v. 27, p. 31–34.

Hyndman, R. D., C. A. Currie and S. P. Mazzotti, 2005, Subduction zone backarcs, mobile belts, and orogenic heat: GSA Today, v. 15, No. 2, p. 4–10, doi:10:1130/1052-5173(2005)015<4:SZBMBA>2.0.C0;2.

Jicha, B. R., D. W. Scholl, B. S. Singer, G. M. Yogodzinski, S. M. Kay, 2006, Revised age of Aleutian Island Arc formation implies high rate of magma production: Geology, v. 34, No. 8; p. 661–664; doi: 10.1130/G22433.1.

Kelemen, P. B., Yogodzinski, G. M., and Scholl, D. W., 2003, Along-strike variation in lavas of the Aleutian island arc: Implications for the genesis of high Mg# andesite and the continental crust, *in* J. Eiler (editor), Inside the subduction factory: American Geophysical Union Geophysical Monograph 138, p. 223–246.

Keller, R. A., D. W. Graham, K. A. Farley, R. A. Duncan, and J. E. Lupton, 2004, Cretaceous-to-recent record of elevated ^{3}He / ^{4}He along the Hawaiian-Emperor volcanic chain, Geochemistry Geophysics Geosystems, v. 5, Q12L05, doi:10.1029/2004GC000739.

Klemperer, S. L., E. L. Miller, A. Grantz, D. W. Scholl and the Bering-Chukchi Working Group*,* 200*2,* Crustal structure of the Bering and Chukchi shelves: Deep seismic reflection profiles across the North American continent between Alaska and Russia, *in* Tectonic Evolution of the Bering Shelf–Chukchi Sea–Arctic Margin and Adjacent Landmasses, E. L. Miller, A. Grantz, and S. L. Klemperer, (editors): Geological Society of America Special Paper 360, p. 1–24.

Klemperer, S. L., E. L. Miller, A. Grantz, D. W. Scholl, and the Bering-Chukchi Working Group*,* 2002, Seismic reflection profiles*, in* Tectonic Evolution of the Bering Shelf–Chukchi Sea–Arctic Margin and Adjacent Landmasses, E. L. Miller, A. Grantz, and S. L. Klemperer (editors): Geological Society of America Special Paper 360, plate 2.

Koppers, A. A. P. and H. Staudigel, 2005, Asynchronous bends in Pacific seamount trails: a case for extensional volcanism? Science, v. 307, p. 904–907.

Kozhurin, A., this volume, Active faulting in the Kamchatsky Peninsula, Kamchatka-Aleutian Junction, *in* Volcanism and subduction at the Kamchatka Peninsula and Adjacent Arcs, J. C. Eichelberger and E. Gordeev (editors): American Geophysical Union, Monograph.

Kulm, L. D., J. M. Resig, T. C. Moore, Jr., and V. J., Rosato, 1974, Transfer of Nazca Ridge pelagic sediments to the Peru continental margin: Geological Society of America Bulletin, v. 85, p. 769–8780.

Levin, V., N. Shapiro, J. Park and M. Ritzwoller, 2002, Seismic evidence for catastrophic slab loss beneath Kamchatka: Nature, v. 418, p. 763–766.

Levashova, N. M and M. L., Bazhenov, 1997, Late Cretaceous paleomagnetism of the East Ranges island arc complex, Kamchatka; implications for terrane movements and kinematics of the northwest Pacific: Journal of Geophysical Research, v. 102, No. B11, p. 24,843–24,857.

Levashova, N. M., M. N. Shapiro, V. N. Beniamovsky, and M. L., Bazhenov, 2000, Paleomagnetism and geochronology of the Late Cretaceous-Paleogene island arc complex of the Kronotsky Peninsula, Kamchatka, Russia; kinematic implications: Tectonics v. 19, No. 5, p. 834–851.

Levin, V., N. M. Shapiro, J. Park and M. H. Ritzwoller, 2005, Slab portal beneath the western Aleutians: Geology, v. 33, No. 4, p. 235–256, doi:1130/G20863.I.

Lizarralde, D., W. S. Holbrook, S. McGeary, N. L. Bangs, and J. B. Diebold, 2002, Crustal construction of a volcanic arc, wide-angle seismic results from the western Alaska Peninsula: Journal of Geophysical Research, v. 107, No. B8, 10.1029/2001JB000230.

Lonsdale, P. 1988, Paleogene history of the Kula plate: offshore evidence and onshore implications: Geological Society of America Bulletin, v. 100, p. 733–754.

Lowey, G., 1998, A new estimate of displacement on the Denali Fault system based on the occurrence of carbonate megaboulders in the Dezadeash Formation (Jura-Cretaceous), Yukon, and the Nutzotin Mountains sequence (Jura-Cretaceous), Alaska, Bulletin of Canadian Petroleum Geology, 46, 3, 379–386.

Ludwig, W. J., S. Murauchi, N. Den, M. Ewing, H. Hotta, R. E. Houtz, T. Yoshii, T. Asanuma, K. Hagiwara, T. Sato, and S. Ando, 1971, Structure of Bowers Ridge: Journal of Geophysical Research, v. 76, No. 26, p. 6350–6366.

Mackey, K. G., K. Fujita, L. V. Gunbina, V. N Kovalev, V. S. Imaev, B. M. Kozmin, and L. P. Imaseva, 1997, Seismicity of the Bering Strait region; evidence for a Bering Block: Geology 25, No. 11, p. 979–982.

Mann, P., 1997, Model for the formation of large transtensional basins in zones of tectonic escape: Geology, v. 25, p. 211–214, doi:10.1130/0091-7613.

Mammerickx, J. and G. F. Sharman, 1988, Tectonic Evolution of the North Pacific During the Cretaceous Quiet Period: Journal of Geophysical Research, v. 93: p. 3009–3024.

Markov, M. S., V. A., Siliverstov, M. Yu., Kotin, and B. K., Dolmatov, 1969, Junction of the east Kamchatka structures and the Aleutian Island Arc: Geotectonics, English translation, v. 3, p. 314–319.

Marlow. M. S., and A. K. Cooper, 1983, Wandering terranes in southern Alaska: the Aleutia microplate and implications for the Bering Sea: Journal of Geophysical Research, v. 88, p. 3439–3446.

Marlow. M. S., A. K. Cooper, and M. A., Fisher, 1987, Petroleum geology of the Beringian continental shelf, *in* D. W. Scholl, A. Grantz, and J. G. Vedder, (editors), Geology and Resource Potential of the Continental Margin of Western North America and Adjacent Ocean Basins—Beaufort Sea to Baja California: Circum-Pacific Council for Energy and Mineral Resources, Earth Science Series, v. 6, p. 103–122, Houston, Texas.

Marlow, M.S., A. K. Cooper, S. V, Dadisman, E. L. Geist, and P. R. Carlson, 1990, Bowers Swell; evidence for a zone of compressive deformation concentric with Bowers Ridge, Bering Sea: Marine and Petroleum Geology, v. 7, pp. 398–409.

Mazzotti, S. and R. D., Hyndman, 2002, Yakutat collision and strain transfer across the northern Canadian Cordillera: Geology, v. 30, No. 6, p. 495–498.

Mazzotti, S., L. J. Leonard, R. D. Hyndman, and J. F. Cassidy, in press, Tectonics, dynamics, and seismic hazard in the Canada-Alaska Cordillera, *in* "Active tectonics and seismic potential of Alaska", J. Freymueller, P. Haeussler, and R. Wesson (editors), American Geophysical Union Monograph.

McElfresh, S. B. Z., W. Harbert, C-Y Ku and J-S Lin, 2002, Stress modeling of tectonic blocks at Cape Kamchatka, Russia, using principal stress proxies from high-resolution SAR: new evidence for the Komandorsky Block: Tectonophysics, v. 354, p. 239–256.

Miller, M., D. Bradley, T. Bundtzen and W. McClelland, 2002, Late Cretaceous through Cenozoic evolution of southwestern Alaska—the impact of dextral strike slip tectonism: Journal of Geology, v. 110, p. 247–270.

Miller, M. S. and B. L. N. Kennett, 2006, Evolution of mantle structure beneath the northwest Pacific: evidence from seismic tomography and paleogeographic reconstructions: Tectonics, v. 25, TC 4002, doi:10.1029/2005TC001909.

Minyuk, P. S., and Y. B. Gladenkov, 2007, Magnetostratigraphy of Paleogene Deposits in Kamchatka: Stratigraphy and Geological Correlation, 2007, v. 15, No. 1, pp. 100–111, Pleiades Publishing, Ltd.

Moore, J. C, 1972, Uplifted trench sediments: southwestern Alaska-Bering shelf edge: Science, v. 175, p. 1103–1105.

Mortera-Gutiérrez, C. A., D. W. Scholl, and R. L. Carlson, 2003, Fault trends on the seaward slope of the Aleutian Trench: Implications for a laterally changing stress field tied to a westward increase in oblique convergence: Journal of Geophysical Research, v. 108, No. B10, 2477, doi:10.1029/2001JB001433.

Muzurov, Ye. L., B. V. Baranov, Yu. V. Borisenko, P. L. Brudastov and L. A. Litvinova, 1989, Sea-floor spreading in the Komandorskiy Basin and structure of the Shirshov Ridge: Doklady Akademii Nauk, SSSR, v. 305 No. 5, p. 1181–1185 (in Russian).

Nokleberg et al., 2005, Metallogenesis and tectonics of the Russian far east, Alaska, and the Canadian Cordillera: United States Geological Survey Professional Paper 1697, 397 pp.

Nokleberg, W. J., G. Plafker and F. H. Wilson, 1994, Geology of South Central Alaska, *in* Geology of Alaska, G. Plafker and H. C. Berg, editors, The Geology of North America (DNAG), v. G-1, The Geological Society of America, Boulder, CO, p. 311–366.

Norton, I. O., 1995: Plate motions in the North Pacific: the 43 Ma non-event: Tectonics, v. 14, p. 1080-1094 10.1029/95TC01256.

Norton, I. O, in press, Speculations on Cretaceous tectonic history of the Northwest Pacific and a tectonic origin for the Hawaii hotspot, *in* Plates, plumes, and planetary processes, G. R. Foulger and D. M. Jurdy (editors): Geological Society of America Special Paper [see http://www.mantleplumes.org/P%5E4/P%5E4Chapters/NortonP4AcceptedMS.pdf.]

Nyst, M. and W. Thatcher, 2004, New constraints on the active tectonic deformation of the Aegean: Journal of Geophysical Research, vol. 109, B11406, doi:10.1029/2003JB002830.

Oldow, J. S., D. S., Lewis, H. G. Avé Lallemant, L. Ferranti, L. Maschio, J. Comstock and J. Freymueller, J., 1999, Displacement partitioning, trench-parallel stretching, and westward migration of the Aleutian arc and collision with Kamchatka: Part 2. GPS geodetic analysis: EOS, Transactions of the American Geophysical Union, v. 80 No. 46, p. F947.

Oldow, J. S., A. W. Bally and H. G. Avé Lallemant, 1990, Transpression, orogenic float, and lithospheric balance: Geology, v. 18, p. 991–994.

Page, B. M., G. A. Thompson, and R. G. Coleman, 1998, Overview: Late Cenozoic tectonics of the central and southern Coast Ranges of California: Geological Society of America Bulletin, v. 110, p. 846–876.

Page, R. A, N. N. Biswas, J. C. Lahr and H. Puplan, 1991, Seismicity of continental Alaska, *in* Neotectonics of North America, D. B. Slemmons, E. R. Engdahl, M. D. Zoback, D. D. Blackwells (editors): Geological Society of America Decade Map Volume, p. 47–68.

Page, R. A., G. Plafker, and H. Pulpan, 1995, Block rotation in east-central Alaska: A framework for evaluating earthquake potential?: Geology, v. 23, No. 7, 629–632.

Pares, J. M. and T. C. Moore, 2005, New evidence for the Hawaiian hotspot plume motion since the Eocene: Earth and Planetary Science Letters, v. 237, p. 951–959.

Park, J., V. Levin, M. T. Brandon, J. M Lees, V. Peyton, E. Gordeev and A. Ozerov, 2002, A dangling slab, amplified arc volcanism, mantle flow and seismic anisotropy near the Kamchatka plate corner, *in* S. Stein and J. Freymueller (editors), Plate boundary zones: American Geophysical Union Geodynamics Series No. 30, p. 295–324, DOI: 10/1029/030GD18.

Parry, W. T., M. P. Bunds, R. L. Bruhn, C. M. Hall and J. M. Murphy, 2001, Mineralogy, $^{40}Ar/^{39}Ar$ dating and apatite fission track dating of rocks along the Castle Mountain fault, Alaska: Tectonophysics, v. 337, p. 149–172.

Patton, W. W., Jr. and J. M. Hoare, 1968, The Kaltag fault, west-central Alaska: United States Geological Survey Professional Paper 600-D, p. D147-D153.

Pedoja, K., J. Bourgeois, T. Pinegina, and B. Higman, 2006, Does Kamchatka belong to North America? An extruding Okhotsk block suggested by coastal neotectonics of the Ozernoi Peninsula, Kamchatka, Russia: Geology, v. 34, No. 5; p. 353–356, doi:10.1130/G22062.1.

Peyton, V., V. Levin, J. Park, J., M. Brandon, J. Lees, E. Gordeev and A. Ozerov, 2001, Mantle flow at a slab edge: Seismic anisotropy in the Kamchatka region: Geophysical Research Letters, v. 28, p. 379–382.

Plafker, G., and H. C. Berg, 1994, The Geology of Alaska, *in* Plafker, G. and Berg, H. C. (editors), The Geology of Alaska: The geology of north America (DENAG), v. G-1: Boulder, CO, Geological Society of America, pp. 1055.

Plafker, G., J. C. Moore and G. Winkler, 1994, Geology of the southern Alaska margin, *in* Plafker, G., and Berg, H. C. (editors), The Geology of Alaska: The geology of north America (DENAG), v. G-1: Boulder, CO, Geological Society of America, p. 389–449.

Portnyagin, M. V., D. P. Savel'ev and K. Hoernle, 2005, Plume-related association of Cretaceous oceanic basalts of eastern Kamchatka: compositions of spinel and parental magmas: Petrology, v. 13, No. 6, pp. 571–588. Translated from Petrologiya, v. 13, No. 6, 2005, pp. 626–645. Original Russian Text Copyright © 2005 by Portnyagin.

Portnyagin, M. V., K. Hoernle, G. Avdeiko, F. Hauff, R. Werner, L. Bindeman, V. Uspensky and D. Garbe-Schonberg, 2005, Transition from arc to oceanic magmatism at the Kamchatka-Aleutian junction: Geology, v. 33, p. 25–28.

Rabinowitz, P. D. and A. Cooper, 1977, Structure and sediment distribution in the western Bering Sea: Marine Geology, v. 24, p. 309–320.

Rabinowitz, P. D., 1974, Seismic profiling between Bowers Ridge and Shirshov Ridge in the Bering Sea: Journal of Geophysical Research, v. 79, p. 4977–4979.

Rea, D. K, I. A., Basov, D. W. Scholl, and J. F. Allan, 1995, Proceedings of the Ocean Drilling Program, Scientific Results, Volume 145: College Station, Texas, Ocean Drilling Program, 711 pp.

Redfield, T., D. W. Scholl, P. Fitzgerald and M. E. Beck, jr. in press, The Extrusion of Alaska: Past, Present, and Future: Geology.

Riegel. S. A., K. Fujita, B. M. Koz'min, V. S. Imaev and D. B. Cook, 1993, Extrusion tectonics of the Okhotsk plate northeast Asia: Geophysical Research Letters, v. 7, p. 607–610.

Ridgway, K. D., J. M. Trop and A. R. Sweet, 1997, Thrust-top basin formation along a suture zone, Cantwell Basin, Alaska Range: implications for development of the Denali fault system: Geological Society of America Bulletin, v. 109, p. 505–523.

Ryan, H.F., and D. W., Scholl, 1989, The evolution of forearc structures along an oblique convergent margin, central Aleutian Arc: Tectonics, v. 8, p. 497–516.

Ryan, H.F., and D. W. Scholl, 1993, Geologic implications of great interplate earthquakes along the Aleutian Arc: Journal of Geophysical Research, v. 98, p. 22,135–22,146.

Rostovtseva, Y. V. and M. N., Shapiro, 1998, Provenance of the Paleocene-Eocene clastic rocks of the Komandorsky Islands: Sedimentology, v. 45, p. 201–216.

Sager, W. W., 2005, What formed Shatsky Rise—A mantle plume or ridge tectonics?, *in* Plumes, Plates and Paradigms, G. Foulger, D. Anderson, J. Natland and D. Presnall (editors), Geological Society of America Special Paper 388, p. 721–734.

Savotsin L. A., B. V. Baranov, T. Z. Grigoryan, and L. R. Merkin, 1986, Tectonics and origin of the western Bering Sea: Transactions (Doklady) of the USSR Academy of Science Earth Science Sections, Scripta Technica, Inc, American Geological Institute, v. 286, No. 1, p. 88–91.

Scholl, D. W., 1999, Plate-boundary driven tectonism of the northern rim of the Pacific Basin forms the Aleutian-Bering region in the early and middle Eocene: Geological Society of America, Abstracts with Programs, Berkeley, California, v. 31, No. 6, p. A92.

Scholl, D. W., J. S. Creager, et al., 1971, Geologic synthesis of Leg 19 (DSDP) results: far north Pacific, Aleutian Ridge, and Bering Sea, *in* J. S. Creager, D. W. Scholl (editors), Initial Reports of the Deep Sea Drilling Project, v. 19: Washington, DC, U.S. Government Printing Office, p. 897–913.

Scholl D. W. and D. K. Rea, 2002, Estimating the Age of the Hawaiian Hotspot; EOS, Transactions of the American Geophysical Union, Fall meeting, v. 83, no. 47, p. F1282–1283.

Scholl, D. W. and R. von Huene, 2007, Crustal recycling at modern subduction zones applied to the past—issues of growth and preservation of continental basement, mantle geochemistry, and supercontinent reconstruction**,** *in* The 4D Framework of Continental Crust, R. D. Hatcher, Jr., M. P. Carlson, J. H. McBride, and J. R. Martínez Catalán (editors): Geological Society of America Memoir 200.

Scholl, D. W., E. C. Buffington, M. S. Marlow, 1975, Plate tectonics and the structural evolution of the Aleutian-Bering Sea region: *in* R. R. Forbes (editor), Contributions to the geology of the Bering Sea Basin and adjacent regions: Geological Society of America Special Paper 15, p. 1–31.

Scholl, D. W., and A. J. Stevenson, 1989, The Aleutian-Bowers-Shirshov Arc system, response to deformation of Alaska ("orocline") by subduction driven impact and escape of crustal masses—exploration of an idea: EOS, Transactions American Geophysical Union, v. 70, p. 1307.

Scholl, D. W., and A. J., Stevenson, 1991, Exploring the idea that early Tertiary evolution of the Alaska orocline and the Aleutian-Bering Sea region is a manifestation of Kula-plate driven Cordilleran tectonism and escape tectonics, Geological Society of America, Abstracts with Programs, San Diego, California, Oct., 21–24. v. 23, p. A435.

Scholl D W., J. R. Hein, M. Marlow and E. C. Buffington, 1977, Meiji sediment tongue: North Pacific evidence for limited movement between the Pacific and North America plates, Geological Society of America Bulletin, v. 88; p. 1567–1576.

Scholl, D. W., A. J. Stevenson, S. Mueller, E. L. Geist, D. C. Engebretson, and T. L., Vallier, 1992, Exploring the notion that southeast-Asian-type escape tectonics and trench clogging are involved in regional-scale deformation of Alaska and the formation of the Aleutian-Bering Sea region, *in*, M. Flower, R. McCabe and T. Hilde, (editors), Southeast Asia Structure, Tectonics, and Magmatism: Proceedings of the Geodynamics Research Institute Symposium, Texas A & M University, College Station, Texas, p. 57–63.

Scholl, D. W., A. J. Stevenson, S. Mueller, E. L. Geist, T. L. Vallier, and D. C. Engebretson, 1994, Regional-scale strain partitioning leading to escape tectonism and formation of offshore arc-trench systems, Alaska-Aleutian-Bering Sea region: Geological Society of America, Abstracts with Programs, Seattle Washington, Oct. 24–27, v. 26, p. 136.

Scholl, D. W., A. J. Stevenson, T. L., Vallier, H. F. Ryan, and E. L. Geist, 1989, Aleutian arc-trench system: perspective of ocean margin evolution controlled by regional changes in plate-boundary conditions: Proceedings of the 28th International Geological Congress, v. 3, p, 52–53.

Scholl, D. W, A. J. Stevenson, M. A. Noble, and D. K. Rea, 2003, The Meiji drift body of the northwestern Pacific—modern and paleoceanographic implications, *in* From greenhouse to icehouse: the marine Eocene-Oligocene transition, D. Prothero (editor): Columbia University Press, p. 119–153.

Scholl, D. W., T. L. Vallier, and A. J. Stevenson, 1986, Terrane accretion, production, and continental growth—a perspective based on the origin and tectonic fate of the Aleutian-Bering Sea region: Geology, v. 14, p. 43–47.

Scholl, D. W., T. L. Vallier, and A. J. Stevenson, 1987, Geologic evolution and petroleum geology of the Aleutian Ridge, *in* D. W. Scholl, A. Grantz, and J. G. Vedder, (editors), Geology and resource potential of the continental margin of western North America and adjacent ocean basins—Beaufort Sea to Baja California: Circum-Pacific Council for Energy and Mineral Resources, Earth Science Series, v. 6, p. 124–155, Houston, Texas.

Seliverstov N. I., 1998, Sea floor structure offshore Kamchatka Peninsula and geodynamics of the Kamchatka-Aleutian junction area: Moscow, Scientific Word Publication, 164 pp., Moscow (in Russian).

Seliverstov, N. I., 1984, Structure of junction zone between Kuril-Kamchatka and Aleutian Island Arc from continuous seismic profiling. Vulkanol. Seismol, v. 3, p. 53–67 (in Russian) [Volcanology Series, 1984, v. 5, p. 175–190, Gordon and Breach Scientific Publishers S. A and OPA Ltd, UK, in English].

Shapiro. M. N., B. I. Slyadnev and A. V. Lander, 1984, Slice-overthrust structure of the northern part of the East Kamchatka Anticlinorium: Geotectoknics, English translation, v. 18, p. 514–521.

Shapiro. M. N., 2005, Kinematics of the Campanian-Maastrichtian island arcs in northeastern Asia in light of drilling results on the Emperor Seamounts: Geotectonics, v. 39, No. 5, p. 408–415.

Sharp, W. D. and D. A. Clague, 2006, 50 Ma initiation of Hawaiian-Emperor bend records major change in Pacific plate motion, Science v. 313, p. 1281–1284.

Shmidt, O. A., 1978, The tectonics of the Komandorsky Islands and structure of the Aleutian Ridge (in Russian): Geological Institute, Academy of Science, USSR, v. 320, Nauka, Moscow (in Russian).

Shillington, D. J., Van Avéndonk, H. J., Holbrook, W. S., Kelemen, P. B., and M. J. Hornbach, 2004, Composition and structure of the central Aleutian island arc from arc-parallel wide-angle seismic data: Geochemistry, Geophysics, Geosystems, v. 5, doi:10.1029/2004GC000715.

Shor. G. G., 1964, Structure of the Bering Sea and the Aleutian Ridge, Marine Geology, v. 1, p, 213–219.

Stavsky, A. P., V. D. Chekhovitch, M. V. Kononov, and L. P. Zonenshain (1988), Palinspastic reconstruction of the Anadyr-Koryak region, based on plate tectonics: Geotectonics, v. 22, No. 6, p. 496–503.

Stavsky, A. P., V. D. Chekhovitch, M. V. Kononov, and L. P. Zonenshain (1990), Plate tectonics and palinspastic reconstruction of the Anadyr-Koryak region, northeastern USSR: Tectonics, v. 9, p. 81–101.

Steinberger, B. and C. Gaina, 2007, Plate-tectonic reconstructions predict part of the Hawaiian hotspot track to be preserved in the Bering Sea: Geology, v. 35, no. 5, p. 407–410; doi: 10.1130/G23383A.1.

Steblov, G. M., Kogan, M. G., King, R. W., Scholz, C. H., Bürgmann, R., and Frolov, D. I., 2003, Imprint of the North American plate in Siberia revealed by GPS: Geophysical Research Letters, v. 30 No. 4, doi: 10.1029/2003GL017805.

Steinberger, B., R. Sutherland, and R. J. O'Connell, 2004, Prediction of Emperor-Hawaii seamount locations from a revised model of global plate motion and mantle flow, *Nature*, v. 430, p. 167–173.

Stock, J. M., 2006, The Hawaiian-Emperor Bend: Older Than Expected: Science v. 313, p. 1250–1251.

Stone, D. B., 1988, Bering Sea-Aleutian Arc, Alaska, *in* The ocean basins and margins, v. 7B, A. E. M. Narin, F. G. Stehli, and S. Uyeda (editors), Plenum Publishing Corp., p. 1–84.

Subarya, C., M. Chlieh, L. Prawirodirdjo, J-P Avouac, Y. Bock, K. Sieh, A. J. Meltzner, D. H. Matawodjaja, and R. McCaffrey, 2006, Plate-boundary deformation associated with the great Sumatra-Andaman earthquake: Nature v. 444, p.44–51.

Sukhov, A. N., N. A. Bogdanov, and V. D. Chekhovich, 2004, Geodynamics and paleogeography of the northwestern Pacific continental margin in the Late Cretaceous: Geotectonics v. 38, No. 1 p. 61–71.

Sukhov, A. N., S. M. Lyapunov, and E. R. Drubetskoy, 1987, New data on geochemistry and K-Ar age of igneous and metamorphic rocks of the Shirshov Ridge: Abstracts of III Congress of Soviet Oceanologists. Section: geology, geophysics and geochemistry. Leningrad, p. 209–210 (in Russian).

Takahashi, N., S. Kodaira, S. L. Klemperer, Y. Tatsumi, Y. Kaneda and K. Suyehiro, 2007, Crustal structure and evolution of the Mariana intra-oceanic island arc: Geology, v. 35, no. 3; p. 203–206, doi: 10.1130/G23212A.

Tapponnier, P., G. Peltzer, A. Y. Le Dain, R. Armijo and P. Cobbing, 1982, Propagating extrusion tectonics in Asia: new insights from simple experiments with plasticine: Geology v. 10, p. 611–616.

Tapponnier, P., G. Peltzer and R. Armijo, 1986, On the mechanics of the collision between India and Asia: *in* M. P. Coward and A. C. Ries (editors), Collision Tectonics: Geol. Society Special Publication 19, pp. 115–157.

Tarduno, J. A., in press, On the motion of Hawaii and other mantle plumes: Chemical Geology.

Tarduno, J. A. and R. D. Cottrell, 1997. Paleomagnetic evidence for motion of the Hawaiian hotspot during formation of the Emperor seamounts: Earth and Planetary Science Letters, v. 153, p. 171– 180.

Tarduno, J. A., R. A. Duncan, D. W. Scholl, R. D. Cottrell, B. Steinberger, T. Thordarson, B. C. Kerr, C. R. Neal, F A. Frey, M. Torii, C. Carvallo, 2003, The Emperor Seamounts: Southward Motion of the Hawaiian Hotspot Plume in Earth's Mantle: Science, v 301. p. 1064–1069.

Tolson, R. B., 1987, Structure and stratigraphy of the Hope basin, southern Chukchi Sea, *in* D. W. Scholl, A. Grantz, A and J. G., Vedder (editors), Geology and resource potential of the continental margin of western North America and adjacent ocean basins—Beaufort Sea to Baja California: Circum-Pacific Council for Energy and Mineral Resources, Earth Science Series, v. 6, p. 59–71, Houston, Texas.

Thompson, G. A., 1999, California Coast Range tectonics in light of geophysical constraints: International Geology Review, v. 41, p. 383–390.

Tsukanov, N. V. and V. P. Zinkevich, 1987, The tectonics of the Kumroch Range (eastern Kamchatka): Geotectonics, English translation, v. 21, p. 535–546.

Tsvetkov, A. A., 1991, Magmatism of the westernmost (Komandorsky) segment of the Aleutian Island arc: Tectonophysics, v. 199, p. 289–317.

Vallier, T. L., H. A. Karl, and M. B. Underwood, 1987, Geologic evolution of the western Aleutian arc and adjacent north Pacific seafloor: EOS, Transactions of the American Geophysical Union, v. 68, p. 1486.

Vallier, T. L., H. A. Karl, L. M. Prueher and D. G. Masson, 1992, Deformation in the western Aleutian fore-arc region caused by impingement of Stalemate ridge on the trench inner wall: Geological society of America Abstracts with Programs, v. 24, p. 87.

Vallier, T. L., D. W. Scholl, M. A. Fisher, T. Bruns, F. H., Wilson, R. von Huene, R. and A. J. Stevenson, 1994, Geologic framework of the Aleutian arc, Alaska, *in* G . Plafker and H. C. Berg (editors), The Geology of Alaska: The geology of north America (DENAG), v. G-1: The Geological Society of America, Boulder, CO, p. 367–388.

Vallier, T. L., C. Mortera-Guiterrez, H. A. Karl, D. G., Masson, L. Prueher, and T. E. Chase, 1996, Geology of the Kula Paleo-Plate, North Pacific Ocean, *in*, J. V. Gardner, M. E Field, and D. C., Twichell, Jr. (editors), Geology of the US Ocean Floor: The view from GLORIA: Cambridge University Press, Cambridge, England, p. 333–353.

Valyashko G. M., G. E. Chernyavsky, N. I. Seliverstov, A. N. Ivanenko, 1993, Back-arc spreading in the Komandorsky Basin: Papers of the Russian Academy of Sciences, V. 338, No. 2, p.212–216 (in Russian).

von Huene, R. and D. W Scholl, 1991, Observations at convergent margins concerning sediment subduction, subduction erosion, and the growth of continental crust: Reviews of Geophysics, v. 29, p. 279–316.

Watson, B. F. and K. Fujita, 1985, Tectonic evolution of Kamchatka and the Sea of Okhotsk and implications for the Pacific Basin, *in* Tectonostratigraphic terranes of the Circum-Pacific region, D. G. Howell (editor): Circum-Pacific Council for Energy and Mineral Resources, Earth Science Series, v. 1, p. 333–348, Houston, Texas

Worrall, D. M., 1991, Tectonic history of the Bering Sea and the evolution of Tertiary strike-slip basins of the Bering shelf: Geological Society of America Special Paper 257, pp. 120.

Yogodzinski, G. M., J. M. Lees, T. G. Churikova, F. Dorendorf, G. Woerner and O. N. Volynets, 2001, Geochemical evidence for the melting of subducting ocean lithosphere at plate edges: Nature. v. 409, p. 500–504.

Yogodzinski, G. M., J. L. Rubinstone, S. M. Kay and R. W., Kay, 1993, Magmatic and tectonic development of the western Aleutians: an oceanic arc in a strike-slip environment: Journal of Geophysical Research, v. 98. No. 7, p. 11807–11834.

Yogodzinski, G. M., O. N. Volynets, A. V. Koloskov, N. I Seliverstov, and V. V. Matvenkov, 1994, Magnesian andesites and the subduction component in a strongly calc-alkaline series at Piip Volcano, far western Aleutians: Journal of Petrology, v. 35, p. 163–204.

Yogodzinski, G. M., R. W. Kay, O. N. Volynets, A. V. Koloskov, and S. M. Kay, 1995, Magnesian andesite in the western Aleutian Komandorsky region: Implications for slab melting and processes in the mantle wedge: Geological Society of America Bulletin, v. 107, p. 505–519.

Yorath, C. J., 1987, Petroleum geology of the Canadian Pacific continental margin, *in* D. W. Scholl, A. Grantz and J. G. Vedder (editors), Geology and resource potential of the continental margin of western North America and adjacent ocean basins—Beaufort Sea to Baja California: Circum-Pacific Council for Energy and Mineral Resources, Earth Science Series, v. 6, p. 283–304, Houston, Texas.

Zinkevich, V. P. and N. V. Tsukanov, 1992, The formation of the accretional structure of eastern Kamchatka in the late Mesozoic and early Cenozoic: Geotectonics, v. 26, No. 4, p. 332–343.

Zinkevich, V. P., A. D., Kazimirov, A. A., Peyve and G. M. Churakov, 1985, New data on the structure of the Cape Kamchatskiy Peninsula, eastern Kamchatka: Doklady Academii Nauk, USSR Earth Science, v. 285, p. 954–958.

Zonenshain, L. P., M. I., Kuzmin and L. M. Natapov, 1990, Geology of the USSR; A plate tectonic synthesis: American Geophysical Union, Geodynamic Series, v. 21, pp. 149–167.

Evolution of the Kurile-Kamchatkan Volcanic Arcs and Dynamics of the Kamchatka-Aleutian Junction

G. P. Avdeiko, D. P. Savelyev, A.A. Palueva, and S. V. Popruzhenko

Institute of Volcanology and Seismology, East Division of Russian Academy of Science, Petropavlovsk-Kamchatsky, Russia

The Cenozoic tectonic evolution of the Kurile-Kamchatkan arc system has been reconstructed based on the spatial-tectonic setting of the volcanic-rock formations and their petrologic-geochemical characteristics, using gravity and seismic data. Three volcanic arc trench systems of different ages that become successively younger toward the Pacific have been recognized in the region: the West Kamchatka (Eocene), Mid-Kamchatka-Kurile (Late Oligocene–Quaternary), and Recent Kurile-Kamchatka systems. The Kamchatka volcanic belts are viewed as the products of these systems, which originated above the subduction zones. The geometry of the present-day Kurile-Kamchatka subduction zone and dynamics of contemporary volcanism can be defined from seismic data. The contemporary Kurile-Kamchatka arc can be subdivided into individual segments in accord with its tectonic evolution and geodynamics. The East Kamchatka segment represents the initial subduction stage (7–10 Ma ago) of the Pacific Plate. The Petropavlovsk segment (the Malka-Petropavlovsk zone of transverse faults) is a zone of discordant superposition of the contemporary Kurile-Kamchatka arc over the older Mid-Kamchatka arc. Within the South Kamchatka segment subduction remained practically unchanged since the Late Oligocene, i.e., since the origin of the Mid-Kamchatka-Kurile arc system, as well as within the three Kurile segments. Geodynamics controlled magma generation and is imprinted in the petrochemical properties of the volcanic rocks. Typical arc magmas are generated at the steady-state geodynamic regime of subduction. Lavas of an intraplate geochemical type are generated at initial and final stages of subduction, and also at the Kamchatka-Aleutian junction.

1. INTRODUCTION

The Kurile-Kamchatkan subduction system is a very appropriate region for the reconstruction of volcanic arc (VA) evolution and of the geodynamic conditions of VA volcanism and magma generation for a number of reasons. First, the Kurile segment of this system is a typical island arc with a steady-state regime of subduction, but Kamchatka is an active continental margin with three VA of different ages. Second, within Kamchatka there are VA temporally positioned at the initial stage of subduction (Eastern Kamchatka) and at the final stage of subduction (the Sredinny Range). Third, typical VA rocks are distributed on the Kuriles and in South Kamchatka, whereas some volcanic rocks with intraplate geochemical characteristics coexist with predominant VA rocks in East Kamchatka and in the Sredinny Range [*Volynets*, 1994]. And finally, a transition from arc to oceanic volcanic rocks takes place at the Kamchatka-Aleutian

Volcanism and Subduction: The Kamchatka Region
Geophysical Monograph Series 172

10.1029/172GM04

junction [*Portnyagin et al.*, 2005]. Additionally, high magnesian basalts and adakites occur in this region [*Volynets et al.*, 1999; *Yogodzinsky et al.*, 2002].

This paper is an attempt to synthesize modern spatial-structural, petrological and geochemical data in relation to the tectonic evolution and volcanism of the Kurile-Kamchatkan VA system, with the aim of reconstruction of geodynamic conditions of different types of VA volcanism and establishing criteria for paleotectonic reconstructions of volcanism of ancient subduction zones.

2. GEOLOGICAL AND GEOPHYSICAL DATA

2.1 Geology Framework of Kamchatka

The Kamchatka peninsula has been developing as an ocean-continent transition zone for a long time. Allochthonous and autochthonous geological formations comprise its structure (Plate 1). Autochthonous terrigenous and volcanogenic complexes were formed during island arc stages of development beginning from the Paleogene. Allochthonous complexes were formed in different geological and geodynamic conditions and were accreted to Kamchatka in the Late Mesozoic-Early Cenozoic time. Now the majority of them, excluding geological complexes of the eastern peninsulas, form a basement for the Kamchatka volcanic arcs (Plate 1). The most ancient rocks of the basement obviously are metamorphic complexes of the Sredinny and Ganalsky Ranges, but their age has been a subject of debate for almost a half century. At first geologists assumed that the metamorphic rocks were Precambrian. Later, it was determined that allochthonous-folded structure of Sredinny and Ganalsky massifs and metamorphism of separate allochthonous units were related to collision processes in Mesozoic and Cenozoic time [*Rikhter*, 1991, 1995; *Konstantinovskaya*, 2001].

Sredinny metamorphic massif (Plate 1) is composed of several main units that differ in structure and degree of metamorphism. The lower unit (Kamchatskaya Unit) contains a high-grade metamorphic core composed of granulite facies rocks [*Rikhter*, 1995]. Amphibolite-facies rocks (Malkinskaya Unit) are thrust over the rocks of Kamchatskaya Unit in periclinal zones, and along the eastern margin of the metamorphic core. Terrigenous, volcanic-siliceous and volcaniclastic rocks were protoliths for the rocks of Kamchatskaya and Malkinskaya Units. Originally these rocks were formed as a result of transportation of terrigenous material to a back-arc basin and volcanic arc. During collision, the continental margin and arc rocks were metamorphosed and intruded by plagiogranites, Rb/Sr dated as 127 Ma [*Vinogradov et al.*, 1991]. Along the eastern margin, the Sredinny metamorphic massif is tectonically covered by Upper Cretaceous terrigenous and volcanic-siliceous deposits of Khosgonskaya and Iruneyskaya Units.

The Ganalsky metamorphic massif (Plate 1) consists of three allochthonous units. The uppermost contains phyllite and chlorite-biotite facies rocks, the middle one includes greenshists and epidote amphibolites, and the lower unit is made of garnet amphibolites [*Rikhter*, 1991]. In contrast to the Sredinny massif, the protoliths for these metamorphic rocks were oceanic basalts, pelagic siliceous rocks, limestones and also VA rocks. Tectonic slices are often separated by metamorphized ultramafics and serpentinite melange. The metamorphism is related to arc-continent collision. $^{39}Ar/^{40}Ar$ age from garnet amphibolites (50.6–47 Ma) indicate that the amphibole-grade metamorphism occurred before the end of Early Eocene [*Konstantinovskaya*, 2001].

Metamorphic rocks also occur in the structure Khavyvenskaya Rise (Plate 1) and comprise blocks in serpentinite melanges on the Ozernoy Peninsula, Kamchatsky Mys Peninsula and northern part of Kumroch Range. These units consist of amphibolites, green slates, and rare quartzites. The metamorphism is related with subduction of an oceanic plate, fragments of which were thrust to the surface in the process of the tectonic reorganization [*Osipenko et al.*, 2005].

Besides metamorphic rocks, the basement of Cenozoic volcanic arcs includes Late Cretaceous – Paleocene units, the composition of which varies for different tectonic zones (Plate 1). The basement of West Kamchatka and of the Mid-Kamchatka arcs (Sredinny Range) is Upper Cretaceous terrigenous deposits (Khosgonskaya and Lesnovskaya Units), volcanic-siliceous rocks of Iruneyskaya Unit, and volcanic formations of VA-type of the Upper-Cretaceous-Paleocene Kirganikskaya Unit. Terrigenous deposits were formed by transportation of material from a continental margin to a back-arc basin, often as turbidites. Volcanic-siliceous deposits of the Iruneyskaya Unit were clearly formed in back-arc spreading conditions.

Within Eastern Kamchatka (in the Valaginsky and Kumroch Ranges, on the Ozernoy Peninsula), the basement is represent by Upper Cretaceous volcanic, volcano-terrigenous and siliceous rocks (Khapitskaya and Kitilginskaya Units), which were formed in the conditions of an ensimatic island arc. Paleocene-Lower Eocene complexes consist of continental-derived turbidites. Deposits of different arc facies were tectonically combined and formed the accretion structure of basement of the modern volcanic arc of Eastern Kamchatka. The east part of Kumroch Ridge and southern part of Valaginsky Ridge are characterized by series of tectonic slices, which comprise the accretionary complex of Paleocene-Early Eocene age (Vetlovka Unit). This unit contains volcaniclastic rocks, pelagic radiolarites, limestones,

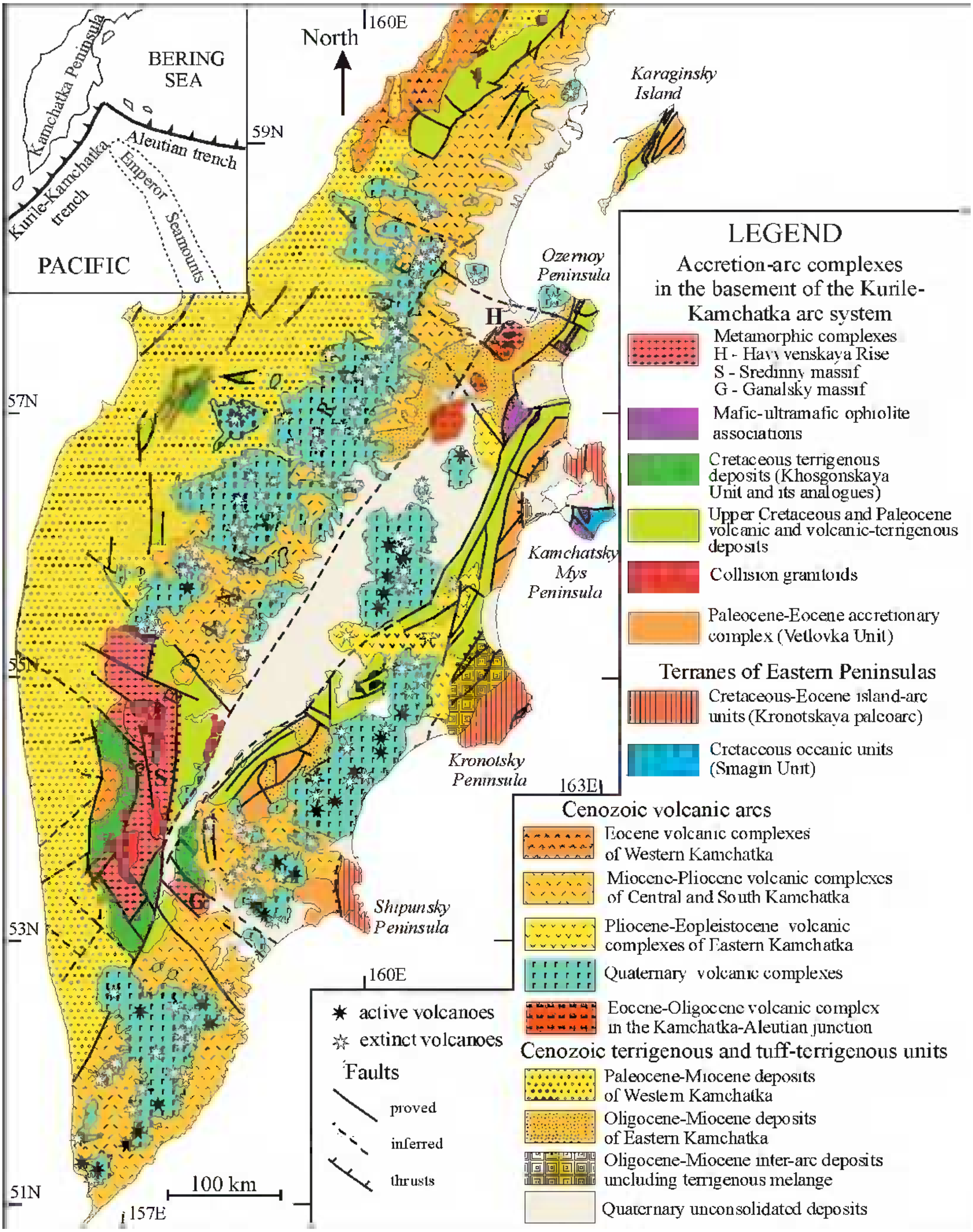

Plate 1. Generalized tectonic map and geologic formation complexes of Kamchatka.

MORB-like basalts, and diabases formed in the Vetlovka oceanic basin [*Konstantinovskaya*, 2001].

Terranes of eastern peninsulas (Kamchatsky Mys, Kronotsky and Shipunsky) form a frontal (tectonic) arc in the modern structure of Kamchatka (Plate 1). They are parts of the Kronotskaya paleoarc formed in the central part of Pacific and accreted to the Kamchatka [*Khubunaya*, 1987; *Levashova et al*., 2000]. Upper Cretaceous-Eocene marine volcanogenic-sedimentary rocks are characteristic for this arc. The peninsulas are separated from the rest of Kamchatka by a long trough, the Tyushevskiy paleobasin, filled with Upper Eocene-Miocene terrigenous sediments. The western border of the Tyushevskiy trough is a large zone of east-trending thrust (Grechishkin Suture) formed as a result of accretion of the Kronotskaya paleoarc. There are two points of view on the time of collision of the Kronotskaya paleoarc with Kamchatka. According to one of them [*Tsukanov*, 1991], it took place in the Middle Eocene phase of compression simultaneously with the main structural reorganization of the entire region. According to other authors [*Avdeiko et al*., 1999; *Konstantinovskaya*, 2001], tectonic accretion of the Kronotskaya paleoarc took place in the Late Miocene (7–10 Ma ago), and resulted in closing of the Tyushevskoy basin and jump of the subduction zone to the present-day position.

Much interest is focused on the structure of Kamchatsky Mys Peninsula where there are ophiolites and volcanic rocks of the OIB and IAB types. This terrane occupies a key position at the Kamchatka-Aleutian junction. The geological structure of this area consists of intrusive, volcanic and sedimentary complexes from the Cretaceous to Quaternary that were formed in a variety of geodynamic conditions (Plate 1). Data on rock composition and age allow us to reconstruct the history of development of this area.

The southern part of the Kamchatsky Mys Peninsula is composed of components of an ophiolite assotiation – ultrabasic rocks, gabbro, dikes and lavas of the basalts, as well as Cretaceous silicic-volcanic and terrigenous sedimentary rocks. Some amphibolites occur as blocks in a serpentinite melange. Volcanoclastic tuff and chert deposits with pillow-basalt, jasper and limestone are melded with in the Smagin Unit. The age of this sequence was estimated to be Albian-Cenomanian by the radiolarian assemblage from jasper in the limestones. This complex contains a suite of MORB-like tholeiites and high-K_2O alkali basalts [*Fedorchuk*, 1992; *Savelyev*, 2003; *Portnyagin et al*., 2005b]. Alkali basalts constitute about 5–7% of the volcanic rocks in the Smagin Unit and their geochemical characteristics correspond to those of ocean island basalts (OIB). The high content of K, P, Nb and LREE in these rocks is similar to alkali basalts of the Emperor Seamount Chain. Thus, composition and age connects the formation of Kamchatsky Mys alkali basalts to activity of the Hawaiian mantle plume [*Avdeiko and Savelyev*, 2005]. Deposits of the Smagin Unit are overlain by Turonian-Campanian sandstones and siltstones of the Pikezh Unit. The northern part of Kamchatsky Mys Peninsula is composed of Cretaceous – Middle Eocenian terrigenous-volcanogenic deposits of the Stolbovskaya Unit similar to those of Kronotsky and Shipunsky Peninsulas of the same age. Primitive tholeiites and high-Al basalts, typical for ensimatic island arcs, predominate in it [*Khubunaya*, 1987; *Tsukanov*, 1991]. During the Early Eocene, ophiolite complexes were eroded from this arc, as evidenced by abundant serpentinite fragments in sandstones of the Stolbovskaya Unit.

A model of geological development was constructed consistent with these data. Early Cretaceous: oceanic crust was formed in the axial zone of a mid-oceanic ridge (ultrabasic rocks, gabbro, basalts MORB-type). Albian-Cenomanian: an intra-oceanic rise was formed on the flanks of an anomalous segment of this mid-oceanic ridge, affected by the adjacent Hawaiian mantle plume (i.e., the Smagin Seamount composed of tuffaceous sediments, tuffs, limestones with jasper, MORB-like tholeiites, and high-K_2O alkali basalts). Turonian-Campanian: the Smagin Seamount migrated into a continental margin into a zone of terrigenous sedimentation (sandstones and siltstones of Pikezh Unit). Campanian-Maastrichtian: Kronotskaya arc began to form on oceanic crust. Active volcanism in this arc continued up to Eocene and volcanogenic-sedimentary deposits accumulated. Middle Eocene: a large tectonic reconstruction occurred as the Pacific plate changed its direction. Collision of Achaivayam-Valaginskaya arc with Kamchatka [*Konstantinovskaya*, 2000]: This is a stage of folding and metamorphism. Possibly at the same time, the Smagin Seamount collided with the Kronotskaya arc. Late Eocene: Volcanism stopped in the Kronotskaya arc. Oligocene and Early Miocene: the Kronotskaya arc continued its passive motion on the Pacific oceanic plate. The Tyushevskiy basin (with accumulated terrigenous deposits) was situated between Kamchatka and the inactive Kronotskaya arc . Kamchatka collided with the Kronotskaya inactive arc and Smagin Seamount in Late Miocene (7–10 Ma ago). This collision caused the latest tectonic reconstruction of East Kamchatka and a jump of the subduction zone to their present-day position. The Smagin Seamount was separated from the rest of the Emperor Seamount Chain.

2.2. Distribution of VA Formations

Three VA complexes of different age were formed within the Kurile-Kamchatka VA system (Fig. 1). The Eocene volcanic and subvolcanic rock complexes from basalts to

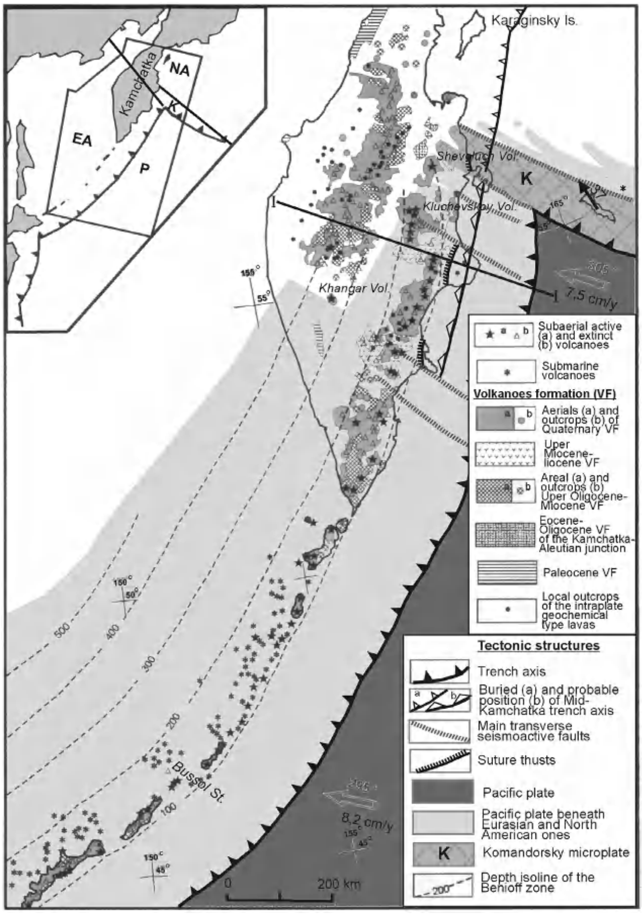

Figure 1. Spatial distribution of Cenozoic subduction-related volcanic formations in the Kurile-Kamchatka island-arc system. I-I location of model cross-section on Fig. 4. On the incut: EA – Eurasian, NA – North American, P – Pacific plates, K – Komandorskaya microplate.

rhyolites (Kinkil unit) stretch out along the western coast and depression of the Parapolsky Dol [*Filatova*, 1988; *Bogdanov, Khain*, 2000].

The associations of Neogene-Quaternary volcanic and intrusive rocks from basalts to dacites and liparites are widespread within the Sredinny ridge of Kamchatka and Southern Kamchatka. Rocks of both normal and alkalic series, i.e. trachybasalts, trachyandesites, etc., occur among them. Some data indicate that the oldest are of Late Oligocene age [*Litvinov, Patoka*, 1999], but other data indicate that they are Miocene [*Sheimovich, Patoka*, 2000]. Detailed geological and petrographic descriptions of these rocks are reported in a number of publications [*Ogorodov et al.*, 1972; *Volynets*, 1994]. *Sheimovitch and Patoka* [2000] distinguish six volcanoplutonic formations in Southern Kamchatka and the Sredinny Range: Miocene andesite, Miocene-Pliocene liparite-dacite, Pliocene basic andesites, Early Pleistocene basalt, Pleistocene-Holocene basaltic andesites (to which all active volcanoes belong), and Holocene basalts (distributed, monogenic volcanism). It should be noted that the name of the formations is the predominant rock type. Two basic features distinguish VA formation complexes of the Sredinny Range from ones of Southern Kamchatka: (1) only typical VA volcanic formations are distributed on Southern Kamchatka, whereas some volcanic rocks of the intraplate non-VA geochemical type occur in the Sredinny Range among the predominant typical VA lavas [*Volynets*, 1994], (2) only two potentially active volcanoes, Ichinsky and Khangar, are in the Sredinny Range [*Melekestsev et al.*, 2001], whereas active volcanism is well-spread within South Kamchatka.

VA volcanic rocks of the Great Kurile Islands have a similar composition. "Green tuff", volcanogenic-siliceous–diatomite, andesite–basaltic andesite, and andesite formation complexes have been described there [*Sergeev, Krasny*, 1987; *Piscunov*, 1987]. The oldest of these is the Oligocene–Middle Miocene green-tuff complex, whose volcanic rocks are represented by basalt, basaltic andesite, andesite, and dacite lavas along with volcanic breccias of the same compositions. Quartz diorite is the only representative of intrusive rocks. The Middle Miocene–Pliocene volcanogenic-siliceous–diatomite complex contains large amounts of andesite and dacite pumice and may be comparable to the rhyolite–dacite rock association of Southern Kamchatka. The andesite–basaltic andesite complex of the Kurile Islands is close both in age and composition to the basaltic andesite rock association of South Kamchatka. Pillow lavas, detrital–pillow breccias, and aquagene tuff are characteristic of this complex. All three pre-Quaternary volcanic-rock complexes occur only at the flanks of the Greater Kurile Islands: on the Shumshu and Paramushir islands (North Kuriles) and on the Urup, Iturup and Kunashir (South Kuriles). Volcanic rocks of the Kurile Islands display evident features of submarine eruption, in contrast to those of the South Kamchatka and Sredinny Range of Kamchatka. The andesite complex of the Kurile Islands is represented by basalt, basaltic andesites, andesites, and dacites of Quaternary volcanoes, many of which are active. The Quaternary submarine volcanoes located on the back-arc part of the Great Kurile Islands were studied in detail during 9 cruises of R/V "Vulkanolog". They also are represented by basalts, basaltic andesites and andesites [*Avdeiko et al.*, 1991].

In East Kamchatka, including the Central Kamchatka Depression, Oligocene–Miocene volcanic rocks of the VA type are absent, in contrast to the Kamchatka Sredinny Range, Southern Kamchatka, and the Kurile Islands. Here, a large group of Pliocene and Pliocene–Early Pleistocene volcanic complexes composed of basalt, andesite, and dacite lavas in variable proportions and of subvolcanic facies of the same rocks have been recognized [*Litvinov, Patoka*, 1999]. There are also modern volcanoes (Fig. 1). In addition, there are some small volcanic bodies of alkaline and subalkaline basalts with intraplate geochemical characteristics [*Volynets et al.*, 1990; Volynets, 1994]. These are Late Miocene rocks and are the oldest volcanic products within the Eastern Kamchatka VA belt.

On the whole, Pliocene–Quaternary VA rocks are most common within the Kurile-Kamchatka system. Their compositions range from basalts to dacites and rhyolites and vary across different regions. Basaltic andesites and andesites are predominant rocks on the Kurile Islands, while basalts and basic basaltic andesite are predominant in Kamchatka.

2.3. Chemical Characteristics of VA Formations

The chemical composition of lavas is most completely studied for the Pliocene-Quaternary association of volcanic rocks [*Avdeiko et al.*, 1991; 1992; *Volynets*, 1994)] Within the Kuriles and Kamchatka lavas there can be distinguished low-K, moderate-K, high-K, and shoshonite-latite series and normal and subalkalic series. Following the criteria of *Miyashiro* [1974], tholeiitic and calc-alkaline differences are distinguished within every series. Calc-alkali, moderate-K series predominate in both Kamchatka and Kuriles and are usually found within frontal zones of the volcanic arcs: on the Kuriles and on east Kamchatka, where they are wide spread, on the Central Kamchatka Depression and on the Sredinny Range, where they appear only sporadically along the eastern margins of these structures [*Volynets*, 1994]. Lavas of high-K series are localized within the rear zones of the Kuriles, south and east Kamchatka and the Sredinny Range. Lavas of shoshonite-latite series occur in the rear zones of the northern Kuriles (and only among basalts), south Kamchatka and Central Kamchatka Depression, but are more common in the Sredinny Range where they are found in the central and rear zones of the volcanic belt.

The distribution of rocks of different series is interrupted by large transverse fault structures, where lavas of the high-K series are found even in the frontal zones of volcanic belts, for example, at the bend of the Kurile arc in the area of Bussole strait [*Avdeiko et al.*, 1992], and in the area of the Malko-Petropavlovsk zone of transverse dislocations in Kamchatka [*Baluev et al.*, 1979].

Among the VA associations of the Kuriles, south and east Kamchatka, a transverse mineralogical and geochemical zonation is well manifested while a longitudinal zonation is less distinct [*Avdeiko et al.*, 1991; *Volynets*, 1994]. Lavas of the frontal volcanic zones are characterized mainly by two-pyroxene phenocrysts, whereas in basalts of the rear zones phenocrysts of orthopyroxene are seldom seen. Phenocrysts of amphibole and biotite are wide spread in andesites and acid rocks and sometimes even in basalts of rear zones while they are absent in analogous rocks of the frontal zone. Similar minerals from different zones also vary in chemical composition [*Volynets et al.*, 1990 b; *Volynets*, 1994; *Osipenko*, 2000].

Transverse geochemical zoning is expressed in increasing concentrations of many incompatible trace elements (K, Rb, Li, Be, Ba, Sr, U, Th, La, Ce, Nb, Ta, Zr, W, Mo) in lavas from front to rear. K/Na, Rb/Sr, La/Yb, Sr/Ca, Th/U, and Mg/(Mg+Fe) (Mg#) ratios, as well as contents of volatile components (H_2O, F, Cl, S), also increase in the same direction. In contrast, contents of Fe, V, and Fe^{2+}/Fe^{3+} decrease in lavas in the same direction. A well pronounced isotope zonation has been defined in the Kurile lavas: $^{87}Sr/^{86}Sr$ and $^{143}Nd/^{144}Nd$ values decrease notably from the front to the rear [*Volynets et al.*, 1988; *Avdeiko et al.*, 1991].

Similar transverse zoning is manifested in the Quaternary VA-type volcanic products of the Sredinny Range, with higher general alkalinity and higher level of the incompatible trace elements concentrations [*Volynets et al.*, 1987; 1990].

Two volcanic zones, front and rear, parallel to the deep-sea trench with a zone of weak volcanic activity between them, are distinctly displayed in the Kuriles and in southern Kamchatka [*Avdeiko et al.*, 1991; 1992]. The volcanic belt of the Central Kamchatka Depression can also be interpreted as a rear zone relative to the frontal one of Eastern Kamchatka (Fig. 1). In any event, the same regularities of geochemical zoning as in the Kuriles and south Kamchatka are characteristic of these zones [*Volynets et al.*, 1990; *Volynets*, 1994].

In addition, lavas of an intraplate geochemical type were discovered and described by *Volynets* [1994] among the Late Cenozoic volcanic rocks of Kamchatka. In contrast to typical VA lavas, these are characterized by high concentrations of Ta, Nb, and Ti, with a Ta-Nb minimum in the rock/primitive mantle spider-diagram that is small or absent [*Volynets*, 1994; *Avdeiko and Savelyev, 2005*]. In addition, they are also characterized by modestly high concentrations of incompatible elements like volcanic rocks of the rear zones (Fig. 2). “Intraplate” lavas of Kamchatka include the following volcanic series: K–Na alkaline basalts (of Late Miocene age in eastern Kamchatka); K–Na alkaline olivine basalts (Pliocene in eastern Kamchatka and Late Pliocene–Holocene in the Sredinny Range, where they comprise a zone of flood-basalt volcanism); K–Na basalt–comendite (of Pliocene–Early Pleistocene age in the Sredinny Range); and K-basalt and associated shoshonite–latite series (Late Miocene–Pliocene in between the Western Kamchatka and Sredinny Range). No systematic transverse geochemical zonation was found among lavas of the intraplate geochemical type.

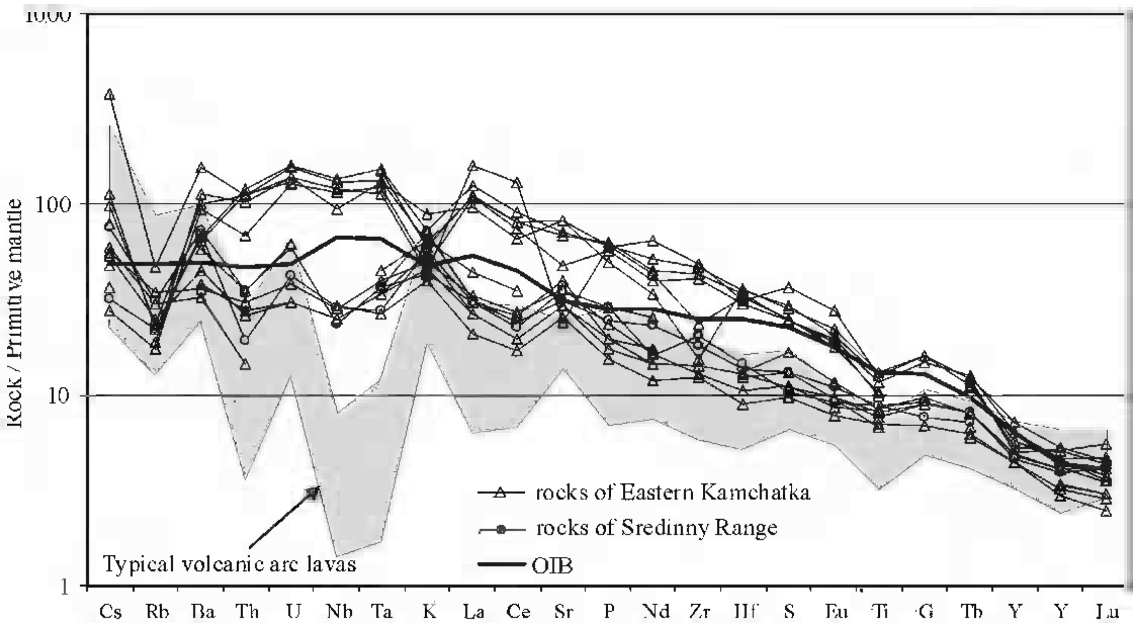

Figure 2. Primitive mantle-normalized trace element for intraplate-type volcanic rocks of Kamchatka. OIB and primitive mantle composition after *Sun and McDonough* (1989), typical arc lavas of Central Kamchatka Depression (35 samples) after *Churikova et al.* (2001)

There are some unusual characteristics of subduction-related volcanic rocks in the Kamchatka-Aleutian junction area. One is the wide distribution here of high-magnesian basalts, basaltic andesites and andesites, including adakites [*Volynets et al.*, 1998; 1999 a]. The volume of magnesian rocks of this area is approximately 10 times more than in all other areas of Kamchatka. Within the magnesian rocks there are certain regularities. Magnesian basalts (Mg# 80–88) of the northern volcanoes (Shiveluch, Kharchinsky, Zarechny) have lower Ca, higher Sc, Y, Yb concentrations and higher K/Ti, La/Yb, Ni/Sc, and La/Ta ratios compared to the similar ones from the Kluchevskaya group of volcanoes. Most of the volcanic rocks of this region are characterized by high alkalinity and high LILE and LREE concentrations. Volcanoes of the Kluchevskaya group are characterized by a very high productivity, supplying about 1/3 of volume of the volcanic material erupted by all Kamchatka volcanoes and two times more than east Kamchatka volcanoes during Holocene time [*Volynets et al.*, 1998; *Kozhemyaka*, 2000]. These unusual features of volcanism reflect the unique geodynamic conditions of the Kamchatka-Aleutian junction.

The data on the distribution, age and chemical composition of VA rocks testify that the volcanic belt of the Sredinny Range is different from the Eastern Kamchatka belt. The origin of the Late Oligocene–Quaternary volcanic belt in the Sredinny Range is still a matter of debate. Some authors interpret it as an independent volcanic arc located above a separate subduction zone under the Sredinny Range. This belt has now completed its development as the result of a blockade of its subduction zone by accretion of the eastern peninsulas to Kamchatka [*Legler, 1977; Avdeiko et al., 1999; Trubizin et al.*, 1998]. Other authors believe that the volcanic belt of the Sredinny Range is related to the present-day Kurile–Kamchatka subduction zone, being a third volcanic zone, a back-arc one relative to the Eastern volcanic zone and the volcanic zone of the Central Kamchatka depression [*Tatsumi et al.*, 1994; *Seliverstov*, 1998]. The origin of the Sredinny Range volcanic belt will be discussed below.

2.4. Gravity Data

The gravity field of the present-day Kurile–Kamchatka arc-trench system has principal gravity features characteristic of such systems, i.e., the presence of conjugate positive and negative free-air gravity anomalies [*Watts et al.*, 1975; 1978]. The positive anomaly extends along the tectonic (frontal) arc, which encompasses the Lesser Kurile Islands and their submarine extension in the Kuriles, as well as the eastern peninsulas in Kamchatka. The positive anomaly is complicated by transverse lower-intensity gravity anomalies along large transverse fault zones in the areas of the Gulf of Avacha in Kamchatka and of the Bussol Strait in the Kuriles [*Watts et al.*, 1978].

The volcanic belts of East Kamchatka, the Central Kamchatka Depression, and the Sredinny Range show a mosaic of alternating Bouguer gravity fields (Plate 2) [*Popruzenko et al.*, 1987]. The character of the anomalies in the areas of volcanic cones is controlled by the structure and composition of the basement rocks, the genetic type and maturity of volcanic centers, the state of isostatic equilibrium, and other factors. For example, local gravity maxima, complicated by gravity ring minima at their margins, mark basalt and some andesite volcanoes. Volcanic calderas produce, depending on their origin, gravity lows (explosive calderas) or highs (collapse calderas).

A characteristic feature of the gravity field in Kamchatka, as compared to other VA systems is the presence of two additional, although less intense, zones of positive gravity anomalies in the area between the Malka–Petropavlovsk zone of transverse faults and the Kamchatka-Aleutian junction. These additional zones are roughly parallel to the principal zone of positive gravity anomalies confined to the eastern peninsulas (Plate 2). One of them, located in the Central Kamchatka Depression, has been delineated rather reliably, while the positive anomaly zone in western Kamchatka is less distinct. The positive anomaly zone in the Central Kamchatka Depression occupies the same position relative to the volcanic belt of the Sredinny Range as does the zone of the eastern peninsulas relative to the volcanic belt of eastern Kamchatka. It coincides nearly completely with the buried part of Khavyvenskaya Rise. The maximum gravity values within this uplift occur on the Khavyvenskaya Rise, which is composed of crystalline schists, serpentinized ultrabasic rock, Late Cretaceous–Paleocene pillow basalt, and tuff, and intruded by a gabbro body with a density of 3.05 g/cm^3. Elsewhere, the anomalous zone of the Khavyvenka highland is covered by a mantle of Cenozoic volcanoclastic rocks, which lowers the value of the positive gravity anomaly. However, the high gravity effect cannot be explained only by the presence of the high-density rocks [*Aprelkov et al.*, 1985]. In our opinion, the buried Khavyvenskaya Rise was the frontal (tectonic) arc of the subduction zone beneath the Sredinny Range. In this case, the positive gravity anomaly is partly a residual anomaly produced by disturbance of isostasy during subduction. We note too that ophiolite complexes are often distributed in frontal arcs.

The presence of a buried paleotrench, indicated by a negative free-air gravity anomaly along the continental rise east of Karaginsky Is. (*Watts et al*., 1975), suggests the separate nature of the subduction zone under the Sredinny Range. The Tyushevskiy trough and the Grechishkin overthrust zone in the Kamchatka correspond to this subduction zone, the latter to the western slope of the paleotrench (Fig. 1).

A model vertical gravity section, showing two subduction zones, is presented in Fig. 3. Our gravity modeling across Kamchatka (profile A – B in Plate 2) indicated that the shape and intensity of the calculated gravity anomaly is close to the measured one if two higher gravity subducting layers with an effective density of +0.08 to +0.1 g/cm^3 and two lower density zones (–0.08 to –0.1 g/cm^3), corresponding to the inferred sites of magma generation, are used into the model.

A third zone of positive gravity anomalies in western Kamchatka seems to mark a Paleogene arc (Plate 2).

2.5. Seismological Data

The spatial distribution of earthquake epicenters recorded during 1962–2005 are shown in Plate 3. A belt of shallow-focus earthquakes (less than 50 km deep) extends along on the continental slope of the deep-sea trench. It is characteristic that all large earthquakes with magnitude more than 7.5 are located within the tectonic arc, above and within the sharp downward bend of the Pacific plate, where the angle of subduction changes from 10–12° to about 50° (Plate 3B). North of the Kamchatka-Aleutian junction, the seismic belt is offset westward, occupying a position relative to the

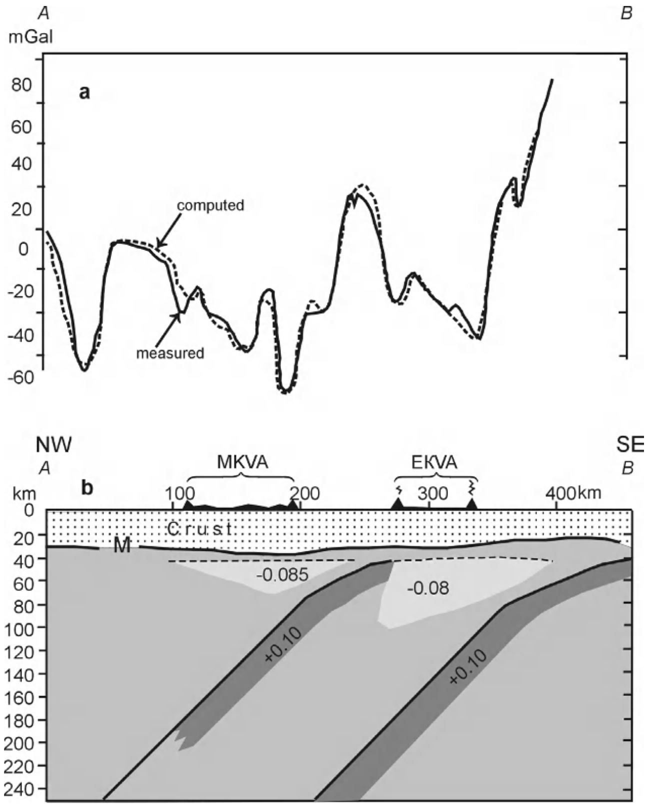

Figure 3. Density model for the mantle at the cross-section along line *A – B* (Plate 2). Earth's crust density heterogeneities were included into calculations.

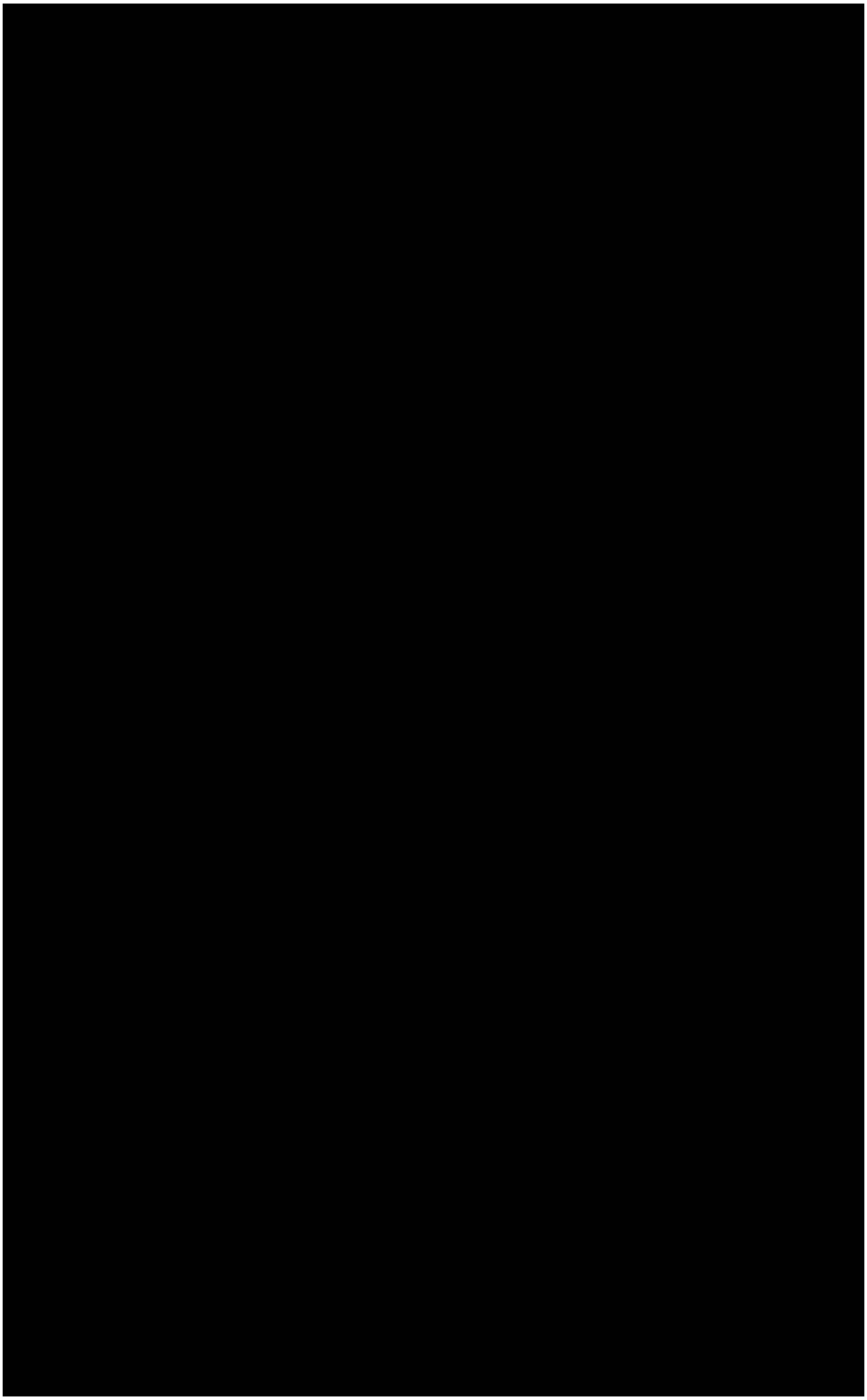

Plate 2. Bouguer gravity anomalies on Kamchatka. A – B – location of model cross-section show in Fig. 3.

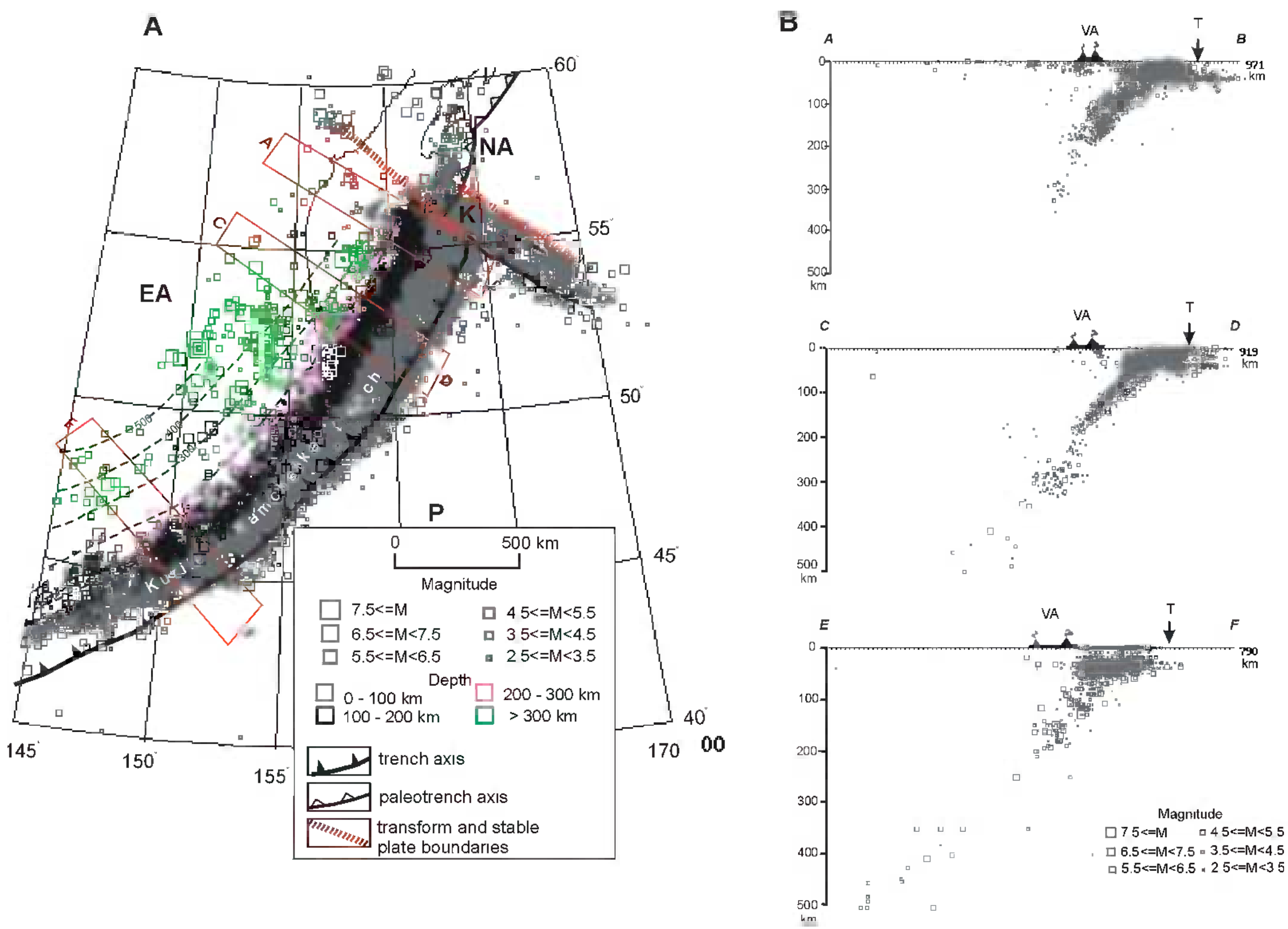

Plate 3. Map of earthquakes epicenters (A) and transverse cross-sections (B) of the Kurile-Kamchatkan Island Arc System. A: Eurasian (EA), North American (NA), Pacific (P) plates, and Komandorskaya microplate (K). B: VA – volcanic arc, T – deep-sea trench.

paleotrench as the seismic belt southward the Kamchatka-Aleutian junction relative to the Kurile-Kamchatka trench. This provides additional evidence in favor of a jump of the subduction zone south of the Kamchatka-Aleutian junction to the present day position. In addition, a great number of shallow-focus earthquakes are recorded in eastern Kamchatka between the Malka-Petropavlovsk zone of transverse faults and a prolongation of the Kamchatka-Aleutian junction on Kamchatka, the segment where we assume the subduction jump took place, whereas few isolated weak earthquakes were recorded in South Kamchatka. This indicates that weak motion still continues along the previous subduction zone, although no longer recorded at greater depths.

2.6. Geodynamic Characteristics of Volcanic Activity

Earlier, *Avdeiko* [1994] discussed the principal geodynamic parameters of volcanism in the Kurile segment of the Kurile-Kamchatka island-arc system based on a subduction model. Benioff seismic zone parameters are known to control aspects of volcanic activity. They exert an effect upon the temperature, pressure, and composition of the melting substratum, the quantity and composition of volatile components participating in the melting process, and the conditions of magma ascent and eruption. Principal parameters include the depth of the subduction zone (to the Benioff zone's upper surface) under the frontal and back-arc volcanoes, the distance between the deep-sea trench axis and the volcanic front, the subduction zone inclination angle, etc.

Recently, in cooperation with V.A. Shirokov, we refined the geometry of the Benioff zone using the data available for the earthquakes in the Kurile–Kamchatka region during the whole period of detailed instrumental observations (1962–2005). The isodepths to the upper surface of the Benioff zone, based on these data, are shown in Fig. 1, and the refined parameters of the structure as it occurs in various portions of the East Kamchatka and Kurile segments of the island-arc system are summarized in Table 1.

The depth of the Benioff focal plane below the volcanic front is nearly constant, at about 110 ± 5 km, and the maximum depth below the back-arc volcanoes farthest from the volcanic front does not exceed 220 km. *Avdeiko* [1994] argued that melting conditions in the mantle wedge are confined to this depth interval of the Benioff plane because of release of volatiles, in general water, from the subducted Pacific plate.

The rate of the Pacific Plate subduction varies from 7.5 cm/year under the Kronotsky Peninsula to 8.3 cm/year at the latitude of Kunashir Is. [*Gorbatov, Kostoglodov*, 1997]. This rate and the distance between the deep-sea trench axis and the volcanic-arc front were used to calculate the time for subduction to 110 km depth where melting of the mantle wedge begins as a result of volatile flux. This time varies from 2.8 m.y. in eastern Kamchatka to 3.2–3.5 m.y. in the southern Kurile Islands.

Table 1. Geodynamic parameters of the Quaternary of Kurile–Kamchatka VA system

Geodynamic parameter	Easthern Kamchatka	Avachinsky Bay	Southern Kamchatka
L_{min}, km	190–200	205	200–205
L_{dir}, km	190–200	205	200–205
L_b, km	130–140	145	140–145
V, cm/y	7.6	7.6	7.7–7.8
$\alpha°$	80–90	90	85–90
$\beta°$	35–51	51	50–51
H_f, km	105–115	115	110
H_{max}, km	195	180	205
t, m.y.	2.8–2.9	3	2.9–3.0
d, km	50–70	70	40–60
T, km	~40	42–47	40–45

Notes: L_{min} and L_{dir} – the distance between the trench axes and volcanic front: minimal (L_{min}) and along the direction of the Pacific plate motion (L_{dir}). L_b – the distance between the trench axis and the bend in the Pacific plate (a change of subduction angle from 10–12º to about 50º, V – the convergence rate [*Gorbatov et al.*, 1097], α - angle between a direction of the Pacific plate motion and the arc strike, β - a subduction angle between 40 – 500 km, the depth beneath the volcanic front (H_f) and the rear volcanoes (H_{max}), t – the time of the Pacific plate to pass from the trench axis down to H_f, d –width of the volcanic arc, T –crustal thickness.

It should be emphasized that the geodynamic parameters of magma generation and volcanic activity are approximately the same in all VA systems throughout the Circum-Pacific Belt. The principal parameters are as follows: the Benioff-zone depth below the volcanic arc varies from 110±10 km beneath a volcanic front up to 220 km beneath the most distant from volcanic front volcanoes; the volcanic-arc width usually is not more then 100 km; and the distance between the deep-sea trench axis, i.e., the subduction starting line and the volcanic front line is not more that 250 km. The position of the volcanic belt in the Kamchatka Sredinny Range does not agree with these parameters. The depth to the present-day Benioff zone in the south of the belt varies from 300 km below the frontal volcanoes to 450 km under the rear-arc volcanoes. As for the area north of Ichinsky volcano, subduction, if present, does not reveal itself in the form of a seismic zone. The width of the Sredinny Range volcanic belt exceeds 100 km, which is comparable with the width of a large volcanic arc. If the volcanic belt of the Sredinny Range is considered as a third volcanic belt connected with present-day subduction zone, then the volcanic arc is as wide as 400 km within this segment of the Kurile–Kamchatka island-arc system.

3. DISCUSSION

3.1. Nature of the Volcanic Belt of the Sredinny Range, Kamchatka

The above geological and geophysical data enable assessment of the conditions of formation of the volcanic belt of the Sredinny Range in Kamchatka. On the one hand, this question is key to reconstructing the history of tectonic development of the Kurile-Kamchatka VA system. On the other hand, it is important for understanding the processes of magma generation related to the subduction.

Connecting the formation of this belt with the present day Kurile-Kamchatka subduction zone is well-described in by *Tatsumi et al*. [1994; 1995]. In their opinion, the unusual position of this belt and the atypical composition of the volcanic rocks are accounted for by melting of K-amphibole-bearing peridotite at the base of the mantle wedge at anomalously high temperatures. Such high temperature is explained by the unusual tectonic setting of the belt at the edge of the Pacific plate having a transform-type boundary with the North American plate. Calculations made by these authors predict a temperature rise of 200–300°C in the boundary of the mantle wedge in comparison with the usual situation.

This explanation could be plausible if the aerial distribution of volcanoes in the Sredinny Range were restricted to the zone of the Kamchatka-Aleutian junction. However, the volcanic belt of the Sredinny Range represented by subduction-related Late Oligocene-Quaternary volcanic formations extends more than 700 km from latitude 54.8°N at Khangar volcano in the south to latitude 60.3° in the north. It should be emphasized, however, that a zone of anomalously increased temperature does exist, and, in our view, causes formation of high-magnesian basalts and lavas of the intraplate geochemical type along with the typical VA lavas [*Volynets*, 1994; *Volynets et al.*, 1999; *Portnyagin et al.*, 2005; *Avdeiko and Savelyev*, 2005].

Seliverstov [1998] believes also that the Sredinny Range volcanic belt formation is connected with the modern Kurile-Kamchatka subduction zone. In his opinion, inclination of the subduction zone in Miocene was more gentle due to subduction of hotter lithosphere. In Pliocene time, the angle of the subducted plate increased and VA belt shifted from the Sredinny Range to the present-day position. This view is unlikely to be the true for the following reasons:

1. It is not clear why subducting Pacific lithosphere should have been hotter in the Miocene. A single cause may be intraplate volcanism, but the age of the nearest volcanoes of the Obruchev rise (Detroit and Meiji Seamounts) is more than 85 m.y. [*Regelous et al.*, 2003].
2. The dip angle of subduction of the young Nasca plate exceeds 23°, whereas the subduction angle zone at the distance of 320–350 km between the Kurile-Kamchatka trench axis and the Sredinny Range volcanic belt must be less than 20°.
3. According to *Seliverstov* [1998], a change of the subduction angle is a continuous process resulting from an increase in the sinking rate due to subduction of a heavier lithosphere. Therefore, the question arises as to why the volcanic zone was offset east ward over a distance of 150 km (distance between paleovolcanic front of the Sredinny Range and volcanic front of eastern Kamchatka), during a continuous process without leaving any trace in the form of volcanoes.

The data discussed in the previous sections suggest that the volcanic belt of the Sredinny Range was an independent volcanic arc, which was formed above its subduction zone, which jumped to its present-day position in the end of Miocene, as incoming positive-buoyancy lithospheric blocks locked subduction. According to *Trubitsyn et al*. [1998], these blocks are represented now by the eastern Kamchatka peninsulas. The location of the volcanic arcs and the axes of the deep-sea trenches that mark the subduction zones, are shown in Fig. 1. The principal lines of evidence for this interpretation are summarized below.

1. Spatial distribution and tectonic setting of the volcanic belts and the absence of Miocene island-arc volcanic rocks in eastern Kamchatka, except Late Miocene intraplate lavas (Fig. 1), indicate that the volcanic belts of the Sredinny Range and eastern Kamchatka (along with the belts of the Central Kamchatka Depression) are independent volcanic arcs. Moreover, frontal and rear-arc volcanic zones separated by a zone of weaker volcanic activity have been recognized within the Sredinny Range volcanic arc, as well as in Southern Kamchatka and in the Kurile Islands.
2. The transverse petrochemical zoning of the Sredinny Range volcanic belt is similar to that of other volcanic arcs, though with higher contents of alkali and incompatible trace elements.
3. Gravity data indicate the doubling, and possibly trebling, of crustal thickness of the Sredinny frontal (tectonic) arc (delineated by a belt of positive anomalies)–volcanic arc systems (Plate 2 and Fig. 3).
4. The seismological data (Plate 3) suggest that some residual movements still occur in the subduction zone of the Sredinny Range. It is also possible that these movements continue in the segment between the Malka–Petropavlovsk and Kamchatka-Aleutian junction of transverse faults. These are transform faults that limit the region (segment) of the subduction zone jump (Fig. 1).
5. A paleotrench corresponding to the Sredinny Range subduction zone has been outlined by gravity and seismic reflection and refraction data east of Karaginsky Island.

The idea of the jump of tectonic zones in Kamchatka, which are regarded as the paleoanalogues of modern VA–trench systems, was put forward by one of the present writers independent of the subduction model [*Avdeiko*, 1971]. Later, *Legler* [1977] elaborated the concept as a subduction-zone offset. However, the mechanism of subduction north of the Kamchatka Peninsula, i.e., to the north of the junction with the Aleutian arc, remained unclear. Based on computer modeling, *Trubitsyn et al.* (1998) showed that subduction and, consequently, volcanism in the northern segment of the Sredinny Range arc had been caused by mantle convection under the Komandorskaya Basin induced by the Pacific Plate motion. A system of back-arc spreading rifts, which corresponds to this interpretation, had previously been discovered within the Komandorskaya Basin [*Baranov et al.*, 1991].

3.2. Tectonic History

The data presented above allow us to interpret Cenozoic tectonic history of the Kurile–Kamchatka region as the development of VA subduction systems of different ages, which were offset discretely and consecutively grew younger toward the Pacific Ocean (Fig. 1 and 4). Obviously, a system of volcanic complexes existed in western Kamchatka in the Paleogene (Fig. 1), of which only isolated outcrops of volcanic sheets and subvolcanic bodies remain [*Bogdanov, Khain*, 2000]. A belt of positive gravity anomalies seems to mark a frontal (tectonic) arc (Plate 2). The intensity of the anomalies has been reduced by partial recovery of isostatic equilibrium.

Beginning from the end of the Oligocene (Fig 4, cross-section 1), a system of two arcs existed within Kamchatka and the Kurile Islands, i.e., the Mid Kamchatka and the South Kamchatka–Kurile arcs. The formation of this system south of the Kamchatka-Aleutian junction was caused by the subduction of the Pacific Plate, while to the north, it was caused by subduction of a young small plate of the Komandorskaya basin. These arcs are marked in the present-day structure by their own volcanic-rock associations (Fig. 1). A frontal (tectonic) arc of this subduction system shown (Fig. 4) now is buried beneath sediments of the Central Kamchatka Depression excluding Havyvenskaya Rise. A positive gravity anomaly marks its position. A paleotrench of this system shown on Fig. 1 is reconstructed as a prolongation of buried trench of Komandorskaya basin and on the basis of geodynamic parameters of modern Kurile-Kamchatka subduction system (Table 1). A portion of sediments deposited on this trench continental slope was eroded, a portion is shown on the generalized map as Oligocene-Miocene deposits of Eastern Kamchatka, and a portion was covered by volcanic rocks of East Kamchatka VA. Fragments of these deposits were carried upward as xenolites during Large Tolbachik eruption (*Fedotov et al.*, 1984).

In the end of the Miocene, the subduction zone of the Pacific Plate within the segment from the Shipunsky Peninsula to the Kamchatka-Aleutian junction was blocked by the accretion of the eastern Kamchatka peninsulas and, probably, some other structural elements of eastern Kamchatka. As a result, the subduction zone jumped to its present-day position, and the Kurile–Kamchatka island-arc system acquired its present-day shape (Fig. 1). Geodynamic conditions changed. The area of the Miocene trench, where a negative isostatic anomaly was present, began to elevate as isostatic equilibrium was restored. In contrast, the Miocene frontal arc began to subside, forming the Central Kamchatka Depression. Opposite movements led to formation of a fault zone probably with a thrust component due to compression.

We postulate the forming of a plate gap, and consequently opening of mantle windows, after cessation of subduction (Fig. 4, cross-section 2). This breakage is possible as a result of increase of plate sinking after eclogitization. P-wave seismic tomography appears to show a gap in the slab at a depth of 450–600 km [*Gorbatov et al.*, 2000, Fig. 7, cross-section E–E']. This cross-section is located in the central part of Kamchatka, where the jump of subduction zone took place. We suggest that the high velocity body in this cross-section at the depth about 600–1000 km was torn away from the Pacific plate after subduction stopped beneath the Sredinny Range. There is no such gap in the cross-section D–D' located beneath southern Kamchatka, where no jump of the subduction zone occurred, i.e. in the segment of the steady-state regime of subduction.

An inter-arc trough formed between frontal and volcanic arcs. It is suture zone, were sediments of the lower slope of the Miocene trench were accumulated. They are shown as Oligocene-Miocene inter-arc deposits including terrigenous mélange on Plate 1. Later some of them were covered Quaternary unconsolidated deposits.

3.3. Volcanic–Tectonic Zonation

Our interpretation of volcanic–tectonic zonation is based on the principle of classifying volcanic arcs by the ages of the subduction zones and the episodes of volcanic activity. The present-day Kurile–Kamchatka VA system can be subdivided into segments based upon variations in geodynamic parameters of the subduction zone, which are also reflected in the spatial distribution and tectonic setting of the volcanoes and by the composition of the volcanic rocks. Since we did not find any effects of the age or the composition of the basement rocks upon the composition of the volcanics in the Kurile–Kamchatka VA system, we do not use this parameter in defining the volcanic–tectonic zonation.

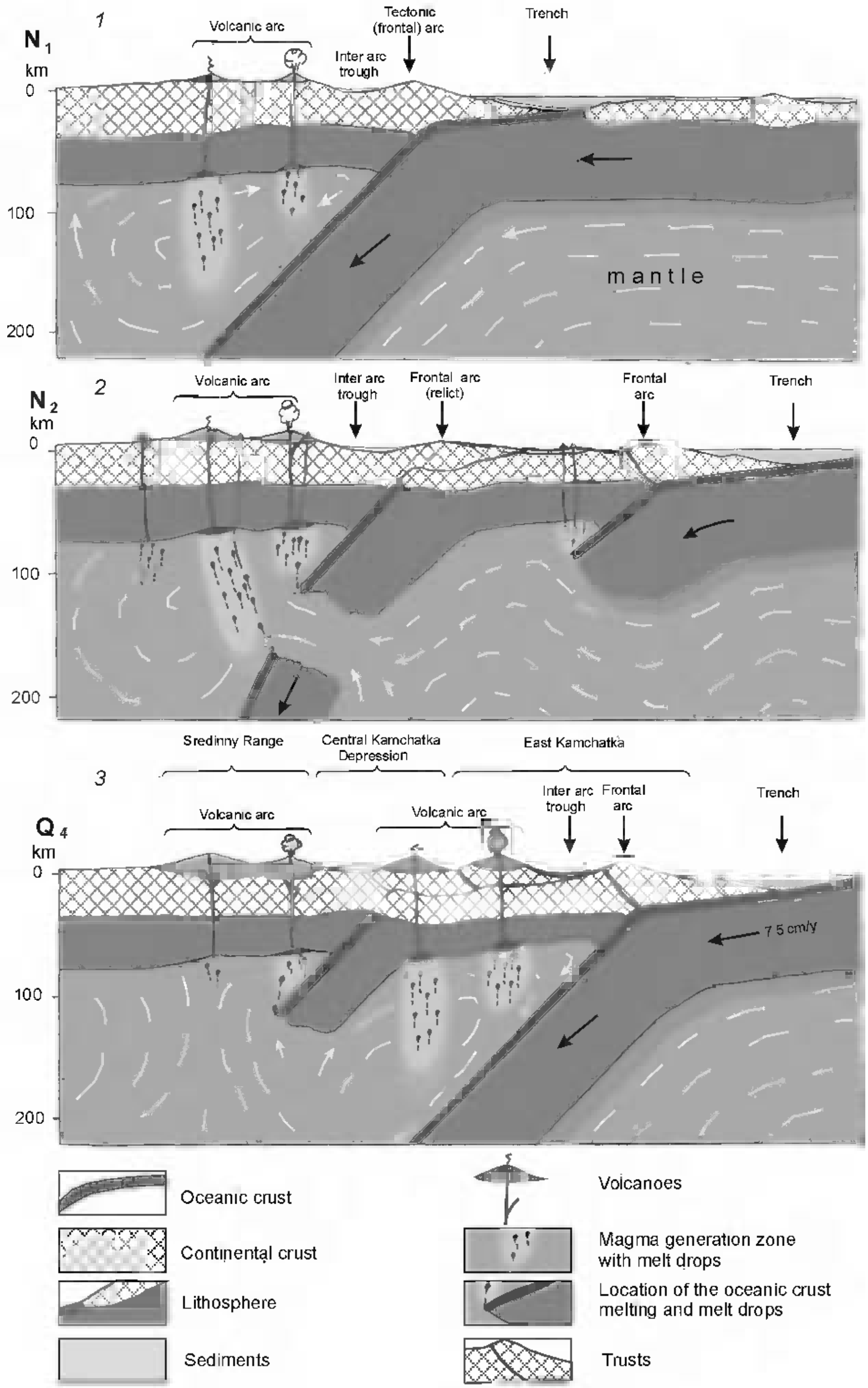

Figure 4. Model cross-sections of evolution of the Kurile-Kamchatka island arc system (after *Avdeiko et al.*, 2001 with correction). See Fig. 1 for location of cross-sections.

Three volcanic arc–deep-sea trench systems of different ages that become successively younger toward the Pacific Ocean have been recognized in the region: the West Kamchatka (Eocene), Mid Kamchatka–Kurile (Late Oligocene-Miocene), and Recent Kurile–Kamchatka systems. These volcanic arcs form the rigid framework of the present-day tectonic structure of the Kurile–Kamchatka island-arc system. Sedimentary troughs separating these arcs are either forearc or back-arc basins.

We recognize the following segments within the Kurile–Kamchatka VA system based on the tectonic evolution and geodynamics of the present-day volcanic activities above the zone of the Pacific Plate subduction under the Eurasian Plate.

The East Kamchatka segment represents the initial stage (7–10 Ma) of an orthogonal subduction process. The subsidence of the Pacific Plate margin to a depth of approximately 110 km, where the separation of initial magmatic melts becomes possible and over which the volcanic front is located, lasted 2.8–2.9 m.y. This implies that subduction must have commenced before the extrusion of the associated oldest volcanic rocks, i.e., in the latest Miocene. This segment consists of various components, with an area where the lithospheric plate carrying normal oceanic crust is underthrust at an angle of 50°, and an area where the oceanic crust, thickened owing to the presence of the Obruchev Rise, is subducted at an angle of about 30°–35°. This segment also includes the Kamchatka-Aleutian junction.

The Petropavlovsk segment (the Malka–Petropavlovsk transverse-fault zone) is a zone of discordant superposition of the present-day Kurile–Kamchatka arc of NE trend upon the Malka–Petropavlovsk segment of the Middle Kamchatka–Kurile VA system, having a NW trend there. In the south Kamchatka segment, as well as in the three Kurile segments, subduction began at the end of the Oligocene. A virtually stationary subduction zone persisted there for about 25-m.y. We postulate that westward shift of the volcanic front was caused by the cooling effect of the subducted Pacific Plate and a consequent shift of the magma-generation zone in the mantle wedge in the same direction as slab motion. We have subdivided the Kurile segment of the Kurile–Kamchatka arc into the North, Middle and South Kurile segments, with different geodynamic characteristics of the subduction zone and subduction-related volcanism (Table 1). Both the frontal and back volcanic zones, separated by a zone of weaker volcanic activity, are distinctly displayed in each segment of the volcanic arcs.

3.4. Geodynamics of the Kamchatka-Aleutian Junction

Geodynamical conditions of this area have evolved over the last 40 Myr due to interaction of the Pacific, North American, Eurasian and Kula plates and Komandorskaya microplate. The junction assumed its present shape during the last 7–10 Myr, after blockage of the Pacific plate subduction under the Sredinny Range of Kamchatka and its jump to the present-day position (Fig. 1 and 4). Both the jump and the arrow-like shape of the Kamchatka-Aleutian junction are in large measure caused by the Hawaiian-Emperor volcanic chain. The proposed geodynamic model of the Kamchatka-Aleutian junction (Fig. 5) assumes gradual westward transfer of motion from oblique subduction of the Aleutian arc to the transform fault near Kamchatka. The braking effect of the motionless North American plate upon the moving and subducting Pacific plate results in a tension and sometimes rupture of the latter (slab-windows) and intrusion of hotter below-slab material into the mantle wedge. One such slab-window probably occurs under the Kluchevskaya group of volcanoes and is the reason for their high productivity and the magnesian composition of their rocks. Additionally, separation of the Pacific slab-edge blocks, their sinking into the mantle, and subsequent heating can lead to generation of small mantle plumes (Fig. 5). One such plume is confirmed by seismic tomography data [*Gorbatov et al.*, 2000; *Levin et al.*, 2002] and by the presence of the OIB-like rocks [*Portnyagin et al.*, 2005]. The large variety of volcanic rocks from usual VA-type up to the intraplate type is caused by varying contributions of mantle materials from the hot below-slab zone, mantle wedge and also by the fluid and/or melt separated from the slab. The role of fluids in magma generation decreases, while the role of slab melt increases in the direction from the Kluchevskaya group of volcanoes to the northern volcanoes Hailula and Nachikinsky [*Portnyagin et al.*, 2005a].

The braking effect also was a cause of forming Komandorskaya microplate, which separated from North American plate. Northwestward motion of this microplate at 3.7 cm/y was determined from GPS data (Fig. 1 and 5) after the Kronotsky 1997 earthquake (*Levin et al.*, 2002).

3.5. Geodynamic Conditions of Magma Generation

Magma generation is one of the most important problems in volcanology and petrology. The Kurile VA system is an appropriate object to solve this problem, because geodynamics conditions varied in space and time during its evolution. Geodynamics controlled the magma generation and geochemical characteristics of volcanic rocks. Magma generation beneath the Kurile Island Arc [*Avdeiko*, 1999] corresponding to a steady-state regime of subduction takes place in the mantle wedge under the influence of fluids derived from the subducted slab. Frontal and rear volcanic zones are formed above two zones of magma generation,

Figure 5. 3D-model of the geodynamics of the Kamchatka-Aleutian junction as a view from North West. Black stars-active volcanoes, white stars – Nachikinsky (N) and Khailula (K) extinct volcanoes located off the edge of Pacific plate, K – Komandorskaya microplate, which separated from North American plate. Some lithosphere blocks are torn off the Pacific plate edge as a result of interaction (breaking) with North American plate. These blocks, having a negative buoyancy, sink into a mantle, are heated, and can form a small mantle plume.

controlled by two levels of dehydration of water-bearing minerals in the slab. Varying composition of the fluids result from differences in compositions of the dehydrating of water-bearing minerals. Amphiboles (including tremolite) and chlorites from the layers 1 and 2 of the oceanic crust are dehydrated beneath the frontal arc zone, and serpentine and talc from the 3B layer are dehydrated beneath the rear one. Additionally, aqueous fluid separating beneath the frontal zone passes upward to the zone of magma generation only through the wedge base, whereas fluid separating beneath the rear zone rises successively through layers 3A, 2 and 1 of oceanic crust as well as a longer way through the mantle wedge to the zone of magma generation. The fluid separating from the slab beneath the rear zone has a higher temperature in comparison with the frontal one. Typical VA magmas are generated beneath the frontal and the rear zones under the steady-state regime of subduction.

What are conditions of the occurrence in Kamchatka of volcanic rocks of an intraplate geochemical type along with the considerably more abundant typical VA rocks? In contrast to the typical VA lavas characterized by the low concentrations of Ta, Nb, and Ti, the intraplate lavas show higher abundances of these elements (Fig. 2) [*Volynets*, 1994; *Avdeiko and Savelyev*, 2005]. The low Ta, Nb, and Ti concentrations in typical VA magmas are due to the fact that these elements, that reside principally in rutile, are poorly soluble in fluids [*Tatsumi et al.*, 1986]. However, partial melting of oceanic-crust basalt under water-saturated conditions is possible at temperatures exceeding 750°C [*Peacock et al.*, 1994], and these melts contain, according to experimental data, higher Ti, Nb, and Ta concentrations especially at depths below 150 km where rutile is unstable [*Ringwood*, 1990]. Thus, appearance of intraplate-type lavas may be due to partial melting of oceanic crust because of higher temperatures that prevail within the slab in the steady-state regime of subduction. Where can there be such higher slab temperatures? It should be noted, first of all, that intraplate-type volcanic rocks are present only within the segment between the zone of the Malka–Petropavlovsk transverse faults and the Kamchatka-Aleutian junction (Fig. 1), i.e. in the segment of the subduction zone that jumped in the Late Miocene. Melting of the frontal edge of the subducting plate was possible at the contact with the hot mantle during the initial stage of the subduction, as, for instance, in eastern Kamchatka during the end of Miocene—beginning the Pliocene (Fig. 4).

Similar conditions for partial melting of the subducting plate seem to have existed at the Kamchatka-Aleutian junction, at the northern edge of the Pacific plate, where the upper mantle has high temperatures [*Tatsumi et al.*, 1994]. Such conditions can occur beneath fracture zones forming slab windows at some distance south the plate edge, where intrusion of hot asthenospheric material through the slab window takes place (Fig. 5).

The formation of the Sredinny Range intraplate-type rocks coincided in time with the subduction zone jump and also connected with a mantle window as we discussed in section 3.2 (Fig. 4). Oceanic crust can melt in a contact with hot under-slab mantle material intruded into slab window.

The termination of subduction under the Sredinny Range might have caused the detachment of the heavier lower portion of the oceanic crust (with underlying lithosphere), its sinking below the eclogitization zone depth (deeper than 150 km), and the intrusion of a hot mantle material from under the slab into the resulting gap (Fig. 4). This might have been accompanied by the melting of layers 1 and 2 of oceanic crust upon the contact with this material.

Thus, we explain the occurrence of intraplate-type rocks in all three instances by the melting the upper portion of the subducted plate (oceanic crust) at its contact with the hotter mantle. We must qualify that this hypothesis is advanced here in the most general form and requires a more thorough evaluation by computing temperature distributions in anomalous areas, seismic tomography, and more detailed petrochemical and geochemical data. Studies aimed at testing this hypothesis have already been initiated within the framework of the Russian–German KALMAR Project. Another scenario for such lavas is low-percentage melting of mantle with little slab input (e.g. *Abratis and Wörner*, 2001). Such scenario is possible for the Sredinny Range and west Kamchatka. A hot mantle material rises in plate gap (Fig. 4. cross-section 2) and higher may give small portion melt as a result of decompression.

4. CONCLUSIONS

We have distinguished the following segments in the present-day Kurile–Kamchatka island-arc system based on the distinctive features of their geological structure and geodynamic parameters: the East Kamchatka, Petropavlovsk, South Kamchatka, North Kurile, Central Kurile, and South Kurile segments. The East Kamchatka segment exemplifies an early subduction stage, the Petropavlovsk segment is complicated by a transverse fracture zone, while the South Kamchatka and Kurile segments have been steady-state for a long time. In contrast, the Mid Kamchatka volcanic arc represented by the Sredinny Range is in a waning stage, because subduction jumped eastward when formation of east Kamchatka capes blocked subduction. Mid Kamchatka arc volcanism extended north of the Kamchatka-Aleutian junction because of subduction of western Komandorsky Basin crust, driven by back-arc spreading. Intraplate-type magmas enriched in Ta, Nb, and Ti are generated by the systems at the onset and cessation of subduction and over slab windows, apparently by melting of slab oceanic basalt.

Other scenarios for appearance of intraplate-type lavas are possible, but all must be consistent with their restriction to the area of the Kurile-Kamchatka system where a jump in subduction took place.

Acknowledgements. We thank Oxana Evdokimova and Dmitry Isaev for help in the preparation of this paper. We are very grateful to John Eichelberger and Pavel Izbekov for discussion and correction of the manuscript. We also thank two anonymous reviewers for valuable comments that obliged us to make some improvements.

REFERENCES

Abratis, M., and Wörner, G., Ridge collision, slab-window formation, and the flux of Pacific asthenosphere into the Caribbean realm. *Geology*, 29, 127–130, 2001.

Aprelkov, S. E., Smirnov, L. M., and Ol'shanskaya, O. N., The Origin of Gravity Anomaly in Central Kamchatka Depression, *in: Modeling of Deep Geological Structures from Gravity and Magnetic Data,* Vladivostok: PED RAS, 68–71, (in Russian), 1985.

Avdeiko G. P., Evolution of geosynclines on Kamchatka. *Pacific Geology*, 3, 1–13, 1971.

Avdeiko G. P., On possible prolongation of the Hawaiian-Emperor chain in Kamchatka, i*n: Jackson, E.D., and Koisumi,I et al. Initial Reports of Deep Sea Drilling Project*. Washington D.C., 55, 851–854, 1980.

Avdeiko, G. P., Geodynamics of Volcanic Occurrences in the Kurile Island Arc and Evaluation of Magma Generation Models. *Geotectonika*, 2, 19–32, (in Russian), 1994.

Avdeiko, G. P., Antonov, A. Ju., Volynets, O. N. et al., Submarine volcanism and zonality of the Kurile Island Arc. Moskow, *Nauka*, 528 p., (in Russian), 1992.

Avdeiko, G. P., Pilipenko, G. P., Palueva, A. A., Napylova, O. A., Geotectonic settings of modern hydrothermal manifestations in Kamchatka. *Volcanology & Seismology*, 20, 695–711, 1999.

Avdeiko, G. P., Popruzhenko, S.V., Palueva, A.A., Modern structure of the Kurile-Kamchatka region and magma-forming conditions, i*n: Geodynamics and volcanism of the Kurile-Kamchatka Island-Arc system*, Petropavlovsk-Kamchatsky, 9–33, (in Russian), 2001.

Avdeiko, G. P., Popruzhenko, S. V., and Palueva, A. A., The Tectonic Evolution and Volcano–Tectonic Zonation of the Kuril–Kamchatka Island-Arc System. *Geotectonics*, 36 (4), 312–327, 2002.

Avdeiko, G. P., Volynets, O. N., Antonov, A. Yu., Tsvetkov, A. A., Kurile island-arc volcanism:structural and petrological aspects. *Tectonophysics*, 199, 271–287, 1991.

Avdeiko, G. P., and Savelyev, D. P., Two types of "intra-plate" lavas on Kamchatka, in *Problems of sources of deep magmatism and plumes*, Proceeding of International Workshop, Petropavlovsk-Kamchatsky – Irkutsk, 229–246, 2005.

Baluev, E. Yu., Perepelov, A. B., Anan'ev, V. V., and Taktaev, V. I., Forearc high-potassium andesites (Kamchatka). *Dokl. Akad. Nauk SSSR*, 279 (4), 977–981, (in Russian), 1979.

Baranov, B. V., Seliverstov, N. I., Murav'ev, A. V., and Muzurov, E. L., The Komandorsky Basin as a product of spreading behind a transform plate boundary. *Tectonophysics*, 199, 237–270, 1991.

Bogdanov, N. A., Khain, V. E., (Eds), Tectonic map of the Sea of Okhotsk region, scale 1:2500000 (2 sheets) with explanatory notes. Moskow, Institute of the Lithosphere of Marginal Seas, 2000.

Churikova, T., Dorendorf, F., and Wörner, G., Sources and fluids in the mantle wedge below Kamchatka: Evidence from across-arc geochemical variation. *Journal of Petrology*, 42, 1567–1593, 2001.

Fedorchuk, A. V., Oceanic and back-arc basin remnants within accretionary complexes: geological and geochemical evidence from Eastern Kamchatka. *Ofioliti,* 17 (2), 219–242, 1992.

Fedotov S. A. et al. (Eds), The 1975–1976 Large Tolbachik Fissure Eruption in Kamchatka, Moscow, Nauka, (in Russian), 1984.

Filatova, N. I., Circum-oceanic volcanic belts. *Nedra*, Moscov, (in Russian), 1988.

Gorbatov, A., Kostoglodov, V., Maximum depth of seismicity and thermal parameter of the subducting slab: general empirical relation and its application. *Tectonophysics*, 277, 165–187, 1997.

Gorbatov, A., Vidiyantoro, S., Fukao, Y. & Gordeev, E., Signature of remnant slabs in the North Pacific from P-wave tomography. *Gephys. J. Int.*, 142, 27–36, 2000.

Harabaglia, P., Doglioni, C., 1998. Topography and gravity across subduction zones. *Geophys. Res. Lett.*, 25 (5), 703–706.

Honda, S., Uyeda, S., Thermal process in subduction zones – a review and preliminary approach on the origin of arc volcanism. *Arc volcanism: physics and tectonics*, Tokio: Errapub, 117 – 140, 1983.

Khubunaya, S. A., The High-Al Plagioclase Tholeite Association of Island Arcs, Moscow: *Nauka*, 1987.

Konstantinovskaia, E. A., Geodynamics of an Early Eocene arc–continent collision reconstructed from the Kamchatka Orogenic Belt, NE Russia. *Tectonophysics*, 325, 87–105, 2000.

Konstantinovskaia, E. A., Arc-continent collision and subduction reversal in the Cenozoic evolution of the Northwest Pacific: an example from Kamchatka (NE Russia). *Tectonophysics*, 333, 75–94, 2001.

Kozhemyaka, N. N., Active volcanoes of Kamchatka: spatial and temporal dynamics of eruptive intensity and productivity. *Volcanology & Seismology*, 22 (1) 25–34, 2000.

Legler, V. A., Development of Kamchatka in Cenozoic according the theory of lithosphere plate tectonics (energy sources of tectonic development and plate dynamics), i*n: Tectonics of lithosphere plate, Moskow, Institute of Oceanology*, 137–169, 1977, (in Russian).

Levashova, N. M., Shapiro, M. N., Ben'yamovskii, V. N., and Bazhenov, M. L., Kinematics of the Kronotskii Island Arc (Kamchatka) from Paleomagnetic and Geological Data. *Geotectonics*, 34 (2), 141–159, 2000.

Levin, V. E., Gordeev, E. I., Bakhtiarov, V. F., Kasahara, M., Preliminary Results From GPS Monitoring in Kamchatka and the Komandorskie Island. *Volcanology and Seismology*, 1, 3–11, 2002, (in Russian).

Levin, V., Shapiro, N., Park, J., and Ritzwoller, M., Seismic evidence for catastrophic slab loss beneath Kamchatka. *Nature*, 418, 763–767, 2002.

Litvinov, A. F., Patoka, M. G. & Markovsky, B. A., (Eds), Map ot the mineral resources of Kamchatka region, scale 1: 500000, St.-Peterburg, Kamchatprirodresource, 19 sheets, 1999.

Miyashiro, A., Volcanic rock series in island arcs and active continental margins. *Amer. J.Sci.*, 274 (4), 321–355, 1974.

Melekestsev, I. V., Braitseva, O. A., Ponomareva, V. V., A new approach to definition of the term "active volcano", i*n: Geodynamics and volcanism of the Kurile-Kamchatka Island-Arc system*, Petropavlovsk-Kamchatsky, 191–203 (in Russian), 2001.

Ogorodov, N. V., Kozhemyaka, N. N., Vazheevskaya, A. A., and Ogorodova, A. S., Volcanoes and Quaternary volcanism of Sredinny Ridge of Kamchatka: Moskow, *Nauka*, 1972, (in Russian).

Osipenko, A. B., Lateral variations in the chemistry of rock-forming minerals in the backarc zone of the Kurile Island: amphiboles. *Volcanology & Seismology*, 22 (1), 143–160, 2000.

Osipenko, A. B., Konilov, A. N., Savelyev, D. P., Krylov, K. A., and Anikin, L. P. Geology and Petrology of Amphibolites from Cape Kamchatskii, Eastern Kamchatka. *Petrology,* 13 (4), 381–404, 2005

Piscunov, B. N., Geological and petrological specificity of island arc volcanism, Moscow, Nauka, (in Russian), 1987.

Portnyagin, M., Hoernle, K., Avdeiko, G., Hauff, F., Werner, R., Binderman, I., Uspensky, V., Garbe-Schönberg, D., Transition from arc to oceanic magmatism at the Kamchatka-Aleutian junction. *Geology*, 33 (1), 25–28, 2005a.

Portnyagin, M. V., Savelyev, D. P., and Hoernle, K. Plume-Related Association of Cretaceous Oceanic Basalts of Eastern Kamchatka: Compositions of Spinel and Parental Magmas. *Petrology*, 13 (6), 571–588, 2005b.

Peacock, S. M., Rushmer, T., Thompson, A. B., Partial melting of subducting oceanic crust. *Earth and Planetary Science Letters*, 121, 227–244, 1994.

Popruzhenko, S. V., Aprelkov, A. E., & Olshanskaya, O. N., The East Kamchatkan volcanic belt as reflected by geophysical data. *Volcanology & seismology*, 9 (2), 200–216, 1990.

Regelous, M., Hofmann, A.W., Abouchami, W., and Galer, S. J. G., Geochemistry of Lavas from the Emperor Seamounts, and the Geochemical Evolution of Hawaiian Magmatism from 85 to 42 Ma. *Journal of Petrology*, 44 (1), 113–140, 2003.

Rikhter, A. V., Structure of metamorphic complexes of the Ganalsky Range (Kamchatka). *Geotectonics*, 25 (1), 75–83, 1991.

Rikhter, A. V., Structure of metamorphic complexes of the Central Kamchatka massif. *Geotectonics*, 29 (1), 65–72, 1995.

Ringwood, A. E., Slab-mantle interactions. 3.Petrogenesis of intraplate magmas and structure of the upper mantle. *Chem.Geol.*, 82, 187–207, 1990.

Savelyev, D. P., Intraplate alkali basalts in the Cretaceous accretionary complex of the Kamchatkan Peninsula (Eastern Kamchatka). *Volcanology & Seismology*, 1, 14–20 (in Russian), 2003.

Sheimovich, V. S., Patoka, M. G., Geology of areas active Cenozoic volcanism. Moscow: *GEOS*, (in Russian), 2000.

Seliverstov, N. I., Geological structure of Near-Kamchatka bottom and geodynamics of junction zone of Kurile-Kamchatka and Aleutian island ars, Moskow, *Nauchnyi Mir*, 1998.

Sergeyev, K. F., Krasny, M. L., (Eds), Geology-geophysical atlas of the Kurile-Kamchatka island system, Leningrad, VSEGEI, 36 sheets, 1987.

Sun, S. S. & McDonough, W. F., Chemical and isotopic sistematics of oceanic basalts; implications for mantle composition and processes. In: Saunders, A. D. & Norry, M. J. (cds) Magmatism in the Ocean Basins. Geological Society, Landon, Special Publications 42, 313–345, 1989.

Tatsumi, Y., Migration of fluid phases and genesis of basalt magmas in subduction zones. *J.Geophys. Res.*, 94 (B4), 4697–4707, 1989.

Tatsumi, Y., Furukawa, Y. Kogiso, T. et al., A third volcanic chain in Kamchatka: thermal anomaly at transform/convergence plate boundary. *Geophys. Res. Lett.*, 21 (7), 537–540, 1994.

Tatsumi, Y., Hamilton, D.L., Nesbitt, R.W., Chemical characteristics of the fluid phase released from a subducted lithosphere and the origin of arc magmas: evidence from high pressure experiments and natural rocks. *J. Volcanol. Geotherm. Res.*, 29 (1–4), 293 – 309, 1986.

Tatsumi, Y., Kogiso, T., Nohda, S., Formation of a third volcanic chain in Kamchatka: generation of unusual subduction-related magmas. *Contrib Mineral. Petrol*. 120, 117 – 128, 1995.

Trubitsin, V. P., Shapiro, M. N., and Rykov, V. V., Numerical modeling of the Prepliocene mantle flow in the junction zone of the Kuril-Kamchatka and Aleutian Island Arcs. *Physics of the Solid Earth*, 4, 10–19 (in Russian), 1998.

Tsukanov, N. V. The Late Mesozoic–Early Cenozoic Tectonic History of the Pacific Coastal Zone of Kamchatka, Moscow: *Nauka*, 1991.

Vinogradov, V. I., Grigoriev, V. S., Leites, A. M., Age of metamorphism of the rocks from the Sredinny Range of Kamchatka. *Izv. Acad. Nauk SSSR. Ser. Geol*. 9, 30–38 (in Russian), 1988.

Volynets, O. N., Geochemical types, petrology and genesis of Late Cenozoic volcanic rocks from the Kurile-Kamchatka island-arc system. *Intern. Geol. Rev.*, 36, 373–405, 1994.

Volynets, O. N., Avdeiko, G. P., Tsvetkov, A. A., Antonov, A. Yu., Markov, I. A., Filosofova, T. M., Mineral zoning in the Quaternary lavas of the Kurile Island Arc. *Intern. Geol. Rev.*, 32 (2), 128–142, 1990.

Volynets, O. N., Melekestsev, I. V., Ponomareva, V. V. & Yogodzinsky, J. M., Kharchinskii and Zarechnyi volcanoes-unique centers of Late Pleistocene magnesian basalts in Kamchatka: structural setting, morphology, globalic structure and age. *Volcanology & Seismology*, 20 (4-5), 383–400, 1999a.

Volynets, O. N., Melekestsev, I. V., Ponomareva, V. V. & Yogodzinsky, J. M., Kharchinskii and Zarechnyi volcanoes-unique centers of Late Pleistocene magnesian basalts in Kamchatka: composition of erupted rocks, *Volcanology & Seismology*, 21 (1), 45–66, 1999b.

Volynets, O. N., Puzankov, Ju.M., Anoshin, G. N., Geochemistry of Neogene-Quaternqry volcanic series in kamchatka. *In: Geochemical typification of magmatic and metamorphic rocks in Kamchatka. Proceeding of the Institute of Geology and Geophysics*, Novosibirsk, 390, 73–114 (in Russian), 1990.

Volynets, O. N., Uspenskiy, V. S., Anoshin, G. N. et al, Geochemistry of Late Cenozoic basalts from East Kamchatka and implications for geodynamic evolution of magma generation. *Volcanology & Seismology*, 12 (5), 560–575, 1992.

Watts, A. B., Gravity field of the Northwest Pacific Ocean basin and its margin: Aleutian island-arc trench system: Geological Society of America Map and Chart Series, MC-10, 1975.

Watts, A. B., Kogan, M. G., Bodine, J. H., Gravity field of the Northwest Pacific Ocean basin and its margin: Kuril island arc-trench system: Geological Society of America Map and Chart Series, MC-27, 1978.

Yogodzinski, G. M., Lees, J. M., Churikova, T. G., Dorendorf, F., Wörner, G. & Volynets, O. N., Geochemical evidence for the melting of subducting oceanic lithosphere at plate edges. *Nature*, 409, 500–504, 2001.

The Origin of the Modern Kamchatka Subduction Zone

Alexander V. Lander

International Institute of Earthquake Prediction Theory and Mathematical Geophysics RAS, Moscow, Russia

Mikhail N. Shapiro

Schmidt Institute of the Physics of the Earth RAS, Moscow, Russia

Within the Kuril-Kamchatka arc, its northern segment has a few conspicuous features lacking to the south of it: the second Quaternary volcanic belt, which ceased its activity only in the Holocene; three peninsulas (Shipunski, Kronotski and Kamchatski Mys) on the Pacific side of Kamchatka composed of the Paleocene-Eocene volcanic-sedimentary formation lacking elsewhere in Kamchatka; the significant decrease of the seismic zone depth from 650 km in the southern segment of the arc to 150–450 km beneath Kamchatka. All these features can be explained by a recent collision of the "Kronotski Arc terrain" with Kamchatka that caused the extinction of the northern part of the older subduction zone and the formation of the modern subduction zone about 150 km eastward. As the result of that, the older Central-Kamchatka volcanic belt gradually ceased its activity and a new Eastern volcanic belt formed at the same distance from the old one. A set of independent lines of evidence supports this model and gives several estimates for the age of the collision. Based on the ages of deformed deposits and the overlying volcanic rocks the time of the collision for the southern part of the Kronotski arc is 5–10 Ma. Calculations based on plate kinematics suggest the time interval of 0–10 Ma, which is in good agreement with the paleomagnetic data. A more accurate estimate was made by using the along-dip extension of the present-day slab to calculate the amount of time since the beginning of subduction: 7 Ma, 5 Ma, and 2 Ma for Shipunski, Kronotski and Kamchatski Mys segments, respectively.

PECULIAR FEATURES OF THE PLIOCENE-QUATERNARY TECTONIC STRUCTURE OF KAMCHATKA

Most present-day subduction zones exist tens or hundreds of million years and the data on their origin are scarce. Kamchatka is one of the exceptions from this rule. Here, the age of the present-day subduction zone is measured by a few million years, and the evidence for its origin can be observed today.

Recent Kamchatka is a part of the entire Kuril-Kamchatka arc with a continuous trench, a volcanic belt, and an inclined seismic zone extending from South Kurils up to Aleutian-Kamchatka juncture. However, in contrast to the southern Kuril part of the arc which has existed since Oligocene, the modern Kamchatka structure was formed only during the last few million years. Still in Pleistocene and even in the beginning of the Holocene (less than 0.1 Ma) there were substantial distinctions

Volcanism and Subduction: The Kamchatka Region
Geophysical Monograph Series 172

10.1029/172GM05

in the development of northern and southern segments of the Kuril-Kamchatka zone. The boundary of the two segments with different geological histories doesn't coincide with the ocean-continental crust transition but goes along Avacha (also named Malki-Petropavlovsk) transverse fracture zone in the southern Kamchatka (Figure 1). Below we shall mean by the Kamchatka segment only the part of the arc located between this fracture zone and the Aleutian juncture.

Three significant features of the Kamchatka segment directly related to the recent geological history make it different from the southern part of the arc.

Two Volcanic Belts

In contrast to the single volcanic belt of southern Kamchatka (a direct continuation of the Kuril belt), one can see two parallel belts of Quaternary volcanic rocks to the north from the transverse Avacha fracture zone (Figures 1) [*Avdeiko et al.,* 2002]. The first, Eastern belt, (a further northward extension of the present-day of the Kuril belt) goes along the Vostochny mountain ridge, somewhat deviating to the west in the northern part of the segment. The second, Central-Kamchatka volcanic belt, (which is absent in the southern segment) goes along the Sredinny mountain ridge, which is located 80–150 km inland and parallel to Eastern belt (Figure 2a).

Now eruptions occur only in the Eastern belt, and the Central-Kamchatka belt has almost lost all activity. However less than a half of a million years ago numerous stratovolcanos were active there and the areal basaltic volcanic activity continued even in the Holocene. The Eastern belt terminates in the area of Shiveluch volcano, which coincides with the northern edge of the Kuril-Kamchatka deep seismic zone. The Central-Kamchatka belt stretches further north to the Kamchatka Isthmus, where it extends by discontinuous exposures of the Neogene and Quaternary volcanic rocks of the Olutor zone. The geochemical characteristics of both volcanic belts are typical for suprasubductional conditions. [*Avdeiko et al.,* 2002].

Although the present-day Eastern belt is a direct continuation of the Kuril volcanic segment, it is much younger. Cenozoic volcanic rocks older than 5 Ma are not known in the Vostochny ridge, to the north from the Avacha fracture zone, whereas in the Southern Kamchatka volcanic series were produced since Oligocene. The oldest floristic complexes among volcanic series of the Central-Kamchatka belt belong to the Middle Miocene [*Shantser,* 1987], but the metamorphic or Cretaceous basement of the belt contains a lot of shallow granitoid intrusions with the age 25–38 Ma. This suggests the age of the Central-Kamchatka belt as the Oligocene or even Late Eocene.

Figure 1. Characteristics of the present-day Kamchatka structure [modified after *Avdeiko et al.,* 2002]. 1) Active volcanoes; 2) Pliocene-Quaternary volcanic series; 3) Oligocene-Miocene volcanic series; 4) Area of local exposures of post-Eocene intrusions and Miocene volcanic series; 5) Paleocene-Eocene "Kronotski Arc" formation (sedimentary / volcanic); 6) Grechishkin suture.

Thus in Pliocene and Quaternary time two parallel volcanic belts stretched for more than 600 km along Kamchatka. On a larger scale these belts were part of echelon structure formed by two great volcanic belts: Kuril-Kamchatka and Kamchatka-Olutor. Such structure, apparently reflected a process of the gradual extinction of the Kamchatka-Olutor belt and prolongation of Kuril-Kamchatka belt to the north.

Kronotski Terrain

The eastern coast of the Kamchatka segment is complicated by three small peninsulas: Shipunski, Kronotski and Kamchatski Mys. They are composed of a geological formation, which extends to the Komandorski block, but is lacking in other parts of Kamchatka (Figure 1). This formation (named Kronotski) includes Paleocene-Eocene volcanic and sedimentary series, which consist mostly of high-aluminous suprasubductional basalts, tuffites, and volcanic greywackes. As a result, three peninsulas and the Komandorski block are considered to be fragments of an ancient island arc, which is also referred to as Kronotski arc [*Khubunaya,* 1987]. Paleomagnetic studies indicate that in Middle Eocene time the active Kronotski arc was located at latitudes of about 40–50° [*Bazhenov et al.,* 1991; *Pecherski, Shapiro*, 1996; *Levashova et al.*, 2000]. However, if at that time the peninsulas were at the same position relative to Kamchatka as now, the corresponding paleolatitudes would be not less than 56°. Hence, in Eocene the Kronotski arc was located at least 500 km further south relative to Kamchatka and moved toward it later.

The zone of Kronotski formation is separated from the rest of Kamchatka by a large suture "Grechishkin thrust". In present-day structure this is a thrust fault or a system of faults extending 120–180 km westward parallel to the Kamchatka trench and plunging to the west. Please note, that the shift of the Grechishkin thrust relative to the modern trench is nearly the same as the distance between axes of two parallel Quaternary volcanic belts. The autochthonous western flank of the thrust is composed of folded Paleocene-Miocene subrasubductional series of the Kronotski formation, which folding rapidly decreases eastward from the main fault. On the other hand, the allochthon of the Grechishkin suture consists mostly of Early Paleogene tuffaceous cherts and terrigenous series including olistoliths and tectonic lens composed of jaspers and oceanic tholeiites. All these series are usually grouped together and commonly referred to as Vetlovski formation. It is characterized by the imbricated structure with the eastern vergency and could be interpreted as the ancient accretionary prism. The Grechishkin thrust, as well as Vetlovski and Kronotski formations, are exposed intermittently along the entire length of the Kamchatka segment of the arc but are absent to the south from the Avacha zone and to the north from the Kamchatski Mys peninsula, where the last exposures of the Vetlovski formation are cut by shoreline about 30 km to the north from it.

Figure 2. Cross-sections of the Kamchatka seismic zone. **a)** Topography of Kamchatka region. Dashed lines are parallel to the vector of the relative Pacific—Eurasia plate motion, as well as the arrow in left-bottom part of the figure. **b**) Projection of all Kamchatka earthquakes to the vertical plane orthogonal to the relative plate motion; **c**) Projection of the earthquakes to the vertical plane parallel to the relative plate motion. Only earthquakes to the north of the Avacha fracture zone are represented in this figure; the topography on the cross-section C´-C´´ (with the factor 20) is shown by a solid line. The position of Avacha transverse fracture zone is indicated in Fig. **a, b** by a grey rectangle and a double-arrow respectively.

Relatively Shallow Seismic Zone

The maximum depth of the seismicity steeply decreases on the vertical plane parallel to the vector of the Pacific—Eurasia plate motion and corresponding to the Avacha transverse fracture zone on the surface [*Fedotov et al.,* 1985; *Gorbatov et al.;* 1997, *Lander,* 2000]. The belt of deep earthquakes with the depths 350–680 km continuously extends for more than 800 km along the Kuril and South Kamchatka arc until the Avacha transverse structure (Figure 2b). Further to the north, only three earthquakes were located in the depth interval of 400–450 km, all in the southern part of the Kamchatka segment within less than 100 km from its Avacha boundary. The depths of all other earthquakes of the Kamchatka segment do not exceed 350 km. Northward from the Avacha zone step, the maximum depth of the earthquakes continues to decrease, reaching about 120 km near the northern edge of the slab in the area of Shiveluch Volcano. This suggests that the depth of the slab in the modern Kamchatka subduction zone is at least 300 km less as compared to the depth of the Kuril slab.

The depth of the earthquakes under the Eastern volcanic belt lies in the range of 90–160 km, which is typical of most active island arcs. But the relation of the Oligocene-Quaternary Central-Kamchatka volcanic belt to a well defined modern or to a hypothetical ancient seismic (subduction) zone is less clear. It cannot be related to the modern Kamchatka seismic zone in its present-day geometry (Figure 2c), because a small number (about 20) of the subduction earthquakes projected vertically onto the area of the Central-Kamchatka belt are too deep (300–450 km) for the typical island arc volcanic region and occur only in a small south-eastern part of the belt. And vice versa, only small, rare shallow earthquakes occur in the main area of the Central-Kamchatka volcanic belt. The same type of shallow seismicity extends westward to the much broader areas of the Okhotski Sea region and has no direct relation to subduction processes.

HYPOTHESES

There are a number of approaches for the interpretation of each of the three features discussed above. According to *Tatsumi et al.,* [1994], the origin of the second volcanic belt in the Kamchatka segment of the arc is related to abnormally high temperatures of the suprasubduction mantle wedge in the vicinity of the edge of the sinking Pacific plate. Presumably it leads to the existence of two different levels of dehydration of the sinking slab and the melting of the mantle wedge, and as a result, to the appearance of two synchronous volcanic belts. *Levin et al.,* [2001] are also suggesting the proximity of the edge of the slab, but it is based on another fact – the decreasing maximum depth of the earthquakes. Using the data on the regional seismic anisotropy they argue the existence of a mantle flow passing around the northern edge of the Kamchatka which causes heating and erosion of the slab. [*Gorbatov et al.,* 1997] give another interpretation of the small depth of the slab as a result of sinking of abnormally warm Hawaiian trace into the Kamchatka subduction zone.

All the above models are focusing on the description of one of peculiar features of the Kamchatka segment, but do not give a simple explanation for the entire data set. These models explain neither the very large difference (10–20 million years) in the origin times of the two volcanic belts, nor the present-day cessation of the activity within the Central-Kamchatka belt. The attempt to explain all the data was made by [*Seliverstov,* 1998]. By this model the Oligocene-Miocene Kamchatka subduction zone originated from the same trench but was at a significantly lower angle as compared to the modern one. The smaller angle of subduction provided the larger distance from the trench to the related Central-Kamchatka volcanic belt. The model suggests that in the Pliocene the angle of subduction abruptly increased resulting in an eastward displacement of the volcanic activity. The sinking of a relatively cold and heavy section of the Pacific plate was suggested as a reason for a quick rotation of the slab. However, there is no independent evidence for the Pliocene rotation of the Kamchatka slab.

An essentially different explanation for the aforementioned features of the Kamchatka segment was suggested many years ago in [*Legler,* 1977; *Avdeiko,* 1971] and further developed in [*Avdeiko et al.,* 2002]. This hypothesis argues for the existence of an ancient subduction zone about 150 km west of the modern one and plunging beneath Kamchatka as well. It suggests that the subduction within the ancient zone has decreased since Pliocene time as the result of collision with some terrains (present-day peninsulas) and formation of the modern subduction zone at the same time east of the colliding blocks. In this case two parallel volcanic belts can be products of two individual subduction zones with separate locations and times of activity, i.e. the Central-Kamchatka belt is the remnant of the ancient zone and the Eastern belt obviously corresponds to the modern one.

When the 1970s papers were written, much data on the Grechishkin suture, the Kronotski arc, and the geometry of the seismic zone were either unknown or not interpreted yet. So, this model can be expanded further to include an explanation of all the peculiar features of the Kamchatka segment described above. The use of new data allows model testing and more accurate estimation of the age of origin of the modern subduction zone.

All data suggest that the collision of Kamchatka with the passive Kronotski arc moving along with the Pacific plate caused the Late Miocene—Pliocene jump of the subduction zone. The Avacha transverse fracture zone is a southern boundary of the area of collision. Further south the Kuril subduction zone has been stable at least since Oligocene time. Therefore the depths of the earthquakes there are close to the deepest for the entire Earth. In contrast, the Kamchatka segment of the subduction zone is a relatively new postcollisional Pliocene-Quaternary structure. The depth of the new zone is increasing with the sinking of the slab, but it is still far from a maximum. That is the reason for the absence of the deepest earthquakes in the Kamchatka segment. This provides an opportunity to estimate the time when the new subduction began and, therefore, the age of the collision. At present the ancient Kamchatska segment of the subduction zone is practically inactive. But its location can be reconstructed by the positions of the Central-Kamchatka volcanic belt, the line of crossing the surface (Grechishkin thrust), and the parallel ancient accretionary prism (Vetlovski formation). As all these structures have nearly the same westward displacement of 100–150 km relative to their present-day analogs, then the old subduction zone likely had a dip angle similar to the modern one.

THE AGE OF THE MODERN KAMCHATKA SUBDUCTION ZONE

In the framework of the last hypothesis we have three independent groups of data for estimating the ages of the collision of the Kronotski arc with Kamchatka or for the onset of subduction of the new slab which are likely the same. Furthermore, the consistency between independent estimates can be a good test on the reliability of the model.

Geological Estimates

The age of the youngest Low-Middle Eocene sediments, which are involved in the deformations related to the Grechishkin thrust, provides the limit for the time of the beginning of collision. The other limit is defined by the age of Pliocene volcanic series of the Eastern belt horizontally overlying the Grechishkin thrust in the Kronotski isthmus. The maximum age of this series was estimated to be about 5 Ma [Gladenkov, 1998]. That means that the age of the end of motion in the Grechishkin thrust, and therefore of the Kronotski arc collision, is within an interval of 5–10 Ma. As the volcanic series overlie the thrust only in a local area, the upper limit strictly speaking can be used only for the nearest part of the arc, i.e. Kronotski peninsula.

Paleomagnetic Estimates

Data on the Eocene Kronotski formation volcanic series show a big latitude difference of the arc relative to Kamchatka. Using certain models for the plate motions in the northwestern Pacific we can try to choose a trajectory of the Kronotski arc fitting both the present-day position and the Eocene paleolatitudes of the arc, thus finding the time of collision.

Based on geological data the Kronotski arc was active between the Late Cretaceous and Paleogene and ceased its activity at the end of the Middle Eocene, approximately 38 Ma. The age interval of Late Eocene—Middle Miocene is represented in the Kronotski Arc formation by the arc slope and shallow marine sedimentary series. The Pliocene-Quaternary shallow marine and continental sedimentary series complete the cross-section of the formation, while the volcanic series of the Eastern belt are at the top in the western part of the Kronotski peninsula. Thus the geological history of the Kronotski formation could be divided into three periods: active arc, passive arc, and “a part of Kamchatka”.

For calculations the Kronotski arc is considered as part of one of the great plates with known kinematics (“reference plate”) for every of the three periods. The following reference plates have been analyzed in different combinations: North America or Pacific for the “active arc” period, the Pacific for the “passive arc” period, Eurasia or North America for the last period. Motion parameters after [*Kraus, Scotese,* 1993] for continental plates and [*Engebretson et al.,* 1985] for the Pacific were used in the calculations. It is necessary to note that for the last 50 million years the Pacific was the only known plate that could ensure a quick north-west motion of the Kronotski arc. The time boundary between active and passive periods is fixed at 38 Ma from geological data (actually ±2 Ma). The last and the most significant free parameter for the model is the age of collision of the Kronotski arc with Kamchatka, i.e. the boundary between the second and third time periods. For every combination of reference plates we tried this parameter from the interval 0 to 45 Ma to choose the best fit for the data. A set of calculated models is shown in Figure 3 as the trajectories in terms of latitude displacement versus time. Any point of the trajectory shows the trial difference of the latitude of the Kronotski arc for the given age with respect to its present-day position.

The measured paleolatitudes of the Kronotski arc are known only for the first “active arc” interval of its history. To decrease the uncertainty of the model we selected the data for the latest series: Lutetian of the Kamchatski Mys peninsula (paleolatitude 47.0±6.4°) and Bartonian series of the Kronotski peninsula (paleolatitude 45.1±4.7°) [*Levashova et al.,* 2000]. These measurements are shown in Figure 3 by filled circles, and two rectangles of the 95% confidence regions. Only the model parameters corresponding to the trajectories that are crossing both rectangles fit the data. The best fitting estimate for the time of the Kronotski Arc—Kamchatka collision is 4 Ma with a confidence interval of 0–12 Ma. There is no evidence for the delay of the collision for different parts of the arc based on paleomagnetic data from different sites.

Seismological Estimates

The most accurate results could be obtained based on the relatively shallow depth of the Kamchatka seismic zone, which is accepted as the modern depth of the slab. We used the along-dip extension of the slab for estimating the amount of time since the beginning of subduction. Relative Neogene Pacific—Eurasia plate motion parameters after [*Kraus*, *Scotese,* 1993; *Engebretson et al.,* 1985] were used to calculate the time necessary the slab to sink to its modern position. This time was taken as an estimate of the age of subduction zone as well as the age of the end of Kronotski Arc—Kamchatka collision. Attributing Kamchatka to the North-American plate instead of Eurasian doesn't change the results.

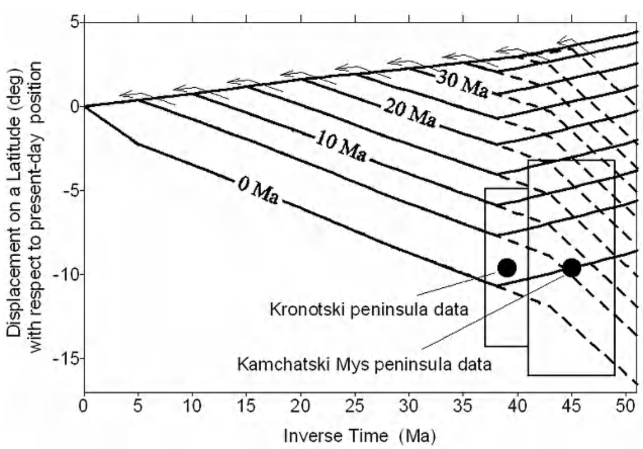

Figure 3. Age of the collision between Kronotski Arc and Kamchatka: paleomagnetic test. A set of the calculated models represented as trajectories in (Time, Latitude displacement) coordinates. Parameters of every trajectory: the sequence of three "reference plates" and the age of collision (marked at the trajectory). Any point of the trajectory shows the latitude difference of the Kronotski arc for a given age with respect to its present-day position. Every trajectory consists of three segments (three intervals of the arc history): right—trajectory of active arc moving with North American (solid line) or Pacific (dashed line) plates; central—trajectory of passive arc (part of Pacific plate), left—motion of the arc as a part of Kamchatka (part of Eurasia or North America—no significant difference). The time of collision corresponds to the bend between central and left segments of the trajectory and marked by broken arrow. The paleomagnetic data for both sites of the Kronotski formation are shown by filled circles, and two rectangles – represent the 95% confidence regions. Model parameters corresponding to the trajectories that are crossing both rectangles fit the data.

The depth of the seismic zone is not constant along the Kamchatka segment of the arc. It decreases in the north direction. We accept that this segment could be divided in three smaller ones (approximately corresponding to three Kamchatka peninsulas) (Figure 2b). The maximum depths of the slab for these subsegments and the corresponding along-dip extensions (numbers in brackets) were estimated as 450 (650) km for Shipunski segment, 350 (500) km for Kronotski segment, 150 (250) km for Kamchatski Mys segment.

According to our model, the estimates of the age of the modern Kamchatka subduction zone are: 7 Ma for Shipunski segment, 5 Ma for Kronotski segment, 2 Ma for Kamchatski Mys segment . This means that the process of collision could be stretched in time. Different parts of the arc were joining Kamchatka at significantly different times. Only the Komandorski block is still moving towards it [*Gordeev et al.,* 2001].

CONCLUSIONS AND GEODYNAMIC RECONSTRUCTIONS

Three types of estimates—geological, paleomagnetic and seismological—have different accuracy and resolution, but are in a good mutual agreement. We may conclude that the collision of the Kronotski arc with Kamchatka began in the southern part of the Kamchatka segment in the time interval approximately 10–7 Ma. A new subduction zone was formed about 7 Ma and gradually expanded to the north during at least 5 million years. In the area of the Aleutian-Kamchatka juncture the new subduction seems to have started not earlier than 2 Ma. It is possible that the expansion of the zone is not completed yet. Both old and new shifted in space trenches existed during that time forming an echelon structure along the Kamchatka segment. It is likely that series of short transform faults connected two trenches at different moments of that time interval (Figures 4b and 4c), however no remnants of such faults remain in the modern structure.

Figure 4 shows the main stages of the interaction between Kronotski arc and Kamchatka, as well as the main episodes of transformation of the northern part of the Kuril-Kamchatka arc in Late Miocene – Quaternary. The locations of Kamchatka and Kronotski arc are based on the plate motion parameters from [*Kraus*, *Scotese,* 1993; *Engebretson et al.,* 1985]. These stages are summarized below.

(38–10 Ma): Since the Oligocene, the Kuril-Kamchatka volcanic arc and the corresponding subduction zone extended to the north continuously from Kuril Islands to Sredinny Ridge of Kamchatka. "Vetlovski" accretionary prism was formed at the place of the present-day Vostochny Ridge of Kamchatka. The trench was located at the line of the present-day peninsu-

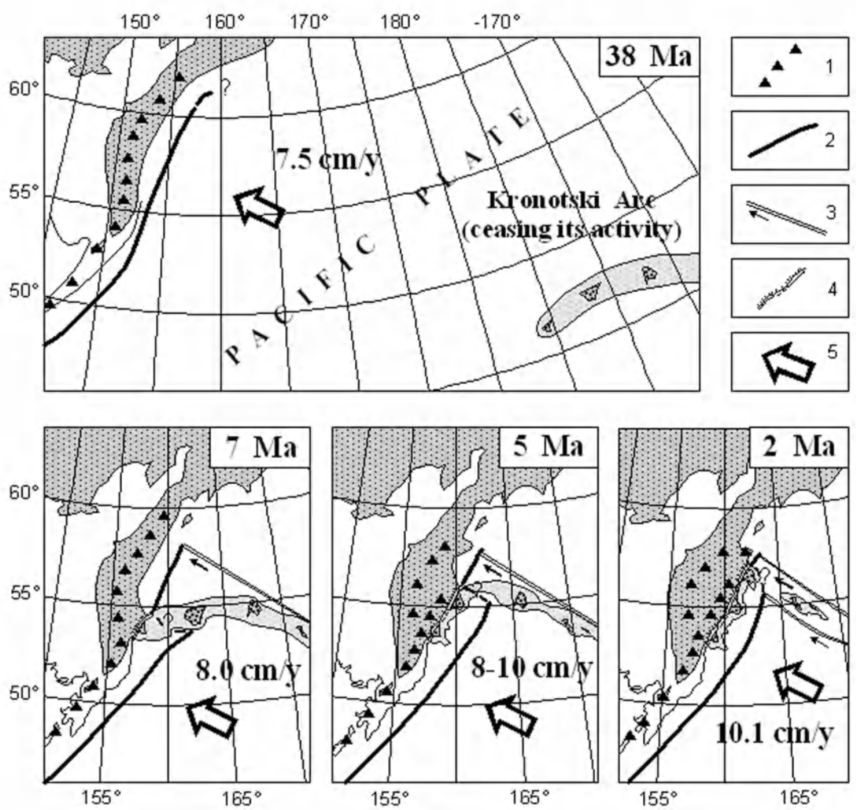

Figure 4. Post-Eocene Kamchatka Subduction Zone History—Geodynamic Reconstructions. 1–Volcanic belts, 2–Trenches, 3–Transform faults, 4–"Grechishkin thrust" suture, 5–Pacific plate velocity vector relative to Eurasia). All maps are in fixed hot spots frame, modern coordinate system. Paleolatitudes of the Eocene Kronotski Arc: after [*Levashova et al.,* 2000]. Plate kinematics: after [*Kraus*, *Scotese,* 1993; *Engebretson et al.,* 1985]. The ages of the collision are estimated from data on maximum depths of earthquakes in different parts of the modern Kamchatka seismic zone.

las. The northern end of the arc is questionable, but most likely it extended to the present-day South Koryakia.

38 Ma ago the Kronotski volcanic arc located nearly 2500 km to the south-east from Kamchatka stopped its activity, became a passive part of the Pacific plate and began to move along with it to the north-west. The passive Kronotski arc consisted of the blocks which later became Kamchatka peninsulas and Komandorski Islands.

(10–7 Ma): The western end of the Kronotski terrain, i.e. Shipunski block collided with Kamchatka. The corresponding segment of the old trench closed and the southern part of the Grechishkin thrust formed at its place. A new trench and subduction zone formed to the east of the Shipunski block as a continuation of the Kuril—South Kamchatka arc.

(5 Ma): Collision of the Kronotski block with Kamchatka occured. A new trench and subduction zone are extended to the north-east as well as the Greshishkin thrust. Volcanism began in the southern part of the Eastern Volcanic Belt of Kamchatka.

(2–0.5 Ma): Kamchatski Mys block joined Kamchatka and the modern structure of the arc shaped. The old trench completely disappeared being replaced by the Grechishkin suture. The Central-Kamchatka volcanic belt is gradually ceased its activity. All sections of the modern Eastern volcanic belt became active.

Acknowledgments. This research was supported by Basic Research Program 13 "Changes of Environment and Climate: Natural Disasters" of the Presidium of Russian Academy of Sciences. We are appreciate to Pavel Izbekov for very helpful remarks and corrections.

REFERENCES

Avdeiko, G.P., Evolution of geosynclines on Kamchatka, *Pacific Geology,* No.3, 1–14, 1971.

Avdeiko, G.P., S.V. Popruzhenko, and A.A. Palueva, The tectonic evolution and volcano-tectonic zonation of the Kuril-Kamchatka island-arc system, *Geotectonics,* 36(4), 312–327, 2002.

Bazhenov, M.L., V.S. Burtman, O.A. Krezhovskikh, and M.N. Shapiro, Paleotectonic reconstruction of the Aleutian Arc-Kamchatka convergence zone, *Geotectonics*, *25*(3), 244–256, AGU, Washington, DC, United States, 1991.

Engebretson D.C., A.Cox, and R.Gordon Relative motions between oceanic and continental plates in the Pacific Basin, *in Geological Society of America. Special Paper 206*, 59 p., 1985.

Fedotov, S.A., A.A. Gusev, G.V. Chernysheva G.V., and L.S. Shumilina, Kamchatka seismic [Benioff] zone (geometry, hypocenter distribution, relationship to volcanism), *Volcanology and Seismology,* No.4, 91–107, 1985, (in Russian).

Gladenkov, Yu.,B., B.A. Salnikov, A.K. Borovtsev et al., *Resolution Interdepartmental workshops on Paleogene and Neogene stratigraphy of Russia: Kamchatka, Koryak Upland, Sakhalin, and Kuril Islands, Explanatory Note to Stratigraphic schemes,* 147 p., Moscow, GEOS, 1998, (in Russian).

Gorbatov A., V. Kostoglodov, G. Suarez and E. Gordeev, Seismicity and structure of the Kamchatka subduction zone. *Journal of Geophysical Research.* Vol. 102, NO. B8, 17883–17898, 1997.

Gordeev, E.I., A.A. Gusev, V.E. Levin, V.F. Bakhtiarov, V.M. Pavlov, V.N. Chebrov, and M. Kasahara, Preliminary analysis of deformation at the Eurasia-Pacific-North America plate junction from GPS data, *Geophysical Journal International*, v.147, 189–198, 2001.

Khubunaya, S.A., *High-alumina plagiotholeitic formation of island arcs,* 167 p., Moscow, Nauka, 1987, (in Russian).

Kraus, J.U. and C.R. Scotese, Global Polygon and Suture Map, *PALEOMAP Progress Report 19-0293*, Department of Geology, University of Texas at Arlington, Texas, 12 p., 1993.

Lander, A.V., Seismicity of the Sea of Okhotsk Region, *in The Tectonic Map of the Sea of Okhotsk Region at a scale of 1:2500 000,* edited by Bogdanov, N.A., and V.E. Khain, 141–145, Institute of the Lithosphere of Marginal Seas of the Russian Academy of Sciences, Moscow, 2000.

Legler, V.A., Cenozoic development of Kamchatka: plate tectonic view, *in Tectonics of Lithospheric Plates (energy sources for tectonic processes and plate dynamics),* 137–169, Shirshov Institute of Oceanology of the Russian Academy of Sciences, Moscow, 1977, (in Russian).

Levashova, N.M., M.N. Shapiro, V.N. Beniamovsky, and M.L. Bazhenov, Paleomagnetism and geochronology of the Late Cretaceous-Paleogene island arc complex of the Kronotsky Peninsula, Kamchatka, Russia: Kinematic implications, *Tectonics,* Vol.19, No.5, 834–851, 2000.

Levin, V., J. Park, J. Lees, M.T. Brandon, V. Peyton, E. Gordeev, and A. Ozerov, Crust and upper mantle of Kamchatka from teleseismic receiver functions, *Tectonophysics*, v358, 233–265, 2002.

Pechersky, D.M. and M.N. Shapiro, Paleomagnetism of Upper Cretaceous and Paleogene volcanogenic series of Eastern Kamchatka; evidence for absolute motions of ancient subduction zones. *Izvestiya, Physics of the Solid Earth*, **32**, 114–137, 1996.

Seliverstov, N.I., *Structure of Kamchatkian Water Area Bottom and Geodynamic of a Junction Zone between the Kuril-Kamchatka and Aleutian Island Arcs,* 164 p., 4 plates, Moscow, Nauchnyi Mir, 1998, (in Russian).

Shantser, A.E., Cenozoic development of Kamchatka—generation and destruction of unstable orogenic uplifts, *in Description of the Tectonic Evolution of Kamchatka,* 109–164, Moscow, Nauka, 1987, (in Russian).

Tatsumi Y., Furukava Y., Kogiso T. et al. A third volcanic chain in Kamchatka: thermal anomaly at transform/convergence plate boundary, *Geophys. Res. Lett.* V.21, No.7, 537–540, 1994.

Three Dimensional Images of the Kamchatka-Pacific Plate Cusp

Jonathan M. Lees[1], John VanDecar[2], Evgenii Gordeev[3], Alexei Ozerov[3], Mark Brandon[4], Jeff Park[4], Vadim Levin[5]

First arrivals of seismic waves were recorded along the Kamchatka arc using broadband seismic stations deployed for one year in 1998–1999. Cross correlation methods were used from a high resolution data set for tomographic inversion of body waves. The P-wave teleseismic tomography shows evidence of slab shoaling along the northern terminus of the Kamchatka subduction zone. Tomographic anomalies corroborate trends in seismicity, geochemistry, heat flow, shear wave splitting, and surface wave inversions. Thermal ablation via contact with asthenosphere, under the proper conditions, is offered as a possible explanation of the observed shoaling of the Kamchatka slab edge.

INTRODUCTION

The Aleutian-Kamchatka corner is a trench-transform junction that forms a cusp on the boundary between the Pacific and North American plates. Unique to this junction is Earth's most extreme example of exposure of an arc cusp where the side-edge of a subducting plate is heated by mantle flow. In this paper we present results from a tomographic study using teleseismic arrivals at an array of seismic stations deployed temporarily in Kamchatka during 1998–1999. Evidence for this fact is manifest: seismicity shallows to the north [*Gorbatov et al.*, 1997], teleseismic tomography shows a deepening of high velocity dipping to the southwest [*Lees*, 2000], high heat flow in the Komandorsky Basin [*Baranov et al.*, 1991], and shear wave splitting indicates trench-parallel sub-slab orientations along the Kamchatka Arc changing to NW trending orientation north of the Aleutian-Kamchatka Junction [*Peyton et al.*, 2001]. Yogodzinski et al. (2001) used the idea of a torn slab and exposed oceanic lithosphere to further explain the presence of calc-alkaline volcanics [*Defant and Drummond*, 1990; *Defant and Kepzhinskas*, 2001; *Hochstaedter et al.*, 1994] just north of the junction, providing a new model for the presence of Adakites found in the central and western Aleutians. Detailed descriptions of Kamchatka tectonics can be found in numerous publications and will not be repeated here [*Gaedicke et al.*, 2000; *Geist and Scholl*, 1994; *Nokleberg et al.*, 2001; *Park et al.*, 2002; *Seliverstov*, 1998].

The question of how the exposed edge of a torn slab interacts with the surrounding mantle has profound worldwide implications for geochemistry of mantle asthenosphere and eruptive magmas and geodynamics of flow in the upper mantle. There is evidence that tears of the kind observed in Kamchatka are ubiquitous in the Pacific Rim. *Kirby et al.* [1996] noted pointedly in their seminal paper on subduction zone seismicity and thermal models that arc cusps around the western Pacific all have shoaling seismic zones towards the cusps. If exposed slab is constantly ablating and being absorbed in the upper mantle we will have to reevaluate our notions on the chemical makeup of the upper mantle [*Lees*, 2000; *Yogodzinski et al.*, 2001]. Fluid flow models of

[1] University of North Carolina, Chapel Hill, Department of Geological Sciences, Chapel Hill, North Carolina, USA
[2] Department of Terrestrial Magnetism, Carnegie Institution of Washington, Washington, DC, USA
[3] Institute of Volcanology and Seismology (IVS), Petropavlovsk-Kamchatsky, Russia
[4] Yale University, New Haven, Connecticut, USA
[5] Department of Geological Sciences, Rutgers University, Piscataway, New Jersey, USA

Volcanism and Subduction: The Kamchatka Region
Geophysical Monograph Series 172

10.1029/172GM06

the upper mantle and models of corner flow will have to be adjusted significantly if stresses associated with tear model flow are correct.

At nearly every cusp around the Pacific Rim there is an observed shoaling of seismicity cusp-ward from the deep subducted plates [*Kirby et al.*, 1996]. Shoaling seismicity is especially pronounced at the Kamchatka-Aleutian junction where the Kamchatka arc terminates against the Bering Fault of the western Aleutians. While in some localities the shoaling seismicity may be attributed to the youth of the subducting lithosphere, in Kamchatka the Cretaceous age of the lithosphere precludes this interpretation. Rather, the old subducting lithosphere requires a completely different interpretation to explain the absence of seismicity in the Kamchatka-Aleutian cusp.

THE EDGE OF A PLATE

The main point of this paper is to present results of three dimensional imaging of the Kamchatka plate as it subducts in the western Pacific. The images were derived via tomographic inversion of P-wave arrivals from teleseismic body waves and show a clear edge of the northern extent of the subducting Pacific plate, confirming earlier results which included analysis of slab events and global surface wave inversion. The P-wave arrivals recorded at 15 broadband stations deployed in 1998–1999, however, offer the best chance so far of imaging the deep part of the slab with clarity and fidelity.

Earthquakes in the subducting Kamchatka slab extend from the surface where the Pacific plate collides with Eurasia down to 600 km depth. Events form a clear Wadati-Benioff zone that dips consistently at about 50 degrees to the west. By plotting events in cross section one can determine a general trend and contour the top of seismicity to be used as a proxy for the extent of the slab in the mantle. Contours of seismicity appear to shoal towards the north where the Aleutian arc terminates at the Kamchatka Peninsula. At the apex of the seismicity the gradient of dip shallows in the vicinity of the Kliuchevskoi group of volcanoes. The lack of deep seismicity in the northern part of the subduction zone is a strong indication that subduction is absent in this region. The overall shape of the slab in Kamchatka, based on seismicity alone, appears to be tongue-like, with the deepest events occurring near the center of the Kamchatka-Kurile arc and shoaling north and south towards the ends.

Tomography

Earlier tomographic inversions of structure in Kamchatka consist of P-wave tomography using the large world wide catalogues suggest that there is no slab extending north of the northern terminus of seismicity as discussed above [*Gorbatov et al.*, 1999; *Gorbatov et al.*, 2000]. These inversions use a combined data set of arrival times extracted from regional arrays of the Geophysical Survey of Russia and travel time arrivals from global (ISC, NEIC) data bases. The presence of considerable noise in these data can be problematic for tomographic inversion. The inversion presented in our analysis is obtained independently from the global dataset, and provides much needed waveform information from the isthmus region of Kamchatka north of the Kamchatka-Aleutian Cusp (KAC). Our results solidify and extend the earlier tomography results and provide details. A study using surface waves (S-wave velocities) [*Levin et al.*, 2002] shows a termination of the slab in KAC region, in agreement with the P-wave analysis presented here. Furthermore, Levin et al. [2002] speculate that the absence of high velocity S-wave anomalies north of KAC is evidence for catastrophic slab loss in the subduction zone. The P-wave results presented below also show no evidence of remnant slab fragments north of the subduction zone.

Heat Flow

Oceanic heat flow in the Kamchatka region is governed primarily by the thickness of the Pacific Plate and local extension in the Komandorsky basin [*Smirnov and Sugrobov*, 1982]. The Komandorsky basin, north of the Bering Islands, is the locus of relatively recent spreading (~5M years) which points to an upper mantle heat source north of the Bering fault. Anomalous heat flow is also observed above the Meiji Sea Mounts, east of Kamchatka and south of the Bering Islands.

Modeling of the thermal regime of the slab, based solely on conduction, as it thrusts into the mantle shows that internal geotherms follow seismicity contours in the upper most part (<100 km) of the slab where the slab appears to bend to the northwest [*Davaille and Lees*, 2004]. Below 100 km depth thermal conduction alone cannot account for the reduction of observed seismicity and additional ablation, perhaps from small scale convection associated with the remnant Meiji Seamounts may account for the drastic reduction of seismicity and the curve of apparent termination of hypocenter trends to the south.

Shear Wave Splitting

Shear wave splitting using SKS seismic waves arriving in Kamchatka revealed evidence for trench parallel orientation of fast directions. This was interpreted as evidence for preferred orientation of olivine crystals deformed to align along the direction of mantle flow as material deforms during slab roll back. Laboratory modeling [*Buttles and Olson*, 1998], aimed at simulating the effect of slab roll back on shear wave splitting in the mantle, confirms observations of trench parallel polarizations in numerous subduction zones around the Pacific Rim [*Russo and Silver*, 1994], including Kamchatka [*Peyton et al.*, 2001]. Recent new observations of source side anisotropy supports this view and provides definitive evidence for placing the locus of the shear wave splitting below the slab 100–400 km depth [*Russo and Lees*, 2005]. Evidence for flow beyond the northern terminus of slab as imaged here is much more sparse but the few points imaged by Peyton et al. [2001] seem to agree, more or less, with the idea that there is a component of flow around the edge of the slab in the north. Local S-wave splitting in the mantle wedge indicated that the fast polarization rotates around near the cusp, suggesting mantle flow distortion above the slab near its edge [*Levin et al.*, 2004]. While the P-wave velocity perturbation images presented in this paper do not show specific evidence of this around the edge flow, the lack of significant high velocity anomalies in the north corroborates the notion that warm material is flowing around the Kamchatka slab to the north.

Geochemistry

The geochemistry of the volcanic rocks in the northern region of the Kamchatka Arc exhibits a unique pattern that supports the termination model of the Pacific plate in the vicinity of the Kliuchevskoi group of volcanoes [*Portnyagin et al.*, 2005; *Yogodzinski et al.*, 2001]. Strong, lateral zonation of older, oceanic-type, volcanic centers in the north versus younger, arc-type, active volcanoes in the south indicates an abrupt change in tectonics bounding the KAC [*Portnyagin et al.*, 2005]. A more detailed, fine line demarcation is suggested by models of Yogodzinski et al. [2001] where the presence of adakitic volcanics are found north of the junction of Kliuchevskoi-Sheveluch axis, but not to the south. The model suggests that slab melts are derived from ablated slab as the Pacific plate plunges into the mantle: the exposed edge provides a source for slab to contaminate rising melts and significantly modify the erupted magmas.

INSTRUMENTATION AND ARRAY DESCRIPTION

The seismic experiment was designed to span the extent of Kamchatka targeting the intersection of the Aleutian-Kamchatka junction. The installation included 15 broadband PASSCAL instruments equipped with Guralp CMG3T sensors (120 s period) deployed for a period of one year. The full complement of seismic stations was active and recording reliably for a period of about 9 months. Details of the installation can be found in earlier publications [*Lees et al.*, 2000; *Peyton et al.*, 2001]. A map of the seismic station locations is provided in Figure 1 where the names of stations are indicated for reference. 107 teleseismic and regional events with more than 10 stations recording were recorded during the time period of the deployment and the source locations for events at angular distances less than 100 degrees are presented in Figure 2 (one event with core-phase arrivals was also used in the analysis). There is reasonably good coverage of events except for gaps in the south east.

An example of a particularly good seismic record is illustrated in Figure 3. This M6.5 event was recorded on April 8, 13:10 GMT and registered a focal depth of 565 km. The waveforms have been re-aligned so that the predicted first arrival is the same for all. The predicted first arrivals are

Figure 1. Map of the Kamchatka-Aleutian region. Showing station locations of the SEKS (Side Edge of Kamchatka Slab) array (red) and permanent GSN stations (MA2, PET) in the region. Stations KGB, KRO, ZUP, PET and PZT are located along the volcanic arc. Station BNG was located on Bering Island. The central Kamchatka depression is located between the Sredeny range and coastal volcanic arc. The Kliuchevskoi volcanic complex is situated in the central Kamchatka depression offset to the northwest from the line of arc volcanoes to the south. The plate boundary between the Pacific and Eurasian Plates is presented as a thick reddish line. Contours along topographic highs in the ocean southeast of station KRO are the oceanic Meiji Seamounts. Magnetic anomaly lineations in the Komandorsky Basin are shown where seafloor spreading has occurred in the last 5 My [*Moore et al.*, 1992].

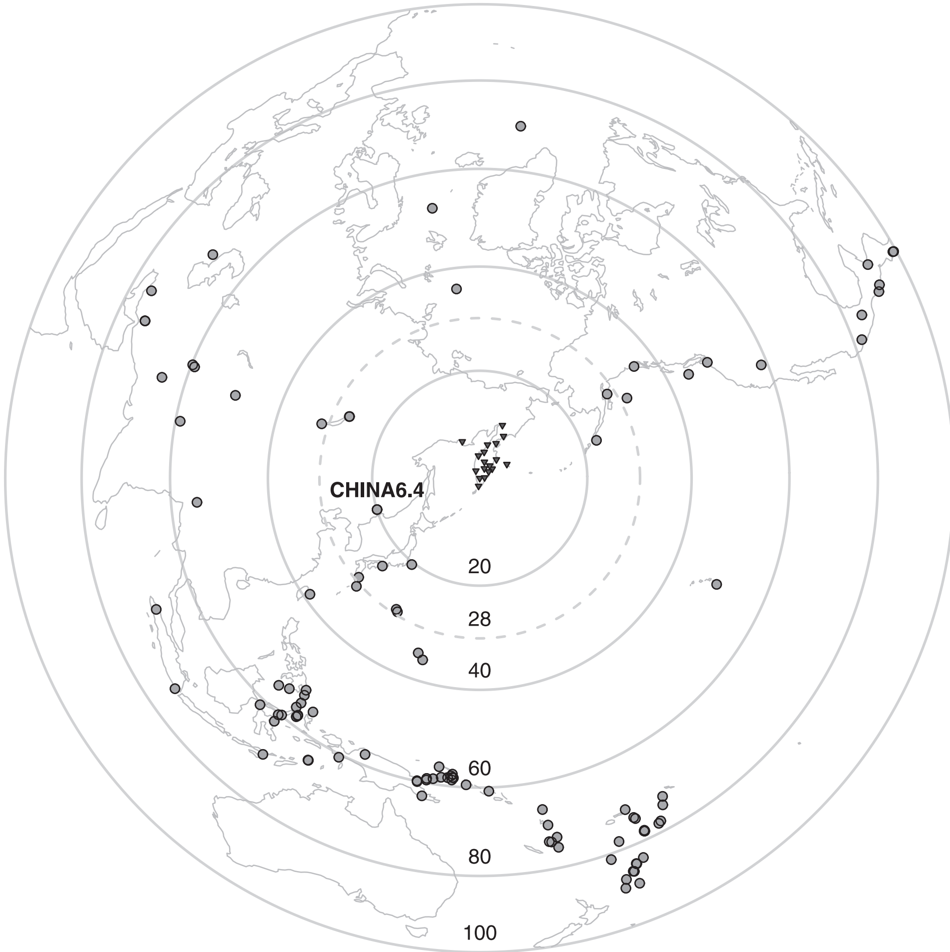

Figure 2. Equal-area projection of the world with Kamchatka at the center. SEKS array is represented as small triangles on the Kamchatka Peninsula. Small circles are earthquake hypocenters for events recorded in 1998–1999 by the SEKS array in Kamchatka. Of 107 events identified, 102 were used in the tomographic inversion. Events with distance less than 30° were excluded except for the notable event marked CHINA64 which occurred on April 8, 1999 at 1:10 GMT. This event was located at 565 km depth.

calculated from a one-dimensional spherically symmetric layered model. The fact that some arrivals come in late and others early indicated that the 1-D model does not adequately explain the travel times and a three-dimensional model is required to account for the discrepancy. The difference between the predicted and observed arrival at each station is called the residual and is used in the tomographic inversions presented in this paper. One especially intriguing observation from this seismic record is the later arrival of the high frequency signals at stations KRO and KGB.

While the analysis of dispersive waves is beyond the scope of this paper, the delay of high frequency waves from this event may be caused by internal structure in the slab that causes waveguide dispersion [*Abers*, 2000]. We note that in the example shown in Figure 3 stations PET and ZUP do not show appreciable evidence of this observation. We have searched for further evidence of waveguides propagating up the slab, in numerous events recorded on the broadband array, but we have not been able to identify this phenomenon independently. It may be that the waveguide modes are excited only in specific circumstances when the slab geometry, source radiation and receiver array are oriented appropriately. Path effects and shallow heterogeneity in the vicinity of the KAC may also play a roll in producing a dispersive wave.

TOMOGRAPHIC MODELING

To derive a three dimensional model of the deep structure below Kamchatka we extracted teleseismic events from the continuous recording and determined P-wave arrival times at first by manual picking and later these were refined by cross correlation [*VanDecar and Crosson*, 1990]. The cross correlation method reduces biases associated with human picking and provides very precise estimates of arrival times used in the inversion. The final data set included 102 events with at least 6 well recorded first arrivals (with most events recorded by 12 or more stations), providing 1161 total raypaths. Relative arrival times were derived using cross-correlation and residual travel times were then inverted for P-wave velocity variations in the subduction zone. A plot of the distribution of events from the global catalogue is presented in Figure 2. The azimuthal coverage is reasonable although notable gaps exist.

At each station residuals are determined by estimating the predicted versus observed arrival times. These are presented graphically via residual spheres, Figure 4. Arrivals coming up the slab from the south-west at stations KGB, KRO, and ZUP, show a clear negative trend, indicating the presence of the strong, high velocity of the subducting slab. Note that at station KGB several arrivals from the north east show the opposite trend. By contrast, arrivals in the northern stations (TKI, OSO, PAN, TIG, and UKH) are either mixed or tend to have positive anomalies. This pattern strongly suggests that structure in the northern part of Kamchatka is significantly different from that in the south. The first cut interpretation of the residual plots, prior to tomographic analysis, shows that P-wave arrivals recorded during this experiment strongly suggest that the edge of the slab resides near the boundary between station KGB and TUM. These travel time residuals comprise the basic data that are used in the tomographic inversion, described next.

Our tomographic models are derived by inverting the relative arrival times for smooth 3D perturbations in the seismic velocity beneath the array. The Earth's interior was parameterized (Figure 5) at 90576 nodes: 37 in the radial direction, 48 in latitude and 51 in longitude, with the velocity (in practice, slowness or 1/velocity) between nodes constrained by splines under tension. Raypaths were determined via a shooting method that traces rays from distant events that arrive teleseismically in Kamchatka. Within the region near Kamchatka where the model is perturbed, rays

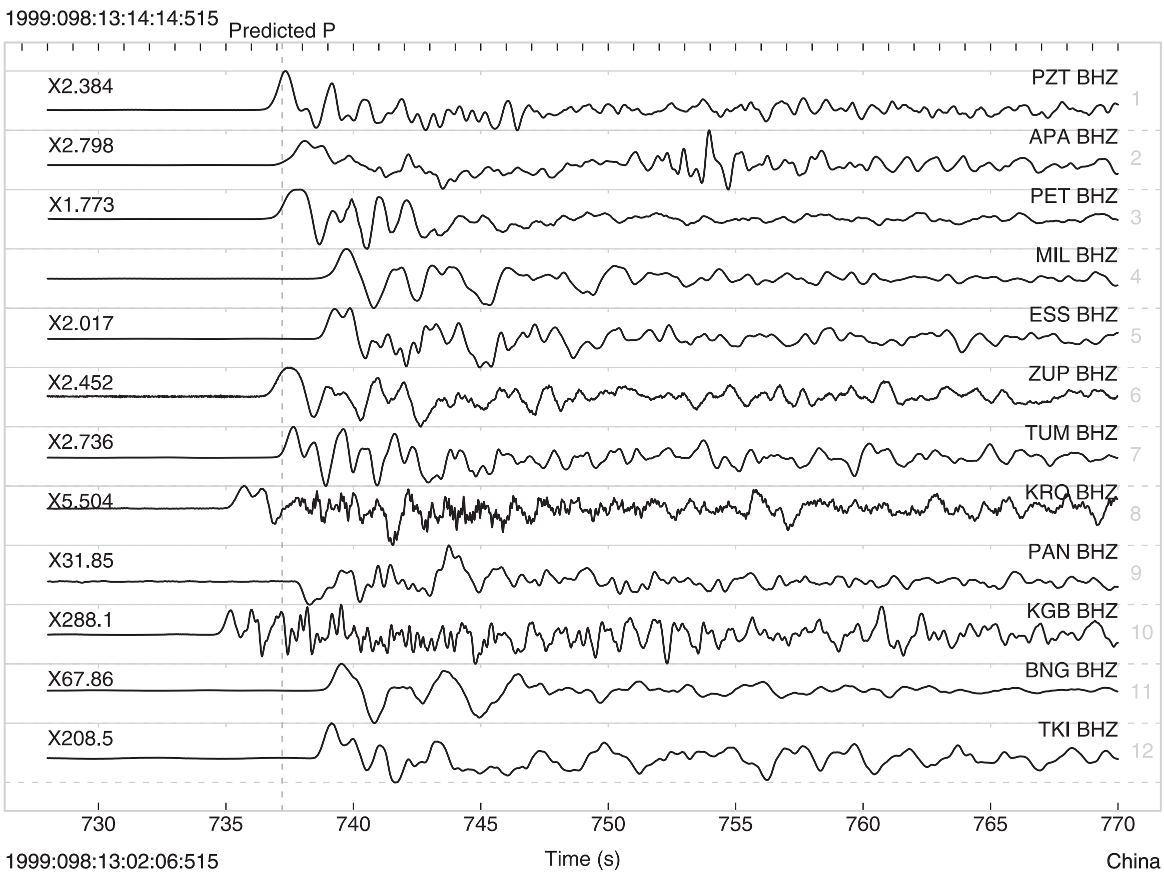

Figure 3. Seismic record of the M6.4 China Event, April 8, 1999 at 1:10 GMT. Signals are arranged from first arrival (PZT, south, top) to north (TKI). The traces have been shifted so the predicted arrival times at each station are aligned. Note that station BNG exhibits a late arrival.

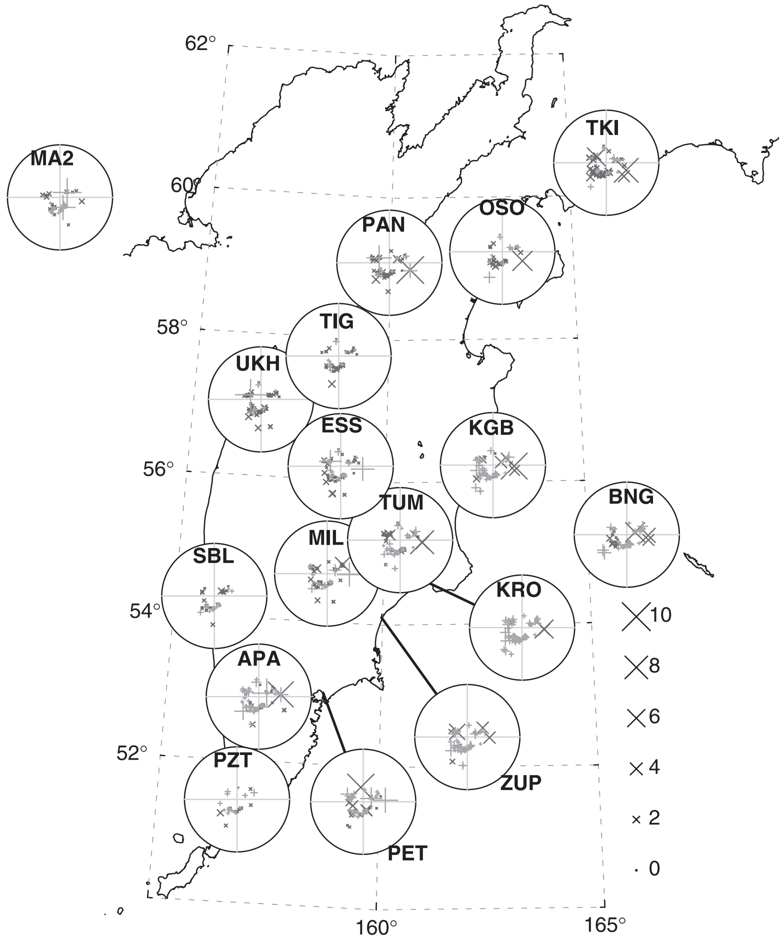

Figure 4. Residual spheres for the data arriving at SEKS stations in 1998–1999. Each sphere represents an equal area projection of incoming rays at each station. Points are plotted at the back azimuth and incident angle of each datum. Darker X-marks and lighter +-marks are positive and negative residuals respectively. Marks are scaled by size in seconds.

bend according to the 3D models; outside this region, the rays follow a radially symmetric 1D Earth model (IASP91 [*Kennett and Engdahl*, 1991]). Once raypaths and residuals are determined, a matrix is inverted and perturbations from the 1D model are plotted showing the 3D variations in velocity required to explain the residual travel times. Apriori smoothness constraints are invoked by requiring first and second spatial derivatives to be small, which reduces large fluctuations when noise is present. Each inversion involves thousands of iterations and >95% residual reduction is typically achieved. Linear and non-linear inversions are explored as well as resolution tests using synthetic models. We confidence in our model results and details of our inversion procedure can be found in *VanDecar et al.* [2003].

The tomographic inversion (Plates 1–3) is presented as a series of horizontal, vertical and rendered representations of the full three-dimensional perturbation model. The first order interpretation shows a clear signature of the subducting slab as a high velocity anomaly inclined at approximately 50 degrees plunging to the north-west in agreement with the seismicity. Noteworthy is the apparent slab shoaling towards the northern terminus of the subduction zone in Kamchatka where the Aleutian Islands intersect with the Kamchatka Arc. This is seen as varying anomalies trending from north to south in the descending horizontal slices (Plate 1), as well as in differences in the presence of high velocities (blue) in vertical slices X versus Z (Plate 2). Since the tomographic model is derived from teleseismic arrivals it is not biased by local data (seismicity) in the subducting slab. The fact that the seismicity shallows in the same way that the tomographic model shoals corroborates the assertion that the slab varies considerably as it approaches its northern terminus. Either the slab has heated up to the extent that it can no longer sustain the stresses required for seismicity, or it simply does not exist. These results corroborate and are independent of surface wave studies that image S-wave propagation in Kamchatka [*Levin et al.*, 2002].

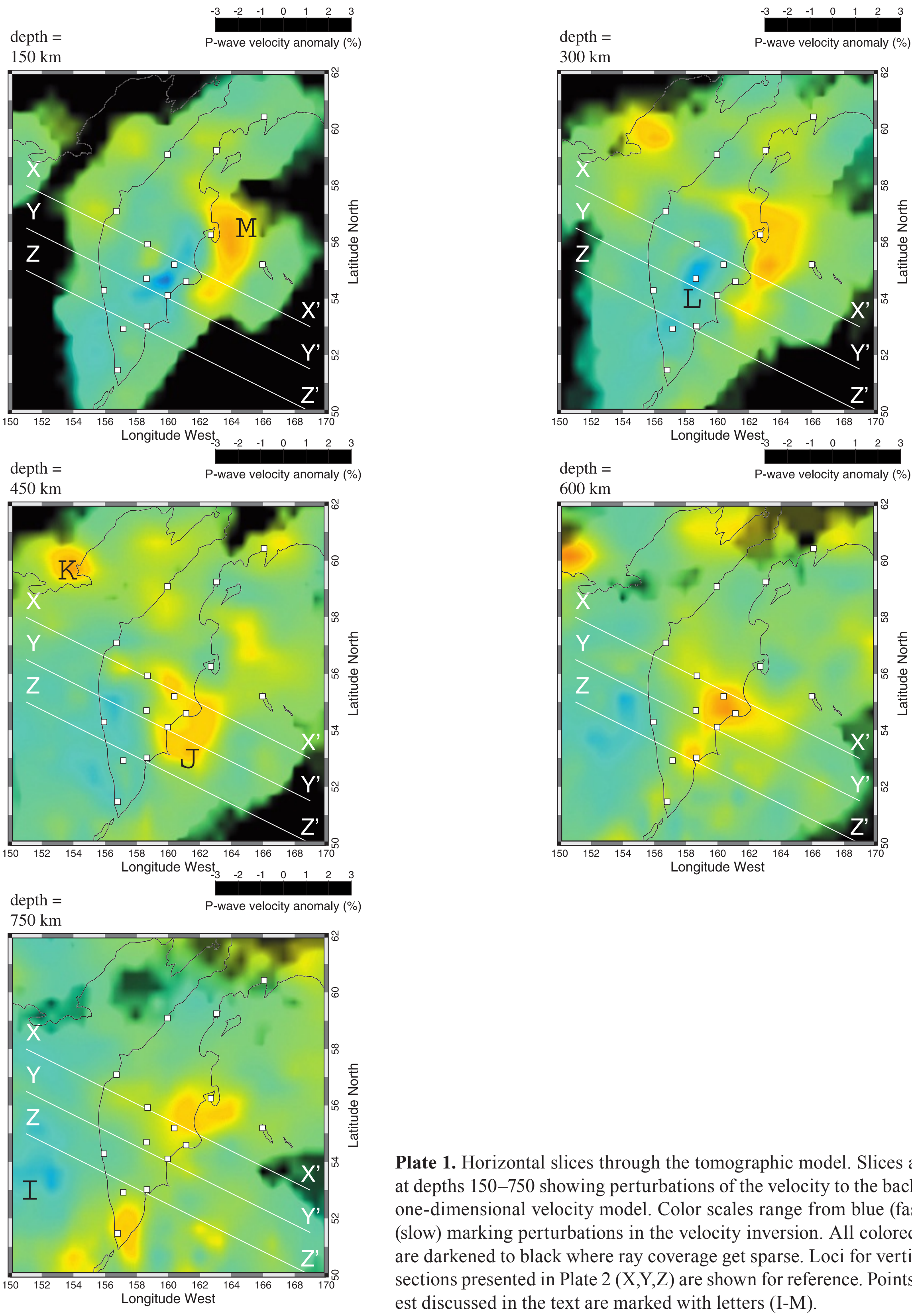

Plate 1. Horizontal slices through the tomographic model. Slices are taken at depths 150–750 showing perturbations of the velocity to the background, one-dimensional velocity model. Color scales range from blue (fast) to red (slow) marking perturbations in the velocity inversion. All colored regions are darkened to black where ray coverage get sparse. Loci for vertical cross sections presented in Plate 2 (X,Y,Z) are shown for reference. Points of interest discussed in the text are marked with letters (I-M).

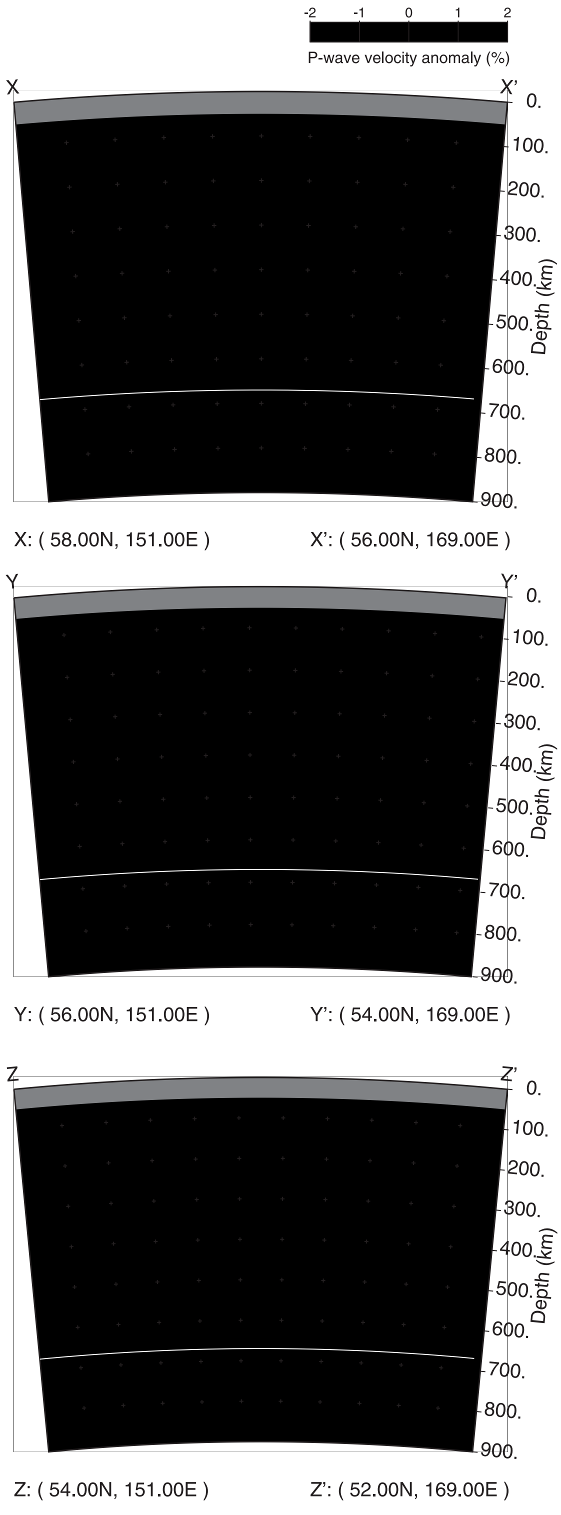

L2 P-wave inversion

Plate 2. Vertical cross sectional slices through the tomographic model. Map orientation of the cross sections is shown in Plate 1.

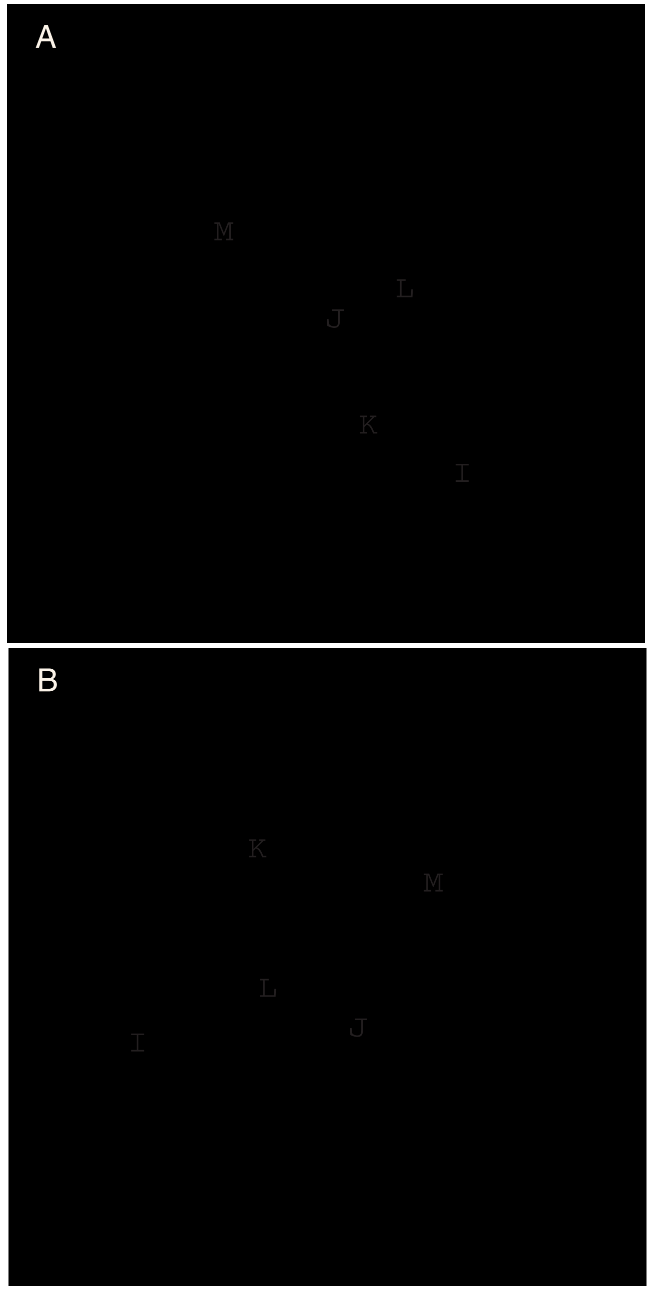

Plate 3. Tomographic image of the Kamchatka Subduction zone rendered in three-dimensions. The cut-off perturbation level is 3% with blue regions being high velocity and red lower velocity perturbations. The slab is a clear high velocity zone approximately 100 km thick plunging into the upper mantle at an angle of ~50°. The green plane represents the top of the subduction zone seismicity, contoured and rendered along with the tomographic images. Gold cones are active volcanoes along the Kamchatka arc and white squares are stations included for reference to the map in Figure 1. The bars represent length scales of 100 km. Points of interest discussed in the text are marked with letters (I–M).

We describe the inversion results by high-lighting important anomalies from the deepest parts of the model to the surface (Plates 1–3). (Please see the "Animated view of the tomographic inversion of Kamchatka subduction zone" on the CDROM accompanying this volume.) At 750 km depth the slab is not evident, but a broadened high velocity can be seen (labeled I) northwest of Kamchatka on the western side of the Sea of Okhotsk. This anomaly merges with the slab at around 600 km depth beneath the sea of Okhotsk. Low velocity perturbations can be seen below station KRO at this depth (labeled J). At 450 km depth the slab is perceived as a high velocity perturbation and a low velocity lineation can be seen in a triangle formed by stations BER, KRO and KGB (labeled L). Another low velocity anomaly is observed north of stations PAN and OSO in the northern section of Kamchatka (labeled K). The subducting slab is best observed at depths 300–150 km. At these depths (especially 300 km depth) there is a noticeable signature of low velocity between BER and KGB (labeled M) where we anticipate mantle flow around the northern terminus of the slab as suggested by analyses of shear wave splitting based on teleseismic S-wave studies.

Resolution analyses of this inversion show that the horizontal resolving power is greater than vertical resolution for teleseismic tomography. In the Kamchatka inversion we suggest that the resolution is on the order of 100 km near the center of the model (300 km depth) where the interpretations are most important. Near the edges of the model, data coverage is poor and smearing and instability prevents us from providing a detailed interpretation.

The shoaling and diminishment of the Kamchatka slab northward appears to corroborate the hypothesis put forward by Yogodzinski et al. [2001], namely, that there exists a significant tear in the slab between the western Aleutians and northern extent of the Kamchatka Arc. Further elaboration of this model is presented via imaging by *Levin et al.* [2005] along the Aleutians. It may be that all slabs exhibit some form of ablation at their edges where cusps are formed on oceanic plates. *Kirby et al.* [1996] show seismicity around the Pacific rim in cross section and notes that at each cusp there is pronounced shoaling towards the point where arcs change direction. As a second, detailed example of this phenomenon, a cross section of seismicity at the Kurile-Japan Trench below Hokkaido shows a similar trend (see illustration in this monograph on seismicity along the Japan-Kurile-Kamchatka subduction zones). There the shoaling does not trend towards the surface as in Northern Kamchatka but rather stops much deeper in the subduction zone. We interpret this as a breach in the slab, although in this case the breach terminates at depth and slab ablation may not have a geochemical signature as observed in Kamchatka. A simple search around the Pacific Rim at other cusps (Central American Cocos plate, Taiwan Pacific plate) confirms the observation that slabs shoal near cusps as suggested in a rough way by *Kirby et al.* [1996]

The absence of high velocity slab in the northern corner of the Kamchatka subduction zone suggests that the slab is either heated to the extent that seismic anomalies are considerably reduced in this region or that the slab simply does not extend into this part of the upper mantle (does not exist). If the slab does not extend into the mantle below the KAC, then a large portion of the slab must have been ablated (or foundered?) during the subduction process. Considering the large number of slab edges across the globe, this implies that the mantle is contaminated with slab material, at least near the edges where subduction shoals and volcanism terminates. Furthermore, the slab window provides a conduit for upper mantle material to flow through the breach, which explains the patterns of shear wave splitting observed in Kamchatka. This may also provide an explanation for the westward shift of the Kliuchevskoi group of volcanoes in the northern terminus: flow around the edge deforms the slab at the northern edge, ablates it and produces the westward warp and uplift. Other mechanisms have been proposed by *Park et al.* [2002].

The subduction of the aseismic Meiji seamounts represents a slight twist in this simple model of slab ablation and mantle

Figure 5. 3-D perspective showing the model parameterization. At the crossing point of each line, the perturbations from the 1-D background model are constrained by splines under tension, with the velocity model calculated to reduce the travel time residuals and fit the data to observations. There are 37 spline knots in the radial direction, 48 in latitude and 51 in longitude. There are a total number of 90576 nodes in the model.

flow. *Davaille and Lees* [2004] suggested that side ablation via conduction alone could not completely explain the shape of the seismicity shoaling trends in northern Kamchatka. They suggested that the presence of the Meiji seamounts, remnants of the Hawaiian plume deformation of the Pacific plate, provides accelerated ablation that can account for the missing slab in the north. The model is based on small scale convection cells forming at the base of the lithosphere and carried into the subduction where they are more prone to erosion. This model, of course, cannot explain the pervasive observation around the Pacific Rim on shoaling of seismicity towards cusps in general. It is useful to keep in mind that the subduction of the Meiji seamounts may contribute to the erosion of the plate and provides an acceleration of the process of terminating the plate to the north.

While subduction was apparently active in the isthmus region of the Kamchatka Peninsula in the last 10 My we see no convincing evidence of high velocity P-wave anomalies associated with remnant slabs in this region. This observation has been used to suggest that catastrophic failure occurred where slab remnants broke away and descended into the deep mantle [*Levin et al.*, 2002]. Slab foundering provides a possible mechanism [*Davies and von Blanckenburg*, 1995] to explain upwelling thermal plumes below the Komandorsky Basin which create associated heat flow anomalies [*Smirnov and Sugrobov*, 1982] and volcanic geochemistry variations [*Portnyagin et al.*, 2005]. An alternative is that a slab window opened and evolved as the Kamchatka-Aleutian junction migrated northward over time allowing thermal intrusions in the isthmus and Komandorsky regions [*Dickinson and Snyder*, 1979]. We suggest that observations related in this paper, especially the shoaling geometry of the slab, is common to other cusps along the Pacific rim and general explanations will have to be found that apply to all these localities to explain the phenomena. Kamchatka Peninsula is one place where a large, land based, regional array can be used to examine the subduction zone seismically. In the future, ocean bottom seismic arrays may be used to image the region between the Kamchatka subduction zone and Aleutian subduction [*Levin et al.*, 2005]. These studies might then settle the question of how the Kamchatka-Aleutian slab window formed and evolved to its present state.

CONCLUSIONS

We conclude that teleseismic P-wave tomography clearly shows the presence of cold subducting Pacific plate slab in southern Kamchatka and an equally discernible absence of slab material subducting north of the termination of volcanism along the Kamchatka Arc. The termination of the slab to the north implies that the slab edge is exposed to the north and mantle material can flow around the edge freely. The motion of slab material around the edge of the slab causes further ablation of the slab that contaminates volcanics at the most northern active volcanoes in Kamchatka (Sheveluch) and provides an explanation for the characteristic shoaling of seismicity to the north. A low velocity anomaly beneath the region where Bering Island resides may be evidence for flow around the northern terminus of the Kamchatka subduction zone.

REFERENCES

Abers, G.A., Hydrated subducted crust at 100–250 km depth, *Earth Planetary Science Letters*, *176*, 323–330, 2000.

Baranov, B.V., N.I. Seliverstov, A.V. Murav'ev, and E.L. Uzurov, Commander Basin: back-transform spreading, *Tectonophysics*, *199*, 237–269, 1991.

Buttles, J., and P. Olson, A laboratory model of subduction zone anisotropy, *Earth Planet. Sci. Lett.*, *164*, 245–262, 1998.

Davaille, A., and J.M. Lees, Thermal modeling of subducted plates: tear and hot spot at the Kamchatka corner, *Earth Planet. Sci. Letts.*, *226* (3–4), 293-304DOI:10.1016/j.epsl.2004.07.024, 2004.

Davies, J.H., and F. von Blanckenburg, Slab breakoff; a model of lithosphere detachment and its test in the magmatism and deformation of collisional orogens, *Earth Planet. Sci. Letts.*, *129* (1-4), 85–102, 1995.

Defant, M.J., and M.S. Drummond, Derivation of some modern arc magmas by melting of young subducted lithosphere, *Nature*, *347*, 662–665, 1990.

Defant, M.J., and P. Kepzhinskas, Evidence suggests slab melting in arc magmas, *Eos (Trans. AGU)*, *82* (6), 65–69, 2001.

Dickinson, W.R., and W.S. Snyder, Geometry of triple junctions related to San Andreas transform, *J. Geophys. Res.*, *84*, 561–572, 1979.

Gaedicke, C., B. Baranov, N. Seliverstov, A. Alexeiev, N. Tsukanov, and R. Freitag, Structure of an active arc-continent collision area: The Aleutian-Kamchatka junction, *Tectonophys.*, *325*, 63–85, 2000.

Geist, E.L., and D.W. Scholl, Large-scale deformation related to the collision of the Aleutian arc with Kamchatka, *Tectonics*, *13* (2), 538–560, 1994.

Gorbatov, A., J. Dominguez, G. Suarez, V. Kostaglodov, D. Zhao, and E. Gordeev, Tomographic imaging of P wave velocity structure beneath Kamchatka Peninsula, *Geophys. J. Int.*, *137*, 269–279, 1999.

Gorbatov, A., V. Kostoglodov, S. Gerardo, and E. Gordeev, Seismicity and structure of the Kamchatka subduction zone, *J. Geophys. Res.*, *102*, 17883–17898, 1997.

Gorbatov, A., A. Widiyantoro, Y. Fukao, and E. Gordeev, Signature of remnant slabs in the North Pacific from P-wave tomography, *Geophys. J. Int.*, *142*, 27–36, 2000.

Hochstaedter, A.G., P.K. Kepezhinskas, M.J. Defant, M.S. Drummond, and H. Bellon, On the tectonic significance of arc volcanism in northern Kamchatka, *J. Geol.*, *102*, 639–654, 1994.

Kennett, B.L.N., and E.R. Engdahl, Travel times for global earthquake location and phase identification, *Geophys. J. Int.*, *105*, 429–465, 1991.

Kirby, S.H., E.R. Engdahl, and R.P. Denlinger, Intermediate-depth intraslab earthquakes and arc volcanism as physical expressions of crustal and uppermost mantle metamorphism in subducting slabs, in *Subduction top to bottom*, edited by G.E. Bebout, D.W. Scholl, S.H. Kirby, and J.P. Platt, pp. 195–214, 1996.

Lees, J.M., Implications of slab tear on geodynamics, seismology and volcano geochemistry, in *Eos (Trans. AGU)*, pp. 1080, 2000.

Lees, J.M., M. Brandon, J. Park, V. Levin, A. Ozerov, and E. Gordeev, Kamchatka: Edge of the Plate, *Iris News Letter*, *2000* (1), 17–19, 2000.

Levin, V., D. Droznin, J. Park, and E. Gordeev, Mantle wedge anisotropy beneath southeastern Kamchatka from local-S birefringence, *Geophys J. Int.*, *158*, 1009–1023, 2004.

Levin, V., N. Shapiro, J. Park, and M. Ritzwoller, Seismic evidence for catastrophic slab loss beneath Kamchatka, *Nature*, *418*, 763–767, 2002.

Levin, V., N. Shapiro, J. Park, and M. Ritzwoller, Slab Portal beneath the western Aleutians, *Geology*, *33* (4), 253–256, 2005.

Moore, G.W., N.A. Bogdanov, K.J. Drummond, X. Golovchenko, R.L. Larson, W.C. Pitman, III, W.A. Rinehart, L. Siebert, T. Simkin, S.M. Tilman, and S. Uyeda, Plate-tectonic map of the Circum-Pacific Region, Arctic Sheet, in *Circum-Pacific Map Series*, pp. 20, United States Geological Survey, 1992.

Nokleberg, W.J., L.M. Parfenov, J.W.H. Monger, I.O. Norton, A.I. Khanchuk, D.B. Stone, C.R. Scotese, D.W. Scholl, and K. Fujita, *Phanerozoic Tectonic Evolution of the Circum-North Pacific*, 122 pp., 2001.

Park, J., V. Levin, M.T. Brandon, J.M. Lees, V. Peyton, E. Gordeev, and A. Ozerov, A dangling slab, amplified arc volcanism, mantle flow and seismic anisotropy near the Kamchatka plate corner, in *Plate Boundary Zones*, edited by S. Stein and J. Freymueller, pp. 295–324, AGU, Washington DC, 2002.

Peyton, V., V. Levin, J. Park, M. Brandon, J. Lees, E. Gordeev, and A. Ozerov, Mantle Flow at a Slab Edge: Seismic Anisotropy in the Kamchatka Region, *Geophys. Res. Lett.*, *28* (2), 379–382, 2001.

Portnyagin, M., K. Hoernle, G. Avdeiko, F. Hauff, R. Werner, I. Bindeman, V. Uspensky, and D. Garbe-Schönberg, Transition from arc to oceanic magmatism at the Kamchatka-Aleutian junction, *Geology*, *33* (1), 25-28DOI:10.1130/G20853.1, 2005.

Russo, R.M., and J.M. Lees, Seismic Anisotropy beneath Pacific Ocean Lithosphere Subducted at Kamchatka, submitted to Journal of Geophysical Research-Solid Earth, 2005.

Russo, R.M., and P.G. Silver, Trench-parallel flow beneath the Nazca Plate from seismic anisotropy, *Science*, *263*, 1105–1111, 1994.

Seliverstov, N.I., *Structure of Kamchatkian Water Area Bottom and Geodynamic of a Junction Zone between the Kuril-Kamchatka and Aleutian Island Arcs (in Russian)*, 164 pp., Nauchnyi Mir, Moscow, 1998.

Smirnov, Y.B., and Y.M. Sugrobov, Terrestrial heat flow in the Northwestern Pacific, *Tectonophysics*, *83*, 109–122, 1982.

VanDecar, J.C., and R.S. Crosson, Determination of teleseismic relative phase arrival times using multi-channel cross correlation and least squares, *Bull. Seis. Soc. Am.*, *80* (1), 150–169, 1990.

VanDecar, J.C., R.M. Russo, D.E. James, W.B. Ambeh, and M. Franke, Aseismic continuation of the Lesser Antilles slab beneath continental South America, *J. Geophys. Res.*, *108*, 2043DOI:10.1029/2001JB000884, 2003.

Yogodzinski, G.M., J.M. Lees, T.G. Churikova, F. Dorendorf, G. Woerner, and O.N. Volynets, Geochemical evidence for the melting of subducting oceanic lithosphere at plate edges, *Nature*, *409*, 500–504, 2001.

Jonathan M. Lees, University of North Carolina, Chapel Hill, Department of Geological Sciences, CB#3315, Mitchell Hall, Chapel Hill, NC 27599-3315

John VanDecar, Department of Terrestrial Magnetism, Carnegie Institution of Washington, 5241 Broad Branch Rd., NW, Washington, DC 20015

Evgenii Gordeev and Alexei Ozerov, Institute of Volcanology and Seismology (IVS), Petropavlovsk-Kamchatsky, Piip Boulevard 9, 683006, Russia

Mark Brandon, Yale University, P.O. Box 208109, 210 Whitney Avenue, New Haven, CT 06520-8109

Jeff Park, Yale University, P.O. Box 208109, 210 Whitney Avenue, New Haven, CT 06520-8109

Vadim Levin, Department of Geological Sciences, Rutgers University, 610 Taylor Road, Piscataway, New Jersey 08854-8066

Thermal Models Beneath Kamchatka and the Pacific Plate Rejuvenation From a Mantle Plume Impact

V. C. Manea and M. Manea

Seismological Laboratory 252-21, CalTech, Pasadena, California, USA

The Northwest Pacific area, comprising the Kamchatka peninsula, is a distinctive area where a series of on going geodynamical processes like: plate rejuvenation from a mantle plume impact, slab detachment, slab edge melting and exotic volcanism, take place. With the help of finite element modeling we infer the thermal structure across Kamchatka in a series of 2D profiles normal to the trench. We chose the location at these profiles based on seismicity, geochemical variation and offshore heat flow measurements.

Assuming that the transition from brittle to ductile behavior inside the subducting slab corresponds to the 650°C isotherm, our thermal models predict a good fit with maximum depth of seismicity (~500 km) for southern Kamchatka only if the exothermic olivine-spinel phase transition is introduced. In the central part of Kamchatka, a good fit is obtained if the hot mantle plume, located just beneath Meiji Guyot seamount, thermally rejuvenates the subducting Pacific plate. Further to the north, the seismicity shallows more (200–100 km) and slab rejuvenation alone cannot provide a thermal structure with a good fit with seismically active subducting slab. A good explanation for such shallow seismicity might be the slab detachment due to cessation of subduction just north of Kamchatka-Aleutians junction. The thermal structure beneath the northernmost active volcano in Kamchatka, Scheveluch, which exhibits a strong adakitic signature, shows that slab edge exposure to the hotter asthenosphere creates the favorable conditions for oceanic crust melting at ~70 km depth, just beneath Scheveluch.

Our numerical models show that plate rejuvenation from a mantle plume, slab edge exposure to hot upper mantle and probably slab detachment play an essential role in subduction slabs thermal structure, seismicity down-dip extension and geochemical variations of lavas in Kamchatka.

INTRODUCTION

One of the consequences of the motion of Earth's tectonic plates is the onset of suduction zones where one plate plunges beneath another. Intense dehydration of the subducted plate can induce partial melting in the mantle wedge, generating thermo-chemical instabilities or plumes, which finally end up in an intense arc volcanism (*Gerya et al., 2003, 2003a*). Other mantle plumes, which are frequently assumed to come from the transition zone or from the core-mantle boundary (*Hansen and Yuen, 1988; Helmberger et al., 1998; Foulger et al., 2000; Nataf, 2000; Shen et al., 2002; Tan et al., 2002; Zhao, 2003; Montelli et al., 2004*), can affect the plate thermal structure through a process called thermal rejuvenation

Volcanism and Subduction: The Kamchatka Region
Geophysical Monograph Series 172

10.1029/172GM07

(*Crough, 1978; Nagihara et al., 1996; Moore et al., 1998*), where an old plate behaves actually like a young plate. Such thermal discontinuities in a plate thermal structure, sometimes coupled with important variations in the subduction rates can produce an interesting phenomenon, called slab detachment, where parts of the subduction slab separate and sink into the mantle (*Von Blanckenburg and Davis, 1995; Davis and Von Blanckenburg, 1995; Wortel and Spakman, 2000; Xu et al., 2000; Levin et al., 2002; Rogers et al., 2002; Gerya et al., 2004*). The Northwest Pacific area, comprising the Kamchatka peninsula, reassembles all of the above geodynamical processes. The old Pacific plate (PAC) subducts beneath Kamchatka at a fast convergence rate of ~7.5 cm/yr (*DeMets, 1992*), producing one of the most active volcanic arcs in the world. A large positive bathymetric feature located at the northern end of the Emperor seamount chain, the Meiji Guyot seamount, is characterized by anomalously high heat flow (> 80 mW/m^2) (*Smirnov & Sugrobov 1979, 1980a,b*) for the old (~90 Ma) Pacific plate. In this area, a non-linear iterative P-wave traveltime tomography of *Gorbatov et al. (2001)* has revealed a mantle plume rising across the 660 km discontinuity, and deflecting subhorizontally in the uppermost mantle.

Levin et al. (2002) imaged the upper mantle seismic structure beneath Kamchatka, and proposed two Quaternary episodes of slab detachment just north of the Aleutian-Kamchatka junction. Whereas extensive slab dehydration of the subducting Pacific slab beneath southern part of the eastern Kamchatka volcanic front (SEVF) is responsible for mantle wedge melting, the slab detachment, upwelling and southward flow of hot and fertile mantle are the main reason for the recent magmatism in southern Kamchatka central depression (SCKD) (*Portnyagin et al., 2005*). Although the convergence rate and the age of the Pacific plate show very little variation along the Kamchatka trench, the intraslab seismicity varies from ~500 km beneath SEVF to ~300 km in the central part of the peninsula (NEVF), and decreases to ~100–200 km further to the north (*Gorbatov et. al, 1997*). The main goal of this paper is to infer the thermal structure beneath Kamchatka which satisfy simultaneously the seismic observations, type of volcanism and geodynamic background. We show that plate rejuvenation from a mantle plume and slab detachment plays an essential role in subduction slabs thermal structure, seismicity down-dip extension and geochemical variations of lavas along EVF and SCKD.

TECTONIC AND GEOLOGIC SETTINGS

Subduction is active only in the southern half of the Kamchatka peninsula, whereas past subduction in the north is indicated by an inactive volcanic arc (*Kepezhinskas et al., 1997*). The PAC subducts near-normal along the Kamchatka subduction zone (KSZ) with a highly variable dip angle, from ~55º in the south to ~35º in the north (*Gorbatov et al, 1997*). The Pacific plate age varies from 104 Ma to 87 Ma (*Renkin and Sclater, 1988*), and the converge rate from 7.8 cm/yr to 7.5 cm/yr (*Gorbatov et al., 1997*) (*Fig. 1*). The seismicity and structure of the KZS was studied in detail by *Gorbatov et al. (1997)*. The subducting Pacific slab is seismically active down to ~450–500 km in southern Kamchatka. Further north, the seismicity shallows in steps, from ~300 km beneath NEVF to ~200 km beneath the Klyuchevskoy group and ~100 km under the Scheveluch group, respectively (*Fig. 2*). The maximum depth of seismicity in subduction zones is controlled mainly by pressure and temperature. *Goto et al. (1983)*, *Spencer (1994)* and *Gorbatov* and *Kostoglodov (1997)* proposed a cut-off temperature of 650°C for the maximum extent of intraslab seismicity. It is assumed that beyond this critical temperature the slab loses its brittle behavior, instead acting like a ductile material. Recent studies suggest that intermediate-depth intraslab earthquakes likely results from mineralogical changes within the subducting slab (*Hacker et al., 2003*). A recent study of *Abers et al. (2006)*, advocates that a mineral reaction front controls the position of the earthquakes in the subducting slab. The linearity of the slab seismicity in the *(p,T)* space seen for the Alaska subduction zone (*Abers et al., 2006*), implies that the breakdown of lawsonite is responsible for the occurrence of seismicity located in the subducted oceanic crust. Beneath Kamchatka, the seismicity is too scatter within the subducting slab and consequently in the (*p,T*) space too. Therefore, we use in this study only the cut-off temperature (T_{cr}=650°C) to constrain the thermal structure inside the subducting slab.

Offshore central Kamchatka heat flow data (*Smirnov and Sugrobov, 1979; 1989a,b*) show unusual high values higher than 80 mW/m^2 just above Meiji Guyot seamount, suggesting that the thermal thickness of the Pacific plate is much smaller in this area. Thus the effective age (thermally defined) is less than the geological age (*Renkin and Sclater, 1988*) (*Fig. 3*). In contrast, the Pacific plate offshore southern Kamchatka shows normal heat flow values (~40–60 mW/m^2) for a ~100 Ma oceanic plate (*Stein, 1995*). Interestingly, *Gorbatov et al. (2001)* revealed a wide cylindrical shaped mantle plume (–2% δv_p anomaly) rising from ~900 km depth and being deflected by the Pacific plate motion toward the Kamchatka trench (*Fig. 4*). The superficial thermal effect of this plume seems to be reflected in the anomalously heat flow values recorded in the Meiji Guyot seamount area. In the northwesternmost Pacific the Aleutian and Kamchatka arcs collide at an angle of ~90º. At this junction, *Levin et al., (2002)* show that a large portal exists, exposing the slab edge to the hotter mantle and facilitating the production of high Mg andesites,

Figure 1. Tectonic setting and position of the four study areas labeled A, B, C and D (black dashed lines). The offshore white contour lines represent the heat flow data from *Smirnov & Sugrobov (1979, 1980a,b)*. The red area just beneath the highest heat flow values (>80 mW/m^2) delimitates the Meiji Guyot seamount (hatched area). The transparent A-A' cross-section is used in *Fig. 2* to project the seismicity beneath Kamchatka. The arrows pointed toward the trench show the Pacific plate convergence rate from *Gorbatov et al. (1997)*. Also the plate age in shown in Ma above these arrows from *Renkin and Sclater (1988)*. Other notations are: SEVF—south eastern volcanic arc; NEVF—north eastern volcanic front; SCKD – south central Kamchatka depression. Some principal active volcanoes are: I - Ilinsky; M - Mutnovsky; A - Avachinscy; Ka - Karymsky; U - Uzon; Ki - Kizimen; T - Tolbachik; K – Kluchevskoy; Sh – Shiveluch. Z - Zhupanova area within EVF where an adakitic signature was found (*Maxim Portnyagin—personal communication, 2005*).

called adakites, through subducting oceanic crust melting. Also, *Yogodzinski et al. (2002)* provide strong geochemical evidence for the melting of subducting crust beneath northern Kamchatka and Aleutians. *Levin et al. (2002)* showed that two episodes of slab detachment occurred beneath northern Kamchatka in the last 10 Ma. The Klyuchevskoy volcanic group lies just above the slab edge itself, and its extraordinary volcanic productivity and high temperature of equilibrium of magmas (*Ozerov, 2000*) are attributed to slab-edge lofting (*Park et al., 2002*). *Portnyagin et al. (2005)* show a strong and opposite variation of Nb/Y, Ba/Nb and Dy/Yb ratios along the southern Central Kamchatka depression (SCKD) in the vicinity of the Kamchatka-Aleutian junction. For example, low NB/Y and Dy/Yb ratios and high Ba/Nb ratio for the SCKD suggest abundant slab dehydration which can contribute to extensive, high-degree mantle wedge melting. Also, the strong adakitic signature (i.e. high Sr contents and high Sr/Y ratios) of Sheveluch group is proposed to be the effect of thermal erosion of the subducting slab edge exposed to hot asthenosphere. In contrast, NCKD is characterized by high NB/Y and Dy/Yb ratios and low Ba/Nb ratio, advocate for a highly diminished fluid influx and therefore explaining the low degree melting beneath the northern volcanoes.

On the other hand, southern Kamchatka (SEVF and NEVF) is the place of a normal calk-alkaline arc volcanism, where the magmatism is proposed to be the result of the lowering of the melting point of peridotite through an influx of volatiles from the dehydration of subducting slab (*Perfit et al., 1980*). An important dissimilarity of southern Kamchatka is that no adakites were found, suggesting that in this region the subducting basaltic crust does not undergo melting.

In this study we divided the study area into four sub regions based on seismicity, geochemical variation and off-shore heat flow measurements (*Fig. 1*). We assume a cut-off temperature of T_{cr}=650°C for the maximum depth of seismicity. For each sub region, we build a series of 2D thermal models following the numerical scheme proposed by *Manea et al. (2005)*. Then, we use MORB phase diagrams (*Schmidt and Poli, 1998; Kerrick and Connolly, 2001; Hacker et al., 2003*) and (*p,T*) paths along the slab surface to investigate the dehydration variations along the oceanic crust beneath the volcanic arc. We also explore the circumstances for the oceanic basaltic crust and mantle wedge peridotite to undergo melting.

MODELING PROCEDURE

The numerical scheme of *Manea et al. (2005)* consists of a system of 2D Navier-Stokes equations and 2D steady state heat transfer equation. Strong temperature-dependence of viscosity is used in the present modeling

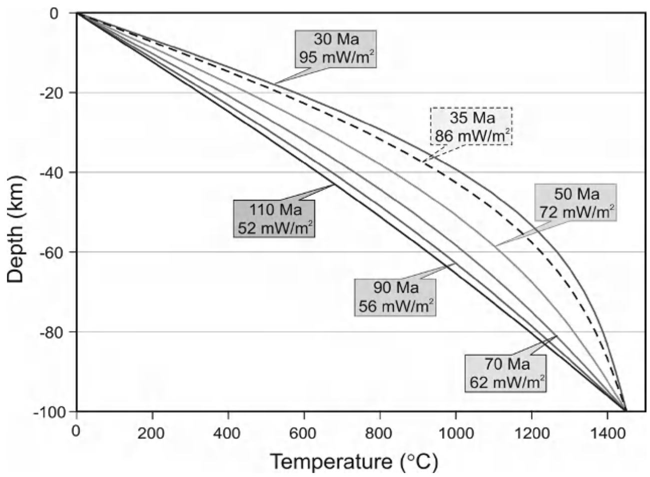

Figure 3. Oceanic isotherms used as boundary condition in the numerical models (using GDH1 model from *Stein and Stein (1992)*.) The insets show the plate age and the modeled surface heat flow. The dashed black curve at 35 Ma (86 mW/m^2) was used to fit our models with the maximum depth of seismicity.

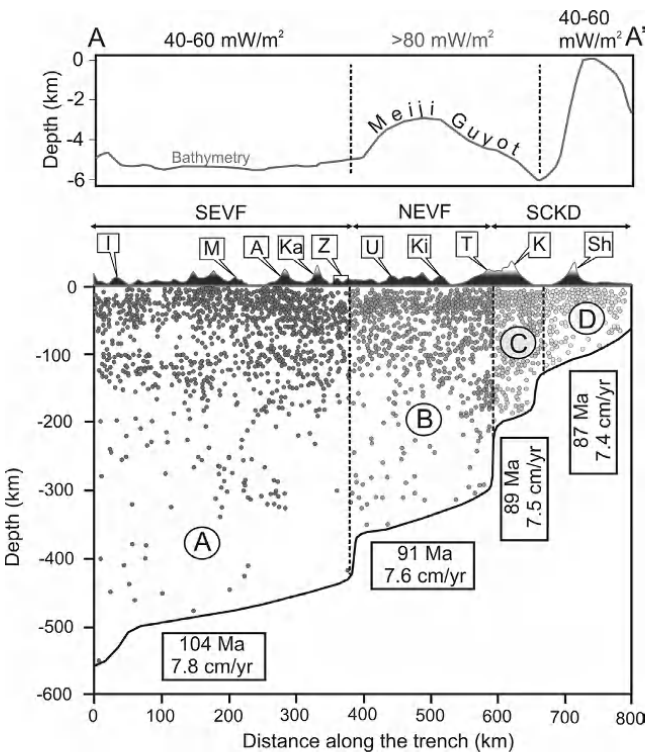

Figure 2. Projection of the seismicity along A-A' cross-section in Fig.1. The seismicity shallows continuously with four important discontinuities from ~500 km in southern Kamchatka (A) to ~100 km at the Kamchatka-Aleutians junction (D). On top, the bathymetry profile show the Meiji Guyot seamount that corresponds to high heat flow values > 80 mW/m^2. Other symbols are from *Fig.1.*

$$\eta = \eta_0 \cdot e^{\left[\frac{E_a}{R \cdot T_0}\cdot\left(\frac{T_0}{T}-1\right)\right]},$$

where the activation energy E_a corresponds to diffusion creep of olivine (*Karato and Wu, 1993*). Other parameters used are: η- mantle wedge viscosity (Pa s), η_0- mantle wedge viscosity at the potential temperature T_0 (10^{20} Pa s), T_0- mantle wedge potential temperature (1,450ºC), *R*- universal gas constant (8.31451 J/mol ºK) and *T*-temperature (ºC).

A finite-element grid extends from 25 km seaward of the Kamchatka trench up to 600 km landward of it, and consists of 15,000 triangular elements with an average resolution of 4 km. The model consists of five thermo-stratigraphic units as follows: upper continental crust, lower continental crust, oceanic lithosphere, oceanic sediments, and mantle wedge. The thermal parameters used for each layer are from: *Peacock and Wang, 1999; Smith et al., 1979; Vacquier et al., 1967.* The continental crust in Kamchatka is divided into two layers: the upper crust (0–15 km depth) and lower crust (15–35 km depth). These depths are consistent with values inferred by *Gorbatov et al. (2000)* and *Levin et al. (2002)*. The shape and dip of the subducting plate beneath the active volcanic arc are constrained by earthquake hypocenter distribution.

The upper and lower boundaries are maintained at constant temperatures of 0ºC at surface and of 1,450ºC in the asthenosphere, respectively. The left, landward vertical boundary condition is defined by a 22.5ºC/km thermal gradient for the continental crust. Below the 35 km depth, the left boundary condition is represented by a low thermal gradi-

Figure 4. Cross-section of the tomographic model (*Gorbatov et al. 2001*). Noticed the low velocity mantle plume which rises from ~900 km depth and is deflected at the surface toward the Kamchatka trench. On top, the Meiji Guyot seamount is assumed to be the bathymetric response of this upwelling. The lower left inset show the position of the B-B'-B" cross-section.

ent of 10ºC/km down to the depth of 100 km. Beneath 100 km depth no horizontal conductive heat flow is specified. Underneath the Moho (35 km), for the left boundary, corresponding to the mantle wedge, zero traction is assumed. At the intersection between the subducted slab and the left boundary, the velocity of the subducting slab is assumed. The right, seaward boundary condition is a one-dimensional geotherm calculated for the oceanic plate using the GDH1 model of *Stein and Stein (1992)*. We use plate age data and heat flow observation to obtain the oceanic geotherm using GDH1 (Fig. 3). In terms of displacement, the velocity of the oceanic plate is taken with respect to the continental plate. Thus the convergence rate of 7.4–7.8 cm/year between the PAC and Kamchatka is used *(Renkin and Sclater, 1988)*. A long-term continuous sliding between the subducting and continental plates along the thrust fault should produce frictional heating. We introduce shear heating along the thrust fault from the trench down to the contact between the slab and continental Moho (35 km). Below Moho and above the slab we assume the presence of serpentine, which exhibits rate-strengthening, stable-sliding and aseismic behavior *(Reinen, 2000)* and therefore decouples the subducting and overriding plates (*Manea et al., 2004*). We introduced in our models a small degree of volumetric frictional heating ($Q_{sh}=\tau v/w$) where τ represents the shear stress (τ=15 MPa on average, using *Byerlee, 1978*), v is the convergence rate and w is the thickness of the oceanic crust involved in friction (200 m).

Due to the deep seismicity (>500 km) for the southernmost profile we include the spinel – olivine exotermic phase transition at 410 km depth. The heat of exotermic reaction is L=90 kJ/kg. For c_p=1 kJ/Kg K, the heat released by this phase change increases the temperature inside la subducting slab by 90 K ($\Delta T=L/c_p$) (*Turcotte and Schubert, 2001*). We use the simplified phase diagram of olivine-spinel transition from *Schmeling et al. (1999)* (~0.3 °C/MPa for T > 600 °C) with a sharp transition from olivine to spinel.

For the northernmost profile, located just beneath the Schveliuch group, we simulate the slab edge exposure to the hot mantle by constructing a series of 2D thermal models parallel with the Kamchatka trench at distances of 50, 100, 150, 200 and 250 km, and normal to the main thermal model. The boundary conditions for these models are: 0°C and 1450°C for the top and bottom, oceanic upper mantle geotherm for the northern boundary and the temperature profile through the main thermal model as southern boundary.

MODELING RESULTS

Thermal Models

The thermal models that correspond to the four subregions are presented in *Fig. 5* through *Fig. 8*. Using as main constraints the geological age (~104 Ma), convergence rate (~7.8 cm/yr) and slab geometry (~55° slab dip), the first thermal model located beneath SEVF shows that the T_{cr} is not consistent with the maxim extent of intraslab seismicity (450–500 km) (*Fig. 5A*). Alternatively, just introducing the exotermic olivine-spinel phase transition, a good agreement between the seismicity and the cut-off temperature is obtained (*Fig. 5B*).

The second area, where the seismicity shallows to 300–350 km beneath NEVF, shows little variation in age, convergence rate and slab geometry (91 Ma; 7.6 cm/yr; ~53° slab dip) compared with the neighbor region to the south. The thermal structure, and correspondingly the 650°C cut-off temperature, calculated with the above parameters, is not consistent with the maximum depth of seismicity (*Fig. 6A*). The mantle plume located just in front of this area seems to be the source for the anomalous heat flow above 80 mW/m^2. We argue that this high value of heat flow reflects a plate thermal rejuvenation, therefore the old 91 Ma Pacific plate behaves like a 35 Ma young oceanic plate (*Fig. 3*). Introducing this rejuvenation effect in our thermal models, we obtain a good fit between the seismicity and cut-off temperature of 650°C (*Fig. 6B*).

The third region corresponds to the inland jump of the volcanic front and an abrupt change of the seismicity from 300–350 km to ~200 km. The little variation in plate age and convergence rate compared with the previous area is not sufficient to explain such shallow seismicity. Even the oceanic plate rejuvenation cannot explain the maximum depth extent of ~200 km of the intraslab seismicity (*Fig. 7*). We discuss later an alternative mechanism which can explain this unusual shallow seismicity, inland shift of the volcanic front

Figure 5. Thermal models for the southernmost study area located beneath SEVF (area A in *Fig. 1*). Notice the resonable fit (T_{cr}=650°C) with the maximum depth of seismicity when we introduced the olivine-spinel phase transition (B) compared with the model without this phase transition (A). The dashed line represent the 650°C isotherm, assumed here to be the transition from brittle to ductile behavior, and therefore a good indicator of the maximum depth of intraslab seismicity. The thick black line shows the surface of the subducting slab. Also, the thick dashed horizontal line represents the Moho (35 km depth).

Figure 6. Thermal models beneath NEVF (area B in *Fig. 1*). Observe the good fit (T_{cr}=650°C) with the maximum depth of seismicity when we introduced the plate rejuvenation from the mantle plume (B) compared with the model without such rejuvenation (A). Other symbols are like in *Fig. 5*.

and the extraordinary lava production of the Klyuchevskoy volcanic cluster.

The last section is located above the Aleutian - Kamchatka junction, where actually the edge of the Pacific slab comes in direct contact with the hot upper mantle material. Here, the seismicity shallows even more (~100 km) than in the previous area, despite the little variation in the slab age and convergence rate. Also the subducting slab dips at only ~33° beneath Schveluch volcano, compared with ~52° just to the south below the neighbor Kluchevskoy volcanic cluster. The modeled thermal structure (*Tcr*=650°C) shows no correlation with the shallow seismicity (*Fig. 8*). Nevertheless, despite this disagreement, the models which include the slab edge heating due to exposure to hot upper mantle, predict temperature above 750°C at ~70 km depth, enough to melt the oceanic basaltic crust (*Fig. 9*).

Slab Dehydration and Melting

The estimated variation of wt% H_2O content with depth along the subducting Pacific slab is presented in *Fig. 10*. We use both, computed *(Kerrick and Connolly, 2001*) and experimentally determined phase diagrams (*Schmidt and Poli, 1998; Hacker et al., 2003*). Using the computed phase diagram and weight percentages of H_2O in metabasalt of *Kerrick and Connolly, 2001* (Fig. 10A), we see that complete and intense (~2.5 wt%) dehydration occur at depths of ~70–80 km just beneath Kluchevskoy group (KCKD) and NEVF when the slab reheating in taking into account. Experimentally phase relationships for basalt at water-saturated conditions of *Schmidt and Poli (1998)* (Fig.10B) show also intense dehydration (>3 wt%) beneath Kluchevskoy group (KCKD) and NEVF at depths of 70–90 km. On the other hand, the cold slab beneath SEVF retains ~0.5–1.0 wt% at greater depths (>100 km). Completely and progressively metamorphic devolatilization occurs beneath SCKD, where the subducted oceanic crust loses all its hydrous phases at shallower depths of ~60 km (Fig. 10A, B). Using the phase diagram of *Schmidt and Poli (1998),* the sequence of hydrous phases in the basaltic crust beneath SEVF, NEVF and KCKD might be as follows. At blueschist conditions, assemblages are composed of lawsonite-glaucophane-chlorite-garnet-clinopyroxene-quartz (field G in *Fig. 10B*). Increasing the temperature lawsonite reacts to zoizite (field F). At depths greater than ~70 km, amphiboles decompose forming chloritoid at T<650°C (field D). Then, blueschist transforms to lawsonite-eclogite (fields A and B) and amphibole-eclogite to zoisite-eclogite (fields C and D). At 90–100 km depth, zoisite breakdown produces an almost dry eclogite for T>700°C (field O). Beneath SCKD, the mineral assemblages are composed by lawsonite-amphibole-chlorite-albite-quartz at low (*p,T*) (field K in *Fig. 10B*). With increasing temperature lawsonite reacts with epidote (fields I and

Figure 7. Thermal models beneath the Kluchevskoy volcanic cluster (area C in *Fig. 1*). High heat flow measurements just in front of this area suggest the Pacific slab is still rejuvenated by the mantle plume (see *Fig. 1*). However, the shallow seismicity (~200 km) cannot be explained by our model (A) even when we introduced slab rejuvenation (B). We argue that in this area slab detachment or necking might be the cause for such unusual shallow seismicity. Other symbols are like in *Fig. 5*.

J) and chlorite decomposes forming garnet (fields E and H). Other minor hydrous phase in the basaltic crust is represented by paragonite which forms at 20–30 km (at 500–650°C) and decomposes at ~70 km (500–700°C< fields E and F). At greater depths (>60–70 km), the oceanic crust beneath SCKD might undergo melting.

Figure 8. Thermal model beneath the northernmost active volcano, Shieveluch (area D in *Fig. 1*). The same as in the previous model, the shallow seismicity (~100 km) cannot be explained by our models, even if the subducting slab has a shallower dip angle of only ~33° compared with ~55° further to the south. Probably slab detachment suggested by *Levin et al. (2002)* might be a reasonable explanation.

We also use the phase diagram for basalt of *Hacker et al. (2003)* (*Fig. 10C*) to reveal the metamorphic sequences in the subducted oceanic crust. Here the metamorphic structure is as follows: from jadeite-lawsonite-blueschist-amphibole-talc facies, the oceanic crust enters at a depth of ~65 km into the stability field of zoisite-amphibole-eclogite with strong dehydration (2.7–3 % H_2O released). Another pulse of strong dehydration (0.3–2.3 % H_2O released) occurs at 90–100 km depth, when the oceanic crust dehydrates completely and transforms into eclogite. Rigorous dehydration occurs through these phase changes, in total more than 5 wt% H_2O being released into the overlying mantle up to a depth of ~100 km. This process would hydrate and lower the melting point of the mantle wedge peridotite. In fact, using wet peridotite *solidus* from *Wyllie (1979)* (~1050°C at 100 km depth), the thermal models predict melting of mantle peridotite beneath the volcanic front only if the mantle wedge is subject to fluid hydration from the oceanic crust. Interestingly, the cold slab surface geotherm beneath SEVF does not intersect *solidus*, predicting no oceanic crust melting (*Fig. 10C*). On the other hand, the oceanic crust beneath NEVF and KCKD seems to approach the

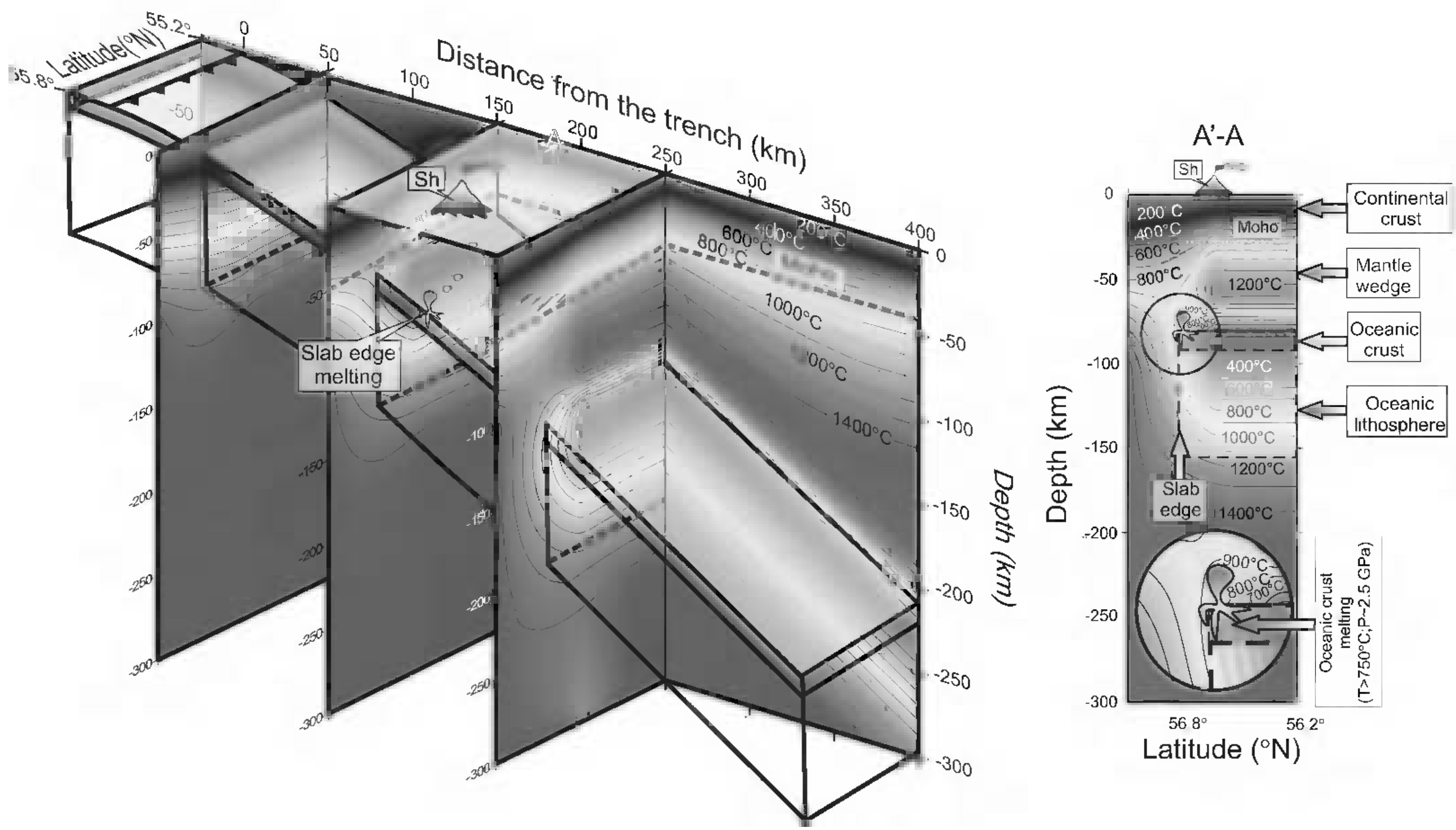

Figure 9. A – 3D Thermal structure of the subducting slab edge exposed to the hotter asthenosphere beneath Aleutian-Kamchatka junction. B – cross-section normal to the main model (*Fig. 8*) where the Shiveluch volcano is located (A-A'). Note the high temperature (T>750°C) at ~70 km which represent the suitable conditions for the oceanic crust to undergo melting and producing adakitic magmas recorded at Shieveluch.

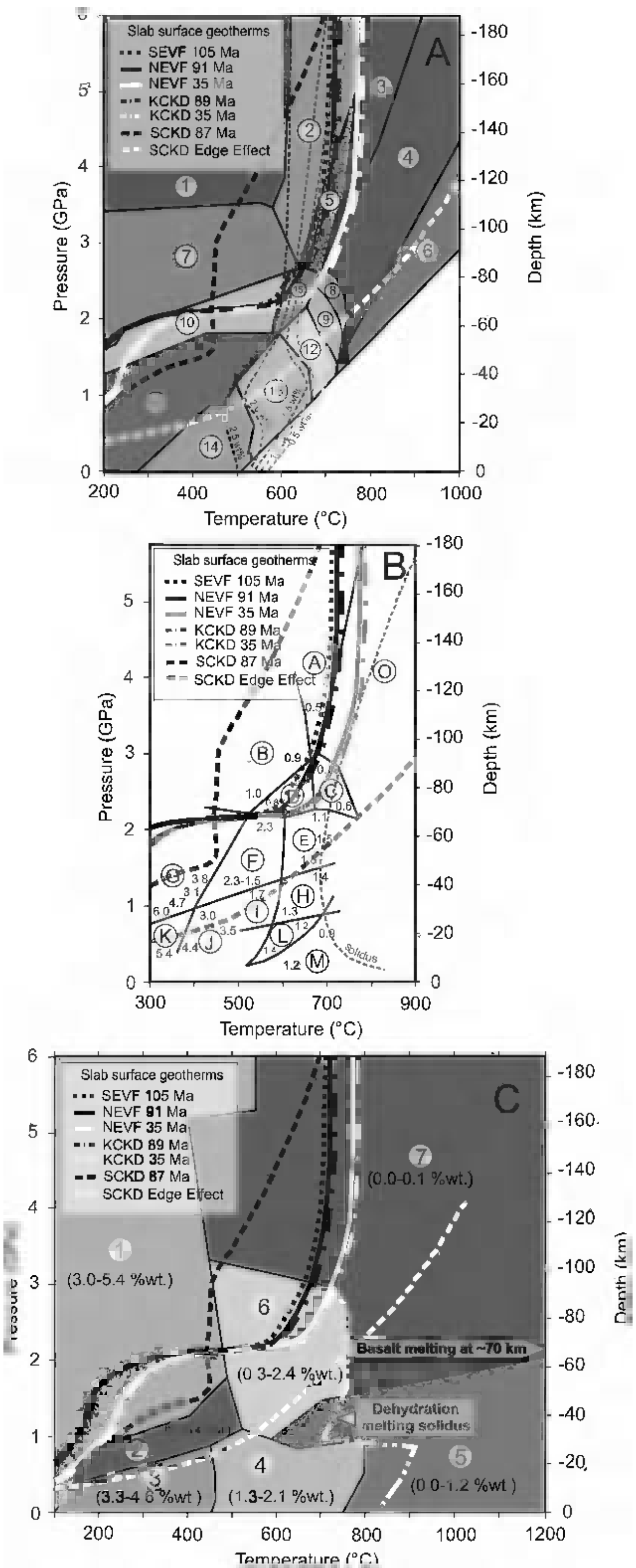

melting conditions at depth of 90–110 km (*Fig. 10 B,C*). Also, the model which incorporates the slab edge exposure to hotter mantle, clearly predicts oceanic crust melting (at ~70 km depth) just beneath Sheveluch, the northernmost active volcano in Kamchatka with a strong adakitic signature. Here, the oceanic crust shows a more complicated metamorphic structure: zeolite-prehnit-pumpellyite-actinolite-greenschist up to ~25 km depth, epidote-amphibolite up to ~35 km depth, then from zoisite-amphibole-eclogite the oceanic crust crosses the *solidus* at ~70 km depth and finally transforms into the anhydrous eclogite.

Figure 10. A. Simplified computed phase diagram from *Kerrick and Connolly (2001)*: 1 – Cpx-Mgs-Grt-Lws-Rt-Coe, 2 – Grt-Cpx-Mgs-F-Lws-Rt-Coe, 3 – Cpx-Dol-Grt-Mgs-F-Rt-Coe, 4 – Cpx-Dol-Grt-F-Rt-Coe, 5 – F-Cpx-Dol-Grt-Mgs-Lws-Rt-Coe, 6 – Cpx-Gt-F-Rt-Coe, 7 – Cpx-Mgs-Gln-Lws-Rt-Coe, 8 – Cpx-Grt-Dol-F-Rt-Qtz-Ky, 9 – Cpx-Gln-Grt-Dol-F-Rt-Qtz-Ky, 10 – Gln-Cpx-Grt-Dol-Lws-Rt-Coe, 11 – Gln-Dol-Chl-Qtz-Spn-Czo-Arg, 12 – Cpx-Gln-Grt-Dol-F-Czo-Rt-Qtz-Ky, 13 - Cpx-Gln-Grt-Dol-F-Czo-Rt-Qtz, 14 - Chl-Pg-Gln-Dol-F-Spn-Czo-Cc, 15 - Gln-F-Cpx-Dol-Grt-Lws-Rt-Qtz. Phase abbreviations are: Chl=chlorite, Coe=coesite, Cpx=clinopyroxene, Czo=clinozoisite, Dol=dolomite, F=fuid, Gln=glaucophane, Grt=garnet, Ky=kyanite, Lws=lawsonite, Mgs =magnesite, Pg=paragonite, Qtz=quartz, Rt=rutile, Spn=sphene. Dashed thin lines represent the wight percentages of H_2O in metabasalt. Thick curves represent the slab geotherms from thermal models presented in *Fig. 5, 6,7, 8 and 9* (see insets for details). B. Experimentally determined mineral assemblages and maximum H_2O contents bound in hydrous phases in H_2O saturated MORB (*Schmidt and Poli, 1998*): O-gar–cpx–coes/stish, A-law–gar–cpx–coes/stish, B- law–cld–gar–cpx–qz/coes, C- zo–gar–cpx–qz/coes, D- zo–cld–gar–cpx–qz/coes, E- amph–zo/epi–para–gar–cpx–qz, F- amph–zo–chl–± para–gar–cpx–qz, G- law–chl–glauc–gar–cpx–qz, H- amph–epi–plag–gar–qz, I- amph–epi–chl–plag–gar–qz, J- amph–epi–chl–ab=plag–qz, K- law–amph–chl–ab–qz, L- epi–amph–plag–qz, M- amph–plag–qz. Thick curves represent the slab geotherms from thermal models presented in *Fig. 5,6,7,8 and 9* (see insets for details). C. Simplified phase diagram for the hydrous MORB (*Hacker et al., 2003*). Metamorphic facies: 1 – jadeite-lawsonite-blueschist-amphibole-talc (3.0-5.4 wt.% H_2O), 2 – lawsonite-epidote-blueschist-jadeite (3.1–5.4 wt.% H_2O), 3 – zeolite-prehnit-pumpellyite-actinolite-greenschist (3.3–4.6 wt.% H_2O), 4 – epidote-amphibolite (1.3–2.1 wt.% H_2O), 5 – garnet-amphibolite-granulite (0.0-1.2 wt.% H_2O), 6 – zoisite-amphibole-eclogite (0.3–2.4 wt.% H_2O), 7 – eclogite-coesite-diamond (0.0-0.1 wt.% H_2O). The slab geotherms for most of the volcanic active Kamchatka (EVF and SCKD beneath Kluchevskoy) show strong slab dehydration (~2.5–5 wt.%) from 60 km down to ~100 km. The model which includes slab edge effect at the Aleutian-Kamchatka junction shows appropriate conditions for the oceanic crust to undergo melting (at 60–70 km depth) and producing adakitic magmas recorded at Shieveluch.

DISCUSSION AND CONCLUSIONS

The slab and mantle wedge thermal structure beneath Kamchatka is studied using numerical models of temperature developed using the numerical scheme of *Manea et al. (2005)*. The thermal models are constrained by slab age, convergence rate, slab geometry, maximum depth of intraslab seismicity and offshore heat flow measurements. Four different areas are considered along Kamchatka, based on their difference in seismicity, volcanic front geometry and geochemical spatial variation (*Fig. 1*). Although the convergence rate and slab age varies slightly along the trench, the maximum depth of seismicity shows some considerable discontinuities. The seismicity shallows continuously from south (~500 km) to the north (~100 km) with a series of four main discontinuities (*Fig. 2*). The thermal structure beneath SEVF (section A in *Fig. 1*) which includes the exothermic olivine-spinel phase transformation shows a good correlation of maximal depth of slab seismicity with the cutoff temperature inside the subducting slab of 650°C. Pacific plate rejuvenation from ~91 Ma to ~35 Ma due to the mantle plume impact, provides a hotter thermal structure beneath NEVF (section B in *Fig. 1*) and a good fit of seismicity (300–350 km) with the position of the cutoff isotherm. Also, these models show strong slab dehydration (~5% wt H_2O) down to depth of ~100 km. Such influx of fluids lowers the mantle peridotite melting point. Our models predict temperature in the mantle wedge beneath the entire EVF well above 1100°C, sufficient to melt hydrated peridotite, and therefore explaining the calcalkaline arc magmatism in this area.

The last two sections (C and D in *Fig. 1*) show a much shallower slab seismicity, from ~200 km beneath the Kluchevskoy volcanic cluster to ~100 km under the Sheveluch area. The slab thermal rejuvenation is not enough to explain such shallow seismicity. A recent study of *Levin et al. (2002)* revealed the seismic structure beneath northern Kamchatka, revealing that significant portions of the subducting slab detached and sank into the mantle. The active volcanism in the Kluchevskoy area lies just above the slab edge itself located at ~200 km depth, therefore explaining probably the lack of seismicity at greater depths. The ~200 km width of the Meiji Guyot seamount covers both the NEVF and SCKD, but only the Kluchevskoy group shows an unusual high magma output. The slab edge lofting proposed by *Levin et al. (2002)* seems to explain better the extreme volcanic activity at the Kluchevskoy cluster than an increased hydrous-fluid input from Meiji Guyot seamount proposed by *Davies (2002)*. The northernmost active volcano in Kamchatka, the Sheveluch volcano, stands also above the slab edge where the Pacific plate ends and come in contact with the hotter upper mantle. The thermal models which integrate the lateral edge heating show that at a depth of ~70 km, just below Sheveluch, the temperature inside the oceanic crust exceeds 750°C (*Fig. 9*) and therefore the *solidus* for basalt (*Fig. 10*). This result is in good agreement with the strong adakitic signature recorded in magmas erupted from Sheveluch. This is not the only area across Kamchatka where adakites were identified. Recently, *Maxim Portnyagin (personal communication 2005*) identified adakitic signatures in Late Neogene dikes in central Kamchatka (Zhupanova area, see *Fig.1*). Such adakitic signatures are in good agreement with the thermal structure beneath NEVF which takes into account the oceanic plate reheating due to Meiji plume impact, where the slab surface geotherm approaches the *solidus* at a depth of ~100 km (*Fig.10 B*).

Recent numerical studies show that two types of plumes might form in the mantle wedge (*Gerya et al., 2006*). Such dual-type plumes can explain the presence of different magmas in volcanic arcs: magmas with adakitic signatures and magmas from peridotitic source. Rates of plumes or buoyant diapirs propagation vary from 0.1 to 3 My (*Gerya et al., 2006; Manea et al., 2005)*, rates which are consistent with transfer times for fluids and slab melts from U-Th isotope measurements (*Hawkesworth et al., 1997*). Also, in these numerical models, intense melting of the mixed plumes (sediments and oceanic crust) occurs at low temperatures, therefore reconciling the cold slab geotherms beneath volcanic arc and the crust melting.

The shallow seismicity (~100 km) beneath Sheveluch cannot be explained by the edge effect alone, and probably the slab detachment revealed by *Levin et al. (2002)* seems to be the reasonable explanation. We did not incorporate the slab detachment into our thermal models, and future studies will focus on the effect of such strong discontinuity in the slab thermal structure and mantle flow around the slab edge. Recent numerical studies of thermomechanical modeling of slab detachment (*Gerya et al., 2004*) show that the rapid detachment process takes place over a few million years, and the detachment occurs at depths of ~100–400 km (*Gerya et al., 2004; Buiter et al., 2002; Houseman and Gubbins, 1997*). The detached fragments of the slab are 300–500°C colder than the surrounding asthenosphere, therefore they might be seen in tomographic images (*Levin et al., 2002*). On the surface, the expression of slab breakoff might be represented by rapid topographic changes (i.e. uplift) and increasing volcanic activities due to melting of subducted oceanic crust. The vigorous volcanic activity at Sheveluch fits well in such scenario.

We conclude that the main effect of the slab rejuvenation from a mantle plume impact is the reducing of maximum depth extent of intraslab seismicity. The slab edge exposure to the upper mantle produces the favorable *P-T* conditions for oceanic crust melting at shallow depths.

Acknowledgments. Very helpful comments and suggestions by Evgenii Gordeev, Yury Perepechko, Victor Sharapov, Maxim Portnyagin, and an anonymous reviewer were very important to improving this manuscript. This is contribution 9152 of the Division of Geological and Planetary Sciences, California Institute of Technology.

REFERENCES

Abers, G. A., van Keken, P. E., Kneller, E. A., Ferris, A., and Stachnik, J. C., 2006. The thermal structure of subduction zones constrained by seismic imaging: Implications for slab dehydration and wedge flow. *Earth Planet. Sci. Lett., 241, 387–397.*

Buiter, S. J. H., Govers, R., and Wortel, M. J. R., 2002. Two-dimensional simulations of surface deformation caused by slab detachment. *Tectonophysics, 354, 195–210.*

Byerlee, J. D., 1978. Friction of rocks. *Pure Applied Geophysics, v. 116, p. 615–626.*

Crough, S. T., 1978. Thermal origin of mid-plate hot-spot swells. *Geophys. J. R. Astronom. Soc., v.68, p. 133.*

Davies, J. H., 2002. Breaking plates. Nature, v. 418, p. 736–737.

Davies, J. H. and von Blanckenburg, 1995. Slab breakoff: a model of lithospheric detachment and its test in the magmatism and deformation of collisional orogens. *Earth Planet. Sci. Lett., 129, 85–102.*

DeMets, C., 1992. A test of present-day plate geometries for northeast Asia and Japan. *Journal of Geophysical Research, v.97, p. 17,627–17,635.*

Foulger, G. R., M. J. Pritchard, B. R. Julian, J. R. Evans, R. M. Allen, G. Nolet, W. J. Morgan, B. H. Bergsson, P. Erlendsson, S. Jakobsdottir, S. Ragnarsson, R. Stefansson and K. Vogfjord, 2001. Seismic tomography shows that upwelling beneath Iceland is confined to the upper mantle, *Geophys. J. Int, 146, 504–530.*

Gerya, T. V., Uken, R., Reinhardt, J., Watkeys, M. K., Maresch, W.V., and Clarke, B.M., 2003. Cold fingers in a hot magma: numerical modeling of diapers in the Bushveld Complex, South Africa. *Geology, 31, 753–756.*

Gerya, T. V. and Yuen, D. A., 2003a. Rayleigh-Taylor instabilities from hydration and melting propel 'cold plumes' at subduction zones. *Earth and Planetary Science Letters, v. 212, p. 47–62.*

Gerya, T. V., Yuen, D. A., and Maresch, W. V., 2004. Thermomechanical modeling of slab detachment. *Earth Planet. Sci. Lett., 226, 101–116.*

Gerya, T.V., Connolly, J. A. D., Yuen, D. A., Gorczyk, W., and Capel, A. M., 2006. Seismic implications of mantle wedge plumes. *Phys. Earth Planet. Int. 16 pg.*

Gorbatov, A., and Kostoglodov, V., 1997. Maximum depth of seismicity and thermal parameter of the subducting slab: general empirical relation and its application. *Tectonophysics, v. 277, p. 165–187.*

Gorbatov, A., Kostoglodov, V., Suárez, G., and Gordeev, E., 1997. Seismicity and structure of the Kamchatka subduction zone. *Journal of Geophysical Research, v. 102, no. B8, p, 17,883–17,898.*

Gorbatov, A., Widiyantoro, A., Fukao, Y., and Gordeev, E., 2000. Signature of remnant slabs in the North Pacific from *P*-wave tomography. *Geophysical Journal International, v. 142, p. 27–36.*

Gorbatov, A., Fukao, Y., Widiyantoro, A., and Gordeev, E., 2001. Seismic evidence for a mantle plume oceanwards of the Kamchatka-Aleutian trench junction. *Geophysical Journal International, v. 146, p. 282–288.*

Goto, K., Hamaguchi, H., and Suzuchi, Z., 1985. Earthquake generating stresses in the descending slab. In: Kobayashi, K., Sacks, I.S. (Eds.), Structures and Processes in the Subduction Zones. *Tectonophysics, 112, 111–128.*

Hacker, B. R., Abers, G. A., and Peacock, S. M., 2003. Subduction Factory 1. Theoretical mineralogy, densities, seismic wave speeds, and H2O contents. *Journal of Geophysical Research, v. 108, 10.1029/2001JB001127.*

Hansen, U. and Yuen, D. A., 2000. Extended- Boussinesq thermal-chemical convection with moving heat sources and variable viscosity. *Earth and Planetary Science Letters 176, 401–411.*

Hawkesworth, C. J., Turner, S. P., McDermott, F., Peate, D. W., and van Calsteren, P, 1997. U-Th isotopes in arc magmas: Implications for element transfer from the subducted crust. *Science, 276, 551–555.*

Helmberger, D. V., Wen, L., Ding, X., 1998. Seismic evidence that the source of the Iceland hotspot lies at the core mantle boundary. *Nature 396 (6708), 251 255.*

Houseman, G. A. and Gubbins, D., 1997. Deformation of subducted oceanic lithosphere. *Geophys. J. Int., 131, 535–551.*

Karato, S., and Wu, P., 1993. Rheology of the upper mantle: a synthesis. *Science, v. 260, p. 771–778.*

Kepezhinskas, P., McDermott, F., Defant, M. J., et al., 1997. Trace element and Sr-Nd-Pb isotopic constraints on a three-component model of Kamchatka arc petrogenesis. *Geochim. Cosmochim. Acta, 61, 577–600.*

Kerrick, D. M. and Connolly, J. A. D., 2001. Metamorphic devolatilization of subducted oceanic metabasalts: implications for seismicity, arc magmatism and volatile recycling. *Earth Planet. Sci. Lett., 189, 19–29.*

Levin, V., Park, J., Brandon, M., Lees, J., Peyton, V., Gordeev, E., and Ozerov, A., 2002. Crust and upper mantle of Kamchatka from teleseismic receiver functions. *Tectonophysics, v. 358, p. 233–265.*

Manea, V. C., Manea, M., Kostoglodov, Currie, C. A., and Sewell, G., 2004. Thermal Structure, Coupling and Metamorphism in the Mexican Subduction Zone beneath Guerrero. *Geophysical Journal International, v.158, p. 775–784 doi: 10.1111/j.1365 - 246X.2004.02325.x.*

Manea, V.C., Manea, M., Kostoglodov, V., Sewell, G., 2005. Thermo-mechanical model of the mantle wedge in Central Mexican subduction zone and a blob tracing approach for the magma transport. *Physics of the Earth and Planetary Interiors, v.149, p. 165–186. doi: 10.1016/JPEPI2004.08.024*

Montelli, R., Nolet, G., Dahlen, F., Masters, G., Engdahl, E., and Hung, S., 2004. Finite-frequency tomography reveals a variety of mantle plumes. *Science, 303, 338–343.*

Moore, W. B., Schubert, G., and Tackley, P., 1998. Three-dimensional simulations of plume-lithosphere interaction at Hawaiian Swell. *Science, 279, 1008.*

Nagihara, S., Lister, C. R. B., Sclater, J. G., 1996. Reheating of old oceanic lithosphere: Deductions from observations. *Earth Planet. Sci. Lett., 139, 91.*

Nataf, H. C., Vandecar, J., 1993. Seismological detection of a mantle plume. *Nature 364 (6433), 115 120.*

Ozerov, A. Y., 2000. The evolution of high-alumina basalts of the Klyuchevskoy volcano, Kamchatka, Russia, based on microprobe analysis of mineral inclusions. *J. Volcanol. Geotherm. Res., 95.*

Park, J., V. Levin, M. T. Brandon, J. M. Lees, V. Peyton, E. Gordeev, and A. Ozerov, 2002. A dangling slab, amplified arc volcanism, mantle flow and seismic anisotropy near the Kamchatka plate corner. *in Plate Boundary Zones*, Stein, S., and Freymueller, J. (eds.), *AGU Geodynamics Series No. 30, AGU, Washington DC, p. 295–324.*

Peacock, S. M., and Wang, K., 1999. Sesimic consequences of warm versus cool subduction metamorphism: Examples from southwest and northeast Japan. *Science, v. 286, p. 937–939.*

Perfit, M. R., Gust, D. A., Bence, A. E., Arculus, R. J., and Taylor, S. R., 1980. Chemical characteristics of island-arc basalts: implications from mantle sources. *Chem. Geol., v.30, p. 227–256.*

Portnyagin, M., Hoernle, K., Avdeiko, G., Hauff, F., Werner, R., Bindeman, I., Uspensky, V., Garbe-Schönberg, D., 2005. Transition from arc to oceanic magmatism at the Kamchatka –Aleutians junction. *Geology, v.33, no. 1, p. 25–28.*

Reinen, L. A., 2000. Slip styles in a spring-slider model with a laboratory-derived constitutive law for serpentinite. *Geophys. Res. Lett., 27, 2037–2040.*

Renkin, M. L., and Sclater, J. G., 1988. Depth and age in the North Pacific. *Journal of Geophysical Research, v. 93, B4, p. 2919–2935.*

Rogers, R. D., Karason, H., and van der Hilst, R.D., 2002. Epeirogenic uplift above a detached slab in northern Central America. *Geology, 30, 1031–1034.*

Schmeling, H., Monz, R., and Rubie, D. C., 1999. The influence of olivine metastability on the dynamics of subduction. *Earth Planet. Sci. Lett., 165, 55–66.*

Schmidt, M. and Poli, S., 1998. Experimentally based water budgets for dehydrating slabs and consequences for arc magma generation. *Earth Planet. Sci. Lett.,, v. 163, p. 361–379.*

Shen, Y., Solomon , S., Bjarnason, I., and Nolet, G., 2002. Seismic evidence for a tilted mantle plume and north-south mantle flow beneath Iceland. *Earth Planet. Sci. Lett., 197, 261–272.*

Smirnov, Ya. B., and Sugrobov, V. M., 1979. Terrestrial heat flow in the Kurile-Kamchatka and Aleutian provinces. I. Heat flow and tectonics (in Russian). *Volcanology and Seismology, v. 1, p. 59–73.*

Smirnov, Ya. B., and Sugrobov, V. M., 1980a. Terrestrial heat flow in the Kurile-Kamchatka and Aleutian provinces. II. The map of measured and background heat flow (in Russian). *Volcanology and Seismology, v. 1, p. 16–31.*

Smirnov, Ya. B., and Sugrobov, V. M., 1980b. Terrestrial heat flow in the Kurile-Kamchatka and Aleutian provinces. III. Assessments of temperature at depth and thickness of the lithosphere (in Russian). *Volcanology and Seismology, v. 1, p. 16–31.*

Smith, D. L., Nuckels, C. E., Jones, R. L. and Cook, G. A., 1979. Distribution of heat flow and radioactive heat generation in northern México. *Journal of Geophysical Research, v. 84, p. 2371–2379.*

Spencer, J. E., 1994. A numerical assessment of slab strength during high- and low-angle subduction and implications for Laramide orogenesis. *J. Geophys. Res. 99, 9227–9236.*

Stein, C. A and Stein, S., 1992. A model for the global variations in oceanic depth and heat flow with lithospheric age. *Nature, 359, 123–129.*

Stein, C. A., 1995. Heat flow of the Earth. *Global Earth Physics, A Handbook of Physical Constants, AGU Reference Shelf 1.*

Tan, E., Gurnis, M., and Han, L., 2002. Slabs in the lower mantle and their modulation of plume formation. *Geochem. Geophys. Geosys., 3, 1067, doi:10.1029/2001GC000238.*

Turcotte, D. L., and Schubert, G., 2002. Geodynamics, 2nd edition, *Cambridge University Press, New York.*

Vacquier, V., Sclater, J. G., and Corry, C. E., 1967. Studies of the thermal state of Earth: The 21st paper: Heat-flow, eastern Pacific. *Bulletin of Earthquake Research Institute, v. 45, p. 375–393.*

Von Blanckenburg, F. and Davies, J. H., 1995. Slab breakoff: a model for syncollisional magmatism and tectonics in the Alps. *Tectonics, 14,120–131.*

Wortel, M. J. R. and Spakman, W., 2000. Subduction and slab detachment in the Mediterranean-Carpathian region. *Science, 290, 1910–1917.*

Wyllie, P. J., 1979. Magmas and volatile components. *American Mineralogy, v. 654, p. 469–500.*

Xu, P. F., Sun, R. M., Liu, F. T., Wang, Q., Cong, B., 2000. Seismic tomography showing subduction and slab breakoff of the Yangtze block beneath the Dabie-Sulu orogenic belt. *Chin. Sci. Bull. 45, 70–74.*

Yogodzinski, G. M., Lees, J. M., Churikova, T. G., Dorendorf, F., Wöerner, G., and Volynets, O. N., 2002. Geochemical evindence for the melting of subducting oceanic lithosphere at plate edges. Nature, 409, 500–504.

Zhao, D., 2004. Global tomographic images of mantle plumes and subducting slabs: insight into deep Earth dynamics. *Phys. Earth Planet. Int., 146, 3–34.*

Magnetic and Seismic Constraints on the Crustal Thermal Structure Beneath the Kamchatka Peninsula

Akiko Tanaka

Planning Headquarters, AIST, On temporary leave from Geological Survey of Japan, AIST

Spectral analysis of aeromagnetic anomalies is applied to estimate the centroid depths of crustal magnetic sources, Zo, beneath the Kamchatka Peninsula, to constrain on crustal thermal regime. One of another potential proxies to assess the crustal thermal structure is the deeper depth limit of seismogenic zone, D_{90}, the depth above that 90 % of earthquakes occur. Estimated Zo agree generally with D_{90} and are consistent with tectonic regime. This indicates that Zo is closely relating to the isotherm and assessing reasonable average thermal regime.

INTRODUCTION

Kamchatka Peninsula lies along an area called the Pacific "Ring of Fire", a zone of frequent earthquakes and volcanic eruptions that stretches in a series of arcs from New Zealand, through Indonesia, Philippines, Japan, Kuril Islands and Kamchatka Peninsula, across the Pacific Ocean via the Aleutian Islands, and down the west coast of the Americas (Plate 1 (a)). Tectonics regime of Kamchatka peninsula is dominated by the subduction zone where Pacific and North Pacific plates converge at a rate of about 80 mm yr^{-1} [DeMets *et al.*, 1990]. The volcanic front is trench-parallel and corresponds to a depth of the slab of about 120 to 140 km (Plate 1 (b)).

Better constraints on the thermal structure of lithosphere are required to understand continental evolution and to monitor these active crustal deformations and activities of earthquakes and volcanoes. Heat flow data provides critical information to help constrain crustal thermal structure. However, these data distributions remain restricted unfortunately, and there is a few heat flow data especially on-land area beneath the Kamthatka Peninsula (Plate 1 (b)). To compensate the shortage of data, the determination of the depth of magnetic sources based on spectrum analysis of magnetic anomaly data [e.g., Bhattacharyya and Leu, 1975a; Spector and Grant, 1970] can be used to estimate regional thermal structures. The obtained basal depth of the magnetic sources is assumed to be the Curie point depth, i.e. the depth at which magnetite passes from a ferromagnetic to paramagnetic state under the effect of increasing temperature, which for most geophysical purposes means they changes from magnetic to non-magnetic state. This analysis is still controversial and the Curie point depth does not necessarily represent an isotherm, 580ºC for pure magnetite. However, the Curie point depths may reflect the broad average temperature and they have been used to estimate the thermal structure in various regions [e.g., Bhattacharyya and Leu, 1975b; Shuey *et al.*, 1977; Connard *et al.*, 1983; Blakely, 1988; Okubo *et al.*, 1989; Tanaka *et al.*, 1999]. Previous studies suggested that there was an inverse correlation between estimated Curie depths and heat-flow measurements as expected [in east and southeast Asia [Tanaka *et al.*, 1999]; in southern California [Ross *et al.*, 2006]].

Another proxy of the crustal thermal structure is the depth distribution of earthquakes. The maximum depth of seismogenic zone is interpreted either as the brittle-ductile transition, the transition from brittle faulting to plastic flow in the continental crust, or as the transition in the frictional sliding process from unstable to stable sliding. This transition depth depends on many factors, such as rock composition, temperature, strain rate, and fluid pressure. Previous studies [e.g., Sibson, 1982, 1984] suggested that this transition is strongly temperature-dependent and the onset of dislocation creep in quartz which is assumed to control this transition

Volcanism and Subduction: The Kamchatka Region
Geophysical Monograph Series 172

10.1029/172GM08

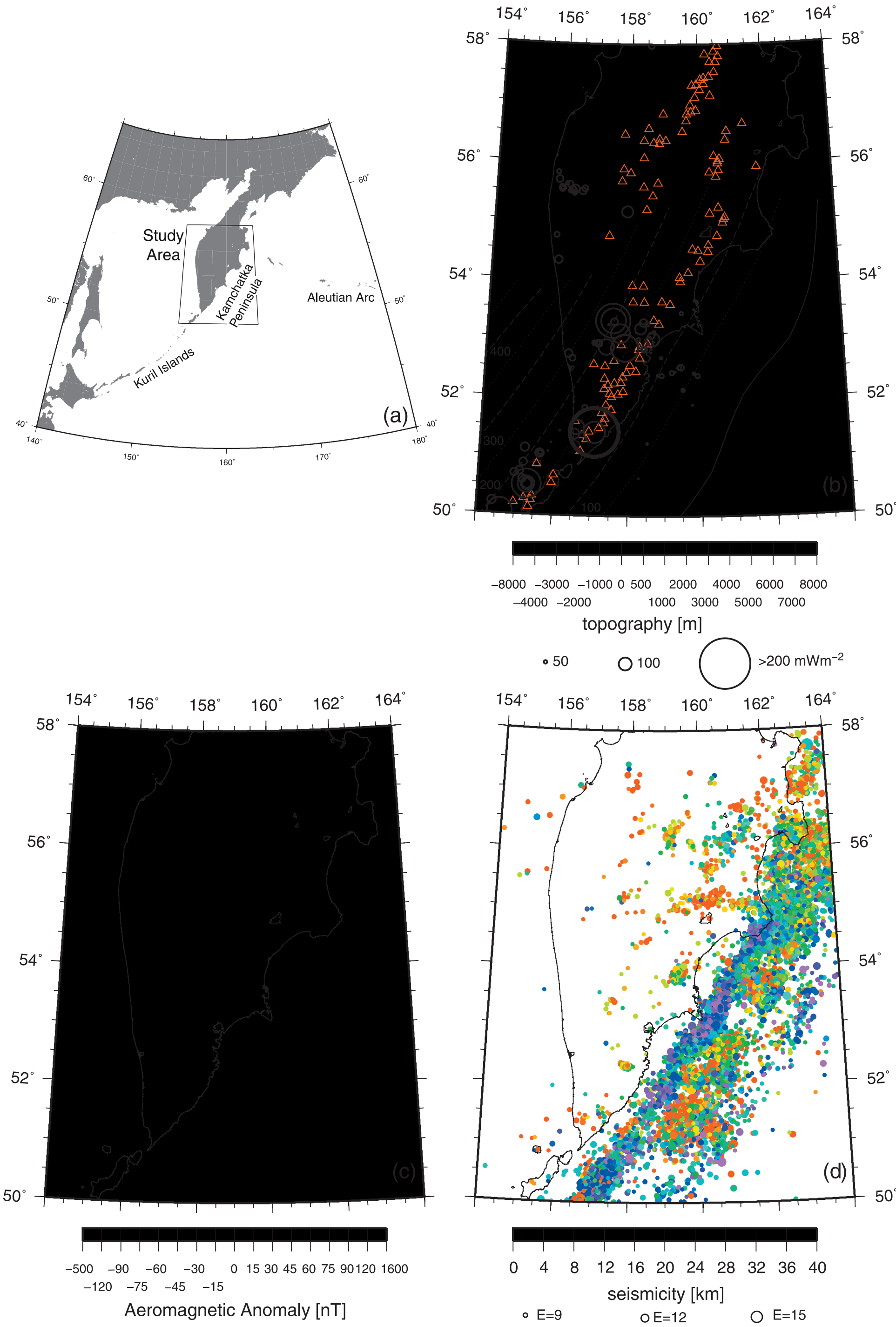

Plate 1. (a) Index map of a part of the Pacific "Ring of Fire". The study area is outlined by the solid line. (b) Heat flow distribution [Yamano, 2004] beneath the Kamchatka peninsula superimposed on the topographic relief map. Size of the circle denotes magnitude of heat flow. Red triangles denote volcanoes with known or inferred Holocene eruptions [Smithsonian Institution, Global Volcanism Program, http://www.volcano.si.edu/]. Solid line shows the location of trench. Dashed and dotted limes are at 50 km intervals in depth of subducting slabs [Gudmundsson and Sambridge, 1998]. (c) Magnetic anomaly map [NGDC, 1997]. (d) Hypocentral distributions for the period from 1962 to 2004 [EMSD]. The diameter of each circle is proportional to the energy class.

is about 300°C. Spatial variations in the maximum depth of seismicity have been correlated with crustal temperature for regions with abundant heat flow data and reliable seismicity [e.g., in southern California [Williams *et al.*, 2001]; in Japan [Tanaka, 2004]].

In this paper, two kinds of proxies to constrain the crustal thermal structure, the centroid of magnetic sources and the lower depth limit of seismogenic zone, are estimated. The correlation between two and its correspondence with tectonic regime indicates that these values are useful to delineate regional crustal thermal structure.

ESTIMATES OF THE CENTROID DEPTH OF MAGNETIC SOURCES

Most previous methods to estimate the basal depth of the magnetic sources are based on calculations of the top bound and the centroid of magnetic sources [Connard *et al.*, 1973; Blakely, 1988, Okubo *et al.*, 1988; Tanaka *et al.*, 1999]. We used the same method to estimate the depth of magnetic sources as described by Tanaka *et al.* [1999]. The method is based on that of Spector and Grant [1970], which assumes a uniform distribution of parameters for an ensemble of magnetized blocks. We could estimate the top bound and the centroid of magnetic source, Zt and Zo respectively, by fitting a straight line through the high-wavenumber and low-wavenumber parts of the radially averaged spectrum of ln $(\Phi_{\Delta T}\,(|\,k\,|)^{1/2})$ and ln $((\Phi_{\Delta T}\,(|\,k\,|)^{1/2})\,/\,|\,k\,|)$, where $\Phi_{\Delta T}$ is the power-density spectra of the total-field anomaly and k is the wavenumber. The basal depth of the magnetic sources, Zb, is calculated from 2 Zo − Zt. Note that only the centroid of magnetic source is estimated because of the data quality as mentioned after this section.

The size of each sub-region was decided considering the complexity of tectonic province, which cause the changes in thermal structure. The region with deep Zo might affect the neighbouring region with shallow Zo, and vice verse. For example, deeper magnetic sources cause magnetic anomalies with longer wavelengths and lower amplitudes, which makes them difficult to distinguish from anomalies caused by shallower sources. To avoid controversies that would interfere between different tectonic provinces, it is required to choose the size and area of each region. On the other hand, the size and spatial resolution of Zo are in a trade-off relationship. We used here the uniform grids of overlapping subregions because this method is reconnaissance technique for estimating the regional crustal thermal structure.

Spector and Grant [1970] concluded that the theoretical possibility of determining Zo and Zt from total magnetic field intensity data, provided that the data of each sub-region cover an area of at least 200 × 200 km, with a maximum grid spacing of 1 km. We estimated the depth of magnetic sources using the magnetic anomaly data in the Former Soviet Union, provided by the National Geophysical Data Center (NGDC) [http://www.ngdc.noaa.gov/seg/fliers/se-0102.shtml] (Plate 1 (c)). These data are based on a mosaic series of 18 sheets at 1:2.5 million scale showing the residual magnetic intensity over the land mass of the U.S.S.R published by the Ministry of Geology of the U.S.S.R. in 1974. The original one-arc-minute digital data contains errors, which were removed by reprocessing of the digitized contour data by NGDC. This map reveals several magnetic features including clusters of high amplitude magnetic anomalies coincide with Quaternary volcanic regions. In this paper, we used this gridded magnetic anomaly datasets in square windows of 2.1° × 2.1°. The two grids overlap each other by about half to increase resolution.

We carefully select the frequency range using the following criteria. For Zo, the spectrum peak shifts towards smaller wavenumbers with increasing the average thickness of magnetic sources. This spectrum peak is specified as the lower limit of wavenumber. The upper limit of wavenumber is specified by both the average thickness of magnetic sources and the truncation error associated with neglecting higher order terms. Tanaka and Ishikawa [2005] suggested that the upper limit of wavenumber for Zo is specified as 0.055 km^{-1}, provided that the average thickness of magnetic sources is about 20 km and the error in the approximation is less than 5 %. This assumption is under possible and reasonable condition. Considering this upper limit, wavenumber range was selected using the correlation coefficient of the least-square linear fit and the change in the trend of the spectrum with increasing wavenumbers. We calculated Zo within this frequency limits as shown in Figure 1. For Zt, the situation is rather complicated, because the power spectrum involves in more noises at shorter wavelengths. By considering the criteria of Spector and Grant [1970], the correct straight-line portion of the spectrum is so ambiguous with noises using grid-spacing of 3 minute as used here. Therefore, only Zo is estimated.

The bottom depth of magnetic sources, Zb, determined from the spectral analysis of residual magnetic anomalies is generally interpreted as the level of the Curie point isotherm, and is useful to estimate the regional thermal structure. However, in this study Zo is estimated and used instead of Zb. Although we cannot prove the justification of it, on the basis of previous results we believe that Zo reflect regional crustal thermal structure to a certain extent. This presumptive evidence is that Zt have almost the same values of 5 km and Zo vary widely with different tectonics settings, so that the basal depths of magnetic sources show wide ranges, all over in East and Southeast Asia [Tanaka *et al.*, 1999].

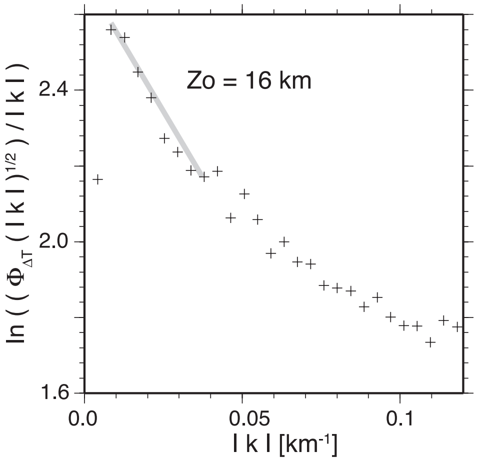

Figure 1. Examples of spectra for the estimation of the centroid (Zo) of magnetic sources using the two-dimensional magnetic anomaly data in a region of extending from 157°E, 52°N to 159.1°E, 54.1°N. Value of 16 km were obtained as Zo using the gradient of spectra defined as $\ln ((\Phi_{\Delta T} (| k |)^{1/2}) / | k |)$, where | k | is the wavenumber and $\Phi_{\Delta T}$ (| k |) is the spectrum of the magnetic anomaly.

As mentioned before Zb = 2 Zo − Zt and Zb is assumed to correspond to 580°C isotherm. This leads to that Zo may correspond to about 350°C isotherm using one-dimensional heat conductive transport model.

Zo VERSUS DEPTH LIMIT OF THE SEISMOGENIC ZONE

The deeper depth limit of seismogenic zone provides an additional constraint on crustal thermal regime. The catalogue of seismicity compiled by the Kamchatkan Experimental-Methodical Seismological Department (EMSD) was used for the hypocentral distribution (Plate 1 (d)). The data were obtained thorough the website http://www.emsd.iks.ru/seismicity-e.html. We selected crustal earthquakes with depth shallower than 40km, and used events larger than energy class (as defined by EMSD) 9.0 in a time interval from 1962 to 2004. The earthquake energy class, K, corresponds to the energy scale for classification using S-wave records of local earthquakes obtained at stations with short-period seismometers, where K = log E (energy in joules). Plate 1 (d) shows that the distribution of seismicity is not ubiquitous, but are concentrated in some restricted areas. Offshore high seismic activity along the eastern coast of the peninsula is related to seismic activity at trench. Poor seismic station coverage limits accuracy of depth estimates of this offshore seismicity. They may contain several outliers due to inaccurate locations or isolated seismic events generated by local anomalies. In order to avoid bias due to few outliers, the deeper depth limit of the seismogenic zone is defined as the depth above which 90 percent of the earthquakes occur, D_{90}. Plates 2 (a) and (b) show contour maps of Zo and D_{90}, which ranges from about 11 to 22 km and about 12 to 33 km, respectively. Note that each square window indicated in Plate 2 by solid line, has yields only one value of Zo or D_{90}. Both patterns are similar to one another, except for moderate values of Zo with deep D_{90} around the point of (54°N, 160°E) and southern part of the peninsula. Shallower Zo and D_{90} lie beneath volcanic areas. The southern part of the peninsula is characterized by higher heat flow (more than 300 mW/m^2) with scatters as shown in Plate 1 (b), suggesting that lithospheric temperatures at depth are higher than those of surrounding areas. Also, deep earthquakes within the slab may contaminate the crustal seismicity due to the poor coverage of land stations for off-shore events. These indicate that Zo may be reliable than D_{90} to delineate regional crustal thermal structure.

Figure 2 shows the deeper depth limit of the seismogenic zone, D_{90}, plotted against calculated centroids of magnetic sources, Zo. Good relationship between D_{90} and Zo, which gives us insight that Zo reflect average crustal thermal regime. Circles and crosses in Figure 2 show the distribution of Kamchatka and Japan [Tanaka and Ishikawa, 2005] respectively. The average values of Zo and D_{90} are about 16 and 25 km of Kamchatka, which are deeper than that of in and around Japan. Thermal structure under arcs may be mainly controlled by subduction processes, which are the cooling effect of subducting cold slab and heating effect of the induced flow in the mantle wedge. These effects depend on some subduction parameters, such as the depth of subducting slab beneath the volcanic front. This depth is about 120 to 140 km and 70 to

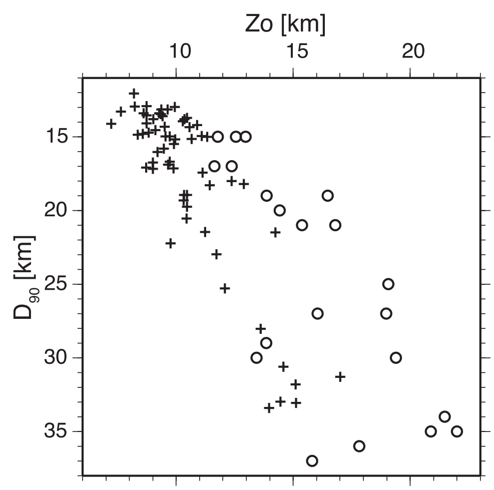

Figure 2. Plot of the depth to the centroid depth of magnetic sources (Zo) against the seismogenic layer thickness (D_{90}). Circles and crosses denote data from Kamchatka peninsula [this study] and Japan [Tanaka and Ishikawa, 2005], respectively.

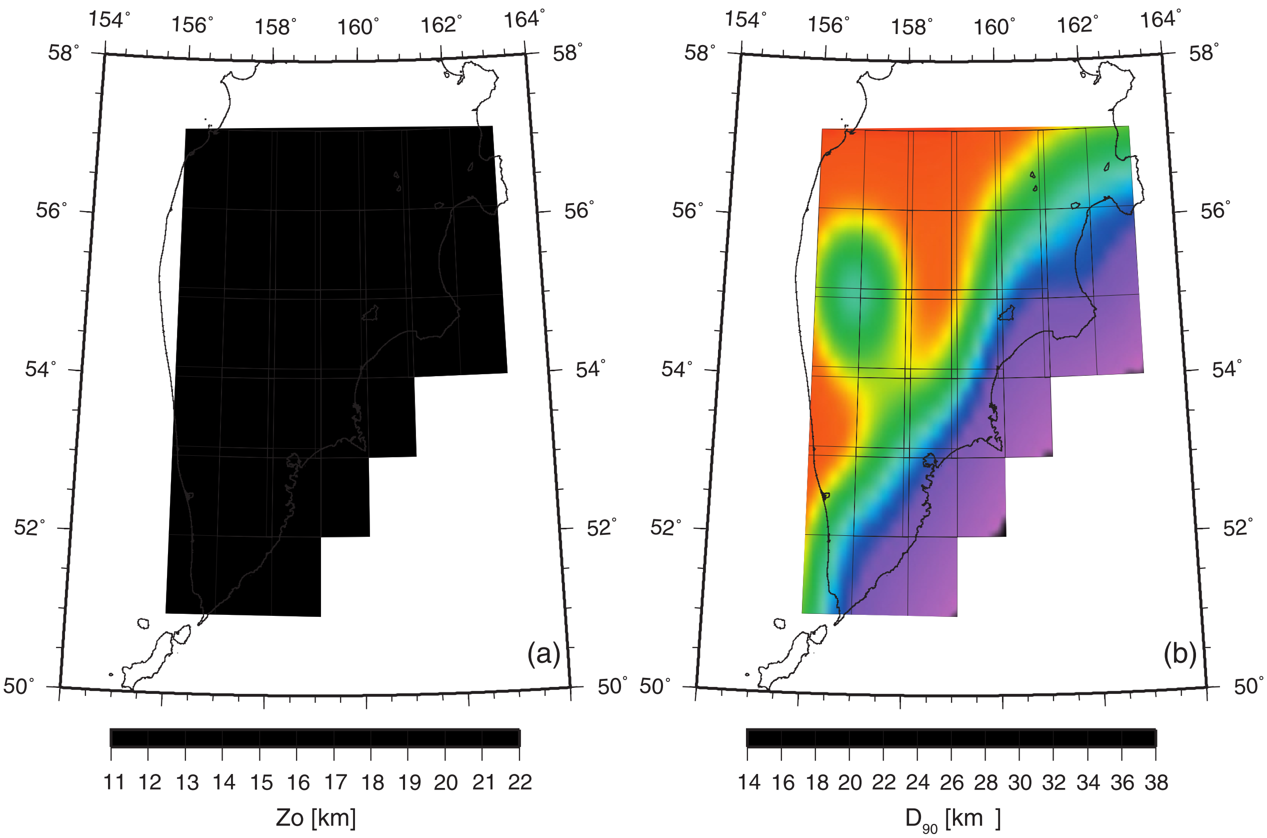

Plate 2. Contour maps of the depth to the centroid depth of magnetized source, Zo (a) and D_{90} (b). Each square represents the area, which uses to calculate Zo and D_{90}.

80 km, for Kamchatka and Japan respectively [Gudmundsson and Sambridge, 1998]. The difference in slab depths at target areas between Kamchatka and Japan may cause the deeper average values of Zo and D_{90}. There is a correlation between Zo and D_{90}, however there are variations of several exceptions around this correlation. One of the reasons to this discrepancy is that the uniform sub-regions we used in this paper might be insufficient large to capture longer wavelengths of magnetic anomalies associated with deeper Zo. The discrepancy might also be caused by data involves errors.

CONCLUSIONS

The complex and dynamical tectonics in the circum-Pacific plate boundaries gives some of the world's most active crustal deformations. Each region is quite diverse, and application of the "comparative subductoology" approach is required to better understand the processes and structures. The Kamchatka peninsula has one of the most active volcanic chains in the world and is a dynamic convergent margin. There are several observations and proxies to assess the crustal thermal structure, although heat flow measurements beneath the Kamthcka Peninsula are not widely distributed. We estimated thermal state within the crust from two different sources, the centroid depth of magnetic sources from magnetic anomaly data and the deeper depth limit of seisogenic layer from seismicity. Both show good correlations, which permits us to image the thermal structure beneath the Kamchatka peninsula, although they may contain some scatters and bias due to the different characteristics and errors. These values combined with multidisciplinary data provide a useful indicator of the crustal thermal structure in these regions.

Acknowledgments. The author wishes to thank two anonymous reviewers for their valuable comments. The author thanks Prof. John Eichelburger, the editor of this special issue, for his encouragement. The author would like to thank Takemi Ishihara for showing me about the magnetic anomaly data. Evgenii Gordeev and Yuzo Ishikawa kindly suggested me about the catalogue of seismicity. The author is grateful to Hannah Ross, who kindly sent her a preprint. The GMT mapping software [Wessel and Smith, 1998] was used to prepare figures.

REFERENCES

Bhattacharyya, B. K., and Leu, L.-K., Spectral analysis of gravity and magnetic anomalies due to two-dimensional structures, Geophysics, 40, 993–1013, 1975a.

Bhattacharyya, B. K., and Leu, L.-K., Analysis of magnetic anomalies over Yellowstone National Park: Mapping of Curie point isothermal surface for geothermal reconnaissance, J.Geophysics. Res., 80, 4461–4465, 1975b.

Blakely, R. J., Curie temperature isotherm analysis and tectonic implications of aeromagnetic data from Nevada, J.Geopgys.Res., 93, 11817–11832, 1988.

Connard, G., Couch, R., and Gemperle, M., Analysis of aeromagnetic measurements from the Cascade Range in central Oregon, Geophysics, 48, 376–390, 1983.

DeMets C., R. G. Gordon, D. F. Argus, and S. Stein, Current plate motions, Geophys. J. Int., 101, 425–478, 1990.

Gudmundsson, O. and M.Sambridge, A regionalized upper mantle (RUM) seismic model, J.Geopgys.Res., 103, 7121–7136, 1998.

Okubo, Y., Tsu, H., and Ogawa, K., Estimation of Curie point temperature and geothermal structure of island arcs of Japan, Tectonophysics, 159, 279–290, 1989.

Ross, H. E., Blakely, R. J., and Zoback, M. D., Testing the use of aeromagnetic data for the determination of Curie depth in California, Geophysics, 71, L51–l59, 2006.

Shuey, R. T., Schellinger, D. K., Tripp, A.C., and Alley, L. B., Curie depth determination from aeromagnetic spectra, Geophys. J.R.astr.Soc., 50, 75–101, 1977.

Sibson, R. H., Fault zone models, heat flow, and the depth distribution of earthquakes in the continental crust of the United States, Bull. Seismol. Soc. Am., 72, 151–163, 1982.

Sibson, R. H., Roughness at the base of the seismogenic zone: contributing factors, J. Geophys. Res., 89, 5791–5799, 1984.

Spector, A., and Grant, F.S., Statistical models for interpreting aeromagnetic data, Geophysics, 35, 293–302, 1970.

Stacey, F. D., and Banerjee, S. K., The physical principles of rock magnetism. Elsevier Scientific Publication company, 195 pp., 1974.

Tanaka, A., Okubo, Y., and Matsubayashi, O., Curie point depth based on spectrum analysis of the magnetic anomaly data in East and Southeast Asia, Tectonophysics, 306, 461–470, 1999.

Tanaka, A., Geothermal Gradient and Heat Flow Data in and around Japan (II): Crustal Thermal structure and its relationship to seismogenic layer, Earth, Planets and Space, 56, 1195–1199, 2004.

Tanaka, A., and Ishikawa, Y., Crustal Thermal Regime Inferred from Magnetic Anomaly Data and its Relationship to Seismogenic Layer Thickness: the Japanese Islands Case Study, Physics of the Earth and Planetary Interiors, 152, 257–266, 2005.

Wessel, P., and Smith, W. H. F., New version of the Generic Mapping Tools released, Eos Trans., AGU, 76 (33), 329, 1995.

Williams, C., Temperature and the seismic/aseismic transition: Observations from the 1992 Landers earthquake, Geophys.Res. Lett., 23, 2029–2032, 1996.

Yamano, M., Heat Flow Data in and around Japan, Digital Geoscience Map DGM P-5, Geological Survey of Japan, 2004.

Correlation of Kamchatka Lithosphere Velocity Anomalies With Subduction Processes

Irina Nizkous[1], Edi Kissling[2], Irina Sanina[1],
Larissa Gontovaya[3] and Valeria Levina[3]

Using arrival times of local earthquakes pressure and shear waves 3D P- and S-velocity model was calculated for the Kamchatka part of Kurile-Kamchtka arc. Maximum depth of the model is 200 km. For calculation 38 seismic stations and 6702 local earthquakes were used. Results of velocity reconstruction show depth and lateral heterogeneity of lithosphere of Kamchatka within mantle wedge and subduction zone, in particular there is pronounce low velocity layer at about 70–130 km depth beneath Eastern-Kamchatkan volcanic belt. Calculated 3D velocity structure is presented by horizontal and vertical cross-sections that illustrate clear correlation between main tectonic elements of the region with deep velocity anomalies. In this paper we show dependence between earthquake epicenter distribution and P- and S-wave velocity change in focal layer. In addition we present local study of velocity structure beneath Klyuchevskoy volcano group and correlation of velocity anomalies with some other geophysical measurements in this area.

INTRODUCTION

Kamchatka peninsula is located in the northern-western side of Pacific Ocean and it is the part of Kurile-Kamchatkan arc that comes across with Aleutian arc further to the north. This geographical position determines deep tectonic structure of the region. Main tectonic elements of Kamchatka are Sredinny Mountain Chain, Central Kamchatkan Depression, Eastern Kamchatkan Mountain Chain, hills of Kamchatka eastern peninsulas—Shipunsky, Kronotsky, Kamchatsky Mys, Kurile-Kamchatkan deep Trench and Central- and Eastern-Kamchatkan volcanic belts (Figure 1). It is assumed that the most part of the seismic activity in the region caused by the seismic focal zone (SFZ) processes [Fedotov, Gusev et al, 1985]. That is why it is very important to investigate deep structure of subduction zone and answer to the number of questions, for example, what part of SFZ cause volcanic activity and how processes of focal zone relate to deep tectonic activity of the region. Recently to answer these questions and reconstruct deep velocity structure many authors use seismic tomography method [Kuzin, 1974, Slavina et al, 1974, Pivovarova et al, 1983, Gorbatov et al, 1999, Gontovaya et al, 2003 and others]. But the results of studies are ambiguous and need additional analysis using various methods of calculations.

In this work we present results of 3D P-wave velocity model reconstruction of crust and upper mantle of the Eastern Kamchatka area using high-resolution tomography technique that gives new insight into subduction processes in this area. In addition we would like to show seismic tomography image of the P-wave velocity structure of the crust beneath famous Klyuchevskoy volcanic group, that located in the northern part of Kamchatka.

DATA

All computations based on the EMSD GS RAS catalogue including 32 years of data registering (1971–2003 years).

[1] Institute of Geospheres Dynamics RAS, Moscow, Russia.
[2] Institute of Geophysics EHT, Zurich, Switzerland.
[3] Institute of Volcanology and Seismology Far east Division of RAS, Petropavlovsk-Kamchatski, Russia.

Volcanism and Subduction: The Kamchatka Region
Geophysical Monograph Series 172

10.1029/172GM09

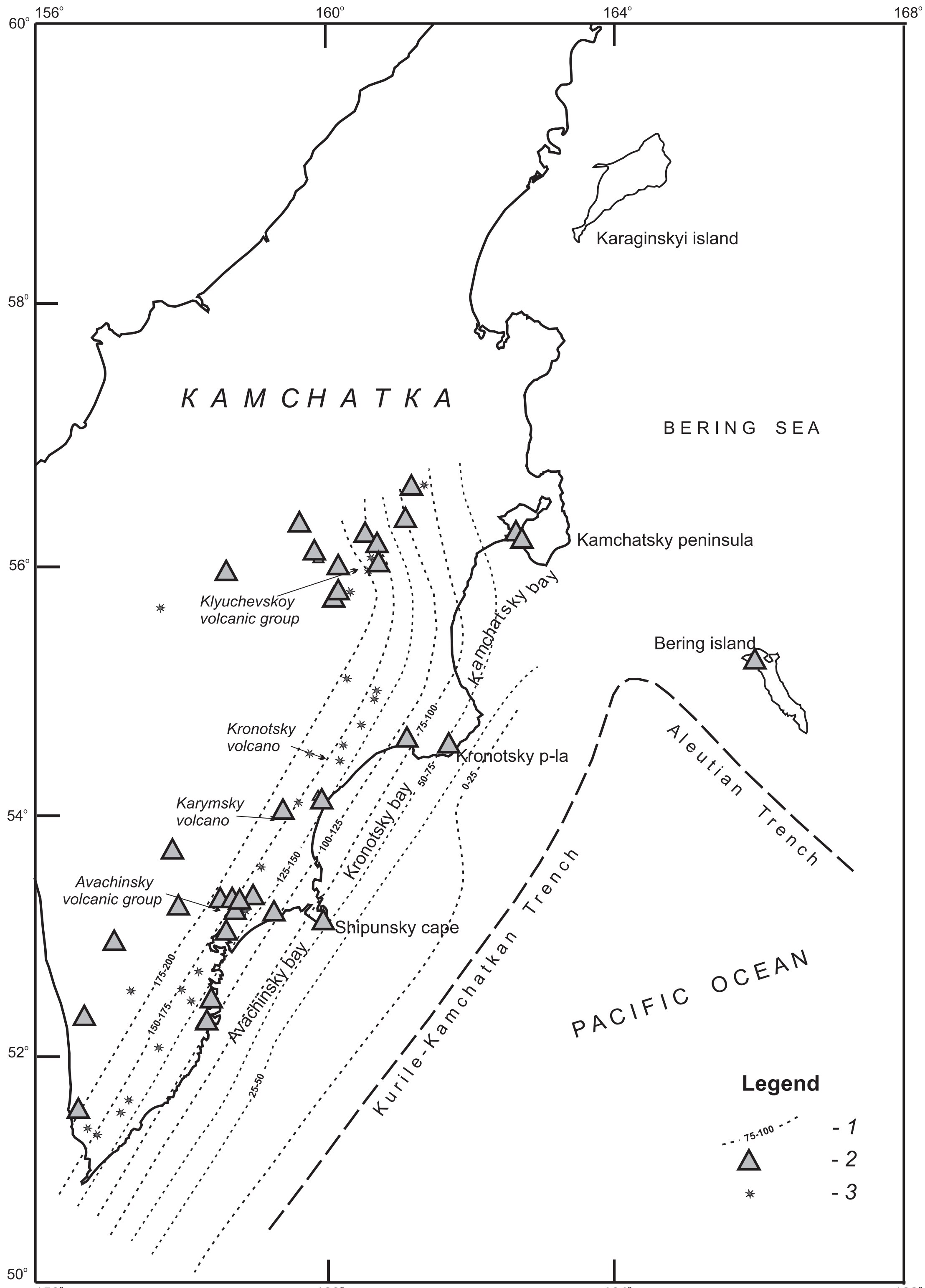

Figure 1. The map of Kamchatka peninsula. Legend: 1 – Pacific plate position according to [Fedotov, Gusev, at al, 1985]; 2 – seismic stations, 3 – volcanoes.

Catalogue includes arrival times of P- and S-waves from local earthquakes with magnitudes M³4 (or energy class Ks³8 in local earthquake classification). For data processing only IP, IS, EP and ES phases with corresponding arrival time errors (0.1 s for IP, 0.2 s for EP and IS, 0.3 s for ES) were used. In addition the following data selection criterion was applied: for each event there should be not less then 8 high quality P wave station records, azimuth gap should be less then 180 degrees and the arrival time error less then ±0.2 s. Finally for further computation we created 6702 events data set included 63515 P-phases and 32954 S-phases recorded by 38 seismic stations of Kamchatka regional network (Figure 1). According to a priori arrival time error estimation for selected data, the uncertainty is about 0.25 s.

COMPUTATION

1D minimum velocity model. Before 3D velocity model reconstruction we calculate new 1D velocity model for the region of study and perform several sensitivity and accuracy tests for given events and seismic stations position. With the help of VELEST software 1D minimum P- and S-wave velocity models [Kissling, 1988, Kissling et al, 1994] were computed based on the 600 earthquakes that in the best way meet the criterion of data selection mentioned above. As initial preliminary 1D velocity model we chose one that is currently used for Kamchatka routine hypocenter location [Kuzin, 1974]. Station delays were calculated relative to Petropavlovsk (PET) seismic station, which is the station of international seismic network (Figure 2).

Comparing initial Kuzin's and computed 1D minimum P- and S-wave velocity models we may conclude that minimum velocity model is characterized by higher velocities (Figure 3), fine layering, so there is no abrupt crust-mantle velocity change. Moho boundary corresponds to approximately 30 km depth and Vp is about 7.5 km/s. Station delays for P- and S-wave arrivals are consistent and reflect geological difference between Central Kamchatka depression (positive station delays) and eastern peninsulas of Kamchatka (negative station delays). Thus for further calculations and all hypocenters relocation we use new minimum 1D velocity model. Final position of the earthquakes was changed: epicenters moved by about ±10 km in the northern and northern-eastern direction and the events depth shift was about ±6 km.

3D velocity model. It is well known that accuracy and reliability of modeling result depend on parameterization of the medium, applied damping coefficients and overall resolution of the model. In our case damping coefficients were assessed with the help of synthetic data set. Parameterization of the medium were chosen in the way that model blocks should be relatively small and the distances corresponded to the arrival time error (having certain velocity value) should be about several percents of linear size of the cell. Based on this assumption and taking into account distribution of earthquakes and seismic stations for further calculations we use 30 km x 30 km x 20 km blocks. Resolution of the model were computed using real data set and quantitatively estimated by diagonal element of resolution matrix

$$R=[M^TM+ L]^{-1}M^TM \qquad (1)$$

M – model parameters matrix (velocities), L – damping parameters matrix. Such resolution assessment takes into

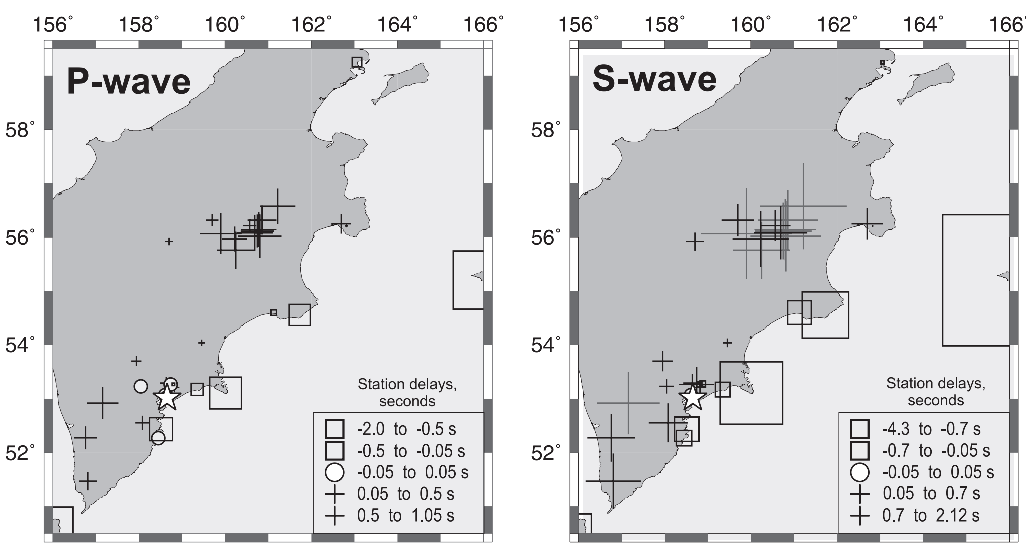

Figure 2. 1D minimum model station delays for P and S waves, calculated relative to Petropavlovsk (PET) seismic station.

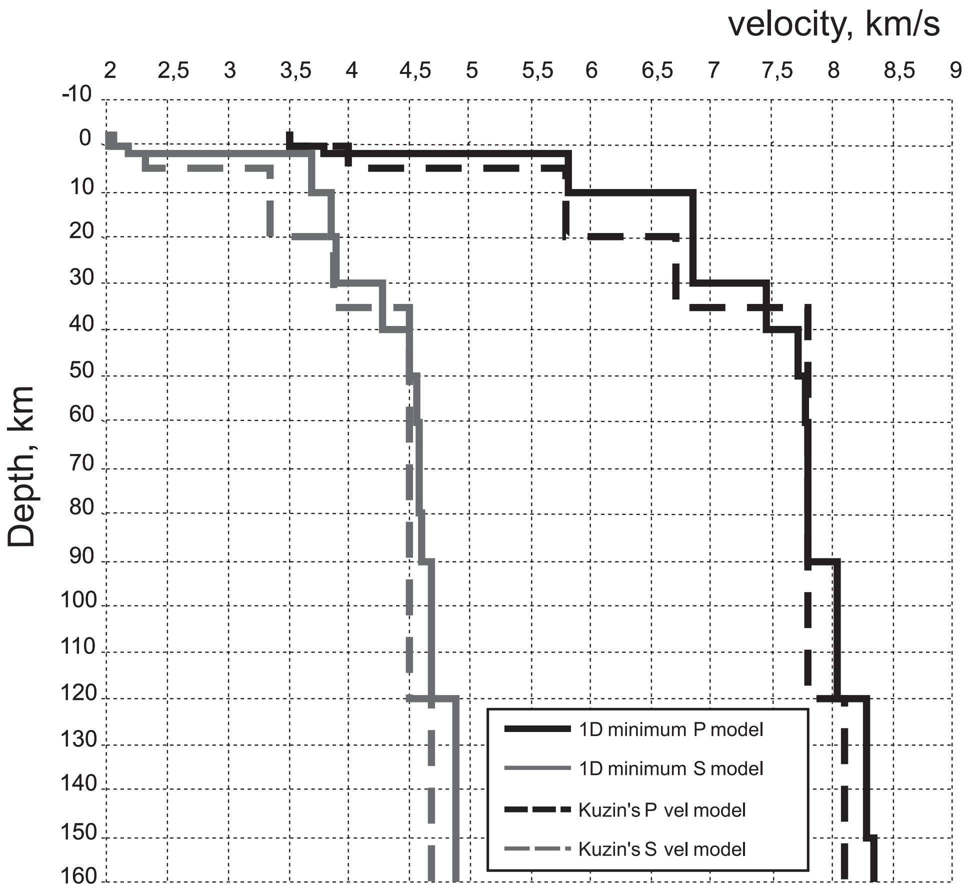

Figure 3. Comparison of 1D minimum velocity models for pressure (P) and shear (S) waves with Kuzin's [Kuzin, 1974] velocity model.

account ray trajectories and doesn't overestimate size of resolved areas.

Model resolution is shown in Figure 4 and demonstrates that starting from 20 km depth area of good and fair resolution is uniform and has maximum square. Deeper then 120 km good resolution region becomes smaller and shifts to the west toward Central Kamchatka Depression. Thus we expect to have the most reliable model results in 20–100 km depth interval. To increase model depth to 200–250 km over 700 deep earthquakes (with hypocenters located deeper then 150 km) were included in computations.

To model spatial P-wave velocity distribution for area of study we use SIMULPS14 software [Evans et al., 1994, Haslinger, Kissling, 2001]. After velocity structure calculation and earthquake relocation root mean square error decreased from 0.502 s to 0.472 s whereas event hypocenters shift was negligible - 0.3 km and 0.2 km in horizontal and vertical directions. This means that 1D minimum velocity model is correct because otherwise hypocenter drift would be essential.

Final 3D velocity distribution is presented in the form of vertical and horizontal cross sections that show percentage velocity change relative to 1D velocity model (Plates 1, 2).

RESULTS AND DISCUSSION

The first profile (Plate 1) crosses Eastern-Kamchatkan volcanic belt and further to the north Eastern Mountain Chain and Kamchatsky bay. At the latitude of Kronotsky peninsula SFZ turns to the north and at the same time Eastern-Kamchatka volcanic belt is shifted to the west [Fedotov et al, 1985]. Analyzing profile velocity structure we define the following layers Kamchatka lithosphere: low velocity crust beneath volcanic belt with –6% up to –10% P-wave velocity variation; high velocity layer in 30–70 km depth interval with low velocity zones located beneath central parts of eastern peninsulas of Kamchatka; low velocity and seismic activity layer – asthenosphere wedge – in 70–130 km depth interval, where Vp variation is about 2–3% that is most likely due to material decompression and high fluid concentration, that is proved by electroconductivity data [Moroz et al. 2004], so we assume that this zone is a magma source for active volcanoes of the Eastern Kamchatka volcanic belt; high velocity layer – Pacific plate – where Vp is about 8.0–8.5 km/s, the top of this layer is at 110–120 km depth where maximum representative earthquakes hypocenters located (with energy class $Ks^{3}10$). It should be noted that the position of Pacific lithosphere is changed in the area of Kurile-Kamchatkan and

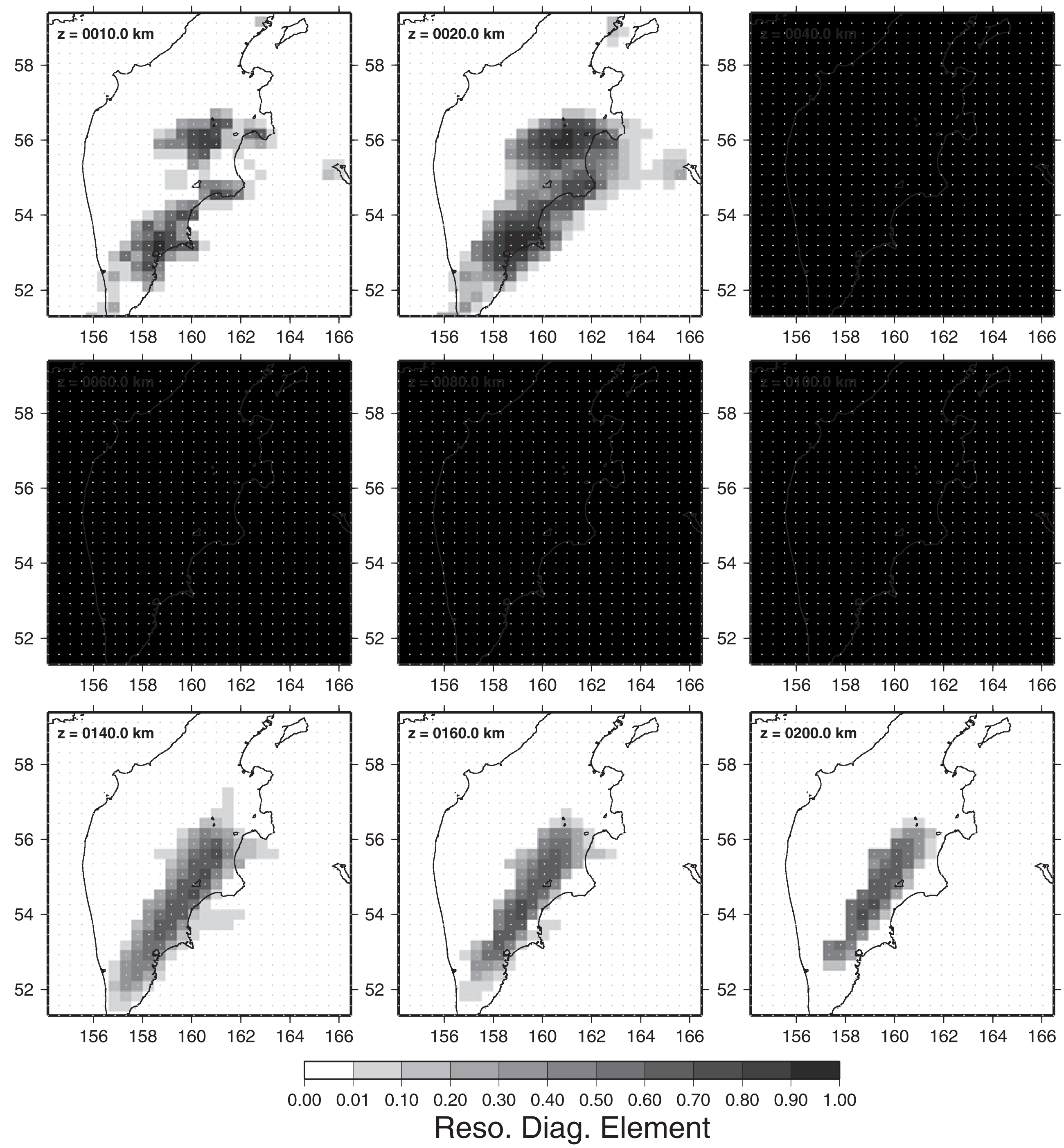

Figure 4. Assessment of spatial resolution for given location of stations and seismic events. Sections made at depths 10 km, 20 km, 40 km, 60 km, 80 km, 100 km, 140 km, 160 km and 200 km.

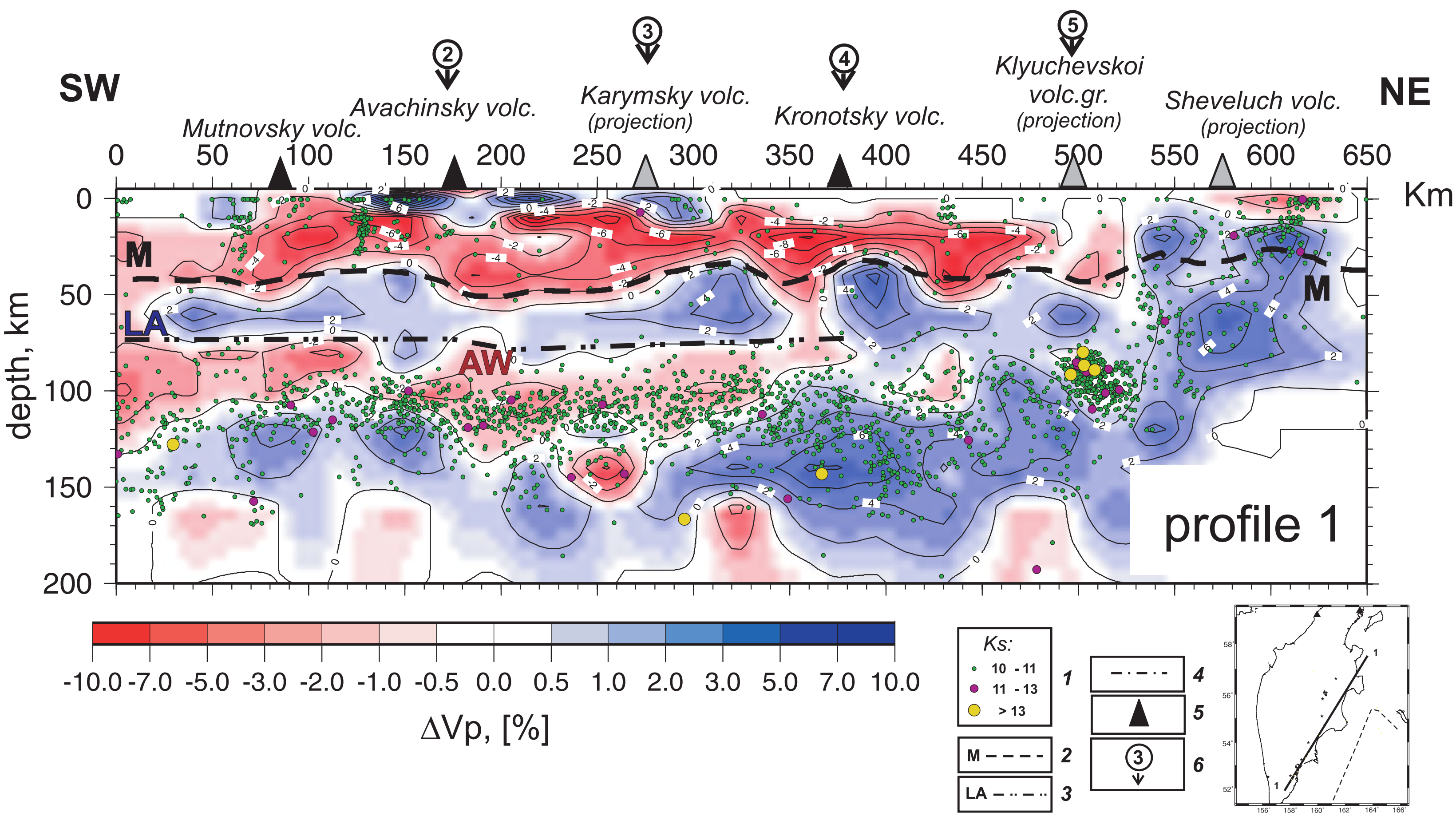

Plate 1. Profile 1 along the eastern coast of Kamchatka that crosses Eastern-Kamchatkan volcanic belt. Tomography results are shown in the way of relative percentage variation of P wave velocity. Legend: 1 – energy class of the earthquakes; 2 – Moho boundary (M); 3 – lithosphere-asthenosphere boundary (LA); 4 – proposed limits of the slab; 5 – volcanoes, 6 – positions of vertical profiles perpendicular to SFZ. AW – asthenosphere wedge.

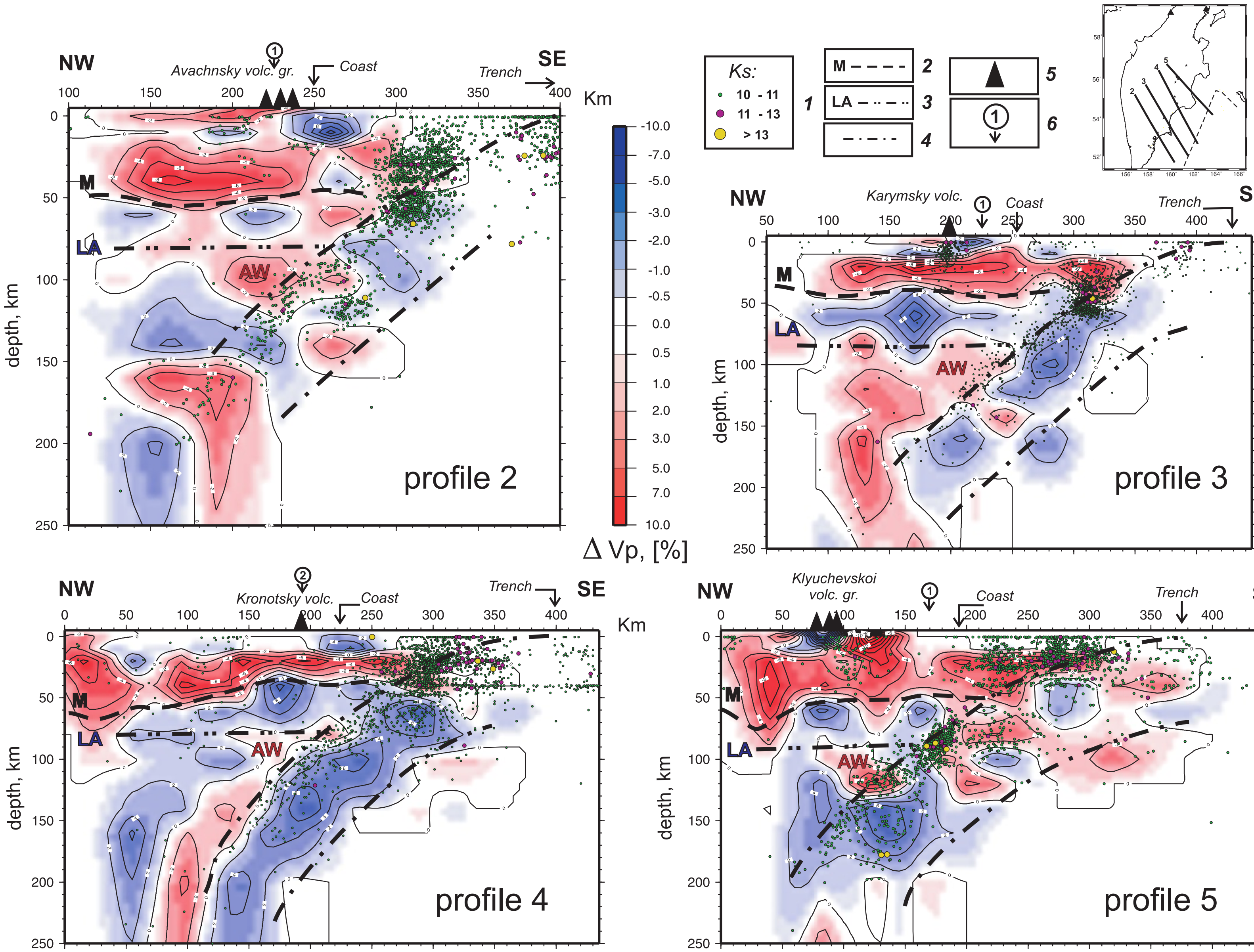

Plate 2. Seismic tomography results for vertical cross sections perpendicular SFZ: profile 2 crosses Avachinsky volcanic group, profile 3 – Karymsky volcano, profile 4 – Kronotsky volcano and profile 5 crosses Klyuchevskoy volcanic group. Legend: 1 – energy class of the earthquakes; 2 – Moho boundary (M); 3 – lithosphere-asthenosphere boundary (LA); 4 – proposed limits of the slab; 5 – volcanoes, 6 – positions of profile 1. AW – asthenosphere wedge.

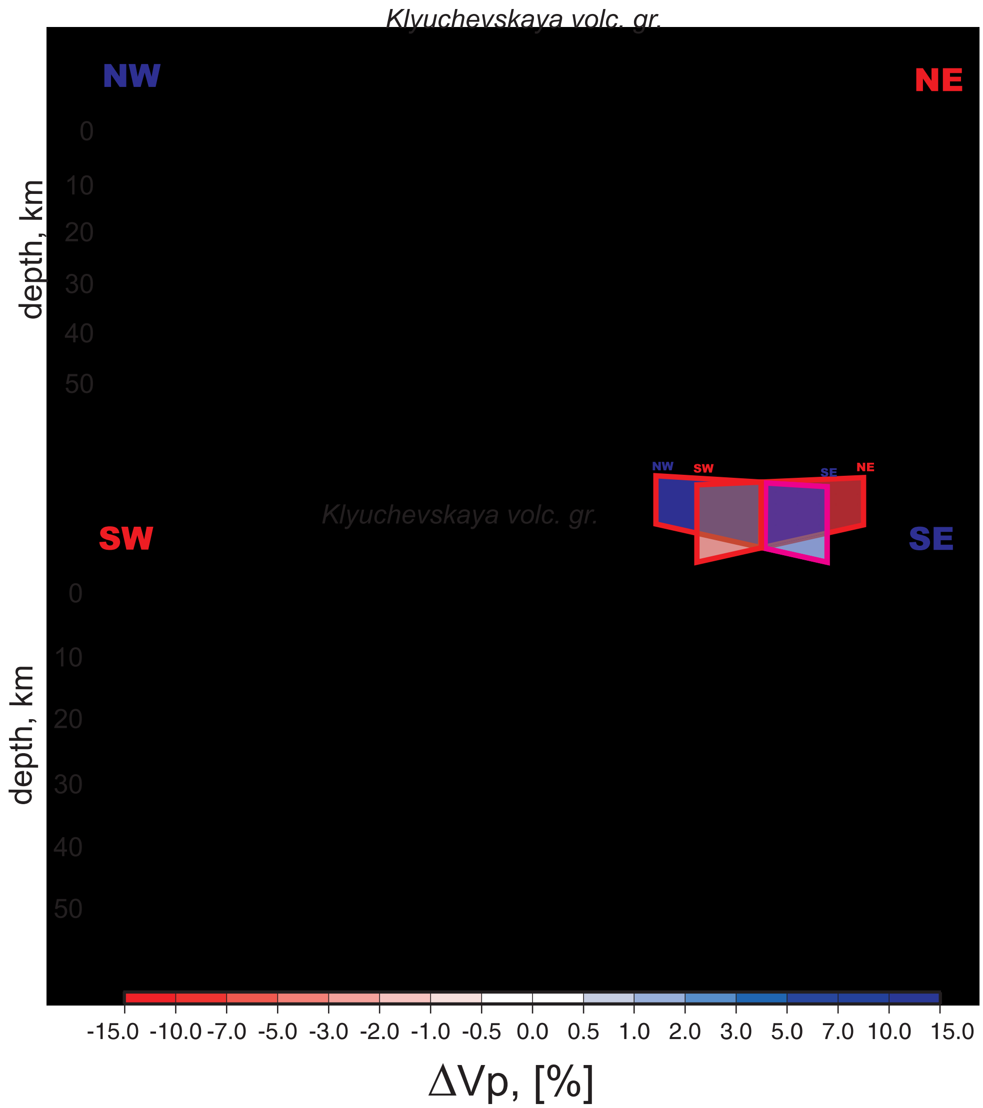

Plate 3. Seismic tomography modeling results for Klyuchevskoy volcanic group, profiles show relative percentage variation of P wave velocity. Green circles denote earthquakes (Ks>5).

Aleutian arc junction (around 500 km mark on the profile) the top of the plate rises up to 50–70 km depth therefore in the northern part of the cross section there are no low velocity crust and asthenosphere wedge.

Vertical profiles perpendicular to Kurile-Kamchatkan arc and SFZ are shown in Plate 2. There are several general characteristics that could be applied to each cross section. First of all P-wave velocity within Pacific plate area increases from southern to northern profiles and the maximum Vp variation (4%) as well as the highest seismicity level are beneath the Kronotsky peninsula area, where as was mentioned above volcanic belt turns to the west. Such high P- wave velocity of Pacific lithosphere most likely not due to material composition of the plate, but refers to increased stress corresponded to tectonic structure turn. Low velocity layer at 70–130 km depth spreads into SFZ area and causes inclination of the focal zone and visible displacement of lithosphere layers along this weakened region. At the same time on all the profiles one can see large deep (at 100–220 km depth) low velocity area with low seismic activity that located in the western part of Kamchatka and projected on the surface to the Central Kamchatka Depression region and possibly related to this tectonic element of Kamchatka.

Whereas the first three profiles characterized by similar velocity structure the last one has several essential differences. Profile characterized by increasing crust thickness and disappearing asthenosphere wedge and moreover it seems that Pacific lithosphere has gaps or so-called “slab windows” [Levin et al., 2002]. All these differences could be explained by specific position of the profile: it crosses Kamchatka bay fault zone where revealed low velocity area evidently indicates the dependency between decompressed upper mantle of the bay and Klyuchevskoy volcanic group. The latter is related to deep processes in the Kurile-Kamchatkan and Aleutian arcs junction area. The mechanism of this relation could be explained in different ways, based on various concepts of tectonic evolution of the region [Avdeiko et al, 2002; Seliverstov, 1998; Lees, Davaille, 1998; Levin et al., 2002]. In our study we assume material movement through “slab window” and Kamchatsky bay fault zone toward Klyuchevskoy volcanic group. In addition to regional tomography results we would like to present local high-resolution tomography image of crust velocity structure beneath Klyuchevskoy volcanic group (Plate 3). Revealed low velocity area in 25–35 km depth interval correlates with some other geophysical parameters variation, in particular with electroconductivity anomalies, and with petrology data that allows supposing that this area is crust magma chamber of active volcanoes in the Klyuchevskoy volcanic group. This local study together with regional tomography image could help in further geodynamic study of this volcanic area.

CONCLUSIONS

With the help of high-resolution seismic tomography we calculated detailed 3D model of velocity structure beneath Eastern Kamchatka that gives a new insight into subduction processes in the western Pacific area. Based on seismic velocity structure analysis we may derive the following main conclusions.

Computed seismic velocity changes correspond to main tectonic elements of Kamchatka. Pacific lithosphere is not homogeneous; the maximum seismic velocity variation within the slab is likely caused by increased stress due to plate turn at the latitude of Kronotsky peninsula. Velocity structure of the Kamchatsky bay area is influenced by the western part of Aleutian arc.

In the upper mantle beneath Eastern-Kamchatkan volcanic belt at depths of about 70–120 km asthenosphere wedge is revealed. It extends up to the latitude of Kronotsky peninsula and probably is the magma source of active volcanoes.

Focal zone mainly corresponds to high velocity gradient areas that separate Pacific lithosphere and continental block. SFZ is not uniform and this is verified by velocity structure and correlation of earthquake hypocenters with Vp variation.

Revealed by seismic tomography study low velocity zone in the crust beneath Klyuchevskoy volcanic group correlates with geophysical and petrophysics data and likely represents crust magma chamber of Klyuchevskoy volcanic group.

Calculated 3D velocity model allows to assume considerable difference in evolution of upper (about 100 km depth) and deeper parts of Kamchatka lithosphere. Obtained result might be useful for further geophysical investigations and construction of global geodynamic model of subduction processes in the area.

Acknowledgments. Authors thank colleagues from Kamchatka EMSD GS RAS for high quality data set and fruitful discussions. Special thanks to our colleagues from Institute of Geophysics ETH, Zurich, and from Institute of Geospheres Dynamics RAS. The work was supported by RFBR grant # 03-05-64650.

REFERENCES

Avdeiko, G. P., Popruzhenko S. V., Palueva A. A., Tectonic evolution and volcano-tectonic zoning of Kurile-Kamchatkan arc system, *Geotectonics,* 4, 64–80, 2002

Ermakov, V. A., Tectonic zoning of Kurile Islands and seismicity problems, *Physics of the Earth,* 1, 30–47, 1997.

Evans, J. R., Eberhart-Phillips, D., Thurber, C. H., User’s manual for SIMULPS12 for imaging Vp and Vp/Vs: A derivative of the “Thurber” tomographic inversion SIMUL3 for local earthquakes and explosions, Open-file Report 94-431, U.S. Geological Survey, 1994.

Fedotov, S. A., Gusev, A. A., Tchernysheva, G. V., Shumilina, L. S., Seismic focal zone of Kamchatka (geometry, earthquake hypocenter location and relation to volcanism), *Volcanology and Seismology*, 4, 91–107, 1985.

Gontovaya, L. I., Sanina, I. A., Senyukov, S. L., Stepanova, M. Yu, About spatial velocity model of Eastern Kamchatka lithosphere (according to seismic tomography data), *Volcanology and Seismology*, 4-5, 150–159, 1995.

Gontovaya, L. I., Levina V. I., Sanina I. A., et al, Velocity heterogeneities of lithosphere beneath Kamchatka, *Volcanology and Seismology,* 4, 56–64, 2003.

Gorbatov, A., Kostoglodov, V., Suarez, G., Gordeev, E., Seismicity and structure of the Kamchatka subduction zone, *J. of Geophys. Res*., 102, 17883–17898, 1997.

Gorbatov, A., Dominguez, J., Suarez, G., et al., Tomographic imaging of the P-wave velocity structure beneath the Kamchatka peninsula, *Geophys. J. Int*., 137, 269–279, 1999.

Haslinger, F., Kissling, E., Investigating effects of 3-D ray tracing methods in local earthquake tomography, *Physics of Earth and Planetary Interiors,* 123, 103–114, 2001.

Kissling, E., Ellsworth, W.L., Ederhart-Pillips, D., Kradolfer, U., Initial reference models in local earthquake tomography, *J. of Geophys. Res*., 99, 19635–19646, 1994.

Kissling, E., Geotomography with local earthquake data, Reviews of Geophysics, 26, 659–698, 1988.

Kuzin, I. P., Focal zone and upper mantle structure in the Eastern Kamchatka area, M.: Nauka, 1974.

Lees J.M., Davaille, A., Heat transport in the torn edge of the Pacific slab in Kamchatka, *in Abstracts of International Seismic Workshop on Kamchatkan-Aleutian Subduction Processes*, 65–66, Petropavlovsk-Kamchatsky: IVGG FED RAS, 1998.

Levin, V., Shapiro, N., Park, J., Ritzwoller, M., Seismic evidence for catastrophic slab loss beneath Kamchatka, *Nature,* 418, 763–766, 2002.

Moroz, Yu. F., Nurmukhamedov, A. G., Deep geoelectric model of Kurile-Kamchatkan and Aleutian arcs junction area, *Physics of the Earth,* 6, 54–67, 2004.

Pivovarova, N. B., Slavina, L. B., Tushko, T. A., Modeling of three-dimensional velocity fields, *in Physics of Seismic Waves and Interior Structure of the Earth,* pp. 139–150, M.: Nauka, 1983.

Seliverstov, N. I., Structure of the bottom of the near Kamchatka water areas and geodynamic of Kurile-Kamchatkan and Aleutian arcs junction area, M.: Scientific World, 1998.

Active Faulting in the Kamchatsky Peninsula, Kamchatka-Aleutian Junction

Andrey Kozhurin

Geological Institute of Russian Academy of Sciences, Moscow, Russia

Active faults of the Kamchatsky Peninsula mark where the peninsula block is deforming. The most prominent fault of the peninsula, striking ENE-WSW in its southeast corner, exhibits dominant right-lateral movement at Holocene slip rate of about 4 mm y^{-1}. Shorter faults striking NW-SE to WNW-ESE southeast of it have dominantly normal displacements. Based on these observations, it is concluded that none of active faults of the peninsula can represent an onshore extension of any of large NW-trending underwater faults of the western Aleutians. It is suggested that movement along active faults accommodate a part of the peninsula block clock-wise rotation caused by northwest-directed differential movements of the fault-bounded longitudinal blocks of the westernmost Aleutians.

INTRODUCTION

With the Kronotsky and the Shipunsky peninsulas to the south, the Kamchatsky Peninsula make a common set of promontories along eastern Kamchatka (see Fig. 1 and Fig. 2), but in terms of present geodynamics the latter is distinctive. While the southern two peninsulas are now part of the leading edge of an overriding plate, the Kamchatsky Peninsula lies west of the Komandorsky segment of the Aleutian arc, north of the northern tip of the Kamchatka subduction zone (Fig. 1). The elevated east portion of the Kamchatsky Peninsula elongates SE-NW, that is, obliquely to the main structural trend of the Kamchatka mainland (Fig. 2). Based on this fact and on evident differences between Cretaceous-Paleogene evolution of northern Kamchatka mainland and the Kamchatsky Peninsula, Markov et al. (1969) interpreted the Kamchatsky Peninsula to likely represent an extreme NW element of the Komandorsky segment of the Aleutian island chain.

Either a part of Kamchatka or that of the Aleutians, the Kamchatsky Peninsula centers the area where the two island arcs meet at nearly a right angle. Their interaction is commonly interpreted in terms of active arc-arc collision that has been occurring since the Kamchatsky Peninsula block docked against the Kamchatka ocean margin some time after the mid Cenozoic (Pechersky et al., 1997; Park et al., 2002). Markov et al. (1969) inferred that the Kamchatka mainland and the Kamchatsky Peninsula meet across a regional fault that runs NNE-SSW directly west of the Nerpichie Lake (see Fig. 3), and that the tighter compressed structure of the northern Kumroch Range of central Kamchatka is a manifestation of the Kamchatka-Aleutians interaction. Geist and Scholl (1994) outlined a zone of intensive thrusting in the portion of east central Kamchatka NW of the peninsula and interpreted it as having resulted from the Kamchatka-Aleutian collision. Based on the seismicity pattern, they suggested also that at present the Kamchatka-Aleutian interaction might be occurring somewhere between the Komandorsky chain and the Kamchatsky Peninsula block. Gaedicke et al. (2000) examined possible relationships between Late Quaternary faults of the peninsula and a system of arc-parallel right-lateral underwater faults of the western Aleutians detected from seismic profiling data (Seliverstov, 1983; Baranov et al., 1991; Seliverstov et al, 1995).

Contributing much to understanding the active processes of the Kamchatka-Aleutian interaction, all the

Volcanism and Subduction: The Kamchatka Region
Geophysical Monograph Series 172

10.1029/172GM10

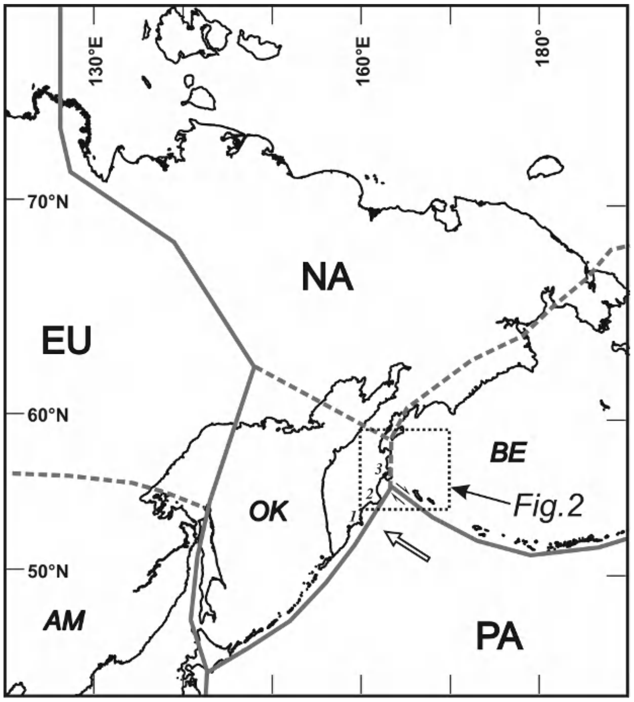

Figure 1. Plate boundaries configuration in NW Pacific. Dashed lines are boundaries of minor plates within major plates. NA = North American Plate, EU = Eurasian Plate, PA = Pacific Plate (DeMets et al., 1990). AM = Amurian Plate, OK = Okhotsk Plate (Zonenshain, Savostin, 1979), BE = Bering Sea Plate (Lander et al., 1994). Open arrow shows direction of NA-PA relative motion. 1 to 3 are for promontories along the Kamchatka east margin: 1 – Shipunsky Peninsula, 2 – Kronotsky Peninsula, 3 – Kamchatsky Peninsula (see also Fig. 2).

works mentioned above incorporated, however, few data on onshore active faulting. The aim of the present paper is to describe geomorphic manifestation of active faulting in the Kamchatsky Peninsula to provide additional insight in the Late Quaternary development of the Kamchatka-Aleutian junction area.

GEOLOGIC AND NEOTECTONIC SETTING

Physiographically, the Kamchatsky Peninsula combines several isolated mountainous massifs surrounding the lowland of the central part of the peninsula with the large lakes Nerpichie and Kultuchnoe (Fig. 3). The massifs are rimmed with successions of marine terraces, development of the oldest of them probably dating back to the beginning of the Middle Quaternary time (Melekestsev, Erlikh, 1974). The massifs are composed of Cretaceous and Paleogene complexes while the lows between them are filled with the Ol'khovskaya suite of late Pliocene to early Quaternary age (Geological, 2002). However, patches of sediments of the Ol'khovskaya suite are present at high altitudes as well in northern and southern regions of the peninsula (Geological, 2002). This presence suggests that modern topography of the peninsula has resulted from mainly Middle and Late Quaternary tectonic vertical movements, slower (~1.6 mm y^{-1}) in the northeast and faster (up to 4.7 mm y^{-1}) in the south (Melekestsev, Erlich, 1974). Judging simply by the massif morphology, block tilting, mostly towards the central part of the peninsula, has been occurring. At the same time, in the southern peninsula, general steepening of marine terraces from younger to older suggests south-directed tilting of the block between the First and Second Pereval'naya rivers (Kozhurin, 1985). Along the southern margin of the peninsula, the inclined form of an unconformity between the Ol'khovskaya suite and underlying rocks (Fig. 2 in Basilyan, Bylinskaya, 1997) may also be evidence of post-Late Pliocene tilting or folding.

Active faults in the region of the Kamchatsky Peninsula, known and inferred from interpretation of aerial images, make up two groups (Fig. 2 and 3). The faults close and parallel to the eastern foothills of the Kumroch Range, west of the Nerpichie Lake, represent the northernmost extension

Figure 2. Regional neotectonic setting of the study area. Thick black lines are active faults, dashed where inferred, ticks on downthrown side. Thinner black dashed lines are major underwater faults (Baranov et al., 1991; Seliverstov, 1995, simplified). Dotted black lines are the Kurile-Kamchatka trench and the Aleutian trench. White dashed line ovals are approximate outlines of NW-SE trending elongated uplifted area in the Kamchatsky peninsula and, for comparison, of NNE-SSW-trending (margin-parallel) uplifts in the Kronitsky Peninsula. CKD = Central Kamchatka Depression, KR = Kumroch Range, EKFZ = East Kamchatka fault Zone, ShV = Shiveluch Volcano. See Fig. 1 for location.

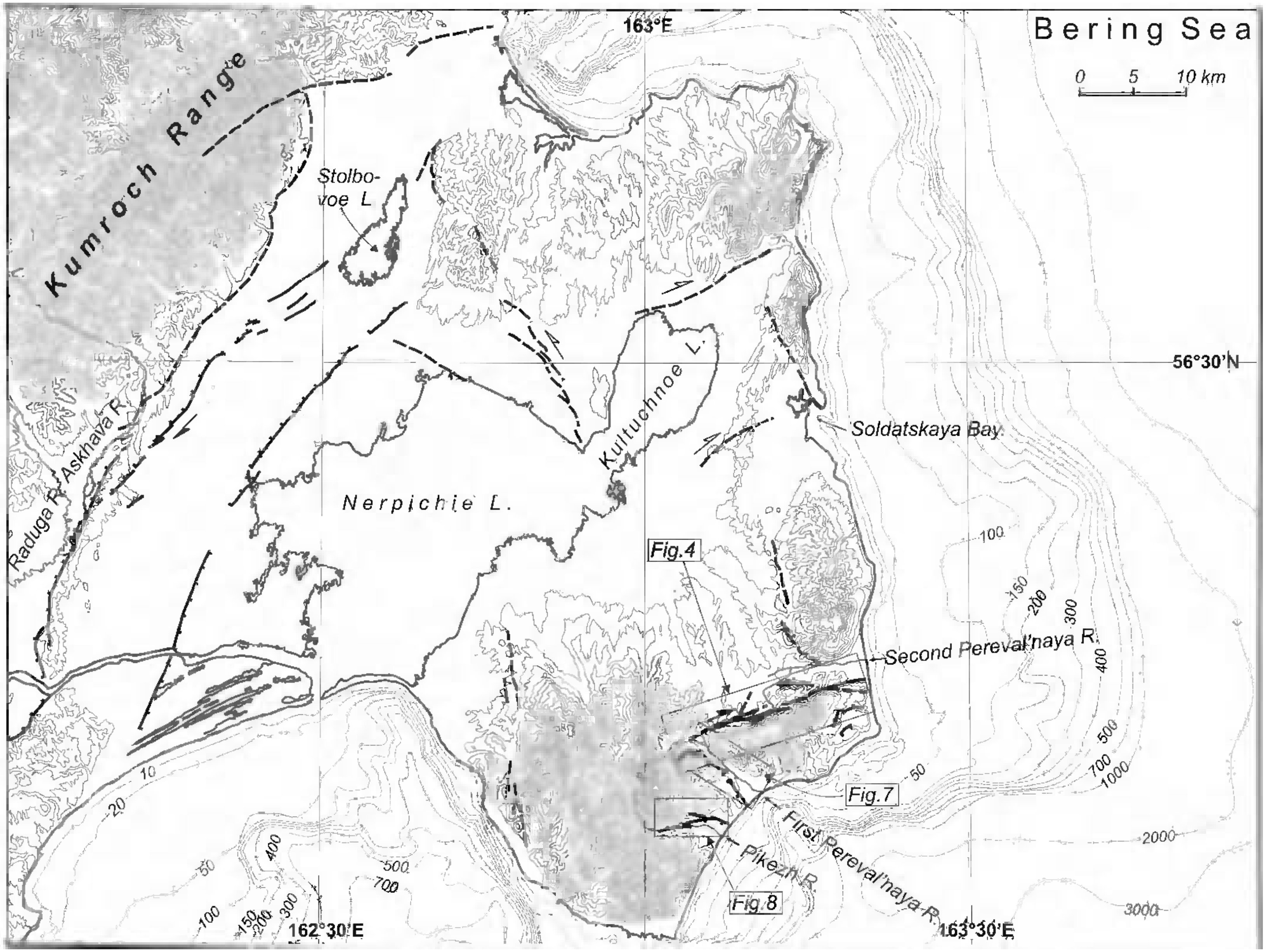

Figure 3. Active faults in the Kamchatsky Peninsula area. Thick black lines are active faults, dashed where inferred, ticks on downthrown side. Arrows mark strike-slip faults, open-headed where lateral movements inferred. Topographic counter interval is 100 m. Bathymetric contours are in meters. See Fig. 2 for location.

of the east branch of the East Kamchatka Fault Zone, the major fault system of the Kamchatka mainland. These faults are mostly normal, with the west sides relatively elevated, and some right-lateral component of movements (Kozhurin, 1990, 2004; Kozhurin et al., 2006). East of these faults, there is a separate net of NW-trending and NE- to ENE-trending faults. These faults do not connect to those of the first group and may therefore relate to internal deformation of the Kamchatsky Peninsula.

ACTIVE FAULTING IN THE KAMCHATSKY PENINSULA

Here I describe a group of active faults concentrated in the southeast corner of the peninsula (see Fig. 3). The faults cut Holocene landforms providing good evidences for their kinematics. This group includes a fault that extends ENE from upstream portion of First Pereval'naya River to the mouth of Second Pereval'naya River (Fig. 4 box on Fig. 3). It is likely that this fault continues farther east, beneath the waters of the Kamchatsky Straight, along one of the canyons on the peninsula continental slope. South of this fault, there are two short NW to WNW-striking faults, one in the First Pereval'naya River valley (Fig. 7 box on Fig. 3), and another in the Pikezh River valley (Fig. 8 box on Fig. 3). Both faults also extend up to the shoreline and may continue some distance into the sea.

ENE-WSW-Trending Fault

The fault stretches as a generally continuous, slightly northward-convex line, probably with a short left-hand step near the middle where its downthrown (northern) side becomes mountainous (Fig. 4). The fault is the northern limit of an uplifted block, which bears well-developed marine terraces on its top and gentler southern slope, the oldest of them reported to be Middle Quaternary in age (Melekestsev, Erlich, 1974). From younger to older, the terrace surfaces become notably steeper suggesting southeast-directed tilting of the uplifted block (Kozhurin, 1985).

All along its length, the fault exhibits evidences for right-lateral offset of Holocene landforms - side-crests, gullies and terrace risers, with offset values ranging from about 2 m to 70–75 m (Table 1). Characteristic features are abandoned channels and curved active channels, as well as shutter ridges (Fig. 5). The vertical component of offset is subdued. The average rate of Holocene right-lateral fault movement may be estimated based on offset of two terraces along one of the left tributaries

Figure 4. *Top*. Fragment of aerial photograph. White arrows point at the fault line. *Bottom*. Black lines are active faults, ticks on downthrown side. Arrows mark strike-slip faults. Dotted lines are rivers and streams courses. For location see Fig. 3.

Table 1. Amplitudes of Right-Lateral Offsets along the ENE-WSW Fault, SE Kamchatsky Peninsula

Fault strike at observation site	Right-lateral displacement, *m*	Vertical separation, *m*	Corresponding figure
70°	5.5	1	
70°	32		Fig. 5B
70°	65–70	~ 5	Fig. 5A
	7		
	30		Fig. 5A
70°	70	~5	
70°	8–10		
	19–20		
	70–75	~5	
70°	72–75	~5	
	37–40		
	35		
	15		
70°	57–58	4–5	
	43–45		
	14–15		
	2		
	20–22		
70°	30—32		
	25		
70°	65	~5	
80°	10–12	0.8–0.9	Fig. 5C
70°	13–14	1.1–1.2	Fig. 6
	23–24	1.2–1.3	Fig. 6

of the First Pereval'naya River, close to the fault's west end (Fig. 6). Both terraces are mantled with soil-pyroclastic deposits with lowermost tephra identified as ash falls from Shiveluch Volcano (Vera Ponomareva, personal communication). The oldest tephra on the lower (younger) terrace (terrace 1 in Fig.6) is SH_{2800} with an age of 2800 ^{14}C yr BP (2900 calibrated years) (Pevzner et al., 1998). On the next higher terrace (terrace 2 in Fig. 6), the oldest tephra is SH_{4800} with and age of 4800 ^{14}C yr BP (5500–5600 calibrated years) (Pevzner et al., 1998). Terrace 2 was traced down to the First Pereval'naya River mouth where ^{14}C dating of its sediments gave an age of 6000 ± 50 ^{14}C yr BP or ~6800 calibrated years BP (Kozhurin, 1990), in reasonable compliance with the tephrochronological dating. Terrace one is displaced right-laterally 13–14 m and Terrace two 23–24 m (Fig. 6). Based on these figures, maximum slip rates can be estimated to be 4.5 to 4.8 mm y^{-1}, for the lower terrace 1, and 4.1 to 4.3 mm y^{-1}, for the higher terrace 2. On each terrace there is about 10–12 cm of loamy soil between the lowermost identified ash and coarser alluvial deposits. Earlier, the rate of accumulation of similar sediments at the base of the west slope of the Kumroch Range was estimated to be 0.1 to 0.4 mm y^{-1} (Kozhurin et al., 2006). This suggests that both terraces can be roughly 500 years older than overlying lowermost tephras, therefore I estimate the terrace ages to be roughly 3.4 ka and 6 ka. Average lateral slip rates based on these observations and reasoning are about 4 mm a^{-1}. Based on this value and the amount of minimal right-lateral offset measured in the fault (2 m, see Table 1), recurrence interval between fault movements can be tentatively estimated as about 0.5 ka.

Figure 5. Right-lateral displacements of geomorphic elements along the ENE-WSW fault of the Kamchatsky Peninsula. White arrows point at the fault scarp. For location of photos see Fig. 4. Insets are plan-view sketches of displacements (field drawings). ***A***. AB = 65–70 m, CD = 30 m. View to S. ***B***. AB = 32 m. View towards WNW. ***C***. AB = 10–12 m, VS (vertical separation) = 0.8–0.9 m View to N. (see Table 1).

Figure 6. *Top.* Photo of terraces in the First Pereval'naya River valley displaced right-laterally in the west part of the fault. *Bottom.* Interpretation (field drawing). Numbers enumerate terraces (see text). MT = marine terrace. Nearly equal length of arrows indicating offset amounts is due to oblique view distortion. View towards E. For location see Fig. 4.

NW-SE-Trending Faults

Fault in the First Pereval'naya River valley. This fault produces a SW-facing scarp on the west (right-hand) slope of the First Pereval'naya River valley (Fig. 7). In the north, where the valley turns northwest, the fault also turns northwest while keeping its southern side uplifted. This relationship indicates a south to southeast dip of the fault plane and a normal sense of fault movement.

The amplitude of vertical separation of topography varies along the fault, being larger, up to 15–20 m, where the fault strikes E-W (in the north) and decreasing to 5–7 m where the fault strikes NW-SE. At places, right-hand stepping of the fault trace is noticeable. Lateral component of motion is very small and apparently left-lateral. Such motion is obviously missing on the E-W-striking portion of the fault and may be present where the fault strikes NW. So, within a stream valley, NW of the Nepropuskovy Creek (see Fig. 7), the fault displaces by ~1 m vertically and 2 m left-laterally a low water divide between two active, shallow channels. On aerial photographs, the courses of two gullies farther NW seem to bend a little along the fault line, probably reflecting left-lateral displacement of up to 20–25 m. However, it should be emphasized that evidence for lateral movement on the fault is scarce and uncertain, so the fault should be considered mostly normal.

Southeast of the First Pereval'naya R. mouth, there is a well-developed underwater canyon that extends, widening seaward, down to the base of the continental slope (see Fig. 3). Since the location and direction of the First Pereval'naya R. valley were obviously predetermined by the fault movements, the canyon may mark the underwater continuation of the fault.

Fault in the Pikezh River valley. In the area of the lower Pikezh River, several short faults combine in a system that borders a triangular-shaped depression filled with well-developed, low marine terraces (Fig. 8). All the faults produce steep, south-facing scarps and, by appearance, look very similar to the fault in the First Pereval'naya River valley. Total vertical separation of the ground surface across segments amounts to 10–12 m. Typically, fault scarps are accompanied by shallow depressions at their foot (see profile inset, Fig. 8), suggesting normal movement along the faults. As in case with the First Pereval'naya River fault, no reliable evidence for lateral fault movement is apparent.

Figure 7. *Top.* Fragment of aerial photograph. *Bottom.* Black lines are active faults, dashed where inferred, ticks on downthrown side. Arrows mark strike-slip faults. Dotted lines are rivers and streams courses. For location see Fig. 3.

Figure 8. *Top*. Fragment of aerial photograph. *Bottom*. Black lines are active faults, dashed where inferred, ticks on downthrown side. Dotted lines are rivers and streams courses. Numbers are measured vertical separation, meters. On scarp profile, 10–12 m is amount of vertical separation of ground surface, 5 m is the width of fault-related depression, dashed lines mark inferred position of major and antithetic fault planes. For location see Fig. 3.

Other faults. Other probable active faults on the peninsula, based solely on interpretation of aerial images, include the following (see Fig. 3).

A fault with undoubtedly Late Quaternary movement extends NW by a set of short, NE-facing scarps from the NE corner of Nerpichie Lake (Fig. 3). Markov et al. (1969) inferred left-lateral movement along the fault but reported no supporting data. Based on interpretation of aerial photographs, Late Quaternary activity can be also expected for the NNW-striking fault starting at the northern margin of the Soldatskaya Bay, where marine terraces appear to be vertically displaced. Finally, we suppose that young vertical movement may have been occurring on about N-S faults south of Nerpichie Lake (Fig. 3).

DISCUSSION

The most conspicuous fault of the peninsula is that extending roughly E-W between the First and Second Pereval'naya rivers. Kinematics of the fault is mainly right-lateral. The vertical component of fault movement is much smaller and is likely normal. Based on ^{14}C and tephrochronological age determinations, the Holocene average lateral slip rate is ~4 mm y^{-1}. In the east, the fault reaches the peninsula shoreline and is likely extending underwater along one of the canyons of the peninsula continental slope.

The NW-striking faults in the First Pereval'naya River valley and the Pikezh River valley exhibit mostly normal movement in recent times. Lateral component is negligibly small and left-lateral. This result evidently contradicts the conclusion of Gadeicke et al. (2000) that the fault along the First Pereval'naya River exhibits up to 250 m of cumulative dextral offset imprinted in topography. I maintain, there is no appreciable evidence of right-lateral movement along any of the right-side tributaries, of size and geomorphic position similar to Nepropuskovy Creek. The Nepropuskovy valley has no terraces and in its downstream portion incises the Holocene terrace of the First Pereval'naya River. Thus, attributing 250 m of plan-view bend of the stream to Holocene cumulative displacement yields a six-times faster lateral slip rate (~2.5 cm y^{-1}), than that estimated by tephrochronology and radiocarbon dating for the ENE-WSW-striking right-lateral fault of the peninsula.

Gaedicke et al. (2000) were apparently the first who attempted to connect the large dextral faults of the Komandorsky segment of the Aleutians with active faults on land on the Kamchatsky peninsula. In their model, the onshore ENE-WSW-striking fault is shown as a continuation of one of the NE-SW-striking splays of the Bering fault zone. (Fig. 9). Since the splay strikes obliquely to the main trace of the Bering F.Z., the sense of movement along it must be mainly reverse (as indicated in Fig.3 in Gaedicke et al., 2000). However, field data indicate that the onshore fault moves laterally and that the vertical component constitutes just a very small portion of the overall fault movement. It seems that the only possible model that incorporates the onshore strike-slip fault as a direct extension of the Bering Fault zone could be that of the counter clockwise rotation of a single block of the westernmost segment of the Aleutian island rise and the southwest portion of the Kamchatsky Peninsula. However, the two faults differ too much in their radius of curvature so that the motion on one of them can not be simply accommodated by the motion on the other.

As for the faults in the First Pereval'naya and Pikezh river valleys, their dominantly normal kinematics and lack of any reliable evidence for dextral movement do not allow them to be linked to the dextral Pikezh fault zone (see Fig. 9).

We must conclude therefore that at present any correlation between onshore faults of the Kamchatsky Peninsula and offshore faults of the western Aleutians must remain provisional, if only by reason of differences in resolution of terrestrial and underwater data. Moreover, I suggest there may be another way of examining the problem. I suggest that active faults in the peninsula do not extend beyond the limits of the peninsula block (roughly, landward of the 1000-m bathymetric contour) and reflect therefore just internal deformation of this block. Large right-lateral faults of the Komandorsky

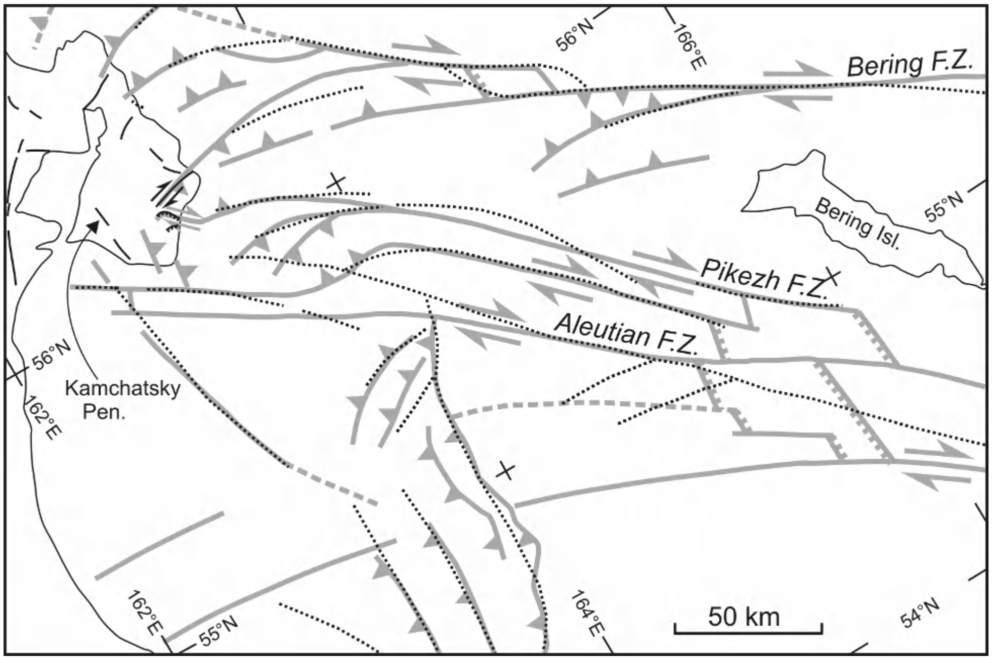

Figure 9. Major fault zones of the westernmost Aleutians. Thick gray lines and kinematic symbols are faults as in Gaedicke et al., 2000. Dotted lines are faults from Seliverstov et al., 1995. Thinner black lines are active faults (this paper). See text for details.

chain, including the Bering F.Z. and the Pikezh F.Z., which accommodate a portion of the transform movement along the Pacific-Aleutian boundary, may be interpreted either to terminate before the eastern limit of the Kamchatsky Peninsula block or to plunge beneath it.

An important consequence of the uniform kinematics of the NW-SE faults of the Komandorsky islands is the decrease in rate of dextral movement from one fault to another with distance from the Aleutian-Pacific interface. This, in turn, implies a gradual northward decrease in the rate of convergence between the Kamchatsky Peninsula block and the longitudinal, fault-bounded blocks of the Komandorsky Island chain. The expected result of this specific multi-block interaction may be some clockwise rotation of the Kamchatsky Peninsula block, some part of this rotation being accommodated by movements along the peninsula faults (Fig. 10).

Supporting evidence for this model include the following:

1) NW-directed movement of longitudinal, fault-bounded slivers of the Komandorsky segment comply with slip vectors and orientation of compression axes obtained from focal plane solutions of strong earthquakes immediately east of the Kamchatsky Peninsula (Cormier, 1975; Zobin et al., 1988) (Fig. 11).
2) Along-arc translation and clock-wise rotation of blocks may be occurring in the central Aleutian Island arc (Geist

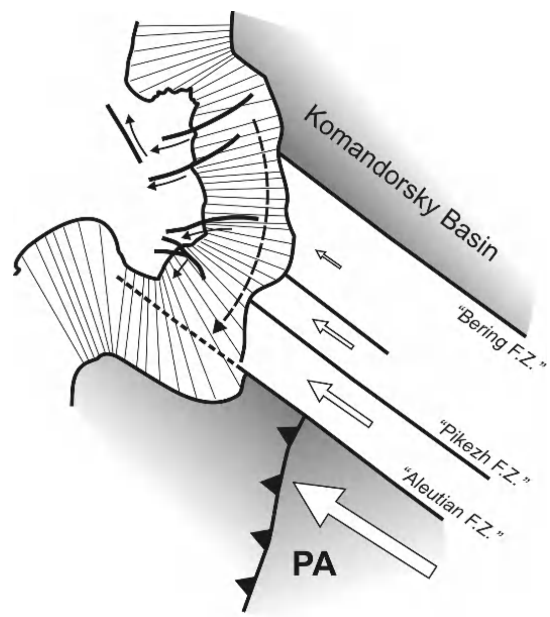

Figure 10. Idealized representation of the Kamchatsky Peninsula – Aleutians interaction. Thick black lines are active faults both known and potential (see Fig. 3) with their inferred underwater extensions. Hatched area is underwater slope of the Kamchatsky Peninsula block. Open arrows indicate direction of movements relative to Kamchatka, longer arrows for faster movements. PA is the Pacific Plate.

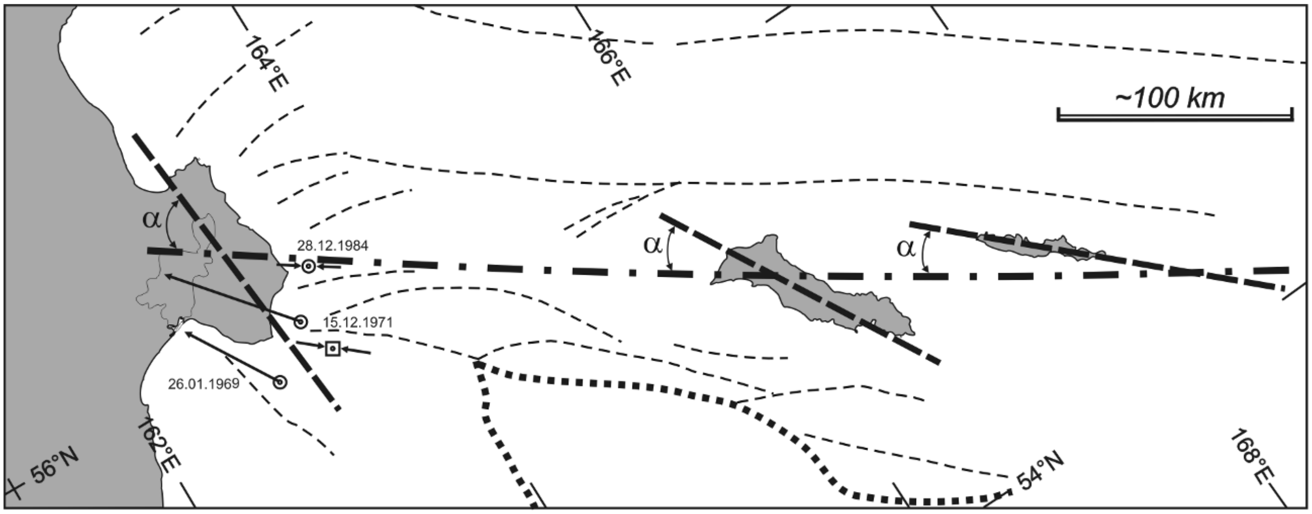

Figure 11. En echelon arrangements of the Komandorsky islands and the Kamchatsky Peninsula. Dashed-dotted line marks the axis of the single elevation of the Kamchatsky Peninsula + Komandorsky Islands, thick dashed lines are axes of the individual islands and the peninsula. Single arrows starting from circles are azimuths of earthquake slip vectors (Cormier, 1975), two opposite arrows show horizontal projection of P-axis (Zobin et al., 1988), quadrangle is location of the 15.12.1971 earthquake as in Zobin et al. (1988). For other symbols see Fig. 9. Note that the obliquity angle α is regularly increasing northwestward.

et al., 1988), probably in association with arc-parallel extension (Lallemant and Oldow, 2000).

3) Similar to the Komandorsky islands (Bering and Medny islands), the elongated Kamchatsky Peninsula block is oriented oblique to the trend of the west Aleutians but at larger angle (see Fig. 11). It may be speculated that the extra obliquity accumulated due to rotation of the peninsula block caused in turn by differential NW-directed movement of the Komandorsky segment.

It follows from above, that the Kamchatka-Aleutian interaction may be occurring somewhere between the Komandorsky chain and the Kamchatsky Peninsula block as suggested by Geist and Scholl (1994) based on seismicity pattern, rather than directly within the peninsula, as later suggested by Gaedicke et al. (2000).

CONCLUSIONS

1. Active faults in the Kamchatsky Peninsula form a specific group independent of active faults in the rest of Kamchatka. The main fault of the peninsula is the about E-W-striking fault moving right-laterally at the rate of ~ 4 mm y^{-1}. Shorter NW-SW faults breaking its southern side are mostly normal.
2. By strike and sense of movement, the faults of the peninsula can not represent direct extensions of the large underwater longitudinal faults of the Komandorsky segment of the Aleutian Islands rise or subordinate elements of their system, and reflect therefore internal deformation of the peninsula block.
3. The probable mechanism of active faulting in the area may be active rotation of the peninsula block caused by lateral pressure applied by the fault-bounded longitudinal blocks of the westernmost Aleutians moving at different rates to the northwest.

Acknowledgements. I am grateful to Jody Bourgeois and Alan Terril for their help in improving the English of the manuscript. I also wish to thank Jody Bourgeois and two anonymous reviewers for many helpful comments. The research was supported in part by the Russian Foundation for Basic Research, Grant # 06-05-064960.

REFERENCES

Avé Lallemant, H. G., Oldow, J. S., Active displacement partitioning and arc-parallel extension of the Aleutian volcanic arc based on Global Positioning System geodesy and kinematic analysis, *Geology,* 28 (8), 739–742, 2000.

Baranov, B. I., Seliverstov, N. I., Murav'ev, A. V., Muzurov, E. L., The Komandorsky Basin as a product of spreading behind a transform plate boundary, *Tectonophysics,* 199, 237–260, 1991.

Basilyan, A. E., Bylinskaya, M. E., The shelf of the Kamchatsky Peninsula, eastern Kamchatka, in the Late Pliocene and Early Quaternary (Ol'khovaya time), *Stratigraphy. Geological correlation,* 5(3), 83–91, 1997.

Cormier, V. F., Tectonics near the junction of the Aleutian and Kuril-Kamchatka arcs and a mechanism for middle Tertiary magmatism in the Kamchatka basin, *Geol. Soc. Amer. Bull.,* 86, 443–453, 1975.

DeMets, C. R., Gordon, R. G., Argus, D. F., Stein, S., Current plate motions, *Geophys. J. Inter*., 101, 425–478, 1990.

Gaedicke, C., Baranov, B., Seliverstov, N., Alexeiev, D., Tsukanov, N. and Freitag, R., Structure of an active arc-continent collision area: the Aleutian – Kamchatka junction, *Tectonophysics*, 325, 63–85, 2000.

Geist, E. L., Scholl, D. W., Large-scale deformation related to the collision of the Aleutian Arc with Kamchatka, *Tectonics,* 13(3), 538–560, 1994.

Geist, Eric L., Childs, Jonathan R., Scholl, David W., The origin of summit basins of the Aleutian Ridge: implications for block rotation of an arc summit, *Tectonics,* 7(2), 327–341, 1988.

Geological Map of Russian Federation. Scale 1:200000. East Kamchatka Series, Ust'-Kamchatsk, Sheets O-58-XXVI, XXXI, XXXII, MNR RF, 2002.

Kozhurin, A. I., Quaternary tectonics of the Kumroch Range and Kamchatsky Mys Peninsula, *Geotectonics,* 2, 76–87, 1985 (in Russian).

Kozhurin, A. I., Recent strike-slip faults in the Kumroch Range and Kamchatsky Peninsula area, Eastern Kamchatka, *Tikhookeanskaya geologiya*, 6: 45–55, 1990 (in Russian).

Kozhurin, A. I., Active faulting at the Eurasian, North American and Pacific plates junction, *Tectonophysics*, 380, 273–285, 2004.

Kozhurin, A. I., Acocella, V., Kyle, P. R., Lagmay, F. M., Melekestsev, I. V., Ponomareva, V., Rust, D., Tibaldi, A., Tunesi, A., Corazzato, C., Rovida, A., Sakharov, A., Tengonciang, A., and Uy, H., Trenching active faults in Kamchatka, Russia: paleoseismological and tectonic implications, *Tectonophysics*, 417, 285–304, 2006.

Lander, A. V., Bukchin, B. G., Droznin, D. V., Kiryushin, A. V., The tectonic environment and source parameters of the Khailino, Koryakiya earthquake of March 8, 1991: Does a Beringia plate exist? *Computational Seismology and Geodynamics (English edition of the Geodinamika i prognoz zemletriaseniy. Vychislitel'naya seismologiya)*, 3, 80–96, 1994.

Markov, M. S., Seliverstov, V. A., Khotin, M. Yu., Dolmatov, B. K., On the conjugation of structures of the Eastern Kamchatka and Aleutian island arc, *Geotectonics,* 5, 52–61, 1969 (in Russian).

Melekestsev, I.V ., Erlikh, E. N. Denudational-tectonic mountainous uplifts, *in History of relief development in Siberia and Far East. Kamchatka, the Kuril and Komandor Islands*, edited by I.V. Luchitsky, pp. 100–141, Nauka, Moscow, 1974 (in Russian).

Park, J., Levin, V., Lees, J., Peyton, V., Gordeev, E., Ozerov, A. A., Dangling Slab, Amplified Arc Volcanism, Mantle Flow and Seismic Anisotropy in the Kamchatka Plate Corner, *in Plate Boundary Zones. Geodynamics Series.30*, edited by S. Stein and J.T. Freymueller, pp. 295–324, 2002

Pechersky, D. M., Levashova, N. M., Shapiro, M. N., Bazhenov, M. L.,Sharonova, Z. V., Palaemagnetism of Palaeogene volcanic series of the Kamchatsky Mys Peninsula, East Kamchatka: the motion of an active island arc, *Tectonophysics,* 273, 219–237, 1997.

Pevzner, M. M., Ponomareva, V.V., Melekestsev, I.V., Chernyi Yar—reference section of the Holocene ash markers at the northeastern coast of Kamchatka, *Volcanol Seismol.*, 19/4, 389–406, 1998.

Seliverstov, N. I., The structure of Kuril-Kamchatka and Aleutian Islands according to single-channel seismic data, *Volcanol. Seismol.*, 2, 53–67, 1983 (in Russian).

Seliverstov, N. I., Sugrobov, V. M., Yanovsky, F. A., On geology and evolution of the Komandorky Basin, *Volcanol. Seismol.*, 1, 38–53, 1995 (in Russian).

Zobin, V. M., Fedotov, S. A., Gordeev, E. I., Guseva, E. M., Mityakin, V.P., Large earthquakes in Kamchatka and Commander Islands in 1962–1986, *Volcanol. Seismol.*, 1, 3–23, 1988 (in Russian).

Zonenshain, L. P., Savostin, L. A., Introduction to geodynamics, Nedra, Moscow, 311 pp., 1979 (in Russian)

High Seismic Attenuation in the Reflective Layers of the Philippine Sea Subduction Zone, Japan

Anatoly Petukhin and Takao Kagawa

Geo-Research Institute, Japan.

Intrinsic seismic attenuation gives additional constraints on the physical properties of the deep medium. However, in many cases attenuation is masked by scattering loss. In this work, the high-frequency Q-value, i.e. parameter of seismic attenuation, is studied in the Kii Peninsula segment of the Philippine Sea subduction zone of Japan. The geometrical spreading factor, which is necessary to exclude before inversion of the Q-value, is calculated numerically using a realistic 3-D velocity model and ray approximation. Generally, estimated "total" Q-values agree well with results of other studies and with common expectations based on tectonic structure, except for one striking result: Q-values for the lower crust and the subducting oceanic crust become extremely low, Q_{total} ~ 20–30f. In order to interpret this result we compiled attenuation-related phenomena that were observed in the studied region: (1) the seismogenic upper crust; (2) aseismic lower crust; (3) reflective lower crust (RLC); (4) belt-like zone of the deep low-frequency tremor generation (LFT), that is parallel to the slab; (5) low-frequency earthquakes (LFE); and (6) reflective subducting oceanic crust (SOC). Analysis of ray coverage reveals that anomalously low Q-value in RLC and SOC can be explained mostly by high scattering attenuation (i.e., low Q_{sc} value) in the reflective layers.

INTRODUCTION

Studies on seismic attenuation are helpful to constrain tectonic models. S-wave attenuation in some cases is more sensitive to cracks and fluids than seismic velocity. In a high-frequency range (f > 1Hz), it is possible to resolve detailed attenuation structures using simple ray approach and linear tomography inversion. The problem is that due to the scattering of waves, random variations of amplitudes become large and inversion becomes unstable. Using wide frequency range and assuming that Q-value (i.e. parameter for seismic attenuation) is frequency independent, inversion can be stabilized. This approach is used in many attenuation tomography studies and gives reasonable correlations between observed attenuation structures and tectonic features [e.g., *Wu and Lees*, 1996; *Roth et al.*, 1999; *Stachnik et al.*, 2004].

Studies on a frequency dependent Q-value can help to resolve the source of attenuation in the subduction zone: Is it mostly intrinsic attenuation, caused by the presence of fluids and/or melts? Alternatively, is it scattering attenuation, caused by the heterogeneous velocity structure? Q-value is expected to approach frequency independence in the first case, and will develop strong frequency dependence in the second case [*Sato and Fehler*, 1998; Chapters 5.2 and 5.3].

To increase the accuracy of the estimation of the frequency dependent Q-value, a method based on realistic physical models needs to be developed. At local and regional distances, first of all, calculations of realistic geometrical spreading need to be considered. Using such a method, a non-uniform Q-structure can be estimated.

In this study, we used our original method of attenuation tomography inversion [*Petukhin et al.*, 2003] and estimated

Volcanism and Subduction: The Kamchatka Region
Geophysical Monograph Series 172

10.1029/172GM11

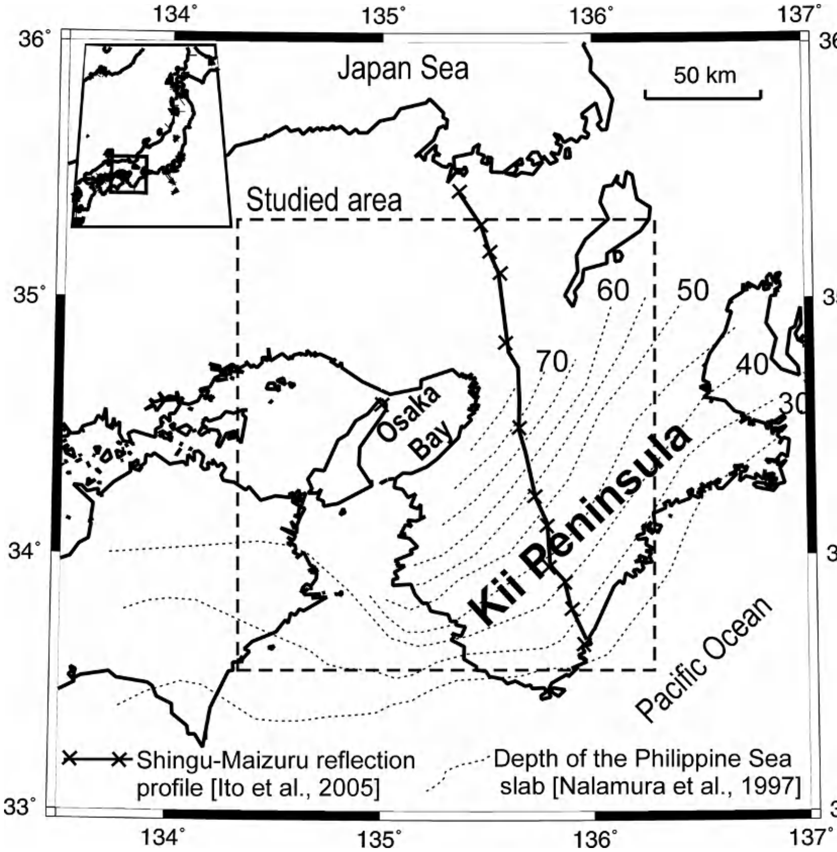

Figure 1. Map of the studied region. Location of the Shingu-Maizuru reflection profile, crossing studied region in NNW-SSE direction, which will be intensively referenced throughout the paper, is also shown.

the structure of Q-value. In order to estimate the Q-value, the effect of elastic attenuation (i.e. mainly geometrical spreading) needs to be first eliminated. The result of this Q-value depends on the exclusion method used. In this study, for high-frequency range, we employed ray approximation and calculated elastic attenuation using ray-theory. For this purpose, we used the *Complete Ray Tracing* (CRT) method [*Červený et al.*, 1988], both for calculating elastic attenuation and for ray tracing. Another feature of this developed method is the use of the double-spectral ratio method in tomographic inversion, to reduce trade-offs between the source and/or site effect and Q-value.

The studied region was the Kii Peninsula segment of the Philippine Sea subduction zone. Many low-frequency earthquakes, which indicate the presence of fluids in the Earth's crust, were observed here. Most of low-frequency earthquakes are located in the junction of the slab and crust [*Obara*, 2002], with some in the central part of studied area, far from volcanic centers [*Ohmi*, 2001].

The Philippine slab is thin (around 30 km) and subjected to an inclined subduction process in a Northwest direction in Western Japan. Due to this complex process, the slab crumples into several folds, one of which is the Kii Peninsula segment. Due to this crumpling effect, the velocity structure in the studied region is essentially three-dimensional. The studied area and slab location are shown in Figure 1.

The 3-D velocity model in the studied area for this work was compiled from seismicity data, travel-time tomography results, seismic exploration results, gravity data and borehole measurements. The data used in the inversion are high-frequency (1–10Hz) high-quality data of CEORKA [*Toki et al.*, 1995] and Hi-net networks [*Obara et al.*, 2000].

Generally, these estimated "total" Q-values agree well with results from other studies and with common expectations based on the tectonic structure, except for one remarkable result when the Q-values for the lower crust and the subducting oceanic crust become extremely low: Q_{total} ~ 20–30f. In order to interpret this result, we compared the estimated Q-structure with other phenomena related to attenuation that were observed in the studied region. Good correlations with the reflective layers [*Ito et al.*, 2005] were found.

METHOD OF *Q*-STRUCTURE INVERSION

Estimation of Q-value by Elimination of Ray-Theory Geometrical Spreading

Spectral inversion. In order to study *S*-wave attenuation in high-frequency range, it was assumed that observed amplitude Fourier spectrum is a product of four terms [e.g., *Iwata and Irikura*, 1988]: (1) source (*S*), (2) elastic path attenuation (*g*), (3) described by the *Q*-value inelastic path attenuation and (4) site (*G*) effects.

$$O = S \cdot g \cdot \exp\left(-\pi \frac{Rf}{vQ(f)}\right) \cdot G. \quad (1)$$

Such a simplified formulation leads to a simple linear tomography inversion methodology. Assignment of initial *Q*-values in blocks is unnecessary and a dependency of the results on the initial model in this case is not present.

In contrast to many other methodologies (e.g., *pulse width method*, [*Wu and Lees*, 1996], *phase pair method*, [*Roth et al.*, 1999]), this inversion method does not assume that *Q*-value is frequency independent, and estimates, separately in many frequency bands, the frequency dependence from inversion. However, from a negative standpoint, because this method uses narrow frequency bands, either data scattering becomes higher, thereby requiring more data for a more stable inversion, or inversion resolution becomes lower.

Frequently, to estimate the path attenuation effect, the *Q*-value is inverted under the assumption that geometrical spreading is spherical (This is true for a uniform velocity model). Actually, elastic attenuation *g* is a complex effect that includes: (1) geometrical spreading in a non-uniform velocity model, (2) reflection and conversion on major velocity discontinuities and (3) free-surface effect.

In this study, elastic path attenuation was calculated using complete ray theory [*Červený et al.*, 1988] in a 3-D velocity model. Travel time inside block *k* was calculated by 3-D ray tracing:

$$T^k = \int_0^{R^k} \frac{dR}{v^k(R)}. \quad (2)$$

Double spectral ratio method. The source and site effects were eliminated using the double spectral ratio scheme [*Chun et al.*, 1987]. The *Q*-values in blocked media were subsequently inverted from the observed double spectral ratios *DSR* using a tomography approach:

$$DSR_{ijnm} = \frac{O_{in} \cdot O_{jm}}{O_{im} \cdot O_{jn}} = \frac{g_{in} \cdot g_{jm}}{g_{im} \cdot g_{jn}} \cdot \exp\left(-\pi \sum_k \left(T^k_{in} - T^k_{im} + T^k_{jm} - T^k_{jn}\right) \cdot \frac{f}{Q^k}\right); \quad (3)$$

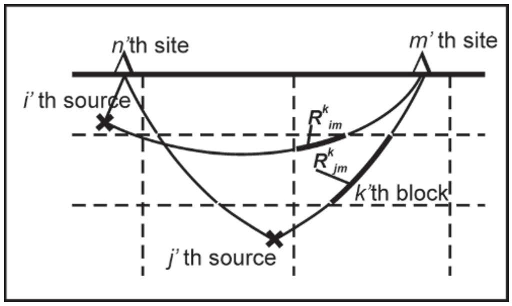

Figure 2. Scheme illustrating the double-spectral ratio tomography inversion procedure, see equation (4). Dashed lines – blocks, solid lines – rays, bold paths are the paths having constant $Q = Q^k$.

Or converted in a linear form, after the removal of the elastic attenuation term and adopting the logarithm:

$$\log DSR'_{ijnm} = -\pi \sum_k \left(T^k_{in} - T^k_{im} + T^k_{jm} - T^k_{jn}\right) \cdot \frac{f}{Q^k}. \quad (4)$$

Here, *i* and *j* - indexes of the source pair, *m* and *n* - indexes of the station pair, *k* - index of medium block with uniform *Q* (see also Figure 2).

The usefulness of the double spectral ratio method in stabilizing inversion was shown by a simple numerical simulation in a previous research [*Petukhin et al.*, 2004], because the method reduces bias due to the trade-offs of the *Q*-value and source/site effect.

Additional measures to stabilize inversion were: (1) selection of data having a uniform coverage; (2) construction of a tomography block model adjusted to an expected *Q*-structure (see below); and (3) layer stripping. Referring to [*Petukhin et al.*, 2003], in order to reduce a possible trade-off between the *Q*-values in seismogenic layer and other blocks, we used a two-step layer-stripping algorithm.

In the first step, only the data of shallow events, whose rays pass within the upper crust, were used to estimate the *Q*-structure in the upper crust. The results of [*Petukhin et al.*, 2004] were used for this step.

In the second step, the data of events from the subduction zone, deeper than 20 km, were used. In this case, the rays pass both through the upper crust and through the deeper part (lower crust/mantle wedge/subducting oceanic crust/slab). In order to determine the *Q*-structure in the deeper part, we fixed the *Q*-structure in the shallow part using the results from the first step of the inversion.

Velocity Model and Tomography Block Model

Following to [*Petukhin et al.*, 2004], for this study we developed a 3-D velocity model for the Kii Peninsula segment (see Figure 3). This model includes: (1) the surface

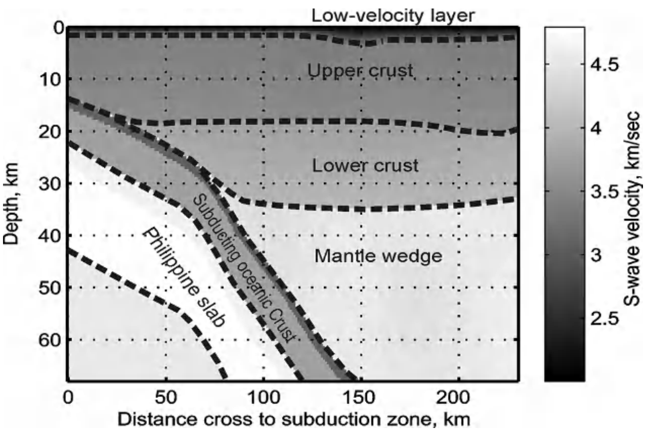

Figure 3. Cross-section of the 3-D velocity model, perpendicular to the subduction zone and passing through the central part of the studied region.

low-velocity layer, (2) seismogenic layer (or upper crust), (3) lower crust, (4) Philippine Sea slab, (5) subducting oceanic crust above the slab, (6) mantle wedge (between the continental crust and subducting oceanic crust), and (7) upper mantle (i.e. below the slab). Based on the case study in [*Petukhin et al.*, 2004], it was assumed that velocities inside each layer have gradient, thus, velocity discontinuities on the layer boundaries are absent. Moreover, in high-frequency range, at the crossing point with velocity interface, the effect of reflection/conversion for upward rays is negligible.

In order to check the compiled 3-D velocity model, we calculated the *P*-wave travel times and compared them with the observed travel times. Analysis of the results reveals that differences between observed and calculated *P*-arrivals are small (maximum value is around +/- 1 sec; standard deviation is around 0.35 sec; the average difference is smaller than the standard deviation and have no distance trend). Hence, the compiled model has no large systematic errors; and can therefore be used for analysis. For more details about the velocity model, refer to [*Petukhin et al.*, 2004].

The whole media of ray propagation was divided into blocks with a constant *Q*-value according to the tectonic structure (see Figure 4): The upper crust (UC), lower crust (LC), mantle wedge (MW) subducting oceanic crust (SOC) and slab (SLB). The UC block was subdivided into 3 smaller blocks with the boundaries along the major fault systems in the studied area. The surface low-velocity layer above the seismogenic layer was considered as an additional block (LV).

The structure of the tomography blocks was constructed based on the following assumptions:

1. The blocks must be large enough. There are two reasons for this. First, in order to solve the ill-conditioned attenuation tomography inversion problem, the ray coverage for each block (i.e., the number of rays crossing this block) should be large (of the order 100–200 rays). Second, the size of the block should be several times larger then the width of the scattered, physical rays. For details, see discussion in [*Petukhin et al.*, 2003].
2. For large blocks, better results are expected if the structure of the blocks themselves will coincide with the tectonic structure in the studied region, which is also an expected *Q*-structure.
3. For the upper crust blocks, natural boundaries between blocks are the major active faults in the studied area. These boundaries also surround the tectonically uniform sub-regions.

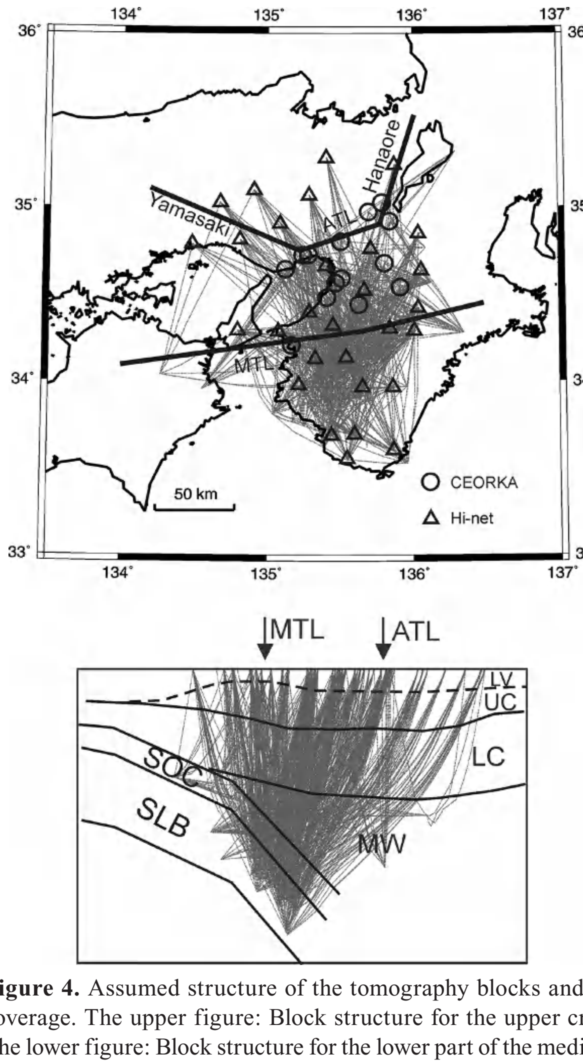

Figure 4. Assumed structure of the tomography blocks and ray coverage. The upper figure: Block structure for the upper crust. The lower figure: Block structure for the lower part of the medium. Blocks and rays on the lower figure are projected to the cross-section that coincides with the Shingu-Maizuru profile (see Figure 1). In the upper figure, locations of the observation sites used in the analysis are also shown.

Data Processing

Processing of data, namely selection of direct *S*-wave window, calculation of amplitude Fourier spectra, removing noise and so on, is an important step of analysis. Accurate (although complicated) data processing reduces scattering of the data, stabilizes inversion and finally improves resolution of inversion.

In this study, we followed our original method of data selection and processing described in [*Petukhin et al*., 2003], with one exception: we used a constant time-window of 3 sec from the *S*-arrival, instead of the time-window used in [*Petukhin et al*., 2003] that was estimated from polarization analysis and was only around 1sec in average. The main advantage of the current method is that a longer window reduces scattering of data points. The disadvantage is that the constant window shifts the *Q*-value estimates to a smaller value.

Frequency range used for the amplitude spectrum calculation is 4–10Hz. The total number of sources used for the second step of inversion is 39, number of sites is 43, number of records is 704 and number of DSR values is 23718. The distribution of ray paths is shown in Figure 4.

RESULTS

In [*Petukhin et al*., 2004], for strong ground motion prediction purposes, we combined some blocks into larger blocks to stabilize the results: MW was combined with LC, and SLB with SOC. In this work, limiting frequency range to higher frequencies, we inverted the *Q*-value separately in LC, MW, SOC and SLB blocks. The results are shown in Figure 5 (plot), Figure 6 (cross-section cartoon) and Table 1. Figure 5 also shows error ranges for the *Q*-value estimates at each frequency. The error ranges demonstrate satisfactory resolution of inversion results (in frequency range 8–10Hz), in sufficient quality to formulate conclusions both on the absolute value differences and on the frequency dependence.

Analysis of the results of inversion indicates that surprisingly low *Q*-values are present in the LC and SOC layers. These *Q*-values cannot be explained by inversion instability alone. In order to confirm the validity of the elastic

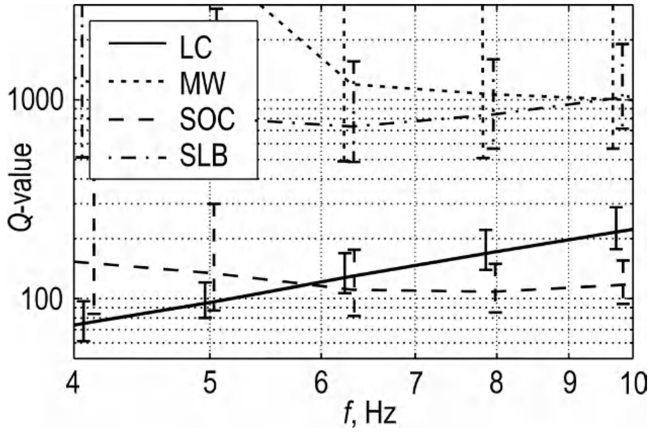

Figure 5. Results of the *Q*-value inversion. Line style of the error bars corresponds to the line style of the results. Due to the inversion instability, indicated by large estimation errors, *Q*-values for the MW and SLB blocks have tendency to rise up at f<5Hz. *Q*-values above the 5Hz have trends comparable with other studies. *Q*-values in the LC and SOC blocks are much smaller than in the MW and SLB blocks.

attenuation model constrained in this inversion, we analyzed residues between the observed and simulated values of the amplitude Fourier spectrum. The results show that the residues have no trend and their absolute value is smaller than that of residues of a similar study of [*Petukhin et al*., 2003], employing a simplified 1-D velocity model.

In order to interpret the results of inversion, in Figure 7 we compiled phenomena, related to attenuation, that were observed in the studied region: (1) seismogenic upper crust; (2) aseismic lower crust; (3) reflective lower crust (RLC) [*Ito*, 1999] in depth range 17–35km and reflective layers (RL) in the SOC, and both are revealed by the deep seismic exploration studies in the region [e.g., *Ito et al*., 2005]; (4) belt-like zone of the deep, low-frequency tremor generation (LFT) parallel to the slab, which was observed using high-sensitivity borehole Hi-net stations [*Obara*, 2002]; (5) few deep, low-frequency earthquakes, (LFE) near the

Table 1. Results of *Q*-value inversion

	Lower Crust	Mantle Wedge	Oceanic Low-Velocity Layer	Philippine slab
Q-value	$15f^{1.0}$	~1000 (f>6)	$\sim30f^{0.6}$	$\sim200f^{0.7}$ (f>6)
		$\propto$ (f<5) [a]		$\propto$ (f<5) [a]

[a]Unstable at lower frequencies f<5Hz.

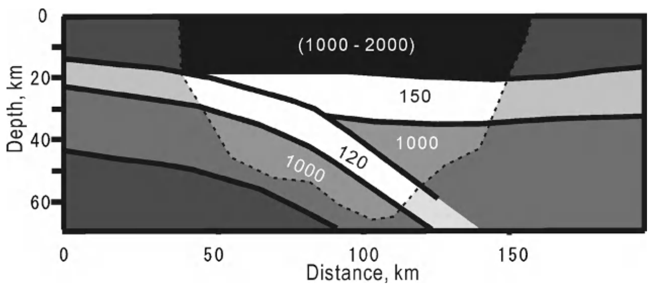

Figure 6. Cross-section cartoon of the results of the *Q*-value inversion. Numbers are estimated *Q*-values at f = 10Hz. Dashed line indicates area covered by rays.

Moho boundary were observed in the central part of the studied area, far from volcanic centers [*Ohmi*, 2001]; (6) the dehydration and/or partial melting in depths ranging from 30–50km, which can explain the presence of the liquid phase in the crust near/above the Moho boundary, which in turn was used [*Katsumata and Kamaya*, 2003] to explain the generation of the LFT and LFE.

The analysis of Figure 7 shows, that anomalously low Q-value in LC and SOC can be explained by two processes: (1) the high intrinsic attenuation (low Q_{in} value) due to the presence of fluids in the LC and SOC, which are indicated by the LFE and LFT phenomena; and (2) the high scattering attenuation (low Q_{sc} value) due to scattering on the crust heterogeneities, indicated by the RLC and RL reflectors. We should mention that the Q_{in} and Q_{sc} values can be combined to the total Q-value, observed in this study, according to the formula:

$$\frac{1}{Q_{total}} = \frac{1}{Q_{in}} + \frac{1}{Q_{sc}}. \tag{5}$$

Although both phenomena have approximately the same depth, they are spatially separated. The main belt of LFT/LFE is moved forward to the slab, while RLC is located in a backward inland area, and RLs in SOC are shifted down. In order to estimate the effects of both phenomena on the inverted Q-value, the ray coverage of used data needs to be analyzed.

ANALYSIS OF RAY COVERAGE EFFECTIVE ZONE AND COMPARISONS WITH OTHER PHENOMENA RELATED TO ATTENUATION

Because of a complex three-dimensional tectonic structure of the studied region, simple projection of rays, earthquakes

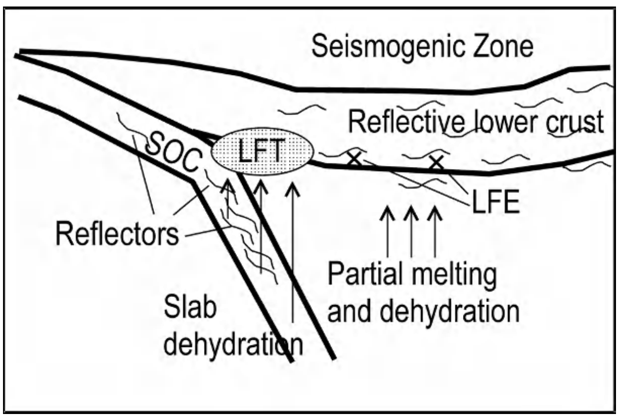

Figure 7. Cartoon of the observed or supposed phenomena, related to attenuation.

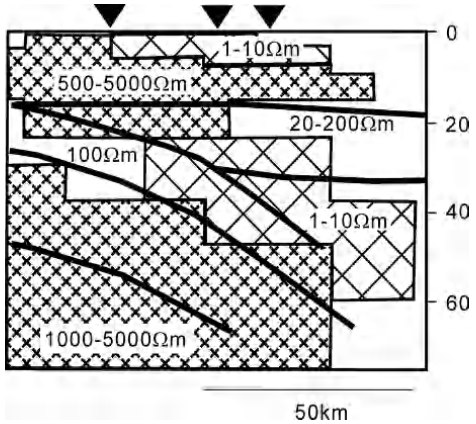

Figure 8. Resistivity model [from *Kasaya et al.*, 2003]. Thick lines present the block boundaries in this study.

and other phenomena into a single cross-section does not provide a clear picture to analyze. In order to avoid this problem we applied a curvilinear projection that is “parallel” to the slab. In fact, all subduction related phenomena are approximately slab-parallel, due to the constancy of the pressure-temperature conditions along the parallel lines.

In order to generate such projection, first, we generated a set of tubes running in "parallel" above the depth isolines of the upper boundary of the slab. The height of the tubes is 3km and width is 3–5 km, depending on the dip angle of the slab under the tube (smaller dip angles produce wider tubes). Subsequently, studied objects, like ray path length or number of earthquake hypocenters, were summarized inside each tube. Finally, we plotted the results along the vertical cross-section in a NNW-SSE direction starting at a point 33.6N, 136.0E that approximately coincides with the Shingu-Maizuru reflection profile in Figure 1. This cross-section was used in many other studies in the Kii Peninsula segment, and our results can be directly compared with those results.

The results of our study and comparisons with results from other studies are shown in Plates 1–3 and Figure 8. The boundaries of the block model are superimposed on each figure, so as to easily compare the locations of the different phenomena.

Plate 1 shows the results for earthquake locations (see Plates 1a and 1b) and ray coverage (in Plate 1c). We can see that these rays effectively cover the UC, LC and SOC blocks, and less effectively the SLB and MW blocks. Although, for some tubes, the coverage in MW seems desirable, the total length of the rays is too short to resolve the Q-value of the tip of mantle wedge. Tectonic earthquakes are located mostly in the UC and SLB blocks. The earthquakes indicate a spread of the brittle crust that should also have high Q-values. This expectation agrees well with our results. The main LFE/

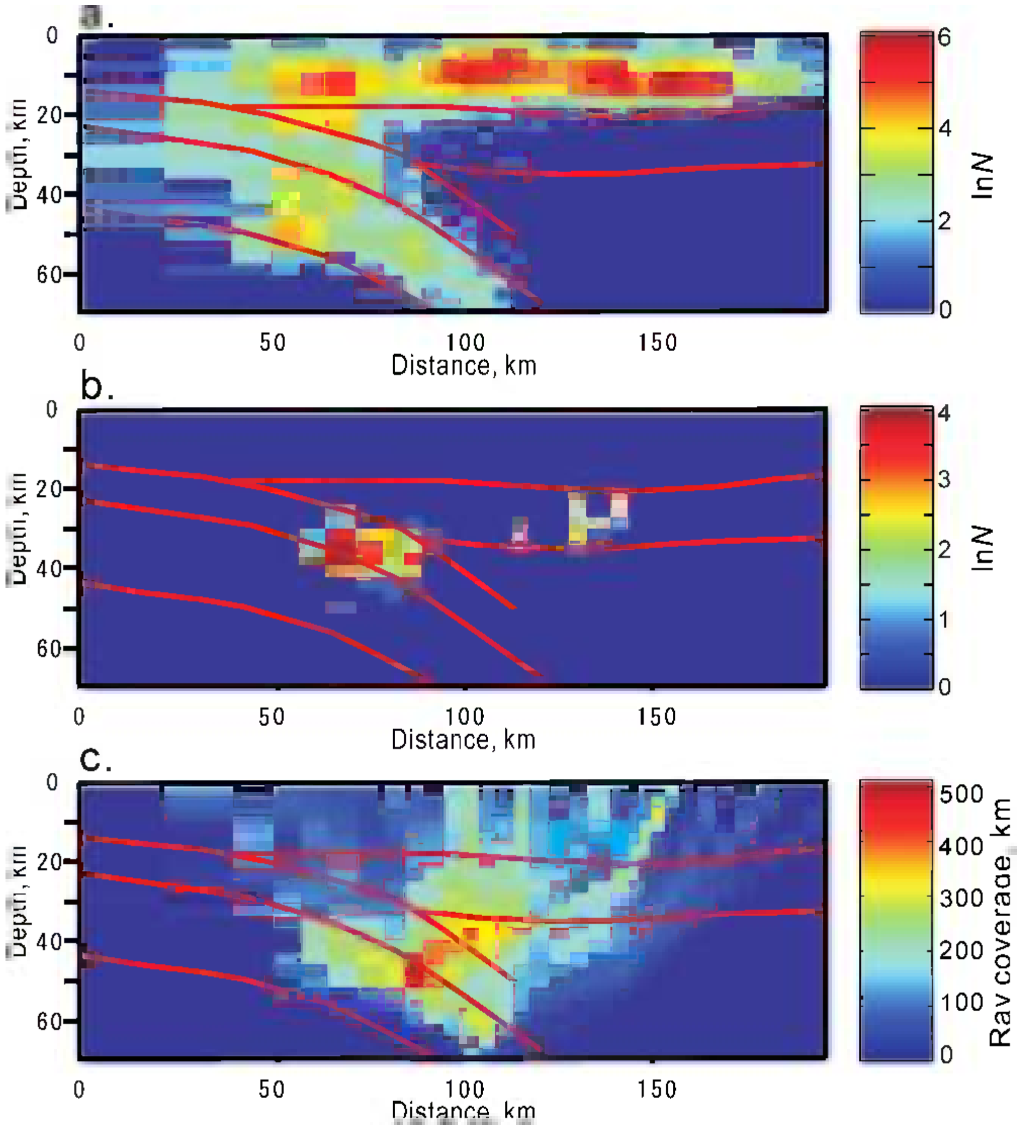

Plate 1. Curvilinear projection of the 3-D distribution of the tectonic earthquakes (a), LFE (b) and the ray coverage (c), on a SSE-NNW profile, which approximately coincides with the Shingu-Maizuru reflection profile, see Figure 1. Tomography blocks used in the inversion are superimposed as reference.

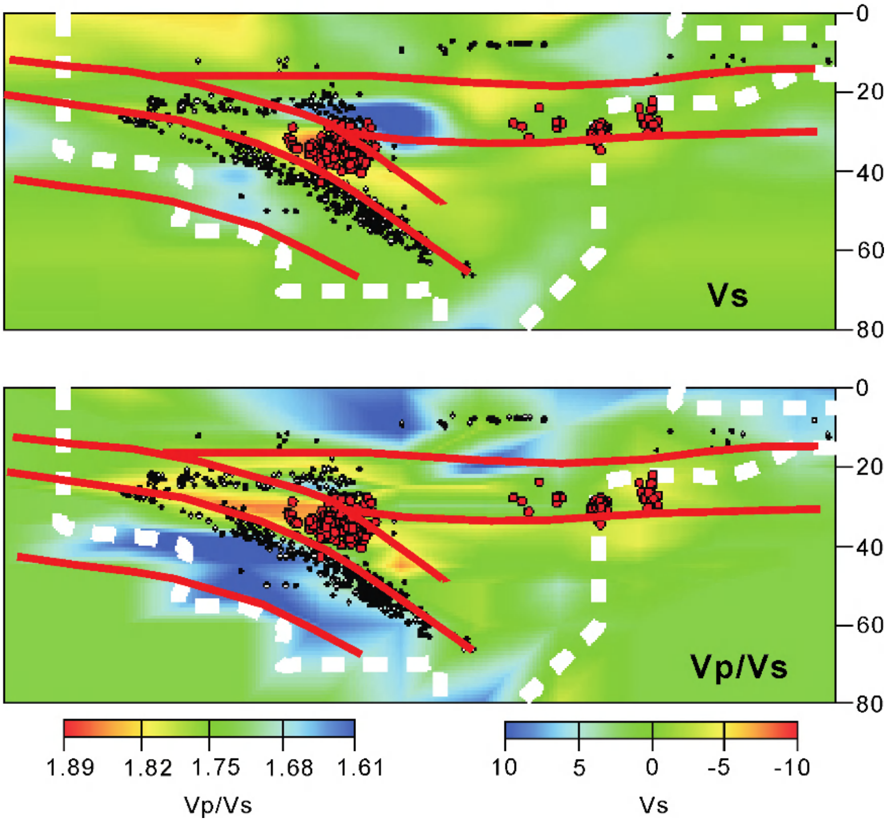

Plate 2. Results of the DD tomography inversion [from *Nakajima and Hasegawa*, 2004]. The block boundaries of our model are superimposed onto the figure (red lines); white dashed line shows area covered by rays in the DD tomography inversion. Note a low V_S and high V_P/V_S zone that coincide with the SOC block in our model.

Plate 3. Reflection cross-section of the Singu-Maizuru profile, [from *Ito et al.*, 2005]. Dark blue color indicates the reflective layers (note intensive reflections in the LC and SOC blocks). Dashed lines and arrows schematically indicate rays and reflection losses.

LFT zone covers the SOC block at the Moho depth, and the second LFE zone is in the LC block under Osaka bay. However, both these zones are located mostly outside of the zone covered by the rays. Therefore, although the LFE and LFT being strong phenomena that definitely should have an effect on attenuation, in our study, they cannot be used to explain low Q-values in the LC and SOC blocks.

In Plates 2 and 3 and in Figure 8 we compiled other phenomena related to attenuation. Plate 2 shows the results from [*Nakajima and Hasegawa*, 2004] of the double-difference velocity tomography inversion (DD tomography, see [*Zhang and Thurber*, 2003]). The results of DD tomography show a high V_P/V_S and low V_S zone that coincides with the LFT zone and even closer coincides with the SOC block in our model. High V_P/V_S value usually serves as an indicator for the presence of fluids, which also results in a low Q-value.

The LFT zone is a strong determinant that can reduce the Q-value. Although the LFT zone is located quite separate from the effective zone covered by the rays, its effect is not 100% negligible. In order to verify its influence on attenuation, we compared the residues for rays crossing the LFT zone and those passing out of the LFT zone. We found the differences to be small but stable in the different distance ranges and frequencies. The differences vary on average from -0.1 to -0.3 log values, with an average standard deviation of 0.45. In future work, it will be necessary to isolate the LFT zone into a separate block.

Figure 8 shows the resistivity model [from *Kasaya et al.*, 2003]. The observed data can be explained as follows: The model has low resistivity in the SOC, MW and in that part of the LC covered by the rays, which also affected by the RLC phenomenon. The SLB and UC have high resistivity. Low resistivity is related to the cracked medium and/or presence of fluids. In both cases, this also results in a low Q-value. Except for the MW block, the proposed resistivity model agrees well with our Q-model.

Plate 3 shows a reflection cross-section of the Singu-Maizuru profile [*Ito et al.*, 2005]. This cross-section clearly indicates reflective layers in the SOC and RLC. The upper boundary of the SOC layer in our block model coincides with the upper boundary of the reflective layers. This boundary can be traced down to a depth of 40–45 km, which is slightly above the lower limit of the rays crossing the SOC block. A thin-layered quasi-parallel structure of the alternating low and high-velocity layers, rather than a single discontinuity, could generate such intensive reflections. Obviously, such a structure should also reflect energy away from these upcoming rays that start from sources located in the slab, below the SOC and RLC layers [e.g., *Nielsen and Thybo*, 2003]. As a consequence of this process, a high loss of energy is expected: The amplitudes of reflected waves, in some cases, are several times larger than the amplitude of direct waves (K.Ito, personal communication). In [*Nielsen and Thybo*, 2003] such reflections of upcoming waves were used to explain the "whispering gallery" phenomena by direct numerical simulations.

DISCUSSION

The large intensity of the reflective layers indicates that loss of energy due to reflections is the most probable candidate to explain low Q-values. However, the reflections on Plate 3 should be assigned to a frequency range of 1–5 Hz and it is expected be smaller at a higher frequency range.

On one side, these reflection losses are an elastic effect, but on another side, the source of the losses is the total volume of the SOC and RLC layer; and the longer the ray path inside the layer, the larger these losses. For these reasons, the losses are described by the scattering Q-value, Q_{sc}. Unlike the regular scattering Q-value, the Q_{sc} of the reflective layer depends on the direction of incidence: Q_{sc} becomes larger, if both the source and the receiver are located on the same side of the reflective layer, so that the reflected energy is additive to the energy of the direct waves; it becomes smaller, if they are on opposite sides, so that the reflected energy represents lost energy.

Further evidence that the low total Q-values in LC and SOC are mostly scattering Q is the fact that Q-values have strong frequency dependence (i.e., $Q \sim f$ for LC and $Q \sim f^{0.6}$ for SOC) that is easier to explain by scattering loss [e.g. *Sato and Fehler*, 1998; Chapter 5.3] than by intrinsic loss [e.g., *Jackson*, 2000; *Sato and Fehler*, 1998, Chapter 5.2]. For the LC, the scattering loss is the only possible explanation for low Q-value. For SOC there are other models and observations that support the possibility for intrinsic loss, due to the presence of fluids that exist because of dehydration of materials near the upper boundary of the slab [*Hacker et al.*, 2003; *Katsumata and Kamaya*, 2003]. The frequency dependence of the Q-value is also an important observation to support the scattering model of loss in SOC.

The presence of the fluids in SOC is explained by dehydration of minerals in the oceanic crust, such as chlorite in altered basalts and serpentin in altered dunites [*Hacker*, 2003]. The source of fluids in LC, in the second zone of LFE, is less obvious. This zone is located just above the deepest tip of the slab, and the melt's upwelling was used to explain the LFE phenomenon [*Katsumata and Kamaya*, 2003]. Another source of this liquid phase could be dehydration of mantle wedge materials drawn down by the subducted plate to a depth of 60–70km.

Another quandary is that this model [*Hacker et al.*, 2003] also predicts dehydration in the tip of the mantle wedge that could imply low Q_{in}. However, the inversion results show that

Q_{total} in the MW is higher than in the SOC. This could be due to strong additional scattering loss in SOC (Of course, the effect of inversion instability could imply a smaller real difference between Q-values in MW and SOC). Another explanation for the high Q in MW is the observation that the presence of water in the supercritical state increases the Q-value, where normally its presents decrease the Q-value [*Sanders et al.*, 1995]. Water can enter this supercritical state during its upward movement from the oceanic crust into the mantle wedge. Interestingly, in the Alaska subduction zone, the Q-value in the cold tip of the mantle wedge is high in contrast to the low Q-value in the hot body of the wedge [*Stachnik et al.*, 2004]. This observation agrees with our results.

Based on the assumption that intrinsic Q_{in} is frequency independent in the analyzed frequency range [see review in *Sato and Fehler*, 1998, Chapter 5.2], but that scattering Q_{sc} is proportional to frequency f, from the total $Q = 30f^{0.6}$, we can estimate that: $Q_{in} \sim 160$ and $Q_{sc} \sim 33f$ in the SOC. A more accurate separation could be made by an analysis of the envelopes: The stronger the scattering, the longer the envelope duration. However, in the case of strongly non-uniform distribution of the scattering parameters, such as in the subduction zone, this kind of analysis is possible only on a direct numerical simulation, [*Nielsen and Thybo*, 2003; *Furumura and Kennet*, 2005], that is an impractical computational problem.

CONCLUSIONS

In this study, Q-structure of the Kii Peninsula segment of the Philippine Sea subduction zone is estimated using the double spectral ratio method of attenuation tomography. The main conclusions are:

1. The Q-values for the lower crust and subducting oceanic crust become extremely low: $Q_{total} \sim 20$–$30f$.
2. Comparison of the estimated Q-structure with other phenomena related to attenuation, namely the spread of a brittle crust indicated by seismicity, reflective lower crust, reflective layers in the subducting oceanic crust, resistivity, low-frequency tremors and low-frequency earthquakes (the last two phenomena are indicative for the presence of fluids) shows high correlation of the low-Q zones with the zones of spreading of the reflective layers.
3. Low Q-values observed in the lower crust block can be explained by the reflective lower crust phenomenon. In this case, there are several mechanisms for the high attenuation: (1) The scattering loss on the velocity inhomogeneities; (2) the reflection loss in the reflective layers; and (3) the intrinsic loss in the cracked medium as indicated by low resistivity.
4. Low Q-values in the subducting oceanic crust can be explained by similar mechanisms, with the following exceptions: The scattering loss has a smaller effect; and the intrinsic loss has a larger effect due to the presence of fluids.

Acknowledgments. We deeply appreciate the National Institute of Earth Science and Disaster Prevention and the Committee of Earthquake Observation and Research in the Kansai Area (CEORKA) for providing the data. Many thanks to the Special Project for Earthquake Disaster Mitigation in Urban Areas (DAIDAITOKU) and Prof. K.Ito for providing the Shingu-Maizuru reflection results and Dr. J.Nakajima for providing the DD tomography results. We are indebted to Dr. A.Gorbatov and an unanimous reviewer for valuable comments that enhanced the article. Dr. W.Dorrance and Dr. J.-T.Nguyen did extensive proofreading and editing of the work.

REFERENCES

Červený, V, L. Klimens, and I. Pšenčík, Complete seismic-ray tracing in three-dimensional structures, in *Seismological algorithms*, edited by Doornbous DJ, Academic Press, New York, 1988.

Chun, K-Y, G.F. West, R.J. Kokoski, and C. Samson, A novel technique for measuring *Lg* attenuation: results from Eastern Canada between 1 to 10 Hz, *Bull.Seismol.Soc.Am*., *77*, 398–419, 1987.

Furumura, T., and B. L. N. Kennett, Subduction zone guided waves and the heterogeneity structure of the subducted plate: Intensity anomalies in northern Japan, *J. Geophys. Res*., *110*, B10302, doi:10.1029/2004JB003486, 2005.

Hacker, B.R., G.A. Abers, and S.M. Peacock, Subduction factory, 1, Theoretical mineralogy, densities, seismic wave speeds, and H_2O contents, *J.Geophys.Res*., *108*, doi:10.1029/2001JB001127, 2003.

Ito, K., Seismogenic layer, reflective lower crust, surface heat flow and large inland earthquakes, *Tectonophysics, 306*, 423–433, 1999.

Ito, K., H. Sato, I. Hirose, Y. Umeda, N. Hirata, T. Ito, S. Abe, T. Kawanaka, and T. Ikawa, Crust and Upper Mantle Structure From Seismic Refraction and Wide-Angle Reflection Surveys and its Relation to Seismic Activity in Southwest Japan, *Eos Trans. AGU*, 86(52), *Fall Meet. Suppl*., Abstract T43A-1364, 2005.

Iwata, T., and K. Irikura, Source parameters of the 1983 Japan sea earthquake sequence, *J.Phys.Earth., 36*, 155–184, 1988.

Jackson, I., Laboratory measurements of seismic wave dispersion and attenuation: Recent progress, in *Earth's Deep Interior: Mineral Physics and Tomography From the Atomic to the Global Scale, Geophys Monogr.Ser*., vol.117, edited by S.Karato et al., pp.265–289, AGU, Washington, D.C.

Kasaya, T., S. Yamaguchi, T. Goto, M. Ueshima, H. Utada, T. Kagiyama, H. Mikada, and K. Suehiro, Exploration of a deep resistivity structure below the Kii peninsula, SW Japan, *Butsuri-tansa*, *56*, 427–437, 2003.

Katsumata, A., and N. Kamaya, Low-frequency continuous tremor around the Moho discontinuity away from volcanoes in the southwest Japan, *Geophys.Res.Lett.*, *30*, doi: 10.1029/2002GL015981, 2003.

Nakajima, J., and A. Hasegawa, Imaging crust, mantle and slab structure around the Shikoku district, Japan, by double-difference tomography and its relationship to the occurrence of nonvolcanic deep tremors, *Eos Trans. AGU*, 85(47), *Fall Meet. Suppl*., Abstract S51B-0161, 2004.

Nakamura M, Watanabe H, Konomi T, Kimura S, and Miura K., Characteristic activities of subcrustal earthquakes along the outer zone of Southwestern Japan, *Annuals of Disas. Prev. Res. Inst., Kyoto Univ*., No. 40 B-1, 1–20, 1997 (in Japanese).

Nielsen, L., and H. Thybo, The origin of teleseismic *Pn* waves: Multiple crustal scattering of upper mantle whispering gallery phases, *J.Geophys.Res*., *108*, doi:10.1029/2003JB002487, 2003.

Obara, K., H. Sadaki, Y. Okada, and S. Aoi, Hi-net: High sensitivity seismograph network in Japan, *AGU 2000 Fall Meeting, Eos Trans., AGU*, 81(48), *Fall Meet. Suppl*.,p.863, 2000.

Obara K., Nonvolcanic deep tremor associated with subduction in Southwest Japan, *Science*, *296*, 1679–1681, 2002.

Ohmi, S., Deep Low-Frequency earthquakes Associated With Active faults in Central-Southwest Japan, *Eos Trans., AGU*, 82(47), *Fall Meet. Suppl*., Abstract S31D-12, 2001.

Petukhin, A., K. Irikura, S. Ohmi, and T. Kagawa, Estimation of *Q*-values in the seismogenic and aseismic layers in the Kinki region, Japan, by elimination of geometrical spreading effect using ray approximation, *Bull.Seismol.Soc.Am*., *93*, 1498–1515, 2003.

Petukhin, A., K. Irikura, T. Kagawa, and S. Ohmi. Study of the HF seismic attenuation in Kinki region, Japan, using the ray theory elastic attenuation effect in 3-D velocity model and the 3-D structure of *Q*-value, *13th World Conference on Earthquake Engineering, Vancouver, B.C., Canada, August 1–6, 2004*, paper No. 633, 2004.

Roth, E.G., D.A. Wiens, L.M. Dorman, J. Hildebrand, and S.C. Webb. Seismic attenuation tomography of the Tonga-Fiji region using phase pair methods, *J.Geophys.Res., 104*, 4795–4809, 1999.

Sanders, C.O., S.C. Ponko, L.D. Nixon, and E.A. Schwartz. Seismological evidence for magmatic and hydrothermal structure in Long Valley caldera from local earthquake attenuation and velocity tomography, *J.Geophys.Res., 100*, 8311–8326, 1995

Sato, H., and M.C. Fehler, *Seismic wave propagation and scattering in the heterogeneous earth*, 308pp., Springer, New York, 1998.

Stachnik, J. C., G. A. Abers, and D. H. Christensen, Seismic attenuation and mantle wedge temperatures in the Alaska subduction zone, *J. Geophys. Res*., *109*, B10304, doi: 10.1029/2004JB003018, 2004.

Toki, K., K. Irikura, and T. Kagawa, Strong motion records in the source area of the Hyogoken-nambu earthquake, January 17, 1995, Japan, *Journal of Natural Disaster Science*, *16*, No.2, pp.23–30, 1995.

Wu, H., and J. Lees, Attenuation structure of Coso geothermal area, California, from wave pulse widths, *Bull.Seism.Soc.Am*., *86*, 1574–1590, 1996.

Zhang, H., and C.H.Thurber, Double-difference tomography: The method and its application to the Hayaward fault, California, *Bull.Seism.Soc.Amer*., *93*, 2003.

A. Petukhin and T. Kagawa, Geo-Research Institute, Itachibori 4-3-2, Nishi-ku, Osaka, 550-0012 Japan. (anatolyp@geor.or.jp)

Seismicity, Earthquakes and Structure Along the Alaska-Aleutian and Kamchatka-Kurile Subduction Zones: A Review

Natalia A. Ruppert

Kamchatka Branch, Geophysical Survey of Russian Academy of Sciences, Petropavlovsk-Kamchatsky, Russia

Jonathan M. Lees

University of North Carolina, Chapel Hill, Chapel Hill, North Carolina, USA

Natalia P. Kozyreva

Kamchatka Branch of Russian Geophysical Survey, Petroparlovsk-Kamchatsky, Russia

We present a review of great earthquakes and seismicity patterns along the Alaska-Aleutian and Kamchatka-Kurile arcs as an overview of one of the longest subduction zone complexes on the planet. Seismicity patterns, double seismic zones and focal mechanism solutions are described and used to illustrate the distribution of stress in the Pacific plate as it collides with North America and Eurasia. Seismicity along the Alaska-Aleutian arc is relatively shallow as compared to the Kamchatka-Kurile arc where the plate is considerably older and thicker prior to entering the subduction zone. Tomographic inversions of the slab generally show high velocity anomalies where seismicity is high, presumably tracking the cold subducting lithosphere.

INTRODUCTION

The Kamchatka-Kurile and Alaska-Aleutian arcs mark one of the most active tectonic margins in the world. Together, they span a length of nearly 6,000 km (Plate 1). The Alaska- Aleutian arc stretches 3,800 km from the Gulf of Alaska westward to Kamchatka, where the two global structures intersect. The Kamchatka-Kurile subduction zone further extends for ~2,000 km from the Bering Sea in the north to Hokkaido Island in the south. This subduction complex extends farther south along the Japan, Izu-Bonin and Mariana trenches.

Volcanism and Subduction: The Kamchatka Region
Geophysical Monograph Series 172

10.1029/172GM12

Due to the curvature of the arc, relative plate motions along the Aleutian trench change from trench-normal in the east to transform in the west. Along the Kamchatka-Kurile arc, the plate motion is almost purely convergent. Convergence rates between the overriding and subducting plates vary from ~6.2 cm/yr in southern Alaska to ~7.2 cm/yr in the central Aleutians [*DeMets et al.*, 1994]. In the Kuriles and Kamchatka, relative plate motions are ~8–9 cm/yr [*DeMets*, 1992]. The age of oceanic lithosphere as it enters the Aleutian trench, varies from 63Ma in the east to ~43Ma in the western Aleutians. Farther west, the age of the subducting lithosphere appears to increase rapidly westward [*Lonsdale*, 1988]. Unlike the Kuriles and Kamchatka, in the Aleutians the oceanic lithosphere ages oceanward of the trench. Kamchatka slab is one of the oldest in the world (>100Ma).

Plate reconstructions indicate that in the Aleutians the rate and relative direction of convergence of the Pacific plate have been fairly constant over the past 43 m.y. [*Wallace and Engebreston*, 1984]. Furthermore, the absolute plate motion of the Pacific plate has not varied significantly during the last 47 m.y. as can be seen by the consistency of the Hawaiian seamount chain [*Dalrymple et al.*, 1977]. Therefore, the geometry of the subduction zone in the Northern Pacific has remained relatively constant over many millennia.

Tectonic processes along the North Pacific margin produce one of the world's most prominent earthquake belts. Shallow earthquakes accommodate slip between the overriding and subducting plates. Earthquakes at intermediate depths, on the other hand, represent deformation within the descending slab. The subduction processes are also made manifest by active arc volcanism, with the exception of the northernmost part of the Alaska subduction zone and the western Aleutians. In the north, the last active volcano is located at ~61ºN, while the subducting slab terminates at ~64ºN. The westernmost presently active subaerial volcano along the Aleutian arc is located 80 km west of Buldir Island (176ºE), it is one of the smallest volcanic centers along the arc. Diminishment of volcanism in the western Aleutians is related to the oblique subduction verging to strike slip motion and perhaps the absence of subduction altogether prior to the collision with the Kamchatka arc [*Yogodzinski et al.*, 2001].

REGIONAL SEISMIC NETWORKS AND EARTHQUAKE CATALOGS

Systemic observations and written records about strong earthquakes, tsunamis, and volcanic eruptions in the region date back to the 18th century when the first Russian explorers arrived in Kamchatka and later moved along the Aleutian arc and into Alaska. Separate accounts and records exist for the southern Kuriles from observations in Japan. Local instrumental observations were initiated in the Russian Far East in the late 1940's and early 1950's with six regional stations. In the late 1950's more seismograph stations were installed, fueled by the creation of the Far East Tsunami Survey. At its peak at the end of the 1980's, there were over 30 regional seismograph stations operating in the Russian Far East. The first digital stations of GSN (Global Seismic Network) were installed in Yuzhno-Sakhalinsk in 1992 with the second station installed in Petropavlovsk-Kamchatsky in 1993. Currently, about 30 real-time seismic stations are located in Kamchatka, jointly operated by the Kamchatka Branch of Russian Geophysical Survey (RGS) and the Institute for Volcanology and Seismology. A permanent network in Kurile Islands includes three stations, operated by the Sakhalin Branch of RGS. A number of temporary seismic deployments have been carried out in addition to the permanent seismic installations. In the late 1990's, Lees et al. [2000] deployed a 15-station broadband seismic array in Kamchatka to investigate the subduction zone structure.

In Alaska, initiation of the regional seismic network commenced in the late 1960's-early 1970's in the wake of the great M9.2 1964 earthquake. This network improved greatly starting in the 1990's due to an expansion of volcano monitoring efforts in the Aleutians and equipment upgrades. Currently, there are ~350 real-time seismic stations operating in Alaska and the Aleutians. This network is managed jointly by the Alaska Earthquake Information Center (AEIC), the Alaska Volcano Observatory (AVO), and the West Coast/ Alaska Tsunami Warning Center (WC/ ATWC). The AEIC serves as the regional data center, collecting, processing and archiving seismic event data.

Kamchatka-Kurile earthquake catalogs were published in the yearly issues of "Earthquakes in the USSR" collection and ISC bulletins (International Seismological Centre). A regional earthquake catalog for Kamchatka dating back to 1962 is complete at a M_W magnitude threshold of 3.8 [*Gorbatov et al.*, 1997]. Earthquake location errors vary from ~40 km in depth and ~20 km in epicenter for events near the trench to ~5 km within a depth range of 45–200 km located landward. For the most recent data, the magnitude of completeness of Kamchatka regional earthquake catalog is close to M_L 2.5.

Systemic publications of earthquake catalogs in Alaska began with installation of the regional seismic network and continue through present at the AEIC ("Earthquakes in Alaska", http://www.aeic.alaska.edu/html_docs/monthly_reports.html). Earthquake detection capabilities in Alaska and the Aleutians vary in space and time and improved with the recent expansion of the regional seismic network. Detailed analysis of the Alaska earthquake catalog completeness is given by Wiemer and Wyss [2000]. In the Aleutians, the magnitude of completeness of the regional earthquake catalog is currently about 2.5, with a higher magnitude threshold in the Near Islands and Komandorsky Islands region. The magnitude threshold for south-central Alaska is approximately 1.5. The AEIC Earthquake catalog is available on the World Wide Web at http:// www.aeic.alaska.edu/db2catalog.html.

GREAT EARTHQUAKES

Convergent plate boundaries are the regions where the world's largest earthquakes originate. Therefore, it is not surprising that five out of the ten largest earthquakes ever recorded in the world were located within the Kamchatka-Kurile and Alaska-Aleutian subduction zones: the M9.2 1964

Table 1. Great earthquakes in Kamchatka-Kurile and Alaska-Aleutian subduction zones.

Date	Region	Lat.(a)	Lon.(a)	Depth, km(a)	M(b)	M_S(a)	M_W(c)
06/25/1904	Kamchatka	52.00	159.00	25		8.3	
05/01/1915	Kuriles	48.40	155.50	30		8.3	
01/30/1917	Kamchatka	55.20	164.50	40		8.1	
09/07/1918	Kuriles	45.50	151.50	25		8.3	
02/03/1923	Kamchatka	53.00	161.00	40	8.5	8.5	
11/10/1938	Alaska	55.50	-158.00	25	8.2	8.7	
04/01/1946	Unimak Island	52.80	-162.50	50	8.1	7.4	
11/04/1952	Kamchatka	52.30	161.00	40	9.0	8.5	
03/04/1952	Hokkaido	42.50	143.00	25		8.6	
03/09/1957	Andreanof Islands	51.30	-175.80	33	8.6		
11/06/1958	Kuriles	44.30	148.50	32	8.3	8.7	
05/04/1959	Kamchatka	53.10	160.30	20		8.0	
10/13/1963	Kuriles	44.80	149.50	47	8.5	8.3	
03/28/1964	Alaska	61.10	-147.60	23	9.2	8.5	
02/04/1965	Rat Islands	51.30	178.60	36	8.7	8.2	
08/11/1969	Kuriles	43.50	147.40	28		8.2	
05/07/1986	Andreanof Islands	51.50	-174.80	19			7.9
10/04/1994	Kuriles	43.80	147.30	14			8.3
06/10/1996	Adak Island	51.56	-177.63	33			7.9
12/05/1997	Kamchatka	54.84	162.04	33			7.8
09/25/2003	Hokkaido	41.81	143.91	27			8.3
11/17/2003	Rat Islands	51.15	178.65	33			7.8
11/15/2006	Kuriles	46.59	153.27	10			8.3
01/13/2007	Kuriles	46.27	154.45	10			8.1

(a) NEIC Significant Worldwide Earthquakes and PDE catalogs http://neic.usgs.gov/neis/epic/epic_rect.html
(b) NEIC Significant Earthuqkes list - http://earthquake.usgs.gov/regional/world/historical.php
(c) Harvard CMT catalog - http://www.globalcmt.org/CMTsearch.html

Great Alaskan, M9.0 1952 Kamchatka, M8.7 1965 Rat Islands, M8.6 1957 Andreanof Islands, and M8.5 1963 Kurile Islands earthquakes (Table 1, Plate 2). The remarkable thing about these earthquakes is that they occurred within a span of 12 years. The earlier events occurred before deployment of the World Wide Standardized Seismograph Network (WWSSN) while later events, such as 1963 and 1964, were recorded by WWSSN stations allowing for a more detailed analysis. Still, few seismic records are available for these events and details of the rupture processes are difficult to unravel. The hazards from such mega-earthquakes include not only violent ground shaking that causes wide-spread destruction of buildings and infrastructure, but also devastating tsunamis. It is important, therefore, to understand the mechanics of these events in order to mitigate future seismic and tsunami hazards.

The first event in the sequence, the M9.0 Kamchatka earthquake, occurred on 4 November, 1952 [*Savarensky et al.*, 1958; *Kanamori*, 1976; *Johnson and Satake*, 1999]. It caused a catastrophic tsunami with run-up wave heights up to 12 m that severely damaged the city of Severo- Kurilsk [*Fedotov*, 1965]. The rupture started in the north and propagated southwest for 600–700 km with a velocity of 3–3.5 km/s [*Ben-Menahem and Toksoz*, 1963]. According to regional seismological studies, aftershocks were concentrated in the northern and southern parts of the rupture zone [*Tarakanov*, 1961]. Average slip based on tsunami wave modeling is estimated at 3.2 m with the maximum slip of up to 11 m [*Johnson and Satake*, 1999]. The slip may represent two asperities, both in the down-dip portion of the ruptured fault: a smaller asperity near the initiation of the rupture and another, larger one, within the second half of the rupture.

Historical written records from Russian explorers contain a detailed account of a major earthquake and subsequent tsunamis that occurred on October 17, 1737 [*Krasheninnikov*, 1949]. From the Holocene tsunami deposits in Kronotsky Bay, Kamchatka, the 1737 and 1952 tsunami deposits have the largest inland propagation [*Pinegina et al.*, 2003]. This may be an indication that the 1737 event was of a similar magnitude and ruptured the same area as the 1952 event.

Other important events in Kamchatka include the 1904 and 1923 earthquakes; both generated destructive tsunamis in Kamchatka. The 1923 event is estimated at ~M8.3–8.5. Russian seismologists concluded that the 1923 earthquake ruptured north of, but not into the 1952 rupture area. The rupture zone of the 1904 event is estimated to be located downdip of the central part of the 1952 event rupture [*Fedotov*,

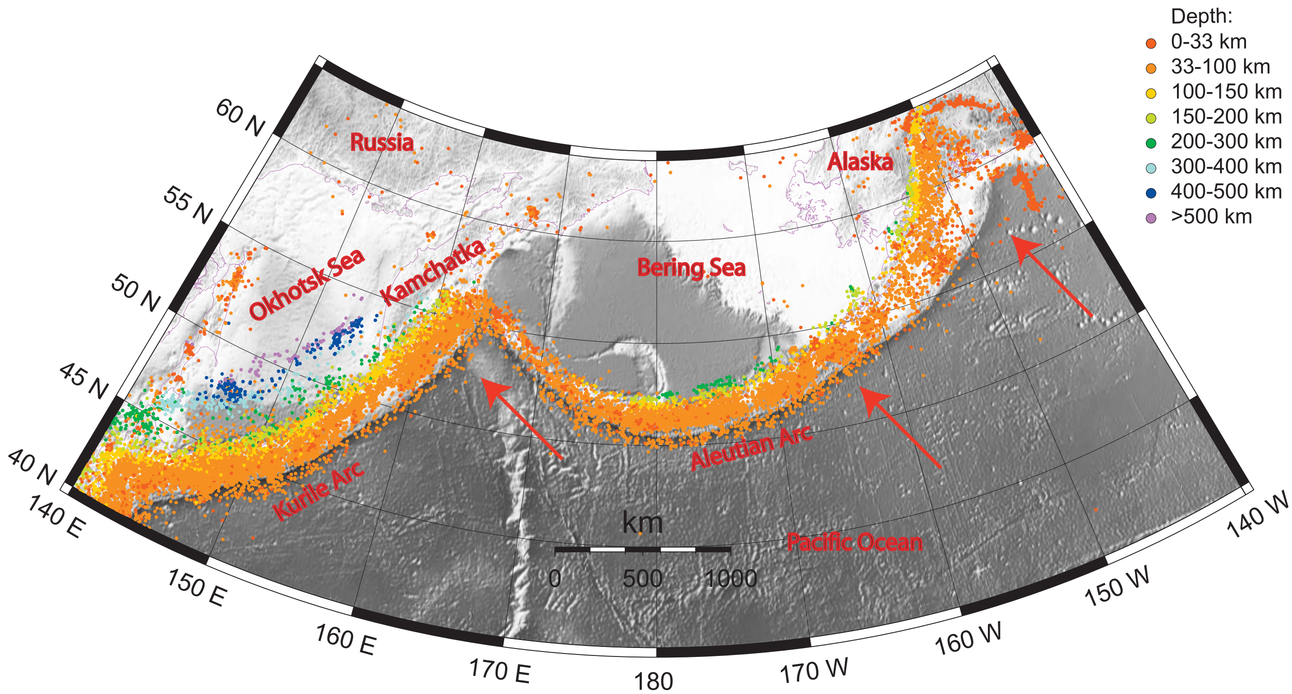

Plate 1. Seismicity distribution in the Alaska-Aleutian and Kamchatka-Kurile subduction zones (PDE catalog 1974–present, M>=4.0). Arrows show relative motion of the Pacific plate.

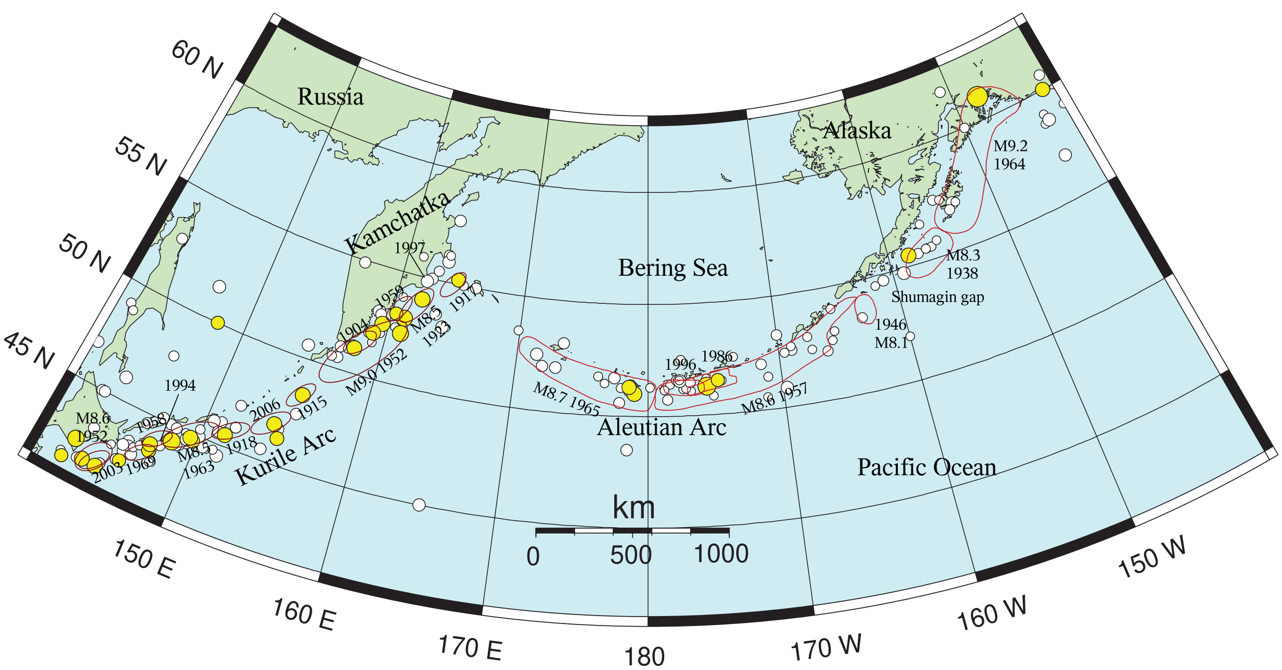

Plate 2. Rupture zones of great earthquakes along the Alaska-Aleutian [*Haeussler and Plafker*, 1995] and Kamchatka-Kurile [*Kuzin et al.*, 2001] subduction zones (red solid lines) and locations of instrumentally recorded magnitude 7+ earthquakes (white circles - M=7.0–7.9, yellow circles - M>=8.0). Event locations and magnitudes are from NEIC catalog of Significant Worldwide Earthquakes. See Table 1 for event details.

1965]. Multiple events in the 7–8 magnitude range have been reported within the Kamchatka subduction zone from both instrumental and historic records [*Fedotov*, 1965]. The most recent and largest of such events was a M7.8 Cape Kronotsky earthquake on December 5, 1997 [*Zobin and Levina*, 2001].

Along the Kurile trench, the subduction zone has recurrently generated earthquakes with magnitudes in the high 7 to mid-8 range over the past two centuries [*Fedotov*, 1965; *Schwartz and Ruff*, 1987]. The central Kurile segment differs from the northern and southern part. This area has a thin, suboceanic crust (<~20km thick), while the crust in the NE and SW is of a subcontinental type with thickness reaching 30 km [*Kuzin et al.*, 2001]. The largest instrumentally recorded event in the Kurile Islands arc was the M8.5 Urup earthquake that occurred on October 13, 1963 [*Beck and Ruff*, 1987; *Balakina*, 1990]. It generated tsunami waves with maximum run-up heights of 4–5 m along a 200-km-long stretch of the Kurile arc [*Solovjov*, 1965]. The rupture started in the south and propagated mainly to the northeast. Beck and Ruff [1987] used long-period P-waves to obtain details of the rupture process. They concluded that the earthquakes ruptured two well- resolved and one poorly-resolved asperity with a scale length of ~60km, estimating a total rupture length of ~250 km. The aftershock locations, however, occupy a region 150–200 km wide and up to 500 km long [*Balakina*, 1990]. There is also a discrepancy between the moment release estimate from the long-period P-waves and the surface waves [*Kanamori*, 1970a]. Beck and Ruff [1987] concluded that in order to match the full moment release determined from surface waves, a long-period component of moment release is necessary to reconcile this difference, indicating that areas of the fault plane surrounding the asperities slipped coseismically.

The latest significant event in the Kuriles (M8.3) occurred on November 15, 2006 in the central arc. Prior to this event, the 250-km-long segment of the arc between the 1918 rupture in the southwest and the 1915 rupture in the northeast has been recognized as a seismic gap [*Fedotov*, 1968]. Its seismic potential was estimated at 8.2–8.5 [*Fedotov*, 1965; *Fedotov*, 1968]. The 2006 Kurile earthquake was followed by an outer rise event (M8.1) on January 13, 2007.

Nanayama et al. [2003] used deposits of prehistoric tsunamis to infer occurrence of larger events generated from longer ruptures in the Kurile margin. They concluded that unusually large tsunamis with deposits extending kilometers inland occurred about every 500 years, on average, over the past 2,000–7,000 years, with the most recent one ~350 years ago. It is possible that such multi-segment earthquakes persistently recur among a larger number of single-segment events. It is very likely that we have not seen the largest event of which the Kurile arc is capable of.

The Alaska-Aleutian arc has a history of repeatedly rupturing in great earthquakes [*Tobin and Sykes*, 1968; *Keller*, 1970; *Sykes*, 1971; *McCann et al.*, 1979]. The most recent sequence that ruptured almost the entire arc from southern Alaska to the western Aleutians began in 1938 with a M8.3 earthquake southwest of Kodiak Island (Plate 2). The only segment of the arc that did not rupture is the so called Shumagin seismic gap [*Davies et al.*, 1981]. Based on GPS observations, however, it has been observed that very little strain is being accumulated in that region [*Lisowski et al.*, 1988; *Larson and Lisowski*, 1994]. The recurrence times of major and great earthquakes alone the Aleutian trench are not very well constrained due to the lack of systemic paleo-seismic and paleo-tsunami observations. It is summarized by *Nishenko and Jacob* [1990].

The largest earthquake along the Alaska-Aleutian subduction zone (M9.2) occurred on March 28, 1964. It is currently the second largest recorded earthquake in the world. It is characterized by a unilateral rupture started in the Prince William Sound region and propagated southwest for ~800 km. Strong ground motion following this event triggered many avalanches and landslides—some being tsunamigenic. Ground deformation was extensive, with some areas east of Kodiak Islands elevated by as much as 10 meters and areas near Anchorage subsided by nearly 3 meters [*Plafker*, 1964]. The maximum reported intensity was XI on the modified Mercalli Intensity scale, indicating major structural damage, including ground fissures and failures. This earthquake generated a damaging, Pacific-wide tsunami wave. Details of the rupture process were estimated from a variety of available seismic records [*Wyss and Brune*, 1967; *Kanamori*, 1970b; *Ruff and Kanamori*, 1980; *Kikuchi and Fukao*, 1987; *Christensen and Beck*, 1994] and from tsunami records [*Johnson et al.*, 1996]. The studies indicate two major moment release areas, or asperities. The larger asperity was located near the epicenter, and a second, smaller one was within the second half of the rupture zone near Kodiak Island. The rupture area estimated from the aftershock locations, however, is larger than that from the waveform inversions. Recurrence interval of this event has been estimated at 400–1000 years based on dating the uplifted terraces and subsidence events [*Plafker*, 1986; *Combellick and Reger*, 1988; *Hamilton et al.*, 2005].

The next largest event along the Alaska-Aleutian margin (M8.7) occurred on February 4, 1965 in the Rat Islands region. The length of the rupture is estimated at 600 km. Three major pulses of moment release were identified from the analysis of teleseismic P-waves which correlate with Rat, Buldir, and Near tectonic blocks [*Geist et al.*, 1988; *Beck and Christensen*, 1991]. This event is characterized by a unilateral rupture propagating from southeast to northwest.

The 9 March 1957 Andreanof Islands event (M8.6) has the longest aftershock zone of the above mentioned events, stretching for ~1200 km along the Aleutian arc [*Johnson et al.*, 1994]. This event is also the least studied and understood of the three great Alaska-Aleutian earthquakes. Since it occurred before the introduction of the WWSSN stations, practically no seismic data are available. This event caused severe damage on Adak and Unimak Islands where local tsunamis reached heights of 13 meters. From surface wave analysis, it was determined that significant moment release occurred only in the western half of the aftershock zone, where the largest slip was estimated from tsunami inversion (up to 7 m). The tsunami source area, however, is smaller, extending ~850 km in length from 180ºE to 168ºW, and does not include the eastern end of the aftershock zone. This event is also unusual because it is characterized by a bi-lateral rupture propagation.

The last significant events in the Aleutians were the M7.9 7 May 1986 Andreanof and the 10 June 1996 Adak earthquakes. Both events reruptured parts of the western end of the 1957 rupture zone [*Johnson et al.*, 1994; *Tanioka and Gonzalez*, 1998]. The M7.8 Rat Islands earthquake in November 2003 was located near the eastern end of the 1965 rupture zone.

Studies of great earthquakes have revealed a large variation in seismicity among subduction zones often explained in terms of differing degrees of mechanical coupling between the subducting and overriding plates [*Kanamori*, 1977; *Ruff and Kanamori*, 1980; *Lay et al.*, 1982; *Peterson and Seno*, 1984]. The asperity model, proposed to explain earthquake occurrence [*Kanamori*, 1981], is based on a notion of fault plane heterogeneity. The strongest regions are referred to as asperities, and the occurrence of the largest earthquakes is attributed to the failure of the largest asperities. Weak portions of a fault may slip along with large events although with smaller displacements. Overall, in the Kuriles, Kamchatka and Aleutians we see major earthquakes (M=7.0–8.0) occurring within the rupture zones of the mega earthquakes (M>~8.5). These major events do not represent complete re-rupturing of asperities and the associated completion of the seismic cycle, but probably represent minor stress adjustments to continued plate motion and increasing deformation of the locked zone. Careful monitoring of large earthquakes could lead to better forecasts of great earthquakes, as well as potential high-slip areas.

SEISMICITY AND GEOMETRY OF SUBDUCTING PLATE

Early discussions of earthquake distributions were based on regional seismic recordings both in Kamchatka-Kurile margin [*Fedotov*, 1965; *Fedotov*, 1968; *Fedotov and Tokarev*, 1974; *Fedotov et al.*, 1985] and in Alaska [*Van Wormer et al.*, 1974; *Lahr*, 1975]. Later seismicity studies with improved earthquake locations provided better seismological constraints on regional tectonics based on data recorded by extensive regional and global networks. Temporary PASSCAL deployments in Kamchatka [*Lees et al.*, 2000] and in Alaska [*Meyers et al.*, 2000; *Ferris et al.*, 2003; *Stachnik et al.*, 2004] provided high quality datasets that utilized both regional and teleseismic earthquake records to delineate crustal thickness and study detailed properties of the subducted plate and mantle. The main target of the Kamchatka deployment was the cusp where the Pacific plate terminates at 55ºN. Investigations of shear wave splitting using SKS arrivals, S-wave velocity using surface waves, and P-wave velocity using body waves showed that the edge of the Pacific plate terminates in the north at the junction of the Aleutians and Kamchatka [*Peyton et al.*, 2001; *Levin et al.*, 2002a; *Park et al.*, 2002; *Russo and Lees*, 2005; *Davaille and Lees*, 2004; *Lees et al.*, this volume].

Kamchatka-Kurile WBZ Seismicity

The Pacific plate is old (>100My) by the time it plunges into the mantle along the Kamchatka Arc. The consequence of this is that the subducting lithosphere is relatively cold and thick and the Wadati-Benioff zone is clearly defined by hypocenters plunging to depths of 600 km south of the southern tip of Kamchatka. Using cross sectional slices perpendicular to the Kamchatka trench, Gorbatov et al. [1997] delineated the surface of hypocentral distribution in Kamchatka and found that the earthquakes dip approximately 49º in the direction WNW towards the Eurasian plate. This trend is fairly consistent along the Kamchatka arc except where the Aleutian arc collides with Kamchatka. There, the hypocenters shoal considerably and shift to the northwest below the Central Kamchatka Depression. The shoaling seismicity towards the north has been the inspiration of several studies of the Kamchatka-Aleutian cusp and most likely represents the northern terminus of the Pacific plate where the plate apparently hangs down, exposed in the mantle [*Davaille and Lees*, 2004; *Lees et al.*, this volume].

To illustrate the structure of seismicity along the Kamchatka-Kurile arc we present plots of the seismicity projected and rotated (Figure 1). The events were extracted from the E. Engdahl database of relocated hypocenters (7504 events from 1964 to 1995) and from the NEIC (National Earthquake Information Center) database (5873 events from 1995 to 2006). Events that had 33 km for depth (a default value) and shallow events that were clearly not in the subduction zone, were removed. We first perform an oblique

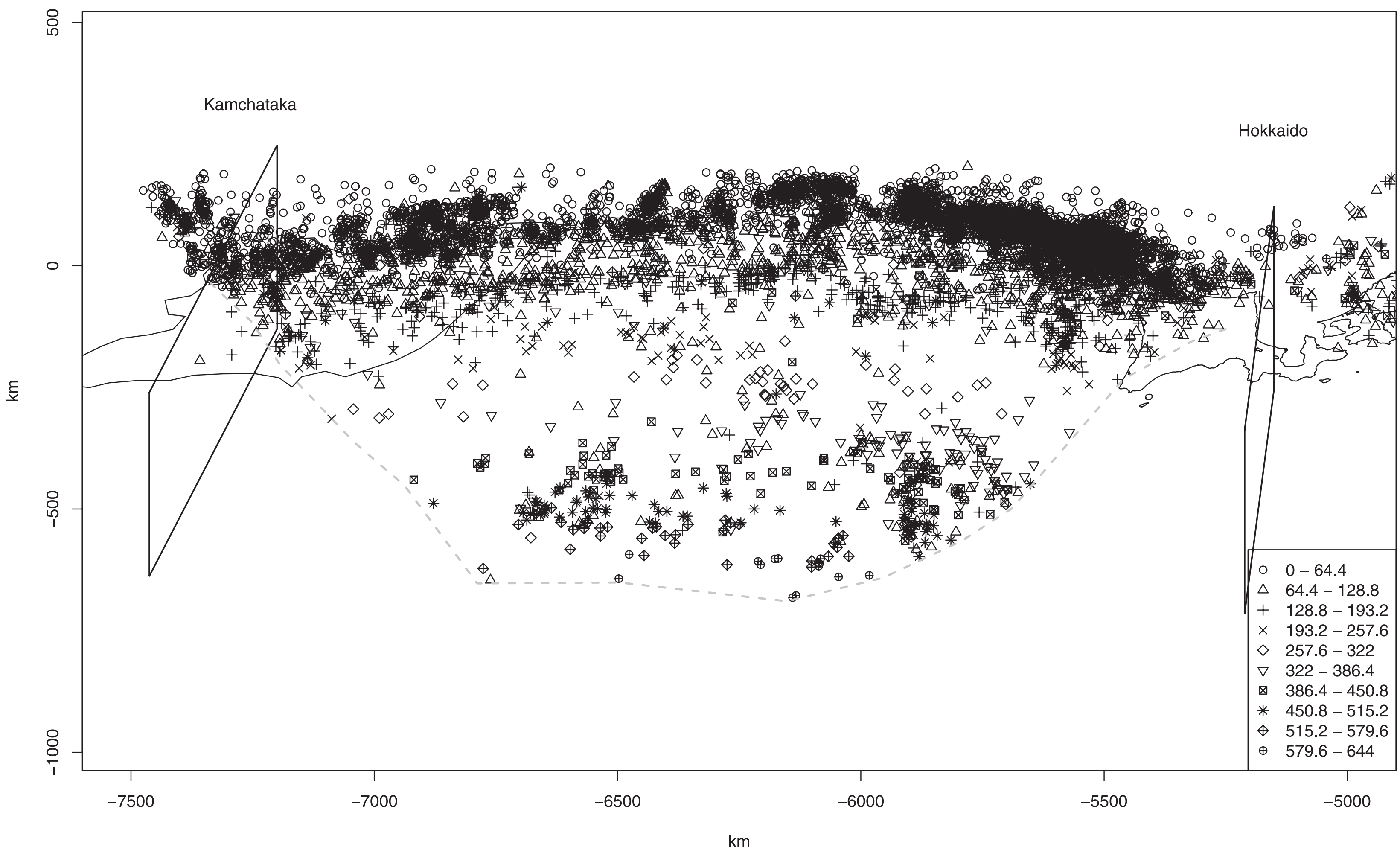

Figure 1. Seismicity from 1964–2006 rotated 49° about the 0 line x-axis. This projection shows the seismicity looking face on at the subduction zone. Events off the slab by more than 250 km are removed. Maps and rectangular markers of the cusps are also rotated and plotted in this projection. A dashed line outlines the lower extent of seismicity in the Kamchatka-Kurile subduction zone. Symbols represent the depths of events.

Mercator projection rotating the Kamchatka-Kurile arc so that the X-axis represents distance along the arc and the vertical axis is perpendicular to the arc in its center. Next we rotate the hypocenters by 49° to view the slab head on, as if standing in Magadan and looking into the earth at the subduction zone (Figure 1). In this view the pattern of seismicity shoaling towards the Kamchatka-Aleutian Cusp and the Kurile-Japan cusp is clear. It is remarkable how similar the edges of the plates appear in this view. Several explanations for the shape of the convex hull of Kamchatka hypocenters have been given [*Peyton et al.*, 2001; *Yogodzinski et al.*, 2001; *Levin et al.*, 2002b; *Park et al.*, 2002; *Lees et al.*, this volume] which relate to slab ablation or slab foundering as the Pacific plate thrusts into the mantle. Davaille and Lees [2004] modeled the contour of seismicity by invoking conduction and small scale convection and they suggested that the presence of the Meiji Seamounts have a considerable influence on the thickness of the slab in Kamchatka [*Lees et al.*, this volume]. Since there is no subducting seamounts in the Hokkaido cusp, however, it would be difficult to invoke this explanation for the southern shoaling of seismicity at the other end of the Kamchatka-Kurile slab. Indeed, shoaling of seismicity at cusps appears to be a common feature around the Pacific Rim [*Kirby et al.*, 1996].

There is a gap in seismicity that occurs between 200–300 km within the Kamchatka slab. This is a common observation in deep slabs around the world [*Kirby et al.*, 1996]. It is assumed that at around 300 km of depth dehydration embrittlement is diminished considerably and so seismicity decreases. Later, deeper earthquakes increase in numbers due to transformational faulting related to phase transitions in the deep part of the upper mantle. In Kamchatka, resumption of seismic activity starts at 400–500 km.

Alaska-Aleutian WBZ Seismicity

Due to the curvature of the arc, relative plate motions along the Aleutian trench vary from normal in the east to transform in the west. Coincident with this change, the maximum depth of seismicity changes from 250 km to 50 km from east to west, where the active volcanism diminishes (Plate 1, Figure 2). The along-strike variation in the maximum depth of seismicity can be explained thermally. It has been suggested that the slab extends at least a few hundred kilometers beneath the seismicity cut-off along the entire arc, including the western Aleutians. Most likely, the slab material exists, but no intermediate focus earthquakes are present because of initiation of high-temperature, steady-state creep [*Creager and Boyd*, 1991]. The alternative explanation is that the slab has been eroded and is simply no longer present in the western Aleutians [*Levin et al.*, 2005].

In the Aleutian arc, the slab seismicity below 100 km is characterized by dips that vary smoothly from shallow (45°) in the eastern Aleutians to steep (60°) in the central Aleutians and slightly shallower and less well resolved dip (~50°) in the far western Aleutians [*Davies and House*, 1979; *Boyd and Creager*, 1991].

The plate boundary in southern Alaska transitions from a transform boundary along the Fairweather-Queen Charlotte strike-slip fault to a convergent boundary along the Aleutian trench. However, the ongoing collision of the Yakutat block between these two regions complicates the interaction between the Pacific and North American plates. Stresses from the collision are transferred deep into the interior region of Alaska, resulting in an abundance of the crustal seismicity and active mountain building. In contrast, the transition from transform motion in the Komandorsky Islands to the convergent boundary in Kamchatka is relatively simple and crustal seismicity in Kamchatka is modest [*Gorbatov et al.*, 1997]. Analysis of the stress partitioning at this corner is discussed in detail by Geist and Scholl [1994].

FOCAL MECHANISMS AND STRESS STATE

The first systematic studies of earthquake focal mechanisms in Kamchatka were carried out in 1950–1960 [*Averianova*, 1969; *Stauder and Mualchin*, 1976]. In general, slabs act as stress guides with the dominant stress oriented in the down-dip direction. At depths shallower than 50 km, focal mechanisms of earthquakes along the convergent boundaries show predominately thrust faulting. It was observed in the Kurile arc that earthquakes with lower angle thrust mechanisms (<30°) span a short interval of only 30 km, or less, in depth. For deeper events, nodal planes steepen by ~10–15° [*Kao and Chen*, 1995]. The authors interpreted the steepening as a transition zone connecting interplate thrust with intermediate depth seismicity within the slab.

Christova [2001] investigated the depth distribution of stress in the Kamchatka slab by examining inversions of focal mechanisms [*Gephart and Forsyth*, 1984]. Christova found that in the shallow parts of the subduction zone (0–60 km) the stress was mostly uniform and conformed to the state expected for a convergent margin: the maximum stress nearly horizontal and normal to the strike of the slab, and the minimum stress in the downdip direction of the slab. In the deeper part of the subduction zone, however, there was considerable heterogeneity and downdip extension-compression was observed. The deepest part of the slab was found to be under down-dip compression, indicating that the slab encounters resistance as it descends into the lower mantle.

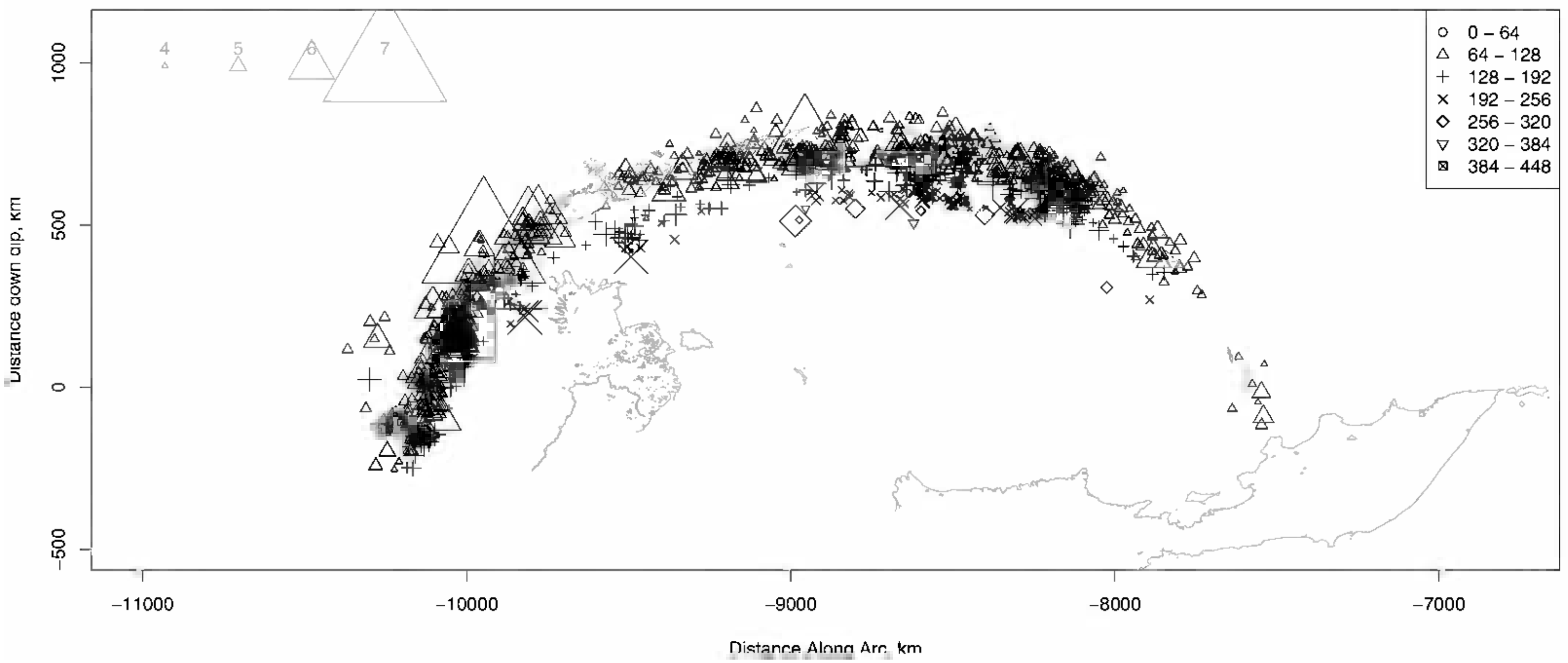

Figure 2. Seismicity plot for the Alaska-Aleutian arc, using an oblique Mercator projection, rotated about a horizontal line by 60º to show the relationship of seismicity down dip along the Aleutian Arc. Events are scaled by size where symbols represent depth levels below sea level. Seismicity in the central Aleutians dips more steeply than in Kamchatka-Kurile arc although does not penetrate nearly as deeply.

Gorbatov et al. [1997] used 21 Harvard CMT solutions to describe the stress state of the Kamchatka slab. He estimated the "thermal parameter" [*Kirby et al.*, 1996] in the Kamchatka seismic zone and found that the maximum depth of seismicity agrees with that predicted from global studies, except north of 55ºN where significant deviations occur near the northern terminus of the slab.

In the Aleutians, normal faulting events occur beneath the trench and in the outer rise, while shallow-angle underthrusting between the trench and the arc is observed, as expected (Plate 3).Thrusting events show steeper dip of inferred fault planes nearer to the arc. Events located near the trenchward edge of the main thrust zone have fault planes averaging ~15º [*House and Jacob*, 1983]. In the eastern Aleutians, Reyners and Coles [1982] found underthrusting for shallow seismicity (<50km). For intermediate depth, aside from the double zone complications, they identified down-dip extension, while the deepest events (200–250 km) showed down-dip compression. In Alaska, the stress regime within the slab is dominated by down-dip extension and along- strike compression [*Li et al.*, 1995; *Lu et al.*, 1997].

Lu and Wyss [1996] examined along-strike variations of the stress directions in the Alaska-Aleutian subduction zone determined through inversion of focal mechanisms of the earthquakes from the main thrust zone. They identified several boundaries across which the stress directions change. The identified boundaries correlate with ends of the aftershock zones of great ruptures and fracture zones.

In summary, for shallow WBZ (above 60 km) we observe thrust-type faulting with minimum stress (extension) oriented down-dip and maximum stress (compression) oriented in the direction of the plate convergence. This is consistent with the slab pull/ridge push dynamics. Stress patterns for the deepest earthquakes (below 200 km) indicate down-dip compression which can be explained by mantle resistance to slab descent. Stress dynamics within the intermediate depth range, however, vary along the arcs indicating that additional forces contribute to the slab dynamics, such as possible unbending forces (Kuriles and Kamchatka), specifics of the subduction zone geometry (Aleutians and Alaska), or material properties of the slab. For example, based on three-dimensional kinematic flow modeling, Creager and Boyd [1991] suggested that gravitational pull is equally strong throughout the Aleutians, producing a component of down-dip extension along the entire arc. However, in the central Aleutians the along-arc extension forced by the geometry of the arc dominates, resulting in along-arc extension and down-dip contraction. In southern Alaska, along-strike orientation of compressional stresses within the intermediate depth range was attributed to the curvature and bend of the slab [*Creager and Chiao*, 1992; *Lu et al.*, 1997]. These details are discussed in the next section.

DOUBLE SEISMIC ZONES

Since the discovery of a double seismic zone beneath the north-eastern Japan arc [*Umino and Hasegawa*, 1975], the search for a similar feature among other convergent zones became a target of many studies. Subsequently, double seismic zones identified on the basis of hypocenter distribution and spatial separation of different orientations of in-plane stresses in a given segment of the underthrust plate were reported for a number of subduction zones [*Fujita and Kanamori*, 1981]. In addition to the north-eastern Japan arc, for example, double seismic zones with down- dip compression in the upper zone and down-dip extension in the lower zone were found in Kamchatka [*Fedotov*, 1968; *Gorbatov et al.*, 1994], the Kuriles [*Veith*, 1977], and the central Aleutians [*Engdahl and Scholz*, 1977]. However, due to the complexity of the subduction process the above stress pattern is not common to all convergent zones. Several mechanisms—phase changes, bending-unbending of the slabs, sagging of the plate, and differential thermal stresses have been proposed to explain the formation of double seismic zones [*Lay*, 1994].

The first reports of double seismic zones in Kamchatka are attributed to Fedotov [1968]. Detailed further analyses supported the initial findings [*Fedotov et al.*, 1985; *Zobin*, 1990]. Kao and Chen [1995] used teleseismic earthquake data recorded between 1963 and 1991 to demonstrate that in central and northern Kuriles, the lower seismic zone starts at depths of ~70–80 km and extends down to 120–150 km. The separation between the zones is up to 40 km in the shallower part and down to 20 km at greater depths. The upper layer is under downdip compression and a lower layer is under downdip extension.

In Kamchatka, Gorbatov et al. [1994] analyzed regionally recorded earthquake data and demonstrated the existence of a double seismic zone with a stress regime identical to the Kurile case, i.e. upper sheet of compressional events and lower sheet of tensional events. The two planes of seismicity are separated by 40 km at a depth of 50 km, and by 10–15 km at 180 km depth below which the two seismic zones merge together. The Kamchatka double seismic zones are confined to between approximately 46–54ºN, and possibly extending to 56ºN.

In the central Aleutians beneath Adak, a double seismic zone has been observed using locally recorded earthquakes. There the lower plane begins at ~100 km, where the two planes are ~25 km apart, and merges into the upper plane at ~175 km depth. As in the double seismic zones in Kamchatka and the Kuriles, focal mechanisms in the upper plane are consistently down-dip compressional, while those in the lower plane are down-dip tensional [*Engdahl and Scholz*, 1977].

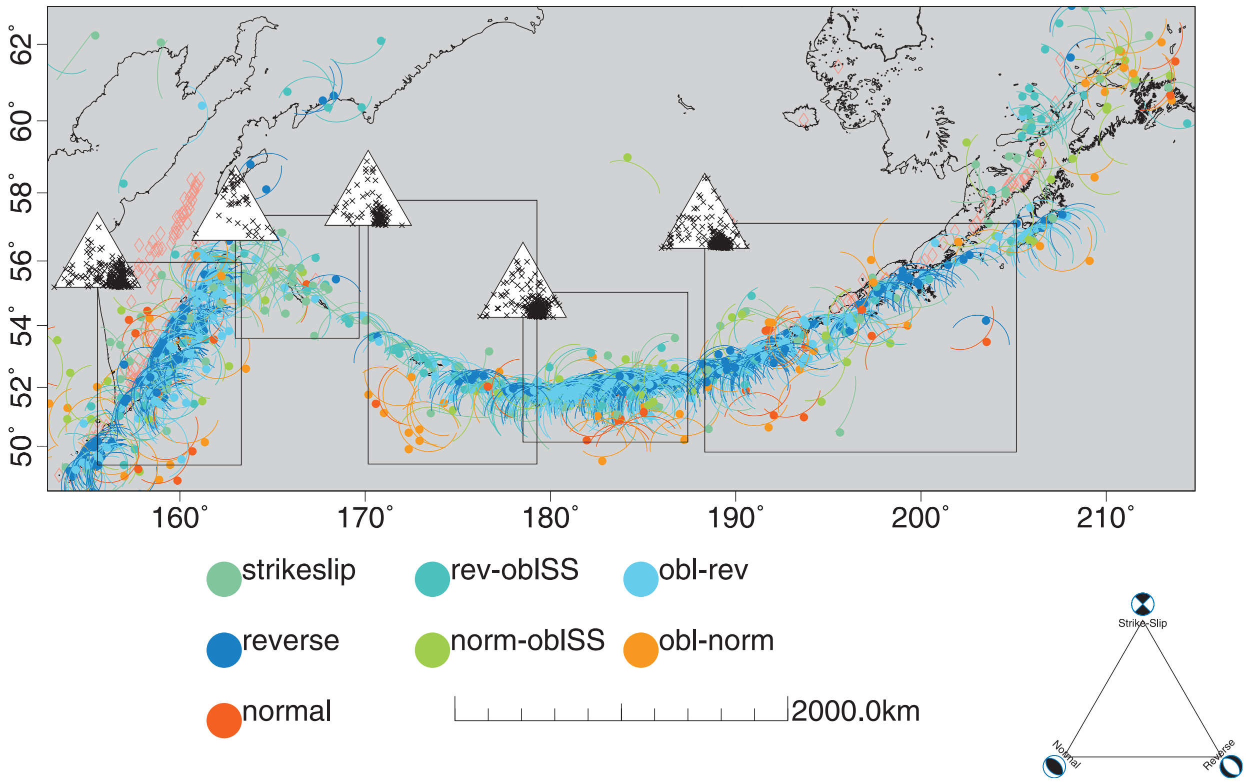

Plate 3. Focal mechanisms plotted as simple arcs and slip vector points. Groups of spatially related events are gathered and plotted on ternary plots [*Lees*, 2000] to show variations of focal mechanisms and stress along the arc moving from the Aleutians to Kamchatka. Note the predominantly strike-slip events in as the Aleutian arc approaches Kamchatka along the Bering fault.

Considerable attention has been paid to the Shumagin Islands region due to an identified seismic gap [*Sykes*, 1971; *McCann et al.*, 1979; *Davies et al.*, 1981]. A local seismic network was established there in 1973 and was operated by the Lamont-Doherty Observatory for 20 years. Based on data recorded by this network, a double seismic zone was also identified [*Reyners and Coles*, 1982; *House and Jacob*, 1983; *Hauksson et al.*, 1984; *Abers*, 1992]. The lower plane begins at ~65 km, where it is separated from the upper plane by ~25 km, and further down converges with the lower plane at ~120 km depth. The upper plane was found to be under down-dip tension. Results for the lower plane are inconclusive although they differ from the upper plane and appear to be consistent with the down-dip tension.

Ratchkovsky et al. [1997] identified a double seismic zone beneath central Cook Inlet in southern Alaska. The lower zone is separated from the upper one by 5–10 km and extends from a depth of 50 km to 90 km, where it merges into the upper zone. In the upper zone, the minimum principal stress is oriented down-dip. In the lower zone, both maximum and minimum principal stresses are rotated 40–60° from the down-dip direction. Below 80 km, the stresses are down-dip extensional. This is similar to the double zone observed in Shumagin Islands.

The double seismic zones identified in Kuriles, Kamchatka and the central Aleutians have similar stress patterns: the upper layer of compressional events and the lower layer of extensional events. This is the most common feature observed elsewhere in the world (e.g., Japan, Mariana Arc, Tonga Arc). This pattern is more easily explained by unbending forces acting within the slab. The double zones in Shumagin Islands and southern Alaska, however, are different. In these regions, both the upper and lower zones are under down-dip extension, with the lower layer still having distinctly different characteristics than the upper layer. Various forces and processes contribute to the slab dynamics. Depending on the geometry and material properties of the slab, some forces may overprint others. In the eastern Aleutians and southern Alaska the slab attains a higher degree of curvature than in central Aleutians and undergoes two distinct bends, a counterclockwise bend at around 59°N and a clockwise bend farther north at 63°N. This geometry apparently generates along-strike compressive stresses [*Creager and Chiao*, 1992]. It may be that this situation arises when along-strike compression overprints the compression within the upper layer of the double zone from unbending of the slab.

SEISMIC STRUCTURE AND TOMOGRAPHIC STUDIES

Kamchatka

Early tomographic analyses (three dimensional inversions) of seismic data in Kamchatka were examined mainly via global tomographic efforts [*van der Hilst et al.*, 1993]. Later in the 1990's Gorbatov et al. [1999] used extensive regional catalogues and global ISC data for inversions of P-wave anomalies. The authors later extended their inversion analyses over a wider range of the Western Pacific and interpreted high velocity anomalies as remnant slabs abandoned in the mantle [*Gorbatov et al.*, 2000]. In 1998–1999 a US-Russian team of investigators installed a temporary array of 15 stations [*Lees et al.*, 2000] extending from the southern tip of Kamchatka to as far north as Korf. The target of this study was to image the edge of the northern terminus of the Kamchatka slab, mainly north of 56°N. These data were used to investigate SKS shear wave splitting [*Peyton et al.*, 2001], dispersion of S-waves [*Levin et al.*, 2002b], receiver functions [*Levin et al.*, 2002a] and propagation of P-waves in the subduction zone [*Lees et al.*, this volume]. Shear wave splitting studies show strong support for mantle flow around the northern edge of the Kamchatka plate, confined to depths below the slab [*Peyton et al.*, 2001; *Russo and Lees*, 2005]. Waves that travel above the slab in the mantle wedge also show evidence of shear wave splitting [*Levin et al.*, 2004a] but not clear patterns of trench parallel mantle flow. In the Kamchatka-Aleutians corner, however, fast polarizations are distorted indicating significant tectonic deformation [*Levin et al.*, 2004b].

Alaska and the Aleutians

A number of tomographic studies used regional seismic data to constrain extent and properties of the subducting plate beneath Alaska [*Kissling and Lahr*, 1991; *Zhao et al.*, 1995; *Searcy*, 1996; *Eberhart-Phillips et al.*, 2006]. These studies were primarily based on data from regional seismic arrays, and inferred the subducting Pacific plate to be 45–55 km thick with a P-wave velocity 3–6% higher than that of the surrounding mantle. The BEAAR deployment in south-central Alaska provided a high quality dataset that included use of both regional and teleseismic earthquake records to delineate crustal thickness and study detailed properties of the subducted plate and mantle beneath the Alaska Range [*Meyers et al.*, 2000; *Ferris et al.*, 2003; *Stachnik et al.*, 2004].

In the Aleutians, shallow slab structure (<60 km) has been investigated via active source seismic soundings [*Abers*, 1994; *Fliedner and Klemperer*, 1999; *Shillington et al.*, 2004; *Van Avendonk et al.*, 2004]. As the Aleutian Islands are remote and isolated, it is difficult to establish a spatially distributed seismic array without significant ocean bottom seismometry. Therefore the regional tomographic inversion approach used on Kamchatka and Alaska are not available for intermediate to deep imaging in the Aleutians. Deep imaging of seismic velocity in the north Pacific was investigated using global earthquake catalogues [*Gorbatov et al.*, 2000], although this study may suffer from significant errors in the general earthquake catalogues. Gorbatov et al. [2000] found high velocity perturbations associated with the Pacific slab extending to 400 km depth although significantly differentiated from deeper high velocity anomalies at 600 km depth where a high velocity is observed to flatten. This was interpreted as a possible remnant slab. In the western Aleutians the Wadati-Benioff zone does not show a significant high velocity slab signature at intermediate depths, although the 600 km perturbation appears to be evident. A study of shear wave speeds using surface wave dispersion [*Levin et al.*, 2005] suggests there is a slab portal in the western Aleutians separating the end of the Wadati-Benioff zones of the Aleutians with Kamchatka. This model agrees with earlier models describing such a slab window [*Peyton et al.*, 2001; *Yogodzinski et al.*, 2001; *Levin et al.*, 2002b; *Lees et al.*, this volume].

CONCLUSIONS

The Alaska-Aleutian and Kamchatka-Kurile arcs comprise one of the longest subduction complexes in the world. Seismicity extends from the trench to 200–300 km deep in the Aleutians. From the central Aleutians earthquakes shoal moderately towards Buldir Island in the western Aleutians where shallow strike slip faulting extends along the Bering fault system to the west. At the collision zone where the Aleutians intersect with Kamchatka, seismicity becomes complicated by collision tectonics. In the Kamchatka-Kurile region earthquakes extend to at least 600 km depth, although a gap in earthquake density is observed between 200–300 km depth. Shoaling of seismicity at both the northern and southern ends of the Kamchatka-Kurile subduction zone has been interpreted as slab erosion. The stress regime within the downgoing slabs varies along the arcs and is controlled by geometry, material properties and thermal structure of the respective slabs. In Kamchatka–Kurile the subducting oceanic plate is much older than in the Aleutians and is therefore colder and thicker. This contrast accounts for the relative differences in seismic density and depth between the two subduction zones.

Five out of the ten largest earthquakes recorded in the world occurred in the North Pacific region. These events not only caused wide-spread damage in nearby population centers, but also generated devastating Pacific-wide tsunamis. In the Kuriles, Kamchatka and Aleutians we also see major earthquakes (M=7–8) occurring within the rupture zones of the mega-earthquakes (M>~8.5). These events may represent minor stress adjustments to continued plate motion and increasing deformation of the locked zone, but do not represent complete rupture of the main asperities. It is important, therefore, to understand the mechanics of these events in order to mitigate future seismic and tsunami hazards. The history, geometry, hypocenter distribution and stress release of the subducting Pacific plate all play a significant role in the evolution of the plate boundary and seismic potential of the Northern Pacific.

Acknowledgements. We thank Dr. Doug Christensen, an anonymous reviewer, and editor Dr. John Eichelberger for thoughtful reviews and suggestions that improved the manuscript. Support for work on this paper was in part provided by the Office of the State Seismologist of Alaska and the Geophysical Institute, University of Alaska Fairbanks (N.A.R.) and by NSF grants EAR-9614639 and EAR 0337462 (J.M.L.).

REFERENCES

Abers, G. A., Relationship between shallow- and intermediate-depth seismicity in the eastern Aleutian subduction zone, *Geophys. Res. Lett., 19*, 2019–2022, 1992.

Abers, G. A., Three-dimensional inversion of regional P and S arrival times in the East Aleutians and sources of subduction zone gravity highs, *J. Geophys. Res., 99*, 4395–4412, 1994.

Averianova, V. N., *Detailed characteristics of seismic foci of the Far Eastern Region*, Nauka, Moscow, 192 pp., 1969.

Balakina, L. M., The Urup earthquake of October 13, 1963 (M~8.4–8.5) in the lithosphere beneath the Kurile Island Arc, *Physics of Solid Earth, 25*, 781–792, 1990.

Beck, S. L., and D. H. Christensen, Rupture process of the February 4, 1965, Rat Islands earthquake, *J. Geophys. Res., 96*, 2205–2221, 1991.

Beck, S. L., and L. J. Ruff, Rupture process of the great 1963 Kurile Islands earthquake sequence: Asperity interaction and multiple event rupture, *J. Geohpys. Res., 92*, 14123–14138, 1987.

Ben-Menahem, A., and M.N. Toksoz, Source mechanism from spectra of long-period surface waves, 2. The Kamchatka Earthquake of November 4, *J. Geophys. Res., 68*, 5207–5222, 1963.

Boyd, T. M., and K. C. Creager, The geometry of Aleutian subduction: Three-dimensional seismic imaging, *J. Geophys. Res., 96*, 2267–2291, 1991.

Christensen, D. H., and S. L. Beck, The rupture process and tectonic implications of the Great 1964 Prince William Sound earthquake, *Pure Appl. Geophys., 142*, 29–53, 1994.

Christova, C., Depth distribution of stresses in the Kamchatka Wadati-Benioff zone inferred by inversion of earthquake focal mechanisms, *J. Geodyn., 31*, 355–372, 2001.

Combellick, R. A., and R. D. Reger, Evaluation of Holocene subsidence events in Cook Inlet estuarine flats near Anchorage, Alaska, as a basis for assessing seismic hazard in southcentral Alaska, in *U.S. Geol.Surv. Open-File Rep. 88–434*, 463–464, 1988.

Creager, K. C., and T. M. Boyd, The geometry of Aleutian subduction: Three-dimensional kinematic flow model, *J. Geophys. Res., 96*, 2293–2307, 1991.

Creager, C., and L. Y. Chiao, Membrane deformation rate and geometry of Aleutian Alaska subduction, in *Wadati Conference* *on Great Subduction Earthquakes*, edited by D. Christensen, M. Wyss, R.E. Habermann, and J. Davies, Univ. of Alaska, Fairbanks, 27 pp., 1992.

Dalrymple, G. B., D. A. Clague, and M. A. Lanphere, Revised age for Midway volcano, Hawaiian volcanic chain, *Earth Planet. Sci. Lett., 37*, 107–116, 1977.

Davaille, A., and J. M. Lees, Thermal modeling of subducted plates: tear and hot spot at the Kamchatka corner, *Earth Planet. Sci. Letts., 226*, *DOI:10.1016/j.epsl.2004.07.024*, 293–304, 2004.

Davies, J. N., and L. House, Aleutian subduction zone seismicity, volcano-trench separation, and their relation to great thrust-type earthquakes, *J. Geophys. Res., 84*, 4583–4591, 1979.

Davies, J. N., L. Sykes, L. House, and K. Jacob, Shumagin seismic gap, Alaska Peninsula: History of great earthquakes, tectonic setting, and evidence for high seismic potential, *J. Geophys. Res., 86*, 3821–3855, 1981.

DeMets, C., Oblique convergence and deformation along the Kurile and Japan trenches, *J. Geophys. Res., 97*, 17615–17625, 1992.

DeMets, C., R.G. Gordon, D.F. Argus, and S. Stein, Effects of recent revisions to the geomagnetic reversal time scale on estimates of current plate motions, *Geophys. Res. Lett., 21*, 2191–2194, 1994.

Eberhart-Phillips, D., D.H. Christensen, T.M. Brocher, R. Hansen, N.A. Ruppert, P.J. Haeussler, and G.A. Abers, Imaging the transition from Aleutian subduction to Yakutat collision in central Alaska, with local earthquakes and active source data, *J. Geophys. Res., 11*, *doi:10.1029/ 2005JB004240*, 2006.

Engdahl, E.R., and C.H. Scholz, A double Benioff zone beneath the central Aleutians: An unbending of the lithosphere, *Geophys. Res. Lett., 4*, 473–476, 1977.

Fedotov, S.A., O zakonomernostyah raspredeleniya sil'nyh zemletryaseniy Kamchatki, Kuril'skih ostrovov i severo-vostochnoy Japonii (Systemic distribution of strong earthquakes in Kamchatka, Kurile Islands and north-eastern Japan), in *Seismcheskoye Rayonirovanie (Seismic zoning)*, Institute of Physics of Earth, USSR Academy of Sciences, Nauka, Moscow, 66–93, 1965 (in Russian).

Fedotov, S. A., O seismicheskom tsikle, seismicheskom rayonirovanii, i dolgosrochnom prognozirovanii zemletryaseniy (Seismic cycle, seismic zoning, and long-term seismic forecast), in *Seismicheskoe Rayonirovanie (Seismic Zoning)*, Institute of Physics of Earth, USSR Academy of Sciences, Nauka, Moscow, 121–150,1968 (in Russian).

Fedotov, S. A., and P. I. Tokarev, Earthquakes, characteristics of the upper mantle under Kamchatka, and their connection with volcanism (according to data collected up to 1971), *Bulletin Volcanologique, 37*, 245–257, 1974.

Fedotov, S. A., A. A. Gusev, G. V. Chernysheva, and L.S. Shumilina, The seismofocal zone of Kamchatka; geometry, distribution of the earthquake foci and relationships with volcanism, *Vulkanologiya i Seysmologiya, 1985-4*, 91–107, 1985 (in Russian).

Ferris, A., G. A. Abers, D. H. Christensen, and E. Veenstra, High resolution image of the subducted Pacific (?) plate beneath central Alaska, 50–150 km depth, *Earth Planet. Sci. Lett., 214*, 575–588, 2003.

Fliedner, M., and S. L. Klemperer, Structure of an island-arc: wide-angle seismic studies in the eastern Aleutian Islands, Alaska, *J. Geophys. Res., 104*, 10667–10694, 1999.

Fujita, K., and H. Kanamori, Double seismic zones and stresses of intermediate depth earthquakes, *Geophys. J. R. Astr. Soc., 66*, 131–156, 1981.

Geist, E. L., J. R. Childs, and D. W. Scholl, The origin of Summit basins of the Aleutian Ridge: Implications for block rotation of an arc massif, *Tectonics, 7*, 327–342, 1988.

Geist, E. L., and D. W. Scholl, Large-scale deformation related to the collision of the Aleutian arc with Kamchatka, *Tectonics, 13*, 538–560, 1994.

Gephart, J. W., and D. W. Forsyth, An improved method for determining the regional stress tensor using earthquake focal mechanism data; application to the San Fernando earthquake sequence, *J. Geophys. Res., 89*, 9305–9320, 1984.

Gorbatov, A., G. Suarez, V. Kostoglodov, and E. Gordeev, A double-planed seismic zone in Kamchatka from local and teleseismic data, *Geophys. Res. Lett., 21*, 1675–1678, 1994.

Gorbatov, A., V. Kostoglodov, S. Gerardo, and E. Gordeev, Seismicity and structure of the Kamchatka subduction zone, *J. Geophys. Res., 102*, 17883–17898, 1997.

Gorbatov, A., J. Dominguez, G. Suarez, V. Kostaglodov, D. Zhao, and E. Gordeev, Tomographic imaging of P wave velocity structure beneath Kamchatka Peninsula, *Geophys. J. Int., 137*, 269–279, 1999.

Gorbatov, A., A. Widiyantoro, Y. Fukao, and E. Gordeev, Signature of remnant slabs in the North Pacific from P-wave tomography, *Geophys. J. Int., 142*, 27–36, 2000.

Haeussler, P., and G. Plafker, Earthquakes in Alaska, *U.S. Geol. Surv. Open-File Rep., 95–624*, 2003.

Hamilton, S., I. Shennan, R. Combellick, Mulholland, J., and Noble, C., Evidence for two great earthquakes at Anchorage, Alaska and implications for multiple great earthquakes through the Holocene, *Quaternary Sci. Rev., 24*, 2050–2068, 2005.

Hauksson, E., J. Armbruster, and S. Dobbs, Seismicity patterns (1963–1983) as stress indicators in the Shumagin seismic gap, Alaska, *Bull. Seism. Soc. Am., 74*, 2541–2558, 1984.

House, L. S., and K. H. Jacob, Earthquakes, plate subduction, and stress reversals in the Eastern Aleutian Arc, *J. Geophys. Res., 88*, 9347–9373, 1983.

Johnson, J. M., Y. Tanioka, L. J. Ruff, K. Satake, H. Kanamori, and L.R. Sykes, The 1957 great Aleutian earthquake, *Pure Appl. Geophys., 142*, 3–28, 1994.

Johnson, J. M., K. Satake, S. R. Holdahl, and J. Sauber, The 1964 Prince William Sound earthquake: Joint inversion of tsunami and geodetic data, *J. Geophys. Res., 101*, 523–532, 1996.

Johnson, J. M., and K. Satake, Asperity distribution of the 1952 Great Kamchatka earthquake and its relation to future earthquake potential in Kamchatka, *Pure Appl. Geophys., 154*, 541–553, 1999.

Kanamori, H., The Alaska earthquake of 1964: Radiation of long-period surface waves and source mechanism, *J. Geophys. Res., 75*, 5029–5040, 1970a.

Kanamori, H., Synthesis of long-period surface waves and its application to earthquake source studies - Kurile Islands earthquake of October 13, 1963, *J. Geophys. Res., 75*, 5011–5027, 1970b.

Kanamori, H., Re-examination of the Earth's free oscillations excited by the Kamchatka earthquake of November 4, 1952, *Phys. Earth Planet. Int., 11*, 216–226, 1976.

Kanamori, H., Seismic and aseismic slip along subduction zones and their tectonic implications, in *Island Arcs, Deep Sea Trenches and Back-arc Basins*, edited by M. Talwani and W.C. Pitman, Maurice Ewing Series, 1, 163–174, 1977.

Kanamori, H., The nature of seismicity patterns before large earthquakes, in *Maurice Ewing Series, 4*, edited by D.W. Simpson, and P.G. Richards, 1–19, 1981.

Kao, H., and W. P. Chen, Transition from interplate slip to double seismic zone along the Kuril- Kamchatka arc, *J. Geophys. Res., 100*, 9881–9903, 1995.

Kelleher, J.A., Space-time seismicity of the Alaska-Aleutian seismic zone, *J. Geophys. Res., 75*, 5745–5756, 1970.

Kikuchi, M., and Y. Fukao, Inversion of long-period P-waves from great earthquakes along subduction zones, *Tectonophysics, 144*, 231–247, 1987.

Kirby, S.H., S. Stein, E. Okal, and D.C. Rubie, Metastable mantle phase transformations and deep earthquakes in subducting oceanic lithosphere, *Rev. Geophys., 34*, 261–306, 1996.

Kissling, E., and J.C. Lahr, Tomographic image of the Pacific Slab under southern Alaska, *Eclogae Geol. Helv, 84*, 297–315, 1991.

Krasheninnikov, S.P., *Opisaniya Zemli Kamchatki (Description of the land of Kamchatka)*, Russian Academy of Sciences, Moscow, 1949 (in Russian).

Kuzin, I.P., L.I. Lobkovsky, and O.N. Solovjova, Characteristics of seismicity in the central Kurile region, *Izvestia, Phys. Solid Earth, 37*, 464–473, 2001.

Lahr, J.C., *Detailed seismic investigation of Pacific-North American plate interaction in southern Alaska*, Ph. D. thesis, Columbia University, New York, 1975.

Larson, K. M., and M. Lisowski, Strain accumulation in the Shumagin Islands: Results of initial GPS measurements, *Geophys. Res. Lett., 21*, 489–192, 1994.

Lay, T., H. Kanamori, and L. Ruff, The asperity model and the nature of large subduction zone earthquakes, *Earthquake Prediction Research, 1*, 3–71, 1982.

Lay, T., Seismological constraints on the velocity structure and fate of subducting lithospheric slabs: 25 years of progress, in *Advances in Geophysics*, 35, edited by R. Dmowska and B. Saltzman, Academic Press, Inc., 185 pp., 1994.

Lees, J. M., Geotouch: Software for three and four dimensional GIS in the Earth Sciences, *Computers & Geosciences, 26*, 751–761, 2000.

Lees, J. M., M. Brandon, J. Park, V. Levin, A. Ozerov, and E. Gordeev, Kamchatka: Edge of the plate, *IRIS News Letter, 2000*, 17–19, 2000.

Lees, J. M., J. VanDecar, E. Gordeev, A. Ozerov, M. Brandon, J. Park, and V. Levin, Three dimensional images of the Kamchatka-Pacific plate cusp, in *AGU Monograph: Volcanism and Tectonics of the Kamchatka Peninsula and Adjacent Arcs*, edited by J. Eichelberger, P. Izbekov, M. Kasahara, J. Lees, and E. Gordeev, this volume.

Levin, V., J. Park, M. Brandon, J. M. Lees, V. Peyton, E. Gordeev, and A. Ozerov, Crust and upper mantle of Kamchatka from teleseismic receiver functions, *Tectonophysics*, *358*, 233–265, 2002a.

Levin, V., N. Shapiro, J. Park, and M. Ritzwoller, Seismic evidence for catastrophic slab loss beneath Kamchatka, *Nature, 418*, 763– 767, 2002b.

Levin, V., D. Droznin, J. Park, and E. Gordeev, Detailed mapping of seismic anisotropy with local shear waves in southeastern Kamchatka, *Geophys. J. Int., 158*, 1009–1023, 2004a.

Levin, V., D. Droznin, J. Park, and E. Gordeev, Mantle wedge anisotropy beneath southeastern Kamchatka from local-S birefringence, *Geophys J. Int., 158*, 1009–1023, 2004b.

Levin, V., N. Shapiro, J. Park, and M. Ritzwoller, Slab portal beneath the western Aleutians, *Geology, 33*, 253–256, 2005.

Li, Z., N. Biswas, G. Tytgat, H. Pulpan, and M. Wyss, Stress directions along the Alaska Wadati- Benioff zone from inversion of focal mechanism data, *Tectonophysics, 246*, 163–170, 1995.

Lisowski, M., J.C. Savage, W.H. Prescott, and W.K. Gross, Absense of strain accumulation in the Shumagin seismic gap, Alaska, 1980–1987, *J. Geophys. Res., 93*, 7909–7922, 1988.

Lonsdale, P., Paleogene history of the Kula plate: offshore evidence and onshore applications, *Geol. Soc. Am. Bull., 100*, 733–754, 1988.

Lu, Z., and M. Wyss, Segmentation of the Aleutian plate boundary derived from stress direction estimates based on fault plane solutions, *J. Geophys. Res., 101*, 803–816, 1996.

Lu, Z., M. Wyss, and H. Pulpan, Details of stress directions in the Alaska subduction zone from fault plane solutions, *J. Geophys. Res., 192*, 5385–5402, 1997.

McCann, W. R., S. P. Nishenko, L. R. Sykes, and J. Krause, Seismic gaps and plate tectonics: seismic potential for major boundaries, *Pure Appl. Geophys., 117*, 1082–1147, 1979.

Meyers, E. V., D. H. Christensen, G. A. Abers, J. C. Stachnik, A. R. Holland, and K. B. Beebe, Broadband (Seismic) Experiment Across the Alaska Range (BEAAR) to determine the crustal and upper mantle structure beneath central Alaska, *Eos Trans. Am. Geophys. Union, 81*, F877, 2000.

Nanayama, F., K. Satake, R. Furukawa, K. Shimokawa, B. F. Atwater, K. Shigeno, and S. Yamaki, Unusually large earthquakes inferred from tsunami deposits along the Kurile trench, *Nature, 424*, 660–663, 2003.

Nishenko, S. P., and K. H. Jacob, Seismic potential of the Queen Charlotte-Alaska-Aleutian seismic zone, *J. Geophys. Res., 95*, 2511–2532, 1990.

Park, J., V. Levin, M. Brandon, J. Lees, V. Peyton, E. Gordeev, and A. Ozerov, A dangling slab, amplified arc volcanism, mantle flow and seismic anisotropy in the Kamchatka plate corner, in *Plate Boundary Zones*, *Geodynamic Series, 30*, edited by S. Stein, and J. Freymueller, 295– 324, 2002.

Peterson, E. T., and T. Seno, Factors affecting seismic moment release rates in subduction zones, *J. Geophys. Res., 89*, 10233–10248, 1984.

Peyton, V., V. Levin, J. Park, M. Brandon, J. Lees, E. Gordeev, and A. Ozerov, Mantle flow at a slab edge: Seismic anisotropy in the Kamchatka region, *Geophys. Res. Lett., 28*, 379–382, 2001.

Pinegina, T. K., J. Bourgeois, L.I. Bazanova, I.V. Melekestsev, and O.A. Braitseva, A millennial- scale record of Holocene tsunamis on the Kronotsky Bay coast, Kamchatka, Russia, *Quaternary Res., 59*, 36–47, 2003.

Plafker, G., Tectonics of the March 27, 1964, Alaska Earthquake, *U.S. Geol. Surv. Professional Paper, 543-I*, 1964.

Plafker, G., Geologic studies related to earthquake potential and recurrence in the "Yakataga seismic gap", *U.S. Geol. Surv. Open-File Rep. 86-92*, 135–143, 1986.

Ratchkovsky, N. A., J. Pujol, and N. Biswas, Stress pattern in the double seismic zone beneath Cook Inlet, south-central Alaska, *Tectonophysics, 281*, 163–172, 1997.

Reyners, M., and K. S. Coles, Fine structure of the dipping seismic zone and subduction mechanics in the Shumagin islands, Alaska, *J. Geophys. Res., 87*, 356–366, 1982.

Ruff, L., and H. Kanamori, Seismicity of the subduction process, *Phys. Earth Planet. Inter., 23*, 240–252, 1980.

Russo, R. M., and J. M. Lees, Seismic anisotropy beneath Pacific ocean lithosphere subducted at Kamchatka, *Eos Trans. Am. Geophys. Union, T23A-0531*, 2005.

Savarensky, E. F., V. G. Tischenko, A. E. Svyatlovsky, A.D. Dobrovolsky, and A.V. Zhivago, Tsunami of November 4–5 1952, *Bulluten of the Seismology Council, Russia, 4*, 1958 (in Russian).

Schwartz, S. Y., and L. J. Ruff, Asperity distribution and earthquake occurrence in the southern Kurile Islands arc, *Phys. Earth Planet. Inter., 49*, 54–77, 1987.

Searcy, C.K., *Crustal and upper mantle velocity structure in Alaska*, Ph.D. thesis, University of Alaska, Fairbanks, 1996.

Shillington, D. J., H. J. A. V. Avendonk, W. S. Holbrook, P. B. Kelemen, and M. J. Hornbach, Composition and structure of the central Aleutian island arc from arc-parallel wide-angle seismic data, *Geochem. Geophys. Geosyst., 5, DOI:10.1029/2004GC000715*, 2004.

Solovjov, S. L., *Zemletryaseniya i tsunami 13 i 20 oktyabrya 1963 g. na Kurilskih ostrovah (Kurile Islands earthquakes and tsunamis of October 13 and 20, 1963)*, Siberian Branch of the Soviet Academy of Sciences, Yuzhno-Sakhalinsk, 1965 (in Russian).

Stachnik, J. C., G. Abers, and D. H. Christensen, Seismic attenuation and mantle wedge temperatures in the Alaska subduction zone, *J. Geophys. Res., 109, DOI:10.1029/2004JB003018*, 2004.

Stauder, W., and L. Mualchin, Fault motion in the larger earthquakes of the Kurile-Kamchatka arc and the Kurile-Hokkaido corner, *J. Geophys. Res., 81*, 1976.

Sykes, L. R., Aftershock zones of great earthquakes, seismicity gaps, and earthquake prediction for Alaska and the Aleutians, *J. Geophys. Res., 76*, 8021–8041, 1971.

Tanioka, Y., and F. I. Gonzalez, The Aleutian earthquake of June 10, 1996 (Mw 7.9) ruptured parts of both the Andreanof and Delarof segments, *Geophys. Res. Lett., 25*, 2245–2248, 1998.

Tarakanov, P. Z., Povtornye tolchki zemletryaseniya 4 noyabrya 1952 g. (Aftershocks of the November 4, 1952 earthquake), in *Publications of Sakhalin Complex Research Institute*, Siberian Branch of Soviet Academy of Sciences, Yuzhno-Sakhalinsk, 1961 (in Russian).

Tobin, D. G., and L. R. Sykes, Seismicity and tectonics of the northeast Pacific Ocean, *J. Geophys. Res., 73*, 3821–3845, 1968.

Umino, N., and A. Hasegawa, On the two-layered structure of deep seismic plane in northeastern Japan arc, *Zisin, 27*, 125–139, 1975 (in Japanese).

Van Avendonk, H. J. A., D. J. Shillington, W. S. Holbrook, and M. J. Hornbach, Inferring crustal structure in the Aleutian island arc from a sparse wide-angle seismic data set, *Geochem. Geophys. Geosyst., 5, DOI:10.1029/2003GC000664*, 2004.

Van der Hilst, R. D., E. R. Engdahl, and W, Spakman, Tomographic inversion of P and pP data for aspherical mantle structure below the Northwest Pacific region, *Geophys. J. Int., 115*, 264–302, 1993.

Van Wormer, J. D., J. Davies, and L. Gedney, Seismicity and plate tectonics in south central Alaska, *Bull. Seism. Soc. Am., 64*, 1467–1475, 1974.

Veith, K. F., The nature of the dual zone of seismicity in the Kuriles arc, *Trans. Am. Geophys. Un., 58*, 1232, 1977.

Wallace, W. K., and D. C. Engebreston, Relationships between plate motions and Late Cretaceous and Paleogene magnetism in southwestern Alaska, *Tectonics, 3*, 295–315, 1984.

Wiemer, S. and M. Wyss, Minimum magnitude of completeness in earthquake catalogs: Examples from Alaska, the Western United States and Japan, *Bull. Seis. Soc. Am., 90*, 859–869, 2000.

Wyss, M., and J. N. Brune, The Alaska earthquake of 28 March 1964: A complex multiple rupture, *Bull. Seism. Soc. Am., 57*, 1017–1023, 1967.

Yogodzinski, G. M., J. M. Lees, T. G. Churikova, F. Dorendorf, G. Woerner, and O. N. Volynets, Geochemical evidence for the melting of subducting oceanic lithosphere at plate edges, *Nature, 409*, 500–504, 2001.

Zhao, D., D. Christensen, and H. Pulpan, Tomographic imaging of the Alaska subduction zone, *J. Geophys. Res., 100*, 6487–6504, 1995.

Zobin, V. M., Earthquake focal mechanisms and seismotectonic deformation in the Kamchatka- Commander region, *J. Geodynamics, 12*, 1–19, 1990.

Zobin, V. M., and V. I. Levina, The rupture process of the Mw 7.8 Cape Kronotsky, Kamchatka, earthquake of 5 December 1997 and its relationship to foreshocks and aftershocks, *Bull. Seis. Soc. Am., 91*, 1619–1629, 2001.

Zweck, C., J. T. Freymueller, and S. C. Cohen, Three-dimensional elastic dislocation modeling of the postseismic response to the 1964 Alaska earthquake, *J. Geophys. Res., 107, 10.1029/2001JB000409*, 2002.

Natalia A. Ruppert, Geophysical Institute, University of Alaska Fairbanks, 903 Koyukuk Drive, PO Box 757320, Fairbanks, AK 99775, USA

Jonathan M. Lees, The University of North Carolina at Chapel Hill, Department of Geological Sciences, Campus Box 3315, Chapel Hill, NC 27599-3315, USA

Natalia P. Kozyreva, Kamchatka Division of Russian Geophysical Survey, 9 Piip Blvd., Petroparlovsk-Kamchatsky, 683006, Russia

Recurrence of Recent Large Earthquakes Along the Southernmost Kurile-Kamchatka Subduction Zone

Yuichiro Tanioka

Institute of Seismology and Volcanology, Hokkaido University, Japan

Kenji Satake

Active Fault Research Center, National Institute of Advanced Industrial Science and Technology (AIST), Japan

Kenji Hirata

Institute for Research on Earth Evolution, Japan Agency for Marin-Earth Science and Technology, Japan

Recurrent large earthquakes in the southernmost part of the Kurile-Kamchatka subduction zone were studied. Previous studies have indicated that the 1994 Sanriku-oki earthquake (Mw 7.8) ruptured only the southern part of the rupture area of the 1968 Tokachi-oki earthquake (Mw 8.2), and left the main rupture interface of the 1968 earthquake intact. Also, the 2003 Tokachi-oki earthquake (Mw 8.1) did not rupture the eastern part of the rupture area of the 1952 Tokachi-oki earthquake (Mw 8.2).

The rupture processes of the 1973 and 1894 Nemuro-oki earthquakes were studied through tsunami waveform analyses. The rupture of the 1973 Nemuro-oki earthquake was concentrated on the plate interface off Nemuro, Hokkaido, and the seismic moment was estimated to be 6.5×10^{20} Nm (Mw 7.8). The 1894 Nemuro-oki earthquake ruptured much larger area than that of the 1973 Nemuro-oki earthquake. The fault length of the 1894 earthquake was about 200 km, and the seismic moment was 28.8×10^{20} Nm (Mw 8.3). In this subduction zone, none of three sets of recent recurrent large earthquakes, the 1968 Tokachi and 1994 Sanriku-oki earthquakes, the 1952 and 2003 Tokachi-oki earthquakes, and the 1894 and 1973 Nemuro-oki earthquakes, have the same rupture processes. Variable rupture patterns of large recurrent earthquakes make it difficult to estimate the source processes of future large earthquakes in this subduction zone. These non-regular recurrences also suggest that, in addition to invariant geometric and material heterogeneities, the dynamic stress heterogeneities are seen to be important for understanding large earthquake complexity in this subduction zone.

Volcanism and Subduction: The Kamchatka Region
Geophysical Monograph Series 172

10.1029/172GM13

1. INTRODUCTION

Many large earthquakes have occurred in the Kurile-Kamchatka region due to subduction of the Pacific plate along the Kurile trench. In this paper, we concentrate on the southernmost part of the Kurile-Kamchatka subduction zone. Figure 1 shows two recent sequences of large underthrusting earthquakes that have ruptured the plate interface along the southern part of the Kurile subduction zone. The southern end of the plate interface was ruptured by the 1968 Tokachi-oki earthquake, and then the 1994 Snariku-oki earthquakes occurred in the same area 26 years later. The plate interface off Tokachi in Hokkaido was ruptured by the 1952 Tokachi-oki earthquake, and the 2003 Tokachi-oki earthquake ruptured the same interface 51 years later. The plate interface off Nemuro, northeast of Tokachi, was ruptured by the 1894 and 1973 Nemuro-oki earthquakes.

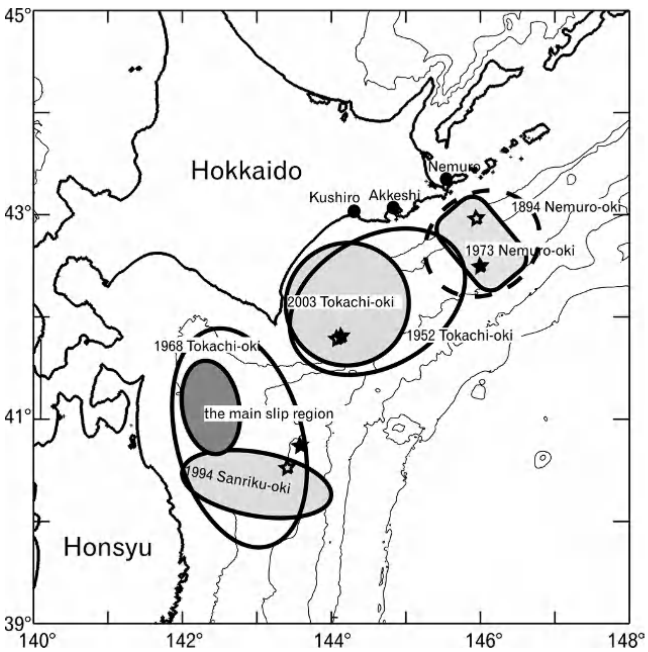

Figure 1. Recent sequences of large underthrusting earthquakes to rupture the plate interface along the southern part of the Kurile subduction zone. Light shaded regions show the rupture areas of the 1994 Sanriku-oki, 2003 Tokachi-oki and 1973 Nemuro-oki earthquakes. Open stars are the epicenter of those earthquakes. Open ellipsoids show the rupture areas of the 1968 Tokachi-oki and 1952 Tokachi-oki earthquakes. A dashed ellipsoid shows the rupture area of the 1894 Nemuro-oki earthquake which is not well determined previously. Solid stars are the epicenters of those three old earthquakes. The dark shaded region shows the main slip region of the 1968 Tokachi-oki earthquake. Note that the 1968 Tokachi-oki earthquake is located off northern Honshu rather than off Tokachi.

In March 2003, the Japanese government made long-term forecast for large earthquakes along the Kurile trench (Earthquake Research Committee, 2004). The estimated probability to have a large earthquake off Tokachi and Nemuro in next 30 years (starting from March 2003) was 60% and 20–30%, respectively. Then the 2003 Tokachi-oki earthquake occurred in September. There is now concern about a future Nemuro-oki earthquake.

In this paper, we first review the previous studies for the 1968 Tokachi-oki and 1994 Sanriku-oki earthquakes as one of the recurrent earthquake sequences. We also review the previous studies for the 1952 and 2003 Tokachi-oki earthquakes as another example of recurrent events in the Kurile subduction zone. Then, the slip distribution of the 1973 Nemuro-oki earthquake is estimated using tsunami waveform inversion. Also, the source process of the 1894 Nemuro-oki earthquake is studied using tsunami waveform data. Finally, the variability of the recurrent earthquakes in the southern end of the Kurile subduction zone is discussed.

2. PREVIOUS STUDIES

2.1 The 1968 Tokachi-oki and 1994 Sanriku-oki Earthquakes

The source process of the 1968 Tokachi-oki earthquake (Mw 8.2) was extensively studied using teleseismic body waves [Kikuchi and Fukao, 1985; Schwartz and Ruff, 1985], teleseismic surface waves [Mori and Shimazaki, 1985] and tsunami waveforms [Satake, 1989]. In general, their results are consistent and show that large moment release occurred in the northern part of the aftershock area (Figure 1). Recently, Nagai et al. [2001] studied the slip distribution of the 1968 Tokachi-oki earthquake in detail using strong-motion data recorded at a regional network and the teleseismic body waves recorded at global networks. They estimated two large slip areas. One is the largest slip area in the northern part of the aftershock area, the same as the previous studies. Another large slip area is in the southern part of the aftershock area.

The source process of the 1994 Sanriku-oki earthquake (Mw 7.8) was also extensively studied using strong motion data [Nakayama and Takeo, 1997], GPS displacement data and tsunami waveform data [Tanioka et al., 1996]. Recently, Nagai et al. [2001] studied the detailed slip distribution using both strong motion and teleseismic body wave data. In general, all of them show that the northern part of the 1968 Tokachi-oki aftershock area, where the largest moment was released by the 1968 event, was not ruptured by the 1994 Sanriku-oki earthquake. The large slip of the 1994 event was concentrated on the southern part of the aftershock area of the 1968 event. Nagai et al. [2001] suggested that the 1994 event re-ruptured the large slip area of the 1968 event estimated in the southern part of the 1968 aftershock area.

These studies indicate that the 1994 Sanriku-oki earthquake was a recurrent earthquake of the 1968 Tokachi-oki earthquake because the rupture area of the 1994 event was within the rupture are of the 1968 event, but the largest slip area of the 1968 event was not ruptured by the 1994 event.

2.2 The 1952 and 2003 Tokachi-oki Earthquakes

The source process of the 1952 Tokachi-oki earthquake (Mw 8.1) was studied using tsunami waveforms [Hirata et al., 2003] and strong motion data [Yamanaka and Kikuchi, 2003]. Hirata et al. [2003] suggested that the largest moment was released at the down-dip edge in the western part of the aftershock area off Kushiro although large moment was also broadly distributed in the eastern part of the aftershock area off Akkeshi (Figure 1). Yamanaka and Kukuchi, [2003] studied the initial part of the moment release of the 1952 event using the nearby strong-motion seismograms. The later part of the moment release was not estimated because waveforms of the strong motion seismograms went off-scale soon after the S-wave arrivals. They show that the initial part of the moment was released at the western part of the aftershock area.

The source process of the 2003 Tokachi-oki earthquake (Mw8.1) was studied extensively using strong motion data [Honda et al., 2004], teleseismic body wave and strong motion data [Yamanaka and Kikuchi, 2003; Yagi, 2004], geodetic and strong motion data [Koketsu et al., 2004] and tsunami waveforms [Tanioka et al., 2004]. In general, all the results from various studies consistently show that the large moment was released by the 2003 event in the western part of the 1952 Tokachi-oki source region estimated by Hirata et al. [2003].

In order to compare the slip areas of the 2003 and 1952 Tokachi-oki earthquakes more accurately, Satake et al. [2006] re-estimated the slip distribution of the 1952 Tokachi-oki earthquake using more accurate tsunami simulation. They show that the source area of the 1952 Tokachi-oki earthquake was indeed larger than that of the 2003 Tokachi-oki earthquake. Although the largest moment for both 2003 and 1952 Tokachi-oki earthquakes were released at the western part of the 1952 aftershock area off Kushiro, the plate interface at the eastern part of the 1952 aftershock area off Akkeshi was only ruptured by the 1952 Tokachi-oki earthquake (Figure 1).

3 THE 1973 NEMURO-OKI EARTHQUAKE

The fault parameters of the 1973 Nemuro-oki earthquake were first estimated by Shimazaki [1974] using surface waves and geodetic data. The location of the fault model estimated by Shimazaki [1974] is shown in Figure 2. Tada [1974] also estimated the fault model using the geodetic data including the vertical deformation observed at tide gauges. Kikuchi and Fukao [1987] estimated the distribution of the moment release using the teleseismic body waves, and their result was generally similar to that of Shimazaki [1974].

In this paper, the slip distribution of the 1973 Nemuro-oki earthquake was estimated from tsunami waveform inversion. The tsunami waveform data recorded at 6 tide gauge stations, Kushiro, Hachinihe, Ofunato, Ayukawa, Sendai, and Onahama, were used for this analysis (Figure 3). The source area of the Nemuro-oki earthquake was divided into 6 subfaults (Figure 2 and 3). The size of the subfaults was 40 km x 40 km. The strike of the fault was assumed to be 240°, as estimated by Tada [1974]. The dip angle of the fault was assumed to be 14°, calculated from the depth contours of the plate interface suggested by Earthquake Research Committee [2004] shown in Figure 2. The rake angle of the fault was assumed to be 100°, similar to that estimated by Kikuchi and Fukao [1987]. The depths of the top edge of shallower subfaults (A, B, C) and deeper subfaults (D, E, F) were 15.0 km and 24.5 km, respectively.

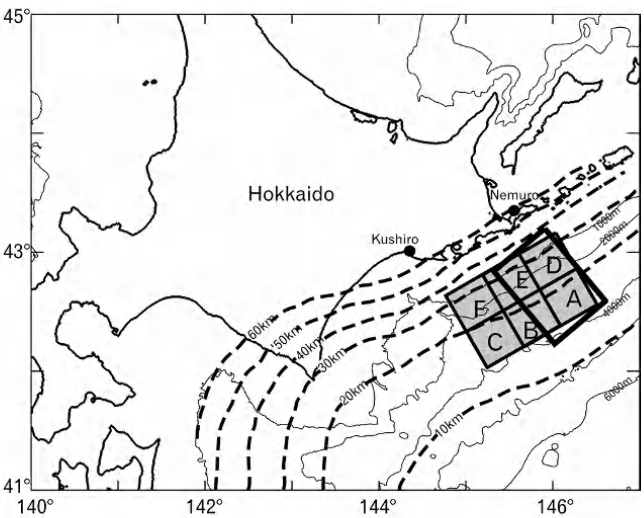

Figure 2. The location of six subfaults to estimate the slip distribution of the 1973 Nemuro-oki earthquake using the tsunami waveform inversion. Thick dashed contours show the depth of the plate interface in this region suggested by Earthquake Research Committee [2004]. A thick rectangle shows the location of the fault model of the 1973 Nemuro-oki earthquake by Shimazaki [1974].

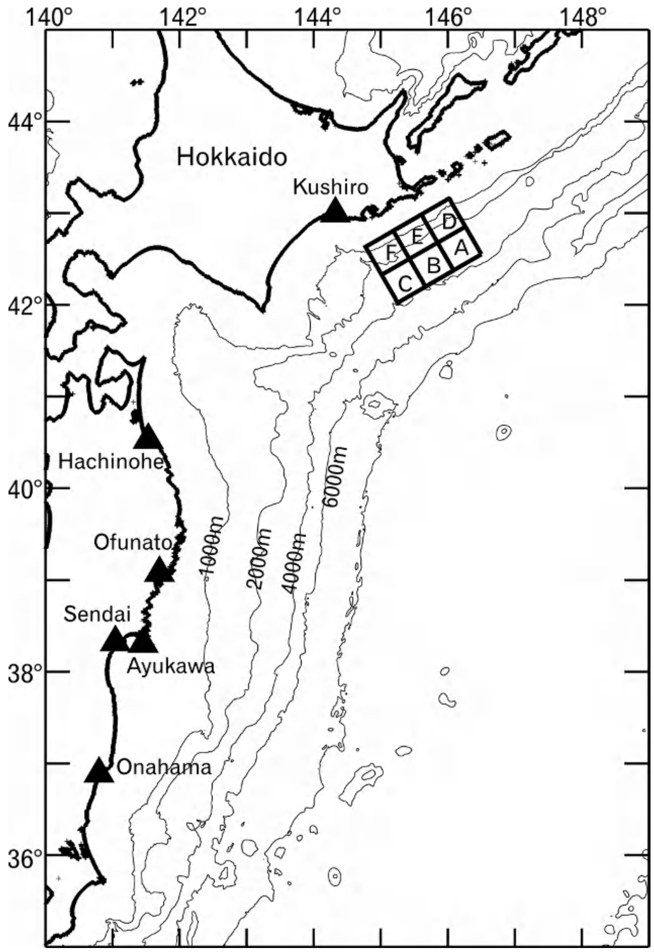

Figure 3. Tsunami computation area. Triangles show the location of the tide gauge stations where the tsunami waveforms were observed. Frames show the location of six subfaults.

To calculate the tsunami Green's functions, finite different approximation of the linear long-wave equations [see Jonshon 1998] was computed in the area shown in Figure 3. The grid size was 20 sec of arc (about 600 m) in deep water; a finer grid (4 sec) was used around the tide gauge stations. The time step for the computation was 1 s to satisfy a stability condition. The initial ocean bottom vertical deformation due to the fault motion was computed using the equations of Okada [1985]. Then, the ocean surface deformation, the initial condition for the tsunami propagation, was calculated from the ocean bottom deformation [see Tanioka and Seno, 2001]. The rise time of the tsunami initial wave was assumed to be 30 s. Green's functions for the 6 stations were computed for each subfault with a unit amount of slip. The method of tsunami inversion is the same as that used by Tanioka and Satake [2001]. For error analysis, the jackknife technique [Tichelaar and Ruff, 1989] was applied.

First, the tsunami waveform inversion was carried out for 5 observed tsunami waveforms, Kushiro, Ofunato, Ayukawa, Sendai, and Onahama because the absolute timing at the tide gauge in Hachinohe did not have enough accuracy to use in the inversion. Table 1 shows the result of the inversion. The comparison between observed and computed tsunami waveforms as a result of the inversion is shown in Figure 4. The timing of the first observed tsunami wave at Hachinohe was corrected to coincide with the arrival time of the computed tsunami wave using the slip distribution estimated by the inversion. Then, we carried out the tsunami waveform inversion again using all six observed tsunami waveforms including the tsunami waveforms at Hachinohe.

The results are shown in Figure 5 and Table 1. The result using all six tsunami waveforms is similar to the result using five waveforms. The observed tsunami waveforms are well explained by the computed waveforms as shown in Figure 6. The largest slip of 2.9 m was estimated at subfault A and D. The small slip of 0.9 m was estimated at subfault B. Essentially, no slip was estimated at subfaults, C, E, and F. This suggests that the slip of the 1973 Nemuro-oki earthquake was concentrated on the plate interface off Nemuro and did not extend into the plate interface off Akkeshi. These results are consistent with the fault model estimated by Shimazaki [1974] (Figure 5). The total seismic moment was 6.5 x 10^{20} Nm (Mw 7.8) by assuming the rigidity of 6 x 10^{10} N/m^2.

4 THE 1894 NEMURO-OKI EARTHQUAKE

Previously, the source of the 1894 Nemuro-oki earthquake was studied from seismic intensity or tsunami heights distributions [Hatori, 1974; Satake et al., 2005]. The tsunami heights of the 1894 Nemuro-oki earthquake were estimated by Hatori [1974] on the basis of the damage report by Omori [1985]. Satake et al. [2005] indicate that the eastward increase of tsunami heights from Kushiro along the Pacific coast of Hokkaido was a characteristic feature of Nemuro-oki earthquake. Although the seismic intensity of the 1894 Nemuro-oki earthquake was slightly larger than that of the 1973 Nemuro-oki earthquake, the pattern of the seismic intensity distributions with the largest intensities

Table 1. Slip distributions using five and six stations

subfault	The results using 5 stations slip, m	The result using all 6 stations slip, m
A	2.4±0.3	2.9±0.4
B	1.2±0.2	0.9±0.2
C	0.1±0.2	0.1±0.1
D	3.2±0.4	2.9±0.4
E	0.0±0.0	0.0±0.0
F	0.0±0.0	0.0±0.0

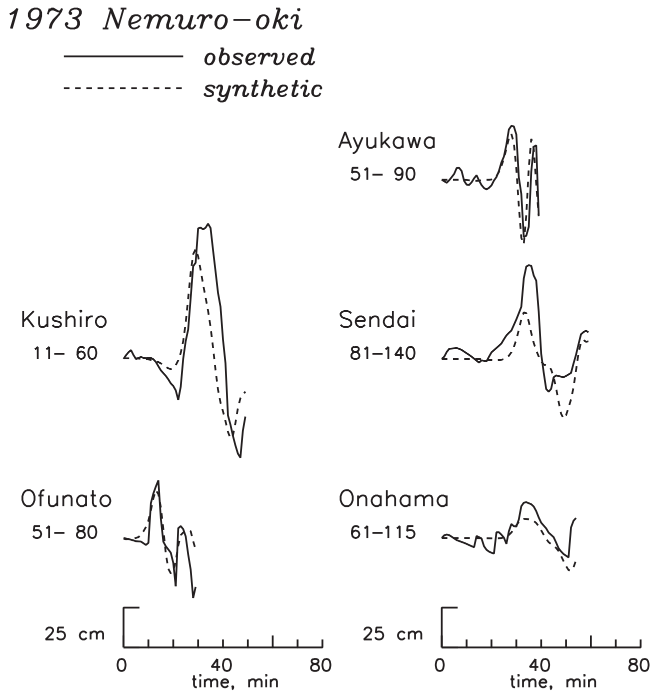

Figure 4. Comparison of the observed (solid) and computed (dashed) tsunami waveforms for the result of the tsunami waveform inversion using five tide gauge stations without Hachinohe. The numbers below the station name indicate the time range of the waveforms (in minutes after the origin time).

at the eastern edge of Hokkaido was similar to each other [Satake et al., 2005]. Hatori [1974] showed the observed tsunami waveform of the 1894 event recorded at the tide

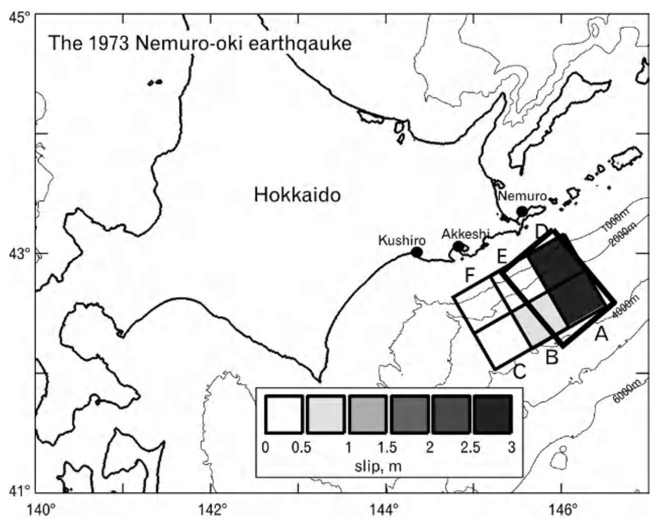

Figure 5. The slip distribution of the 1973 Nemuro-oki earthquake estimated by the tsunami waveform inversion using all six tide gauge records. A thick rectangle shows the location of the fault model of the 1973 Nemuro-oki earthquake by Shimazaki [1974].

gauge at Ayukawa and he compared that tsunami waveform with the observed tsunami waveform of 1973 Nemuro-oki earthquake at the same tide gauge (Figure 7). He suggested that the differences between the two observed tsunami waveforms at Ayukawa should be related to the differences of the tsunami sources between the 1894 and 1973 Nemuro-oki earthquakes.

In this paper, we try to find a fault model of the 1894 Nemuro-oki earthquake using the observed tsunami waveform at Ayukawa. Considering the poor accuracy of clocks in those days, we decided to use the waveform only without an absolute timing. The tsunami numerical computation was carried out using the finite different approximation of the linear long-wave equations [see Jonshon 1998]. The details of the computation are the same as those for the 1973 Nemuro-oki earthquake. No focal mechanism solution has yet been estimated for the 1894 event. Therefore, the strike and dip of the fault were assumed to be the same as those of the 1973 Nemuro-oki earthquake, 240° and 14°, respectively. The rake of the fault is assumed to be 90°. The width of the fault was fixed to be 100 km (Figure 8). We varied fault

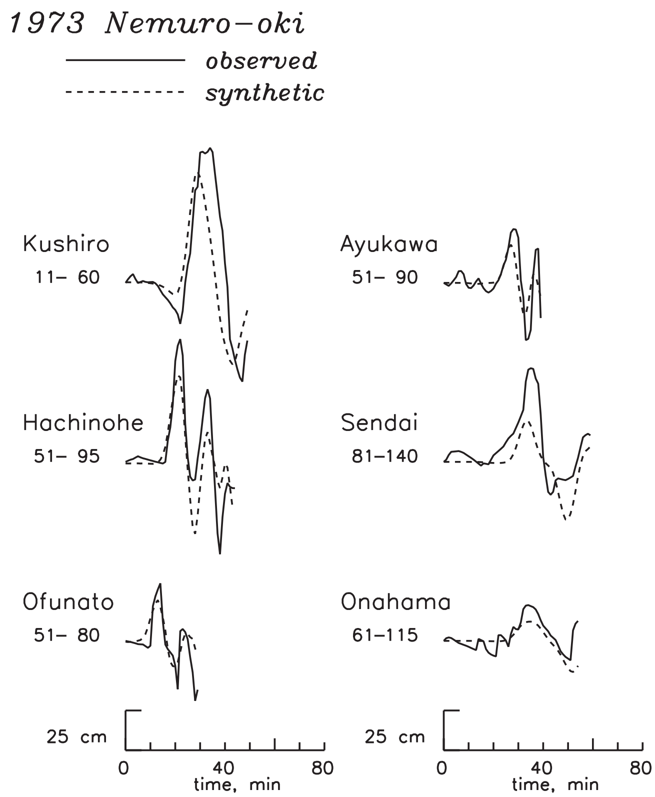

Figure 6. Comparison of the observed (solid) and computed (dashed) tsunami waveforms for the result of the tsunami waveform inversion using all six tide gauge stations. The numbers below the station name indicate the time range of the waveforms (in minutes after the origin time).

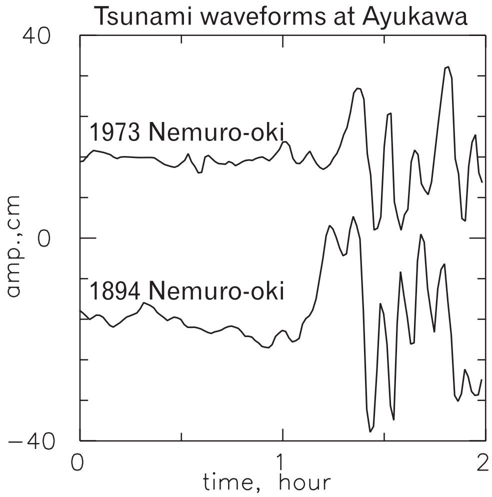

Figure 7. Comparison of observed tsunami waveforms at Ayukawa for the 1973 Nemuro-oki and 1894 Nemuro-oki earthquakes. Both waveforms are displayed to align the origin time of the earthquakes.

length as 100 km, 150 km, and 200 km. The slip amount for each fault model is determined by comparison of observed and computed tsunami waveforms.

The observed and computed tsunami waveforms from thee fault models with diferent lengths are compared in Figure 9. The computed tsunami waveform from the 200 km-long fault best explains the first phases of the observed tsunami. The computed tsunami waveforms from other fault models cannot explain the first wave of the observed tsunami waveform, in particular the period of the first leading wave. We therefore conclude that the fault length of the 1894 Nemuro-oki earthquake was approximately 200 km, much larger than that of the 1973 Nemuro-oki earthquake, 40–80 km. The slip amount was estimated to be 2.4 m by comparison of observed and computed amplitudes between the largest peak and the first trough. The total seismic moment of the 1894 Nemuro-oki earthquake was 28.8 x 10^{20} Nm (Mw8.3) by assuming the rigidity of 6 x 10^{10} N/m^2. This estimate was much larger than the estimated seismic moment of the 1973 Nemuro-oki earthquake.

5. DISCUSSION

The previous studies indicate that the 1994 Sanriku-oki earthquake (Mw 7.8) ruptured only the southern part of the rupture area of the 1968 Tokachi-oki earthquake (Mw 8.2), and did not rupture the main part of the rupture interface of the 1968 Tokachi-oki earthquake. Also, the previous studies show that the 2003 Tokachi-oki earthquake (Mw 8.1) did not rupture the eastern part of the rupture area of the 1952 Tokachi-oki earthquake (Mw 8.2). The tsunami waveform analyses of the 1973 Nemuro-oki and 1894 Nemuro-oki earthquakes indicate that the rupture area of the 1894 Nemuro-oki earthquake was much larger than the 1973 Nemuro-oki earthquake. In the southernmost part of the Kurile-Kamchatka subduction zone, none of three sets of recurrent large underthrust earthquakes had the same rupture area. Variable rupture patterns of large underthrust earthquakes make it difficult to estimate the source processes of future large earthquakes in this subduction zone. In addition to these recent earthquakes, tsunami deposit studies indicate that unusual large tsunami have occurred in this subduction zone with long (about 500 yrs) recurrence interval [Nanayama et al., 2003]. It makes the rupture history of large earthquakes in this subduction zone more complicated.

The same type of non-characteristic behavior and complex recurrence of large subduction zone earthquakes is suggested for the 1957 (Mw=8.6), 1986(Mw=8.0), and 1996(Mw=7.9) Aleutian Islands earthquakes and the 1963 (Mw=8.5) and 1995(Mw=8.0) Kurile Islands earthquakes by Schwartz [1999]. These non-regular recurrence behaviors are not consistent with physical models of earthquake rupture where slip complexity is exclusively controlled by invariant geometric and material heterogeneities but suggested that dynamic stress heterogeneities are also important. Recent theoretical study by Shaw [2004] concludes that irregularities of recurrences created by dynamic stress heterogeneities arising through frictional instabilities are seen to remain substantial even for large fixed geometric and material heterogeneities. The results in this paper are also consistent with their theoretical study.

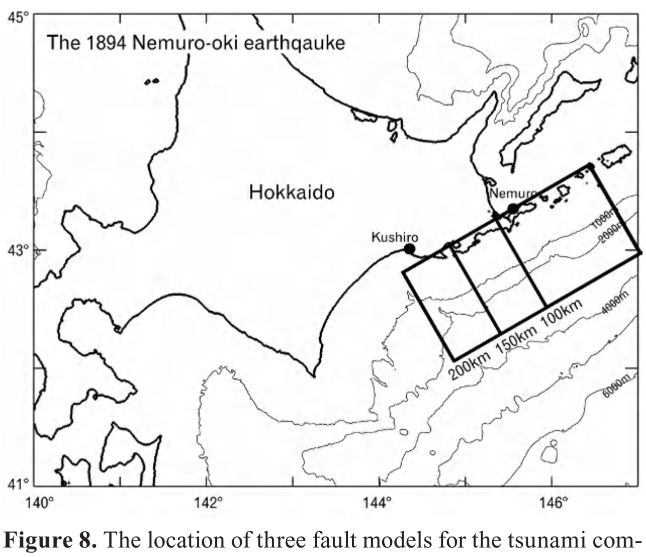

Figure 8. The location of three fault models for the tsunami computations of the 1894 Nemuro-oki earthquake. Three fault models with different fault lengths, 100 km, 150 km, and 200 km, were used for the tsunami computations.

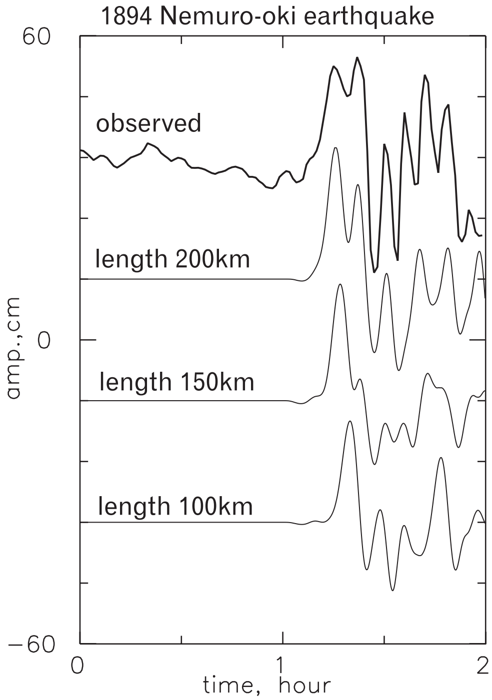

Figure 9. Comparison of the observed (thick) and three computed (thin) tsunami waveforms obtained from three fault models with different fault lengths, 100 km, 150 km,and 200km. The location of the fault models are shown in Figure 8. The slip amount was 2.4 m for all three fault models.

6. CONCLUSION

The 1973 Nemuro-oki earthquake ruptured the plate interface off Nemuro with the seismic moment of 6.5 x 10^{20} Nm (Mw 7.8). The rupture area was consistent with the result of Shimazaki [1974]. The 1894 Nemuro-oki earthquake ruptured much larger area than that of the 1973 Nemuro-oki earthquake. The estimated fault length for the 1894 earthquake is approximately 200 km, and the estimated seismic moment is 28.8 x 10^{20} Nm (Mw 8.3). In the southernmost part of the Kurile-Kamchatka subduction zone, three sets of recent recurrent large earthquakes, the 1968 Tokachi and 1994 Sanriku-oki earthquakes, the 1952 and 2003 Tokachi-oki earthquakes, and the 1894 and 1973 Nemuro-oki earthquakes, did not exhibit the same rupture processes. Variable rupture patterns of the large recurrent earthquakes make it difficult to estimate the source processes of future large earthquakes in this subduction zone.

These non-regular recurrences also suggest that, in addition to invariant geometric and material heterogeneities, the dynamic stress heterogeneities are seen to be important for understanding large earthquake complexity in the southernmost part of the Kurile-Kamchatka subduction zone.

Acknowledgments. We thank Dr. Eric Geist and an anonymous reviewer for constructive comments. This study was partly supported by Grants-in-Aid for Scientific Research in Japan (C:17540386).

REFERENCES

Earthquake Research Committee, Long-term evaluation of seismicity along the Kuril Trench, *Publications of Earthquake Research Committee II*, 1–74, 2004

Hatori, T., Source area of the tsunami off the Nemuro Peninsula in 1973 and its comparison with the tsunami in 1894, *Special Bull. Earthq. Res. Inst. Univ. Tokyo,* **13**, 67–76, 1974 (in Japanese with English abst.).

Hirata, K., E.L. Geist, K. Satake, Y. Tanioka, and S. Yamaki, Slip distribution of the 1952 Tokachi-oki earthquake (M 8.1) along the Kuril trench deduced from tsunami waveform inversion, *J. Geophys. Res.*, **108**, 2196 doi:10.1029/2002JB001976,2003

Honda, R., S. Aoi, N. Morikawa, H. Sekiguchi, T. Kunugi, and H. Fujiwara, Ground motion and rupture process of the 2003 Tokachi-oki earthquake obtained from strong motion data of K-NET and KiK-net, *Earth Planets and Space*, **56**, 317–322, 2004

Jonshon, J. M., Heterogeneous coupling along Alaska-Aleutians as inferred from tsunami, seismic, and geodetic inversions, *Advance in Geophysics*, **39**, 1–110, 1998

Kikuchi M., and Y. Fukao, Iterative deconvolution of complex body waves from great earthquakes–The Tokachi-oki earthquakes of 1968, *Phys. Earth Planet. Inter.*, **37**, 235–248, 1985

Kikuchi M., and Y. Fukao, Inversion of long-period P-waves from great earthquakes along subduction zone, *Tectonophysics*, **144**, 231–247, 1987

Koketsu, K., K. Hikima, S. Miyazaki, and S. Ide, Joint inversion of strong motion and geodetic data for the source process of the 2003 Tokachi-oki, Hokkaido, earthquake, *Earth Planets and Space*, **56**, 329–334, 2004

Mori, J., and K. Shimazaki, Inversion of intermediate-period Rayleigh waves for source characteristics of the 1968 Tokachi-oki earthquake, *J. Geophys. Res.*, **90**, 11374–11382, 1985

Nagai, R., M. Kikuchi, and Y. Yamanaka, Comparative study on the source process of recurrent large earthquakes in Sanriku-oki region: The 1968 Tokachi-oki earthquake and the 1994 Sanriku-oki earthquake, *Jishin 2*, **52**, 267–289, 2001 (in Japanese with English abst.)

Nakayama, W. and M. Takeo, Slip history of the 1994 Sanriku-Haruka-oki, Japan, earthquake deduced from strong motion data, *Bull. Seismol. Soc. Am.*, **87**, 918–931, **1997**.

Nanayama, F., K. Satake, R. Furukawa, K. Shimokawa, B.F. Atwater, K. Shigeno, and S. Yamaki, Unusually large earthquakes inferred from tsunami deposits along the Kurile trench. *Nature*, **424**, 660–663, 2003.

Okada, Y., Surface deformation due to shear and tensile faults in a half-space, *Bull. Seim. Soc. Am.*, **75**, 1135–1154, 1985

Omori, F., Reports of the Hokkaido earthquake on May 22, 1894, *Reports of the Imperial Earthquake Investigation Committee*, **3**, 27–36, (in Japanese), 1895.

Satake, K., Inversion of tsunami waveforms for the estimation of heterogeneous fault motion of large submarine earthquakes: 1968 Tokachi-oki and the 1983 Japan Sea earthquakes, *J. Geophys. Res.*, **94**, 5627–5636, 1989

Satake, K., F. Nanayama, S. Yamaki, Y. Tanioka, and K. Hirata, Variability among tsunami sources in the 17^{th}–21^{st} centuries along the southern Kurile trench, *K. Satake (ed), Tsunamis: Case Studies and Recent Developments*, 157–170, 2005

Satake, K., K. Hirata, S. Yamaki, and Y. Tanioka, Re-estimation of tsunami source of the 1952 Tokachi-oki earthquake, *Earth Planets and Space*, **58**, 1–8, 2006

Schwarts S. Y., Noncharacteristic behavior and complex recurrence of large subduction zone earthquakes, *J. Geophys. Res.,* **104**, 23,111–23,125, 1999

Schwartz S.Y., and L.J. Ruff, The 1968 Tokachi-oki and the 1969 Kurile Islands earthquakes: Variability in the rupture process, *J. Geophys. Res.*, **90**, 8613–8626, 1985

Shaw, B. E., Dynamic heterogeneities versus fixed heterogeneities in earthquake models, *Geophys. J. Int.*, **156**, 275–286, 2004

Shimazaki, K, Nemuro-oki earthquake of June 17, 1973: lithospheric rebound at the upper half of the interface, *Phys. Earth Planet. Inter.*, **9**, 314–327, 1974

Tada, T., Fault model and crustal movement of the 1973 Nemuro-oki earthquake, *Jishin 2*, **27**, 120–128, 1974

Tanioka, Y, K. Hirata, R. Hino, and T. Kanazawa, Slip distribution of the 2003 Tokachi-oki earthquake estimated from tsunami waveform inversion, *Earth Planets and Space*, **56**, 373–376, 2004

Tanioka, Y., L. Ruff, and K. Satake, The Sanriku-oki, Japan, earthquake of December 28, 1994 (Mw 7.7): Rupture of a different asperity from a previous earthquake, *Geophy. Res. Lett.*, **23**, 1465–1468, 1996

Tanioka, Y. and K. Satake, Coseismic slip distribution of the 1946 Nankai earthquake and aseismic slip caused by the earthquake, *Earth Planets and Spac*e, **53**, 235–241, 2001

Tanioka, Y., and T. Seno, Sediment effect on tsunami generation of the 1896 Sanriku tsunami earthquake, *Geophys. Res. Lett.*, **28**, 3389–3392, 2001

Tichelaar, B.W., and L.J. Ruff, How good are our best model? Jackknifing, bootstrapping, and earthquake depth, *EOS, Trans. Am. Geophys. Union*, **70**, 593,605–606, 1989

Yagi, Y., Source rupture process of the 2003 Tokachi-oki earthquake determined by joint inversion of teleseismic body wave and strong ground motion data, *Earth Planets and Space*, **56**, 311–316, 2004

Yamanaka, Y. and M. Kikuchi, Source processes of the Tokachi-oki earthquake on September 26, 2003, inferred from teleseismic body waves, *Earth Planets Space*, **55**, e21–e24, 2003

Spatial Relationship Between Interseismic Seismicity, Coseismic Asperities and Aftershock Activity in the Southwestern Kuril Islands

Hiroaki Takahashi and Minoru Kasahara

Institute of Seismology and Volcanology, Graduate School of Science, Hokkaido University, Sapporo, 060-0810, Japan

We investigate the spatiotemporal relationship between background seismic activity, coseismic asperities and aftershock activity in the southwestern Kuril Islands using high precision earthquake catalogue produced by Hokkaido University since 1976. Seismicity maps clearly indicate that coseismic asperity patches correspond to low seismic activity regions surrounded by high activity areas. This seismicity pattern in and around the asperity does not vary with time, which may suggest invariant stable frictional conditions in the temporal domain. We infer that these observations reflect the frictional nature of the asperity and its surrounding area. This spatial variation of seismic activity may be due to the variations of the yielding threshold point to the shear stress for earthquake faulting, which is due to the spatial variation of frictional parameters on the plate interface. It is feasible to recognize unknown asperities from epicenter distributions during the interseismic period. A similar relationship between asperity distribution and aftershock activity might also be due to the frictional variations on the plate interface.

1. INTRODUCTION

In the southwestern Kuril Islands where the Pacific plate is subducting beneath the Okhotsk plate, large earthquakes have frequently occurred. Predominant focal mechanisms are shallow dipping thrusts on the plate interface (Fig. 1). Intraslab events have also occurred but are rare. *Utsu* (1972) found that the rupture areas of large interplate earthquakes do not overlap each other during one seismic cycle. He divided the southern Kuril trench into several segments and pointed out a seismic gap off Nemuro. The 1973 Nemuro-oki earthquake (M_{JMA}7.4) filled this gap. This was a primary example which supports the ideas of characteristic earthquakes, earthquake cycles and seismic gaps proposed by several researchers such as *Utsu* (1972) and *Fedotov et al.* (1970). These have been fundamental ideas for earthquake forecasting in this region.

Recently, slip distributions of large earthquakes have been obtained using several methods. For example, slip distribution models of the 2003 Tokachi-oki earthquake (M8.0), off south-eastern Hokkaido, have been analyzed by teleseismic body waves (e.g. *Yamanaka and Kikuchi*, 2003), strong motion data (e.g. *Honda et al.*, 2004), and geodetic data (e.g. *Miura et al.*, 2004). Many of those studies clearly indicate that coseismic slip distribution in a focal region is inhomogeneous. *Lay and Kanamori* (1980) define an asperity as a area of a fault where a large seismic moment is released by a large earthquake. This is practically equivalent to a patch with relatively large coseismic slip during an earthquake. We believe that coseismic inhomogeneous slip distribution is due to the irregularities on the plate interface. It is proposed that this property might induce a variety of background seismicity behavior.

Volcanism and Subduction: The Kamchatka Region
Geophysical Monograph Series 172

10.1029/172GM14

Yamanaka and Kikuchi (2004) examined the slip distributions of large interplate earthquakes occurring along the northern Japan Trench using JMA's strong motion and teleseismic data, and produced an 'asperity map'. *Yamanaka and Kikuchi* (2001) also examined asperities off southeastern Hokkaido. They clearly mapped the locations, dimensions and slip distributions of asperities of major subduction earthquakes occurring since 1952 along the southwestern Kuril and northern Japan Trenches.

Yamanaka and Kikuchi (2004) and *Nagai et al.* (2001) came to the conclusion that recurrent large interplate earthquakes in the northern Japan Trench have been the result of repeat faulting of the same asperities. They also pointed out that M8 class earthquakes sometimes resulted in simultaneous faulting of several neighboring M7 class asperities. This invariant asperity model is one of the predominant theories used to understand the seismic cycle along the subduction system.

These hypothesesis associated with asperities might be adaptable to the southwestern Kuril Trench, which is the northeastern neighbor of the Japan Trench. As mentioned above, *Yamanaka and Kikuchi* (2001) already produced an asperity map in this region. In 2003, a recurrent event, the 2003 Tokachi-oki earthquake (M8.0), occurred in the same region as the previous 1952 event (M8.2). *Yamanaka and Kikuchi* (2003) compared the asperity distribution of the former 1952 (M8.2) and the 2003 (M8.0) events, and came to the conclusion that these earthquakes occurred by faulting of a same asperity. This implies that the invariant asperity hypothesis might be applicable to this region as we expect.

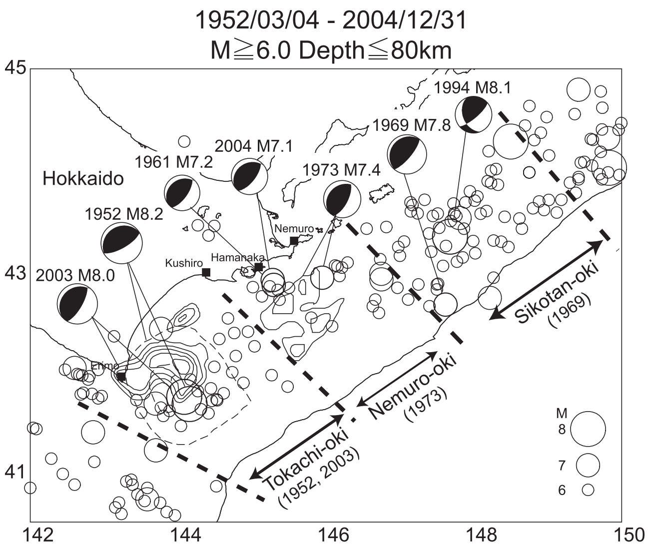

Figure 1. Seismicity map in southwestern Kuril trench. Major interplate earthquakes with focal mechanisms and their rupture segments (*Fukao and Furumoto*, 1975, for 1969 event; *Shimazaki*, 1974, for 1973 event; *Yamanaka and Kikuchi*, 2003, for 1952 and 2003 events; Yamanaka, 2004b, for 1961 and 2004 events) are shown. The epicenter and mechanism of the 1994 intraslab earthquake is also indicated (*Kikuchi and Kanamori*, 1995). Contours are the asperities of the 1952, 1973 and 2003 earthquakes (*Yamanaka and Kikuchi*, 2001, *Yamanaka and Kikuchi*, 2003). Contour intervals are 1m.

We have observed seismicity in the region and been aware of the inhomogeneous hypocenter distribution in the spatial domain. After the occurrence of the 2003 Tokachi-oki earthquake, we observed the similarity of the location of the 2003 coseismic asperity and consecutively low seismicty area off Erimo cape. This might imply a relationship between the spatial variation of background seismicity and coseismic asperity distribution. In this paper we investigate seismic activity during interseismic and aftershock periods, in and around asperities and examine their spatial and temporal depending characteristics.

2. SEISMOLOGICAL OBSERVATION IN HOKKAIDO

In the Hokkaido Islands, which are located in the southwestern edge of the Kuril Islands, the Japan Meteorological Agency (JMA) started earthquake observations by sensory intensity and seismometers in 1872 and 1881, respectively, and the observation network has been continuously improved since then. But detailed discussion of the spatiotemporal change of seismicity including M<5 earthquakes has been difficult because JMA observed the earthquakes mainly by a strong motion seismometer network (*e.g. Mochizuki et al.,* 1978).

Hokkaido University started microseismic observations in 1966 at Kamikineusu station. We began the hypocenter determination in 1976 with seven stations and have made efforts to improve the seismological network. Fig. 2 shows the epicenter distribution and magnitude-frequency diagram of Hokkaido University and JMA catalogues during the same period. Hokkaido University located nearly 1000 events but only 100 were located by JMA. This clearly shows higher event detectability by Hokkaido University than JMA. In 1996, Hokkaido University and Sapporo District Meteorological Observatory of JMA started to exchange their digital seismic waveform data in real time. At this time the mean event detection ability of these institutes became the same. The Japan Agency for Marine-Earth Science and Technology's three cabled permanent ocean bottom seismographs, off southeastern Hokkaido (e.g. *Hirata et al*., 2002) have also been sent to JMA and Hokkaido University in real time since 2000. Vast waveform data from the Hi-net (High Sensitivity Seismograph Network of Japan) operated by the National Institute for Earth Science and Disaster Prevention (NIED) have been transmitted to JMA and

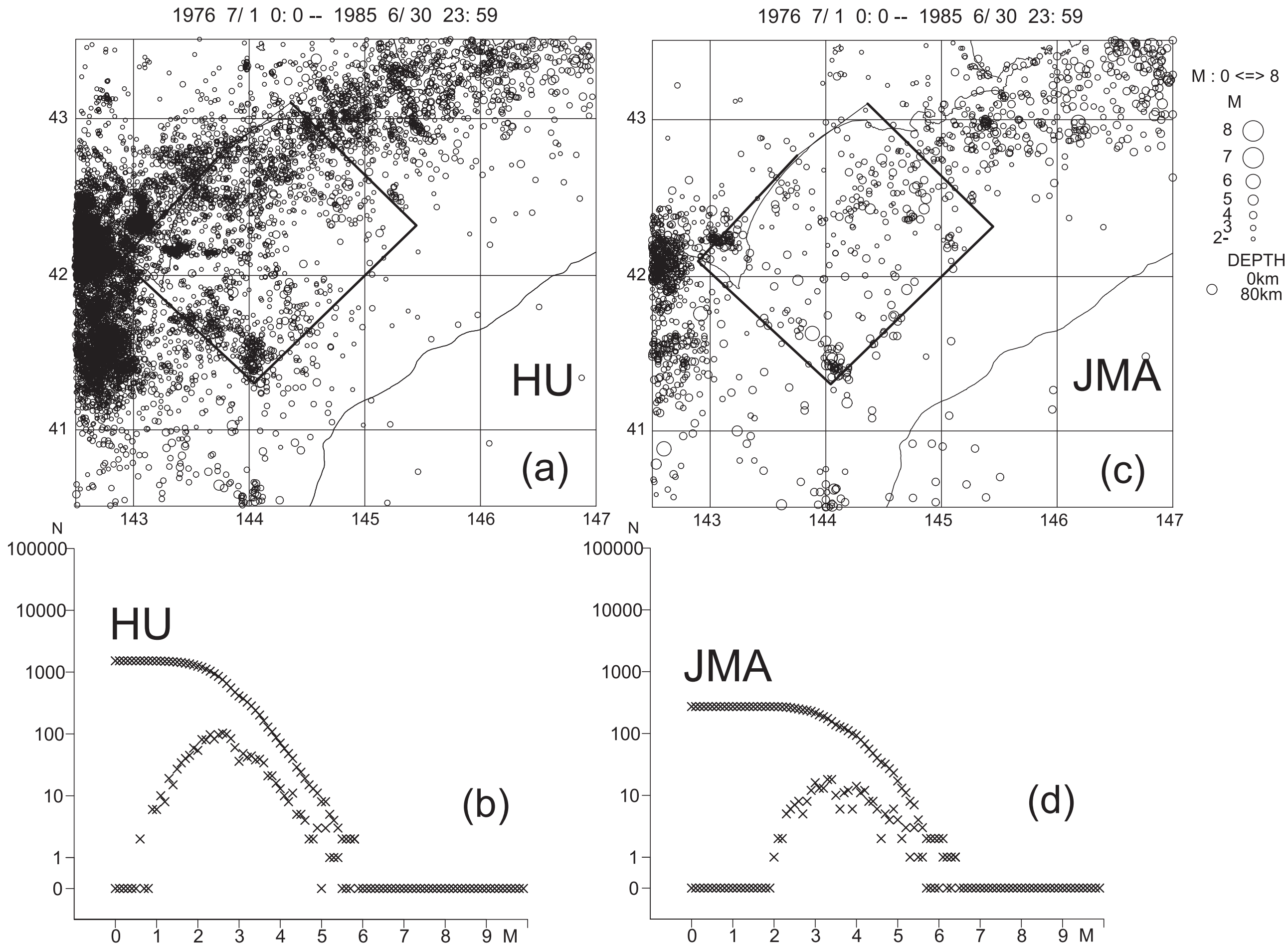

Figure 2. (a) Epicenter map based on Hokkaido University catalogue. (b) Magnitude-frequency and total earthquake number diagrams in the rectangle shown in (a). (c) Epicenter map based on JMA catalogue. (d) Magnitude-frequency and total earthquake number diagrams in the rectangle shown in (c).

Hokkaido University in real time since 2001. Currently, the total number of non-strong motion seismological stations in Hokkaido is 191 (Hokkaido University: 51; JMA: 30; Hi-net: 110), and all waveform data are open for general use.

In this study we investigated the properties of background seismicity in the spatiotemporal domains along the southwestern Kuril Trench. As mentioned above, the Hokkaido University earthquake catalogue had kept higher hypocenter detection ability than JMA. Therefore, we hereafter refer mainly to the Hokkaido University earthquake catalogue for seismicity investigations.

3. ASPERITIES, INTERSEISMIC SEISMICITY AND AFTERSHOCK ACTIVITY IN THE SOUTHWESTERN KURIL ISLANDS

As shown in Fig. 1, there have been several large interplate earthquakes since 1952, these are the 1952 Tokachi-oki (M8.2), the 1969 Hokkaido-Toho-Oki (M7.8) and the 1973 Nemuro-oki (M7.4) earthquakes. We consider this series as the latest earthquake cycle in this region. The 2003 Tokachi-oki earthquake (M8.0) may be the opening event to the next earthquake cycle, similar to the 1952–1973 series.

Here we try to investigate characteristics of seismic activity based on Hokkaido University and JMA earthquake catalogues in and around the asperities of the large interplate events mentioned above examined by *Yamanaka and Kikuchi* (2001) and *Yamanaka and Kikuchi* (2003). The 1969 event (M7.8) was excluded because it is far outside of observation network. In this study we used earthquakes shallower than 80km in depth, which show seismic activity in the seismogenic layer of this subduction zone, with location errors less than 10km. We also confirmed that seismicity in and around the subducting plate is not contaminated the seismicity in the overriding plate in this region.

3-1. The 1952 Tokachi-oki Earthquake (M_{JMA}8.2) and the 2003 Reccurent Tokachi-oki Earthquake (M_{JMA}8.0) Segment

The Tokachi-oki area is one of the notable focal regions where M8 class earthquakes have recurred. The former event occurred in 1952 (M8.2). This event ruptured the entire segment shown in Fig. 1 (*Satake et al*., 2006). The recent earthquake in 2003 (M8.0) filled in eastern half of the 1952 rupture area (*Satake et al*., 2006, *Tanioka et al*., 2004, *Takahashi and Kasahara*, 2004).

Asperities of these two recent earthquakes were estimated by *Yamanaka and Kikuchi* (2003). Though strong motion waveforms of the 1952 event recorded only the first half of the full duration because of instrumental problems, their efforts succeeded to partially determine the asperity of this event. They concluded that the 'seismic' asperities of these two Tokachi-oki earthquakes were the same.

Fig. 3 shows the epicenter distribution from 1976 to just before the 2003 mainshock from the Hokkaido University's catalogue. It is apparent in this figure that there are low seismicity patches surrounded by high seismicity regions. To clarify this property, a contour map of cumulative earthquake number bound by 0.08 degrees in latitude and longitude is shown in Fig. 4a. This clearly shows the inhomogeneous density of seismic activity. Fortunately, we already know the location of the asperity of the 2003 earthquake as mentioned above (*Yamanaka and Kikuchi*, 2003). Superimposing the maps of the earthquake density and the asperity location by *Yamanaka and Kikuchi* (2003) point out the fact that the locations and dimensions of the low seismicity patches labeled A and B agree fairly well with that of the 2003 asperity location (Fig. 4b).

Relatively large aftershocks of the 2003 event mainly occurred in patch-C as shown in Fig. 4 and Fig. 5. Maximum slip of these aftershocks by *Yamanaka* (2005) was only

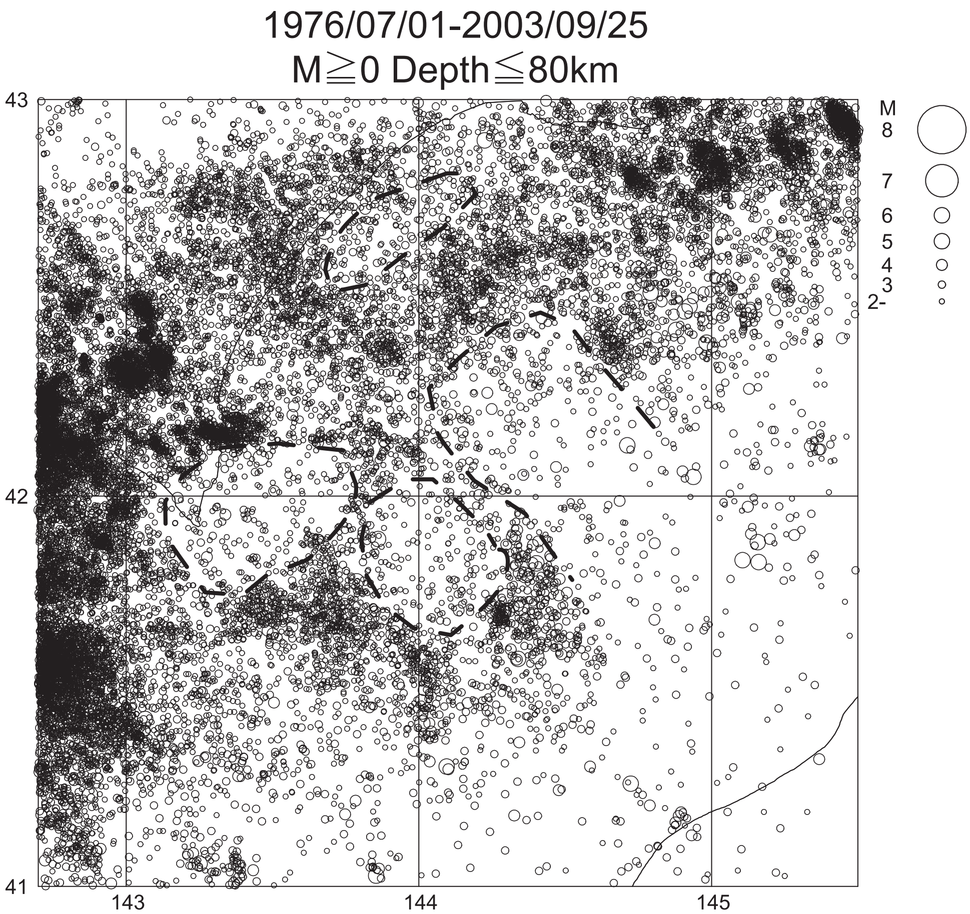

Figure 3. Background seismic activity in the Tokachi-oki segments where the 1952 (M8.2) and the 2003 (M8.0) recurrent earthquake occurred by Hokkaido University catalogue. Dashed lines indicate low seismic activities patches.

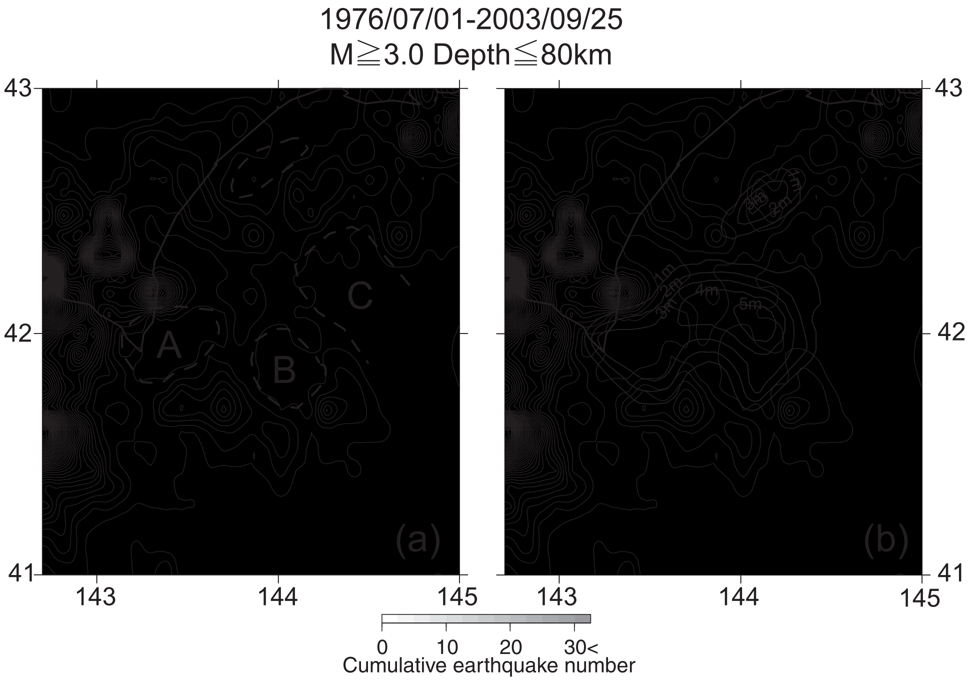

Figure 4. (a) Contouring of the cumulative earthquake number by the Hokkaido University catalogue and low seismicity patches indicated in Fig. 3. Contour interval is every 10 events. (b) Same as Fig. 4(a) with the 2003 Tokachi-oki earthquake asperity by *Yamanaka and Kikuchi* (2003).

0.3m, which is only 5% of the mainshock maximum slip. These relatively small moment releases in patch-C are almost the same as estimated by geodetic data including afterslip (*Miyazaki et a*l., 2004; *Ozawa et al*., 2004). *Miyazaki et al*. (2004) suggest that steady-state velocity strengthening friction means steady slip during the interseismic period. On the other hand, *Satake et al*. (2006) show the large coseismic slip (~3.48m) in the patch-C at the 1952 Tokachi-oki earthquake from tsunami data. This implied stress accumulation during interseismic phase. Therefore, we infer the possibility that most of the accumulated stress in patch-C still remains.

3-2. The 1973 Nemuro-oki Earthquake (M_{JMA}7.4) Segment

The Neromo-oki segment is located adjacent and to the east of the Tokachi-oki segment. The former Nemuro-Hanto-oki earthquake (M7.4) occurred in 1973. The largest aftershock (M7.1) occurred at a detached location from the mainshock epicenter. *Yamanaka and Kikuchi* (2001) also pointed out that the locations of the asperities of the 1973 mainshock and largest aftershock were clearly different. Therefore, we propose two asperities in this segment.

Fig. 6a displays the background seismicity since 1976, and Fig. 6b shows the density contour of cumulative earthquake number along with the 1973 mainshock and largest aftershock asperities by *Yamanaka and Kikuchi* (2001).

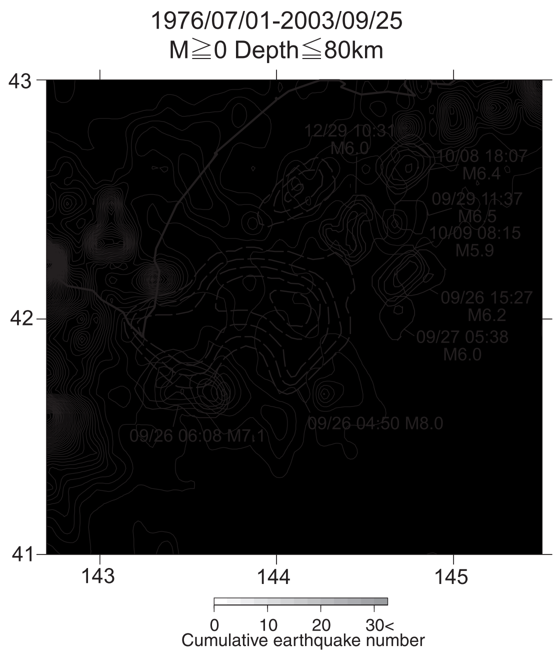

Figure 5. Asperities of mainshock and major aftershocks of the 2003 Tokachi-oki earthquake (*Yamanaka*, 2005) with contouring of cumulative earthquake number as in Fig. 4. Mainshock asperity is shown by dashed line. Contour intervals are 1m for mainshock, 0.2m for largest aftershock (M7.1), and 0.05m for others, respectively.

These figures clearly indicate that background seismicity has been extremely low in the whole Nemuro-oki segment since 1976. There were no M>5 earthquakes in the asperity region during this period. This seismic gap fully covers the 1973 mainshock asperity, extends trenchward and into the southwestern regions. The size of this gap is about 150km long by 100km wide. On the other hand, there has been a high seismicity rate at the onshore region of the 1973 asperity. This region is situated downdip of the extension of the 1973 asperity.

The high seismicity rate in the region eastward of the 1973 asperity was due to the aftershocks of the 1994 Hokkaido-Toho-oki intraslab event (M8.2) (e.g. *Kikuchi and Kanamori*, 1995). Therefore, it is difficult to extract the properties of the background seismicity in the area of the largest 1973 aftershock asperity.

3-3. The off Hamanaka Earthquake Sequence in 2004–2005 (M7.1 and M6.9) and 1961(M7.2 and M6.9)

An earthquake with M7.1 occurred on 29 November 2004 inshore Hamanaka (Fig.1), which corresponds to the coastal portion of the Nemuro-oki segment discussed above. The largest aftershock M6.9 occurred to the southeast of the mainshock on 6 December 2004. These focal mechanisms show typical thrust faulting mechanisms on the plate interface (Fig.1) (*NIED*, 2005).

In this area there was an earthquake sequence in 1961 with M7.2 and M6.9. *Yamanaka and Kikuchi* (2001) located these asperities. It is noteworthy that the epicenter locations of the mainshock and aftershock were nearly the same as the 2004 events. In addition, strong motion waveforms of these two events at the several JMA stations were very similar (*Yoshida et al*., 2005). These facts strongly imply that the 2004 earthquakes were the recurrent events of the 1961 sequence. Asperities of the 1961 and 2004 events were examined by *Yamanaka* (2004a, 2004b, 2004c). *Yamanaka* (2004a) concluded by comparing the location and slip distribution of asperities of these events that the 2004 M7.1 event was the recurrent earthquake of the 1961 (M7.2).

The spatial distribution of background seismicity, aftershocks, and asperities in the focal region shows interesting patterns. Fig. 7a and 7b display the background seismicity for the 7 years prior to the occurrence of the 2004 sequence by the JMA catalogue and its earthquake density map, respectively. There are remarkable seismic gaps among the seismic clusters. The asperities of the 2004

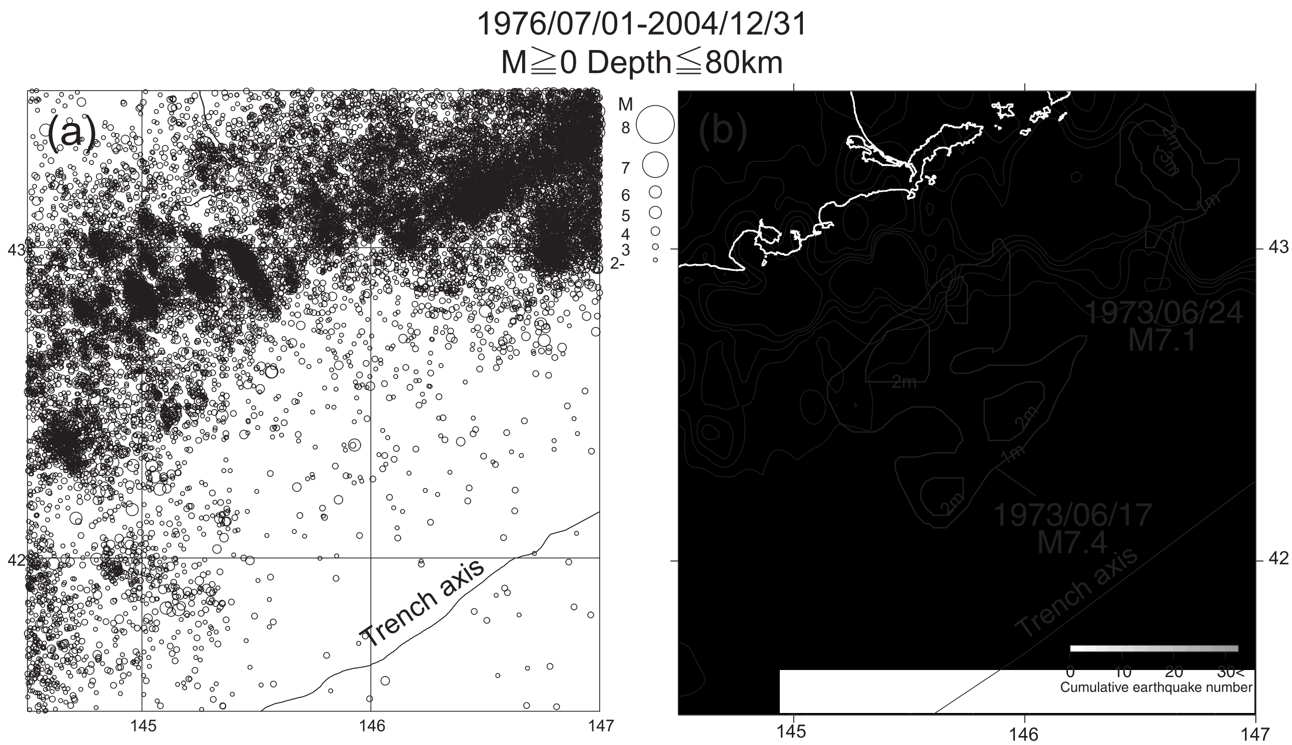

Figure 6. (a) Background seismic activity in the Nemuro-oki segment where the 1973 (M7.4) earthquake occurred using the Hokkaido University catalogue. (b) Contouring of cumulative earthquake number and the 1973 mainshock (M7.4) and largest aftershock (M7.1) asperities by *Yamanaka and Kikuchi* (2001).

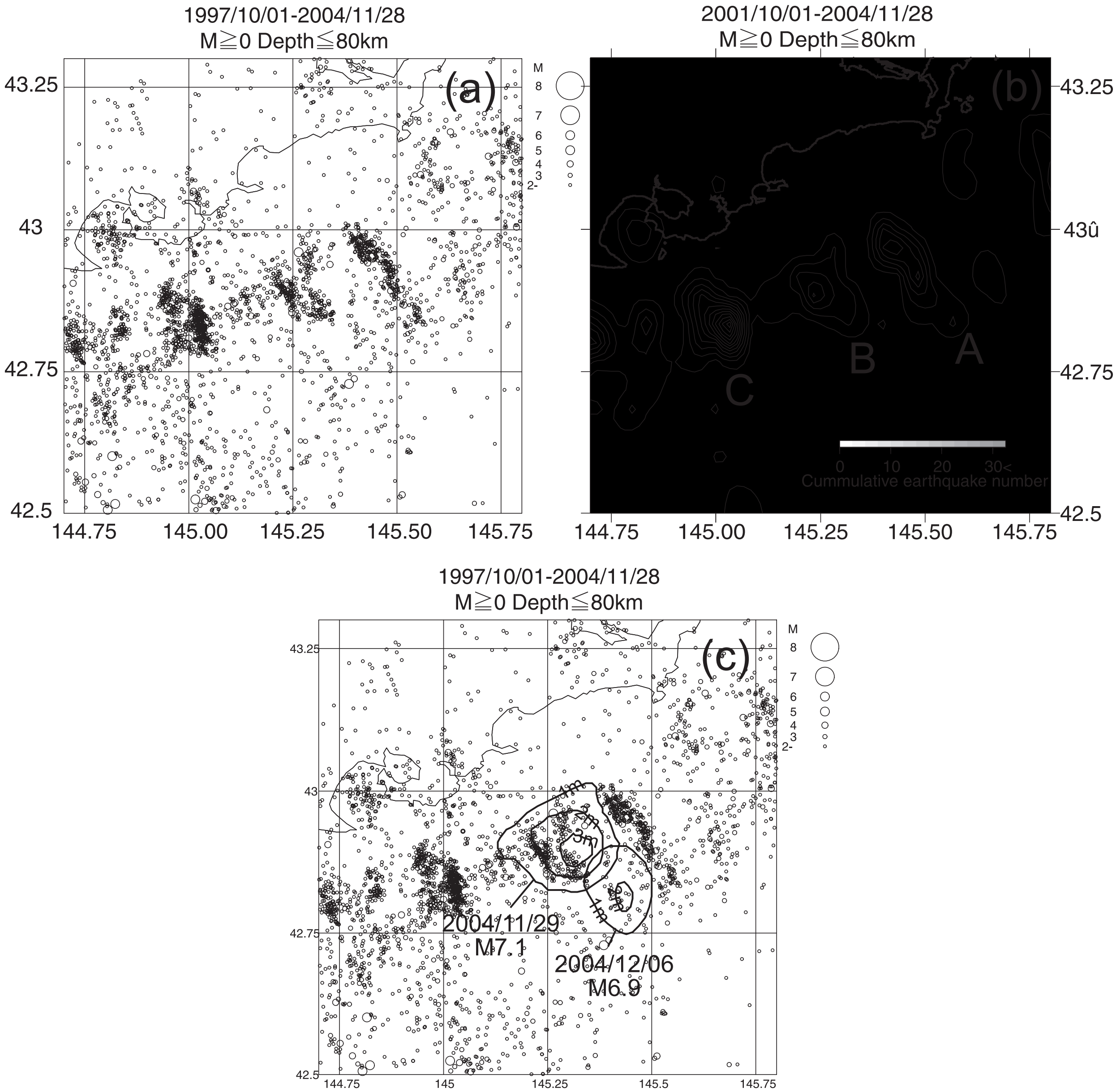

Figure 7. (a) Background seismic activity off Hamanaka region by JMA catalogue. (b) Contouring of cumulative earthquake number. Contour interval is every 10 events. (c) Background seismicity and asperities of the 2004 mainshock (M7.1) and largest aftershock (M6.9) inferred by *Yamanaka* (2004a, 2004c).

mainshock (M7.1) and largest aftershock (M6.9) determined by *Yamanaka* (2004a, 2004b, 2004c) were also superimposed on the background seismicity (Fig. 7c). These asperities are located in the seismic gap without overlapping the seismicity clusters. This suggests that the seismic gap is the seismic asperity. Location of the mainshock and largest aftershock asperities were segregated. This indicated that these events occurred by faulting on neighboring independent asperities as mentioned by *Yamanaka* (2004c).

Fig. 8 shows the locations of the asperities of the 2004 mainshock and largest aftershock and their aftershocks. This demonstrated that aftershocks of these earthquakes mainly occur in the areas surrounding of the mainshock asperity, and very few in the asperities. This aftershock distribution is analogous with that of the background seismicity as shown in Fig. 7. In other words, background seismic activity and aftershocks mostly occur around the edge of the asperity.

4.

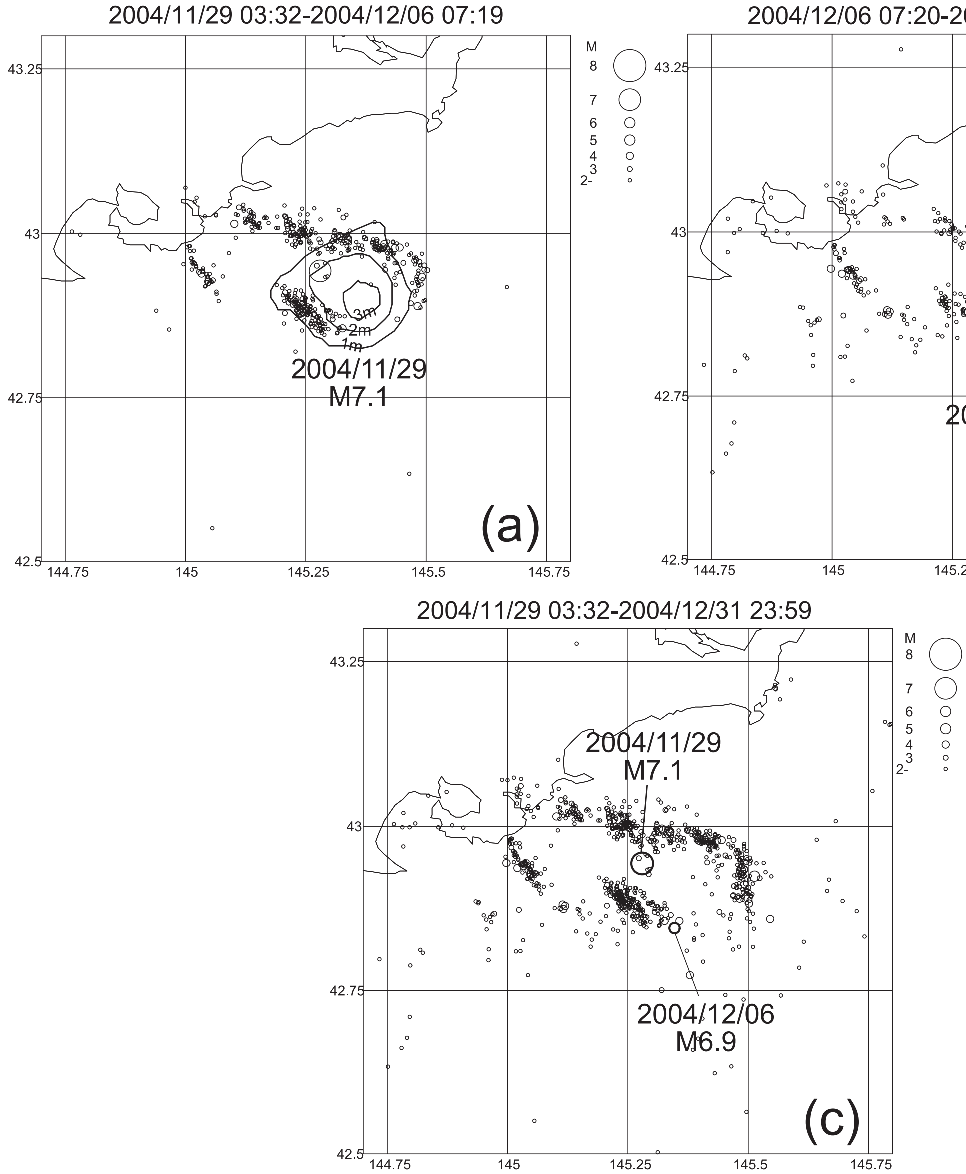

Figure 8. (a) Asperity (*Yamanaka*, 2004a) and aftershock activity of the 29 November 2004 event (M7.1). (b) Asperity (*Yamanaka*, 2004c) and aftershock activity of the 6 December 2004 event. (c) Total aftershock distribution of the 2004 earthquake sequence off Hamanaka. Aftershocks surrounds asperities.

DISCUSSION

4-1. Asperities and Interseismic Seismicity

Backgound seismicity in the southwestern Kuril Islands clearly shows the existence of low seismicity patches during interseismic periods. Locations of these patches correspond to the asperities of the largest earthquakes. In other words, seismic activity in asperities is generally low compared with the surrounding area during the interseismic phase. Earthquake density maps shown in Fig. 4, 6 and 7 are the integral expression of earthquake numbers in the time domain, and these suggest that low seismic activity in the asperity is a non-time dependent property.

This characteristic low seismic activity in the asperity has been observed in different size earthquakes that range from M6.9 to M8.0. This fact implies this phenomenon is not dependent on the dimensions of the asperity, and might indicate fractal characteristic as proposed by *Seno* (2003).

Plate interface depth data (*Iwasaki et al*., 1989; *Katsumata et al*., 2003, *Nakanishi et al*., 2004) indicate that low seismicity patches and active regions coexist at the same depth. This implies that this property is not due to changes of the vertical loading stress and/or thermal conditions on the plate interface (e.g. *Scholz*, 1990; *Nakatani*, 2003). Therefore, spatial variations of frictional properties on the plate interface by its nature may induce this heterogeneous seismicity pattern. *Miyazaki et al*. (2004) also indicates a possible along strike spatial variation of frictional properties at the same depth from postseismic deformation data observed by GPS associated with the 2003 Tokachi-oki earthquake.

Moment release at the asperity of the 1952 and 2003 Tokachi-oki earthquakes show that the seismic coupling coefficient was close to 100% (*Yamanaka and Kikuchi*, 2004). This indicates that the Tokachi-oki asperity could store up elastic strain without releasing stress during the interseismic period. In brief, coupling strength on the asperity has been consistently strong since 1952. On the other hand, it is a reasonable idea that high seismic activity in the area surrounding the asperity is due to a lower yielding point than the inner asperity at the same shear stress conditions.

There are several candidates to generate this frictional variation on the plate interface which induce heterogeneous seismicity, e.g. geometrical shape, changes in materials, water interactions on the plate interface. *Scholz and Small* (1997) suggest that subducting seamounts induce strong coupling and act as barriers to suppress the rupturing of the megathrust. This hypothesis was supported by several researchers who revealed the spatial distribution of seamounts and coseismic asperities in the Nankai Trough and Kuril Islands (e.g. *Kodaira et al*. 2000; *Hirata et al*. 2003). Effects of materials and water on the plate interface are also one of the possible parameters controlling properties of the plate interactions (e.g. *Kasahara*, 2003, *Kasahara et al*., 2003). However, structural and physical data on the plate interface in this region are difficult to come by. We hope future surveys of the deep structure along these asperities and high seismicity regions will reveal more information as in the northern Japan Trench (e.g. *Fujie et al*., 2002).

The observed relationship between background seismic activity and asperities suggest that asperities which are not yet mapped could be extracted from epicenter mapping as shown in this study. Determining the location of unknown asperities will help to focus detailed geophysical surveys which can reveal the status of the asperity and provide input to numerical strong ground motion predictions of destructive earthquakes. Of course, the ability to locate asperities depends on the precision of epicenter locations, observation period and event detectability of the seismographic network. We hope that the high accurate continuous observations made by Hokkaido University will enable further studies of the phenomena associated with subducting seismic activity.

4-2. Aftershock Period

The observation of low seismicity rate in the asperity and relatively high seismicity rate in the surrounding area might be applied to aftershock activity. Fig. 9 shows the one month of aftershocks for the 1973 and the 2003 earthquakes. Most of aftershocks occurred outside coseismic asperities. This relation is rather clear in the case of the 2004 off Hamanaka sequence (Fig. 7).

This spatial compartmentalization of asperities and aftershocks has already been observed in several earthquakes (*Mendoza and Hartzell*, 1988, *Houston and Engdahl*, 1989, *Nagai et al*., 2001, *Yamanaka and Kikuchi*, 2004). Detailed examination in the 1968 (M7.9) and 1994 (M7.6) recurrent earthquakes in the northern Japan Trench by *Nagai et al*.(2001) and *Yamanaka and Kikuchi* (2004) determined that the aftershock distribution of both earthquakes was quite similar. These indicate that the invariant asperity model is applicable not only to the mainshock asperity but also relatively small asperities which generate aftershocks. Stress changes in the surrounding area by mainshock faulting may induce seismicity if both the asperity and the surrounding area have velocity weakening frictional properties but different threshold points of faulting, higher for asperity and lower for the surrounding area. This hypothesis can be

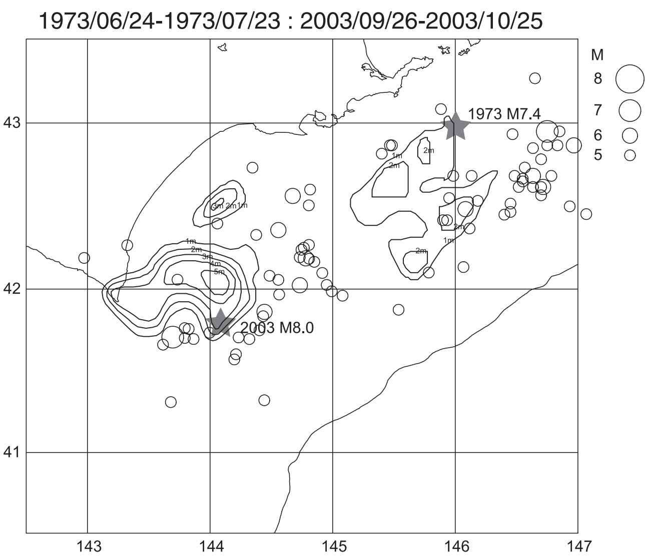

Figure 9. One month aftershock distribution of the 1973 Nemuro-Hanto-oki earthquake (M7.4) and the 2003 Tokachi-oki earthquake (M8.0) with their asperities examined by *Yamanaka and Kikuchi* (2001, 2003) based on JMA catalogue.

directly applicable to observed spatial variations of seismic activity during the interseismic phase.

4-3. The Largest Low Seismicity Region

Finally, we check a wide-area of seismicity southeastern off Hokkaido (Fig. 10). It clearly indicates the low seismicity area near the trench axis astride the Numuro-oki and Tokachi-oki segments, which is shown by a polygon. This feature is not apparent because a cumulative event number diagram in this polygon shows M ≥ 3 event detectability (Fig. 10).

Plate interface depth there is very shallow (10–15km depth from sea level) (*Iwasaki et al*., 1989, *Nakanishi et al*., 2004). This implies possible relatively weak coupling, frictionally stable, and stable sliding on the plate interface (*e.g. Yabe*, 2004), which is characterized by steady-state velocity strengthening (*Scholz*, 1990). These conditions suggest possible aseismic faulting on the plate interface.

On the other hand, there is a high seismicity region along the trench axis off Sanriku, southern adjacent region of the Tokachi-oki segment. *Umino et al*. (1995) confirmed that earthquakes occurring there are situated on the plate interface using *sP* depth phases. Furthermore, a large tsunami earthquake (M8.0) occurred there in 1896 (*Tanioka and Satake*, 1996). These facts indicate the possible ability to generate earthquakes near the trench axis region. Recent seafloor deformation data in the Peru-Chile trench reveal full coupling from 2km to 40km depth on the plate interface (*Gagnon et al.,* 2005). These facts suggest possible seismic faulting near the trench axis.

Tsunami sediment analysis reveals that paleo-megatsunamis have recurrently struck southeastern Hokkaido coast (*Hirakawa et al*, 2000; *Nanayama et al*., 2003). These unusual tsunami events might be induced by multi-segment rupture of both the Tokachi-oki and Numueo-oki regions. We propose a hypothesis that faulting of these mega-earthquakes extends to the trench axis including the seismic gap shown in Fig. 10.

Recent seismic activity along the trench axis has been obviously low. From the point of view of tsunami hazard assessment, it is desirable to clarify the earthquake genesis ability there by geophysical methods.

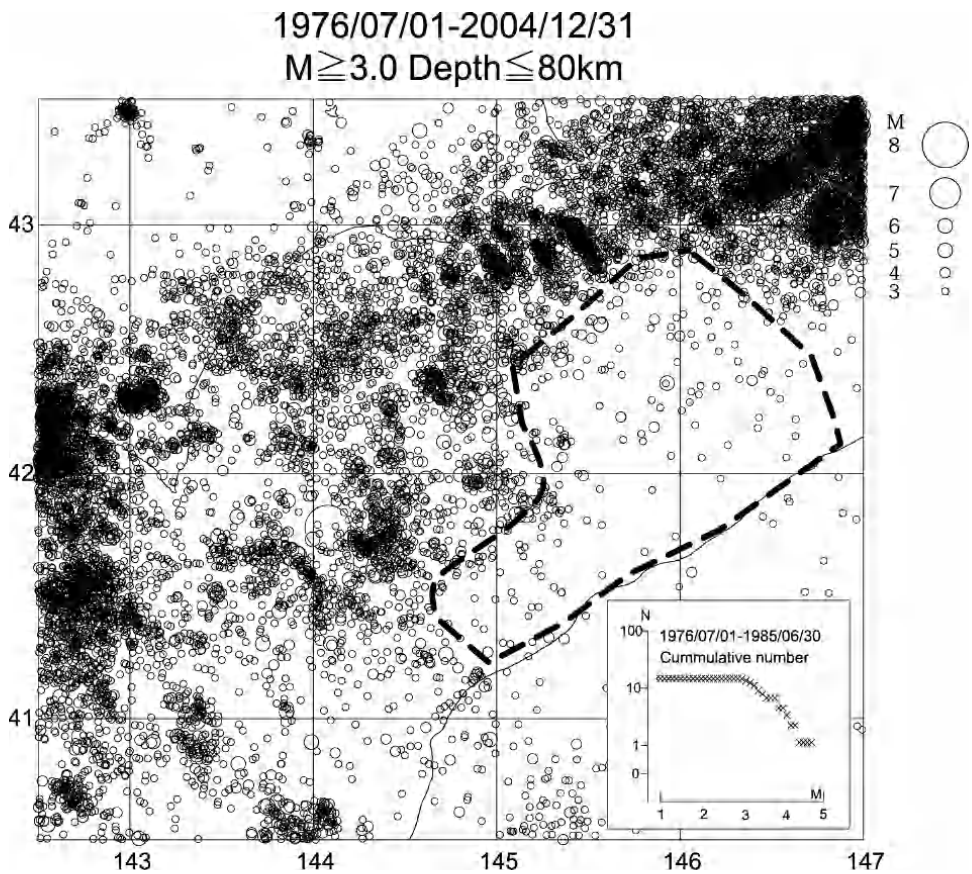

Figure 10. A largest seismic gap near trench axis by Hokkaido University catalogue. Inset indicates a cumulative earthquake number diagram in the polygon during a first decade of the observation period.

5. SUMMARY

Microseismicity catalogues produced by Hokkaido University clearly indicate that seismicity in the coseismic asperities have been low through the interseismic phase. These low seismicity patches are surrounded by high seismicity areas at the same depth. This relation between asperity and background seismicity is a commonly observed feature of the spatial distribution of mainshock asperity and aftershock activity as already pointed out by several studies.

Low seismicity rates in asperities do not vary with time, which suggest stable frictional properties in the temporal domain. This indicates spatial variations of the frictional coefficient on the plate interface causing this heterogeneous seismic activity. In other words, the spatial variation of seismic activity directly reflects the frictional variations on the plate interface. Observed interseismic and aftershock activity suggest that both asperities and their surroundings have steady-state velocity weakening, but different yielding threshold points to the shear stress. Asperities might define a patch where the yielding point to the shear stress is higher than the surrounding area. High steady seismicity around the asperities are caused by faulting of small asperities with low yielding points. Unknown asperities are detectable if high precision earthquake catalogues are available, which will provide important data to estimate the strong ground motion induced by destructive earthquakes.

Acknowledgments. We thank the staff of the Institute of Seismology and Volcanology, Hokkaido University, Drs. Y. Motoya, I. Maeda, S. Suzuki, Messers M. Okayama, M. Ichiyanagi, M. Takada, and T. Yamaguchi, and the Japan Meteorological Agency, who have operated and determined hypocenter routinely. We also thank anonymous reviewers for their constructive comments. Figures are partially drawn by SEIS-PC for WINDOWS (*Ishikawa and Nakamura,* 1997) and GMT (*Wessel and Smith,* 1995).

REFERENCES

Fedotov, S. A., N. A. Dolbilkina, V. N. Morozov, V. I. Myachkin, V. B. Preobrazensky and G. A. Sobolev, Investigation on earthquake prediction in Kamchatka, *Tectonophys*, **9**, 249–258, 1970.

Fujie, G., J. Kasahara, R. Hino, T. Sato, M. Shinohara, and K. Suyehiro, A significant relation between seismic activities and reflection intensities in the Japan Trench region, *Geophys. Res. Lett*., **29**, doi:10.129/2001GL013764, 2002.

Fukao, Y., and M. Furumoto, Foreshocks and multiple shocks of large earthquakes, *Phys. Earth Planet. Int*., 10, 355–368, 1975.

Gagnon, K., C. D. Chandwell, and E. Norabuena, Measuring the onset of locking in the Peru-Chile trench with GPS and acoustic measurements, *Nature*, 434, 205–208, 2005.

Hirakawa K., Y. Nakamura and T. Echigo, Large paleo-tsunamis along the Pacific coast of Tokachi region, Hokkaido (In Japanese), *Earth Monthly*, *Special Issue*, **31**, 92–98, 2000.

Hirata, K., M. Aoyagi, H. Mikada, K. Kawaguchi, Y. Kaiho, R. Iwase, S. Morita, I.Fujisawa, H. Sugioka, K. Mitsuzawa, K. Suyehiro, H. Kinoshita, and N. Fujiwara, Real-time geophysical measurements on the deep seafloor using submarine cable in the southern Kurile subduction zone, *IEEE Journal of Oceanic Engineering*, **27**, 170–181, 2002.

Hirata, K., E. Geist, K. Satake, Y. Tanioka, and S. Yamaki, Slip distribution of the 1952 Tokachi-Oki earthquake (M8.1) along the Kuril Trench deduced from tsunami waveform inversion, *J. Geophys. Res*., **108**, 2196, doi:10.1029/2002JB001976, 2003.

Honda, R., S. Aoi, N. Morikawa, H. Sekiguchi, T. T. Kunugi, and H. Fujiwara, Ground motion and rupture process of the 2003 Tokachi-oki earthquake obtained from strong motion data of K-NET and KiK-net, *Earth Planets Space*, **56**, 317–322, 2004.

Houston, H., and E. R. Engdahl, A comparison of the spatiotemporal distribution of moment release for the 1986 Andreanof Islands earthquake with relocated seismicity, *Geophys. Res. Lett*., **16**, 1421–1424, 1989.

Ishikawa, Y.and K. Nakamura, SEIS-PC for Windows95, *Abstracts of the 1997 Joint Assembly of Earth and Planetary Science Societies*, P78, 1997.

Iwasaki, T., H. Shiobara, A. Nishizawa, T. Kanazawa, K. Suyehiro, N. Hirata, T. Urabe and H. Shimamura, A detailed subduction structure in the Kurile trench deduced from ocean bottom seismographic refraction studies, *Tectonophysics*, **165**, 315–336, 1989.

Kasahara J., ed., *The role of water in earthquake generation*, University of Tokyo Press, 392pp, 2003.

Kasahara, J., K. Mochizuki, A. Kamimura, M. Nakamura, R. Hino, T. Yamada, T. Sato, P.P. Moghaddam,. M. Nishino, Y. Nakamura and T. Kanazawa, Non-asperities at subduction zones and estimation of materials at plate boundary, *J. Geogra*., **112**, 814–827, 2003.

Katsumata K., N. Wada, and M. Kasahara, Newly imaged shape of the deep seismic zone within the subducting Pacific plate beneath the Hokkaido corner, Japan‐Kurile arc‐arc junction, *J. Geophys. Res*., **108**, 2565, doi:10.1029/2002JB002175, 2003.

Kikuchi, M., and H. Kanamori, The Shikotan earthquake of October 4, 1994: lithospheric earthquake, *Geophys. Res. Lett*., 22, 1025–1028, 1995.

Kodaira, S., N. Takahashi, A. Nakanishi, S. Miura, and Y. Kaneda, Subducted seamount imaged in the rupture zone of the 1946 Nankaido earthquake, *Science*, **289**, 104–6, 2000.

Lay, T., and H. Kanamori, Earthquake doublets in the Solomon Islands, *Phys. Earth Planet. Inter*., **21**, 283– 304, 405, 1980.

Mendoza, C., and S. H. Hartzell, Aftershock patterns and main shock faulting, *Bull. Seismo. Soc. Am*., **78**, 1438–1449, 1988.

Miura, S., Y. Suwa, A. Hasegawa, and T. Nishimura, The 2003 Tokachi-Oki earthquake—How much has the great event paid back slip debts?, *Geophys. Res. Lett*., **31**, L05613, doi:10.1029/2003GL019021, 2004.

Miyazaki, S., P. Segall, J. Fukuda, and T. Kato, 2004, Space time distribution of afterslip following the 2003 Tokachi-oki earthquake: Implication for variations in fault zone frictional properties, *Geophys. Res. Lett*., **31**, L06623, doi:10.1029/2003GL019410, 2004.

Mochizuki, E., E. Kobayashi, and M. Kishio, Hypocenter determination ability of JMA seismological observation system during 1965–1974, *Quarterly Journal of Seismology*, **42**, 23–30, 1978.

Nagai, R., M. Kikuchi, and Y. Yamanaka, Comparative study on the source processes of recurrent large earthquakes in Sanriku-oki region: the 1968 Tokachi-oki earthquake and the 1994 Sanriku-oki earthquake, *Zishin*, 2, **54**, 267–280, 2001.

Nakanishi A., A. J. Smith, S. Miura, T. Tsuru, S. Kodaira, K. Obana, N. Takahashi, P. R. Cummins, and Y. Kaneda, Structural factors controlling the coseismic rupture zone of the 1973 Nemuro-Oki earthquake, the southern Kuril Trench seismogenic zone, *J. Geophys. Res*., **109**, B05305, doi:10.1029/2003JB002574, 2004.

Nakatani, M., Physicochemical interpretation of time-depend healing of frictional strength: A quantitative analysis with absolute rate theory, *J. Geograph*., **112**, 961–969, 2003.

Nanayama, F., K. Satake, R. Furukawa, K. Shimokawa, B. F. Atwater, K. Shigeno, and S. Yamaki, Unusually large earthquakes inferred from tsunami deposits along the Kuril trench, *Nature*, **424**, 660–663, 2003.

NIED, Earthquake Mechanism Information, at http://www.fnet.bosai.go.jp/.

Ozawa, S., M. Kaidzu, M. Murakami, T. Imakiire, and Y. Hatanaka, Coseismic and postseismic crustal deformation after the Mw8 Tokachi-oki earthquake in Japan, *Earth Planets Space*, **56**, 675–680, 2004.

Satake, K., K. Hirata, S. Yamaki, and Y. Tanioka, Re-estimation of tsunami source of the 1952 Tokachi-oki earthquake, *Earth Planets Space ,* **58**, 535–542, 2006.

Scholz, *The mechanics of Earthquakes and Faulting*, Cambridge University Press, 1990.

Scholz, C. H., and C. Small, The effect of seamount subduction on seismic coupling, *Geology*, **25**, 487–490, 1997.

Seno, T., Fractal asperities, invasion of barriers, and interplate earthquakes, *Earth Planets Space*, **55**, 649–665, 2003.

Shimazaki K., Nemuro-oki Eathquake of June 17, 1973: A lithospheric rebound at the upper half of the interface, *Phys. Earth Planet. Int*., 9, 314–327, 1974.

Takahashi, H. and M. Kasahara, The 2003 Tokachi-oki earthquake, off southeastern Hokkaido, Japan, *Zishin*, **2**, 57, 115–130, 2004.

Tanioka, Y., and K. Satake, Fault parameters of the 1896 Sanriku tsunami earthquake estimated from tsunami numerical modeling, *Geophys. Res. Lett*., **23**, 1549–1552, 1996.

Tanioka, Y., K. Hirata, R. Hino, and T. Kanazawa, Slip distribution of the 2003 Tokachi-oki earthquake estimated from tsunami waveform inversion, *Earth Planets Space*, **56**, 373–376, 2004.

Umino, N., A. Hasegawa, and T. Matsuzawa, sP depth phase at small epicentral distances and estimated subducting plate boundary, *Geophys. J. Int*., **120**, 356–366, 1995.

Utsu, T., Large earthquakes near Hokkaido and the expectancy of the occurrence of a large earthquake off Nemuro, *The report of coordinating committee for earthquake prediction*, **7**, 7–12, 1972.

Yabe, Y., A proposal of new interpretation of spatiotemporal variation in seismicity and its application to plate interface east off NE Japan, *Zishin*, 2, **56**, 485–495, 2004 (Japanese with English abstract).

Yamanaka, Y., and M. Kikuchi, Asperity map in Hokkaido, *Program and Abstract of the Seismological Society of Japan*, B52, 2001.

Yamanaka, Y. and M. Kikuchi, Source processes of the recurrent Tokachi-oki earthquake on September 26, 2003, inferred from teleseismic body waves, *Earth Planets Space*, **55**, e21–e24, 2003.

Yamanaka, Y., and M. Kikuchi, Asperity map along the subduction zone in northeastern Japan inferred from regional seismic data, *J. Geophys. Res*., **109**, 1307307, doi10.1029/2003JB002683, 2004.

Yamanaka, Y., *EIC earthquake note*, No. 158, at http://www.eri.u-tokyo.ac.jp/sanchu/Seismo_Note/, 2004a.

Yamanaka, Y., *EIC earthquake note*, No. 158+ at http://www.eri.u-tokyo.ac.jp/sanchu/Seismo_Note/, 2004b

Yamanaka, Y., *EIC earthquake note*, No. 159 at http://www.eri.u-tokyo.ac.jp/sanchu/Seismo_Note/, 2004c

Yamanaka, Y., Rupture process of the 2003 and 1952 Tokachi-oki earthquakes, *Earth Monthly*, *Special Issue*, **49**, 34–39, 2005.

Yoshida, Y., T. Yoshida, K. Nakamura, and T. Aketagawa, Aftershock distribution and source process of the Off Kushiro earthquake on November 24, 2004, *Abstracts of the 2005 Japan Earth and Planetary Sciences Joint Meeting*, S052P-007, 2005.

Wessel, P., and W. H. F. Smith, New Version of the Generic Mapping Tools Released, *EOS Trans. AGU*, **76**, 329, 1995.

Late Pleistocene-Holocene Volcanism on the Kamchatka Peninsula, Northwest Pacific Region

Vera Ponomareva, Ivan Melekestsev and Olga Braitseva

Institute of Volcanology and Seismology, Petropavlovsk-Kamchatsky, Russia

Tatiana Churikova[1]

Geowissenschaftliches Zentrum Göttingen, Universität Göttingen, Germany

Maria Pevzner and Leopold Sulerzhitsky

Geological Institute, Moscow, Russia

Late Pleistocene-Holocene volcanism in Kamchatka results from the subduction of the Pacific Plate under the peninsula and forms three volcanic belts arranged in en echelon manner from southeast to northwest. The cross-arc extent of recent volcanism exceeds 250 km and is one of the widest worldwide. All the belts are dominated by mafic rocks. Eruptives with SiO_2>57% constitute ~25% of the most productive Central Kamchatka Depression belt and ~30% of the Eastern volcanic front, but <10% of the least productive Sredinny Range belt.

All the Kamchatka volcanic rocks exhibit typical arc-type signatures and are represented by basalt-rhyolite series differing in alkalis. Typical Kamchatka arc basalts display a strong increase in LILE, LREE and HFSE from the front to the back-arc. La/Yb and Nb/Zr increase from the arc front to the back arc while B/Li and As, Sb, B, Cl and S concentrations decrease. The initial mantle source below Kamchatka ranges from N-MORB-like in the volcanic front and Central Kamchatka Depression to more enriched in the back arc. Rocks from the Central Kamchatka Depression range in $^{87}Sr/^{86}Sr$ ratios from 0.70334 to 0.70366, but have almost constant Nd isotopic ratios ($^{143}Nd/^{144}Nd$ 0.51307–0.51312). This correlates with the highest U/Th ratios in these rocks and suggest the highest fluid-flux in the source region.

Holocene large eruptions and eruptive histories of individual Holocene volcanoes have been studied with the help of tephrochronology and ^{14}C dating that permits analysis of time-space patterns of volcanic activity, evolution of the erupted products, and volcanic hazards.

INTRODUCTION

Models of active volcanism along subduction zones presume that lithospheric plates have been moving uniformly over thousands of years and that magma in subduction zones is generated continuously and at a constant rate. However, eruptions of magma at the surface are episodic or clustered, rather than constant or periodic in time [e.g. *Cambray* and *Cadet*, 1996; *Sigurdsson*, 2000; *Gusev* et al., 2003]. Furthermore, the volcanic belt may consist of vents, scattered out over a much wider zone and erupting more variable magmas than anticipated by a simple model of subduction-generated magma flow. In Kamchatka, subduction is responsible for most of recent volcanism [e.g. *Volynets*,

[1]Now at Institute of Volcanology and Seismology, Petropavlovsk-Kamchatsky, Russia

Volcanism and Subduction: The Kamchatka Region
Geophysical Monograph Series 172

10.1029/172GM15

1994; *Churikova* et al., 2001, 2007; *Avdeiko* et al., 2006; *Portnyagin et al.*, 2007a, b]. However, its spatial distribution and time patterns are rather complicated. In this paper, we present data on the latest period of volcanic activity in Kamchatka, which started 50–60 ka BP [*Erlich* et al., 1979]. It was during this period when dominantly pyroclastic classical conic stratovolcanoes started to form, which now comprise a typical volcanic landscape of Kamchatka (Fig. 1).

The Kamchatka Peninsula overlies the northwestern margin of the Pacific plate subducting under Kamchatka at ~8 cm/yr [*DeMets*, 1992]. In the north, the Kamchatka subduction zone terminates at the transform fault zone of the Western Aleutians (Figs. 2A, B). Close to the northern terminus of the subduction zone, slab dip is believed to shallow from 55° to 35°, with probable loss of a slab fragment [*Levin* et al., 2002; *Park* et al., 2002]. Plate geometry in this northwest "corner" is currently under debate [e.g. *Riegel* et al., 1993; *Mackey* et al., 1997; *McElfresh* et al., 2002; *Bourgeois* et al., 2006]. Some authors treat Kamchatka as a part of the North American plate [e.g. *Park* et al., 2002], while others locate it on a smaller Okhotsk block (or microplate) [e.g. *Zonenshain* and *Savostin*, 1979; *Riegel* et al., 1993] and add a Bering block east of it [e.g. *Lander* et al., 1994; *Mackey* et al., 1997]. Whatever the plates' evolution may have been, it is likely recorded in the time-space patterns of Kamchatka volcanism and in geochemical affinities of the volcanic rocks. The best example of this connection are findings of adakite-like rocks in northern Kamchatka, probably reflecting the edge of the subducting Pacific plate being warmed or ablated by mantle flow [*Volynets* et al., 1997b, 1999b, 2000; *Peyton*, 2001; *Yogodzinski* et al., 2001a]. Research aimed at understanding of the nature of various volcanic zones in Kamchatka and their relation to the changing tectonic environment is currently going on in many areas of Kamchatka [e.g., *Avdeiko* et al., 2006; *Churikova* et al., 2001, 2007; *Duggen* et al., 2007; *Perepelov*, 2004; *Perepelov* et al., 2005; *Portnyagin* et al., 2005, 2007a, b; *Volynets* et al., 2005] and hopefully will result in the understanding of this dynamic region.

SPATIAL DISTRIBUTION

Traditionally, recent Kamchatka volcanoes are assigned to two volcanic belts: Eastern volcanic belt and Sredinny Range (SR). The Eastern belt may be further subdivided into the Eastern volcanic front (EVF) and the Central Kamchatka Depression (CKD) volcanic zone (Fig. 2A). In fact, all the belts are not exactly linear and have a complicated structure (Fig. 2B). This might reflect subduction of sea mounts [e.g. *Churikova* et al., 2001] and peculiarities of the tectonic situation near a triple junction of lithospheric plates [e.g. *Yogodzinski* et al., 2001a; *Park* et al., 2002; *Portnyagin* et al.,

Figure 1. Eastern volcanic front, view to the south. Active Komarov volcano at the foreground, two late Pleistocene cones of Gamchen massif farther south, and Kronotsky volcano at the background. Classic cones of dominantly pyroclastic stratovolcanoes started to form only in late Pleistocene [*Braitseva* et al., 1974]. Photo courtesy Philippe Bourseiller.

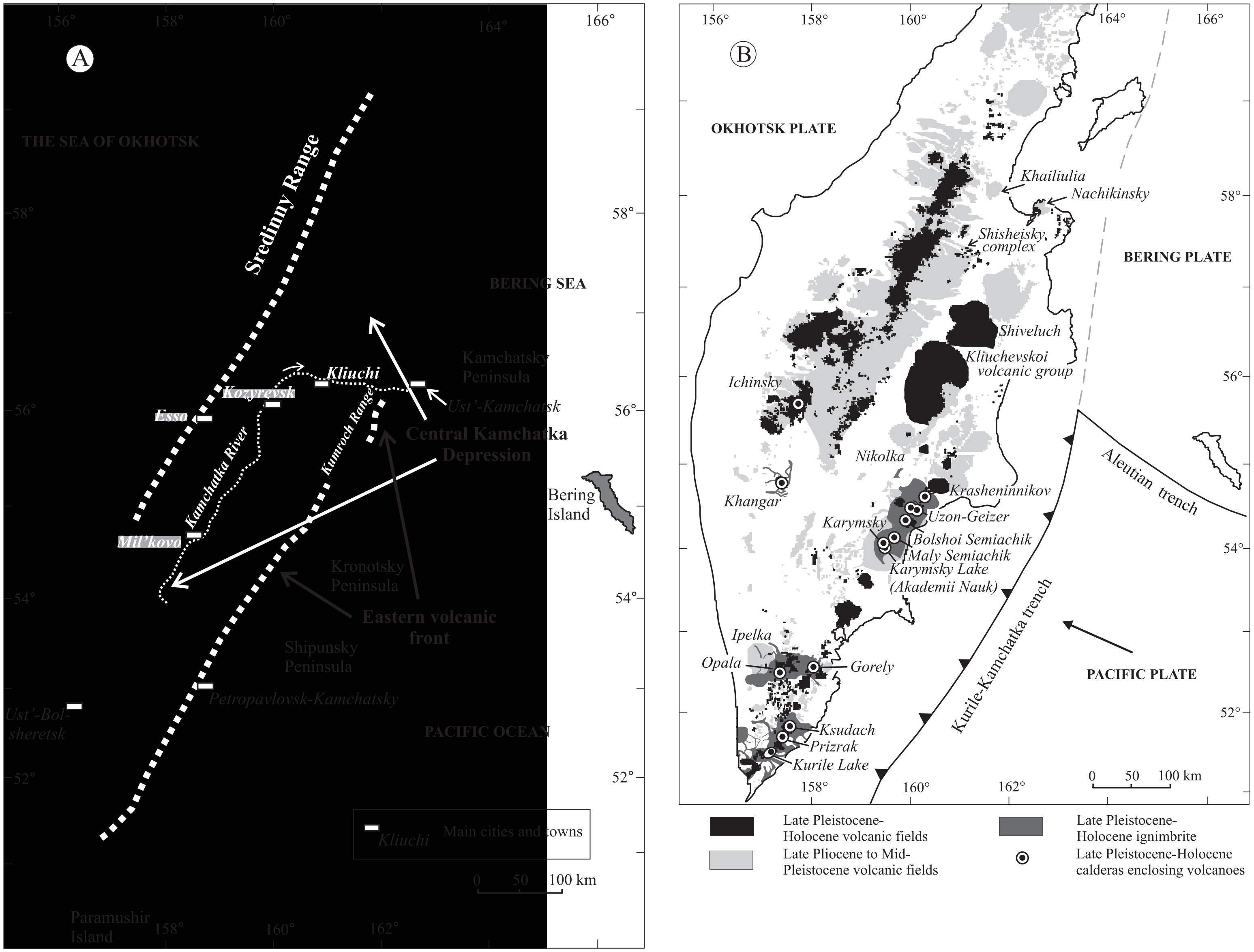

Figure 2. A. Shaded SRTM elevation model of Kamchatka showing main topographic features. Image released by NASA/JPL/NIMA. Dashed white lines shematically show EVF and SR volcanic belts. For SR volcanic belt, a line along its axial part is shown: from the southernmost Khangar volcano to the northern terminus of the late Pleistocene volcanism. **B**. Sketch map of late Pliocene-Holocene Kamchatka volcanic fields based on the 1:100 000 and 1:300 000 unpublished geological maps by Ivan Melekestsev, and *Map of Mineral Resources of Kamchatka region* (1:500 000) [1999]. Volcanic fields include debris avalanche and lahar deposits at the volcanoes foot. Gray dashed line shows a presumed boundary of the Bering plate [*Lander* et al., 1994]. Late Pleistocene-Holocene calderas and selected volcanoes are labeled.

2005; 2007b]. Distribution of the late Pleistocene-Holocene volcanic vents follows in general that of the preceding late Pliocene - mid-Pleistocene volcanic fields (Fig. 2B). The latter, however, cover far larger areas and comprise extensive mafic lava plateaus and huge shield volcanoes, still preserved in the topography [*Braitseva* et al., 1974].

There is no evident spatial correlation between late Pleistocene-Holocene volcanic centers and major active fault systems that bound main neotectonic structures of the peninsula (Fig. 3A). The only regional fault system that may be spatially linked to volcanism is found along the axis of the EVF and is different, both geometrically and kinematically, from other, "amagmatic", fault systems. The faults comprising this system exhibit dominantly normal displacement, probably with a small left-lateral component, and form a graben-in-graben structure ~130 km long and 10–18 km-wide [*Florensky* and *Trifonov*, 1985; *Kozhurin*, 2004].

Historically active volcanoes are located only in the Eastern volcanic belt (both in the EVF and CKD) (Table 1). This is likely the reason for a widely accepted opinion that Sredinny Range volcanism either is dying [e.g. *Avdeiko* et al., 2002, 2006] or is already dead [e.g. *Park* et al., 2002]. "Historical" time in Kamchatka, however, is very short—200–300 years—and tephrochronological studies and ^{14}C dating show that some Sredinny Range volcanoes have been active as recently as few hundreds of years ago [*Pevzner*, 2004, 2006]. Late Pleistocene-Holocene volcanic fields cover large areas in the Sredinny Range not lesser than in the eastern Kamchatka (Fig. 3A), [*Ogorodov* et al., 1972].

Three late Pleistocene-Holocene volcanic belts (those of EVF, CKD and SR) in plan view are arranged in en echelon manner from southeast to northwest (Fig. 2B). Within the belts, most of the eruptive centers are concentrated in 15–10 km wide axial areas. Best expressed is the EVF, which lies 200–250 km west of the Kurile-Kamchatka trench. It trends for ~550 km from SW to NE, from Kambalny volcano at the south to a relatively small group of late Pleistocene cinder cones dotting the eastern slope of the Kumroch Range almost as far north as the mouth of the Kamchatka River (Fig. 2A). These cones (including Kovrizhka and Krasny (Fig. 4B)) are commonly disregarded, in which case the EVF is considered to stretch only up to the Gamchen volcanic group and then step westward to the CKD via Kizimen volcano (Fig. 3A) [e.g. *Churikova* et al., 2001; *Park* et al., 2002]. EVF *per se* has a more or less linear plan view with westward offshoots to Opala volcano in the south and to Bakening volcano (against Shipunsky Peninsula) (Fig. 3A). The volcanic front consists of rather tightly spaced stratovolcanoes only 15–30 to 60 km apart from each other. Maly Semiachik and Krasheninnikov volcanoes consist of 2–3 overlapping cones stretching along the axial fault zone (Figs. 3A and 5), while Zhupanovsky, Kozelsky-Avachinsky-Koriaksky, Gorely and Koshelev volcanoes form prominent across-front ranges [*Holocene volcanoes in Kamchatka*, http://www.kscnet.ru/ivs/volcanoes/holocene]. Most of 5–18 km wide collapse calderas and associated ignimbrite fields are located in the EVF, forming chains between Kronotsky and Karymsky lakes and then from Ksudach to Kurile Lake (Fig. 2B) and (Table 2).

The next volcanic belt to the northwest is the CKD one, hosting the most vigorous volcanoes of Kamchatka (Figs. 2, 3 and 4). Most of the volcanic centers, including large volcanoes and clusters of monogenetic vents, are concentrated in a 150-km-long belt from Tolbachik lava field in the south to Shiveluch volcano in the north. A few smaller monogenetic vents are scattered over old Nikolka volcano ~30 km south of this zone, and near old Nachikinsky volcano ~150 km NE of Shiveluch. Some authors trace this zone farther south via monogenetic vents at old Ipelka volcano (west of Opala) and then to a back-arc western volcanic zone of the Kurile arc (Fig. 3A) [*Melekestsev* et al., 1974; *Laverov*, 2005]. A number of monogenetic vents scattered on the eastern slope of the Sredinny Range in the Elovka River basin (sometimes called "Shisheisky Complex") 60–80 km NNW of Shiveluch (Fig. 2B) likely also should be attributed to the CKD rather than to SR volcanic zone based on their geochemical features [*Portnyagin* et al., 2007b]. Geographically, however, many of those belong to Sredinny Range, so in (Table 1) we enlist the Holocene vents from this group (Bliznetsy, Kinenin and Shisheika, (Fig. 4B) under "Sredinny Range". No ignimbrite-related calderas are known to date in CKD; 3–5 km wide summit calderas on Plosky Dalny (Ushkovsky) and Plosky Tolbachik volcanoes resulted from the collapse due to lava drainage [*Melekestsev* et al., 1974].

The next late Pleistocene-Holocene volcanic belt to the northwest, that of SR, starts from the isolated Khangar intra-caldera volcano in the south, then widens for 100 km farther north and finally merges into a single narrow belt following the axis of the Sredinny Range (Figs. 2A and B). Unlike EVF and CKD with their conic stratovolcanoes, SR hosts mostly lava fields and a few shield-like volcanoes (with the exception of Khangar and Ichinsky intra-caldera edifices).

The widest possible cross-arc extent of recent volcanism (and one of the widest worldwide) forms a ~250x250 km^2 zone stretching from the Pacific coast inland along the projection of the Aleutian trend (Fig. 3B). This unusually wide range of recent volcanism coincides with slab shallowing [*Gorbatov* et al., 1997] and likely results from the subduction of the Emperor Seamount chain [*Churikova* et al., 2001].

Table 1. Kamchatka volcanoes active in Holocene

Name	Location of an active crater, Lat. N Long.E	Description	Last dated eruption, AD or ^{14}C yr BP	Dominating Holocene rocks
		Eastern volcanic front		
Central Kamchatka Depression				
Shiveluch	56° 38' 161° 19' (Young Shiveluch)	Late Pleistocene stratovolcano with a collapse crater hosting Holocene Young Shiveluch eruptive center	AD 2007	Medium-K, high-Mg and Cr basaltic andesite -andesite series
Plosky Dalny (Ushkovsky)	56° 04' 160° 28'	Late Pleistocene stratovolcano with two summit calderas and Holocene flank vents (e.g., Lavovy Shish)	≤8600	Medium- and high-K basalt - basaltic andesite
Kliuchevskoi	56° 03' 160° 39'	Holocene stratovolcano with numerous flank vents	AD 2007	Medium-K basalt-basaltic andesite
Bezymianny	55° 58' 160° 36'	Holocene stratovolcano with growing lava dome	AD 2007	Medium-K basaltic andesite-andesite series
Plosky Tolbachik	55° 49' 160° 23'	Late Pleistocene stratovolcano with two summit calderas, active in Holocene	AD 1975–76	High-K basalt
Tolbachik lava field (south and northeast of Plosky Tolbachik)		Numerous Holocene cinder cones and associated lava field	AD 1975–76	High-K, high-Al basalt and medium-K, high Mg basalt
Kizimen	55° 08' 160° 20'	Holocene volcano made of lava domes and flows	AD 1927–28	Medium-K basaltic andesite - dacite series
Eastern volcanic front				
Vysoky	55° 04' 160° 46'	Holocene stratovolcano	~2500	Transitional from low- to medium-K basaltic andesite-andesite series
Komarov	55° 02' 160° 44'	Holocene stratovolcano, likely successor to Vysoky	<1000	Transitional from low- to medium-K calc-alkaline andesite
Gamchen (Baranii Cone)	54° 58' 160° 43'	Holocene dominantly pyroclastic volcano with flank lava domes	~2500	Low-K basaltic andesite-andesite
Kronotsky	54° 45' 160° 32'	Late Pleistocene stratovolcano with Holocene flank cinder cones	AD 1923	Low-K basalt-basaltic andesite; andesite?
Cinder cones between Kronotsky Lake and Krasheninnikov caldera		Numerous cinder cones with lava flows, maar	~3400 (Zametny Cone)	Medium-K tholeiitic basaltic andesite
Krasheninnikov	54° 38' 161° 19' (Northern Cone)	Two coalesced Holocene stratovolcanoes with flank vents inside a late Pleistocene caldera	400–500	Medium-K tholeiitic basalt-dacite series
Cinder cones south of Krasheninnikov caldera		A number of cinder cones	3200–3300 (Duga Cone)	Medium-K tholeiitic basaltic andesite-andesite

Table 1. *Cont.*

Name	Location of an active crater, Lat. N Long.E	Description	Last dated eruption, AD or ^{14}C yr BP	Dominating Holocene rocks
Kikhpinych	54° 29' 160° 16' (Savich Cone)	Two coalesced Holocene stratovolcanoes and a lava dome	~500	Low-K basalt-basaltic andesite
Taunshits	54° 32' 159° 48' (young dome)	Late Pleistocene stratovolcano with Holocene collapse crater and lava dome	~2400	Medium-K calc-alkaline basaltic andesite-andesite
Monogenetic craters inside Uzon caldera		Dalnee Lake tuff ring and a number of maars	Small phreatic eruption in AD 1989; Dalnee Lake 7600-7700	Dalnee Lake -medium-K tholeiitic basaltic andesite
Monogenetic lava domes in Bolshoi Semiachik caldera		Lava domes, some with lava flows	Ezh and Korona domes ~ 5600	Low-K andesite
Maly Semiachik	54° 07' 159° 39' (Troitsky Crater)	Three coalesced stratovolcanoes inside a late Pleistocene caldera	AD 1952	Medium-K tholeiitic basalt-andesite series and low-K basalt (?)
Karymsky	54° 03' 159° 27'	Holocene caldera enclosing a stratovolcano	AD 2007	Medium-K calc-alkaline basaltic-andesite-rhyolite series
Tuff rings near the northern shore of the Karymsky Lake		At least two Holocene tuff rings	AD 1996	Medium-K calc-alkaline basaltic andesite
Cinder cones in Levaia Avacha River valley (east of Bakening): Zavaritsky, Veer, etc.		Scattered cinder cones with lava flows, maar	1600-1700 (Veer Cone)	Medium-K basalt-basaltic andesite
Novo-Bakening	53° 57' 158° 06'	Large monogenetic center with lava flows	Early Holocene	Medium-K andesite - dacite
Bakening	53° 55' 158° 05'	Late Pleistocene stratovolcano	Early Holocene	Medium-K andesite
Cinder cones south of Bakening		Scattered cinder cones with lava flows, maars	~600 (Kostakan)	Medium-K basalt-basaltic andesite
Zhupanovsky	53° 35' 159° 08'	Late Pleistocene-Holocene volcanic range made of stratovolcanoes and lava domes	AD 1956-57	Transitional from low- to medium-K basalt-andesite series
Lava cones and flows west of Zhupanovsky		Lava cones with extensive and thick lava flows	~1600	Medium-K andesite
Koriaksky	53° 19' 158° 43'	Late Pleistocene-Holocene stratovolcano	AD 1956-57	Medium-K basalt-andesite series
Avachinsky	53° 15' 158° 50'	Late Pleistocene stratovolcano with a collapse crater hosting Young Cone Holocene stratovolcano	AD 2001	Low-K basaltic andesite-andesite series
Kozelsky	53° 14' 158° 53'	Late Pleistocene stratovolcano with a collapse crater	Early Holocene	Low-K basaltic andesite-andesite series

Table 1. *Cont.*

Name	Location of an active crater, Lat. N Long.E	Description	Last dated eruption, AD or ^{14}C yr BP	Dominating Holocene rocks
Cinder cones south of Nachikinsky Lake (north of Tolmachev lava field)		A number of cinder cones	?	?
Cinder cones north of Viliuchinsky		Scattered cinder cones with lava flows	Middle Holocene	Medium-K basaltic andesite
Viliuchinsky	52° 42' 158° 17'	Late Pleistocene stratovolcano	Early Holocene	Medium-K basaltic andesite
Tolmachev lava field		Late Pleistocene-Holocene cinder cones and associated lava field	1600-1700	Medium-K basaltic andesite
Chasha Crater (Tolmachev lava field)	52° 38' 157° 33'	A large monogenetic crater	~4600	Transitional from medium to high-K rhyolite
Opala	52° 33' 157° 20'	Late Pleistocene-Holocene volcano on the rim of the late Pleistocene caldera with flank vents including a large crater Baranii Amphitheater with lava domes inside	AD 1776	Transitional from medium to high-K basaltic andesite-rhyolite series
Cinder cones and maar SSW of Opala caldera		Two cinder cones and maar	Early Holocene?	?
Gorely	52° 33' 158° 02' (Active Crater)	Late Pleistocene-Holocene volcanic ridge inside the late Pleistocene caldera	AD 1986	Medium- and high-K basaltic andesite - andesite
Mutnovsky	52° 28' 158° 10' (Active Crater)	Late Pleistocene volcanic massif with a Holocene stratovolcano	AD 2000	Low- and medium-K basalt-basaltic andesite
Asacha	52° 21' 157° 50'	Large volcanic center with Holocene cinder cones at the western flank	?	?
Khodutkinsky Crater (NW of Khodutka)	52° 05' 157° 38'	Large monogenetic crater with a lava dome	~2500	Medium-K rhyolite
Khodutka	52° 04' 157° 43'	Late Pleistocene-Holocene stratovolcano	~2000?	Low-K basalt-andesite series
Cinder cones W-SW of Khodutka		Cinder cones with lava flows	Holocene	?
Ksudach	51° 49' 157° 32' (Stübel Cone)	Large caldera complex with 3 Holocene calderas and Stübel stratovolcano	AD 1907	Low-K basaltic andesite-rhyolite series
Zheltovsky	51° 35' 157° 20'	Late Pleistocene stratovolcano with Holocene lava domes	AD 1923	Low-K basalt-andesite series
Iliinsky	51° 30' 157° 12'	Holocene stratovolcano with flank vents inside a Holocene collapse crater on the pre-Iliinsky volcano	AD 1901	Transitional from low- to medium-K tholeiitic basalt to dacite series

Table 1. *Cont.*

Name	Location of an active crater, Lat. N Long.E	Description	Last dated eruption, AD or ^{14}C yr BP	Dominating Holocene rocks
Kurile Lake caldera		Holocene caldera enclosing lava domes	~7600	Transitional from low- to medium-K basaltic andesite to rhyolite series
Ukho and Gorely cinder cones (NW of Koshelev)		Cinder cones with lava flows	~6000	Medium-K basalt
Dikii Greben'	51° 27' 156° 59'	Holocene extrusive massif	~1600	Medium-K dacite - rhyolite
Koshelev	51° 21' 156° 45' (Eastern Cone)	Pleistocene volcanic ridge with Holocene cinder cone and lava flows	AD 1741 ?	Medium-K basaltic andesite to dacite series
Kambalny	51° 18' 156° 53'	Holocene stratovolcano	AD 1767	Low-K basalt-basaltic andesite
		Sredinny Range		
Tobeltsen	58° 15' 160° 44'	Cinder cone with lava flows	~3500	Medium-K basalt
X Cone	58° 10' 160° 48'	Lava cone with a lava flow	~4000	Medium-K basalt
Spokoiny (Kutina[1])	58° 08' 160° 49'	Late Pleistocene-Holocene stratovolcano	~5400	Transitional from medium to high-K dacite-rhyolite
Nylgimelkin (Atlasov[1])	57° 58' 160° 39'	Small shield-like volcano topped with two cinder cones (likely one eruption)	~5500	Medium-K basalt
Ozernovsky	57° 35' 160° 38'	Cinder cone with lava field	9000–10,000	Medium-K basalt
Titila	57° 24' 160° 07'	Shield-like volcano	2500–3000	Transitional from medium to high-K basalt
Sedanka lava field		Cinder cones and associated lava flows	2500–3000	Transitional from medium to high-K basalt
Kinenin Maar	57° 21' 160° 58'	Maar with some juvenile tephra	~1100	Medium-K basaltic andesite
Bliznetsy ("Twins")	57° 21' 161° 22'	Lava domes and flows	~3000	Medium-K andesite
Gorny Institute	57° 20' 160° 11'	Late Pleistocene-Holocene stratovolcano	<700	Transitional from medium to high-K basaltic andesite-dacite
Shisheika	57° 09' 161° 05'	Lava dome and flow	4200	Medium-K andesite-dacite
Alney	56° 41' 159° 38'	Pleistocene volcanic massif with a Holocene eruptive center	<350	Medium-K andesite

Table 1. *Cont.*

Name	Location of an active crater, Lat. N Long.E	Description	Last dated eruption, AD or ^{14}C yr BP	Dominating Holocene rocks
Kireunsky (east of Alney)	56° 41' 159° 44'	Cinder cone and lava flow	~2600	Medium-K andesite
Lava flow in Levaia Belaia River (east of Alney)	56° 38' 159° 43'	Cinder cone and lava flow	~2600	Medium-K basaltic andesite-andesite
Kekuk Crater	56° 34' 158° 02'	Tuff ring?	7200–7300	Medium-K dacite
Ichinsky	55° 41' 157° 44'	Late Pleistocene-Holocene stratovolcano	AD 740	Transitional from medium to high-K andesite-dacite
North Cherpuk	55° 36' 157° 38'	Cinder cone and lava flow	~6500	Medium-K basaltic andesite-andesite
South Cherpuk	55° 33' 157° 28'	Cinder cones and lava field	~6500	Medium-K basalt-basaltic andesite
Khangar	54° 45' 157° 23'	Late Pleistocene-Holocene stratovolcano inside a late Pleistocene caldera	~400	Medium-K dacite-rhyodacite

[1] Volcano names as in *Ogorodov* et al., 1972. Other names in parentheses in column 1 are other names used for this volcano in the literature. Volcano names in parentheses in column 2 indicate a summit in the volcanic massif whose coordinates are provided. Classification of the Holocene erupted products is based on SiO_2-K_2O classification by *LeMaitre* [1989]. The rock series, which are close to the classification lines or cross it, but form individual trends, are marked as transitional. Volcano data from the following sources: Central Kamchatka Depression and Eastern volcanic front [*Bindeman* and *Bailey*, 1994; *Braitseva* and *Melekestsev*, 1990; *Braitseva* et al., 1991, 1998; *Churikova* et al., 2001; *Dirksen* et al., 2002; *Dorendorf* et al., 2000b; *Fedotov* and *Masurenkov*, 1991; *Melekestsev* et al., 1992, 1995, 1996a, 2003b; *Ozerov*, 2000; *Ponomareva,* 1990; *Ponomareva* et al., 2004, 2006b; *Selyangin* and *Ponomareva*, 1999; *Vlodavets*, 1957; *Volynets* et al., 1989, 1999a]; Sredinny Range [*Bazanova* and *Pevzner*, 2001; *Churikova* et al., 2001; *Dirksen* et al., 2003; *Pevzner*, 2004, 2006; *Pevzner* et al., 2000; *Volynets*, 2006]. Question mark indicates that the data are lacking.

AGE ESTIMATES

Very few radiometric age determinations exist for late Pliocene - mid-Pleistocene volcanic rocks, underlying the late Pleistocene - Holocene volcanoes. A few $^{40}Ar/^{39}Ar$ determinations on lava plateaus in different parts of Kamchatka demonstrate that they span from 6 to 1 Ma [*Volynets* et al., 2006]. K/Ar dates obtained on various volcanic rocks in the area from Bakening to Mutnovsky volcanoes cover 0.5 to 5 Ma range, with two groups of welded tuffs dated at around 1.5 and 4 Ma [*Sheimovich* and *Karpenko*, 1997; *Sheimovich* and *Golovin*, 2003]. Lava plateaus underlying Kliuchevskoi volcanic group were dated at ~260–270 ka [$^{40}Ar/^{39}Ar$, *Calkins*, 2004]. Mid-Pleistocene age was also attributed to the oldest preserved stratovolcanoes (e.g. Gorny Zub, the oldest stratovolcano within the Kliuchevskoi volcanic group) based on their relationship with glacial deposits [*Melekestsev* et al., 1971; *Braitseva* et al., 1995].

In late Pleistocene, both volcanic and non-volcanic mountains of Kamchatka hosted extensive alpine glaciers, which deposited moraines at the surrounding lowlands. Glacial deposits identified on the air- and space images, indicate two stages of the late Pleistocene glaciation with maxima assigned to ~79–65 and 24–18 ka BP based on North America analogues (Early and Late Wisconsinian) [*Braitseva* et al., 1995]. Recently obtained ^{14}C ages related to the last glacial maximum (LGM) deposits yield ~21 ka BP and fit well into the latter interval [*Braitseva* et al., 2005].

Since very few radiometric ages are available for the late Pleistocene volcanoes, age estimates for them are based mostly on their morphology and on the stratigraphic relationship of their products with the LGM deposits. Volcanoes, which started to form ~50–60 ka BP, between the two glacial maxima, are only moderately reshaped by erosion and surrounded by moraines. Preliminary data indicates that this period of volcanic activity was preceded by rather a long repose [*Melekestsev* et al., 1974; *Calkins*, 2004], however, this needs to be confirmed by further

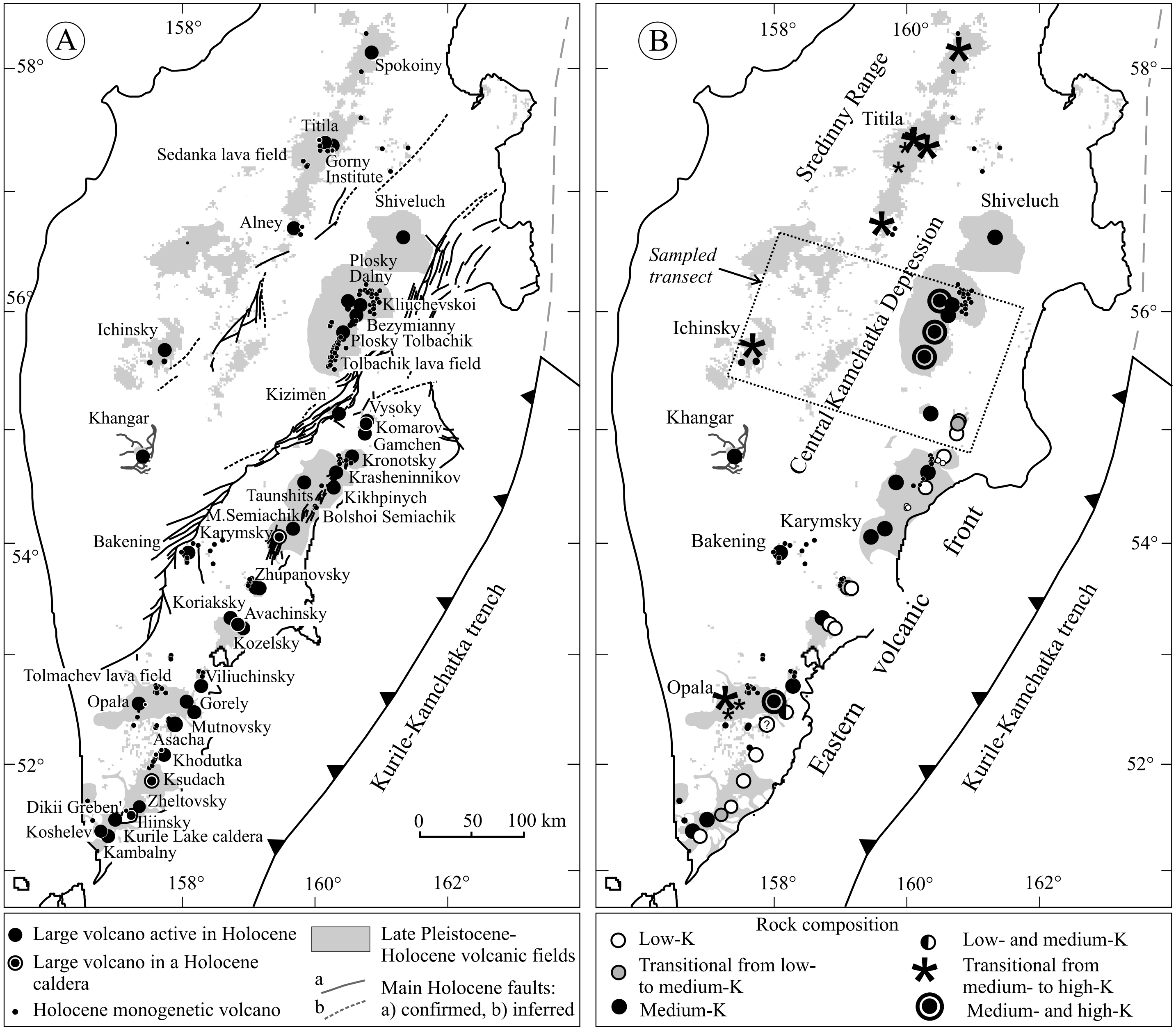

Figure 3. Holocene volcanism in Kamchatka. For details see Table 1. **A**. Kamchatka volcanoes active in Holocene. Major active fault zones by *Kozhurin* [2004]. **B**. Composition of the Holocene erupted products based on SiO_2-K_2O classification by *LeMaitre* [1989]. The rock series, which are close to the classification lines or cross it, but form individual trends, are marked as transitional.

Table 2. Late Pleistocene and Holocene calderas associated with ignimbrites

Caldera Name	Age (Method)	Caldera dimension (km)	References
Ichinsky III	Late Pleistocene (Stratigraphy)	5x3	*Erlich*, 1986; *Volynets* et al., 1991
Khangar II	38–40 ka (^{14}C)	8	*Braitseva* et al., 1995, 2005
Krasheninnikov	35–38 ka (^{14}C)	12x10	*Florensky*, 1984*; Erlich*, 1986
Uzon-Geizerny twinned caldera	39 ka (^{14}C)	18x9	*Florensky*, 1984; *Erlich*, 1986; *Leonov and Grib*, 2004
Bolshoi Semiachik II	Late Pleistocene (Stratigraphy)	10	*Erlich*, 1986; *Leonov and Grib*, 2004
Maly Semiachik	~20 ka (Stratigraphy)	7	*Selyangin* et al., 1979; *Erlich*, 1986; *Leonov and Grib*, 2004
Karymsky	7.9 ka (^{14}C)	5	*Braitseva* et al., 1995; *Erlich*, 1986
Akademii Nauk (Karymsky Lake)	28–48 ka (Fission-track)	5	*Ananiev* et al., 1980; *Erlich*, 1986; *Leonov and Grib*, 2004
Gorely II	33–34 ka (^{14}C)	12x9	*Erlich*, 1986; *Braitseva* et al., 1995
Opala	39–40 ka (^{14}C)	15	*Erlich*, 1986; *Braitseva* et al., 1995
Ksudach I	Late Pleistocene (Morphology)	9	*Erlich*, 1986; *Melekestsev* et al., 1996b
Ksudach II	Late Pleistocene (Morphology)	8	*Melekestsev* et al., 1996b
Ksudach III	8.8 ka (^{14}C)	?	*Braitseva* et al., 1995; Melekestsev et al., 1996b; *Volynets* et al., 1999a
Ksudach IV	6 ka (^{14}C)	?	" "
Ksudach V	1.8 ka (^{14}C)	6x3	*Braitseva* et al., 1995, 1996; *Volynets* et al., 1999a
Prizrak I	Late Pleistocene (Morphology)	6	*Melekestsev* et al., 1974; *Erlich*, 1986
Prizrak II	Late Pleistocene (Morphology)	?	
Kurile Lake (-Iliinsky)	7.6 ka (^{14}C)	7	*Ponomareva* et al., 2004

Note: Calderas are enlisted from north to south. Roman numbers indicate a number of this caldera in a sequence of Quaternary calderas in the volcanic center.
Most of the calderas are superimposed not on individual volcanic cones but on volcanic complexes, which combine edifices of different ages.

dating efforts. Younger volcanoes preserve most of their original topography and many of them continued their activity into the Holocene [*Braitseva* et al., 1995].

Better age estimates are available within the range of the ^{14}C method, the last 40–45 ka. *Braitseva* et al. [1993] described a special technique for estimating age of volcanic deposits by dating associated paleosol horizons. A number of ^{14}C-dated ignimbrites related to the large calderas fall within a period of 30–40 ka BP (a warm interstadial) (Table 2) and serve as markers for dating other volcanic deposits [*Braitseva* et al., 1995, 2005]. In CKD, late Pleistocene eolian sandy loams preserve tephra layers deposited during the last 40 ka. The stratigraphic position of these tephras also suggests that explosive volcanic activity peaked at 35–40 ka BP [*Braitseva* et al, 2005]. It may be glacial unloading, that caused an upsurge of explosive activity at this time. On the other hand, this cluster of dates may be explained by the fact that only these ignimbrites are associated with datable paleosols, which did not form during earlier or later colder climates. The best ^{14}C-dated volcanic deposits and landforms (>3000 dates) are the Holocene ones, and we discuss them in a special section below.

Figure 4. A. Highest volcanoes of the Kliuchevskoi group: Kliuchevskoi, 4835 m a.s.l.; Kamen', 4585 m; Plosky massif with higher Plosky Blizhny, 4057 m (on the right), and flat Plosky Dalny (or Ushkovsky), 3903 m; Bezymianny, 2869 m a.s.l. View from the south. **B.** Shaded SRTM elevation model showing the volcanoes of the Central Kamchatka Depression and northern parts of EVF and Sredinny Range. A part of the image released by NASA/JPL/NIMA.

HOLOCENE VOLCANISM

Post-glacial volcanic deposits, both tephra and lava, are well preserved in Kamchatka This permits detailed reconstructions of eruptive activity over the last 10–11.5 ka. One of the main tools in the Holocene studies is a so-called soil-pyroclastic cover, which is a continuously accumulating sequence of tephra and soil layers (Fig. 6). In Kamchatka, such cover is Holocene in age: ^{14}C dates obtained for its lowermost parts commonly are as old as ~9.5–10 ka, and in rare cases, go back almost to 12 ka [*Braitseva* et al., 2005; *Pevzner* et al., 2006]. The Holocene soil-pyroclastic cover blankets most of Kamchatka, while older sequences of this kind have been mostly removed during glaciation and occur only in isolated outcrops. We ascribe a Holocene age to an eruption based on relationship of its products with the LGM deposits and presence of its tephra in the soil-pyroclastic cover. In the literature some volcanoes are ascribed to Holocene time based on "freshness" of their lava flows [e.g. *Vlodavets*, 1957; *Ogorodov* et al., 1972]. In fact, "freshness" of the lava flows depends not only on their age but also on thickness of the overlying soil-pyroclastic cover, which is accumulating faster near active volcanoes. This means that, for example, in many parts of Sredinny Range, far from most active volcanoes, a lava flow will retain its primary topography longer than, say, in Kliuchevskoi volcanic group (Fig. 7). Thus, "freshness" of volcanic landforms alone is not a sufficient criterion for determining Holocene eruptions. In addition, several cases have been reported of fresh-looking lava flows that, in fact, had been deposited over a glacier and then were "projected" onto the underlying surface when the glacier melted [*Leonov* et al., 1990; *Ponomareva*, 1990]. World catalogues of the Holocene volcanoes [e.g., *Simkin* and *Siebert*, 1994] include a lot of "fresh" volcanoes in their Kamchatka listing, especially for SR, based on old Russian publications. Re-examination of SR volcanic centers has allowed us confrim Holocene status only for some of them (Fig. 3A), [*Pevzner*, 2006].

Distribution and Types of the Holocene Volcanic Edifices

In Kamchatka, 37 large volcanic centers have been active during the Holocene. In addition, a few hundred monogenetic vents (cinder cones, maars, isolated craters, lava domes, etc.) were formed. Holocene eruptions took place in most of the late Pleistocene volcanic fields, excluding only few in SR (Fig. 3A).

In Kamchatka, most of the stratovolcanoes, which were active throughout Holocene, started to form either in the end of late Pleistocene or in Holocene [*Braitseva* et al., 1995]. Shield-like volcanoes are not typical for Holocene and likely only Titila in SR and Gorely in South Kamchatka may be termed in this way. A few Holocene volcanic edifices are composed of andesitic-rhyodacitic lava domes. Examples include Young Shiveluch, Kizimen, and Dikii Greben' volcanoes [*Melekestsev* et al., 1991, 1995; *Ponomareva* et al., 2006].

Some stratovolcanoes (e.g., Krasheninnikov, Fig 4, Maly Semiachik, and Bezymianny), are built of 2–4 overlapping cones. It is presumed that when the volcano reaches some elevation limit, not allowing magma to erupt through its summit crater, the magma conduit shifts and a new cone starts to form at the flanks of the earlier one. In case this shift is impossible due to limited permeability of the upper crust, a lowering of the edifice by explosion or collapse may happen, and then the activity will continue [*Braitseva* at al., 1980; *Ponomareva*, 1990].

Of 37 recently active large Kamchatka volcanoes, at least 18 have been modified by major sector collapses, some of them repetitively [*Ponomareva* et al., 2006]. The largest sector collapses identified so far on Kamchatka volcanoes, with volumes of 20–30 km^3 of resulting debris-avalanche deposits, occurred at Shiveluch and Avachinsky volcanoes in the late Pleistocene. During the Holocene the most voluminous sector collapses have occurred on extinct Kamen' (4–6 km^3) and active Kambalny (5–10 km^3) volcanoes. The largest number of repetitive debris avalanches (>10 during just the Holocene) occurred at Shiveluch volcano. Large failures occurred on both mafic and silicic volcanoes and were mostly related to volcanic activity.

In the Holocene, five collapse calderas associated with explosive eruptions were formed, all within the EVF: Karymsky, three calderas on Ksudach volcanic massif, and Kurile Lake caldera (Fig. 2B), (Table 2). Karymsky and Kurile Lake caldera-forming eruptions were separated by only a couple of centuries [*Braitseva* et al., 1997a]. Holocene ignimbrites commonly are not welded.

There are several lava fields in Kamchatka, the largest of them are the Sedanka, Tolbachik, and Tolmachev fields (Fig. 3A). Sedanka and Tolmachev cinder cones are scattered over a large territory. Mid- to late Holocene vents in the Tolbachik field form a 3–5 km wide belt, that stretches for 40 km in a SSW-NNE direction, then crosses late Pleistocene Plosky Tolbachik volcano (where it is responsible for Plosky Tolbachik's Holocene activity) and then goes for another 14 km to the northeast (Fig. 5B). This alignment may suggest that the position of the vents is determined by a system of faults [*Piip*, 1956]. Some volcanoes host many flank cinder cones, Kliuchevskoi definitely being a leader (>50 cones) (Fig. 4B). Some cinder cones occur as isolated vents not associated with any large volcanoes or cone clusters (Fig. 3A).

Another type of monogenetic eruptive center in Kamchatka is large craters that have produced voluminous rhyolitic tephra falls. Three such Holocene craters are located in South Kamchatka: Chasha Crater, situated among the mafic cinder cones of the Tolmachev lava field [*Dirksen* et al., 2002]; Baranii Amphitheater on the ESE slope of Opala volcano; and Khodutkinsky Crater northwest of Khodutka volcano (Tables 1 and 3) [*Melekestsev* et al., 1996a; http://www.kscnet.ru/ivs/volcanoes/holocene]. Chasha and Khodutkinsky craters have magmas different from those of the adjacent volcanoes, while Baranii Amphitheater rhyolite fits into the overall geochemical trend for Opala volcano [*Fedotov* and *Masurenkov*, 1991]. The closest historical example of such a volcanic vent is Novarupta near Katmai volcano, Alaska [*Hildreth*, 1983]. Unlike Katmai, no caldera collapse was associated with these Kamchatka craters, that allowed I.V. Melekestsev [1996a] to call them "craters of sub-caldera eruptions".

Ages of Volcanic Cones and How They Grow

Reconstruction of the eruptive histories of the Holocene volcanoes based on geological mapping, tephrochronology and radiocarbon dating have allowed us to 1) determine the ages and growth rates of volcanic edifices; 2) identify temporal patterns of the eruptive activity; 3) document and date the largest explosive eruptions (Table 3); and 4) correlate their tephras over Kamchatka in order to obtain a tephrochronological framework for dating various deposits [*Braitseva* and *Melekestsev*, 1990; *Braitseva* et al., 1980, 1984, 1989, 1991, 1997a, b, 1998; *Melekestsev* et al., 1995, 1996b; *Ponomareva*, 1990; *Ponomareva* et al., 1998, 2004, 2007; *Selyangin* and *Ponomareva*, 1999; *Volynets* et al., 1989, 1999a].

Ages of some stratovolcanoes were determined based on the assumption that initial construction of such edifices was by continuous explosive activity. At the foot of all the Holocene stratovolcanoes we have identified tephra packages that meet the following criteria: 1) they underlie the oldest lava flows from the volcano; 2) are widely dispersed and easily identified around the volcano; 3) consist of a number of individual layers sometimes separated by thin sandy loam horizons; and 4) overlie thick paleosol layers suggesting that no activity from the volcano took place earlier. Radiocarbon dates on such paleosols or other associated organic matter have allowed us to date these tephra packages and thus constrain when cone-building eruptions started on various eruptive centers (Table 4). Ages of Kizimen and Dikii Greben extrusive volcanoes have been estimated based on the stratigraphic position of their initial tephra relative to the LGM deposits and the 7.6 ka Kurile Lake caldera ignimbrite, respectively.

Growth rates have been estimated for some stratovolcanoes [*Braitseva* et al., 1995]. The largest Holocene volcano, Kliuchevskoi (~4800 m a.s.l.) started to form at 1700 m on the slope of Kamen' volcano at ~5.9 ka (^{14}C) (or ~6.8 calibrated ka) and likely reached its modern height within about 3000 years, after which its first flank vents

Figure 5. A. Krasheninnikov volcano, view to the south. This Holocene volcano is nested in a ~35–38 ka old caldera and consists of two large coalesced cones. The northern cone is crowned with a caldera enclosing a smaller cone with a lava cone inside. Large cones as well as numerous monogenetic vents north and south of the late Pleistocene caldera are aligned along the regional fault zone parallel to the general strike of the volcanic belt [*Florensky* and *Trifonov*, 1985]. **B.** Cinder cones north of Krasheninnikov caldera. The cones are aligned along the regional fault zone. Krasheninnikov volcano is in the background. Photos courtesy Vasilii Podtabachny.

started to form. This is about the duration of the main cone-building phase for other large volcanoes (Young Cone of Avachinsky, North Cone of Krasheninnikov, Karymsky, etc.). Small edifices with volumes of ~2 km^3, e.g. each of the two cones composing Kikhpinych volcano or Stübel Cone in Ksudach massif, formed in the main during a few hundred years.

Eruptive activity of all the studied volcanoes was organized in spurts, with alternating active and repose periods. Repose periods as long as 1000–3000 years were rather common. Longer repose periods with the durations of >3000 years occurred at Bezymianny, Kikhpinych, Zheltovsky, Dikii Greben', and Kambalny volcanoes [*Melekestsev* et al., 2001]. The longest known period of quiescence (~3500 years), after which the volcano was able to resume its activity, was at Dikii Greben' volcano [*Ponomareva* et al., 2006]. Even volcanoes notable for their frequent historic eruptions and intense magma supply like Shiveluch or Avachinsky appeared to have had ~900 years-long repose periods (or at least periods of low activity) [*Braitseva* et al., 1998; *Ponomareva* et al., 2007]. Zones of cinder cones behaved much as the large volcanoes: their eruptions tended to cluster into active periods separated by quiescence not exceeding 3000–4000 years [*Braitseva* et al., 1984; *Dirksen* and *Melekestsev*, 1999]. In certain cases, we can identify long periods of volcanic rest shared by several neighboring volcanoes. For example, three such periods recorded by thick paleosols have been documented for the southernmost part of Kamchatka, which hosts five active volcanoes (Zheltovsky, Iliinsky, Dikii Greben', Koshelev and Kambalny). The earlier two periods of quiescence lasted for a minimum of 1400 to 1500 years, and the latest one—for 750 years [*Ponomareva* et al., 2001]. Long (up to 3500 years) repose periods do not seem

Table 3. The largest explosive eruptions in Kamchatka during the last 10,000 years

Source volcano	Tephra code	Average ^{14}C age, yr BP (or calendar age for historical eruptions)	Volume of tephra, km^3	Composition of tephra
Shiveluch	SH_{1964}	AD 1964	0.6-0.8	Andesite
	SH_{1854}	AD 1854	~1	" "
	SH_1	250	≥2	" "
	SH_2	950	≥2	" "
	SH_3	1400	≥2	" "
	SH_{1450}	1450	≥2	" "
	SH_5	2550	~1	" "
	SH_{2800}	2800	≥1	" "
	SHsp	3600	~1	Basalt
	SH	3750	≥1	Andesite
	SHdv	4100	≥2	" "
	SH_{4700}	4700	≥2	" "
	SH_{4800}	4800	≥2	" "
	SH_{5600}	5600	≥1	" "
	SH_{6850}	6850	1.2	" "
	SH	7900	≥1	" "
	SH	8100	≥2	" "
	SH	8200	≥1	" "
	SH	8300	≥2	" "
Bezymianny	B_{1956}	AD 1956	1.8-2	" "
Kizimen	KZ	7550	4-5	Dacite
Khangar	KHG	6850	14-16	Dacite-rhyodacite
Karymsky caldera	KRM	7900	13-16	Rhyodacite
Avachinsky	II AV_3	3300	>1.2	Basaltic andesite
	II AV_1 (AV_1)	3500	≥3.6	" "
	IAv24 (AV_2)	4000	≥0.6	Andesite-basaltic andesite
	IAv20 (AV_3)	4500	≥1.1	Andesite
	IAv12 (AV_4)	5500	≥1.3	" "
	IAv2	7150	≥8–10	" "
Chasha Crater	OPtr	4600	0.9–1	Rhyolite
Opala, Baranii				
Amphitheater Crater	OP	1500	9–10	" "
Khodutkinsky Crater	KHD	2500	1–1.5	Rhyodacite
Ksudach, Stübel cone	$KSht_3$	AD 1907	1.5–2	Basaltic andesite-dacite
	$KSht_1$	950	0.8–1	" "
Ksudach calderas	KS_1	1800	18–19	Rhyolite
	KS_2	6000	7–8	Andesite
	KS_3	6350	0.5–1	Rhyodacite-andesite
	KS_4	8850	1.5–2	Andesite
Iliinsky	ZLT	4850	1.2–1.4	" "
Kurile Lake caldera	KO	7600	140–170	Rhyolite-basaltic andesite

Note: Volcanoes are enlisted from north to south. Radiocarbon ages are averaged to nearest 50 yrs. Original ages are from *Bazanova* and *Pevzner*, 2001; *Bazanova* et al., 2004; *Braitseva* et al., 1997a,b, 1998; *Dirksen* et al., 2002; *Pevzner* et al., 1998; *Ponomareva* et al., 2004, 2007, and Zaretskaya et al., 2007. For Avachinsky eruptions new tephra codes are from *Bazanova* et al., 2004, and old codes (in parentheses) are from *Braitseva* et al., 1997a,b; 1998.

to exhibit any specific chemical or spatial association. Data on the Holocene eruptive histories of Kamchatka volcanoes show that long repose periods can occur both at dominantly basaltic (e.g. Kikhpinych) and rhyodacitic (Dikii Greben') volcanoes, dominantly explosive (e.g. Ksudach) and effusive (Dikii Greben') volcanoes, and those located closer to the Kamchatka trench (Kikhpinych) and farther west (Kizimen) [*Melekestsev* et al., 2001].

Figure 6. Holocene soil-pyroclastic cover in Kamchatka. **A**. EVF, Maly Semiachik volcano region. Local tephra: MS - cinder of the initial cone-building eruptions from Kaino-Semiachik, the youngest cone of Maly Semiachik volcano (7300–7400 ^{14}C yr BP); Maly Semiachik - stratified cinders from Kaino-Semiachik (~4000 ^{14}C yr BP). Regional marker tephras: KRM - a package of the Karymsky caldera deposits (7900 ^{14}C yr BP); KO - a thin ash layer from the Kurile Lake caldera (7600 ^{14}C yr BP). A person is ~155 cm tall. Photo courtesy Oleg Seliangin. **B**. Northern part of Sredinny Range, Sedanka lava field. Regional marker tephras: KHG - Khangar volcano (6850 ^{14}C yr BP). KS_1- Ksudach (1800 ^{14}C yr BP). A knife is ~25 cm long.

Largest Explosive Eruptions

Table 3 lists major Holocene explosive eruptions in Kamchatka. Large eruptions took place in various parts of Kamchatka (Table 3), (Fig. 3A). The largest eruption was associated with formation of Kurile Lake caldera and yielded a tephra volume of 140–170 km^3, making it the largest Holocene eruption in the Kurile–Kamchatka volcanic arc and ranking it among Earth's largest Holocene explosive eruptions. Tephra from the Kurile Lake caldera-forming eruption was dispersed mostly to the northwest at a distance of ~1700 km [*Ponomareva* et al., 2004]. The second largest explosive Holocene eruption was associated with a caldera at Ksudach (KS_1) (Table 3). Its tephra was dispersed to NNE and covered most of Kamchatka providing a wonderful marker for Holocene studies [*Braitseva* et al., 1996, 1997b]. Tephras associated with other caldera-forming and larger sub-caldera eruptions reached volumes of 9–19 km^3. Most large tephras ranged from andesite to rhyolite in composition. The only large mafic (basaltic andesite) tephra erupted from Avachinsky volcano and yielded a volume of ≥3.6 km^3.

Dated tephra layers are widely used for dating and correlating various volcanic and non-volcanic deposits [*Braitseva* et al., 1997b] as well as archaeological sites [*Braitseva* et al., 1987] and serve as a main tool in reconstructing eruptive histories of the Holocene volcanoes [*Braitseva* and *Melekestsev*, 1990; *Braitseva* et al., 1980, 1984, 1989, 1991, 1998; *Melekestsev* et al., 1995; *Ponomareva*, 1990; *Ponomareva* et al., 1998, 2004, 2007; *Selyangin* and *Ponomareva*, 1999; *Volynets* et al., 1989, 1999a], paleoseismic events (tsunami and faulting) [*Pinegina* et al., 2003; *Bourgeois* et al., 2006; *Kozhurin* et al., 2006], and environmental change [e.g. *Dirksen*, 2004]. As of now, no Kamchatka tephra has been positively identified in the Greenland ice cap, but some peaks in the GISP-2 core have been tentatively correlated with the largest Kamchatka eruptions based on age estimates [*Braitseva* et al., 1997a]. Finding the Aniakchak tephra from Alaska in Greenland ice [*Pearce* et al., 2004] suggests the possibility of finding Kamchatka tephras there as well.

In Figure 8, there are two peaks of magma output in explosive eruptions at AD 200–700 and BC 6650–4900, with

Figure 7. A. Late Pleistocene cinder cone and lava flow in the central part of Sredinny Range. Both cinder cone and lava flow look very fresh; however, tephra of this eruption is not present in the soil-pyroclastic cover. Lava is bare in many places, but soil-pyroclastic cover can be found in the depressions on its surface and is as old as that overlying the LGM deposits. **B.** Flat surface on the foreground is a ~2 ka old lava flow overlain by more than a 3 m thick soil-pyroclastic cover (Kliuchevskoi volcano foot). Original topography of the lava flow is smoothed and lava crops out mostly in the river valleys. A young lava flow likely formed in late 1800-ies is at the far left. A ~3.5 ka old cinder cone is at the right.

especially high production between BC 6600 and 6400 ("a century of catastrophes" [*Melekestsev* et al., 1998]). During these peaks, larger eruptions are *relatively* more frequent, whereas the frequency of all eruptions (above some certain size level, say, 1 km^3) remains near average [*Gusev* et al., 2003]. Considering the general temporal structure of the event sequence, one can say that in the discussed time-ordered list of eruptive volumes, large-size explosive eruptions happen in tight clusters "too often" (as compared to a randomly-shuffled list of the same events). The reality of this tendency was successfully checked by statistical analysis and is called "order clustering" of the largest explosive eruptions [*Gusev* et al., 2003].

In addition, we analyzed magma output rate averaged over small time intervals. We found that this rate, as a function of time (at time scales 300–10,000 yrs), has a well-expressed episodic character. This fact contradicts commonly assumed random or periodic temporal distribution of eruptions [e.g. *Wickman*, 1966; *Ho* et al., 1991; *Jones* et al., 1999] and supports qualitative conclusions about non-uniform or episodic character of volcanism derived from the distribution of tephra layers in deep-sea boreholes [*Kennet* et al. 1977; *Cambray* and *Cadet*, 1996; *Cao* et al., 1995; *Prueher* and *Rea*, 2001] or from the on-land tephrostratigraphy [*Braitseva* et al., 1995].

Mafic intrusion into a silicic magma chamber has been proved to be a common trigger for an explosive eruption [*Sparks* and *Sigurdsson*, 1977]. In Kamchatka, cases of such triggering have been demonstrated for most of the large explosive eruptions [e.g., *Volynets,* 1979; *Melekestsev* et al., 1995; *Volynets* et al., 1999a; *Eichelberger* and *Izbekov,* 2000; *Ponomareva* et al., 2004]. So the observed clusters of larger explosive eruptions over a large territory might have been caused by large-scale changes in the crustal stress field that have allowed an ascent of deeper mafic melts over most of the Kamchatka volcanic region. A typical explanation of such a phenomenon is glacial unloading [*Wallman* et al., 1988], but it hardly can be applied to the younger of the two Kamchatka volcanic peaks (AD 200–700). We hope that further detailed studies of spatial-temporal patterns of the well-dated Holocene Kamchatka volcanism combined with the records of the largest crustal and subduction-related earthquakes will allow us to explain its episodic character.

Volcanic Hazard Assessment

Volcanic hazard assessment has been implemented for many Holocene volcanoes based on their reconstructed eruptive histories [e.g. *Melekestsev* et al., 1989; *Ponomareva* and *Braitseva*, 1991; *Bazanova* et al., 2001]. About 80% of the ~350,000 people inhabiting Kamchatka concentrate in three cities: Petropavlovsk-Kamchatsky and Elizovo, located ~30 km south of Koriaksky and Avachinsky volcanoes, and Kliuchi, located 30 km north of Kliuchevskoi and 45 km south of Shiveluch volcanoes. For the historical period (~300 years), these sites have experienced volcanic influence only by minor ashfalls and flooding in outermost suburbs. During the Holocene, the main hazard for these territories was also associated with tephra falls and lahars. Recurrence of large tephra falls (with thickness of buried tephra ≥1 cm) in Petropavlovsk-Kamchatsky during the last 8000 yrs was ~1 fall per 420 yrs [*Bazanova* et al., 2005]. In Kliuchi (Fig. 2A), an average recurrence of large tephra falls in Holocene was ~1 fall per 700 years; however, it reached a value of 1 per 300 years during the last 1000 years [*Pevzner* et al., 2006]. Such remote towns as Ust'-Bolsheretsk received only

Table 4. Radiocarbon ages of some volcanic edifices

Volcano	Onset of edifice formation, yr B.P. (^{14}C)	Reference
Kliuchevskoi	~5900	*Braitseva* et al., 1995
pre-Bezymianny	10,000–11,000	*Braitseva* et al., 1991; *Braitseva* et al., 1995
Bezymianny	~4700	" "
Kizimen	12,000–11,000	*Braitseva* et al., 1995; *Melekestsev* et al., 1995
Komarov	1500	*Ponomareva*, 2000, unpublished data
Gamchen (Baranii Cone)	3600	*Ponomareva* et al., 2006
Krasheninnikov		*Ponomareva*, 1990; *Braitseva* et al., 1995
North Cone	5500	" "
Mid-North Cone	1300	
Kikhpinych		*Braitseva* et al., 1989; *Braitseva* et al., 1995
West Cone	4200	" "
Savich Cone	1400	
Maly Semiachik		
Paleo-Semiachik	20,000?	*Braitseva* et al., 1980, 1995; *Melekestsev* et al., 1989
Meso-Semiachik	11,000	
Kaino-Semiachik	7300–7400	
Karymsky	5300	*Braitseva* and *Melekestsev*, 1990; *Braitseva* et al., 1995
Avachinsky (Young Cone)	3500	*Braitseva* et al., 1995; *Bazanova* et al., 2003
Ksudach (Stübel Cone)	1600	*Braitseva* et al., 1995; *Volynets* et al., 1999a
Iliinsky	7600	*Ponomareva* et al., 2004
Dikii Greben'	7600	" "

two large tephra falls during the last 8500 years [*Bazanova* et al., 2005]. A long-term prediction of sector collapses on Kliuchevskoi, Avachinsky and Koriaksky volcanoes [*Melekestsev* and *Braitseva*, 1984; *Melekestsev* et al., 1992] highlights the importance of closer studies of their structure and stability.

AMOUNT OF ERUPTED MATERIAL

Estimates of the eruptive volumes and mass were done based on the detailed maps of the late Pleistocene-Holocene volcanoes compiled by I.V.Melekestsev. The total mass of rocks erupted during the late Pleistocene-Holocene is estimated at 18 to 19 x 10^{12} tonnes [*Melekestsev*, 1980]. CKD volcanic belt was the most productive (~40% of all the eruptives) (Fig. 9A). The EVF production was less at 35%. SR (25%) was subordinate to both other belts. Mafic rocks dominated in all the belts. Andesite-rhyolite constituted 25–30% of the total volume erupted in CKD and EVF and only ~6% of that erupted in Sredinny Range. Within EVF, most of silicic rocks were erupted in South Kamchatka. In Holocene, CKD and EVF belts produced almost similar amount of eruptives, while SR belt productivity dropped (Fig. 9A).

The highest magma production rate both during the last 60 and 11.5 ka was in CKD (Fig. 9B). In late Pleistocene, production rate in CKD and EVF was almost twice higher than that in Holocene. Late Pleistocene magma production rate in SR was smaller than that in CKD and EVF, but not that dramatically smaller than in Holocene. It is unclear whether this Holocene drop in SR production rate means the end of volcanic activity in SR or just reflects a relatively quiet period.

The largest late Pleistocene-Holocene stratovolcanoes yielded volumes up to 320 km^3 or mass of ~0.74 x 10^{12} tonnes (including tephra) [*Melekestsev*, 1980]. Examples include Kronotsky, Kamen', and Old Avachinsky (before the sector collapse). The largest Holocene edifice is that of Kliuchevskoi (270 km^3 or 0.6 x 10^{12} tonnes). The smallest Holocene stratovolcano, Stübel Cone, has a volume of ~2 km^3 and mass of the rocks of ~0.005 x 10^{12} tonnes. The largest Holocene explosive eruption produced 140–170 km^3 (0.18 x 10^{12} tonnes) of tephra and 7-km-wide Kurile Lake caldera [*Ponomareva* et al., 2004]; other eruptions ranked far below (Table 3). Most of the late Pleistocene calderas are significantly larger (up to 18 km, Table 2) and are surrounded by thick packages of welded tuffs. We suggest that most of the late Pleistocene caldera-forming eruptions were at least equal to the largest Holocene eruption (Kurile Lake caldera) or larger. Volume of individual Holocene lava eruptions reached 2–5 km^3 [*Pevzner* et al., 2000; *Ponomareva* et al., 2006].

COMPOSITION OF ROCKS

Late Pleistocene-Holocene volcanic rocks in Kamchatka cover wide range of compositions. One of their most interesting features is a high proportion of mafic varieties (basalt-andesite) compared to that of silicic rocks (Fig. 9); [*Volynets*, 1994]. The amount of the sedimentary component is limited in most of the Kamchatka volcanic rocks [*Kersting* and *Arculus*, 1995; *Tsvetkov* et al., 1989; *Turner* et al., 1998] and the most mafic varieties do not show any sign of crustal contamination [e.g. *Volynets* et al., 1994; *Dorendorf* et al., 2000a], offering a chance to investigate a relatively simple system. In addition, a certain amount of more silicic rocks (dacite-rhyolite) is present in Kamchatka, mostly related to caldera systems and associated crustal magma chambers. Studies of magma evolution on the individual centers show that most of the silicic rocks have been derived from mafic melts through fractionation and mixing with related melts [e.g. *Kadik* et al., 1986; *Ivanov*, 1990; *Volynets* et al., 1989, 1999a; *Leonov* and *Grib*, 2004]. O and Sr isotopes studies, however, have shown that some of silicic rocks have been influenced by crustal and meteoritic/hydro-thermal water [*Bindeman* et al., 2004]. In this paper, we discuss mafic products since these are most reflective of mantle processes.

Large variations of the volcanic rocks in Kamchatka and adjacent volcanic arcs clearly represent the result of several factors that control conditions of the mantle melting and future melt evolution during ascent and chamber residence before eruption. These factors may vary from arc to arc and are mainly related to crustal thickness, mantle fertility, composition and thermal state of the subducted plate [*Pearce* and *Parkinson*, 1993; *Plank* and *Langmuir*, 1988, 1993], temperature of the mantle wedge and subducted slab [*England et al.*, 2004; *Manea et al.*, 2005], and the amount and compositions of subducted fluids and sediments [*Plank* and *Langmuir*, 1993; *Duggen et al.*, 2007].

Cross-arc Chemical Zonation

Cross-arc chemical zonation of the Late Pleistocene-Holocene Kamchatka volcanic rocks from east to west at different latitudes is most pronounced in their enrichment in alkalies and incompatible trace elements [*Volynets*, 1994; *Tatsumi* et al., 1995; *Avdeiko* et al., 2006; *Davidson*, 1992,

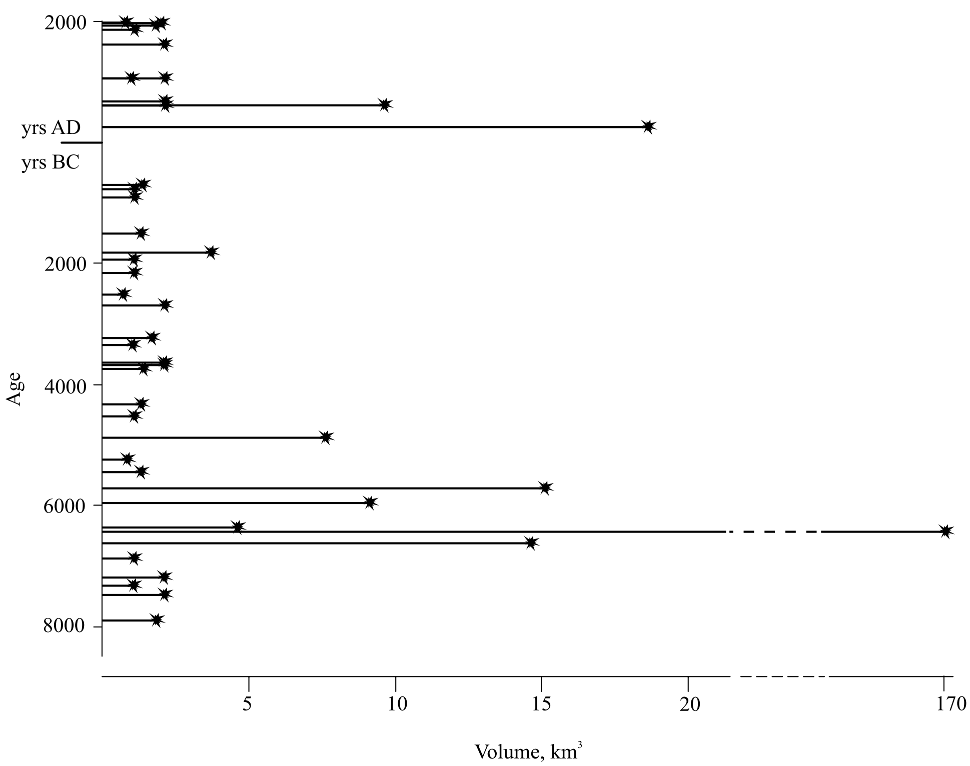

Figure 8. Volumes of the products from the largest explosive eruptions in Kamchatka in Holocene (for details see Table 3). Ages are radiocarbon ages converted to calibrated years (cal yr BP) using CALIB 5.0 [*Stuiver* et al., 2005]. Two peaks of magma output in explosive eruptions can be identified at AD 200–700 and BC 6650–4900, with especially high production between BC 6600 and 6400 (“a century of catastrophes” [*Melekestsev* et al., 1998]).

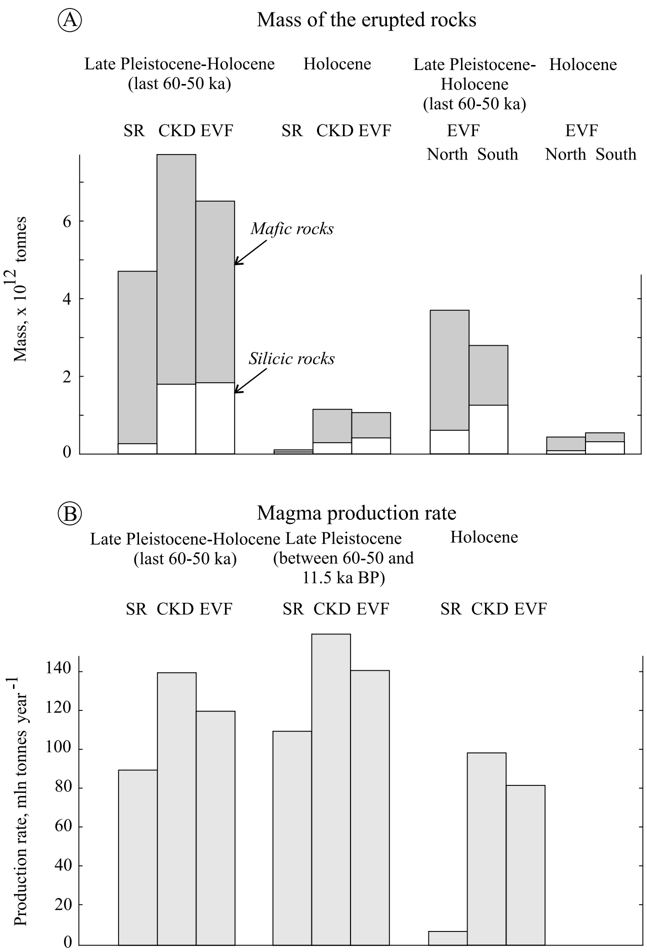

Figure 9. Mass of the late Pleistocene- Holocene erupted rocks (**A**) and magma production rate (**B**) by volcanic belts: SR - Sredinny Range, CKD - Central Kamchatka Depression, EVF - Eastern volcanic front. In **A**, gray and white fillings show mafic and silicic rocks, respectively. CKD was the most and SR - the least productive volcanic belts in Kamchatka during late Pleistocene-Holocene.

pers.comm.]. Some authors argue that the currently active subduction zone may be responsible for all the magma-generating processes during this period [*Tatsumi* et al., 1995; *Churikova* et al., 2001]. Others suggest the simultaneous existence of two subduction zones: one beneath the Eastern Volcanic Front and the Central Kamchatka Depression and the second one beneath the Sredinny Range [*Avdeiko* et al., 2006].

To evaluate both hypotheses, mafic volcanic rocks densely sampled along an E-W transect have been studied for major and trace element compositions as well as isotopes of Sr, Nd, Pb, U, Th, O and Hf [*Churikova* et al., 2001; *Dorendorf* et al., 2000a, b; *Münker* et al., 2004; *Wörner* et al., 2001]. This 220-km-long transect is comprised by 13 Upper Pleistocene and Holocene stratovolcanoes and two large lava fields. It stretches from EVF through CKD into the back arc of SR (Fig. 3B). Since the compositions of CKD rocks north and south of the Kamchatka River are significantly different, we consider them separately as NCKD and SCKD, respectively. The transect was fitted to follow the widest possible cross-arc extent of recent volcanism, which is one of the widest worldwide.

In terms of major element composition the rocks of the EVF belong to the low- to medium-K tholeiitic and calc-alkaline series (Fig. 10). Low-K rocks stretch along the EVF and are present on the other volcanoes closest to the trench (Kronotsky, Kikhpinych, some volcanoes of Bolshoi Semiachik massif, Zhupanovsky, Avachinsky, Mutnovsky, Khodutka, Ksudach, Zheltovsky, Kambalny) (Fig. 3B), (Table 1); [e.g. *Fedotov and Masurenkov*, 1991; *Duggen at el*., 2007]. The rocks of the back arc (SR) are medium to high-K calc-alkaline. SCKD and NCKD rocks have intermediate position between EVF and SR. Near Ichinsky volcano, we found HFSE (high field strength elements)-enriched basalts with intra-plate affinities (here: basalts of within-plate type - WPT). Recent studies have discovered rocks of this type in northern parts of Sredinny Range [*Volynets* et al., 2005]. Some more alkaline rocks (shoshonitic and K-alkaline basaltoids, alkaline basalts and basanites) were described in SR [*Perepelov et al*., 2005]. Those will not be considered in the following discussion, however, because they belong to Paleogene and Miocene.

Trace elements patterns for EVF, CKD and SR rocks are shown in (Fig. 11). All rocks have typical arc-signatures with strong but variable LILE and LREE enrichment and low HFSE. LILE and HFSE concentrations increase from the front to the back-arc. All rocks are depleted in Nb and Ta, REE, and HREE compared to NMORB. However, Nb-Ta-depletions in back arc rocks compared to neighboring LILE's are much smaller than in the EVF and CKD rocks. All the SR rocks contain a variable amount of the enriched OIB-like mantle component. The amount of this component changes from low addition on Ichinsky volcano (so called SR (IAB)) to highly enriched (up to 30–35%) in intra-plate basalts (so called SR (WPT)) [*Churikova at al*., 2001, 2007; *Münker* et al., 2004; *Volynets et al*., 2006].

Along the transect under study the depth to the slab changes from 100 km for EVF to 400 km for SR [*Gorbatov* et al., 1997]. Some CKD samples are close to a primary mantle-derived melt composition. However, EVF and SR rocks and most of CKD rocks were obviously affected by some mineral fractionation, therefore, direct comparison of trace element concentrations is impossible. For comparison, the data from each volcano were normalized to 6% MgO following the approach used by [*Plank* and *Langmuir*, 1988]. The normalized data for selected trace elements and element ratios versus depth to the slab surface are shown in Figures 12 and 13. Most of incompatible trace elements, i.e. HFSE (Zr, Nb, Hf, Ta), LILE (Sr, Ba, Rb, Be, Pb, U, Th), LREE, some major elements (K, Na) and certain element ratios (K/Na, La/Yb, Sr/Y, Nb/Yb) are positively correlated with slab depth. Similar cross-arc changes in element concentrations and their ratios have been recently found south of the described transect [*Duggen et al.*, 2007; *Portnyagin et al.*, 2007a]. At the same time Y and the HREE are almost constant from front to back arc (Fig. 12H". The WPT at Ichinsky have higher concentrations of Na_2O, TiO_2, P_2O_5, Sr and all HFSE and REE, and are depleted in SiO_2 and Rb compared to the Ichinsky IAB-SR.

Isotope data for the northern transect are summarized in Figure 14. The data plot close to the MORB field; variations in all isotope systems are small and inside the previously reported ranges for Kamchatka [*Kepezhinskas* et al., 1997; *Kersting* and *Arculus*, 1995; *Tatsumi* et al., 1995; *Turner* et al., 1998]. There is a general increase in $^{87}Sr/^{86}Sr$ and $^{143}Nd/^{144}Nd$ from

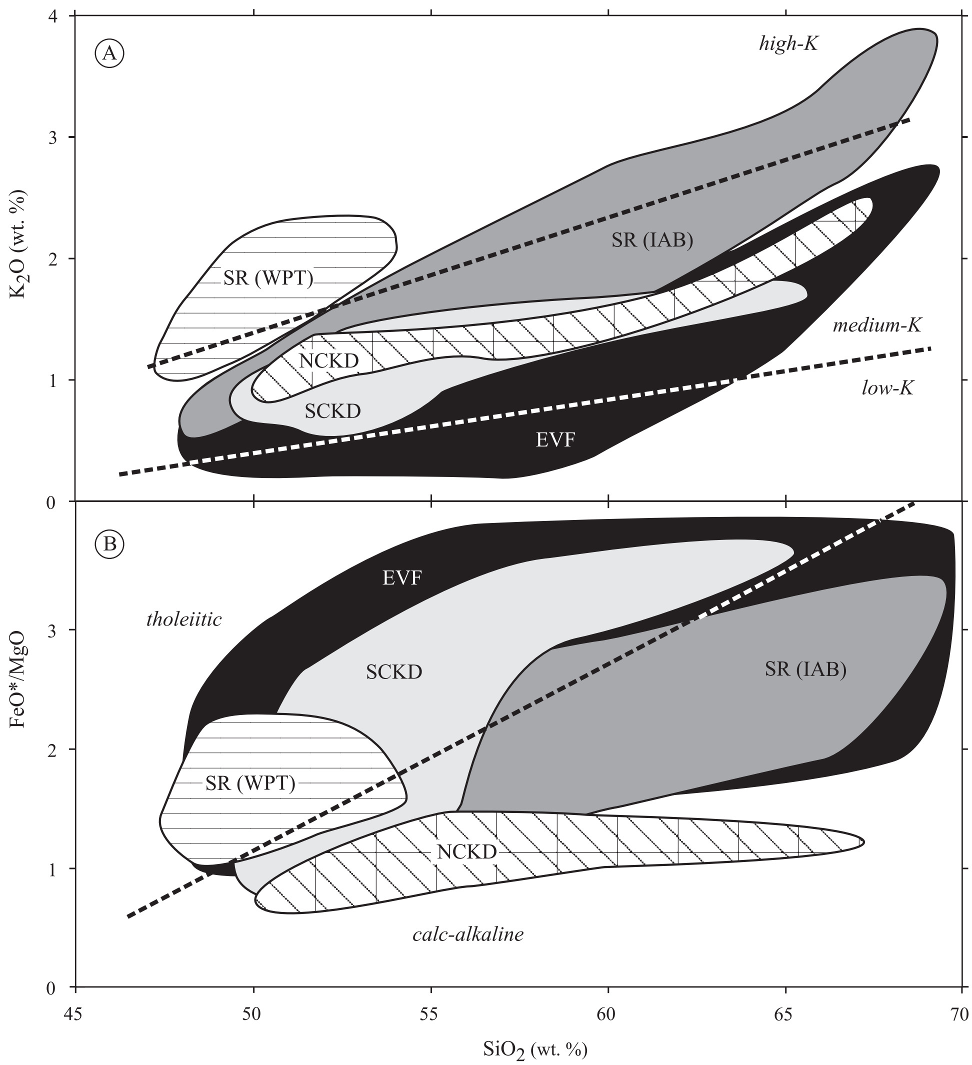

Figure 10. K_2O (**A**) and FeO*/MgO (**B**) vs. SiO_2 for late-Pleistocene-Holocene volcanic rocks of the Kamchatka Peninsula. The rocks of different volcanic regions or of specific composition are combined in the fields marked by different colors. Only medium-K calk-alkaline rocks are shown for SCKD region. Data from *Fedotov* and *Masurenkov* [1991]; *Dorendorf* et al. [2000a, 2000b]; *Churikova* et al. [2001]; *Leonov* and *Grib* [2004]; *Ivanov* et al. [2004]; *Volynets* et al. [2005]. EVF – Eastern Volcanic Front; SCKD – volcanoes of the Central Kamchatka Depression south of the Kamchatka River; NCKD - those north of the Kamchatka River; SR (IAB) – island-arc basalt type rocks of Sredinny Range; SR (WPT) – within-plate type rocks of Sredinny Range. Element concentrations are given in wt.%. Classification lines for (A) after *Le Maitre* et al. [1989] and for (B) after *Miashiro* [1974]. FeO* - all iron expressed as FeO.

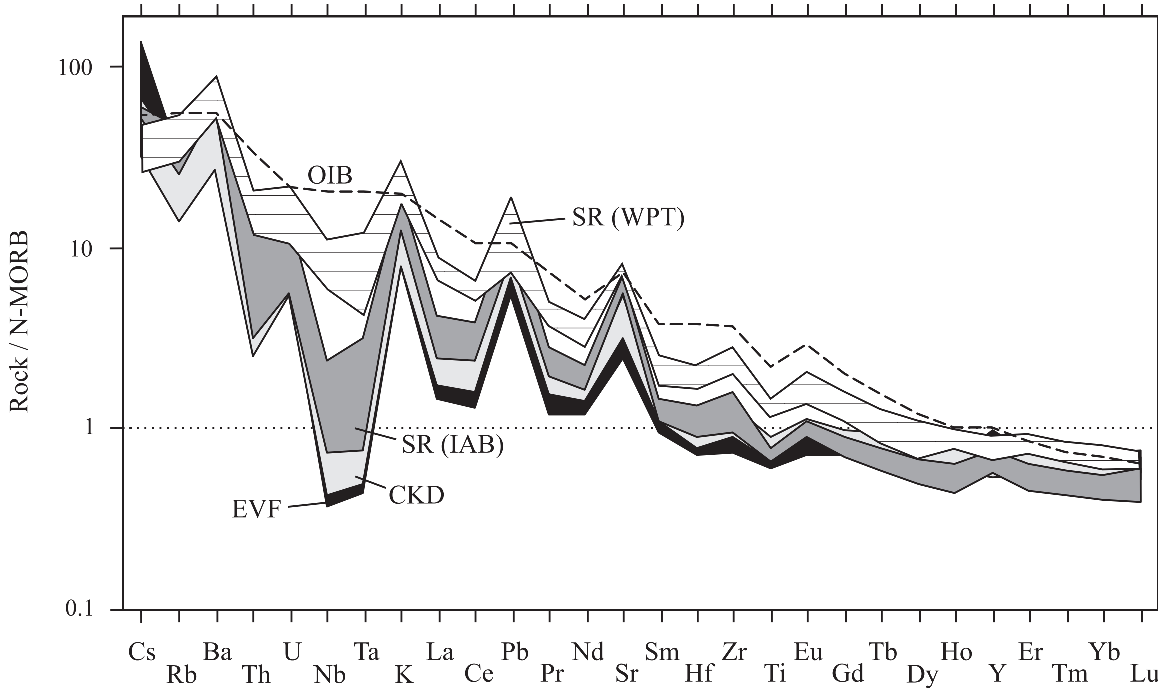

Figure 11. NMORB-normalized trace element patterns for mafic rocks of the different regions of Kamchatka. The order of incompatible elements is derived from *Hofmann* [1988] with Cs and all REE added. For clarity, each zone is expressed by a compositional field. SR (WPT) are significantly more enriched in all trace elements compared to all other lavas. Data from *Churikova* et al. [2001] and *Volynets* et al. [2005]. NMORB and OIB values after *Sun* and *McDonough* [1989].

the EVF to the CKD and a decrease from the CKD to the SR with strongest ^{87}Sr-enrichment in CKD samples. Three trends could be distinguished on Figure 14, suggesting involvement of three different components. A component low in ^{87}Sr/^{86}Sr (<0.7031) and high in ^{143}Nd/^{144}Nd (~0.5131) is a MORB source within the mantle wedge. From the MORB field one array trends to higher Sr-isotope ratios with unchanged Nd-ratios. Slab fluids (or slab melts) are expected to have such composition. The second array tends to lower Nd-isotope ratios with a correlated increase in Sr-isotopes. Such a trend probably results from mixing with an enriched mantle component and formed mainly by the SR back-arc rocks.

Using Pb isotopes data for the Kamchatka rocks and pelagic sediments from ocean drilling near Kamchatka, K*ersting* and *Arculus* [1995] argued that subducted sediments play a minor role in Kamchatka magma generation. These data were also confirmed by Be isotopes [*Tsvetkov* et al., 1989]. Recently, however, new data imply that subducted sediments/melts play a more important role in the genesis of the Kamchatka rocks [*Duggen et al.*, 2007; *Portnyagin et al.*, 2007a].

The degree of partial melting required for generation of the volcanic rocks of Kamchatka decreases from arc front to back arc. The rocks of the EVF display the highest source degree of melting of 14–20%, the CKD and SR "normal" arc rocks show lower degrees of melting, down to 9–12%, and samples with intraplate signatures in back arc show the lowest degree of melting at 7% [*Churikova* et al., 2001; *Portnyagin* et al., 2007a].

On Th/Yb versus Ta/Yb diagram [*Pearce,* 1983] (Fig. 15), all samples from the EVF and NCKD and most samples from SCKD fall into the field of depleted mantle sources. However, the SR rocks form an array reaching from the oceanic arc towards an enriched mantle component. The existence of the enriched source was evidenced by the high-precision measurements of Nb/Ta, Zr/Hf, Lu/Hf ratios together with Hf isotopes [*Münker* et al., 2004].

Despite that, based on LREE and LILE concentrations, fluid contribution does not change across Kamchatka (Ce/Pb, Ba/Zr ratios do not show systematic change) (Figs. 13B, F), elements more sensitive to arc fluid transport show strong cross-arc variations. Using volatile and fluid-mobile elements in melt inclusions from Kamchatka's olivines, different fluid compositions were found across Kamchatka. While fluid released in EVF and CKD carries high amounts of B, Cl and S [*Portnyagin et al.*, 2007a], the fluid below SR is enriched in Li and F (Fig. 16),[*Churikova* et al., 2004, 2007]. We argue that the dehydration of different water-rich minerals at different depths explains the difference in fluid

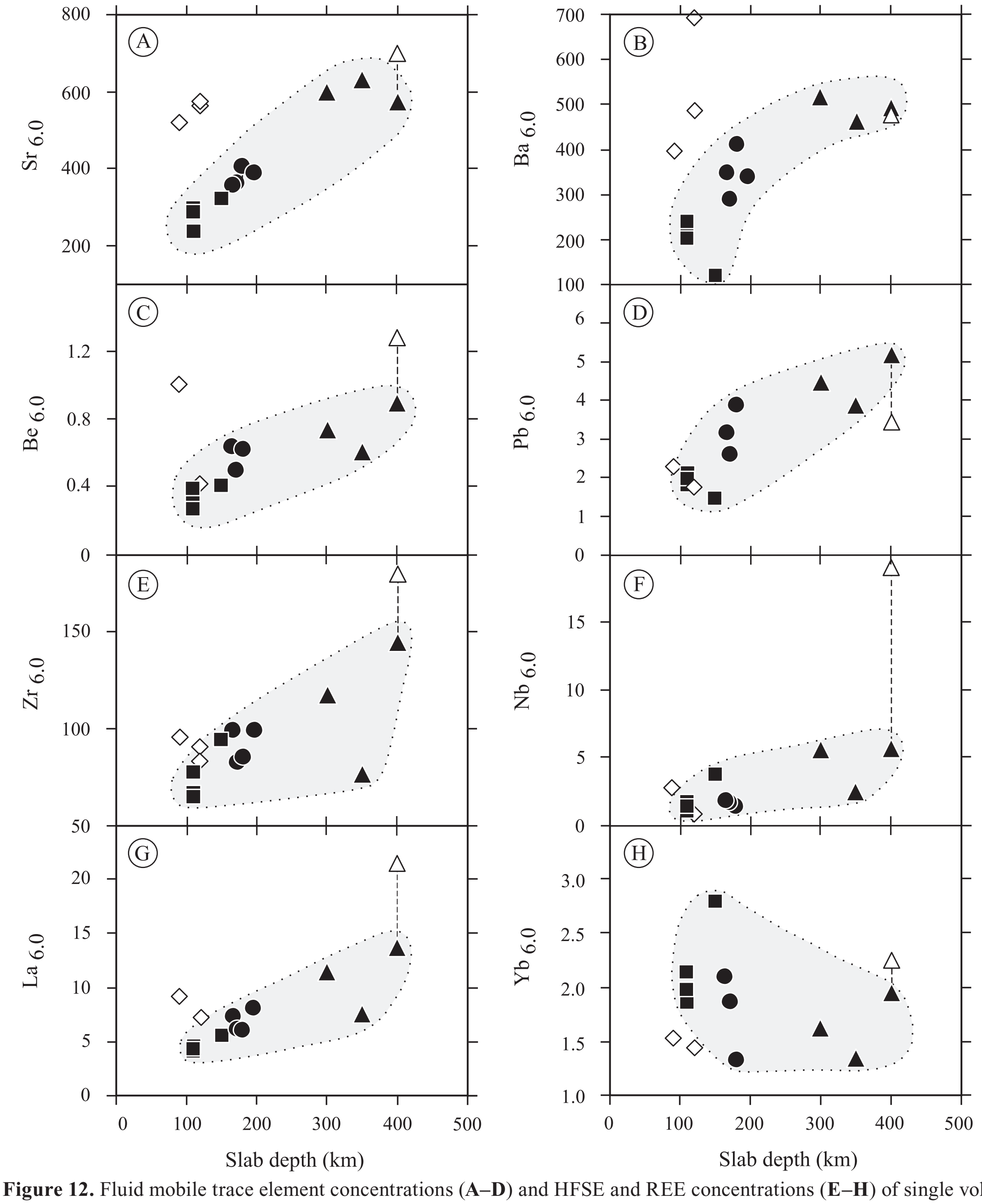

Figure 12. Fluid mobile trace element concentrations (**A–D**) and HFSE and REE concentrations (**E–H**) of single volcanoes in relation to the depth of the slab surface below the volcanoes for the northern Kamchatka transect. For correct comparison of differently fractionated volcanic series the data from each volcano were normalized to 6% MgO following the approach used by [*Plank* and *Langmuir*, 1988]. The shaded fields were drawn to underline the trends of the typical arc magmas. The typical arc series of Ichinsky are connected by a dotted line with the WPT, occurring at the same volcano. Positive linear trends are well-defined for $Sr_{6.0}$, $Ba_{6.0}$, $Be_{6.0,}$ $Pb_{6.0}$, $Zr_{6.0}$, $Nb_{6.0}$, $La_{6.0}$ and a week negative trend for $Yb_{6.0}$ which are marked by shaded fields. However, the trends for HFSE and REE are less well defined than for the fluid mobile elements. Squares – EVF; circles – SCKD; diamonds – NCKD; triangles – SR. Element concentrations are given in ppm. Modified after *Churikova* et al. [2001].

composition across the Kamchatka arc and may significantly influence the chemical composition of the rocks.

Systematic geochemical variations from front-arc to back-arc argue for a single subduction zone. Trace element patterns seem to be mostly governed by slab fluid and variable source compositions in the mantle wedge. Rate of magma production by individual volcanoes depends on fluid flux, mantle wedge heterogeneity and the location of their magmatic sources with respect to the dehydrating slab.

Chemical Variations Along the Kamchatka arc

No significant changes in chemical composition of the late Pleistocene-Holocene rocks have been found along EVF [*Volynets,* 1994] or northern part of SR (from Ichinsky to ~50 km north of Titila) (Fig. 17A) [*Volynets* et al., 2005; *Volynets*, 2006]. In CKD, however, systematic changes in trace element ratios were observed from Kliuchevskoi group northwards to Nachikinsky and Khailulia volcanoes, that suggests a transition from fluid-induced melts through

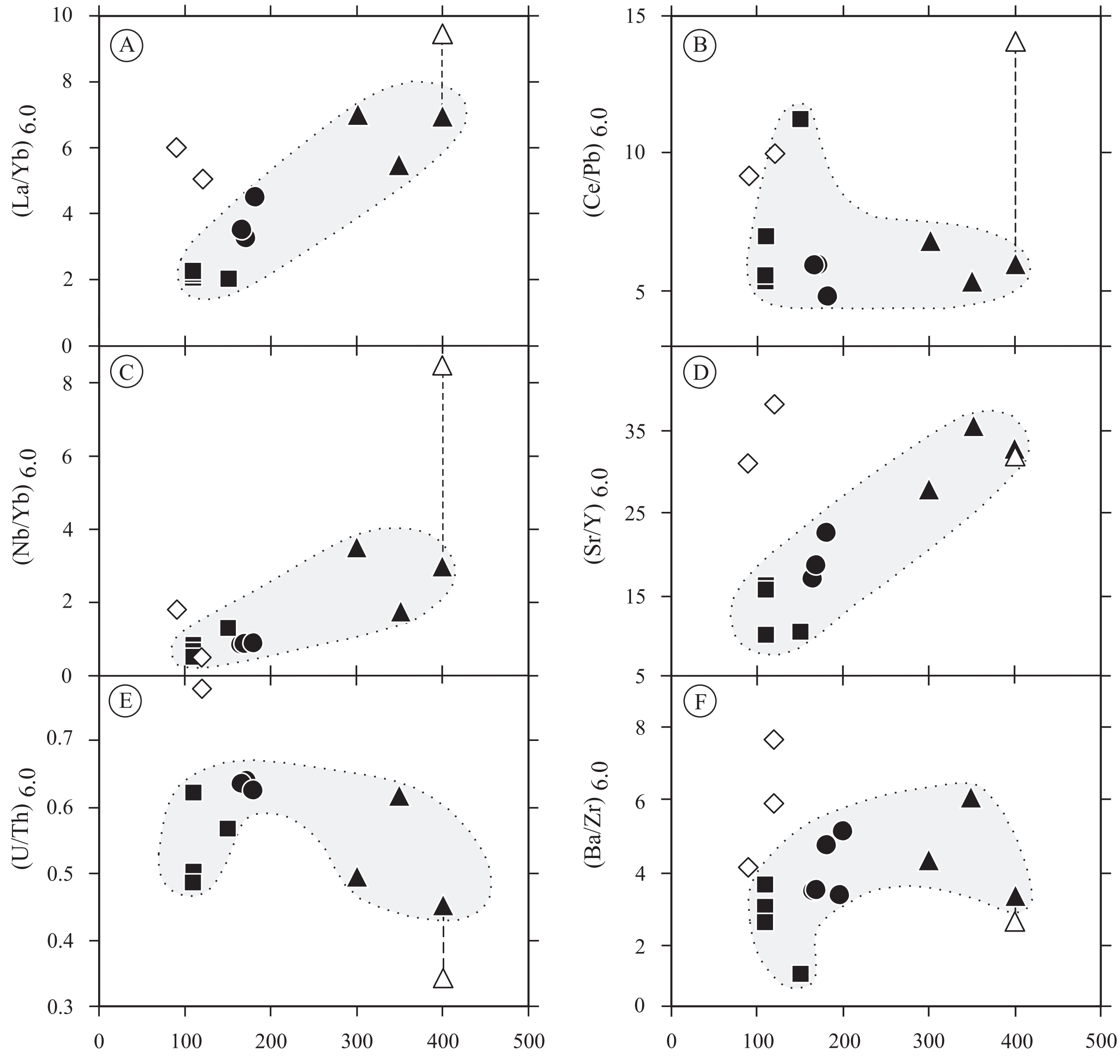

Figure 13. 6% MgO-normalized incompatible trace element ratios of single volcanoes in relation to the depth of the slab surface below the volcano. Positive linear trends exist for $(La/Yb)_{6.0}$, $(Nb/Yb)_{6.0}$ and $(Sr/Y)_{6.0}$. The $(Ce/Pb)_{6.0}$, $(Ba/Zr)_{6.0}$ and $(U/Th)_{6.0}$ ratios do not show regular trends. Symbols as in Fig. 12. Modified after *Churikova* et al. [2001].

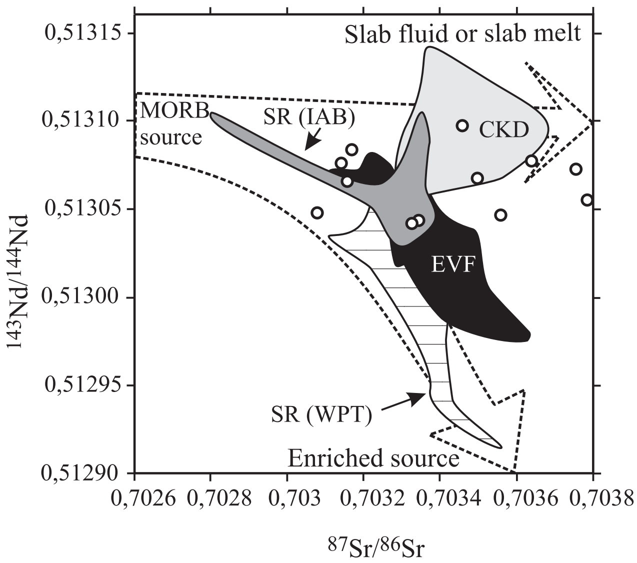

Figure 14. $^{143}Nd/^{144}Nd$ vs $^{87}Sr/^{86}Sr$ for Kamchatka rocks. Data from *Churikova* et al [2001]; *Dorendorf* et al. [2000a, b] and *Volynets* [2006]. The points of leached clinopyroxene from mantle xenoliths for Kamchatka [*Dorendorf*, 1998; *Koloskov*, 1999] are marked by white circles and shows for Nd-isotopes a comparable and for Sr-isotopes an even larger range than observed in the volcanic rocks. Arrows are drawn schematically to show three-component mixing between slab fluid, MORB and enriched mantle source. SR rocks show mixing line between MORB and OIB sources.

slab-influenced source to intra-plate melt compositions (Fig. 17B), [*Portnyagin* et al., 2005]. Khailulia and most of Nachikinsky, however, likely started to form in early-mid-Pleistocene times, so they are significantly older than the late Pleistocene-Holocene Tolbachik, Kliuchevskoi and Shiveluch. These changes might reflect variations of melts both in space and time.

CKD Volcanoes

The best studied volcanoes in Kamchatka are in CKD, with the Kliuchevskoi group south of the Kamchatka River (SCKD) and the NCKD group with Shiveluch, Zarechny and Kharchinsky volcanoes north of the river (Fig. 4) [e.g. *Ozerov*, 2000; *Khubunaya* et al., 1995, *Volynets* et al., 1999b; *Dorendorf* et al., 2000a, *Kersting* and *Arculus,* 1994; *Mironov* et al., 2001; *Portnyagin* et al., 2005, 2007a, b]. The reason for CKD's high volcanic activity could be related to intra-arc

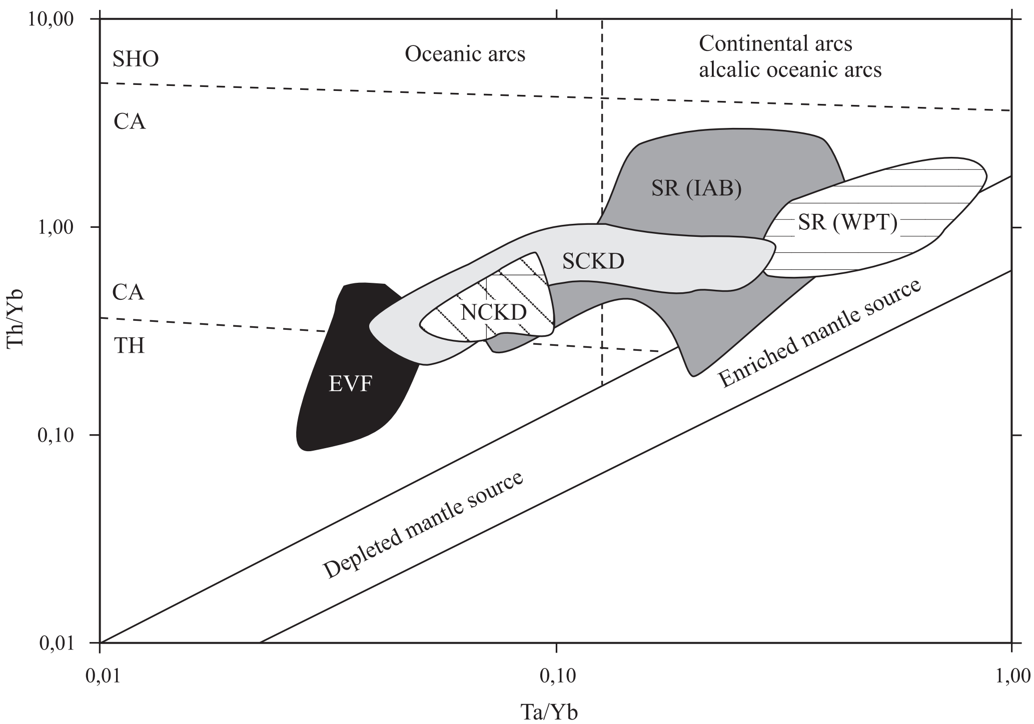

Figure 15. Th/Yb vs. Ta/Yb after *Pearce* [1983]. Nearly all samples from EVF and SCKD as well as most NCKD samples fall into the field of oceanic arcs formed from depleted mantle sources. In a contrast, the SR samples trend towards an enriched mantle composition (shaded field). SHO - shoshonitic series; CA - calc-alkaline series; TH - tholeiitic series. Data from *Churikova* et al [2001]; *Dorendorf* et al. [2000b], *Ivanov* et al. [2004], and *Volynets* et al. [2005].

rifting and upwelling in this area. Yogodzinski et al. [2001a] suggested that mantle wedge below CKD is extraordinary hot because of a hot mantle flow around the edge of the subducting Pacific plate. Even if the degree of melting is not very high (around 12%), a large volume of mantle could be involved in this melting due to massive decompression below the rift. CKD rocks are enriched in ^{87}Sr, and elevated U/Th and Ba/Zr ratios (Figs. 14 and 16), [e.g. *Churikova* and *Sokolov*, 1993, *Dorendorf* et al., 2000a, *Wörner* et al., 2001]. We conclude that the high magma production rate in CKD may be caused by: (1) intra-arc rifting, following upwelling and enhanced decompression melting and (2) enhanced fluid-flux from the Emperor Seamounts Chain.

Most of SCKD rocks are medium-K calc-alkaline basalt-andesite series (Fig. 10). At the same time, on Plosky Tolbachik volcano and Plosky massif high-K tholeiitic rocks occur along with "normal" medium-K calc-alkaline volcanic rocks. High-K rocks are enriched in all incompatible elements, but exhibit low HFSE, and therefore fall off the across-arc trend for most geochemical parameters. Despite the fact that such rocks were found only on a few volcanoes, they have significant volumes and so merit further detailed examination. For example, in the Tolbachik lava field, individual eruptions produced up to 1–2 km^3 of high-K basalt and the total for the Holocene rocks of this composition approaches to 70 km^3 [*Braitseva* et al., 1984; *Flerov* et al., 1984].

NCKD volcanoes (Shiveluch, Zarechny, Kharchinsky) display trace element patterns distinct from the SCKD [*Yogodzinski* et al., 2001a; *Portnyagin* et al., 2005]. They have high Sr/Y ratios of ~35 and La/Yb of ~5 (Figs. 10, 12, 13), which by far exceed compositions on the across-arc trend (Figs. 10B, 12, 13, 17). Such a pattern is typical for adakites, for which an origin from slab melting is assumed [*Defant* and *Drummond*, 1990]. The adakite-type signatures were explained by tearing of the slab and warming of the slab edge by hot asthenospheric mantle [*Volynets* et al., 1997b; *Yogodzinski* et al., 2001a].

Other Rock Types

Rare rock types occur locally and include shoshonite-latite series [*Volynets*,1994], avachite (high-Mg basalt found near Avachinsky volcano), allivalites (Ol-Pl highly crystallized rocks which occur mostly as inclusions in low-K mafic and silicic tephras), high-K high-Mg phlogopite-bearing and hornblende-bearing basalt—basaltic andesite found only in one tephra from Shiveluch volcano [*Volynets* et al., 1997a], etc.

Unlike most other arcs, Kamchatka rocks are rich in mantle-derived xenoliths (mostly dunites, harzburgites, and clinopyroxenites, with fewer wehrlites) [*Koloskov*, 1999; *Bryant* et al., 2005; *Dektor* et al., 2005] that provide an opportunity to directly observe mantle material altered by subduction processes. Trace elements indicate that Kamchatka xenoliths are depleted in Nb and Ta relative to Ba and light REEs [*Turner et al.*, 1998; *Yogodzinski et al.*, 2001b].

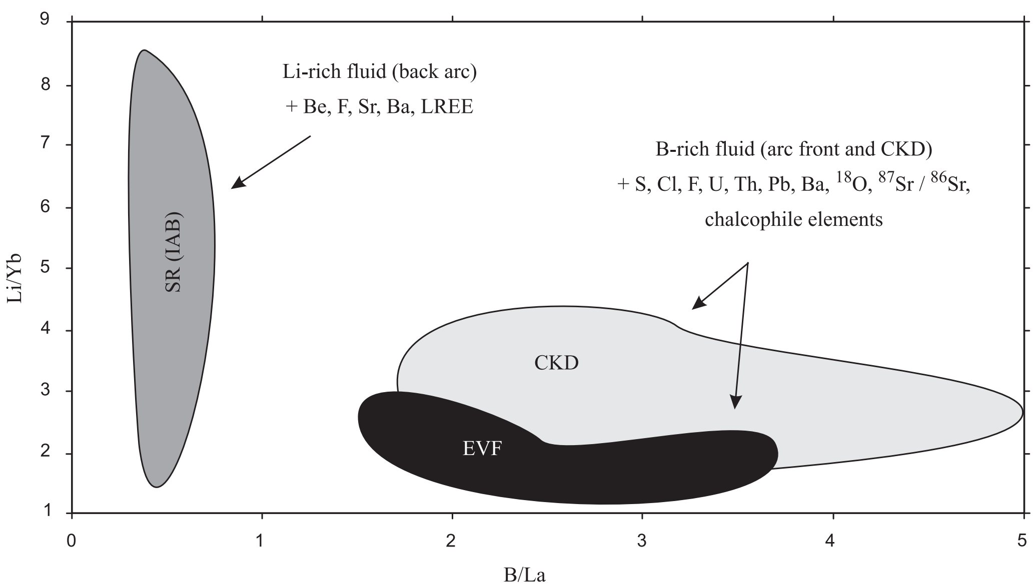

Figure 16. B-Li systematics in melt inclusions from olivines from rocks across the Kamchatka arc, showing the decoupling of B and Li. This results in high B/La in arc front magmas and a strong increase in Li/Yb towards the back arc. Field as in Figure 10.

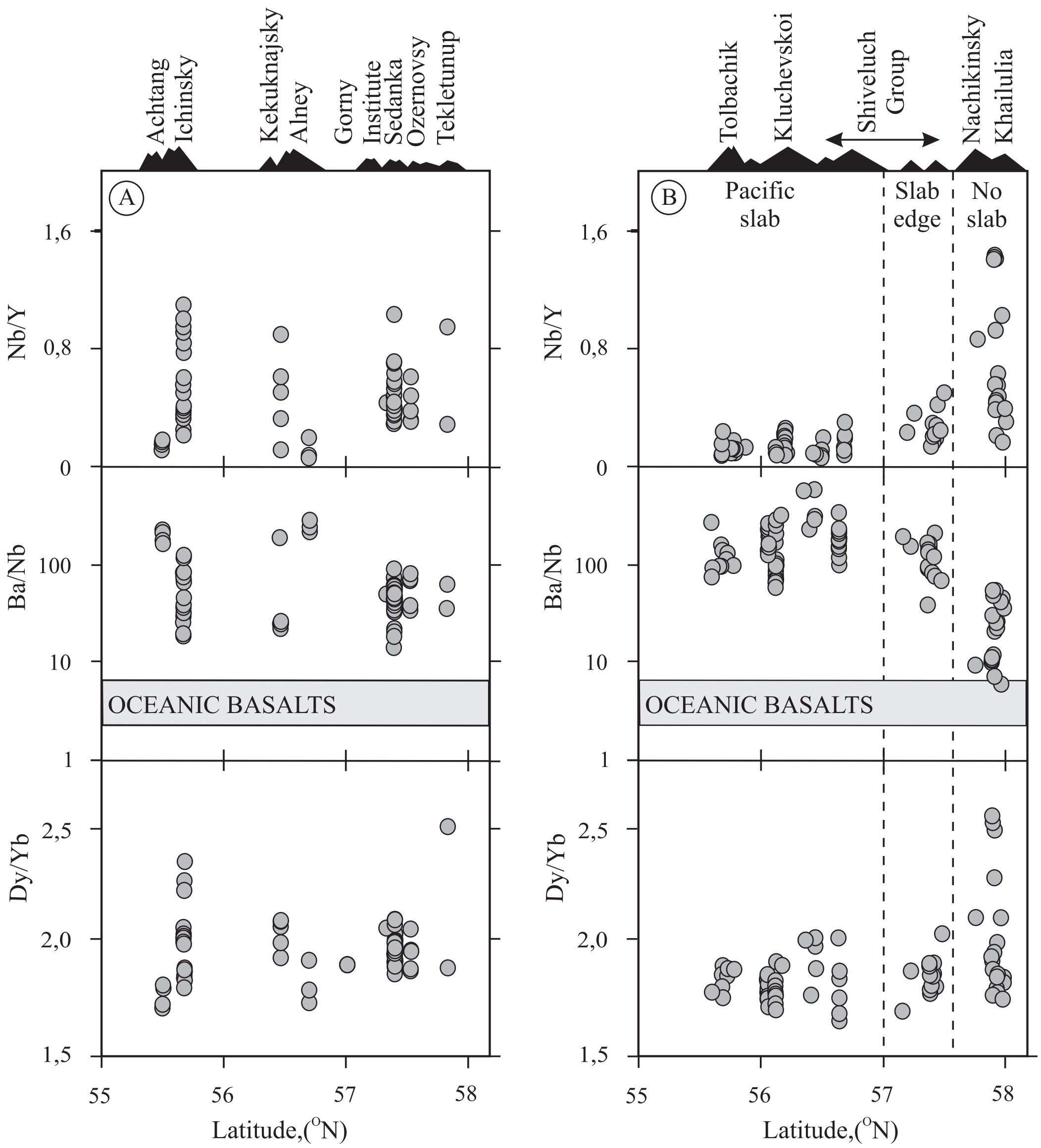

Figure 17. Along-arc variations of trace element ratios in SR (A) and CKD (B) lavas. No systematic changes have been found along the Sredinny Range (A) while the CKD lavas show a transition from fluid-induced melts over Pacific slab through slab-influenced magmas above the slab edge to intra-plate compositions farther north (B). The range of Ba/Nb for oceanic basalts (MORB and OIB) is shown after *Sun* and *McDonough* [1989]; the range of Nb/Y and Dy/Yb for oceanic basalts covers the entire range shown in diagrams. Data sources: (A) - *Volynets* [2006]; (B) - modified after *Portnyagin* et al. [2005].

CONCLUSION: FUTURE TASKS

Changes in the spatial-temporal patterns of volcanism and composition of volcanic rocks reflect large-scale tectonic processes. Further steps in understanding Quaternary volcanism in Kamchatka should, in our opinion, combine radiometric dating of the volcanic rocks with studies of their geochemical affinities. In addition to across-arc variations in rock composition, more along-arc traverses should be studied. Special attention must be paid to northern Kamchatka, where volcanism seemingly extends beyond an active subduction zone (Fig. 2B).

Even in the best studied Kliuchevskoi group, some volcanoes like Udina or Zimina (southeastern part of the group, (Fig. 4) were last visited in 1970-ies and their rocks have never been analyzed in detail. The Kliuchevskoi volcanic group has been recording tectonic processes in the Kamchatka-Aleutian "corner" or triple junction (Fig. 2B) starting from at least mid-Pleistocene, so changes in production rates and compositions of its rocks, once reconstructed, can shed light on the evolution of this structure.

Similar efforts should be made in the studies of the pre-late Pleistocene volcanism including voluminous late Pliocene-Early Pleistocene lava plateaus in Sredinny Range and spectacular shield volcanoes. Of special interest are volcanic fields that existed during only one period and did not resume their activity later (Fig. 2B) (e.g. lava field NE of Shiveluch and fields in the northernmost part of the peninsula). These volcanic deposits likely record major events in the plate history of the region.

At the Holocene scale, attempts of correlating paleovolcanic and paleoseismic records [*Bourgeois* et al., 2006; *Kozhurin* et al., 2006; *Pinegina* et al., 2003] and identifying periods of overall high tectonic activity and natural catastrophes [*Melekestsev* et al., 1998, 2003a,b] are most intriguing. Near their sources, both volcanic and seismic events can produce marked changes in the landscape, building volcanoes, triggering large debris flows and floods, producing conspicuous ground deformation, and reorienting river drainages. At a distance, large earthquakes and volcanic eruptions also leave their mark, causing tsunamis, heavy ash falls, and atmospheric pollution. Major subduction-zone events may include many of these proximal and distal components, which combine their effects and cause more serious and variable consequences than anticipated for individual volcanic or seismic events alone. Studies of such recent geological catastrophes in Kamchatka, based on distal correlations of various deposits with the help of marker tephra layers, hopefully will help to understand the space-time patterns of catastrophic events, make long-term forecasts of future episodes, and to model potential natural catastrophes around the Pacific Rim.

Acknowledgements. The research was supported by grants ## 05-05-64776, 06-05-64960 and 06-05-65037 from the Russian Foundation for Basic Research; by the Russian Academy of Sciences Program "Environmental and Climate Change"; by the Russian Ministry of Industry and Science projects #43.700.11.0005, 43.043.11.1606 and State Contract with Federal Agency of Science and Innovations' Department of Survey and New Technologies Development #01.700.12.0028 to Tatiana Churikova and NSF grant #EAR-0125787 to Joanne Bourgeois. Geochemical studies would not be possible without continuous support and attention from Gerhard Wörner to whom the authors are most grateful. The field work in 1996–2000, 2002, and 2004 was supported by the grants from the National Geographic Society to Vera Ponomareva. We thank John Eichelberger for editing the first version of this manuscript. We appreciate the help from Gene Yogodzinski and an anonymous reviewer, whose comments and suggestions have allowed us to improve the manuscript.

REFERENCES

Ananiev, V. V., N. A. Titaeva, and A. N. Troshin (1980), Uran-Ionium and track dating of the volcanic rocks, in *A volcanic center: structure, dynamics and substance of the Karymsky center*, edited by Masurenkov Yu. P., pp. 199–235, Nauka, Moscow, (in Russian)

Avdeiko, G.P., S.V. Popruzhenko, and A.A. Palueva (2002), The tectonic evolution and volcano-tectonic zonation of the Kuril-Kamchatka island-arc system, *Geotectonics, 36*(4), 312–327.

Avdeiko G. P., Palueva A.A., and O. A. Khleborodova (2006), Geodynamic conditions of volcanism and magma formation in the Kurile-Kamchatka island-arc system, *Petrology*, *14* (3), 230–246.

Bazanova, L. I., O. A. Braitseva, M. Yu. Puzankov, and L. D. Sulerzhitsky (2003), Catastrophic plinian eruptions of the initial cone-building stage of the Young Cone of Avachinsky volcano (Kamchatka), *Volcanol. and Seismol.*, (6), 20–40 (In Russian).

Bazanova, L. I., and M. M. Pevzner (2001), Khangar: One more active volcano in Kamchatka, *Transactions (Doklady) of the Russian Academy of Sciences, Earth Sciences*, *377A*, 307–310.

Bazanova, L. I., O. A. Braitseva, I. V. Melekestsev, and M. Yu. Puzankov (2001), Expected hazard from the Avachinsky volcano eruptions, in *Geodynamics and volcanism of the Kurile-Kamchatka island arc system.* Petropavlovsk-Kamchatsky. 390–407, (In Russian).

Bazanova, L. I., O. A. Braitseva, I. V. Melekestsev, and L. D. Sulerzhitsky (2004), Catastrophic eruptions of Avachinsky volcano (Kamchatka) in Holocene: chronology, dynamics, geological effect, environmental impact and long-term forecast. *Volcanol. and Seismol.*, (6), 15–20, (In Russian).

Bazanova, L. I., O. A. Braitseva, O.V. Dirksen, L. D. Sulerzhitsky, and T.Danhara (2005) Ashfalls from the largest Holocene eruptions along the Ust'-Bol'sheretsk - Petropavlovsk-Kamchatsky traverse: sources, chronology, recurrence. *Volcanol. and Seismol.*, (6), 30–46, (In Russian).

Bindeman, I. N., and J. C. Bailey (1994), A model of reverse differentiation at Dikii Greben' volcano, Kamchatka: progressive basic magma vesiculation in a silicic magma chamber, *Contrib. Mineral. Petrol., 117*, 263–278.

Bindeman, I. N., V. V. Ponomareva, J. C. Bailey, and J.W. Valley (2004), Kamchatka Peninsula: a province with high-$\delta^{18}O$ magma sources and large $^{18}O/^{16}O$ depletion of the upper crust, *Geochimica et Cosmochimica Acta, 68*(4), 841–865.

Bourgeois J., T. K. Pinegina, V.V. Ponomareva, and N.E. Zaretskaia (2006), Holocene tsunamis in the southwestern Bering Sea, Russian Far East and their tectonic implications, *The Geol. Soc. Amer. Bull., 11*(3/4), 449–463; doi: 10.1130/B25726.1.

Braitseva, O. A., I.V. Melekestsev, and E.N. Erlikh (1974) , Recent volcanic activity, in *Kamchatka, Kurile and Commander Islands*, edited by I. V. Luchitsky, Nauka, Moscow, pp. 369–394, (in Russian).

Braitseva, O. A., I. A. Egorova, L. D. Sulerzhitsky, and I. A. Nesmachny (1980), Maly Semiachik volcano, in *A volcanic center: structure, dynamics and substance of the Karymsky center*, edited by Yu. P. Masurenkov, Nauka, Moscow, pp. 199–235, (In Russian).

Braitseva, O. A., I. V. Melekestsev, G. B. Flerov, V. V. Ponomareva, L. D. Sulerzhitsky, and S. N. Litasova (1984), Holocene volcanism of the Tolbachik regional zone of cinder cones, in *Great Tolbachik Fissure Eruption, Kamchatka, 1975-1976*, edited by S. A. Fedotov, Nauka, Moscow, pp. 177-222, (In Russian).

Braitseva, O. A., S. N. Litasova, and A. K. Ponomarenko (1987), Application of tephrochronology for dating a key archaeological site in Eastern Kamchatka, *Volcanol. and Seismol.*, *5*(5), 507–514.

Braitseva, O. A., I. V. Florenskii, V. V. Ponomareva, and S. N. Litasova (1989), The history of the activity of Kikhpinych volcano in the Holocene, *Volcanol. and Seismol.*, *7*(6), 845-872.

Braitseva, O. A., and I. V. Melekestsev (1990), Eruptive history of Karymsky volcano, Kamchatka, USSR, based on tephra stratigraphy and ^{14}C dating, *Bul.l Volcanol., 53*, 195–206.

Braitseva, O. A., I. V. Melekestsev, G. E. Bogoyavlenskaya, and A. P. Maksimov (1991), Bezymianny volcano: eruptive history and activity dynamics, *Volcanol. and Seismol.*, *12*(2), 165–194.

Braitseva, O. A., L. D. Sulerzhitsky, S. N. Litasova, I. V. Melekestsev, and V. V. Ponomareva (1993), Radiocarbon dating and tephrochronology in Kamchatka, *Radiocarbon, 35*(3), 463–476.

Braitseva, O. A., I. V. Melekestsev, V. V. Ponomareva, and L. D. Sulerzhitsky (1995), The ages of calderas, large explosive craters and active volcanoes in the Kuril-Kamchatka region, Russia, *Bull. of Volcanology, 57*(6), 383–402.

Braitseva, O. A., I. V. Melekestsev, V. V. Ponomareva, and V. Yu. Kirianov (1996), The caldera-forming eruption of Ksudach volcano about cal. AD 240, the greatest explosive event of our era in Kamchatka, *J. Volcanol. Geotherm. Res., 70*(1-2), 49–66.

Braitseva, O. A., L. D. Sulerzhitsky, V. V. Ponomareva, and I. V. Melekestsev (1997a), Geochronology of the greatest Holocene explosive eruptions in Kamchatka and their imprint on the Greenland glacier shield, *Trans. Russian. Acad. Sci., 352*(1), 138–140.

Braitseva, O. A., V. V. Ponomareva, L. D. Sulerzhitsky, I. V. Melekestsev, and J. Bailey (1997b), Holocene key-marker tephra layers in Kamchatka, Russia, *Quaternary Res., 47*(2), 125–139.

Braitseva, O. A., L. I. Bazanova, I. V. Melekestsev, and L. D. Sulerzhitsky (1998), Largest Holocene eruptions of Avachinsky volcano, Kamchatka, *Volcanol. and Seismol.*, *20*, 1–27.

Braitseva, O. A., I. V. Melekestsev, and L. D. Sulerzhitsky (2005), New data on the Pleistocene deposits in the Central Kamchatka Depression, *Stratigraphy and Geological correlation*, *13*(1), 99–107.

Bryant, J. A., G. M. Yogodzinski, and T. G. Churikova (2005), Petrology of metasomatised mantle xenoliths from Shiveluch Volcano, Kamchatka, *Goldschmidt Conference Abstracts. Subduction Zone Magmatism*, A642.

Calkins, J. (2004), ^{40}Ar/^{39}Ar geochronology of Khapitsa Plateau and Studyonaya River basalts and basaltic andesites in Central Kamchatka Depression, Kamchatka, Russia, *Abstracts IV JKASP International workshop.*

Cambray, H., and J.-P. Cadet (1996), Synchronisme de l'activite volcanique d'arc: Mythe ou realite?, *C. R. Acad. Sci. Paris, 322*, 237–244.

Cao, L. Q., R. J. Arculus, and B. C. McKelvey (1995), Geochemistry and petrology of volcanic ashes recovered from Sites 881 through 884: A temporal record of Kamchatka and Kurile volcanism, in *Proceedings of the Ocean Drilling Project, Scientific Results, 145*, edited by D. K. Rea et al., College Station, Texas, Ocean Drilling Program, pp. 345–381.

Churikova, T. G., and S. Yu. Sokolov (1993), The magmatic evolution of Ploskie Sopky volcano, Kamchatka (analyses of Sr isotopic geochemistry), *Geochemistry, 10*, 1439–1448.

Churikova, T., F. Dorendorf, and G. Wörner (2001), Sources and fluids in the mantle wedge below Kamchatka, evidence from across-arc geochemical variation, *J. Petrol., 42*(8), 1567–1593.

Churikova, T., G. Wörner, N. Mironov, A. Kronz, P. Pletchov, and M. Portnyagin (2004), Halogens and Sulfur Across the Kamchatka Arc, *AGU Fall Meeting, EOS*, (7), F540.

Churikova, T., G. Wörner, N. Mironov, and A. Kronz (2007), Volatile (S, Cl and F) and fluid mobile trace element compositions in melt inclusions: Implications for variable fluid sources across the Kamchatka arc, *Contributions to Mineralogy and Petrology,* in press, DOI 10.1007/s00410-007-0190-z.

Defant, M. J., and M. S. Drummond (1990), Derivation of some modern arc magmas by melting of young subducted lithosphere, *Nature (London), 347*, 662–665.

Dektor, C. L., G. M. Yogodzinski, and T. G. Churikova (2005), Petrology of ultramafic xenoliths from Kharchinsky Volcano, Russia, *Goldschmidt Conference Abstracts. Subduction Zone Magmatism*, A643.

DeMets, C. (1992), Oblique convergence and deformation along the Kuril and Japan trenches, *J. Geophys. Res., 97*, 17615–17625.

Dirksen, O. V., and I. V. Melekestsev (1999), Chronology, evolution and morphology of plateau basalt eruptive centers in Avacha River area, Kamchatka, Russia, *Volcanol and Seismol., 21*(1), 1–28.

Dirksen, O. V., V.V. Ponomareva, and L. D. Sulerzhitsky (2002), Eruption from Chasha Crater - a unique large silicic eruption at a monogenetic basaltic lava field, *Volcanol. and Seismol.,* (5), 3–10, (In Russian).

Dirksen, O. V., L. I. Bazanova, and M. Portnyagin (2003), Chronology of the volcanic activity in the northern part of Sredinny Range (Sedanka lava field) in the Holocene, in *Volcanism and geodynamics*, Materials of the II Russian symposium on volcanology and paleovolcanology, Ekaterinburg, 871–874.

Dirksen, V. (2004), Holocene Vegetation Changes in Eastern Kamchatka Based on Pollen and Macrofossil Records, *Eos Trans. AGU, 85*(47), Fall Meet. Suppl., Abstract PP21B-1378.

Dorendorf, F. (1998), *Genesis of Quaternary volcanic rocks from Kamchatka, Russia*, Ph. D. Thesis, Geochemishes Institute, Göttingen University, Germany.

Dorendorf, F., U. Wiechert, and G. Wörner (2000a), Hydrated sub-arc mantle: a source for Kluchevskoy volcano / Kamchatka, *Earth Planet. Sci. Lett., 175*, 69–86.

Dorendorf, F., T. Churikova, A. Koloskov, and G. Wörner (2000b), Late Pleistocene to Holocene activity at Bakening volcano and surrounding monogenetic centers (Kamchatka): volcanic geology and geochemical evolution, *J. of Volcanology and Geothermal Research. 104*, 131–151.

Duggen, S., Portnyagin, M., Baker, J., Ulfbeck, D., Hoernle, K., Garbe-Schönberg, D., and N. Grassineau (2007), Drastic shift in lava geochemistry in the volcanic-front to rear-arc region of the Southern Kamchatkan subduction zone: Evidence for the transition from slab surface dehydration to sediment melting, *Geochimica et Cosmochimica Acta*, *71*(2), 452–480.

Eichelberger, J. C., and P. Izbekov (2000), Eruption of andesite triggered by dyke injection: contrasting cases at Karymsky volcano, Kamchatka and Mount Katmai, Alaska, *Royal Soc. London Phil. Trans., ser. A, 358*, 1465–1485.

England, P., R. Engdahl, and W. Thatcher (2004), Systematic variation in the depths of slabs beneath arc volcanoes, *Geophys. J. Int*., 156, 377–408.

Erlich, E. N., I.V. Melekestsev, and O.A. Braitseva (1979), Evolution of Recent Volcanism, in *Quaternary Volcanism and Tectonics in Kamchatka,* edited by E. N. Erlich and G. S. Gorshkov, *Bull. Volcanol., 42*, 93–112.

Erlich, E. (1986), Geology of the calderas of Kamchatka and Kurile Islands with comparison to calderas of Japan and the Aleutians, Alaska, *U. S. Geol. Surv. Open-File Report. 86*-291. 300 p.

Fedotov, S. A., and Yu. P. Masurenkov (eds) (1991), *Active volcanoes of Kamchatka*, *Vol.1*, 302 p., *Vol.2*, 415 p., Nauka, Moscow.

Flerov G.B., V.N.Andreev, V.A.Budnikov, and A.I.Tsyurupa (1984), Petrology of the erupted products, in *Great Tolbachik Fissure Eruption, Kamchatka, 1975-1976*, edited by S. A. Fedotov, Nauka, Moscow, pp. 223-284, (In Russian).

Florensky, I.V. (1984), On the age of Uzon and Krasheninnikov calderas, *Volcanol. and Seismol.,* (1), 102–105, (In Russian).

Florensky I. V. and V. G. Trifonov (1985), Neotectonics and volcanism in the East Kamchatka volcanic zone, *Geotektonika,* (4), 78–87 (In Russian).

Gorbatov, A., V. Kostoglodov, G. Suarez, and E. I. Gordeev (1997), Seismicity and structure of the Kamchatka subduction zone, *J. Geophys. Res., B, 102*(8), 17,883–17,898.

Gusev, A. A., V. V. Ponomareva, O. A. Braitseva, I. V. Melekestsev, and L. D. Sulerzhitsky (2003), Great explosive eruptions on Kamchatka during the last 10,000 years: self-similar irregularity of the output of volcanic products, *J. Geophys. Res., 108*(B2), 2126, doi: 10.1029/2001JB000312.

Hildreth, W. (1983), The compositionally zoned eruption of 1912 in the Valley of Ten Thousand Smokes, Katmai National Park, Alaska, *Journal of Volcanology and Geothermal Research, 18*(1-4), 1–56.

Ho, C. H., E. I. Smith, D. L. Feuerbach, and T. R. Naumann (1991), Eruptive probability calculation for the Yucca Mountain site, USA: statistical estimation of recurrence rates, *Bull. Volcanol., 54*, 50–56.

Hofmann, A. W. (1988), Chemical differentiation of the Earth; the relationship between mantle, continental crust, and oceanic crust, in *Isotope geochemistry; the Crafoord symposium. Earth and Planetary Science Letters*, edited by E. Welin, Amsterdam, Elsevier, pp. 297–314.

Holocene volcanoes in Kamchatka, http://www.kscnet.ru/ivs/volcanoes/holocene

Ivanov, B.V. (1990), *Types of the andesite volcanism within the Pacific volcanic belts,* 213 p., Nauka, Moscow (In Russian).

Ivanov, A.V., A.B. Perepelov, M.Yu. Puzankov, T.A. Yasnygina1, Yu.M. Malykh1, and S.V. Rasskazov (2004), Rift- and arc-type basaltic volcanism of the Sredinny Ridge, Kamchatka: case study of the Payalpan volcano-tectonic structure. *Metallogeny of the Pacific Northwest: Tectonics, Magmatism and Metallogeny of Active Continental Margins (Khanchuk, A.I. et al. Eds) Dalnauka, Vladivostok*, 345–349 (In Russian).

Jones, G., D. K. Chester, and F. Shooshtarian (1999), Statistical analyses of the frequency of eruptions at Furnas Volcano, Sao Miguel, Azores, *J. Volcanol. Geotherm. Res., 92*, 31–38.

Kadik, A.A., A.P. Maksimov, and B.V. Ivanov (1986), *Physico-Chemical Conditions of Crystallization and Genesis of Andesites*, 158 p., Nauka, Moscow (In Russian).

Kennett, J. P., A. R. McBirney, and R. C. Thunell (1977), Episodes of Cenozoic volcanism in the circum-Pacific region, *J. Volcanol. Geotherm. Res., 2*, 145–163.

Kepezhinskas, P., F. McDermott, M. J. Defant, A. Hochstaedter, M. S. Drummond, C. J. Hawkesworth, A. Koloskov, R. C. Maury, and H. Bellon (1997), Trace element and Sr-Nd-Pb isotopic constraints on a three-component model of Kamchatka Arc petrogenesis, *Geochimica et Cosmochimica Acta, 61*, 577–600.

Kersting, A. B., and R. J. Arculus (1994), Kliuchevskoi volcano, Kamchatka, Russia – the role of high-flux recharged, tapped, and fractionated magma chamber(s) in the genesis of high-Al_2O_3 from high-MgO basalt, *J. of Petrology, 35*(1), 1–42.

Kersting, A. B., and R. J. Arculus (1995), Pb systematics of Kliuchevskoi volcano, Kamchatka, and North Pacific sediments: Implications for magma genesis and sediment recycling in the Kamchatka arc, *Earth Planet Sci. Lett., 136*, 133–148.

Khubunaya, S. A., N. A. Zharinov, Ya. D. Muravyev, V. V. Ivanov, G. E. Bogoyavlenskaya, T. Yu. Novgorodtseva, Yu. V. Demyanchuk, V. A. Budnikov, and S. M. Fazlullin (1995), 1993 eruption of Shiveluch volcano, *Volcanol. and Seismol., 17*, 1–20.

Koloskov A.V. (1999), *Ultramafic inclusions and volcanic rocks as self-adjusted geological system*, 224 p., Nauchnij Mir, Moscow (In Russian).

Kozhurin, A. I. (2004), Active faulting at the Eurasian, North American and Pacific plates junction, *Tectonophysics, 380*, 273–285.

Kozhurin, A., V. Acocella, P. R. Kyle, F. M. Lagmay, I. V. Melekestsev, V. Ponomareva, D. Rust, A. Tibaldi, A. Tunesi, C. Corazzato, A. Rovida, A. Sakharov, A. Tengonciang, and H. Uy (2006), Trenching active faults in Kamchatka, Russia: paleoseismological and tectonic implications, *Tectonophysics*, *417*, 285–304.

Lander, A. V., Bukchin, B. G., Droznin, D. V., and A.V. Kiryushin (1994), The tectonic environment and source parameters of the Khailino, Koryakiya earthquake of March 8, 1991: Does a Beringia plate exist? *Computational Seismology and Geodynamics*

(English edition of the Geodinamika i prognoz zemletriaseniy. Vychislitel'naya seismologiya), 3, 80–96.

Laverov, N. P. (Ed) (2005), *Recent and modern volcanism in Russia*, Moscow, Nauka Publishers, 604 p. (In Russian)

Le Maitre, R. W., P. Bateman, A. Dudek, J. Keller, M. J. Lameyre Le Bas, P. A. Sabine, R. Schmid, H. Sorensen, A. Streckeisen, A. R. Woolley, and B. Zanettin (1989), *A classification of igneous rocks and glossary of terms*, Blackwell, Oxford.

Leonov, V. L., E. N. Grib, and L.A. Kartasheva (1990), On the structure and age of Taunshits volcano. *Voprosy Geographii Kamchatki,* 10, 156–166 (in Russian).

Leonov, V. L., and E. N. Grib (2004), *Structural position and volcanism of the Kamchatka Quaternary calderas*, 189 p., Dalnauka, Vladivostok.

Levin, V., N. Shapiro, J. Park, and M. Ritzwoller (2002), Seismic evidence for catastrophic slab loss beneath Kamchatka, *Nature, 418*, 763–767.

Mackey, K. G., K. Fujita, L. V. Gunbina, V. N. Kovalev, V. S. Imaev, B. M. Kozmin, and L. P. Imaseva (1997), Seismicity of the Bering Strait region: evidence for a Bering Block, *Geology, 25*, 979–982.

Manea, V.C., M. Manea, V. Kostoglodov, and G. Sewell (2005), Thermal models, magma transport and tomographic imaging for the Kamchatka subduction zone, in *Plates, Plumes, and Paradigms,* edited by G.R. Foulger, J.H. Natland, D.C. Presnall and D.L. Anderson, *Geological Society of America Special Volume 388,* 861 pp,

Map of Mineral Resources of Kamchatka region (1:500 000) [1999].

McElfresh, S. B. Z., W. Harbert, C.-Y. Ku, and J.-S. Lin (2002), Stress modeling of tectonic blocks at Cape Kamchatka, Russia using principal stress proxies from high-resolution SAR: new evidence for the Komandorskiy Block, *Tectonophysics, 354*, 239–256.

Melekestsev, I.V., 1980. Volcanism and Relief Formation. Moscow: Nauka. 212 pp.

Melekestsev, I. V., O. A.Braitseva, L. D.Sulerzhitsky, N. N.Kozhemyaka, N. V. Ogorodov, I. A.Egorova, and E. G.Lupikina (1971), The age of volcanoes of the Kurile-Kamchatka volcanic region, in *Volcanism and the Deep Interior of the Earth,* pp. 68–75, Nauka, Moscow (in Russian).

Melekestsev, I. V., O. A. Braitseva, E. N. Erlich, and N. N. Kozhemyaka (1974), Volcanic mountains and plains, in *Kamchatka, Kurile and Commander Islands*, edited by I. V. Luchitsky, Nauka, Moscow, pp. 162–234, (in Russian).

Melekestsev, I. V., and O. A. Braitseva (1984, English translation 1988), Gigantic rockslide avalanches on volcanoes, *Volcanol. Seismol*., 6: 495–508.

Melekestsev, I. V., O. A. Braitseva, and V. V. Ponomareva (1989), Prediction of volcanic hazards on the basis of the study of dynamics of volcanic activity, Kamchatka, in *Volcanic Hazards Assessment and Monitoring: IAVCEI Proceedings in Volcanology*, I. Berlin - ...Tokyo. Springer-Verlag, pp. 10–35.

Melekestsev, I. V., O. N. Volynets, V. A. Ermakov, T. P. Kirsanova, and Yu. P. Masurenkov (1991), Shiveluch volcano, in *Active volcanoes of Kamchatka, 1*, edited by S. A. Fedotov and Yu. P. Masurenkov, pp. 84–92, Nauka, Moscow.

Melekestsev, I. V., S. N. Litasova, and L. D. Sulerzhitsky (1992), On the age and scale of the directed-blast catastrophic eruption of the Avachinsky volcano (Kamchatka) in the Late Pleistocene, *Volcanol. and Seismol., 13*(2), 135–146.

Melekestsev, I. V., V. V. Ponomareva, and O. N. Volynets (1995), Kizimen volcano (Kamchatka) - future Mt. St.Helens?, *J. Volcanol. Geotherm. Res., 65*, 205–226.

Melekestsev, I. V., O. A. Braitseva, L. I. Bazanova, V. V. Ponomareva, and L. D. Sulerzhitsky (1996a), A particular type of catastrophic explosive eruptions with reference to the Holocene subcaldera eruptions at Khangar, Khodutka Maar, and Baraniy Amfiteatr volcanoes in Kamchatka, *Volcanol and Seismol., 18*, 135–160.

Melekestsev, I. V., O. A. Braitseva, V. V. Ponomareva, and L. D. Sulerzhitsky (1996b), Holocene catastrophic caldera-forming eruptions of Ksudach volcano, Kamchatka, *Volcanol. and Seismol., 17*, 395–421.

Melekestsev, I. V., O. A. Braitseva, V. V. Ponomareva, and L. D. Sulerzhitsky (1998), A century of volcanic catastrophes in the Kurile-Kamchatka region in Early Holocene time, in *Global environmental change*, edited by N. L. Dobretsov and V. I. Kovalenko, pp.146–152, Sibir' Division of RAS Publishing House, Novosibirsk.

Melekestsev, I. V., O. A. Braitseva, and V. V. Ponomareva (2001), A new approach to defining a term "active volcano", in *Geodynamics and Volcanism of the Kurile-Kamchatka Island-Arc System,* edited by B. V. Ivanov, pp. 191–203, Petropavlovsk-Kamchatsky, (In Russian).

Melekestsev, I. V., O. A. Braitseva, V. V. Ponomareva, L.I. Bazanova, M. M. Pevzner, and L.D. Sulerzhitsky (2003a), Holocene geological catastrophes at Kamchatka and Kurile islands. *Transactions (Doklady) of the Russian Academy of Sciences. Earth science sections, 389*/3, 342–345.

Melekestsev, I. V., O. A. Braitseva, V. V. Ponomareva, L.I. Bazanova, Pinegina T.K., and O.V. Dirksen (2003b) AD 0–650 - a period of the strongest natural catastrophes in Kamchatka. *Volcanol. and Seismol.,* (6), 3–23 (In Russian).

Miyashiro, A. (1974), Volcanic rock series in island arcs and active continental margins, *Am. J. Sci*., 274, 321–355.

Mironov, N. L., M. V. Portnyagin, P. Yu. Pletchov, and S. A. Khubunaya (2001), Final Stages of Magma Evolution in Klyuchevskoy Volcano, Kamchatka: Evidence from Melt Inclusions in Minerals of High-Alumina Basalts. *Petrology*, *9*(1), 46–62.

Münker, C., G. Wörner, G. Yogodzinski, and T. Churikova (2004), Behaviour of high field strength elements in subduction zones: constraints from Kamchatka–Aleutian arc lavas, *Earth and Planetary Science Letters, 224*, 275– 293.

Ogorodov, N. (Ed.) (1972), *Volcanoes and Quaternary volcanism of Sredinny Range, Kamchatka*, 190 pp., Nauka Publishers, Moscow, (In Russian).

Ozerov, A. Yu. (2000), The evolution of high-alumina basalts of the Klyuchevskoy volcano, Kamchatka, Russia, based on microprobe analyses of mineral inclusions, *J. Volcanol. Geotherm. Res., 95*, 65–79.

Park, J., V. Levin, M. Brandon, J. Lees, V. Peyton, E. Gordeev, and A. Ozerov (2002), A dangling slab, amplified arc volcanism, mantle flow and seismic anisotropy in the Kamchatka plate corner, in *Plate Boundary Zones, Geodynamics Series, v. 30,* edited by S. Stein and J. T. Freymueller, pp. 295–324, Washington, D.C., American Geophysical Union.

Pearce, J. A. (1983), Role of the sub-continental lithosphere in magma genesis at active continental margins, in, *Continental basalts and mantle xenoliths; papers prepared for a UK Volcanic Studies Group meeting at the University of Leicester*, edited by C. J. Hawkesworth and M. J. Norry, pp. 230–249, Shiva Publ., Nantwich.

Pearce, N. J. G., J. A. Westgate, W. J. Eastwood, and W. T. Perkins (2004), Identification of Aniakchak (Alaska) tephra in Greenland ice core challenges the 1645 BC date for Minoan eruption of Santorini, *Geochemistry, Geophysics, Geosystems G3*, *5*(3), doi: 10.1029/2003GC000672.

Perepelov, A. B. (2004), Neogene-Quaternary shoshonite-latite magmatism of the Kamchatka Sredinny Range: Tekletunup Volcano (geochemistry, petrology, geodynamic interpretation), *Volcanol. and Seismol.*, (4), 1–15, (In Russian).

Perepelov, A. B., A. V. Ivanov, M. Yu. Puzankov and S. I. Dril (2005), Lithospheric control on depth of island-arc magma generation beneath Kamchatka, *www. MantlePlumes.org, Discussing the origing of "hotspot" volcanism,* http://www.mantleplumes.org/Kamchatka.html

Pevzner, M. M. (2004), The First Geological Data on the Chronology of Holocene Eruptive Activity in the Ichinskii Volcano (Sredinnyi Ridge, Kamchatka). *Transactions (Doklady) of the Russian Academy of Sciences/Earth Science Section, 395A*(3), p. 335–337.

Pevzner, M. M. (2006), Holocene volcanism of the Northern Kamchatka: space-temporal patterns. *Transactions (Doklady) of the Russian Academy of Sciences/Earth Science Section*, *409A* (6), 884–887.

Pevzner, M. M., Ponomareva, V.V., and I.V.Melekestsev (1998), Chernyi Yar - reference section of the Holocene ash markers at the northeastern coast of Kamchatka, *Volcanol. and Seismol., 19*(4), 389–406.

Pevzner, M.M., I.V.Melekestsev, O.N.Volynets, and V.A.Melkii (2000), South Cherpuk and North Cherpuk - the largest Holocene monogenetic volcanoes on the Sredinnyi Range of Kamchatka, *Volcanol. Seismol. 21*, 667–681.

Pevzner, M. M., V. V. Ponomareva, and L. D. Sulerzhitsky (2006), Holocene soil-pyroclastic successions of the Central Kamchatka depression: ages, structure, depositional features, *Volcanol. and Seismol.,* (1), 24–38, (In Russian).

Peyton, V., V. Levin, J. Park, M. T. Brandon, J. Lees, E. I. Gordeev, and A. Ozerov (2001), Mantle flow at a slab edge: Seismic anisotropy in the Kamchatka region, *Geophys. Res. Lett., 28*, 379–382.

Piip, B. I. (1956), Kliuchevskaya Sopka and Its Eruptions in 1944–1945 and the Past. *Trans. Volc. Lab. AN SSSR, Issue 11,* (in Russian).

Pinegina, T., J. Bourgeois, L. Bazanova, I. Melekestsev, and O. Braitseva (2003), A millennial - scale record of Holocene tsunamis on the Kronotskiy Bay coast, Kamchatka, Russia, *Quaternary Research, 59,* 36–37.

Plank, T., and C. H. Langmuir (1988), An evaluation of the global variations in the major element chemistry of arc basalts, *Earth and Planetary Science Letters, 90*, 349–370.

Plank, T., and C. H. Langmuir (1993), Tracing trace elements from sediment input to volcanic output at subduction zones, *Nature (London), 362*, 739–743.

Ponomareva, V. V. (1990), The history of Krasheninnikov volcano and the dynamics of its activity, *Volcanol. and Seismol., 9,* 714–741.

Ponomareva, V. V., and O. A. Braitseva (1991), Volcanic Hazards Assessment in the Area of lake Kronotskoye, Uzon caldera and Valley of Geysers, *Volcanol. and Seismol., 12*(1), 42–69.

Ponomareva, V. V., M. M. Pevzner, and I. V. Melekestsev (1998), Large debris avalanches and associated eruptions in the Holocene eruptive history of Shiveluch volcano, Kamchatka, Russia, *Bull. Volcanol., 59*(7), 490–505.

Ponomareva, V. V., L. D. Sulerzhitsky, O. V. Dirksen, and N. E. Zaretskaia (2001), Holocene paleosols as records of intervals of volcanic quiescence in the Kurile Lake region, South Kamchatka, in *"TEPHRAS, chronology, archaeology", Les dossiers de l'Archéologie,* (1). CDERAD, edited by E. Juvigné and J. P. Raynal, pp. 91–100.

Ponomareva, V. V., P. R. Kyle, I. V. Melekestsev, P. G. Rinkleff, O. V. Dirksen, L. D. Sulerzhitsky, N. E. Zaretskaia, and R. Rourke (2004), The 7600 (^{14}C) year BP Kurile Lake caldera-forming eruption, Kamchatka, Russia: stratigraphy and field relationships, *J. Volcanol. Geotherm. Res., 136*, 199–222.

Ponomareva, V.V., I. V. Melekestsev, and O. V. Dirksen (2006), Sector collapses and large landslides on Late Pleistocene-Holocene volcanoes in Kamchatka, Russia, *J. Volcanol. Geotherm. Res., 158*, 117–138.

Ponomareva, V. V., P. R. Kyle, M. M. Pevzner, L. D. Sulerzhitsky, M. Hartman (2007), Holocene eruptive history of Shiveluch volcano, Kamchatka Peninsula, Russia. This volume.

Portnyagin, M., Hoernle, K., Avdeiko, G., Hauff, F., Werner, R., Bindeman, I., Uspensky, V., and D. Garbe-Schönberg (2005), Transition from arc to oceanic magmatism at the Kamchatka-Aleutian junction, *Geology, 33*, 25–28.

Portnyagin, M., K. Hoernle, P. Plechov, N. Mironov, and S. Khubunaya (2007a), Constraints on mantle melting and composition and nature of slab components in volcanic arcs from volatiles (H_2O, S, Cl, F) and trace elements in melt inclusions from the Kamchatka Arc, *Earth and Planetary Science Letters, 255*(1-2), 53–69.

Portnyagin, M., Bindeman, I., Hoernle, K., Hauff, F. (2007b) Geochemistry of primitive lavas of the Central Kamchatka Depression: Magma generation at the edge of the Pacific Plate. This volume.

Prueher, L. M., and D. K. Rea (2001), Tephrochronology of the Kamchatka-Kurile and Aleutian arcs: evidence for volcanic episodicity, *J. Volcan. Geotherm. Res., 106*, 67–87.

Riegel, S. A., K. Fujita, B. M. Koz 'min, V. S. Imaev, and D. B. Cook (1993), Extrusion tectonics of the Okhotsk plate, northeast Asia, *Geophysical Research Letter, 20*(7), 607–610.

Salters, V.J.M. and N.Shimizu (1988), World-wide occurrence of HFSE depleted mantle, *Geochim. Cosmochim. Acta, 52*, 2177–2182.

Seliverstov, N. I. (1997), Evolution of a junction zone between the Kuril-Kamchatka and Aleutian island arcs: A geodynamic model, *Volcanol. and Seismol., 19*(3), 269–286.

Selyangin, O. B., O. A. Braitseva, I. A. Egorova, L. D. Sulerzhitsky, I. A. Nesmachny (1979), Geological and tephrochronological studies of recent volcanoes, in *Problems of deep magmatism*, pp. 31–49, Nauka, Moscow, (in Russian).

Selyangin, O. B., and V. V. Ponomareva (1999), Gorelovsky volcanic center, South Kamchatka: structure and evolution, *Volcanol. and Seismol., 21*(2), 163–194.

Sheimovich, V. S., and M. I. Karpenko (1997), K-Ar age of volcanism in South Kamchatka, *Volcanol. and Seismol., 18*(2), 231–236.

Sheimovich, V. S., and D. I. Golovin (2003) Age of the silicic volcanic rocks in the Bolshe-Banny springs region, *Volcanol. and Seismol.,* 1, 21–25, (In Russian).

Sigurdsson, H. (2000), Volcanic episodes and rates of volcanism, in *Encyclopedia of Volcanoes,* edited by H. Sigurdsson, pp. 271–279, Academic Press, San Diego... Toronto.

Simkin, T., and L. Siebert (1994), *Volcanoes of the World*. Second edition. 347 p. Geoscience Press, inc. Tucson, Arizona.

Sparks, S. R. J., and H. Sigurdsson (1977), Magma mixing: a mechanism for triggering acid explosive eruptions, *Nature, 267*, 315–318.

Stuiver, M., Reimer, P.J., and Reimer, R.W. (2005), CALIB 5.0 ^{14}C age calibration program, www.calib.org

Sun, S. S., and W. F. McDonough (1989), Chemical and isotopic systematics of oceanic basalts; implications for mantle composition and processes, in *Magmatism in the ocean basins. Geological Society Special Publications,* edited by A. D. Saunders and M. J. Norry, pp. 313–345, Geological Society of London, London.

Tatsumi, Y., T. Kogiso, and S. Nohda (1995), Formation of a third volcanic chain in Kamchatka; generation of unusual subduction-related magmas, *Contributions to Mineralogy and Petrology, 120*, 117–128.

Tsvetkov, A. A., N. G. Gladkov, and O. N. Volynets (1989), Problem of sediment subduction and 10Be isotope in lavas of Kuril Islands and Kamchatka Peninsula, *Doklady Akademii Nauk SSSR, 306*, 1220–1225.

Turner, S., F. McDermott, C. Hawkesworth, and P. Kepezhinskas (1998), A U-series study of lavas from Kamchatka and the Aleutians: constraints on source composition and melting processes, *Contributions to Mineralogy and Petrology, 133*, 217–234.

Vlodavets, V.I. (ed) (1957) *Catalogue of the active volcanoes of the USSR*. In: *Bull Volcanol stancii*, 25, 180 pp. (in Russian)

Volynets, O. N. (1979), Heterotaxitic lavas and pumices (on the problem of magma mixing), in *Problems of Deep Magmatism*, edited by V. S. Sobolev, pp. 181–197, Nauka Publishers, Moscow, (In Russian).

Volynets, O. N., V.V. Ponomareva, and A. A. Tsyurupa (1989), Petrological and tephrochronological studies of Krasheninnikov volcano, Kamchatka, *Int. Geol. Rev., 31*(1), 1107–1122 .

Volynets, O. N., M. G. Patoka, I. V. Melekestsev, and M. I. Zubin (1991), Ichinsky volcano, in *Active volcanoes of Kamchatka,* edited by S. A. Fedotov and Yu. P. Masurenkov, Vol. 1, pp. 282–294, Nauka, Moscow.

Volynets, O. N. (1994), Geochemical types, petrology and genesis of Late Cenozoic volcanic rocks from the Kurile-Kamchatka island-arc system, *Int. Geol. Rev. 36*(4), 373–405.

Volynets, O. N., V. V. Ponomareva, and A. D. Babansky (1997a), Magnesian basalts of Shiveluch andesite volcano, Kamchatka, *Petrology, 5*(2), 183–196.

Volynets, O., G. Wörner, A. Babansky, F. Dorendorf, T. Churikova, G. Yogodzinski, Y. Goltsman, and A. Agapova (1997b), Variations in geochemistry and Sr-Nd isotopes in lavas from the Northern Volcanic Group, Kamchatka; evidence for distinct sources at a subducting transform system, *Eos, Transactions*, F804, American Geophysical Union 78, Washington.

Volynets, O. N., V. V. Ponomareva, O. A. Braitseva, I. V. Melekestsev, and Ch. H. Chen (1999a), Holocene eruptive history of Ksudach volcanic massif, South Kamchatka: evolution of a large magmatic chamber, *J. Volcanol. Geotherm. Res., 91*, 23–42.

Volynets, O. N., I. V. Melekestsev, V. V. Ponomareva, and J. M. Yogodzinski (1999b), Kharchinsky and Zarechnyi volcanoes, unique centers of Late Pleistocene magnesian basalts in Kamchatka: Composition of erupted rocks, *Volcanol. and Seismol., 21*(1), 45–66.

Volynets, O. N., A. D. Babanskii, and Yu. V. Gol'tsman (2000), Variations in isotopic and trace-element composition of lavas from volcanoes of the Northern Group, Kamchatka, in relation to specific features of subduction, *Geochem. Intern., 38*(10), 974–989.

Volynets, A. O. (2006), *Pleistocene-Holocene volcanism of Sredinny Range, Kamchatka: rock composition and geodynamic interpretation*, Ph. D. thesis, Moscow State University, 195 pp.

Volynets A. O., T. G. Churikova, and G. Wörner (2005), Geochemistry of the volcanic rocks of Sredinny Range, Kamchatka, *Vestnik KRAUNC, Earth science series, 2*(6), 21–33.

Volynets A., Woerner G., Churikova T., and P. Layer (2006), The source of Pleistocene-Holocene volcanism in the Sredinny Range back arc, Kamchatka: constraints from trace elements and isotopic compositions, Abstracts of the 5th Biennial Workshop on Subduction Processes emphasizing the Japan-Kurile-Kamchatka-Aleutian Arcs. Sapporo, Japan, 40–42.

Wallman, P. C., G. A. Mahood, and D. D. Pollard (1988), Mechanical models for correlation of ring-fracture eruptions at Pantelleria, Strait of Sicily, with glacial sea-level drawdown, *Bull. Volcanol., 50*, 327–339.

Wickman, F. E. (1966), Repose patterns of volcanoes, I. Volcanic eruptions regarded as random phenomena, *Ark. Mineral. Geol., 4*, 291–301.

Wörner, G., T. Churikova, W. Leeman, V. Liebetrau, S. Tonarini, and A. Heuser (2001), Fluid-Mobile Trace Element and U-series Isotope Variations Across Kamchatka: Timing and effects of slab dehydration, *Margins Meeting, Schriftenreihe D. Geol. Ges., 14*, 236–237.

Yogodzinski, G. M., J. M. Lees, T. G. Churikova, F. Dorendorf, G. Woerner, and O. N. Volynets (2001a), Geochemical evidence for the melting of subducting oceanic lithosphere at plate edges, *Nature, 409*, 500–504.

Yogodzinski, G. M., T. Churikova, A.V. Koloskov, and J. Roth (2001b), Trace element features of subduction-related metasomatism from ultramafic xenoliths of the Kamchatka arc, *AGU Fall Meeting, EOS*, 82(47), F1199.

Zonenshain, L. P., and L. A. Savostin (1979), *Inrtoduction to geodynamics,* 311 pp., Nedra, Moscow, (in Russian).

Zaretskaya, N. E., V.V. Ponomareva, and L.D. Sulerzhitsky (2007), Radiocarbon dating of large Holocene volcanic events within South Kamchatka (Russian Far East), *Radiocarbon*. In press.

Vera Ponomareva, Institute of Volcanology and Seismology, Piip Boulevard, 9, Petropavlovsk-Kamchatsky, 683006, Russia, ponomareva@kscnet.ru

Geochemistry of Primitive Lavas of the Central Kamchatka Depression: Magma Generation at the Edge of the Pacific Plate

Maxim Portnyagin[1,2], Ilya Bindeman[3], Kaj Hoernle[1,4], and Folkmar Hauff[1]

New and published major and trace element and isotope (O, Sr, Nd) compositions of the Late Quaternary rocks from the Central Kamchatka Depression (CKD) are used to demonstrate systematic changes in magma genesis along the northern segment of the Kamchatka Arc, above and north of the subducting Pacific slab edge. We envision a number of possible petrologic scenarios for magma generation beneath the CKD and formulate quantitative mass-balance models which lead to three major conclusions departing significantly from previous interpretations of the CKD rocks. First, this study demonstrates that eclogite melts contribute to the composition of virtually all CKD lavas and could be the major agent transferring material from the subducted slab to the mantle wedge, including fluid-mobile elements (e.g., K, Ba). Second, thermal state of the mantle wedge beneath the CKD has primary control on the major composition of primitive magmas, favoring production of low temperature andesitic and dacitic mantle melts toward the slab edge. Third, hydrous slab-fluids might not be required to generate CKD magmatism. Instead, strong enrichment in LILE, high $\delta^{18}O$ and $^{87}Sr/^{86}Sr$, in some CKD magmas could originate from assimilation of hydrothermally-altered mafic lithosphere. Several concurring factors could facilitate partial melting of the subducting slab beneath the all CKD volcanoes and favor variable modification of the eclogite melts during interaction with the mantle wedge. Large input from slab melting makes CKD magmatism unique in Kamchatka and may contribute to the CKD volcanoes being the most productive arc volcanoes on Earth.

1. INTRODUCTION

The Kamchatka Peninsula forms the northern part of the Kuril-Kamchatka volcanic arc in the NW Pacific Ocean, a part of the circum Pacific "Ring of Fire", and represents one of the most volcanically active regions on Earth. The largest and most productive arc volcanoes on Earth occur in the Central Kamchatka Depression (CKD), located adjacent to the Kamchatka-Aleutian Arc junction. During recent decades the CKD volcanoes have been the subject of many geochemical studies aimed at tracing their magmatic evolution, reconstructing the composition of mantle sources and understanding the reasons for the exceptional productivity of the volcanoes [e.g., *Kersting and Arculus,* 1994, 1995; *Kepezhinskas et al*, 1997; *Hochstaedter et al.* 1996; *Pineau et al.* 1999; *Turner et al.* 1998; *Volynets* 1994; *Volynets et al.* 1997; 1998; 1999; 2000; *Yogodzinski et al.* 2001; *Dorendorf et al.* 2000; *Churikova et al.* 2001; *Ishikawa et al.* 2001; *Dosseto et al.* 2003; *Bindeman et al.* 2004, 2005; *Portnyagin*

[1] Leibniz Institute for Marine Sciences, IfM-GEOMAR, Kiel, Germany.
[2] Vernadsky Institute of Geochemistry and Analytical Chemistry, Moscow, Russia.
[3] Department of Geological Sciences, University of Oregon, Eugene, Oregon, USA.
[4] SFB574, University of Kiel, Kiel, Germany.

Volcanism and Subduction: The Kamchatka Region
Geophysical Monograph Series 172

10.1029/172GM16

et al. 2005a]. These authors interpret the compositional variations of CKD magmas as resulted from the following processes: 1) primary magmas are derived from the depleted MORB-source under abundant fluid flux from the subducting Pacific plate; 2) small amounts of sediment-derived fluids/melts are input into magma generation zones; 3) the subducting Pacific Plate melts beneath Shiveluch Group of volcanoes; 4) relatively long time lapse between the release of U-rich fluid from the slab and eruption of magmas (~150 k.y.) compared to other island-arcs; and 5) mantle upwelling north of the subducting Pacific slab edge caused decompression melting and produced alkalic magmas from the northernmost CKD volcanoes.

In this paper we use a compilation of ~900 analyses of the Late Quaternary volcanic rocks from the CKD in order (1) to summarize the previous and new results, (2) to demonstrate along-arc geochemical zonation in major and trace elements and isotope ratios in northern Kamchatka, (3) to elucidate possible petrologic scenarios of magma origin, (4) to constrain quantitative models, and (4) to evaluate the results in light of recent geophysical studies at the Kamchatka-Aleutian Arc junction.

1.1. Northern Segment of the Kamchatka Arc

Holocene to Late Pleistocene volcanism in the Kamchatka Arc is concentrated within two main zones: the Eastern Volcanic Belt and the Sredinny Range (Figure 1A). The Eastern Volcanic Belt includes southern and northern segments, which are distinct in geographic position relative to the Kamchatka trench, longevity of volcanism, volcanic productivity and geochemistry of erupted lavas [e.g., *Fedotov and Masurenkov* 1991; *Park et al.* 2002; *Avdeiko et al.* 2002; *Ponomareva et al.* 2007a]. In the northern segment, recent volcanism is concentrated within the CKD, which is lowland between the Eastern Ridges, mainly composed by accretionary terrains [*Konstantinovskaia,* 2001] and the Sredinny Range of Kamchatka (Figure 1A).

The Klyuchevskoy Group is the largest cluster of volcanoes in the CKD and was formed during the Late Pleistocene-Holocene on thick pedestal of the Middle to Late Pleistocene plateau basalts [*Melekestsev,* 1980]. The Klyuchevskoy Group includes Klyuchevskoy volcano, the most active arc volcano on Earth [e.g., *Melekestsev,* 1980; *Fedotov and Masurenkov,* 1991; *Kersting and Arculus* 1994], active Plosky Tolbachik and Bezymianny volcanoes, hydrothermally-active Ushkovsky volcano and several other large extinct volcanoes (Ostry Tolbachik, Malya and Bolshaya Udina, Ostaraya and Ovalanaya Zimina, Kamen'). The largest zone of monogenetic volcanism is spatially related to Plosky Tolbachik volcano (Tolbachinsky Dol areal volcanic field) [e.g. *Fedotov,* 1983]. Monogenetic cinder cones are also abundant on the south-western slope of the Ushkovsky (Plosky Sopki) volcano and on the eastern slope and at the foot of the Klyuchevskoy volcano [*Fedotov and Masurenkov,* 1991; *Ponomareva et al.* 2007a]. The Shiveluch Volcanic Group (some times referred to as the Northern Group of CKD volcanoes [e.g., *Volynets et al.* 2000; *Yogodzinski et al.* 2001]) includes highly active Shiveluch volcano [e.g., *Ponomareva et al.* 2007b] and dormant Zarechny and Kharchinsky volcanoes with spatially related zone of monogenetic cinder cones [*Volynets et al.* 1998]. Shisheisky Volcanic Complex, consisting of the Late Pleistocene to Holocene extrusions and lava flows, forms a separate volcanic cluster ~50 km to the north from Shiveluch volcano and extends the volcanic chain further north along the CKD. Nachikinsky and Khailulia volcanoes are located at the northern end of the CKD, on the north-west trending Alpha Fracture Zone (F.Z.) extending from the Bering Sea to Kamchatka [*Portnyagin et al.* 2005a]. There is a general decrease in the size of the volcanic structures and overall Quaternary magma production from south to north along the CKD [*Fedotov and Masurenkov* 1991; *Ponomareva et al.* 2007a].

1.2. Specific Conditions of Subduction

The northern segment of the Kamchatka Arc is adjacent to the Kamchatka-Aleutian Arc junction, where lithospheric plates of different age and origin meet in a complexly structured and tectonically active framework (see review in [*Park et al.* 2002]). The Pacific plate entering the Kamchatka trench has an inferred age between ~87Ma at the Kamchatka-Aleutian junction and ~95 Ma at the southern tip of Kamchatka [*Renkin and Sclater*, 1988]. Despite the narrow age interval, the plate structure and geophysical parameters change significantly along strike. Meiji seamount, the northernmost in the Emperor Seamount chain, is located immediately south of the Komandorsky Islands (westernmost Aleutian Arc), suggesting that older Emperor Seamounts may be subducting beneath central and northern Kamchatka. Further south, only the Pacific Plate, normal oceanic plate without intraplate volcanism, is subducting beneath southern Kamchatka. The heat flow from the Pacific sea-floor at the arc junction is significantly higher (>80mW/m^2) compared to more southern localities (40–60 mW/m^2) [e.g., *Smirnov and Sugrobov, 1980*]. The lithospheric plate subducting beneath the CKD was thus suggested to be anomalously hot for its Cretaceous age because of thermal anomaly inherited from the Hawaiian hot-spot [*Gorbatov et al.* 1997, *Davaille and Lees*, 2004] or lithosphere rejuvenation due to deep mantle upwelling [*Gorbatov et al.* 2001; *Manea et al.* 2006].

In order to reconcile the transition from subduction of the Pacific Plate beneath Kamchatka to strike-slip plate movements along the Western Aleutian Arc several authors proposed that the Pacific Plate is likely torn along the Western Aleutian F.Z. so that the Pacific Plate edge is subducting beneath Kamchatka at the arc junction [e.g., *Yogodzinski et al.* 2001; *Park et al.* 2002; *Levin et al.* 2002; *Davaille and Lees*, 2004]. The data presented in *Davaille and Lees* [2004] suggests that the Pacific Plate may be torn along the Bering F.Z. Tracing this regional fault along its strike to Kamchatka, the edge of the subducted plate can be proposed to locate at ~57.3^{o}N beneath axial zone of the CKD. The largest CKD volcanoes likely take place above the subducting Pacific Plate, 60 to 200 km south-west from its edge. The Shisheisky Complex occupies the position nearly above the proposed slab edge. Farther north, the Komandorsky Plate was previously subducted beneath northern Kamchatka [e.g., *Baranov et al.* 1991; *Fedorov and Shapiro,* 1998; *Kepezhinskas et al.* 1996; *Park et al.* 2002]. The mantle tomography data [*Levin et al.* 2002] however suggests that neither previously subducted portions of the Pacific Plate nor Komandorsky Plate underlie the most northern Nachikinsky and Khailulia volcanoes. The Komandorsky Plate subducted beneath northern Kamchatka was proposed to have broken off and sunk into the deep mantle during the Cenozoic triggering asthenospheric upwelling [*Levin et al.* 2002; *Portnyagin et al.* 2005a].

Seismic data suggest progressively shallower subduction dips of the Pacific Plate toward its northern edge, from 45^o beneath Tolbachik volcano to 25^o beneath Shiveluch volcano, [*Fedotov and Masurenkov* 1991; *Gorbatov et al.* 1997; *Park et al.* 2002]. The upward bending of the Pacific plate towards the Kamchatka-Aleutian junction and its northern edge results in large variations in depths to the subducting slab beneath the active volcanoes along the CKD (80–180 km) whereas the distance from the volcanoes to the Kamchatka trench remains nearly constant (~200–250 km). Since the crustal thickness beneath the CKD is relatively constant (30–35 km) [e.g., *Balesta,* 1981; *Park et al.* 2002; *Bogdanov and Khain*, 2000], the mantle wedge thickness (i.e., "mantle column" beneath a volcano) decreases substantially towards the slab edge. The length of the mantle column, which can be potentially involved in magma generation, decreases from ~165 km beneath Tolbachik to ~55 km beneath Shiveluch volcano and may be even less above the slab edge (Table 3).

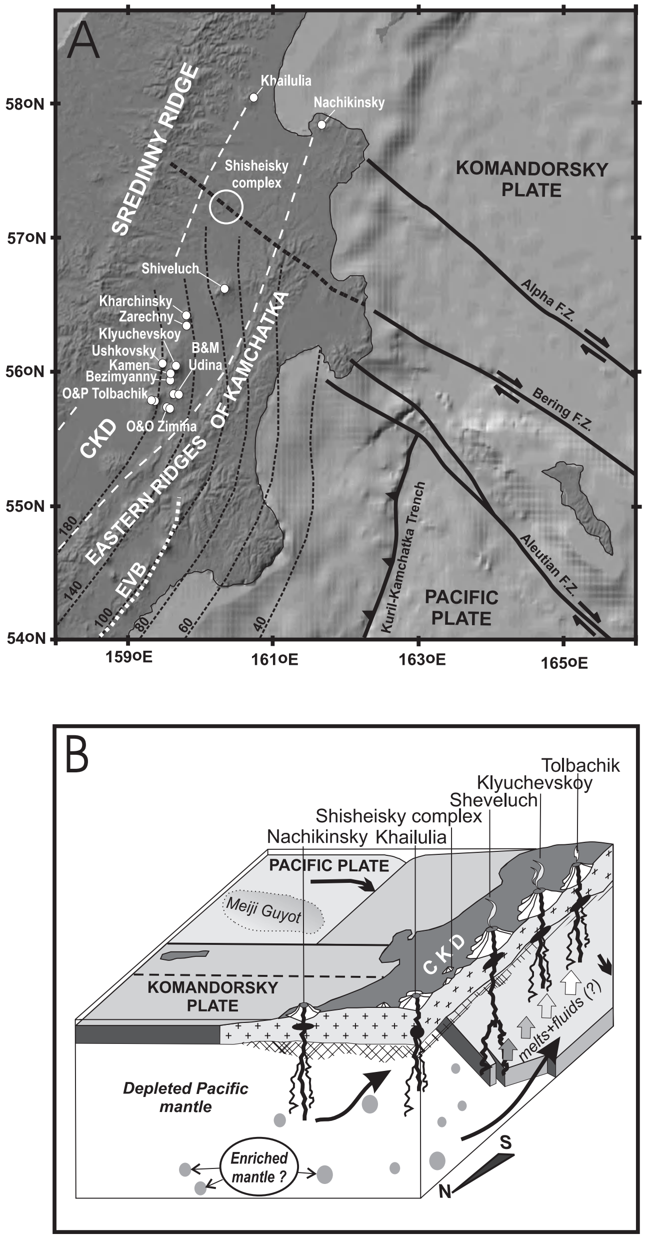

Figure 1. A) Schematic map of the Kamchatka-Aleutian arc junction and neighboring areas. Bathymetric and relief background map was produced in ETDB/PAC [2002]. Short-dash lines show depths to subducting Pacific Plate after *Gorbatov et al.* [1997]. Thick lines are major fracture zones (F.Z.). Approximate borders of the Central Kamchatka Depression (CKD) are shown in dashed lines. White circles denote volcanoes. "O&P Tolbachik" indicates Ostry and Plosky Tolbachik volcanoes and neighboring Tolbachinsky Dol areal volcanic field; "O&O Zimina"—Ostraya and Ovalnaya Zimina volcanoes; "B&M Udina"—Bolshaya and Malaya Udina volcanoes. Thick dotted line denotes position of the volcanic front in the central part of the Eastern Volcanic Belt (EVB). B) Geodynamic framework of magma generation beneath CKD (modified from *Portnyagin et al.* [2005a]. The Pacific Plate is likely torn along the Western Aleutian F.Z. The largest volcanoes in CKD (Tolbachik, Klyuchevskoy, Shiveluch) originate above subducted Pacific Plate. Shisheisky Complex could be formed above the slab edge. No subducted slab underlies volcanoes at the northern end of CKD (Nachikinsky and Khailulia).

1.3. Geochemical Database

In this work we have compiled ~900 chemical analyses of volcanic rocks from the CKD. With some exceptions (Kharchinsky and Nachikinsky volcanoes), we focused mainly on the most recent Late Pleistocene, Holocene and historical volcanic rocks, which might be representative of the present-day magma generation in the CKD.

The present compilation includes data from the following sources: (1) GEOROC database of the Max-Plank Institut für Chemie (Mainz, Germany), (2) research papers and reviews mainly published in Russian language and not included in the GEOROC bank [*Krivenko,* 1990; *Fedotov and Masurenkov,* 1991; *Fedotov,* 1983], (3) reports of the Russian Geologic Survey [*Pilipchuk et al.* 2006], (4) our unpublished analyses. Unlike existing web databases, analyses of the same samples published in different papers were mostly identified and linked excluding incomplete and multiple records. Analyses obtained before 1970 [e.g., *Erlich,* 1966] were not included because their quality can hardly be assessed and some data do not match more recent results. The data base was also screened for analyses of questionable quality and of highly altered rocks (L.O.I. > 3 wt %).

This compilation and complete list of references is available as auxiliary material on the CD-Rom accompanying this manuscript. The geochemical data base on the CKD magmatism is a subject of ongoing development and the latest version is available on request from the first author.

Our original analyses were obtained at the Leibniz Institute for Marine Geosciences IFM-GEOMAR (Kiel, Germany). Details of the analytical technique are reported elsewhere [*Portnyagin et al.* 2005a]. Representative analyses of volcanic rocks from the Shisheisky Complex, which are first published here, are shown in the Table 1. New Sr, Nd and O isotope data on rocks from different CKD localities are given in Table 2.

The northern Kamchatkan volcanoes are not equally represented in the data base (Figure 2). Different numbers of analyses for different volcanoes point to naturally biased interest of most researchers to active volcanism. The largest amount of data, more than 400 major element analyses, is available for Klyuchevskoy volcano; more than 100 analyses exist for Tolbachik volcano, 80 analyses for Shiveluch volcano (additional 86 analyses for Shiveluch volcano are provided by *Ponomareva et al.* [2006b], this volume). Large data set also exists for Nachikinsky volcano resulting from its interesting tectonic position. Information about other volcanoes is less abundant. Volcanoes from southeastern part of the CKD (Bolshaya and Malaya Udina, Ostraya and Ovalnaya Zimina) are not represented in the data base. Data from these volcanoes were last published more than 40 years ago [e.g., *Erlich,* 1966]. Obtaining new compositional data from these volcanoes could be an important direction for future studies, particularly aimed at evaluating *across-arc* variations in the CKD.

We also note that better understanding of the origin of the CKD volcanism requires collection of reliable age data and careful examination of geochemical trends of magmas erupted from the same or neighboring volcanic centers through time. Detailed investigation of the Middle to Late Pleistocene lavas composing huge volumes of plateau basalts in the basement of the Klyuchevskoy Group and erupted through short interval of time at the rate comparable to the productivity of the Hawaiian shield volcanoes [*Melekestsev*, 1980] also provide an intriguing direction for the future studies.

2. ALONG-ARC GEOCHEMICAL VARIATIONS

2.1. An Overview of Major Element Systematics

The CKD rocks span a large compositional range (Figure 3 and 4). The majority of rocks are medium-K, low- to medium-Fe basalts to andesites of normal alkalinity. High- to medium-K low Mg subalkaline basalts and basaltic andesites, which often tend to have Fe-rich compositions, were very abundant at the initial stages of the CKD volcanism in the Middle-Late Pleistocene [e.g. *Melekestsev,* 1980]. Presently, high-K rocks are restricted to the southern and western part of the Klyuchevskoy Group (Tolbachik, Ushkovsky), occur in the Shiveluch Volcanic Group and compose the Late Pleistocene cinder cones and lava flows near Nachikinsky volcano. In contrast to southern Kamchatka, low-K rocks and highly evolved rocks (dacites and rhyolites) are extremely rare in the CKD and have not been documented among Holocene eruptions [e.g., *Fedotov and Masurenkov,* 1991; *Krivenko,* 1991; *Volynets,* 1994; *Ponomareva et al.* 2007b]. Modal and chemical compositions of CKD rocks exhibit systematic variations along the strike of the volcanic arc [e.g., *Fedotov and Masurenkov,* 1991; *Yogodzinski et al.* 2001; *Volynets,* 1994; *Volynets et al. 1997*; 1999; 2000; *Churikova et al.* 2001], but these variations have not been evaluated in detail thus far.

Rocks from the southern and western parts of the Klyuchevskoy Group (Tolbachik and Ushkovsky volcanoes) and spatially related monogenetic volcanic fields of cinder cones and lavas are medium- to high-K basalts and trachybasalts, ranging to trachyandesites at Ushkovsky volcano (Lavovy Shish vent, V. Ponomareva, 2006, pers. comm.) (Figure 3). Phenocrysts are rare in primitive basalts and usually represented by high-Fo olivine and Ca-pyroxene. Evolved rocks are plagioclase-pyroxene phyric. Hydrous phases (amphibole, phlogopite) are absent. A very common rock type is high-K trachybasalt with giant plagioclase

Table 1. Major and trace element composition of the Shisheisky Complex rocks

##	Sample name	Mg#	SiO_2	TiO_2	Al_2O_3	Fe_2O_3	FeO	MnO	MgO	CaO	Na_2O	K_2O	P_2O_5	LOI	H_2O	CO_2	Total	V	Cr	Co	Ni	Zn	Ga	Rb	Sr	Y	Zr	Nb	Ba
1	162	70.6	53.71	0.64	15.28	3.22	3.68	0.13	8.86	7.75	3.91	0.93	0.22	0.83			99.16												
2	6137	77.0	54.43	0.52	14.20	1.94	4.67	0.11	12.05	6.80	3.95	0.72	0.14	0.71			100.24												
3	166	65.4	60.25	0.58	16.49	4.95	0.69	0.10	5.45	6.08	4.56	0.95	0.12	0.75			100.97												
4	165	65.9	60.34	0.53	16.59	3.81	1.19	0.09	5.00	5.49	5.00	1.00	0.10	0.68			99.82												
5	336	69.0	61.25	0.41	16.25	3.18	1.14	0.06	5.00	3.94	5.80	1.64	0.07	0.59			99.33												
6	261	68.9	62.49	0.53	14.69	1.36	2.79	0.09	5.00	3.94	6.00	1.73	0.18	0.46			99.26												
7	287	65.7	62.73	0.45	16.07	2.87	1.44	0.08	4.33	4.55	4.90	1.27	0.13	0.38			99.20												
8	1314	68.3	56.93	0.65	15.39	2.29	4.02	0.11	7.34	6.56	4.25	0.95	0.16	0.44			99.09												
9	203/4	64.7	50.49	1.34	15.12	2.48	6.84	0.16	9.34	7.95	4.00	1.00	0.24	0.71			99.67												
10	7196/3	72.0	53.44	0.68	13.46	2.13	5.98	0.16	11.41	8.28	3.19	1.35	0.12	0.63			100.83												
11	7199	70.4	52.36	0.69	15.92	1.98	5.29	0.13	9.42	8.28	4.10	1.18	0.11	0.42			99.88												
12	1306	67.0	54.96	0.99	14.17	3.69	4.15	0.12	8.51	5.71	3.96	0.95	0.14	0.31			97.66												
13	259/2	69.9	56.15	0.70	14.67	1.98	5.17	0.14	9.06	6.52	4.29	1.23	0.17	1.14			101.22												
14	3096/1	74.5	58.60	0.58	15.86	1.75	3.23	0.11	7.88	5.00	4.40	1.55	0.18	0.22			99.36												
15	285	42.5	50.97	0.98	17.75	5.10	5.10	0.20	4.02	9.27	3.35	0.82	0.20	1.29			99.05												
16	3136	55.0	73.81	0.14	13.94	0.31	0.93	0.02	0.83	1.50	5.24	1.14	0.18	0.16			98.20												
17	6128	52.7	68.52	0.28	16.00	0.80	1.26	0.05	1.24	1.36	5.11	3.54	0.08	0.76			99.00												
18	305	51.7	72.92	0.05	14.85	0.12	0.64	0.02	0.45	1.25	6.00	2.31	0.06	0.58			99.25												
19	329	44.0	61.78	0.53	17.50	3.32	1.58	0.11	2.01	5.00	5.25	1.64	0.24	1.12			100.08												
20	200/1	55.1	58.80	0.89	17.12	2.21	4.35	0.13	4.36	6.88	4.00	1.20	0.27	0.52			100.73												
21	201	50.4	56.94	0.89	18.08	3.10	3.84	0.13	3.78	6.96	4.22	1.28	0.26	1.00			100.48												
22	3270	51.1	60.29	0.53	17.56	2.71	2.21	0.11	2.73	5.87	5.25	1.57	0.19	0.66			99.68												
23	1293	50.7	60.33	0.59	17.67	2.85	2.30	0.10	2.81	5.29	5.00	1.50	0.20	0.37			99.01												
24	3092	66.9	60.98	0.57	16.83	1.04	3.02	0.08	4.49	4.38	4.95	1.45	0.16	0.70			98.65												
25	G-206	69.1	49.96	0.85	14.90		8.46	0.16	10.62	9.92	2.59	0.78	0.22		0.38	0.04	98.88	237	759	46	136	71	14	12	356	18	77	4	191
26	G-202	70.3	52.57	0.79	16.75		6.49	0.12	8.62	8.17	3.60	1.01	0.18		0.16	0.01	98.47	163	429	30	175	58	21	20	455	16	93	4	379
27	G-200	72.3	52.21	0.79	13.89		7.87	0.14	11.51	7.75	3.07	1.05	0.18		0.14	0.01	98.61	206	837	41	240	66	16	19	344	18	79	4	338
28	G-1304/1	70.6	53.47	0.65	15.59		6.71	0.12	9.05	7.50	3.67	1.13	0.16		0.17	0.01	98.22	160	552	30	149	62	21	21	412	17	84	5	431
29	G-1305	71.3	51.74	0.72	14.37		7.50	0.14	10.46	7.89	2.95	1.04	0.47		0.54	0.12	97.94	185	889	37	182	67	15	23	390	15	81	7	338
30	G-1286	70.1	52.82	0.72	14.68		7.44	0.14	9.77	8.23	3.01	1.09	0.19		0.35	0.03	98.47	184	772	36	146	71	18	23	414	15	80	4	374
31	G-6247	69.8	58.37	0.64	15.52		5.26	0.09	6.82	5.75	4.29	1.33	0.20		0.36	0.01	98.64	126	391	21	121	59	15	27	527	12	95	5	394
32	G-1303	70.5	53.03	0.63	15.36		7.01	0.13	9.42	7.28	3.58	1.09	0.15		0.19	0.02	97.89	169	604	32	177	66	17	19	373	16	82	3	398
33	G-3277	73.6	56.10	0.71	15.19		5.73	0.10	8.98	6.16	4.07	1.56	0.21		0.13	0.01	98.95	130	552	24	203	55	16	29	463	17	105	7	457
34	K2-107	54.5	62.55	0.47	17.53		3.96	0.09	2.66	5.06	5.06	1.56	0.23		0.29	0.00	99.46	87	52	11	2	56	21	35	604	12	120	2	595
35	K2-108	56.7	58.03	0.71	17.05		5.97	0.11	4.38	6.66	4.32	1.36	0.29		0.31	0.02	99.21	156	119	19	13	65	20	31	617	16	115	3	481
36	K2-109	70.7	52.94	0.79	16.67		6.48	0.12	8.76	8.27	3.64	1.03	0.17		0.12	0.01	99.00	173	457	29	169	58	16	19	465	16	92	3	360
37	K2-110B	48.8	56.52	0.74	18.44		6.46	0.12	3.45	7.02	4.54	1.30	0.33		0.31	0.01	99.24	143	<18	18	<2	76	20	27	689	18	120	3	442
38	K2-111	53.2	63.41	0.53	17.42		3.52	0.07	2.24	4.25	5.43	1.73	0.20		0.13	0.00	98.93	72	<18	10	7	48	21	40	545	10	111	5	620
39	K2-112	47.9	62.30	0.46	17.77		3.98	0.10	2.05	4.89	5.12	1.63	0.29		0.58	0.01	99.18	75	<18	9	<2	65	19	38	692	17	134	3	635
40	RG	15.7	73.53	0.54	12.42		1.30	0.04	0.11	0.62	3.49	5.53	0.18				99.18	64.4	1.8						43.3	11.7	158	7.7	324

Note.
#1-24 are from the Report of the Russian Geologic Servey [Pilipchuk et al. 2006] (wet chemical data);
#25-39 are analyses from this study obtained at IfM-GEOMAR (Kiel) by the XRF technique. Details of the analytic technique can be found in the work by [Portnyagin et al., 2005a, Supplement]
#40 is average composition of rhyolitic glasses from partially melted/reacted xenoliths in the Shisheisky Complex rocks. Major elements are by electron probe (average from 13 analyses), trace elements by ion probe (average from 3 analyses).
Major elements in wt %; trace elements in ppm. Mg# refers to 100*MgO/(MgO+FeO) calculated on molar basis, where FeO is total Fe content expresed as FeO.

Table 2. New data on the O-Sr-Nd isotope composition of primitive to moderately evolved CKD volcanic rocks

Area	Sample	Mg#	SiO_2 (wt%)	TiO_2 (wt%)	K_2O (wt%)	$\delta^{18}O_{SMOW}$, ‰	Phase	$^{87}Sr/^{86}Sr$	2σ (ppm)	$^{143}Nd/^{144}Nd$	2σ (ppm)
Tolbachik Areal	K01-25	67.5	50.85	0.88	0.72	5.56	ol	0.703314	3	0.513090	3
Tolbachik Areal	K01-30	65.0	50.02	1.28	1.27	5.61	ol	0.703405	3	0.513065	4
Tolbachik Areal	K01-40	46.1	51.63	1.65	2.03	6.05	ol				
Tolbachik Areal	K01-49	48.6	50.81	1.58	1.75	5.38	ol				
Tolbachik Areal	K01-52	62.0	50.42	1.25	1.34	5.56	ol				
Tolbachik Areal	K01-54	60.1	50.41	1.15	1.15	5.60	ol	0.703345	2	0.513072	7
Tolbachik Areal	K01-58	61.9	50.75	1.24	1.33	5.37	ol				
Kluchevskoy volcano	V 68-37	47.7	53.52	1.14	1.17	7.18	ol				
Kluchevskoy volcano	AP 60-31	53.6	53.05	1.06	1.07	6.00, 6.37, 6.09	ol	0.703624	3	0.513082	4
Kluchevskoy volcano	Byl 69-38	52.0	53.36	1.09	1.17	6.98	ol				
Kluchevskoy volcano	Bel 70-46	49.3	53.45	1.12	1.17	7.17	ol				
Kluchevskoy volcano	ZaV 50-49	54.1	53.37	1.03	1.08	7.04	ol				
Kluchevskoy volcano	PiiP 79-50	54.8	53.59	1.06	1.06	6.90	ol	0.703655	3	0.513073	4
Sheveluch volcano	K1-14B	57.6	53.57	0.86	1.08	5.68, 5.55*	ol	0.703314*	3	0.513100	3
Sheveluch volcano	K1-18B	69.4	50.55	0.84	1.93	5.72*	ol	0.703676*	2	0.513045	4
Sheveluch volcano	K1-19	61.1	57.30	0.70	1.16	5.93, 5.81*	ol	0.703346*	2	0.513115	3
Zarechny volcano	K1-22	70.2	52.60	0.87	1.31	6.37*	ol	0.703505*	2	0.513084	3
Shisheisky Complex	G-206	69.1	49.96	0.85	0.78	5.40	ol	0.703315	3	0.513046	5
Shisheisky Complex	G-200	72.3	52.21	0.79	1.05	6.05	ol	0.703565	3	0.513040	6
Shisheisky Complex	G-1304/1	70.6	53.47	0.65	1.13	6.22	ol	0.703527	3	0.513053	3
Shisheisky Complex	G-1305	71.3	51.74	0.72	1.04	5.72	ol	0.703432	2	0.513054	3
Shisheisky Complex	G-1286	70.1	52.82	0.72	1.09	6.01	ol				
Shisheisky Complex	G-6247	69.8	58.37	0.64	1.33	6.96	opx	0.703452	2	0.513023	5
Shisheisky Complex	G-1303	70.5	53.03	0.63	1.09	6.11	ol	0.703582	3	0.513029	5
Shisheisky Complex	G-3277	73.6	56.10	0.71	1.56	5.43	ol (xen)	0.703404	3	0.513058	4
Shisheisky Complex	K2-108	56.7	58.03	0.71	1.36			0.703498	2	0.513046	3
Shisheisky Complex	K2-110B	48.8	56.52	0.74	1.3	5.98	amph	0.703473	2	0.513083	3
Shisheisky Complex	K2-111	53.2	63.41	0.53	1.73			0.703511	2	0.513061	2
Shisheisky Complex	K2-112	47.9	62.30	0.46	1.63	6.32	amph	0.703507	3	0.513077	2
Nachikinsky volcano	N44-A	54.1	52.12	1.89	1.92	5.21**	ol	0.703311	3	0.512979	7
Nachikinsky volcano	N45-A	48.4	52.65	1.88	2.01	5.14**	ol	0.703303	2	0.512984	7

Note. Sr and Nd isotope analyses are obtained on a multi-collector TRITON thermal ionization mass spectrometer (TIMS) at IfM-GEOMAR (analyst F.Hauff). Sr and Nd isotopic ratios are normalized within run to $^{86}Sr/^{88}Sr$= 0.1194 and $^{146}Nd/^{144}Nd$= 0.7219 respectively and all errors are reported as 2σ. Over the course of the study normalized NBS-987 gave $^{87}Sr/^{86}Sr$= 0.710250± 0.000008 (N=18) and $^{143}Nd/^{144}Nd$= 0.511847± 0.00006 (N=9) was obtained for La Jolla and $^{143}Nd/^{144}Nd$= 0.511712± 0.00006 (N=8) for our in-house monitor Spex. Further details of the analytical technique can be found in [Portnyagin et al. 2005a, Supplement]

Oxygen isotope composition of mineral phenocrysts ($\delta 18O_{SMOW}$) separated from crushed rocks was analyzed by laser fluorination at the University of Oregon and California Institute of Technology, see Bindeman et al. [2004, 2005] and Portnyagin et al. [2005a] for previously reported analyses and analytical details. The overall analytical uncertainty on single measurements was better than 0.20‰ (2σ).More than one δ18O value reported for some samples refer to the analyses of different crystals.Mineral analyzed for oxygen isotope composition is indicated in "phase" collumn (ol (xen)- olivine (xenocrystic); opx - orthopyroxene, amph - amphibole).

Complete major and trace element analyses of rocks can be found in the Suplementary Materials accompanying this manuscript. Analyses of O and Sr marked with asterisk (*) were previously reported by Bindeman et al. [2005]; those with two asterisks (**) are from Portnyagin et al. [2005a].

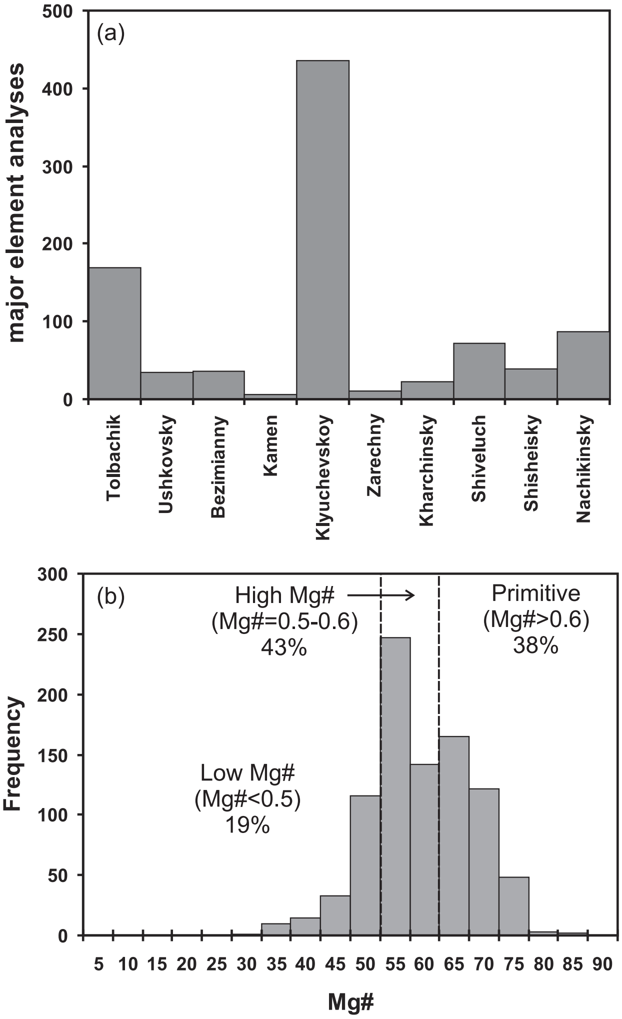

Figure 2. A) Availability of chemical data for northern Kamchatkan volcanoes (major element analyses). Note highly biased interest of researchers in the largest and most active volcanoes. No data published since the 1960's and 1970's exist for the Udina and Zimina Volcanic Groups. B) Histogram of Mg# in volcanic rocks of the CKD. Note predominance of primitive (Mg#>0.6) and high Mg# (Mg#=0.5–0.6) rocks.

phenocrysts (up to 2 cm). The mega-plagiophyric trachybasalts compose the pedestal of the Klyuchevskoy Group and, although geochemically not completely identical (M. Portnyagin, unpublished data), were last erupted from the Southern Vent of the Great Fissure Tolbachik Eruption in 1975–1976 [*Fedotov,* 1983]. These rocks belong to Fe-rich series and have the lowest SiO_2 and the highest FeO (here and thereafter FeO refers to total Fe expressed as FeO) compared to rocks from other CKD volcanoes (Figure 3, 4). These basalts are also distinctively enriched in TiO_2, CaO, K_2O and have relatively low Na_2O and Al_2O_3 when compared to other CKD rocks at similar MgO (Figure 4). Detailed description of rocks from the Tolbachik volcano and the neighboring Tolbachinsky Dol areal volcanic field can be found in the work by [*Fedotov* 1983].

Klyuchevskoy volcano, its predecessor Kamen' volcano and Bezymianny volcano predominantly comprise medium-K, olivine-pyroxene-plagioclase-phyric basaltic andesites (Klyuchevskoy and Kamen') and two-pyroxene-plagioclase and amphibole-plagioclase andesites (Bezymianny). The rocks belong to the medium-Fe arc series and have SiO_2, TiO_2, FeO, CaO, Na_2O intermediate between Tolbachik rocks and those from volcanoes located further north (Figure 3, 4). A distinctive feature of the Klyuchevskoy rocks is relatively low K_2O content (Figure 3B). Low-MgO, high-Al basaltic andesites (Al_2O_3 up to 20 wt %) are common eruptive projects of Kluchevskoy (Figure 4). Rocks from Klyuchevskoy volcano are described in numerous publications [e.g., *Khrenov et al.* 1989; *Khubunaya et al.* 1994; *Kersting and Arculus,* 1994; *Ariskin et al.* 1995; *Dorendorf et al.* 2000; *Ozerov,* 2000; *Mironov et al.* 2001].

Volcanoes located to the north of the Kamchatka River (Shiveluch, Zarechny, and Kharchinsky) predominantly comprise medium- to low-Fe, medium-K calc-alkaline basalts, basaltic andesites and andesites (Figure 3). With rare exception, rocks from Kharchinsky volcano, related cinder cones and from the Baidarny Spur of the Late Pleistocene Shiveluch volcano edifice are similar to rocks from Klyuchevskoy volcano yet tend to have higher K_2O content [e.g. *Volynets et al.* 1999; 2000]. Rocks from Zarechny volcano and many rocks from Shiveluch volcano are high Mg# calc-alkaline basaltic andesites and andesites [e.g. *Volynets et al.* 1997; 1999, 2000; *Churikova et al.* 2001; *Ponomareva et al.* 2007b] and have lower FeO, CaO, TiO_2 and higher SiO_2 and Na_2O at similar MgO compared to Klyuchevskoy volcano (Figure 4). A distinctive feature of these rocks is the wide occurrence of amphibole, which is common not only in andesites but is also present in more basic rock types together with Ca-pyroxene and olivine. Rare rocks with Mg-rich phlogopite phenocrysts, which are unique in the CKD, were described on Kharchinsky volcano (crater extrusion) and among the Holocene pyroclastic deposits of Shiveluch volcano (basaltic tephra, 3600 BP) [*Volynets et al.* 1999; 2000; *Ponomareva et al.* 2007b]. Petrologic information about the northern CKD volcanoes is relatively abundant [*Fedotov and Masurenkov,* 1991; *Volynets et al.* 1997; 1998; 1999; 2000; *Churikova et al.* 2001], although the amount of high quality geochemical data is still relatively small compared to the great emphasis to these volcanoes in the literature. To some extent, this gap is filled by the large data set on the Holocene products of Shiveluch volcano presented in the work by *Ponomareva et al.* [2006b].

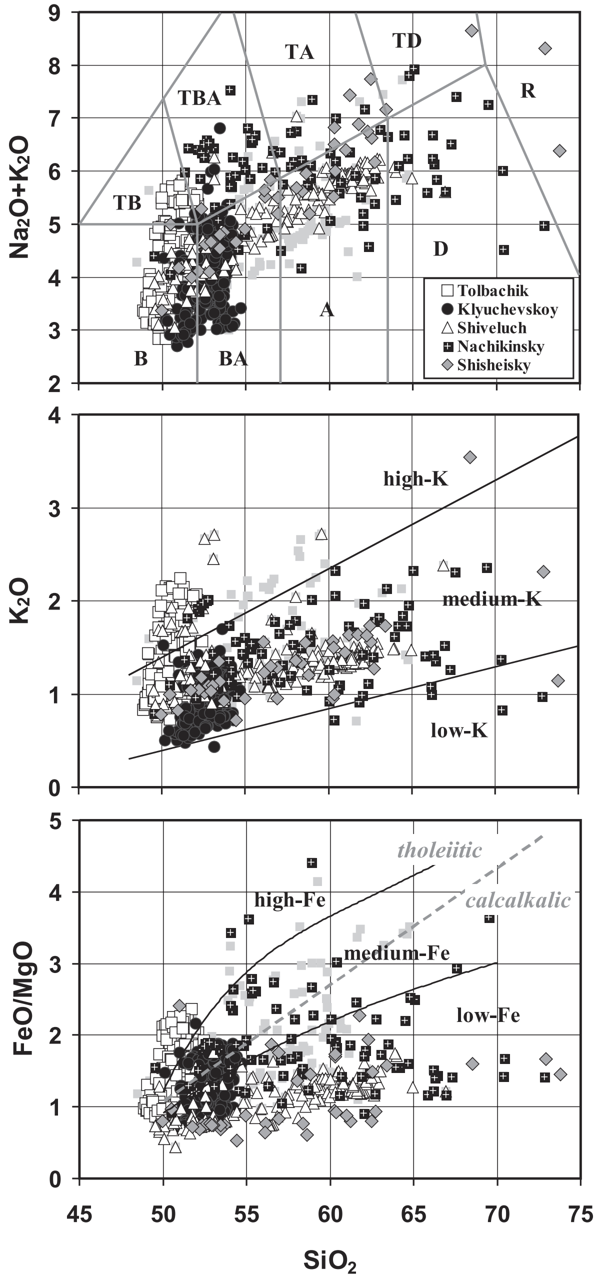

Figure 3. Classification diagrams for the Quaternary CKD lavas: A) SiO_2 vs. total alkalis [*Le Bas et al.* 1986], B) SiO_2 vs. K_2O showing fields of low-, medium- and high-K arc series after *Gill* [1981], and C) SiO_2 vs. FeO/MgO showing tholeiitic vs. calc-alkalic series after *Miashiro* [1974] and low-, medium- and high-Fe series after *Arculus* [2003]. Symbols (except grey squares) are explained in the legend and specify compositions of five large volcanic centres along the arc strike (from south to north: Tolbachik volcano, Klyuchevskoy volcano, Shiveluch volcano, Shisheisky Complex and Nachikinsky volcano). Grey squares represent analyses of CKD volcanic rocks not denoted by other symbols. FeO throughout this paper refers to total Fe in sample expressed as FeO.

Geochemical data on rocks from the remote Shisheisky Complex are sparse. This volcanic complex is very unusual for the CKD because there is no large volcano in the vicinity and the volcanic activity was related to numerous small monogenetic lava vents and extrusions forming several NW-SE trending chains coinciding with the strike-slip Western Aleutian F.Z.. The majority of the Shisheisky Complex rocks are medium-K low-Fe, strongly calc-alkaline basalts, basaltic andesites and andesites with Mg#>0.6 and SiO_2 up to 63 wt% (Figure 4, Table 1). Evolved andesites, dacites and rhyolites also present in subordinate amount. A peculiar feature of the Shisheisky Complex rocks is the absence of plagioclase phenocrysts in all rock types. Olivine and clinopyroxene phenocrysts occur in basalts and basaltic andesites. Amphibole and Mg-rich orthopyroxene (Mg#=0.86–0.90, our unpublished data) are the major phenocryst phases in high-Mg# andesites and dacites. Quartz xenocrysts surrounded by shells of dacitic to rhyolitic glasses (Table 1) including peculiar low-Al (Al_2O_3 <1 wt %) clinopyroxene crystals, very similar to those described in primitive andesites from Mexico [*Blatter and Carmichael,* 1998], occur in some andesites. Additionally, xenogenic mantle olivines (Fo=89–90 mol%, CaO<0.05 wt%, NiO=0.35–0.38 wt%, $\delta^{18}O_{olivine}$ =5.43 ‰, Table 2 and our unpublished data) were found in andesite G3277 (Table 1). In the general CKD systematics, the Shisheisky basalts are broadly similar to high-Mg# basalts from other CKD localities (Figure 4). More SiO_2-rich rock varieties, primitive andesites and dacites, have the lowest FeO, CaO, TiO_2 and the highest SiO_2 and Na_2O at similar MgO compared to all volcanoes in the CKD (Figure 4) and represent the most extreme calc-alkaline rocks in the CKD (Figure 3). Some additional information of the Shisheisky Complex can be found in the reports of the Geologic Survey [*Pilipchuk et al.* 2006] and will be published elsewhere (Portnyagin et al. 2007, manuscript in preparation).

Rocks of Nachikinsky volcano at the northern end of the CKD span a particularly large compositional range. The oldest, Pliocene-Early Quaternary (?), rocks are low-Fe, medium- to low-K pyroxene and amphibole andesites and dacites (Figure 3, 4), which are geochemically similar to the Pliocene andesites from the isthmus of Kamchatka [*Fedorov and Shapiro,* 1998; *Kepezhinskas et al.* 1997]. The most recent Late Pleistocene rocks are moderately Fe-rich, high- to medium-K olivine-plagioclase-pyroxene trachybasalts and basaltic trachyandesites sampled near Nachikinsky volcano. In comparison with high-K trachybasalts from Tolbachik volcano, these rocks have higher Na_2O, Al_2O_3 and lower CaO (Figure 4). Data on rocks from Nachikinsky volcano and from neighboring areas were published by [*Litvinov et al.* 1991; *Portnyagin et al.* 2005a].

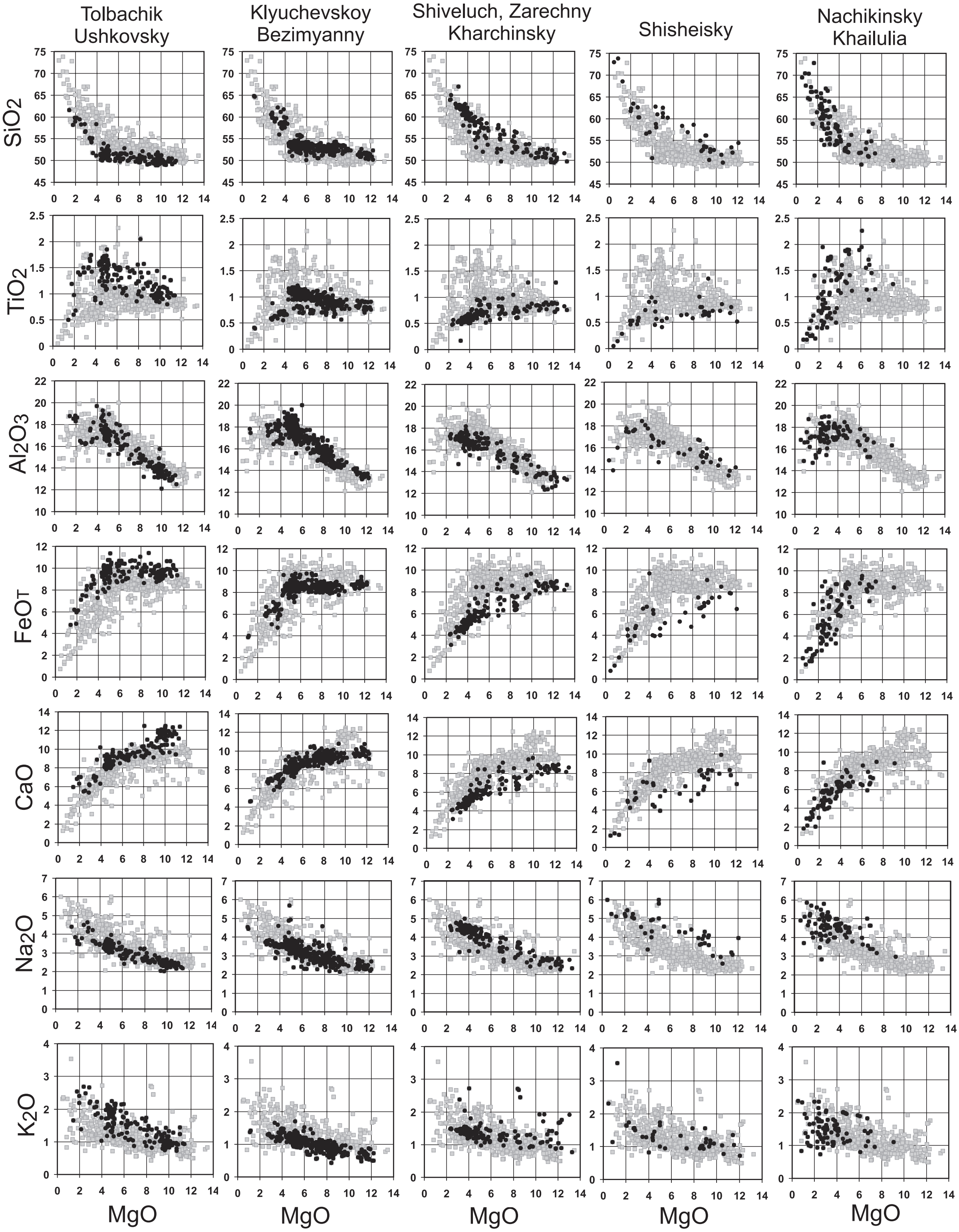

Figure 4. Concentrations of major element oxides in the CKD lavas. Volcanoes are grouped according to their location along the arc strike and similarity in chemical composition. Grey symbols correspond to all lavas from the CKD; black dots denote lavas from volcanoes specified at the top of each diagram.

2.2. Major Elements in Primitive Magmas

An overview of the major element systematics of CKD magmas given in the previous section reveals some systematic changes in magma geochemistry along the arc strike. It, however, remains unclear to what extent the variations are related to compositional diversity of parental magmas or reflect different fractionation paths of similar parental magmas which might also involve substantial crustal assimilation or crustal derivation [e.g., *Bindeman et al.* 2004]. To resolve this question, we focus on the most primitive rocks, which have compositions that are close to being in equilibrium with the mantle wedge and thus could represent weakly fractionated parental melts. Fortunately, such rocks are very abundant in the CKD (Figure 2B). Following *Kelemen et al.* [2003a], we classify as "primitive" those rocks which have Mg#>0.6 where Mg#=MgO/(MgO+FeO) calculated on molar basis. We note that the criterion of Mg#>0.6 to screen evolved rocks is rather strict and excludes the majority of rocks referred in literature to as "high-magnesian". For example, among 86 analyses of high Mg# basalts, basaltic andesites and andesites (Mg#=0.51–0.74) from the Holocene Shiveluch deposits reported by [*Ponomareva et al.* 2007b] only 23 samples fulfill the criterion Mg#>0.6 and can be considered as primitive.

Here we assume that the primitive CKD rocks are informative of the parental melt compositions. Strictly speaking, this assumption is fully applicable only to aphyric primitive rocks, which are rare in the CKD and occur mainly in the Tolbachinsky Dol and Shisheisky Complex. Some of so called "primitive" rocks can originate by accumulation of mafic phenocrysts in highly evolved magma and are not representative of the true parental melts [e.g. *Portnyagin et al.* 2005b]. Nevertheless, we illustrate in the following paragraphs that major and incompatible trace elements in the primitive CKD rocks vary very systematically along the arc, and this systematics can hardly be generated by accumulation or fractionation of mafic minerals. We believe that the complex analysis of statistically large data set adopted here does allow assessing variability of the parental CKD melts, although differentiation processes also can not be excluded as responsible for some additional scatter of the primitive rock compositions.

The average primitive compositions for each volcano are shown in Table 3 and plotted versus inferred distance from the Pacific slab edge in Figure 5. As illustrated by the data, concentrations of major elements in the primitive magmas change very regularly along the CKD. Primitive rocks of Tolbachik volcano have exclusively basaltic compositions. SiO_2 concentrations in primitive rocks become increasingly variable to the north, and the average compositions change to andesitic in the Shisheisky complex. Primitive basalts occur in all localities, while primitive andesites were found only in the proximity to the inferred slab edge. Other major elements strongly correlate with SiO_2 (Figure 5, 6) so that the average and maximum SiO_2 and Na_2O in primitive rocks monotonously increase from south toward the slab edge, and FeO, TiO_2 and CaO decrease. Al_2O_3 tends to increase to the north except in magmas from Zarechny and Kharchinsky volcanoes, which have low Al_2O_3 concentrations. K_2O concentrations do not vary systematically (Figure 5, 6). The lowest K_2O was found in the Klyuchevskoy rocks, the highest in Zarechny, Kharchinsky, Shiveluch and Shisheisky rocks.

Occurrence of high-Mg# and primitive andesites is a distinctive feature of the CKD volcanoes. In global systematics of primitive andesites, the rocks have relatively low CaO, TiO_2 but high Na_2O, FeO and MgO at a given SiO_2 content compared to classic Adak-type primitive andesites from the Western Aleutian Arc and southern Chile [*Kay*, 1978; *Yogodzinski et al.* 1995; *Stern and Kilian*, 1996; *Bindeman et al.* 2005] and are more similar to primitive andesites from Piip volcano in the Western Aleutian Arc [*Yogodzinski et al.* 1994] (Figure 6).

Primitive rocks of Nachikinsky volcano exhibit very scattered compositions. Early Quaternary (?) high Mg# rocks of this volcano have andesitic and dacitic compositions and fall on extrapolations of trends defined by the CKD magmas from southern localities, having even more Si-rich and Fe-, Ca- and Ti-poor compositions (Table 3, Figure 5). The Late Pleistocene high Mg# rocks of Nachikinsky volcano and primitive melt inclusions in olivine (Fo_{84-86}) from these rocks [*Portnyagin et al.* 2003 and unpublished data] have low-Si, high-Ti and high-K trachybasaltic compositions (Table 3, Figure 5), which are unlike any other primitive magma in the CKD, and indicate distinct conditions of magma generation beneath Nachikinsky volcano in the Late Pleistocene in comparison to the southern CKD volcanoes.

It is interesting to note that the compositional trends of the primitive CKD magmas are qualitatively very similar to those which can be inferred from the compositions of more evolved magmas as was previously suggested by [*Volynets,* 1994] and on the global basis by [*Plank and Langmuir*, 1988]. This is well demonstrated by the strong correlations between average compositions of primitive magmas and the compositions corresponding to MgO=6 wt%, derived from the compositional trends of all rocks from a particular volcano plotted versus MgO [e.g., *Plank and Langmuir*, 1988] (Figure 7). These correlations demonstrate that, at least in the case of the CKD, compositional peculiarities of low-MgO rocks should be in many aspects inherited from their parental magmas (see also [*Grove et al.* 2003; *Kelemen et al.* 2003a; *Green et al.* 2004]). Strongly calc-alkaline low-CaO high-SiO_2 low-Mg# andesites to dacites from the northern volcanoes (Shiveluch, Shisheisky), for example, might be derived from low-CaO and high-SiO_2 basalt andesitic parental melts [e.g. *Volynets et al.* 1997], whereas tholeiitic trend of the southern volcanoes (Tolbachik, Ushkovsky, Klyuchevskoy) toward relatively high-CaO low-SiO_2 low-Mg# basalts and basaltic andesites implies predominantly high-CaO low-SiO_2 basaltic parental magmas [e.g. *Fedotov,* 1983].

2.3. Trace Elements in Primitive Magmas

Trace element geochemistry of the northern Kamchatka lavas has been discussed in many publications over the past years [e.g., *Kepezhinskas et al.* 1997; *Hochstaedter et al.* 1996; *Turner et al.* 1998; *Churikova et al.* 2001; *Dorendorf et al.* 2000; *Volynets et al.* 2000; *Münker et al.* 2004; *Portnyagin et al.* 2005a]. Here we briefly evaluate the systematics of selected trace elements (Ni, V, Y, Zr, Nb, Sr, Ba) in primitive magmas, primarily because these elements span several geochemical groups (e.g., LILE, HFSE, REE-proxy Y) and thus allow us to constrain mass-balance models involving partial melting and fluid and melt fluxing. Additionally, analyses of these elements are relatively abundant in the literature, since they are routinely determined by XRF and their analytical precision is satisfactory. Our goal here is to assess along-arc variations of a range of trace elements, and to evaluate correlations of these trace elements with major elements in primitive lavas (Table 3, Figure 5 and 8).

2.3.1. Nickel. Concentrations of Ni are high in all primitive magmas (100–240 ppm in the volcano averages, Table 3) and do not correlate with major and incompatible trace elements (Figure 5). Primitive rocks from single volcanoes exhibit correlations of Ni and MgO (for example, Klyuchevskoy rocks) suggesting that our compilation of primitive rocks includes rocks differentiated to some extent. This variability in refractory elements, however, can be explained by minor (several percent) fractionation/accumulation of olivine and does not affect the major conclusions of this study. Noteworthy, primitive andesites from the Shisheisky Complex have Ni content even higher compared to the majority of primitive basalts and basaltic andesites from the southern Klyuchevskoy and Tolbachik volcanoes (Figure 5, Table 1, 3), which can not be explained by accumulation of olivine in the Shisheisky andesites, which are typically free of magmatic olivine phenocrysts and have significantly lower MgO content than primitive CKD basalts.

2.3.2. Vanadium and yttrium. Systematics of V, Y (and heavy REE: Dy through Lu; our unpublished data) in the primitive CKD magmas is very similar to that of TiO_2. Concentrations of these elements correlate strongly with major elements (Si, Fe, Ca, and Na) along the arc strike. The highest V and Y concentrations were found in the Tolbachik volcano lavas. Their concentrations decrease to the north, have minimum values in magmas of the Shisheisky Complex and then increase again in magmas of Nachikinsky volcano at the northern end of the volcanic belt (Figure 5). Because Ti and V are compatible elements with Fe-Ti oxides and Y is not compatible, the coupled behavior Ti, V and Y precludes fractionation of Fe-Ti oxides as the main reason for the compositional variability in the CKD primitive rocks.

Fractionation between heavy REE is rather weak in the majority of the CKD rocks [*Portnyagin et al.* 2005a]. Dy/Yb in primitive basalts and andesites from the southern CKD volcanoes including Shiveluch volcanic group are similar and relatively low (1.7–2.0), yet slightly higher on average compared to N-MORB (1.5–1.9 [*Hofmann,* 1988; *Sun and McDonough*, 1989]). Thus, primitive andesites from Kamchatka do not exhibit strong garnet signature in their REE patterns unlike high-Mg# andesites from the neighboring Western Aleutian Arc [*Yogodzinski et al.* 1995]. Primitive basalts and melt inclusions from Nachikinsky volcano have distinctively high Dy/Yb (up to 2.5) indicating a greater role for garnet in their source compared to the southern CKD volcanoes [*Portnyagin et al.* 2005a].

2.3.3. Niobium and zirconium. Enrichment in Nb (up to 60 ppm) and Zr (up to 250 ppm) is a characteristic feature of the most recent rocks and primitive melt inclusions from Nachikinsky volcano (Figure 5). They have high Nb/Y (up to 1.4) and Zr/Y (up to 14) exceeding those in typical MORB [*Hofmann,* 1988; *Sun and McDonough*, 1989] and suggest derivation from relatively fertile mantle sources (see also Figure 10). Rocks from southern localities have significantly lower Nb (0.6–5 ppm) and also lower Zr (70–200 ppm) within primitive MORB range. Among CKD rocks, the lowest Nb concentrations and Nb/Y ratios are characteristic of Klyuchevskoy, Zarechny and Shiveluch rocks (Figure 5). Rocks from the Shisheisky Complex and Tolbachik volcano have slightly higher Nb, although its concentrations are still far below those of the Nachikinsky rocks. Zr/Y ratio (not shown) increases from the south towards the slab edge, reaching very high values in magnesian andesites from the Shisheisky Complex (up to 11), almost as high as in Nachikinsky volcano. Some Kharchinsky rocks also have high Zr and Zr/Y, which however do not correlate with the major elements.

Table 3. Average compositions of CKD primitive magmas and parameters of magma generation

Volcano	Ushkovsky		Tolbachik		Klyuchevskoy		Zarechny		Kharchinsky		Shiveluch		Shisheisky Complex		Nachikinsky		Primitive dacite
Latitude (degrees North)	56.12		55.7		56.05		56.36		56.44		56.63		57.36		57.86		
Longitude (degrees East)	160.5		160.3		160.63		160.82		160.8		161.32		161.3		162.68		
Slab depth (km)[a]	180		180		160		140		140		90		80				
Distance from slab edge (km)	140		170		140		100		100		60		0		-100		
Mantle collumn (km)[b]	145		145		125		105		105		55		45				
Primitive magmas	Rocks	n	Rocks	n	Rocks	n	Rocks	n	Rocks	n	Rocks	n	Rocks	n	Melt.inc.	n	
SiO_2 (wt%)	50.9	4	50.5	75	52.8	174	54.5	8	51.9	18	54.1	27	56.4	24	48.0	20	64
TiO_2(wt%)	1.19	4	1.07	75	0.89	174	0.86	8	0.84	18	0.79	27	0.70	24	2.07	20	0.4
Al_2O_3 (wt%)	14.5	4	13.8	75	15.1	174	13.4	8	13.8	18	14.9	27	15.4	24	14.7	20	17
FeO total (wt%)	9.6	4	9.6	75	8.6	174	8.1	8	8.5	18	7.7	27	6.5	24	11.2	20	3.5
MnO (wt%)	0.18	4	0.18	75	0.17	174	0.16	8	0.17	18	0.15	27	0.12	24	0.09	20	0.1
MgO (wt%)	9.2	4	9.9	75	9.1	174	9.9	8	11.5	18	9.4	27	8.6	24	9.5	20	4.0
CaO (wt%)	10.3	4	11.2	75	9.6	174	8.4	8	8.9	18	8.3	27	6.7	24	9.5	20	3.5
Na_2O (wt%)	2.57	4	2.47	75	2.77	174	3.05	8	2.89	18	3.03	27	4.19	24	3.23	20	5.5
K_2O (wt%)	1.23	4	1.03	75	0.81	174	1.43	8	1.39	18	1.34	27	1.14	24	1.25	20	1.6
P_2O_5 (wt%)	0.34	4	0.26	75	0.16	174	0.24	8	0.25	18	0.27	27	0.17	24	0.36	20	0.1
$^{87}Sr/^{86}Sr$	0.70337	2	0.70336	15	0.70357	28	0.70346	8	0.70358	7	0.70353	18	0.70348	7	0.70299[j]	1	~0.70350
$^{143}Nd/^{144}Nd$	0.51308	2	0.51309	15	0.51309	27	0.51309	7	0.51309	8	0.51307	15	0.51305	7	0.51307[j]	1	~0.51305
d^{18}O olivine (‰)			5.5	7	6.2	12	6.4	3	6.4	1	5.8	6	5.9	7	5.1[j]	2	5.1-6.0
Ni (ppm)	137	4	135	30	116	63	150	8	186	17	109	13	170	10	212	13	70-150
V (ppm)	282	4	289	28	248	45	221	4	240	15	193	9	173	10	256	13	~50
Y (ppm)	23	4	22	28	17.8	45	17.5	6	16	14	17	12	16	10	20	13	~10
Sr (ppm)	307	4	301	31	317	64	616	8	591	19	460	16	420	10	559	13	~630
Zr (ppm)	111	4	99	29	80	54	78	6	93	14	81	10	87	10			~120
Nb (ppm)	4.1	4	2.6	23	1.5	26	1.2	3	1.9	10	2.5	11	3.7	10	26	13	2-6
Ba (ppm)	304	4	280	31	267	66	657	8	571	20	369	16	366	10	152	13	~600
Parental magmas (Fo_{91}, NNO)																	
Olivine added (mol %)[d]	11.2		9.4		9.3		5.3		2.2		5.4		1.9		13.1		0.0
SiO_2 (wt%)	49.5		49.4		51.5		53.6		51.5		53.3		56.1		46.8		64
TiO_2(wt%)	1.04		0.96		0.80		0.81		0.82		0.74		0.69		1.76		0.4
Al_2O_3 (wt%)	12.7		12.3		13.5		12.6		13.5		14.0		15.1		12.5		17
FeO total (wt%)	9.7		9.7		8.8		8.2		8.5		7.8		6.5		11.1		3.5
MnO (wt%)	0.16		0.16		0.15		0.15		0.17		0.14		0.12		0.08		0.1
MgO (wt%)	14.1		13.9		13.2		12.1		12.3		11.7		9.4		15.3		4.0
CaO (wt%)	9.0		10.0		8.6		7.9		8.7		7.8		6.6		8.1		3.5
Na_2O (wt%)	2.24		2.21		2.48		2.87		2.82		2.86		4.11		2.74		5.5
K_2O (wt%)	1.07		0.92		0.73		1.35		1.36		1.26		1.12		1.06		1.6

Table 3. *Cont.*

Volcano	Ushkovsky	Tolbachik	Klyuchevskoy	Zarechny	Kharchinsky	Shiveluch	Shisheisky Complex	Nachikinsky	Primitive dacite
Parental magmas (Fo_{91}, NNO) cont.									
P_2O_5 (wt%)	0.30	0.23	0.14	0.23	0.24	0.25	0.17	0.31	0.1
T (°C) @ 0.001 GPa, dry[e]	1353	1345	1336	1333	1331	1323	1312	1387	1311
T (°C) @ 1 GPa, H_2O present[f]	1298	1287	1271	1262	1264	1253	1228	1437	1206
Mixing model (1)									
Amount of dacite in mixture (m.f.)[g]	0.063	0.035	0.202	0.319	0.133	0.291	0.455		1
Degree of melting (m.f.)	0.040	0.054	0.063	0.056	0.077	0.070	0.071		-
Reaction model (2A)									
Assimilation rate (M_a/M_c)	1.038	1.047	1.063	1.084	1.067	1.072	1.078		-
Liquid mass increase (M/M_o)	2.44	2.30	2.07	1.83	1.96	1.84	1.41		-
H_2O in melt (wt%)[i]	2.6	2.9	3.4	4.0	3.7	4.0	5.4		8
Flux melting model (2B)									
Amount of dacite in source (m.f.)	0.022	0.021	0.059	0.070	0.067	0.061	0.114		-
Degree of melting (m.f.)	0.070	0.037	0.130	0.140	0.141	0.122	0.168		-
H_2O in source (wt%)[h]	0.19	0.18	0.48	0.57	0.55	0.50	0.93		-
H_2O in melt (wt%)[i]	2.3	3.7	3.4	3.8	3.6	3.8	5.2		8

Notes:

a) Estimated after *Gorbatov et al.* [1997].
b) Estimated assuming crustal thickness 35 km beneath all volcanoes [*Fedotov and Masurenkov*, 1991; *Park et al.* 2002].
c) Compositions of parental melts calculated in the Petrolog 2.0 software [Danyushevsky et al. 2002] from the average primitive compositions by addition of olivine (0.1% increment) until equilibrium with olivine Fo91; oxygen fugacity was assumed to correspond to the Ni-NiO buffer.
d) Amount of olivine added to the composition of primitive melt to achieve equilibrium with olivine Fo91.
e) Temperature of saturation of parental magmas with olivine at 0.001 GPa pressure and dry conditions (H_2O=0) calculated according the model by [*Ford et al.* 1983].
f) Temperature of saturation of parental magmas with olivine at 1 GPa (i.e., below the Kamchatkan crust) under hydrous conditions. Amount of water in melt was estimated from the "reaction model" (2A) with H_2O in dacite component 8 wt%. Decrease of liquidus temperature due to water addition was acconted according the model by [*Falloon and Danyushevsky*, 2000] and the slope of olivine liquidus 50 °/GPa [*Ford et al.* 1983].
g) Here and thereafter "m.f." refers to mass fraction.
h) and i) Amount of water in melt (h) and its mantle source (i) calculated from the different models. Initial mantle H_2O content was assumed to be 116 ppm, H_2O bulk partition coefficient 0.012 [*Stolper and Newman*, 1994] and amount of H_2O in primitive dacite component 8 wt%.
j) Sr and Nd isotope composition of primitive trachybasalt P-74-02; O-isotope composition of olivine from samples N44-A and N45-A [*Portnyagin et al.* 2005a].

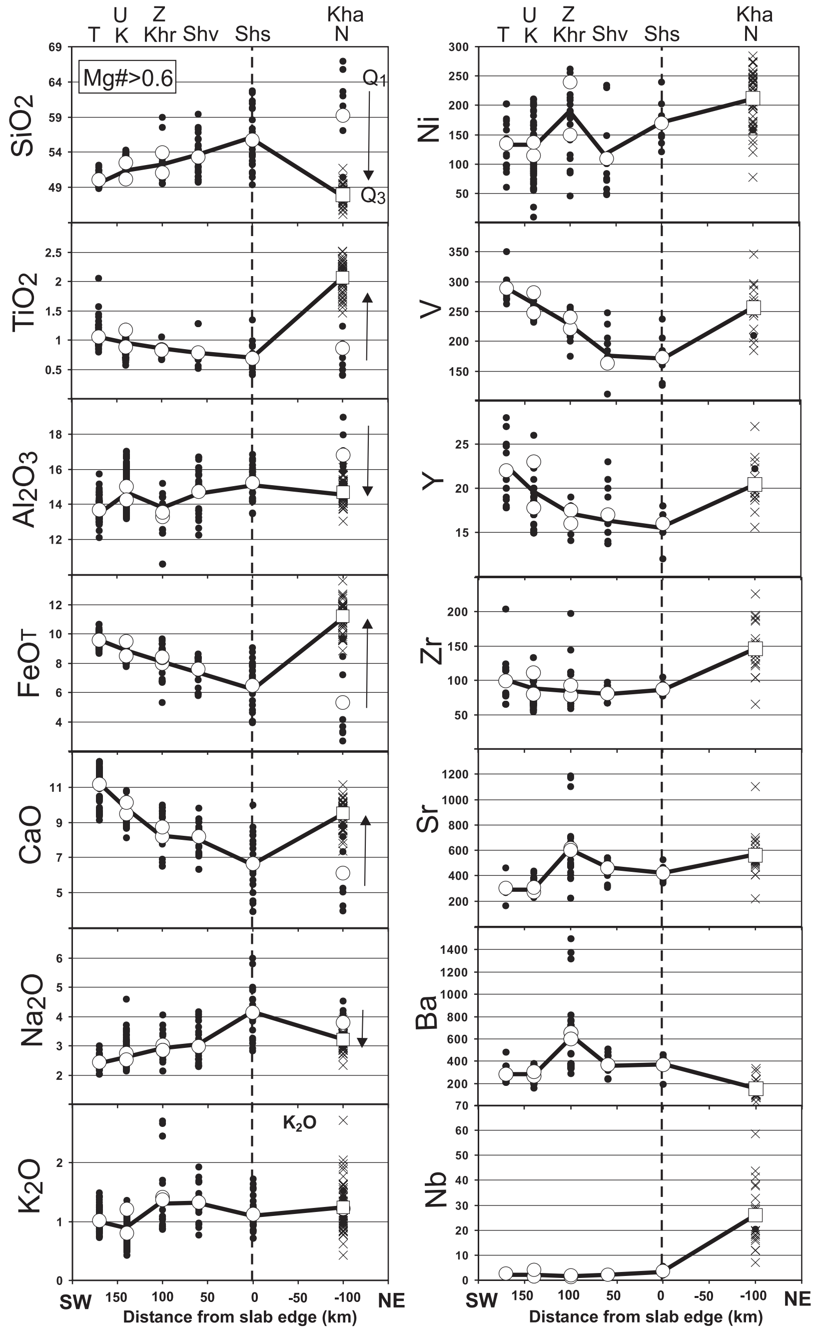

Figure 5. Along-arc variations of major and trace elements in primitive (Mg#>0.6) CKD lavas plotted versus inferred distance from the Pacific slab edge along the SW-NE arc strike. Labels at the top correspond to volcanoes: T—Tolbachik, U – Ushkovsky, K—Klyuchevskoy, Z – Zarechny, Khr – Kharchinsky, Shv – Shiveluch, Shs – Shisheisky complex, Kha – Khailulia, N – Nachikinsky. Black dots are compositions of all primitive lavas; large open circles are volcano averages (see Table 3); oblique crosses are compositions of melt inclusions in primitive olivine (Fo_{86-88}) from the most recent Nachikinsky lavas [*Portnyagin et al.* 2003 and unpublished data]; open square is average composition of the Nachikinsky melt inclusions (Table 3). Solid line connects volcano averages for the Late Pleistocene-Holocene compositions along the CKD. Labelled arrow shows evolution of compositions of Nachikinsky primitive magmas from Early Quaternary (Q_1) through Late Pleistocene (Q_3) [*Portnyagin et al.* 2005a]. The Pacific Plate is proposed to be torn along the Bering F.Z. [*Davaille and Lees*, 2004].

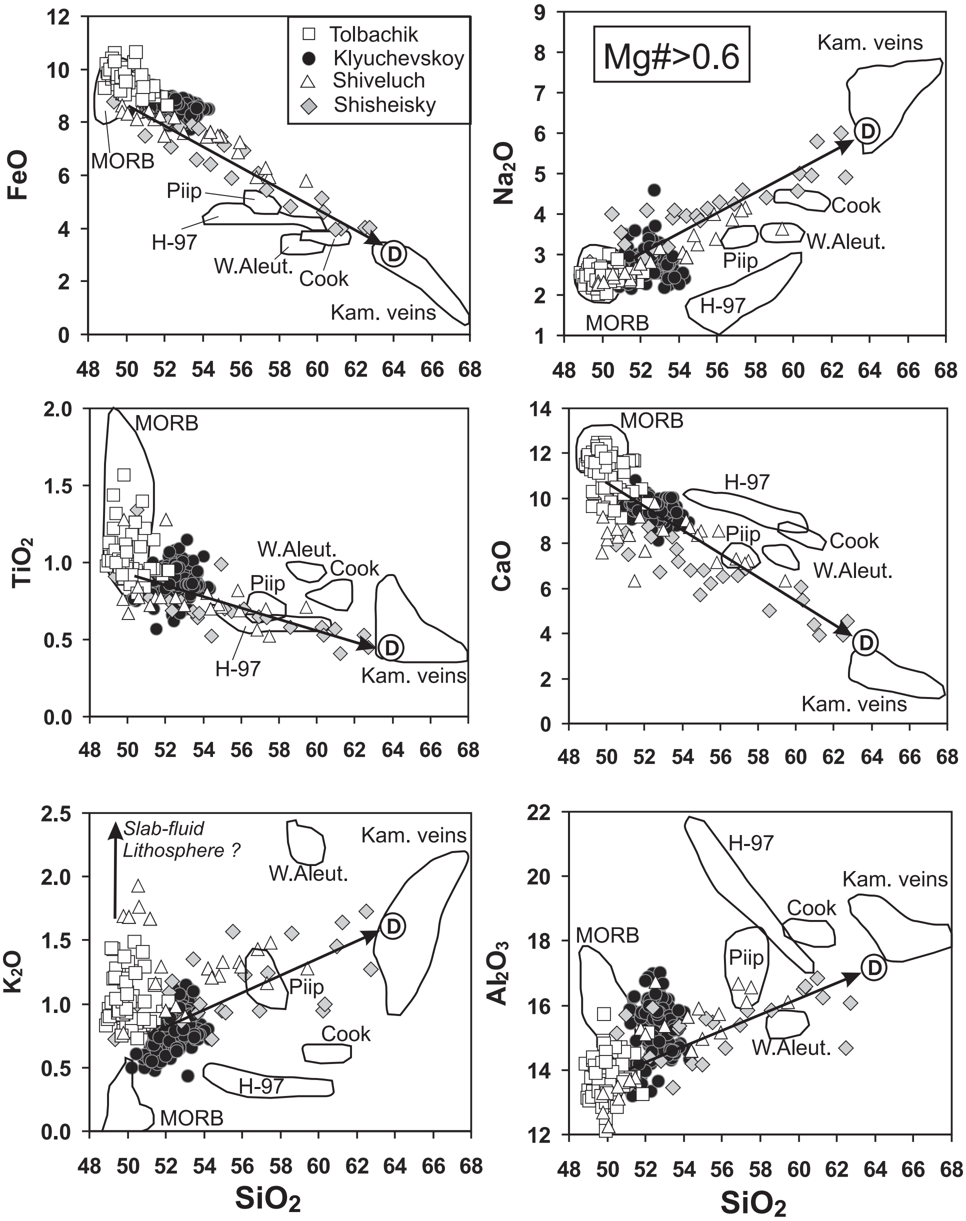

Figure 6. Variations of major elements in primitive (Mg#>0.6) magmas from Tolbachik, Klyuchevskoy, Shiveluch volcanoes and Shisheisky Complex. Fields are labelled as follows: "MORB"—compositions of primitive Pacific MORB compiled from PETDB web data base [PETDB, 2004]; "Piip" – high Mg# andesites from Piip volcano [*Yogodzinski et al.* 1994]; "W.Aleut." – high Mg# andesites from the Kamchatsky Strait, Western Aleutian Arc [*Yogodzinski et al.* 1995]; "Cook" – high Mg# andesites from Cook Island, Southern Chile [*Stern and Kilian*, 1996]; "Kam. veins" – throndhjemitic veins in mantle xenoliths from Tymlat area on the isthmus of Kamchatka [*Kepezhinskas et al.* 1995, 1996]; "H-97" – water-saturated partial melts from fertile peridotite KLB-1 [*Hirose*, 1997]. Encircled "D" refers to the inferred composition of the primitive dacite component. Arrows denote general trends of the primitive CKD rocks.

2.3.4. Strontium and barium. Rocks from the Klyuchevskoy Group have relatively low Sr concentrations (200–400 ppm) and low Sr/Y (10–20) (Figure 5, 8). Rocks from more northern volcanoes are substantially enriched in Sr (400–1200 ppm) and have high Sr/Y (up to 80) as was emphasized by many authors [e.g., *Volynets et al.* 1999; 2000; *Yogodzinski et al.* 2001]. Thus, both Sr and Sr/Y increase from the south towards the slab edge. This effect

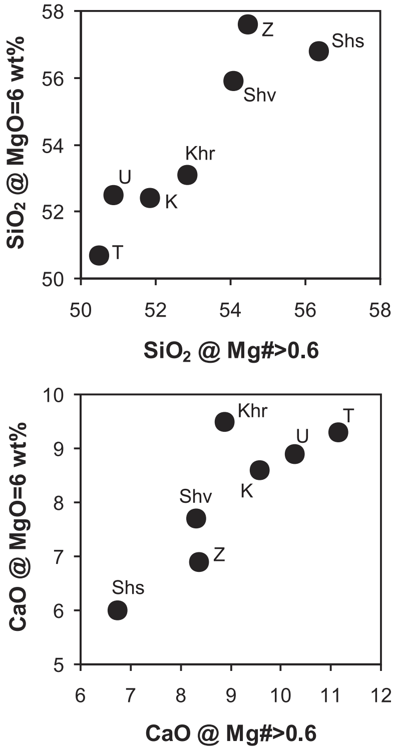

Figure 7. Comparison of average compositions of primitive lavas (Mg#>0.6) and compositions at MgO=6 wt. % inferred from approximation of all data for every particular volcano [*Plank and Langmuir*, 1988]. Labels refer to volcano names as in Figure 5. Good correlations imply that differences in composition of evolved lavas are inherited from differences in their parental magmas. In particular, difference in the composition of parental magmas readily explains contrasting tholeiitic (e.g., Tolbachik) and calc-alkaline (e.g., Shiveluch) trends as suggested previously by [*Volynets et al.* 2000; *Kelemen et al.* 2003b; *Green et al.* 2004].

is evident even when comparing the most southern volcanoes, Tolbachik and Klyuchevskoy, which have systematically different Sr/Y (Table 3). We note, however, that the maximum Sr concentrations and Sr/Y ratios were found in rocks from Kharchinsky volcano (Figure 5, 8), which do not have distinct major element compositions, being high-K basaltic andesites. Magnesian andesites from the Shisheisky Complex and Shiveluch volcano have somewhat lower Sr/Y (~50) than Kharchinsky rocks but still significantly higher than rocks from the Klyuchevskoy Group. North of the slab edge, Nachikinsky rocks have on average similar Sr concentrations and slightly lower Sr/Y ratios compared to the Shiveluch Group. Concentrations of Ba vary within a relatively narrow interval (200–600 ppm) in the majority of the CKD rocks. Exceptionally high Ba concentrations (up to 1500 ppm) and Ba/Nb (up to 600) are characteristic of rocks from Kharchinsky and Zarechny volcanoes (Figure 5, 8), which as noted above also have high Sr and Sr/Y. Compared to the southern volcanoes, Nachikinsky rocks have slightly lower Ba concentrations and distinctively lower Ba/Nb (7–23) and Ba/Zr (0.7–2.5) approaching compositions of oceanic basalts [*Portnyagin et al.* 2005a] (Figure 8).

2.4. Oxygen Isotopes

Presently available data set on oxygen isotope composition of lavas and minerals from the northern segment of the Kamchatka arc includes about 100 published analyses [e.g., *Pokrovsky and Volynets*, 1999; *Pineau et al.* 1999; *Volynets et al.* 2001; *Dorendorf et al.* 2000; *Bindeman et al.* 2004; 2005; *Portnyagin et al.* 2005a]. In this study we focus on laser fluorination analyses of olivine crystals from primitive to intermediate lavas, which provide direct information about the composition of mantle sources and are generally more precise (external precision is ~0.1‰) compared to bulk rock analyses [e.g., *Bindeman et al.* 2004]. Amphibole analyses were also used for Shiveluch volcano and Shisheisky Complex. Amphibole has O isotope values 0.2–0.4‰ higher than olivine with which it is in equilibrium at high temperatures of basaltic magmas, and the oxygen isotope compositions of olivine and amphibole differ only by this slight amount for magmas of similar compositions [*Eiler*, 2001; *Bindeman et al.* 2004]. New 22 analyses of olivine and amphibole from the CKD rocks obtained with the help of high precision laser fluorination technique are shown in Table 2.

The distinctive and spectacular feature of CKD magmatism is the large range of oxygen isotope compositions ($\delta^{18}O_{olivine}$ = 5.1–7.2‰) and prevalence of compositions with unusually high $^{18}O/^{16}O$ compared to the majority of subduction-related magmas [e.g., *Eiler et al.* 2000] (Figure 8, 9). To our knowledge, these are the highest $\delta^{18}O_{olivine}$ values measured to date. The lowest $\delta^{18}O_{olivine}$ (5.1–5.2‰) in the northern Kamchatka, which are within the range of MORB olivine compositions (5.0–5.4‰) [*Eiler*, 2001], were reported for olivines from Khailulia and Nachikinsky trachybasalts, which also have very low Ba/Nb, La/Nb and MORB-like $^{87}Sr/^{86}Sr$ [*Portnyagin et al.* 2005a]. Olivines separated from more evolved rocks of these volcanoes have higher $\delta^{18}O_{olivine}$ (up to 5.8 ‰). Olivine and amphibole phenocrysts from southern CKD lavas have systematically higher $\delta^{18}O_{olivine}$ than MORB. Olivines from Tolbachik lavas exhibit relatively small range of compositions slightly higher than the MORB range ($\delta^{18}O_{olivine}$ = 5.4–6.0 ‰, Table 2). Compositions of olivine and amphibole from other volcanoes are highly scattered. Particularly large range is observed for Klyuchevskoy volcano ($\delta^{18}O_{olivine}$ = 5.8–7.2 ‰), where the oxygen isotope composition of olivine phenocrysts appears to correlate with K_2O, U, Ba, LREE in the host lavas [*Dorendorf et al.* 2000]. High $\delta^{18}O_{olivine}$ (6.4–6.5 ‰) were also reported for olivines from Zarechny and Kharchinsky volcanoes [*Bindeman et al.* 2005]. Compositions of amphibole and olivine from Shiveluch volcano [*Bindeman et al.* 2004; 2005] and Shisheisky Complex (Table 2) fall in the intermediate range ($\delta^{18}O_{olivine}$ = 5.4–6.2‰, $\delta^{18}O_{amphibole}$ = 5.5–6.4‰).

When $\delta^{18}O$ in minerals are plotted versus SiO_2 in their host rocks, two distinct trends can be recognized (Figure 9). Tolbachik, Klyuchevskoy, Zarechny, Kharchinsky and some Shisheisky high-Mg# (Mg# > 0.55) rocks define a steep trend toward extremely high $\delta^{18}O_{olivine}$ (up to 7‰) at relatively low $SiO_2 \leq 54$wt%. Primitive to moderately fractionated rocks from Shiveluch, Shisheisky and Nachikinsky volcanoes define a shallow trend of only slightly increasing $\delta^{18}O_{olivine}$ (up to ~6 ‰) over a large increase in SiO_2 (up to 63 wt%). Both trends converge at low $\delta^{18}O_{olivine}$ (5.2–5.4 ‰) and SiO_2 (48–50 wt %) to values in the range of primitive Nachikinsky rocks (Figure 9), characteristic of typical MORB [*Eiler*, 2001].

2.5. Neodymium and Strontium Isotopes

Nd isotope ratios in the CKD rocks from the literature sources [*Kepezhinskas et al.* 1997; *Dorendorf et al.* 2000; *Volynets et al.* 2000; *Churikova et al.* 2001; *Dosseto et al.* 2003; *Portnyagin et al.* 2005a; *Bindeman et al.* 2004; 2005] and obtained in this works (Table 2) fall within relatively narrow interval ($^{143}Nd/^{144}Nd$=0.51302–0.51316 excluding 4 analyses), which is entirely within the range of typical values for the Pacific and depleted Indian MORB ($^{143}Nd/^{144}Nd$>0.5130) (Figure 8). Along-arc variations in Nd isotope ratios are not systematic except for somewhat lower values compared to other volcanic complexes measured for Shisheisky lavas (0.51302–0.51308) and two new analyses of trachybasalts from Nachikinsky volcano (0.52974–0.52984).

Available estimates for Nd isotope composition of sediments possibly subducting beneath Kamchatka range from ~0.51234 [*Plank and Langmuir,* 1998] to 0.51264–0.51276 [*Duggen et al.* 2006] depending on the amount of volcanic ash layers in the sedimentary columns assumed to derive the average sediment composition. These values are significantly less radiogenic compared to generally MORB-like Nd-isotope ratios in the CKD rocks. The bulk amount of subducted sediments involved in genesis of the most CKD magmas is therefore limited by 1–2 wt % or less, considering mantle – sediment melt mixtures [e.g. *Kersting and Arculus,* 1995; *Kepezhinskas et al.* 1997; *Turner et al.* 1998; *Ishikawa et al.* 2001; *Churikova et al.* 2001]. Somewhat higher amount of sedimentary material compared to other volcanoes could be

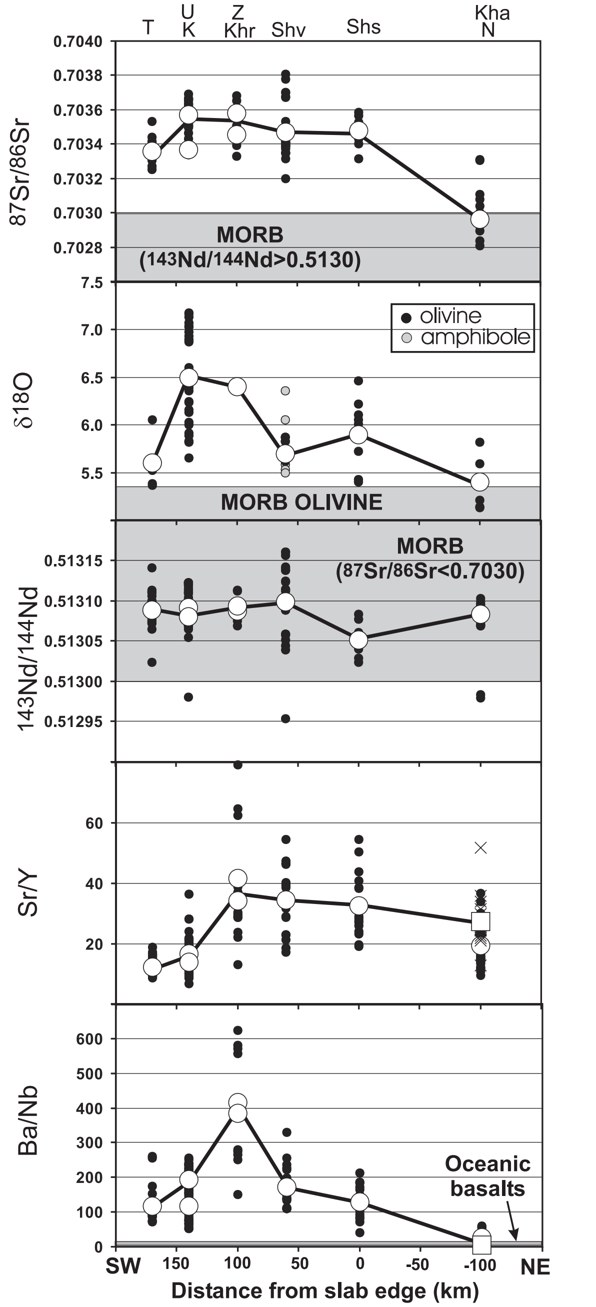

Figure 8. Along-arc variations of trace element and isotope ratios in CKD rocks (all data including low-Mg# rocks). Symbols are the same as in Figure 5. Range of MORB compositions is after [*Sun and McDonough*, 1989; *PETDB*, 2004; *Eiler*, 2001]. Sr and Nd isotope data are from [*Kepezhinskas et al.* 1997; *Dorendorf et al.* 2000; *Volynets et al.* 2000; *Churikova et al.* 2001; *Dosseto et al.* 2003; *Portnyagin et al.* 2005a; *Bindeman et al.* 2004; 2005; and this study]. Laser fluorination O isotope data on olivine and amphibole separates are from this study and [*Dorendorf et al.* 2000; *Bindeman et al.* 2004; 2005]. Trace elements are from numerous sources (see reference list in the Supplementary Data Tables).

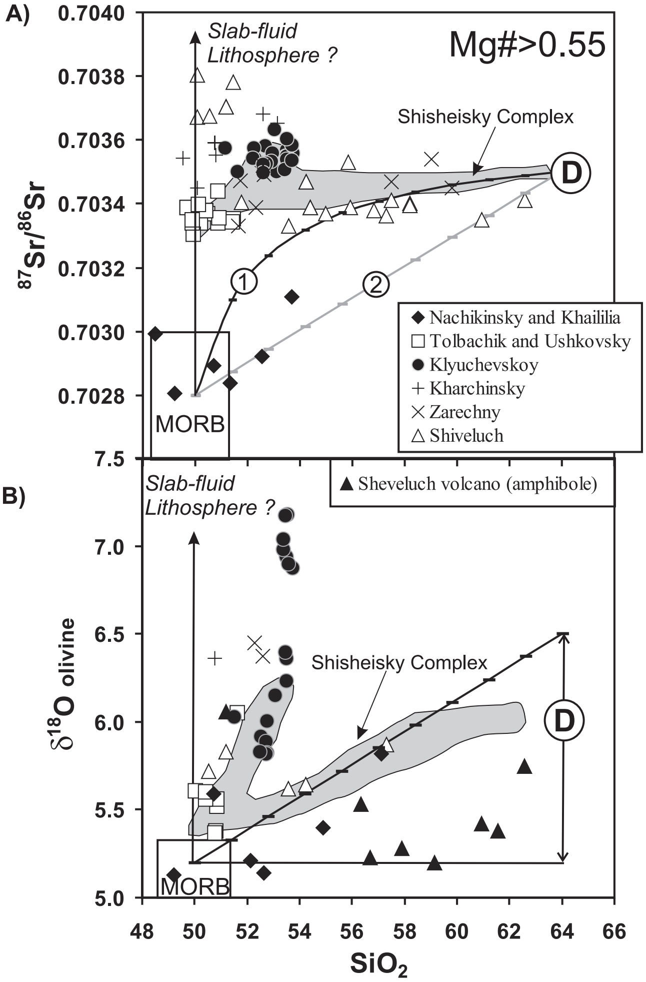

Figure 9. Variations of $^{87}Sr/^{86}Sr$ (A) and $\delta^{18}O_{olivine}$ (B) versus SiO_2 concentrations in primitive to slightly evolved (Mg#>0.55) CKD rocks. The amphibole O-isotope analyses were converted to values in equilibrium with olivine by subtraction of 0.3 ‰ from the $\delta^{18}O_{amphibole}$ values. Data sources are listed in the caption to Figure 8. Compositional field of depleted MORB is after [*PETDB*, 2004; *Eiler*, 2001]. Encircled "D" refers to the inferred composition of the primitive dacite component in plot (A) and to the range of possible compositions in plot (B). Labelled curves demonstrate trajectories of mixing between the primitive dacite melt component and (1) depleted MORB and (2) primitive trachybasalt from Nachikinsky volcano (sample P-74-02 from [*Portnyagin et al.* 2005a]). The mixing trajectories coincide in the lower diagram. Tick marks correspond to 10% increment of the primitive dacite in the mixture. The mixing curves were calculated assuming the following compositions. MORB: SiO_2 = 50 wt%, $^{87}Sr/^{86}Sr$ =0.7028, Sr = 90 ppm; dacite component: SiO_2 = 64 wt%, $^{87}Sr/^{86}Sr$= 0.7035, Sr = 600 ppm; Nachikinsky trachybasalt: SiO_2 = 50 wt%, $^{87}Sr/^{86}Sr$= 0.7028, Sr=579 ppm. Vertical arrow demonstrates expected compositional effect of fluid fluxed mantle melting and/or assimilation of mafic lithosphere.

involved in the genesis of the Shisheisky Complex rocks, shifting $^{143}Nd/^{144}Nd$ to lower values. More quantitative estimates of the amount of sediments involved in the genesis of the CKD magmas would be possible with data on Pb-isotope compositions of the CKD rocks, which is beyond the scope of this work.

Sr isotope ratios reported in [*Kepezhinskas et al.* 1997; *Dorendorf et al.* 2000; *Volynets et al.* 2000; *Churikova et al.* 2001; *Dosseto et al.* 2003; *Portnyagin et al.* 2005a; *Bindeman et al.* 2004; 2005] and from this study (Table 2) vary from MORB-like for the northernmost Nachikinsky volcano ($^{87}Sr/^{86}Sr$ =0.7028–0.7031) to significantly more radiogenic in rocks from the southern CKD volcanoes originating above the subducting Pacific Plate ($^{87}Sr/^{86}Sr$ =0.7033–0.7038) (Figure 8). Overall, relatively radiogenic $^{87}Sr/^{86}Sr$ at given $^{143}Nd/^{144}Nd$ in the majority of the CKD rocks compared to oceanic basalts (e.g. MORB) were interpreted as reflecting involvement of Sr-rich Nd-poor fluids from subducting altered oceanic crust in magma genesis beneath CKD [e.g. *Kepezhinskas et al.* 1997; *Turner at al.* 1998; *Dorendorf et al.* 2000; *Churikova et al.* 2001]

Tolbachik and Ushkovsky rocks have relatively low $^{87}Sr/^{86}Sr$ falling within narrow range (0.7033–0.7035). Klyuchevskoy rocks have systematically more radiogenic Sr isotope compositions (0.7035–0.7037). Further to the north, the Sr isotope compositions scatter from the Tolbachik-like (~0.7033) to significantly more radiogenic ($^{87}Sr/^{86}Sr$ up to 0.7038 in some Shiveluch rocks). In general, volcanoes located at intermediate distances (60–100 km) from the inferred slab edge tend to have the most radiogenic Sr compositions, whereas Shisheisky rocks have intermediate compositions (0.7033–0.7036). Sr isotope ratios do not correlate with SiO_2 (or other major elements) in primitive rocks (Figure 9). The most SiO_2-rich primitive andesites from Shiveluch volcano and Shisheisky complex have relatively low $^{87}Sr/^{86}Sr$ (~0.7034–0.7035), whereas compositions of basaltic rocks from Zarechny, Kharchnisky and Shiveluch volcanoes are very scattered and extend to significantly more radiogenic values (0.7033–0.7038, Figure 8, 9).

Two samples from Nachikinsky volcano (N45A, N44A, Table 2) have slightly higher $^{87}Sr/^{86}Sr$ (0.70330–0.70331) compared to other Nb-rich basalts from this volcano (~0.7029–0.7030) [*Portnyagin et al.* 2005a], which correlate with relatively low $^{143}Nd/^{144}Nd$ (0.52974–0.52984). Compositionally these basalts are similar to some alkaline basalts from the area nearby Ichinsky volcano in the Sredinny Range [*Churikova et al.* 2001] and suggest involvement enriched (EM-1?) material in the genesis of some recent rocks from the northernmost volcanoes in the CKD.

3. DISCUSSION

3.1. Major Components in the CKD Magmas

Several previous works identified the major sources that contribute to the compositional diversity of the CKD magmas to be (i) mantle wedge, (ii) subducting plate, and (iii), possibly, an overriding lithospheric plate [e.g., *Kepezhinskas et al.* 1997; *Churikova et al.* 2001; *Münker et al.* 2004; *Dosseto et al.* 2003; *Bindeman et al.* 2004; *Portnyagin et al.* 2005a]. The picture is however far from the quantitative understanding of the importance of these sources in creating compositional diversity of the CKD magmas. Thus, our first goal here is to identify the principle geochemical components contributing to the CKD magmas, which would make possible to elucidate their sources and propose quantitative and predictive geochemical models explaining much of the geochemical variability in the CKD in terms of few compositional variables and processes.

As evident from simple binary diagrams (Figure 6, 9), the major and trace element and Sr-Nd-O isotope variations of the primitive CKD magmas can be at first glance described in terms of three-component mixing. Much of the major element variations are explained by mixing of basaltic and dacitic primitive melts. Primitive basalts clearly require mantle source. The origin of the primitive dacitic component introducing "adakitic" signature to the northern CKD rocks [e.g. *Yogodzinski et al.* 2001] is uncertain and should be specifically discussed. Third component(s) contributes to high K_2O, Ba, Sr, $^{87}Sr/^{86}Sr$ and $\delta^{18}O$ but has little or no effect on major and moderately incompatible (Ti, Y, V) element contents. High Ba/Nb and $^{87}Sr/^{86}Sr$ suggest that this component may be hydrous fluid derived from the subducting plate [e.g. *Kepezhinskas et al.* 1997; *Churikova et al.* 2001]. While extremely high $\delta^{18}O$ in some CKD rocks suggest massive crustal assimilation [*Bindeman et al.* 2004]. Below we discuss the key compositional features of these major components and their possible origin.

3.2. Mantle Component(s)

High Mg# and Ni content in primitive CKD rocks leave no doubts that their primary melts were derived from the mantle wedge or, at least, interacted with high-Mg# mantle peridotite on their way to surface. Composition of the pristine mantle wedge below Kamchatka, that is mantle composition as it was before involvement in magma generation processes, has been discussed in numerous publications [e.g., *Kersting and Arculus* 1995; *Turner et al.* 1998; *Kepezhinskas et al.* 1997; *Churikova et al.* 2001; *Münker et al.* 2004; *Portnyagin et al.* 2005a]. Most of these works focused on the isotope composition of the mantle wedge. Major and trace element composition of the mantle is more difficult to constrain because the estimates depend on the processes involved, and there have been few attempts specifically addressing this important question [e.g., *Hochstaedter et al.* 1996; *Kepezhinskas et al.* 1997].

In general, CKD basalts and, particularly, those from Tolbachik and Ushkovsky volcanoes are similar to primitive MORB in terms of major elements (Figure 6). High CaO, TiO_2 and Na_2O in these basalts suggest relatively fertile lherzolitic mantle beneath northern Kamchatka, which is similar to common MORB source or even more fertile beneath the northernmost Nachikinsky volcano [*Portnyagin et al.* 2005a]. Melting of fertile (primitive mantle-like [*McDonough and Sun,* 1995]) to slightly Nb-depleted mantle beneath CKD is also in agreement with the Nb-Y systematics in the primitive magmas (Figure 10). Significantly Nb-enriched sources are apparently required for parental Nachikinsky magmas.

There appears to be little evidence for the large scale two-stage mantle melting proposed for the origin of the CKD magmas [e.g. *Hochstaedter et al.* 1996]. At least, the idea about re-melting residues after extraction Ushkovsky magmas beneath Klyuchevskoy volcano [*Hochstaedter et al.* 1996] clearly does not meet our data (Figure 10). Parental magmas of these volcanoes can be produced by different degrees of melting of the same fertile source similar to the primitive mantle. Weather the residues of the plateau basalts in the basement of the Klyuchevskoy Group can serve as the source of the present-day magmatism [*Churikova et al.* 2001] is difficult to assess with presently available data. In general, the variations of Nb at similar Y in the average CKD compositions (except Nachikinsky magmas) can be explained by no more than ~1% of previous melt extraction from initially homogeneous and fertile source. This can readily reflect initial mantle heterogeneity rather than multiple melt extraction beneath the CKD.

On the other hand, assuming derivation of Nb entirely from the mantle wedge may be not valid for CKD where Nb-rich slab melts were likely involved in magma genesis [e.g. *Kepezhinskas et al.* 1997; *Münker et al.* 2004]. In this case, the composition of the CKD mantle wedge prior to subduction-related metasomatism, which variably enriched mantle wedge in Nb and other trace elements, could be more depleted than indicated by the composition of parental magmas. This alternative explanation of compositional heterogeneity of the CKD magma sources is supported by decoupling Nb/Ta and Zr/Hf in the CKD rocks [*Münker et al.* 2004] and applied as working hypothesis in our work. On the basis of this data we assumed for all CKD volcanoes (except Nachikinsky) initially depleted mantle source of the same composition as estimated by [*Workman and Hart*, 2005]

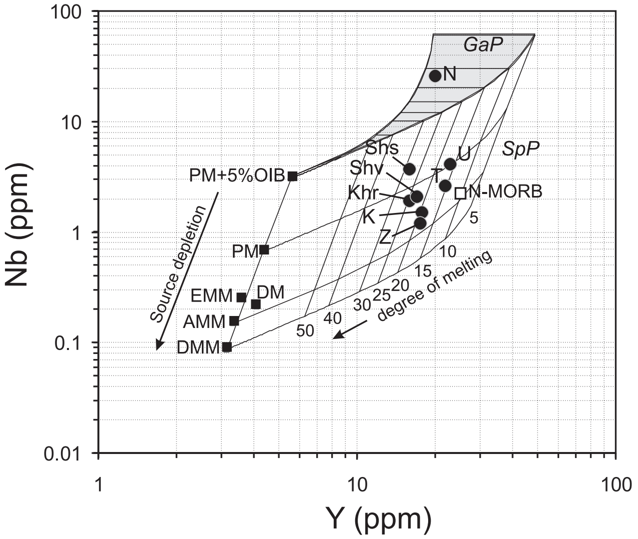

Figure 10. Systematics of Nb and Y concentrations in average compositions of primitive CKD magmas. Volcanoes are labelled as in Figure 5. Solid squares demonstrate compositions of different mantle sources of oceanic magmas: depleted MORB mantle (DMM), enriched MORB mantle (EMM) and average MORB mantle (AMM) [*Workman and Hart*, 2005]; depleted mantle (DM) [*Salters and Stracke*, 2004]; primitive mantle (PM) [*McDonough and Sun*, 1995]; primitive mantle plus 5% of average ocean island basalts (PM+5%OIB) [*Sun and McDonough*, 1989]. Trajectories of batch modal partial melting are calculated after [*Shaw*, 1970]. Curves labelled as "*SpP"* were calculated for DMM, PM and PM+5%OIB and refer to melting in spinel facies (ol:opx:cpx: spl=57:28:13:2) and bulk partition coefficients 0.0034 (Nb) and 0.088 (Y) [*Workman and Hart*, 2005]. Shaded field labelled as "*GaP"* encloses melt compositions produced by mixing of melts from Nb-enriched PM+5%OIB source in garnet facies (ol:opx: cpx:ga =53:8:34:5) [*Salters and Stracke*, 2004] and melts from the same source composition in spinel facies (as above); bulk partition coefficients for garnet peridotite were assumed 0.0047 (Nb) and 0.26 (Y) [*Salters and Stracke*, 2004]. The diagram is constructed in a way similar to the Nb-Yb diagram by [*Pearce and Parkinson*, 1993] and aimed at distinguishing source enrichment/depletion and variations in degrees of partial melting. In general, the approach provides a minimum estimate for the source depletion before melting because enrichment of mantle source in Nb can associate with metasomatism by slab-derived melts.

for the Average MORB Mantle (AMM). Alternative estimate for the CKD mantle wedge, for example, as "Depleted MORB Mantle" by [*Salters and Stracke*, 2003] does not affect the major conclusions of the study, although absolute values of estimated parameters of magma origin (degree of melting, amount of enriched component etc.) are certainly model dependent. High concentrations of Nb, Zr and Ti in the Nachikinsky primitive melts require mantle source more enriched in incompatible trace elements (Figure 10). Quantitative modeling of these magmas was beyond the scope of this work and will be presented elsewhere.

With regard to the isotope data, all authors have agreed thus far that the CKD mantle wedge is compositionally similar to common MORB asthenospheric mantle, based on the rather homogeneous and relatively radiogenic MORB-like Nd isotope ratios in lavas and mantle xenoliths [e.g., *Kepezhinskas et al.* 1997; *Churikova et al.* 2001]. The conclusion is further confirmed by the low $^{87}Sr/^{86}Sr$ (<0.7030) and $\delta^{18}O$ (~5.2 ‰) in rocks from Nachikinsky and Khailulia volcanoes, which were derived from the mantle only weakly modified by subduction-related processes compared to the southern CKD volcanoes [*Portnyagin et al.* 2005a]. Although these northern CKD magmas originate from the mantle more enriched in trace elements than required for the majority of the CKD rocks (Figure 10), residues after extraction of a few percent melt from the Nachikinsky-type magma sources can potentially serve as the sources of the abundant subduction-related CKD magmatism. Therefore, isotope compositions of the Nachikinsky magmas can be informative of the CKD mantle wedge prior subduction-related metasomatism and point to low $^{206}Pb/^{204}Pb$ (~18), low $^{87}Sr/^{86}Sr$ (<0.7030) and high $^{143}Nd/^{144}Nd$ (~0.5131) mantle wedge composition. Our new data (samples N44A and N45A in Table 2) suggest that slightly isotopically enriched mantle with EM-1 "flavor" could be also involved in the origin of the northernmost Nachikinsky magmas (Figure 1B). There is, however, no evidence that enriched mantle sources contributed to the majority of subduction-related magmas in the southern CKD.

3.3. Primitive Dacitic Component

Presence of primitive high-SiO_2 (dacitic or 'adakitic') component is a distinctive feature of primitive magmas from the CKD, recognized and interpreted as such by most researchers [*Volynets et al.* 1997; 2000; *Yogodzinski et al.* 2001; *Churikova et al.* 2001; *Münker et al.* 2004]. We estimated the composition of this component by little extrapolating the compositional trends of primitive (Mg#>0.6) Shisheisky basalts, basaltic andesites and andesites to SiO_2=64 wt% (Figure 6, 9, 11; Table 3), that is, to the limit of real compositions of primitive rocks occurring in the Shisheisky Complex. Unfortunately, trace element data were not available for the most extreme magnesian andesites with SiO_2=60–63 wt% (Table 1). Estimation of trace element content in the dacitic end-member was thus not as straightforward as for major elements and required some more extrapolation (e.g. Figure 11D). The estimated primitive dacite component (Table 3) has trondhjemitic composition with high Mg# (~0.68), Ni (70–150 ppm), SiO_2 (~64 wt %), Na_2O (~5.5 wt %), Al_2O_3 (~17 wt %), moderately high K_2O (~1.6

wt %) and low FeO (~3.5 wt %), CaO (~3.5 wt. %), MgO (~4 wt. %) and TiO_2 (~0.4 wt %). The dacitic melt has low concentrations of Y (~10 ppm) but high Zr (~120 ppm), Sr (~600 ppm) and LILE (e.g., Ba~600 ppm). $^{87}Sr/^{86}Sr$ (~0.7035) is moderately radiogenic but somewhat lower compared to many basalts and basaltic andesites from the other parts of the CKD. Nd isotope composition ($^{143}Nd/^{144}Nd$~0.5134) is slightly less radiogenic than the majority of basaltic CKD rocks. Oxygen isotope compositions of amphiboles from Shiveluch and Shisheisky andesites, which approach the composition of the primitive dacitic component, scatter from MORB-like (~5.2‰) up to ~6 ‰.

Presence of amphibole in the Shisheisky complex primitive andesites suggests hydrous nature of the dacitic component. Assemblage of high Mg# orthopyroxene and amphibole in primitive Kamchatkan andesites could crystallize under water saturated conditions at 0.2–0.3 GPa pressure (5.5–6.5 wt % H_2O in melt) and temperature 940–960°C as demonstrated in experimental study by *Blatter and Carmichael* [2001] on compositionally similar andesites from Mexico. Even higher H_2O concentration (up to ~11 wt. % [*Grove et al.* 2003]) is required to stabilize amphibole with Mg# ~0.78 on liquidus at inferred ΔfO_2(NNO) ~ +2 for andesites from Shisheisky Complex (our unpublished data). Thus mineral-

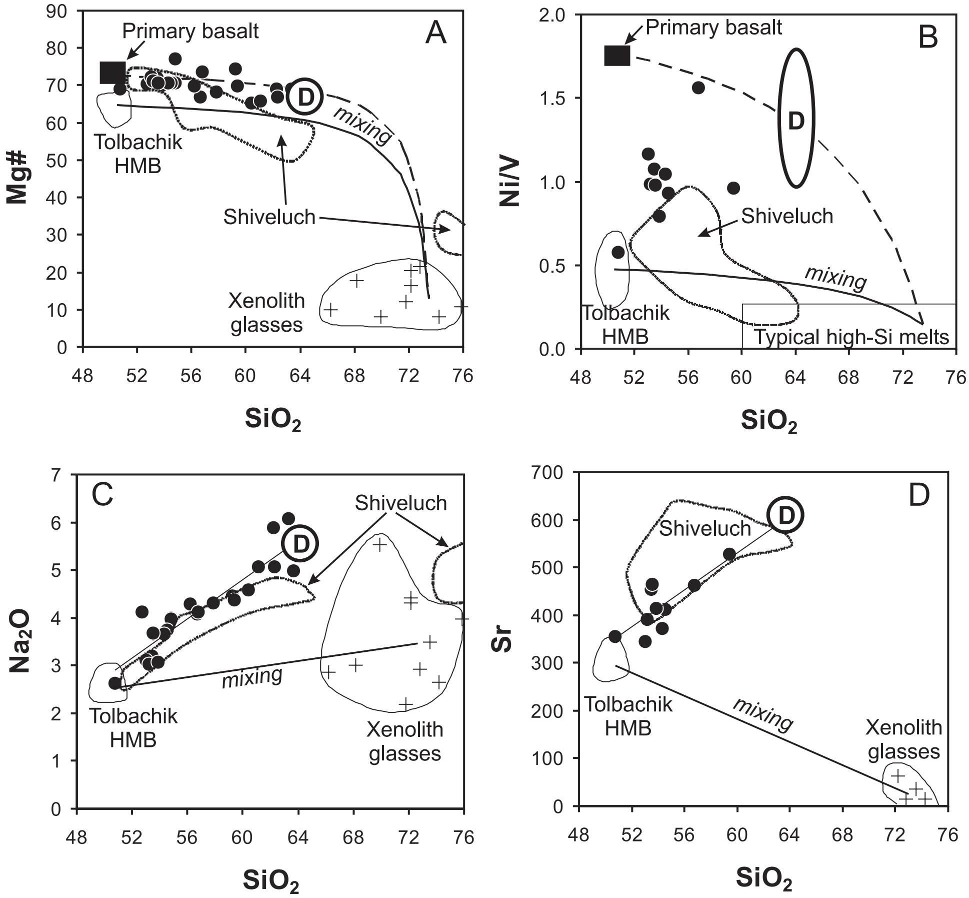

Figure 11. Illustration of possible effects of mixing basalts and evolved rhyolitic melts on creating compositional peculiarity of the Shisheisky Complex rocks. The compositions of the Shisheisky rocks are shown by solid circles (this study and [*Pilipchuk et al.* 2006]). The line of linear regression of the Shisheisky data is shown in plots C and D. Encircled "D" denotes inferred composition of the primitive dacite component. Rhyolitic glasses from partially melted xenoliths from the Shisheisky complex rocks are shown by crosses. Fields of Tolbachik primitive basalts, rocks and interstitial glasses from Shiveluch volcano (typical calc-alkalic rock series) are shown for reference. Rectangular field in plot B encloses composition of typical high SiO_2 (>60 wt %) magmas of Kamchatka [*Krivenko et al.* 1990; this study]. Solid labelled lines denote mixing curves between the average compositions of primitive Tolbachik basalts (solid line), primary mantle melt (dashed line) and rhyolitic melts. Note that mixing primary basaltic magmas and rhyolites can hypothetically explain high Mg# and Ni/V (and Ni content) in the Shisheisky series. The mixing model cannot explain high Na_2O and Sr in primitive andesites.

ogical data testify for highly hydrous nature of the primitive dacitic component with H_2O=5.5–11 wt %.

Compositions which are most similar to the inferred primitive dacite component were reported for metasomatic "adakitic" veins from mantle xenoliths in the Miocene alkali basalts from the Kamchatka Isthmus [*Kepezhinskas et al.* 1995, 1996]. These veins may therefore represent intrusive analogues of primitive dacitic melts "frozen" in the lithospheric mantle beneath northern Kamchatka.

3.4. Origin of Primitive Dacitic Component by Crustal Processes

Several hypotheses have been proposed to explain the origin of high Mg# andesites and adakites in island-arc settings, which may also be applicable to the origin of primitive dacitic component in the CKD magmas: (1) crystal fractionation; (2) mixing of primitive basaltic melts and rhyolites, or assimilation of granitic rocks in basalts; (3) direct slab melting; (4) hydrous fluid flux mantle melting, (5) interaction of slab melts with the overlying mantle wedge [e.g., *Kay*, 1978; *Defant and Drumond*, 1990; *Sen and Dunn,* 1994; *Hirose*, 1997; *Yogodzinski et al.* 1994, 1995; *Kelemen et al.* 1995; 2003a,c; *Blatter and Carmichael*, 1998, 2001; *Shimoda et al.* 1998; *Tatsumi,* 1981, 2001; *Tatsumi and Ishizaka,* 1981; *Tatsumi et al.* 2003; *Carmichael*, 2002; *Grove et al.* 2002; 2003; 2005; *Bindeman et al.* 2005].

Early crystallization of Fe-Ti oxides and/or amphibole from hydrous and highly oxidized magmas can drive fractionating magma toward high SiO_2 compositions without sharp decrease of Mg# [e.g., *Moore and Carmichael,* 1998]. The origin of primitive andesites from Shisheisky Complex through fractional crystallization of primitive basalts seems however unlikely because of several reasons. First, amphibole and Fe-Ti oxides are not present among phenocrysts in primitive basalts and basaltic andesites from Shisheisky Complex, whose crystallizing assemblage consist of high-Mg olivine, orthopyroxene, clinopyroxene and moderately oxidized chromium spinel (Cr/(Cr+Al)=0.60–0.78, Fe^{+3}/(Fe^{+3}+Cr+Al)=0.1–0.2, our unpublished data). Amphibole together with orthopyroxene appears only in primitive andesites at SiO_2>58 wt % and is particularly common in low-Mg# evolved rocks. Second, all primitive Shisheisky rocks have extremely high Ni (up to 200 ppm, Table 1), Ni/V (Figure 11B) and exhibit very weakly decreasing Mg# over large range of SiO_2 (Figures 3 and 11) compared to typical calc-alkaline trend of crystallization of Shiveluch rocks governed by early appearance of amphibole and Fe-Ti oxides on liquidus [e.g., *Volynets et al.* 1997]. And finally, massive crystallization of Fe-Ti oxides would lead to decoupling of Ti and V from other incompatible elements in primitive magmas (e.g. Y, REE), which is not the case for Shisheisky rocks with essentially identical Ti/Y in basalts (230–300) and andesites (250–320).

Elevated $\delta^{18}O$ and $^{87}Sr/^{86}Sr$, quartz xenocrysts and somewhat unradiogenic $^{143}Nd/^{144}Nd$ in the Shisheisky andesites (Figure 8, 9) suggest that assimilation of continental-type (?) crustal material could be important process in their genesis [e.g. *Bindeman et al.* 2005]. In order to test this hypothesis, we consider here the simplest way to generate high Mg# andesites through mixing of primitive basalts of mantle origin and rhyolitic melts, which can originate either by extensive fractionation of basaltic magmas or by partial melting of the Kamchatka crust (Figure 11). As examples of crustal rhyolitic melts, we use in the modeling the compositions of high-Si glasses surrounding partially melted/reacted with matrix melt quartz xenocrysts from Shisheisky rocks (Table 1). As illustrated in Figure 11A, high SiO_2 and Mg# in primitive andesites can be indeed explained by mixing of primitive basaltic and rhyolitic melts as was also proposed for calc-alkaline rocks world-wide [e.g. *Brophy,* 1987; *Conrad et al.* 1983; *Kay and Kay,* 1985; *Blatter and Carmichael,* 1998]. The typical primitive basalts from Tolbachik volcano, which are among the most primitive in the CKD, however can not serve as an appropriate basaltic end-member for such mixing because Mg# of the Shisheisky rocks is even higher than in Tolbachik primitive basalts. In order to fit the mixing line with the Shisheisky compositions, the basaltic end-member should have composition of primary mantle melt with MgO~14 wt% and Mg#~0.75 (Table 3). Similarly, high Ni content and high Ni/V, Ni/Sc etc. ratios in the Shisheisky andesites can only be explained if the rhyolitic melts mix directly with primary mantle melts with Ni~500 ppm and Ni/V > 1.5 (Figure 11B). Although the mixing of primary basaltic melts with crustal rhyolitic melts is hypothetically possible, the model however fails to explain high Na_2O and Sr in the Shisheisky andesites (Figure 11 C, D). Appropriate rhyolitic melt end-member in such mixture fitting the trend of Shisheisky rocks should have Na_2O up to 10 wt% and Sr up to 1000 ppm. Rhyolites of such composition are not known in Kamchatka and can hardly be produced by crystallization of basaltic magmas, which commonly involve plagioclase, or low-degree partial melting of plagioclase-bearing crustal material (see also discussion in [*Kelemen et al.* 2003c]). Finally, it should be noted that perfect mixing of basaltic and rhyolitic melts might be improbable in nature [*Campbell and Turner*, 1985; *Bindeman and Bailey,* 1994; *Blatter and Carmichael,* 1998]. Assimilation of crustal material is energy consuming process and should likely cause massive crystallization [e.g. *Reiners et al.* 1995; *Bohrson and Spera,* 2001], which is not observed in nearly aphyric andesites from Shisheisky complex.

Although our detailed investigation identified some xenogenic material in the Shisheisky andesites (mantle olivine, quartz), the amount of the material is small (<1%) and was found only in large volume of crushed rock. We interpret the observations as evidence for rather rapid transport of the Shisheisky magmas through the crust, so that xenogenic material was not completely reacted with the host magma. Xenogenic, sometimes abundant crustal material was also described in basaltic magmas throughout the CKD [e.g. *Fedotov*, 1983]. Therefore, there is no reason to believe that the primitive andesites from the Shisheisky complex are different from other CKD rocks due to the presence of xenogenic material and they are contaminated much stronger as compared to other rocks in the CKD.

Summarizing all observations above, we conclude that the processes of crustal fractionation, mixing and assimilation do not provide plausible explanation for the origin of the primitive dacite component in primitive CKD magmas and, in general, geochemical zonation along the CKD.

3.5. Origin of Primitive Dacitic Component by Slab or Mantle Melting

Alternative explanation for the origin of the primitive dacitic component is related to melting of the subducting Pacific Plate beneath Kamchatka [e.g. *Yogodzinski et al.* 2001] (Figure 12). In particular, primitive dacite component is enriched in trace elements which are weakly soluble in hydrous fluids (e.g., Zr, Nb and also Th and LREE, our unpublished ICP-MS data on Shisheisky andesites) [e.g., *Tatsumi et al.* 1986; *Brenan et al.* 1995; *Keppler,* 1996; *Green and Adam*, 2003]. These elements should be most likely transported in sediment- and/or basalt derived melts (or supercritical fluids) [e.g., *Rapp et al.* 1999; *Johnson and Plank,* 1999; *Tatsumi,* 2001; *Kelemen at al.* 2003a,c].

Our modeling indicates that the pattern of highly incompatible elements (K, Ba, Nb, Sr) in the primitive dacite component can be indeed produced by ~5–10% partial melting of eclogite composed by 80% MORB and 20% of local sediments (Figure 13A). High Mg# and Ni content however preclude the dacite component from being a direct slab-derived eclogite melt as was also argued for high-Mg# andesites from the Aleutian Arc and elsewhere [e.g., *Kay*, 1978; *Yogodzinski et al.* 1994; 1995; *Tatsumi* 2001; *Kelemen et al,.* 2003a]. Moreover, the eclogitic melts are expected to have strong garnet signature (high Dy/Yb, Ti/Y) and significantly lower Y, Zr and Ti contents compared to the inferred dacitic component in the CKD magmas (Figure 13A). These geochemical features imply that processes of modification of slab melts on their way through mantle wedge should be involved in the origin of the dacitic component. Although pattern of highly incompatible elements in the dacitic component mimics closely that of eclogite melts, less incompatible and major elements in the component may reflect re-equilibration of eclogite melts with mantle wedge.

Limited interaction of eclogite melts with the mantle wedge was widely proposed to explain the origin of high Mg# andesites [e.g., *Kay,* 1978; Yogodzinski et al. 1994, 1995]. Melts leaving the subducting slab are however in compositional disequilibrium with the overlying mantle peridotite, and a critical aspect of eclogite melt – peridotite interaction is whether the eclogitic melts can survive below the wet solidus of peridotite, which is placed by different authors between ~800 and 1000°C at 2–3 GPa [*Green*, 1973; *Wyllie*, 1979; *Thompson*, 1992; *Mysen and Boettcher*, 1975; *Grove et al.* 2002; 2003]. The processes occurring at the slab-mantle interface are poorly known, and two different scenarios of the interaction between eclogite melts and mantle should be considered (Figure 12): (i) all eclogite melt is exhausted during the reaction with mantle peridotite producing secondary olivine-free pyroxenite, and (ii) liquid never disappear during the reaction with the mantle wedge but evolves toward equilibrium with mantle peridotite.

According to the first scenario, the likely fate of eclogite melts, when they react with peridotite converting it to olivine- and melt-free high Mg# (garnet) pyroxenite, is "thermal death" [*Yaxley and Green*, 1998; *Rapp et al.* 1999; *Kelemen et al.* 2003c; *Sobolev et al.* 2005]. The hybridized mantle, consisting of "blobs" of pyroxenite, can be melted later through decompression or water-rich fluid flux, for example, resulting from the breakdown of serpentinites in the deeper portions of the subducting plate [e.g., *Ringwood,* 1990; *Rüpke et al.* 2002]. Although we did not model quantitatively the conversion of mantle peridotite to olivine-free pyroxenite and subsequent fluxed melting of the secondary pyroxenite (high-Mg# eclogite), the process appears to be capable to produce appropriate high-SiO_2 melts (primitive dacitic component) involved in the CKD magma origin. The partial melts from pyroxenite should be silica-rich like in the case of eclogite melting [e.g. *Rapp et al.* 1999]. The pattern of highly incompatible elements in secondary pyroxenite melts could be inherited from reacted eclogite melts but Mg# and Ni should be significantly higher compared MORB eclogite melting [*Sobolev et al.* 2005].

Following the second scenario of eclogite melt-mantle interaction, eclogitic melts leaving the subducting slab are proposed to react with the mantle wedge so that the liquid never completely solidifies during the interaction and changes its composition towards basalt as the reaction proceeds [e.g., *Yogodzinski et al.* 1994; *Tatsumi* 2001; *Kelemen et al.* 2003a,c]. Eclogite melt – mantle interaction can gener-

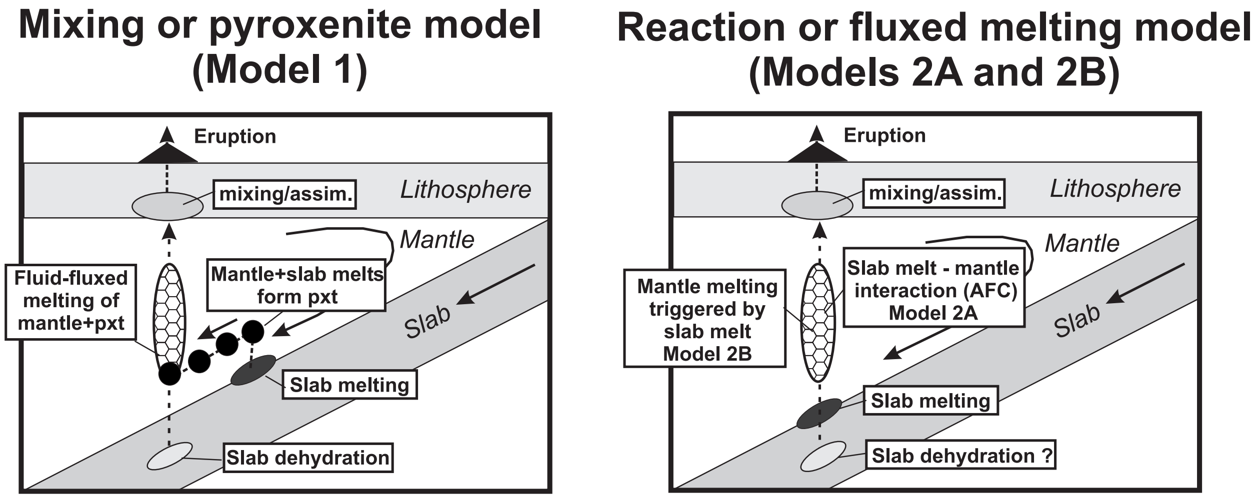

Figure 12. Schematic illustration of possible scenarios for magma generation beneath the CKD. Model 1 assumes reaction of eclogite melts with mantle peridotite producing secondary high-Mg# pyroxenites in the mantle wedge, which are melted on later stage together with surrounding peridotite material. Model 2 suggests continuous reactive interaction between eclogitic melts and mantle wedge peridotite. Hydrous eclogitic melt triggers mantle melting (model 2A) or, in alternative view, assimilates mantle material as the slab melt rises, heats and decompresses in the mantle wedge (model 2B). All models assume that some shallow assimilation may follow mantle melting and occurs in the overriding plate. Combination of different mechanisms of magma origin can certainly take place beneath the CKD. See further explanations in text.

ate high Mg# and Ni content in the dacite component, while significantly increasing concentration moderately incompatible elements (Ti, Y, HREE) and reducing initially high Sr/Y, Zr/Y and Ti/Y ratios in the resultant melt [*Tatsumi* 2001; *Kelemen et al.* 2003a,c]. We were able to closely reproduce Ba, Nb, K, Sr, Na, Ti and Y in the primitive dacite component by numerical simulation this kind of slab melt – mantle interaction (Figure 13B) and conclude that the dacite component can represent a product of limited interaction between mantle and eclogite slab-derived melts (see electronic Supplement Methods for details of modeling). An exception is high Zr concentration in the dacite component, which was not reproduced in our modeling and increased only slightly during the simulated mantle–eclogite melt interaction (Figure 13B). In order to explain high Zr concentrations in the dacite component, eclogite melts reacting with mantle wedge should also have about 2–3 times higher concentrations of this element. It is possible that partition coefficients during slab melting beneath Kamchatka were significantly lower compared to those used in our modeling (compilation by [*Kelemen et al.* 2003c]), or the composition of subducting plate was more Zr-rich than N-MORB. If we assume that igneous component in the composite eclogite was enriched basalt with Zr~150 ppm (~2 times higher than N-MORB), like that recovered from Meiji and Detroit Seamounts [*Regelous et al.* 2003], closer fit between modeled composition and the dacite component can be achieved.

Compositions of low to moderate degree partial eclogite melts at ~3 GPa pressures in presence H_2O were shown to have andesitic to rhyolitic compositions with high Na_2O, low CaO, MgO and FeO [e.g. *Sen and Dunn,* 1994; *Rapp and Watson,* 1995, *Proteau et al.* 1999]. On the other hand, experiments demonstrated that primitive andesites with SiO_2 up to 60 wt% can also be produced by direct melting of fertile peridotite under low temperature (<1150°C) water-saturated conditions [e.g., *Green*, 1973; *Hirose* 1997; *Hirose and Kawamoto,* 1995] or be in equilibrium with olivine and orthopyroxene under upper mantle conditions [*Tatsumi,* 1981; *Baker et al.* 1994; *Grove et al.* 2003]. SiO_2 in partial melts increases with increasing water pressure and source depletion [e.g. *Falloon and Danyushevsk*y, 2000], and thus dacitic melts also could be produced by partial melting of mantle peridotite. The low-temperature hydrous mantle melt compositions are broadly similar to eclogitic melts yet have higher Mg# reflecting equilibrium with mantle minerals [*Hirose* 1997]. It seems therefore likely that eclogite-derived, hydrous and siliceous melts can approach equilibrium with mantle peridotite very quickly by little modification of their composition. Although the experimental melts by *Hirose* [1997] have higher CaO, Al_2O_3 and lower Na_2O, FeO and K_2O compared to primitive andesites from Kamchatka (Figure 6), we suggest that the primitive dacitic melt (and the parental melts of all CKD volcanoes) could be in equilibrium with the mantle mineral assemblage (olivine + orthopyroxene ± clinopyroxene) at pressures of

1–1.5 GPa, as has also been argued for magnesian andesites from Northern California, Japan and Mexico [e.g., *Tatsumi,* 1981; *Blatter and Carmichael* 2001; *Grove et al.* 2003]. In this case, high SiO_2 and low CaO, MgO, FeO, TiO_2, Y, V in the primitive dacite melt compared to partial melts from fertile peridotite [e.g., *Hirose* 1997; *Hirose and Kawamoto*, 1995; *Gaetani and Grove*, 1998] may indicate re-equilibration of eclogite melts with more depleted mantle [e.g., *Falloon and Danyushevsky*, 2000; *Grove et al.* 2003].

In summary, we favor the origin of the primitive dacite component due to slab melting followed by eclogite melt-mantle interaction, which appears to explain both major and trace element composition of the dacitic component. In principle, we can not exclude that the primitive dacite component can also originate through melting of delaminated lower crustal blocks under mantle conditions or through melting of veined lithospheric mantle impregnated by eclogite melts [e.g., *Kepezhinskas et al.* 1995]. In this case, origin of the dacite

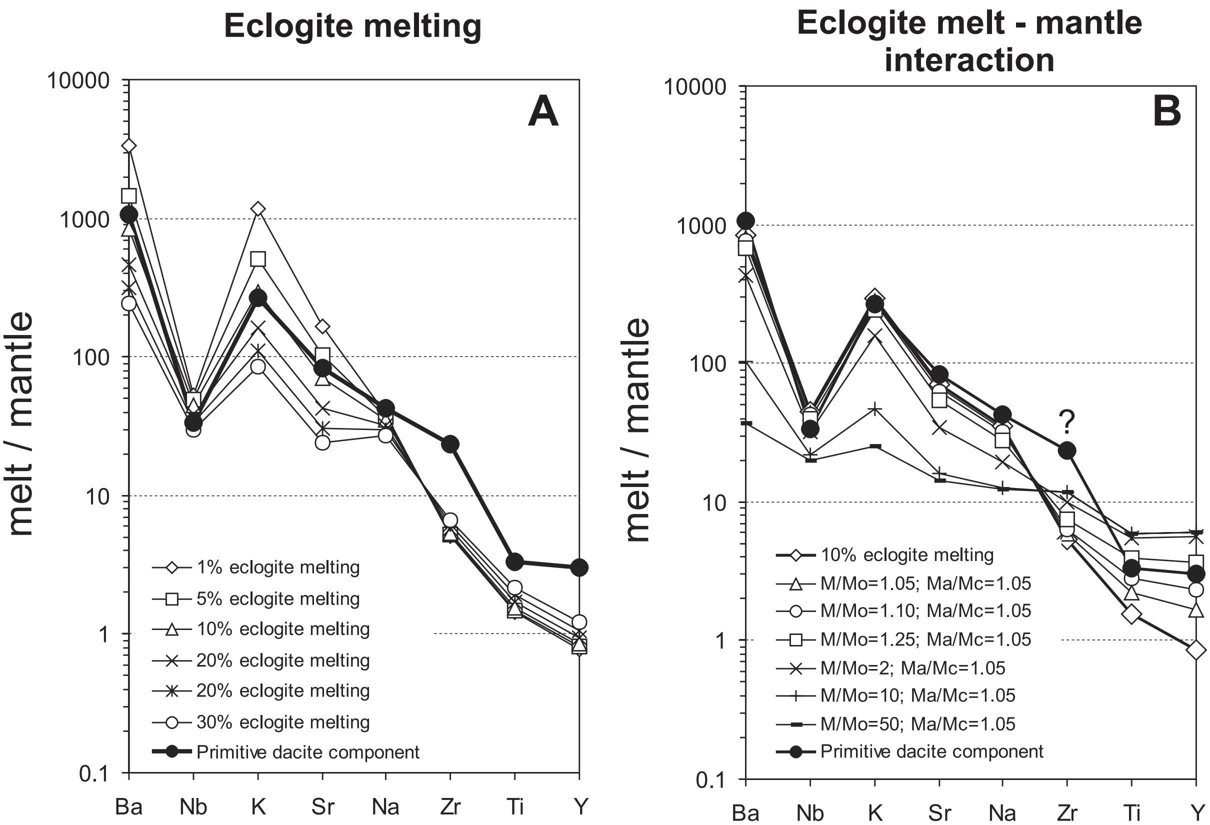

Figure 13. Results of modelling eclogite melting (Figure A) and eclogite melt – mantle interaction (Figure B). Eclogite melting was modelled assuming source composition composed by 90% NMORB [*Sun and McDonough*, 1989] and 10% Kamchatkan sediments [*Plank and Langmuir,* 1998]. Eclogite mode was 59% pyroxene, 40% garnet, 1% rutile. Melting was assumed to be batch and modal. Partition coefficients are from compilation [*Kelemen et al.* 2003c]. Interaction of melt produced by 10% of eclogite melting with mantle peridotite was modelled using AFC model [*De Paolo,* 1981] at constant assimilation rate (M_a/M_c, mass of assimilated material per mass crystallized material) and different extent of the reaction expressed in the value of the liquid mass increase (M/M_o). Mantle composition was the Average MORB Mantle (AMM) [*Workman and Hart*, 2005]. Bulk partition coefficients between melt and fertile peridotite are from compilation [*Kelemen et al.* 2003c]. Note similar concentrations of highly incompatible elements (Ba, Nb, K, Sr) in the primitive dacite component and eclogite melts of 5–10% of melting (plot A). Moderately incompatible elements (Zr, Ti, Y) are systematically lower in the eclogite melts at any degree of melting and are buffered by residual garnet. Interaction of the eclogite melts with spinel peridotite (plot B) causes sharp increase in concentrations of moderately elements (e.g. Ti, Y) and has little effect on concentrations of highly incompatible elements so that Sr/Y, Zr/Y, Ti/Y decrease quickly at small increase of the liquid mass. Good coincidence of incompatible elements (except Zr, see text) in the primitive dacite component and modelled product of eclogite-melt-mantle interaction is approached at the liquid mass increase M/M_o=1.1.–1.25. See text and Supplementary Materials for more details and discussion.

component may be not related to the ongoing subduction beneath CKD [e.g., *Park et al.* 2002]. This scenario is difficult to distinguish from processes of slab melt – mantle interaction outlined above. Moreover, crustal origin of the primitive dacite component fails to explain increasing amount of the dacite component toward the Pacific slab edge.

3.6. Fluid and/or Lithospheric Component(s)

Slab-derived hydrous fluids enriched in incompatible elements (e.g., LILE, B, U) were proposed to play important role in generating CKD magmatism [e.g., *Hochstaedter et al.* 1996; *Kepezhinskas et al.* 1997; *Turner et al.* 1998; *Dorendorf* et al. 2000; *Ishikawa et al.* 2001; *Churikova et al.* 2001]. Assessing the fluid component in the CKD magmas is however not straightforward and depends on assumption of elements and ratios which are informative about involvement of the slab fluids in magma genesis.

The primitive dacite component (modified eclogite melt), which we favor in this study, has many compositional features which are traditionally ascribed to hydrous slab-derived fluids (for example, high H_2O, high LILE and low Nb content). Involvement of eclogite melts in magma generating processes is difficult to distinguish from addition of hydrous fluids (see also [*Kelemen et al.* 2003a]), and we demonstrate in the following chapters that hydrous fluids indeed might not be required to explain the composition of the majority of CKD rocks. Involvement of hydrous fluids might be only required to account for exceptionally high Ba/Nb (>250) and Sr/Y (>60) in some rocks from volcanoes located at intermediate distances (50–100 km) from the slab edge (Figure 8).

Dorendorf et al. [2000] proposed that large amount of hydrous fluid might be responsible for unusually high $\delta^{18}O$ in Klyuchevskoy rocks correlating with high K/Ti, U/Th, La/Yb. The amount of hydrous fluid (with $\delta^{18}O$~20‰) involved in magma generating processes must be in this case of the order of 10–20%. This large amount of fluid can hardly be reconciled with direct fluid-fluxed melting and should lead to an enormously high degree of melting (>30%) beneath CKD [e.g. *Hirschmann et al.* 1999; *Eiler,* 2000; *Katz et al.* 2003]. This large amount of hydrous slab fluid was thus proposed to be accumulated in the mantle over a long period of time without causing any melting. According to *Dorendorf et al.* [2000] model, the mantle was probably too cold to melt, and the accumulation of high $\delta^{18}O$ fluid occurred through formation of hydrous minerals in the mantle wedge, which was re-heated and melted at a later stage.

Alternatively, *Bindeman et al.* [2004; 2005] proposed the origin of high $\delta^{18}O$ CKD magmas through assimilation of crustal material beneath Kamchatka. Because the high $\delta^{18}O$ was found in very primitive magmas and high Fo olivines, the model requires assimilation of mafic crustal and/or mantle rocks, which would not strongly alter the composition of primitive magmas in terms of major elements (e.g., SiO_2, FeO, CaO, Na_2O). The majority of the Kamchatkan crust is Cretaceous mafic to ultramafic arc basement that was accreted to Kamchatka several million years ago [e.g., *Kamenetsky et al.* 1995; *Konstantinovskaia,* 2001]. These rocks, hydrothermally-altered by seawater, have high $\delta^{18}O$ (up to 11‰ for mafic granulites and amphibolites, [*Bindeman et al.* 2004, and references therein] and thus could represent the common assimilant beneath CKD. The large amount of assimilation (up to 50%, see Figure 3 in [*Bindeman et al.* 2005]) required by the model could be explained if abundant magmatism in the CKD caused abnormally hot conditions in the lower crust favoring extensive crustal assimilation by ascending primitive magmas [e.g., *Reiners et al.* 1995].

Delamination of lower crustal, high-$\delta^{18}O$ basement due to subduction erosion [*von Huene et al.* 2004] or due to the corner mantle flow [*Kelemen et al.* 2003b] could also deliver the older arc blocks into the zone of magma generation as proposed in the Andes and other areas of thickened crust and slab-crust coupling [*Kay et al.* 2005]. A third possible explanation is that present-day volcanism in CKD occupies the former fore-arc of the Eocene-Pliocene volcanic arc of the Sredinny Ridge of Kamchatka [e.g., *Avdeiko et al.* 2002; *Park et al.* 2002]. Mafic rocks reworked by shallow high-$\delta^{18}O$ slab-fluids in the former fore-arc region could be mobilized by the present-day magmatism beneath CKD.

In summary, available data on the CKD rocks suggest that the importance of water-rich fluids in generating CKD magmatism might be overestimated. The key observation is that eclogite melts can explain many compositional features of the CKD magmas, which were traditionally ascribed to the involvement of hydrous fluids (e.g. high LILE/HFSE). Some other geochemical features can hardly be explained through mantle melting triggered either by eclogite melts or by hydrous fluids (for example, extremely high-$\delta^{18}O$ in Klyuchevskoy magmas). Plausible explanation could be massive assimilation of hydrothermally altered mafic arc lithosphere beneath CKD. Significant contribution from the lithosphere to the budget of highly incompatible elements (e.g., U and Th) provides also elegant explanation for relatively small or no ^{238}U excesses in the CKD rocks, which were previously interpreted as evidence for unusually long time lapsed since fluid release from subducting plate [*Turner et al.* 1998].

3.7. Quantitative Multi-Component Models of CKD Magma Origin

3.7.1. General approach. The well established systematics of the end-member components contributing to the CKD magmas can be parameterized using quantitative mass balance models, which describe variability of the magmas in terms of finite number of parameters and can be predictive for some other compositional parameters, which are difficult to estimate directly from analysis of rock samples (for example, water content in primary melts). Unlike previous attempts to establish the mass balance between slab and mantle components in the CKD magmas [e.g., *Churikova et al.* 2001], our primary task here is to assess the contribution of mantle and dacite/eclogite melts to the composition of the magmas, because (as shown below) these components rather than fluids appear to exert the maximum control on the elemental budget. We account for the fluid and/or lithosphere contribution by difference between the measured concentration in primitive magma and estimated contribution from mantle and dacite melt.

Details of the modeling can be found in the Auxiliary material on the CD-Rom accompanying this manuscript, and the main results are illustrated in Figures 14–17 and Table 3. These models provide new quantitative constraints on the origin of the unusually voluminous and geochemically enigmatic magmatism in CKD and are instructive as for the evaluation of different petrologic models, as for explaining the compositional differences between volcanoes. We intentionally limited our modeling to eight minor and trace elements spanning different geochemical groups: Na, Ti, Ba, Nb, Zr, Sr, K and Y, because these element proxies display similar behavior to the rest of the elements in the periodic table, and serve as indicators of the degree of partial melting. We applied our models to the average compositions of primitive magmas, which differ from the estimated primary melts equilibrated with olivine Fo_{91} by only 2–11% of olivine fractionation (Table 3). This has small effect on concentrations of incompatible elements and thus results of our modeling are applicable to primary melt compositions.

Below, we consider two end member models that present equal solutions to our mass balance modeling: mixing and reaction models. In both models, we can successfully account for the elemental balance by considering three major contributors to the magma compositions: mantle, dacitic component (derivate of eclogitic melt) and slab fluid (±lithosphere). Relative inputs from mantle, dacitic component and slab fluid to the budget of trace elements and estimated parameters of mantle melting (degree of melting, amount of eclogitic melt, etc.) are highly dependent on the proposed petrologic scenario.

3.7.2. Mixing or pyroxenite model (Model 1). The key observation that serves as the basis of this model is the wide range of major element concentrations in primitive Kamchatkan melts, which can be ascribed to simple mixing between primitive basaltic and dacitic melts occurring in the mantle wedge or lithosphere (Figure 6). Basaltic melts are viewed to originate through fluid flux mantle melting. Dacitic component is considered to originate from non-peridotitic source such as secondary pyroxenite (see chapter 3.5), which could be melted simultaneously with mantle peridotite under hydrous fluid flux, for example, resulting from the breakdown of serpentinites in the deeper portions of the subducting plate [e.g., *Ringwood,* 1990; *Rüpke et al.* 2002].

Schematic illustration of the "mixing model" is presented in Figure 12. Equations and detailed description is given in the Supplementary Materials. As a result of our modeling, we are able to parameterize the composition of primitive magmas in terms of degree of mantle melting (F) required to produce basaltic end-member, absolute amount of dacitic component in the mixture with basalt (y) and relative contribution of dacite, mantle and fluid (±lithosphere) to the trace element budget of primitive magma (Figures 14–15, Table 3).

This model predicts large contribution from mantle wedge and fluid (±lithosphere) for magmas from all volcanoes. Except for Shisheisky magmas, the model suggests that more than 50% of LILE (Ba, K, Sr) in the CKD magmas is accounted for by slab fluid (±lithosphere). Significant contribution from eclogitic melt (>20% of LILE, Na and Zr) is predicted for Klyuchevskoy, Zarechny, Shiveluch and Shisheisky magmas (Figure 14). According to the mixing scenario, the amount of dacitic component increases steadily towards the edge of the subducted plate from less than 5% in Tolbachik lavas up to 50% in Shisheisky lavas (Figure 15). This correlation is however pre-determined by the applied mass balance equations solved on the basis of SiO_2 in the volcano averages. Degrees of mantle melting estimated with the mixing model range from ~4 to 8 % and tend to increase toward the slab edge or with decreasing depths to subducted plate (Figure 15).

3.7.3. Reaction or melt flux-melting mode (Model 2). This model suggests that primitive dacitic melt is a common component involved in mantle melting beneath all CKD volcanoes, which acts as trigger of mantle melting and principle agent transferring a number of major (e.g., Na) and trace elements (e.g., LILE, REE) from subducting plate to the mantle wedge beneath CKD (Figure 14). We suggest that the hydrous dacite melts originate through little modification of eclogite melts as they enter mantle wedge above the subducted plate and migrate upward. A key consideration of this scenario is that the thermal gradient in the mantle above subduction zones is inverted and that the temperature of the melts increases as they rise and decompress. This reaction or melt flux-melting [*Grove et al.* 2002; 2003; 2005; *Kelemen et al.* 2003a] results in increase of initial liquid mass

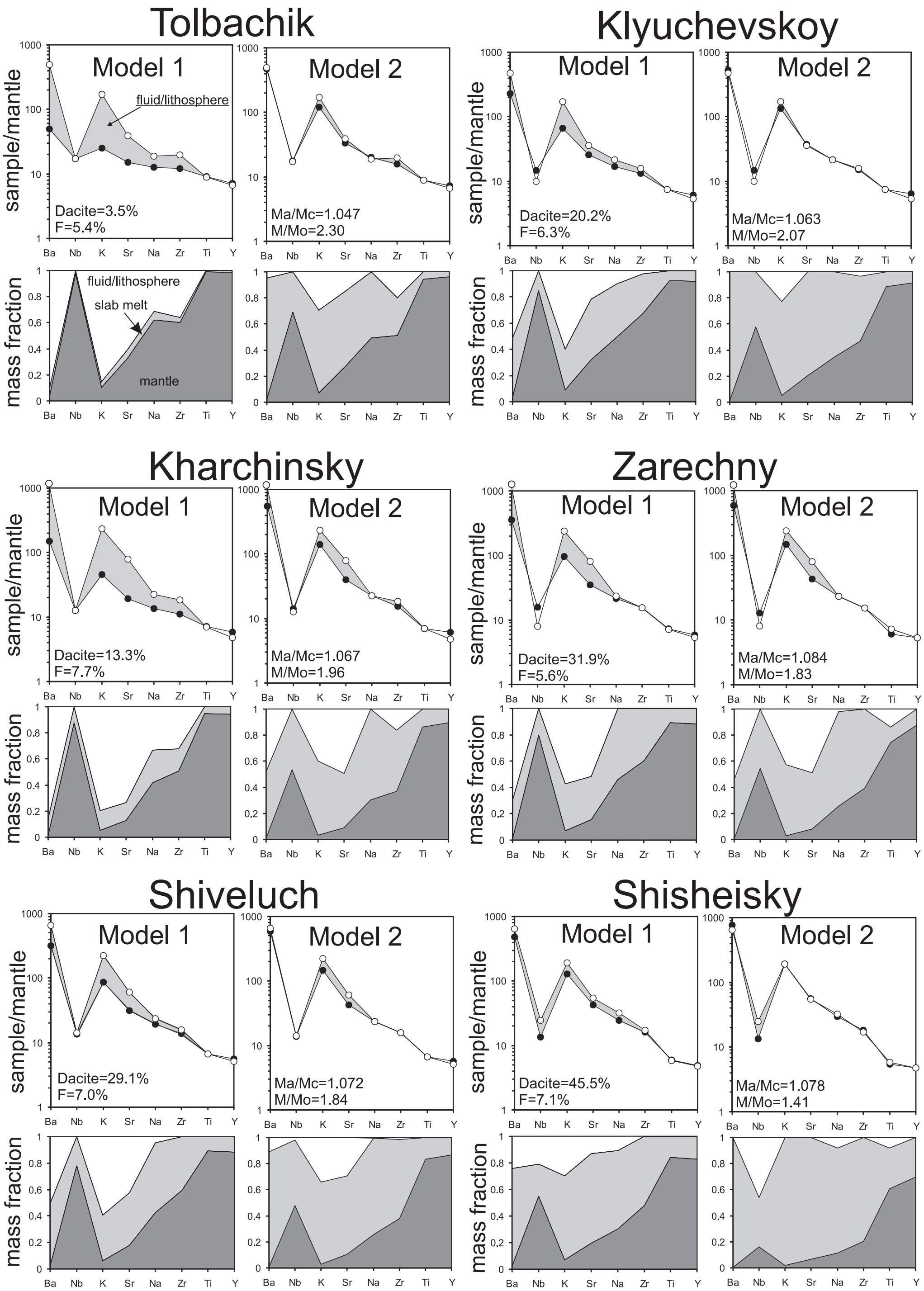

Figure 14. Results of quantitative mass-balance modeling of the CKD primitive magmas. Estimated parameters of mantle melting (Model 1) are amount of dacite component in the mixture ("Dacite", wt %) and degree of mantle melting (F, wt %); extent of eclogite melt—mantle interaction (Model 2) is characterized by the AFC rate (M_a/M_c) and the increase of the initial liquid mass (M/M_o). An excess of trace elements in the modeled CKD magmas over those provided by primitive dacite component and depleted mantle, if it exists, is assigned to the contribution from fluid (±lithosphere). Note little contribution from fluid (±lithosphere) required to explain the composition of all CKD magmas by the reaction model (Model 2). Details of modeling can be found in Auxiliary material on the CD-Rom accompanying this manuscript.

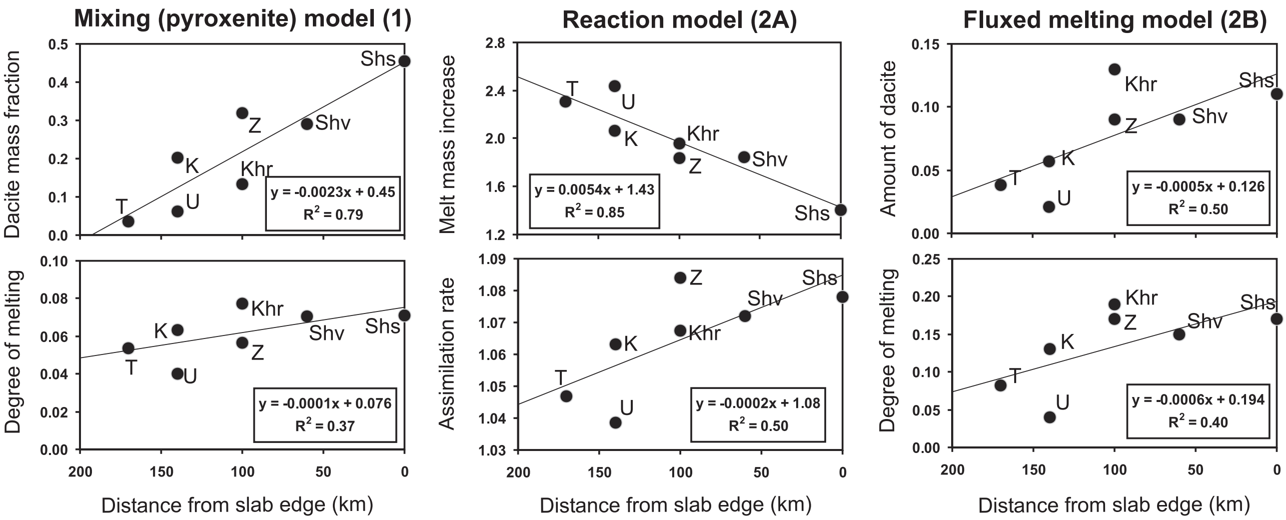

Figure 15. Correlation of estimated parameters of magma generation beneath the CKD with distance from volcanoes to the edge of the subducting Pacific Plate. Note that strong correlation with the amount of dacite component in magma (Model 1) could be expected from the mass balance applied and existing correlation between SiO_2 in average compositions and the distance from the slab edge to volcanoes. Other correlations were not pre-determined by the fitting procedure.

and dilution of slab-derived components as dacite melt rises through the mantle wedge encountering shallower and hotter mantle (Figure 13B). According to this scenario, the melt traversing inverted thermal gradient finds itself out of equilibrium with surrounding mantle. The major and trace element variability of the CKD lavas (Figure 6) can thus be explained by different extents of modification of the eclogite (or dacite) melts during interaction with the mantle wedge. The extent of the interaction could be largely controlled by the mantle temperature. The higher the average temperature in the mantle column, traversed by the dacitic melts, the more mantle material is assimilated by the eclogitic melts before magmas segregate beneath the colder lithosphere.

We simulated dacite melt – mantle interaction in two ways: mantle AFC (Model 2A) or melt fluxed mantle melting (Model 2B) (see Supplementary Methods for details) [*De Paolo,* 1981; *Kelemen,* 1995; *Kelemen et al.* 2003c]. As a result, we are able to parameterize primitive magma compositions in terms of relative contributions from mantle, dacite (slab) melt and fluid ± lithosphere to the balance of trace elements in erupted magma and in terms of AFC rate (M_a/M_c) and increase of liquid mass (M/M_o) (model 2A) or degree of melting (F) and amount of dacite in the source (x^d) (model 2B) (Figure 14–17, Table 3). Both models 2A and 2B result in very similar balance between different components in the composition of the primitive CKD magmas. The results of the melt flux-melting (model 2B) are therefore not graphically represented in Figure 14.

The reaction model favors a very large contribution from dacitic melt to the budget of highly incompatible elements (>40% LILE, Nb, Na, Zr) for all volcanoes. Compositions of Tolbachik and Klyuchevskoy magmas were interpreted to originate through melting resulting from the flux of hydrous fluids [e.g., *Dorendorf et al.* 2000; *Ishikawa et al.* 2001; *Churikova et al.* 2001]. Our reaction model successfully reproduces Tolbachik and Klyuchevskoy compositions with very little contribution from fluid (±lithosphere) to the budget of LILE, which is dominated in this scenario by the dacitic melt (Figure 14). While we are the first to propose an eclogitic melt flux model for CKD magmatism, this model concurs nicely with slab melt-fluxing models offered for the neighboring Aleutians and elsewhere [*Yogodzinski et al.* 1994; 1995; *Kelemen et al.* 1995; 2003a and references therein]. Furthermore, the slab melts can account for concentrations of highly fluid-mobile elements (e.g., B, Pb, U, Sb, As and H_2O), if melting of slab material occurs under fluid flux from deeper portions of subducted slab (for instance, from serpentinites [e.g., *Ringwood,* 1990; *Ulmer and Trommsdorff,* 1995; *Rüpke et al.* 2002]), and the highly fluid-mobile elements were initially transported by the hydrous fluids and inherited by the slab melts. Our preliminary data indicate however that the systematics of highly volatile element (e.g., B) is a bit more complex and decoupled from LILE [*Ishikawa et al.* 2001].

Relatively high fluid (±lithosphere) input to the budget of LILE (>40% Ba, K and Sr) is estimated for Kharchinsky and Zarechny volcanoes (Figure 14), which have the highest $^{87}Sr/^{86}Sr$, Ba/Nb and elevated $\delta^{18}O$ (Figure 8, 9). Unlike the mixing model, this hydrous fluid-like enrichment [*Eiler et al.* 2000; *Dorendorf et al.* 2000] can be ascribed to previous mantle metasomatism or more likely to assimilation of lithospheric material [e.g., *Bindeman et al.* 2004].

In a regional plate tectonic context, the reaction model reveals a strong negative correlation between increase of liquid mass (M/M_o) produced during reaction of eclogite-melt and peridotite and distance from the slab edge so that M/M_o~1.4 for Shisheisky Complex and ~2.3 for southern Tolbachik and Ushkovsky volcanoes (Figure 15). Overall, amount of assimilation and amount of crystallization of mantle peridotite are comparable. The calculated M_a/M_c ratios range from ~1.04 for Tolbachik magmas to ~1.08 for Zarechny volcano and generally tend to increase toward the slab edge (Figure 15) and correlate negatively with M/M_o (Figure 16A). Excellent correlations are found for the amount of melt mass increase (M/M_o) and major elements in volcano averages (e.g. SiO_2, Figure 16B). The later correlation is particularly important and was not pre-determined by our modeling based on trace elements content.

The model of mantle melting triggered by slab melt (model 2B) reveals generally higher degrees of melting compared to the mixing model, which range from ~4% for Ushkovsky up to 20% for volcanoes near the slab edge (Figure 15). The amount of the dacitic component varies from ~3% for Ushkovsky up to ~13% for Kharchinsky volcano and correlates strongly with the estimated degrees of melting and major element compositions (Figure 16 C, D).

In summary, different petrologic scenarios and related numerical models can quantitatively explain the origin of the geochemical zoning along the CKD. On the basis of all observations, we tentatively favor the reactive interaction of eclogitic melts with the mantle wedge as the main process operating beneath CKD and causing the geochemical zonation along the arc strike. We however do not exclude that mixing of pyroxenite and peridotite derived melts or combination of different mechanisms of slab melt- mantle interac-

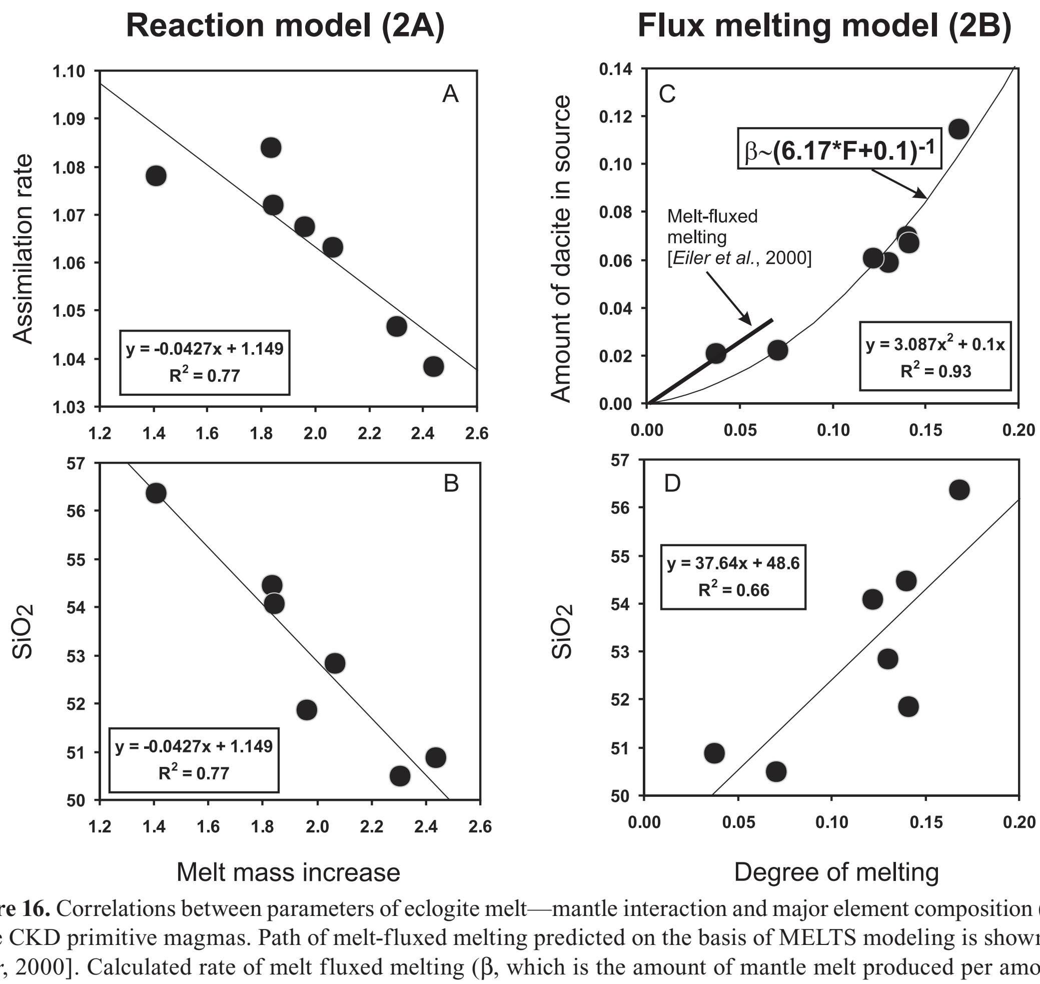

Figure 16. Correlations between parameters of eclogite melt—mantle interaction and major element composition (SiO_2) of the CKD primitive magmas. Path of melt-fluxed melting predicted on the basis of MELTS modeling is shown after [*Eiler*, 2000]. Calculated rate of melt fluxed melting (β, which is the amount of mantle melt produced per amount of hydrous dacite melt flux to the mantle) is shown in the inset in figure C. Note that strong correlations with SiO_2 (and presumably with all other major elements, Figure 6) were not pre-determined by our fitting procedure. These correlations allow predicting major element composition in the primary CKD melts from modeling trace elements.

tion is also possible. Reconciling these scenarios requires better knowledge of the geochemical systematics of highly fluid mobile elements in magmas (e.g., H_2O, B, As, Sb), as well as compositions of lower crust and lithospheric mantle beneath Kamchatka, timing of interaction between mantle and slab melts, and potentially important role of high Mg# pyroxenitic sources in magma generation.

Noteworthy, negative correlation between TiO_2 and Na_2O observed in the CKD and in primitive arc lavas worldwide [*Kelemen et al.* 2003a] can hardly be explained by the mantle melting fluxed with solute-poor water-rich fluid [e.g. *Tatsumi et al.* 1986; *Eiler et al.* 2000] or due to simple process of bulk assimilation of mantle peridotite by slab melts [*Yogodzinski et al.* 1994]. These correlations can however be readily explained with both models proposed in this study. According to the reaction model, 40 to 90 % of Na_2O in the CKD magmas is slab-derived (Figure 14). This element cannot be regarded as immobile and mantle-derived in the case of the CKD magmatism and also in many other volcanic arcs [*Pearce and Peate*, 1995; *Kelemen et al.* 2003a]. Estimation degrees of mantle melting on the basis of widely adopted approach employing Na_2O concentrations normalized to MgO=6 wt% [*Plank and Langmuir*, 1988] maybe not a good approach in this case and would lead erroneous conclusions. Heavy REE, Y, V are poorly soluble in both slab-derived melts and fluids [e.g., *Brenan et al. 1995; Ayers et al.* 1997*; Stalder et al.* 1998; *Rapp et al.* 1999; *Johnson and Plank,* 1999; *Prouteau et al.* 2001; *Green and Adam*, 2003] and should provide more reliable information about degrees of partial mantle melting in subduction zones.

3.8. Where and why Does the Slab Melt Beneath the CKD?

With respect to the common presence of eclogitic melt component in the CKD lavas, which make the lavas very distinctive in Kamchatka, previous workers suggested rather sharp change in conditions of magma generation along the CKD from fluid-dominated beneath Klyuchevskoy volcano to slab-melt-dominated beneath Shiveluch volcano [e.g., *Volynets et al.* 2000; *Kepezhinskas et al.* 1997; *Yogodzinski et al.* 2001; *Churikova et al.* 2001; *Münker et al.* 2004]. Our results show that maximum contribution from slab melting is indeed observed for lavas originating above the proposed slab edge. There is however no sharp change in the composition of lavas along the arc strike and virtually all lavas in the CKD require variable amount of the dacitic (eclogitic melt) component involved in their genesis. Moreover, an estimate of the *absolute* amount of the slab melt involved in the CKD magma genesis depends on the estimated *total magmatic flux* through the Moho along the CKD, which is currently somewhat uncertain [*Fedotov and Masurenkov,* 1991; *Ponomareva et al.* 2007a]. Given the magmatic productivity tends to decrease to the north (from Klyuchevskoy to Shiveluch) and is clearly vanished above the slab edge (Shisheisky Complex), the amount of slab melting maybe broadly the same beneath all CKD volcanoes or, at least, does not drastically vary along the CKD. In our opinion, these observations have fundamental importance and should be explained by any plausible model on the origin of CKD magmatism.

Melting of relatively fast subducting ~90 Ma old Pacific Plate beneath northern Kamchatka is generally not expected from the thermal models of subduction zones established at the end of the last century [e.g., *Davies and Stevenson*, 1992; *Peacock et al.* 1994]. To reconcile these models with the occurrence of adakitic lavas in Kamchatka, *Yogodzinski et al.* [2001] proposed that the slab melts at its edge, which is exposed to heating by the surrounding hot mantle. However, *Davaille and Lees* [2004] showed recently that the conductive heating alone cannot account for the seismic observations beneath northern Kamchatka and is not efficient enough to heat the subducting slab at significant distances from its edge. It is therefore difficult to explain a significant contribution from slab melting for volcanoes located up to 170 km to the south from the slab edge by the model employing highly localized slab melting at its edge.

On the other hand, recent models of the thermal state of the mantle wedge in subduction zones invoking strongly temperature and stress dependent mantle viscosity suggest that the mantle wedge above subduction zones could be hot enough to provide sufficient heating to melt sediments and/or basalts in upper parts of the subducting plates beneath volcanic arcs worldwide [e.g., *Furukawa,* 1993; *van Keken et al.* 2002; *Conder et al.* 2002; *Kelemen et al.* 2003c; *Peacock et al.* 2005; *Manea et al.* 2005; 2007]. Adopting these models to Kamchatkan magmatism allows slab melting beneath all volcanoes in Kamchatka, not only beneath CKD [*Manea et al.* 2005]. The recent models can thus explain occurrence of slab melts at far distances from the slab edge but do not explain why magmas with strong slab melts signatures are particularly abundant in the CKD compared to southern Kamchatka.

Here we propose that some other concurring factors facilitate slab melting and/or favor production of high-SiO_2 primitive magmas beneath the CKD compared to other localities in Kamchatka. These factors could be (1) anomalously hot subducting plate, (2) short and cold mantle wedge columns at the slab edge.

To explain the high heat flow from the sea-floor offshore northern Kamchatka (>80 mW/m2 [*Smirnov and Sugrobov,* 1980]) and absence of deep (>200 km) subduction related earthquakes beneath the northern Kamchatka, the Pacific plate entering the northern part of the Kuril-Kamchatka trench was proposed to be thermally thinned

[*Gorbatov et al.* 1997; *Davaille and Lees,* 2004; *Manea et al.* 2006]. Apparent "thermal" age of the Pacific Plate at the Kamchatka-Aleutian junction was estimated as 30–40 My, that is 2–3 younger than the real Cretaceous (~90 My) age of the subducting oceanic crust. In this respect, the northern part of the Kamchatka arc is quite different from its southern part, where the subducting oceanic plate is characterized by the lower heat flow (40–60 mW/m^2) well corresponding to the age of ~90 Ma [*Gorbatov et al.* 1997]. Whatever the reasons for the thermally young Pacific Plate at the Kamchatka-Aleutian junction, this can be an important, if not a crucial, factor in facilitating partial slab melting beneath the entire northern segment of the Kamchatka Arc. Additionally, because of the higher temperatures in the interior of the Pacific Plate subducting beneath CKD, it can be more hydrated than cold oceanic plate to the south providing particularly abundant fluid release proposed beneath the CKD [*Ishikawa et al.* 2001; *Dorendorf et al.* 2000; *Churikova et al.* 2001].

3.9. Thermal State of Mantle Beneath CKD

Given that slab melting may not be restricted to the slab edge, one can suggest that some other factors may cause preferential preservation and appearance of magmas with strong eclogite melt signatures in the proximity of the slab edge. It seems that particularly important factors governing the composition of erupted arc magmas are length and thermal state of mantle wedge columns involved in magmatism [*Plank and Langmuir,* 1988; *Kelemen et al.* 2003c]. In order to make quantitative constraints on the thermal state of the mantle wedge beneath CKD, temperature of primary melts should be estimated. This estimate however depends dramatically on the amount of water in the inferred parental magmas [e.g., *Hirose,* 1997; *Gaetani and Grove,* 1998; *Falloon and Danyushevsky,* 2000].

The water content in parental CKD magmas is poorly known [*Sobolev and Chaussidon,* 1996; *Khubunaya and Sobolev*, 1998; *Portnyagin et al.* 2007]. In order to estimate it for all volcanoes, we applied here the ability of our models to predict compositional parameters of parental melts, which were not determined on the basis of whole rock compositions, for example, water content. Mineralogical data suggest that the H_2O concentrations in the primitive dacite component could be as high as 5.5–11 wt% (on average ~8 wt %). Using this average estimate for the dacite component, we can predict H_2O concentrations in all parental CKD magmas and their sources by using parameters of dacite melt – mantle interaction independently estimated from the concentrations of non-volatile elements (Figure 14–15, Table 3). The results are illustrated in Figure 17 and Table 3.

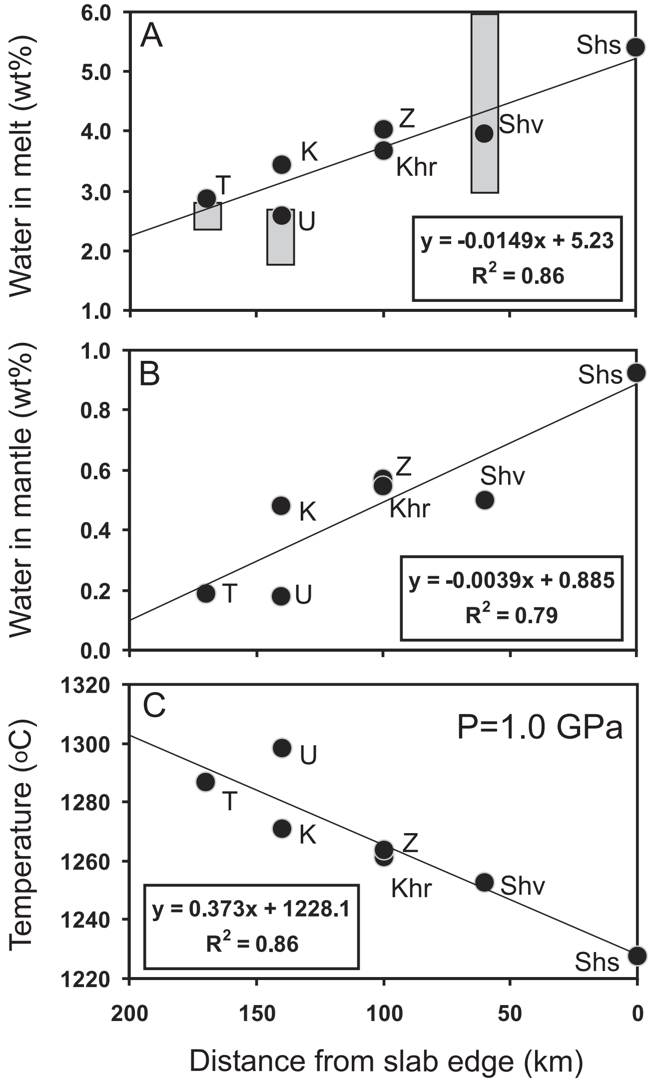

Figure 17. Correlations between predicted concentrations of H_2O in parental CKD magmas (A), H_2O in their mantle sources (B) and temperature of the parental melts at the base of the crust (C) with the distance from the slab edge. Gray rectangles encounter directly estimated concentrations of H_2O for primitive melts of Tolbachik volcano [*Portnyagin et al.* 2007], Klyuchevskoy volcano [*Sobolev and Chaussidon,* 1996; *Khubunaya and Sobolev,* 1998; *Portnyagin et al.* 2007] and H_2O concentrations in evolved (and likely degassed [*Blundy et al.* 2006]) Shiveluch melts [*Tolstikh et al.* 2003].

Average concentrations of H_2O in parental CKD magmas and their mantle sources are predicted to increase from the most southern Tolbachik and western Ushkovsky volcanoes (2.5–3 wt% H_2O in the parental melts, ~0.2 wt% H_2O in the mantle) toward the slab edge and reach the highest values in the Shisheisky primitive melts (~5.5 wt% H_2O in the parental melt, ~0.9 wt% H_2O in the mantle). These estimates are broadly similar to the directly measured water content in primitive melt inclusions in olivine from Tolbachik and Klyuchevskoy volcanoes (up to 3 wt% [*Sobolev and Chaussidon,* 1996; *Khubunaya and Sobolev*, 1998; *Portnyagin et al.* 2007]). Predicted H_2O~4 wt% in the average Shiveluch parental melt appears to be in agreement with up to 7 wt% of H_2O measured in evolved dacitic to rhyolitic melt inclusions in plagioclase from Shiveluch andesites [*Tolstikh et al.* 2003; *Blundy et al.* 2006].

By using these H_2O estimates, we are now able to calculate "wet" temperatures of the CKD mantle sources assuming that the parental CKD magmas were in equilibrium with the mantle below the crust (Table 3). These temperatures monotonously decrease toward the slab edge and range from ~1300°C for Tolbachik and Ushkovsky volcanoes to ~1220°C for Shisheisky Complex (Figure 18) in qualitative agreement with thermomechanical modeling of subduction and mantle wedge beneath CKD [*Manea et al.* 2006] also predicting decrease of the average mantle temperatures toward the slab edge.

We concluded previously that all parental CKD magmas including the most SiO_2-rich andesites could be in equilibrium with mantle peridotite. The major element systematics of the CKD magmas can be therefore explained by variations of mantle temperatures, at which eclogite melts were re-equilibrated with mantle material (Figure 18). The mantle wedge temperature can also control the amount of peridotite material assimilated by hydrous eclogite melts. In other words, we propose here that primitive andesitic melts with strong eclogite melt signature formed near the slab edge originate through re-equilibration of eclogite melts with relatively low temperature mantle wedge. The reaction involved small amount of assimilated peridotite and resulted in strong eclogite melt signature in primary magmas. Higher mantle temperatures further south from the slab edge caused more peridotite material to assimilate and resulted in less hydrous basaltic primary melts with more diluted eclogite melt signature. In some aspects this model is similar to that proposed by *Kelemen et al.* [2003a,b] for island-arc magmas world-wide.

Variability of the primitive magmas compositions in the CKD increases toward the slab edge (Figure 5) and can be likely related to the length and to the possible thermal heterogeneity of the mantle columns beneath volcanoes (Figure 18). According to our model, the whole range of melt compositions may be present in the mantle wedge beneath all volcanoes in the CKD. Short mantle columns near the slab edge may however favor rapid extraction of various primary melts from high- and low-temperature parts of the mantle wedge and their limited homogenization on the way to surface. This can explain why high-temperature (basaltic) and low-temperature (andesitic) primitive magmas occur in the CKD in the same localities and were erupted over short interval of time (for example, in Shisheisky Complex). In contrast, long and hotter mantle columns to the south (Figure 18) result in extensive interaction of eclogite melts with mantle peridotite, effective mixing of magmas from different parts of the mantle column and eruption of low-SiO_2 basalts and basaltic andesites of small compositional range (for example, Tolbachik volcano).

One of the interesting conclusions from our modeling is that amounts of water in magmas and their sources are lower for the most productive CKD volcanoes (Klyuchevskoy Group) compared to less productive volcanoes near the slab edge (Figure 17). It seems that enhanced volcanic productivity along the CKD correlates rather with the highest mantle temperatures, the longest mantle columns and, possibly, with mantle fertility beneath the CKD. Although the magnitude of the water-bearing fluid and/or melt flux from subducting plate might be important factor contributing to the magmatic flux through the Moho and the composition of arc magmas [e.g. *Tatsumi et al.* 1985], the thermal and compositional structure of the mantle wedge appear to exert primary control on the composition and volumes of erupted magmas in the CKD and world-wide [e.g., *Furukawa*, 1993; *Tamura et al.* 2002; *Kelemen et al.* 2003b; *England et al.* 2004].

In summary, due to the pronounced change in physical parameters of magma generation at the Kamchatka-Aleutian junction, the Kamchatka Arc may represent rather unique place in the world where transition from "cold" (=hot mantle) subduction zone, favoring generation of basaltic parental magmas in the mantle wedge, to "hot" (=cold mantle) subduction zone with common high-Mg# andesites [e.g. *Kelemen et al.* 2003a], occurs over ~170 km along the arc strike. Partial melting of the subducting Pacific Plate may however be important process beneath all volcanoes in the CKD and not only restricted to the edge of the subducting plate.

3.10. Recent Transition to Oceanic-Type Magmatism in Northern Kamchatka

The discussion above referred to the largest CKD volcanoes exhibiting strong subduction-related signatures. In this respect, lavas erupted from the northernmost volcanoes in Kamchatka arc, Nachikinsky and Khailulia, are clearly different from typical arc-type rocks and are more similar to magmas originating in oceanic settings. The specific features of these magmas are low LILE/HFSE and LREE/HFSE (e.g., Ba/Nb, La/Nb), MORB-like $^{87}Sr/^{86}Sr$ and $\delta^{18}O$, which suggest minimal to negligible amounts of slab-derived components (fluid or melt) in their sources. The HFSE and LREE enrichment and high Dy/Yb of the northern rocks are consistent with derivation through low-degree melting of fertile garnet-bearing mantle at temperatures well exceeding 1300°C (Table 3) [*Portnyagin et al.* 2005a].

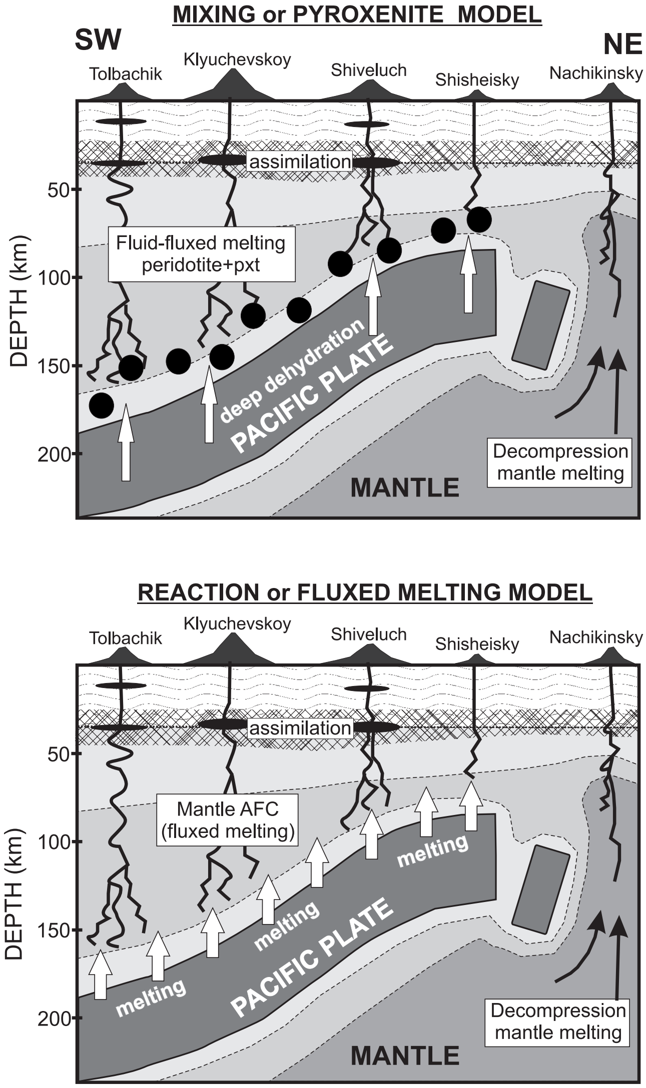

Figure 18. Geodynamic models of primary magma origin along the CKD. Schematic distribution of temperatures in the mantle is shown by gradations of grey; darker grey tone corresponds to hotter temperature. Characteristic feature of the mantle wedge is inverted thermal gradient above the subducting Pacific Plate. Normal gradient is proposed to characterize mantle column beneath Nachikinsky volcano to the north of the slab edge. The temperature field is qualitatively similar to numerically predicted by *Manea et al.* [2007]. (A) Mixing model suggests that major and trace element zoning along the CKD originates due to mixing of basaltic and dacitic melts, which originate from fluid-fluxed melting of hybrid mantle consisting of pyroxenite "blobs" in peridotite matrix. The pyroxenite is proposed to form through reaction between mantle wedge and eclogitic melts at shallow mantle depths. Absolute amount of pyroxenite involved in melting could be similar beneath all volcanoes but their relative amount compared to mantle increases toward the slab edge. (B) Reaction model implies that slab melting occurs beneath all volcanoes and could be particularly abundant at the slab edge. Eclogite melts leave the slab and interact with the mantle wedge on their rise according to the AFC or flux mantle melting scenario. The average extent of this interaction and increase of liquid mass as expressed in the average compositions of erupted primitive magmas correlate with the length of mantle column, distance from the slab-edge and the thermal state of the mantle wedge. Extent of this interaction is larger beneath the southern Klyuchevskoy Group volcanoes and smaller beneath the northern Shiveluch Group. Short mantle columns can favor incomplete mixing between magmas originating in different parts of the mantle wedge and can explain larger variability of primitive magmas toward the slab edge. Magmas to the north of the slab edge are thought to originate due to short-lived upwelling and decompression melting of fertile mantle. The upwelling could be caused by detachment of slab fragments as discussed in the text. All magmas in the CKD could also interact with the shallow lithosphere. The assimilation of lithospheric material could be particularly large beneath the largest and highly active Kamchatkan volcanoes, where lithosphere could be hotter and melted more easily.

The prominent change in geochemistry of lavas erupted at the northern end of the CKD arc correlates with geophysical data indicating that the Pacific slab is subducting beneath the Klyuchevskoy and Shiveluch volcanic groups and that neither a remnant of the Komandorsky Plate nor part of the Pacific Plate underlies northern Kamchatka [*Levin et al.* 2002]. Therefore, as was argued by [*Portnyagin et al.* 2005a], the abrupt shift in geochemistry of lavas at the northern end of the CKD can be generally ascribed to the absence of a subducting slab, the ultimate source of water-bearing melts or fluids triggering arc magmatism, beneath the Nachikinsky and Khailulia volcanoes (Figure 18). Moreover [*Portnyagin et al.* 2003; 2005a] demonstrated that the principle mechanism of magma generation in this region is also different compared to Klyuchevskoy and Shiveluch volcanic groups, being closed-system, pressure-release (decompression) melting of fertile peridotite.

What could be the reasons for mantle decompression beneath northern Kamchatka? *Levin et al.* [2002] proposed two episodes of slab detachment and loss beneath Kamchatka. The detachment of the Komandorsky Plate (5–10 My ago), subducted previously beneath north Kamchatka, correlates with the late Miocene transition from arc-type to alkaline oceanic-type volcanism in the Kamchatka Isthmus [*Kepezhinskas et al.* 1997]. Later detachment of a fragment of the Pacific Plate (~2 My ago) could have been responsible for triggering mantle upwelling and decompression melting beneath the northern part of the CKD, as deeper mantle filled the void left by the sinking slab fragment [*Hole et al.* 1991]. Effective extraction of deep mantle melts from residual mantle could be facilitated in the case of northern Kamchatka by rapid channeling along deep portions of the Alpha Fracture Zone. Thus, the mantle upwelling driven by the slab detachment was likely a short-lived process, produced very small amounts of magmas and magmatism in northern Kamchatka appears to be decreasing. Replacement of the subarc mantle with hot and fertile mantle from depth could however have enhanced melt production beneath the Klyuchevskoy and Shiveluch volcanoes [*Park et al.* 2002; *Levin et al.* 2002; *Portnyagin et al.* 2005a].

The tectonic model described above is applicable to the origin of the most recent magmas in northern Kamchatka. Older rocks from Nachikinsky volcano are significantly less HFSE-enriched, medium-K rocks including high Mg# andesites and dacites. The origin of these rocks cannot be explained solely by crustal AFC from parental HFSE-enriched magmas unless the mass of assimilated crustal material highly exceeds the mass of crystallized melt [*Portnyagin et al.* 2005a]. More likely, the arc-type magmas originated from melting of slab-fragments and/or subduction-modified mantle that survived beneath the northern end of CKD into the Quaternary. The decrease of the subduction-related signature with decreasing age in the rocks from Nachikinsky volcano could reflect replacement of a subduction-modified mantle wedge with unmodified asthenosphere and thermo-mechanical erosion of the subducting Pacific slab edge. We speculate further that the erosion might progressively remove material from the slab edge shifting the physical boundary of the slab to the south. The process might affect conditions of magma generation beneath the entire northern segment of the Kamchatka arc, and the temporal changes can likely be assessed through detailed geochemical studies.

4. CONCLUSIONS

The key observations from our work are regular geochemical changes along the northern segment of the Kamchatka Arc, which were established for major and trace elements, radiogenic (Sr) and stable (O) isotope ratios in primitive (Mg#>0.6) lavas. The geochemical zoning can be explained in light of the recent geophysical data suggesting that the subducting Pacific Plate is torn beneath the Central Kamchatka Depression. Extension of the Bering F.Z. in Kamchatka divides the CKD into two parts, southern and northern, where conditions of magma generation change from subduction-related in the south to non-subduction-related (intraplate- or oceanic-like) in the north.

Recent magmas erupted north of the Bering F.Z. have very weak to negligible contributions from subducted material and originate through decompression melting of fertile mantle peridotite. Detachment of a fragment of the Pacific Plate (~2 My ago) could have been responsible for triggering shortly lasting mantle upwelling and decompression melting beneath the northern part of Kamchatka, as deeper mantle filled the void left by the sinking slab fragment.

Highly abundant subduction-related volcanism in the southern part, including Shiveluch and Klyuchevskoy Volcanic Groups, originates above the subducting Pacific Plate near its northern edge. Compositions of parental magmas in this region require contribution from at least 3 principle components, which are (i) depleted mantle, (ii) eclogite melts and (iii) slab-derived fluid and/or lithospheric component. In this work we provide first quantitative solution for the mass balance between these components in the primitive magmas of Kamchatka, which is presented in the framework of a number of plausible petrologic scenarios.

The model invoking mixing between basaltic mantle-derived melts and dacitic, eclogite- or, more likely, pyroxenite-derived melts suggests similar degrees of fluid-triggered melting of a heterogeneous (pyroxenite + peridotite) mantle source along the arc strike and steadily increasing contribution of the pyroxenite-derived melts toward the slab edge. Pyroxenites are viewed within this model as products of reaction between slab melts and mantle peridotite at shallower depths. Hydrous, slab-derived fluids cannot explain high $\delta^{18}O$ in many CKD basalts, which can more likely result from massive assimilation of mafic hydrothermally altered lithosphere beneath CKD.

Alternatively, the along-strike geochemical zonation can be explained by a progressively smaller extent of reactive interaction between eclogitic slab melts and mantle wedge toward the slab edge, the process which is largely controlled by mantle temperatures decreasing beneath the CKD from south to north. The composition of basaltic lavas from the most productive southern CKD volcanoes (Tolbachik and Klyuchevskoy) can be readily explained without involvement of slab fluids in magmatic processes and can originate through extensive modification of H_2O-rich eclogitic melts by interaction with the mantle wedge or through melt-fluxed mantle melting. Contribution from mafic lithosphere beneath Kamchatka might be also required in this scenario to explain the most extreme LILE concentrations and high Sr and O isotope ratios in some CKD lavas.

The involvement of eclogitic melts in magma genesis at distances up to 170 km from the slab edge suggests that the Pacific Plate near the Kamchatka-Aleutian junction could be thermally rejuvenated prior subduction allowing partial slab melting beneath all CKD volcanoes. Although we do not exclude enhanced slab melting at the slab edge, the increasing contribution of slab melts to the northern CKD magmas might be confused by low-temperature peridotite-hydrous melt equilibrium, favoring production of andesitic primary melts. The eclogitic melt signature can be better preserved beneath the northern CKD volcanoes because of smaller amount of assimilated peridotite material, which is required for eclogite melts to achieve equilibrium with mantle peridotite at lower mantle temperatures above the slab edge.

Finally we note that, despite significant progress in our understanding of magma generation processes at the Kamchatka-Aleutian junction, the origin of the outstanding magmatic productivity of the northern Kamchatkan volcanoes on the global scale still remains unanswered on a quantitative basis. The high magmatic output might be facilitated by several competing factors such as high fluid flux, high mantle temperatures, fast mantle turn-over of the mantle wedge, slab melting and remobilization of hydrated arc roots in magmatic processes. It seems very likely however that the fundamental reasons must be casually related to the specific geodynamic situation at the Kamchatka-Aleutian junction. Moreover, enhanced volcanic activity is one of the distinctive features of all regions associated with discontinuities in the subducting plate.

Acknowledgements. We particularly thank Gennady Avdeiko, Sergei Khubunaya and Nikita Mironov for their generous support in the field, many-year friendship and collaboration. We thank Vitaly Uspensky for donation of samples from Shisheisky complex and Khailulia volcano; Sonja Storm and Nikita Mironov for their help with maintaining the data base on Kamchatkan volcanism; Lasse Heuer and Silke Hauff for preparation of samples for chemical analyses; Dagmar Rau and Dieter Garbe-Schönberg for performing XRF and ICPMS analyses; Leonid Danyushevsky, Svend Duggen, Vera Ponomareva for fruitful discussions and stimulating ideas on the role slab melts in subduction zones. Insightful reviews from Christopher Nye and Gene Yogodzinski helped to improve clarity of the manuscript. Editorial handling by Pavel Izbekov is kindly acknowledged. This research was supported by the Deutsche Forschung Gemeinschaft (HO1833/4 and SFB574, contribution number 101), the Bundes Ministerium für Bildung und Forschung (KOMEX-II and KALMAR projects) and the Russian Foundation for Basic Research (grant 06-05-64873). Oxygen isotope research was funded by NSP (EAR-0537872, IB).

REFERENCES

Ayers, J. C., S. K. Dittmer, and G. D. Layne (1997), Partitioning of elements between peridotite and H_2O at 2.0–3.0 GPa and 900–1100°C, and application to models of subduction zone processes, *Earth Planet. Sci. Lett.*, *150,* 381–398.

Arculus, R. J. (2003), Use and abuse of the terms calcalkaline and calcalkalic, *J. Petrol.*, *44*, 929–935.

Ariskin, A. A., G. S. Barmina, A. Y. Ozerov, and R. L. Nielsen (1995) Genesis of high-alumina basalts from Klyuchevskoi volcano, *Petrology*, *3*, 496–521.

Avdeiko, G. P., S. V. Popruzhenko, and A. A. Palueva (2002) Tectonic evolution, volcanic and tectonic regions of the Kuril-Kamchatka island-arc system, *Geotectonics*, *4*, 64–80. (in Russian)

Baker, M. B., T. L. Grove, and R. Price (1994), Primitive basalts and andesites from the Mt. Shasta region, N. California: products of varying melt fraction and water content, *Contrib. Mineral. Petrol.*, *118*, 111–129.

Balesta, S. T. (1981), *Crust and magmatic chambers in the areas of modern volcanism*, 132 pp., Nauka, Moscow. (in Russian)

Baranov, B. V., N. I. Seliverstov, A.V. Murav'ev, and E. L. Muzurov (1991), The Kommandorsky basin as a product of spreading behind a transform plate boundary, *Tectonophysics*, *199*, 237–270.

Bindeman, I. N., and J. C. Bailey (1994), A model of reverse differentiation at Dikii Greben' Volcano, Kamchatka: progressive basic magma vesiculation in a silicic magma chamber, *Contrib. Mineral. Petrol.*, *117*, 263–278.

Bindeman, I. N., V. V. Ponomareva, J. C. Bailey, and J. W. Valley (2004), Volcanic arc of Kamchatka: a province with high- $\delta^{18}O$ magma sources and large-scale $^{18}O/^{16}O$ depletion of the upper crust, *Geochim. Cosmochim. Acta*, *68*, 841–865.

Bindeman, I. N., J. M. Eiler, G. M. Yogodzinski, Y. Tatsumi, C. R. Stern, T. L. Grove, M. Portnyagin, K. Hoernle, and L. V. Danyushevsky (2005), Oxygen isotope evidence for slab melting in modern and ancient subduction zones, *Earth Planet. Sci. Lett.*, *235*, 480–496.

Blatter, D. L., and I. S. E. Carmichael (1998) Plagioclase-free andesites from Zitacuaro (Michoacan), Mexico: petrology and experimental constraints, *Contrib. Mineral. Petrol.*, 132, 121–138.

Blatter, D. L., and I. S. E. Carmichael (2001), Hydrous phase equilibria of a Mexican high-silica andesite: A candidate for a mantle origin?, *Geochim. Cosmochim. Acta*, 65, 4043–4065.

Blundy, J., K. Cashman, and M. Humphreys (2006), Magma heating by decompression-driven crystallization beneath andesite volcanoes, *Nature*, 443, 76–80.

Bogdanov, N. A., and V. E. Khain (Eds.) (2000), Tectonic map of the Sea of Okhotsk region: map and explanatory notes, scale 1 : 2,500,000. Moscow, Nedra. (in Russian)

Bohrson, W. A., and F.J. Spera (2001), Energy-constrained open-system magmatic processes II: Application of energy -constrained assimilation-fractional crystallization (EC-AFC) model to magmatic systems, *J. Petrol.*, *42* (5), 1019–1040.

Brenan, J. M., H. F. Shaw, F. J. Reyrson, and D. L. Phinney (1995), Mineral-aqueous fluid partitioning of trace elements at 900° C and 2.0 GPa: Constraints on the trace element chemistry of mantle and deep crustal fluids, *Geochim. Cosmochim. Acta*, *59*, 3331–3350.

Brophy, J. G. (1987), The Cold Bay volcanic center, Aleutian volcanic arc, II. Implications for fractionation and mixing mechanisms in calc-alkaline andesite genesis, *Contrib. Miner. Petrol.*, 97, 378–388.

Campbell, I.H., and J. S. Turner (1985) Turbulent mixing between fluids with different viscosities, *Nature, 31*3, 39–42.

Carmichael, I. S. E. (2002), The andesite aqueduct: perspectives on the evolution of intermediate magmatism in west-central (105–99°W) Mexico, *Contrib. Mineral. Petrol.*, *143*, 641–663.

Churikova, T., F. Dorendorf, and G. Wörner (2001), Sources and fluids in the mantle wedge below Kamchatka, evidence from across-arc geochemical variation, *J.Petrol.*, *42*, 1567–1593.

Conder, J. A., D. A. Wiens, and J. Morris (2002) On the decompression melting structure at volcanic arcs and back-arc spreading centers, *Geophys. Res. Lett.*, *29 (15)*, doi:10.1029/2002GL015390.

Conrad, W. K., S. M. Kay, and R. W. Kay (1983) Magma mixing in the Aleutian arc: Evidence from cognate inclusions and composite xenoliths, *J. Volcanol. Geotherm. Res., 18,* 279–295.

Danyushevsky, L., A. W. McNeill, and A. V. Sobolev (2002), Experimental and petrological studies of melt inclusions in phenocrysts from mantle-derived magmas: an overview of techniques, advantages and complications, *Chem. Geol.*, *183*, 5–24.

Davaille, A., and J.M. Lees (2004), Thermal modeling of subducted plates: tear and hotspot at the Kamchatka corner, *Earth Planet. Sci. Lett.*, *226*, 293–304.

Davies, J.H., and D.J. Stevenson (1992), Physical model of source region of subduction zone volcanics, *J. Geophys. Res.*, *97* (B2), 2037–2070.

Defant, M.J., and M.S. Drummond (1990), Derivation of some modern arc magmas by melting of young subducted lithosphere, *Nature*, *347*, 662–665.

De Paolo, D.J. (1981), Trace element and isotopic effects of combined wallrock assimilation and fractional crystallization, *Earth Planet. Sci. Lett.*, *53*, 189–202.

Dorendorf, F., U. Wiechert, and G. Wörner (2000), Hydrated sub-arc mantle: a source for the Kluchevskoy volcano, Kamchatka/Russia, *Earth Planet. Sci. Lett.*, *175*, 69–86.

Dosseto, A., B. Bourdon, J.-L. Joron, and B. Dupre (2003), U-Th-Pa-Ra study of the Kamchatka arc: New constraints on the genesis of arc lavas, *Geochim. Cosmochim. Acta*, *67*, 2857–2877.

Duggen, S., M. Portnyagin, J. Baker, D. Ulfbeck, K. Hoernle, D. Garbe-Schönberg, and N. Grassineau (2007) Drastic shift in lava geochemistry in the volcanic-front to reararc region of the Southern Kamchatkan subduction zone: Evidence for the transition from slab surface dehydration to sediment melting, *Geochim. Cosmochim. Acta*, *71*, 452–480.

Eiler, J. M., A. Crawford, T. Elliott, K.A. Farley, J. W. Valley, and E. M. Stolper (2000), Oxygen Isotope Geochemistry of Oceanic-Arc Lavas, *J. Petrol.*, *41*, 239–256.

Eiler, J. (2001), Oxygen isotope variations of basaltic lavas and upper mantle rocks, in *Stable Isotope Geochemistry*, edited by J.W. Valley, and D.R. Cole, pp. 319–364, Reviews in Mineralogy and Geochemistry, vol. 43, Mineralogical Society of America, Geochemical Society, Washington, DC.

England, P., R. Engdahl, and W. Thatcher (2004), Systematic variation in the depths of slabs beneath arc volcanoes, *Geophysical Journal International*, *156* (2), 377–408.

Erlikh, E.N. (Ed.) (1966), *Petrochemistry of the Kuril-Kamchatka Volcanic Province*, 278 pp., Nauka, Moscow. (in Russian)

ETDB/PAC (2002), Expert Tsunami Database for Pacific, Version 4.8 [CD-ROM], Tsunami Laboratory, ICMMG SD RAS, Novosibirsk, Russia, July 31.

Falloon, T. J., and L. V. Danyushevsky (2000), Melting of Refractory Mantle at 1.5, 2 and 2.5 GPa under Anhydrous and H_2O-undersaturated Conditions: Implications for the Petrogenesis of High-Ca Boninites and the Influence of Subduction Components on Mantle Melting, *J. Petrol.*, *412*, 257–283.

Fedorov, P. I., and M. N. Shapiro (1998), Neogene volcanics of the Kamchatka isthmus and geodynamics of the Aleutian-Kamchatka junction, *Geotectonics*, *32*, 122–137. (in Russian).

Fedotov, S. A. (Ed.) (1983), *The Great Tolbachik Fissure Eruption; geological and geophysical data 1975–1976,* pp. 353, Cambridge Univ. Press, Cambridge, United Kingdom.

Fedotov, S. A., and Yu.P. Masurenkov (Eds.) (1991), *Active volcanoes of Kamchatka*, vol. 1, 302 pp., Nauka, Moscow.

Ford, C. E., D. G. Russel, J.A. Graven, and M. R. Fisk (1983), Olivine-liquid equilibria: temperature, pressure and composition dependence of the crystal/liquid cation partition coefficients for Mg, Fe^{2+}, Ca and Mn, *J.Petrol.*, *24*, 256–265.

Furukawa, Y. (1993), Magmatic processes under arcs and formation of the volcanic front, *J. Geophys. Res.*, *98* (B5), 8309–8319.

Gaetani, G.A., and T.I. Grove (1998), The influence of water on melting of mantle peridotite, *Contrib. Mineral. Petrol.*, *131*, 323–346.

GEOROC (2005), Geochemistry of rocks of the Oceans and Continents, http://georoc.mpch-mainz.gwdg.de/georoc/, MPI für Chemie, Mainz, Germany.

Gill, J. B. (1981), *Orogenic andesites and plate tectonics*, 390 pp., Springer-Verlag, Berlin-Heidelberg.

Gorbatov, A., V. Kostoglodov, G. Suarez, and E. Gordeev (1997), Seismicity and structure of the Kamchatka subduction zone, *J. Geophys. Res.*, *102* (B8), 17833–17898.

Gorbatov, A., Y. Fukao, S. Widiyantoro, and E. Gordeev (2001), Seismic evidence for a mantle plume oceanwards of the Kamchatka-Aleutian trench junction, *Geophysical Journal International*, *146*, 282–288.

Green, D. H. (1973), Experimental melting studies on a model upper mantle composition at high pressure under water-saturated and water- undersaturated conditions, *Earth Planet. Sci. Lett.*, *19*, 37–53.

Green, D. H., M. . Schmidt, and W. O. Hibberson (2004), Island-arc Ankaramites: Primitive Melts from Fluxed Refractory Lherzolitic Mantle, *J. Petrol.*, *45* (2), 391–403.

Green, T. H., and J. Adam (2003), Experimentally-determined trace element characteristics of aqueous fluid from partially dehydrated mafic oceanic crust at 3.0 GPa, 650–700°C, *Eur. J. Mineral.*, *15* (5), 815–830.

Grove, T. L., S. W. Parman, S. A. Bowring, R.C. Price, and M. B. Baker (2002), The role of an H_2O-rich fluid component in the generation of primitive basaltic andesites and andesites from the Mt. Shasta region, N. California, *Contrib. Mineral. Petrol.*, *142*, 375–396.

Grove, T. L., L. T. Elkins-Tanton, S. W. Parman, N. Chatterjee, O. Müntener, and G. A. Gaetani (2003), Fractional crystallization and mantle-melting controls on calc-alkaline differentiation trends, *Contrib. Mineral. Petrol.*, *145* (5), 515–533.

Grove, T. L., M. B. Baker, R. C. Price, S. W. Parman, L. T. Elkins-Tanton, N. Chatterjee, and O. Müntener (2005), Magnesian andesite and dacite lavas from Mt. Shasta, northern California: products of fractional crystallization of H_2O-rich mantle melts, *Contrib. Mineral. Petrol.*, *148* (5), 542–565.

Ishikawa, T., F. Tera, and T. Nakazawa (2001), Boron isotope and trace element systematics of the three volcanic zones in the Kamchatka arc, *Geochim. Cosmochim. Acta*, *65*, 4523–4537.

Johnson, M. C., and T. Plank (1999), Dehydration and Melting Experiments Constrain the Fate of Subducted Sediments, *Geochem. Geophys. Geosyst.,* 1 (Paper number 1999GC000014. Dec. 13, 1999.).

Hirose, K., and T. Kawamoto (1995), Hydrous partial melting of lherzolite at 1GPa: the effect of H_2O on the genesis of basaltic magmas, *Earth Planet. Sci. Lett.*, *133*, 463–473.

Hirose, K. (1997), Melting experiments on lherzolite KLB-1 under hydrous conditions and generation of high-magnesian andesitic melts, *Geology*, *25* (1), 42–44.

Hirschmann, M. M., P. D. Asimov, M. S. Ghiorso, and E. M. Stolper (1999), Calculation of Peridotite Partial Melting from Thermodynamic Models of Minerals and Melts. III. Controls on Isobaric Melt Production and the Effect of Water on Melt Production, *J. Petrology*, *40* (5), 831–851.

Hochstaedter, A. G., P. Kepezhinskas, M. Defant, M. Drummond, and A. Koloskov (1996), Insights into the volcanic arc mantle wedge from magnesian lavas from the Kamchatka arc, *J. Geophys. Res.—Solid Earth*, *101* (B1), 697–712.

Hofmann, A. W. (1988), Chemical differentiation of the Earth: the relationship between mantle, continental crust and oceanic crust, *Earth Planet. Sci. Lett.*, *90*, 297–314.

Hole, M. J., G. Rogers, A. D. Saunders, and M. Storey (1991), Relation between alkalic volcanism and slab window formation, *Geology*, *19*, 657–660.

Kamenetsky, V. S., A. V. Sobolev, J.-L. Joron, and M. P. Semet (1995), Petrology and Geochemistry of Cretaceous Ultramafic Volcanics from Eastern Kamchatka, *J. Petrol.*, *36* (3), 637–662.

Katz, R. F., M. Spiegelman, and C. H. Lagmuir (2003), A new parameterization of hydrous mantle melting, *Geochem. Geophys., Geosyst.*, *4* (9), 1073, doi: 10.1029/2002GC000433.

Kay, R. W. (1978), Aleutian magnesian andesites: melts from subducted Pacific ocean crust, *J. Volcan. Geotherm. Res.*, *4*, 117–132.

Kay, S. M., and R. W. Kay (1985), Aleutian tholeiitic and calc-alkaline magma series: I. The mafic phenocrysts, *Contrib. Mineral. Petrol., 90,* 276–290.

Kay, S. M., Godoy, E., Kurtz, A. (2005), Episodic arc migration, crustal thickening, subduction erosion, and magmatism in the south-central Andes, *Geol. Soc. Am. Bull. 117 (1-2)*, 67–88.

Kelemen, P. B. (1995), Genesis of high Mg# andesites and the continental crust, *Contrib. Mineral. Petrol.*, *120*, 1–19.

Kelemen, P. B., K. Hangøj, and A. R. Greene (2003a), One view of the geochemistry of subduction-related magmatic arcs, with and emphasis on primitive andesite and lower crust, in *Treatise on Geochemistry*, pp. 593–659, Elsevier, Amsterdam.

Kelemen, P. B., J. L. Rilling, E. M. Parmentier, L. Mehl, and B. R. Hacker (2003b), Thermal structure due to solid-state flow in the mantle wedge beneath arcs, in *Inside the Subduction Factory. Geophysical Monograph 138*, edited by J. Eiler, pp. 293–311, Am. Geophys. Union, Washington, D.C..

Kelemen, P. B., G. M. Yogodzinski, and D. W. Scholl (2003c), Along-Strike Variations in the Aleutian Island Arc: Genesis of High Mg# andesite and Implications for continental Crust, in *Inside the Subduction Factory. Geophysical Monograph 138*, edited by J. Eiler, pp. 223–276, American Geophysical Union, Washington, D.C.

Kepezhinskas, P. K., M. J. Defant, and M. S. Drummond (1995) Na-metasomatism in the island arc mantle by slab melt-peridotite interaction: Evidence from mantle xenoliths in the North Kamchatka arc, *J. Petrol.*, *36*, 1505–1527.

Kepezhinskas, P. K., M. J. Defant, and M. S. Drummond (1996), Progressive enrichment of island arc mantle by melt-peridotite interaction inferred from Kamchatka xenoliths, *Geochim. Cosmochim. Acta*, *60*, 1217–1229.

Kepezhinskas, P., F. McDermott, M. J. Defant, A. Hochstaedter, M. S. Drummond, C. J. Hawkesworth, A. Koloskov, R. C. Maury, and H. Bellon (1997), Trace element and Sr-Nd-Pb isotopic constraints on a three-component model of Kamchatka Arc petrogenesis, *Geochim. Cosmochim. Acta*, *61* (3), 577–600.

Keppler, H. (1996), Constraints from partitioning experiments on the composition of subduction-zone fluids, *Nature*, *380*, 237–240.

Kersting, A. B., and R. J. Arculus (1994), Klyuchevskoy volcano, Kamchatka, Russia: the role of high-flux recharged, tapped, and fractionated magma chamber(s) in the genesis of high-Al_2O_3 from high-MgO basalt, *J. Petrol.*, *35*, 1–41.

Kersting, A. B., and R. J. Arculus (1995), Pb isotope composition of Klyuchevskoy volcano, Kamchatka and North Pacific sediments: Implications for magma genesis and crustal recycling in the Kamchatkan arc, *Earth Planet. Sci. Lett.*, *136*, 133–148.

Khrenov, A. P., V. C. Antipin, L. A. Chuvashova, and E. B. Smirnova (1989), Petrochemical peculiarities of Klyuchevskoy volcano basalts, *Volkanologiya i Seismologiya*, *3*, 3–15. (in Russian)

Khubunaya, S. A., S. O. Bogoyavlenskiy, T. Y. Novgorodtseva, and A. I. Okrugina (1994), The mineralogy of the Klyuchevskoi magnesian basalts depicting the fractionation in the magma chamber, *Volkanologiya i Seismologiya*, *15* (3), 315–338. (in Russian)

Khubunaya, S. A., and A. V. Sobolev (1998), Primary Melts of Calc-Alkaline Magnesian Basalts from the Klyuchevskoi Volcano, Kamchatka, *Dokl. Earth Sci.*, *360* (4), 537–539.

Krivenko, A. . (Ed.) (1990), *Geochemical types of magmatic and metamorphic rocks of Kamchatka.* 259 pp., Institute of geology and geophysics, AN SSSR, Siberian Branch, Novosibirsk. (in Russian)

Konstantinovskaia, E. A. (2001), Arc-continent collision and subduction reversal in the Cenozoic evolution of the Northwest Pacific: an example from Kamchatka (NE Russia), *Tectonophysics, 333 (1-2)*, 75–94.

Le Bas, M. J., R. W. Le Maitre, A. Streckeisen, and B. Zanettin (1986), A chemical classification of volcanic rocks based on the total alkali-silica diagram, *J. Petrol.*, *27*, 745–750.

Levin, V., N. Shapiro, J. Park, and M. Ritzwoller (2002), Seismic evidence for catastrophic slab loss beneath Kamchatka, *Nature*, *418*, 763–767.

Litvinov, A. F., A. V. Belyy, and V. B. Lopatin (1991), Upper Cenozoic volcanism in the Ozernoy Peninsula, eastern Kamchatka, *Vulkanologiya i Seismologiya*, *2,* 12–27. (in Russian)

Manea, V. C., M. Manea, V. Kostoglodov, and G. Sewell (2005), Thermal Models, Magma Transport and Velocity Anomaly Estimation beneath Southern Kamchatka (Chapter 31), in *Plates, Plumes & Paradigms*, *Geol. Soc. Am.,* Spec. vol. 388, edited by G. R. Foulger, D. L. Anderson, J. H. Natland, and D. C. Presnall, pp. 381–431.

Manea, V. C., and M. Manea (2007), Thermal models beneath Kamchatka and the Pacific plate rejuvenation from a mantle plume impact, this volume.

McDonough, W. F., and S.-S. Sun (1995), The composition of the Earth, *Chem. Geol.*, *120*, 223–253.

Melekestsev, I. V. (1980), *Volcanism and Relief Formation*, Nauka, Moscow, 212 pp. (in Russian)

Mironov, N. L., M. V. Portnyagin, P. Y. Pletchov, and S. A. Khubunaya (2001), Final Stages of Magma Evolution in Klyuchevskoy Volcano, Kamchatka: Evidence from Melt Inclusions in Minerals of High-Alumina Basalts, *Petrology*, *9* (1), 46–62.

Moore, G., and I. S. E. Carmichael (1998), The hydrous phase equilibria (to 3 kbar) of an andesite and basaltic andesite from western Mexico: constraints on water content and conditions of phenocryst growth, *Contrib. Mineral. Petrol.*, *130*, 304–319.

Münker, C., G. Wörner, G. M. Yogodzinski, and T. Churikova (2004), Behaviour of high field strength elements in subduction zones: constraints from Kamchatka-Aleutian arc lavas, *Earth Planet. Sci. Lett.*, *224*, 275–293.

Mysen, B. O., and A. L. Boettcher (1975), Melting of a hydrous mantle, I. Phase relations of natural peridotite at high pressures and temperatures with controlled activities of water, carbon dioxide and hydrogen, *J. Petrol.*, *16*, 520–548.

Ozerov, A. Y. (2000), The evolution of high-alumina basalts of the Klyuchevskoy volcano, Kamchatka, Russia, based on microprobe analyses of mineral inclusions, *J. Volcanol. Geotherm. Res.*, *95*, 65–79.

Park, J., V. Levin, M. Brandon, J. Lees, V. Peyton, E. Gordeev, and A. Ozerov (2002), A dangling slab, amplified arc volcanism, mantle flow and seismic anisotropy in the Kamchatka plate corner, in *Plate Boundary Zones*, *Geodynamic Series*, vol. 30, edited by S. Stein, and J.T. Freymueller, pp. 295–324, American Geophysical Union, Washington, D.C..

Peacock, S. M., T. Rushmer, and A. B. Thompson (1994), Partial melting of subducting oceanic crust, *Earth Planet. Sci. Lett.*, *121* (1-2), 227–244.

Peacock, S. M., P. E. van Keken, S. D. Holloway, B. R. Hacker, G. A. Abers, and R. L. Fergason (2005), Thermal structure of the Costa Rica—Nicaragua subduction zone, *Physics of The Earth and Planetary Interiors*, *149* (1-2), 187–200.

Pearce, J. A., and I. J. Parkinson (1993), Trace element models for mantle melting: application to volcanic arc petrogenesis, in *Magmatic Processes and Plate Tectonics*, edited by H.M. Prichard, T. Alabaster, N. B. Harris, and C. R. Neary, pp. 373–403, Geological Society Special Publication, London.

Pearce, J. A., and D. W. Peate (1995), Tectonic implications of the composition of volcanic arc magmas, *Annual Review of Earth and Planetary Sciences*, *23*, 251–285.

PETDB (2004), Petrological Database of the Ocean Floor, http://www.petdb.org.

Pilipchuk, N. A., V. S. Uspensky, N. F. Krikun, and V. I. Nikolaeva (2006), *The state geologic map of the Russian Federation, scale 1: 200 000*, *Eastern Kamchatka Series, sheet O-57-XXX.* Explanation notes, VSEGEI, St.-Peterburg. (in Russian)

Pineau, F., M.P. Semet, N. Grassineau, V.M. Okrugin, and M. Javoy (1999), The genesis of the stable isotope (O,H) record in arc magmas: the Kamchatka's case, *Chem. Geol.*, *135*, 93–124.

Plank, T., and C. H. Langmuir (1988), An evaluation of the global variations in the major element chemistry of arc basalts, *Earth Planet. Sci. Lett.*, *90*, 349–370.

Plank, T., and C. H. Langmuir (1998), The chemical composition of subducting sediment and its consequences for the crust and mantle, *Chem. Geol.*, *143*, 325–394.

Pokrovsky, B. G., and O. N. Volynets (1999), Oxygen-isotope geochemistry in volcanic rocks of the Kurile-Kamchatka arc, *Petrology*, *7*, 227–251.

Ponomareva, V., T. Churikova, I. Melekestsev, O. Braitseva, M. Pevzner, and L. Sulerzhitsky (2007a), Late Pleistocene-Holocene Volcanism on the Kamchatka Peninsula, Northwest Pacific Region, this volume.

Ponomareva, V., P. Kyle, M. Pevzner, L. Sulerzhitsky, and M. Hartman (2007b), Holocene Eruptive History of Shiveluch Volcano, Kamchatka Peninsula, Russia, this volume.

Portnyagin, M. V., K. Hoernle, and G. P. Avdeiko (2003), Evidence for decompressional melting of garnet peridotite at the Kamchatka-Aleutian junction, *Geochim. Cosmochim. Acta*, *67* (18), Suppl. 1, Goldschmidt Conference Abstracts, A381.

Portnyagin, M., K. Hoernle, G. Avdeiko, F. Hauff, R. Werner, I. Bindeman, V. Uspensky, and D. Garbe-Schönberg (2005a), Transition from arc to oceanic magmatism at the Kamchatka-Aleutian junction, *Geology*, *33 (1)*, 25–28.

Portnyagin, M. V., K. Hoernle, P. Y. Plechov, N. L. Mironov, and S. A. Khubunaya (2007), Constraints on mantle melting and composition and nature of slab components in volcanic arcs from volatiles (H_2O, S, Cl, F) and trace elements in melt inclusions from the Kamchatka Arc, *Earth Planet. Sci. Lett.*, *255 (1-2)*: 53–59.

Prouteau, G., B. Scaillet, M. Pichavant, and R. Maury (2001), Evidence for mantle metasomatism by hydrous silicic melts derived from subducted oceanic crust, *Nature*, *410*, 197–200.

Rapp, R. P., and E. B. Watson (1995), Dehydration Melting of Metabasalt at 8–32 kbar: Implications for Continental Growth and Crust-Mantle Recycling, *J.Petrol.*, *36* (4), 891–931.

Rapp, R. P., N. Shimizu, M. D. Norman, and G. S. Applegate (1999), Reaction between slab-derived melts and peridotite in the mantle wedge: experimental constraints at 3.8 GPa, *Chem. Geol.*, *160*, 335–356.

Renkin, M. L., and J. G. Sclater (1988), Depth and age in the north Pacific, *J. Geophys. Res.*, *93*, 2919–2935.

Reiners, P. W., B. K. Nelson, and M. S. Ghiorso (1995), Assimilation of Felsic Crust by Basaltic Magma—Thermal Limits and

Extents of Crustal Contamination of Mantle-Derived Magmas, *Geology*, *23* (6), 563–566.

Regelous, M., A. W. Hofmann, W. Abouchami, and S. J. G. Galer (2003), Geochemistry of lavas from the Emperor Seamounts, and the geochemical evolution of Hawaiian Magmatism from 85 to 42 Ma, *J. Petrol.*, *44* (1), 113–140.

Ringwood, A. E. (1990), Slab-mantle interactions 3. Petrogenesis of intraplate magmas and structure of the upper mantle, *Chem. Geol.*, *82*, 187–207.

Rüpke, L., J. Phipps Morgan, M. Hort, and J.A.D. Connolly, Are the regional variations in Central American arc lavas due to differing basaltic versus peridotitic slab sources of fluids?, *Geology*, *30* (11), 1035–1038, 2002.

Salters, V. J. M., and A. Stracke (2004), Composition of the depleted mantle, *Geochem. Geophys. Geosyst.*, *5* (5), Q05004, doi:10.1029/2003GC000597.

Sen, C., and T. Dunn (1994), Dehydration melting of a basaltic composition amphibolite at 1.5 and 2.0 GPa: implications for the origin of adakites, *Contrib. Mineral. Petrol.*, *117*, 394–409.

Shaw, D. M. (1970), Trace element fractionation during anatexis, *Geochim. Cosmochim. Acta*, *34*, 237–243.

Shimoda, G., Y. Tatsumi, S. Nohda, K. Ishizaka, and B. M. Jahn (1998), Setouchi high-Mg andesites revisited: geochemical evidence for melting of subducting sediments, *Earth Planet. Sci. Lett.*, *160*, 479–492.

Smirnov, Y. B., and V. M. Sugrobov (1980), Terrestrial heat flow in the Kuril-Kamchatka and Aleutian provinces: II, The map of measured and background heat flow, *Vulcanologya i Seismologiya*, *1*, 16–31. (in Russian)

Sobolev, A. V., and M. Chaussidon (1996), H_2O concentrations in primary melts from island arcs and mid-ocean ridges: Implications for H_2O storage and recycling in the mantle, *Earth Planet. Sci. Lett.*, *137*, 45–55.

Sobolev, A. V., A. W. Hofmann, S. V. Sobolev, and I. K. Nikogosian (2005), An olivine free mantle source of Hawaiian shield basalts, *Nature*, *434*, 590–597.

Stalder, R., S. F. Foley, G. P. Brey, and I. Horn (1998), Mineral-aqueous fluid partitioning of trace elements at 900–1200°C and 3.0–5.7GPa: New experimental data for garnet, clinopyroxene, and rutile, and implications for mantle metasomatism, *Geochim. Cosmochim. Acta*, *62* (10), 1781–1801.

Stolper, E., and S. Newman (1994), The role of water in the petrogenesis of Mariana Trough magmas, *Earth Planet. Sci. Lett.*, *121* (3-4), 293–325.

Stern, C. R., and R. Kilian (1996), Role of the subducted slab, mantle wedge and continental crust in the generation of adakites from the Andean Austral Volcanic Zone, *Contrib. Mineral. Petrol.*, *123*, 263–281.

Sun, S.-S., and W. F. McDonough (1989), Chemical and isotopic systematics of oceanic basalts: implications for mantle composition and processes, in *Magmatism in the Ocean Basins*, edited by A.D. Saunders, and M. J. Norry, pp. 313–345, Geological Society Special Publication, London.

Tamura, Y., Y. Tatsumi, D. Zhao, Y. Kidp, and H. Shukuno (2002), Hot fingers in the mantle wedge: new insights into magma genesis in subduction zones, *Earth Planet. Sci. Lett.*, *197*, 105–116.

Tatsumi, Y. (1981), Melting experiments on a high-magnesian andesite, *Earth Planet. Sci. Lett.*, *54*, 357–365.

Tatsumi, Y., and K. Ishizaka (1981), Existence of andesite primary magma: an example from southwest Japan, *Earth Planet. Sci. Lett., 53*, 124–130.

Tatsumi, Y., D. L. Hamilton, and R.W. Nesbitt (1986), Chemical characteristics of fluid phase released from a subducted lithosphere and origin of arc magmas: evidence from high-pressure experiments and natural rocks, *Journal of Volcanology and Geothermal Research*, *29*, 293–309.

Tatsumi, Y. (2001), Geochemical modeling of partial melting of subducting sediments and subsequent melt-mantle interaction: Generation of high-Mg andesites in the Setouchi volcanic belt, southwest Japan, *Geology*, *29* (4), 323–326.

Tatsumi, Y., H. Shukuno, K. Sato, T. Shibata, and M. Yoshikawa (2003), The Petrology and Geochemistry of High-Magnesium Andesites at the Western Tip of the Setouchi Volcanic Belt, SW Japan, *J. Petrol.*, *44* (9), 1561–1578.

Thompson A. B. (1992), Water in the Earth's upper mantle, *Nature*, *358*, 295–302.

Tolstykh, M. L., V. B. Naumov, A. D. Babansky, G. E. Bogoyavlenskaya, and S. A. Khubunaya (2003), Chemical Composition, Volatile Components, and Trace Elements in Andesitic Magmas of the Kurile–Kamchatka Region, *Petrology*, *11* (5), 407–425.

Turner, S., F. McDermott, C. Hawkesworth, and P. Kepezhinskas (1998), A U-series study of lavas from Kamchatka and the Aleutians: constraints on source composition and melting processes, *Contrib. Mineral. Petrol.*, *133*, 217–234.

Ulmer, P., and V. Trommsdorff (1995) Serpentine Stability to Mantle Depths and Subduction-Related Magmatism, *Science*, *268* (5212), 858–861.

van Keken, P. E., B. Kiefer, and S. M. Peacock (2002), High resolution models for subduction zones: implications for mineral dehydration reactions and the transport of water into deep mantle., *Geochem, Geophys. Geosyst.*, *3(10)*, 1056, doi:10.1029/2001GC000256.

Volynets, O. N. (1994), Geochemical types, petrology, and genesis of the late Cenozoic volcanic rocks from the Kurile-Kamchatka island-arc system, *International Geology Review*, *36* (4), 373–403.

Volynets, O. N., V. V. Ponomareva, and A. D. Babansky (1997), Magnesian basalts of Shiveluch andesite volcano, Kamchatka, *Petrology*, *5* (2), 183–196.

Volynets, O. N., I. V. Melekestsev, and V.V. Ponomareva, J. M. Yogodzinski (1998) Kharchinsky and Zarechnyi volcanoes—unique centers of Late Pleistocene magnesian basalts in Kamchatka: structural setting, morphology, geologic structure and age, *Volcanology and Seismology*, 20 (4-5), 383–400.

Volynets, O. N., I. V. Melekestsev, V. V. Ponomareva, and J. M. Yogodzinski (1999), Kharchinsky and Zarechnyi volcanoes, unique centers of Late Pleistocene magnesian basalts in Kamchatka: Composition of erupted rocks. *Volcanology and Seismology*, 21 (1), 45–66

Volynets, O. N., A. D. Babanskii, and Y. V. Gol'tsman (2000), Variations in Isotopic and Trace-Element Composition of Lavas from volcanoes of the Northern Group, Kamchatka, in Relation to Specific Features of Subduction, *Geochemistry International*, *38* (10), 974–989.

von Huene, R., Ranero, C.R., Vannucchi, P. (2004), Generic model of subduction erosion, *Geology* 32 (10), 913–916.

Workman, R. K., and S. R. Hart (2005), Major and trace element composition of the depleted MORB mantle (DMM), *Earth Planet. Sci. Lett.*, *231* (1-2), 53–72.

Wyllie, P. J. (1979), Magmas and volatile components, *Am. Mineral.*, *64*, 469–500.

Yaxley, G. M., and D. H. Green (1998), Reactions between eclogite and peridotite: mantle refertilisation by subduction of oceanic crust, *Scweiz. Mineral. Petrogr. Mitt.*, *78*, 243–255.

Yogodzinski, G. M., O. N. Volynets, A. V. Koloskov, N. I. Seliverstov, and V. V. Matvenkov (1994), Magnesian andesites and the subduction component in a strongly calc-alkaline series at Piip volcano, Far Western Aleutians, *J. Petrol.*, *35* (1), 163–204.

Yogodzinski, G. M., R. W. Kay, O. N. Volynets, A. V. Koloskov, and S. M. Kay (1995) Magnesian Andesite in the Western Aleutian Komandorsky Region: Implications for Slab Melting and Processes in the Mantle Wedge, *Geol. Soc. Am. Bull.*, *107* (5), 505–519.

Yogodzinski, G. M., J. M. Lees, T. G. Churikova, F. Dorendorf, G. Wörner, and O. N. Volynets (2001), Geochemical evidence for the melting of subducting oceanic lithosphere at plate edges, *Nature*, *409*, 500–504.

An Estimation of Magmatic System Parameters From Eruptive Activity Dynamics

Yurii Slezin

Institute of Volcanology and Seismology FED RAS, Petropavlovsk-Kamchatsky, Russia

Eruptive activity dynamics characterizes the changes in eruptive regime over time. Eruptive activity can be characterized by: the relation between eruptions and repose periods, the mass flow rate of eruption, the type and structure of the erupted products, and their velocity at the conduit exit. These characteristics and their evolution over time depend on both the structure of the magmatic system and on some external factors. These factors define the boundary conditions and include the eruptive prehistory. This study deals with the inverse problem: reconstruction of the structure of the magmatic system using the eruptive activity dynamics. The critical role of the sharp jump-like changes in eruption regime and intensity described theoretically in [*Slezin*, 1983, 1984, 1998, 2003a] is emphasized and the additional information needed to obtain a unique solution is discussed. Using this inverse approach in conjunction with a "chamber-conduit" model, some geometrical parameters of the following magma systems were estimated: Shiveluch, Mt St Helens, and Bezymianny.

1. GENERAL CHARACTERISTICS OF THE MAGMATIC SYSTEM OF AN ERUPTING VOLCANO.

1.1. The Substance

1.1.1. Magma. Magma is a silicate melt in the depth of the Earth, which contains dissolved volatile components (mostly water). When the ambient pressure is reduced or crystallization occurs, volatiles are exsolved. Magma almost always has some crystal content, which is usually not taken into account *directly* in the description of magma flow, although some models consider crystal content as a factor influencing magma rheology [Papale, 1999; Melnik and Sparks, 2005]. Magma is assumed to be in a liquid state with a given density and viscosity and, in certain cases, with a given yield stress. During an eruption, magma loses its volatiles and is transformed into volcanic products, which appear on the surface.

Volcanism and Subduction: The Kamchatka Region
Geophysical Monograph Series 172

10.1029/172GM17

1.1.2. Volcanic products. The eruptive products result from the magma separation into volatile and nonvolatile components: i.e. a gas and a condensed phase. The latter can be lava or pyroclastics. The type and structure of the volcanic products depends on the composition of the initial magma as well as on the eruption dynamics. Lava is a viscous liquid; pyroclasts are the magma fragments dispersed in gas flow and usually described as solid particles. The transformation of magma into volcanic products occur during eruption in a volcanic conduit, where melt with bubbles and gas-pyroclastic mixture can flow.

1.2. The Magma System Geometry

The mass flow rate of erupting volcanic products averaged over a time interval, which includes several successive eruptions of a volcano treated as "events", is nearly constant [Kovalev, 1971; Tokarev, 1977]. This fact and the observed proportionality between a single erupted mass of magma to the duration of the repose interval, preceding that eruption [Tokarev, 1977; Simkin, T., Siebert, L., 1984], implies the existence of some holding capacity, where the magma is stored during the repose intervals [Kovalev, 1971; Kovalev and Slezin, 1974]. This capacity is often referred to as a peripheral magma chamber, which is fed from deeper parts of the magma system. The existence of the peripheral magma chambers under volcanoes (later referred as "magma chambers") has been demonstrated by geological and geophysical studies [Luchitsky, 1971; Farberov, 1974].

Because of the high intensity of eruptions and the short duration of them with respect to the duration of the repose intervals one can assume, as a first order model of an erupting volcano, a "chamber-conduit" system being isolated in all directions except the conduit exit to atmosphere. More complicated models can include a magma chamber feeding from the depth during an eruption and some heat and mass (volatile components mostly) exchange with the external medium.

1.2.1. Magma chamber. This is an approximately isometric capacity filled with magma on the order of a few to thousands of cubic kilometers. In models, the magma chamber is usually described as a vertical cylinder which height is less than the diameter. The upper boundary of a magma chamber is situated at a depth varying from a few kilometers to a few tens of kilometers from the Earth surface.

1.2.2. Volcanic conduit. In the solid crust the conduit appears initially as a fissure, which later can transform to a cylinder. Such a transformation proceeds very rapidly near the surface at the conditions of a very intense gas-pyroclastic flow. The cross-sectional area, as well as the volume of a conduit, is significantly less than those of a chamber. In existing models a vertical conduit with a constant cross-sectional area is usually assumed.

2. THE DYNAMICS OF THE ERUPTIVE ACTIVITY OF A VOLCANO: GENERAL CHARACTERISTICS

The principal feature of the eruptive activity of a volcano is its intermittence, which usually includes overlapped periods of approximate periodicity. The main rhythm is alternation of the eruptions-events and repose intervals. The larger periods are called cycles of activity, every one of which includes several eruptions with regularly varying characteristics. Every individual eruption is a non-uniform process with regularly changing successive stages including paroxysms and pauses. There is no objective true criterion to distinguish a repose interval between eruptions from a pause in an eruption. Kovalev et al. [1971] proposed to define eruption as a process, not as an event.

In the course of every cycle of activity, and often during every individual eruption, not only variation of the magma mass flow rate is observed, but also variation of the eruption regime. Sometimes very large and sharp changes in the type and velocity of the erupting volcanic products are related to a large and sharp change of the magma mass flow rate. These sharp changes from one steady (quasi-steady) regime to another may provide us with important information about the structure of the magma system.

2.1. The Principal Eruption Regimes and the Types of Volcanic Products

The regime of a volcanic eruption depends on the continuous phase (gas, magma) in the eruption flow at the exit of the conduit.

The volatile component of magma as a rule is composed of at least 95% water [Fedotov (ed.), 1984; Yirabayashi et al., 1984; Menyailov et al., 1985, 1988]. In mechanical models of magma flow, the volatile component is usually treated as 100% water. The exsolved gas phase appears in the form of bubbles. Initial dissolved mass fraction and solubility of water in magma are of such values that at the atmospheric pressure at the conduit exit, the volume flow rate of gas is tens or hundreds times that of the condensed phase. The volume relation between phases in the flow depends on the relative velocities. Consequently, the condensed phase can keep its continuity only if its velocity at the conduit exit is much less than that of the gas phase.

Extensive escape of gas from magma can be provided by two mechanisms: 1) fast uplift of bubbles through the liquid and 2) continuous leakage of gas through a system of channels in condensed phase. This results in three basic regimes of eruption and three corresponding types of volcanic products: 1) effusive regime: there is a bubbly flow in the conduit; the excessive amount of gas escapes with floating bubbles; the eruption produces lava flows; 2) extrusive regime: the excessive amount of gas escapes through the permeable system of interconnected bubbles; the eruption of a very viscous lava forms an extrusive dome; 3) explosive regime: the eruption of the gas-pyroclastic flow, in which gas is a continuous phase and pyroclastics is the dispersed phase. The conditions of realization of any of these regimes were found by the author [Slezin, 1979, 1995b, 2003a].

2.2. The Types of Eruptions and the Evolution of the Flow Structure in a Volcanic Conduit

An eruption-event usually includes several successive regimes. The most complete succession of regimes is demonstrated by so called "catastrophic explosive eruptions" (CEE). The most thoroughly investigated eruption of that type is the eruption of Mount St. Helens in 1980 [Lipman and Mullineaux, 1981]. In this case a moderate "intrusive-explosive" regime changed to a gas-pyroclastic flow of high intensity (catastrophic phase), then to the extrusive regime of low intensity. There was a repose interval between catastrophic and extrusive phases. All the regime changes were very sharp.

During a gas-pyroclastic eruption, all types of the flow take place in the conduit: homogeneous liquid, bubbly liquid, partly destroyed foam and gas-pyroclastic mixture, which is observed at the surface. In the starting and finishing stages of an eruption of this type a steady flow of the gas-pyroclastic mixture is absent in the conduit, and bubbly liquid or partly destroyed foam [*Slezin*, 1980, 1995b, 2003a] is instead erupted. In the final stage an extrusive regime (eruption of partly destroyed foam) takes place [*Slezin*, 1995a].

2.3. Theoretical Basis

2.3.1. Eruption. The sharp transitions from a moderate stage of an eruption to a catastrophic and vice versa are results of a smooth change of the governing parameters of the magma system [*Slezin,* 1984, 1991, 2003a]. They also can be initiated by external factors (such as landslides) if these external factors change the governing parameters in a due direction.

The basic features of the magma system outlined above allow us, as a first approximation, to reduce the problem of eruption dynamics to the description of the quasi-steady flow of degassing magma in a vertical conduit with nearly constant (slowly varying) geometry under a given (slowly varying) pressure difference between conduit ends. The behavior of such flow, including jump-like changes of regimes, is described using equations of hydrodynamics for a steady-state two-phase two-component flow with relevant boundary conditions for the conduit ends and for the boundaries between zones [*Slezin*, 1983, 1998, 2003a].

The recent development of numerical models allowed taking into account additional parameters such as time dependence, variation of magma rheology, heat and mass transfer through the chamber and conduit walls, viscous dissipation, variation of magma properties in two spatial dimensions and in time [e.g. *Papale*, 1999; *Melnik* and *Sparks*, 2005; *Vedeneeva* et al.,2005]. These models provide more accurate solutions for specific aspects of an eruption, and are in a good agreement with the results of this study.

For the analysis of effects the following three basic governing parameters were selected: 1) depth of the magma chamber (length of the conduit), H; 2) excess pressure in the magma chamber, p_{ex}, (equal to total pressure minus static pressure of overlying conduit magma column without bubbles); 3) "conductivity parameter of the conduit" $\sigma = b^2/\eta$, where b is a characteristic cross sectional dimension of the conduit, and η is viscosity. It has been demonstrated, that the dependence of the flow rate on any pair of basic governing parameters has a "cusp singularity" and in a certain area every point in a plane of the arguments has three images on the folded plane of the function. This is a standard "catastrophe" of two-parameter sets of functions [*Poston* and *Stewart*, 1980] (Figure), which describes jumps of a function under smooth changes of the arguments.

This explains abrupt changes in eruption regime: the transition from moderate to catastrophic explosive regime is a result of the conductivity parameter increase (Figure) or the conduit length decrease (e.g. due to a volcano summit destruction by explosions or landslide). Conversely, the transition from catastrophic to extrusive regime is a result of decreasing excess chamber pressure and/or conduit

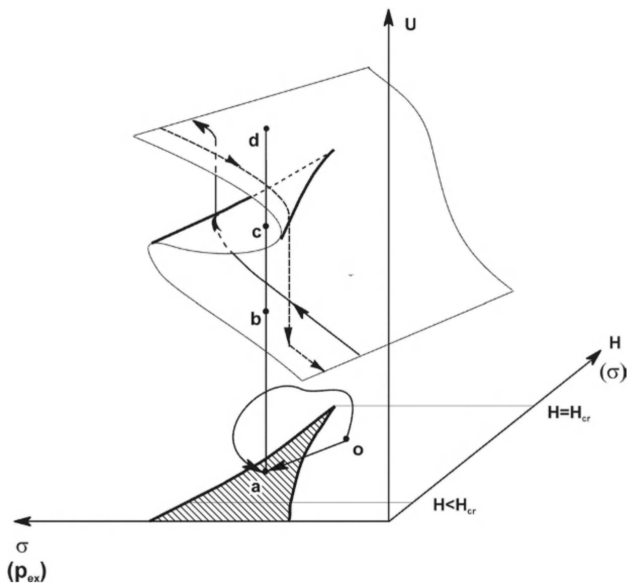

Figure. Magma ascent velocity U as a function of conduit conductivity parameter σ and conduit length H. Note that analytical solution for U as a function of excess pressure in the magma chamber p_{ex} and σ has the same form. Vertical scale is logarithmic. The hatched cusp on the plane of arguments encompasses parameters σ, H, and p_{ex} at which the "catastrophe" scenario is possible. For example, at point a the magma ascent velocity can be b, c, and d corresponding to three eruption regimes with different magma flow rates. The jump-like changes of the magma ascent velocity can be caused by increase of conduit conductivity or by decrease of the excess pressure in magma chamber (indicated by arrows). The straight trajectory leading from point o to point a on the plane of arguments intersects the cusp boundary and leads the function to the catastrophe scenario, whereas the trajectory going from o to a around the cusp leads the function to the point d without any sharp changes of magma velocity. The later case is rather exotic, as it requires a gradual change of H or c_0. Please refer to the text for discussion.

conductivity. The flow velocity jump can be seen as the result of the positive feedback when positive effect of the decrease of the liquid flow region length and average flow density in the conduit prevails over the negative effect of the viscous friction increase. This may become possible due to a several orders of magnitude difference of friction coefficients between zones of liquid and gaseous flow in case when the conduit length is not very large.

2.3.2. An approach to the inverse problem. It appeared that sharp jump-like changes of the eruptive regime could be realized only in a narrow range of parameters of a volcanic system, which is helpful for solving the inverse problem. The very fact of the sharp change of regime applies strict limits on the values of the parameters. The additional quantities such as magma mass flow rate values before and after the jump, duration of the certain stages of eruption, flow velocity, total mass erupted during a certain stage of eruption, and the magma properties, obtained by studying of the erupted volcanic products, give information, which in nearly all cases, is sufficient to allow full reconstruction of the magma chamber and conduit parameters.

Because the system of hydrodynamic equations for the two-component two-phased flow can be solved only by numerical methods, in practice a series of direct problems were solved and the proper structure of the magma system boundary conditions and prehistory chosen.

3. ESTIMATING OF THE PARAMETERS AND EXAMPLES

3.1. Magma Chamber Parameters

3.1.1. The depth of the upper boundary (conduit length). In the most cases after a repose period, a new eruption is started by breaking a new conduit in the shape of a fissure in the solid rocks overlying the chamber, or in a plug sealing up the upper part of the conduit after a previous eruption. The normal evolution of eruption after such a start is connected with widening of the new conduit (destruction of the plug) by the flow. Sometimes this process is very sharp and catastrophic. An increase in magma mass flow rate as well as magma velocity, leads to the transformation from an effusive or extrusive regime to a gas-pyroclastic regime with mass flow rate increase by two or more orders of magnitude [*Slezin,* 1984, 1998, 2003a]. At the end of eruption the reverse sharp transformation with a corresponding mass flow rate decrease (usually with a bigger amplitude than at the start) is probable [*Slezin*, 1991*,* 2003a].

It was found that the sharp jump-like increase of magma mass rate can take place only if the magma chamber depth (conduit length) is less than some critical value H_{cr}, which depends at a first approximation on the initial content of the water dissolved in magma c_0 only [*Slezin*, 1994]. In the cited paper the empirical formula for the H_{cr} is given:

$$H_{cr} = 356(c_0 - 0.01), \qquad (1)$$

where H is in km and c_0 is a wt. fraction.

One can conclude that if the jump-like transition took place the water content must be not less than 0.01 and that if the water content is known the chamber depth must be less than it is given by expression (1). One can estimate the low limit of the possible water content in magma if the magma chamber depth is known.

Additional data allow a more accurate estimation of magma chamber depth. If a magma chamber depth is large enough that the fragmentation level has not reached it, only the conduit is effectively evacuated and the loss of magma is not very large. As a result, the time interval between the end of the gas-pyroclastic stage and the beginning of the extrusive stage must be small. The closer a chamber is located to the surface, the deeper its relative evacuation and the longer the time interval between catastrophic and extrusive stages. This dependence is confirmed qualitatively by observations of the eruptions of Bezymyanny in 1956 (magma chamber depth is 12 km and the interval no more than a few days) and Mt. St. Helens in 1980 (magma chamber depth is 7.2 km and the interval 3 weeks) [Lipman and Mullineaux, 1981; Rutherford et al, 1985]. After the catastrophic eruption of Shiveluch in 1964 the repose interval before the start of the extrusive stage was 16 years, and the author suggested that magma chamber depth must be less than that of the Mount St. Helens (i.e. less than 7 km) [*Slezin*, 1995a]. Recently the depth was estimated to be between 5 and 6 km based on the pressure at which melt inclusions in phenocrysts of the erupted products were entrapped [*Dirksen et al.,* 2006].

3.1.2. Magma chamber diameter. Estimation of the horizontal dimensions of a magma chamber is possible for shallow chambers which are deeply evacuated during a large catastrophic eruption. In this case the evacuated volume of the conduit as a first approximation can be neglected relative to the chamber evacuated volume, and all the magma erupted can be assumed to have been transported from the chamber.

The degree of magma chamber evacuation ("magma drawdown" Δ [*Spera* and *Crisp*, 1981]) can be calculated using formulas given in [*Slezin*, 1987] if the volume fraction of a gas phase near the upper boundary of the magma chamber at the end of a catastrophic stage of eruption is known. This fraction can be calculated by the method of [*Slezin*, 1998, 2003a] if the magma chamber depth and the dissolved water content are known.

Magma chamber evacuation is a result of magma foaming and can proceed up until the start of foam destruction in the magma chamber (i.e. the fragmentation level enters the magma chamber), which causes stopping of the eruption of condensed material. A large negative value of the p_{ex} causes conduit wall and chamber ceiling destruction that may lead to conduit blocking. The beginning of disruption of the silicate foam in the chamber is taken as a condition of the catastrophic stage ceasing. This process starts approximately when the volume fraction of bubbles corresponds to the state of tight packing, and this last was taken as a formal condition in the model.

If the magma chamber depth and the dissolved water content are found independently, magma drawdown Δ can be calculated. The horizontal cross-sectional area of a cylindrical magma chamber can then be calculated by dividing the total volume of the erupted products reduced to the magma density in the chamber by the value of Δ. Using this method, this area was found by the author for the volcano Shiveluch [*Slezin,* 2005] to be little more than 0.5 km^2. For the volcano Mt. St. Helens, for which the chamber cross sectional area was known, the value of the coefficient *a* in the water solubility law in magma $c = ap^{1/2}$ was estimated [*Slezin*, 1987]. It appeared to be close to the value obtained using experimental data for the appropriate magma composition.

3.1.3. Vertical dimension. In some cases the vertical dimension of a magma chamber can also be estimated. For the shallow chamber, where the fragmentation level reached upper boundary of it, the value Δ can be calculated using formulas given in [*Slezin*, 1987, 2003a] if the dissolved water content of the magma is known and the lower boundary of the magma chamber is deeper than the level where bubble nucleation starts. The value of Δ in this case is about 3 km assuming an initial dissolved water content of about 5%. The value of Δ can also be calculated by dividing the total erupted volume reduced to the dense magma by the cross-sectional area of the chamber if this is known. The value of Δ was calculated using this last method for the 76 caldera-forming eruptions in [*Spera* and *Crisp*, 1981] and in most cases it was significantly less than the maximum (~3 km). This fact can be explained by the assumption that the lower boundary of the magma chamber is above the level of bubble nucleation. In this case Δ can be calculated by the same formulas from [*Slezin*, 1987, 2003a] substituting the vertical chamber dimension h_1 instead of the level of the bubble nucleation start z_1. The value h_1 is found iteratively provided that the calculated Δ is equal to Δ obtained from field data.

All of the calculations described above must be treated as estimates because the accuracy of data used is not quite high. For example, one of the main sources of uncertainty for the chamber evacuation model is the value of the coefficient *a* in the expression for water solubility. The result is very sensitive to this value, which is found experimentally for melts of similar, but not exactly the same composition, and under similar, but not exactly the same conditions.

3.2. Conduit Parameters

A volcanic conduit is characterized by its length, area and shape of cross-section. The first parameter was discussed in the previous section, whereas the last one is closely related to the conductivity parameter σ described in the first section:

$$\sigma = b^2/\eta \tag{2}$$

Magma mass flow rate, which can be measured on every stage of an eruption, is proportional to the product of the conduit cross-sectional area, magma density and magma velocity. The total resistance of a volcanic conduit approximately equal to the resistance of the liquid flow zone. Magma velocity in the liquid flow zone is proportional to the product of the driving pressure difference and conductivity parameter. Conductivity parameter σ and magma velocity can be found by numerical calculations for the conditions of jump-like change of regime and the conditions before and after the jump. If the magma mass flow rate is known then the conduit cross-sectional area can be calculated. If the magma viscosity is known independently (using experimental data for melts of similar composition at similar thermodynamic conditions) the characteristic dimension b can be found and also the shape of the cross section and parameters of the fissure if the shape is fissure-like. If the viscosity varies along the conduit average value should be used.

Using this method the radius of the cylindrical conduit for the 1964 eruption of Shiveluch was estimated to be approximately 70 m. In this case the cylindrical shape of the conduit cross section corresponding to catastrophic stage was postulated as an independent assumption [*Slezin*, 2005].

For Mt. St. Helens with a deeper situated magma chamber and a less intensive eruption the magma velocity was estimated at U~0.5 m/s and the conductivity parameter $\sigma \sim 10^{-4}$ $m^2\ Pa^{-1}\ s^{-1}$ [*Slezin*, 2003b]. Knowing the erupting magma volume rate reduced to dense magma (~8000 m^3/s [Lipman and Mullineaux, 1981]) the cross-sectional area can be found ($S = 16000\ m^2$) and the cross-sectional dimension b, or viscosity η for a given shape. If the cross section has a circular shape, the viscosity must be ~10^9 Pa s. At the same time the viscosity of a melt with the composition of Mt. St. Helens magma at the pressure and temperature corresponding to magma fragmentation in accordance to experimental data of [*Williams* and *McBirney*, 1979] must be about 10^6 Pa s. Taking this latter value and using formula (2) b is estimated to be approximately 10 m. So below the fragmentation level the conduit cross-section supposed to be a fissure with a width of 10 m and about 1600 m in length.

3.3. Other Characteristics of a Magma System

"Chamber-conduit" is the first approximation in volcanic magma system modeling. Peripheral chambers are fed from deeper situated magma-generating zones through some feeding channels. The last ones can include intermediate chambers and conduits. The deep part of a magma system also affects eruption dynamics, and some features of the latter bear some information about the former. Heat and mass transfer in the depth are much more inertial processes than at shallower depths. Consequently, the dynamic effects related to the deeper parts of the magma system must be connected with the longer time intervals. They may be connected with cycles of volcanic activity including several eruptions and repose periods and with the evolution of volcanic groups or volcanic centers composed of several individual volcanoes.

Little was made in this field for the time being. Only a constant flow or episodic impulses from the depth were taken into account as external affects, and cycles of activity were described only as a probable result of a deep zone dynamics (for example: [*Kovalev et al*., 1971; *Slezin*, 2005]). Recently the dynamics of extrusive eruptions were analyzed quantitatively in [*Melnik* and *Sparks*, 2005] with the help of a transient model, which incorporated many characteristics including the constant feeding of the chamber from depth, volatile diffusion in melt and decompression-induced crystallization. Such transient models should be very useful for solving the inverse problem.

4. CONCLUSION

It can be concluded that in most cases for volcanoes which erupt "in full cycle" including catastrophic explosive stage the geometrical structure of the upper part of magma system can be reconstructed with satisfactory accuracy using a very simple model. The model describes a "chamber-conduit" system, which geometrical parameters can be found for any individual volcano. The approach relies on using the conditions for eruption stability and sharp changes between main eruptive regimes. Quantitative results can be obtained using rather simple model and approximate data.

Catastrophic explosive eruptions and caldera-forming eruptions are common for andesitic volcanoes in subduction zones. The outlined approach can be used to reconstruct the structure of magma systems beneath volcanoes of Pacific subduction zones, particularly the Kurile-Kamchatka and Aleutian island arcs. The magma system structure must depend on the magma generation process, which, in its turn, depends on the local tectonic setting and on specific features of the local subduction process. Hence the studying and modeling of the volcanic activity dynamics and reconstruction of the magma systems structure of the volcanoes along Pacific Fire Ring may throw light on the total geodynamic situation and on specific features of the subduction process and magma generation in different parts of this global structure. In the North-West part of the Pacific Ring of Fire it would be interesting to compare Aleutian and Kurile-Kamchatka island arcs. It will be especially interesting to examine the specific tectonic features and magma generation process found at the junction of these Island Arcs, where the Shiveluch volcano and the Kliuchevskaya volcanic group are located.

Advanced numerical models, which appeared in recent time, take into account some additional factors such as variation of magma rheology, heat and mass transfer through the chamber and conduit walls, viscous dissipation, variation of magma properties in two spatial dimensions and in time [Papale, 1999; *Melnik* and *Sparks*, 2005; Vedeneeva et al., 2005]. These models combined with the described approach will likely yield more accurate quantitative results.

Acknowledgments. I am grateful to Joanna Malcolm, Oleg Melnik and Pavel Izbekov for useful comments and for improving the English of the manuscript.

REFERENCES

Dirksen, O., M. C. S. Humphreys, P. Pletchov, O. Melnik, Y. Demyanchuk, R.S.J. Sparks, and S. Mahony. (2006) The 2001–2004 dome-forming eruption of Shiveluch volcano, Kamchatka: Observation, petrological investigation and numerical modelling, *Journal of Volcanology and Geothermal Research*, *155* (3-4), 201–226.

Farberov, A. I., (1974), Magmatic chambers under volcanoes of Eastern Kamchatka on the base of geophysical data. *Nauka, Novosibirsk.* 88 pp. (In Russian).

Fedotov S. A. (ed.) (1984). The Great Fissure Tolbachik Eruption, Kamchatka 1975–1976, *Nauka, Moscow.* 637 p.

Hirabayashi, J., Ossaka, J., Ozawa, T., and Yoshida, M. (1984). Change in chemical composition of volcanic gases and sublimates collected after the 1983 eruption of Miyakejima. *Bull. Volcanol. Soc. Jap. 29.* S308 S318.

Kovalev, G. N., (1971), On the energetics of the active volcanism. Volcanism and the depth of the Earth. *Proceedengs of the III All Union Volcanol. Conference. Nauka, Moscow*, 41–46. (In Russian).

Kovalev, G. N., Kalashnikova, L. V. and Slezin, Yu. B., (1971), On the connection between eruptions energy and preceding dormant periods duration of the active volcanoes, *Geologia & Geofisika 3*, 137–140. (In Russian).

Kovalev, G. N., and Slezin, Yu. B., (1974), Some aspects of the volcanic dynamics, *Geodynamics of volcanism and geothermal process (IV AllUnion Volcanol. Conf., Abstracts),* 167. (In Russian).

Lipman, P. W. and Mullineaux, D. R. (eds.), (1981), *The 1980 Eruptions of Mount St. Helens, Washington,* 844 pp., U.S. Geological Survey Professional Paper 1250.

Luchitsky, I. V., (1971), Foundations of paleovolcanology. *AN SSSR, Moscow.* V. 2, 382 pp. (In Russian).

Melnik, O., R. S. J. Sparks, (2005), Controls on conduit magma flow dynamics during lava dome building eruptions, *J. Geophys. Res.,* 110, B02209, doi: 10.1029/2004JB003183.

Menyailov, I F., Nikitina, L. P. and Shapar V. N. (1985), Geochemical monitoring the state of some active volcanoes in Kamchatka and Kurile Islands (USSR). *Per. Minera. Vol. 55,* 55–74.

Menyailov, I F., Nikitina, L.P. and Shapar V. N. (1988), Variations in composition of fumarolic gases at Shiveluch volcano (Kamchatka). *Rendiconti della sosieta italiana di mineralogia e petrologia, Vol. 43,* 1185–1194.

Rutherford M. J., Sigurdsson H., Carey S., and Davis A., (1985), The May 18, 1980 eruption of Mount St. Helens. 1. Melt composition and experimental phase equilibria, *J. Geophys. Res.*, *90. No B4*, 2929–2947.

Papale, P. Numerical Simulation of Magma Ascent along Volcanic Conduits., (1999), *Phys. Chem. Earth (A) Vol.24 No 11–12,* pp. 957–961.

Poston, T,, Stewart, I., (1978), Catastrophe theory and its applications, *Pitman* ,London, 510 pp.

Simkin, T., Siebert, L., (1984), Explosive eruptions in space and time: duration, intervals and a comparison of the world's active belts. *Explosive Volcanism: Inception, evolution and hazards,* National Academy Press, Washington, DC, 110–121.

Slezin, Yu. B., (1979), The conditions of origin of the dispersion regime in volcanic eruption. *Vulcanol, and Seismol. 3*, 69–76 (In Russian).

Slezin, Yu. B., (1980), Stationary dispersion regime at the explosive volcanic eruptions, *Volcanol. and Seismol.,* 2, 56–66. (In Russian).

Slezin, Yu. B (1983), The dynamics of dispersion regime in volcanic eruptions: 1. Theoretical description of magma movement through volcanic conduit, *Vulcanol. and Seismol., 5*, 9–17. (In Russian).

Slezin, Yu. B. (1984), The dynamics of dispersion regime in volcanic eruptions: 2. The condition of magma mass rate instability and the nature of catastrophic explosive eruptions, *Vulcanol. and Seismol., 1*, 23–35. (In Russian).

Slezin, Yu. B., (1987), Mechanism of magma chamber evacuation leading to caldera formation, *Vulcanol. and Seismol., 5,* 3–15. (In Russian).

Slezin, Yu. B. (1991), Changes in magma mass rate during a large explosive eruption, *Vulcanol. and Seismol, 1.,* 35–45. (In Russian).

Slezin Yu. B. (1994), The Effect of the magma properties on the character of eruption (the Results of a numerical experiment), *Vulcanol. and Seismol,, 4–5*, 121–127. (In Russian).

Slezin Yu. B. (1995a), The mechanism of extrusive eruptions, *Vulcanol. and Seismol., 4–5,* 76–84. (In Russian). English translation: Slezin Yu. B. (1996), The mechanism of extrusive eruptions. *Volc. Seis.*, *17,* 449–460.

Slezin Yu. B. (1995b), Principal regimes of volcanic eruptions, *Vulcanol. Seismol., No 2,* 72–82. English translation: Slezin Yu. B. (1995), Principal regimes of volcanic eruptions, *Volc. Seis., 17,* 193–206.

Slezin Yu. B. (1998), The mechanism of volcanic eruptions (a steady state model), *Nauchny Mir, Moscow,* 127 p. (In Russian).

Slezin, Yu. B. (2003a), The mechanism of volcanic eruptions (a steady state approach), *J. of Volcanol. and Geothermal Res, 122,* 7–50.

Slezin, Yu. B., (2003b), The characteristics of a volcanic conduit as a result of the analysis of magma mass rate changes, *Proc. 2nd AllRussian Symposuum on Vlcanology and Paleovolcanology, Ekatrinburg, 2003,* 896–900. (In Russian).

Slezin, Yu. B. (2005), The Characteristics of the Shiveluch Magma System, *Vulcanol. and Seismol., 2,* 3–7. (In Russian).

Spera, F. J., and Crisp J. A., (1981), Eruption volume, periodicity, and caldera area: relationships and inferences on development of compositional zonation in silicic magma chambers, *J. Volcanol. and Geotherm. Res., 11*, 169–187.

Tokarev, P. I., (1977), Some natural features of a volcanic process. In: *Magma genesis and its connection with volcanic process. Nauka, Moscow*, 25–40. (In Russian).

Vedeneeva E. A., Melnik O E ,Barmin A. A., Sparks R. S. J. (2005), *Geophys. Res. Letters, Vol 32,LO5303, doi:10.1029/ 2004GL020954.*

Williams H., and McBirney A. R., (1979). Volcanology. *Freeman, Cooper, San Francisco, CA, USA*, 397 pp.

Yurii B. Slezin, Institute of Volcanology and Seismology, Piip Blvd., 9, Petropavlovsk-Kamchatsky. 683006. Russia, e-mail: slezin@kscnet.ru

Diverse Deformation Patterns of Aleutian Volcanoes From Satellite Interferometric Synthetic Aperture Radar (InSAR)

Zhong Lu[1], Daniel Dzurisin[2], Charles Wicks, Jr.[3], John Power[4],
Ohig Kwoun[5], and Russell Rykhus[5]

Interferometric synthetic aperture radar (InSAR) is capable of measuring ground-surface deformation with centimeter-to-subcentimeter precision at a spatial resolution of tens of meters over a large region. With its global coverage and all-weather imaging capability, InSAR has become an increasingly important measurement technique for constraining magma dynamics of volcanoes over remote regions such as the Aleutian Islands. The spatial distribution of surface deformation data derived from InSAR images enables the construction of detailed mechanical models to enhance the study of magmatic processes. This paper summarizes the diverse deformation patterns of the Aleutian volcanoes observed with InSAR. These include the following: 1) inflation of Mount Peulik Volcano preceding a seismic swarm at nearby Becharof Lake in 1998; 2) persistent volcano-wide subsidence at Aniakchak and Fisher Volcanoes; 3) magmatic intrusion and associated tectonic stress release at Akutan Volcano; 4) magmatic intrusion at Makushin Volcano associated with a small eruption in 1995; 5) complex patterns of transient deformation during and after the 1992–93 eruption at Seguam Volcano; 6) subsidence caused by a decrease in pore fluid pressure in an active hydrothermal system beneath Kiska Volcano; and 7) lack of expected deformation associated with recent eruptions at Shishaldin, Pavlof, Cleveland, and Korovin Volcanoes. We also present preliminary InSAR results for the Katmai Volcano group, and Chiginagak and Dutton Volcanoes. These studies demonstrate that deformation patterns and associated magma supply mechanisms in the Aleutians are diverse and vary between volcanoes. These findings provide an improved understanding of magmatic plumbing systems in the Aleutians.

1. INTRODUCTION

The general eruption cycle of a volcano can be conceptualized as a series of events from deep magma generation to surface eruption, including such stages as partial melting, initial ascent through the upper mantle and lower crust, crustal assimilation, magma mixing, degassing, shallow storage, and finally, ascent to the surface [Dzurisin, 2003]. This process is complex, varying from one eruption to the next and from volcano to volcano. However, in many cases, volcanic eruptions are preceded by pronounced ground deformation in response to increasing pressure in magma reservoirs or upward intrusion of magma [Dvorak and Dzurisin, 1997]. Magma reser-

[1] U.S. Geological Survey (USGS), Earth Resources Observation & Science (EROS) Center and Cascades Volcano Observatory, Vancouver, Washington, USA; lu@usgs.gov
[2] USGS, Cascades Volcano Observatory, Vancouver, Washington, USA; dzurisin@usgs.gov
[3] USGS, Earthquake & Volcano Hazards Programs, Menlo Park, California, USA; cwicks@usgs.gov
[4] USGS, Alaska Volcano Observatory, Anchorage, Alaska, USA; jpower@usgs.gov
[5] SAIC, contractor to the USGS EROS Center, Sioux Falls, South Dakota, USA; okwoun@usgs.gov, rykhus@usgs.gov

Volcanism and Subduction: The Kamchatka Region
Geophysical Monograph Series 172

10.1029/172GM18

voirs typically occur at or below the brittle-ductile transition in the crust (~5 km beneath volcanoes). Even though the slow ascent of magma to that depth generally is not marked by earthquakes [e.g., Sibson, 1982], magma accumulation causes surface deformation. This deformation can be subtle—especially if intrusion occurs episodically in a series of small events or gradually over a long time period. Therefore, surface deformation patterns can provide important insight into the structure, plumbing, and state of restless volcanoes [Dvorak and Dzurisin, 1997; Dzurisin, 2003 and 2007]. Deformation can be the first sign of increasing levels of magmatic activity, preceding increased seismicity or other precursors that signal impending intrusions or eruptions.

The Aleutian arc contains about 8 percent of the world's active volcanoes and more than 85 percent of the nation's historically active volcanoes. During the past decade, there has been an average of 3–4 explosive eruptions per year in the arc. Aleutian volcanoes span the entire spectrum in eruptive style, size, volume, and magma composition. Although the rate of eruptive activity is very high, deformation monitoring using the Global Positioning System (GPS) has been possible at only a few Aleutian volcanoes, owing to the remote location, hostile climate, difficult logistics, and high cost of field operations.

Interferometric synthetic aperture radar (InSAR) imaging is a recently developed remote sensing technique involving the use of two or more synthetic aperture radar (SAR) images to image surface topography and subtle changes due to deformation [e.g., Massonnet & Feigl, 1998; Zebker et al., 2000]. InSAR combines phase information from two or more SAR images of the same area acquired from similar vantage points at different times to produce an interferogram. The interferogram, depicting range changes between the radar and the ground, can be further processed with a digital elevation model (2-pass InSAR) to image surface deformation at a horizontal resolution of tens of meters over areas of ~100 km by 100 km with centimeter-to-subcentimeter precision under favorable conditions. Because SAR operates at a microwave wavelength (from a few millimeters to tens of centimeters), it can penetrate clouds and rain during the day and at night. Therefore, all-weather satellite InSAR images with the potential for measuring subtle ground surface deformation are useful for studying the magma plumbing systems of Aleutian volcanoes. SAR satellites that can provide InSAR capability for deformation mapping are described in Table 1.

To better understand magmatic processes, numerical models are often employed to invert the InSAR-derived surface deformation for physical parameters of a magma body. The spatial resolution of surface displacement data provided by InSAR makes it possible to constrain models of volcanic deformation with a variety of source geometries, such as the spherical point pressure source (Mogi source) [Mogi, 1958], the dislocation source (sill or dike source) [Okada, 1985], the ellipsoid source [Davis, 1986; Yang et al., 1988], the penny-shaped crack source [Fialko et al., 2001], etc. The most widely used source in volcano deformation modeling is the point source embedded in elastic homogeneous half-space [Mogi, 1958]. Even though the point source is simplest, it can fit observed deformation data remarkably well. The four parameters used to describe the point source are horizontal location coordinates (x, y), depth, and pressure or volume change. Another frequently used model is the rectangular elastic dislocation source [Okada, 1985], which requires eight model parameters: horizontal location coordinates, depth, length, width, strike and dip of the dislocation surface, and the slip directed perpendicular to the dislocation surface (i.e., expansion or contraction). Nonlinear least-squares inversion techniques are often used to optimize the source parameters [e.g., Cervelli et al., 2001]. Multiple InSAR images allow evaluation of the temporal progression of a deformation source and the associated magmatic process.

2. INSAR-BASED DEFORMATION SURVEY OF ALEUTIAN VOLCANOES

2.1. Augustine Volcano

Augustine Volcano (Plate 1a), an 8-by-11-km island stratovolcano in Cook Inlet, erupted in 1935, 1963–64, 1976, 1986, and January–March 2006, each time producing andesitic pyroclastic flows and lava domes from vents in the summit area. Multiple InSAR images constructed from SAR images acquired from 1992 to 2004 by the European Remote Sensing Satellite (ERS)-1 and ERS-2 (Table 1) show no sign of significant volcano-wide deformation. Throughout that period, a sector of the volcano's north flank mantled by 1976 and 1986 pyroclastic flows experienced subsidence/compaction at a rate of about 3 cm per year (Plate 1a). The observed deformation can be used to study physical characteristics of the 1986 flows [Masterlark et al., 2006].

2.2. Katmai Volcano Group

The Katmai group (Plate 1b) consists of five volcanoes: Martin, Mageik, Trident, Novarupta, and Katmai. In 1912, Katmai was the site of the world's largest volcanic eruption of the 20th century. The eruption produced ~20 km^3 of air-fall tephra, 11–15 km^3 of ash-flow tuff, and the Novarupta lava dome in the Valley of Ten Thousand Smokes [Miller et al., 1998; Hildreth, 1983]. Eruptive activity in the Katmai group since 1912 has included lava flows from the New Trident vent on Trident Volcano, the youngest of which erupted in 1963. The first application of InSAR to study surface deformation

Table 1. Spaceborne SAR sensors capable of deformation mapping

Mission	Agency	Period of Operation[1]	Orbit Repeat Cycle	Frequency	Wave-length	Incidence Angle at Swath Center	Resolution
Seasat	NASA[2]	06/27 to 10/10, 1978	17 days	L-band 1.2 GHz	25 cm	20 to 26 degrees	25 m
ERS-1	ESA[3]	07/1991 to 03/2000	3, 168, and 35 days[4]	C-band 5.3 GHz	5.66 cm	23 degrees	30 m
SIR-C/X-SAR	NASA, DLR[5], and ASI[6]	04/09 to 04/20, 1994, and 09/30 to 10/11, 1994	6-month, 1-, 2-, 3-day[7]	L-band 1.249 GHz	24.0 cm	17 to 63 degrees (L- & C-band)	10–200 m (30 m typical)
				C-band 5.298 GHz	5.66 cm		
				X-band 9.6 GHz	3.1 cm	54 degrees (X-band)	
JERS-1	JAXA[8]	02/1992 to 10/1998	44 days	L-band 1.275 GHz	23.5 cm	39 degrees	20 m
ERS-2	ESA	04/1995 to present	35 days	5.3 GHz	5.66 cm	23 degrees	30 m
Radarsat-1	CSA[9]	11/1995 to present	24 days	C-band 5.3 GHz	5.66 cm	10 to 60 degrees	10–100 m
Envisat	ESA	03/2002 to present	35 days	C-band 5.331 GHz	5.63 cm	15 to 45 degrees	20–100 m
ALOS	JAXA	Jan 2006 to present	46 days	L-band 1.270 GHz	23.6 cm	8 to 60 degrees	10–100 m

[1] Information was current in January 2006.
[2] National Aeronautics and Space Agency
[3] European Space Agency
[4] To accomplish various mission objectives, the ERS-1 repeat cycle was 3 days from July 25, 1991, to April 1, 1992, and from December 23, 1993, to April 9, 1994; 168 days from April 10, 1994, to March 20, 1995; and 35 days at other times.
[5] German Space Agency
[6] Italian Space Agency
[7] During days 3–4 of the second mission, SIR-C/X was commanded to retrace the flight path of the first mission to acquire repeat-pass InSAR data with a 6-month time separation. From day 7 to the end of the second flight, the shuttle was commanded to repeat the flight path of the previous days to acquire 1-day, 2-day, and 3-day repeat-pass InSAR data.
[8] Japan Aerospace Exploration Agency
[9] Canadian Space Agency

in the Aleutian arc was at New Trident [Lu et al., 1997]. An ERS-1 interferogram indicated about 8 cm of uplift from 1993 to 1995 in an area about 2 km across, indicating a source about 1 km beneath the New Trident vent. Multiple InSAR images from 1995 to 2000 were processed to prospect for any additional deformation in the Katmai region. Plate 1b is an image averaged from five coherent interferograms that collectively span from 1995 to 2000. No significant (i.e., larger than 2–3 cm range change) large-scale deformation is indicated.

2.3. Peulik Volcano

Peulik Volcano (Plate 1c), a stratovolcano located on the Alaska Peninsula, is known to have erupted in 1814 and 1852 [Miller et al., 1998]. InSAR images that collectively span from July 1992 to August 2000 show that a deformation source located about 7 km beneath Peulik, presumably a magma body, inflated about 23 cm between October 1996 and September 1998. The average inflation rate was about 1.4 cm/month from October 1996 to September 1997 (Plate 1c); peaked at 2.3 cm/month between June 26, 1997, and October 9, 1997; and dropped to 0.5 cm/month from October 1997 to September 1998. Any deformation that occurred before October 1996 or after September 1998 was too small to be detected [Lu et al., 2002b]. An intense earthquake swarm occurred near Becharof Lake about 30 km northwest of Peulik from May to October 1998, around the end of the inflation period. Calculated static stress changes in the epicentral area due to the inflation beneath Peulik appear too small to provide a causal link, but the timing is suggestive nonetheless. The 1996–98 inflation episode at Peulik demonstrates that satellite InSAR can be used to detect magma accumulation beneath dormant volcanoes at least several months before other signs of volcanic or tectonic unrest are apparent.

2.4. Chiginagak Volcano

Chiginagak Volcano (Plate 1d) is a symmetric composite cone with a base about 8 km in diameter [Miller et al., 1998]. Snow and ice cover much of the uppermost part of the cone.

Historical eruptions occurred in 1929 and 1971. A fumarole issues from snow and ice on the northeast flank. Thick clouds of steam were observed issuing from this area in l997, 2000, and 2005. In October 1997, increased steaming, snowmelt, and sulfur smell were observed, and a thermal anomaly was registered on Advanced Very High Resolution Radiometer (AVHRR) satellite imagery. InSAR images acquired between 1992 and 2000, including a 1997–98 image that spans the 1997 eruption (Plate 1d), reveal no significant large-scale deformation.

2.5. Aniakchak Volcano

Aniakchak Caldera (Plate 1e) is 10 km in diameter, more than 1 km deep, and perennially ice-free. It formed by collapse about 3,430 years ago during the eruption of more than 50 km^3 of andesite-to-dacite magma [Miller et al., 1998]. Many dacitic eruptions have occurred since the caldera-forming event, most recently in May 1931, which suggests the presence of a large, silicic magma reservoir. InSAR images from 1992 through 2002 show that the floor of Aniakchak Caldera subsides about 13 mm/year (Plate 1e) [Kwoun et al., 2006]. The depth of the deformation source (~4 km) suggests that subsidence can be explained by the cooling or degassing of a shallow magma body and/or the reduction of pore-fluid pressure in a cooling hydrothermal system. Ongoing deformation of the volcano detected by InSAR, in combination with magmatic gas output from at least one warm spring and infrequent, low-level bursts of seismicity below the caldera, indicate that the magmatic system is still active.

2.6. Veniaminof Volcano

Mount Veniaminof (Plate 1f) is a broad central mountain, 35 km wide at the base, truncated by a spectacular steep-walled, ice-filled summit caldera about 10 km in diameter [Miller et al., 1998]. Glacier ice and perennial snow pack obscure much of the volcano's flanks. Frequent small eruptions, producing diffuse, ash-laden plumes, have been observed. Plate 1f shows an averaged InSAR image obtained by stacking multiple interferograms that collectively span from 1992 to 2000. Even though the image is not coherent in the summit area or upper flanks of the volcano due to snow and ice, any volcano-wide deformation can be ruled out.

2.7. Pavlof Volcano

Pavlof Volcano (Plate 1g) is approximately 7 km in base diameter and has active vents on the north and east sides, close to the summit [Miller et al., 1998]. Pavlof is the most active volcano in the Aleutian arc with almost 40 relatively well-documented eruptions dating back to 1790. Pavlof eruptions are typically strombolian to vulcanian in character and consist of the rhythmic ejection of incandescent bombs and ash. Recent vigorous eruptions occurred from 1986 to 1988 and from 1996 to 1997. The 1996–97 strombolian eruption produced lava fountains, lava flows, lahars, and ash plumes [Miller et al., 1998]. Examining InSAR images spanning intervals before, during, and after the 1996–97 eruption, we found no significant, volcano-wide deformation in areas where the images are coherent. Plate 1g shows an averaged interferogram comprising images that collectively span from 1992 to 2000; no significant deformation is apparent.

2.8. Dutton Volcano

Mount Dutton (Plate 1g) is a small calc-alkaline volcanic center with an approximate diameter of 5 km. The volcano consists of a central multiple-dome complex [Miller et al., 1998]. Although historical eruptions have not been reported, a swarm of shallow earthquakes (largest event $M_L = 4.0$) occurred beneath the volcano in July–August 1988. The seismic activity was interpreted as due to the fracturing of country rock as a dike intruded beneath Mount Dutton, which could be precursory to an eruption. Plate 1g shows an averaged interferogram that spans from 1992 to 2000. The image is coherent over most of the volcano, and any deformation is insignificant. However, Mount Dutton could have experienced an episode in 1988 similar to the one at Mount Peulik in 1996–98. In the latter case, deformation began two years before the Becharof Lake seismic swarm in 1998, but it did not persist after the swarm.

2.9. Shishaldin Volcano

Shishaldin Volcano (Plate 2a) is located near the center of Unimak Island in the eastern Aleutians. The spectacular symmetric cone has a base diameter of approximately 16 km and a small summit crater that typically emits a steam plume, occasionally with small amounts of ash. Shishaldin is the third most active volcano in the Aleutian arc, having erupted at least 28 times since 1775, including recent eruptions in 1995–96 and 1999. Multiple InSAR images, each spanning one year or more, show no significant deformation in coherent parts of the images before, during, or after the 1995–96 or 1999 eruptions (Plate 2a) [Moran et al., 2006]. This suggests that any pre-eruption inflation is compensated by subsequent withdrawal of a roughly equivalent volume of magma (resulting in no net deformation), which in turn suggests that magma accumulation and transport occur relatively quickly.

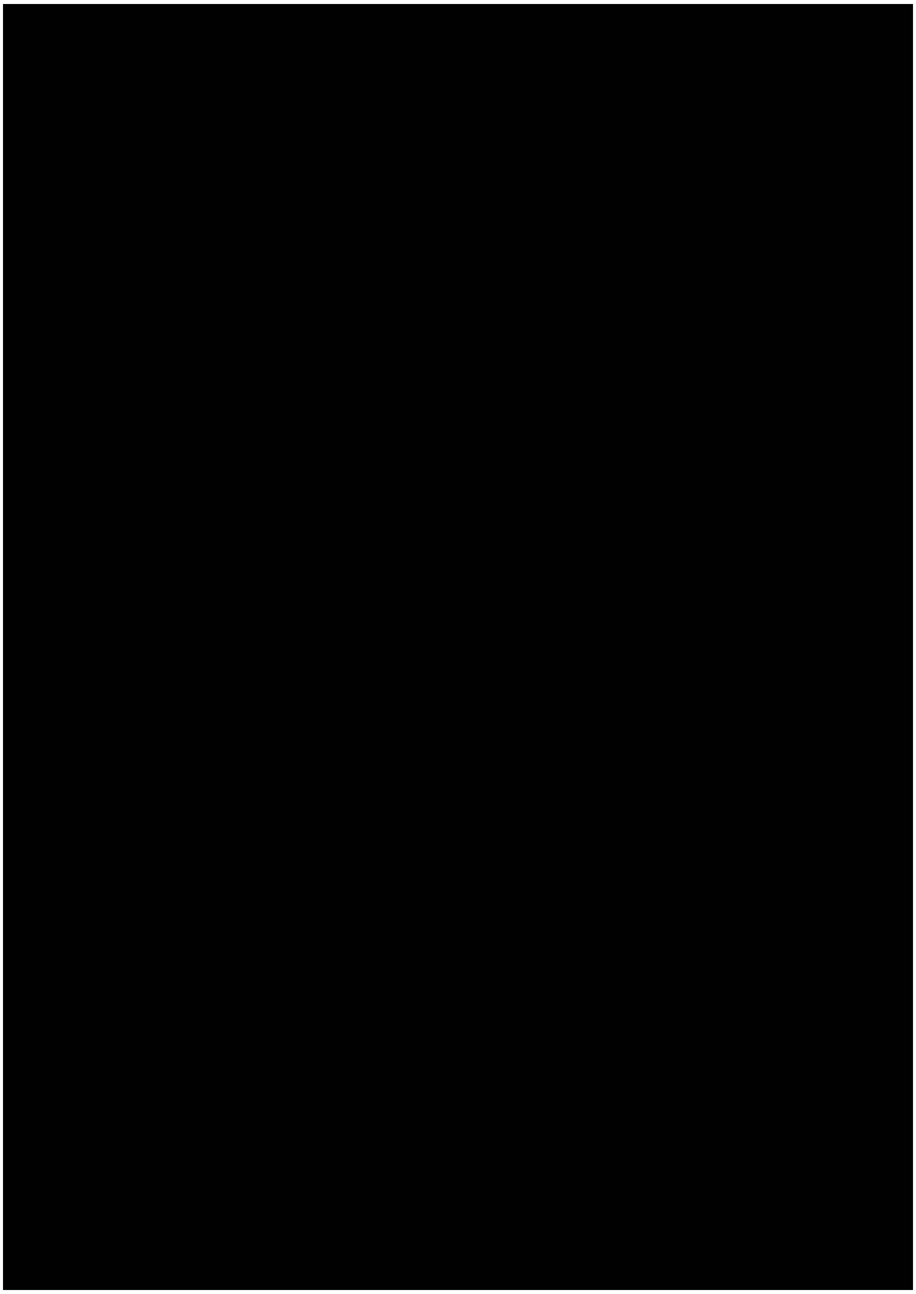

Plate 1. InSAR images for volcanoes in the eastern segment of the Aleutian arc. (a) InSAR image of Augustine volcano (1992-1993), depicting deformation associated with compaction of the 1986 pyroclastic flow deposits outlined by the white dashed line. (b) Averaged interferogram for the Katmai volcano group, showing no significant deformation during 1995-2000. VTTS – Valley of Ten Thousand Smokes; ND – Novarupta Dome; KT – Katmai caldera; NT – New Trident; MG – Mageik; MT – Martin. (c) InSAR image of Peulik volcano showing ~17 cm of uplift centered on the volcano's southwest flank from October 1996 to October 1997. (d) InSAR image (1997-1998) bracketing the October 1997 eruption of Chiginagak volcano, showing no significant deformation associated with the eruption. Localized subsidence (dashed line) was most likely caused by outgassing from an active fumarole. (e) Averaged InSAR image of Aniakchak Volcano showing that the caldera subsided about 13 mm/yr from 1992 to 2002. (f) Averaged interferogram of Veniaminof volcano, showing no significant deformation during 1992-2000. (g) Averaged interferogram (1992-2000) for Pavlof and Dutton volcanoes, showing no detectable deformation. Each interferometric fringe (full color cycle) represents 2.83 cm of range change between the ground and the satellite unless otherwise noted. The color change from red to yellow, blue, and red in a fringe represents a relative increase in satellite-to-ground distance or an away-from-satellite ground motion. Interferograms are draped over DEM shaded relief images. Areas without interferometric coherence are gray.

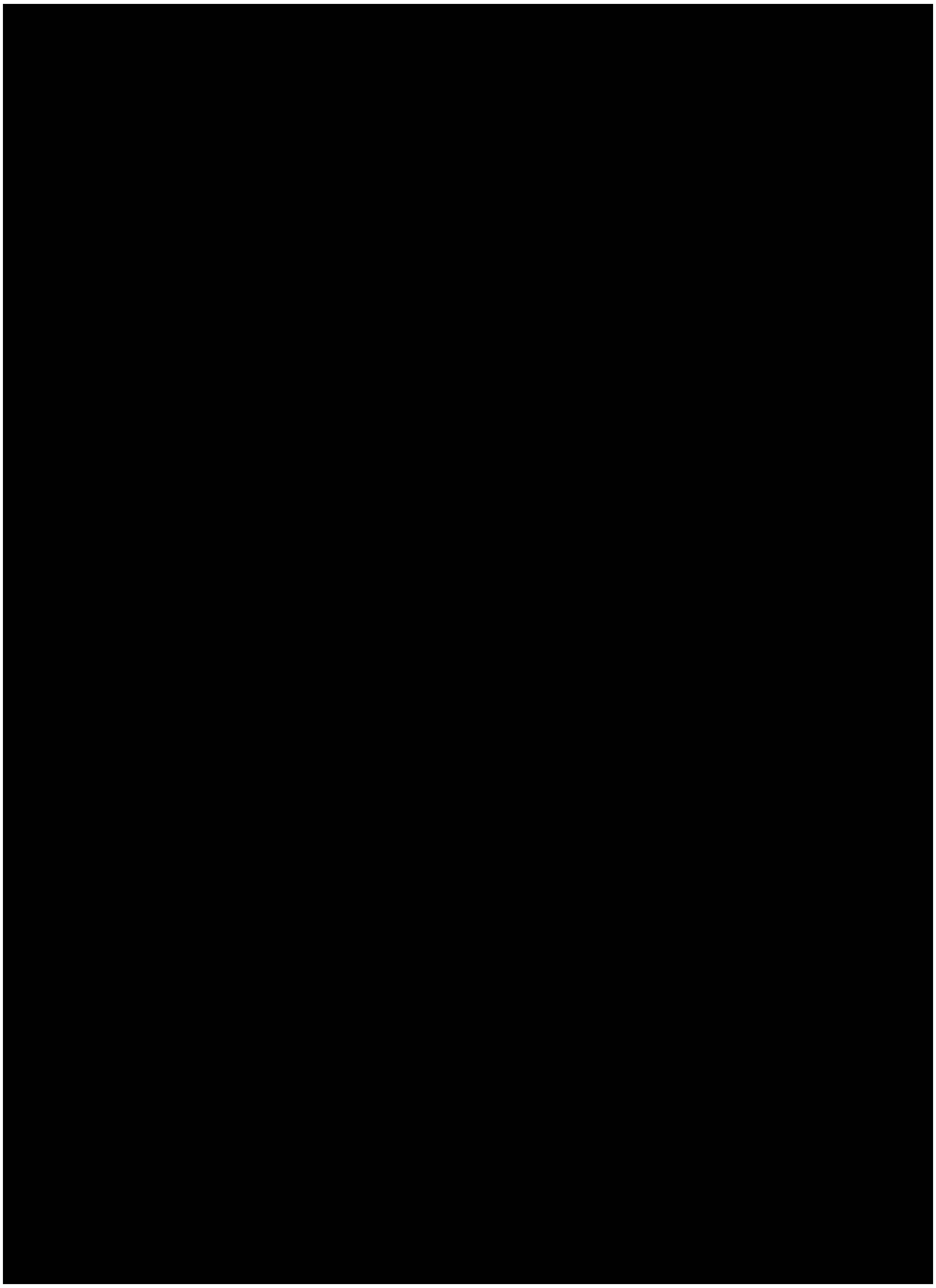

Plate 2. InSAR images for volcanoes in the central segment of the Aleutian arc. (a) InSAR image (1998–1999) of Shishaldin Volcano that shows no significant deformation associated with the volcano's 1999 eruption. (b) InSAR image of Fisher volcano, showing volcano-wide subsidence during 1993–1995. (c) Aseismic inflation of Westdahl volcano depicted by a 1993–1998 InSAR image. Circle marks the surface projection of a shallow magma reservoir beneath Westdahl Peak. (d) A 1993-1995 interferogram of Makushin volcano, showing about 7 cm inflation associated with a likely eruption in January 1995. (e) L-band JERS-1 InSAR image showing the complex deformation field at Akutan Volcano that accompanied an intense earthquake swarm in March 1996. Thick dashed line represents a zone of ground cracks that formed during the swarm. Dashed lines (A-A' and B-B') represent normal faults that were reactivated. (f) Deformation interferogram of Okmok volcano, showing inflation of about 20 cm during 2002–2003. Each interferometric fringe (full color cycle) represents 2.83 cm of range change between the ground and the satellite unless otherwise noted. The color change from red to yellow, blue, and red in a fringe represents a relative increase in satellite-to-ground distance or an away-from-satellite ground motion. Interferograms are draped over DEM shaded relief images. Areas without interferometric coherence are gray.

2.10. Fisher Volcano

Fisher Caldera (Plate 2b) is 11 km wide, 18 km long, and filled with active fumaroles. It formed about 9,000 years ago and is one of the largest calderas in the Aleutian arc. Its last significant eruption occurred in the 1820s, but hydrothermal activity remains strong. Multiple interferograms spanning from 1992 to 2000 indicate that the volcano has been subsiding. Plate 2b shows the result for 1993–95: a maximum of about 3 cm of volcano-wide subsidence. This observation is consistent with GPS measurements in the area [Mann and Freymueller, 2003]. Subsidence is most likely due to depressurization of the vigorous hydrothermal system beneath Fisher Caldera.

2.11. Westdahl Volcano

Westdahl Volcano, a young glacier-clad shield volcano, was frequently active during the latter half of the 20th century with documented eruptions in 1964, 1978–79, and 1991–92 [Miller et al., 1998; Lu et al., 2004]. The background level of seismic activity since the last eruption was generally low (about five M < 3 earthquakes per year). InSAR images from 1991 to 2000 show that Westdahl Volcano deflated during its 1991–92 eruption and is re-inflating at a rate that could produce another eruption in the near future (Plate 2c). The images suggest that rates of post-eruptive inflation and co-eruptive deflation are approximated by exponential decay functions with time constants of about six years and a few days, respectively [Lu et al., 2000b, 2003b]. This behavior is consistent with a deep, constant-pressure magma source connected to a shallow reservoir (about 6 km below sea level) by a magma-filled conduit. The magma flow rate is governed by the pressure gradient between the deep source and the shallow reservoir [Lu et al., 2003b].

2.12. Makushin Volcano

Makushin Volcano (Plate 2d), a broad, ice-capped, truncated stratovolcano, is one of the more active volcanoes in the Aleutians, having produced at least 17 relatively small explosive eruptions since the late 1700s [Miller et al., 1998]. Additional smaller eruptions probably occurred during this period but were unrecorded, either because they occurred when the volcano was obscured by clouds or because the eruptive products did not extend beyond the volcano's flanks. Several independent InSAR images, each spanning the time period from October 1993 to September 1995, show evidence of about 7 cm of uplift (Plate 2d) centered on the volcano's east flank. The uplift was interpreted as pre-eruptive inflation associated with a small, poorly documented explosive eruption on January 30, 1995 [Lu et al., 2002c].

2.13. Akutan Volcano

Akutan Volcano (Plate 2e), the second most active volcano in Alaska [Miller et al., 1998], was shaken in March 1996 by an intense earthquake swarm accompanied by extensive ground cracking but no eruption. InSAR images from both the L-band Japanese Earth Resources Satellite (JERS)-1 (Table 1) and C-band ERS-1/ERS-2 (Table 1) show uplift by as much as 60 cm on the western part of the island associated with the swarm. The L-band JERS-1 interferogram (Plate 2e) displays greater coherence, especially in areas with loose surface material or thick vegetation where C-band interferograms lose coherence. The JERS-1 interferogram also shows subsidence of a similar magnitude on the eastern part of the island, as well as displacements along faults (A–A' and B–B' in Plate 2e) that were reactivated during the seismic swarm [Lu et al., 2000a, 2005b]. The axis of uplift and subsidence strikes about N70°W and is roughly parallel to 1) a zone of fresh cracks on the volcano's northwest flank, 2) normal faults that cut the island, and 3) the inferred maximum compressive stress direction. Multiple InSAR images spanning time intervals both before and after the swarm suggest that the northwest flank was uplifted 5–20 mm/year relative to the southwest flank, probably by magma intrusion [Lu et al., 2005b].

2.14. Okmok Volcano

Okmok Volcano (Plate 2f), a broad shield topped with a 10-km-wide caldera, produced blocky, basaltic lava flows during relatively large effusive eruptions in 1945, 1958, and 1997 [Miller et al., 1998]. Multiple InSAR images reveal 1) surface inflation of more than 18 cm from 1992 to 1995 and subsidence of 1–2 cm from 1995 to 1996, prior to the 1997 eruption; 2) more than 140 cm of surface deflation during the 1997 eruption; and 3) 5–15 cm/year inflation from 1997 to 2004, after the 1997 eruption [Lu et al., 1998, 2000c, 2003c, 2005a; Mann et al., 2002]. Plate 2f is a Radarsat-1 (Table 1) InSAR image that depicts about 20 cm of inflation from 2002 to 2003. Numerical modeling suggests that the magma reservoir responsible for the deformation is located about 3 km beneath the center of the caldera and about 5 km northeast of the 1997 eruptive vent [Mann et al., 2002; Lu et al., 2005a].

2.15. Cleveland Volcano

Cleveland Volcano (Figs. 3a and 3b), a stratovolcano in the central-western Aleutian arc, is frequently observed emitting steam and ash. Most of the activity is characterized as profuse steaming from the summit crater with intermittent emissions of ash and occasional debris flows. Recent explosive eruptions occurred in February–April 2001 and

July 2005 (www.avo.alaska.edu). Multiple interferograms before, during, and after the 2001 and 2005 eruptions do not reveal any significant volcano-wide deformation. Plates 3a and 3b show two interferograms spanning the 2001 and 2005 eruptions, respectively.

2.16. Korovin Volcano

Korovin Volcano (Plate 3c) is a stratovolcano on Atka Island in the central Aleutian arc. It has a basal diameter of 7 km and two summit vents 0.6 km apart. Intercalated lava flows and pyroclastic rocks make up the volcano. Korovin erupted in 1951, 1953–54, 1973, 1976, 1986–87, and 1998. An interferogram spanning the 1998 eruption is shown in Plate 3c. It indicates that deformation associated with the eruption is either lacking or too small to be detected by ERS-1/ERS-2 (Table 1) InSAR.

2.17. Kiska Volcano

Kiska Volcano (Plate 3d) is the westernmost historically active volcano in the Aleutian arc. Sequential InSAR images show a circular area about 3 km in diameter centered near the summit that subsided as much as 10 cm from 1995 to 2001, mostly during 1999–2000 (Plate 3d). Based on the shallow source depth from modeling (< 1 km), the copious amounts of steam that were vented during recent eruptions, and recent field reports of vigorous steaming and persistent ground shaking near the summit area, the observed subsidence is attributed to decreased pore-fluid pressure in a shallow hydrothermal system beneath the summit area [Lu et al., 2002a].

2.18. Seguam Volcano

Seguam Island (Plate 3e) consists of two late Quaternary calderas. The western caldera dominates the western half of the island and includes Pyre Peak (commonly referred to as Seguam Volcano), a 3-km-wide central cone. Historical eruptions occurred in 1901, 1927, and 1977, mostly from vents at or near Pyre Peak. The historically inactive eastern caldera is somewhat larger than its western counterpart and contains a central cone and several vents. In late December 1992 a small satellite cone a few km southwest of Pyre Peak erupted, sending an ash plume to 1,200 m. Intermittent explosive eruptions were reported from May 28, 1993, to August 19, 1993. InSAR images spanning various intervals from 1992 to 2000 document co-eruptive and post-eruptive deformation (Figs. 3e–3g). Interferograms that span the 1992–93 eruption are characterized by a relatively broad pattern of uplift that is roughly centered on the eastern (historically inactive) caldera and elongated along the long axis of Seguam Island. Deformation during the first few years following the eruption was dominated by two separate regions of subsidence, each having radial symmetry roughly centered on the east and west calderas, respectively. During the later post-eruption intervals, the pattern of deformation in the eastern caldera changed from subsidence to broad uplift. A model that combines magma influx, thermoelastic relaxation, and poroelastic effects accounts for the observed deformation [Lu et al., 2003a; Masterlark and Lu, 2004; Price, 2004].

3. SUMMARY

The satellite InSAR technique has proven to be a powerful space-borne geodetic tool for studying a variety of volcanic processes by analyzing surface deformation patterns along the Aleutian arc [Lu et al., 1997, 1998, 2000a–c, 2002a–c, 2003a–c, 2004, 2005 a–b] and at other volcanoes worldwide [e.g., Amelung et al., 2000; Massonnet et al., 1995; Pritchard and Simons, 2004; Rosen et al., 1996; Zebker et al., 2000; Sturkell et al., 2006; Wicks et al., 1998, 2002]. InSAR's all-weather, large-area imaging capability makes it particularly useful in this regard.

InSAR is an excellent technique for detecting subtle deformation of the ground surface, which can be used to identify restless volcanoes long before seismic or other precursory signals are detected. This is well illustrated by InSAR results for Westdahl and Mount Peulik Volcanoes. Each has a magma reservoir ~6–7 km deep, which is below the brittle-ductile transition that typically occurs ~5 km beneath volcanoes [Sibson, 1982]. Therefore, the slow ascent of magma to the reservoirs generally is not marked by earthquakes. The 1996–98 inflation episode at Mount Peulik most likely would have gone undetected if not for the occurrence of the Becharof Lake earthquake swarm, which was the impetus for the InSAR study of the area [Lu et al., 2002b]. Even though the 1996–98 epicenters are not well constrained, it is clear that most of the activity occurred 20–45 km northwest of Mount Peulik, and few if any earthquakes occurred within 10 km of the volcano. We suspect that such episodes are relatively common and an integral part of the eruption cycle for volcanoes with characteristically long repose periods [e.g., Wicks et al., 2002]. Many of these episodes occur aseismically because magma accumulates gradually and preferentially near the brittle-ductile transition in the crust. In such cases, inflation episodes will likely go undetected unless the intrusion rate is high enough to cause brittle failure or the regional stress field is such that a small amount of incremental stress is sufficient to trigger earthquakes along favorably oriented faults at some distance from the volcano. In light of the Mount Peulik results, we suspect that the eruption cycle

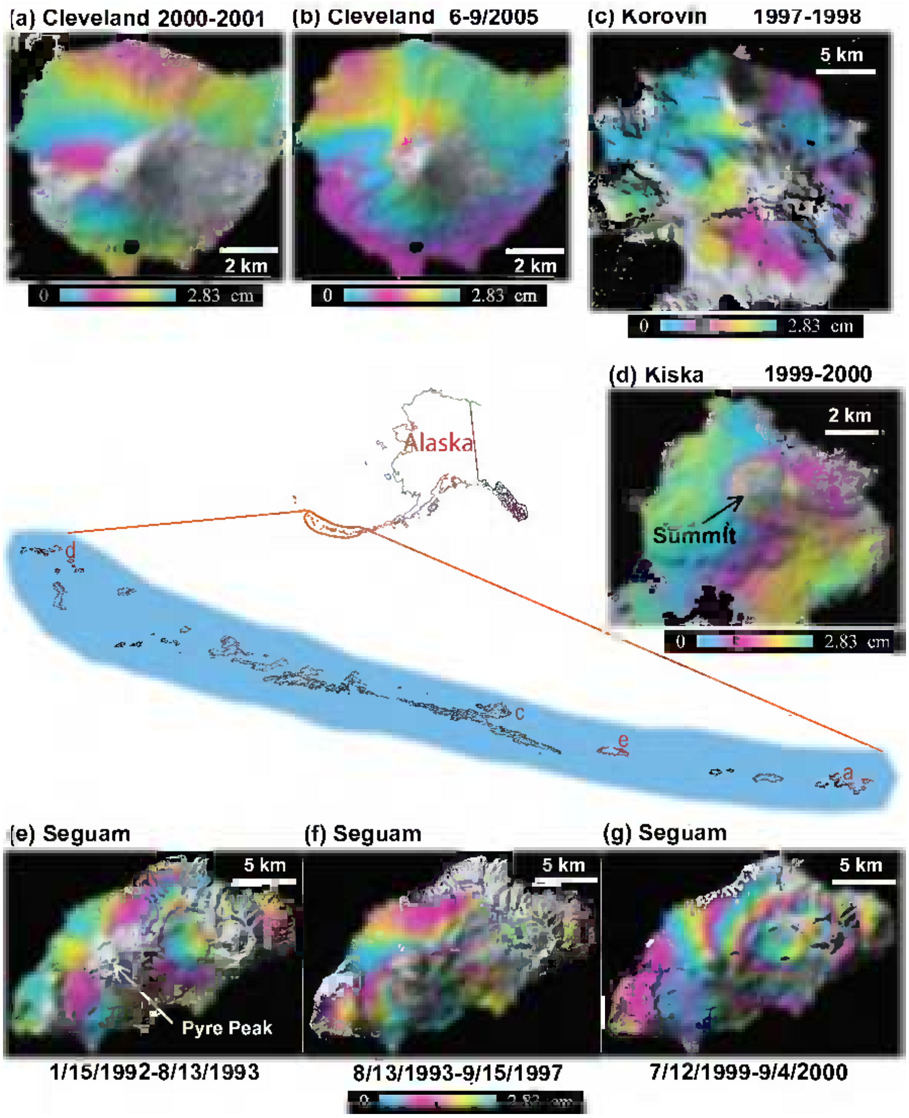

Plate 3. InSAR images for volcanoes in the western segment of the Aleutian arc. (a) InSAR image (2000–2001) of Cleveland volcano that shows no significant deformation associated with the volcano's 2001 eruption. (b) InSAR image (June-September 2005) of Cleveland volcano that shows no significant deformation associated with the volcano's July 2005 eruption. (c)InSAR image (1997-1998) of Korovin volcano, showing no significant deformation associated with the 1998 eruption. (d) InSAR image of Kiska volcano (August 1999-August 2000), showing subsidence of the summit related to hydrothermal activity. (e) InSAR image (January 15-August 13, 1993) of Seguam, showing deformation associated with the 1993 eruption. (f) InSAR image (1993-1997) of Seguam, showing deformation in the first few years after the 1993 eruption. (g) InSAR image of Seguam, showing deformation during 1999-2000, 6-7 years after the 1993 eruption. Each interferometric fringe (full color cycle) represents 2.83 cm of range change between the ground and the satellite. The color change from red to yellow, blue, and red in a fringe represents a relative increase in satellite-to-ground distance or an away-from-satellite ground motion. Interferograms are draped over DEM shaded relief images. Areas without interferometric coherence are gray.

at other dormant stratovolcanoes is much more eventful than has been recognized previously. Such volcanoes might inflate episodically during long periods of apparent quiescence until some threshold is reached, triggering magma's final ascent to the surface. If so, InSAR provides a valuable tool for tracking a volcano's progress from one eruption to the next and for identifying quiescent volcanoes that warrant careful monitoring.

InSAR can image deformation over a large region, which makes it an attractive tool for studying a complex deformation field such as the one that accompanied the 1996 seismic swarm at Akutan Volcano. To adequately characterize such a complex deformation field using a more conventional geodetic technique (e.g., electronic distance measurement (EDM), tiltmeters, strainmeters, or even GPS) would require measurements at a very large number of benchmarks or instrument stations. For remote volcanoes such as those in the Aleutian arc, the resulting workload would be prohibitive. A conventional geodetic network would have to be extensive enough to capture the entire deformation field at each potentially active volcano, as well as dense enough to adequately characterize possible small-scale complexities. InSAR overcomes this limitation of conventional geodesy, at least in areas of adequate radar coherence, by providing a more spatially complete image of the deformation field. In the future, combining areal measurements from InSAR with three-dimensional measurements from GPS will almost surely advance our understanding of the dynamics of magmatic processes.

Based on deformation patterns observed with InSAR at about 20 Aleutian volcanoes, we can make the following statements:

1. Deformation patterns at Aleutian volcanoes are diverse. This probably reflects the fact that Aleutian volcanoes span a broad spectrum of eruptive styles, sizes, magma compositions, and local tectonic settings. Differing deformation patterns suggest differences in the magma plumbing systems as well. For example, Unimak Island hosts three active volcanoes: Westdahl, Fisher, and Shishaldin. In terms of eruption frequency, Shishaldin is the most active among the group, and Fisher is the least active. Our InSAR analysis suggests that Westdahl is persistently inflating at a rate that declined since the last eruption in 1991–92 and that there is a magma reservoir ~6 km below the sea level beneath Westdahl Peak (circle in Plate 2c). Because Shishaldin is more active than Westdahl, one might expect more deformation at Shishaldin. However, InSAR shows that, on the contrary, significant deformation was lacking before, during, and after the 1995–96 and 1999 eruptions at Shishaldin [Moran et al., 2006]. Deformation at Fisher differs from that observed at either Westdahl or Shishaldin: Fisher is subsiding at a rate of 1–2 cm/year. Even though these three volcanoes are only 10–20 km apart, their deformation behaviors are remarkably different.
2. The more frequently active volcanoes, such as Shishaldin, Pavlof, and Cleveland, exhibit little or no measurable deformation. All of these three volcanoes are stratovolcanoes, have symmetric cones, and erupt frequently. Interferograms that span time intervals before, during, and after recent eruptions do not show any significant deformation. Plausible explanations include the following: 1) pre-eruptive inflation is balanced by co-eruptive deflation, resulting in little or no net deformation; 2) the magma reservoirs are deep, so inflation or deflation causes only broad, subtle deformation of the surface that is difficult to detect, especially if the area of radar coherence is limited [Moran et al., 2006]; 3) no significant pre-eruptive and co-eruptive deformation is associated with these eruptions; and 4) the magma reservoir is very shallow and its strength is small (i.e., pressure or volume changes in the reservoir are small), so deformation only occurs over a small area (a few km in radius) near the summit where coherence is lost owing to perennial ice or snow. The third possibility is puzzling, because considerable deformation has been observed with InSAR in association with similar-sized eruptions and intrusions at other Aleutian volcanoes. Considering the size of recent eruptions at these volcanoes, the last alternative also seems unlikely [Moran et al., 2006]. If pre-eruption inflation were compensated by subsequent withdrawal of a roughly equivalent volume of magma (resulting in no net deformation, alternative 1), the InSAR studies suggest that magma transport and accumulation occur relatively quickly. Further study requires better temporal sampling than is available from current SAR satellites and an L-band sensor to defeat interferometric decorrelation due to snow/ice cover. Better monitoring of this type of volcano also requires observations from continuous GPS and seismometers to capture localized or short-term deformation, if it exists.
3. Through numerical modeling, InSAR-derived images can be used to infer sources that cause observed deformation. However, modeling cannot uniquely characterize the source(s), for at least two reasons. First, numerical inversion solutions are inherently non-unique, i.e., any deformation field can be modeled equally well by different sets of superimposed sources. Only by limiting the solution to a single source, or a small number of sources, can we make inferences about the cause of observed deformation (e.g., magmatic or hydrothermal, or in the first case, sphere, ellipsoid, dike, or sill). A second reason that numerical models are non-unique is that volcanic deformation can be caused by changes in either mass or pressure, in either the

magmatic or hydrothermal system. For example, magma can be added to a reservoir from below or withdrawn to feed an intrusion or eruption. Alternatively, exsolution of volatiles during cooling and crystallization of reservoir magma can increase reservoir pressure with no change in mass, and subsequent escape of exsolved volatiles can depressurize the reservoir with negligible mass change [Dzurisin, 2007]. In the latter case, ground uplift might be observed if fluids released from cooling magma are trapped underground at lithostatic pressure, but subsidence can be expected when fluids escape into the hydrostatically pressured part of the system [Fournier, 2007]. At large calderas in particular, numerical simulations have suggested hydrothermal fluid flow can produce significant ground surface deformation [Hurwitz et al., 2007].

4. For the deforming Aleutian volcanoes discussed in this paper, we attribute most of the observed uplifts (e.g., Westdahl, Peulik, and Makushin) to magma intrusion, in large part because the model sources are located at 5-7 km depth. This is deeper than hydrothermal fluids are thought to exist in active volcanic environments [Fournier, 2007]. On the other hand, we interpret persistent subsidence at Kiska volcano as being due to fluid loss from the hydrothermal system, mainly for two reasons: (1) the model deformation source is only about 1 km deep, and (2) steam emissions are commonly observed at the volcano [Lu et al., 2002a]. For the reasons discussed above, we realize that a deep model source is not synonymous with magma, nor is a shallow source at a steaming volcano compelling evidence for a hydrothermal deformation mechanism. In the absence of additional information from microgravity measurements, fluid geochemistry, or scientific drilling, any conclusion about the source(s) of ground deformation is necessarily reduced to a plausibility argument. We believe that magmatic, hydrothermal, and tectonic sources all play a role in causing the surface deformation observed at Aleutian volcanoes. In specific cases, one of these mechanisms is likely to be dominant. We have tried here to identify those mechanisms for a few of the Aleutian volcanoes, recognizing that the available data are inherently ambiguous. Because magma is denser than hydrothermal fluid, high-precision gravity surveys in conjunction with surface deformation and groundwater measurements can help to resolve this ambiguity in some cases [Gottsmann and Rymer, 2002].
5. For some of the Aleutian volcanoes including Okmok, Akutan, Seguam, and Westdahl, InSAR deformation mapping was conducted intensively using SAR images from all of the available sensors (ERS-1, ERS-2, JERS-1, Radarsat-1, and Envisat) (Table 1). For these volcanoes, multi-temporal InSAR images enable construction of virtual magma plumbing systems that can be used to constrain models of magma accumulation and to help anticipate future eruptions. For other volcanoes, including Chiginagak, Veniaminof, and Korovin, InSAR results are still quite preliminary and comprehensive analyses are yet to be completed. Nonetheless, results presented in this paper can serve as a basis for more thorough analyses in the future.

Our studies suggest that some Aleutian volcanoes are much more active, in terms of magma movement as indicated by surface deformation from InSAR, during repose periods than reliance solely on seismic signals might suggest. That is not to say that InSAR is the final piece in a puzzle that has occupied volcanologists for decades. In fact, we are far from a complete understanding of the eruption cycle at most of Earth's highly diverse volcanoes includes those summarized in this paper. As a result, the discovery of ground deformation (or lack thereof) at a given volcano using InSAR or any other geodetic technique does not necessarily result in better allocation of monitoring resources or more informed assessments of volcano hazards. We know that some volcanoes erupt without deforming and others deform without erupting. Likewise, some eruptions are preceded or accompanied by intense seismic activity or copious releases of magmatic gases, while others are not. The challenge in the Aleutians and elsewhere is to better understand why this is the case. For that endeavor, more and better information about how volcanoes deform is surely an advantage—and InSAR is an important new source of such information.

With more operational SAR sensors available for rapid and frequent data acquisitions, future InSAR will escort volcano monitoring to an important phase wherein magma accumulation in the middle to upper crust can be observed long before the onset of short-term precursors to an eruption. Ultimately, more widespread use of InSAR for volcano monitoring could shed light on a poorly understood but important part of the eruption cycle, i.e., the time period between eruptions when a volcano seems to be doing essentially nothing. This potential makes InSAR a promising space-based, long-term volcano monitoring tool. Combining applications of the InSAR technique with observations from continuous GPS, gravimeters, strainmeters, tiltmeters, seismometers, and volcanic gas sensors will surely improve our capability to forecast future eruptions, thus enabling improved volcano hazard assessment and more effective eruption preparedness.

Acknowledgments. ERS-1, ERS-2, Envisat, Radarsat-1, and JERS-1 SAR images are copyrighted © 1991–2005 European Space Agency (ESA), Canadian Space Agency (CSA), and Japan Aerospace Exploration Agency (JAXA), respectively, and were provided by Alaska Satellite Facility (ASF), ESA, and JAXA.

The research summarized in the paper was supported by funding from the NASA Radarsat Program, NASA Solid Earth & Natural Hazards Program, USGS Volcano Hazards Program, USGS Land Remote Sensing Program, and USGS contract O3CRCN0001. We thank ASF, JAXA, and ESA staff members for their special efforts in making SAR data available to us on a timely basis. We also thank J. Freymueller, D. Mann, T, Masterlark, V. McConnell, D. Meyer, S. Moran, W. Thatcher, T. Neal, and many other colleagues for contributions to this research. Constructive comments and edits by J. Eichelberger, P. Lundgren, B. Penga, D. Steinwand, and P. Burns were greatly appreciated.

REFERENCES

Amelung, F., S. Jonsson, H. Zebker, and P. Segall (2000), Widespread uplift and 'trapdoor' faulting on Galapagos volcanoes observed with radar interferometry, *Nature*, *407*, 993–996.

Cervelli, P., M. H. Murray, P. Segall, Y. Aoki, and T. Kato (2001), Estimating source parameters from deformation data, with an application to the March 1997 earthquake swarm of the Izu Peninsula, Japan, *J. Geophys. Res.*, *106* , 11,217–11,237.

Davis, P. M. (1986), Surface deformation due to inflation of an arbitrarily oriented triaxial ellipsoidal cavity in an elastic half-space, with reference to Kilauea Volcano, Hawaii, *J. Geophys. Res.*, *91*, 7429–7438.

Dvorak, J., and D. Dzurisin (1997), Volcano geodesy: The search for magma reservoirs and the formation of eruptive vents, *Rev. Geophys.*, *35*, 343–384.

Dzurisin, D. (2007), *Volcano Deformation – Geodetic Monitoring Techniques*, 441 pp., Springer-Praxis Publishing Ltd, Chichester, UK.

Dzurisin, D. (2003), A comprehensive approach to monitoring volcano deformation as a window on eruption cycle, *Rev. Geophys.*, *Review of Geophysics*, *41*, 10.1029/2001RG000107.

Fialko, Y., Y. Khazan, and M. Simons (2001), Deformation due to a pressurized horizontal circular crack in an elastic half-space, with applications to volcano geodesy, *Geophys. J. Int.*, *146*, 181–190.

Fournier, R. (2007), Hydrothermal system and volcano geochemistry, in *Volcano Deformation—Geodetic Monitoring Techniques*, by D. Dzurisin, 323–342, Springer-Praxis Publishing Ltd, Chichester, UK.

Gottsmann, J., and H. Rymer (2002), Deflation during caldera unrest: Constraints on subsurface processes and hazard prediction from gravity-height data, *Bull. Volcanol.*, *64*, 338–348.

Hildreth, W. (1983), The compositionally zoned eruption of 1912 in the Valley of Ten Thousand Smokes, Katmai National Park, Alaska: *Journal of Volcanology and Geothermal Research*, *18*, 1–56.

Hurwitz, S., L. Christiansen, and P. Hsieh (2007), Hydrothermal fluid flow and deformation in large calderas: Inferences from numerical simulations, *J. Geophys. Res.*, *112*, B02206, doi:10.1029/2006JB004689.

Kwoun, O., Z. Lu, C. Neal, and C. Wicks (2006), Quiescent deformation of the Aniakchak Caldera, Alaska, mapped by InSAR, *Geology*, *34*, 5–8.

Lu, Z., T. Masterlark, and D. Dzurisin (2005a), Interferometric Synthetic Aperture Radar (InSAR) Study of Okmok Volcano, Alaska, 1992–2003: Magma Supply Dynamics and Post-emplacement Lava Flow Deformation, *Journal of Geophysical Research*, *110*, B02403, DOI:10.1029/2004JB003148.

Lu, Z., C. Wicks, O. Kwoun, J. Power, and D. Dzurisin (2005b), Surface deformation associated with the March 1996 earthquake swarm at Akutan Island, Alaska, revealed by C-band ERS and L-band JERS radar interferometry, *Canadian Journal of Remote Sensing*, *31*, 7–20.

Lu, Z., R. Rykhus, T. Masterlark, and K. Dean (2004), Mapping recent lava flows at Westdahl volcano, Alaska, using radar and optical satellite imagery, *Remote Sensing of Environment*, *91*, 345–353.

Lu, Z., C. Wicks, D. Dzurisin, J. Power, W. Thatcher, and T. Masterlark (2003a), Interferometric synthetic aperture radar studies of Alaska volcanoes, *Earth Observation Magazine (EOM)*, *12* (3), 8–18.

Lu, Z., T. Masterlark, D. Dzurisin, R. Rykhus, and C. Wicks (2003b), Magma Supply Dynamics at Westdahl Volcano, Alaska, Modeled from Satellite Radar Interferometry, *Journal of Geophysical Research*, *108*, 2354, 10.1029/2002JB002311.

Lu, Z., E. Fielding, M. Patrick, and C. Trautwein (2003c), Estimating Lava Volume by Precision Combination of Multiple Baseline Spaceborne and Airborne Interferometric Synthetic Aperture Radar: the 1997 Eruption of Okmok Volcano, Alaska, *IEEE Transactions on Geoscience and Remote Sensing*, *41*, 1428–1436.

Lu, Z., T. Masterlark, J. Power, D. Dzurisin, and C. Wicks (2002a), Subsidence at Kiska volcano, Western Aleutians, Detected by Satellite Radar Interferometry, *Geophysical Research Letters*, *29*, 1855, doi:10.1029/2002GL014948.

Lu, Z., C. Wicks, D. Dzurisin J. Power, S. Moran, and W. Thatcher (2002b), Magmatic Inflation at a Dormant Stratovolcano: 1996–98 Activity at Mount Peulik Volcano, Alaska, Revealed by Satellite Radar Interferometry, *Journal of Geophysical Research*, *107*, 2134, doi:10.1029/2001JB000471.

Lu, Z., J. Power, V. McConnell, C. Wicks, and D. Dzurisin (2002c), Pre-Eruptive Inflation and Surface Interferometric Coherence Characteristics Revealed by Satellite Radar Interferometry at Makushin Volcano, Alaska: 1993–2000, *Journal of Geophysical Research*, *107*, 2266, doi:10.1029/2001JB000970.

Lu, Z., C. Wicks, J. Power, and D. Dzurisin (2000a), Ground deformation associated with the March 1996 earthquake swarm at Akutan volcano, Alaska, revealed by satellite radar interferometry, *Journal of Geophysical Research*, *105*, 483–21,496.

Lu, Z., C. Wicks, D. Dzurisin, W. Thatcher, J. Freymueller, S. McNutt, and D. Mann (2000b), Aseismic inflation of Westdahl volcano, Alaska, revealed by satellite radar interferometry, *Geophysical Research Letters*, *27*, 1567–1570.

Lu, Z., D. Mann, J. Freymueller, and D. Meyer (2000c), Synthetic aperture radar interferometry of Okmok volcano, Alaska: Radar observations, *Journal of Geophysical Research*, *105*, 10791–10806.

Lu, Z., D. Mann, and J. Freymueller (1998), Satellite radar interferometry measures deformation at Okmok volcano, *EOS Transactions*, *79*, 461–468.

Lu, Z., and J. Freymueller (1998), Synthetic aperture radar interferometry coherence analysis over Katmai volcano group, Alaska, *Journal of Geophysical Research*, *103*, 29887–29894.

Lu, Z., R. Fatland, M. Wyss, S. Li, J. Eichelberger, K. Dean, and J. Freymueller (1997), Deformation of New Trident volcano measured by ERS-1 SAR interferometry, Katmai national Park, Alaska, *Geophys. Res. Lett.*, *24*, 695–698.

Mann, D., and J. Freymueller (2003), Volcanic and tectonic deformation on Unimak Island in the Aleutian Arc, Alaska, *J. Geophys. Res.*, *108*, 2108, doi:10.1029/2002JB001925.

Mann, D., J. Freymueller, and Z. Lu (2002), Deformation associated with the 1997 eruption of Okmok volcano, Alaska, *J. Geophys. Res.*, *107*, 10.1029/2001JB000163.

Massonnet, D., P. Briole, and A. Arnaud (1995), Deflation of Mount Etna monitored by spaceborne radar interferometry, *Nature*, *375*, 567–570.

Massonnet, D., and K. Feigl (1998), Radar interferometry and its application to changes in the Earth's surface, *Rev. Geophys.*, *36*, 441–500.

Masterlark, T., and Z. Lu (2004), Transient volcano deformation sources imaged with InSAR: Application to Seguam island, Journal of Geophysical Research, *J. Geophys. Res. 109*, B01401, doi:10.1029/2003JB002568.

Masterlark, T., Z. Lu, and R. Rykhus (2006), Thickness distribution of a cooling pyroclastic flow deposit: Optimization using InSAR, FEMs, and an adaptive mesh algorithm, *Journal of Volcanology and Geothermal Research*, *150*, 186–201.

Miller, T.M., R.G. McGimsey, D.H. Richter, J.R. Riehle, C.J. Nye, M.E. Yount, and J.A. Dumoulin (1998), Catalog of the historically active volcanoes of Alaska, *USGS Open-File Report*, *98-582*, 1998.

Mogi, K. (1958), Relations between the eruptions of various volcanoes and the deformations of the ground surface around them, *Bull. Earthquake Res. Inst. Univ. Tokyo*, *36*, 99–134.

Moran, S., O. Kwoun, T. Masterlark, and Z. Lu (2006), On the absence of deformation signals from InSAR interferograms bracketing the 1995–1996 and 1999 eruptions of Shishaldin Volcano, Alaska, *Journal of Volcanology and Geothermal Research*, *150*, 119–131.

Okada, Y. (1985), Surface deformation due to shear and tensile faults in a half-space, *Bull. Seismol. Soc. Am.*, *75*, 1135–1154.

Price, E. (2004), Dynamic deformation of Seguam Island, Aleutian Islands, Alaska, 1993–2000: Implications for magmatic and hydrothermal processes, *J. Geophys. Res.*, *109*, 10.1029/2003JB002671.

Pritchard, M., and M. Simons (2004), Surveying volcanic arcs with satellite radar interferometry: The central Andes, Kamchatka, and beyond, *Geological Society of America (GSA) Today*, *14*, 4–11.

Rosen, P., S. Hensley, H. Zebker, F. H. Webb, and E. J. Fielding (1996), Surface deformation and coherence measurements of Kilauea volcano, Hawaii, from SIR-C radar interferometry, *J. Geophys. Res.*, *101*, 23109–23125.

Sibson, R. (1982), Fault zone models, heat flow, and the depth distribution of seismicity in the continental crust of the United States, *Bull. Seismol. Soc. Am.*, *72*, 151–163.

Sturkell, E. and others (2006), Volcano geodesy and magma dynamics in Iceland, *Journal of Volcanology and Geothermal Research, 150*, 14–34.

Wicks, C., W. Thatcher, and D. Dzurisin (1998), Migration of fluids beneath Yellowstone Caldera inferred from satellite radar interferometry, *Science*, *282*, 458–462.

Wicks, C.W. Jr., Dzurisin, D., Ingebritsen, S., Thatcher, W., Lu, Z., and Iverson, J. (2002), Magmatic activity beneath the quiescent Three Sisters volcanic center, central Oregon Cascade Range, USA, *Geophys. Res. Lett.*, *29*, doi: 10.1029/2001GL014205.

Yang, X.-M., P. M. Davis, and J. H. Dieterich (1988), Deformation from inflation of a dipping finite prolate spheroid in an elastic half-space as a model for volcanic stressing, *J. Geophys. Res.*, *93*, 4249–4257, 1988.

Zebker, H., F. Amelung, and S. Jonsson (2000), Remote sensing of volcano surface and internal processing using radar interferometry, *Remote Sensing of Active Volcanism*, AGU Monograph, edited by P. Mouginis-Mark et al., 179–205.

Holocene Eruptive History of Shiveluch Volcano, Kamchatka Peninsula, Russia

Vera Ponomareva[1], Philip Kyle[2], Maria Pevzner[3], Leopold Sulerzhitsky[3], and Melanie Hartman[2]

The Holocene eruptive history of Shiveluch volcano, Kamchatka Peninsula, has been reconstructed using geologic mapping, tephrochronology, radiocarbon dating, XRF and microprobe analyses. Eruptions of Shiveluch during the Holocene have occurred with irregular repose times alternating between periods of explosive activity and dome growth. The most intense volcanism, with frequent large and moderate eruptions occurred around 6500–6400 BC, 2250–2000 BC, and 50–650 AD, coincides with the all-Kamchatka peaks of volcanic activity. The current active period started around 900 BC; since then the large and moderate eruptions has been following each other in 50–400 yrs-long intervals. This persistent strong activity can be matched only by the early Holocene one.

Most Shiveluch eruptions during the Holocene produced medium-K, hornblende-bearing andesitic material characterized by high MgO (2.3–6.8 wt %), Cr (47–520 ppm), Ni (18–106 ppm) and Sr (471–615 ppm), and low Y (<18 ppm). Only two mafic tephras erupted about 6500 and 2000 BC, each within the period of most intense activity.

Many past eruptions from Shiveluch were larger and far more hazardous then the historical ones. The largest Holocene eruption occurred ~1050 AD and yielded >2.5 km^3 of tephra. More than 10 debris avalanches took place only in the second half of the Holocene. Extent of Shiveluch tephra falls exceeded 350 km; travel distance of pyroclastic density currents was >22 km, and that of the debris avalanches ≤20 km.

INTRODUCTION

Large explosive eruptions can have a profound impact on the environment and seriously affect human lives. At the same time, the eruptions document critical moments in the life of a magmatic system and provide valuable information on its conditions. Of special interest are volcanoes that have frequent large explosive eruptions during their lifetime.

Shiveluch volcano is located near the northern end of Central Kamchatka Depression (Fig. 1) and is one of the most active volcanoes on the Kamchatka Peninsula. The average magma discharge is ~0.015 km^3 year^{-1}, an order of magnitude higher than typical of island arc volcanoes [*Melekestsev* et al. 1991; *Davidson* and *DeSilva*, 2000]. Shiveluch has experienced many flank failures with formation of large debris avalanches. These are likely a consequence of the high magma supply rate and repetitive dome formation [*Ponomareva* et al., 1998; *Belousov* et al.,

[1] Institute of Volcanology and Seismology, Petropavlovsk-Kamchatsky, Russia
[2] Department of Earth and Environmental Science, New Mexico Institute of Mining and Technology, Socorro, New Mexico, USA
[3] Geological Institute, Moscow, Russia

Volcanism and Subduction: The Kamchatka Region
Geophysical Monograph Series 172

10.1029/172GM19

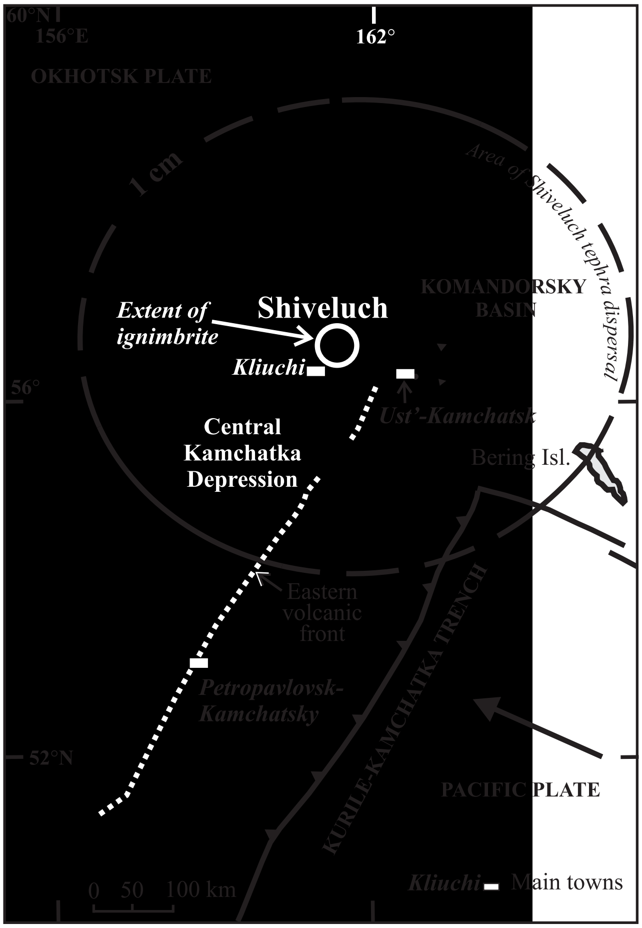

Figure 1. Map of Kamchatka showing the location of Shiveluch volcano and nearby towns of Kliuchi and Ust'-Kamchatsk. Shiveluch is located at the northern end of Central Kamchatka depression—a major graben structure located behind the Eastern volcanic front. The 1 cm limit for tephra erupted from Shiveluch is indicated. Base map is a shaded SRTM elevation model from NASA/JPL/NIMA.

1999]. Shiveluch mainly erupts high magnesium andesite, which has an adakitic character. Generation of the Shiveluch magmas may involve some slab melting as it is located over the edge of the subducting Pacific plate and warming or ablation of the slab by mantle flow may be responsible for magma generation [*Volynets* et al., 2000; *Peyton* et al., 2001; *Yogodzinski* et al., 2001; *Park* et al., 2002]. Numerous tephra layers erupted from Shiveluch serve as excellent markers in Holocene studies [*Braitseva* et al., 1997a; *Pevzner* et al., 1998]. Due to its frequent explosive eruptions, Shiveluch poses hazard not only to the towns of Kliuchi and Ust'-Kamchatsk, located at a distance of 45–85 km, but also for aviation. Everyday dozens of flights from Europe and North America to the Far East pass close to the Kamchatka Peninsula and could easily intercept ash clouds from large eruptions of Shiveluch.

Good preservation of the Holocene deposits on the flanks and surrounding apron of Shiveluch has allowed us to reconstruct the last ~10 ka of eruptive activity using geologic mapping, tephrochronology, radiocarbon dating and geochemical analyses. Preliminary descriptions of a few individual eruptions were given by *Volynets* et al. [1997]; *Ponomareva* et al. [1998] and *Pevzner* et al. [1998]. In this paper we give a detailed account of the stratigraphy and composition of the Holocene deposits at Shiveluch volcano. 101 radiocarbon dates on paleosols, charcoal and wood samples are used to construct the eruptive history. We examine how activity has fluctuated with time and determine the duration of repose periods. This allows us to put the current ongoing activity into a historical perspective. We also briefly document the variation of magma composition with time and examine the potential hazards of eruptions from Shiveluch.

GENERAL DESCRIPTION AND HISTORICAL ERUPTIONS

Shiveluch volcano consists of a younger Holocene and older late Pleistocene eruptive centers (Figs. 2 and 3A, B). Young Shiveluch (2,800 m a.s.l.) is a cluster of lava domes nested in a 9-km-wide collapse crater cut into the south side of the Old Shiveluch stratovolcano (3,283 m a.s.l.). The southward facing opening of the crater was likely controlled by a system of normal faults with vertical displacements of ~500 m [*Melekestsev* et al., 1974]. Several Holocene lava domes were emplaced on the western slopes of Old Shiveluch. Most of the Holocene ignimbrites and debris avalanche deposits occur to the south of the volcano (Fig. 3A, B). The tephra-falls were dispersed in all directions depending on the prevailing wind at the time of eruption. Lahar deposits descend down all the radial valleys and form fans around the volcano. Old Shiveluch hosts summit and valley glaciers (Fig. 3B).

Written records of Shiveluch activity date back to 1739 [*Gorshkov* and *Dubik*, 1970]. In 1854 a large explosive eruption occurred [*Ditmar,* 1890]. This eruption deposited a voluminous pumice fall NNE of the volcano, moderate volumes of ignimbrite on the southern slope, and extensive lahar deposits that can be traced down all the valleys on the southern and western slopes [*Ponomareva* et al., 1998]. Smaller eruptions reported from 1879–1883, 1897–1898, 1905, 1928–1929 and 1944–1950, resulted in emplacement of lava domes with accompanying minor ash falls [*Gorshkov* and *Dubik,* 1970; *Meniailov,* 1955].

The most recent large eruption of Shiveluch occurred on November 12, 1964. It involved a sector collapse, subsequent phreatic explosion, a powerful plinian eruption resulting in fall and ignimbrite deposits and accompanying lahars [*Gorshkov* and *Dubik,* 1970; *Belousov*, 1995]. Lava domes have been growing in the 1964 crater since 1980, occasionally producing block-and-ash and pumice flows, landslides, and minor ash falls, most recently in 2007 [*Dvigalo*, 1984; *Gorelchik* et al., 1997; *Khubunaya* et al., 1995; *Zharinov* et al., 1995; *Fedotov* et al., 2004; http://www.kcs.iks.ru/ivs/kvert/volcanoes/Sheveluch/index_eng.html]. The 2005 eruptions were the largest since 1964 but they still rank below the latter in magnitude.

TYPES OF SHIVELUCH DEPOSITS

Holocene volcanic deposits, interlayered with paleosol horizons, form a soil-pyroclastic sequence on the slopes and foot of Shiveluch which has been continuously accumulating during the last ~10 ka (Fig. 4). At distances >7 km from the crater, the Holocene deposits include tephra fall, pyroclastic density current deposits, debris avalanche and debris flow (lahar) units. They are underlain by assorted glacial or pre-Holocene debris avalanche deposits. The Holocene deposits are well exposed in a number of deep radial valleys (Figs. 3 and 4).

Tephra fall deposits. Typical proximal tephra fall deposits at Shiveluch are andesitic pumice lapilli tuffs produced by Plinian eruptions (Fig. 4A, B; Table 1). In more distal localities the pumice lapilli transition into coarse ash, commonly enriched in mineral grains and basaltic andesitic in composition, and then to a fine dominantly vitric andesitic-dacitic ash [Braitseva et al., 1997a]. Many fall units have distinct dispersal axes, e.g. tephras shown at Figure 5A, which depend on the wind direction at the time of eruption. Such fall deposits are usually unstratified and ungraded (Fig. 4A) and were likely emplaced continuously over a short time interval. Some pumice fall layers have wider dispersal directions (Fig. 5B, C) possibly due to varying wind directions and they have normal or reverse grading (Fig. 4B). The largest fall deposits have estimated volumes of 2–3 km^3 and their 1 cm isopachs reach ~350 km downwind from the eruptive center. This is about the limit that the tephra can be recognized in the soil-pyroclastic cover (Fig. 1). Other types of tephra fall deposits include: 1) those associated with explosions on lava domes (commonly fine to coarse dark-pink or pale ash); 2) co-ignimbrite falls (very fine white vitric ash); and 3) those produced by phreatic eruptions (gray fine matrix commonly enriched in rock fragments). These tephra fall deposits normally are less voluminous than the Plinian ones.

Two Shiveluch tephra layers are mafic in composition and differ from the typical andesite tephra [*Volynets* et al., 1997]. The older one is informally called the “dark package” and is a dark-gray stratified coarse ash and small lapilli of

Figure 2. View of Shiveluch looking northeast showing the older snow covered Pleistocene volcano and in front the mainly Holocene Young Shiveluch. The current active andesite lava dome has a gas plume and is surrounded to the south by an apron of young deposits many resulting from the 1964 and subsequent eruptions. Photo taken by Yuri Demianchuk in October, 2005.

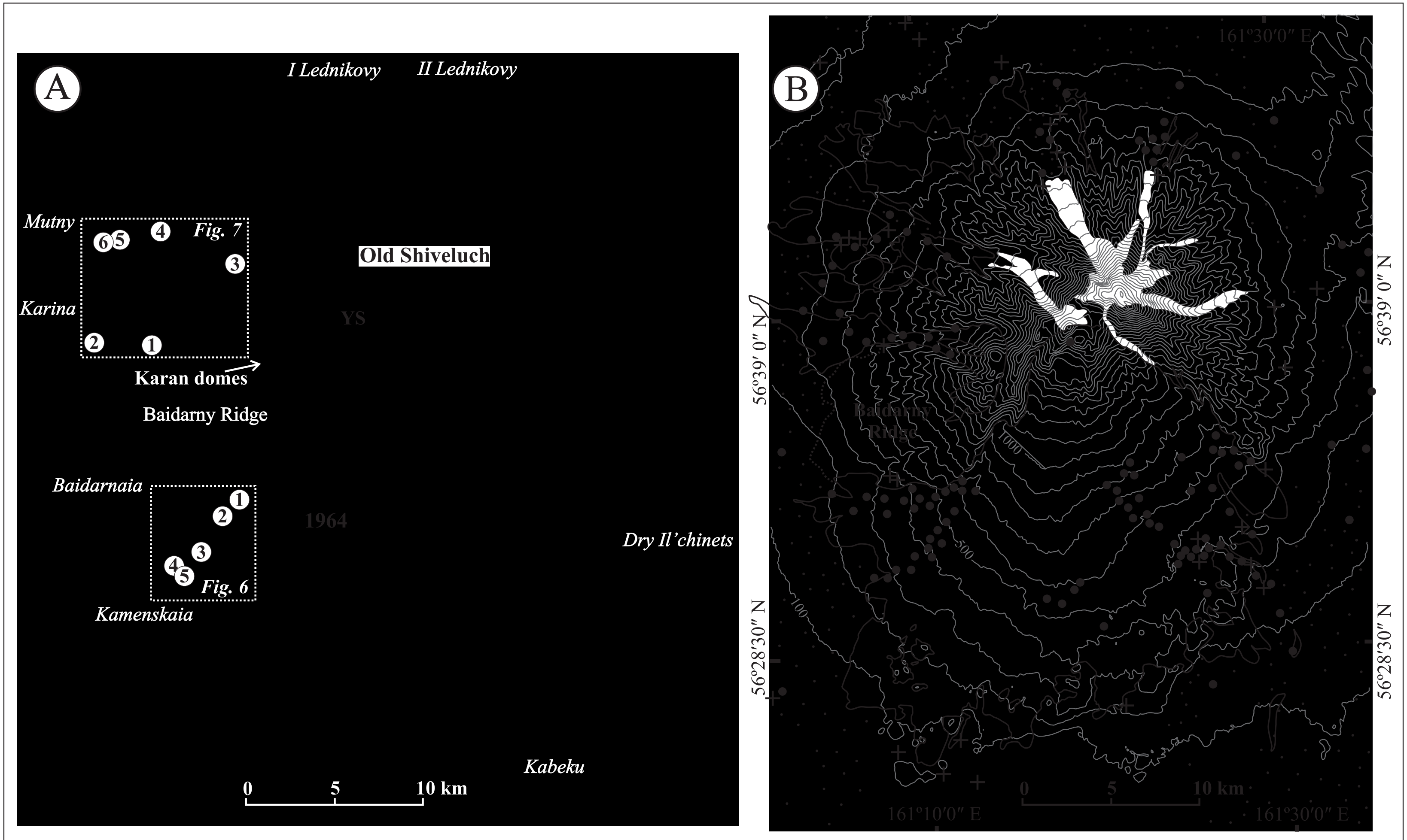

Figure 3. A. Landsat (ETM+) image of Shiveluch volcano. The main topographic features and river valleys are labeled. YS - Young Shiveluch. The light colored apron of the 1964 debris avalanche deposit and ignimbrite is visible extending to the south. Numbered circles in Kamenskaia and Mutny-Karina valleys show locations of the sections in Figures 6 and 7, respectively. **B.** Contour map (100m intervals) of Shiveluch volcano. The extent of Holocene deposits is outlined. Lahar deposits are shown by small black dots. Black crosses show proximal sites where sections of early-late Holocene soil-pyroclastic sequence were measured, filled black circles indicate the location of measured sections through the mid-late Holocene deposits. Summit glaciers are shown with white filling. Space images and SRTM data processing by Dmitrii Melnikov.

Table 1. Representative Whole Rock Major and Trace Element Analyses of Pumice Clasts from Shiveluch

Eruption number	1 (SH_{1964})	8	16	18	25	28 (SHsp)	29	32	39	46	47	58
SiO_2	60.59	60.41	57.65	60.71	59.72	51.43	55.96	57.11	61.16	52.65	62.55	58.80
TiO_2	0.54	0.54	0.66	0.50	0.54	0.83	0.60	0.62	0.53	0.72	0.48	0.63
Al_2O_3	16.59	16.39	16.42	16.67	16.30	13.69	14.93	15.73	16.69	15.21	16.67	16.43
Fe_2O_3	5.19	5.29	6.23	4.80	5.27	9.43	7.03	6.23	4.90	8.13	4.49	6.01
MnO	0.10	0.10	0.12	0.09	0.10	0.16	0.12	0.11	0.10	0.14	0.09	0.11
MgO	3.73	3.77	4.67	3.19	3.85	10.58	8.50	5.62	3.18	9.25	2.35	3.91
CaO	5.97	5.91	6.54	5.47	5.83	8.36	7.22	6.52	5.72	7.77	5.12	6.23
Na_2O	4.59	4.51	4.35	4.66	4.30	2.71	3.67	4.02	4.55	3.14	4.40	4.20
K_2O	1.29	1.39	1.22	1.30	1.34	1.70	1.06	1.40	1.36	0.90	1.46	1.43
P_2O_5	0.17	0.18	0.21	0.17	0.18	0.36	0.16	0.20	0.18	0.17	0.18	0.20
L.O.I.	0.47	0.92	1.44	2.09	1.85	0.78	0.23	1.41	1.89	1.17	2.02	1.78
Total	99.22	99.42	99.51	99.65	99.27	100.03	99.50	98.98	100.25	99.25	99.80	99.73
S	265	514	410	99	278	588	199	235	484	82	274	1200
Cl	538	353	878	569	519	224	292	527	475	272	316	547
V	116	106	129	98	106	261	165	127	106	233	70	122
Cr	117	111	136	94	123	591	508	254	85	563	52	104
Ni	29	30	45	25	33	157	146	61	25	173	15	27
Cu	37	27	47	25	28	54	63	48	33	70	15	41
Zn	54	51	60	52	55	77	64	61	58	74	54	59
Ga	18	17	19	19	19	16	16	18	18	16	18	19
As	7	7	5	6	6	2	3	5	6	4	6	6
Rb	21	23	20	21	23	38	16	23	22	16	30	25
Sr	556	580	539	568	537	482	459	552	586	393	544	528
Y	13	14	16	12	13	21	14	14	13	16	12	17
Zr	111	110	123	119	115	93	89	109	112	91	119	122
Nb	2	1	2	2	2	2	2	1	2	3	2	2
Mo	1	1	1	1	1	1	<1	<1	1	<1	1	2
Ba	408	465	399	431	447	467	341	473	404	328	456	443
Pb	6	9	7	6	7	7	5	8	9	6	7	8
Th	1	4	1	<1	<1	1	<1	<1	1	3	<1	1
U	1	2	1	2	1	1	1	1	<1	1	1	<1

Analyses were made by XRF in New Mexico Institute of Mining and Technology, USA. Description of the analyzed samples: eruption number (sample number; facies of the deposit). 1 (00K69; ignimbrite); 8 (00K67; ignimbrite); 16 (00K50; fall); 18 (00K51; fall); 25 (00K55; fall); 28 (00K15; fall); 29 (00K22; ignimbrite); 32 (00K58; fall); 39 (00K30; fall); 46 ("dark package", 97058/2; fall); 47 (00K32; fall); 58 (00K44; fall). Eruption codes of marker tephras are given in parentheses. In the text and on the diagrams we refer to contents of SiO_2 in analyses, recalculated to 100%, LOI free.

basaltic andesite composition (Table 1, eruption 46). The younger, coded SHsp, is a unique high-K, high-Mg olivine- and phlogopite-bearing basaltic lapilli tephra (Table 1, eruption 28) [*Volynets* et al., 1997].

Deposits of pyroclastic density currents are common at Shiveluch and are typically pumiceous ignimbrites (Fig. 4C) and various cross-bedded (surge) deposits. Most of these deposits directly overlie pumice fall units and likely formed as a result of a column collapse. We did not find block-and-ash flow deposits in any of our sections and found only a few minor non-pumiceous density current deposits likely derived from dome collapse. One ignimbrite (Table 1, eruption 29) is zoned from light andesitic pumice at the base to black mafic scoria on the top. Most of the ignimbrites were deposited south of the volcano but a few ignimbrites are found also on its western and northwestern slopes (Fig. 3B). The most distal ignimbrite (from SH_1 eruption) occurs in the Kabeku Valley 22 km from the eruptive vent. The original extent of some ignimbrites was greater but they are buried at the extremities by younger lahar deposits. Most of the ignimbrites have volumes usually < 0.5 km^3. A younger and extensive ignimbrite formed by SH_1 eruption is ≤1 km^3 (Fig. 5B).

Debris avalanche deposits. The most prominent debris avalanche on Shiveluch is late Pleistocene in age and resulted

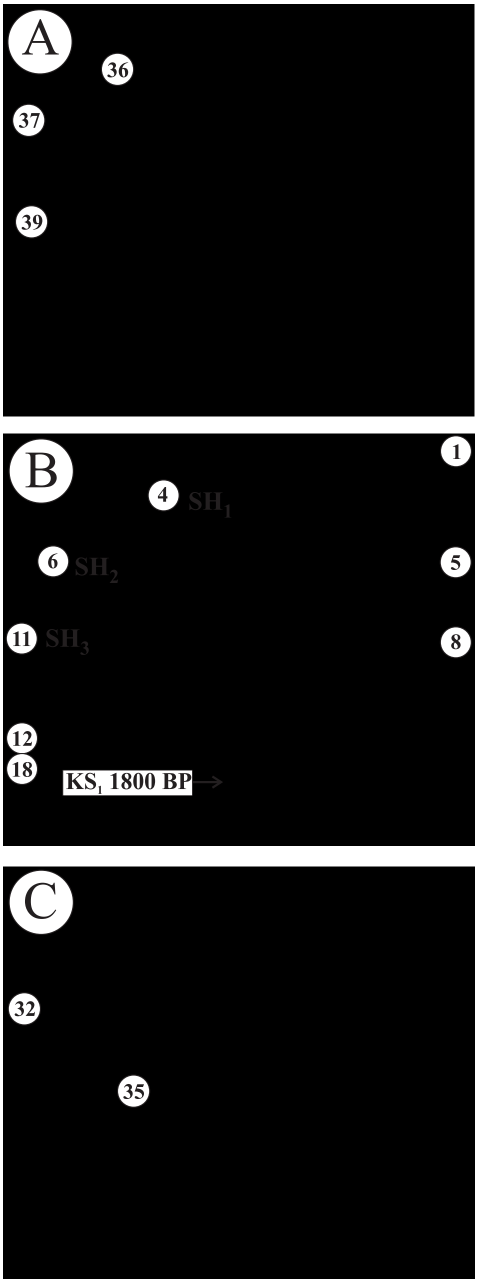

Figure 4. Selected sections showing the pyroclastic units around Shiveluch volcano. Units are labeled with their eruption numbers in white circles. **A**. Mid-Holocene pumice fall units interlayered with thin organic-rich paleosols and fine tephra 16 km southeast of the crater. A handle of a shovel is ~50 cm long. **B**. Upper part of the soil-pyroclastic sequence 16 km southeast of the crater. Marker tephra layers SH$_1$, SH$_2$, and SH$_3$ from Shiveluch and KS$_1$ from Ksudach volcano are labeled. Note the wedge-shaped SH$_3$ ignimbrite separating tephra-fall and paleosol layers. **C**. Coarse-grained ignimbrites interlayered between packages of tephra-fall and paleosol layers. SE sector, 14 km from the crater. A standing person is ~180 cm tall.

in the formation of the 9 km-wide crater which dissects Old Shiveluch volcano. Large hummocks of this debris avalanche are found on the southern slope of the volcano (Fig. 3A) [*Melekestsev* et al., 1991; *Belousov* et al., 1999; *Ponomareva* et al., 2006]. More than 10 mid- to late Holocene debris avalanche deposits are exposed on the southern slope and 2 occur on the western slope of Shiveluch at distances ≥7 km from the active vent [*Ponomareva* et al., 1998]. The prehistoric deposits are labeled with Roman numbers I–XIII (Figs. 6–10). Travel distances of individual Holocene avalanches exceeded 20 km, and volumes reached 3 km^3. When the avalanche deposits are not obscured by younger deposits they display a typical hummocky topography. Some debris avalanche deposits are completely buried under younger volcanic products but in outcrops they exhibit typical “block facies” often underlain by “mixed facies” [*Glicken*, 1986; *Belousov* et al., 1999]. When one considers the high magma discharge rates during the Holocene, it is likely there are more debris avalanche deposits which are not exposed or have not been identified.

In plan view most of the debris avalanche deposits look similar to the 1964 deposit which is narrow near vent and spreads out in a broad apron (Fig. 3A). These likely originated from a collapse of tightly spaced domes located close to the modern one. Debris avalanche deposits V and XII occur in a wide area extending from Baidarnaia to Dry Il’chinets Rivers (Fig. 3A) [*Ponomareva* et al., 1998]. This distribution suggests they originated from collapse of domes which once occupied the whole area of the late Pleistocene collapse crater. At least one of the deposits (X on Fig. 6) may have originated from Baidarny Ridge based on the dispersal of this deposit only in the southwestern sector of the volcano’s foot and the presence of a collapse scarp on the ridge (Fig. 2). *Ponomareva* et al. [1998] gives more details on the distribution of the debris avalanche deposits and *Belousov* et al. [1999] provides characteristics of some of those.

Lahars (debris flows) likely accompanied most of Shiveluch eruptions due to the presence of glaciers and long-lived snow cover at the volcano. The lahar deposits have rounded rock fragments suspended in a coarse sandy matrix. They are exposed in all the valleys and merge into a discontinuous ring plain around the volcano (Fig. 3B).

STRATIGRAPHY

Our field work at Shiveluch has identified 60 large Holocene eruptions (Figs. 6–10). Eruptions are individually numbered but since tephra falls of 8 of them are distinct in some way and are used as markers, these eruptions are given the identifier code SH for Shiveluch [*Braitseva* et al., 1997a, b] (Table 2).

At distances >15 km from Shiveluch the Holocene soil-pyroclastic sequence is dominated by pumice and ash falls separated by paleosols. Included in these sequences are regional marker tephra layers from volcanoes throughout Kamchatka (Figs. 4B, 6–10; Table 2). Studies of the historical deposits (e.g. those of the 1944–1950 and 1964 Shiveluch eruptions and the 1956 Bezymianny eruptions) show that even when there is a short time interval between eruptions, their deposits are separated by paleosols. Because the paleosols form rapidly, when volcanic deposits directly overlie each other and are not separated by paleosols, we have assigned them to the same eruption.

Most fall deposits erupted from Shiveluch look similar and are difficult to uniquely identify in many sections. Direct tracing of tephra layers from section to section was helpful. About 200 sections were measured around Shiveluch mostly along river valleys (Fig. 3B). In cases when correlation of the deposits from adjacent valleys was uncertain, pits up to 4-m-deep were dug on the divides to allow the tephra layers to be traced. All measured sections are over 7 km from the eruptive center. Early Holocene deposits are exposed >10 km from the crater (Fig. 3B). For this reason our eruptive history only includes mid-late Holocene deposits, which reached distances ≥7km from source and 10–12 km for early Holocene units. Some distal tephra falls from Shiveluch have been examined and dated in many sites throughout the Kamchatka Peninsula and are used as markers for volcanological, paleoseismological and paleoclimate research (e.g. *Braitseva* et al., 1983, 1991; *Pevzner* et al., 1998, 2006; *Bourgeois* et al., 2006; *Kozhurin* et al., 2006). These markers are included in Table 2; their ^{14}C ages are also shown on Figures 6–10. We have used tephra thickness data from distal sites to construct isopach maps and estimate eruption volumes.

There is nearly continuous outcrop along the banks of rivers radiating out from Shiveluch. Significant differences can be seen in pyroclastic deposits from bank to bank along the rivers. So we therefore measured sections on both banks of each valley. Two examples of correlation of the sections down two river valleys are shown on Figures 6 and 7. Kamenskaia valley drains to the southwest and exposes deposits erupted during the last ~1.5 ka (Figs. 3A and 6). Mutny valley descends from Old Shiveluch to the northwest (Fig. 3A) exposing deposits erupted during the last ~9.5 ka. As the pyroclastic sequence in Mutny valley is >4 m thick, we show only the part between the KS_1 and SHdv marker tephra layers (Fig. 7). Direct tracing of tephra layers and other deposits has allowed us to compile summary sections through the deposits exposed in each of

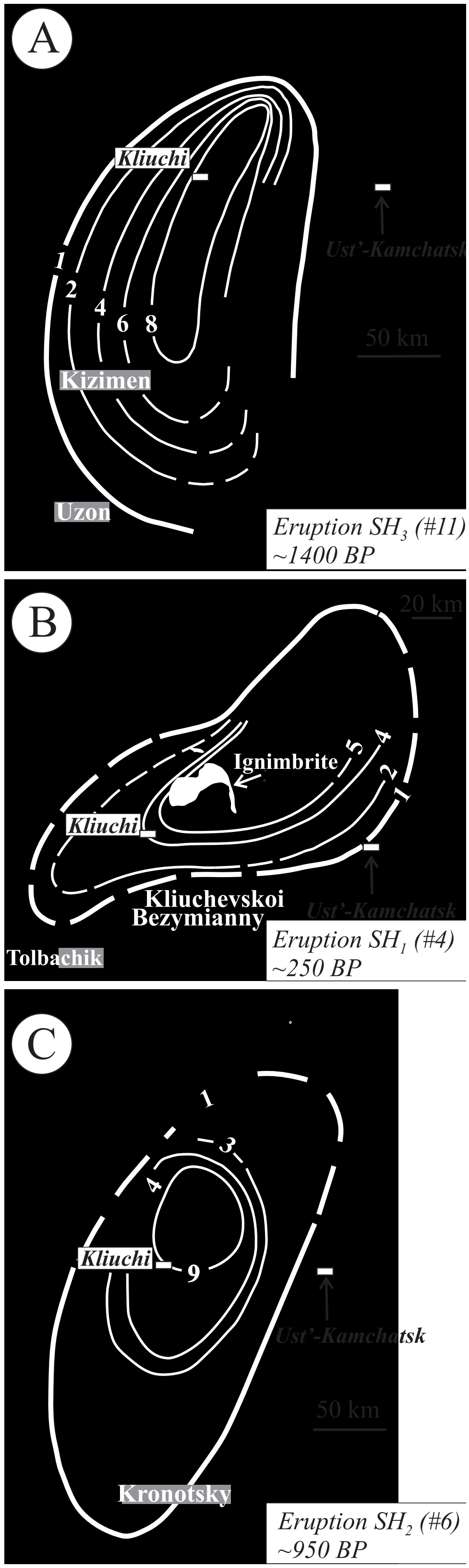

Figure 5. Representative isopach maps for Shiveluch eruptions showing the dispersal of SH_1, SH_2 and SH_3 tephra fall units. Isopach are dashed where inferred and thicknesses are in cm.

Table 2. Holocene Marker Tephra Layers Identified at Shiveluch Volcano, Kamchatka

Source volcano	Code	Rounded ^{14}C age (yr BP)	Description	Composition	Characteristic features
Shiveluch	SH_{1964}		White pumice lapilli	A	Medium K_2O content, high Cr and Sr content, presence of Hb, Ol
Bezymianny	B_{1956}		Gray coarse to fine ash (1–3 cm)	A	Medium K_2O content, presence of Hb
Shiveluch	SH_1	250	Thinly stratified white fine to coarse ash	A	Medium K_2O content, high Cr and Sr content, presence of Hb
"	SH_2	950	Normally graded light gray coarse ash and pumice lapilli	A	Medium K_2O content, high Cr and Sr content, presence of Hb
"	SH_3	1400	Dirty-yellow pumice lapilli	A	Medium K_2O content, high Cr and Sr content, presence of Hb, Ol
Ksudach	KS_1	1800	Pale yellow (upper 1–2 cm gray) fine ash (6-8 cm)	D	Low K_2O content, absence of Hb
Shiveluch	SH_5	2550	Yellow pumice lapilli in the western sector and coarse yellow ash in other sectors	A	Medium K_2O content, high Cr and Sr content, presence of Hb, Ol
"	SHsp	3600	Stratified dark-gray cinder lapilli and coarse ash	B	High K_2O, MgO, Cr and Sr content, presence of Hb, Ol and Ph
"	SHdv	4100	Normally graded pale yellow coarse to fine ash	A	Medium K_2O content, high Cr and Sr content, presence of Hb
Kliuchevskoi	KL	5800–6000	Black coarse ash (0.5–1.5 cm)	BA	Medium K_2O content
Ksudach	KS_2	6000	Iron-stained ochre fine ash (0.5 cm)	A	Low K_2O content, absence of Hb
Khangar	KHG	6950	Bright yellow fine ash (3–4cm)	D	Medium-high K_2O content, presence of Bi and Hb
Kizimen	KZ	7550	Yellow fine ash (1–2 cm)	D	Medium K_2O content, presence of Hb
Plosky	PL	8600	Dark-brown coarse ash (1cm)	BA	High K_2O content
Plosky	PL	~9500	Dark-brown coarse ash (1cm)	BA	High K_2O content

Note. Tephra layers are listed in chronological order. Ages are the rounded average radiocarbon ages from *Braitseva* et al [1988, 1995, 1997a, b] and *Volynets* et al. [1997]. In description average thicknesses of distal marker tephra layers in the Shiveluch area are given in parentheses. Composition of the tephra are A – andesite; BA-basaltic andesite; D – dacites; RD – rhyodacite; R - rhyolite. Hb, hornblende; Ol, olivine; Bi, biotite; Ph, phlogopite.

these valleys. In the same way we compiled summary sections for each of the radial valleys (Fig. 8) and combined them into a summary section through the Holocene pyroclastic succession at Shiveluch foot (Fig. 9). The summary section is the basis for the reconstruction of the Shiveluch Holocene eruptive activity. ^{14}C dates obtained in different valleys complement each other and provide a detailed framework for timing the eruptions.

Reconstruction of the eruptive history of Shiveluch and an understanding of the repose periods can only be determined using sections measured along multiple river valleys. Eruptive units were dispersed in different directions and some of them are absent on the southern slope of the volcano traditionally visited by researchers. Belousov et al. [1999] examined the pyroclastics on the southern slope and concluded that the volcano produced only one strong eruption (SH_3) between 1600 and 1000 BP. Our data show that actually this period includes a period of enhanced activity with at least three more large eruptions in addition to the SH_3 one (Figs. 9–10) with fallout axes directed to the N and SE (Fig. 8).

We think that the tephra layers younger than ~9.5 ka (eruption #52, Fig. 9) are equally well preserved in all the sectors around Shiveluch. Older tephra have been examined in fewer outcrops which hampers an understanding of their dispersal and eruptive volumes. Smaller early Holocene debris avalanche deposits may also be buried under younger deposits. Debris avalanche deposits VII and XI and two pyroclastic density current deposits have been recognized only on the western slope and were likely associated with eruptions of the Karan domes (Figs. 9 and 10).

The various facies of an eruption are given on Figure 10. At least 6 eruptions started with debris avalanches and then produced pumice falls and ignimbrites or surge deposits. Five debris avalanches were followed only by deposition of ignimbrite and only 2 by tephra falls. More than 20 eruptions produced fall and pyroclastic density current deposits. Eighteen eruptions produced only fall deposits including 14 andesitic pumice fall deposits, 2 phreatic tephras and 2 basaltic fall deposits.

ERUPTION VOLUMES

The 1964 eruption (SH_{1964}) produced ~2 km^3 of debris avalanche and 0.3–0.4 km^3 each of fall deposits and ignimbrite [*Gorshkov* and *Dubik*, 1970]. As this was the last major eruption these deposits are easily identified around the volcano. The SH_{1964} tephra fall deposit can be traced SE downwind of the volcano to the Pacific coast. In the Ust'-Kamchatsk region (Fig. 1) the fall was 2–3 cm thick. Ash from the SH_{1964} eruption was also observed to fall at Bering Island (Fig. 1), ~330 km from source [*Gorshkov* and *Dubik*, 1970]. Now only minor traces of this ash are found there. The 1964 eruption can serve as a model for a large eruption from Shiveluch but examination of pre-historic deposits shows that larger eruptions have occurred in the past.

Only approximate volumes for pre-historic ignimbrite, surge and debris avalanche deposits can be estimated since many are obscured by younger eruptives or are partly eroded. Furthermore, calculation of tephra fall vol-

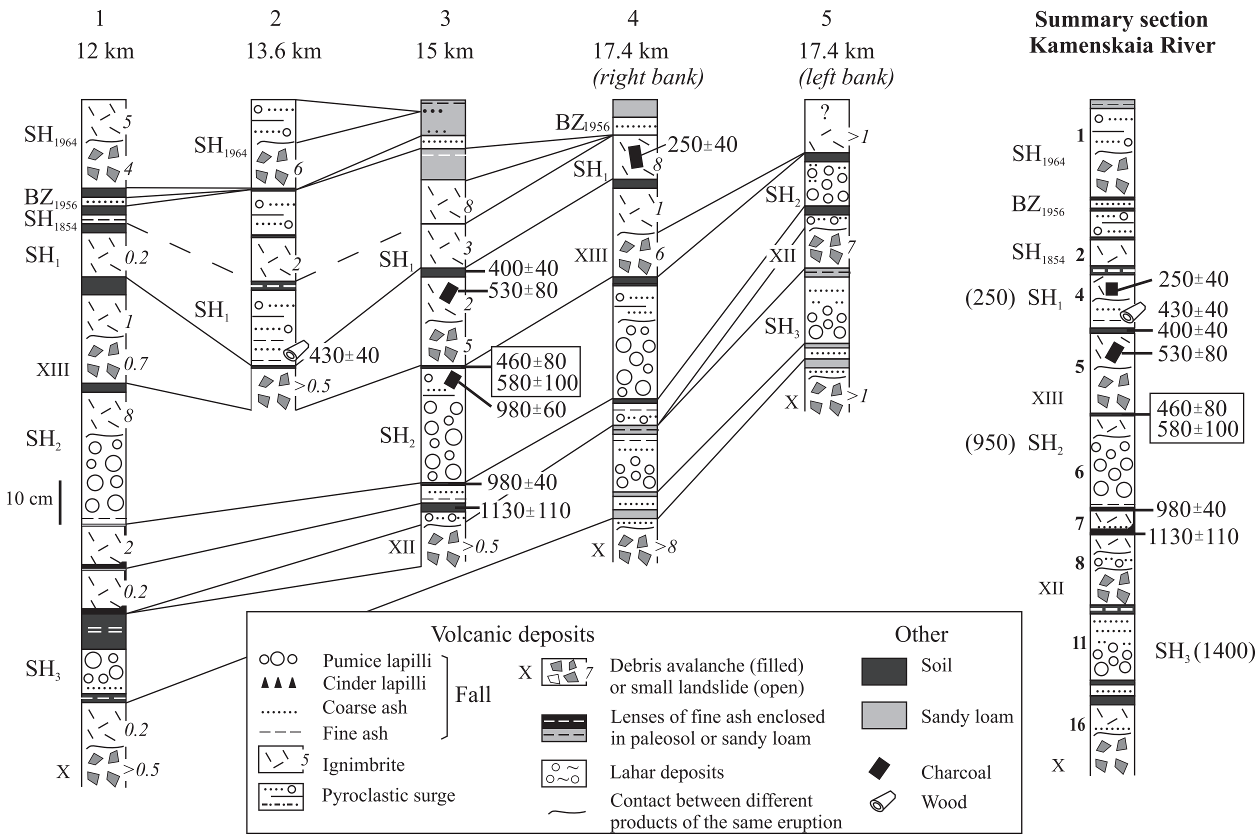

Figure 6. Summary and individual measured stratigraphic sections in the Kamenskaia River. Locations of the sections are shown on Figure 3A. Distance from the eruptive vent is shown above the columns. Inferred correlations are dashed. Rounded radiocarbon ages of marker tephra layers are given in the parentheses. Codes and ages of marker tephra layers as in Table 2. Roman numbers are debris avalanche deposits [from *Ponomareva* et al., 1998]. Radiocarbon dates obtained on successive alkaline extractions from the same sample are shown in boxes. See "Table 3" (available on the CD-ROM accompanying this volume). for details on the dated samples. The 10-cm scale (on the left) is for fall and surge deposits only. Lahar and debris avalanche deposits and ignimbrites are not to scale and their thicknesses in meters are shown to the right of the columns by italic numbers. Numbers of the eruptions are shown left of the summary section.

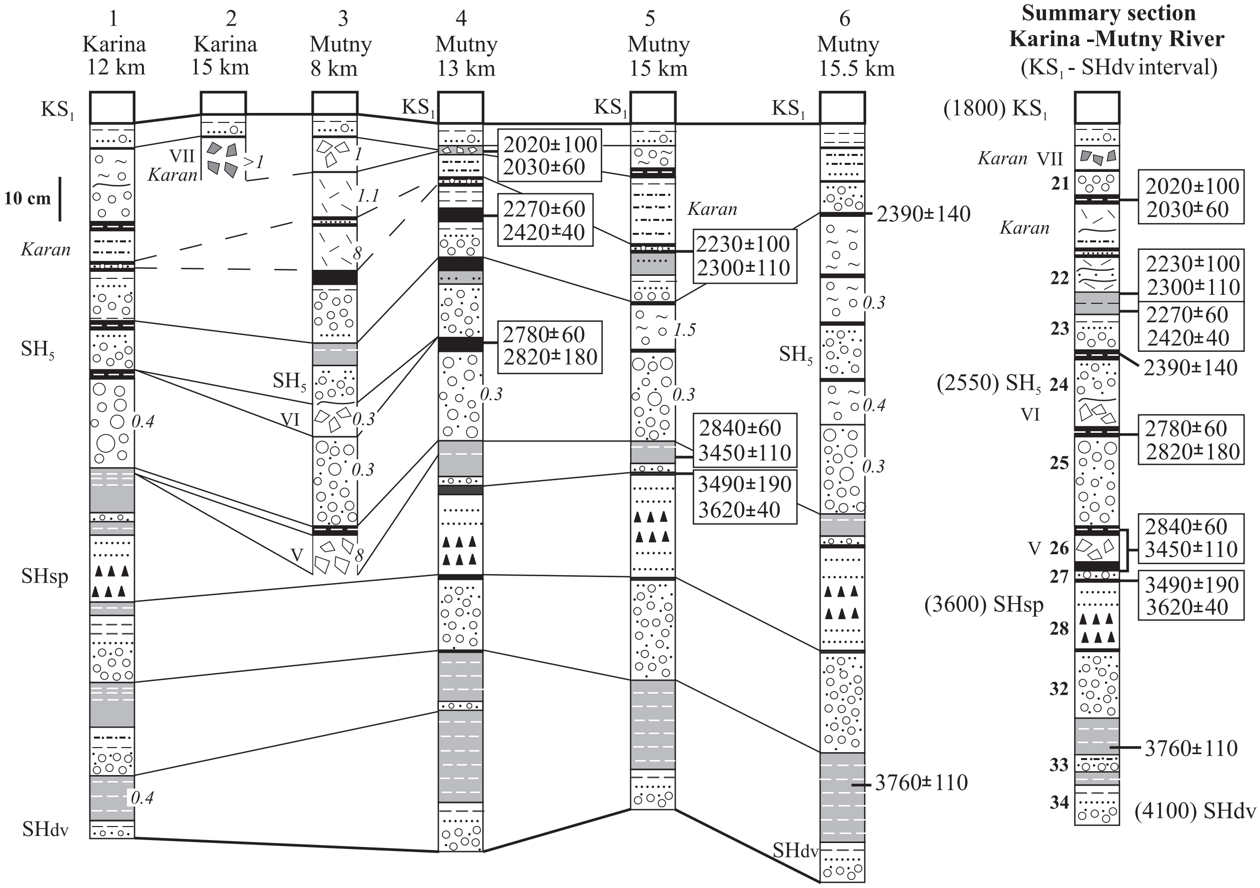

Figure 7. Summary and individual measured stratigraphic sections in the Karina and Mutny Rivers. Locations of the sections are shown on Figure 3A. Only the sections between the 1800 BP KS_1 and 4100 BP SHdv marker tephra layers are shown. Some deposits in these sections were probably erupted from the Karan domes and not from the main crater. Symbols are the same as Figure 6. Lahar deposits are not included into the summary section.

umes are hampered because identification and correlation of many distal deposits are difficult. Estimated volumes for the SH_2 tephra show it is the largest tephra fall deposit (Fig. 5C). The SH_1 eruption had the largest ignimbrite deposits and co-ignimbrite fall tephra (Fig. 5B). The smallest eruptions which are detectable >7 km from the crater, are estimated to have tephra fall volumes of ~0.01 km^3. Such small volume eruptions likely occurred during periods of dome growth. Here we use the 1964 eruption as a reference and classify eruptions with >1 km^3 of erupted products as the largest, 1–0.5 km^3 as large, 0.5–0.1 km^3 as moderate, and <0.1 km^3 as small or minor. For deposits erupted in historic times, including the Plinian eruptions in 1854 (SH_{1854}) and 1964 (SH_{1964}) and dome related eruptions in 1944–1950 and 1980–2005, we can calculate their volumes from field data. When these are compared to contemporary data on tephra dispersal, it shows that we tend to under-estimate the volumes of past eruptions.

RADIOCARBON DATING

Reconstructed eruptive history is based on 101 conventional radiocarbon dates on paleosols, charcoal and wood associated with the pyroclastic deposits (Table 3 available on the CD-ROM accompanying this volume; Fig. 9). Of those, sixteen dates have been earlier published by *Ponomareva* et al. [1998] and three dates - by *Belousov* et al. [1999]. The radiocarbon dates provide additional time constraints when used in conjunction with earlier dated marker tephras from Shiveluch and other volcanoes (Figs. 9 and 10; Table 2).

For radiocarbon dating, we used methods given in *Braitseva* et al. [1992, 1993], which can be summarized as follows. ^{14}C dates from soil layers, which formed over a long time interval, were obtained using successive alkaline extractions (Table 3: available on the CD-ROM accompanying this volume). In such cases we used the younger date for the soil underlying and the older date for the soil overlying the tephra

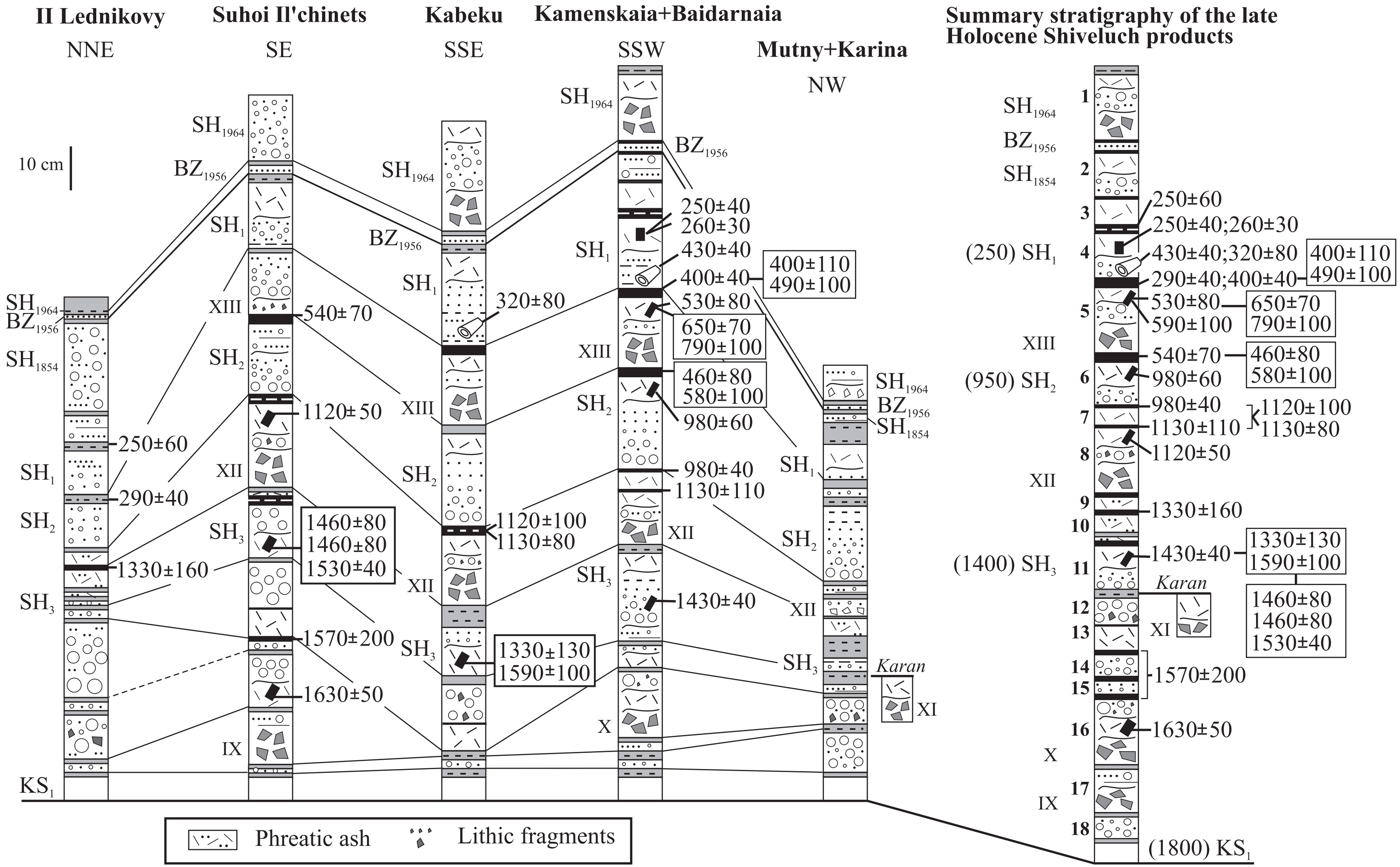

Figure 8. Correlation of late Holocene deposits exposed in 5 river valleys radiating out from Shiveluch volcano. The summary sections for each of the valleys and correlations were used to construct the summary stratigraphic section of the late Holocene history of Shiveluch. The KS_1, ~1800 BP marker tephra layer from Ksudach volcano is at the base of each section. For designations see Figure 6 and Table 2. The 10-cm scale (on the left) is for fall deposits as measured 15–17 km from their eruptive vent. Debris avalanche deposits and ignimbrites are not to scale.

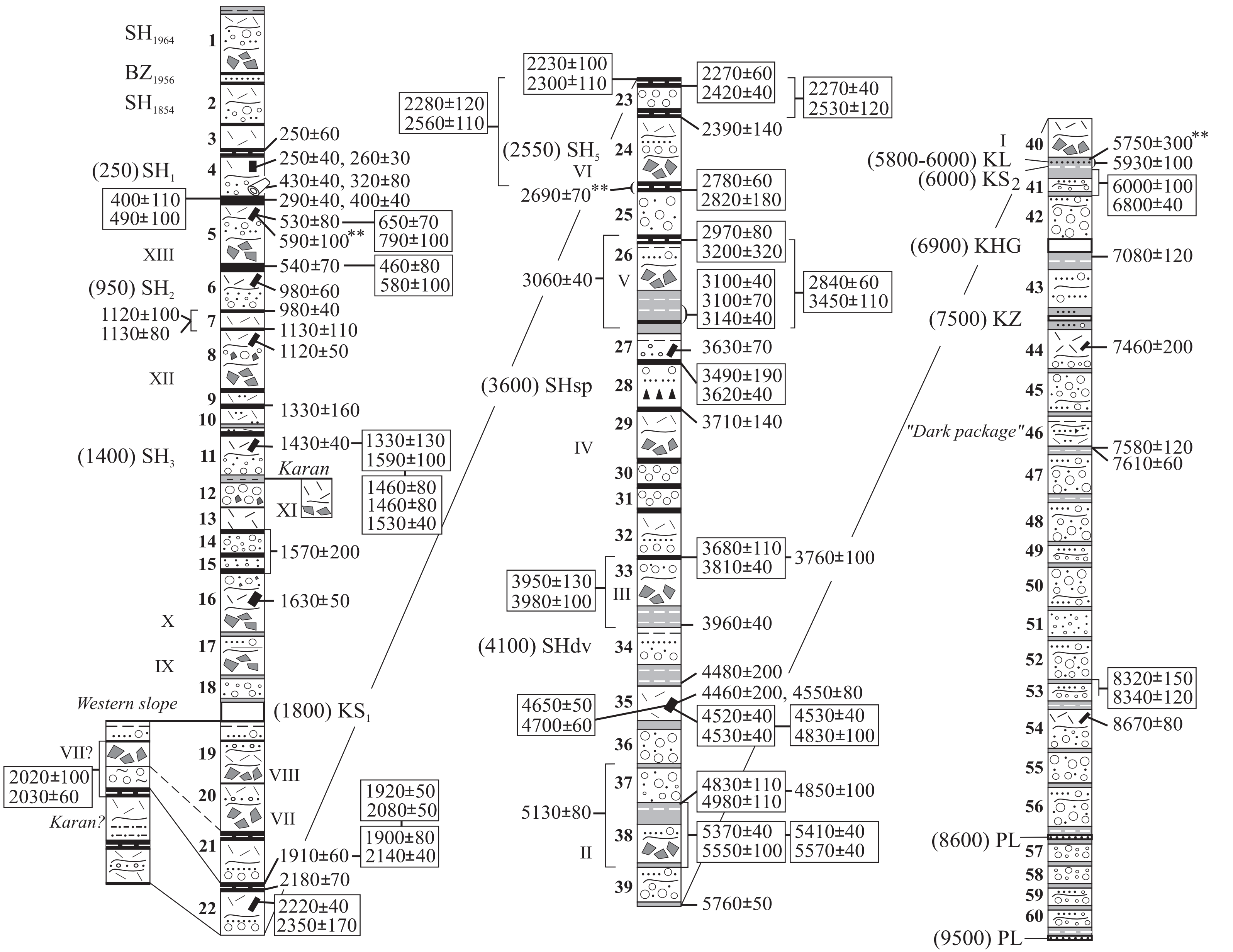

Figure 9. Summary stratigraphy of the Holocene deposits surrounding Shiveluch volcano. Deposits from Karan eruptive centers to the west of Shiveluch are shown left and right of the main column. Symbols are given on Figures 6 and 8. Marker tephra codes are from Table 2. ^{14}C dates are from "Table 3" (available on the CD-ROM accompanying this volume). Dates marked with a double asterisk are from *Belousov* et al. [1999]. ^{14}C dates with square brackets are on paleosols in places where other deposits enclosed within the bracket were not present (pinched out).

deposit. A date obtained on a long-lived soil or peat layer without subdivision into extractions gives its mean age and so may differ significantly from the age of under- or overlying deposits [*Braitseva* et al., 1993]. Wood found in debris avalanche deposits may have been redeposited and can yield older ages. The stratigraphic relationships and ages of the marker tephra layers also help to constrain the ^{14}C dating uncertainty. In Figures 6–8 we provide radiocarbon dates obtained in the individual valleys. In Figure 9 and in Table 3 (available on the CD-ROM accompanying this volume) we provide all the available dates. In Figure 10, we choose the dates we consider provide meaningful ages close to the ages of the eruptions. These are mainly dates on charcoal from the ignimbrites, and the youngest and the oldest dates on paleosols. Approximate ^{14}C ages were then estimated for each of the eruptions. For estimating the duration and timing of active and repose periods (Fig. 12) we have calibrated the ^{14}C ages using CALIB 5.0 [*Stuiver* et al., 2005]. In some parts of the summary stratigraphy, where the dates are rare or lacking (e.g. early Holocene, Fig. 10), we had to rely mostly on marker tephra layers and estimated the ages of individual eruptions dividing the age span between marker layers or between the calibrated dates by the number of the enclosed eruptions.

According to the requirements of the Radiocarbon http://www.radiocarbon.org/Authors/author-info.pdf, we report radiocarbon dates as years BP (e.g., 1000 BP) and calibrated ages as years BC or AD, or (only in Table 4 (available on the CD-ROM accompanying this volume)) as cal years BP. Approximate age estimates in the running text, e.g. ~10 ka, are calibrated ages as well.

COMPOSITION OF ERUPTED PRODUCTS

The major and trace element composition of ejecta from representative eruptions were determined by XRF (Table 1; Table 4 (available on the CD-ROM accompanying this volume)). All of these analyses are on pumice or scoria samples from pyroclastic deposits and should represent the bulk compositions of the magmas erupted at Shiveluch. Glasses from the tephra fall deposits were analyzed by electron microprobe to characterize their compositions and to allow them to be used in tephrochronological studies (Table 5).

Most Holocene erupted products are medium-K, hornblende-bearing andesites [*Gill*, 1981] having a range of SiO_2 from 56 to 64% but many analyses have between 60 and 63% SiO_2 (Fig. 11A, B; Table 4 (available on the CD-ROM accompanying this volume)). The andesites are characterized by high-Mg olivines, which contain Cr spinel inclusions. Compared to other medium-K andesites in Kamchatka the andesite from Shiveluch has higher Mg, Ni, Sr, and Cr contents and Ni/Co, Cr/V and Sr/Y ratios and lower Y contents [e.g., *Churikova* et al., 2001; *Kepezhinskas* et al., 1997; *Melekestsev* et al., 1991; *Volynets* et al., 1994, 1999; 2000; *Yogodzinski* et al., 2001]. The high Sr/Y ratios and low Y concentrations are typical of adakites [*Defant* and *Drummond*, 1993] which are derived in part from slab melting.

Table 5. Representative Electron Microprobe Analyses of Glass

Eruption	1 (SH_{1964})	4 (SH_1)	6 (SH_2)	8	11 (SH_3)	12	13	16	22	32	35	44	47	51
SiO_2	75.06	74.86	75.52	76.06	75.46	76.75	75.88	74.26	75.86	74.35	75.19	75.59	78.06	74.27
TiO_2	0.25	0.24	0.26	0.23	0.24	0.26	0.26	0.23	0.22	0.33	0.23	0.22	0.17	0.35
Al_2O_3	13.89	14.08	13.84	13.24	13.94	12.96	13.33	13.97	13.77	14.12	13.77	13.46	12.72	14.25
FeO	1.24	1.04	1.11	0.92	1.25	1.07	1.19	1.40	1.09	1.52	1.24	1.06	0.76	1.48
MnO	0.03	0.03	0.01	0.04	0.02	0.01	0.02	0.03	0.03	0.04	0.02	0.02	0.01	0.03
MgO	0.31	0.31	0.22	0.13	0.30	0.15	0.29	0.39	0.25	0.41	0.29	0.22	0.19	0.32
CaO	1.27	1.32	1.16	0.90	1.27	0.87	1.10	1.47	1.16	1.37	1.13	0.96	0.97	1.33
Na_2O	5.03	4.89	4.60	4.80	4.35	4.46	4.67	5.11	4.50	4.93	4.47	5.44	4.01	4.41
K_2O	2.75	2.98	3.07	3.38	2.95	3.19	2.99	2.92	2.92	2.74	2.81	2.87	2.82	3.37
P_2O_5	0.04	0.06	0.07	0.04	0.03	0.05	0.04	0.04	0.03	0.04	0.03	0.03	0.04	0.05
SO_2	0.03	0.01	0.02	0.01	0.02	0.03	0.04	0.02	0.01	0.02	0.02	0.02	0.02	0.02
F	0.03	0.06	0.04	0.18	0.03	0.04	0.04	0.05	0.05	0.04	0.68	0.05	0.19	0.03
Cl	0.11	0.13	0.11	0.09	0.15	0.18	0.17	0.15	0.11	0.12	0.12	0.10	0.05	0.12
Total	100.03	100.01	100.01	100.03	100.01	100.01	100.01	100.03	100.01	100.04	100.02	100.04	100.02	100.03

Analyses were made by Cameca SX-100 electron microprobe at New Mexico Institute of Mining and Technology. Multiple analyses for the individual pumice clasts were corrected for sodium loss, normalized to 100% and averaged. Description of the analyzed samples: eruption number (sample number; facies of the deposit). 1 (00K69; ignimbrite); 4 (00K68; ignimbrite); 6 (00K66; ignimbrite); 8 (00K67; ignimbrite); 11 (00K45; ignimbrite); 12 (00K9; fall); 13 (00K64; ignimbrite); 16 (00K65; ignimbrite); 22 (00K62; ignimbrite); 32 (00K21; ignimbrite); 35 (00K27; ignimbrite); 44 (00K31; ignimbrite); 47 (00K32; fall); 51 (00K41; fall). Eruption codes of marker eruptions are given in parentheses.

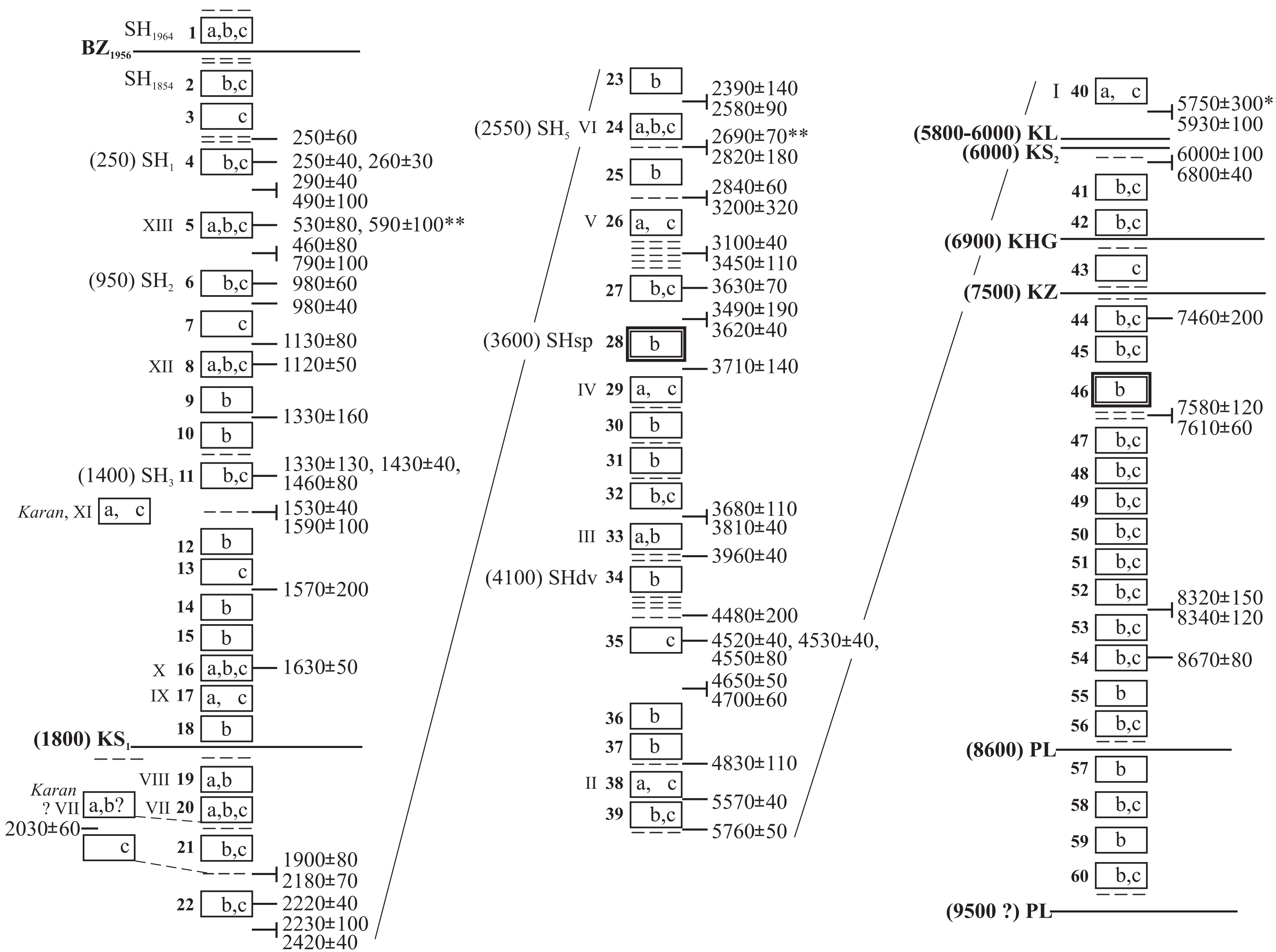

Figure 10. Summary of the eruptive history of Shiveluch volcano during the Holocene. Sixty individual eruptions have been identified and are numbered. Letters inside the boxes give the facies of the deposits: a - debris avalanche deposit; b - fall deposit; c – pyroclastic density current (ignimbrite/surge) deposits. Highlighted boxes for eruptions 28 and 46 show basaltic-andesite eruptions. Short dashed horizontal lines between the boxes are for weak eruptions probably associated with periods of dome growth. Important marker tephra layers are indicated by long horizontal lines "Table 2". Selected ^{14}C dates show dates from charcoal within ignimbrites (tie line to the center of a box) and the youngest dates obtained below an eruption and the oldest dates above the next unit. Radiocarbon dates marked with an asterisk are from *Belousov* et al. [1999].

Mafic (56–58% SiO_2) members of this sequence are few and are represented both by light-colored pumice and dark-gray scoria. In some cases, lower SiO_2 content in the rock coincides with a presence of relatively mafic glass (Fig. 11C; Table 5); it might be interpreted as an input of more mafic material into the magma feeding system. Banded pumices with alternating layers of andesitic and basaltic andesitic material have been described for Shiveluch, that reflects simultaneous presence of both magmas in a chamber [*Volynets*, 1979]. Other mafic andesite varieties contain silicic glass and their bulk composition might reflect enrichment of andesitic pumice with mineral grains including those from disintegrated ultramafic xenoliths (Fig. 11C) [*Volynets* et al., 1997]. This latter case resembles changes of Shiveluch tephra composition downwind due to eolian segregation: as it has been described earlier, its bulk composition may change from silicic andesite (proximal pumice lapilli) to basaltic andesite (sand-size tephra enriched in mineral grains) and then again to silicic andesite or dacite (very fine ash) [*Braitseva* et al., 1997a]. Bulk analyses of lapilli from the andesitic sequence show coherent geochemical trends consistent with fractional crystallization (Fig. 11A); [*Volynets* et al., 1997]. The Shiveluch tephra have high MgO (2.3–6.8 wt %), Cr (47–520 ppm), Ni (18–106 ppm) and Sr (471–615 ppm) and low Y (<18 ppm).

SHIVELUCH ACTIVITY DURING THE HOLOCENE

The volume of eruptions from Shiveluch volcano over the last 10 ka are given in Figure 12. We have arbitrarily assigned a volume of 0.5 km^3 for units which have similar thicknesses and distribution to the 1964 deposits. Debris avalanche deposits with unknown or <1 km^3 volumes [*Ponomareva* et al., 1998] are assigned a volume of 0.5 km^3. Periods of dome growth were identified in the stratigraphic record by the presence of the tephra layers similar to those erupted from domes between 1944 and 2005. Typically these consisted of minor pumiceous or lithic-rich coarse tephra fallout, including pink (oxidized) fine and coarse tephra. Five periods of small or infrequent eruptions and low activity are shaded on Figure 12.

The eruptive activity of Shiveluch during the Holocene (Figs. 9, 10 and 12) has been characterized by Plinian eruptions alternating with periods of dome growth. Plinian eruptions with eruption volumes ≥0.6–0.8 km^3 have occurred at least 23 times during the Holocene giving an average of over 2 Plinian eruptions per 1000 years. At the same time, Shiveluch activity has not been uniform with time. Periods of large and moderate eruptions separated by only 50–100 years intervals, often were followed by long periods of small eruptions.

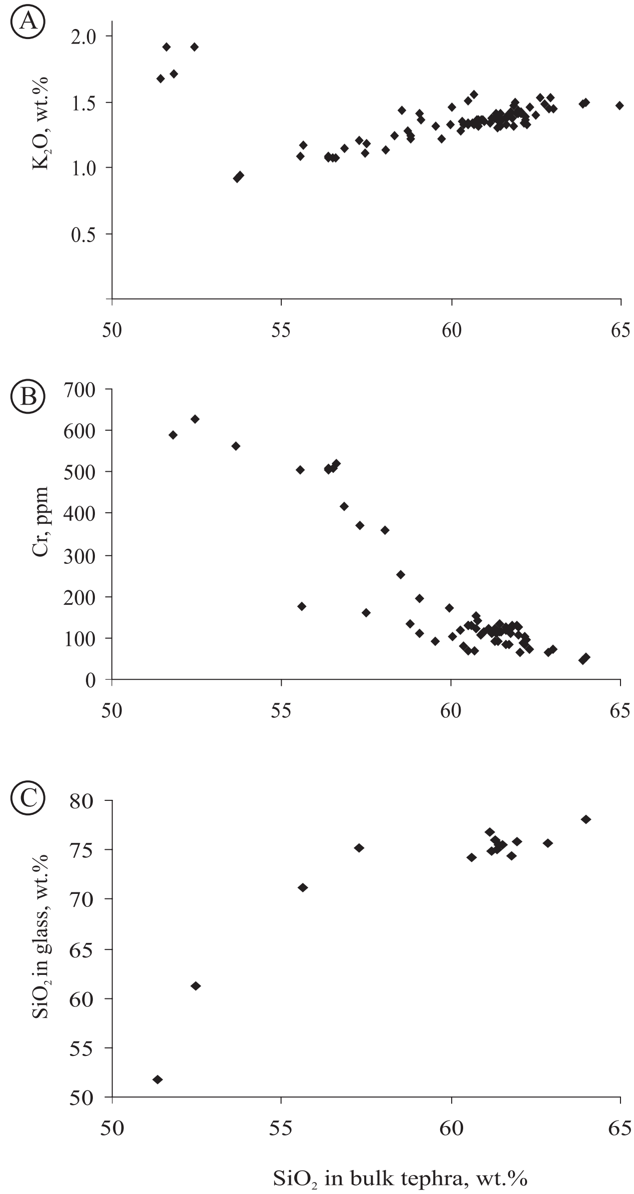

Figure 11. Silica variation diagrams showing K_2O and Cr contents in pumice and scoria samples representative of the bulk composition of the erupted tephra. Groundmass glasses are rhyolitic although the parental eruptions were andesitic. The smooth linear trend in the K_2O plot is consistent with the magmas evolving from a basaltic andesite parent by fractional crystallization. The "basic" (~52% SiO_2) SHsp eruption is more potassic than the evolved andesitic rocks and is not related to the normal andesitic rocks erupted from Shiveluch. See "Table 4" (available on the CD-ROM accompanying this volume) and "Table 5" for the data.

Shiveluch had 3 distinct periods of frequent moderate to large eruptions. These were from ~8500 to 6400 BC, with 16 eruptions; from ~2600 to 1700 BC, with 5 eruptions and since ~900 BC with 16 eruptions including eruptions from the Karan domes on the western flank of the volcano. Within these periods there were times when the large and moderate eruptions were only ~50 years apart. These times were 6500–6400 BC, 2250–2000 BC, and 50–650 AD. Unusual mafic eruptions ("dark package" and SHsp) occurred during the 2 earlier periods. The earliest and the latest periods fit well into periods of intensified activity noted throughout Kamchatka [*Braitseva* et al., 1995]. The 2250 to 2000 BC activity with the unique SHsp correlates with periods of strong mafic eruptions, documented on many Kamchatka volcanoes, including the growth of the young cones of Avachinsky and Gamchen volcanoes and vigorous activity of flank vents on Kliuchevskoi volcano [*Braitseva* et al., 1995; *Kozhurin* et al., 2006].

Long periods with little deposition of tephra >7 km from the vent, happened several times in the volcano's life (Fig. 12). The longest quiet period between 6400 and 4600 BC had only one large plinian eruption at ~5500 BC and intermittent minor activity. The last relatively calm period took place between 1800 and 900 BC with small collapse deposits found in Mutny, Baidarnaia and Dry Il'chinets rivers.

The eruptive frequency of Shiveluch activity was irregular. The current period of activity seems to have started around 900 BC; since then the large and moderate eruptions follow each other in 50–400 yrs-long intervals. Over the ~1.5 ka there was at least 5 largest, 3 large, 2 moderate eruptions and 5 debris avalanches including the largest one during the Holocene. This persistent and strong activity can be matched only by the early Holocene one.

Explosive eruptions associated with debris avalanches were small to large, but never the largest (Fig. 12). During some of them explosive events were likely provoked by sector collapses, otherwise the activity might have been restricted to another dome formation as it was shown for the 1964 eruption by *Belousov* [1995]. Only 2 pre-historic debris avalanches were immediately followed by a large pumice fall similar to the 1964 eruption. In 3 more cases explosive events included moderate to small pumice fall and extensive pyroclastic density currents. In other cases explosive activity was weak. In most cases debris avalanche-associated eruptions did not follow each other but were separated by one or more Plinian eruptions. The largest Plinian eruptions, such as SH_1, SH_2 and SH_3, followed within a 50–200-yrs long intervals after the debris avalanche-associated eruptions.

During the Holocene most Shiveluch eruptions were andesitic (Fig. 12). No other Kamchatka volcano has consistently produced andesite like Shiveluch during the Holocene. Most of other "andesitic" volcanoes, including Bezymianny and Kizimen, also erupted large amounts of mafic material during their lifetime [*Braitseva* et al., 1991; *Melekestsev* et al., 1995]. The persistent andesitic eruptions from Shiveluch suggest the existence of a steady andesitic magma chamber under the volcano. Petrologic models show that the andesite at Shiveluch could fractionate from basaltic andesite. Basaltic andesite has erupted a number of times, most recently in 1854, but it also occurs as mafic bands in some andesitic pumice [*Volynets* et al., 1979, 1997]. As it was discussed earlier, two mafic tephras, "dark package" and SHsp, erupted about 6500 and 2000 BC, respectively, likely reflect some important events in the magma feeding system, especially the later one, which has no analogues in any other Shiveluch products but has a certain similarity to the basalts of nearby Kharchinsky volcano [*Volynets* et al., 1997]. There is no distinct relationship between composition of the erupted products and the size of an eruption or its position within the active period. We only can note that the two mafic tephras appeared close to the end of the corresponding periods of activity. Based on seismic data, replenishment of this supposed crustal chamber starts from the depth of at least 100 km and was registered even before small explosive eruptions [*Gorelchik* et al., 1997]. Irregularity of Shiveluch activity, correlation of its main peaks with the regional ones, stability of magma composition and replenishment of the crustal chamber from a deep source even before small explosive eruptions suggest that pulses of Shiveluch activity are governed by a deep-seated process.

Shiveluch eruptive history clearly demonstrates that historical activity was far less hazardous than some of the preceding eruptions. The largest historical eruptions (in 1854 and 1964) were not the largest ones on the geological record (Fig. 12), and their tephra fall was dispersed mainly to the north and east, respectively, where the closest villages were located farther than 80 km from the volcano (Fig. 1). Some 150–200 years before the 1854 eruption a far stronger eruption (SH_1) occurred, which produced pumice fall and voluminous ignimbrite >22 km long, and caused extensive debris flows (lahars) down all the valleys. Pyroclastic density currents were dispersed mostly in the southern sector with minor offshoots into Mutny and II Lednikovy valleys (Fig. 3A, B). Prominent features of deposits on the southern slope are carbonized spruce trunks still standing in an upright position. Fall deposits combine pumice fall and co-ignimbrite fall, and are commonly stratified. The fall dispersal pattern is shown on Figure 5B. The present day thickness of compacted SH_1 tephra in Kliuchi town, ~45 km to the southwest, is ~4 cm.

The impact of future eruption will depend on the season and snow cover. Future eruptions could result in Plinian eruptive columns which collapse giving pyroclastic density currents. These could ignite a large forest fire and destroy roads and buildings. Tephra falls ~6–8 cm thick could occur in Kliuchi. Lahars will also descend to the Kamchatka River,

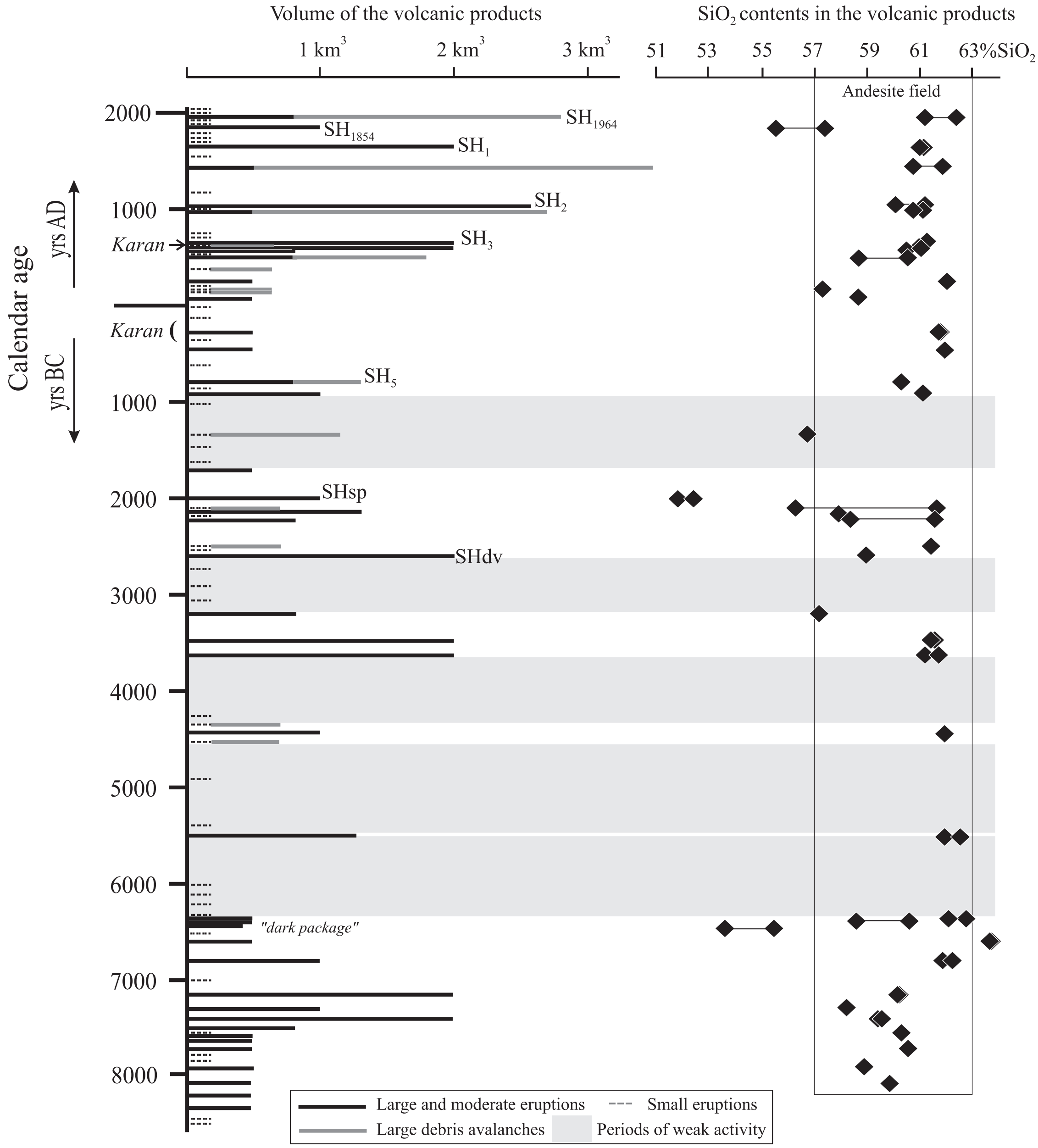

Figure 12. Volumes of eruptive products and the Holocene eruptive history of Shiveluch volcano. Ages are in calendar years AD or BC. Codes of the eruptions as in Table 2. Periods of Karan domes activity are shown to the left of the age axis. The SiO_2 contents of the erupted products show most eruptions were andesitic (the range in analyses for the same eruption are shown by tie lines). The figure is based on the data from "Table 3" and "Table 4" (available on the CD-ROM accompanying this volume).

which will bring sediment load down to Ust'-Kamchatsk. A lahar in winter could break ice on the river (as in 1854) and may cause an unexpected ice drift towards the river mouth.

The largest Holocene eruption from Shiveluch was likely SH_2, which occurred ~1050 AD and yielded more than 2.5 km^3 of tephra. Its pumice fall was dispersed in all the directions from the volcano and can be traced southwards as far as Uzon caldera (Fig. 5C). In Kliuchi, the thickness of a compacted tephra from this eruption (~9 cm) exceeds that of any other tephra from Shiveluch deposited during the Holocene. Its ignimbrite, on the contrary, is limited to the most proximal area (<8 km from the crater).

The forecast of future large eruptions from Shiveluch, based on its eruptive history, is ambiguous. We noted that since ~900 BC the volcano is in its active period, the longest one in the Holocene (Fig. 12). A number of recent eruptions (SH_1, SH_2, SH_3 etc.) were the largest in the eruptive history of the volcano. In most cases, debris avalanche-associated eruptions were followed by Plinian eruptions. So after the 1964 eruption, which started from a debris avalanche, we might expect a large to largest Plinian eruption in future. At the same time, it is not clear why past active periods were shorter than the modern one and why they gave way to long periods of weak activity.

CONCLUSIONS

1) Pyroclastic deposits surrounding Shiveluch volcano show it has been active throughout the Holocene. Eruptive activity has included numerous Plinian eruptions, deposition of debris flows and debris avalanches and periods of lava dome growth. Many past eruptions from Shiveluch, were larger and more hazardous than historical eruptions. The tephra fall of the ~1050 AD eruption (SH_2) exceeded 2.5 km^3. Tephra falls from Shiveluch eruptions often exceeded 350 km making them good stratigraphic markers.

2) Eruptive activity at Shiveluch alternated between periods of strong and weak activity. Active periods were ~8500–6400 BC, 2600–1700 BC and from ~900 BC to the present. Within these periods there were times when the large and moderate eruptions were ~50 years apart. These times were 6500–6400 BC, 2250–2000 BC, and 50–650 AD. The oldest and youngest peaks of activity coincide with periods of increased eruptive activity shown by volcanoes throughout Kamchatka. The 2250–2000 BC eruptions may correlate with a period of increased mafic eruptions seen at many Kamchatka volcanoes.

3) The current period of activity started around 900 BC and is the longest in the Holocene. Debris avalanche events were usually followed 50 to 200 yrs later by Plinian eruptions. The 1964 Shiveluch eruption commenced with a debris avalanche so a large Plinian eruption may occur in the near future.

4) During the Holocene Shiveluch has erupted mainly medium-K, hornblende-bearing andesite (56–63% SiO_2) characterized by high MgO (2.3–6.8 wt %), Cr (47–520 ppm), Ni (18–106 ppm) and Sr (471–615 ppm), and low Y (<18 ppm). Two mafic tephras including a high-K, high-Mg olivine- and phlogopite-bearing basalt were erupted. The mafic eruptions occurred during peaks of activity indicating changes in the magma supply system.

5. In order to better understand magmatic processes under Shiveluch, more mineralogical and geochemical data on the eruptive deposits are necessary. In future studies, analysis of the evolution of tephra compositions with respect to periods of eruptive activity and eruption volume is desirable. Large and largest eruptions from Shiveluch produced tephra layers, which are good markers for Holocene studies. However, most of the Shiveluch tephra have similar bulk, mineral and glass compositions. In order to be able to use them as markers more detailed characterization and geochemical fingerprinting are required.

*Acknowledgements***.** This research was supported by grants ## 05-05-64776, 06-05-64960 and 06-05-64960 from the Russian Foundation for Basic Research and NSF grant #EAR-0125787 to Joanne Bourgeois. The 1999 and 2000-field work was supported by grants ## 6543-99 and 6831-00 from the National Geographic Society. We are very grateful to Olga Braitseva who shared her 1978 field data and to Ivan Melekestsev for allowance to use his unpublished map of the Shiveluch deposits. Support from the New Mexico Institute of Mining and Technology helped to cover the field expenses of Melanie Hartman. Philip Kyle acknowledges support from the Office of Polar Programs, NSF. Lab expenses at NMT were partially supported by a grant to MH from the Geological Society of America. We thank Andrei Babansky (IGEM) for additional analyses of major elements and Dmitry Melnikov for space images processing.

REFERENCES

Belousov, A. B. (1995), The Shiveluch volcanic eruption of 12 November 1964-explosive eruption provoked by failure of the edifice, *J. Volcanol. Geotherm. Res*., 66, 357–365.

Belousov, A., Belousova, M., and B. Voight (1999), Multiple edifice failures, debris avalanches and associated eruptions in the Holocene history of Shiveluch volcano, Kamchatka, Russia, *Bull. Volcanol*., *61*, 324–342.

Bourgeois, J., Pinegina, T. K., Ponomareva, V. V., and N. E. Zaretskaia (2006), Holocene tsunamis in the southwestern Bering Sea, Russian Far East and their tectonic implications, *The Geol. Soc. Amer. Bull*., 11 (3/4), 449–463; doi: 10.1130/B25726.1.

Braitseva, O. A., Melekestsev, I. V., and V. V. Ponomareva (1983), Age divisions of the Holocene volcanic formations of the Tolbachik Valley, *The great Tolbachik fissure eruption: geological and geophysical data 1975–1976, Cambrige Earth Sci. Series*, 83–95.

Braitseva, O. A., Sulerzhitsky, L. D., Litasova, S.N., Grebzdy E.I. (1988), Radiocarbon dates for the Holocene soil-pyroclastic cover in the Kliuchevskoi volcano group, *Volcanol. and Seismol., 6*, 317–325.

Braitseva, O. A., Melekestsev, I. V., Bogoyavlenskaya, G. E., and A. P. Maksimov (1991), Bezymianny volcano: eruptive history and activity dynamics, *Volcanol. and Seismol., 12*(2), 165–194.

Braitseva, O. A., Litasova, S. N., and L. D. Sulerzhitsky (1992), Validity of radiocarbon dating in regions of active volcanism in Kamchatka, *Quaternary International, 13/14,* 143–146.

Braitseva, O. A., Sulerzhitsky, L. D., Litasova, S. N., Melekestsev, I. V., and V. V. Ponomareva (1993), Radiocarbon dating and tephrochronology in Kamchatka. *Radiocarbon 35*(3), 463–476.

Braitseva, O. A., Melekestsev, I. V., Ponomareva, V. V., and L. D. Sulerzhitsky (1995), The ages of calderas, large explosive craters and active volcanoes in the Kuril-Kamchatka region, Russia, *Bull. Volcanol., 57*(6), 383–402.

Braitseva, O. A., Ponomareva, V. V., Sulerzhitsky, L. D., Melekestsev, I. V., and J. Bailey (1997a), Holocene key-marker tephra layers in Kamchatka, Russia, *Quaternary Research, 47*(2), 125–139.

Braitseva, O. A., Sulerzhitsky, L. D., Ponomareva, V. V., and I. V. Melekestsev (1997b), Geochronology of the greatest Holocene explosive eruptions in Kamchatka and their imprint on the Greenland glacier shield, *Transactions (Doklady) of the Russian Academy of Sciences. Earth science sections*, *352*(1), 138–140.

Braitseva, O. A., Bazanova, L.I., Melekestsev, I. V., and L.D. Sulerzhitsky (1998) The largest Holocene eruptions of Avachinsky volcano, Kamchatka, *Volcanol. and Seismol., 20,* 1–27.

Churikova, T., Dorendorf, F., and G. Woerner (2001), Sources and fluids in the mantle wedge below Kamchatka, evidence from across-arc geochemical variation, *J. of Petrology*, *42*(8), 1567–1594.

Davidson, J. and S. DeSilva (2000), Composite volcanoes. *in* Sigurdsson, H., ed., Encyclopedia of Volcanoes: San Diego, CA, Academic Press, p. 663–682.

Defant, M.J. and M.S. Drummond (1990), Derivation of some modern arc magmas by melting of young subducted lithosphere, *Nature (London), 347,* 662–665.

Ditmar, K. (1890), *Reisen und Aufenthalt in Kamtschatka in den Jahren 1851–1855. Th. 1. Beitrage zur Kenntniss des Russischen Reiches,* Bd. 7, Spb

Dvigalo, V. N. (1984), Growth of the dome in the crater of Shiveluch volcano in 1980–1981 according to photogrammetric data, *Volcanol. and Seismol.,* (2), 104–109 (in Russian).

Fedotov, S.A., Zharinov, N.A., Dvigalo, V.N., Seliverstov, N.I., Khubunaya, S.A. (2004), The 2001–2004 eruptive cycle of Shiveluch volcano, *Volcanol. and Seismol.,* (6), 3–14 (in Russian).

Gill, J. (1981), *Orogenic Andesites and Plate Tectonics*. Berlin: Springer, 390 pp.

Glicken, H. (1986), *Rockslide-debris avalanche of May 18, 1980, Mount St. Helens volcano, Washington. The University of California. Santa Barbara,* Ph. D. Dissertation, 303.

Gorelchik, V. I., Shirokov, V. A., Firstov, P. P., and O. S. Chubarova (1997), Shiveluch volcano: seismicity, deep structure and forecasting eruptions (Kamchatka), *J. Volcanol. Geotherm. Res., 78,* 121–132.

Gorshkov, G. S. and Yu. M. Dubik (1970), Gigantic directed blast at Shiveluch volcano (Kamchatka), *Bull. Volcanol., 34,* 261–288.

Kepezhinskas, P., McDermott, F., Defant, M. J., Hochstaedter, A., Drummond, M. S., Hawkesworth, C. J., Koloskov, A., Maury, R. C., and H. Bellon (1997), Trace element and Sr-Nd-Pb isotopic constraints on a three-component model of Kamchatka Arc petrogenesis, *Geochimica et Cosmochimica Acta, 61*(3), 577–600.

Khubunaya, S. A., Zharinov, N. A., Muravyev, Ya. D., Ivanov, V. V., Boloyavlenskaya, G. E., Novgorodtseva, T. Yu., Demyanchuk, Yu. V., Budnikov, V. A., and S. M. Fazlullin (1995), 1993 eruption of Shiveluch volcano, *Volcanol. and Seismol., 17*, 1–20.

Kozhurin, A., Acocella, V., Kyle, P. R., Lagmay, F. M., Melekestsev, I. V., Ponomareva, V. V., Rust, D., Tibaldi, A., Tunesi, A., Corazzato, C., Rovida, A., Sakharov, A., Tengonciang, A., and H. Uy (2006), Trenching active faults in Kamchatka, Russia: paleoseismological and tectonic implications, *Tectonophysics, 417*: 285–304

Melekestsev, I. V., Braitseva, O. A., Erlich, E. N., and N. N. Kozhemyaka (1974), Volcanic mountains and plains. In: Luchitsky I. V. (Ed.) *Kamchatka, Kurile and Commander Islands*, pp. 162–234, Nauka Press, Moscow (in Russian).

Melekestsev, I. V., Volynets, O. N., Ermakov, V. A., Kirsanova, T. P., and Yu. P. Masurenkov (1991), Shiveluch volcano. In: Fedotov S. A., Masurenkov Yu. P. (Eds.) *Active volcanoes of Kamchatka. 1,* pp. 84–92, Nauka Press, Moscow.

Melekestsev, I. V., Ponomareva, V. V., and O. N. Volynets (1995), Kizimen volcano (Kamchatka) - future Mt. St.Helens?, *J. Volcanol. Geotherm. Res., 65,* 205–226.

Meniailov, A. A. (1955), Shiveluch volcano - geological structure, composition of products and eruptions. *Transactions of the Laboratory of Volcanology, USSR Academy of Sciences, 9*, 265 pp. (in Russian).

Park, J., Levin, V., Lees, J., Peyton, V., Gordeev, E., and A. Ozerov (2002), A Dangling Slab, Amplified Arc Volcanism, Mantle Flow and Seismic Anisotropy in the Kamchatka Plate Corner. In: Stein S. and Freymueller J. T. (Eds.) *Plate Boundary Zones. Geodynamics Series, 30*, DOI: 10/1029/030GD18

Pevzner, M. M., Ponomareva, V. V., and I. V. Melekestsev (1998), Chernyi Yar - reference section of the Holocene ash markers at the northeastern coast of Kamchatka, *Volcanol. and Seismol*., *19*(4), 389–406.

Pevzner, M. M., Ponomareva, V. V., and L. D. Sulerzhitsky (2006), Holocene soil-pyroclastic successions of the Central Kamchatka depression: ages, structure, depositional features, *Volcanol. and Seismol*., 1, 24–38 (in Russian).

Peyton, V., Levin, V., Park, J., Brandon, M., Lees, J., Gordeev, E. and A. Ozerov (2001), Mantle flow at a slab edge: Seismic anisotropy in the Kamchatka Region, *Geophysical Research Letters*, *28*(2), 379–382.

Ponomareva, V. V., Pevzner, M. M., and I. V. Melekestsev (1998), Large debris avalanches and associated eruptions in the Holocene eruptive history of Shiveluch Volcano, Kamchatka, Russia, *Bull. of Volcanol.*, *59*, 490–505.

Ponomareva, V. V., Melekestsev, I. V., and O. V. Dirksen (2006), Sector collapses and large landslides on late Pleistocene-Holocene volcanoes in Kamchatka, Russia, *J. Volcanol. Geotherm. Res., 158*, 117–138.

Stuiver, M., Reimer, P.J., and Reimer, R.W. (2005), CALIB 5.0 ^{14}C age calibration program, www.calib.org

Volynets, O. N. (1979), Heterotaxitic lavas and pumices on the problem of magma mixing . In: Sobolev, V. S. (Ed.) , *Problems of Deep Magmatism*, pp. 181–197, Nauka Press, Moscow (in Russian).

Volynets, O. N. (1994), Geochemical Types, Petrology, and Genesis of Late Cenozoic Volcanic Rocks from the Kurile-Kamchatka Island-arc System, *International Geology Review*, *36*, 373–405.

Volynets, O. N., Ponomareva, V. V., and A. D. Babansky (1997), Magnesian basalts of Shiveluch andesite volcano, Kamchatka, *Petrology*, *5*(2), 183–196.

Volynets, O. N., Melekestsev, I. V., Ponomareva, V. V., and J. M. Yogodzinski (1999), Kharchinsky and Zarechnyi volcanoes, unique centers of Late Pleistocene magnesian basalts in Kamchatka: Composition of erupted rocks, *Volcanol. and Seismol., 21*(1), 45–66.

Volynets, O. N., Babanskii A. D., and Yu. V. Gol'tsman (2000), Variations in Isotopic and Trace-Element Composition of Lavas from Volcanoes of the Northern Group, Kamchatka, in Relation to Specific Features of Subduction, *Geochemistry International*, *38*, 1067–1083.

Yogodzinksi, G. M., Lees, J. M., Churikova, T. G., Dorendorf, F., Woerner, G., and O. N. Volynets (2001), Geochemical evidence for the melting of subducting oceanic lithosphere at plate edges, *Nature*, *409*, 500–504.

Zharinov, N. A., Bogoyavlenskaya, G. E., Khubunaya, S. A., and Yu. V. Demyanchuk (1995), A new eruption cycle of Shiveluch volcano, 1980–1993, *Volcanol. and Seismol., 17*, 21–30.

Vera Ponomareva, Institute of Volcanology and Seismology, Petropavlovsk-Kamchatsky, Russia

Philip Kyle, Department of Earth and Environmental Science, New Mexico Institute of Mining and Technology, Socorro, New Mexico, USA

Maria Pevzner and Leopold Sulerzhitsky, Geological Institute, Moscow, Russia

Melanie Hartman, Department of Earth and Environmental Science, New Mexico Institute of Mining and Technology, Socorro, New Mexico, USA

Periodicities in the Dynamics of Eruptions of Klyuchevskoi Volcano, Kamchatka

A. Yu. Ozerov, P. P. Firstov, and V. A. Gavrilov

Institute for Volcanology and Seismology, Russian Academy of Sciences,
Petropavlovsk-Kamchatsky, Russia

Detailed studies of volcanic tremor envelopes with frequencies ranging from $5.5 \cdot 10^{-6}$ to $2.5 \cdot 10^{-2}$ Hz (50 hrs - 40 sec), recorded during the Klyuchevskoi volcano eruptions of 1983 and 1984, revealed five major frequencies: $1.1 \cdot 10^{-2}$ Hz (T_1 = 1 min 34 sec), $2.5 \cdot 10^{-3}$ Hz (T_2 = 6 min 10 sec), $4.2 \cdot 10^{-4}$ Hz (T_3 = 40 min), $5.1 \cdot 10^{-5}$ Hz (T_4 = 5 hrs 30 min), $7.7 \cdot 10^{-6}$ Hz (T_5 = 36 hrs), as well as superpositions of their harmonics. In the 1993 eruption, fluctuations in the volcanic tremor envelopes have frequencies of T_I = 2 hrs 48 min and T_{II} = 6 hrs 12 min, which correspond to periodicities in the dynamics of eruptions identified by visual observations since 1932. The distribution of peak amplitudes has been found to vary in relation to eruption intensity—increasing eruption strength correlates with an increase in the amplitude of low frequency peaks, and vice versa. It is concluded that volcanic tremor allows monitoring of eruption dynamics. Possible reasons for the occurrence of periodicities are discussed, but a comprehensive model for this phenomenon has not yet been developed.

1. INTRODUCTION

A basic task of volcanology is the study of the dynamic characteristics of eruptions. Such a study allows identifying major peculiarities of eruptive processes and understanding the basic functioning patterns of active magmatic systems.

Detailed studies were conducted at one of the most active volcanoes in the world—Klyuchevskoi volcano in Kamchatka, Russia, a large basaltic stratovolcano with a height of sea level of 4,822 m. Seismic data indicate that the volcano's feeding system originates in the upper mantle and reaches the surface in the form of a vertical conduit. No large inhomogeneities, which might be interpreted as magmatic chambers within the feeding system, have been discovered. Klyuchevskoi eruptions are characterized by isolated explosions, continuous outburst of incandescent magmatic material, and relatively liquid lava flows (Figure 1). Data on the structure of the feeding system of the Klyuchevskoi volcano, on characteristics of its eruptive activity reported by previous investigators, and our long-term studies are reviewed by *Ozerov et. al.,* [1997].

Compositions of all varieties of the volcano's eruption products fall within the common evolutionary calc-alkaline trend of basalts [*Ozerov,* 2000]. High-aluminous (4.5–6 % MgO) and aluminous (6–8 % MgO) basalts predominate within the eruptive edifice; magnesium (8–10 % MgO) and high-magnesium (10–12 % MgO) basalts are subordinate and occur as isolated lava flows and pyroclastic deposits of flank eruptions.

Two terms, "intensity" and "periodicity", of eruption are used in the present paper. These words have not been strictly defined in the volcanological literature. Without any claims to universality, the authors use these terms as follows: intensity of eruption is a descriptive characteristic that is in practice based upon one or more eruption parameters, such as height of bomb or ash ejection, frequency of explosions, size

Volcanism and Subduction: The Kamchatka Region
Geophysical Monograph Series 172

10.1029/172GM20

Figure 1. Fire fountains at the Klyuchevskoi volcano summit crater, 1984. Crater diameter 750 m. Bomb ejection height 200 m. Photo by A. Yu. Ozerov.

of ejecta, dimension of eruptive cloud, length of ash plumes, etc. Such characteristics as seismicity (volcanic tremor, volcanic earthquakes) and emission of acoustic energy can also be indicators of the eruption intensity. Thus, the term “intensity of eruption” is used as a parameter, whose pure physical meaning has not yet been determined. Moreover, its meaning can be identified only after developing a physical model for the eruption. In turn, creation of such a model is impossible without searching and systematizing eruption parameters that might allow the physical understanding of the eruptive process. Discovering and describing patterns in eruption parameters is the point of the present paper.

The term “periodicity” in modern volcanological papers can be applied to at least three types of phenomena of completely different nature, intensity and time scale:

1. Periodical recurrence of eruptions at the same volcano (regular successive recurrence of intra-eruptive and eruptive phases). In this case, the period consists of the eruption phase and the dwell phase, their regular recurrence giving the periodicity itself. A period can last from a few months to hundreds or thousands of years. To single out this periodicity, geological and tephrochronological data concerning eruptive events are generally used, as well as statistical treatment of historical information of the volcano behavior.

Examples of such periodicities occurred during the 1986 26–27 day fire fountain episodes at Kilauea volcano, Hawaii [*Tilling et al.,* 1987] and during the 2003–2005 half-year episodes of andesite eruptions at Bezymianny volcano in Kamchatka (as observed by the authors). A possible reason for regular recurrence of events at volcanoes with viscous magmas was discussed by *Melnik and Sparks,* 1999; *Melnik, 2000; Barmin et al., 2002*.

2. Periodicity manifesting itself in the course of a single eruptive period of the volcano. For basalt volcanoes, it can be a succession of single explosions (the period consists of an explosion phase and a dwell phase between the explosions), as well as by bomb ejection (the period consists of an intensive fusillade and relative quiet) and by ash emissions (the period combines intervals of tephra production and relative quiet). For andesite volcanoes, periodicity may be present

in the dynamics of an extrusive dome (period consists of a growth phase accompanied by explosions and/or pyroclastic flows, and a phase of relative quiet). Stable periodicity can be observed with the period lasting for minutes, hours, a few days, or more. Such periodicity can best be revealed as the result of continuous observations, and is rather well determined using seismic methods. This type of periodicity does not always occur in the course of an eruption.

At Klyuchevskoi volcano, periodicity of 6–7 hours was first identified in 1932 during the operation of the Tuila flank breakout [*Novograblenov,* 1933], as well as a period of 5 minutes in the summit eruption dynamics [*Troitsky,* 1937]. Periodicity was also reported at Kilauea, Hawaii, the 1959, 1969–72 and 1983–86 eruptions, where rhythmically repeating fountaining cycles were observed lasting from several tens of minutes to a few hours [*Swanson et al.,* 1979; *Koyanagi et al.,* 1987; *Wolfe et al.,* 1987]. During the 1975 Great Tolbachik Fissure Eruption (Kamchatka), a period of 2–3 hours was observed [*Gorelchik et al.,* 1978]. The 1989, 1999 and 2000 eruptions at Etna, Italy, showed periods lasting from an hour to a few hours [*Delfa et al.,* 2001; *Privitera et al.,* 2003]. In the course of the 1991 eruption of Avachinsky volcano (Kamchatka), a 6-hour periodicity was observed (authors' data). The above observations refer to basaltic volcanism; however periodicities lasting for hours or longer occur at andesite volcanoes also. During 1990 eruption of Redoubt volcano (Alaska), two activity intervals were determined, in which dome failure episodes occurred in 4.5 and 7.8 days [*Page et al.,* 1994]. At Soufriere Hills volcano, Montserrat in 1997, periodicities from 8 to 18 hours were determined [*Voight et al.,* 1998; *Druitt et al.,* 2002].

3. Periodicity of single explosions the same eruption episode, consisting of hundreds to thousands of similar explosions. Dwell intervals between the explosions are commonly characterized by a total absence of activity in the crater and, as a rule, last much longer (3–30 minutes) than the explosions themselves.

Explosions proper, presenting the supply of magmatic matter onto the surface, can have several patterns in their development. Some of them fade monotonously and quickly, in 10–15 seconds. In the course of other, more durable venting events (20–40 seconds, rarely up to one minute and more), modulations might sometimes appear in the acoustic noise intensity and visible volume of the emitting gas with typical period of about 1 second. These fluctuations determine the third type of periodicities in the eruptive activity. Series (pulse groups) are typically observed consisting of 10–20 one second periods. The following pattern occurs: explosion (3–5 seconds), some weakening (10–20 seconds) followed by pulsing (10–25 seconds). Such periodicity can be qualitatively fixed in the course of the regime observation; better, it can be recorded by seismograms, but best and most reliable, is the acoustic record. Periodicities of this kind are typical for andesite volcanism.

This type of periodicities was first mentioned by *Tokarev and Firstov* [1967] *and Farberov et al.* [1983] in considering eruptions of Karymsky volcano. *Benoit and McNutt* [1997] identified this periodicity within the Arsenal Volcano seismic signal and named the process "chugging". The process was studied in detail in the course of joint Russian-American work at the Karymsky volcano during 1996–1999, and by American researchers at the San-Guy volcano eruption [*Lees et al., 1997; Johnson and Lees,* 1999]. A possible mechanism for this short-period process has been described in the paper by *Ozerov et al.* [2003].

In the present paper, the second (minute to hour) type of periodicity is considered for single explosions and bomb ejection in the dynamics of the Klyuchevskoi basalt volcano eruption.

2. OBSERVATIONS AND ANALYSIS

Investigation of the Klyuchevskoi volcano eruptive process was conducted on three parameters: analysis of historical data on eruption periodicities, detailed visual observations of eruption dynamics, and analysis of seismological data obtained during the eruptions. These volcanological-geophysical surveys made it possible to distinguish periodicities at various levels.

Since 1932, volcanologists have reported periodicities of minutes, hours and multi-hours in the eruptions of the Klyuchevskoi volcano through visual observations of bombfall, lava outburst and steam-gas emissions. Systematization and analysis of these data identified five major groups of periodicities (Figure 2): 1–22 min, 28–55 min, 1.5–7 hrs, 12 hrs and 24 hrs [*Ozerov and Konov,* 1988; *Konov and Ozerov,* 1988]. However, visual observations over the course of the eruptions are quite subjective and desultory in character and not always suitable for statistical treatment.

Development of geophysical methods for the studies of volcanic processes allowed continuous surveys of different geophysical fields in the course of the eruption. One of the most striking manifestations of eruption is volcanic tremor [*Tokarev,* 1982; *Koyanagi at al.*, 1987; *Chouet at al.,* 1994; *Julian*, 1994; *Neuberg,* 2000, *Chouet at al.,* 2003]. Monitoring of volcanic tremor is a remote method allowing the study of eruption dynamics, and, in some cases, even the estimation of volume of erupted material [*Tokarev,* 1981; *Gordeev at al.,* 1985].

We carried out studies of volcanic tremor (0.8 – 1.0 Hz) continuously recorded during the eruptions of 1983, 1984

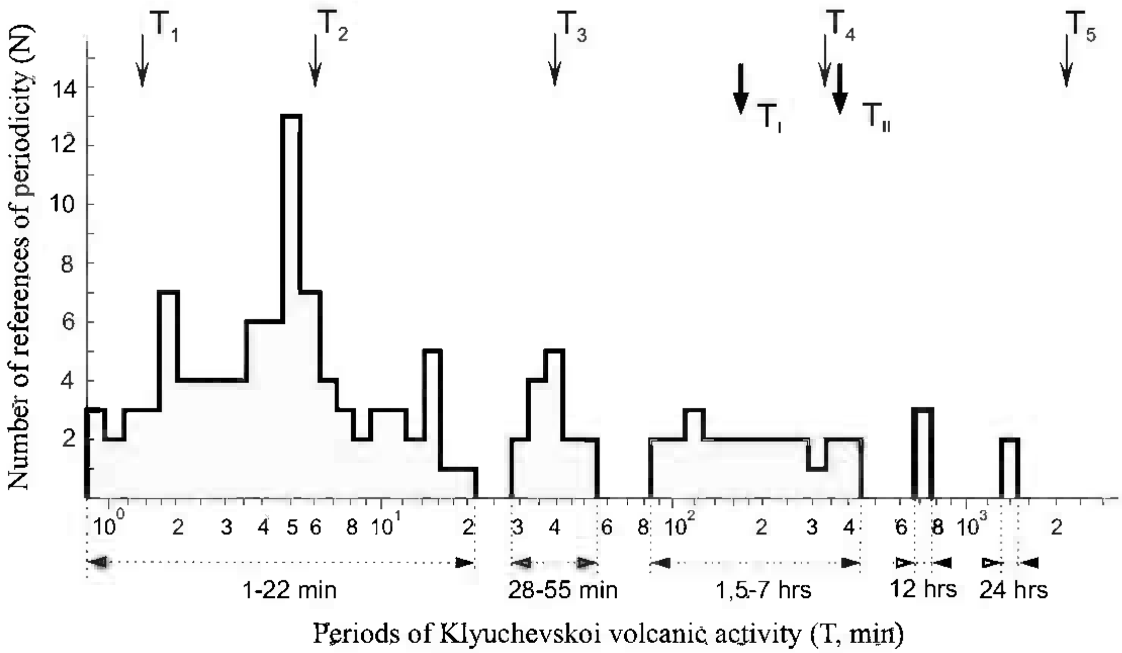

Figure 2. Histogram of observed periodicities in the eruptive activity of the Klyuchevskoi volcano from 1932 to 1978 – by visual data, and by seismic data (1983–84 and 1993). Abscissa axis in the logarithmic scale – periods of volcanic activity in minutes (T, min); ordinate axis – number of occurrences of individual temporal periodicity (N). Vertical arrows indicate basic periodicities determined by seismic data: thin arrows – for the eruptions of 1983–84 (T_1–T_5), bold ones – for those of 1993 (T_I and T_{II}).

and 1993. The data, obtained at the regional seismic sites (using electrodynamic seismometer SM-2 with $T_0 = 1.2$ sec) located around the Klyuchevskoi volcano. These were the "Apokhonchich" and "Podkova" stations, placed 14.8 and 14.6 km away from the crater, respectively. For the 1983 and 1984 eruptions, on the vertical channel, the maximum amplitude of volcanic tremor (displacement_amplitude, measured in microns - μm) was measured as a basic value. A series of the enveloping maximum tremor amplitudes with sampling ranging from 10 seconds to 15 minutes were developed, with the length of the series ranging from 240 to 6624 points. The subsequent statistical processing was based upon these data. Methods including the calculation of the autocorrelation functions (autocorrelograms) and functions of intercorrelation of two random processes (crosscorrelograms) were used for determining the periodicities. Spectral estimations were made using the method of maximum entropy.

These techniques identified periodicities within the frequency range from $5.6 \cdot 10^{-6}$ Hz (T_{max} – 50 hours) to $2.5 \cdot 10^{-2}$ Hz (T_{min} – 40 sec) [*Ozerov and Konov,* 1988; *Konov and Ozerov,* 1988]. In order to test the hypothesis of the influence of lunar and solar tides on eruption dynamics, coefficients have been calculated for correlation between the series of seismological data for three time intervals (June 19 – July 01, 1984; July 09–16, 1984; and August 01–12, 1984) and corresponding series of corrections for tidal gravity variation (Δg values measured in milligals were sampled from the diagram once an hour).

During the 1993 eruption, the Podkova seismic station recorded the rate of ground oscillations in μm/sec. The level logger registered the mean-square value of the ground velocity for volcanic tremor (vertical component) with the time constant of 3200 seconds. This value was used as the intensity of tremor. For the intervals where periodicity occurred, spectral power density of the volcanic tremor intensity in $(\mu m/s)^2/(1/min)$ was constructed. This method allows recognition of the periods of 15 minutes and more.

It should be noted that the present research was not aimed at studying the carrier frequency of the Klyuchevskoi volcano tremor (0.8 – 1.0 Hz), considered by *Tokarev* [1966]; *Gordeev at al.* [1986]. The present work is based on investigating the volcanic tremor envelope, that is, superimposed on the volcanic tremor amplitude-modulated oscillations with a wide range of periods (from 40 sec to 50 hrs), due to melt movement within the volcano feeding system and magma fragmentation in the effluent channel.

3. RESULTS

Volcanic tremor in 1983–1984 was studied in the most detail. In many cases, distinct periodicities can be traced on the initial rows of the charts. On Figure 3, pulsations of tremor amplitude with periods of 1 minute 34 seconds (a) and 5 hours 30 minutes (b) are clearly seen. However, such an obvious pattern is rare and a thorough study of periods is possible only through the application of a complex statistical processing. Analysis of these results made it possible to single out a basic series of 47 distinct spectral peaks (frequencies), with a number that remained stable for 19 months. The observed changes of the spectral composition of the enveloping volcanic tremor in time, as well as sharp excitation of these frequencies, identified a set of five major frequencies (corresponding periods are given in brackets): $f_1 = 1.1 \cdot 10^{-2}$ Hz (T_1 = 1 min 34 sec); $f_2 = 2.5 \cdot 10^{-3}$ Hz (T_2 = 6 min 10 sec); $f_3 = 4.2 \cdot 10^{-4}$ Hz (T_3 = 40 min); $f_4 = 5.1 \cdot 10^{-5}$ Hz (T_4 = 5 hrs 30 min); $f_5 = 7.7 \cdot 10^{-6}$ Hz (T_5 = 36 hrs) (Figure 4). Though the set of spectral peaks of the enveloping tremor remained constant during the 1983–1984

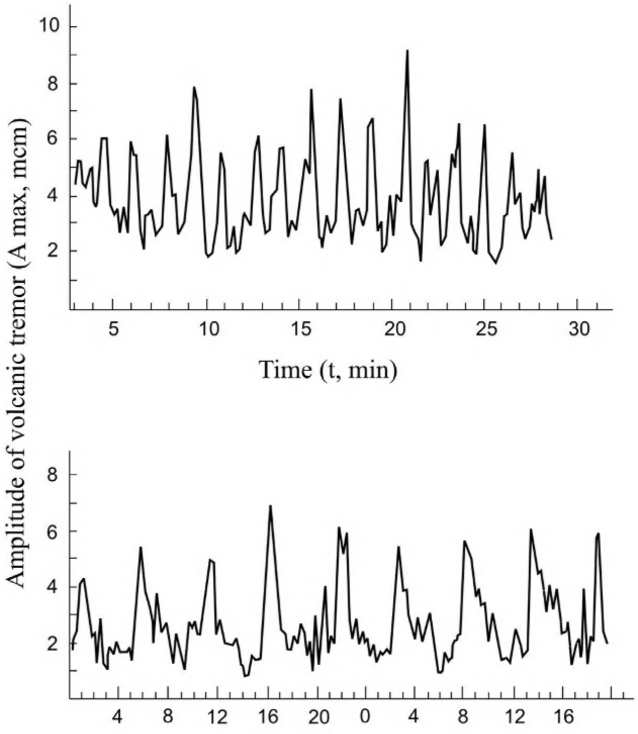

Figure 3. Volcanic tremor amplitude for time intervals: a. – from 03 hours 03 minutes to 03 hours 29 minutes of July 23rd, 1984 (time step is 10 seconds); b. - 00 hours of August 14th, 1984 (time step is 15 minutes). X-line – time scale, in fig. (a) – minutes (t, min) and in fig. (b) – hours (t, hour). Y-line – maximum amplitude of volcanic tremor in microns (A max).

eruption, their amplitudes varied depending upon the variation of the eruption intensity. When the intensity of the eruption increased, a sharp increase of the amplitude of low frequency peaks took place.

Cross-correlation analysis of corrections series for tidal gravity variations and respective series of values of volcanic tremor envelope has revealed ~12 hrs and ~ 24 hrs periodicities in the 1984 tremor component (Figure 5). More precise (up to minutes) definition of the periods mentioned is difficult given the method we use. However, comparison of period duration, forms and variation dynamics in cross-correlograms we obtained with those reported by *Melchior* [1966] is consistent with the assumption that they are determined by lunar-solar tidal process.

Studies of volcanic tremor during the 1993 eruption showed the following fluctuation (Figure 6): On June 28, about 17:00 UT, when volcanic tremor (I) reaches an intensity of 0.7 μm/s, a clear periodic constituent appears, which remained until July 2, 3.5 days later; the amplitude excursion of tremor intensity was 0.2–0.3 μm/s. In the power density spectrum of volcanic tremor intensity – S(ω) – calculated for the given time interval, the spectral maximum has a period of 2 hrs 48 min. Later, a smooth increase of tremor intensity is observed. On July 10, at a value of 3 μm/s, abrupt deep fluctuations of tremor intensity amplitude occurred, which returned to the periodic oscillations of tremor intensity. This mode remained for 9.5 days, until 12:00 UT on July 20; the average level of tremor intensity was 3–4 μm/s, with an amplitude excursion of 3.5–6 μm/s. For this interval, a spectral power density maximum of tremor intensity occurs at 6 hrs 12 min. On July 21, about 21:00 UT, the intensity of volcanic tremor starts gradually increasing, and by July 22 it reaches 7.5–8 μm/s, while the periodic oscillations of the intensity disappear. Thus, fluctuations with periods of 2 hrs 48 min and 6 hrs 12 min are clearly distinguished in the dynamics of the 1993 eruption (see Figure 6 b and c). The data suggest that with increasing intensity of the eruption, periods that are more durable become active.

Correlation of the results of volcanic tremor studies for 1983–1984 with the periodicities of previous years (1932–1978) determined by visual observations, shows that four major periods ($T_1 - T_4$) agree well with four groups of periods singled out in the historical surveys. However, periodicity of 36 h (T_5) has not been reported for any the past eruptions, which might be due to the fact that such a durable periodicity is difficult to document by visual observations. Periods described in the 1993 eruption correspond well to the third group of periodicities singled out from visual data. Results also reveal that ~ 12- and ~ 24-h periodicities, conditioned by distorting tidal process, have been found when analyzing historical eruptions of 1932–1978 (Figure 2).

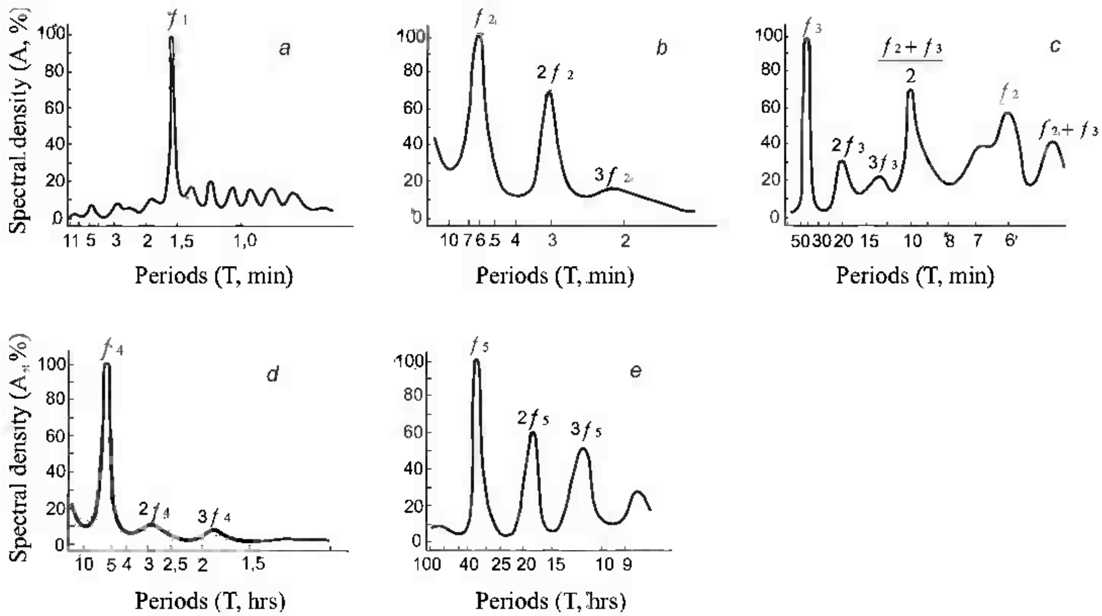

Figure 4. Spectra of the volcanic tremor envelope for various time intervals in 1984: 3-4 a.m., June 23 (a.), 1-2 a.m., August 23 (b.), 3-7 p.m., June 25 (c.), midnight, August 14 – 1 a.m., August 16 (d.), and June 19 – July 2 (e.). X-line – T – periods, in minutes (a., b. and c.) and hours (d. and e.). Y-line - spectral density in % (A, %). a.-e.: basic frequencies (f_1 – f_5) and corresponding periods (T_1 - T_5). $f_1 = 1.1{\cdot}10^{-2}$ Hz (T_1 = 1 min 34 sec); $f_2 = 2.5{\cdot}10^{-3}$ Hz (T_2 = 6 min 10 sec); $f_3 = 4.2{\cdot}10^{-4}$ Hz (T_3 = 40 min); $f_4 = 5.1{\cdot}10^{-5}$ Hz (T_4 = 5 hrs 30 min); $f_5 = 7.7{\cdot}10^{-6}$ Hz (T_5 = 36 hrs). b.-e.: first and second harmonics of basic frequencies (b. – $2f_2$ and $3f_2$, c. – $2f_3$ and $3f_3$, d. – $2f_4$ and $3f_4$, e. – $2f_5$ and $3f_5$); c.: superpositions of basic frequencies f_2 and f_3 - (f_2+f_3) and (f_2+f_3)/2).

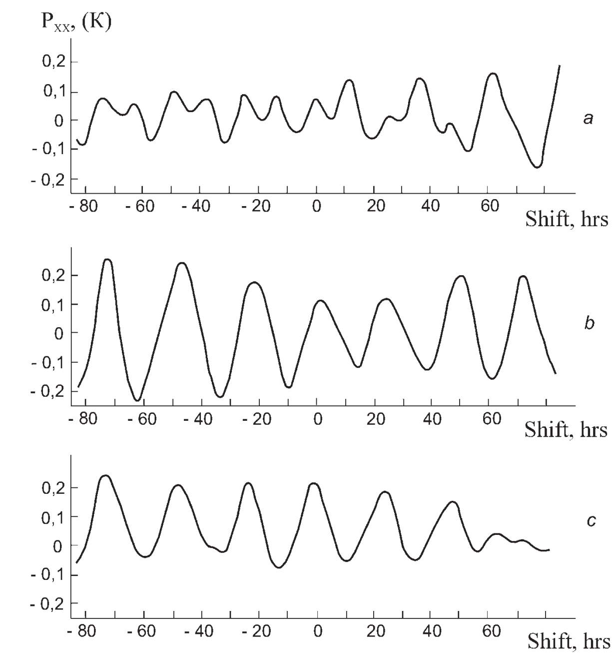

Figure 5. Cross-correlograms of corrections series for tidal gravity variation and corresponding series of tremor envelope values for the intervals of: a. – 1 pm 19.06.–1 am 01.07.1984; b. – 2 am 09.07. – 1 am 16.07.1984; c. – 2 am 01.08. – 1 am 12.08.1984

4. DISCUSSION

Periodicities in the eruptive activity of the Klyuchevskoi volcano may be accounted for by the existence of natural oscillations of magma (viscoelastic fluid) in the output conduit and magmatic chamber; and/or by resonance oscillations at specific frequencies active under certain conditions. Values of these frequencies are evidently controlled by the geometry of resonators comprising the volcanic system, as well as by physical characteristics of magma and enclosing rocks. In discussing the possible reasons of the occurrence of these periodicities, preference should be given to the processes of degassing in the upper part of the magmatic column. Degassing depends upon pressure variations. The latter may be caused either by magma oscillations in the feeding system of the volcano (system of connected resonators), or by hydrodynamic waves spreading through the magmatic column and formed by resonator fluctuations.

Droznin [1980] and *Slezin* [1980] report that the diversity of types of volcanic eruptions is well accounted for by the flow regime of a two-phase mixture: melt and gas. Another explanation for periodicities in volcano eruption dynamics may be spontaneous onset of auto-oscillations during the migration of the two-phase mixture along the magmatic conduit. Auto-oscillation regimes depending upon the magma discharge rate may occur on different levels of the supply conduit.

Interesting models explaining the abrupt periodical intensifications in the eruption dynamics of Kilauea and Etna volcanoes have been developed. *Vergniolle and Jaupart* [1986, 1990] assumed that at Kilauea the mechanism of this phenomenon was conditioned by different regimes of two-phase flows, and they created an attractive and original experimental installation. For Etna volcano, Italian researchers developed models involving a near-surface magmatic reservoir. *Delfa et al.* [2001] considered intensification and weakening of fountaining to be due to reservoir exhaustion and refilling, while *Privitera et al.* [2003] explained them by redistribution of the gas phase within the reservoir. An indispensable condition in the above models is the presence of a near-surface magmatic chamber, thus involving a structural barrier modifying the parameters of ascending two-phase magmatic mixture.

These models are inapplicable for the Klyuchevskoi volcano, since there is apparently no near-surface chamber in its feeding system [*Utnasin et al.,* 1976; *Anosov et al.,* 1978; *Fedotov et al.,* 1988; *Ozerov et al.,* 1997; *Gorelchik et al.,* 2004]. This is also evidenced by new tomographic imaging [*Lees et al.,* 2006 (in the present volume)]. It is important that several groups of periodicities (Fig. 2, 3, 4, 6) have been distinguished in the Klyuchevskoi eruption dynamics, which differ in orders of magnitude – from the first minutes to a few tens of hours. Accordingly, following the models suggested by *Vergniolle and Jaupart* [1990], *Delfa et al.* [2001] and *Privitera et al.* [2003], one would have to postulate several chambers greatly differing in size within the feeding systems of the Klyuchevskoi volcano. Therefore, however tempting it might be, to explain the existing number of periodicities by means of structural barriers (magmatic chambers) of various orders of magnitude, it is inconsistent with present knowledge of the Klyuchevskoi volcano structure.

Studies of the stability of Klyuchevskoi magma feeding system under external effects have revealed that eruption dynamics is influenced by lunar-solar tidal deforming processes. Tidal forces may affect a reservoir filled with magma, compressing and stretching it. As a result, magma in the output conduit would oscillate with tidal frequencies corresponding to the periods of 12 and 24 hours. A model for such phenomena has been developed in *Shimozuru* [1975].

Interpretations suggested thus far do not cover all the possible patterns controlling periodicities at Klyuchevskoi volcano. However, having succeeded in modeling short (~1 s)

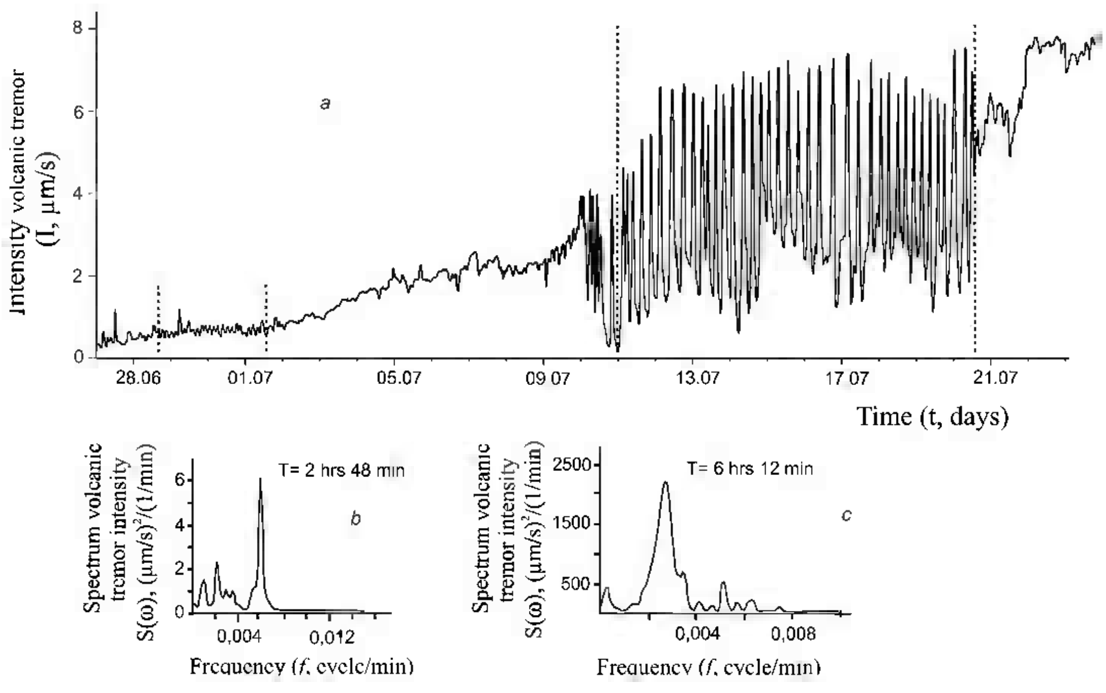

Figure 6. Diagram of changes of the volcanic tremor intensity for the interval from June 27 until July 24, 1993 (a.), and power density spectra of the volcanic tremor intensity (b. and c.) for two time intervals depicted in the (a.) diagram by vertical dotted lines: 7 p.m., June 28 – 3 a.m., July 2 (b.), and midnight, July 11 – 2 p.m., July 20 (c.). In fig. (a): X-line – time, measured in days (t, days), Y-line – Intensity of volcanic tremor (I, μm/s). In fig. (b) and (c): X-line – frequency measured in the cycles per minute (*f*, cycle/min); Y-line – spectral density power of volcanic tremor intensity - S(ω), (μm/s)^2/(1/min).

periodicities in the eruptive process of Karymsky volcano [*Ozerov et al.,* 2003], we continue our studies of the periodicities' at Klyuchevskoi in order to find the causes of this phenomenon. Results obtained will contribute to understanding the dynamics of magmatic systems. Knowledge of patterns of changes in eruption intensity as recorded in seismic data may contribute to better evaluation of risks to aviation and local settlements during an eruption.

Acknowledgments. Authors acknowledge Evgenii I. Gordeev, Jaroslav D. Muraviov, Alexander S. Konov, Andrei I. Farberov, Gennadii I. Anosov, Valentina I. Gorelchik, Aleksandr S. Storcheus, John C. Eichelberger, Maxim G. Gavrilenko, Iskander R. Abubakirov, Olga S. Chubarova, Olga I. Diachkova, Annie F. Sashenkova for their contribution to the research. The authors would like to thank Dr. Tom Miller for his great assistance in editing and preparing the manuscript for publication. The present research is supported by the grants of RFBR № 06-05-64590-a, 07-05-10052-k, 05-05-64730-a and Grants of FEB RAS 06-III-A-08-331, 06-III-B-08-368, 07-III-Д-08-095.

REFERENCES

Anosov, G. I., S. K. Bikkenina, and A. A. Popov (1978), *Deep seismic sounding of Kamchatka*, Nauka, Moscow, 129 p.

Barmin, A. A., O. Melnik, and R. S. J. Sparks (2002), Periodic behavior in lava dome eruptions, *Earth and Planetary Science Letters,* 199, 173–184.

Benoit, J. P., and S. R. McNutt (1997), New constraints on source of volcanic tremor at Arsenal Volcano, Costa Rica, using broadband seismic data, *Geophys. Res. Lett.,* 24, 449–452.

Chouet B., P. Dawson, T. Ohminato, M. Martini, G. Saccorotti, F. Giudicepietro, G. De Luca, G. Milana, and R. Scarpa (2003), Source mechanisms of explosions at Stromboli Volcano, Italy, determined from moment-tensor inversions of very-long-period data, *J. Geophys. Res.,* 108 (B1), 2019, doi:10.1029/2002 JB001919.

Chouet, B. A., R. A. Page, C. D. Stephens, J. C. Lahr, and J. A. Power (1994), Precursory swarms of long-period events at Redoubt Volcano (1989–1990), Alaska: Their origin and use as a forecasting tool, *J. Volcanol. Geotherm. Res.,* 62, 95–135.

Delfa, S. La., G. Patane, R. Clocchiatti, J. L. Joron, and J. C. Tanguy (2001), Activity of Mount Etna preceding the February 1999 fissure eruption: inferred mechanism from seismological and geochemical data, *J. Volcanol. Geotherm. Res.*, 105, 121–139.

Druitt, T. H., S. R. Young, B. Bartie, C. Bonadonna, E. S. Calder, A. B. Clarke, P. D. Cole, C. L. Harford, R. A. Herd, R. Luckett, G. Ryan, and B. Voight (2002), Episodes of cyclic Vulcanian explosive activity with fountain collapse at Soufriere Hills Volcano, Montserrat, *Druitt, T.H., Kokelaar, B.P. (eds), The Eruption of Soufriere Hills Volcano, Montserrat, from 1995 to 1999. Geological Society, London, Memoirs,* 21, 281–306.

Droznin, V. A. (1980), *Physical model for the volcanic process*, Nauka, Moscow, 91 p.

Farberov, A. I., A. B. Storcheus, and E. S. Pribulov (1983), Studies of weak seismicity of Karymsky volcano, August 1978, *Volcanology and Seismology*, 3, 78–89.

Fedotov, S.A., N.A. Zharinov, and V.I. Gorelchik (1988), Deformation and earthquakes of Klyuchevskoy volcano, *Volcanology and Seismology*, 2, 3–42.

Gordeev, E. I. (1985), The Main Properties of Volcanic Tremor of Some Kamchatkan Volcanoes, *Volcanology and Seismology,* 3, 68–77.

Gordeev, E. I., Yu. Yu. Mel'nikov, V. I. Sinitsin, and V. N. Chebrov (1986), Volcanic tremor of the Klyuchevskoy volcano (eruption of the apical crater in 1984), *Volcanology and Seismology*, 5, 39–53.

Gorelchik V. I., V. T. Garbuzova, and A.V. Storcheus (2004), Deep-seated processes beneath Klyuchevskoi volcano as inferred from seismological date, *Volcanology and Seismology*, 6, 21–34.

Gorelchik V. I., V. V. Stepanov, and V. P. Khanzutin (1978), Volcanic tremor at the Great Tolbachik Fissure Eruption in 1975 // In the book *"Geological and geophysical data on the Great Tolbachik Fissure Eruption in 1975–1976"*, Moscow, Nauka, 146–159.

Johnson, J. B., and J. M. Lees (1999), Plugs and Chugs - Strombolian activity at Karymsky, Russia, and Sangay, Ecuador, *J. Volc. Geotherm. Res., 101,* 67–82.

Julian, D. R. (1994), Volcanic tremor: Nonlinear excitation by fluid flow, *J. Geophys. Res,* 99, No B6, 11,859–11,877, June 10.

Konov, A. S. and A. Yu. Ozerov (1990), Klyuchevskoi eruptive activities and volcanic tremors: correlation of periodic events, *Volcanology and Seismology*, Vol. 10, No. 3, 360–385. (Translated from Russian—*Volcanology and Seismology*, 3, 21–38, 1988).

Koyanagi, R. Y., B. Chouet, and K. Aki (1987), Origin of volcanic tremor in Hawaii. 1. Data from the Hawaiian volcano observatory 1969–1985, *U.S. Geol. Surv. Prof. Pap.*, 1350, 1221–1257.

Lees J. M., N. Symons, O.S. Chubarova, V. I. Gorelchik, and A.Yu. Ozerov (2006), Tomographic Images of Klyuchevskoy Volcano P-wave Velocity, Submitted to AGU Monograph: *Volcanism and Tectonics of the Kamchatka Peninsula and Adjacent Arcs*, "in press".

Lees, J. M., A. Y. Ozerov, and E. I. Gordeev (1997), Quasi-periodic Eruptions on Karymsky Volcano, Kamchatka, 1996, *AGU Spring Meeting.* V22A-05.

Melchior, P. (1966), The Earth Tides, *Pergamon Press, Oxford-London-Edinburg-New-York-Paris-Frankfurt,* 445 p.

Melnik, O. (2000), Dynamics of two-phase conduit flow of high-viscosity gas-saturated magma: large variations of sustained explosive eruption intensity, *Bull. Volcanol.,* 62, 153–170.

Melnik, O. and R. S. J. Sparks (1999), Nonlinear dynamics of lava dome extrusion, *Nature,* 492, 4 November, 37–41.

Neuberg, J. (2000), External modulation of volcanic activity, *Geophys. J. Int.,* 142, 232–240.

Novograblenov, P. T. (1933), Lateral crater eruption at Klyuchevskoy volcano, *Proceedings State Geographic Society*, 52–54.

Ozerov, A. Y. (2000), The evolution of high-alumina basalts of the Klyuchevskoy volcano, Kamchatka, Russia, based on microprobe analyses of mineral inclusions, *J. Volcanol. Geotherm. Res.*, 95, 65–79.

Ozerov, A. Yu. and A. S. Konov (1988), Regularities the dynamics of the Klyuchevskoy volcano eruption, *Proceeding Kagoshima International Conference of Volcanoes*, Japan, 63–65.

Ozerov, A. Yu., A. A. Ariskin, Ph. Kyle, G. E. Bogoyavlenskaya, and S. F. Karpenko (1997), Petrological-geochemical model for genetic relationships between basaltic and andesitic magmatism of Klyuchevskoi and Bezimyannyi volcanoes, Kamchatka, *Petrology*, Vol. 5, № 6, 550–569. (Translated from Russian—*Petrologiya*, Vol. 5, No. 6, 614–635, 1997).

Ozerov, A. Yu., I. O. Ispolatov, and J. M. Lees (2003), Modeling Strombolian eruptions of Karymsky volcano, Kamchatka, Russia, *J. Volcanol. Geotherm. Res.*, 122, 265–280.

Page, R. A., J.C. Lahr, B.A.Chouet, J. A.Power, and C. D. Stephens (1994), Statistical forecasting of repetitious dome failures during the waning eruption of Redoubt Volcano, Alaska, February–April 1990, *J. Volcanol. Geotherm. Res.,* 62, 183–196.

Privitera, E., T. Sgroi, and S. Gresta (2003), Statistical analysis of intermittent volcanic tremor associated with the September 1989 summit explosive eruptions at Mount Etna, Sicily, *J. Volcanol. Geotherm. Res.*, 120, 235–247.

Shimozuru, D. (1975), Lava lake oscillations and the magma reservoir beneath a volcano, *Bull. Volcanologigue*, XXXIX – 4, 1–11.

Slezin, Yu. B. (1980), Interaction of particles in the permanent gas-pyroclastic flow in the volcanic channel, *Volcanology and Seismology*, 5, 40–47.

Swanson, D. A., D. A. Duffield, D. B. Jackson, and D. W. Peterson (1979), Chronological narrative of the 1969–1971 Mauna Ulu eruption of Kilauea volcano, Hawaii, *U.S. Geol. Surv. Prof. Pap.*, 1056, 1–55.

Tokarev, P. I. (1966), *Eruptions and seismic regime of the Klyuchevskoi group volcanoes*, Nauka, Moscow, 120 p.

Tokarev, P. I. (1981), Volcanic tremor, *Volcanology and Seismology*, 3, 55–72.

Tokarev, P. I. (1982), Volcanic Micro-Tremors, *Volcanology and Seismology,* 6, 56–78.

Tokarev, P. I. and P. P. Firstov (1967), Seismological studies of Karymsky volcano, *Bulluten' Vulkanol. Stanciy*, 43, 9–22.

Troitsky A. P. (1937) On the behavior of the Klyuchevskoy volcano crater in 1935, *Proceedings State Geographic Society,* vol. XIX, 6, 969–974.

Vergniolle, S. and C. Jaupart (1986), Separated two-phase flow and basaltic eruptions, *J. Geophys. Res.*, 91, 12842–12860.

Vergniolle, S., and C. Jaupart (1990), The dynamics of degassing at Kilauea volcano, Hawaii, *J. Geophys. Res.*, 95, 2793–2809.

Voight, B., R. P. Hoblitt, A. B. Clarke, A. B. Lockhart, A. D. Miller, L. Lynch, J. McMahon (1998), Remarkable cyclic ground deformation monitored in real-time on Montserrat, and its use in eruption forecasting, *Geophys. Res. Lett.,* 25, No 18, 3405–3408, September 15.

Wolfe, E. W., M. O. Garcia, D. B. Jackson, R. Y. Koyanagi, C. A. Neal, and A. T. Okamura (1987), The Pu‘u‘O‘o eruption of Kilauea volcano, episodes 1–20, January 3, 1983 to June 8, 1984, *U.S. Geol. Surv. Prof. Pap.*, 1350, 471–508.

Utnasin, V. K., A. I. Abdurakhmanov, G. I. Anosov, Yu.A. Budyansky, V.I. Fedorchenko, Ye.K. Markhinin, and S.T. Balesta (1976), Types of magma foci of island arc volcanoes and their study by the method of deep seismic sounding of Kamchatka, *Volcanoes and Tectonosphere*, Tokai University Press, 123–137.

A. Yu. Ozerov, P. P. Firstov and V. A. Gavrilov, Institute for Volcanology and Seismology, FED RAS, Piip blvd., 9, Petropavlovsk-Kamchatsky, 683006, Russia. (ozerov@ozerov.ru; first41@mail.ru; vgavr@kscnet.ru)

Tomographic Images of Klyuchevskoy Volcano P-Wave Velocity

Jonathan M. Lees[1], Neill Symons[2], Olga Chubarova[3], Valentina Gorelchik[3,4], and Alexei Ozerov[3]

Three-dimensional structural images of the P-wave velocity below the edifice of the great Klyuchevskoy group of volcanoes in central Kamchatka are derived via tomographic inversion. The structures show a distinct low velocity feature extending from around 20 km depth to 35 km depth, indicating evidence of magma ponding near the Moho discontinuity. The extensive low velocity feature represents, at least to some degree, the source of the large volume of magma currently erupting at the surface near the Klyuchevskoy group.

INTRODUCTION

Tomographic inversion for three-dimensional compressional wave velocity at volcanoes has been relatively routine since the early 1980's. Examples of three dimensional structure derived from seismic travel time inversion include Mount St. Helens [*Lees*, 1992], Mount Rainier [*Lees and Crosson*, 1990; *Moran et al.*, 1999], Kilauea[*Ellsworth and Koyangi*, 1977; *Haslinger et al.*, 2001; *Rowan and Clayton*, 1993; *Thurber*, 1984], Pinatubo [*Mori et al.*, 1996], Etna [*Aloisi et al.*, 2002], Unzen [*Ohmi and Lees*, 1995], Campei Flegrei [*Aster and Meyer*, 1988], Medicine Lake [*Evans and Zucca*, 1988], Vesuvius [*De Natale et al.*, 1998; *Zollo et al.*, 1998], Yellowstone [*Benz and Smith*, 1984; *Clawson et al.*, 1989; *Husen and Smith*, 2004; *Iyer et al.*, 1981; *Miller and Smith*, 1999; *Yuan and Dueker*, 2005], Mount Spurr, AK, [*Brown et al.*, 2004], Long Valley, CA, [*Dawson et al.*, 1990; *Dawson et al.*, 1987; *Hauksson*, 1988; *O'Doherty et al.*, 1997; *Peppin*, 1985; *Sanders*, 1993; *Sanders et al.*, 1995; *Sanders et al.*, 1994], as well as numerous others. In nearly all these cases low velocities were observed below the edifice of the volcanoes and they were interpreted as evidence for magma accumulation, sometimes called the magma plexus [*Benz et al.*, 1996]. In this paper we apply tomographic inversion methods to data collected on a regional network of seismic stations near Klyuchevskoy volcano, Kamchatka, Russia.

Klyuchevskoy volcano is one of the most active volcanoes in the Pacific Rim [*Fedotov and Masurenkov*, 1991]. Construction of most of the 4800 m tall edifice occurred over the past 7000 years (Figures 1 and 2). It has erupted numerous times in the recent past and, along with Bezymianny [*Gorshkov*, 1959] and Tolbachik [*Fedotov et al.*, 1979] volcanoes, represents possibly the most productive volcanic center of all subduction zones. On a larger scale it is important to note that Klyuchevskoy volcano and nearby related volcanic centers lie in the central Kamchatka depression off the axis of the coastal arc. Klyuchevskoy and Sheveluch are the northern most active volcanoes of the Kamchatka arc, which coincides with the collision of the western Aleutians and the Kamchatka Peninsula. Seismic and geochemical analyses have shown that the Klyuchevskoy-Sheveluch axis straddles the northern terminus of the subducting Kamchatka slab [*Lees et al.*, 2007; *Yogodzinski et al.*, 2001]. Furthermore, the subducting slab shallows noticeably at its northern terminus [*Lees et al.*, 2007]. According to current models, warm mantle material erodes the slab as it is pressed around the unconstrained slab edge, causing magmas north of Klyuchevskoy

[1] University of North Carolina, Chapel Hill
[2] Sandia National Laboratories
[3] Institute for Volcanology and Seismology Far-East Branch of the Russian Academy of Sciences, Petropavlovsk-Kamchatsky
[4] Deceased

Volcanism and Subduction: The Kamchatka Region
Geophysical Monograph Series 172

10.1029/172GM21

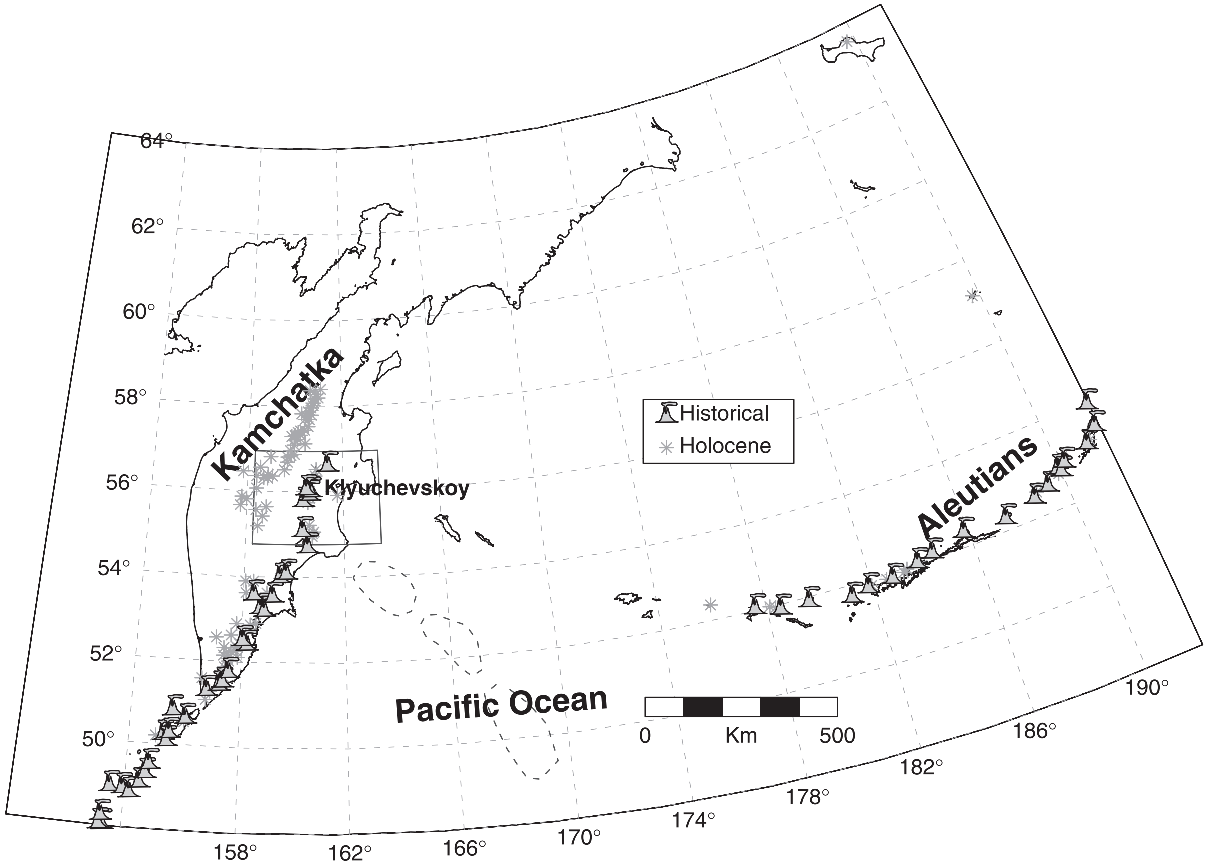

Figure 1. Map of the Kamchatka-Aleutian subduction zones showing the relationship of the target region of this study to volcanism on the subducting Pacific Plate. The Aleutians terminate near Kamchatka where the Bering Island represents the last land masses situated over the Bering faults. The target region for the tomographic inversion is the rectangular patch including the Klyuchevskoy group, extending from Kizimen in the south to Sheveluch in the north. The bounds of the tomographic inversion are limited by the station array and local earthquake event catalogue available for travel time inversion. Active arc volcanoes are represented by larger triangles and smaller ones are inactive

to have distinct geochemical signatures associated with slab melt [*Yogodzinski et al.*, 2001].

Given the large flux of magma at the surface of the Klyuchevskoy group (about 0.17 cubic km/year,) we expect to see a large accumulation of magma stored in the crust or upper mantle. Active source seismic data acquired along the coast of Kamchatka have been used in the past to suggest that there is nearly no signature of a large magma body immediately below Klyuchevskoy, although a small accumulation was postulated below Bezymianny Volcano [*Anosov et al.*, 1978; *Utnasin et al.*, 1976]. Petrologic and geochemical analysis of Klyuchevskoy volcanic material suggests that the Klyuchevskoy group has a typical calc-alkaline composition [*Kersting and Arculus*, 1995; *Ozerov*, 2000]. Ozerov et al. [1997] conclude that magma genesis at Klyuchevskoy occura between 150–60 km depth where high-magnesium basalts are formed. They further suggest that there is no evidence for significant magma accumulation above 20 km depth and that at least two narrow, separate conduit systems feed into the active Bezymianny and Klyuchevskoy volcanoes. In the 20–30 km range they infer the presence of two distinct diverging conduits where fractionation occurs. The model suggests that the physical divergence ultimately produces the geochemical differentiation observed in the surface products: most Klyuchevskoy magmas are basaltic, whereas those at Bezymianny are andesitic-dacitic. A large concentration of hypocenters is evident in this zone indicating either tectonic or magmatic activity at 20–30 km depth, although the patterns of seismicity do not show explicitly the diverging conduits proposed by Ozerov et al.[1997].

DATA

Data used in this study consisted of over 1444 well-located events extracted from the extensive catalogue in Petropavlovsk-Kamchatsky [*Gorelchik et al.*, 1990]. Data ranged from 1981–

1994 and were obtained from the KEMSD (Kamchatkan Experimental Methodological Seismological Department) and the IVGG (Institute of Volcanic Geology and Geochemistry). Events were recorded on paper records and picked by hand by the authors. P and S wave arrival times were determined at the observatory in Petropavlovsk and estimated errors were typically between .05 and .15 s. Hypocenters were located initially using a standard one-dimensional velocity model derived for the Klyuchevskoy region. Events were chosen only if they were well recorded at more than 5 stations and were deemed of high quality by the observers who performed the manual arrival time estimations. Typically, these earthquakes had root mean square residuals of 0.48 s (standard deviation 0.2 s), a median lateral location error of 1.5 km and a median gap of 124 degrees. (The large gap is due to the sparse network in operation during the 1980's and 1990's). Travel time arrivals (6461 P-wave and 9115 S-wave) were extracted, filtered for outlier high fluctuations and the data set was inverted for P-wave velocity.

INVERSION METHODOLOGY

The methods used in this study follow that of Symons and Crosson[1997]. It is based on finite difference calculations of travel times for forward modeling similar to that developed by Benz [1982]. The target region is divided into blocks 5 km to a side, varying in depth according to divisions of the layered model used for simple 1-dimensional event locations. Travel times are calculated using a finite difference method [*Hole*, 1992; *Vidale*, 1988] which provides a solution to the

Figure 2. Detailed topographic map of the target region inverted in this study. The Klyuchevskoy group is near the center of the inversion target region. Cross sections are plotted for later reference to vertical slices through the velocity perturbation results. The deep graben running from southwest to northeast through the target region is known as the central Kamchatka depression. The Klyuchevskoy group is located within the Central Kamchatka depression, in contrast to the more southerly volcanoes of the Kamchatka arc that form a volcanic clear front along the Kamchatka trench. Red triangles are volcanoes and black inverted triangles are station locations.

eikonal equation at nodes of a 3-D grid. Continuous travel-time is then constructed by tri-linear interpolation.

The target region is defined as a vector (**m**) of the *p* slowness (1/velocity) values at every node in a three-dimensional grid plus four hypocenter coordinates for each of *q* earthquakes used in the inversion. Since inversion of seismic travel times is inherently non-linear, the approach is to solve a series of linear inversions. Linearizing the travel-time about a reference model and writing the residual (observed minus calculated travel-time) of the *i-th* earthquake at the *j-th* receiver as

$$r_{ij} = \sum_{k=1}^{p+4q} \frac{\partial T_{ij}}{\partial m_k} \delta m_k \tag{1}$$

we have, in matrix form

$$\mathbf{J}\delta\mathbf{m} = \mathbf{r} \tag{2}$$

where **J** is the partial derivative matrix and $\delta\mathbf{m}$ is the correction required to make the reference model fit the data.

In general, equation (2) will be inconsistent and under-constrained, and $(\mathbf{J}^{\mathrm{T}}\mathbf{J})^{-1}$ will not necessarily exist. We regularize the problem by augmenting the system with additional constraint equations to penalize departure of the final model from *a priori* assumptions. For example, the Laplacian operator has been widely used as a smoothing operator in inversion studies [*Constable et al.*, 1987; *Lees*, 1992]. This constraint forces models to be smooth by requiring gradients to be small.

Since we are interested in finding a smooth final model that is consistent with the observations (rather than just finding smooth perturbations) we modify the constraint equations as follows. If **L** is the discrete Laplacian operator that acts only on the slowness nodes of our solution vector **m**, then $\mathbf{b}_0=\mathbf{L}\,\mathbf{m}_0$ is the roughness of the current model $\mathbf{m}_0$. Since $\mathbf{m}=\mathbf{m}_0+\delta\mathbf{m}$, roughness will be minimized in the final model, **m**, if

$$\mathbf{b_0} + \mathbf{L}\delta\mathbf{m} = \mathbf{0} \tag{3}$$

A weighted version of this equation is added as a constraint to Equation (2) and solved by least squares. Since the combined system of equations is sparse (on the order of 0.001% non-zero elements) we use an iterative conjugate gradient method [*Paige and Saunders*, 1982] to simultaneously solve the entire problem in a least-squares sense for all slowness and hypocenter parameters.

Equation (1) is only a linearization of the true problem so we require multiple iterations to find a final solution. Iteration is continued until the norm of the solution vector $\delta\mathbf{m}$ reaches some prescribed low level. In practice the system typically converges in fewer than ten iterations.

An illustration of the sensitivity of the inversion method is presented in Plate 1. (Please see the "Animated view of the tomographic inversion of subsurface of Kliuchevskoi volcano" on the CDROM accompanying this volume.) Point spread functions are used to estimate the resolving power of the inversion. These represent the response of the inversion methods to a model that has a 7 km diameter perturbation located at points of interest in the model. Tests show that the derived perturbations in the zone of interest (below Klyuchevskoy complex) are well-resolved (to within 7 km, or 1.5 block radius) with data used in this study. We are thus confident that the larger anomalies derived from these data represent real structures and do not reflect spurious noise or other adverse affects. At the edges of the models where ray coverage is limited, on the other hand, the inversion results are not conclusive and we refrain from interpretation. The interpretations described below take a conservative stance and are thus restricted to regions that have a good resolution and low standard error. Anomalies that extend beyond a typical 2–3 block radius are considered to be well resolved and open to interpretation with confidence.

RESULTS

The P-wave velocity anomalies show considerable heterogeneity near the surface with fluctuating high and low perturbations (Plates 2 and 3). The first anomalous regions appear between Klyuchevskoy and Sheveluch as high velocity perturbations at depths of 5–7 km. The high and low velocity anomalies are very heterogeneous (alternating between high and low) between 9 and 13 km depth. An apparent high velocity ridge or lineation is evident along an axis from Klyuchevskoy and Sheveluch and 50–80 km diameters high velocity is evident north east of Kizimen volcano. From 13–20 km a broad lower velocity anomaly is observed in abroad region between Klyuchevskoy and Sheveluch. This region has a lateral extent of more than 100 km. Around 21–23 km depth there is a broad higher velocity anomaly that extends over the whole model. Beginning at 23 km depth a concentrated, nearly circular, low velocity anomaly is clearly defined below the Klyuchevskoy complex. It has a radius of about 12 km and is offset from the peak of Klyuchevskoy by 10 km. This low velocity anomaly extends to depths of 35–37 km, although loss of resolution at these depths prevents us from providing clear delineation of the anomaly much below 33–35 km depth. To illustrate the degree of this perturbation, the low velocities at 25–27 km depth range from 5.3 to 4.5 in the center of the anomalous region. The standard 1-D velocity model used for this region at these depths is typically 6.8–7.7 km depth. Assuming a background velocity of 7.34 km/s the estimates from our 3-D

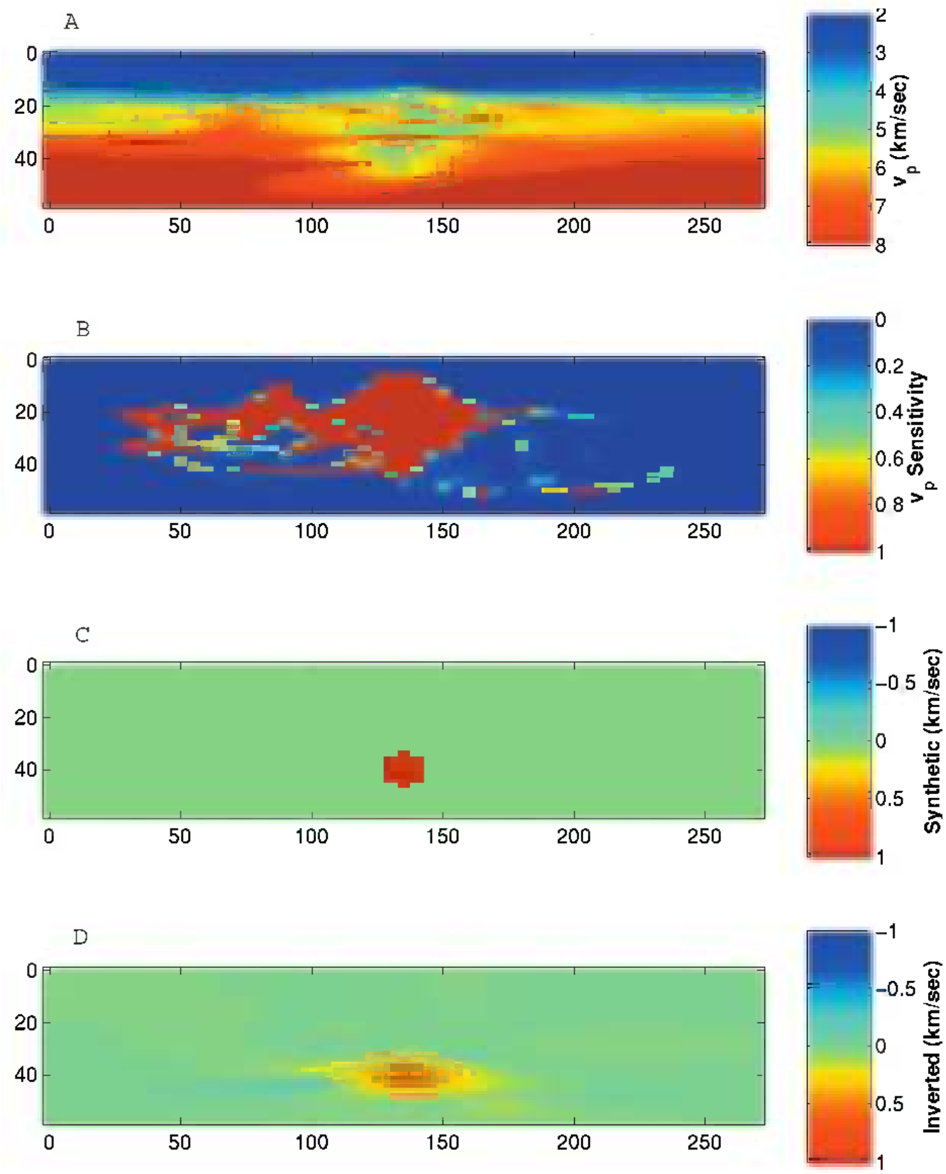

Plate 1. Cross section and point spread function of tomographic inversion. A) Cross section through the tomographic model. B) Sensitivity estimates of the inversion through the cross section in (A). C) Spike inserted in model at depth of 20 km. D) Result of inversion of spike. Note that the synthetic blob is relatively well resolved at 20 km depth.

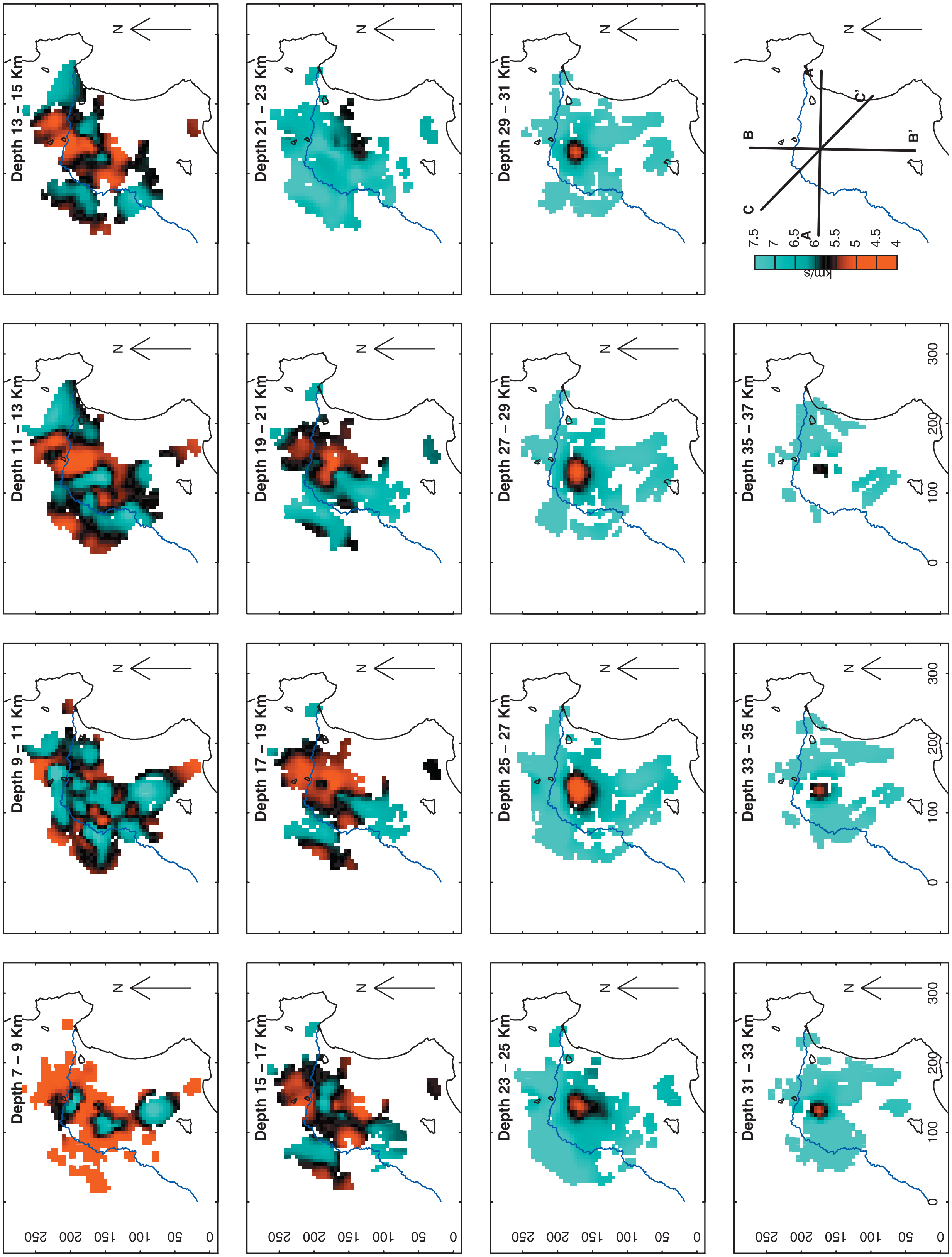

Plate 2. Horizontal slices through the tomographic model of the Kliuchevskoi group. Layers are extracted from the model at 2 km intervals, where the depths are provided in each panel. The color scale (4–7.5 km/s) is provided in the lower right panel along with a small map showing the loci of vertical cross sections in Figure 5. Red colors are lower velocity and blue are higher velocity variations.

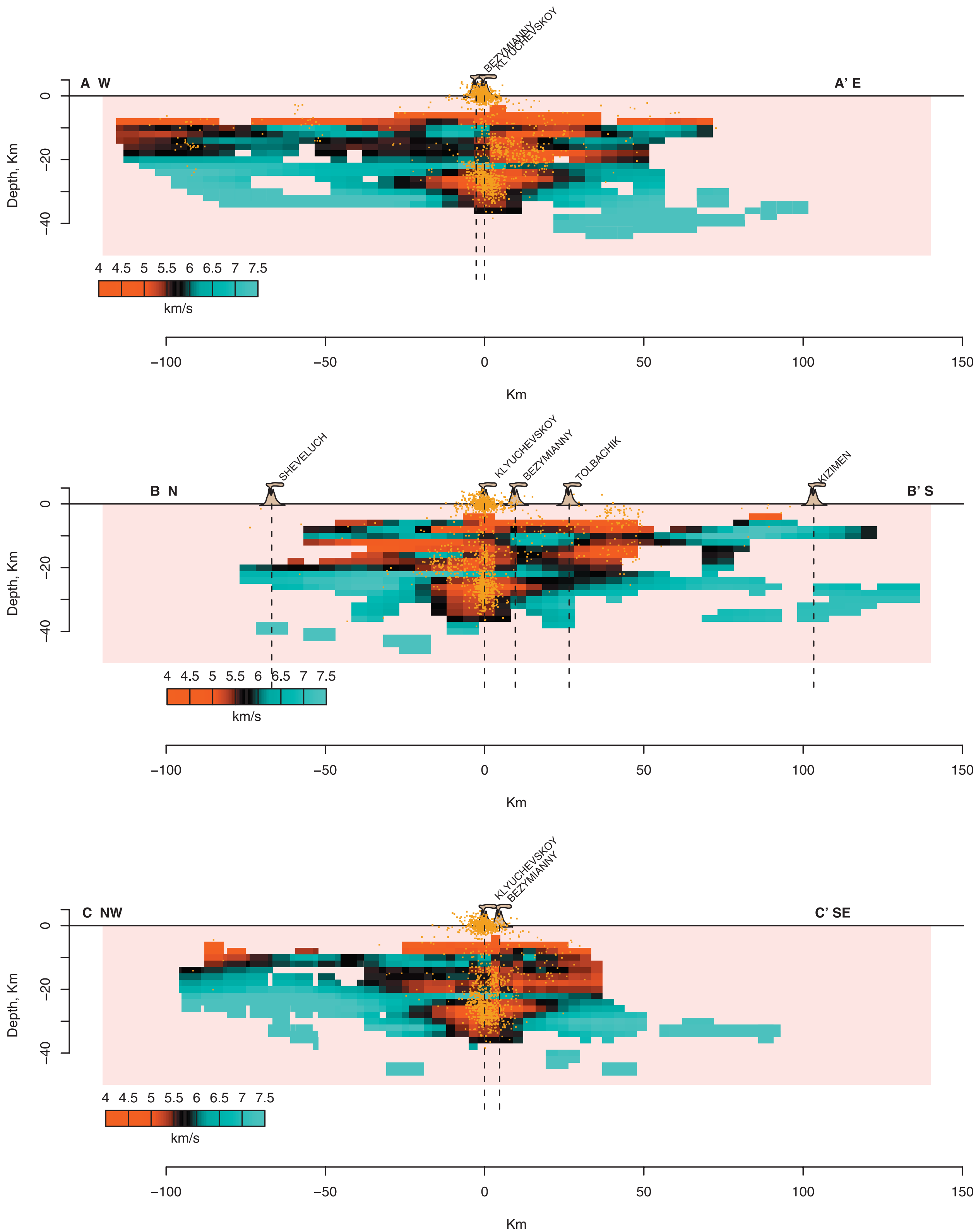

Plate 3. Inversion results for Klyuchevskoy group, vertical cross sections. These sections correspond to the map diagram in Figure 2 and the lower left panel of Figure 4. Red regions represent low velocity, blue high velocity. Yellow points are locations of local earthquakes used in this study, projected from a 20 km swath about the line of cross section. Note the correlation of hypocenters to the low velocity accumulations at depth.

model suggest perturbations ranging from 27–38%. Even if these values are over-estimated, they represent a significant perturbation at these depths. The low velocity anomaly at 23–35 km depth coincides with the concentration of deep seismicity below the Klyuchevskoy volcanic complex.

The distribution of high and low velocity anomalies is particularly evident when viewed in cross section (Plate 3). The low velocity anomaly situated below the Klyuchevskoy group has a cylindrical or conical shape tapering down towards the Moho (23–35 km depth). A higher velocity sill or layer is above this and in the shallower regions, above 12 km depth, numerous heterogeneous anomalies are distributed throughout the cross sections. Although velocity perturbations can be attributed to a variety of sources, we assume that the shallow regions in this part of Kamchatka are related to the complex structures accumulated over the course of subduction and accretion of the Kamchatka arc. Shallow anomalies may be associated with lithologic variations, hydrothermal alteration, and distribution of faults and cracks, in addition to geothermal fluctuations. Without additional *a priori* information constraining the interpretation of these complex variations it is difficult to assign a specific interpretation to a particular anomaly on an individual basis.

In the case of the deeper anomaly (21–35 km depth) below the edifice we are confident that the velocity variation is most likely due to the presence of a significant amount of partial melt or, alternatively, an intense thermal anomaly. The deep anomaly furthermore coincides with deep long period events similar to those found below Mt. Fuji [*Nakamichi et al.*, 2004]. Measurements of seismic P-wave velocities for igneous rocks in laboratory environments suggest that perturbations greater than 50% indicate a considerable proportion of partial melt in samples [*Sato et al.*, 1989]. It is rare to find tomographic inversions with perturbations of this magnitude, although some exceptions are notable [*Horiuchi et al.*, 1997]. This is partially due to issues related to regularization introduced in the calculations because of inconsistencies in the data [*Lees*, 2007]. It may, however, be due to the fact that large accumulations of melt or partial melt, on batholithic spatial scales at least, are simply not present in the deeper parts of the crust [*Coleman et al.*, 2004; *Glazner et al.*, 2004]. On the other hand, it may be that significant percentages of partial melt exist but are distributed in a way that is masked and invisible to tomographic analysis. The non-uniqueness of the tomographic inversion, coupled with the lack of additional constraining information (such as thermal history, density, or lithology derived from xenoliths, for example) makes it impossible to determine unequivocally the exact perturbation magnitude associated with images derived via seismic inversion.

While it is clear that a significant velocity anomaly is present below Klyuchevskoy (Plate 3), the resolving power of the data is not sufficient to delineate individual structures internal to anomalies discussed here. The 25% perturbation suggests there is a significant heat anomaly at 20–30 km depth and it is likely that there is a substantial amount of melt accumulated in this zone. The resolving capabilities of this data set are not fine enough to allow for the isolation of individual conduits connected to specific active volcanic centers like Klyuchevskoy, Bezymianny or Tolbachik. Rather, we see a broad subsurface region with low enough velocity to suggest that significant melt is present and most likely provides a magma storage region that feeds these volcanic centers. The images produced in this study fall into an intermediate scale for tomographic investigation below volcanic regions. At smaller scales, shallow anomalies interpreted as magma accumulation have been observed above 10 km [*Lees*, 1992]. At larger scales, anomalous low velocities are observed in the upper mantle below calderas like Yellowstone[*Clawson et al.*, 1989] and Long Valley[*Sanders et al.*, 1995]. At the caldera scale, amplitudes of anomalous features, compared to expected melt accumulates anticipated for such large scale eruptions, are relatively small. Furthermore, large amplitude, extensive low velocities are often absent in mid-ocean ridge spreading centers where it is known that a considerable flux of volcanic material emerges along axes. The position and amplitude of the anomalies below Klyuchevskoy, on the other hand, provide strong evidence for significant melt accumulations and support the idea that lower crustal storage is probably present at the northern terminus of the Kamchatka arc.

It has been noted that the northern terminus of the Kamchatka arc represents the northern terminus of subducting Pacific plate where the plate apparently exposes an edge as it plunges into the mantle [*Lees*, 2006; *Levin et al.*, 2002; *Park et al.*, 2002; *Yogodzinski et al.*, 2001]. Yogodzinski et al. [2001] showed that adakitic material, derived from slab contamination of the upper mantle, is present at Sheveluch but not at Klyuchevskoy. The lack of significant slab material north of the Klyuchevskoy group allows the slab to bow upward below Klyuchevskoy where the plate is deformed by shoaling. The results of this study do not shed new light on this process, although it may be that shoaling slab creates a state of buoyancy that encourages a large flux of magma. The slab window created by the opening of the Pacific slab north of Kamchatka (below the Bering Islands) provides an upper mantle thermal conduit that may accentuate magmatism in this subduction zone [*Lees et al.*, 2007].

Active source seismic investigations of the Klyuchevskoy region indicated low attenuation of seismic waves at shallow depths below Klyuchevskoy, although the authors report a corresponding shadow zone below Bezymianny[*Anosov et al.*, 1978]. The absence of a significant attenuating body below Klyuchevskoy precluded the possibility of a large magma body below the edifice, although a small low velocity region was postulated for Bezymianny. Anosov et al. [1978] recognized that there must be a deeper source of magma at depth and hypothesized magma accumulation below 20 km. Images presented here delineate the deep magma accumulation, although we cannot draw conclusions here, due to resolution limitations, about the presence or absence of magma accumulations below Klyuchevskoy or Bezymianny.

CONCLUSION

Tomographic P-wave images of Klyuchevskoy volcano show a significant P-wave anomaly ranging from 20–40 km below the edifice of the Klyuchevskoy group. This anomaly appears narrow in the 20 km depth range and broadens laterally around 30–35 km depth, perhaps suggesting ponding and accumulation at the Moho discontinuity. We cannot yet determine the level of percent melt in this region, although the size of the anomaly strongly suggests that a significant amount of magma resides at depth below the Klyuchevskoy group and is most likely the main source feeding this very active region along the Kamchatka Subduction zone.

Acknowledgements. Support for this work was provided in part by grants NSF EAR 0337462 and NSF EAR-0440054. The authors are grateful to Seth Moran for helpful comments.

REFERENCES

Aloisi, M., O. Cocina, G. Neri, B. Orecchio, and E. Privitera, Seismic tomography of the crust underneath the Etna Volcano, Sicily, *Phys. Earth Planet. Int.*, *134* (3-4), 139–155, 2002.

Anosov, G. I., S. K. Bikkenina, and A. A. Popov, *Glubinnoe seismicheskoe zondirovanie Kamchatki: Deep seismic sounding of Kamchatka (in Russian)*, 129 pp., Nauka, Moscow, 1978.

Aster, R. C., and R. P. Meyer, Three-dimensional velocity structure and hypocenter distribution in the Campi Flegrei caldera, Italy, *Tectonophysics*, *149*, 195–218, 1988.

Benz, H., B. A. Chouet, P.B. Dawson, J. C. Lahr, R. A. Page, and J. A. Hole, Three-dimensional P and S-wave velocity structure of Redoubt Volcano, Alaska, *J. Geophys. Res.*, *101* (4), 8111–8128, 1996.

Benz, H. M., Simultaneous inversion for lateral velocity variations and hypocenters in the Yellowstone region using earthquake and refraction data, University of Utah, 1982.

Benz, H. M., and R. B. Smith, Simultaneous inversion for lateral velocity variations and hypocenters in the Yellowstone region using earthquake and refraction data, *JGR. Journal of Geophysical Research. B*, *89* (2), 1208–1220, 1984.

Brown, J., S.G. Prejean, H. Zhang, and J. Power, Double difference earthquake relocation and tomography at Mount Spurr Volcano, Alaska, 1991 to 2004, *Eos, Transactions, American Geophysical Union*, *85* (47), S51A-0140, 2004.

Clawson, S.R., R.B. Smith, and H.M. Benz, P wave attenuation of the Yellowstone Caldera from three-dimensional inversion of spectral decay using explosion source seismic data, *J. Geophys. Res.*, *94* (6), 7205–7222, 1989.

Coleman, D.S., W. Gray, and A.F. Glazner, Rethinking the emplacement and evolution of zoned plutons; geochronologic evidence for incremental assembly of the Tuolumne Intrusive Suite, California, *Geology*, *32* (5), 433–436, 2004.

Constable, A.C., R.L. Parker, and C.G. Constable, Occam's inversion: A practical algorithm for generating smooth models from electromagnetic sounding data, *Geophysics*, *52* (3), 289–300, 1987.

Dawson, P.B., J.R. Evans, and H.M. Iyer, Teleseismic tomography of the compressional wave velocity structure beneath the long Valley region, California, *J. Geophys. Res.*, *95* (B7), 11021–11050, 1990.

Dawson, P.B., H.M. Iyer, J.R. Evans, and U. Achauer, Inversion of teleseismic travel time residuals to investigate the three-dimensional P-velocity structure of the crust and upper mantle, the Long Valley, California, region, *International Union of Geodesy and Geophysics, General Assembly*, *19* (1), 55, 1987.

De Natale, G., P. Capuano, C. Troise, and A. Zollo, Seismicity at Somma-Vesuvius and its implications for the 3D tomography of the volcano, in *J. Volc. Geoth. Res.*, edited by F.J. Spera, B. de Vivo, R.A. Ayuso, and H.E. Belkin, pp. 175–197, 1998.

Ellsworth, W.L., and R.Y. Koyangi, Three-dimensional crust and mantle structure of Kilauea Volcano, Hawaii, *J.Geophys. Res.*, *82* (33), 5379–5394, 1977.

Evans, J.R., and J.J. Zucca, Active high-resolution seismic tomography of compressional wave velocity and attenuation structure at Medicine Lake volcano, northern California Cascade Range, *J. Geophys. Res.*, *93*, 15016–15036, 1988.

Fedotov, S.A., S.T. Balesta, V.I. Gorelchik, G.B. Flerov, and V.B. Enman, The 1975–1976 strong fissure eruption of the Tolbachik Volcano, Kamchatka, *Abstracts of Papers—Pacific Science Congress*, *14*, 90–91, 1979.

Fedotov, S.A., and Y.P. Masurenkov, Active Volcanoes of Kamchatka, pp. 302, Nauka, Moscow, 1991.

Glazner, A.F., J.M. Bartley, D.S. Coleman, W. Gray, and R.Z. Taylor, Are plutons assembled over millions of years by amalgamation from small magma chambers?, *GSA Today*, *14* (April/May), 4–11, 2004.

Gorelchik, V.I., O.S. Chubarova, and V.T. Garbuzova, Seismicity of the region of the Northern group of volcanoes in Kamchatka, 1971–1983, *Volcanology and Seismology*, *10* (N3), 141–157, 1990.

Gorshkov, G.S., Gigantic eruption of the volcano Bezymianny, *Bull. Volcanol.*, *20*, 77–109, 1959.

Haslinger, F., C.H. Thurber, M. Mandernach, and P.G. Okubo, Tomographic image of P-velocity structure beneath Kilauea's East Rift Zone and South Flank; seismic evidence for a deep magma body, *Geophys. Res. Lett.*, *28* (2), 375–378, 2001.

Hauksson, E., Absence of evidence for a shallow magma chamber beneath Long Valley Caldera, California, in downhole and surface seismograms, *J. Geophys. Res.*, *93* (11), 13,251–13,264, 1988.

Hole, J.A., Nonlinear high-resolution three-dimensional seismic travel time tomography, *Geophys. J. Int.*, *97*, 6553–6562, 1992.

Horiuchi, S., N. Tsumura, and A. Hasegawa, Mapping of a magma reservoir beneath Nikko-Shirane volcano in northern Kanto, Japan, from travel time and seismogram shape anomalies, *J. Geophys. Res.*, *102* (B8), 18071–18090, 1997.

Husen, S., and R.B. Smith, Probabilistic earthquake resolution in three-dimensional velocity models for the Yellowstone National Park region, Wyoming, *Bull. Seismol. Soc. Am.*, *94* (3), 880–896, 2004.

Iyer, H.M., J.R. Evans, G. Zandt, R.M. Stewart, J.M. Coakley, and J.N. Roloff, A deep low-velocity body under the Yellowstone caldera, Wyoming: Delineation using teleseismic P-wave residuals and tectonic interpretation, *Geol. Soc. Am. Bull.*, *92* (Part I), 792–798, 1981.

Kersting, A.B., and R.J. Arculus, Pb isotope composition of Klyuchevskoy Volcano, Kamchatka and North Pacific sediments; implications for magma genesis and crustal recycling in the Kamchatkan arc, *Earth Planet. Sci. Letts.*, *136* (3-4), 133–148, 1995.

Lees, J.M., The magma system of Mount St. Helens: Non-linear high resolution P-wave tomography, *J. Volc. Geoth. Res.*, *53* (1-4), 103–116, 1992.

Lees, J.M., Tomography Of Crustal Magma Bodies, in *Cities on Volcanoes*, Quito, Ecuador, 2006.

Lees, J.M., Tomography of Crustal Magma Bodies: Implications For Magmatic Systems, in *J. Volc. Geoth. Res.*, pp. in Review, 2007.

Lees, J.M., and R.S. Crosson, Tomographic imaging of local earthquake delay times for 3-D velocity variation in western Washington, *J. Geophys. Res.*, ***95*** (B4), 4763–4776, 1990.

Lees, J.M., J. VanDecar, E. Gordeev, A. Ozerov, M. Brandon, J. Park, and V. Levin, Three Dimensional Images of the Kamchatka-Pacific Plate Cusp, in *Volcanism and Tectonics of the Kamchatka Peninsula and Adjacent Arcs*, edited by J. Eichelberger, J.M. Lees, P. Izbekov, and E. Gordeev, pp. in press, 2007.

Levin, V., N. Shapiro, J. Park, and M. Ritzwoller, Seismic evidence for catastrophic slab loss beneath Kamchatka, *Nature*, *418*, 763–767, 2002.

Miller, D.S., and R.B. Smith, P and S velocity structure of the Yellowstone volcanic field from local earthquake and controlled-source tomography, *J. Geophys. Res.*, *104* (7), 15,105–15,121, 1999.

Moran, S.C., J.M. Lees, and S.D. Malone, P-wave velocity structure in the greater Mount Rainier area from local earthquake tomography, *J. Geophys. Res.*, *104* (10), 10,775–10,786, 1999.

Mori, J.J., D. Eberhart-Phillips, and D.H. Harlow, Three-dimensional velocity structure at Mount Pinatubo; resolving magma bodies and earthquake hypocenters, in *Fire and mud; eruptions and lahars of Mount Pinatubo, Philippines*, edited by C.G.e. Newhall and R.S.e. Punongbayan, pp. 371–382, 1996.

Nakamichi, H., M. Ukawa, and S.i. Sakai, Precise hypocenter locations of midcrustal low-frequency earthquakes beneath Mt. Fuji, Japan, *Earth, Planets and Space*, *56* (12), e37–e40, 2004.

O'Doherty, K.B., C.J. Bean, and J. McCloskey, Coda wave imaging of the Long Valley Caldera using a spatial stacking technique, *Geophys. Res. Lett.*, *24* (13), 1547–1550, 1997.

Ohmi, S., and J.M. Lees, Three-dimensional P and S-wave velocity structure below Unzen Volcano, *J. Volc. Geoth. Res.*, *65*, 1–26, 1995.

Ozerov, A.Y., The evolution of high-alumina basalts of the Klyuchevskoy Volcano, Kamchatka, Russia, based on microprobe analyses of mineral inclusions, *J. Volc. Geoth. Res.*, *95*, 65–79, 2000.

Ozerov, A.Y., A.A. Ariskin, F. Kayl, G.Y. Bogoyavlenskaya, and S.F. Karpenko, Petrological-geochemical model for genetic relationships between basaltic and andesitic magmatism of Klyuchevskoy and Bezymyannyy volcanoes, Kamchatka, *Petrology*, *5* (6), 614–635, 1997.

Paige, C.C., and M.A. Saunders, LSQR: An algorithm for sparse linear equations and sparse least squares, *Trans. Math. Software*, *8*, 43–71, 1982.

Park, J., V. Levin, M.T. Brandon, J.M. Lees, V. Peyton, E. Gordeev, and A. Ozerov, A dangling slab, amplified arc volcanism, mantle flow and seismic anisotropy near the Kamchatka plate corner, in *Plate Boundary Zones*, edited by S. Stein and J. Freymueller, pp. 295–324, AGU, Washington DC, 2002.

Peppin, W.A., New evidence for magma bodies south of Long Valley Caldera, Mammoth Lakes, California, *Eos, Transactions, American Geophysical Union*, *66* (46), 959, 1985.

Rowan, L.R., and R.W. Clayton, The three-dimensional structure of Kilauea Volcano, Hawaii, from travel time tomography, *J. Geophys. Res.*, *98* (3), 4355–4375, 1993.

Sanders, C.O., Reanalysis of S-to-P amplitude ratios for gross attenuation structure, Long Valley Caldera, California, *J. Geophys. Res.*, *98* (12), 22,069–22,079, 1993.

Sanders, C.O., S.C. Ponko, L.D. Nixon, and E.A. Schwartz, Seismological evidence for magmatic and hydrothermal structure in Long Valley caldera from local earthquake attenuation and velocity tomography, *J. Geophys. Res.*, *100* (5), 8311–8326, 1995.

Sanders, C.O., S.C. Ponko, L.D. Nixon, E.A. Schwartz, and Anonymous, Local earthquake attenuation and velocity tomography for magmatic and hydrothermal structure in Long Valley Caldera, California, in *Seismol. Res. Lett.*, pp. 56, 1994.

Sato, H., I.S. Sacks, and T. Murase, The use of laboratory velocity data for estimating temperature and partial melt fraction in the low velocity zone: Comparison with heat flow and electrical conductivity studies, *J. Geophys. Res.*, *94*, 5689–5704, 1989.

Symons, N.P., and R.S. Crosson, Seismic Velocity Structure of the Puget Sound Region from 3-D Non-linear Tomography, *Geophys. Res. Lett.*, *21*, 2593–2596, 1997.

Thurber, C.H., Seismic detection of the summit magma complex of Kilauea volcano, Hawaii, *Science*, *233*, 165–167, 1984.

Utnasin, V.K., A.I. Abdurakhmanov, G.I. Anosov, Y.A. Budyansky, V.I. Fedorchenko, Y.K. Markhinin, and S.T. Balesta, Types of magma foci of island arc volcanoes and their study by the method of deep seismic sounding of Kamchatka, in *Volcanoes and Tectosphere*, pp. 123–137, Tokai University Press, 1976.

Vidale, J.E., Finite-difference traveltime calculation, *Bull. Seis. Soc. Am.*, *78*, 2062–2076, 1988.

Yogodzinski, G.M., J.M. Lees, T.G. Churikova, F. Dorendorf, G. Woerner, and O.N. Volynets, Geochemical evidence for the melting of subducting oceanic lithosphere at plate edges, *Nature*, *409*, 500–504, 2001.

Yuan, H., and K. Dueker, Teleseismic P-wave tomogram of the Yellowstone plume, *Geophys. Res. Lett.*, *32*, no.7, 4, 2005.

Zollo, A., P. Gasparini, J. Virieux, G. Biella, E. Boschi, P. Capuano, R. de Franco, P. Dell'Aversana, R. de Matteis, G. De Natale, G. Iannaccone, I. Guerra, H. Le Meur, and L. Mirabile, An image of Mt. Vesuvius obtained by 2D seismic tomography, in *J. Volc. Geoth. Res.*, edited by F.J. Spera, B. de Vivo, R.A. Ayuso, and H.E. Belkin, pp. 161–173, 1998.

Minor- and Trace Element Zoning in Plagioclase From Kizimen Volcano, Kamchatka: Insights on the Magma Chamber Processes

Tatiana Churikova[1,2], Gerhard Wörner[2], John Eichelberger[3], and Boris Ivanov[1]

Major and trace elements in whole rocks as well as major (Al, Si, Na, Ca, K), minor (Fe) and trace (Sr, Ba, Mg) elements in plagioclase phenocrysts were investigated in lavas from Kizimen volcano, Kamchatka. Quaternary Kizimen volcano was active during Holocene times and is intriguing in several aspects: (1) its lavas often contain unusually high proportions of incorporated basalt and basaltic andesite magma as enclaves; (2) banded texture is common in lavas; (3) large phenocrysts of plagioclase and hornblende associate with olivine and orthopyroxene in the same sample; (4) mafic enclaves and evolved dacites show a REE cross-over patterns; (5) MORB-like Sr-Nd isotope values exclude crustal contamination. Mafic enclaves and host dacitic lavas are both hybrid and represented by mixtures of mafic and silicic end-members in different proportions. These end-members are likely derivates of the same basaltic parent assuming a significant amount of amphibole fractionation. To understand magma chamber processes of the Kizimen volcano and the origin of its magmas, we used major and trace element zoning patterns in plagioclase phenocrysts from mafic enclaves and evolved hosts. According to our data, mafic and silicic magmas maintain some identity as physically distinct domains, while sometimes exchanging only heat but at other times heat, melt, and crystals between them. Processes in the magma chamber that occurred before eruption are: (1) crystal growth and fractionation, (2) recharge and magma mixing, and (3) resumed crystallization in high-temperature dacite heated by mafic magma.

1. INTRODUCTION

Magma chamber processes play an important role in the formation of igneous rocks. These processes include crystallization, melt differentiation, convection, and magma mixing. Experimental and numerical models of magma chamber processes [e.g. *Marsh*, 1989] allow study of the effects of physical parameters such as density and viscosity as a function of melt composition, temperature gradients inside the chamber and near the contact with country rock, geometry of the magma chamber, etc. However, such models need to be calibrated with natural systems, and it is difficult to apply them directly because many of these parameters are not well constrained.

One approach to better understand mixing dynamics in magmas is the study of the crystallization histories of minerals in volcanic rocks, using major, minor, and trace element zoning in plagioclase in relation to magma

[1] Institute of Volcanology and Seismology Far East Division Russian Academy of Sciences, Kamchatka, Russia
[2] Geowissenschaftliches Zentrum Göttingen, Universität Göttingen, Germany
[3] Alaska Volcano Observatory, Geophysical Institute, University of Alaska Fairbanks, Fairbanks, Alaska, USA

Volcanism and Subduction: The Kamchatka Region
Geophysical Monograph Series 172

10.1029/172GM22

compositions and crystallization conditions. Plagioclase is the best mineral for such kind of research because it faithfully records the changes in magma compositions at variable temporal and spatial scales without significant subsequent re-equilibration [*Grove et al.* 1981, *Davidson and Tepley*, 1997; *Ginibre et al*., 2002a, 2002b]. However, controls on its composition are also rather complex and difficult to separate. Numerical modeling [e.g. *Allĕgre et al*., 1981] has provided insights into the kinetics of plagioclase growth and resorption. Experimental studies have elucidated the influence of some important factors (e.g. P, T, melt composition, H_2O content in the melt) on the An–Ab system (e.g. *Drake and Weill*, 1975; *Bindeman et al.,* 1998).

Recently, significant variations in minor, trace elements and isotope ratios between individual growth zones of natural plagioclase crystals at the scale of several microns were revealed using SIMS and TIMS techniques [*Churikova and Sokolov*, 1993; *Brophy et al*., 1996; *Davidson and Tepley* 1997; *Tepley et al*., 2000]. These variations have been attributed to processes occurring during magma storage and ascent, including fractional crystallization, magma mixing, degassing, assimilation, and temperature effects. The spatial resolution of the SIMS and TIMS is insufficient to reveal chemical variations in individual growth zones at a micron scale. The electron microprobe allows to measure the major, minor and trace elements (if concentrations > 100 ppm) in minerals with a spatial resolution of only a few microns [e.g. *Ginibre et al*., 2002a, b]. Such an approach allows studying a greater number of crystals at higher spatial resolution and at significantly lower cost.

In this study we report the results of microprobe analyses on plagioclase phenocrysts from basalts, basaltic andesites and dacites of Kizimen volcano (Kamchatka, Figure 1). Tephrachronological work on the eruption history of Kizimen has shown that the volcano formed during the Quaternary [*Melekestsev et al.,* 1992] synchronously with an associated graben and was active until Late Holocene time. Its structural setting, and indeed its morphology and petrology, is strikingly similar to Unzen Volcano in Japan [*Nakada & Motomura*, 1999; *Browne et al*., 2006]. At present, there is intense fumarolic activity on the slope of the volcano.

Our geochemical investigation of Kizimen volcano was conducted in several stages. First, we analyzed the major and trace elements as well as isotope ratios of Sr, Nd (in three samples) and Pb (in one sample) in whole rocks. Then we studied six plagioclase phenocrysts from three representative samples for major (Al, Si, Na, Ca, K), minor (Fe) and trace (Sr, Ba, Mg) elements.

2. GEOLOGICAL SETTING, PETROGRAPHY AND MINERALOGY OF SAMPLES STUDIED

Kizimen Volcano, one of the active volcanoes of the Kurile-Kamchatka arc, is located on the eastern margin of the Central Kamchatka Depression (CKD) in the area of Schapinsky graben midway between the Eastern Volcanic Front (EVF) and CKD at the latitude of the Kliuchevskaya Group (Figure 1). The northwestern part of the volcano is cut by NE-SW-trending, westward-dipping normal faults, which form a series of cliffs with good exposures of the volcano's flank and its basement. A single reported eruption, in 1928, was very modest and no deposits were found.

Four cycles of activity have been identified in the eruptive history of the volcano (Figure 1), with ages from 12–11 Ka to present [*Melekestsev et al*., 1992]. Holocene eruptions produced lava flows and a dome complex of basaltic andesite to dacite composition in the upper part of volcano (Figure 1). Andesite and dacite lava flows contain abundant cognate mafic enclaves of more primitive composition (Figure 2a). The most recent summit lava has an unusual high proportion of up to 35 vol % of large (> 20 cm) mafic enclaves of basaltic andesite composition. Dacitic lavas with a few percent of enclaves of smaller size are more common (Figure 2b). We did not find any correlations between shape of enclaves and their composition. There are also abundant conspicuously banded lavas, with an apparent thickness of mafic layers from a few millimeters to 20–25 cm (Figure 2c) thick. All andesite to dacite lavas are hornblende-bearing medium-potassic, and calc-alkaline in composition (Figure 3), and the enclaves are basaltic to basaltic andesites [*Churikova et al*., 2001b].

All samples from basalts to dacites contain plagioclase, hornblende, orthopyroxene, olivine, Ti-magnetite and glass. The amount of olivine decreases from 5 vol% in basalts to a trace in dacite. Basalts are also richer in orthopyroxene compared to dacites, 20 vol% and 10 vol%, respectively. In contrast, the amount of hornblende increases from 5 vol% in basaltic enclaves to 10–15 vol% in andesites and dacites. The amount of plagioclase and Ti-magnetite is rather similar in all rocks, about 20–25 vol% and 2–3 vol%, respectively. Additionally, basalts and basaltic andesites have about 5% of high-Ca clinopyroxene, whereas dacites often contain 0.5–1 vol% quartz [Trusov & Pletchov, 2005].

The composition of minerals in all types of rocks is surprisingly similar: Fo_{79-72} olivine, $En_{63-65}Wo_{1-2}$ orthopyroxene, titanomagnetite, and high-Mg amphibole. Only plagioclases show conspicuous compositional variations.

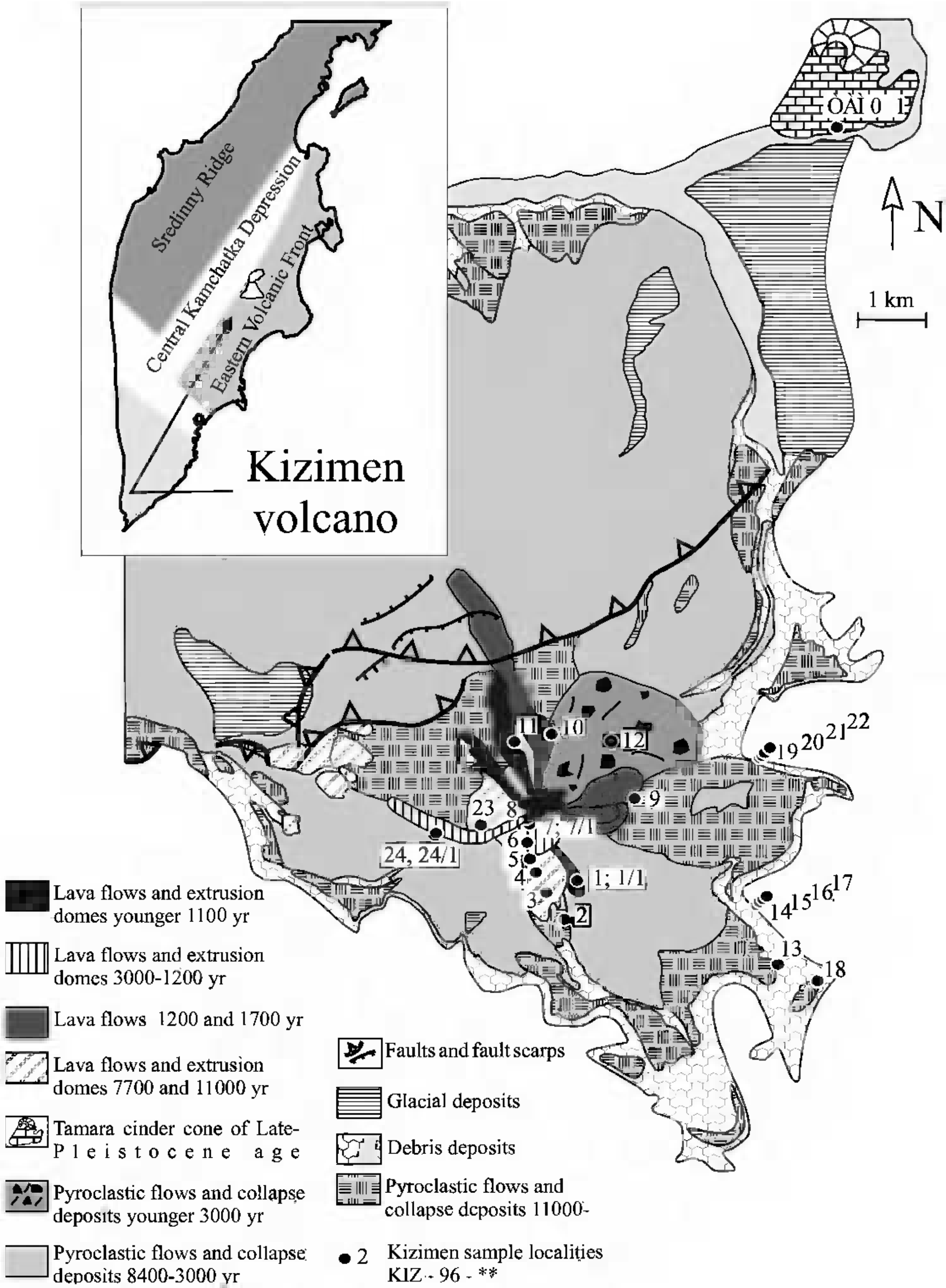

Figure 1. Schematic map of the Kizimen volcano and its surroundings [after *Melekestsev at all*, 1992]. Inset shows the location of Kizimen volcano at the border between Eastern Volcanic Front and Central Kamchatka Depression. All ages are in B.P.

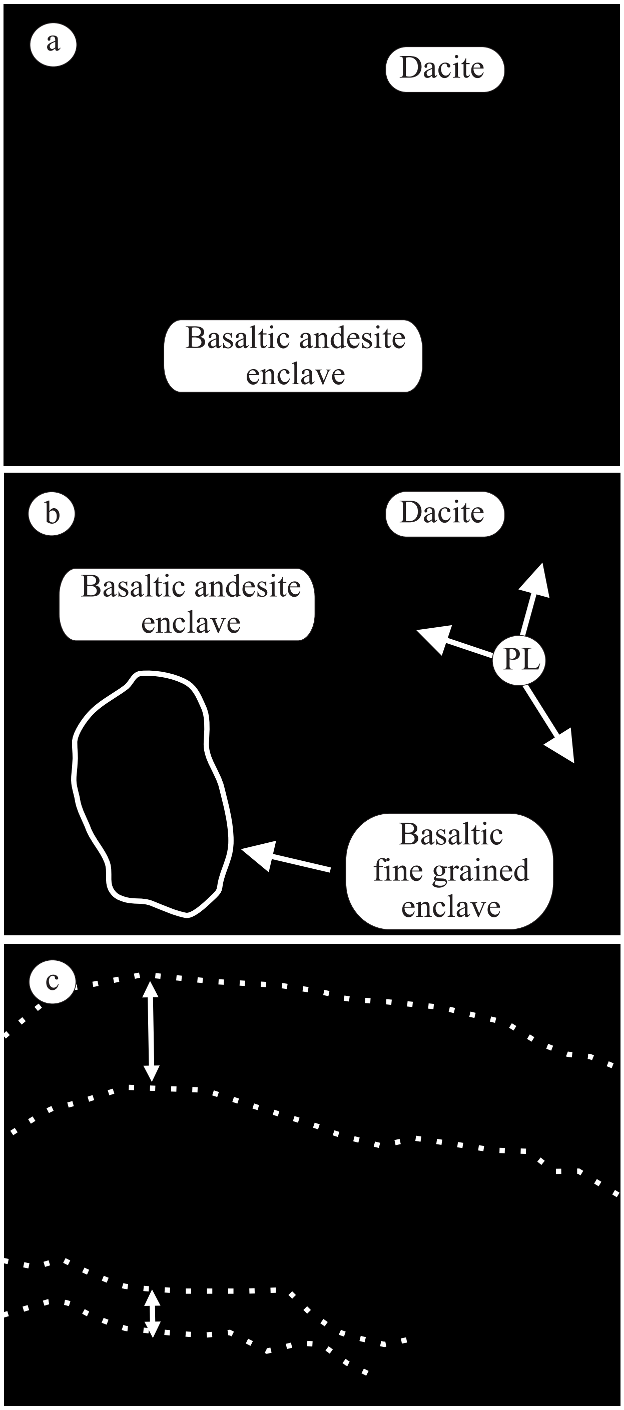

Figure 2. (a) Large basaltic andesite enclave (17*20 cm) in a dacitic lava; (b) 5-cm-diameter fine-grained enclave of basaltic composition inside a larger basaltic andesite enclave in dacitic host. Plagioclase crystals of more than 1 cm in size are found in both, host dacite and mafic enclave (shown by arrows); (c) fragment of the banded lava, the thickness of the layers is shown by double arrows.

In our view, the most prominent characteristic of Kizimen rocks is the occurrence of large phenocrysts of plagioclase and hornblende (up to 2 cm) co-existing with olivine and orthopyroxene.

3. ANALYTICAL METHODS

Analyzes were performed in Geowissenschaftlisches Zentrum of Göttingen Georg-August Universität, Abteilung Geochemie, Germany. Major elements and some trace elements (Sc, V, Cr, Co, Ni, Zn, Ga, Rb, Sr, Zr, and Ba) were determined in 19 samples by X-ray fluorescence analysis on glass discs, prepared with a lithium tetraborate flux. Fe_2O_3 was determined titrimetrically with $KMnO_5$ and the loss on ignition (LOI) by weight difference at heating to 1100°C. The analytical uncertainty (±2σ, rel. %) for all major elements is better than 1 % except for Fe, Na (2%) and LOI (10%), whereas for trace elements it is better than 5 %.

Additional trace elements were analyzed in 7 samples by ICPMS. The analytical uncertainty for most elements was better than 10 rel. %, except for Nb and Ta (15–20 rel. %), which was estimated based on repeated analyses of rock standards JB-3 and JA-2.

Isotope ratios for Sr, Nd, and Pb were measured with a Finnigan MAT 262 RPQ II+ mass-spectrometer at Göttingen using standards NBS987 (0.710245) for Sr, LaJolla (0.511847) for Nd and NBS981 (recommended values from *Todt et al.*, 1984) for Pb. Statistical errors (±2σ) were estimated to be less than 0.004% for Sr and Nd and less than 0.1% for Pb. For details see Dorendof et. al. [2000a, b] and Churikova et al.[2001a].

Major (Si, Al, Ca, Na, and K), minor (Fe) and trace (Sr, Mg, Ba) elements in six plagioclase grains were analyzed using JEOL8900 electron microprobe. This study was combined with textural observations using back scattered electron (BSE) images (multiply accumulated to increase mass resolution) where BSE intensity corresponds to An content. The BSE images were used to locate quantitative measurement points along profiles from core to rim. The central parts and the rims of microlites in the same samples were also analyzed for comparison.

Details of the technique for major and trace element determination with electron microprobe JEOL8900 WDS were described in Ginibre et al. [2002a]. Microprobe quantitative point analyses for Al, Si, Na, Ca, K, Ba, Sr, Fe, Ti, Ba, Mg were performed at 20 kV acceleration voltage and 40 nA beam current, with 2 to 5 µm beam size. Alkali elements (Na, K) and major elements (Al, Si, Ca) were analyzed during the first 90 s (16 s counting time on peak). Minor (Fe) and trace elements (Sr, Ba, Mg) were then analyzed over 4 min counting time on the peak.

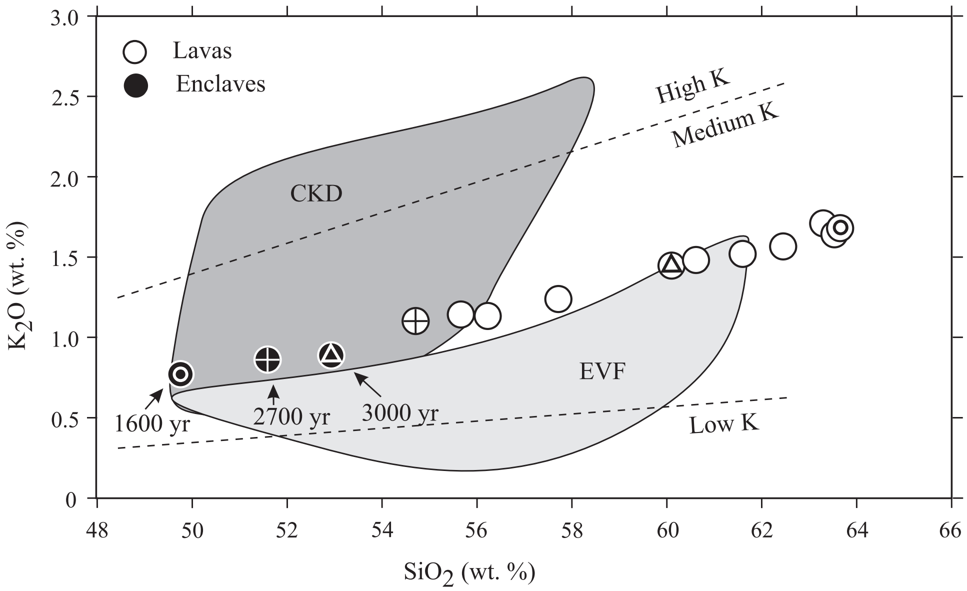

Figure 3. K_2O vs. SiO_2 for Kizimen volcano whole rocks. Rock chemistry within the mafic enclaves changes with time towards more mafic compositions. Compositional fields of EVF and CKD are shown for the comparison [after *Churikova et al.*, 2001a]. The pairs of rocks (host rock – mafic enclave) for three eruptions are shown by additional symbols (crosses, circles and triangles). Ages are taken from Melekestsev et al. (1992) and given in B.P.

The detection limits for Ba, Sr, Fe, Mg, and Ti, as well as the ranges of concentrations and analytical uncertainties for the analyses at the concentrations measured are given in Ginibre et al. [2002b]. Typical analytical uncertainties calculated from counting statistics for each analysis were 19 ppm for Mg, 60–70 ppm for Fe, 110–120 ppm for Sr, 70–75 ppm for Ba and 28–31 ppm for Ti.

4. RESULTS

4.1. Whole-Rock Geochemical Data From Kizimen Volcano.

Lavas and mafic enclaves define linear trend in K_2O versus SiO_2 compositional space (Figure 3). Enclaves in dacites become more mafic in more recent lavas. Kizimen lavas appeared to be transitional between the EVF and the CKD, i.e. they are more enriched in alkalis than the rocks of EVF but depleted in alkalis as compared to basalts and basaltic andesites of CKD (Figure 3). This is part of the systematic compositional trend from the Eastern Volcanic Front (EVF) through the Central Kamchatka Depression (CKD) to the back arc [*Churikova et al.*, 2001a].

Trace element patterns for products of the Kizimen volcano are typical for arc volcanism. They are characterized by strongly but variably enriched fluid mobile trace elements (LILE and LREE: K, Cs, U, Ba, Rb, Sr, Pb, La, and Ce) and relatively depleted HFSE (Nb, Ta, Hf, Zr, Ti) and HREE (from Tb to Yb) elements. The enrichment increases with increasing element compatibility. Ba, Rb, U, Th, and K have more than 10 times higher concentrations compared to NMORB. However, the andesitic and dacitic lavas show a stronger gradient from the most incompatible to less incompatible elements than the basaltic and basaltic-andesitic enclaves (Figure 4). This results in a cross-over pattern because the HREE concentrations in dacitic rocks are lower than in basaltic rocks.

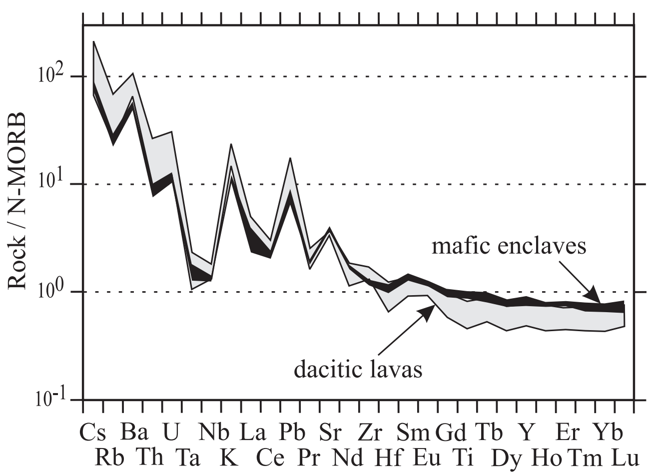

Figure 4. Trace element patterns for Kizimen lavas (gray field) and mafic enclaves (black field). All data are normalized to NMORB [after *Sun & McDonough*, 1989].

Sr- and Nd-isotope ratios for the three most mafic rocks are very close to each other ($^{87}Sr/^{86}Sr$: 0.703352 – 0.703370; $^{143}Nd/^{144}Nd$: 0.513045-0.513048). They fall within the range of Kamchatka rocks (i.e., where the fields for EVF, CKD and Sredinny Ridge of the back arc overlap; *Churikova et al.*, 2001a) and are close to the MORB-field.

Thus rocks of Kizimen volcano are represented by typical arc lavas of medium-K calc-alkaline series with strong but variable LILE and LREE enrichment and low HFSE. Mafic enclaves and evolved dacites show a REE cross-over patterns. In isotope space they are close to NMORB.

4.2. Zoning Trends in Plagioclase Phenocrysts From Kizimen Volcano

We studied the plagioclase phenocrysts from host lavas and its enclaves in three samples: a) dacite lava from the one of the summit flows (KIZ-07; 60.10 wt% SiO_2), b) a basaltic-andesite enclave in this lava flow (KIZ-07/1; 52.90 wt% SiO_2), and c) a mafic enclave from a second summit flow (KIZ-01/1; 49.70 wt% SiO_2; Table 1, Figure 1). All three samples were erupted during the current eruptive cycle [*Melekestsev et al.,* 1992], which began 3,000 years ago. Morphologically, three types of plagioclases were distinguished in all studied rocks.

Pl-1 occurs predominantly in mafic enclaves and less frequently in the host dacite. Pl-1 is characterized by euhedral shape and 20–50-micron-wide zones of growth (Figure 5a). The cores of these crystals sometimes have patchy textures (Figure 5a) or they are relatively homogeneous (not shown). Cores and mantles are compositionally uniform, whereas rims are characterized by steep compositional gradients.

Pl-2 crystals, found only in host dacitic lavas, show very narrow oscillatory zonation (5–50 μm) throughout. Pl-2 has usually numerous dissolution surfaces in the mantle zone, with subsequent regrowth (Figure 6a). The outermost zones are very narrow (5–10 μm).

Pl-3 crystals were observed in both mafic enclaves and in host dacite. It has subhedral to irregular shapes. Pl-3 crystals have continuous (from tens to first hundreds of microns) sieved zones. In some grains such zones make up more than 50% of the crystal. However, the outermost rims of these crystals are well formed and show clear contact with groundmass (Figures 5b, 6b). The cores of Pl-3 crystals show numerous narrow growth zones that are texturally similar to the Pl-2 phenocrysts from the dacitic lavas. We analyzed different zones in 2 grains of Pl-1, in 2 grains of Pl-2 and in 2 grains of Pl-3 (1 from enclave and 1 from host lava) for major (Al, Si, Na, Ca, K), minor (Fe) and trace (Sr, Ba, Mg) elements. Point measurements were taken along profiles from core to rim with spot size 2–5 μm (Figures 5 and 6; Table 2).

4.2.1. Pl-1 in mafic enclaves. Pl-1 phenocrysts from basalt and basaltic andesite enclaves are characterized by the absence of any significant zoning in their cores (Figure 5a), which composition is the most calcic found in Kizimen rocks (An_{86}-An_{93}, see insert in Figure 5a). These cores sometimes have partly sieved texture (Figure 5a) and include hornblende and patches of more sodic plagioclase (An_{77}, see points 6 and 7 on the Figure 5a). The mantle zone between core and rim is close in composition to the core (An_{77}-An_{93}). Cores and their mantles are low in Ba (< 50 ppm) and moderately high in Sr (300 – 550 ppm). Fe and Mg concentrations are high (up to 5000 ppm and 300 – 500 ppm, respectively).

Rims of Pl-1 are very different from the cores and mantle zones. The thickness of the outer rims varies from several microns to 100 microns. Composition of the rims is more sodic (An_{74-36}) than the inner parts of the grains, and An content decreases outwards. Sr and Ba concentrations in the rim increase to 900 ppm and 500 ppm, respectively, whereas Fe and Mg decrease to 2800 ppm and 200 ppm, respectively (Figure 5a). Plagioclase microlites in the enclaves are similar in composition to rims of Pl-1.

4.2.2. Pl-2 in dacitic lavas are relatively large in size (up to 2 cm, Figures 2b, 6a) and characterized by narrow oscillatory zonation. In contrast to Pl-1 from the enclaves, the cores and mantle zones of Pl-2 are rather sodic (An_{40} – An_{50}) and show higher Sr (500 – 750 ppm) and Ba (150–300 ppm) concentrations and lower Fe (1500–2000 ppm) and Mg (100–150 ppm). Because elemental concentrations change so strongly from one growth zone to another, the zoning patterns of Pl-2 are much more variable compared to the Pl-1 phenocrysts from the mafic enclaves (Figure 6a). The thickness of the outermost rims is less than 50 microns. The rims differ in chemical composition from the cores and mantle zones of the crystals. However, in contrast to Pl-1, the rims of Pl-2 are enriched in anorthite component, Fe, and Mg and depleted in Ba and Sr (Figures 6a, 7) compared to the core and mantle zones. Microlites of the dacitic host are similar in chemical composition to the rim of Pl-2.

4.2.3. Pl-3 in dacitic lavas and mafic enclaves are surprisingly similar in crystal morphology and chemical composition. Three distinct growth zones are present in these grains: (I) oscillatory-zoned, compositionally uniform inner core, (II) a sieve-textured zone with a thickness from 50 up to 200 microns and (III) about 50-micron-wide outermost rim (Figures 5b, 6b). Cores of Pl-3 phenocrysts are similar in composition to cores of Pl-2 phenocrysts from dacitic lavas. They are low in An, Fe, and Mg at relatively high concentrations of Ba and Sr. In the sieve-

Table 1. Chemical composition and isotope data for whole rocks of the Kizimen volcano.

Sample	TAM-01	KIZ-01	KIZ-01/1[b]	KIZ-02	KIZ-04	KIZ-05	KIZ-07	KIZ-07/1	KIZ-08	KIZ-09
SiO_2	51.75[a]	64.11	50.23	62.63	62.14	57.10	60.43	53.28	58.13	63.88
TiO_2	0.84	0.58	1.23	0.65	0.68	0.90	0.77	1.11	0.94	0.62
Al_2O_3	15.87	16.30	19.04	16.60	17.73	17.54	16.96	18.48	17.25	16.25
Fe_2O_3	9.43	2.43	5.38	2.70	2.82	3.48	3.85	4.25	3.66	2.43
FeO	0.43	3.05	5.62	3.22	2.59	4.83	3.11	5.34	4.22	3.13
MnO	0.19	0.13	0.19	0.14	0.13	0.17	0.15	0.19	0.17	0.13
MgO	8.49	2.46	5.26	2.68	2.72	4.05	3.12	4.44	3.61	2.43
CaO	9.29	5.38	9.35	5.91	5.77	7.28	6.38	8.54	7.12	5.47
Na_2O	2.74	3.72	2.77	3.74	3.70	3.32	3.60	3.28	3.47	3.77
K_2O	0.73	1.67	0.77	1.58	1.52	1.16	1.47	0.90	1.26	1.74
P_2O_5	0.23	0.16	0.17	0.15	0.19	0.16	0.16	0.19	0.18	0.15
Total	100	100	100	100	100	100	100	100	100	100
Li	7.9	16.3	14.2			10.2				
Be	0.51	0.79	0.52			0.63				
Sc	31	15	26	17	15	21	18	26	24	15
V	221	114	300	137	146	208	163	250	199	115
Cr	481	17	15	16	26	10	12	11	19	13
Co	36	14	30	18	14	29	17	26	21	13
Ni	166	n.d.[c]	2	n.d.	1	7	n.d.	n.d.	n.d.	n.d.
Zn	79	55	79	61	57	68	63	74	65	55
Ga	15	16	17	16	15	17	15	18	16	15
Rb	15	38	14	34*	32*	26	31*	17*	25*	41*
Sr	380	319	370	328	318	330	320	368	325	304
Y	16	16	21	19*	15*	20	22*	24*	22*	18*
Zr	86	121	86	124	115	102	117	96	117	126
Nb	2.4	4.2	2.9	5.0*	6.0*	3.5	4.0*	3.0*	4.0*	4.0*
Cs	0.50	1.50	0.52			0.47				
Ba	358	676	310	593	608	458	567	376	451	655
La	7.62	10.16	5.85			7.73				
Ce	19.02	22.39	15.18			19.37				
Pr	2.69	3.32	2.34			2.76				
Nd	13.10	13.54	11.99			12.79				
Sm	3.72	2.89	3.36			3.23				
Eu	1.11	0.95	1.14			1.04				
Gd	3.29	2.58	3.28			2.97				
Tb	0.52	0.36	0.54			0.44				
Dy	3.38	2.28	3.33			2.94				
Ho	0.67	0.55	0.74			0.65				
Er	2.06	1.46	2.18			1.85				
Tm	0.32	0.20	0.30			0.26				
Yb	2.05	1.39	2.00			1.72				
Lu	0.31	0.24	0.29			0.28				
Hf	2.27	1.91	1.99			1.88				
Ta	0.19	0.21	0.17			0.17				
Tl	0.03	0.27	0.10			0.10				
Pb	2.15	5.30	1.95			3.01				
Th	0.91	3.19	1.02			1.42				
U	0.45	1.45	0.49			0.79				
$^{87}Sr/^{86}Sr$			0.703352							
$^{143}Nd/^{144}Nd$			0.513045							
$^{206}Pb/^{204}Pb$										
$^{208}Pb/^{204}Pb$										
$^{207}Pb/^{204}Pb$										

[a]Major elements, Sc, V, Cr, Co, Ni, Zn, Ga, Sr, Zr, Ba and elements marked by stars were determined by XRF analyses, other trace elements were achieved by ICP-MS. Major elements are given in weight percent, trace elements in ppm.
[b]Samples KIZ-01/1, KIZ-07/1 and KIZ-24/1 are mafic enclaves in lavas KIZ-01, KIZ-07 and KIZ-24, respectively.
[c]Not detected

Table 1. (continued).

Sample	KIZ-11	KIZ-17/2[d]	KIZ-18	KIZ-19	KIZ-21	KIZ-22	KIZ-23	KIZ-24	KIZ-24/1
SiO_2	56.07	57.72	62.30	51.53	56.72	62.40	64.26	55.43	52.28
TiO_2	0.98	0.85	0.68	1.23	1.10	0.65	0.59	1.04	1.30
Al_2O_3	17.73	17.32	16.69	16.90	17.63	16.84	16.31	17.67	18.15
Fe_2O_3	2.92	2.78	2.49	3.04	3.21	3.14	2.63	3.11	4.35
FeO	5.56	4.88	3.56	8.21	5.08	2.96	2.77	5.56	5.86
MnO	0.17	0.17	0.14	0.22	0.18	0.13	0.13	0.17	0.19
MgO	4.19	4.17	2.75	5.35	3.12	2.91	2.39	4.22	4.48
CaO	7.75	7.29	5.91	9.82	7.54	5.81	5.37	8.29	9.25
Na_2O	3.32	3.35	3.80	2.77	3.75	3.57	3.73	3.22	3.07
K_2O	1.15	1.29	1.54	0.73	1.40	1.43	1.68	1.11	0.88
P_2O_5	0.17	0.18	0.15	0.22	0.27	0.16	0.15	0.17	0.19
Total	100	100	100	100	100	100	100	100	100
Li				3.8				8.5	11.7
Be				0.44				0.56	0.56
Sc	21	22	18	35	26	16	13	22	33
V	220	190	133	316	187	130	108	246	324
Cr	16	47	20	42	11	34	19	24	21
Co	27	20	21	37	20	14	13	27	27
Ni	6	20	1	25	n.d.	8	2	2	n.d.
Zn	71	76	58	94	83	60	57	72	80
Ga	16	17	16	18	19	15	15	19	17
Rb	24*	28*	33*	9	15*	30*	36*	21	16
Sr	332	359	324	276	299	341	320	328	335
Y	23*	24*	20*	32	34*	15*	19*	20	23
Zr	98	124	124	104	140	109	124	99	90
Nb	4.0*	4.0*	3.0*	4.1	6.0*	3.0*	4.0*	3.1	3.2
Cs				0.31				0.79	0.59
Ba	459	466	606	164	200	591	669	419	323
La				6.49				6.52	7.02
Ce				19.11				16.57	18.10
Pr				2.73				2.83	2.59
Nd				13.11				12.73	13.08
Sm				3.86				3.25	3.91
Eu				1.14				1.08	1.27
Gd				4.04				3.12	3.53
Tb				0.70				0.47	0.63
Dy				4.37				3.08	3.88
Ho				0.94				0.76	0.75
Er				2.89				1.97	2.23
Tm				0.42				0.27	0.34
Yb				2.77				1.72	2.38
Lu				0.42				0.30	0.32
Hf				2.80				2.10	2.17
Ta				0.21				0.14	0.19
Tl				0.05				0.09	0.10
Pb				2.03				2.73	2.63
Th				0.59				1.57	0.91
U				0.38				0.77	0.61
$^{87}Sr/^{86}Sr$								0.703347	0.703370
$^{143}Nd/^{144}Nd$								0.513048	0.513047
$^{206}Pb/^{204}Pb$									18.32
$^{208}Pb/^{204}Pb$									38.03
$^{207}Pb/^{204}Pb$									15.50

[d]Samples KIZ-17/2, KIZ-19, KIZ-21 and KIZ-22 are from old volcano basement, other samples are Quaternary age.

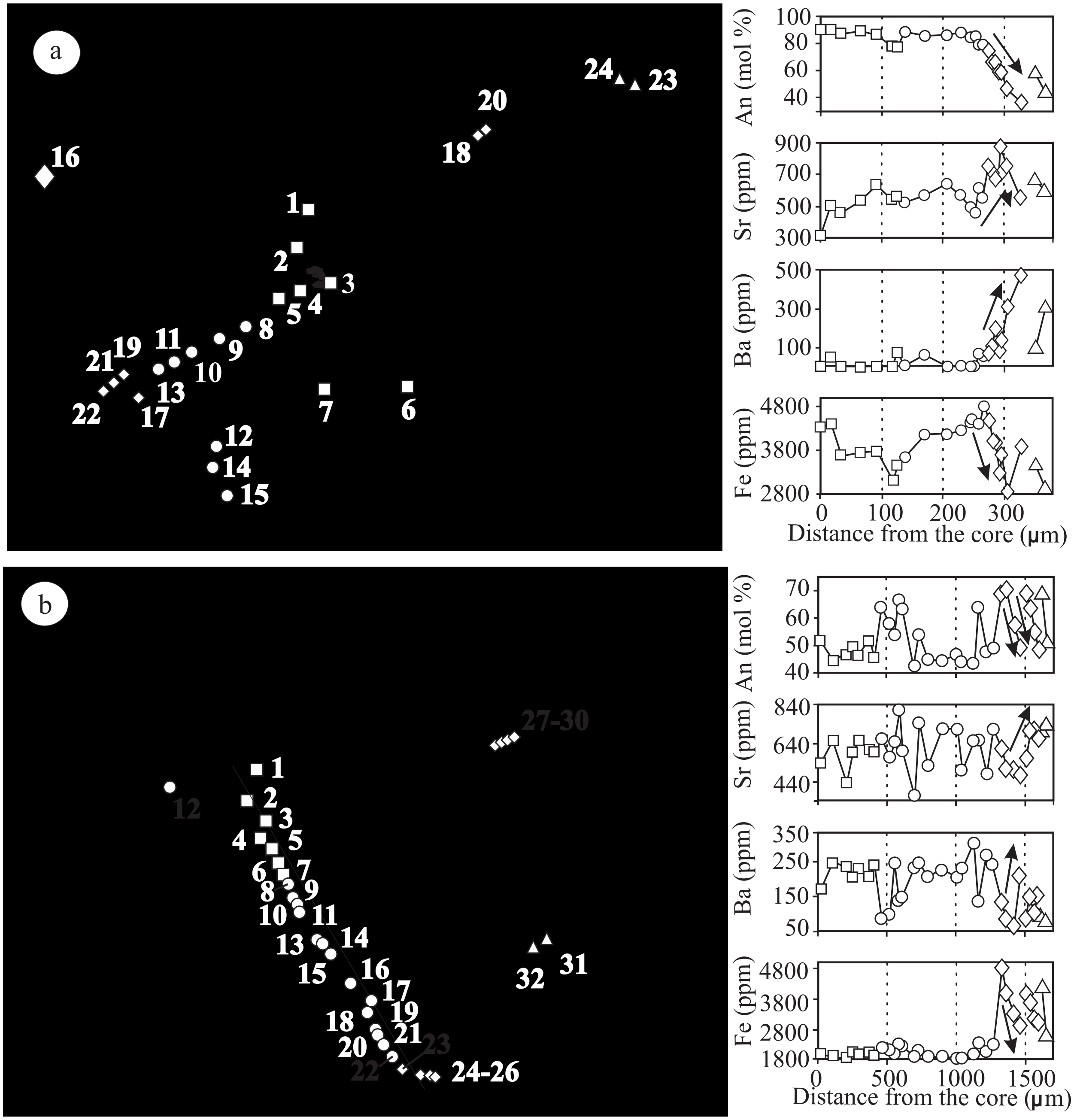

Figure 5. Electron microprobe traverses across plagioclase phenocrysts from a representative basaltic enclave. (a) unresorbed plagioclase and (b) resorbed plagioclase. Compositional profiles are shown in mol. % for An content and in ppm for Sr, Ba, and Fe concentrations. The abrupt in chemical composition near the crystal margins is indicated by arrows. Squares are data from the crystal cores, circles from the mantle, diamonds represent the rim and triangles are for microlites.

textured zone the plagioclase composition becomes more calcic up to An_{80}, whereas concentrations of Fe and Mg increase up to 5000 ppm and 550 ppm, respectively, and Sr and Ba values decrease. The rim zone Pl-3 is more sodic than the sieve-textured zone, but not quite as Ab-rich as the core. Microlites near Pl-2 phenocrysts are similar in chemical composition to zones II and III of Pl-3 (inset Figures 5b, 6b).

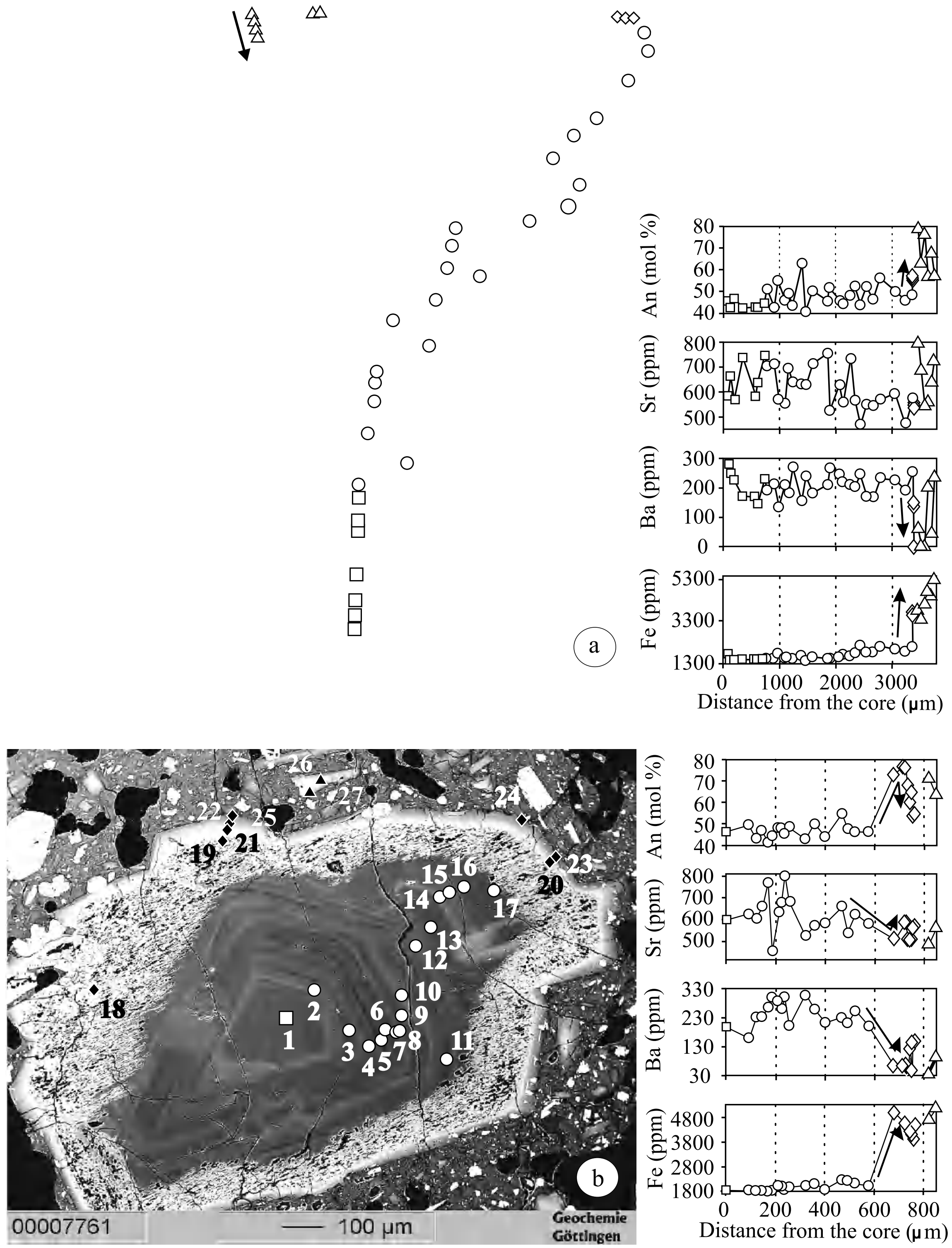

Figure 6. Electron microprobe traverses across plagioclase phenocrysts from typical dacitic lava: (a) unresolved plagioclase PI-2 and (b) resorbed plagioclase PI-3. Symbols are the same as in Figure 5.

Table 2. Microprobe analyses of the plagioclase phenocrysts from the Kizimen volcano (Kamchatka).

Description	S[a], μm	Na_2O	SiO_2	K_2O	Al_2O_3	CaO	Total	Fe	Ti	Sr	Mg	Ba	An
					Pl 1 from enclave KIZ-07/1 (Fig. 5a)								
core	0	1.10[b]	43.91	0.02	34.56	18.26	98	4330	150	313	295	n.d.[c]	90.1
core	16	1.09	45.29	0.02	35.12	17.83	99	4400	102	507	314	50	89.9
core	33	1.40	45.91	0.02	34.67	17.27	99	3669	84	456	362	n.d.	87.1
core	66	1.18	45.22	0.02	34.77	17.48	99	3747	96	532	320	n.d.	89.0
core	92	1.53	46.38	0.03	34.73	17.26	100	3778	84	634	362	n.d.	86.0
mantle	118	2.54	47.83	0.03	32.92	15.60	99	3109	60	541	392	n.d.	77.1
mantle	125	2.48	48.10	0.07	32.62	15.55	99	3459	120	558	531	71	77.3
mantle	138	1.25	45.47	0.01	34.90	17.56	99	3661	96	524	368	n.d.	88.5
mantle	170	1.59	46.34	0.02	34.20	17.14	99	4159	120	566	482	64	85.5
mantle	207	1.46	46.04	0.03	34.22	17.21	99	4190	102	642	440	n.d.	86.5
mantle	230	1.32	45.94	0.03	34.48	17.58	99	4236	60	566	398	n.d.	87.9
mantle	246	1.77	46.46	0.02	33.93	17.02	99	4462	156	490	482	n.d.	84.0
mantle	252	1.60	46.16	0.03	34.25	17.15	99	4516	132	456	434	n.d.	85.4
mantle	259	2.31	48.00	0.05	33.32	15.69	99	4407	150	608	519	64	78.7
mantle	266	2.22	47.68	0.04	33.13	15.95	99	4827	186	549	501	50	79.7
rim	275	2.91	49.12	0.06	32.24	14.66	99	4485	174	752	501	64	73.3
rim	282	3.62	50.84	0.09	31.04	13.37	99	3980	186	718	464	106	66.7
rim	285	3.64	51.31	0.09	31.13	13.53	100	3980	180	676	476	199	67.0
rim	292	4.59	53.37	0.11	29.61	11.57	99	3257	198	701	332	78	57.8
rim	295	4.49	53.28	0.13	29.94	12.12	100	3700	204	879	386	135	59.4
rim	305	5.92	56.29	0.18	27.69	9.36	99	2829	126	752	211	312	46.2
rim	328	6.94	58.83	0.31	25.47	7.44	99	3879	228	549	229	483	36.5
M[d], core	351	4.55	53.40	0.11	29.49	11.69	99	3459	198	667	344	99	58.3
M, rim	367	6.16	57.05	0.23	26.70	8.88	99	2923	144	600	241	312	43.7
					Pl 1 from enclave KIZ-01/1								
core	7	1.47	46.19	0.03	35.02	17.21	100	3008	n.d.	1436	308	n.d.	92.0
core	33	2.24	48.13	0.05	33.50	15.90	100	2907	n.d.	1808	362	92	87.4
core	43	1.38	46.20	0.03	34.85	17.29	100	3568	84	1301	332	50	92.5
core	63	2.36	48.53	0.05	33.40	15.83	100	3000	n.d.	1402	398	163	86.8
mantle	130	1.63	45.44	0.04	33.33	17.12	98	4524	138	414	669	n.d.	85.1
mantle	150	1.66	46.93	0.03	34.20	17.07	100	4081	132	482	416	n.d.	91.0
mantle	190	1.80	47.09	0.03	34.20	16.85	100	4602	132	431	476	71	90.2
mantle	207	2.09	47.78	0.04	33.75	16.44	100	4151	174	439	482	n.d.	88.5
mantle	227	1.46	46.47	0.03	34.50	17.34	100	4477	108	456	428	99	92.1
mantle	263	1.19	45.88	0.03	35.04	17.73	100	4415	102	431	356	64	93.6
mantle	307	1.25	45.99	0.03	34.82	17.57	100	4547	96	532	368	99	93.2
mantle	320	1.84	47.32	0.04	34.07	16.68	100	4508	108	684	398	n.d.	89.9
rim1[e]	327	4.12	52.77	0.10	30.60	12.56	100	3801	156	684	350	64	74.8
rim1	333	6.04	57.07	0.21	27.32	9.26	100	3801	174	591	302	199	59.7
rim2	343	1.94	47.42	0.04	33.79	16.47	100	4858	156	482	416	43	89.3
rim2	353	3.14	50.45	0.08	31.79	14.15	100	5278	204	541	482	71	81.5
M, core	363	3.92	52.03	0.09	30.80	12.71	100	3832	126	718	398	92	76.0
M, rim	373	6.01	57.45	0.24	27.26	9.09	100	3335	168	727	247	199	59.2
					Pl 2 from dacitic lava KIZ-07 (Fig. 6a)								
core	92	6.14	55.92	0.30	26.54	8.83	98	1702	n.d.	591	109	284	43.5
core	127	6.45	58.37	0.31	26.80	8.36	100	1438	n.d.	667	109	248	41.0
core	196	6.53	58.57	0.29	26.91	8.32	101	1415	n.d.	574	60	227	45.6
core	346	6.01	57.17	0.25	27.51	9.36	100	1477	60	743	96	170	40.6
core	577	6.39	58.28	0.31	26.68	8.47	100	1485	n.d.	591	103	170	41.5
core	612	6.19	58.25	0.31	26.80	8.49	100	1461	60	642	72	149	42.3
core	738	6.23	58.00	0.29	27.15	8.99	101	1516	60	752	78	234	43.6
mantle	773	5.46	56.04	0.21	28.50	10.09	100	1531	n.d.	710	84	192	49.9
mantle	900	6.49	58.34	0.30	26.86	8.51	100	1524	54	718	84	213	41.3
mantle	981	5.05	54.73	0.20	29.28	11.03	100	1733	n.d.	574	90	135	54.0
mantle	1096	6.01	57.91	0.28	27.26	8.93	100	1524	60	558	84	213	44.3
mantle	1154	5.68	56.52	0.23	28.17	9.85	100	1586	n.d.	701	115	185	48.3
mantle	1235	6.32	58.15	0.34	26.76	8.55	100	1508	54	642	115	270	41.9

Table 2. (continued)

Description	S[a], µm	Na_2O	SiO_2	K_2O	Al_2O_3	CaO	Total	Fe	Ti	Sr	Mg	Ba	An
mantle	1396	4.11	52.75	0.12	30.76	12.66	100	1663	60	634	103	156	62.6
mantle	1465	6.72	59.10	0.32	26.45	8.05	101	1399	n.d.	634	66	241	39.1
mantle	1592	5.49	56.64	0.25	28.09	9.89	100	1601	n.d.	718	84	185	49.2
mantle	1858	6.06	57.74	0.27	27.20	8.90	100	1531	60	760	90	213	44.1
mantle	1892	5.42	56.00	0.21	28.36	10.25	100	1555	n.d.	532	78	270	50.5
mantle	2065	6.10	57.73	0.31	27.44	9.01	101	1586	60	634	84	248	44.1
mantle	2135	6.29	57.89	0.30	27.16	8.79	100	1726	60	558	90	220	42.8
mantle	2262	5.87	56.48	0.24	28.07	9.75	100	1640	60	743	72	213	47.2
mantle	2342	5.28	55.42	0.20	28.75	10.43	100	1788	66	574	109	206	51.6
mantle	2435	6.31	58.29	0.28	27.20	8.66	101	2169	60	473	96	248	42.4
mantle	2550	5.29	55.47	0.20	28.62	10.36	100	1819	54	558	115	170	51.4
mantle	2665	6.01	57.61	0.28	27.47	9.08	100	1834	n.d.	549	115	170	44.7
mantle	2792	4.92	54.59	0.20	29.44	11.21	100	2130	60	574	139	234	55.1
mantle	3058	5.57	56.24	0.23	28.11	9.89	100	1959	66	600	109	227	48.8
mantle	3242	5.96	57.48	0.28	27.37	9.14	100	1881	n.d.	473	109	192	45.1
mantle	3369	5.70	56.94	0.24	27.83	9.50	100	2091	78	574	115	255	47.2
rim	3370	4.98	54.92	0.20	28.80	11.19	100	3630	138	574	308	149	54.7
rim	3381	4.97	55.08	0.19	28.84	10.99	100	3653	120	549	332	n.d.	54.4
rim	3382	5.04	54.87	0.20	28.86	10.97	100	3599	102	558	308	135	53.9
M1, core	3462	2.38	48.45	0.04	33.49	15.84	100	3840	156	803	295	64	78.4
M1, mantle	3519	4.16	52.89	0.10	30.41	12.59	100	3428	162	693	368	n.d.	62.2
M1, mantle	3577	2.69	49.42	0.06	32.77	15.37	100	4174	138	549	452	n.d.	75.7
M1, rim	3635	4.82	54.55	0.17	29.20	11.28	100	4773	276	566	476	206	55.8
M2, core	3692	3.65	51.39	0.08	31.27	13.49	100	4524	210	651	513	50	66.8
M2, rim	3750	4.69	54.37	0.18	29.26	11.43	100	5402	312	735	488	241	56.8
					Pl 2 from dacitic lava KIZ-07								
core	21	5.83	56.38	0.26	27.27	9.40	99	2021	60	583	115	213	46.4
core	75	5.77	56.51	0.22	27.68	9.66	100	1912	60	465	84	241	47.4
core	139	5.74	56.84	0.25	27.77	9.50	100	2060	54	651	127	263	47.1
core	204	5.38	55.99	0.21	28.42	10.17	100	1974	54	667	90	142	50.5
core	268	5.74	56.84	0.24	27.76	9.51	100	1990	60	634	133	284	47.1
core	439	5.89	57.18	0.26	27.57	9.36	100	2083	n.d.	498	133	156	46.0
core	450	5.81	57.28	0.25	27.68	9.38	100	1998	60	456	103	227	46.4
mantle	514	4.56	53.75	0.18	29.72	11.68	100	2223	78	566	96	78	58.0
mantle	525	4.96	54.64	0.19	29.16	11.02	100	2215	84	574	121	185	54.5
mantle	611	4.67	53.87	0.17	29.85	11.65	100	2239	78	507	96	206	57.4
mantle	621	5.65	57.07	0.25	27.81	9.39	100	2052	60	549	109	241	47.2
mantle	686	5.84	56.99	0.24	27.70	9.47	100	1982	54	693	90	220	46.6
mantle	750	4.35	52.77	0.13	30.61	12.48	100	2417	78	532	127	106	60.9
mantle	761	5.30	55.41	0.23	28.58	10.46	100	2573	108	558	362	121	51.5
mantle	782	3.32	50.94	0.10	31.81	13.79	100	2565	84	558	133	57	69.2
mantle	793	3.23	50.87	0.09	31.92	14.10	100	2557	78	659	121	106	70.3
mantle	804	5.82	56.91	0.23	27.85	9.59	100	2005	60	515	109	170	47.0
mantle	814	5.27	55.46	0.21	28.76	10.48	100	2083	60	659	115	234	51.7
mantle	825	4.18	52.71	0.13	30.72	12.52	100	2557	78	524	133	106	61.9
mantle	836	5.03	55.12	0.21	28.70	10.63	100	2394	108	549	181	177	53.2
mantle	846	5.70	56.91	0.24	27.93	9.67	100	2091	66	482	133	170	47.7
mantle	932	5.98	57.05	0.25	27.80	9.30	100	2130	54	566	133	220	45.5
rim1	996	4.43	53.19	0.17	29.95	12.02	100	3762	102	414	344	85	59.4
rim1	1018	5.35	55.75	0.22	28.31	10.49	100	3723	174	642	308	177	51.3
rim2	1039	5.75	56.80	0.25	27.86	9.49	100	2371	66	727	175	177	47.0
rim2	1058	3.76	51.72	0.13	30.87	13.22	100	3078	132	887	163	106	65.5
rim2	1075	2.98	50.16	0.08	32.42	14.57	100	2892	96	490	127	99	72.6
rim2	1093	5.08	54.64	0.20	28.97	11.00	100	3692	138	634	332	291	53.9
M1, core	1125	2.58	49.10	0.05	32.83	15.28	100	4470	186	574	513	n.d.	76.4
M1, rim	1157	5.05	54.89	0.16	28.94	11.07	100	3817	192	701	362	213	54.3
M2, core	1179	4.29	53.55	0.15	29.92	12.12	100	4050	174	718	380	121	60.4
M2, rim	1200	5.10	55.18	0.20	28.69	10.75	100	3716	162	684	302	206	53.2

Table 2. (continued)

Description	S[a], μm	Na_2O	SiO_2	K_2O	Al_2O_3	CaO	Total	Fe	Ti	Sr	Mg	Ba	An
Pl 3 from enclave KIZ-07/1 (Fig. 5b)													
core	22	5.27	55.34	0.21	28.53	10.49	100	2013	114	541	133	170	51.7
core	111	6.07	57.02	0.29	27.17	9.07	100	1897	n.d.	659	109	248	44.5
core	211	5.91	56.45	0.23	27.60	9.60	100	1866	n.d.	431	103	234	46.7
core	256	5.57	55.06	0.23	28.28	10.09	99	2060	60	600	96	206	49.3
core	300	5.85	56.58	0.27	27.32	9.35	99	1974	66	659	103	227	46.2
core	378	5.24	54.85	0.20	28.50	10.60	99	2021	54	608	115	206	52.2
core	411	5.95	56.90	0.25	27.25	9.06	99	1936	48	591	103	241	45.0
mantle	467	3.88	51.64	0.12	30.78	12.83	99	2200	102	667	90	85	64.1
mantle	522	4.58	53.18	0.16	29.79	11.68	99	2114	60	566	115	99	58.0
mantle	556	5.00	54.55	0.18	29.04	10.78	100	1982	78	651	115	248	53.8
mantle	589	3.61	50.99	0.12	31.20	13.27	99	2332	66	819	121	142	66.6
mantle	611	3.96	51.57	0.14	30.85	12.82	99	2223	54	600	139	149	63.6
mantle	700	6.28	57.46	0.29	26.69	8.59	99	1904	78	363	121	234	42.4
mantle	733	4.95	54.60	0.20	28.92	10.91	100	2107	60	752	109	248	54.3
mantle	800	6.00	56.85	0.27	27.32	9.10	100	1912	54	524	115	206	44.9
mantle	900	6.10	57.05	0.26	27.43	9.05	100	1904	60	718	96	227	44.4
mantle	1011	5.74	56.43	0.27	27.52	9.41	99	1866	54	718	109	206	46.8
mantle	1044	6.24	57.10	0.27	27.05	8.94	100	1858	60	498	115	227	43.5
mantle	1133	6.04	57.25	0.29	26.95	8.67	99	2005	54	659	90	305	43.4
mantle	1167	3.94	51.42	0.13	30.88	13.07	99	2379	108	659	121	135	64.2
mantle	1222	5.66	56.59	0.25	27.73	9.46	100	2060	60	482	127	270	47.3
mantle	1267	5.55	55.72	0.23	28.08	9.94	100	2262	60	718	103	241	49.1
R[f]	1333	3.20	51.52	0.24	30.75	13.35	99	4843	246	617	416	135	68.7
R	1367	3.27	50.43	0.07	31.81	14.14	100	3957	156	507	458	85	70.2
rim1	1422	4.69	53.63	0.13	29.81	11.56	100	3327	180	507	295	57	57.2
rim1	1467	5.62	55.69	0.16	28.04	9.87	99	2930	102	473	235	213	48.8
rim2	1511	3.35	50.36	0.09	31.68	13.98	99	3941	132	566	464	85	69.4
rim2	1541	4.02	52.29	0.09	30.44	12.69	100	3653	204	710	380	149	63.2
rim2	1570	4.94	54.44	0.13	29.13	11.02	100	3148	162	710	283	106	54.8
rim2	1600	5.60	56.68	0.17	28.07	9.74	100	3039	132	667	235	156	48.5
M, core	1622	3.39	50.62	0.08	31.41	14.10	100	4198	180	710	513	92	69.4
M, rim	1656	5.50	55.24	0.16	28.78	10.55	100	2604	162	743	235	78	51.0
Pl 3 from dacitic lava KIZ-07 (Fig. 6b)													
core	0	5.92	56.94	0.26	27.90	9.63	101	1850	n.d.	600	103	199	46.6
mantle	91	5.52	56.05	0.23	28.37	10.16	100	1842	78	625	121	163	49.8
mantle	121	6.12	57.89	0.30	27.08	8.79	100	1850	60	608	103	234	43.4
mantle	145	5.85	56.61	0.25	28.05	9.74	100	1858	72	659	109	234	47.2
mantle	170	6.43	58.55	0.32	26.67	8.48	100	1827	60	769	103	270	41.4
mantle	188	5.94	57.81	0.28	27.55	9.01	101	1873	n.d.	456	103	305	44.9
mantle	212	5.77	56.40	0.22	28.25	9.96	101	2037	n.d.	634	115	291	48.2
mantle	224	5.72	56.33	0.22	28.28	9.90	100	2013	n.d.	676	115	263	48.3
mantle	236	5.98	57.20	0.25	27.69	9.26	100	1873	102	803	96	305	45.4
mantle	255	5.47	56.68	0.24	28.02	9.69	100	1967	90	684	90	206	48.7
mantle	321	6.15	57.94	0.28	27.21	8.76	100	2044	60	524	96	312	43.3
mantle	358	5.46	55.60	0.22	28.50	10.27	100	2107	72	574	115	263	50.3
mantle	400	6.09	57.59	0.29	27.23	8.99	100	1881	60	583	103	213	44.1
mantle	467	4.93	54.68	0.18	29.47	11.20	100	2278	72	659	133	234	55.1
mantle	491	5.75	56.68	0.23	28.02	9.86	101	2231	78	541	109	213	48.0
mantle	521	5.95	56.89	0.25	27.76	9.62	100	2122	108	625	109	255	46.5
mantle	576	5.89	56.92	0.27	27.79	9.60	100	2044	96	583	127	206	46.7
R	679	2.80	49.65	0.15	31.79	14.31	99	4998	216	507	470	64	73.1
rim	721	2.52	48.81	0.06	32.71	15.41	100	4578	186	583	549	64	76.9
rim	727	2.58	48.99	0.07	32.74	15.41	100	4485	132	591	494	71	76.5
rim	733	3.52	51.08	0.09	30.97	13.61	99	4415	162	507	458	50	67.7
rim	745	4.51	53.00	0.14	29.88	12.19	100	4205	192	507	350	128	59.4
rim	752	3.84	52.03	0.11	30.68	13.15	100	4034	162	515	398	43	65.0
rim	758	5.06	55.16	0.19	28.57	10.88	100	3879	186	566	344	149	53.7

Table 2. (continued)

Description	S[a], μm	Na_2O	SiO_2	K_2O	Al_2O_3	CaO	Total	Fe	Ti	Sr	Mg	Ba	An
rim	764	5.05	55.03	0.18	28.64	10.91	100	4485	216	574	308	156	53.8
M, core	818	3.08	49.91	0.08	31.84	14.35	99	4749	180	490	537	43	71.7
M, rim	848	3.88	52.01	0.13	30.41	12.80	99	5200	306	566	555	99	64.1

[a] S - distance from the phenocryst core in microns.

[b] Major elements (Na_2O, SiO_2, K_2O, Al_2O_3 and CaO) are given in wt. %, minor and trace elements (Fe, Ti, Sr, Mg and Ba) - in ppm.

[c] n.d. - not detected.

[d] M - microlite. One or two plagioclase microlites were analysed near by each plagioclase phenocrysts – M1 and M2, respectively.

[e] Outer rims in some grains were measured at different edges of crystal – rim1 and rim2, respectively.

[f] R – resorption zone.

5. DISCUSSION

Kizimen rocks reveal many features commonly attributed to magma mixing: a) presence of olivine and orthopyroxene of constant composition (Fo_{79-72} and $En_{63-65}Wo_{1-2}$, respectively) in all rocks, independent of melt composition; b) coexistence of olivine and quartz; and c) coexistence of plagioclases with high-An core and low-An rims and with low-An cores at high-An rims. Mixing between silicic and mafic end-members is consistent with the observed linear trends on all two-component diagrams for this volcano (e.g. Figure 3). The abundance and size of enclaves in many lava flows as well as numerous banded lavas suggest that the mixing processes play an unusually profound role in magma genesis at Kizimen volcano.

If all Kizimen rocks from dacitic host lavas to mafic enclaves are indeed hybrids, the temporal trend for mafic enclaves on the SiO_2-K_2O diagram either suggests that magma chamber recharge is getting more mafic or that the proportion of the mafic end-member increases with time (Figure 3).

From Sr and Nd isotope data, which are very similar in all rocks and close to MORB values, there is not evidence for any crustal contamination.

Trace element patterns of variably differentiated magmas, which crystallized from the same parent should have sub-parallel patterns, where more evolved rocks are more enriched in all incompatible elements. This is valid however, only as long as olivine, clino- and orthopyroxene, plagioclase, and spinel (or magnetite) are the only crystallizing phases. This is because all of them have low partition coefficients for incompatible trace elements. Theoretically, the observed cross-over patterns could be explained as a result of magmas coming from different mantle sources. However, cross-over patterns on spider diagrams for the rocks of Bakening volcano were modeled by *Dorendorf et. al*. [2000b] as depletion of the dacitic magma in HREE by extensive hornblende fractionation from basaltic melt. We suggest that basalts and dacites of Kizimen volcano were also affected by a strong amphibole signature and thus originated from similar mantle melts. This is reasonable, because all lavas at Kizimen, including the mafic varieties, are rich in amphibole.

According to petrographical and geochemical data (Fo_{72-78} olivine, Mg# 41 to 50 of whole rocks, abundance of low-An plagioclase, and low Cr and Ni concentrations in whole rocks), mafic enclaves are already fractionated compared to primary mantle melts and are contaminated by incorporation of more evolved material, which may or may not be derived directly from the host. Similarly, the presence of high-An plagioclase and traces of olivine in Kizimen dacites suggest that the host lavas are contaminated by mafic debris from enclaves. Thus, both host and enclaves are hybrids formed by mixing of more extreme end-members.

Over the last decade it was shown that trace elements in zoned minerals are a useful tool to identify mixing end-members [e.g. *Brophy at al*., 1996; *Davidson and Tepley*, 1997; *Ginibre at al*., 2002a, 2002b]. Our discussion of mixing end-members and mixing events is based on trace element variations in plagioclase. The Mg and Fe content in plagioclase phenocrysts shows two trends when plotted against An (Figure 7). Cores of Pl-1 phenocrysts from mafic enclaves are highest in An (An_{75}-An_{94}), Mg (300–550 ppm) and Fe (2900–4600 ppm) compared to all other crystals. These high-An, high-Mg, and high-Fe plagioclases probably have grown in a relatively mafic source. Rare crystals of "mafic" plagioclases reveal some resorption in the core (Figure 5a), but the mantle zone and outer rim are never resorbed. This observation suggests that Pl-1 mainly crystallized from a relatively high-temperature melt and was not dissolved during the later mixing events before eruptions. Experimental values of Kd_{Mg} in plagioclase vary between 0.025 and 0.05 [e.g. *Bindeman et al*. 1998]. Using Kd_{Mg} of 0.035, the calculated MgO concentration in the most mafic melt is 3.17±0.5 wt%, which is of the same order as MgO concentration in whole rock composition of mafic enclaves (Table 1, samples KIZ-01/1; KIZ-07/1; KIZ-24/1). High-An plagioclases were found in all enclaves but only traces of Pl-1 were found in host lavas. Therefore, these feldspars are considered phenocrysts from a magma close to the mafic end-member.

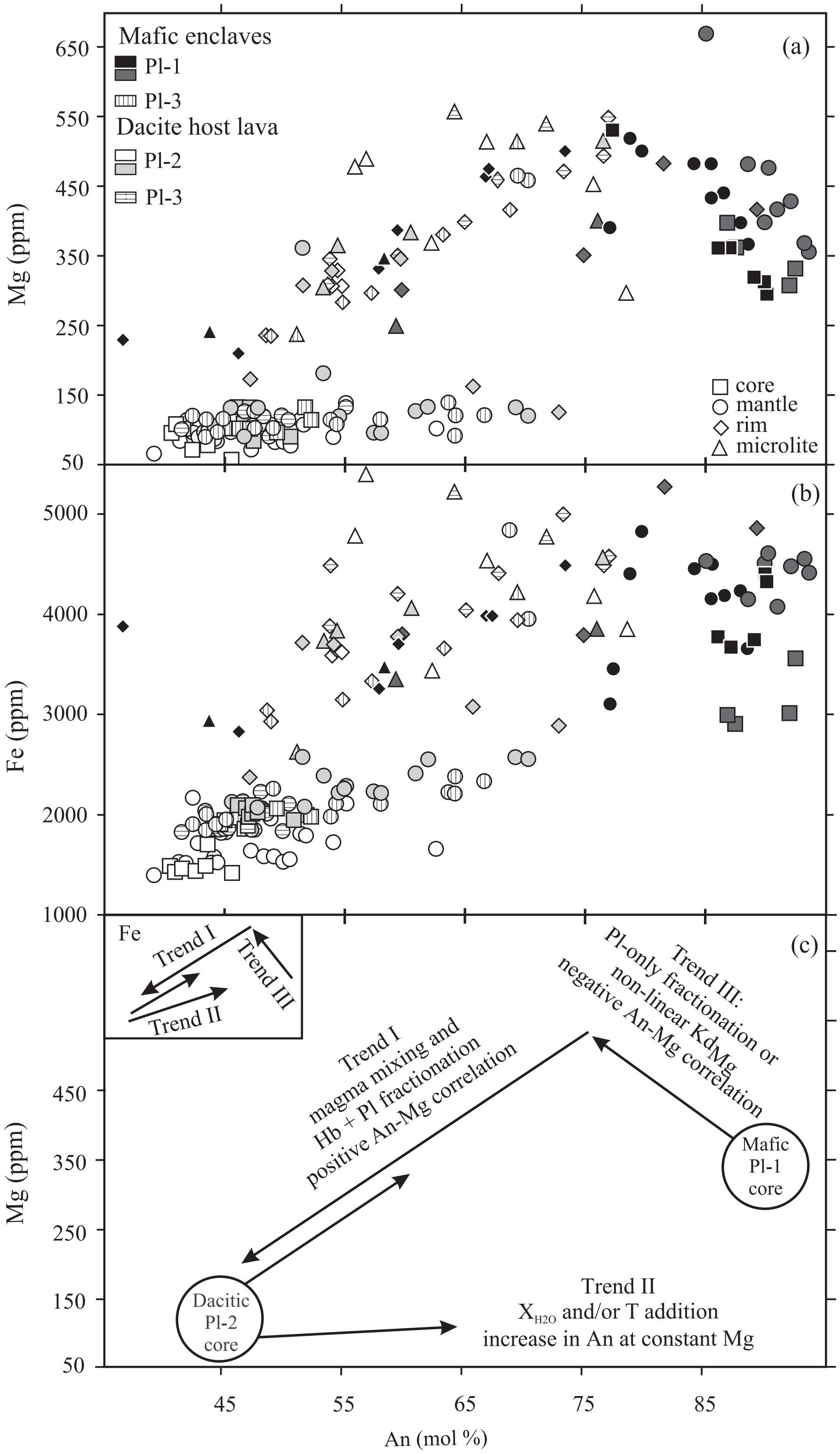

Figure 7. Mg (a) and Fe (b) variations with An-content in Kizimen plagioclase: squares – cores, circles – middle zones, diamonds – rims, triangles - microlites; (c) schematic evolution of the crystals. Arrows show direction of evolutionary trends from core to rim. See text for further explanation and discussion of the trends.

In contrast, the cores of Pl-2 from the host dacitic lava are lowest in An (An_{40}-An_{50}), Mg (50–100 ppm), and Fe (1500–2000 ppm). These low-An plagioclases probably formed in the evolved end-member, but are now found in both, the mafic enclave and the host dacite.

The sodic and low-Mg (and low-Fe) cores of the plagioclases Pl-3 from both mafic enclaves and host lavas are similar to Pl-2 from the host lavas (Figures 5b, 6, 7). Similarity of compositions of Pl-2 and Pl-3 suggests that all these crystals formed in the same relatively evolved melt.

Mantle zones and rims of plagioclases from enclave and lava show different histories. Pl-1 from enclaves displays a typical fractionation trend (Trend I in Figure 7c) with decreasing An and Mg content from core to rim. Mantles zones and rims from Pl-2 of the host lavas show two different trends. One falls on the differentiation trend I (correlated, outward decreasing An, Mg, and Fe). The second trend II, which is also represented in mantles and rims of sodic plagioclase (Pl-2 and all grains Pl-3) is characterized by increasing in An from core to rim at nearly constant Mg content and slightly increasing Fe content. Apparently, these two separate trends could be explained by two different processes. Trend I likely represents a differentiation trend overprinted by repeated mixing events between different members of the differentiation series. This is consistent with the reversals in An between core and rim (Figure 7c). Dissolution features near the rims of sodic plagioclases are then explained by mixing between more extreme melt compositions: low-temperature dacitic magma and high-temperature basaltic melt. This is consistent with the observation that this late-grown An-rich plagioclase rim is also characterized by high concentrations of Mg and low of Ba and Sr contents (for example, point 18, Figure 6b). Microlites then grew from the hybrid melt with compositions similar to the rims of these phenocrysts.

Crystals which grew from the basaltic high-temperature melt in mafic enclaves (Pl-1, Figure 5a) before incorporation of enclaves in the host dacite did not subsequently dissolve significantly. The abrupt change in chemical composition at their late-grown rims relative to their inner zones (decreasing An, Mg and Fe and increasing Ba and Sr, Figure 5a) also suggests a magma mixing processes just before or during eruption. The fact that these crystals are rather homogeneous in their cores with respect to An and minor and trace elements (Figure 5a) argues that they record a quiet growth environment in the mafic end-member magma before mixing.

Cores of the most sodic low-An plagioclases fall on the continuation of trend I (Figure 7) and are probably the result of mixing late in the differentiation process.

Trend II is more difficult to explain. It is characterized by repetitive cycles of increasing and decreasing An content, however, without correlated changes in Mg (or with slight increase in Fe) content. This observation excludes simple mixing of variably differentiated magmas to explain resorption and An variations (Figure 7b). It was shown that Kd_{Mg} in plagioclase varies within a very narrow range, and correlates weakly with T [*Longhi et al.,* 1976] and An content [*Bindeman et al*. 1998]. In the presence of hornblende and Opx crystallization and decreasing Mg (and Fe) in the melt, the effect of variable An on Mg (and Fe) partitioning is inconsistent with the observed constant Mg concentrations [see *Ginibre et al*., 2002b for a more detailed discussion of the An-dependent trace element partitioning in plagioclase]. This trend could then be caused by either increasing temperature and/or increasing water content in the melt. Low An content and concentrations of magnesium (and Fe) in these plagioclases indicate that the melt was certainly not more mafic. At increased temperature, the sodic plagioclase would dissolve in hotter melt and the new more An-rich plagioclase starts to grow. Consequently, variable An at constant Mg could reflect a thermal rather than a compositional disturbance of the host melt. An increase in temperature aided by incomplete mixing when heat from a high-temperature basaltic/basaltic-andesite magma is transported into the low-temperature host dacite by thermal conduction could occur without effect on trace elements in the melt and in crystallized plagioclase.

Alternatively, variable An at constant Mg may be expected when the water content in the melt increases. In this case, a single plagioclase phenocryst may have moved into (and out of) a water-rich boundary layer of the magma chamber [*Ginibre et al*., 2002a]. However such repeated movements of phenocrysts are less likely in the highly viscous dacite melt and therefore we favor the first scenario of "thermal" mixing.

Finally, an unusual behavior of Mg vs. An (less so for Fe) was found in Pl-1 grains from mafic enclaves: increasing Mg at decreasing An from cores to mantle (Trend III in Figure 7). Such Mg (and Fe) behavior was only observed in the highest-An zones of the crystals ($An_{75\text{-}95}$). Because trend for Mg are more pronounced compare to Fe (Figures 7a and 7b), our future discussion would be based on Mg content in plagioclases. Several scenarios are considered to explain this trend:

(1) The continuous replenishment of the magma chamber by a high-Mg melt. The existence of sieved textures in the core of some Pl-1 (Figure 5a) could suggest magma mixing events in the early stages of the plagioclase crystallization. However, negative correlations between An and Mg (and Fe) in plagioclase Pl-1 is observed along the core and mantle zone of the crystal. Also, continuous recharge would be expected to result in resorption and subsequent regrowth, which is not

observed in Pl-1 mantle. On the basis of these arguments, we rule out an origin from highly mafic magmas.

(2) Considering the linear relation between An and Mg partitioning in plagioclase [*Bindeman et al.,* 1998], the zoning could indicate an early phase of crystallization where plagioclase was the only phase. As a result, prior to the onset of olivine and pyroxene fractionation, the An content could decrease while Mg (and Fe) increases. This explanation was tested by a fractional crystallization model of a melt similar in composition to the most mafic end-member enclave (represented by a high-Al basalt KIZ-01/1, Table 1) based on the COMAGMAT program at 1% of H_2O and NNO buffer. The pressure in the model (125 MPa) was taken from petrological experiments [*Churikova et al*., 2001b; *B. Browne*, personal comm.], assuming that the magma chamber was not at a significantly different depth during melt evolution and later mixing.

As shown in Figure 8, the modeled compositions fall close to the observed magma compositions at Kizimen and are consistent with decreasing An in the plagioclase coupled with increasing Mg and Fe in the melt (Figure 8a, b, f) very early in the crystallization sequence. Thus, this model is consistent with Trend III. Observed olivine and pyroxene compositions are also reproduced well in the model: olivines and clinopyroxenes in mafic enclaves are $Fo_{79\text{-}75}$ and $En_{44}Fs_{16}Wo_{40}$ [see also *Trusov & Pletchov*, 2005], and modeled compositions are $Fo_{78,5\text{-}76}$ and $En_{43\text{-}46}Fs_{12\text{-}17}Wo_{40\text{-}42}$, respectively.

However, the most calcic plagioclase calculated in the model is at $An_{84\text{-}85}$, whereas inner parts of Pl-1 in basalt and basaltic andesite enclaves show values up to An_{93}. We would argue that this deviation between modeled and observed plagioclase compositions could be a result of the parameters chosen for the model, which may not be completely appropriate but cannot be better constrained. According to our calculations, Trend III (i.e. increasing Mg and Fe with decreasing An) could therefore be controlled by melt composition and Pl-only fractionation in the first stages of high-Al melt evolution.

We do not imply, however, that this melt was a primary magma. Low MgO (4–5%), Ni (less than 2 ppm), Cr (11–20 ppm) and relatively high K_2O (0,9%) suggest that all enclaves represent already fractionated compositions. The existence of resorbed cores inside of some grains of Pl-1 and the presence of numerous fine-grained basaltic inclusions (enclaves within enclaves) inside the mafic enclaves (Figure 2b) also suggest that the enclave's magma was itself affected by magma mixing events. The crystallization P-T conditions where plagioclase would crystallize first at suppressed Ol and Cpx crystallization are very limited, and according to our model would be possible in subsurface conditions from 1 to 3 Kbar (about 10 km). We believe that such scenario

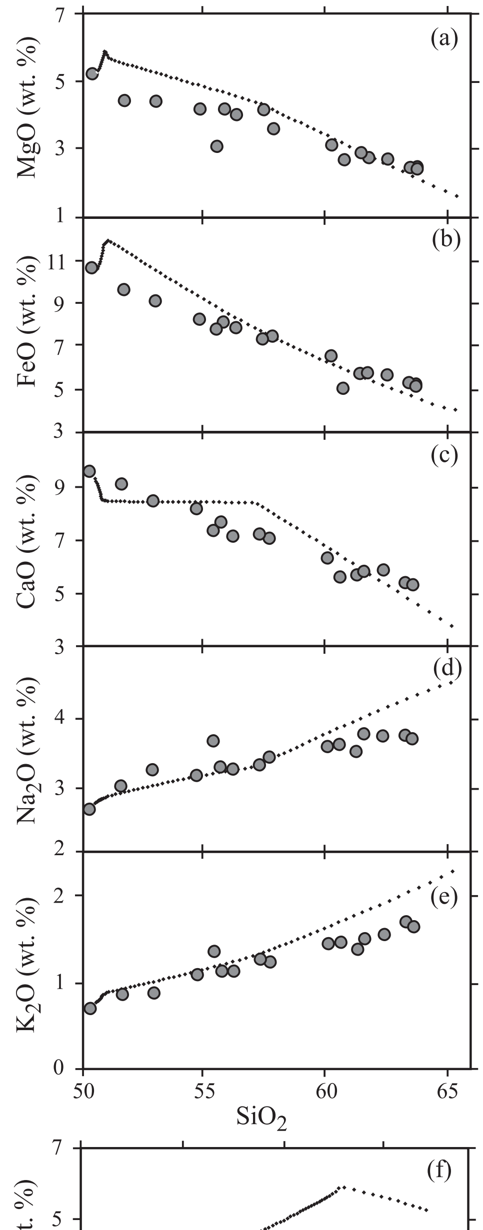

Figure 8. Model calculations (dotted line) of the fractional crystallization of basaltic magma from the Kizimen volcano (sample KIZ-96-01/1) in comparison with observed whole rock compositions (gray circles). Calculations were conducted using COMAGMAT program [*Ariskin et al*., 1993] for P=125Mpa, NNO buffer and H_2O=1%. Due to Pl fractionation during the first stage of crystallization the residual melt is enriched in MgO.

is possible at Kizimen volcano, but other alternatives are possible.

(3) An other explanation of the trend III is non-linear behavior of Kd_{Mg} in high-An plagioclases.

Sato [1989] noted that, due to kinetic disequilibrium, the distribution coefficients determined by the experiments may not represent the true equilibrium values and that as a result partitioning in experiments are significantly different from natural systems.

Experimentally determined Kd_{Mg} in plagioclase varies in a narrow range and is expected to be linear and almost independent from melt composition [e.g. *Bindeman et al.,* 1998]. In this case the positive correlation of An and Mg in plagioclases would be expected. In fact, positive correlation between An and Mg (and Fe) was observed for relatively sodic plagioclases from the Kizimen volcano (Figure 7c, Trend I). However, at An_{75-95} we clearly observe the negative correlation between An and Mg in plagioclases (Figure 7c, Trend III). From our point of view, this may testify to non-linear behavior of Kd_{Mg} (and Kd_{Fe}) in high-An plagioclases. We have a reason to claim that such participation of Mg (and Fe) in high-An plagioclases could be found not only at the complex Kizimen volcano, but also in more primitive systems.

McNeill and Danyushevsky [1996] studied the melt inclusions in minerals from MORB basalts from the Costa Rica Rift (Borehole 896A) where Ol, Cpx and Sp were first crystallized phases. According to their data An in plagioclases and MgO and FeO in the equilibrium melts have a positive correlations (Figures 9a, b drawn using data from Tables 3, 7 of *McNeill and Danyushevsky*, 1996). However, we could observe the trends of negative correlations An with MgO and FeO in all Ca-rich (An_{83-95}) plagioclases (Figure 9c, d, data from Table 3, *McNeill and Danyushevsky*, 1996).

We suggest that negative correlations between An and Mg (less to Fe) in high-An plagioclases at Kizimen could indeed be a function of non-linear behavior of Kd_{Mg}, for example, due to non-equilibrium processes in the Pl-melt system and not directly controlled by melt composition. To our knowledge, this effect has not been documented before and requires additional experimental work for an understanding of Kd_{Mg} and Kd_{Fe} in high-An plagioclases.

Figure 10 shows a schematic model of the magma system below Kizimen volcano, which summarizes our interpretations. Mafic magma (with high-An Pl-1) is introduced to the dacitic magma chamber (with sodic Pl-2) bringing the two magmas in direct contact. This process forms hybrids where two contrasting domains, the enclaves and host lava, show the effects of both chemical and physical mixing (Figure 2c). Pl-2 of bearing dacite, engulfed in mafic magma would be exposed to high temperature, resulting in plagioclase dissolution and transition of Pl-2 in Pl-3. The newly hybrid melt around this plagioclase would be more mafic, resulting in more calcic rims on the resorbed sodic mantle zones of

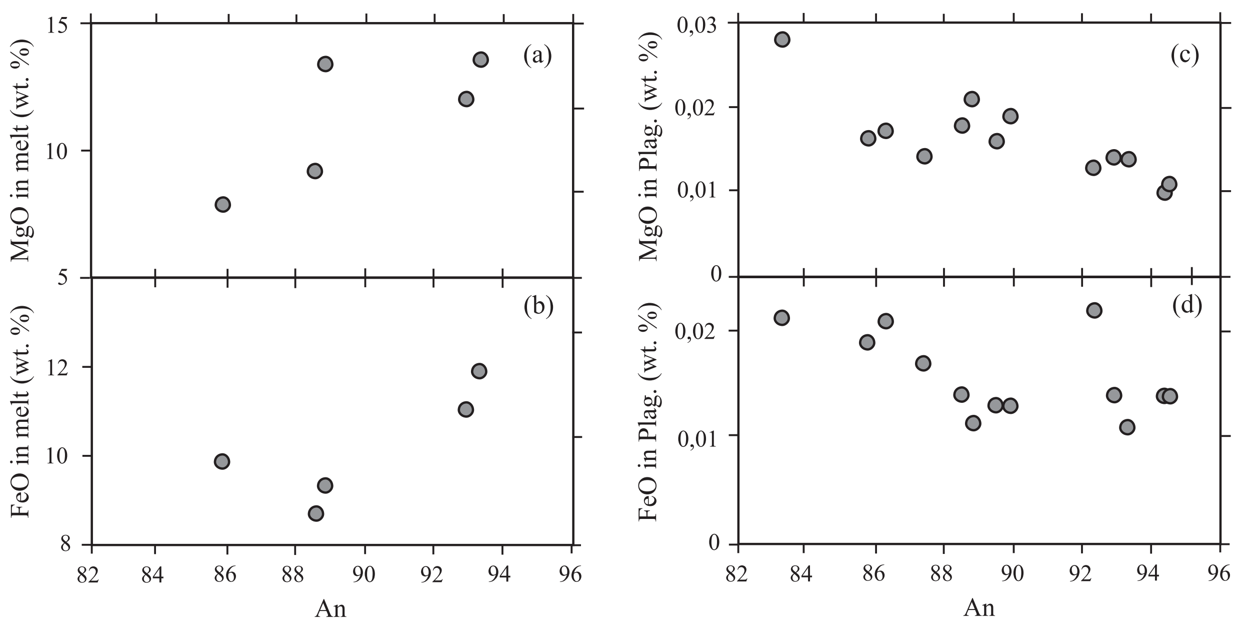

Figure 9. MgO and FeO in melt inclusions versus An component of host plagioclase (a, b) and MgO and FeO concentrations in plagioclase versus An component (c, d) from MORB basalts of the Costa Rica Rift (Borehole 896A; data from *McNeill and Danyushevsky*, 1996, Tables 3, 7).

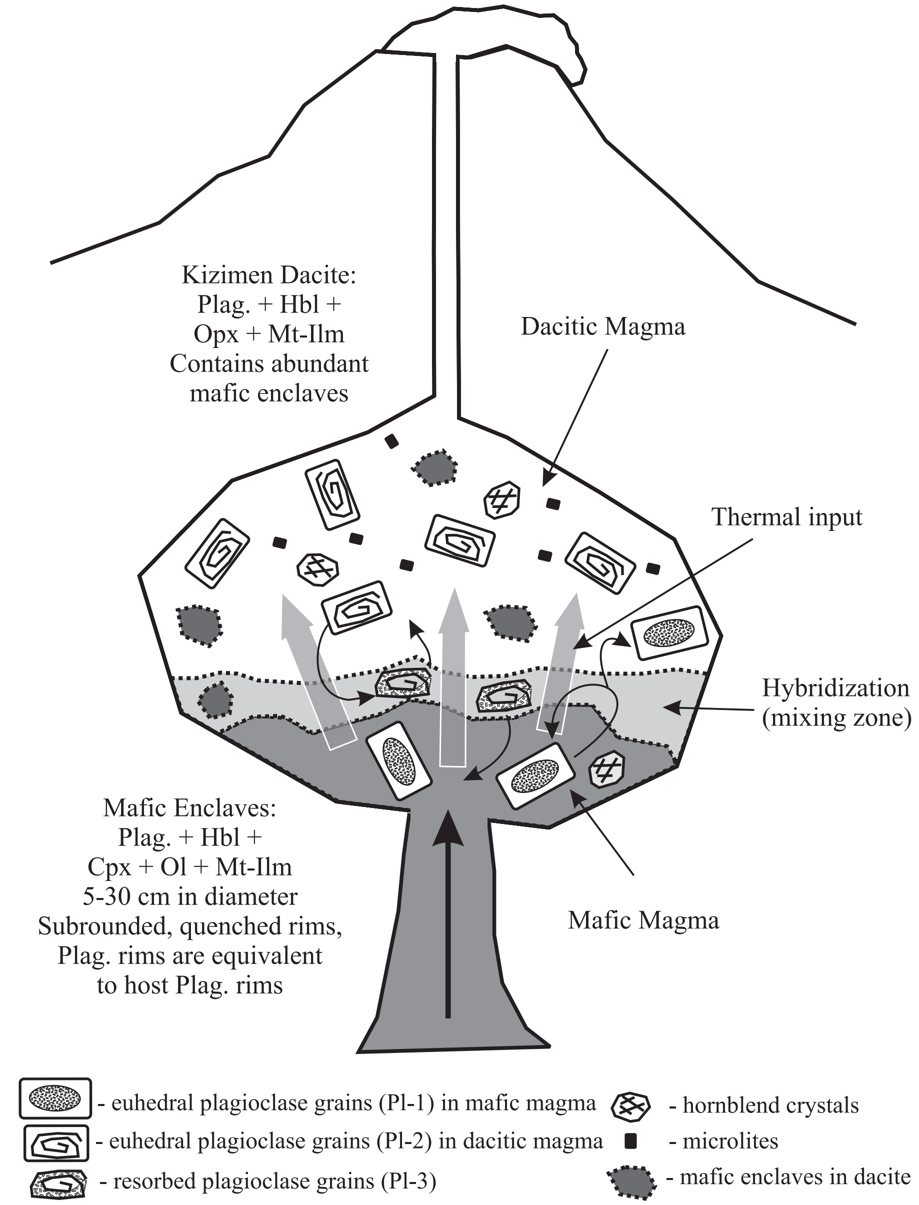

Figure 10. Schematic cartoon illustrating different processes in magma chamber of the Kizimen volcano. Due to a recharge of the basaltic magma inside dacitic magma chamber interactions between two melts are complex. Melts and their crystals could be changed by direct physical and chemical mixing within the mixing zone forming hybrid magma and streaky lavas or by thermal conduction only. Mafic plagioclase grains from basalt would be not significantly influenced by these processes while acid plagioclases would dissolve at higher temperature conditions and overgrow by new rims from surrounding hybrid and/or overheated melts. The movement of the plagioclase crystals are shown by arrows. More discussion see in text.

Pl-3 (e.g. Pl-3 and trend I on Figure 7). Some Pl-3 is returned to the host dacite through mechanical dispersion of mixing products, while some remains as phenocrysts in enclaves.

Mafic Pl-1 from basalt that was entrained in the hybrid zone was not affected by the low-temperature dacite melt and was not resorbed. However it will be overgrown by a more Ab-rich rim precipitated from the new hybrid melt. Such plagioclases are rare in host lava. But we did observe them in significant quantities in the enclaves, which are hybridized mafic magma.

The recharge and mixing process was not sufficiently effective so as to involve the entire magma volume and thus full homogenization in the magma chamber is not achieved. Some portions of dacitic magma may not have been directly involved in the chemical hybridization process, but were nevertheless subjected to heat from recharge. At increased temperatures, the rims of sodic Pl-2 recrystallized to more An-rich composition, forming trend II on Figure 7.

We speculate that episodic rise of basaltic recharge is particularly frequent (and thus causes a high proportion of mafic enclaves) in an extensional tectonic regime and is sustaining a dynamic and poorly mixed magma body at shallow depth below Kizimen. Interactions between magmas at Kizimen are complex, and apparently share many similarities with interactions at Unzen [*Eichelberger et al.*, 2006].

6. CONCLUSIONS

Based on textural evidence from plagioclase growth zones and major, minor and trace element contents, we conclude that:

1) All rocks of Kizimen volcano, including mafic enclaves, are hybrids and represent mixture of mafic and acid end-members in different proportions. These end-members are likely to be derived melts from the same parental melt by crystal fractionation including amphibole.

2) The unusual negative correlation of Mg with An in high-An plagioclase can be explained by fractional crystallization of the high-Al basalt with Pl-only fractionation or by non-linear behavior of Kd_{Mg} in Pl-melt system.

3) Incomplete mixing maintains the physical identity of distinct, though somewhat hybridized, end-members. While (incomplete) chemical mixing is abundant, we also observe evidence for the transport of heat (or increased water content) only in the variation of An content in plagioclase at constant trace element concentrations.

4) The trend within mafic enclaves toward more mafic compositions with time at Kizimen indicates that generation (by fractional crystallization) of the evolved dacite is not keeping pace with mafic recharge and outputs are likely directly triggered by inputs.

Acknowledgments. Martin Streck, Pavel Izbekov and Andrey Babansky are thanked for their detailed and constructive comments on an earlier version of this manuscript. Brandon Browne and Boris Gordeichik helped a lot with graphics preparation. This work was possible with a support of grant DFG #Wo362/15-1+2 to G.W., DFG-RFBR grant #00-0504000 to T.C. and G.W., projects of "Program 13" of RAS Presidium, Ministry of Industry and Science projects #43.700.11.0005, 43.043.11.1606 and State Contract with Federal Agency of Science and Innovations' Department of Survey and New Technologies Development #01.700.12.0028 to T.C.

7. REFERENCES

Allégre, C. J., A. Provost, and C. Jaupart, Oscillatory zoning: a pathological case of crystal growth, *Nature*, 294, 223–228, 1981.

Ariskin, A. A., G. S. Barmina, M. Ya. Frenkel, and R. L. Nielsen, COMAGMAT: a Fortran program to model magma differentiation processes, *Computers and Geosciences*, 19, 1155–1170, 1993.

Bindeman, I. N., A. M. Davis, and M. J. Drake, Ion microprobe study of plagioclase—basalt partition experiments at natural concentration level of trace elements, *Cosmochim Geochim Acta* 62, 1175–1193, 1998.

Brophy, J. G., M. J. Dorais, J. Donnelly-Nolan, and B. Singer, Plagioclase zonation in hornblende gabbro inclusions from Little Glass Mountain, Medicine Lake volcano, California: implications for fractionation mechanisms and the formation of composition gaps, *Contrib Mineral Petrol*, 126, 121–136, 1996.

Browne, B. L., J. C. Eichelberger, L. Patino, T.A. Vogel, J. Dehn, K. Uto, and H. Hoshizumi, Generation of porphyritic and equigranular mafic enclaves during magma recharge events at Unzen Volcano, Japan, *J. Petrol*, *47*, 301–328, 2006.

Churikova, T. G., and S. Yu. Sokolov, The magmatic evolution of Ploskie Sopky volcano, Kamchatka (analyses of Sr isotopic geochemistry), *Geochemistry*, 10, 1439–1448, 1993.

Churikova, T., F. Dorendorf, and G. Wörner, Sources and Fluids in the Mantle Wedge Below Kamchatka, Evidence from Across-Arc Geochemical Variation, J. of Petrology, 42 (8), 1567–1593, 2001a.

Churikova, T., B. Ivanov, J. Eichelberger, S. Trusov, J. Gardner, A. Belousov, B. Browne, P. Izbekov, and G. Wörner, Kizimen Volcano: An Unzen-like Magma System in Kamchatka, *AGU Fall Meeting, EOS*, 82 (47), F1381, 2001b.

Davidson, J. P., F. J. Tepley, Recharge in volcanic system: evidence from isotope profiles of phenocrysts, *Science*, 275, 826–829, 1997.

Drake, M. J., and D. F. Weill, Partition of Sr, Ba, Eu2+, Eu3+ and other REE between plagioclase feldspar and magmatic liquid: an experimental study, *Geochim Cosmochim Acta*, 39, 689–712, 1975.

Dorendorf, F., U. Wiechert, and G. Wörner, Hydrated sub-arc mantle: a source for the Kluchevskoy volcano, Kamchatka Russia, *Earth and Planetary Science Letters*, 175, 69–86, 2000a.

Dorendorf. F., T. Churikova, A. Koloskov, and G. Wörner, Late Pleistocene to Holocene activity at Bakening volcano and surrounding monogenetic centers (Kamchatka): volcanic geology and geochemical evolution, *Journal of Volcanology and Geothermal Research*, 104, 131–151, 2000b.

Eichelberger, J. C., P. Izbekov, and B. Browne, Bulk chemical trends at arc volcanoes are not liquid lines of descent, *Lithos*, 87, 135–154, 2006.

Ginibre, C., A. Kronz, and G. Wörner, High-resolution quantitative imaging of plagioclase composition using accumulated backscattered electron images: new constraints on oscillatory zoning, *Contrib Mineral Petrol*, 142, 436–448, 2002a.

Ginibre, C., G. Wörner, and A. Kronz, Minor- and trace-element zoning in plagioclase: implications for magma chamber processes at Parinacota volcano, northern Chile, *Contrib Mineral Petrol*, 143, 300–315, 2002b.

Grove, T. L., M. B. Baker, and R. J. Kinzler, Coupled CaAl-NaSi diffusion in plagioclase feldspar: Experiments and application to cooling rate speedometry, *Geochim Cosmochim Acta*, 58, 2113–2121, 1981.

Longhi, J., D. Walker, and J. F. Hays, Fe and Mg in plagioclase. *In: Proc 7th Lunar Sci Conf*, 1281–1300, 1976.

Marsh, B. D., Magma chambers, *Annu Rev Earth Planet Sci*, 17, 439–474, 1989.

Melekestsev, I. V., V. V. Ponomareva, and O.N. Volynets, Volcano Kizimen (Kamchatka)—future Sent-Helens, *Volcanology and seismology*, 4, 3–31, 1992.

McNeill, A. W., and L. V. Danyushevsky, Composition and crystallization temperatures of primary melts from hole 896A basalts: evidence from melt inclusion studies. *In: Proc. ODP, Scientific results*, 148, 21–35, 1996.

Nakada, S., and Y. Motomura, Petrology of the 1991–1995 eruption at Unzen; effusion pulsation and groundmass crystallization, *J. Volcanol. Geotherm. Res. 89,* 173–196, 1999.

Sato, H., Mg-Fe partitioning between plagioclase and liquid in basalts of Hole 504B, ODP Leg 111: A study of melting at 1 atm, *Proc. Ocean Drilling Program, Sci. Results*, 111, 17–26, 1989.

Sun, S. S., and W. F. McDonough, Chemical and isotopic systematics of oceanic basalts; implications for mantle composition and processes, *in: Saunders, A.D. & Norry, M.J. (eds) Magmatism in the ocean basins. Geological Society Special Publications. London: Geological Society of London,* 313–345, 1989.

Tepley, F. J. III, J. P. Davidson, R. I. Tilling, and J. G. Arth, Magma mixing, recharge and eruption histories recorded in plagioclase phenocrysts from El Chichon Volcano, Mexico, *J Petrol*, 41, 1397–1411, 2000.

Todt, W., R. A. Cliff, A. Hanser, and A.W. Hofmann, ^{202}Pb-^{205}Pb spike for Pb isotope analysis. *Terra Cognita*, 4, 209, 1984.

Trusov, S. V., and P. Yu. Pletchov, Formation of antidromic series of the Kizimen volcano (Kamchatka). *International petrographical Meeting „Petrography of XXI century", June, Apatiti*, 2005 (in Russian).

Alaska Volcano Observatory, Geophysical Institute, University of Alaska Fairbanks, USA

Geowissenschaftliches Zentrum Göttingen, Universität Göttingen, Germany

Institute of Volcanology and Seismology, Piip Avenue, 9, Petropavlovsk-Kamchatsky, 683006, Russia

Dynamics of the 1800 ^{14}C yr BP Caldera-Forming Eruption of Ksudach Volcano, Kamchatka, Russia

Benjamin J. Andrews[1], James E. Gardner[1], Steve Tait[2],
Vera Ponomareva[3], and Ivan V. Melekestsev[3]

The 1800 ^{14}C yr BP Ksudach KS_1 rhyodacite deposits present an opportunity to study the effects of caldera collapse on eruption dynamics and behavior. Stratigraphic relations indicate four Phases of eruption, Initial, Main, Lithic, and Gray. Well-sorted, reverse-graded pumice fall deposits overlying a silty ash compose the Initial Phase layers. The Main, Lithic, and Gray Phases are represented by pumice fall layers interbedded with pyroclastic flow and surge deposits (proximally) and co-ignimbrite ashes (distally). Although most of the deposit is <30 wt.% lithics, the Lithic Phase layers are >50 wt.% lithics. White and gray pumice are compositionally indistinguishable, however vesicle textures and microlite populations indicate faster ascent by the white pumice prior to eruption of the Gray Phase. The eruption volume is estimated as ~8.5 km^3 magma (dense rock equivalent) and ~3.6 km^3 lithics. Isopleth maps indicate mass flux ranged from 5–10x10^7 kg/s during the Initial Phase to >10^8 kg/s during the Main, Lithic, and Gray Phases. Caldera Collapse during the Lithic Phase is reflected by a large increase in lithic particles and the abrupt textural change from white to gray pumice; collapse began following eruption of ~66% of the magma, and finished when ~72% of the magma was erupted. Stratigraphic, granulometric, and component analyses indicate simultaneous eruption of buoyant plumes and non-buoyant flows during the Main, Lithic, and Gray Phases. Although mass flux did not change significantly following caldera collapse, the Gray Phase of eruption was dominated by non-buoyant flows in contrast to the earlier Phases that erupted mostly buoyant plumes.

1. INTRODUCTION

Understanding the effects of caldera collapse on explosive eruption dynamics constitutes a fundamental question in volcanology. Caldera collapse may significantly alter the vent structure and, as a result, may change the eruption behavior (Dobran et al., 1993). Of particular interest are changes in mass flux, magma ascent rate, the potential for transitions of eruption regime from buoyant, Plinian behavior to dominantly pyroclastic flow generation), and the timescales over which these changes occur. The most recent caldera-forming eruption of Ksudach volcano (Figure 1) provides an opportunity to examine these processes in detail because distinct eruption phases can be recognized in the deposits and most of the tephra was deposited from a buoyant, Plinian column (Braitseva et al., 1996), allowing for an estimation of variations in mass flux throughout the eruption.

[1] Department of Geology and Geophysics, Jackson School of Geosciences, The University of Texas at Austin, Austin Texas
[2] Laboratoire de Dynamique des Systemes Geologiques, Institut de Physique du Globe, Paris, France
[3] Institute of Volcanology and Seismology, Petropavlovsk-Kamchatsky, Russia

Volcanism and Subduction: The Kamchatka Region
Geophysical Monograph Series 172

10.1029/172GM23

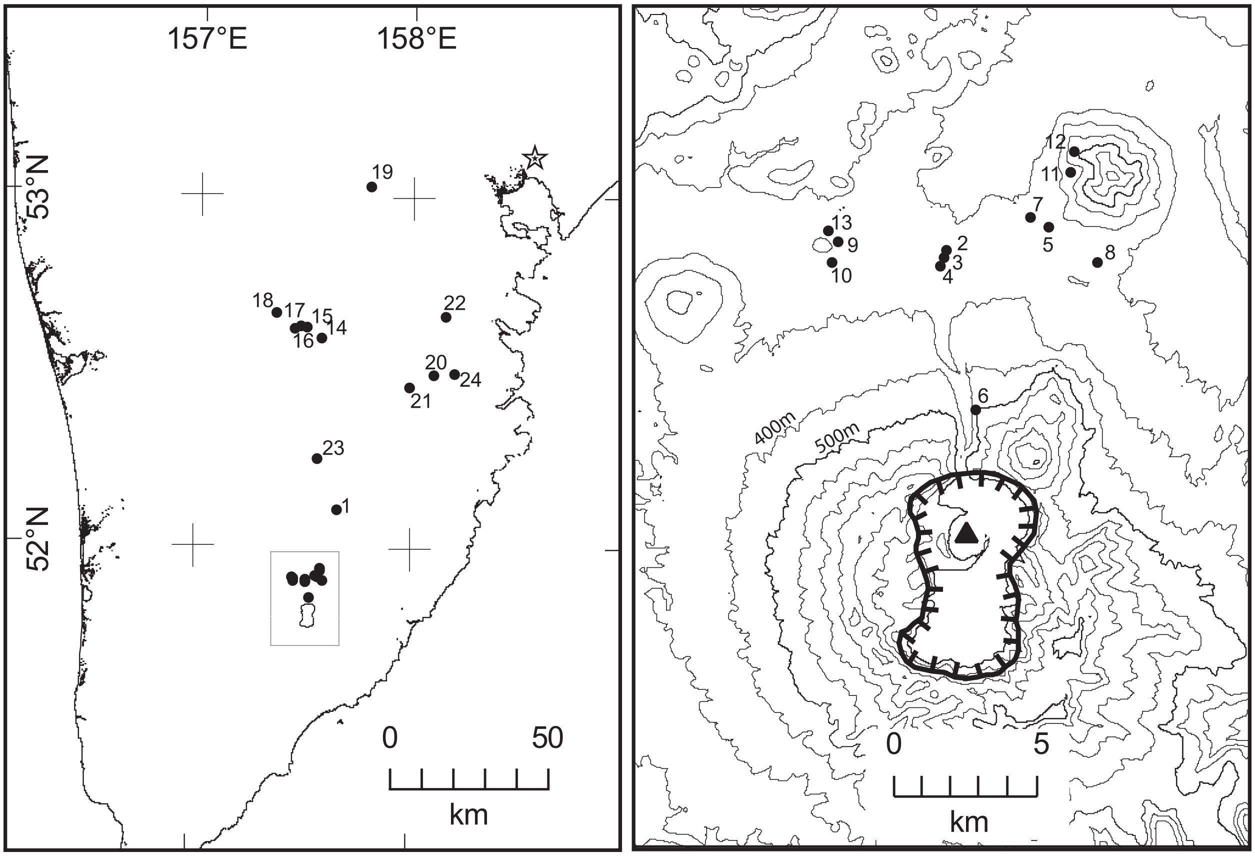

Figure 1. Location of Ksudach and sample locations. Locations of Petropavlosk-Kamchatsky and Stübel Cone' Volcano are indicated by the star and triangle, respectively. Contour interval in insert is 100 m.

The KS_1 eruption occurred in 1800 ^{14}C yr BP forming the ~4x6.5 km Caldera V when 8–9 km3 (DRE) of rhyodacite magma erupted (Braitseva et al., 1996; Volynets et al., 1999; this study). The KS_1 eruption initiated with phreatomagmatic activity but quickly changed to magmatic fall and pyroclastic flow eruption (Braitseva et al., 1996). Column heights ranged from 22 to 30 km during the eruption (Bursik et al, 1993; Braitseva et al., 1996). During the course of the eruption, the dispersal axis of the eruption plumes rotated from a north-northeast to more northerly direction, while the pumice color changed abruptly from white to gray. Bulk compositions of the two pumice types are identical, suggesting that the color difference results from different sizes and distributions of Fe-oxide microlites (Volynets et al., 1999).

In this paper we build on the earlier works with the aim of providing more detailed data on the evolution of the dynamics of the KS_1 eruption. One specific objective was to look for evidence in the deposits for the onset of caldera collapse and how this may have affected the dynamics. The total KS_1 deposit volume, mass fluxes throughout the eruption, and the timing of caldera collapse have been constrained through stratigraphic and component analyses. Relative magma ascent rates and changes in conduit geometry have been derived through analysis of vesicle textures and microlite number densities in pumice in conjunction with estimates of discharge rate.

2. METHODS

2.1 Field Studies

Stratigraphic sections were logged at 24 locations (Figure 1). At every location, the thickness of each tephra layer present was measured. The five largest lithic clasts were sampled from the excavated volumes of most pyroclastic fall layers and the long and short axes of each were measured. Samples analyzed for grain-size distribution and componentry were collected immediately after stratigraphic observations, and their stratigraphic locations are noted in Table 1. All samples were collected as bulk samples large enough to be representative of the layer from which they were taken; thus bulk sample weights range from ~0.1 to 2 kg. Care was taken to sample only portions of a layer that could be considered "massive." In instances where a layer was graded, samples were collected either from the base and top, or their location within the layer was noted.

2.2 Granulometric and Component Studies

Samples were wet sieved in 0.5ϕ size fractions from the coarsest particles to 4.0ϕ ($\phi = -\log_2$[diameter in mm]). Mass fractions of each size were determined from the dry weights. After drying and weighing, sizes of the fractions finer than 4ϕ were measured using a Spectrex Laser Grain Size Analyzer to 7ϕ. Several fall samples were too coarse to fully retrieve from the field and were dry sieved in the field in 1ϕ intervals down to -2ϕ; the finer fraction was then wet sieved in the laboratory. Componentry of the coarse fractions of those field samples was determined prior to discarding, using "pumice" and "lithic" as designators.

Granulometric and component analyses (Table 1) were combined with field observations of depositional structures and stratigraphic facies to distinguish layers as fall, flow, or surge deposits, following the criteria of Walker (1981). Pumice and ash fall layers are described by a high degree of sorting ($\sigma_\phi < 2.0\phi$) and a unimodal grain-size distribution. Layers with polymodal grain-size distributions frequently occur; in general, the coarser modes of these deposits are well-sorted. Pyroclastic flow deposits are characterized by poorer sorting, whereas surge deposits are finer grained, moderately sorted, and commonly have internal structures. Well-sorted layers relatively enriched in fine-grained material are termed co-ignimbrite ashes ($Md_{50} < 4\phi$).

Component mass fractions have been analyzed for 39 samples (Figure 1, Table 1). Random splits of 500 particles were taken from each size fraction 2ϕ and coarser and counted with the aid of a binocular stereo zoom microscope (up to 40x) and 10x hand lens. Weight fractions were calculated from modal fractions by determining average weights for each particle type in each size fraction: 100 pumice and 100 lithics were separated from each 0.5ϕ size fraction between -2ϕ and 2ϕ, crystals were separated at -1ϕ and 1.5ϕ; average weights for each component in a particular size fraction were measured, or interpolated from a best fit equation for those size fractions not measured directly. For size fractions with fewer than 500 particles, all particles were counted, and for those fractions with fewer than 100 particles, the individual component masses weighed.

Component types were determined observationally during fieldwork, sieving, and component analysis. The types of particles observed are pumice (white or gray), crystal, poorly-vesicular juvenile (obsidian) clasts, gray lithic, altered lithic, and granitoid. Pumice, the most common component of nearly all samples, is typically equant, although some white pumice, particularly in the smaller (<1ϕ) size fractions, are highly elongated. Crystals, often with adhering glass, and occasionally clotting together, are almost entirely plagioclase and pyroxene; magnetite and ilmenite may occur as discrete crystals but are generally indistinguishable from small black juvenile clasts. Juvenile, non-vesicular volcanic particles are generally black, glassy, roughly equant, and have <10 vol.% vesicles. Gray lithics are non-altered lava and porphyritic rocks. Some altered volcanic lithics are present, and are distinguished by their weathered and/or oxidized appearance. Pieces of granitoid rocks and occasional cumulates are differentiated from crystal clots by a generally finer grain-size, closer packing, and more equant particle shape. Feldspars and pyroxenes appear to be the dominant phases within granitoid particles.

2.3 Textural Analysis of White and Gray Pumice

White and gray pumice lapilli from stratigraphic site KSU-23 were selected for bulk vesicularity measurements, and back-scattered electron imaging and image analysis during component analysis. Groups of 5 pumice from the 0ϕ size fraction were selected and analyzed for average bulk density, using the methods of Gardner et al. (1996). Bulk vesicularities were calculated from the bulk density by assuming a non-vesicular density of 2500 kg/m^3.

Polished thin sections were made of 10 pumice from KSU-23H and KSU-23b, separated from the 0ϕ size fractions of each sample. Reflected and transmitted light images were taken of the pumice. The slides were then carbon coated and imaged using back-scattered electron (BSE) imaging. The resulting high contrast images were converted to binary images using Scion Image®, and vesicularities of individual pumice and portions of pumice analyzed. Long and short dimensions of vesicles were measured in each image and used to calculate bubble size and aspect ratio. Coalescing vesicles were treated as their multiple, constituent vesicles during measurement. Plagioclase and oxide volumetric microlite number densities, N_v, were calculated from these images using the expression:

$$N_v = \left(\frac{N}{A}\right)^{3/2}$$

where N is the number of microlites counted in an area A of an image (derived from Hammer et al., 1999).

Table 1. Granulometric data for KS_{-1} samples. Graphic mean and standard deviation, M_z and σ_g, are presented in units of ϕ. Sample componentry data are presented as wt% of each component. See Figure 1 for sample locations.

Sample	*Phase*	*Type*	M_z	σ_g	*pumice*	*crystal*	*glass*	*alt.-lith.*	*lithic*	*granitoid*
KSU-01A	Init.	fall	3.17	2.01	73.8	6.0	10.7	0.1	9.2	0.2
KSU-01B	Init.	fall	-0.01	1.82	66.1	10.1	3.8	0.9	18.8	0.3
KSU-01C	Init.	fall	0.35	1.88	45.7	6.8	1.5	1.8	43.9	0.4
KSU-01D	Main	flow	-1.57	2.05	63.3	1.9	1.3	2.7	29.1	0.3
KSU-01F	Main	fall	.69	3.25	70.6	1.5	0.9	1.2	25.6	0.2
KSU-01G	Main	fall	-0.73	0.75	23.0	8.3	13.3	7.0	47.7	0.8
KSU-01H	Lith.	fall	-0.65	0.68	28.6	8.2	1.6	3.4	56.9	0.7
KSU-01I	Lith.	fall	-1.56	1.69	88.8	2.6	7.2	2.5	29.7	0.3
KSU-01J	Lith.	fall	-0.72	0.98	6.9	1.8	0.9	0.4	89.6	0.4
KSU-09F	Gray	fall	-0.20	2.49						
KSU-10A	Init.	fall	3.99	1.68						
KSU-10B	Init.	fall	-0.76	2.11						
KSU-10D	Main	fall	1.79	2.56						
KSU-10F	Main	fall	-2.48	2.45						
KSU-10H	Lith.	fall	-0.45	2.47						
KSU-10I	Lith.	fall	-1.58	2.71						
KSU-10J	Lith.	fall	-2.38	1.62						
KSU-12A	Init.	fall	-2.30	1.93	55.0	1.5	1.3	1.2	40.2	0.8
KSU-12B	Init.	fall	-2.55	2.06	69.1	1.0	0.9	2.22	6.1	0.7
KSU-12D	Main	fall	-3.19	1.65	65.3	1.0	3.9	2.1	26.5	1.3
KSU-12E	Main	fall	-1.58	2.68	41.4	2.6	5.2	1.1	48.5	1.2
KSU-12F	Gray	fall	2.75	2.92	73.7	1.5	5.7	0.0	18.8	0.2
KSU-12G	Gray	fall	-3.37	2.04	81.9	1.1	1.2	4.9	10.2	0.8
KSU-14A	Gray	fall	2.66	1.82	60.8	3.9	4.4	0.0	30.9	0.0
KSU-14B	Gray	fall	1.60	2.54	68.8	2.4	5.0	0.0	24.1	0.0
KSU-14C	Gray	fall	-0.23	1.76	68.9	4.6	3.8	0.0	22.9	0.2
KSU-14D	Gray	fall	1.46	1.91	51.4	6.8	2.5	0.0	38.9	0.3
KSU-14E	Lith.	fall	1.22	0.86	34.5	12.3	2.3	0.3	50.3	0.3
KSU-14F	Main	fall	0.69	1.38	56.5	8.7	1.8	0.1	32.7	0.3
KSU-14G	Main	fall	0.48	1.29	54.1	12.3	2.2	0.1	31.0	0.2
KSU-14H	Main	fall	0.49	1.23	56.8	12.6	0.8	0.0	29.8	0.1
KSU-14I	Main	fall	3.27	2.11	79.9	5.3	1.2	0.0	13.6	0.1
KSU-19A	Gray	fall	1.32	0.76						
KSU-23A	Gray	fall	-1.70	1.67	71.8	2.7	18.3	1.2	5.1	0.0
KSU-23C	Lith.	fall	0.06	1.07	14.1	3.7	16.5	0.0	64.6	1.1
KSU-23D	Lith.	fall	-0.73	1.47	33.3	3.8	17.4	0.2	41.6	2.1
KSU-23F	Lith.	fall	-0.42	1.53	38.3	8.9	14.8	5.4	27.1	4.1
KSU-23H	Main	fall	-1.62	1.58	74.5	2.8	8.2	2.8	10.8	0.3
KSU-23I	Main	fall	-1.05	1.59	66.9	6.0	7.5	3.9	13.7	1.4
KSU-23L	Init.	fall	1.91	2.34	80.5	6.6	4.2	0.7	6.9	1.0
KSU-01E	Main	flow	1.12	3.14	87.3	2.2	3.1	1.1	6.2	0.0
KSU-09C	Main	flow	5.16	1.43						
KSU-10C	Main	flow	3.71	2.16						
KSU-10G	Main	flow	4.44	2.30						
KSU-10K	Gray	flow	-0.12	2.10						
KSU-10L	Gray	flow	-0.08	1.94						
KSU-12C	White	flow	4.88	1.43	97.1	0.4	0.5	0.1	1.8	0.1
KSU-12I	Gray	flow	-0.03	3.04	75.6	3.7	7.2	0.7	12.3	0.3
KSU-21D	Main	flow	-0.58	1.17						
KSU-21E	Main	flow	3.88	2.78						
KSU-21F	Init.	flow	0.12	1.00						
KSU-23B	Gray	flow	1.94	2.87	40.7	3.0	3.0	0.3	53.0	0.1
KSU-23E	Lith.	flow	1.63	2.76	53.9	6.3	0.6	0.1	39.4	0.1
KSU-23G	White	flow	1.80	2.65	48.7	8.2	1.9	0.6	40.5	0.1
KSU-23J	White	flow	3.42	2.53	72.7	4.7	2.4	0.3	19.9	0.1
KSU-23K	White	flow	1.91	2.57	79.0	6.5	5.3	0.1	8.4	0.5

3. RESULTS

3.1 Tephra Stratigraphy and Granulometric and Component Analysis

The KS_1 deposit decreases in thickness and complexity with distance (Figure 2), from >20 m at 4 km from the caldera, to approximately 10 cm at 100 km. The abrupt change from white to gray pumice that is ubiquitous in the upper portion of the sequence provides a distinct time horizon in the deposits. Proximal deposits are composed of numerous flow, surge, and fall layers. In general, the number of correlative fall deposits increases with distance, and the fraction of total deposit composed of fall layers increases from ~30% to 100% within 25 km from the caldera. Ash fall layers occupy similar stratigraphic positions in medial and distal locations as do flow and surge layers in proximal locations.

The decrease in stratigraphic complexity with distance is particularly apparent when across-axis variations in proximal and distal deposits are compared. In proximal areas, correlation of individual layers is difficult (Figure 3a). Flow deposits several meters thick at one section may be absent only a few kilometers away, and erosion by pyroclastic density currents may or may not have removed underlying fall and flow deposits. This is in marked contrast to distal deposits, where fall layers are highly correlative across many tens of kilometers (Figure 3b).

The color change, stratigraphic relations, and componentry have been used to group layers into four distinct eruptive phases of the deposit. These phases are an Initial Phase of mainly reversely-graded fall deposition; a Main Phase of fall and flow deposition; a Lithic-rich Phase dominated by fall deposition; and a Gray Phase of fall and flow deposition (Figure 2, section KSU-01). It should be noted that the interbedded proximal fall and flow layers and medial and distal fall and ash layers are not graded. That is, individual fall layers of a particular phase have relatively constant modes at individual sites despite the occurrence of interbedded fine-grained layers. Isopachs and isopleths were mapped for the pumice fall and ash fall layers of each eruption phase, all of which are strongly elongate to the north-northeast. Those

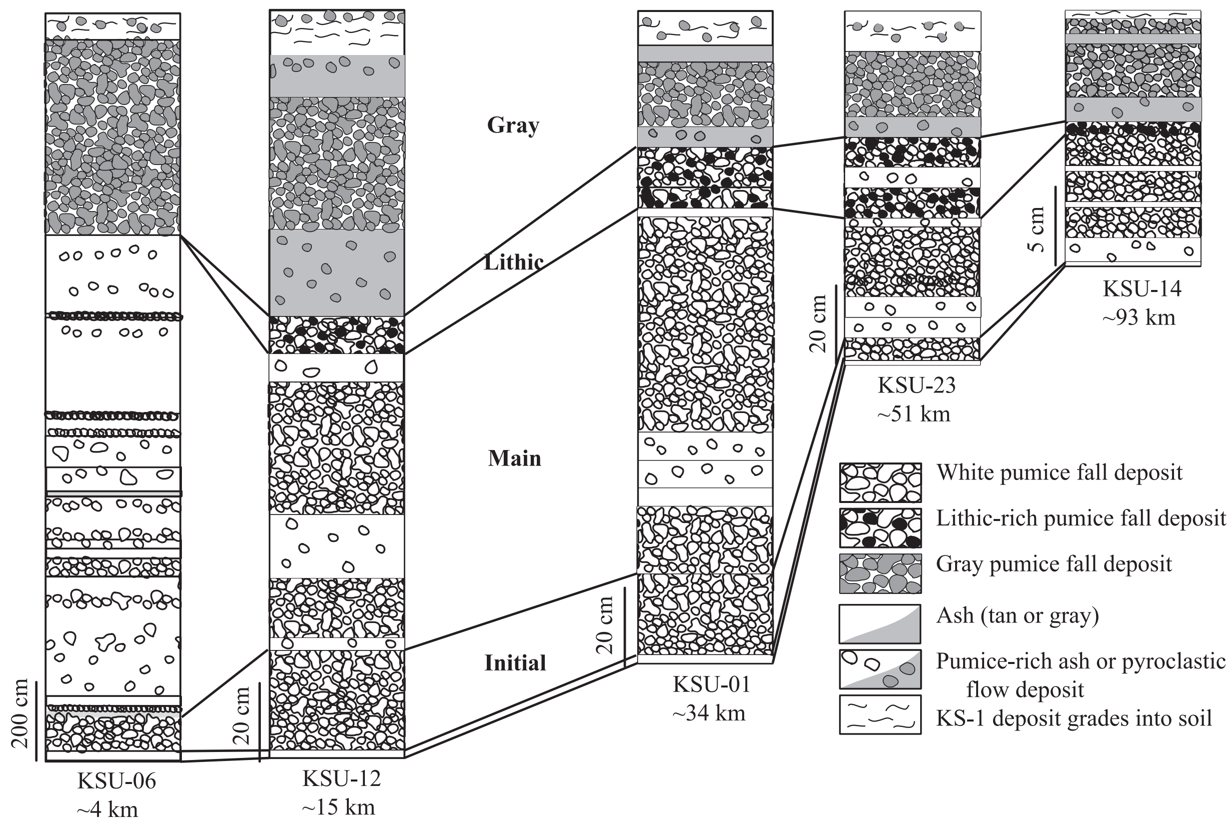

Figure 2. Fence diagram illustrating variations in stratigraphy with distance from the caldera. The complexity of the deposits decreases significantly with distance from the volcano. This is particularly true with regard to interbedding of pumice falls with pyoclastic flows and/or coignimbrite ashes. See Figure 1 for sample locations.

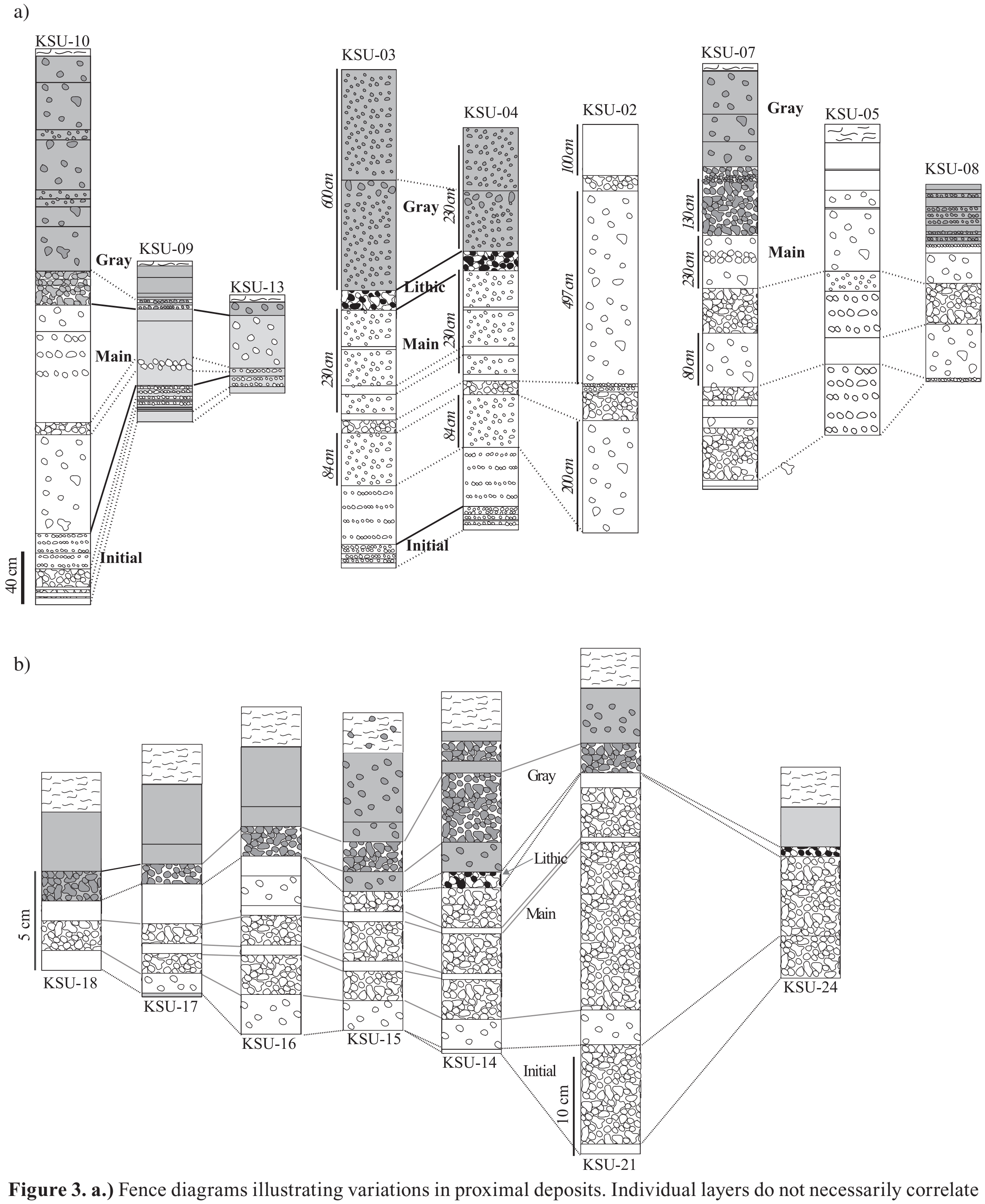

Figure 3. a.) Fence diagrams illustrating variations in proximal deposits. Individual layers do not necessarily correlate well between proximal deposits. Deposit thicknesses can vary substantially over relatively short distances. Pumice fall layers may be present at one location, but completely absent a few hundred meters away (e.g. sites KSU-07, KSU-08, and KSU-05). Locations of fences are shown in Figure 1; stratigraphic legend is shown in Figure 2. **b.)** Fence diagram illustrating across-axis variation in distal stratigraphy. The stratigraphic complexity apparent in proximal deposits (Figure 3a) is largely missing in more distal sections. Pumice fall layers dominate the deposits prior to the white to gray change in pumice color. Gray Phase deposits are represented almost universally by pumice fall layers overlain by ash. See Figure 1 and 2 for sample locations and stratigraphic legend.

a)

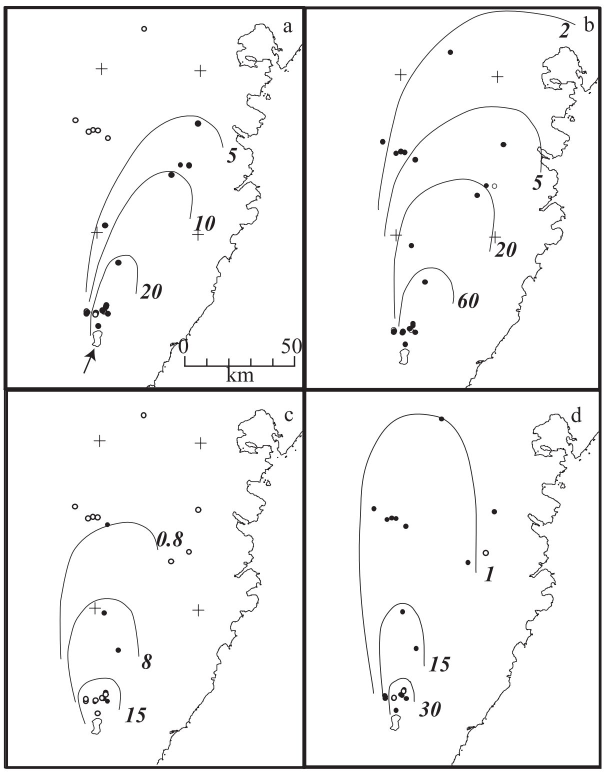

b)

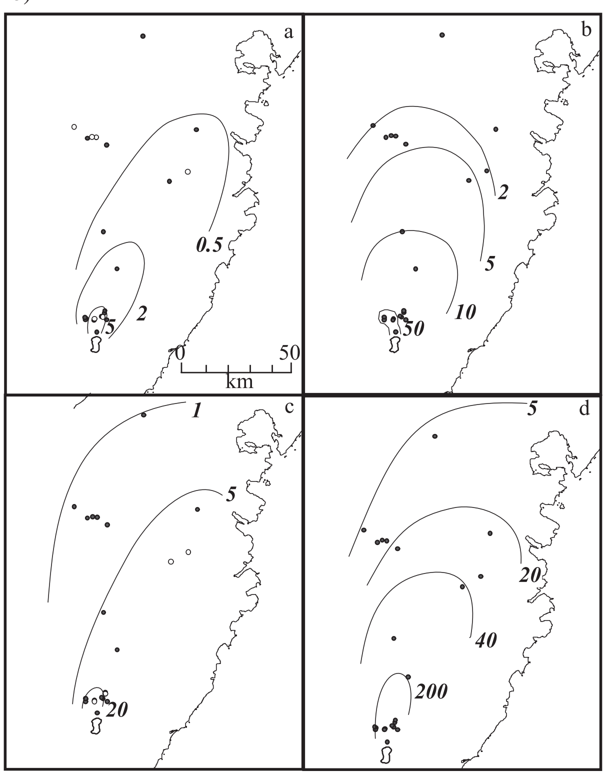

isopachs indicate that the depositional axis rotated ~30° to a more northerly direction during the eruption, in agreement with Bursik et al. (1993), and Braitseva et al. (1996) (Figures 4 and 5).

Volumes for the pumice fall layers were calculated from each isopach map, following the methods of Pyle (1989) and Fierstein and Nathenson (1992). In addition, co-ignimbrite ash volumes were calculated from isopachs of ash and pumice-bearing ash layers. Pyroclastic flow volumes were not directly calculated in this study, but are estimated at 3–4 km^3 of tephra by Braitseva et al. (Table 2). We estimate the total KS_1 deposit

Figure 4a. Pumice fall isopach maps. These maps represent the sum of pumice fall deposits at a particular site for a) Initial, b) Main, c) Lithic, and d) Gray eruption phases. Note that the depositional axis is elongate to the northeast of Ksudach, and rotated to a more northerly position as the eruption progressed. Contour value is in cm and indicated by the bold numbers. The location of Ksudach is indicated by arrow. Sample sites where the isopached eruption phase was not found are indicated by hollow circles.
Figure 4b. Isopach maps of cumulative fine-grained ash fall deposits for a) Initial, b) Main, and c) Gray eruption phases and d) total KS_1 deposit thickness. Contour interval is in cm.

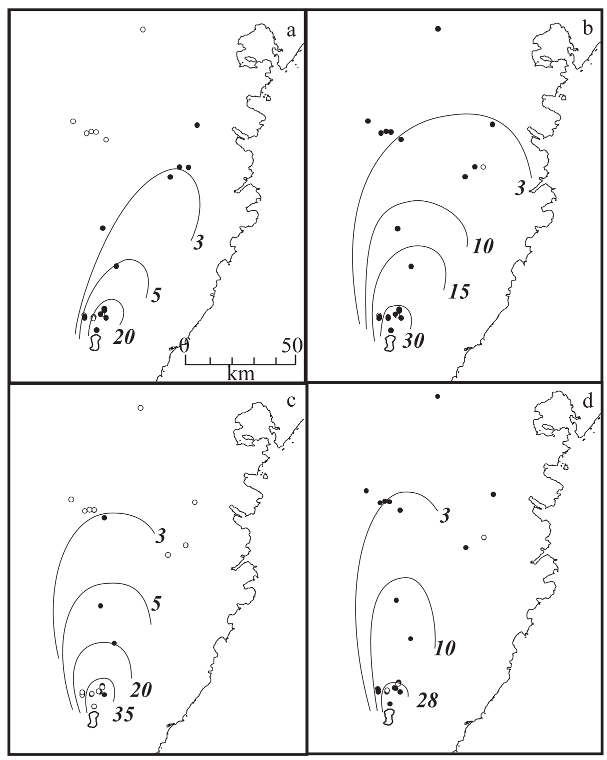

Figure 5. Pumice fall isopleth maps for a) Initial, b) Main, c) Lithic, and d) Gray eruption phases. Isopleth shapes indicate column height was greatest during the Main and Lithic Phases, slightly less during the Gray Phase, and lowest during the Initial Phase. Contour interval is in mm.

volume to be 20–25 km^3 (8–9 km^3 DRE) slightly larger than the 18–19 km^3 (8 km^3 DRE) calculated by Volynets et al. (1999) (Table 2). This estimate incorporates the pyroclastic flow deposit volume of 3–4 km^3 estimated by Braitseva et al. (1996). All deposit volumes are converted to magma dense-rock equivalent (DRE) and lithic volumes, by subtracting the lithic fraction from the deposits and assuming a bulk juvenile deposit density of 1100 kg/m^3 (Paladio-Melosantos et al., 1996) and magma density of 2500 kg/m^3.

3.1.1 Initial Phase. Proximally, the Initial phase of deposition is defined by a reversely-graded, well-sorted, unimodal fall deposit, overlying poorly to moderately sorted silty ash layers (Figure 6). Braitseva et al. (1996) suggest that the lower ash layers were produced by phreatomagmatic explosions. The Initial Phase deposits contain ~70 wt.% pumice, with lithics and juvenile poorly-vesicular particles present in equal amounts (~10 wt.% each), and ~6 wt.% crystals (Figure 6). In proximal sections, the Initial Phase deposits are thicker

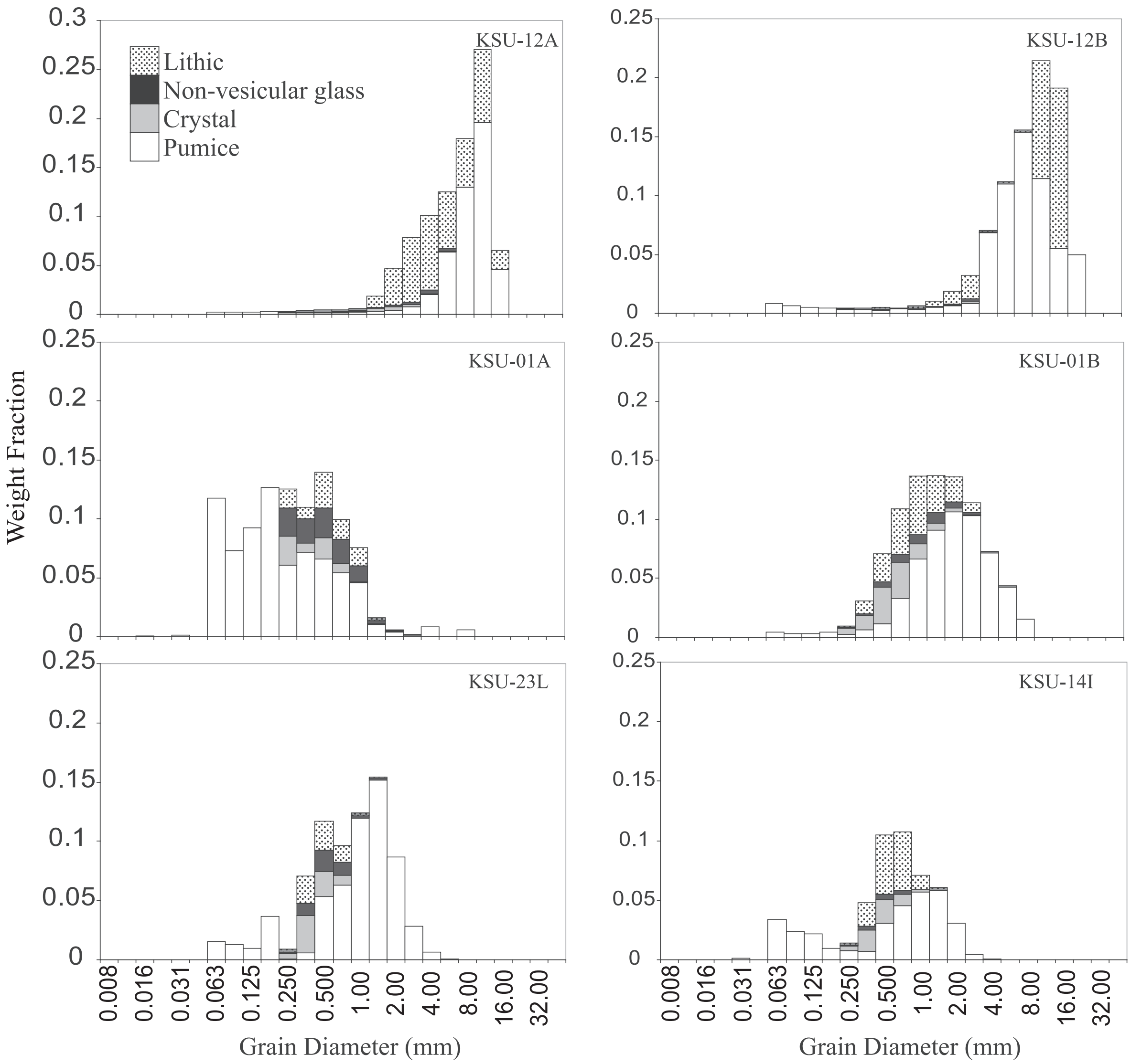

Figure 6. Initial Phase grain size plots. Stratigraphic height increases from left to right. Samples KSU-12A and KSU-12B exhibit prominent fin-grained tails and are skewed toward coarser grain sizes. The lowest sample from KSU-01, A, shows no sorting, however, the overlying Initial fall, B, displays excellent sorting, albeit with a fine-grained tail. The pumice bearing ashes from sites KSU-23 and KSU-14 both show distinct bimodal distributions. In general, the denser particles (i.e. not pumice) are well-sorted—this is particularly evident in samples KSU-12A, -01B, and -23L. Sample locations are shown in Figure 1.

Table 2. Eruptive volume calculated using the method of Pyle (1989) and Fierstein and Nathenson (1992). Volumes are displayed for pumice fall layers from the four eruptive phases, pyroclastic flow and ash layers from all phases except the Lith.ic phase. Total eruptive volume as calculated from the total deposit thicknesses and compared with sumn of individual volume layers. The number of isopachs, *N*, and 1- or 2-line approximation are noted.

Phase	*Type*	*N*	*1- or 2-line*	*Volume (km^3)*
Initial	Pumice fall	3	1	3.3
	Flow/ash	3	2	0.4
Main	Pumice fall	4	2	9.8
	Flow/ash	3	2	4.3
Lithic	Pumice fall	3	1	1.4
Gray	Pumice fall	3	1	2.1
	Flow/ash	3	2	4.1
Total	Complete deposit	4	2	20.2
	Sum of individual layers			25.5

than 1 m, and multiple ash layers are frequently interbedded within the pumice fall layer (Figure 3b). The mode of fall layers increases in diameter upward through the deposits by as much as a factor of 4 (Figure 6). Distally, the Initial Phase is represented by a single coarse, bimodal ash fall layer (Figure 3a). The thickness of the Initial Phase deposits decreases to <5 cm ~100 km from the caldera. Down-axis, the coarse mode decreases in size from 8 to 0.7 mm and the deposit becomes richer in pumice and poorer in crystals.

3.1.2 Main Phase. The Main Phase of the KS_1 deposit is composed of interbedded fall and flow layers at proximal locations, pumice and ash fall layers at medial sites, and coarse and fine-grained ash fall layers at distal sites. The total thickness deposits decreases from >12 m at ~4 km from the caldera to less than 7 cm at ~100 km from the caldera (Figure 2). Main Phase fall layers are frequently bimodal or fines-enriched (Figure 7). Pumice accounts for 63–75 wt % of most Main Phase fall layers, but for greater than 85 wt.% of the coarsest medial layers (KSU-01G and H).

Pyroclastic flow and surge deposits frequently compose up to 90% of proximal Main Phase deposits. The contacts between many proximal fall layers and pyroclastic flow layers are often uneven, so that the thicknesses of fall layers pinch and swell as much as 1 m over length scales of ~10–100 meters. Pyroclastic flow deposits often contain lenses of rounded pumice. Flow deposits do not appear to form large, laterally continuous sheets, but rather numerous lobes complexly interbedded with fall deposits and each other (Figure 3b). Cross-stratified and laminated surge deposits are also present, particularly on topographic highs. Proximal, coarse fall layers overlying fine-grained ash layers show prominent fine-grained tails or secondary modes.

In medial and distal deposits, the Main Phase is dominated by pumice fall layers in which pumice are occasionally ash-coated (Figure 2). Ash fall layers compose up to 30% of the total Main phase thickness in medial and distal deposits; ash layers closer than ~60 km to the caldera are often pumice-bearing, whereas those in distal areas are generally free of coarse pumice. Medial and distal falls are relatively enriched in material <0.063 mm.

3.1.3 Lithic Phase. The Lithic Phase of the KS_1 deposit consists of one to several fall layers that contain 40–70 wt.% lithics. That constrasts with the <30 wt.% lithics in fall layers of other phases at the same locations (Figure 8). Lithic Phase layers are often missing at proximal localities, but are very distinctive at medial and distal sites, where they occur immediately below the white-to-gray change in pumice color. Pumice in the Lithic Phase is however always white. Two distinct fall layers separated by a centimeter-thick ash layer are observed at medial localities, but merge into one with distance. The total Lithic Phase thickness ranges from ~20 cm at 35 km from the caldera, to ~1 cm at 100 km from the caldera.

The Lithic Phase fall deposits are well sorted with fine-skewed grain size distributions. The pumice:crystal ratios (5–10:1) in those layers are very similar to those in fall layers of the other phases. In contrast, the lithic:crystal proportions of the Lithic Phase layers are substantially higher than in other layers (up to 15:1 versus ~2:1). These relationships indicate the componentry of the Lithic phase layers results from a 300–400% increase in lithic material rather than removal of pumice.

3.1.4 Gray Phase. Interbedded fall, flow, and ash deposits compose the Gray Phase KS_1 deposits, defined by having gray pumice in the deposit. Near the caldera, the pumice fall deposits are up to 5 m thick and are overlain by flow deposits <1 m thick (Figures 2 and 3b). At a distance of 15 km, the Gray Phase consists of 20-cm-thick pyroclastic-flow deposits overlain by a 30-cm-thick fall deposit, which is in turn overlain by a 25-cm-thick stratified pyroclastic-flow deposit. With distance those layers grade into pumice-bearing ash beds overlain by pumice fall deposits. Distally, a second, thin gray fall is observed near the top of the sections. Gray Phase deposits are ~6 cm thick in sections ~100 km from the caldera.

Pumice composes 65–80 wt% of Gray Phase deposits. The pumice fall deposits are typically well-sorted, but have minor secondary modes of very fine-grained ash (Figure 9). Lithics comprise 10–20 wt.%, similar to fall layers before the lithic phase, and crystals and non-vesicular juvenile particles are generally present in concentrations less than

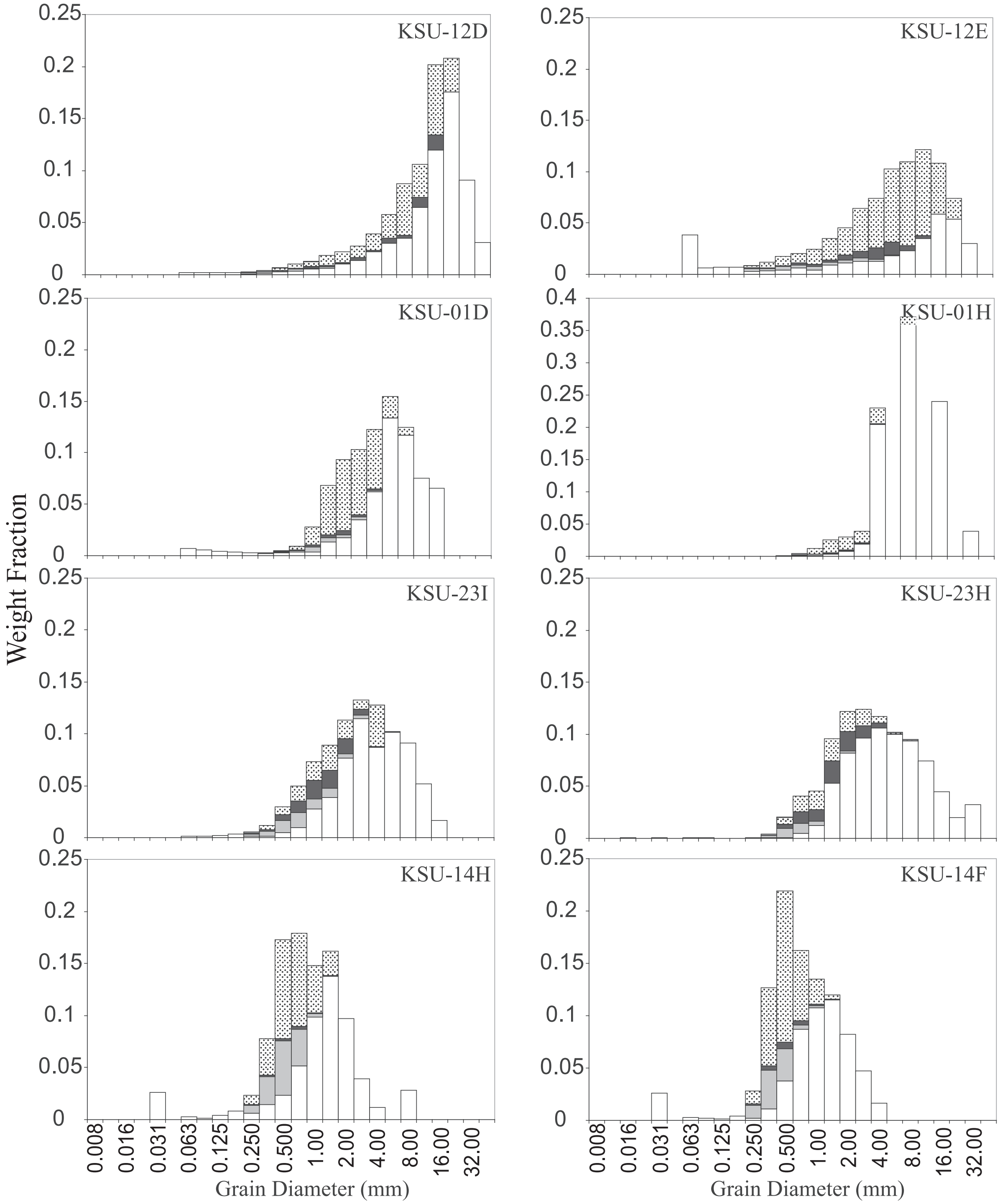

Figure 7. Grain size distributions and componentry of Main Phase fall deposits. Many Main Phase fall deposits are enriched in fine grained material; this is most apparent in samples from proximal locations such as KSU-12, but even well sorted fall deposits (e.g. KSU-23I) have minor fine-grained modes. The distal deposits, KSU-14H and -14F, display bimodal and fine skewed distributions, however, componentry data indicate that these distributions are the products of well-sorted pumice and dense particle distributions. See Figures 1 and 6 for samples locations and component legend.

Table 3. Pumice vesicularities as measured optically and with pycnometer for samples KSU-23H (white) and KSU-23A (Gray). The number of samples averaged for each measurement, *N*. Vesicularity is given as volume percent. Standard deviation of measurements is noted in italics.

Sample	*Method*	*N*	*Ves (%)*
KSU-23H	pyconmeter	15	78.2(*3.8*)
	optically	21	78.6(*4.3*)
KSU-23A	pycnometer	5	75.2(*3.3*)
	optically	17	75.1(*3.5*)

5 wt.%. The lowest gray ash layer in distal areas, however, has 40 wt.% lithics.

Stratigraphically, pyroclastic flow layers in proximal sections correlate with medial and distal bimodal pumice-bearing ash layers. Component analyses indicate the fine modes comprise well-sorted distributions of dense particles (primarily lithics and crystals). Proximal and medial pyroclastic flow and ash layers have componentry similar to the fall layers.

3.2 Textural Analysis

Bulk vesicularities of white and gray pumice are generally in the range of 75–80 vol% (Table 3). On average, white pumice are slightly more vesicular than gray pumice, but their ranges overlap. Despite their similar vesicularities, the shapes of vesicles in white and gray pumice are distinctly different (Table 4). White pumice contains vesicles that are typically 2–3 times more voluminous than those contained in gray pumice. Number densities of gray vesicles, $4–8x10^4/mm^3$, are ~4 times greater than those in white pumice, $1–2x10^4/mm^3$. Vesicles in white pumice generally have greater average aspect ratios (3:1 versus 2:1) than

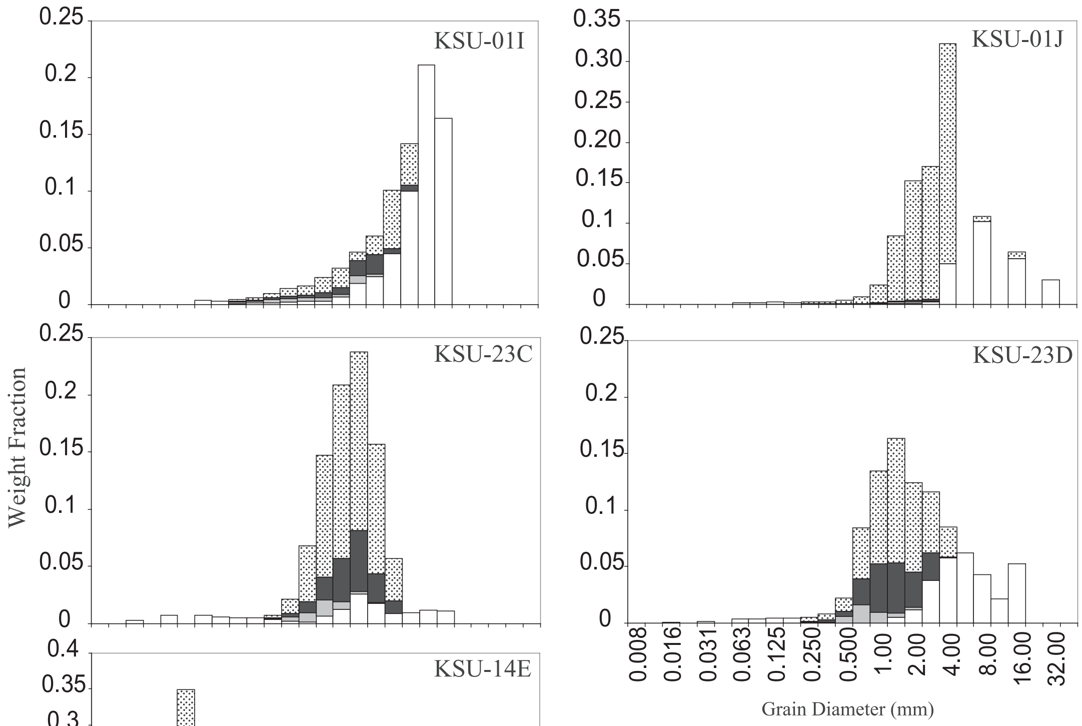

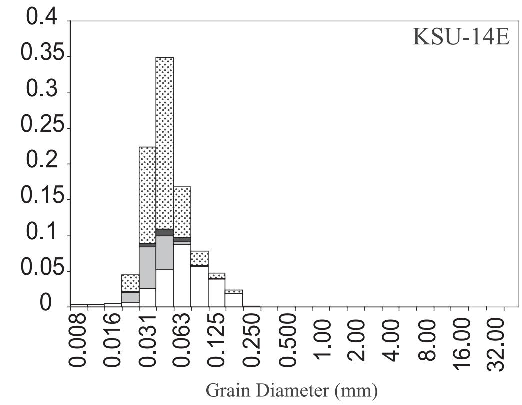

Figure 8. Lithic Phase grain size distributions. Lithic Phase fall deposits are very well sorted and can contain greater than 70 wt% lithics. The fine-grained tails present in Main and Gray Phase deposits (Figures 7 and 9) are largely absent in Lithic Phase fall deposits. Sample locations and component legend are shown in Figures 1 and 6, respectively.

Table 4. Vesicle aspect ratios and sizes as calculated from BSE images of pumices KSU-23H (white) and KSU-23A (Gray). Aspect ratios, *a:b*, are defined as the ratio of long to short axis, and are calculated from an average of *N* vesicles for each pumice. Vesicle volumes are calculated by treating the vesicles as oblate spheroids, *Vo*, spheres, *Vs*, and prolate spheroids, *Vp*.

Sample	*N*	*a:b*	*Vo* ($10^4 \mu m^3$)	*Vs* ($10^4 \mu m^3$)	*Vp* ($10^4 \mu m^3$)
KSU-23H	36	2.7	6.5	9.6	8.0
	20	2.0	2.3	3.7	1.2
	39	3.2	18.8	33.7	11.5
	16	2.5	5.1	8.1	2.6
	39	3.1	19.0	33.4	12.5
	39	2.8	20.4	34.4	12.8
	22	2.9	9.2	15.7	5.3
	42	4.1	12.8	2.6	13.0
	52	3.2	29.8	53.3	21.9
KSU-23A	34	2.1	3.7	5.4	2.3
	19	2.2	2.5	3.7	1.5
	19	1.9	0.5	0.8	0.2
	12	3.9	0.9	1.7	0.6
	34	3.5	25.0	46.7	22.6
	34	1.4	8.7	10.4	2.5
	22	1.9	4.0	5.6	3.0
	26	1.5	8.7	10.8	3.1
	9	1.6	4.2	5.2	2.1

those in gray pumice; significantly, highly elongate vesicles with aspect ratios greater than 25:1 and "woody" or fibrous textures are common in white pumice (Figure 10), but are absent from gray pumice. White and gray pumice also differ in microlite contents. White pumice contain <1000/mm^3 plagioclase or pyroxene microlites and 0–1000/mm^3 Fe-Ti oxide microlites. Gray pumice contain ~1000/mm^3 plagioclase and pyroxene, and ~10,000/mm^3 Fe-Ti oxide microlites (Figure 11, Table 5).

4. INTERPRETATION AND DISCUSSION

4.1 Eruption Dynamics

Maximum lithic isopleths from pumice fall deposits are shown in Figure 5. Column heights have been calculated from isopleth shapes using the method of Carey and Sparks (1986). Buoyant mass fluxes have been estimated from column heights, using the model of Sparks (1986) and assuming a temperature of 900ºC (Izbekov et al., 2003). A range in column height and mass flux is estimated based upon maximum and minimum possible extents for individual isopleths (Table 6). Because each phase erupted both buoyant plumes and pyroclastic flows, we estimate the average total mass fluxes for each eruption phase by dividing the total mass erupted during that phase by the duration of the phase. Durations of were estimated by dividing the mass of the fall deposits by the mass flux of the buoyant column.

Variations in column height and mass flux versus cumulative volume erupted are displayed in Figure 12. The eruption began with a small phreatomagmatic explosion (Braitseva et al., 1996), but then quickly evolved into a magmatic, Plinian eruption with a column 25–30 km tall, corresponding to a mass flux of 5–10x10^7 kg/s. During the Initial Phase ~1.6 km^3 of magma was deposited as falls and less than 0.25 km^3 as ash. Nearly 6 km^3 of magma and ~1.5 km^3 of lithics was erupted during the Main Phase. Two thirds of that volume was deposited from a buoyant plume 30–36 km tall, with 2.4 km^3 of magma was deposited by pyroclastic flows. Total mass flux during this period was 2–6x10^8 kg/s. Although the Lithic Phase has the smallest volume, 0.26 km^3 of magma and 0.6 km^3 lithics, column height exceeded and intensity of eruption nearly equaled that of the Main Phase (Figure 12). During the Gray Phase, mass flux remained comparable to that of the Lithic Phase, but column height decreased to that of the Initial Phase of eruption (Figure 12). Unlike the preceding eruption intervals, more Gray Phase material was deposited by pyroclastic flows and co-ignimbrite ash falls, 2 km^3 magma and 1.5 km^3 lithics, than from a buoyant plume, 0.8 km^3 magma and <0.1 km^3 lithics. We believe that the increased partitioning of material into non-buoyant pyroclastic flows resulted in less material being present in the buoyant plume, producing an effective decrease in the buoyant mass flux, and thus the plume did not rise as high as during the Main and Lithic Phases.

4.2 Simultaneous Generation of Plumes and Flows

Layers with polymodal size distributions may be products of deposition from mixed sources (e.g., pumice fall and co-ignimbrite ash) or from aggregation of fine-grained material into larger particles (Brazier et al., 1983; Carey and Sigurdsson, 1983). In deposits with accretionary lapilli (e.g. KSU-12E), the origin of bimodal size distributions is apparent. In deposits lacking such salient features, the origin of polymodal size distributions is constrained by stratigraphic relations. For example, sample KSU-01D is a bimodal layer in which most pumice is coated with fine ash, with a prominent 3.5 mm mode and a minor <0.05 mm mode (Table 1,

Table 5. Volumetric number densities of oxide and plagioclase microlites are given for white and Gray pumice. Number densities are reported as microlites per mm^3.

Sample	*Plag*	*Oxide*
White	0	800–1300
Gray	0–1000	9800–10500

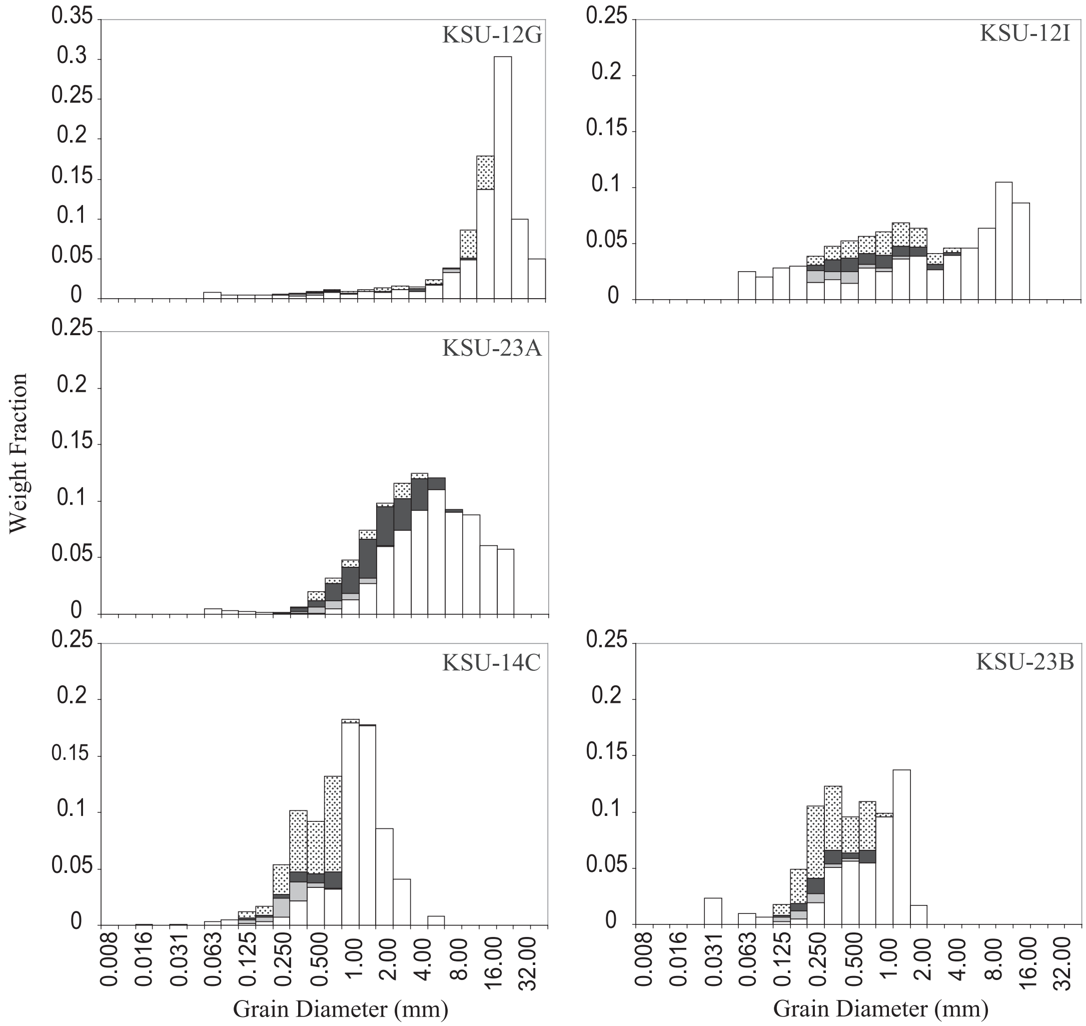

Figure 9. Gray Phase grain size distributions and componentry. Gray phase fall deposits are generally well sorted, though, as with those of the Main phase, they often have fine grained tails. The overlying pyroclastic flow (KSU-12I) and ash (KSU-14B) deposits display polymodal grain size distributions, with medium-grained modes comprised of dense, normal distributed particles. See Figures 1 and 6 for sample locations and component legend.

Figure 7). This layer correlates stratigraphically to pyroclastic flow layers at more proximal sites, and so it is likely KSU-01D is a mixed deposit formed by simultaneous deposition of pumice and ash falls from two plumes, one Plinian and one coignimbrite (Criswell, 1987; Carey et al., 1990; Wilson and Hildreth, 1997; Wilson and Hildreth, 1998).

The following proximal stratigraphic relationships suggest that pyroclastic flows were emplaced over certain sectors of the volcano, while at the same time pumice-fall layers were being deposited over other sectors. Proximal areas have highly variable sequences of interbedded falls and flows (Figure 3b). Those fall layers are not traceable across areas where flow deposits are present. Instead, individual layers are only traceable where pyroclastic flow deposits are absent. Main and Gray Phase fall layers are not graded above and below flow or ash layers. Instead, those layers are bi-modal and appear to be enriched in fine-grained ash. The coarse modes of pumice-rich ashes are similar *to* those of Plinian falls. These relationships

Table 6. Column heights and mass discharge rates (MDR) as calculated using the methods of Carey and Sparks (1986) and Sparks (1986). Three to four isopleths were averaged for each phase

Phase	*Height (km)*	*MDR (kg/s)*
Initial	25–30	5–10x10^7
Main	30–36	2–6x10^8
Lithic	30–37	1–4x10^8
Gray	27–30	2–3x10^8

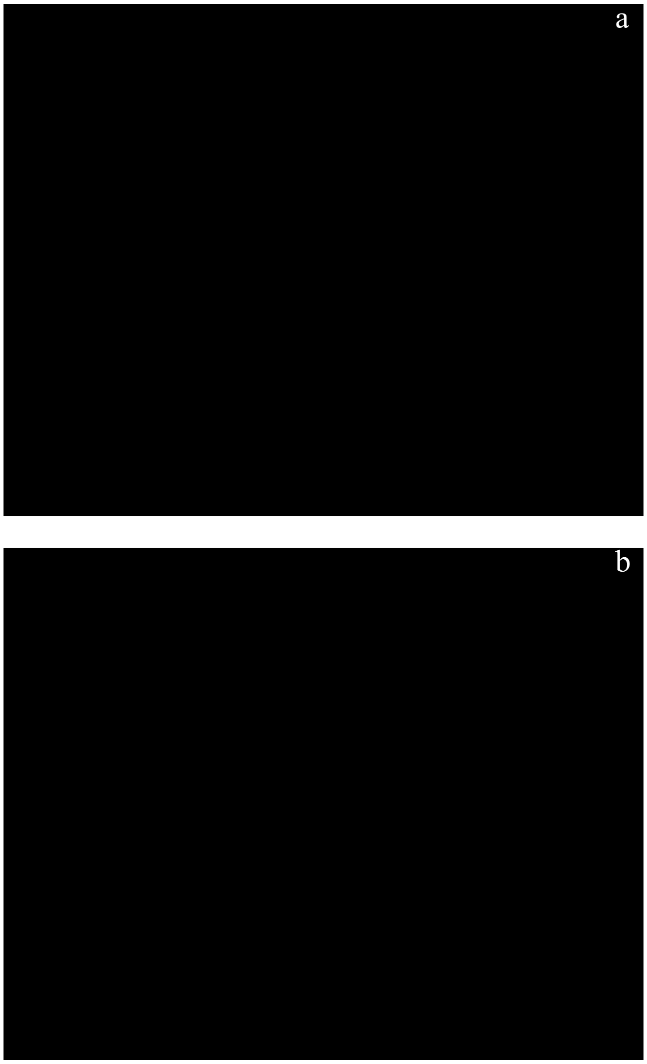

Figure 10. BSE images of a) white and b) gray pumice illustrating differences in vesicle shape and distribution. Note that white pumice contain larger, more elongate vesicles than gray pumice. Vesicle aspect ratios in white pumice can be greater than 20, whereas in gray pumice the vesicles are generally more equant (Table 4).

indicate that tephra was simultaneously deposited from vent-sourced and co-ignimbrite plumes.

Similar behavior (e.g., simultaneous eruption of a buoyant plume and non-buoyant flows) was observed during the 1980 Mount St. Helens (Criswell, 1987) and 1991 Pinatubo eruptions (Paladio-Melosantos et al., 1996), and is suggested to have occurred during the 79 A.D. Vesuvius eruption (Carey and Sigurdsson, 1987) and 1912 Katmai-Novarupta eruption (Houghton et al., 2004). Column instability manifests itself when insufficient air is entrained for the column to become buoyant, at which point the column partially or completely collapses and non-buoyant pyroclastic flows are shed. When instability begins, discrete flows are generated, at least initially, over certain sectors of the volcano (e.g., Neri et al. 2002; Kaminski et al., 2005), rather than the entire column collapsing and depositing material on all flanks of the mountain. Numerical and analog studies by Wilson et al. (1980), Dobran et al. (1993), and Neri et al. (2002) predict column instability when mass flux typically exceeds 10^8 kg/s. Interestingly, the Plinian column of the KS_1 eruption became unstable when mass flux exceeded 10^8 kg/s.

Unlike earlier eruption phases, the Gray Phase erupted a greater volume as pyroclastic flows than as a buoyant column. In addition, the relative proportion of fine ash in bimodal fall samples is greater in Gray Phase samples than in samples from

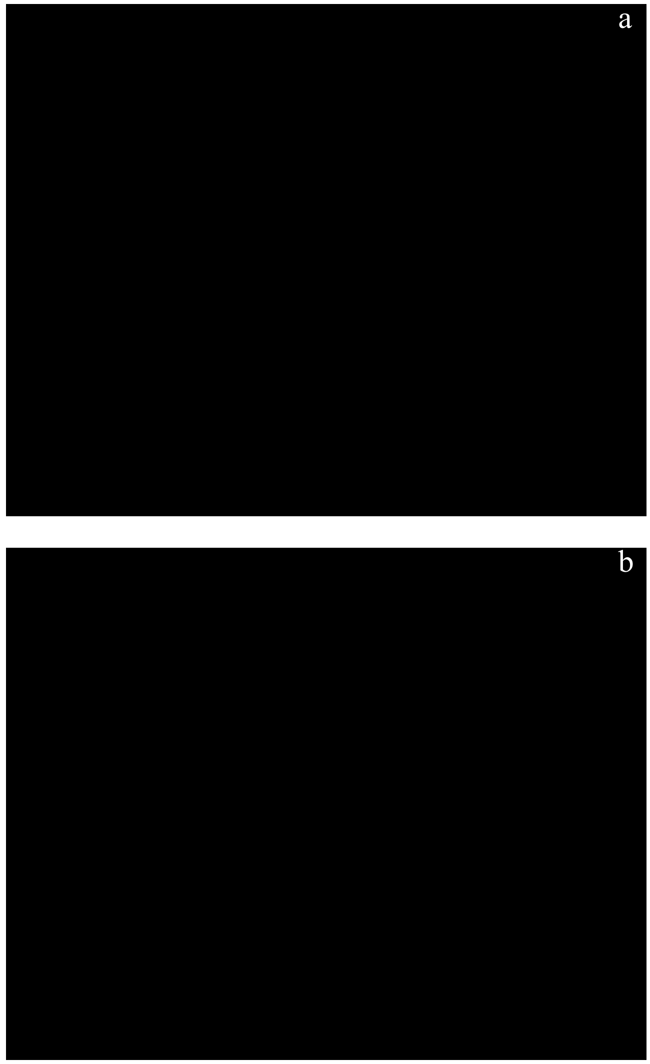

Figure 11. BSE images of a) white and b) gray pumice illustrating differences in microlite content. Note that Fe-Ti oxide, plagioclase, and pyroxene microlites are present in gray pumice but not present in white (Table 5).

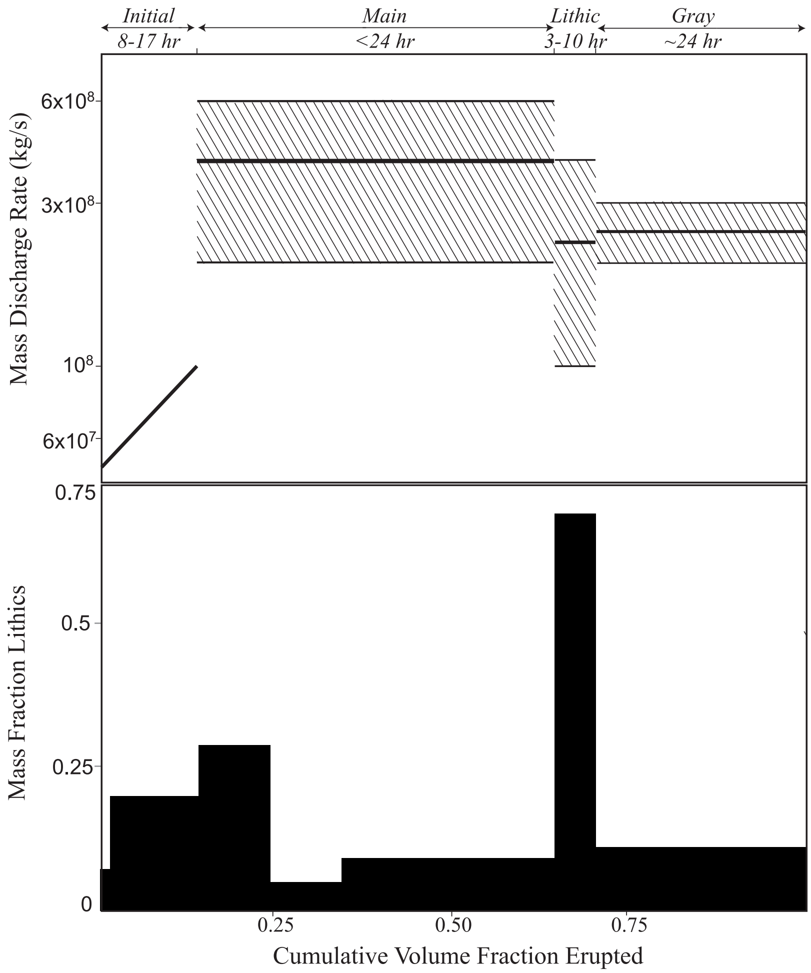

Figure 12. Eruption timeline. Average mass flux is indicated by the bold line and diagonal-hatched regions; the mass fraction of lithic clasts erupted is shown by the gray regions. The approximate durations and volume erupted during each phase of eruption are indicated at the top and bottom, respectively, of the figure.

other phases. That greater relative proportion of fine ash probably reflects a greater proportion of co-ignimbrite ash to Plinian ash fall. These observations suggest that a higher proportion of pyroclastic flows were generated during the Gray Phase than in earlier phases (Figures 6–9) even though mass flux was lower than during the Main Phase (Figure 12). Given the fact that the white and gray pumice were both derived from essentially identical magma, in principle the reverse correlation might be expected. This may indicate a strong dependence of column behavior on vent geometry, and hence that a rapid change in geometry may have taken place (i.e. caldera collapse) preceding eruption of the Gray Phase (Wilson et al., 1980).

4.3 Timing of Caldera Formation

Braitseva et al. (1996) and others have argued conclusively that Caldera V formed during the KS_1 eruption, but one question that remains is when did the caldera collapse during this eruption? Throughout the Initial, Main, and most of the Gray Phases, lithics constitute ~25 wt.% or less of the deposits. During the Lithic Phase, however, lithics account for greater than 50 wt.% of the deposits. Although the total volume of lithics in Lithic Phase deposits is less than that of either the Main or Gray Phases, the rate at which they were erupted is substantially greater. Given estimates for mass fluxes for the different phases, lithic ejection rates for the Lithic Phase are up to 1.4×10^8 kg/s, whereas those of the Main and Gray phases are ~4.3×10^7 kg/s. It is unlikely this represents solely rapid widening of a central vent, because that would have led to a substantial increase in mass flux (Wilson et al., 1980; Woods, 1988), which is not observed (Figure 12). Instead, we propose that the large increase in lithics resulted from collapse of the caldera during the Lithic Phase and continued into the beginning of the Gray Phase, given that its lowest deposit has up to 40 wt% lithics.

Assuming that caldera collapse occurred during the Lithic phase of the eruption, then it formed after ~66% of the volume had been erupted. Interestingly, the amount of magma erupted prior to the Lithic phase, ~7 km^3, is equal to the collapse volume estimated by Braitseva et al. (1996). This contrasts with observations of typical caldera formation (e.g., Bacon, 1983), in which the majority of volume is inferred to have erupted after caldera collapse. Gardner and Tait (2000) noted a similar relation between erupted volume and collapse timing at Volcán Ceboruco, where approximately ~75% of the magma erupted prior to caldera formation. Changes in mass flux during the KS_1 producing eruption are also similar to those of the caldera-forming eruption of Volcán Ceboruco in which mass flux decreased during the initiation of collapse (Gardner and Tait, 2000). Gardner and Tait (2000) suggest that a critical volume of magma must be erupted prior to caldera collapse, and that there may be some fundamental difference in the mechanics of large and small caldera collapses; large calderas seem to begin to collapse early (volumetrically) in the eruption, whereas small calderas may initiate near the conclusion of the eruption (Browne and Gardner, 2004). Indeed, Roche and Druitt (2001) describe a set of collapse criteria that predict early, coherent, "piston" collapse of large calderas and late piecemeal collapse of small calderas.

4.4 The Difference Between White and Gray Pumice

Collapse of Caldera V seems to correspond to the change in pumice texture, from white to gray pumice. The abrupt change in pumice color occurring in the KS_1 deposit seems to mark a correlatable time horizon. Similar abrupt changes in pumice color during caldera-forming eruptions are not uncommon and usually reflect a substantial change in composition, such as those of the 1912 Katmai, 7.7 k.a. eruptions Crater Lake (e.g., Hildreth, 1983; Bacon and Druitt, 1988). In contrast, the bulk compositions of the Ksudach pumice are the same: rhyodacitic 71.5–72 wt.% SiO_2 (Volynets et al., 1999; Izbekov et al., 2003). Moreover, magnetite-ilmenite geothermometry indicates that the magma(s) that formed the white and gray pumice equilibrated at similar temperatures, ~892 +/-7 °C and oxygen fugacities of -11.5 +/-0.2 ($\log f_{O2}$), respectively (Izbekov et al., 2003). Both pumice types have the same phenocryst assemblage (plagioclase, orthopyroxene, clinopyroxene, magnetite and ilmenite) and consist of greater than 90% glass. Thus a single magma body was tapped throughout the KS_1 eruption.

White and gray pumice differ markedly in microlite populations and vesicle textures, despite their identical compositions (Tables 4 and 5). That change in texture may record the transformation of the conduit and vent structure. The elongated vesicles (Table 4) in white pumice could result from a higher strain rate from greater shear (Manga et al., 1998). If so, then this would argue for slower ascent velocity of the gray magma, because the mass flux of the Gray Phase is similar to that of the Main and Lithic Phases (Figure 12).

Support for slower decompression is found in the differences in microlite content between the white and gray pumice (Table 5). Plagioclase and pyroxene microlites are present in number densities of ~1000 mm^{-3} in gray pumice and <1000 mm^{-3} in white. Because time is required for crystals to nucleate and grow (Geschwind and Rutherford, 1995,; Hammer and Rutherford, 2002; Couch, 2003), the marked increase in plagioclase, pyroxene, and Fe-Ti microlites in the gray pumice suggest that the gray magma decompressed more slowly.

Interestingly, the mass flux of the Gray phase is similar to that of the Main and Lithic phases and greater than that of the Initial phase (Table 6), yet pumice appear to record two different ascent rates, with gray pumice ascending slower than white ones. Given that mass flux was similar between Lithic and Gray phases, the change in velocity may suggest that the conduit cross-sectional area increased a change that could be consistent with caldera collapse. Lastly, the higher proportion of pyroclastic flows generated during the Gray phase is also consistent with a change in vent geometry, such as might occur through caldera collapse. All else being equal, if the exit velocity decreases while the area of the conduit increases, then these effects should both combine to make column collapse more likely, and hence lead to a greater proportion of pyroclastic flows.

5. CONCLUSION

Field and stratigraphic observations indicate that the KS_1 eruption progressed in four distinct phases of eruption: Initial, Main, Lithic, and Gray. Granulometric and component analyses suggest fall deposition by both vent sourced and co-ignimbrite plumes. Mass flux varied during the eruption by as much as an order of magnitude, from 5–10x10^7 kg/s during the Initial Phase, to a maximum of 2–6x10^8 kg/s in the Main Phase. Mass flux during the Lithic Phase dropped by as much as a factor of 3, before increasing during the Gray Phase to 2–3x10^8 kg/s. When mass flux exceeded 10^8 kg/s, buoyant plumes and non-buoyant pyroclastic flows were simultaneously erupted. Caldera collapse is probably marked by the major influx of lithics during the Lithic Phase. Collapse thus occurred after eruption of ~6.1 of the 8.5 km^3 of magma (DRE) erupted. Changes in conduit and column dynamics were heralded by collapse, leading to slower magma ascent, marked by the white-gray pumice transition, and increased generation of pyroclastic flows.

Acknowledgements. Pavel Izbekov kindly assisted us in the field and organized this volume. We thank Ken Severin for assistance with the microprobe was invaluable, Brandon Browne and Robert Nicholson for useful insights and comments on grain size and component analysis, and John Eichelberger for discussions regarding caldera collapse. Thoughtful reviews by B. Browne and J.L. Macias greatly improved this manuscript. Funding was provided by the Alaska Volcano Observatory.

REFERENCES

Bacon, CR, 1983. Climactic eruption of Mount Mazama and formation of Crater Lake caldera, Oregon. United States Geological Survey Professional Paper: 141–142.

Bacon, CR and TH Druit, 1988. Compositional evolution of the zoned calcalkaline magma chamber of Mount Mazama, Crater Lake, Oregon. Contributions to Mineralogy and Petrology, 98: 224–256.

Braitseva, OA, IV Melekestsev, VV Ponomareva, and VY Kirianov, 1996. The caldera-forming eruption of Ksudach volcano about cal. A.D> 240: the greatest explosive event of our era in Kamchatka, Russia. Journal of Volcanology and Geothermal Research, 70: 49–65.

Brazier, S, RSJ Sparks, SN Carey, H Sigurdsson, and JA Westgate, 1983. Bimodal grain size distribution and secondary thickening in air-fall ash layers. Nature, 301: 115–119.

Browne, B, and JE Gardner, 2004. The nature and timing of caldera collapse as indicated by accidental lithic fragments from the ~1000 A.D. eruption of Volcán Ceboruco, Mexico. Journal of Volcanology and Geothermal Research, 130: 93–105.

Bursik, M, IV Melekestsev, and OA Braitseva, 1993. Most recent fall deposits of Ksudach Volcano, Kamchatka, Russia. Geophysical Research Letters, 20: 1815–1818.

Carey, SN, and H Sigurdsson, 1983. Influence of particle aggregation on deposition of distal tephra from the May 18, 1980, eruption of Mount St. Helens volcano. Journal of Geoyphysical Review, 87: 7061–7072.

Carey, S and RSJ Sparks, 1986. Quantitative models of the fallout and dispersal of tephra from volcanic eruption columns. Bulletin of Volcanology, 48: 109–125.

Carey, S and H Sigurdsson, 1987. Temporal variations in column height and magma discharge rate during the 79 A.D. eruption of Vesuvius. Geological Society of America Bulletin, 99: 303–314.

Carey, S, H Sigurdsson, JE Gardner, and W Criswell, 1990. Variations in column height and magma discharge during the May 18, 1980 eruption of Mount St. Helens. Journal of Volcanology and Geothermal Research, 43: 99–112.

Cioni, R, R Sulpizio, and N Garruccio, 2003. Variability of the eruption dynamics during a subplinian event; the Greenish Pumice eruption of Somma-Vesuvius (Italy). Journal of Volcanology and Geothermal Research, 124: 89–114.

Couch, S, 2003. Experimental investigation of crystallization kinetics in a haplogranite system. American Mineralogist, 88: 1471–1485.

Criswell, CW, 1987. Chronology and pyroclastic stratigraphy of the May 18, 1980 eruption of Mount St. Helens, Washington. Journal of Geophysical Research, B, 92: 10237–10,266.

Dobran, F, A Neri, and G Macedonio, 1993. Numerical simulations of collapsing volcanic columns. Journal of Geophysical Research, B, 98: 4231–4259.

Fierstein, JE and M Nathenson, 1992. Another look at the calculation of fallout tephra volumes. Bulletin of Volcanology, 54: 156–167.

Gardner, JE, RME Thomas, C Jaupart, and S Tait, 1996. Fragmentation of magma during Plinian volcanic eruptions. Bulletin of Volcanology, 58: 144–162.

Gardner, JE, and S Tait, 2000. The caldera-forming eruption of Volcán Ceboruco, Mexico. Bulletin of Volcanology, 62: 20–33.

Geschwind, C-H and MJ Rutherford, 1995. Crystallization of microlites during magma ascent: the fluid mechanics of the 1980–1986 eruptions at Mount St. Helens. Bulletin of Volcanology, 57: 356–370.

Hammer, JE, KV Cashman, RP Hoblitt, and S Newman, 1999. Degassing and microlite crystallization during the pre-climactic events of the 1991 eruption of Mt. Pinatubo, Philippines. Bulletin of Volcanology, 60, 355–380.

Hammer, JE and MJ Rutherford, 2002. An experimental study of the kinetics of decompression-induced crystallization in silicic melt. Journal of Geophysical Research, B, 107.

Hildreth, W, 1983. The compositionally zoned eruption of 1912 in the Valley of Ten Thousand Smokes, Katmai National Park, Alaska. Journal of Volcanology and Geothermal Research, 18: 1–56.

Houghton, BF, CJN Wilson, J Fierstein, and W Hildreth, , 2004. Complex proximal deposition during the Plinian eruptions of 1912 at Novarupta, Alaska. Bulletin of Volcanology, 66: 95–133.

Izbekov, P, JE Gardner, B Andrews, VV Ponomareva, and IV Melekestsev, 2003. Petrology of Holocene caldera-forming eruptions at Ksudach, Kamchatka. EOS Transactions AGU, 84(46), Fall Meeting Supplement, Abstract V42B-0347.

Kaminski, E, S Tait, and G Carazzo, 2005. Turbulent entrainment in jets with arbitrary buoyancy. Journal of Fluid Mechanics, 526: 361–376.

Manga, M, J Castro, KV Cashman, and M Loewenberg, 1998. Rheology of bubble-bearing magmas. Journal of Volcanology and Geothermal Research, 87: 15–28.

Neri, A, A DiMuro, and M Rosi, 2002. Mass partition during collapsing and transitional columns by using numerical simulations. Journal of Volcanology and Geothermal Research, 115: 1–18.

Paladio-Melosantos, MLO, RU Solidum, WB Scott, RB Quiambao, JV Umbal, KS Rodolfo, BS Tubianoso, PJ de los Reyes, RA Alonso, and HB Ruelo, 1996. Tephra falls of the 1991 eruptions of Mount Pinatubo. In: Fire and Mud: 512–535.

Pyle, DM, 1989. The thickness, volume, and grain-size of tephra fall deposits. Bulletin of Volcanology, 51: 1–15.

Roche, O and TH Druitt, 2001. Onset of caldera collapse during ignimbrite eruptions. Earth and Planetary Science Letters, 191: 191–202.

Sparks, RSJ, 1986. The dimensions and dynamics of volcanic eruption columns. Bulletin of Volcanology, 48: 3–15.

Volynets, ON, VV Ponomareva, OA Braitseva, IV Melekestsev, and ChH Chen, 1999. Holocene eruptive history of Ksudach volcanic massif, South Kamchatka: evolution of a large magmatic chamber. Journal of Volcanology and Geothermal Research, 91: 23–42.

Walker, GPL, 1981. Plinian eruptions and their products. Bulletin of Volcanology, 44: 223–240.

Wilson, L, RSJ Sparks, and GPL Walker, 1980. Explosive volcanic eruptions, IV, The control of magma properties and conduit geometry on eruption column behavior. Geophysical Journal of the Royal Astronomical Society, 63, 117–148.

Wilson, CJN, and WH Hildreth, 1997. The Bishop Tuff: new insights from eruptive stratigraphy. Journal of Geology, 105: 407–439.

Wilson, CJN, and WH Hildreth, 1998. Hybrid fall deposits in the Bishop Tuff, California; a novel pyroclastic depositional mechanism. Geology, 26: 7–10.

Woods, AW, 1988. The fluid dynamics and thermodynamics of eruption columns. Bulletin of Volcanology, 50: 169–193.

Benjamin J. Andrews, Department of Geology and Geophysics, Jackson School of Geosciences, The University of Texas at Austin, 1 University Station C1100, Austin, TX 78712-0254, email: andrewsb@mail.utexas.edu

Late Pleistocene and Holocene Caldera-Forming Eruptions of Okmok Caldera, Aleutian Islands, Alaska

Jessica F. Larsen[1,2], Christina Neal[1,3], Janet Schaefer[1,4], Jim Beget[1,5], and Chris Nye[1,4]

Okmok volcano, in the central Aleutian arc, Alaska, produced two caldera-forming eruptions within the last ~12,000 years. This study describes the stratigraphy, composition, and petrology of those two eruptions. Both eruptions initially produced small volumes of felsic magmas, followed by voluminous andesite and basaltic andesite. The Okmok I eruption produced >30 km^3 DRE of material on Umnak Island, and Okmok II ~15 km^3. However, a significant proportion of material not accounted for here was deposited into the oceans during both events. The Okmok I pyroclastic flow deposits contain evidence for interaction with snow/ice, particularly along the northern flanks of the caldera. Although both Okmok I and II eruptions involved a phreatomagmatic component, the accumulation of a large volume (>15km^3) of volatile-rich, mafic-intermediate magma in the shallow crust may provide the driving force for the catastrophic eruptions. Agglutinate deposits associated with Okmok II indicate energetic lava fountaining simultaneous with caldera-collapse, similar to other descriptions of mafic-intermediate caldera-forming deposits such as in the New Hebrides.

1. INTRODUCTION

Okmok Volcano is a stunning example of an oceanic arc caldera, and is now one of the best studied of the Aleutian arc volcanoes (Figure 1). Early work on Okmok was conducted by the U.S. Geological Survey (e.g. Byers, 1959, 1961) in response to an eruption in 1945, observed by the WWII military base at Fort Glenn. The resulting work by Byers (1959, 1961) provided information that was not expanded upon until 20–30 years later. Studies in the 1970s–1980s focused mainly on the origin of primary Aleutian arc magmas and subduction zone mass recycling (e.g. Marsh, 1979, 1982; Brophy, 1986; Myers and Marsh, 1987; Miller et al., 1992; Kay and Kay, 1994; Fournelle et al., 1994; Class et al., 2000). Nye and Reid (1986) studied the most primitive basalts of Cape Idak and concluded that they were the product of high degrees of partial melting in the mantle wedge. Miller et al. (1992, 1994) focused mainly on the closely spaced (45 km) tholeiitic Okmok caldera (TH) and calc-alkaline (CA) Recheshnoi systems, and concluded that their magmatic series' can be modeled by extensive fractionation, but from separate sources undergoing different degrees of partial melting of the mantle wedge. None of the prior studies sought to place the Okmok volcanic series in stratigraphic context, or provide absolute age control. Thus, no detailed stratigraphic descriptions of the two caldera-forming eruption deposits have been published until very recently II (Burgisser, 2005).

The purpose of this study is to provide a fundamental description of the stratigraphy, physical, and chemical characteristics of the two late Pleistocene-Holocene caldera-

[1] Alaska Volcano Observatory
[2] Geophysical Institute, University of Alaska, Fairbanks, 99775
[3] U.S. Geological Survey, Anchorage, Alaska, 99508.
[4] State of Alaska, Division of Geological and Geophysical Surveys, Fairbanks, AK, 99709
[5] Dept. of Geology and Geophysics, University of Alaska, Fairbanks, 99775

Volcanism and Subduction: The Kamchatka Region
Geophysical Monograph Series 172

10.1029/172GM24

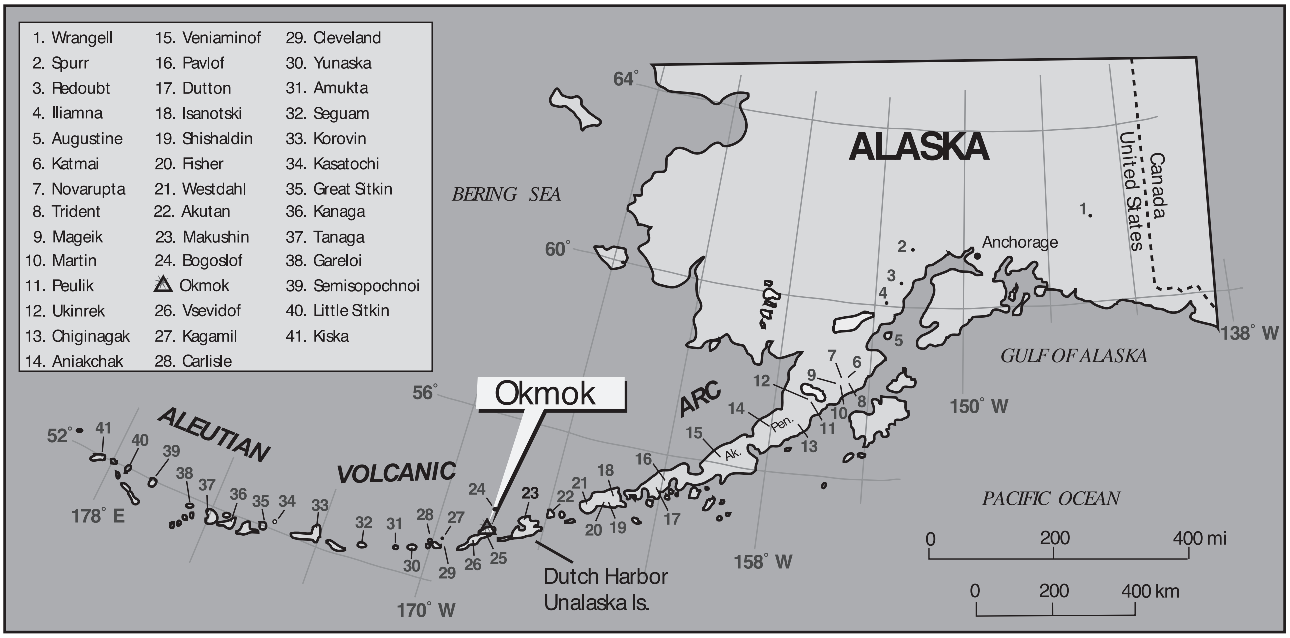

Figure 1. Location map of Okmok volcano, Alaska.

forming eruption deposits. The present study provides the first detailed description available of the late Pleistocene Okmok I caldera-forming eruption. The I and II eruptions were geochemically and volumetrically unique, and are important to understand the eruption history and chemical cycles of Okmok volcano. We also discuss unique features inherent to each eruption that yield clues about the physical environment of Okmok volcano in the late Pleistocene, which may also be important for their eruptive mechanisms.

2. GEOLOGIC SETTING

Umnak island lies 100 km southwest of Dutch Harbor, Unalaska Island, which is a productive port for fisheries in the north Pacific and Bering seas (Figure 1). There are three main volcanic centers on Umnak Island: Pleistocene-Holocene Recheshnoi and Vsevidof volcanoes in the southwest region of the island, and Okmok volcano in the northeastern Umnak Island region (Figures 1 and 2). Okmok volcano consists of a ~30 km diameter shield with a 10 km diameter caldera dominating the northeastern portion of Umnak Island rocks (Byers, 1959; Miller et al., 1998). The modern edifice probably rests on a base of Tertiary volcanic and altered sedimentary rocks. Two currently inactive, glaciated cones, Jag Peak and Mount Tulik, and smaller Pleistocene-Holocene cinder cones are also constructed on the flanks (Figure 2). The caldera consists of two, nested craters, with the high, North and East Arcuate rims outlining the Okmok I caldera. The slightly smaller Okmok II caldera rim is coincident with the Okmok I rim to the south and west, but lies within the North and East Arcuate rims along the north and east (Figure 2). No soils exist beneath the Okmok I unit on Umnak Island. However, one radiocarbon date from a thin soil between the Okmok I deposits from on westernmost Unalaska Island (03JLOK64), and another from beneath distal tephras near the city of Unalaska about 100 km away, indicate the Okmok I eruption occurred about 12,000 ^{14}C yBP (Bean, 1999; Begét et al., 2005). The Okmok II caldera-forming eruption has a ^{14}C radiocarbon age date of 2050 +/-50 yBP from charred grass found within the basal Plinian fall deposit.

The pre-caldera volcanic history of Okmok was predominantly effusion of now variably palagonitized, basaltic lava flows (Byers, 1959; Kay and Kay, 1994; Miller et al., 1992; Nye and Reid, 1986). The oldest dated lavas belong to the Ashishik Basalt formation, which were Ar dated by Bingham and Stone (1972), and are up to ~2 million years old . The primitive lava flows exposed along Cape Idak (Figure 3) are probably older than the Ashishik basalts (e.g., Byers, 1959; Nye and Reid, 1986). Pre-caldera palagonitized pyroclastic rocks are also exposed in places around the flanks and within the caldera walls (Figure 3), yet their absolute ages are unknown (Byers, 1959, 1961). Pleistocene-Holocene, andesitic-dacitic dikes and plugs are exposed within the caldera walls and near the caldera outlet along upper Crater Creek. These rocks are glassy, highly fractured or shattered, and have pillow lavas and pillow fragment breccias in proximity, indicating they were erupted against or beneath glacial ice.

The most silicic known Okmok deposit is the Pleistocene, glassy rhyolite lava flow exposed high along the outer wall of the North Arcuate rim (Figure 3). Several pre-caldera II basaltic cinder cones, lava flows, and a fissure vent also crop out on the flanks, and show some evidence for glacial erosion, particularly along the north and northwest flanks.

Byers (1959) originally mapped the Crater Creek Basalt formation, which is the most significant deposit intermediate in age to Okmok I and II, and forms a bench between the modern caldera floor and the North Arcuate Rim that extends partway along the banks of upper Crater Creek (Figure 3). Although grouped as basaltic by Byers (1959), they range from basalt to andesite (Figure 4). Multiple explosive, scoria-producing eruptions during this time period (not shown in Figure 4), resulted in several thick sequences of scoria lapilli, bomb, and lithic lapilli fall and surge deposits exposed along the north, east, and south flanks. The thickest intracaldera scoria deposit is exposed mainly along the south flanks, originating from a violent, long-lived, phreatomagmatic eruption (Wong, 2004). The timing of those eruptions relative to effusion of the Crater Creek lavas is unknown.

Approximately 14 separate vents have erupted within the modern caldera since the Okmok II CFE. The deposits range from lava flows across the caldera floor, to spatter and tuff

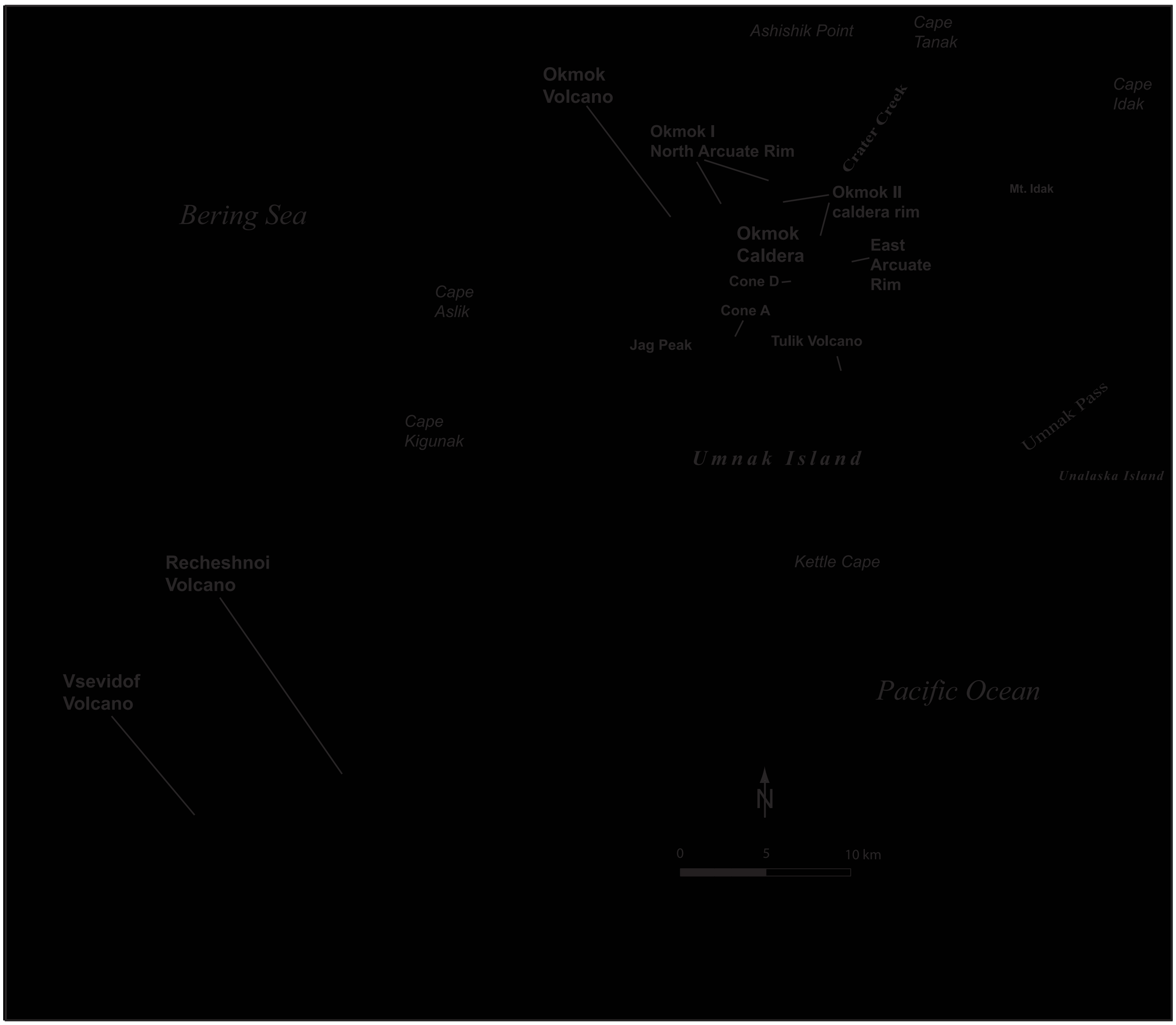

Figure 2. Shaded relief image of Umnak Island showing major geographic features, such as Vsevidof and Recheshnoi volcanoes to the southwest. This figure illustrates the dominance of Okmok caldera in the northeast part of the island, and the "table lands" morphology from the thick pyroclastic flow deposits from the Okmok I and II eruptions.

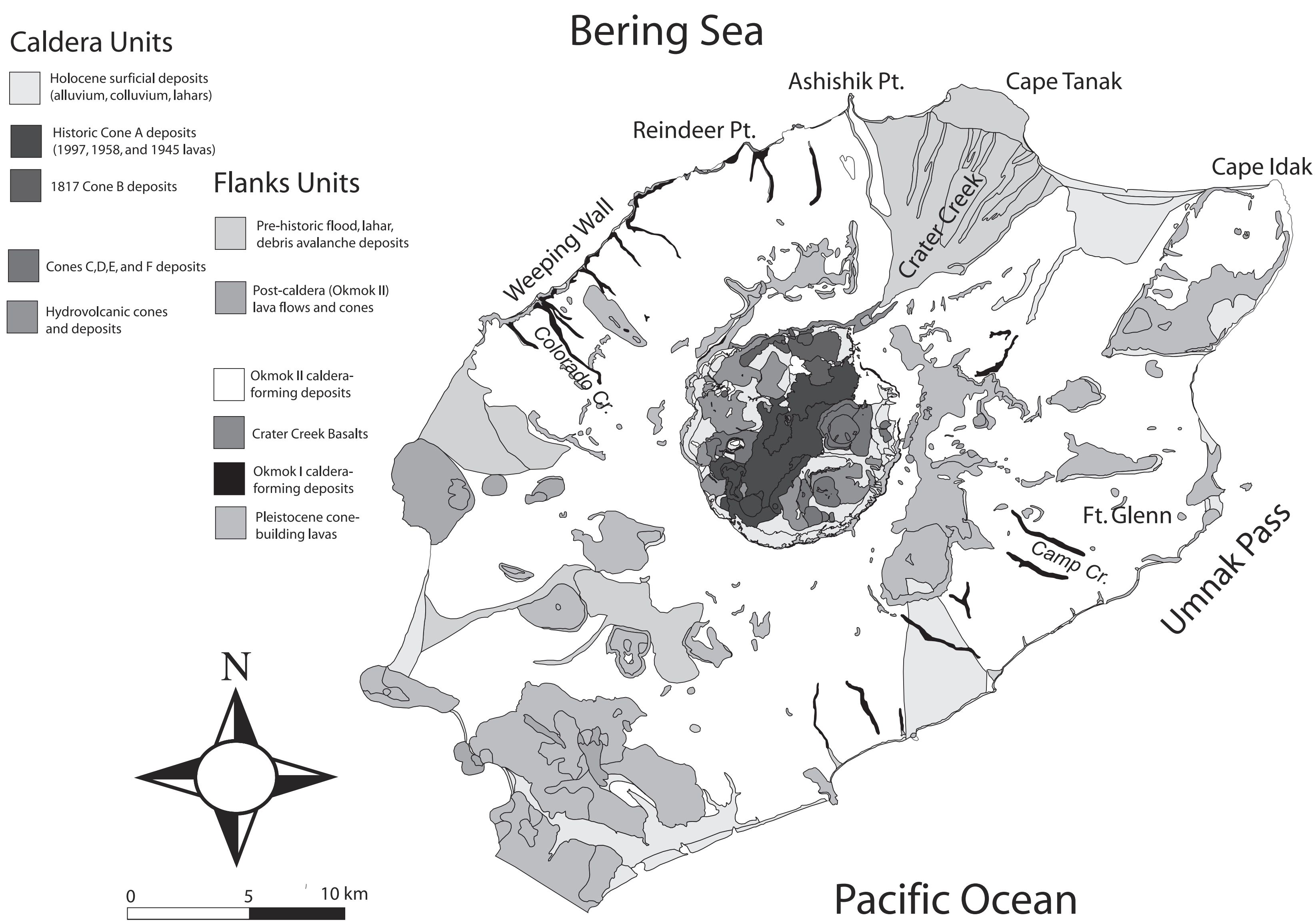

Figure 3. Simplified geologic map of the northeast portion of Umnak Island. This map shows units mapped by AVO geologists, as well as those from the work of Byers (1959). The units shown are simplified versions of the original map polygons, combined primarily by their relative ages and types of deposits they represent. The original map is too complex to display clearly using grayscale format on a journal page, and will be published separately (Larsen et al., in prep; Neal et al., in prep).

cone deposits erupted both sub-aerially and sub-aqueously within caldera lakes. . During the last 70 years Okmok has erupted 7 times (e.g., Grey, 2003), most recently in 1997, with a largely effusive eruption of basalt covering part of the caldera floor (McGimsey and Wallace, 1999). Many of the historic eruptions of Okmok produced tephra deposits, ash clouds, and lava flows, originating from Cone A. The 1945 and 1958 eruptions were similar to the 1997 event, and each produced lava flows that covered part of the modern caldera floor (Figure 3). The 1817 eruption was the largest during recorded history (e.g., Grewingk, 1850; Byers, 1959; Wolfe and Begét, 2002), produced from Cone B. This eruption resulted in another breakout flood from the caldera, originating from a small lake that had been dammed by lava flows from Cone B. The flood and associated lahars inundated an Aleut village located at Cape Tanak (Grewingk, 1850; Begét et al., 2005).

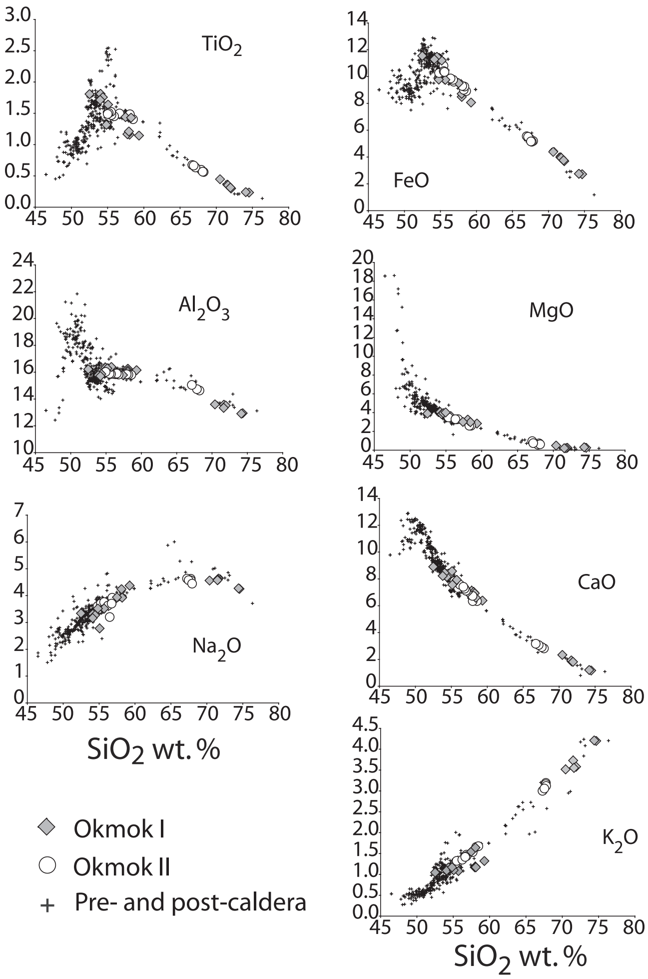

Figure 4. Harker diagrams showing Okmok I and II whole rock compared with rest of the Pleistocene-Holocene Okmok magmatic series. This figure shows that although the two caldera-forming eruptions produced similar composition pyroclastic deposits, distinct differences are observed. The most prominent difference lies in the evolved samples, which are dacitic in the case of Okmok II and rhyolitic in Okmok I.

Since the Okmok II eruption, the caldera was breached along the north rim by at least one catastrophic flood between 1400 and 1000 years ago (e.g., Byers, 1959; Wolfe, 2001). This event drained a lake that filled much of the caldera to 150 m depth after the second caldera-forming eruption (Begét et al., 2005), a smaller version of which now feeds Crater Creek.

3. FIELD AND ANALYTICAL METHODS

The Alaska Volcano Observatory conducted fieldwork between 1998 and 2004, installing seismic and geodetic monitoring networks and producing a revised geologic map (e.g., Figure 3) and hazards report (Begét et al., 2005). Geologic fieldwork consisted of geologic mapping, describing and correlating eruptive stratigraphy, sampling for geochemistry and petrology and Ar and ^{14}C dates, describing and sampling tephras, and graduate student thesis projects (Wolfe, 2001; Almberg, 2003; Grey, 2003; Burgisser, 2005).

Pumice and scoria chips analyzed by the Washington State University (WSU) Geoanalytical Laboratory provide the major and trace element compositions reported in Tables 1 and 2. Each juvenile clast was hand-picked, cleaned in deionized water in an ultrasonic bath to remove surface ash and soil, and then dried for several days at less than 100 °C. All samples were partially crushed to pea-sized or smaller grains, weighed, and 50 gram splits sent to WSU. X-ray fluorescence analyses were conducted following the methods outlined in Johnson et al. (1999). ICP-MS analyses for trace elements were conducted following the procedures described in Knaack et al. (1994).

4. RESULTS

4.1 Okmok I and II Major Oxide Compositions

Okmok I and II eruption products are compositionally classified following Le Maitre (1989). The major oxide compositions of both Okmok I and II products are similar and range between ~53 to ~74 wt. % SiO_2 (Tables 1 and 2). Basaltic andesite to andesite scoria from both eruptions are between 53 to ~58 wt. % SiO_2, and are similar to most products from known Pleistocene to Holocene eruptions of Okmok volcano (Figure 4). In the Okmok II samples there may be a small gap between the pyroclastic flow and andesite fall juvenile clasts, with the andesite fall samples confined to ~57–58 wt. %, and the pyroclastic flow scoria mostly below about

Table 1. Okmok I major oxide compositions of bulk juvenile pumice and scoria

Sample	99JLOK10A	99JLOK15D1	99JLOK15D2	99JLOK16F	99JLOK18A	99JLOK18B
SiO_2	52.75	71.52	70.48	55.09	58.11	59.27
TiO_2	1.81	0.36	0.45	1.64	1.17	1.14
Al_2O_3	16.18	13.39	13.59	16.18	16.07	16.14
FeO	11.39	4.10	4.46	11.23	8.86	8.11
MnO	0.21	0.13	0.14	0.21	0.20	0.20
MgO	3.99	0.24	0.43	3.74	3.04	2.78
CaO	9.04	1.90	2.31	7.80	6.91	6.41
Na_2O	3.17	4.58	4.56	2.77	4.24	4.37
K_2O	1.11	3.72	3.51	1.10	1.17	1.32
P_2O_5	0.34	0.05	0.07	0.25	0.22	0.25
Total	99.53	98.00	98.22	98.46	99.25	99.83

Sample	99JLOK18C	99JLOK20A	99JLOK20D	99JLOK22B	00JLOK29d	00JLOK29k
SiO_2	58.07	54.04	71.64	58.21	54.10	55.71
TiO_2	1.17	1.78	0.35	1.42	1.76	1.42
Al_2O_3	16.17	15.98	13.66	15.89	15.94	16.40
FeO	8.73	11.43	3.93	8.98	11.29	9.77
MnO	0.20	0.23	0.14	0.20	0.22	0.20
MgO	3.10	3.83	0.25	2.86	3.87	3.70
CaO	6.96	8.12	1.93	6.56	8.27	7.99
Na_2O	4.20	3.21	4.51	3.92	3.16	3.51
K_2O	1.18	1.07	3.55	1.65	1.10	1.08
P_2O_5	0.22	0.31	0.04	0.31	0.30	0.23
Total	99.37	99.02	98.34	99.39	99.54	99.03

Sample	00JLOK42_3	00JLOK42_4	00JLOK42Da	00JLOK42Dd	02JLOK59	04JLOK005
SiO_2	54.43	54.11	54.34	71.92	58.03	52.51
TiO_2	1.72	1.72	1.74	0.32	1.18	1.81
Al_2O_3	15.78	15.73	15.68	13.50	16.27	16.28
FeO	11.41	11.36	11.34	3.76	8.47	11.60
MnO	0.22	0.22	0.22	0.13	0.21	0.21
MgO	3.71	3.83	3.81	0.27	3.19	3.99
CaO	8.06	8.30	8.16	1.82	7.05	8.89
Na_2O	3.27	3.31	3.24	4.67	4.21	3.33
K_2O	1.12	1.11	1.17	3.58	1.17	1.05
P_2O_5	0.29	0.30	0.31	0.03	0.23	0.33
Total	99.31	98.99	98.55	97.84	99.21	98.92

Sample	04JLOK025b	04JLOK025c	04JLOK025_1	04JLOK025_2
SiO_2	56.01	53.44	74.06	73.97
TiO_2	1.49	1.80	0.24	0.25
Al_2O_3	15.85	16.19	12.87	12.94
FeO	10.03	11.01	2.70	2.71
MnO	0.21	0.22	0.07	0.08
MgO	3.45	3.96	0.18	0.18

Table 1. *Cont.*

Sample	04JLOK025b	04JLOK025c	04JLOK025_1	04JLOK025_2
CaO	7.67	8.91	1.20	1.22
Na_2O	3.65	2.98	4.27	4.25
K_2O	1.35	1.15	4.37	4.37
P_2O_5	0.29	0.34	0.03	0.03
Total	99.55	99.61	96.19	96.32

Table 2. Okmok II major element compositions of bulk juvenile pumice and scoria

Sample	98JLOK1a	98JLOK1b	98JLOK2a	98JLOK2b	98JLOK3a	98JLOK4b	98JLOK4g
SiO_2	56.82	55.50	55.24	54.79	55.88	67.73	55.68
TiO_2	1.47	1.47	1.50	1.51	1.46	0.61	1.48
Al_2O_3	15.91	16.03	16.00	16.06	15.98	14.74	15.88
FeO	9.60	10.10	10.16	10.30	10.03	5.32	10.16
MnO	0.21	0.20	0.21	0.21	0.20	0.16	0.21
MgO	3.16	3.59	3.64	3.80	3.51	0.57	3.52
CaO	7.14	7.83	7.99	8.26	7.60	2.87	7.69
Na_2O	3.92	3.69	3.71	3.61	3.70	4.67	3.76
K_2O	1.47	1.32	1.28	1.20	1.36	3.16	1.34
P_2O_5	0.31	0.28	0.28	0.27	0.28	0.17	0.28
Total	98.42	99.14	98.47	98.66	98.57	97.68	98.74

Sample	98JLOK5a	98JLOK6Ha	98JLOK6Hb	99JLOK4b	99JLOK4gbase	99JLOK4g_3
SiO_2	55.50	58.14	58.47	67.75	55.47	55.47
TiO_2	1.45	1.42	1.40	0.61	1.51	1.52
Al_2O_3	15.98	15.79	15.80	14.76	15.91	15.86
FeO	10.13	9.04	8.97	5.37	10.33	10.43
MnO	0.20	0.21	0.21	0.16	0.21	0.21
MgO	3.57	2.73	2.73	0.66	3.60	3.52
CaO	7.80	6.57	6.50	2.88	7.77	7.89
Na_2O	3.77	4.13	3.96	4.45	3.63	3.49
K_2O	1.32	1.66	1.66	3.19	1.27	1.33
P_2O_5	0.28	0.32	0.30	0.17	0.29	0.29
Total	99.23	98.36	99.98	98.00	99.66	98.10

Sample	99JLOK4g_5	99JLOK4g_7	99JLOK4g_10	00JLOK27a	00JLOK27b	00JLOK42b
SiO_2	55.28	55.66	55.71	55.11	55.56	67.09
TiO_2	1.50	1.46	1.47	1.48	1.48	0.65
Al_2O_3	15.85	15.90	15.94	16.10	16.04	15.02
FeO	10.51	10.27	10.18	10.33	10.16	5.31
MnO	0.21	0.20	0.20	0.21	0.21	0.17
MgO	3.64	3.54	3.52	3.73	3.60	0.94
CaO	7.95	7.76	7.80	8.03	7.91	3.04
Na_2O	3.53	3.58	3.57	3.48	3.49	4.61
K_2O	1.26	1.34	1.32	1.27	1.29	2.99
P_2O_5	0.28	0.28	0.27	0.26	0.27	0.18
Total	99.44	99.13	99.06	99.15	99.39	98.56

Table 2. *Cont.*

Sample	02JLOK63f	04JLOK004	04JLOK006	04JLOK008	04JLOK017	04JLOK018
SiO_2	58.07	67.83	56.64	57.67	67.10	56.24
TiO_2	1.49	0.60	1.45	1.44	0.66	1.49
Al_2O_3	16.08	14.70	15.88	15.74	15.03	15.91
FeO	8.81	5.17	9.85	9.42	5.45	9.99
MnO	0.21	0.16	0.20	0.20	0.17	0.21
MgO	2.90	0.69	3.23	2.94	0.76	3.35
CaO	6.49	2.87	7.35	6.81	3.06	7.54
Na_2O	3.97	4.75	3.68	3.93	4.62	3.63
K_2O	1.62	3.06	1.42	1.53	2.95	1.35
P_2O_5	0.36	0.17	0.29	0.31	0.20	0.29
Total	99.24	96.84	99.11	99.29	97.19	98.88

Sample	04JLOK019	04JLOK025a	04JLOK029b	04JLOK037e1	04JLOK037e2
SiO_2	56.82	67.54	56.88	58.03	58.11
TiO_2	1.47	0.63	1.45	1.42	1.42
Al_2O_3	15.86	14.81	15.84	15.84	15.79
FeO	9.83	5.34	9.77	9.24	9.25
MnO	0.21	0.17	0.21	0.21	0.21
MgO	3.13	0.71	3.18	2.82	2.81
CaO	7.21	2.97	7.25	6.61	6.57
Na_2O	3.72	4.65	3.71	3.90	3.89
K_2O	1.44	3.01	1.41	1.62	1.62
P_2O_5	0.30	0.18	0.29	0.32	0.32
Total	98.42	97.69	99.33	99.77	100.18

55 wt.% SiO_2. This gap may be a sampling artifact because of the small number of andesite fall deposits sampled with coarse enough lapilli (> 1 cm). Both caldera-forming eruptions also produced early-erupted Plinian fall deposits that are among the most evolved products erupted at modern Okmok volcano (e.g., Miller et al., 1992). The early Okmok II Plinian fall pumice is 67–68 wt. % SiO_2 rhyodacite, and the silicic component of Okmok I is rhyolitic at 70–72 wt. % SiO_2.

4.2 Okmok I Petrography

Okmok I eruption products are nearly aphryic (<5 wt. % phenocrysts), and the rhyolitic pumice from the early stages of the Okmok I eruption are nearly crystal free with flattened tube vesicle textures. The rare phenocrysts are plagioclase with minor augitic pyroxene. No Fe-Ti oxides were found in thin sections or grain mounts made from magnetically separated crystals. Some pumices also have mm-scale domains of dark grey to brown glass containing microlites (<200 µm). The basaltic andesite to andesite scoria from the fall and thick pyroclastic flow deposits contain a range of crystal types, sizes, and textures, but are again phenocryst-poor. The main phenocryst is plagioclase, with two pyroxenes, titanomagnetite, and rare olivine. Only microphenocrysts and microlites (<200 µm) exist in some scoria fragments. Sparse plagioclase phenocrysts, 350 to 1000 µm size, are severely resorbed and sieve textured. The scorias also contain crystal clots and crystalline inclusions containing plagioclase, pyroxenes, Fe-Ti oxides, and olivine..

4.3 Okmok II Petrography

The Okmok II Plinian rhyodacite pumices contain plagioclase, hypersthene, augite, and titano-magnetite, with plagioclase the most abundant phenocryst. No ilmenite exists in the samples studied either because it was not a stable phase in the magma, or it is sparsely distributed in the very crystal-poor (< 5 % by volume) rhyodacite pumice. The groundmass is clear glass with no microlites. The phenocrysts found in the andesite fall scorias are plagioclase, hypersthene, and titanomagnetite. Plagioclase-dominant crystal clots are common and contain associated pyroxenes, Fe-Ti oxides, and trace olivine. The groundmass glass is mostly clear and microlite-free, yet discrete regions also contain abundant plagioclase microlites with skeletal shapes that indicate rapid nucleation and growth, either during post-eruptive cooling or magmatic ascent and degassing (e.g., Lofgren, 1980)

Okmok II basaltic andesite scoria have heterogeneous phenocryst populations, with plagioclase, hypersthene, augite, titano-magnetite, and sparse olivine, mainly in crystal clots as seen in the andesite fall scoria lapilli. The most abundant mineral is plagioclase, with compositions between An_{30} and An_{95}, with approximately three populations evident: $\geq An_{90}$, $\sim An_{60}$, and $\sim An_{30}$. The $>An_{90}$ plagioclase crystals are variably sieved and fritted, with ragged edges. Intermediate, An_{60} plagioclase crystals are clean and euhedral, as are the An_{30} phenocrysts. There are abundant plagioclase and pyroxene microlites in the groundmass, making compositional analyses of the groundmass glass problematic. The plagioclase microlites are skeletal, indicating rapid nucleation and growth during magma ascent and post-eruptive cooling (e.g., Lofgren, 1980; Hammer and Rutherford, 2002). The crystal clots are diverse, some mainly plagioclase and Fe-Ti oxides, whereas others are dominated by intergrown plagioclase and pyroxene. The crystal clots are partially resorbed with disequilibrium textures, similar to the anorthitic plagioclase phenocrysts. Crystal-rich lithic inclusions exist in most scoria clasts, and these may represent pre-caldera lavas, or sub-caldera intrusives that were fragmented, forming cored lapilii and bombs.

4.4 Okmok I and II: Volume Estimates

Dense rock equivalent (DRE) volume estimates of subunits within the caldera-forming deposits have been made using the thicknesses and distributions of the measured outcrop sections (Figure 5). Okmok I volume estimates are complicated because outcrops are sparse and the thickest sections are limited to the north flanks where steep terrain confounds complete section measurements in some places. Thus, minimum and maximum on-island volume estimates have been formulated by assuming deposition at all azimuths versus deposition only in the quadrants in which the Okmok I deposits are exposed, primarily omitting the western sector of the island. The basal breccia deposits best observed at Colorado Creek (Figure 3) have a maximum estimated volume of ~1 km^3. The Okmok I basal surge and fall layers comprise 4–6 km^3, the main pyroclastic flow deposits are 14 to 21 km^3, and the top surge layers are 2 to 3 km^3. The total volume estimate for Okmok I on Umnak Island ranges from ~ 21 to ~ 31 km^3, within the bounds described above. These estimates do not account for the estimated total volume of the depression thought to remain from the Okmok I eruption (~50 km^3), or the volume of material that was deposited into the oceans. In contrast, the Okmok II deposits are usually significantly thinner than Okmok I, which leads

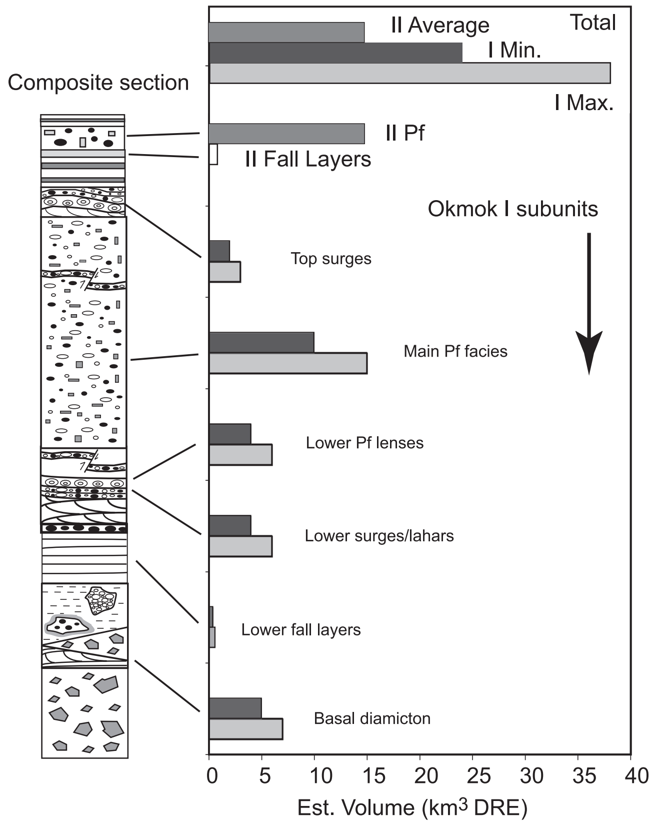

Figure 5. On-island volume estimates for different deposits within the Okmok I and II eruption sequences. The white bar represents the Okmok II Plinian rhyodacite and andesite fall deposits. The medium grey bar represents the Okmok II pyroclastic flow deposits. The black bar represents the maximum volume estimates for different units within the Okmok I sequence. The light grey bar represents the minimum volume estimates for the Okmok I sequence. The maximum and minimum estimates for Okmok I were made assuming deposition over all flanks uniformly, and then deposition confined only to the northwest to south flanks, omitting the west flanks region where outcrops were not found. The maximum on-island estimates for both eruptions represent minimum estimates of the total volume of material ejected during each eruption, because a significant amount of material was lost to the oceans.

to significantly lower eruptive volume estimates. Burgisser (2005) notes the total volume of the initial rhyodacite and andesite Plinian fall deposits are ~0.5 km^3, whereas the main pyroclastic flow deposits are estimated to be ~15 km^3 on-island.

4.5 Okmok I Stratigraphy

Okmok I is best exposed between 2 to 10 km from the present caldera rim, and depositional characteristics differ

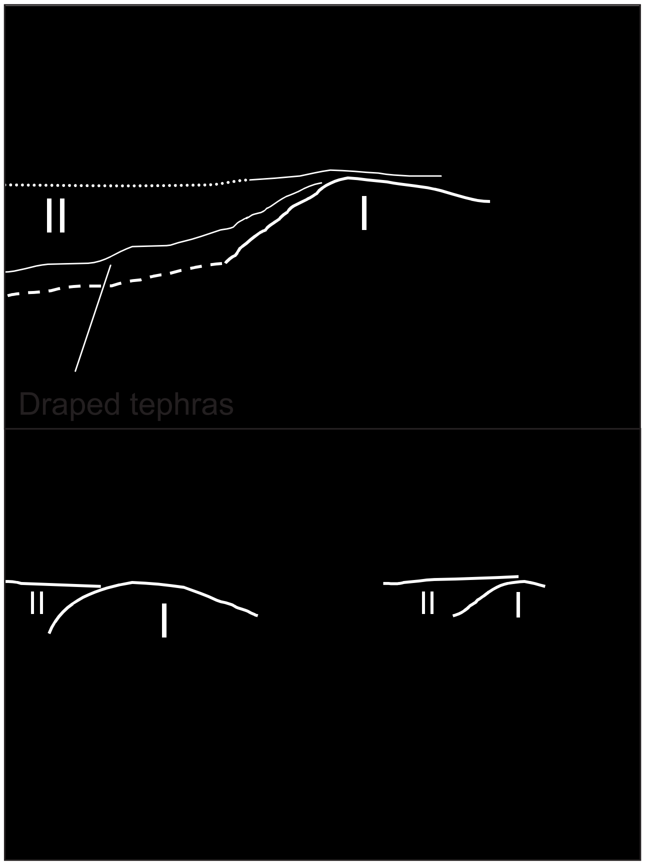

Figure 6. This figure shows two locations where the Okmok I top surface shows a regular pattern of undulations. The stream channels cut across the undulatory surface, exposing a cross section perpendicular to the axis of the undulations. From this, it appears that the undulations are oriented parallel to the slope, and probably perpendicular to the general direction of flow of the Okmok I pyroclastic flows. The undulations have wavelengths up to ~100 m and amplitudes of ~20 m. This surface characteristic is found on all flanks of the volcano where Okmok I outcrops. In contrast, the surface of the Okmok II pyroclastic flow deposits forms a relatively smooth plateau around all flanks of the volcano. I-Okmok I pyroclastic flow deposits. II-Okmok II deposits.

significantly with volcano sector. The most distal exposure studied is on the southwest end of Unalaska Island (Figure 2), and it provides evidence that the eruption involved both mafic-intermediate and rhyolite magmas. Only Okmok II deposits are exposed along the southwest flank, along with post-II Holocene deposits and older basalt flows from flank vents. The Okmok I eruptive sequence is determined based on a continuation of pyroclastic flow and lahar deposits that show no obvious signs of time breaks, such as soil development or fluvially eroded surfaces. Most of the sub-units are gradational or are interlayered with those they overlie. The basal breccia deposits are not well exposed, and are thus not as certainly grouped within the Okmok I sequence. However, the chaotic breccia described below does grade upward into the series of pyroclastic flow deposits recognized in all sectors as belonging to the Okmok I sequence.

The Okmok I pyroclastic flow deposits are exposed in all sectors except the west flanks of the caldera, and are the thickest and most widely exposed part of the sequence. A few locations show internal flow structure, lithic accumulations, and interfingering with surge and lahar deposits, possibly indicating semi-continuous aggradation of the deposits. However, the sparse and incomplete exposures and indurated nature of the deposits has made it difficult to fully assess emplacement mechanisms. Okmok I also has an undulatory upper surface that could also relate to bed forms resulting from emplacement (Figure 6).

4.5.1 North sector basal and chaotic breccia deposits. The basal deposits (Figures 7a and 8a) consist of 10 to 12 m of poorly sorted material containing angular lithic cobbles and boulders (up to 1.5 m) in a sandy, ash-rich matrix. The unit is massive, yet locally contains weak imbrication of lithic clasts and a slight normal grading at the top. Regions of this unit are reddish and oxidized, and contain prismatic lithic blocks. This unit does not contain abundant juvenile lapilli. The prismatic blocks, reddish oxidation, and the ash-rich matrix indicate an early explosion or lateral blast in the Okmok I eruption sequence. At 00JLOK42 on Reindeer Point (Figure 9), the topmost portion of this basal unit lies directly below juvenile pyroclast-rich, ash fall and surge layers. The contact has a 2–3 cm thick layer of dark grey coarse ash overlying the wavy upper surface of the lithic-rich clastic unit.

The basal lithic boulder rich deposit grades upward at 01JLOK47 Colorado Creek (Figures 7 and 9) into a section that includes discrete domains of tan pumice and black scoria and ash layers that are chaotically interbedded within an indurated, massive, poorly sorted, "muddy", brown to red silt to fine lapilli size matrix, which also contains juvenile lapilli with average sizes of 0.5 to 1 cm (Figure 8b). Some domains contain tan-colored, rounded pumice lapilli with average grain sizes of 2–3 cm, with diverse characteristics from very well sorted, to very poorly sorted domains containing light grey-tan ash, as well as larger 0.5 to 2 cm size dark scoria and lithics. A second class of domains comprise chaotically arranged, dark black to grey, poorly sorted, scoria-rich, matrix supported material. The matrix is 0.5 mm or less grain size, with scoria fragments of 1–2 cm, and rare 3–5 cm clasts. Surrounding these lenses, the muddy indurate matrix is red and oxidized, and appears baked, indicating the scoria lenses probably came from hot pyroclastic flows early in the Okmok I eruption. Also enclosed within this chaotic unit are domains of poorly sorted, lithic rich material, with angular fragments, reddish oxidized matrix and clasts, and average lithic sizes of 12 to 30 cm on the longest axes, with the largest boulders up 1–2 m in length. These discrete lenses also contain sections of finer grained, variably fines-depleted, wavy and cross-bedded laminations. Figure 8b shows tan pumice, dark scoria, and boulder-rich domains chaotically distributed throughout this unit. In general, there is no layering or orientation to the diverse domains. It appears that the individual tan pumice, scoria, and ash layers were formerly deposited uniformly along the ground surface, and then an extremely scouring flow ensued, which ripped the layers up and redistributed them chaotically within the muddy material forming the mass of the flow. The chaotic breccia deposits have only been observed at Colorado Creek and have an unknown distribution pattern.

4.5.2 North sector surge and lahar deposits. At Colorado Creek and Reindeer Creek outcrops, the chaotic breccia grades up into indurated deposits that bear the characteristics of surge bedding (Figure 8a). Composed primarily of rhyolite and andesite juvenile pyroclasts, the surge deposits contain only sparse lithics. The surge character of the deposits manifests as a series of laminated, pinch and swell layers that are poorly sorted, predominantly 1–2 mm ash. Cross-bedding and reversely graded, discrete layer sets are common features in this part of the depositional sequence. Some layers within this unit are composed of sub rounded to rounded juvenile fragments 0.5 to 3 cm on a side, with the

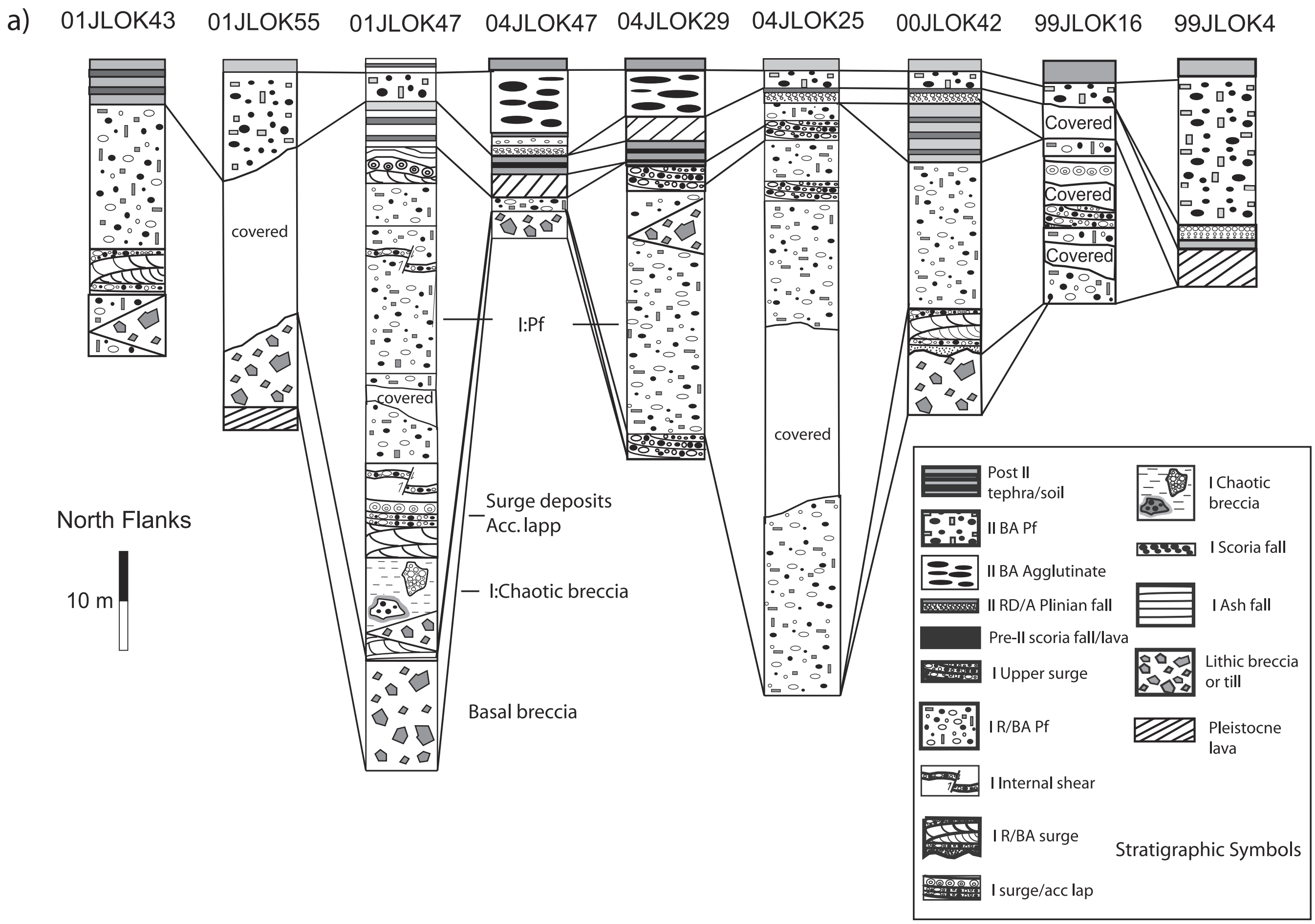

Figure 7. a) Stratigraphic fence diagram showing the variations in thickness and deposit character for Okmok I and II along the north flanks region of the volcano. The legend shows the symbols used for each type of deposit plotted. The locations of the individual sections are shown in Figure 9. The fence diagrams show that the Okmok I deposits are much more complex along the north flanks region. For example, in the Colorado Creek section (01JLOK47), the stratigraphic column shows the chaotic breccia, wet surge/lahar deposits, and accretionary lapilli in the lower and upper surge beds that occur within the Okmok I sequence.

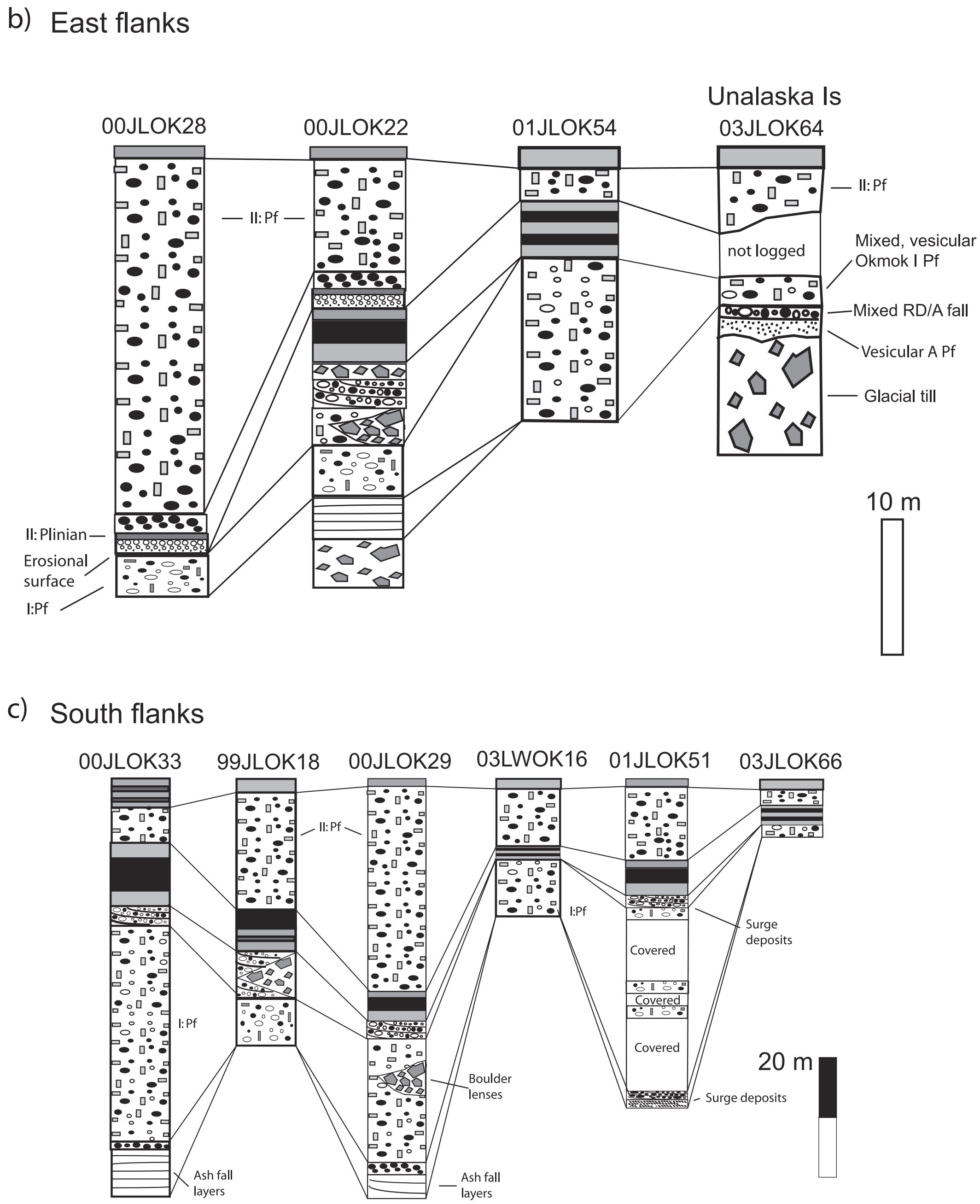

Figure 7. b) Stratigraphic fence diagram showing the variations in thickness and deposit character for Okmok I and II along the east flanks region of the volcano, including one outcrop on Unalaska Island. c) Stratigraphic fence diagram showing the variations in thickness and deposit character for Okmok I and II along the south flanks region of the volcano, including one outcrop on Unalaska Island. Most of the Okmok I deposits exposed in this region are the massive pyroclastic flow deposits.

largest fragments up to 5–6 cm maximum length. Locally at Reindeer Creek, fragments of scoria up to 13 cm on a side exist rarely. Indeed, some of the friable tan pumice clasts are so rounded that they appear to be as eroded as if they were transported by water .

Abundant accretionary lapilli are present near the top of this unit in most sections, but are particularly well preserved at 01JLOK47 Colorado Creek (Figure 7a). The accretionary lapilli are vuggy with hollow cores, 1–2 cm average size, with the largest up to 5 cm across. Also at this horizon in the

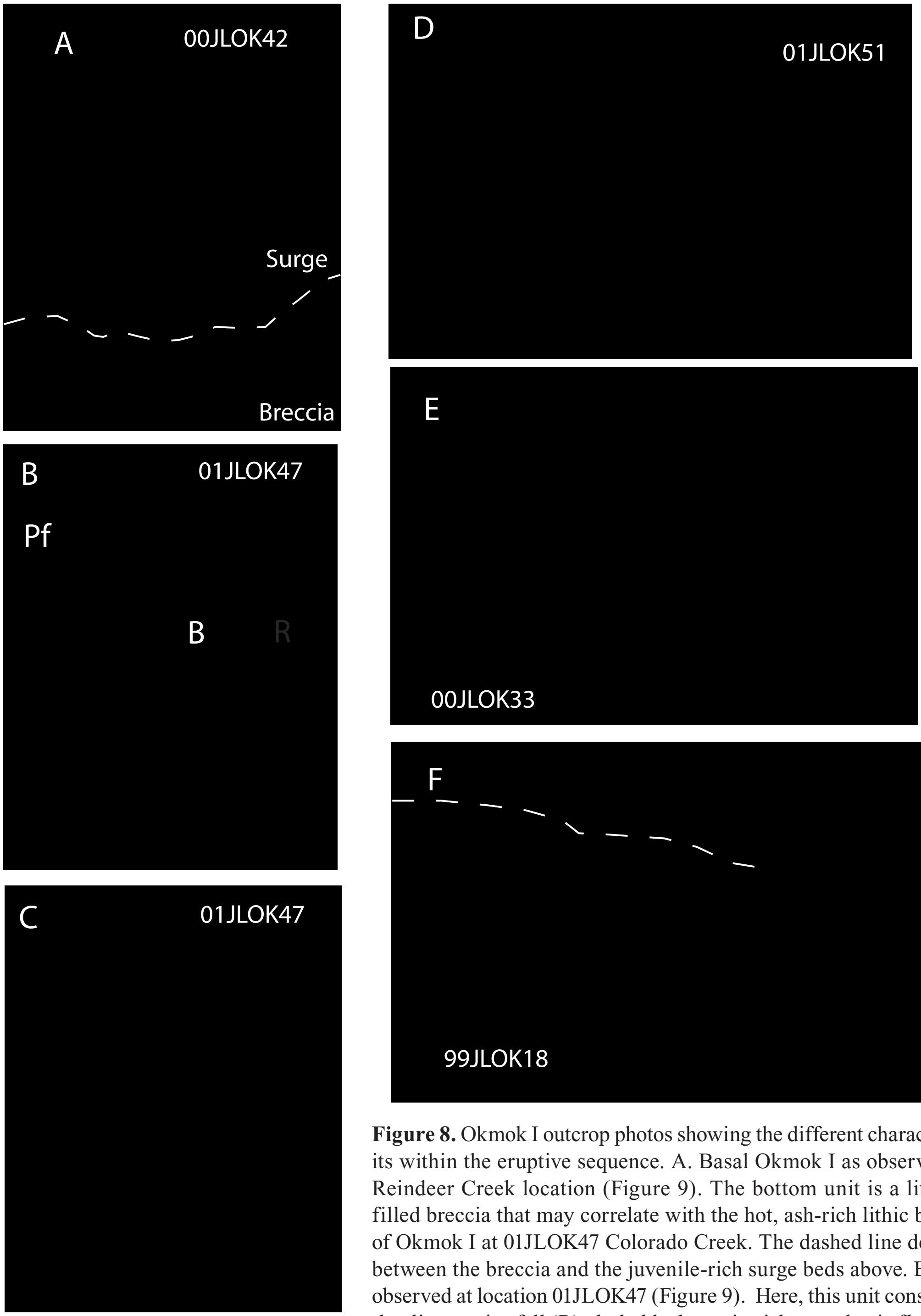

Figure 8. Okmok I outcrop photos showing the different characteristics of deposits within the eruptive sequence. A. Basal Okmok I as observed at 00JLOK42, Reindeer Creek location (Figure 9). The bottom unit is a lithic-rich, boulder filled breccia that may correlate with the hot, ash-rich lithic breccia at the base of Okmok I at 01JLOK47 Colorado Creek. The dashed line denotes the contact between the breccia and the juvenile-rich surge beds above. B. Chaotic breccia observed at location 01JLOK47 (Figure 9). Here, this unit consists of domains of rhyolite pumice fall (R), dark, black scoria-rich pyroclastic flow lenses (Pf), ash layers, sediment, and lithic boulder domains (B) chaotically deposited with no regular internal structure. C. Cemented, poorly sorted, sandy hyperconcentrated flow deposits, probably associated with syn-eruptive lahars. D. Wavy, scoria-rich surge bedding beneath the massive Pf facies of the Okmok I sequence, outcropping on the south flanks at 01JLOK51 Kansas Creek (Figure 9). E. Massive, poorly sorted, mingled rhyolite and basaltic-andesite pyroclastic flow of Okmok I. F. Wavy, lithic-rich surge and lahar layers at the top of Okmok I on the southcoast, at Vermont Creek (99JLOK18; Figure 9). The dashed line denotes the top surface of the Okmok I deposits.

Colorado Creek section, internal shear structures are present, and they offset the individual surge layers. Locally at Colorado Creek, cemented or indurated, fissile or "scabby" deposits are interlayered with the juvenile-rich surge beds (Figure 8c). These layers are poorly sorted, and are rich in sand, ash, and lithic fragments, which have grain sizes ranging up to several cm. These layers probably represent lahars that formed at the same time the pyroclastic surges formed and flowed along the north flanks of the volcano.

4.5.3 North sector pyroclastic flow deposits. The surge and lahar layers grade upward into massive deposits rich in juvenile pyroclasts, and are matrix supported, and poorly sorted. In places, the transition into massive, lithic-bearing pyroclastic flow deposits is an interfingering contact with the surge and lahar layers. The main pyroclastic flow deposit contains predominantly dark grey juvenile scoria, lithics, and 0–10% by volume (by outcrop inspection) of friable tan pumice lapilli concentrated in various regions throughout

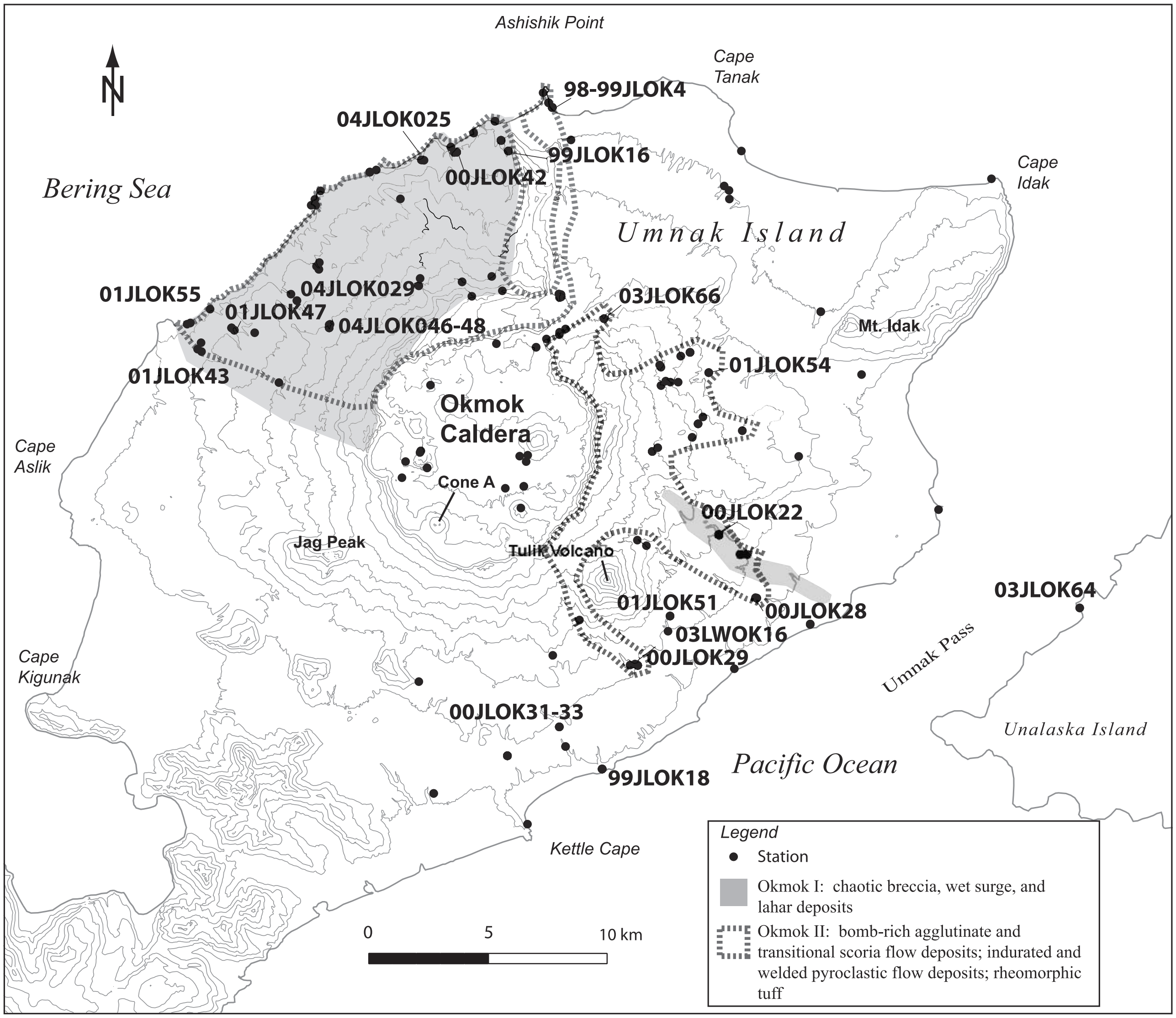

Figure 9. Map showing the approximate distribution of notable facies within the Okmok I and II depositional sequences. The light grey area outlines the extent of the Okmok I basal chaotic breccia and associated surge and lahar deposits on the north and east flanks. The area outlined by the dashed line represents combined distribution of spatter, ribbon, and cauliflower bomb-rich agglutinate and transitional, scoria flow deposits, indurated and welded pyroclastic flow deposits, and rheomorphic tuff associated with the Okmok II eruption. The labeled locations are all Okmok I and II map stations visited by J. Larsen. Only the stations shown in the fence diagrams in Figures 7a–c are labeled in bold font.

the deposit. The lithic clasts vary in abundance relative to the juvenile scoria and pumice, depending on stratigraphic height and outcrop location, and are a mixture of basaltic lava fragments, altered volcanics, and possibly older sedimentary rock fragments. At the base of the 01JLOK47 section (Figures 7a, 9), the average lithic and scoria sizes are 1cm. The pyroclastic flow deposits are locally reversely graded to clasts that are up to 10 cm, over ~30 meters in stratigraphic height from the base.

4.5.4 North sector upper surge bedding. At most locations, the uppermost deposits from the Okmok I eruption are wavy, with local laminations, cross bedding, and pinch and swell layers (Figure 7). Along the north flanks, accretionary and armored lapilli up to 5 cm in size occur locally. The armored lapilli are scoria fragments rimmed by dark grey, coarse ash layers. At Colorado Creek, the surge deposits have higher percentages of tan pumice lapilli (~50 vol. % than earlier Okmok I deposits. It is uncertain whether the increase in tan pumice resulted from an increase in the more silicic component at the end of the eruption, or simply represents local concentrations of the less dense tan pumice towards the top of the pyroclastic flow deposits.

4.5.5 East sector and Unalaska Island. The Okmok I deposits along the east flanks are mainly confined to the deep stream channels proximal to the caldera (Figure 7b). The most complete section in the eastern sector was observed at 00JLOK22 Camp Creek (Figure 7b). Approximately 5 m above the stream, the deposits are moderately fissile, extremely poorly sorted, and contain1 cm to 0.5 m sized lithics with little or no juvenile material. The lithic lapilli and boulders are sub-rounded to angular. They are primarily aphyric or fine-grained basalt, with minor amounts of granitoid and sedimentary rocks. Above this, a complex series of layers grade up into a poorly sorted, massive, juvenile pyroclast rich flow deposit. The complex layers have muddy or sandy matrices, are indurated and fissile, pinch and swell, and contain coarse ash and angular lithic fragments up to 3 cm in size. The juvenile pyroclast rich layers in this sequence contain 80 to 90 % ash and lapilli, with grain sizes from 2 mm to 1 cm diameter. It is likely that these basal layers correlate with the surge and lahar deposits from relatively early in the eruptive sequence along the north flanks.

Above this at Camp Creek are massive pyroclastic flow deposits that contain differing percentages of juvenile ash, lapilli, and lithic fragments depending on position within the outcrop. The base of the pyroclastic flow deposit here is rich in juvenile scoria, with clasts up to 2–5 cm on a side. At the top , the pyroclastic flow deposit also contains concentrations of tan pumice, dark grey scoria, and lithic clasts up to 3 cm. Discrete, clast-supported lenses filled with basaltic lithic boulders that are up to 1 m in size are prevalent at the top of the Okmok I pyroclastic flow deposit at this location. Above this are wavy and laminated layers containing poorly sorted, finer-grained juvenile scoria, with fragments 0.5 cm diameter, and lithics up to 3–4 cm across their long axes. The laminated layers comprise medium ash size particles.

The distal site on Unalaska Island (03JLOK64; Figure 7b) shows a relatively undisturbed, ~15 m thick Okmok I section resting on a thin soil atop glacial till. The basal unit consists of 20 cm thick, vesiculated, dark grey andesitic pyroclastic flow deposit that likely represents a pyroclastic surge that traversed Umnak Pass. It is moderately sorted, and contains 1–2 mm up to 0.5 cm juvenile scoria lapilli in a reversely graded sequence. Above this is an 8 cm thick, fines-poor, well sorted, mixed rhyolite and andesite pumice and scoria fall deposit. It has average lapilli that are 1–2 cm, with rare lapilli up to 4 cm. The main pyroclastic flow deposit is ~ 1m thick, partly indurated, and contains juvenile scoria and tan pumice that are 0.5 to 2 cm in size on average. This subunit is partly vesicular, and has a fissile and cemented character. The vesicular nature of the flow deposits here indicates either a phreatomagmatic phase of the eruption, or incorporation of water as the flows traveled across Umnak Pass. This outcrop shows that both rhyolite and basaltic andesite to andesite magmas were involved in the Okmok I eruption, as shown by the mingled fall deposits in the middle of the Unalaska outcrop section.

4.5.6 South sector. In general, Okmok I exposed along the south consists only of the main pyroclastic flow sequence. However, at location 00JLOK29 in Missouri Creek (Figure 7c) fine ash layers exist at stream level. They alternate from tan to dark grey, are wavy or irregularly bedded, and may have been reworked. Most fine upward from coarse to fine ash size particles. Above the fine ash layers is a 1–2 m thick, well-sorted, fines-poor scoria fall deposit, containing clasts with average sizes of 1–3 cm. These scoriaceous layers may represent an early fall sequence near the beginning of the Okmok I eruption. However, the layers are very poorly preserved due to cold springs seeping through the outcrop at this location. Above the finely layered ash and scoria fall deposits, another series of wavy, cross-bedded, dark grey to black scoria and dark ash deposits exist, and probably represent surge deposits. Locally at Missouri Creek, the scoria fragments range in size to 15 cm blocks, similar in grain size, pyroclast type, and character to the 2.5 m thick subunit found at the base of section 01JLOK51 at Kansas creek (Figures 3, 7c, 8d, 9). The south flank surge deposits probably correlate with the surge and lahar sequence near the base of the Okmok I deposits exposed along the east and north flanks.

Excepting the two localities described above, Okmok I exposures along the south flanks consist of thick, poorly sorted and massive pyroclastic flow deposits (Figure 8e). Generally, they are dark grey to black, ash matrix supported, poorly sorted, massive, and contain abundant dark scoria clasts and locally 3–12 % by volume lithic fragments (99JLOK18 Vermont Creek; Figures 3, 7c, 8f, 9). In all outcrops studied, the lithics are heterolithologic, containing fragments of basaltic lava, granitoids, palagonitized pyroclastics, and sedimentary clasts that may be altered or contain secondary mineralization. Most juvenile pyroclasts are dark grey, relatively dense, and glassy with only a small percentage of visible plagioclase phenocrysts. The largest scoria size locally at Vermont Creek is 15 cm. There are also local concentrations (<10 to ~50 vol. %) within the main pyroclastic flow deposit of tan, friable, highly vesicular rhyolite pumice.

The top of the pyroclastic flow deposits along the south flanks consists of, locally cross-bedded surge layers that correlate with the upper surge deposits exposed in the north and east flanks regions. Locally, the cross-bedded sub-unit contains lithic boulder lenses at 99JLOK18 Vermont Creek (Figures 7c, 8f, 9). The entire sub-unit is fissile, with conjugate partings, fines rich, yet poorly sorted, and locally incises the pyroclastic flow unit beneath. Lithic clasts are rounded to angular, with some that are very angular, faceted or prismatic. They comprise a mixture of lithologies including granitoid blocks, altered sedimentary clasts, oxidized, vesicular basalts, and clasts of the older palagonitized pyroclastics. The largest clast found at 99JLOK18 Vermont Creek is 34 cm across. It is possible that the non-juvenile, lithic boulder rich deposits atop the main pyroclastic flow unit along the south flanks resulted from lahars generated at same time as the surges evident from the top of the section at other locations.

4.6 Okmok II Stratigraphy

The physical details of the Okmok II deposits are described by Burgisser (2005), and will be summarized here following that work. The first episode of the Okmok II eruption deposited a buff colored dacitic (67 to 68 wt. % SiO_2) pumice fall directed to the north-northwest. The thickest deposits occur along the north flanks (e.g., 04JLOK047, 00JLOK42, 99JLOK4; Figures 7a, 9, 10), with the greatest thickness measured of the Plinian fall phase of ~120 cm at location 00JLOK42 at Reindeer Creek. At this location (Figure 9), the 80 cm thick sequence is reversely graded from fine ash (0.2 mm) to pumice blocks (10 cm)and ends with a second 4 cm thick fine ash deposit (e.g., Figure 10a). Above this is a 34 cm thick pumice lapilli fall, with a median grain size of 2 mm. Burgisser (2005) used lithic clast sizes to estimate a plume height of 30 km, and the depositional pattern indicates a vent along the northern rim of the caldera as the source of the first eruptive phase. The second fall deposit resulted from a plume directed to the east, forming a slightly darker buff colored dacitic deposit, 7 cm thick at the 98JLOK6 Camp Creek location (Figure 9), containing dense, blocky and glassy juvenile fragments. The third fall sequence is dark grey, glassy, andesite scoria, that also had an east directed depositional pattern, and ranges in grain size from fine to coarse ash (0.1 to 1 mm) at Camp Creek. Within this sequence are mixed rhyodacite and andesite fall deposits, indicating a period of simultaneous eruption of the two different magmas. Although scant erosion or reworking exists between the first and second fall deposits, no evidence was found for a significant time break, such as soil development or fluvial erosion (Burgisser, 2005).

One observation not noted by Burgisser (2005) is a dacitic pyroclastic flow deposit that correlates with the Plinian fall phase, at location 04JLOK046 (Figure 10b). It is likely that this flow resulted as a pyroclastic flow via sedimentation from the margins of the eruptive plume.

The thick basaltic andesite pyroclastic flow deposits from the Okmok II eruption blanket the northeast quadrant of Umnak Island, forming plateau surfaces that are cut by modern stream channels. Those deposits have a sharp contact with the fall deposits below, with no soil development in between, and scoured the underlying pumice and ash in some locations (Burgisser, 2005). Some of the deposits are massive, structureless and poorly sorted with an average of 20wt% of lithics and 80 wt% of juvenile basaltic andesite to andesite (53–56 wt. % SiO_2) scoria. Thicknesses are highly variable, averaging from ~30 to 50 m from the caldera rim to ~10 km distance at the coast. A common facies change occurs on hills and paleohighs where the deposits feature low angle cross-stratification, improved sorting, and a maximum thickness of a few decimeters. A similar cross-stratified facies is exposed on Unalaska Island, where the deposit has a thickness of 1 m on the western shore. Burgisser (2005) concludes that the massive and stratified facies of the Okmok II pyroclastic sheet were deposited from a single, voluminous density current.

Two other distinct facies of the Okmok II pyroclastic flows exist on Umnak Island. Primarily along the north to northwest flanks, thick accumulations of black, ropy-textured spatter, ribbon bombs, and angular lithic fragments form fines-poor agglutinate deposits (e.g., Figure 10c). Although a couple of similar outcrops exist along the eastern and southern flanks (04JLOK042 and 044; Figure 9), it is rare to find the spatter bomb-rich facies away from the north to north-

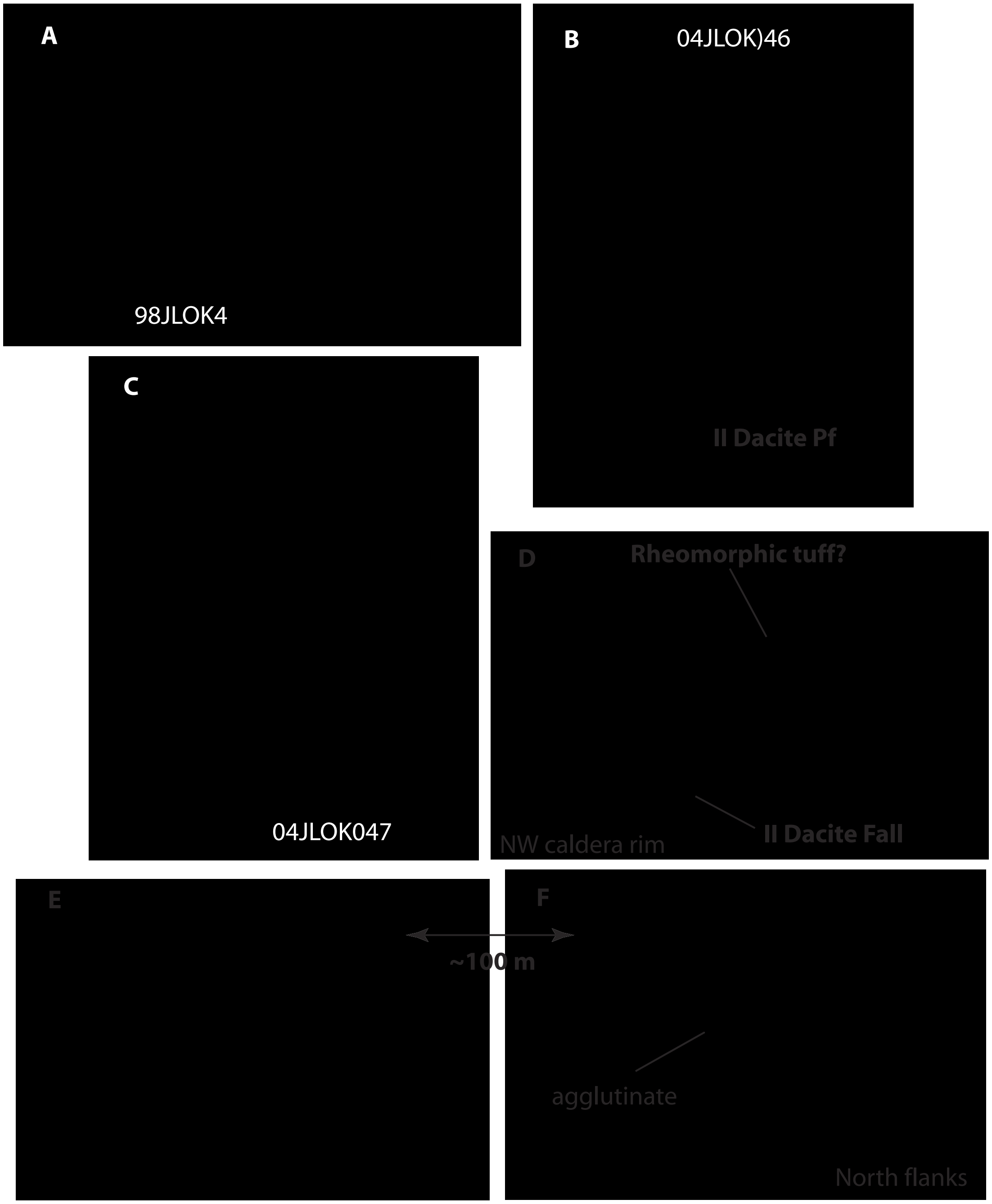

Figure 10. Okmok II outcrop photos showing different deposits within the eruptive sequence. A. Plinian rhyodacite fall layers as viewed at Ashishik point (Figure 2). Although thinner than outcrops at Reindeer Creek (00JLOK42; Figure 9), the deposit at Ashishik point has most of the internal structure as described by Burgisser (2005). B. One section at 04JLOK046 (Figure 9) also includes a poorly sorted, massive, pumice-rich rhyodacite pyroclastic flow deposit that correlates with the Plinian fall deposit. C. Location 04JLOK047 shows spatter-rich agglutinate deposit correlating with the Okmok II basaltic-andesite pyroclastic flow facies. Individual spatter and bombs here reach ~2 m across. D. Along the northwest caldera rim, the proximal Okmok II deposits may include a rheomorphic tuff, correlating with the spatter agglutinate and spatter/Pf transitional flows that outcrop along the northern flanks region. E. Massive facies of the Okmok II pyroclastic flow deposits (e.g., Burgisser, 2005). F. Across the stream from photo E, the Okmok II basaltic-andesite forms spatter-rich agglutinate/flow deposit at the same stratigraphic height.

west flanks. The agglutinate deposits are at approximately the same stratigraphic height everywhere, juxtaposed next to massive Okmok II pyroclastic flow deposits and commonly separated by an intervening stream channel (Figures 10e,f). Individual bombs almost 2 meters across exist at location 04JLOK47, which is nearly 4 km away from the caldera rim (Figures 10c, 9). The largest lithic fragments measured reach ~37 cm at the same location. Here, the concentration of lithics to juvenile bombs is approximately 50:50.

A proximal to distal transition follows from the near-vent, fines-poor, lithic-rich, sintered or incipiently welded aggregates, to distal outcrops (>5 km) that look more like the massive pyroclastic flow facies, but that contain a relatively high percentage of ~5–10 cm cauliflower scoria, ribbon bombs, and angular lithics relative to matrix. Such transitional deposits exist in several places in the north, east, and south flanks (04JLOK042, 044, 045; Figure 9) and at those locations they comprise mainly spatter and ribbon bombs and lithic fragments, but appear to have a greater concentration of ash in the matrix than the deposits described at 04JLOK046. The transitional deposits are partially welded and columnar jointed, and are laterally in contact with the massive pyroclastic flow facies of Okmok II, with an intervening stream channel.

Densly welded tuff associated with the Okmok II eruption is exposed at two proximal locations, 04JLOK040 and high along the northwest caldera rim (Figures 10d and 9). On the northwestern part of the caldera rim, the top portion of the Okmok II deposits may be a rheomorphic tuff (Figure 10d). However, access this location was not examined closely because of its location, exposure, and almost constantly inclement weather. The densely welded tuff at 04JLOK040 contains fiamme in a finer grained matrix, whereas the outcrop just across the stream channel is loose, unconsolidated "massive" facies of Okmok II, similar to the relationship shown in Figures 10e and f.

5. DISCUSSION

5.1 Okmok I: Eruptive Sequence and Depositional Mechanisms

Combining the evidence observed at all outcrops provides for an initial interpretation of the Okmok I eruptive sequence and how the eruption products were deposited. Although the Okmok I deposits lack an easily deciphered, neatly layered eruptive sequence, the correlated stratigraphy (Figure 7) provides for an approximation. Along the north flanks, the basal, lithic and ash-rich deposits indicate that a lateral blast or hot debris flow may have initiated the eruptive sequence. Following this, the distal site at Unalaska indicates that the first erupted, basaltic andesite or andesite juvenile material was expelled explosively producing proximal scoria fall and pyroclastic flows and surges that traveled across Umnak Pass. This agrees with evidence for the domains in the chaotic breccia filled with black scoria pyroclastic flow material, which baked the matrix enclosing them. Shortly thereafter, the eruption plume produced rhyolite and andesite fall deposits, preserved in the mixed fall outcrop on Unalaska Island (Figure 9) and the south flanks, but disrupted by scouring debris flows, surges, and lahars on the north flanks. The eruption of a large amount of juvenile material, deposited via pyroclastic flows and surge clouds followed down all flanks of the edifice. Along the north and east flanks, syneruptive lahars also formed during this phase of the eruption. The deposits at the top of the Okmok I sequence along all flanks have been interpreted as resulting from surges accompanying late-stage phreatomagmatism, which generated the accretionary lapilli observed at the same stratigraphic level along the north flanks. Despite studies documenting eolian reworking (Smith and Katzman, 1991) and hybrid fall deposits creating surge-like characteristics within large ash flow sheets (Wilson and Hildreth, 1998), we were not able to conduct granulometry to help decipher the origins of those deposits because they are too indurated. Given the evidence for phreatomagmatism at the same straigraphic level, it is probably simplest to describe them as surge deposits related to a late-stage phreatomagmatic component to the eruption. The complex nature of the Okmok I deposits, particularly in the north sector make it difficult to estimate the timing of edifice collapse, yet the boulder-filled lenses high in the stratigraphic sequence in the east sector may indicate that it happened relatively late during the eruption.

5.2 Okmok I: Interactions With Snow and Ice

Pyroclastic flows can generate floods and lahars as a result of interactions with snow and ice (Major and Newhall, 1989, through melting of the substrate. Incorporation of water as they travel downslope results in deposits that show characteristics indicating water interactions (e.g., Pierson, 1995; Walder, 2000a and b. The scouring power of hot pyroclastic flows as they travel over snow and ice is also well known from recent eruptions, such as 1980 Mount St Helens, 1989 Redoubt, and 1985 Nevado del Ruiz (Major and Newhall, 1989; Pierson et al., 1990; Pierson and Janda, 1994; Waitt et al., 1994). The presence of lahar deposits interlayered with the surge units along the north flanks indicate that snow and ice were probably present along the north and east flanks of Okmok during the Late Pleistocene. The extreme rounding and eroded surfaces of some of the juvenile scoria and pumice in the surge beds indicate fluvial transport, which is possible if enough water was liberated to generate lahars. Given the occurrence of this eruption during the end of the last glacial period in the Aleutians (e.g., Black, 1975), it is reasonable that snow and glacial ice were present on the north and possibly east flanks of the pre-Okmok I edifice when the eruption occurred.

The Okmok I chaotic breccia deposits (Figures 8 and 9) also indicate that pyroclastic flows scoured a wet substrate, including older volcanic deposits, snow, ice, and glacially derived sediments. Those deposits are is similar to those described by Allen and McPhie (2001) generated during the climactic eruption of the Kos Plateau Tuff, in the Eastern Aegean, Greece. At Kos, the chaotic breccia resulted from the interaction of scouring pyroclastic flows with unconsolidated, wet sediments. At Redoubt, Waitt et al. (1994) describe unusual flow deposits that resulted from scouring pyroclastic flows traveling over the Drift River glacier, and incorporating glacial ice and snow. The ice diamict unit at Redoubt also bears some resemblance to the Okmok I chaotic breccia. It is possible that the chaotic breccia observed at Okmok could represent the remains of a similar mass flow deposit.

One interesting feature of the Okmok I ash flow sheet is its upper undulatory surface (Figure 6). The waves are oriented perpendicular to the down slope direction, presumably perpendicular to the direction of travel of the pyroclastic flows. Their broad distribution, regular wavelength, and orientation relative to the slope make it unlikely that they are erosional features. Similarly, these characteristics also make it unlikely that they formed due to compaction by post-depositional melting of an unstable, snow or ice substrate. It is most likely that they represent waveforms associated with the upper Okmok I pyroclastic flow deposits. Since the top of the Okmok I depositional sequence consists of thick surge beds, the undulations may represent waveforms associated with the mechanics of pyroclastic density current flow and deposition.

5.3 Okmok II: Agglutinate Facies and Implications for Eruption Mechanisms

The Okmok II basal stratigraphy indicates that this eruption began with a Plinian column of rhyodacite issuing from a vent along the north rim of the caldera (Burgisser, 2005). Fallout from the eruptive plume traveled to the north to northwest, shedding localized pyroclastic flows . The second rhyodacitic phase started with the wind blowing to the east. Given the high proportion of glassy and blocky clasts, the internal discontinuous layering of the deposit, and the likely presence of a lake within parts of the caldera left by Okmok I, this event probably was marked by phreatomagmatic explosions. Interestingly, the drastic compositional shift from rhyodacite to andesite occurs without significant change in eruptive style or vent location (e.g., Figure 10a). The eruption of andesite continued with fewer phreatomagmatic explosions. Catastrophic failure of the edifice ensued after the eruption increased strongly in energy and volume, producing the voluminous basaltic andesite pyroclastic flows deposited on all azimuths of the edifice.

The widespread spatter, lithic, and ribbon bomb-rich outcrops along the north to northwest flanks of Okmok indicate diverse eruptive mechanisms during the basaltic andesite phase of the Okmok II eruption. The location of the spatter-rich, fines-poor outcrops in close lateral contact with massive facies of the Okmok II pyroclastic flows indicates that they formed as a separate deposit, during the same eruptive event. The lithic-rich nature of the spatter agglutinate deposits across the north to northwest flanks indicates that they may have formed synchronously with edifice collapse. The concentration of these deposits along the north to northwest flanks, and the existence of rheomorphic tuff on the northwest caldera rim, and welded tuff proximal to the caldera in the Crater Creek region (Figure 9), indicate that the vent producing the spatter agglutinate deposits may have been located along the northern part of the caldera, perhaps the same that produced the early Plinian stage of the eruption (e.g., Burgisser, 2005). Another vent located along the eastern part of the caldera probably also produced spatter, and was perhaps coincident with the vent that was the source of the second Plinian fallout deposits (e.g., Burgisser, 2005).

The Siwi sequence, Tanna volcano, Vanuatu (Allen, 2005) shows similar physical characteristics within the pyroclastic flow deposits. Allen (2005) attributes the agglomerate facies at Siwi to energetic lava fountaining simultaneous to column collapse and caldera formation. Allen (2005) concludes that the fountaining resulted from ejection of a large amount of basaltic magma as the caldera floor subsided into the remnants of the magma chamber. On the other hand, Freundt and Schminke (1995) concluded that Hawaiian-style lava fountaining probably did not accompany emplacement of the basaltic ignimbrite from Tejeda caldera, Gran Canaria. However, Freundt and Schminke (1995) also describe subsidence of the caldera floor as a primary cause of explosive ejection of the large volumes of P1 basalt, which agrees with the conclusions of Allen (2005) for the Siwi pyroclastics. In the case of Okmok, the large ribbon and spatter bombs, and fines-poor nature of the proximal outcrops indicate fountaining accompanied caldera-collapse during the Okmok II eruption. Fountaining could have issued from vents along the east and north rims during Okmok II, perhaps coincident with the vents producing the two Plinian episodes early in the eruption (e.g., Burgisser, 2005). This would explain the prevalence of the spatter-rich, indurated, and welded outcrops of Okmok II occurring mainly over those sectors of the volcano.

The distribution of the Okmok II spatter agglutinate facies shows much farther traveled, larger scoria bombs than described from the Siwi sequence, in which the agglutinate facies is confined to proximal and medial outcrops extending no further than approximately 1 km from the caldera (Allen, 2005). In the case of Okmok, the spatter accumulations containing the largest bombs extend conservatively up to ~4 km from the caldera rim. The more distal outcrops between ~4 to 10 km, near the coast, tend to have fines-rich matrices, indicating that they may actually be flow deposits that contain spatter generated originally by fountaining, but entrained in pyroclastic flows related to column-collapse. Ballistics calculations using the program Eject of Mastin (2001) provide estimates of the distance basaltic andesite spatter would travel from the vent during lava fountaining during the Okmok II eruption. Assuming dense clasts (~2.5 g/cm^3), 1 m in diameter, ejected at a velocity of 100 to 200 m/s, estimated distances of travel are approximately 2 to 3.5 km. Typical vent exit velocities of Hawaiian-style lava fountaining at Kilauea probably do not exceed 100 m/s at most, and are generally lower than that (Mangan and Cashman, 1996; Mastin, 2002). This implies that either the fines-poor deposits are actually lithic-rich, spatter-fed flows, or that the exit velocities of the fountaining phase of the eruption were higher than typically estimated from much less explosive basaltic eruptions. The weak imbrication of cauliflower and ribbon bombs (e.g., 04JLOK047) indicates that the agglutinate flowed at least locally. The violence of the Okmok II eruption could have caused the mass discharge rates of the fountaining phase to be quite high, with deposition of spatter a farther distance than in less explosive Hawaiian-style eruptions.

5.4 What Causes Okmok's Catastrophic Eruptions?

The Okmok caldera-forming basaltic andesite and andesite products are common compared with the majority of sampled Okmok magmas erupted since about 2 million years ago. That both eruptions were preceded by volumetrically minor, but compositionally more evolved magmas, may be significant in terms of the processes leading up to catastrophic eruptions at this tholeiitic arc volcano. In this regard, the Okmok caldera-forming eruptions are similar to the 14.1 Ma Tejeda caldera eruptions, Gran Canaria (Freundt and Schminke, 1995). The Gran Canaria event began with eruption of mixed rhyolite-trachyte magmas, followed with emplacement of basaltic ignimbrite during the later stages of the eruption. As is the case with the Okmok caldera-forming eruptions, the relative volumes of evolved magmas erupted during the Gran Canaria events are also smaller than the co-erupted basalt. Freundt and Schminke (1995) conclude that several factors contributed to the unusually high mass discharge rates of the Tejeda P1 basalt, including the magma's relative buoyancy and pressure as it reached the magma chamber, degassing of the felsic magmas within the chamber, and then subsidence of the roof during collapse, which is though to have helped to expel the mass of basalt.

However, not all basaltic and basaltic-andesite caldera-forming eruptions involve magmas as felsic as rhyodacites and rhyolites. In fact, some mafic-intermediate caldera-forming eruptions, like the Siwi sequence, are relatively uniform in composition (e.g., Robin et al., 1994; Allen, 2005). Phreatomagmatism, particularly during the early phases of the eruption cycles, is commonly observed associated with basaltic to andesitic ignimbrites from ocean island arc volcanoes (e.g., Freundt and Schminke, 1995; Robin et al., 1994; Allen, 2005). Robin et al. (1994) conclude that the highly explosive interaction between magma and external groundwater is an important trigger for the subsequent eruption of mafic-intermediate magma in smaller arc calderas in the New Hebrides. However, Okmok is notable in the large volumes (>15 km^3) of mafic-intermediate magma erupted. The DRE estimates from this work and derived from Burgisser (2005) point to large accumulations of potentially volatile-rich basaltic andesite to andesite magma in the shallow crust beneath the edifice. Aleutian arc mafic-intermediate magmas commonly display petrological features, such as high An content plagioclase (e.g., Sisson and Grove, 1993), like those observed in the Okmok CFE products. Most likely, the Okmok CFE magmas erupted explosively by virtue of their volatile-rich natures and the edifice collapse resulting from withdrawal of the large volumes of accumulation magma beneath the edifice. The associated rhyodacite and rhyolite may represent older, evolved magmas trapped within the crust, or fractionates associated with the large accumulations of mafic-intermediate magmas in the shallow crust. The phreatomagmatic nature of some of the eruptive deposits may thus be an ancillary feature as the magma erupted through local lakes or snowfields.

6. CONCLUSIONS

This study presents general stratigraphic, petrologic, and compositional descriptions of two caldera-forming eruptions of Okmok volcano Alaska within the last ~12,000 years. These two eruptions are remarkable for their explosive release of relatively large volumes of basaltic andesite magmas.

- The two caldera-forming eruptions initially tapped small volumes of rhyolite (I) and rhyodacite (II) magmas followed by much greater volumes of andesite and basaltic andesite magmas. The eruption of felsic magmas prior to caldera collapse at Okmok is a common element of the caldera-forming eruptions.

- The Okmok I eruption produced ~ 30 km^3 DRE material on Umnak Island, while Okmok II produced ~15 km^3. Both estimates are minima, however, since a significant proportion of material flowed into the oceans.
- The Okmok I pyroclastic flow deposits show evidence for interaction with snow/ice, particularly along the northern flanks. In particular, lahar deposits interlayered with pyroclastic flows and surge deposits are prominent within outcrops along the north flanks and to a limited extent along the east flanks of the volcano. This is consistent with the estimated age of Okmok I of ~12,000 ^{14}C yBP, which was late in the last glacial maximum period.
- Both Okmok I and II eruptions involved phreatomagmatic explosions. Previous studies consider this important in the case of triggering catastrophic eruptions of mafic-intermediate magmas. At Okmok, large accumulations of volatile-rich basaltic andesite to andesite can explain both the explosivity of the eruptions, as well as subsequent failure of the edifice. It is uncertain whether the small volume of felsic magmas erupted early in each CFE are important factors in the catastrophic nature of those eruptions as well.
- An energetic and voluminous period of lava fountaining took place during the caldera-collapse phase of the Okmok II eruption. The lithic-rich nature of the spatter agglutinate layers indicates that this phase accompanied the caldera-collapse. It is possible that the vents for the fountaining were coincident with those estimated for the initial Plinian phases, along the north and east caldera rim.

Acknowledgements. Work supported by the Alaska Volcano Observatory and the Volcano Hazards Program of the U.S. Geological Survey. The authors would like to thank Tom Sisson and Charlie Bacon for careful reviews of the manuscript. We thank Bering Pacific Ranches Ltd., Pat Harvie, Tim and Mala Webb, Cowboy Rob, and Lonnie and Susan Kennedy and family for lodging, logistics, and good company. We thank helicopter pilots Bill Springer, Rick Farish, and Joe Trudo and Maritime Helicopters for their excellent support of our field work. We thank Don and Kris Graves, Magone Marine, and Jimmer McDonald for excellent marine logistical support and transportation. We thank the Aleut Corporation and the U.S. Fish and Wildlife Service Alaska Maritime National Wildlife Refuge for granting access to the lands of Umnak Island.

REFERENCES

Allen S. R., and J. McPhie (2001), Syn-eruptive chaotic breccia on Kos, Greece, associated with an energetic pyroclastic flow, *Bull. Volcanol., 63,* 421–432

Allen, S. R. (2005) Complex spatter- and pumice-rich pyroclastic deposits from and andesitic caldera-forming eruption: The Siwi pyroclastic sequence, Tanna, Vanuatu, *Bull. Volcanol., 67,* 27–41.

Almberg, L. D. (2003), Hydrovolcanism in Okmok Caldera, Alaska, *University of Alaska Fairbanks unpublished M.S. thesis,* 57 p.

Bean, K. W. (1999), The Holocene eruptive history and stratigraphy of Makushin volcano, Unalaska Island, Alaska, *University of Alaska Fairbanks unpublished M.S. thesis*, 130 p.

Begét, J. E., J. F. Larsen, C. A. Neal, C. J. Nye, and J. R. Schaefer (2005), Preliminary volcano-hazard assessment for Okmok Volcano, Umnak Island, Alaska, *Alaska Division of Geological & Geophysical Surveys Report of Investigation 2004-3,* 32 p., 1 sheet, scale 1:150,000.

Bingham, D. K. and D. B. Stone, (1972), Palaeosecular Variation of the Geomagnetic Field in the Aleutian Islands, Alaska, *Geophys. Journ. Royal Astr. Soc., 28,* 317–335.

Black, R. F. (1975), Late Quaternary geomorphic processes: Effects on the ancient Aleuts of Umnak Island in the Aleutians, *Arctic*, 28, 159–169.

Brophy, J. G., 1986. The Cold Bay volcnaic center, Aleutian volcanic arc I; Implications for the origin of high-alumina arc basalt, *Contrib. Min. Pet.* 93, 368–380.

Burgisser, A. (2005), Physical volcanology of the 2,050 bp caldera-forming eruption of Okmok volcano, Alaska, *Bull. Volcanol.,* 67, 497–525.

Byers, F. M.Jr. (1959), Geology of Umnak and Bogoslof Islands, Aleutian Island, Alaska, *U.S. Geol. Surv. Bull.,* 1028-L, 107–367.

Byers, F. M.Jr. (1961), Petrology of three volcanic suites, Umnak and Bogoslof Islands, Aleutian Islands, Alaska, *Geol. Soc. Am. Bull., 72,* 93–128.

Class, C., D. M. Miller, S. L. Goldstein, and C. H. Langmuir (2000), Distinguishing melt and fluid subduction components in Umnak volcanics, Aleutian Arc, *Geochem., Geophys., Geosyst., 1,* paper number 1999GC000010 [15,355 word, 11 figures, 5 tables].

Fournelle, J. H., B. D. Marsh, and J. D. Myers (1994), Age, character, and significance of Aleutian arc volcanism: in *The Geology of Alaska: Boulder, Colorado, Geological Society of America, The Geology of North America G-1,* edited by G. Plafker, and H.C. Berg, eds., 723–758.

Freundt, A., and H-U Schminke (1995), Eruption and emplacement of a basaltic welded ignimbrite during caldera formation on Gran Canaria, *Bull. Volcanol., 56,* 640–659.

Grewingk, C. (1850), Grewingk's geology of Alaska and the Northwest Coast of America, *Rasmuson Library Historical Translation Series 11,* The University of Alaska Press, edited by Marvin W. Falk, translation by Fritz Jaensch published 2003, 242 p.

Grey, D. M. (2003), Post-caldera eruptions at Okmok volcano, Umnak Island, Alaska, with emphasis on recent eruptions from Cone A, *University of Alaska Fairbanks unpublished M.S. thesis,* 135 p.

Hammer, J. E., and Rutherford, M. J., 2002. An experimental study of the kinetics of decompression-induced crystallization in silicic melt. *J. Geophys. Res.,* 107, DOI 10.1029/2001JB000281.

Hildreth, W. (1981), Gradients in silicic magma chambers; implications for lithospheric magmatism. Granites and rhyolites*, J. Geophys. Res., 86,* 10153–10192

Johnson D. M., P. R. Hooper, and R. M. Conrey (1999) XRF Analysis of Rocks and Minerals for Major and Trace Elements on a

Single Low Dilution Li-tetraborate Fused Bead *Advan. X-ray Anal. 41*, 843–867.

Kay, S. M., and R. W. Kay (1994), Aleutian magmas in space and time, in *The Geology of Alaska: Boulder, Colorado, Geological Society of America, The Geology of North America G-1,* edited by G. Plafker, and H.C. Berg, eds., 687–722.

Knaack, C., Cornelius, S. B., and Hooper, P. R., 1994. Trace Element Analyses of Rocks and Minerals by ICP-MS, Geo-Analytical Lab Technical Notes, Washington State University, December, 1994.

Le Maitre, R. W. (1989) A classification of igneous rocks and glossary of terms. *Blackwell Scientific Publications,* 193p.

Lofgren, G. E., (1980), Experimental studies on the dynamic crystallization of silicate melts, in *Physics of Magmatic Processes*, edited by R. B. Hargraves, 487–551.

Major, J. J., and C. G. Newhall (1989) Snow and ice perturbation during historical volcanic eruptions and the formation of lahars and floods: A global review. *Bull. Volcanol.,* 52, 1–27.

Mangan, M. M., and K. V. Cashman (1996) The structure of basaltic scoria and reticulite and inferences for vesiculation, foam formation, and fragmentation in lava fountains, *J. Volcanol. Geotherm. Res.,* 87, 15–28.

Marsh, B. D. (1979) Island arc development; some observations, experiments, and speculations, *J. Geol.,* 87, 687–713.

Marsh, B. D., 1982. The Aleutians, in *Andesites; Orogenic Andesites and Related Rocks,* John Wiley, New York, edited by R. Thorpe, 99–115.

Mastin, L. G. (2001) A Simple Calculator of Ballistic Trajectories for Blocks Ejected during Volcanic Eruptions, *U.S. Geol. Surv., Open-File Report 01-45,* 18 p.

Mastin, L. G. (2002) Insights into volcanic conduit flow from and open-source numerical model, *Geochem., Geophys., Geosyst.,* 3, 10.1029/2001GC000192.

McGimsey R. G., Wallace K. L. (1999) Volcanic activity in Alaska and Kamchatka; summary of events and response of the Alaska Volcano Observatory. *US Geol. Surv. Open File Report 99-448,* 42 p.

Miller, T. P., R. G. McGimsey, D. H. Richter, J. R. Riehle, C. J. Nye, M.E. Yount, and J. A. Dumoulin (1998), Catalog of the Historically Active Volcanoes of Alaska, *U.S. Geol. Surv. Open-File Report 98-582,* 104 p.

Miller, Thomas P., and Smith, Robert L., 1987. Late Quaternary caldera-forming eruptions in the eastern Aleutian arc, Alaska, *Geology*, 15, 434–438.

Miller, D., C. Langmuir, S. Goldstein, and A. Franks, 1992. The importance of parental magma composition to calc-alkaline and tholeiitic evolution: evidence from Umnak Island in the Aleutians, *J. Geophys. Res.* 97, 321–343.

Miller, D., S. Goldstein, and C. Langmuir, 1994. Cerium/lead and lead isotope ratios in arc magmas and the enrichment of lead in continents, *Nature* 368, 514–520.

Myers, J. D., and Marsh, B. D., 1994. Aleutian lead isotopic data: Additional evidence for the evolution of lithospheric plumbing systems, *Geochim. Cosmochim. Acta,* 51, 1833–1842.

Nye, C. J., and M. R. Reid (1986), Geochemistry of primary and least fractionated lavas from Okmok Volcano, central Aleutians: Implications for arc magmagenesis, *J. Geophys. Res., 91,* 10271–10287.

Pierson, T. C., R. J. Janda, J. C. Thouret, and C. A. Borrero (1990), Perturbation and melting of snow and ice by the 13 November 198 eruption of Nevado del Ruiz, Colombia, and consequent mobilization, flow and deposition of lahars, *J. Volcanol. Geotherm. Res., 41,* p 17–66.

Pierson, T. C., and R. J. Janda (1994) Volcanic mixed avalanches; a distinct eruption-triggered mass-flow process at snow-clad volcanoes, *Geol. Soc. Am. Bull.,* 106, 1351–1358.

Pierson, T. C. (1995), Flow characteristics of large eruption-triggered debris flows at snow-clad volcanoes: Constraints for debirs-flow models, *J. Volcanol. Geotherm. Res.,* 66, 283–294.

Robin, C., J-P Eissen, M. Monzier (1994), Ignimbrites of basaltic andesite and andesite compositions from tanna, New Hebrides Arc, *Bull. Volcanol.,* 56, 10–22.

Smith, G. A., and D. Katzman (1991) Discrimination of eolian and pyroclastic-surge processes in the generation of cross-bedded tuffs, Jemez Mountains volcanic field, New Mexico, *Geology*, 19, 465–468.

Waitt, R. B., C. A. Neal, C. A. Gardner, T. C. Pierson, and J.J. Major (1994), Unusual ice diamicts emplaced during the December 15, 1989 eruption of Redoubt Volcano, Alaska, in *The 1989–1990 eruptions of Redoubt Volcano, Alaska,* edited by B. A. Chouet and T.P . Miller, *J. Volcanol. Geotherm. Res.,* 62, 409–428.

Walder, J. S. (2000a), Pyroclast/snow interactions and thermally driven slurry formation. Part 1: Theory for monodisperse grain beds, *Bull. Volcanol.,* 62, 105–118.

Walder, J. S. (2000b), Pyroclast/snow interactions and thermally driven slurry formation. Part 2: Experiments and theoretical extension to polydisperse tephra, *Bull. Volcanol., 62,* 119–129.

Wilson, C. J. N, and W. Hildreth (1998) Hybrid fall deposits in the Bishop Tuff, California: A novel pyroclastic depositional mechanism, *Geology*, 26, 7–10.

Wolfe, B. A. (2001), Paleohydrology of a catastrophic flood release from Okmok caldera and post-flood eruption history at Okmok Volcano, Umnak Island, Alaska, *University of Alaska Fairbanks unpublished M.S. thesis,* 100 p.

Wolfe, B. A., and J. E. Begét (2002), Destruction of an Aleut village by a catastrophic flood release from Okmok caldera, Umnak Island, Alaska, *Abstracts with Programs, Geological Society of America,* 34.

Wong, L. J. (2004), Physical volcanology of a sub-plinian and phreatomagmatic eruption at Okmok Volcano, Alaska: implications for explosive mafic volcanism: *University of Alaska Fairbanks unpublished M.S. thesis,* 117 p.

Preliminary Study on Magnetic Structure and Geothermal Activity of Tyatya Volcano, Southwestern Kuril Islands

Noritoshi Okazaki[1], Hiroaki Takahashi[2], Kenji Nogami[3], Hiromitsu Oshima[2], Hiromu Okada[2], and Minoru Kasahara[2]

We carried out reconnaissance surveys of the magnetic and geothermal fields on Tyatya volcano, Kunashiri Island, southwestern Kuril Islands. Two characteristic features were in the magnetic anomalies: topography dependent ones and locally scattered ones of which origin was unknown. Modeling of the topography dependent anomalies indicates that the Tyatya edifice is uniformly magnetized with magnetization of 7 A/m and any significant anomalies, that suggest the existence of thermally demagnetized parts, are not found. The result agrees with low heat discharge rate of 0.6 Mw from volcano surface. Judging from these ground-based data, it can be concluded that the volcanic activity of the shallower part of Tyatya volcano is very inactive at present.

INTRODUCTION

Tyatya volcano, at the Kunashiri Island in southwestern edge of the Kuril volcanic chain, a typical island arc volcano associated with the subducting Pacific plate, and is the largest and highest (1822m) composite stratovolcano in the southwestern Kuril arc (Figure 1). Initial historical eruption was recorded in 1812. Nakagawa et al. [2002] summarized this eruption spouted lava flow from the central cone and partially filled summit caldera. Recent major eruption (VEI=4) occurred in 1973 at both the northern and southern flanks with sub-Plinian and Strombolian explosions [Markhinin et al., 1974, Abdurakhmanov and Steinberg, 1999]. This was the largest eruption in the southwestern Kuril Islands during the 20th century. After several succeeding eruptions in 1974, 1975, 1978 and 1981, volcanic activity has seemed to be calm.

It is important to monitor the volcano because eruptive ash from this volcano possibly causes fatal hazard to jet aircrafts flying the north Pacific air routes between Asia and North America. However, there had been little data concerning this volcano, because the volcano is located in a remote place, far from human habitation. Therefore, we are obliged to make geophysical/geological studies without delay.

Magnetic survey is one of the basic methods to investigate magnetic subsurface structure and to delineate thermal condition within volcanic body because the magnetization of rocks is strongly sensitive to the temperature [e.g. Nishida and Miyajima, 1984]. Heat discharge measuring on ground surface provides another basic parameter to estimate state of thermal condition of volcano interior. These data may play important roles to the geophysical understanding of volcano structure and status.

International cooperative volcanological research exploration on Tyatya volcano between Japan and Russia was done from 30 July to 3 August 1999. Using this occasion, we carried out reconnaissance surveys of geomagnetic and geothermal fields during this expedition. In this short paper we report preliminary results of magnetic structure and geothermal aspects of Tyatya volcano.

[1] Geological Survey of Hokkaido, Sapporo, 060-0819, Japan (okazaki@gsh.pref.hokkaido.jp)
[2] Institute of Seismology and Volcanology, Graduate School of Science, Hokkaido University, Sapporo, 060-0810, Japan
[3] Volcanic Fluid Research Center, Tokyo Institute of Technology, Kusatsu, 377-1711, Japan

Volcanism and Subduction: The Kamchatka Region
Geophysical Monograph Series 172

10.1029/172GM25

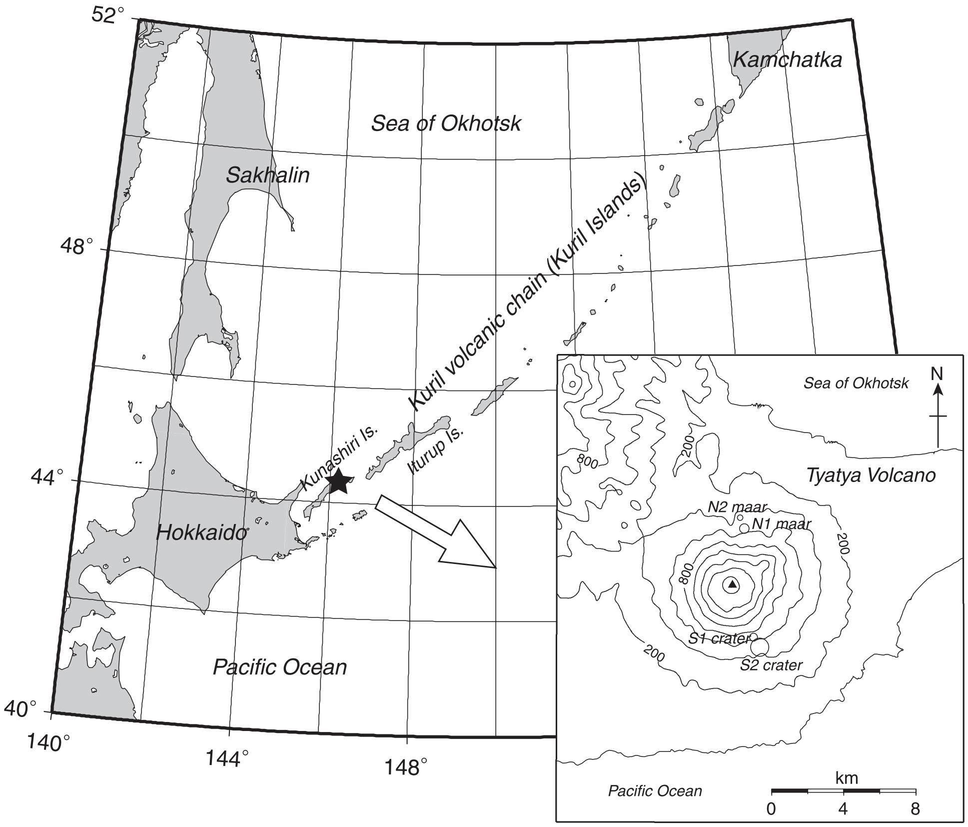

Figure 1. Map showing the Kuril volcanic chain and the topography of Tyatya volcano. Four open circles show the craters (N1, N2, S1 and S2) formed by the 1973 explosive eruption.

MAGNETIC AND GEOTHERMAL SURVEYS

We observed magnetic total force intensity using the Gem System Overhauser proton magnetometer GSM-19 with 0.1 nT sensitivity and 0.01 nT resolutions. A mean value of two to four times measurements was regarded as the geomagnetic field at each point. In the measurements, the height of the sensor was fixed at 2 m. We applied no corrections for diurnal variations amplitudes of several tens of nanotesla at most because the observed anomalies were up to several thousands of nanotesla as shown in Figure 2. Geographical locations of each observation point were determined from standard point positioning technique by Garmin GPS receiver with accuracy less than 30 m.

We measured 30 points along the A-B profile of a southeastern slope of the volcanic edifice and in the summit caldera as shown in Figure 2a. However, we could not established observation points on northern side of the volcano because of a limited schedule for observation. Figure 2b shows the total force intensity with topography along the profile A-B. This indicates a general tendency that the total force intensity increases with topographical elevation. In addition to above, several measured values vary widely near the caldera rim and around S2 crater as shown in broken ellipses in Figure 2b.

It was difficult to determine the reference value to extract the anomalies caused by the volcanic edifice from the observed values because the regional magnetic anomalies have not been measured. Therefore, a field intensity of 49,000 nT was assumed as a reference value based on the mean value observed at three points on the southern foot of the volcano.

We carried out geothermal survey at the central cone in summit caldera and the S2 crater where was formed by 1973 explosive eruption (Figure 1). There were no geothermal manifestations along a geomagnetic profile except for two places. Surface temperatures were measured using a thermal imaging camera, Thermo Tracer TH5104 by NEC Sanei Instruments with 2.2 micro radian instantaneous field of view, and a thermistor thermometer. Visible but weak fumarolic activities were observed in and around the crater of summit cone. Observed maximum temperature in this area was 93 °C, which was equal to the boiling point. Total heat discharge rate on summit cone

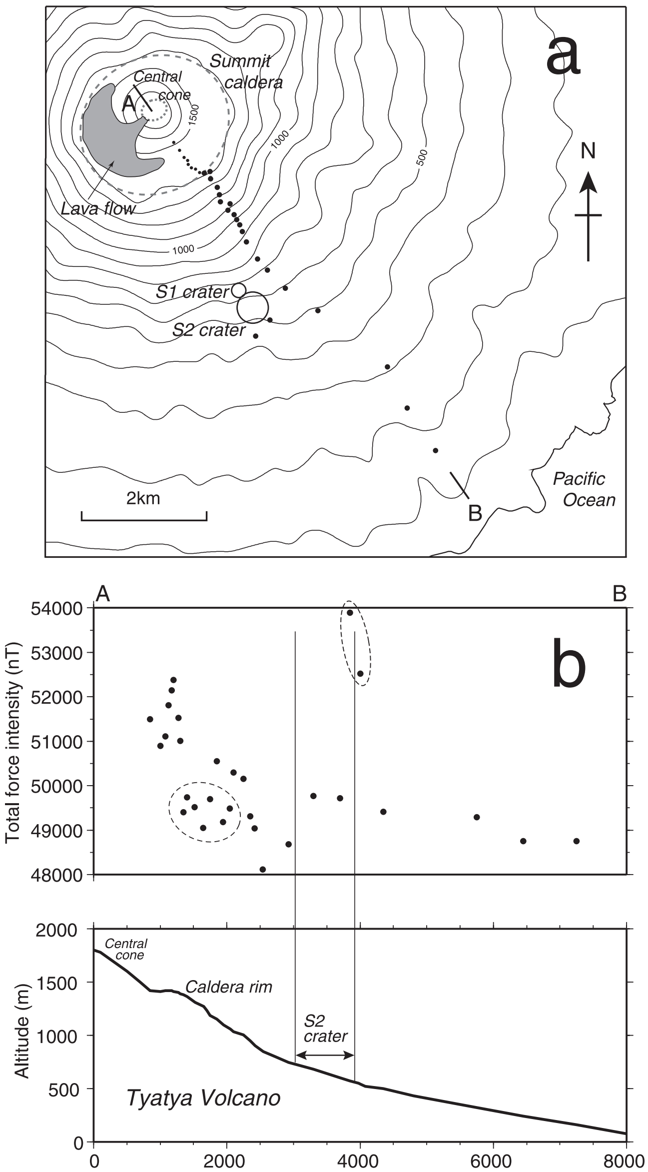

Figure 2. a: Map showing the survey area. Solid circles show the observation points of the magnetic total force intensity. Dashed lines show a crater rim of central cone and a summit caldera rim. b: Magnetic total force intensity (solid circle) along the profile A-B in Fig.2a is shown, with the topographic cross-section of Tyatya volcano. The solid circles surrounded by two broken ellipses show the magnetic fields around the caldera rim and the S2 crater.

was estimated as 0.6 Mw through the geothermal images using equations proposed by Kagiyama et al. [1979]. This value indicated low geothermal activity in this part. Though the sulfur sublimations were recognized in the S2 crater, we could not observe any geothermal anomalies there, indicating the geothermal activity had been terminated in this crater.

MAGNETIC STRUCTURE OF TYATYA VOLCANO

As mentioned above, magnetic anomalies are classified by the following two types: (1) correlated with the topographical altitude, (2) scattered observed at the outer slope near the summit caldera rim and around the S2 crater (Figure 2b).

In many case, volcano edifice is approximated by a circular cone [e.g. Nishida and Miyajima, 1984]. One can calculate the magnetic anomalies on the surface of a magnetized circular cone by Rikitake and Hagiwara [1965]. Surface geology showed that this volcano was composed of basaltic-andesitic and andesitic lava flows and pyroclastic ejecta [Nakagawa et al., 2002]. However, we have little knowledge about the inner geological structure and do not have any information about the rock magnetization of Tyatya volcano. In addition, the present magnetic survey covered only a limited area. Therefore, we made simple model calculations assuming circular cones for the convenience of comparison between observed and calculated anomalies as shown in Figure 3. Model I represents a uniformly magnetized circular cone, while model II and III show magnetized circular cones of which central part are replaced by weakly and strongly magnetized cylinders, respectively. Figure 3 indicates calculated magnetic anomaly pattern on the surface of the topography along the profile A-B (NW-SE direction), assuming the cones are magnetized in the same direction as the geomagnetic field in the region concerned (inclination is 57°).

Among the three models, model II should be rejected because the calculated anomalies indicate sharp decrease to minus values from the summit caldera rim toward the caldera floor, in contrast to the observed anomalies. Sharp increase of the calculated anomalies at the southern caldera rim for model III can not reproduce the observed ones. In conclusion, the uniformly magnetized edifice (model I) is most preferable between three models, although the model is by no means unique. In more detail, the Tyatya edifice is approximated by three piled up cones, U, M and L as shown in Figure 4. Magnetization intensity of the edifice is adjusted to 7 A/m to match anomaly amplitudes by trial-and-error procedure (Figure 4). The estimated magnetization is reasonable for basaltic-andesite rock.

DISCUSSIONS AND CONCLUDING REMARKS

Estimated reasonable model (Figure 4) implied that the summit caldera was not filled by weakly magnetized materials. Nakagawa et al. [2002] proposed that the summit caldera had been formed as a result of cylinder-like subsidence of the summit caused by migration and/or drain back of magma toward the reservoir just beneath the summit. Several examples of this phenomenon, i.e. Katmai [Abe, 1992] and

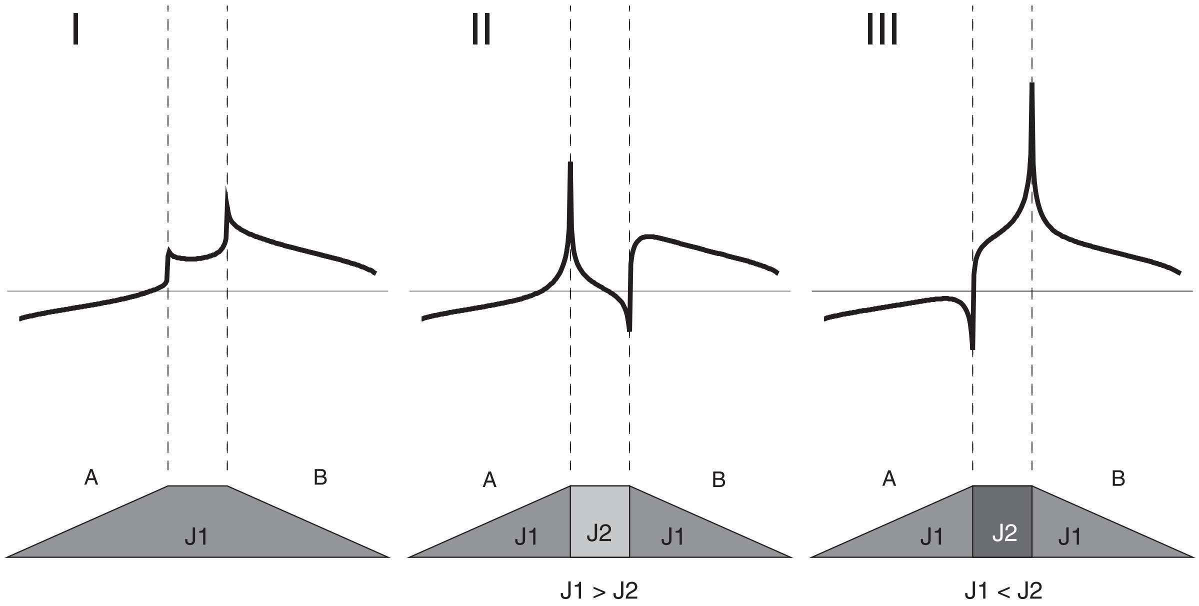

Figure 3. Schematic illustration of magnetic anomaly models along the profile A-B (NW-SE direction) in Fig.2a. Magnetic inclination is assumed to be 57°. I: A uniformly magnetized circular cone, II: a magnetized circular cone with weakly magnetized cylinder, and III: a magnetized circular cone with strongly magnetized cylinder.

Miyakejima volcanoes [Furuya et al, 2003], indicate that this case forms deeper cylinder-like calderas on the summit area. As Tyatya volcano has no such a cylinder-like depression on the summit, the following volcanic activities must have refilled this depression and the crater fill must have the same magnetization as the edifice: the crater fill may not be originated from the fall back ashes on dacitic magma because model II was rejected. Therefore, it is suggested that the magma component before and after the crater formation has been not too invariant.

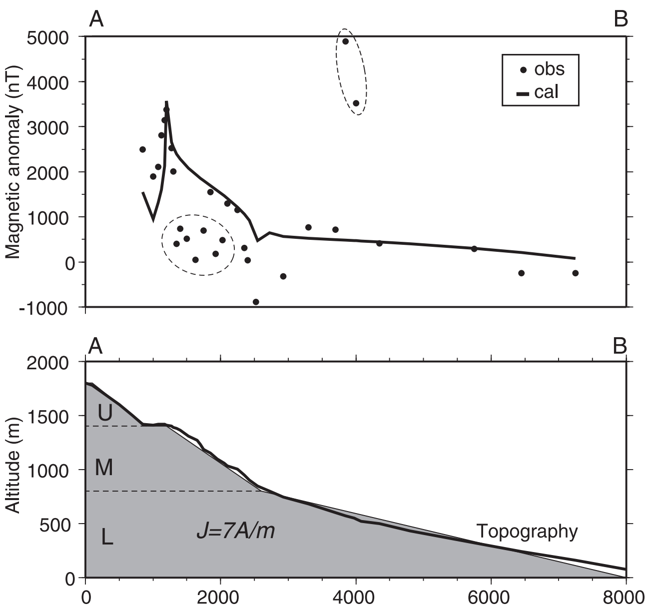

Figure 4. Observed (solid circles) and model (solid curve) magnetic field along the profile A-B in Fig.2a are shown, with the corresponding model cross-section of Tyatya volcano which is composed of three circular cones U, M and L. The solid circles surrounded by two broken ellipses show the magnetic anomalies around the summit caldera and the S2 crater.

The 1973 eruption was started at 12:10 (local time) from N1 and N2 maars at the northern flank of this volcano (Figure 1). This eruptive stage had continued only less than 3–5 hours. After several hours, new eruptions restarted from the S1 and S2 craters at the southern flank (Figure 1).

Considering the low heat discharge rate (0.6 Mw) and the magnetic anomalies which do not support the thermal demagnetization, the thermal activity is low in the shallower part of Tyatya volcano. Negligible seismicity observed by Hokkaido University also supports the low thermal activity after the 1973 event [Kasahara et al, 1986]. However, we should take special precautions against eruption because Tyatya volcano has sometimes erupted with few precursors like the 1973 event, which may be caused by rapid magma intrusion from deeper part.

Acknowledgements. This survey was carried out by complete support of Asahi Shinbun Company as a part of the Japan-Russia Joint Scientific Study of Tyatya Volcano in Kunashiri Island in 1999, which is specialist exchange of the visa-free exchanges of Japan and Russia. We would like to thank K. Takahashi, H. Hayashi and other members of the secretariat of the company. We are also much indebted to staff of the Kuril Conservation State of Nature and members of the Sapporo Alpinist Society for their logistic support during the fieldwork. We express our gratitude deeply for being able to carry out this survey by the understanding of Japanese Government Ministry of Foreign Affairs, Hokkaido government, and Russian government. We are thankful to anonymous reviewer and Dr. Evgenii Gordeev for their constructive comments. Figures were partially drawn using GMT software [Wessel and Smith, 1995].

REFERENCES

Abdurakhmanov, A. I. and G. S. Steinberg, TYATYA VOLCANO Morphology and Geological Structure of the volcano, Institute of Volcanology and Geodynamics Russian Academy of Natural Science, 1–20, 1999.

Abe, K., Seismicity of the caldera-making eruption of Mount Katmai, Alaska in 1912, Bull. Seism. Soc. Am.,82, 175–192, 1992.

Furuya, M., S. Okubo, W. Sun, Y. Tanaka, J. Oikawa, H. Watanabe, and T. Maekawa, Spatiotemporal gravity changes at Miyakejima Volcano, Japan: Caldera collapse, explosive eruptions and magma movement, J. Geophys. Res., 108, 2219, 2003.

Kagiyama, T., K. Uhira, T. Watanabe, F. Masutani, and M. Yamaguchi, Geothermal survey of the Volcanoes Kirishima, Bull. Earthq. Res. Inst., Univ. Tokyo, 54, 187–210, 1979 (in Japanese with English abstract).

Kasahara, M., T. Ogawa, and S. Suzuki, Seismic swarm immediately before and in the early stage of the 1973 great eruption of volcano TiaTia, Kunashiri Island, Geophys. Bull. Hokkaido Univ., 49, 33–40, 1996 (in Japanese with English abstract).

Markhinin, E. K., Y. A. Anikiev, V. M. Grannik, et al., Eruption of Tyatya volcano, in Kuril Isles in July of 1973, Geologiya Geofizika, 10S, 20–31. 1974 (in Russian).

Nakagawa, M., Y. Ishizuka, T. Kudo, M. Yoshimoto, W. Hirose, Y. Ishizaki, N. Gouchi, Y. Katsui, A. W. Soloovyow, G. S. Sreinberg, and A. I. Abdurakhmanov, Tyatya Volcano, southwestern Kuril arc: Recent eruptive activity inferred from widespread tephra, The Island Arc, 11, 236–254, 2002.

Nishida, Y., and E. Miyajima, Subsurface structure of Usu volcano, Japan, as revealed by detailed magnetic survey, J. Volcanol. Geotherm. Res., 22, 271–285, 1984.

Rikitake, T., and Y. Hagiwara, Magnetic anomaly over a magnetized circular cone, Bull. Earthq. Res. Inst., Univ. Tokyo, 43, 509–527, 1965.

Wessel, P., and W. H. F. Smith, New version of the generic mapping tools released, Eos Trans. AGU, 76(33), 329–336, 1995.